GTI ENERGY

REPORT

GTI ENERGY PROJECT NUMBER 21728

HFTS-1 Final Report

DE-FE0024292

Report Issued:
September 29, 2023

Prepared For:
Mr. Gary Covatch
Project Manager
US Department of Energy
National Energy Technology Laboratory
3610 Collins Ferry Road
Morgantown, WV 26505
304-285-4589
Gary.Covatch@NETL.DOE.GOV

GTI Energy Technical Contacts:
Mr. Jordan Ciezobka
Sr. Manager, R&D
847-768-0924
jciezobka@gti.energy

Dr. Debotyam Maity
Sr. Data Engineer
847-768-0523
dmaity@projeo.com

1700 S. Mount Prospect Rd.
Des Plaines, Illinois 60018
www.gti.energy

Signature Page

Print or typed		
First M. Last	***Signature***	***Date***
AUTHOR:		
	Title:	
REVIEWED BY:		
	Title:	
APPROVED BY:		
	Title:	

Legal Notice

This information was prepared by GTI Energy for U.S. Department of Energy.

Neither GTI Energy, the members of GTI Energy, the Sponsor(s), nor any person acting on behalf of any of them:

a. Makes any warranty or representation, express or implied with respect to the accuracy, completeness, or usefulness of the information contained in this report, or that the use of any information, apparatus, method, or process disclosed in this report may not infringe privately-owned rights. Inasmuch as this project is experimental in nature, the technical information, results, or conclusions cannot be predicted. Conclusions and analysis of results by GTI Energy represent GTI Energy's opinion based on inferences from measurements and empirical relationships, which inferences and assumptions are not infallible, and with respect to which competent specialists may differ.

b. Assumes any liability with respect to the use of, or for any and all damages resulting from the use of, any information, apparatus, method, or process disclosed in this report; any other use of, or reliance on, this report by any third party is at the third party's sole risk.

c. The results within this report relate only to the items tested.

Table of Contents

Signature Page i
Legal Notice ii
Table of Contents iii
Table of Figures xviii
List of Tables xxxvii
Abstract 39
Executive Summary 40
Published Art 42
Summary 42
Reference to publications 42
Background 46
Introduction 46
Test Sites 46
Project structure 48
HFTS-1 Phase 1 Midland Basin Test Program 50
Introduction 51
Overview of results 51
Coring Through the Stimulated Reservoir Volume (SRV) 51
Proppant Analysis 53
Water Quality 54
Air Quality 55
Variable Rate Fracturing (VRF) 55
Tracer Results 56
Microseismic 57
Geocellular Earth Modeling 57
Predictive Analytics Natural and Hydraulic Fracture Modeling 57
Conclusions 57
Core fracture description of the HFTS Phase 1 slant core 60
Abstract 60
Introduction 60

Slant core: acquisition, handling, and preparation for analysis 61
Systematic Description Methodology 63
Depth and Number 63
Orientation 63
Aperture and fill 63
Length and height 63
Morphology and surface features 63
Fracture origin 64
Fracture Description and Criteria for Fracture Classification 64
Natural fractures 64
Hydraulic fractures 66
Hydraulic fractures with proppant pack 69
Hydraulic fractures reactivating weak planes, such as bedding or natural fractures. 72
Drilling-induced fractures (from drilling the slant well) 72
Core recovery and handling 73
Fracture Distribution 74
Discussion 74
Conclusions 77
Natural and Hydraulic Fracture Density Prediction and Identification of Controllers 78
Abstract 78
Introduction 78
Data collection 79
Multivariate Analytics 80
Results 83
Discussion and Model Utility 84
Future model improvements 86
Conclusions 86
Downhole Microseismic Mapping 87
Abstract 87
Introduction 87
Microseismic Fracture Mapping Project Objectives 88
Project Plan and Setup 89
MSM Quality Assurance 89
Microseismic Velocity Model Optimization 91
Microseismic Data Quality 92
Prior wells and geophone setup 94

Well Completion and Fracturing Sequence 95
Microseismic Monitoring (MSM) 98
Representative Fracture Geometry from MSM 99
Perforation Cluster Design Comparison 101
Fracture Azimuth and Complexity 102
Downhole Deformation Measurements (Tiltmeters) 107
MSM Data Relative to the "Slant Well" Post-Fracturing Whole Core 110
Observations and Conclusions 111
Using microseismic frequency-magnitude distributions from hydraulic fracturing as an incremental tool for fracture completion diagnostics. 113
Abstract 113
Introduction 113
Method 117
Result: hydraulic fracture stage data 122
Overburden stress estimation 124
Result: spatial variations 125
Result: temporal variations 132
Discussion 136
Conclusion 137
Using stage level microseismic analysis to ground truth cored hydraulic fractures. 138
Abstract 138
Introduction 138
Application of Microseismic 139
Classification of hydraulic fractures in the core 140
Application of KDE plots 141
Results 141
Discussion 142
Conclusions 143
Using stage level microseismic analysis to gain insight into fracture efficiency and completion effectiveness. 145
Abstract 145
Introduction 145

Method 146
Stacked Heat Maps 146
Kernel Density Estimation (KDE) Maps 147
Results 149
Discussion 153
Conclusions 153
Surface seismic Monitoring at HFTS Phase1 154
Abstract 154
Introduction 154
Data and Field description 156
Methods 158
Results and Discussions 160
Conclusion 163
Interwell Communication Study at HFTS Phase 1 165
Abstract 165
Introduction 165
Methods 166
Results 168
Discussion 171
Conclusions and Recommendations 172
Proppant Transport at HFTS 1 Phase 1 site 173
Summary 173
Introduction 173
Sample Preparation 175
Method 175
Introduction to circular Hough Transform 176
Classification using machine learning. 179
Workflow validation 182
In-situ stress model definition 184
Results 185
Correlation with petrophysical logs 189
Interaction between natural and hydraulic fractures 191
Correlation with perforation clusters. 194

Conclusions 195
Proppant Analysis from Fracture Faces to Study Trapping and Crushing Behavior 196
Summary 196
Introduction 196
Methods 197
Results & Discussion 201
Conclusions 205
Well Interference Diagnosis through Integrated Analysis of Tracer and Pressure Interference Tests 207
Abstract 207
Introduction 207
Field Information, Observations and Analysis 209
Well Configuration and Stimulation Sequence: 209
Fluid Tracer Test Analysis: 210
Proppant Tracer (Radioactive Tracer) Tests Analysis: 211
Pressure Interference Tests Analysis: 212
Modeling and Sensitivity Analysis 214
Summary 217
Conclusions 218
Conclusions based on Fluid and Proppant Tracer Tests 218
Integrating Pressure Responses with Tracer Responses 218
Conclusions based on Pressure Interference Modeling 219
Environmental Impact Analysis on the Hydraulic Fracture Test Site (HFTS Phase 1) 220
Abstract 220
Objective 220
Methods 220
Observations 220
Significance 220
Introduction 220
Description of the Hydraulic Fracture Test Site 222
Methods 222
Groundwater Monitoring 222
Air Quality Analysis 222
Produced Water Chemistry and Microbiology 223
Results and Discussion 224
Groundwater Quality 224

Air Quality 226
Water Characterization 229
Microbial Control 236
Conclusions 237
HFTS-1 Phase 2 Enhanced Oil Recovery (Huff n Puff) 240
Introduction 241
Literature Review on the Application of Enhanced Oil Recovery in Shale formations 241
Gas/ CO_2 Huff n Puff 241
Surfactant injection/ Huff n Puff 242
Biological EOR 242
Bakken Formation 243
Eagle Ford Formation 244
Wolfcamp Formation 245
Background Information on Enhanced Oil Recovery (EOR) from Hydraulically Fractured Reservoir Using Cyclic Gas Injection 247
Overview of the Project Objectives & Results 249
Field Operations 249
Executive Summary 249
Field Demonstration 250
Field Tests & Results 254
Gas Injection 254
Post Injection Data Monitoring 256
Data Compilation 262
Background Data 262
Geology 262
PVT 262
Acquired Data 263
Experimental & Modeling Studies 268
Laboratory Tests & Results 268
Simulation Results 272
New Findings/Lessons Learned 275
HFTS-1 Phase 3 Liner Refracturing 277
Introduction 278
Background 278
Sealed wellbore pressure monitoring (SWPM) 283

VFR Analysis 283
Pre- and Post-refracturing perforation efficiency 287
Pre-refracturing perforation imaging 287
Post-refracturing perforation imaging 291
Impact of re-frac and in-fill fracs on SRV 295
Evolution 1 [Pre-pump baseline measurements] 296
Evolution 2 [Zgabay 4H pre-load] 296
Evolution 3 and 4 [re-frac and in-fill frac] 297
Evolution 5 and 6 [POP and flowback monitoring] 300
Integrated analysis 303
Mapping pre-existing and new fracture network 304
Proppant log 304
Core integration 309
Integrated analysis with DSS strain response 313
Integrated analysis with pressure gauges 314
Proppant log: value proposition and other considerations 316
Fiberoptic crosswell monitoring during refrac operations. 317
Refrac and new infill production response 325
References 327
Appendix A: Phase 1 Fracture Characterization by BEG 350
Project findings covered in this report. 351
LAREDO_SuggA171_6TW Slant Well Fracture Characterization: Systematic Description 351
LAREDO_SuggA171_6TW Slant Well Fracture Characterization: Systematic Description Methodology 351
Slant core: acquisition, handling, and preparation for analysis 351
Slant core: proppant analysis 353
Results—spreadsheet format 354
Depth and number 354
Orientation 355
Lateral and vertical extent 355
Morphology and surface features 355
Proppant 356

Aperture and fill 356
Faults 358
Fracture origin 358
Summary of Results and Criteria for Fracture Classification 358
Natural fractures 358
Hydraulic fractures 361
Hydraulic fractures with proppant pack 365
Hydraulic fractures reactivating weak planes, such as bedding or natural fractures. 367
Drilling-induced fractures (from drilling the slant well) 369
Core Recovery 369
Damage during sawing into sections and transportation and other handling up to point of CT scan. 370
Fractures created because of handling/desiccation after CT scan. 370
Proppant analysis 370
Use of results for modeling 371
References 371
Appendix B: Phase 2 Fracture Characterization by BEG 372
Introduction 373
Fracture Description 373
Key findings from fracture description and proppant analysis 373
Hydraulic Fractures 381
Planes reactivated during HF. 384
Natural Fractures, Sets 1 and 2, bed-parallel, others 385
Faults 388
Drilling induced fractures 389
Planes reactivated during drilling. 390
Planes reactivated during CH. 391
Discussion of bed-parallel break interpretation 391
Discussion of hydraulic fracture occurrence in the cores 392
Conclusions: fracture description 392
Laredo Sugg E 197 5TW Slant Well Proppant Analysis 393
Proppant Analysis Overview 393
Results and Discussion 398
Summary 405
References 405
Acknowledgements 406

Appendix C: Phase 3 Eagle Ford Project Fracture Characterization by BEG 407
Report Contents 408
Fracture Description 408
Methods 408
Results 409
Hydraulic Fractures 411
Natural Fractures 415
Bed-parallel fractures 416
Unascribed natural fractures 417
Drilling induced and core handling fractures 417
Proppant 419
Statistical analysis of fracture distribution 420
Discussion of aspects of fracture description findings 428
References 429
Acknowledgements 430
Appendix D: Environmental Monitoring of the Hydraulic Fracturing Test Site (HFTS) Operations 431
Legal Notice 432
Executive Summary 432
Introduction 434
Objectives 436
Description of the HFTS Site 437
Groundwater Monitoring 438
Methods and Approach 439
Results and Discussion 440
Produced Water Characterization 444
Methods and Approach 445
Results and Discussion 447
Air Quality Analysis 454
Methods and Approach 454
Results and Discussion 456
Discussion of Overall Environmental Impact 459
Conclusions 460
References 462

Appendix 462
Appendix E: Scaleup and Demonstration of Membrane Distillation 479
Executive Summary 480
Acknowledgements 481
Introduction 481
Wastewater from Hydraulic Fracturing 481
Current Management Strategies 483
Membrane Distillation 483
Study Objectives 484
Laboratory scale studies 484
Materials and Methods 484
Biological treatment 486
Activated carbon treatment. 486
Chemical Oxidation 487
Results and Discussion 487
Effect of membrane properties on DCMD performance with raw produced water 487
DCMD performance with pretreated produced water 489
Impact of produced water on membrane characteristics 491
Impact of specific organics on DCMD performance 493
DCMD performance with synthetic solutions of volatile salts 495
Conclusions 496
Pilot scale demonstration 497
Materials and Methods 497
Pilot plant design 497
Pilot plant setup and operation 498
Pilot plant set-up with pretreatment 501
Results and Discussion 503
Trial 1 503
Trial 2 508
Conclusions 514
Conclusions 514
References 515
Appendix 522
Appendix F: Forecasting of Benefits of Membrane Distillation in the Treatment of Produced Water for Beneficial Use 527

Legal Notice 528
Acknowledgment 528
Executive Summary 528
Introduction 532
Objectives 535
Overall Approach 536
Background 537
Summary of Information Considered in the Analysis 538
Membrane Distillation and Potential Heat Sources 541
Membrane Distillation 541
Minimum Heat Required to Treat Produce Water 542
Comparison of Heat Sources 543
Bakken Shale 547
Produced Water in the Bakken 547
Produced Water Life-Cycle Analysis for the Bakken 549
Summary of the Bakken Results 552
Permian Shale 553
Produced Water Generation in the Permian 553
Produced Water Lifecycle in the Permian 555
Summary of the Permian Results 556
Cost of Treatment with Membrane Distillation 557
Example Cost Model Output 558
Cost Sensitivity to the Price of Pre-commercial Gas 565
Conclusions 566
References 567
Appendices 569
Appendix A: Basis for Minimum Heat Demand for Membrane Distillation 569
Appendix B: Heat Pumps Applied to the Membrane Distillation Process 570
B.1 Summary: 571
B.2 Objective 571
B.3 Results 571
B.4 Heat and Mass Transfer Calculation 573

B.5 Discussion and Conclusions: 574
Appendix C: Heat Transfer from Diesel Engine Exhaust 575
C.1 Summary: 575
C.2 Objective: 576
C.3 Model Heat Transfer System: 577
C.4 Model Results: 578
C.5 Discussion and Conclusion 580
C.6 Nomenclature: 582
C.7 Model Development 584
Appendix D: Analysis of the Bakken Production Data 590
D.1. Summary 590
D.2 Status of the Existing Bakken Wells 591
D.3. Life Cycle Analysis for the Bakken 619
Appendix E: Analysis of the Permian Basin (Texas) Production 621
E.1 Summary 621
E.2 Lifecycle in the Permian 627
Appendix F. Flaring Regulations in the Permian 628
Appendix G: Cost Analysis Model Inputs and Outputs 630
G.1 Input Parameters: 630
G.2 Technical Outputs: 631
G.3 Cost Output Parameters: 631
Appendix G: Microbiological Analysis of Hydraulic Fracture Test Site (HFTS) Operations 636
Legal Notice 637
Executive Summary 637
Introduction 638
Objective 639
HFTS Site & Operations Description 639
Methods and Approach 641
Sampling 641
Microbiological Analysis 642
Chemistry Results 642
Injection Water 642
Produced Water 643
Microbiological Results 647
Metagenomic Sequencing Results 648
Poseidon Tank 650

Injection Water 651
Produced Water 652
Early Produced Water Microbiology 654
Late Produced Water Microbiology 656
Post Biocide Water Microbiology 656
Discussion 656
Microbial Control 657
TOC, S, N shaping microbial PW communities. 658
Conclusions 659
Recommendations 660
References 660
Appendix A: Produced Water Chemistry 661
Appendix B: Relative Abundance of Dominant Phylotypes in HFTS Water Samples 666
Appendix H: Impact of Stress Shadowing and Reservoir Heterogeneity on the Propagation of Complex Fractures: Comparison with Field Data 669
Disclaimer 670
Abstract 670
Introduction 671
Preparation and analysis of field core data 672
Introduction 672
Objectives 673
Methods 673
Presentation of Core Data – Cores 1 to 4 674
Presentation of Core Data – Cores 5 and 6 675
Analysis of Core Data 677
Impact of inter-stage stress interference on natural fracture reactivation. 678
Conclusion 679
Non-planar Fracture Propagation from Multiple Perforation Clusters in Horizontal Wells 680
Summary 680
Introduction 680
Model Formulation 682
Wellbore Storage 682

Multiple Fracture Propagation: Parametric Analysis 683
Impact of Operationally Controllable Variables. 684
Impact of number of clusters and stage size. 684
Impact of perforation parameters. 685
Impact of Formation Properties. 686
Impact of matrix permeability. 686
Impact of lateral heterogeneity. 688
Inter-Stage Stress Shadow Effects 693
Infill Well Hydraulic Fracturing 696
Conclusions 698
Proppant Distribution Among Multiple Perforation Clusters in a Horizontal Wellbore 699
Summary 699
Introduction 700
Simulation of Proppant Transport (Step 1) 701
Proppant Transport Efficiency Correlations (Step 2) 702
Modeling Proppant Distribution among Multiple Clusters in a Fracturing Stage (Step 3) 704
Calculation of Proppant Distribution among Multiple Clusters 704
Implications of the PTE versus PFR curve 705
Incorporation of the PTE Correlation into a Multi-Cluster Hydraulic Fracturing Model 706
Multi-Cluster Hydraulic Fracturing Model 706
Results and Discussion 708
Proppant and Fluid Distribution in the HFTS 6SU Well 713
Conclusions 715
Effect of Reservoir Heterogeneity on the Vertical Migration of Hydraulic Fractures 716
Summary 716
Introduction 716
Mathematical Model 717
Results and Discussion 718
Investigation of Fracture Propagation Behavior near a Layer Boundary 718
Conclusions 744
A Peridynamics Model For The Propagation of Hydraulic Fractures in Naturally Fractured Reservoirs 745
Summary 745
Introduction 745

Mathematical Model 747
Definition of Natural Fracture (Pre-existing Fracture) in Peridynamics 747
Verification: Comparison with Experimental Results (Interaction of a Hydraulic Fracture with a Single Natural Fracture) 748
Growth of Multiple Hydraulic Fractures in Naturally Fractured Reservoirs 756
3-D Interaction between a hydraulic fracture and a natural fracture 760
Simulations with HFTS Log Data 767
Conclusions 772
Hydraulic Fracture Diagnostics and Stress Interface Analysis by Water Hammer Signatures in Multi-Stage Pumping Data 773
Summary 773
Introduction 774
Simulation Model for Water Hammer Signature in Wellbore-Fracture System 774
Recent Approaches to Use Water Hammer for Diagnostic Purposes 776
Impact of R, C, and I 777
Impact of Wellbore Geometry and Injection Fluid 778
Impact of Shut-in Process 778
Data Requirements for Water Hammer Analysis 779
Workflow of Water Hammer Simulation for Single-Stage Data 780
Estimation of ISIP by Water Hammer Simulation 781
Water Hammer Simulation for Multi-Stage Fracturing 782
Conclusions 785
References 785

Table of Figures

Figure 1: Location of HFTS 1 (Loving County Texas). Right insert is a plan view of 11 horizontal wells, as well as the slant core well. Air and water quality monitoring locations are also highlighted. 47

Figure 2: Phase 2 location relative to Phase 1 wells in Reagan Co, Texas. 47

Figure 3: Phase 3 location in DeWitt Co, Texas hosted by Devon Energy. 48

Figure 4: HFTS sponsors and participants. 49

Figure 5: A) Depiction of continuous core sections collected adjacent to the stimulated producing Upper Wolfcamp well. B) Whole core interval after clamshell core barrel extraction method. Hydraulic fracture plane shown in right panel. C) Example of a hydraulic fracture cutting a natural fracture captured in the core. 53

Figure 6: Oily sludge in jar collected from core. After washing, proppant and other particles can be identified and quantified in count, shape, size, color, etc. 54

Figure 7: Air quality results from HFTS site near Midland TX. The data shown is the deviation from baseline air quality before HFTS operations began. 55

Figure 8: Example of a rate pulse and the resulting pressure pulse created with Variable Rate Fracturing. 56

Figure 9: VRF well performance uplift relative to offset wells. Proppant loading is noted in the legend. 56

Figure 10: The core is left whole while the aluminum tube is bisected and opened to reveal core ("clamshell" method). Example test on section 9,408–9,411 ft, where the core has several fractures. Top right is the CT scan for this 3 ft section. 61

Figure 11: (a) CT scan and photograph of slabbed core from 9,312 to 9,315 ft measured depth (MD). This core section has multiple breaks and was treated with red epoxy prior to slabbing. (b) In places the force of introducing epoxy (red material) had widened existing fractures from their original width of 1–2 mm to around 1 cm. 62

Figure 12: Core section from 9,539 to 9,541 ft. (a) Slabbed section inside aluminum tube. (b) Slice through CT scan of this interval. Pale carbonate layer and can be seen in whole core (a). Fracture face cannot be observed without removing core from tube. (c) Core has been removed from tube and inverted on the bench. The act of slabbing and removing core from the tube has generated a new complete break, the beginnings of which is visible as partial hairline fracture on CT scan. 62

Figure 13: Natural fractures in the slant core. (a) Parted, Set 1 fracture with patchy calcite on fracture face, 9,365.10 ft. MD. (b) Intact, Set 2 composite fracture, 9,689.35 ft. MD; there are three segments, the middle segment is offset up-hole from the other two by a few millimeters. Slight deviation of the fracture path at the tips indicates stresses ahead of the tips were modified by the presence of the approaching neighbor. (c) Euhedral calcite crystals on fracture face at 9,292.8 ft indicating this fracture was open in the subsurface. 64

Figure 14: Lower-hemisphere stereograms of poles to calcite-filled natural fractures. (a) Set 1, (b) Set 2. Data from ConocoPhillips analysis. 65

Figure 15: Calcite-filled fractures associated with concretions. Some fractures are internal to concretions stopping at boundaries (IF). Others develop in shale surrounding concretions (SC) and most likely develop as result of strain localization around concretion. Example from Core 4 at 9,667 ft. 65

Figure 16: Faults in Core 4 at 9,675–9,681 ft MD. (a) CT scan of faulting and soft-sediment deformation (9,678–9,681 ft). (b) CT scan of fault in c, which has oblique slickensides. 66

Figure 17: Lower-hemisphere stereogram of poles to hydraulic fractures. Data from ConocoPhillips analysis; n = 321. 66

Figure 18: Hydraulic-fracture doublet indicating propagation to the west (orange mark = core top). (a) Whole core with two nonparallel fractures. (b) Core pieces pulled apart. (d–f) Fracture faces in b. (f) Example from Core 3 just above 9,521 ft. 67

Figure 19: Examples of twist hackles (TH). Dashed line = initiation plane. Local direction of growth is normal to that line (white arrow). Overall fracture propagation direction given by yellow arrow. (a) 9,435 ft in Upper Wolfcamp; view downhole. TH initiate at pyrite layer. Propagation down and west. (b) 11,678.5 ft in Middle Wolfcamp; view uphole. TH initiate at bedding plane. Propagation up and east. 68

Figure 20: Example of twist hackles with anomalous orientation. At 9,372.45 ft, looking downhole, hackles suggest downward propagation. Twist-hackle asymmetry suggests overall propagation is to the east (left in photo)..... 68

Figure 21: Sand pack in a hydraulic fracture at 9,488.90 ft in Upper Wolfcamp. (a) 3 ft section of core with location of sand pack figured in b at base of section, where two HFs are in proximity—termed a doublet. Slightly uphole is a complex in which a hydraulic fracture interacts with a Set 2 natural fracture (Figure 17). (b) Detail of doublet. (c) Face of fracture at 9,488.9 ft looking uphole. 69

Figure 22: Sand pack in a complex hydraulic fracture at 9,488.85 ft in Core 3. (a) CT scan of fracture; proppant dark gray. (b) Intact core; fracture complex approximately 1 cm wide. (c) Sand pack viewed uphole with core piece below fracture removed. Sand has since been removed for analysis. Hydraulic fractures at this location have complex geometry that may have favored trapping of sand pack. 70

Figure 23: Sand pack in complex hydraulic fracture adjacent to concretion at 9,561.7 ft in Core 3. (a) Sand on outer surface of core with multiple breaks visible. (b) CT circumferential scan. 71

Figure 24: Possible interaction between HF and Set 2 natural fracture (NF) at 9,458.8 ft. (a) View of uphole face with thick sand patches on HF surface and some on NF face. We did not observe cement on face of NF; it was interpreted as such based on their orientation. At this location (out of view) an intact Set 1 NF also occurs with cement, although crosscutting relations were not clear. 71

Figure 25: (a) CT scan of section with bed-parallel fracture (BPF) bounded by two hydraulic fractures (HF). (b) Photograph of bed-parallel fracture surfaces, which are smooth and planar. Drilling mud has partly invaded at the margins. 72

Figure 26: Drilling-induced fractures. (a) Petal centerline shape at 9,391 ft viewed looking downhole. (b) Irregular, saddle-shaped fracture at 11,564 ft. 73

Figure 27: Likely core recovery fracture at 9,634 ft. Irregular surface with a sharp point (p), suggesting the break initiated within the core. 73

Figure 28: (a) Likely core-handling fracture at 9,479.6 ft. Irregular surface with some drilling mud splatters. (b) Post-CT scan break at 9,346.8 ft. It is irregular with a rough surface and has no drilling mud inside. 74

Figure 29: Distribution of different fracture types along the length of the cores for Upper Wolfcamp (left) and Middle Wolfcamp (right). 75

Figure 30: Diagram of plumose structure on a joint surface (from Cobain et al. (2015), their figure 6A). Note local direction of propagation indicated by twist hackles is up at the top and down at the base. 76

Figure 31: HFTS Phase 1 area located in core of Laredo's leasehold. Modified from Trowbridge et al., 2017. 78

Figure 32: Schematic diagram showing Slant Core Well (SCW) position relative to the most proximal Upper and Middle Wolfcamp horizontal wellbores (UWC and MWC, respectively) as well as the most adjacent legacy vertical wells. All horizontal wells in the test site area were drilled from North to South including the SCW. The SCW trajectory comes within 89 ft of the UWC wellbore and 135' of the MWC well. 79

Figure 33: Schematic showing location of slant core well (SCW) relative to HFTS well package. 6 horizontal wells in the Upper Wolfcamp (UWC) and 5 horizontals in the Middle Wolfcamp (MWC). Order of operations: Drill 11 horizontal wells; recomplete 2 legacy vertical wells and complete 11 new horizontals with pressure monitors, microseismic monitors, cross-well seismic, and downhole logging; run tracers and fiber coil production logs; monitor post-frac pressure; drill and core slant well. Modified from Courtier et al., 2017. 80

Figure 34: Relative stratigraphic position of formations within the Lower Permian system. 80

Figure 35: CT scan images of the SCW. Each image displays 3 ft of core. Hydraulic and natural fracture interpretations are noted. Two main sets of natural fractures are identified and are primarily classified based on calcite mineral fill. Hydraulic fractures are quantified as large planes of varying complexity that have been intersected by the core (Gale et al., 2018). 81

Figure 36: A) Well log tracks displaying fracture measurements over the cored intervals, lithological information, and mechanical properties. Several log tracks contain multiple logs. Log track key is shown on right and color coded by log curve color. B) Hydraulic fracture density log in blue and natural fracture density log in brown filled to 10' moving average curve (black line). Logs displayed represent the upper cored interval. 82

Figure 37: A) Natural Fracture Model (NFM) with initial 31 variables ranked by significance. B) Data correlation table (above) contains natural fracture intensity, brittleness, gamma ray, acoustic impedance, stress gradient, Young's modulus, weak interface model properties, Poisson's ratio, water saturation, neutron porosity, shallow resistivity, bulk density, deep resistivity, pyrite, total organic carbon, k-feldspar, heterogeneous rock analysis, quartz, total porosity, effective porosity, photoelectric factor, permeability, illite, unbound water, clay, calcite, bound water, unbound oil, effective water saturation, stress, and chlorite. 422 samples were initially evaluated. Actual versus predicted plot (below) shows a correlation coefficient of 0.909. C) Final variables evaluated within NFM after collinearity analysis. Variables are ranked by significance (blue) with model sensitivities shown in yellow. D) NFM after collinearity analysis leaves 12 variables retained in the model. Data correlation table (above) contains natural fracture intensity, stress gradient, Young's Modulus, brittleness, permeability, gamma ray, shallow resistivity, pyrite, bulk density, k-feldspar, unbound water, and weak interface model properties. 422 samples were evaluated to understand which variables are most significant and have the highest model sensitivity. Actual versus predicted plot (below) shows a correlation coefficient of 0.804. E) NFM predicted versus actual log responses. The actual natural fracture density is shown with black curve. Predicted natural fracture density shown in red. 82

Figure 38: A) HFM with initial 33 variables ranked by significance. B) Data correlation table (above) contains hydraulic fracture intensity, bulk density, shallow resistivity, stress, stress gradient, total porosity, effective porosity, k-feldspar, Poisson's ratio, heterogeneous rock analysis (HRA), HRA absolute value, neutron porosity, deep resistivity, pyrite, permeability, illite, photoelectric factor, unbound water, Young's modulus, gamma ray, total organic carbon, effective water saturation, water saturation, calcite, brittleness, quartz, chlorite, acoustic impedance, unbound oil, bound water, clay, NFM model results, and the weak interface model results. 874 samples were initially evaluated to understand which variables are most significant and have the highest model sensitivity. Actual versus predicted plot (below) shows a correlation coefficient of 0.896. C) HFM significant variables with model sensitivities after collinearity analysis. D) HFM with final 18 variables. Data correlation table (above) contains shallow resistivity, stress gradient, total porosity, heterogeneous rock analysis and absolute value, neutron porosity, pyrite, unbound water, Young's Modulus gamma ray, total organic carbon, effective water saturation, brittleness, chlorite, acoustic impedance, NFM results, weak interface model results. Actual versus predicted plot (below) shows a correlation coefficient of 0.887. E) HFM predicted versus actual log responses. The actual hydraulic fracture density is shown with black curve. Predicted hydraulic fracture density shown in red. 83

Figure 39: Final model results. HFM on the left. Black curve represents the calculated 10' moving average and is filled with blue showing interval intensity. NFM on the right. 10 ft moving average curve in black is filled with brown showing natural fracture density. The red curve on each log track shows the predicted response results from the NLMVA. 84

Figure 40: Impact of four most significant variables on natural fracture intensity. 85

Figure 41: Impact of four most significant variables on hydraulic fracture intensity. 85

Figure 42: Illustration of chevron well pattern (end view). 87

Figure 43: Three-dimensional (3D) and two-dimensional (2D) views of the subsurface project wells. 89
Figure 44: Final VTI Velocity Model 1 used during Phase 1 and 2 stages. 92
Figure 45: Listening distance. 93
Figure 46: Typical background noise levels. 94
Figure 47: Offset well production (vertical wells). 94
Figure 48: Project wells and existing wellbores (drainage patterns are shown for illustration only). 95
Figure 49: Geophone and tiltmeter arrays. 96
Figure 50: Zipper fracturing completions sequence: Phase 1 (Fracturing Crew 1), Wells 7U and 8U (yellow square); Phase 1 (Fracturing Crew 2), Wells 5U, 6U, and 6M (yellow triangle); Phase 2 (Fracturing Crew 1), Wells 7M and 8M (black oval); Phase 2 (Fracturing Crew 2), Wells 3U and 4U (black oval); Phase 3 (Fracturing Crew 2), Wells 4M and 5M (black dotted square). 97
Figure 51: Side view of all real-time microseismic events (colored by fracturing stage). 97
Figure 52: Map view of all real-time microseismic events (colored by fracturing stage). 97
Figure 53: Side view of fracture height in the MW formation (color by formation). 98
Figure 54: Example of fracture geometry (fracture length and height). 98
Figure 55: Map view of MSM events from simultaneously stimulated stages on Wells 6M and 7U. 99
Figure 56: Average MSM height growth for all wells. 100
Figure 57: Example of typical fracture height and time relationship, well 5U. 100
Figure 58: Example of typical fracture height and time relationship, well 7M. 101
Figure 59: Perforation design and resulting fracture geometry on Well 4U. 101
Figure 60: Comparison of Well 4U Stage 10 (five clusters) and Stage 13 (three clusters). 102
Figure 61: Well, 7U perforation design and resulting fracture geometry. 102
Figure 62: Map view of primary (black) and secondary (red) azimuths of selected project stages. 103
Figure 63: Primary and secondary fracture azimuths for all stages. 103
Figure 64: Average event-cloud width measurements for all wells. 104
Figure 65: Map view of low complexity stages. 104
Figure 66: Final fracture gradients, all wells. 105
Figure 67: Interaction between adjacent stages, Well 5U Stages 4, 5, and 6. 105
Figure 68: Average fracture half-length (ft) per well. 106

Figure 69: End view (gun barrel view) of all stages colored by formation. 106
Figure 70: Example of fracture length and time relationship, Well 5U Stage 19. 107
Figure 71: Example of fracture length and time relationship, Well 7M Stage 20. 107
Figure 72: Deformation detected during Well 8U Stage 12. 108
Figure 73: Deformation detected during Well 7U Stage 12. 108
Figure 74: Deformation detected during Well 7M Stages 12 through 16. 109
Figure 75: Correlating microseismic measurements during tiltmeter deformation detection. 109
Figure 76: Core cut along Well 6SW adjacent to Well 6U Stages 19 through 24. 110
Figure 77: Core cut along Well 6SW interval adjacent to Well 6U Stages 22 through 24. 110
Figure 78: Core cut along Well 6SW interval adjacent to Well 6M Stages 12 through 17. 111
Figure 79: Test site well schematic showing the (a) test site location, (b) gun-barrel view looking north, and (c) map view looking down. We indicate all the wells hydraulically fractured as part of the experiments. The slant well was used to acquire through fracture core samples (Gale et al., 2018; Maity et al., 2018) and a vertical well W12 was used in microseismic monitoring. The colored box inserts in (b) highlight the wells that were fractured together in the zipper fracturing sequence (Table 3). 114
Figure 80: Cumulative frequency-magnitude distribution of events for two selected hydraulically fractured stages at HFTS. We can clearly see the higher uncertainty for (a) due to low event count compared to (b) which has a higher event count and lower uncertainty band (Eq. 3). The magnitude of completeness (M_C) for both stages is similar, but the calculated slope of the distribution varies significantly. 118
Figure 81: Estimation of magnitude of completeness using goodness of fit approach for microseismic catalog data from a randomly selected hydraulic fracturing stage at HFTS. The synthetic fits to the actual catalog are shown in subplots (a), (b) and (c) for three arbitrary values of Mm. The goodness of fit as a function of Mm is shown in subplot (d). The selected data fit instances from subplots (a), (b) and (c) are highlighted in subplot (d). The selected M_C is highlighted in subplot (d). For this case, we find the best fit to be 83.4%. 119
Figure 82: Diagnostic Nolte-Smith interpretation guide depicting fracture propagation modes. From Britt et al. (1994). 121
Figure 83: Applicability of maximum likelihood estimate for catalogs from test site: (a) observed magnitude range for various HFTS study wells and (b) comparison between b-value calculated for various catalogs using both the maximum likelihood and the least square error estimates. We did not observe any microseismic event of significant magnitude. 122
Figure 84: Impact of microseismic survey design (source to receiver separation) on catalog quality: (a) source to receiver distance for various wells and (b) stage-wise M_C behavior for three selected wells compared with the mean source to receiver distance for corresponding stages. 123

Figure 85: Variation in ISIP with stage (toe to heel) for wells W7 and W8. The stress shadow effect and resulting gradual rise in ISIP can be seen towards the toe section. Local stress reversal is evident, particularly for well W7. 124

Figure 86: Relationship between b-value calculated in depth and in-situ differential stress along pilot well W6. 126

Figure 87: Ant-track (variance) attribute highlighting potential discontinuities within (a) UWC and (b) MWC formations close to the hydraulically fractured wells. Section identifying stages where microseismic data is unavailable is highlighted in (b). 126

Figure 88: Map view of UWC wells showing distribution of (a) b-value and (b) associated uncertainty measure. Major identified lineaments from ant track discontinuity maps (Figure 87a) are superimposed on top. Dotted insert shows the approximate location of cored section along the slant well. 127

Figure 89: Map view of MWC wells showing distribution of (a) b-value and (b) associated uncertainty measure. Major identified lineaments from ant track discontinuity maps (Figure 87b) are superimposed on top. Section identifying stages where microseismic data is unavailable is highlighted in (a). Dotted insert shows the approximate location of cored section along the slant well. 128

Figure 90: Normal stress change due to strike-slip failure along defined vertical fault plane, modeled for a linear displacement of approximately 3.3 ft. The stress change is modeled along the direction of S_{Hmin}. 129

Figure 91: Based on stress models for UWC and MWC formations, critically stressed natural fractures for well W4 landed in UWC formation at (a) no pressurization, (b) 200 psi pressurization, and (c) 500 psi pressurization; and for well W9 landed in MWC formation at (d) no pressurization, (e) 200 psi pressurization, and (f) 500 psi pressurization. The percentage values reported in each panel represents the proportion of critically stressed fractures compared with the total fractures for that well at specified pressurization. The critically stressed fractures are highlighted in red. 130

Figure 92: 3D Seismic derived brittleness compared with microseismic derived spatial b-value distribution for (a) UWC and (b) MWC wells. There seems to be a good correlation between areas showing high brittleness and areas with high b-values and vice versa. The areas with significant mismatch between these two properties generally show higher uncertainty (σ). The black arrow highlights one such location in UWC formation. Section identifying stages where microseismic data is unavailable is highlighted in (b). 132

Figure 93: Temporal distribution showing b-value, rate of occurrence, distribution of seismic events with depth and fracturing treatment pressure for four stages: (a) stage A, (b) stage B, (c) stage C, and (d) stage D. 134

Figure 94: Nolte-Smith exponent 'e' based on fracturing treatment pressure for stages in Figure 93: (a) stage A, (b) stage B, (c) stage C, and (d) stage D. For stage A, there are significant portions of the treatment where the value is close to unit slope as shown by the shaded regions. For

stage B, the value of the slope is approximately 0.3 for most of the treatment. For stage C and stage D, we see significant negative distribution of slope highlighted by the shaded regions. . 135

Figure 95: Distribution of 3D seismic derived ant-tracks close to (a) stage A in well W3 and (b) stage B in well W10. The locations of stages are identified by the red inserts. 136

Figure 96: Whole core were successfully obtained in 4 separate runs (Core 1-4) in the Upper Wolfcamp portion of the slant well after the 6SU and 6SM wells were completed. Core segments 5-6 were collected in the Middle Wolfcamp for a total of 594 ft of whole core. Downhole microseismic data were also collected throughout the completion of these wells. 139

Figure 97: Image of the two "fracture planes" identified by planar microseismic event clouds which were used to alter planned core location to better intersect with both planes and thus increase likelihood of encountering hydraulic fractures. 140

Figure 98: Evolution of KDE microseismic anomalies over stages 23 and 24 on the Sugg A 171 6SU. (a) shows the far field events present in the data prior to ramp up of casing pressure, the events snap to a location intersecting a proppant pack with colored sand linked to Stage 23 in (b), later in the treatment, (c), the anomaly migrates to the heel of the stage over an area of high certainty hydraulic fractures and remains there for the duration of the treatment. Early in Stage 24 the anomaly reoccupies the same location over Core 1 as in the previous stage. 142

Figure 99: 36 minutes into the treatment of Stage 23, a high-density cloud of microseismic events gathers around the core intervals 2 and 3 in the same location a large proppant pack, b), and was seen in the core. The microseismic concentration at 36 minutes into treatment of the stage likely is showing the fracture network that emplaced the proppant encountered in the Slant Core. 142

Figure 100: Proprietary geocellular model of calcite volume. (b): Proprietary geocellular model of clay volume. On both figures, notice the arresting of events in the center of the figure coinciding with elevated calcite/lower clay volume. The cyan microseismic events are from Stage 24, purple events are Stage 23. 143

Figure 101: Location view map. 146

Figure 102: Comparison of the histogram vs. KDE (scikit-learn.org) 147

Figure 103: Kernel density estimate (KDE) with different bandwidths of a random sample of 100 points from a standard normal distribution. Grey: true density (standard normal). Red: KDE with h=0.05. Black: KDE with h=0.337. Green: KDE with h=2. 148

Figure 104: Kernel density estimate (KDE) algorithm comparison. 148

Figure 105: Evolution of Gaussian KDE microseismic time series map view over Stage 23. (a) Stacked heat map over stage 23. (b) KDE map shows elapsed time at 9 minutes into pump schedule. Microseismic events have initial far field event in the beginning of completion. (c) Ramp up at 15 minutes but microseismic event cloud jump to wellbore not until around 36 minutes. (d) Later event cloud jumps back to wellbore at 72 minutes. (e) Heelward extent towards end stage (elapsed time 135 minutes) could be the effect of stress shadowing. (f) Pump schedule over Stage 23. 150

Figure 106: Evolution of Gaussian KDE microseismic time series map view over Stage 24. (a) KDE map shows microseismic event cloud at elapsed time ~8 minutes. Far-field microseismic event occurred prior to ramp up. (b) Microseismic event cloud snap back to the wellbore, right after pumping at elapsed time 18 minutes. Later in the treatment, Figure c to f, the microseismic event migrates toward the toe perf cluster of the stage throughout the reminder treatment of the stage 24. It indicates the 2nd and 3rd perf which are close to the heel of the stage 24, were not efficient. (g) Pump schedule over stage 24. 151

Figure 107: fastKDE time series heat map at elapsed time 21 minutes 31 second over stage 24; black dots show the actual microseismic events. (a) Map view. (b) Gun barrel view. (c) Profile view. (d) pump schedule over stage 24. 152

Figure 108: Index maps showing the location of the Hydraulic Fracturing Test Site (HFTS) within the Midland Basin in Reagan County, Texas. Maps provided by Laredo Petroleum, Inc. (LPI) and Gas Technology Institute (GTI Energy). 155

Figure 109: Map view of two arrays of 3C geophones (red dots) that recorded seismic waveforms during the fracture stimulation of two Middle Wolfcamp wells (4S and 5S) located about 8,000 ft. below the geophone arrays. Each array consisted of 24 GS-One 3C geophones spaced 220 ft.-apart; for each array, 20 geophones were deployed in a magnetic north-south direction (353.5° azimuth) with four geophones deployed orthogonal, intersecting the 20-geophone line at its midpoint. The picture at right shows a geophone deployment at the HFTS site where the GSOne 3C sensor is buried with only its top surface showing above ground. 157

Figure 110: Map showing the location of regional events (solid red dots) reported in the ANSS catalog during the fracturing of horizontal wells in Reagan County. The blue, yellow and green circles drawn on the map have a radius of 500 km, 1,000 km, and 1,500 km respectively. 159

Figure 111: Map showing the location of nearby station from the United States National Seismographic Network (red pyramids) used for waveform comparison with LPLD events recorded at Reagan County site (yellow star). The circle (blue) drawn on the map has a radius of 120 miles. 160

Figure 112: Stacked waveform (panel-a) and spectrogram (panel-b) of a long duration event identified during hydraulic fracturing of one of the toe stages. Color scale shows amplitude in decibel, with warmer colors corresponding to higher amplitude. 161

Figure 113: Seismic waveform (panel a) and spectrogram plot (panel b) of United States National Seismographic Network (USNSN) data recorded for similar timeframe as LPLD event observed in the current study and shown in Figure 112. 162

Figure 114: Filtered seismograms of vertical (left panel) and horizontal (right panel) components showing the record of LPLD event. Red rectangle marks the time interval of observed LPLD event. 163

Figure 115: Permian Basin (source: Encyclopedia Britannica). 166

Figure 116: Wellbore positioning and spacing of the 12 newly drilled wells in the HFTS. 166

Figure 117: Proppant traced wells highlighted with corresponding tracer color utilized. 167

Figure 118: 3U, 5M, 5U and 6TW wells labeled in white were not traced. 167

Figure 119: Break down of oil (OFT) and frac fluid (CFT) tracer injection intervals for 3 and 4 segment wells. 168

Figure 120: 6U well, stage 30. 168

Figure 121: 6M well, stage 13. 169

Figure 122: 4U well, stage 2 – 5 cluster design. 169

Figure 123: 4U well stage 28 – 3 cluster design. 169

Figure 124: Frac fluid communication matrix for the HFTS horizontal wells. 170

Figure 125: Oil communication matrix for the HFTS horizontal wells. 171

Figure 126: Location of test site along with the Schematic view of the UWC (dotted curves) and MWC (solid curves) wells at HFTS; (a) test site location, (b) map view, (c) section view. 173

Figure 127: Classifier confidence comparison for (a) proppant and (b) natural calcite. The training data results for the model are shown with the solid line and the dotted lines show results for two separate datasets where the model is applied. 181

Figure 128: Results from controlled classification tests showing samples distributed within a segregated matrix (a) with particle type populating each grid highlighted in (b) and results from the classification workflow in (c). The percentage values in (c) are that of particles identified accurately in relation to the particle type populating a particular grid cell. 182

Figure 129: Classification and QC workflow to inspect and validate classifier results for proppant & calcite detection and classification. The first connectors are indicated. 183

Figure 130: Sample scan sub-section images from Core 3 at depths (a) 9,570ft, (b) 9,573ft and (c) 9,576ft. Corresponding size distributions are shown in (d), (e) and (f). The number on each bar indicates total proppant particles of the corresponding mesh size fraction identified by classification workflow in the samples referenced in (a), (b) and (c). We observe significant proppant in the middle core tube but negligible proppant in the straddling tubes. 184

Figure 131: Lateral and vertical variation of proppant particles: (a) vertical variation in UWC, (b) Lateral variation in UWC, (c) Vertical variation in MWC and, (d) Lateral variation in MWC. 186

Figure 132: Relative size distribution of identified proppant particles: (a) UWC cored interval and, (b) MWC cored interval. For most of cored interval, mesh 100 size fraction dominates. 187

Figure 133: Relative proppant vs. natural calcite distribution: (a) UWC core, and (b) MWC core. 189

Figure 134: Example of fracture complexity from core # 3 at 9,460ft. The computed tomography scan of the intact core is shown in (a) and snapshot of the core sludge sample from processing is shown in (b). 190

Figure 135: Proppant distribution correlated with petrophysical measurements for a part of the UWC cored interval: (a) proppant distribution, (b) porosity, (c) rock type and (d) in-situ stress gradient with brittleness. The aquamarine-colored bands in (a), (b) and (d), highlight the

locations with significant carbonate layers as seen in (c). Only the depth horizon with significant identified proppant is shown. 191

Figure 136: Proppant distribution correlated with petrophysical measurements for the MWC cored interval: (a) proppant distribution, (b) porosity, (c) rock type and (d) in-situ stress gradient with brittleness. The aquamarine-colored bands in (a), (b) and (d), highlight the locations with significant carbonate layers as seen in (c). 191

Figure 137: Distribution of average natural and hydraulic fractures compared with distribution of identified proppant and natural calcite count along the UWC cored section. Note that the average fracture densities are relative and not scaled as per the vertical axes. 192

Figure 138: Geomechanical state of fractures: (a) section A, (b) section B and (c) section C as highlighted in Figure 137. The percentage fractures reported are those that fall strictly above the Mohr-Coulomb failure line for coefficient of friction of 0.6. 193

Figure 139: Map view of the hydraulically fractured wells W4 in UWC and W9 in MWC formations. The relative proppant count distribution identified along the cored interval is highlighted using bars along the well for two size fractions: (a) mesh 40/70 distribution and (b) mesh 100 distribution. The clusters are colored similarly for the same stage (e.g., clusters 69, 79 and 71 belong to the same stage). The bars are colored according to the average vertical offset from well W4. 194

Figure 140: Fracture face sample collection from core. (A) Example 3 ft interval of core before sampling. (B) Samples bagged to be transported to Bureau of Economic Geology labs. (C) Example of a dry fracture face. (D) Brushing method of dry fracture faces using paper and brushes. (E-F) Example of rough and/or wet fracture faces that were either scraped with heavy duty paper or rinsed with water into jars (G). 197

Figure 141: Cleaning and sieving of fracture face samples. (A-C) Bagged and jarred samples were rinsed into a detergent bath and cleaned with paint bushes. (D-E) When no oily mud remained, samples were wet-sieved into 4 size fractions: >500 µm, 250-500 µm, 120-250 µm, and 63-120 µm. (F-G) Fractionated samples were then put into separate containers where excess water, clumps of paper fibers, and floating aluminum shavings were removed with a pipette, followed by air-drying. 198

Figure 142: Weighing and imaging of fracture face samples. (A-C) Each fractionated size was weighed on a high-precision balance and then put into labeled tubs. (D-E) Samples were laid out in monolayers on a black background to be imaged with a macro lens attached to a mounted DSLR camera. 199

Figure 143: Photoshop image preparation. (A) Original image from DSLR. (B) Modified image with all particles lightened for total count. (C) Modified image with darker particles removed and proppant, calcite, and/or aluminum highlighted. 200

Figure 144: Image analysis protocol, depth 9,487.9, 250-500 µm size fraction. (A) Sample image contains base and red proppant, shale, and aluminum. (B) Conversion to 8-bit with a 2 px median smoothing. (C) Thresholding of bright particles only, ignoring shale. (D) LUT inversion with holes filled. Blue box from A-D shows example of proppant with darker interior and bright

perimeter needing infill after thresholding. (E) Watershed algorithm applied to touching particles. Orange box in D shows proppant touching aluminum, which is then separated in E. (F) Proppant counts based on circularity, which exclude angular calcite and elongate aluminum. Green boxes in A and F show automation error which counted a piece of aluminum (solid box) and excluded a red proppant (dashed box). In larger size fractions error is negligible, whereas in smaller size fractions error is ~5% underestimated by automation. 200

Figure 145: (A) Complex hydraulic fracture with 1 cm sand pack and (B) hydraulic fracture with thinner sand patches. (C) Base along with potential red proppant and (D) potential yellow proppant measured in situ before sample collection. 202

Figure 146: Randomly chosen examples of 63-120 µm, we observe rounded particles across all 6 core examples highlighted showing minimal grain crushing. Upper Wolfcamp: (A) 9,380.2 ft, (B) 9,478.2 ft, (C) 9,514.9 ft, & (D) 9,709.7 ft. Middle Wolfcamp: (E) 11,534.1 ft & (F) 11,661.4 ft. 203

Figure 147: Examples of resin-coated sand changing colors due to high temperatures and pressures. (A) Red resin-coated sand before autoclaving (left) and after (right). (B) Fresh blue resin-coated proppant imaged with a macro lens. (C) Blue proppant recovered from fracture face at 11,683.6 ft has a more sky-blue appearance versus the greenish tinge of the unpumped blue proppant from (B). 204

Figure 148: Part of 250-500 µm image from depth 9485.9 illustrating difficulty of characterizing colored proppant after retrieval from the subsurface. Clear-to-white base proppant is abundant and obvious. Blue boxes are red proppant. Purple box is yellow proppant. Green boxes are grains that could be either oxidized base, faded red or yellow proppant. Dashed orange boxes are examples of other colored particles found within samples that are not proppant. 206

Figure 149: Pressure interference between Well 0 and well A, no interference between Well 0 and Well B (Awada et al., 2015) 208

Figure 150: Well configuration showing UWC and MWC wells (circles) using gun-barrel view. MWC wells are 325 ft deeper and chevroned 330 ft horizontally offset to UWC wells. 209

Figure 151: Well stimulation sequence, ZF denotes zipper fracturing. 210

Figure 152: Water soluble chemical tracer analysis during flowback/production. Each sub-figure represents an inter-well tracer test with tracer injected in a well (enclosed by a square) and observed at all wells. The numbers on the well (and the color) represents the normalized tracer concentration at that well (high numbers indicate more tracer observed). 210

Figure 153: Proppant communication between wells based on radioactive tracer (Red: Indium; Blue: Antimony; Yellow: Scandium) presence at each well. Cross mark denotes the well where the RA tracer was injected. 211

Figure 154: Bottomhole pressure monitored in 11 wells during pressure interference testing. Arrows in the figure represent pressure interference events. 212

Figure 155: Pressure interference between the source (UWC3) and monitor (UWC4) well, as the source well is restarted. 213

Figure 156: Summary of pressure interference test. Arrows represent interference between well pairs and the corresponding number is the response time in minutes. 214

Figure 157: Effective model to capture the pressure interference between fractured wells during production. 215

Figure 158: Forward model and the inverse problem. 215

Figure 159: a) Pressure response at the monitor well due to production from the source well, b) Response Time as a function of offset between the propped fractures, c) Response Time as a function of matrix permeability, d) Response Time as a function of the overlap between the propped fractures. 216

Figure 160: History match of the simulation with field data. Pressure interference captured when propped fractures are hydraulically connected by IU fractures. 216

Figure 161: Sensitivity study to analyze the impact of length of the critical path, IU fracture permeability and IU fracture length on Response Time (T_r). 217

Figure 162: Location of the Hydraulic Fracture Test Site in Reagan, Texas, USA. 222

Figure 163: Groundwater Salinity Changes during HFTS Experiment. 226

Figure 164: BTEX, Methane, and VOC 12-hour Averages during HFTS Experiment. 229

Figure 165: Total Dissolved Solids with Time in Produced Waters Collected from the Three Shale Wells at the HFTS. 231

Figure 166: Sulfate Vs. Time in Produced Waters Collected from Three Wells Selected for Sampling at the HFTS. 232

Figure 167: Nitrate Vs. Time in Produced Waters Collected from the Three Wells Selected for Sampling at the HFTS. 232

Figure 168: Total Organic Carbon Vs. Time in Produced Waters Collected from Three Wells at the HFTS. 233

Figure 169: Balanced Equations Describing the Microbial Oxidation of Organic Matter Using Nitrate and Sulfate 234

Figure 170: Comparison of Oxidant and TOC Conversion in the Downhole Aquatic Environment During the Initial 14 Days of Flowback Release. 235

Figure 171: Location of EOR test wells and other potential test locations. 251

Figure 172: Plan view of EOR test site showing the horizontal injector and monitor wells, and vertical wells. 252

Figure 173: Plan view of EOR test site showing the horizontal, vertical, and slant wells as well as the location of BHP gauges 253

Figure 174: Trajectory of the Second Slant Core Well. Run #1: Cut 69′ with 100% recovery; Run #2: Cut 73′ with 99.5% recovery (72.65′); Run #3: Cut 53′ with 99.4% recovery (52.7′); Run #4: Cut 66′ with 100% recovery (65.9′). 254

Figure 175: Pressure and Rate data in the injector well during gas injection. 254

Figure 176: Produced gas rates in the 6NU well. Once the gas rate increased by 1000 mcf, the well was shut in. 255

Figure 177: EOR pilot well layout indicating wells which were shut in due to the severity of their increased gas production (red dashed boxes) and the wells with increased gas production that were not shut in (Orange dashed boxes). 256

Figure 178: Gas injection timeline in the 5NU well showing the cumulative injected gas plot at the bottom. 257

Figure 179: Production profile showing decline trends for Sugg A 197-195 5SU before and after gas injection. 257

Figure 180: Production profile showing decline trends for Sugg A 197-195 4SU before and after gas injection. 258

Figure 181: Production profile showing decline trends for Sugg A 197-195 3SU before and after gas injection. 258

Figure 182: Production profile showing decline trends for Sugg A 184 1NM before and after gas injection. 259

Figure 183: Production profile showing decline trends for Sugg A 184 1NU before and after gas injection. 260

Figure 184: Production profile showing decline trends for Sugg A 197-198 3NU before and after gas injection. 260

Figure 185: Production profile showing decline trends for Sugg A 197-198 6NU before and after gas injection. 261

Figure 186: Production profile showing decline trends for Sugg A 197-198 5NU (injector well) before and after gas injection. 261

Figure 187: Pressure drawdown profile of the test site wells showing bottom hole pressure responses before and after injection. 262

Figure 188: Geology variations and similarities between the two areas A (HFTS Phase I) and B-North (HFTS EOR phase) by Laredo. 263

Figure 189: Location of this SUGG A 142 3NU well (indicated by the red star) compared to the EOR test wells (B North). 263

Figure 190: Results from fiber optic injection profiling monitoring using Distributed Temperature Sensing (DTS). 265

Figure 191: Results from fiber optic production profiling using Distributed Temperature Sensing (DTS). 265

Figure 192: Results from fiber optic production allocation monitoring using Distributed Acoustic Sensing (DAS). 266

Figure 193: Gas injection rate (top) and bottom-hole pressure (bottom) in the 5NU during acoustic response monitoring and injection/production logging. 266

Figure 194: DTS pressure and temperature monitoring in Sugg E 197-198 5NU showing that the "hot spots" during injection are in the middle of stage 27 and stage 25 with the south end of stage 24. 267

Figure 195: Acoustic activity volumes near 5NU horizontal well during HP injection and post-injection. 267

Figure 196: Fully populated active volumes in Sugg E 197-198 5NU horizontal well (depth viewed from above). 268

Figure 197: Fully populated 3D active volumes in Sugg E 197-198 5NU horizontal well (the red line) viewed from the SW. 268

Figure 198: Gas compressibility factor (Z-factor) of gas as a function of pressure. 271

Figure 199: Variations in saturation pressures as a function of gas injection mol%. 271

Figure 200: Liquid volume drop-out as a function of pressure. 272

Figure 201: Slim tubes study to determine the MMP. 272

Figure 202: Pressure match for the well Sugg E 197-198 5NU. Dark blue line is simulated reservoir pressure; light blue line is simulated BHP; and dark red dots are the gauge pressures. 273

Figure 203: Regions with enhanced permeability around the hydraulic fracture (top) and the pressure distribution within the fracture (bottom). 274

Figure 204: The drainage profile showing different SRV areas around the fracture. Colors represent the pressure (red being the highest pressure) in the matrix (left) and in the fracture (right). 274

Figure 205: Comparing gas injection performance predictions for the scenarios outlined in the Table 20. 275

Figure 206: Conceptual illustration of the test program as planned. 278

Figure 207: Project location along with observation, refrac, and new infill wells. 280

Figure 208: Project timeline. 280

Figure 209: Core testing examples for Zgabay 14H. 281

Figure 210: Refrac well perforation design. 282

Figure 211: Operational summary at Zgabay unit during infill operations. 283

Figure 212: Production interference test plan with POP (Put On Production) sequence. 283

Figure 213: SWPM - Zgabay 3H/ 4H active wells with Zgabay 11H, 12H, 13H, 14H monitor wells. 284

Figure 214: Hydraulic interaction plot indicating estimated fracture half lengths associated with various fracture Zgabay 3H and 5H refrac stages. We see good overlap between VFR response and the distance of these observation wells from the correpesponding refrac wells. 285

Figure 215: Zgabay 3H stage 34 to Zgabay 14H response. New fracture as well as probable fracture reactivation are highlighted. 285

Figure 216: VFR response comparison. Red dots indicate Zgabay 3H response & blue dots indicate 5H response at 14H. 287

Figure 217: Observed ovality along Zgabay 5H during perforation imaging. 288

Figure 218: Perforation area as a function of well position along Zgabay 5H well. 289

Figure 219: Perforation are as a function of depth along Zgabay 5H. The vertical lines indicate plug depth and red lines show erosion trend line. 290

Figure 220: Observed pre-refracturing per stage directional increase in bias. 290

Figure 221: Cluster vs. perforation efficiency for observed perforations in Zgabay 5H before refracturing. 291

Figure 222: Parted casing observed in the well could have been due to a frac hit from in-fill fracturing operations at the site. 291

Figure 223: Post refracturing perforation area as a function of well position in Zgabay 5H. Note that outliers have been omitted in this display. 292

Figure 224: Post refracturing perforation area increase as a function of depth. Outliers have been removed. 293

Figure 225: Post fracture per stage directional increase bias in Zgabay 5H post refracturing. 294

Figure 226: Cluster vs. perforation efficiency for observed perforations in Zgabay 5H after refracturing. 294

Figure 227: Mean post refracturing area increase vs. phase range. Right perforation (when looking from top) seems to have eroded more (57%) compared to left perforations. Also, the high side seems to have eroded 40% more compared to low side. 295

Figure 228: Wells (LHS: map view and RHS: gun-barrel view) at the test site. 295

Figure 229: Zgabay 4H preload strain change response at Zgabay 14H. Pressure gauge locations are identified using dotted inserts. 297

Figure 230: Rayleigh frequency shift, strain change rate along Zgabay 14H with definable communication zones. 297

Figure 231: Zgabay 14H RFS DSS strain change during fracturing operations. 298

Figure 232: Strain change after refrac and after infill fracturing periods from 12,000 ft to 14,650 ft. 299

Figure 233: Strain change after refrac and after infill fracturing periods from 14,650 ft to 18,000 ft. 299

Figure 234: Strain change during refrac with Zgabay 14H casing pressure measured at 13,400' in Lower EagleFord. 300

Figure 235: Accumulated RFS strain change waterfall during Evolution 5 monitoring. 301

Figure 236: Time lapse strain profiles during refrac-infill and parent well flowback operations. Negative strain change indicates compression in fiber due POP (green trace)/ flowback (red trace) operations. 302

Figure 237: Examples of conductive fracture clustering within each conductive corridor. 302

Figure 238: RFS strain change before and after the refrac and infill operations. Example of strain reversal is noted for reference. 303

Figure 239: Test site including well representations showing site complexity. 304

Figure 240: Proppant-log workflow. 305

Figure 241: 3D visualization of proppant-log output 306

Figure 242: Proppant log response relative to offset from parent wells. 306

Figure 243: Sealed wellbore pressure monitoring results with interpreted fractures. Red indicates lack of communication. 306

Figure 244: Side view showing relative location of Zgabay 14H, Zgabay 3H and Zgabay 5H laterals. We observe limited fracture height growth above 60 to 70 ft vertically during restimulation or 3H and 5H wells (Figure 243). 307

Figure 245: Preload operations - high level observations (pressure response above and below fracture gradient during preload operations showing stronger response in the heel vs. the toe. Offset pressure changes, i.e., parent fracture network growth is only observed above fracture gradient 308

Figure 246: Using derived attributes (β) to interpret proppant source. 309

Figure 247: Using derived attributes (α) to interpret propped fracture corridors. 309

Figure 248: Roughness based fracture classification for hydraulic fractures in HFTS-1 Phase 3 core. Reds highlight fractures where textural roughness dominates, greens highlight very smooth fractures, blues indicate presence of simple propagational features whereas yellows highlight complex propagation artifacts. 310

Figure 249: Fracture roughness measure along the cored interval along Zgabay 14H for identified hydraulic fractures. 310

Figure 250: Fracture clustering at HFTS-1 Phase 3 site. The figure on the left highlights the gradual rise and fall in roughness observed along the core, likely governed by stress effects. The confidence boundaries in the figure on the right are for asymptotic normal distribution of coefficients using Pearson's correlation coefficient. 311

Figure 251: Grain size distribution (GSD) interpreted from digital fracture surface maps. Notice that rocks with more quartz (larger GSD) tend to have higher roughness (complex propagational or textural roughness). 311

Figure 252: Comparison of gamma ray log vs. fracture roughness including basic type classification of textural roughness vs. others. Highlighted sections indicate quartz or carbonate rich zones and hydraulic fractures with textural roughness. 312

Figure 253: Hydraulic fracture density (distribution) compared with proppant distribution along cored interval. 313

Figure 254: Observed communication observed broadly along various sections of the monitoring well lateral during Zgabay 4H preload operations. 313

Figure 255: DSS strain change rate snapshot measured along Zgabay 14H fiber during Zgabay 4H preload operations. Proppant log attributes are overlayed for reference. 314

Figure 256: Pressure drawdown observed at various depths along the Zgabay 14H monitoring well. 315

Figure 257: Pressure gauge readings prior to refracturing/ infill fracturing operations. We note responses are being directly correlated to propped zones as interpreted from the log. 315

Figure 258: Lack of hydraulic fractures (core characterization, BEG) correlates with lack of propped zones from proppant log and high reservoir pressure (lack of drainage). 316

Figure 259: Identification of potential targets for infill fracturing guided by proppant log. 316

Figure 260: Instrumented wells (black) and known geologic features. 318

Figure 261: Mapped fracture interceptions along the Zgabay 12H and Zgabay 14H fibers during refracturing operations. 319

Figure 262: Cluster efficiency observations from crosswell response. 320

Figure 263: Fracture interception morphology with cluster counts vs. new fracture interception far-field. 320

Figure 264: Zgabay 5H on Zgabay 14H fracture corridor analysis. 320

Figure 265: Zgabay 3H on Zgabay 12H fracture corridor analysis. 321

Figure 266: Interpreted fracture azimuth across re-stim stages. 321

Figure 267: Fracture corridor interpretation for a sample stage. Note that we would consider prior stage reactivation when evaluating the corridor width. However, non-interception is not included in evaluating the corridor. 322

Figure 268: Total observed extensional strain (Stage-wise) across identified fracture corridors for various well pairs. 322

Figure 269: Total interpreted fracture corridor summary statistics. 323

Figure 270: New fracture corridor statistics (total without reactivation). 323

Figure 271: Interpreted fracture corridor gap (Zgabay 5H stage 20 on Zgabay 14H). 324

Figure 272: Interpreted fracture corridor overlap (Zgabay 5H stage 10 on Zgabay 14H). 324

Figure 273: Percent of total extensional strain in new fracture corridor only (nm/ m) for both Zgabay 3H to 12H and Zgabay 5H to 14H observations. 324

Figure 274: Skewness of new fracture corridor cumulative extensional strain for the two refrac wells. 325

Figure 275: Zgabay 3H well production before (dotted) and after (solid) refrac operations. 325

Figure 276: Zgabay 5H well production before (dotted) and after (solid) refrac operations. 325

Figure 277: Zgabay A unit wells (non-infill or non-refrac wells) showing production before and after operations. 326

List of Tables

Table 1: HFTS-1 phase highlights. 46

Table 2: Completion order, fracturing stages monitored, and observation wells. 90

Table 3: Completion sequence for various wells in the pad. Also, highlighted are the corresponding observation wells and number of stages with available microseismic data: modified from Stegent & Candler (2018). The colors represent wells fractured in each zipper fracturing sequence and correspond with rectangles in Figure 79b. 115

Table 4: Ordinary and adjusted coefficients of determination for b-value vs. ISIP data for various UWC and MWC wells from HFTS study. 123

Table 5: Treatment design for the two Middle Wolfcamp wells 158

Table 6: Description of cores, depths and sample numbers from HFTS slant core well. Depths reported are the measured depths along the well. 174

Table 7: Comparison between core fracture description and tracer results for UWC and MWC formations. Communication data is based on tracer study within the study area (Wood et al., 2018). In the two rows, we report average numbers for wells within the two formations where we introduced tracers, i.e., the average number of wells in said formations where we observed oil or water tracers 188

Table 8: Parameters and Methods for Groundwater Quality Analysis at the HFTS. 223

Table 9: Groundwater Quality Results during the HFTS Experiment 225

Table 10: Air Quality Results for HFTS Experiment. 228

Table 11: Characteristics of Impoundments that Store Water for Hydraulic Fracturing at the HFTS. 230

Table 12: Average Copies / mL of Bacteria (BA), Sulfate Reducing Bacteria (SRB), Denitrifying Bacteria (DNB), and Methanogens (Meth) over 550 of Production at the HFTS. 233

Table 13: Completion summary of the EOR pilot wells; injection well is highlighted. 252

Table 14: Operations timeline for the fiber optic injection profiling/production allocation monitoring on the Sugg A 197-198 5NU 264

Table 15: Summary of the samples that were analyzed, and quality controlled by CoreLab. 269

Table 16: Analysis of the reservoir fluid composition by CoreLab. 269

Table 17: Analysis of the reservoir fluid properties by CoreLab. 270

Table 18: Analysis of the synthetic and injection gas composition by CoreLab. 270

Table 19: Summary of the swelling gas experiment conducted by CoreLab at 157°F. 271

Table 20: Summary of all different gas injection simulation cases ran by Nitec. BHP limits of 3500 psia set for all injection cases. 275

Table 21: Completion design summary for Zgabay 3H and Zgabay 5H refrac wells. 282

Table 22: Zgabay 3H SWPM summary (15 ft cluster spacing). 285
Table 23: Zgabay 5H SWPM summary (20 ft cluster spacing). 285
Table 24: Reactivation vs. new fracture arrivals in Zgabay 14H (Zgabay 3H active) 286
Table 25: Zgabay 14H measurement phases from Neubrex. 296
Table 26: Zgabay wells POP order followed during monitoring. 301

Abstract

Despite the long history of hydraulic fracturing, the optimal number of fracturing stages during multi-stage fracture stimulation in horizontal wells can be a complex subject. In addition to the increased expense of multistage fracturing in horizontal wells, increasing the number of fracturing stages does not always correlate with a commensurate increase in production. The problem is the application of a uniform fracture stimulation design to all stages with no consideration for geological variations along the wellbore. The result is an inefficient use and costly waste of energy and water.

Optimization of the fracturing process requires an understanding of the cause-and-effect relationship between fracturing parameters and local geological properties at a given location along the wellbore. Realizing that the generalized rock mechanics theories and hypotheses are not truly applicable to fractured and laminated shales, quantifiable impacts of a shale's geomechanical and depositional features are a prerequisite for design and implementation of optimized hydraulic fractures. The overarching goal of this project is to understand and define the relationships of shale geology and fracture dynamics using detailed field data that includes coring of the fracture domain.

Finally, resource recovery from shale formations is estimated to be less than fifteen percent. Research proposed in this project will establish the foundations for investigating enhanced recovery techniques for increased resource recovery in existing fracture treated wells. Natural gas as an EOR fluid is in the initial stages of being used broadly in the oil and gas industry and as such, many aspects of the process need to be researched and addressed prior to widespread acceptance. In addition, re-fracturing techniques, particularly using cemented liners also need to be further investigated. This project explores several of these EOR techniques in greater detail, not just at the theoretical level, but through actual field test sites.

This report delves into the research program, identified tasks, several studies, observations, results, and conclusions under the Hydraulic Fracturing Test Site (HFTS) project. This test project is subdivided into three distinct phases and each phase is discussed in detail under separate sections. The original test site for Phase 1 as well as the Phase 2 site are in Midland Basin in Texas and operated by Laredo Petroleum. In the first two phases, the program targeted the Wolfcamp formation in Midland Basin. Phase 3 of the study targeted the EagleFord play in South Texas with Devon Energy as the operator. Significant conclusions from this study include: 1) lateral and vertical fracture growth mapping as well as proppant transport behavior, 2) Use of field gas and its applicability for huff n puff EOR injection in the Midland Basin, 3) Development and validation of proppant log, both at core scale as well as in-fill well implementation by analyzing drilling mud return samples, 4) Applicability of liner refracturing including best practices for enhanced unit level productivity. This report will detail all these studies as well as technical results and conclusions from said studies. These include general subsurface characterization work, completion designs as implemented, studies looking at fracture geometry, high resolution microseismic study, advanced crosswell strain mapping studies including drainage characterization, core characterization results, proppant analysis (core and observation wells), geochemistry, etc. to name a few.

Executive Summary

The HFTS project addresses the environmentally prudent development of shale oil and gas resources which require the drilling and completing of tens-of-thousands horizontal wells in multiple vertically stacked geologic horizons. Non optimal development can result in drilling a substantial number of unnecessary wells resulting in a waste of resources such as water, steel casings, and other infrastructure. It adds to emissions issues and land footprint. Too few wells from the perspective of well spacing and inefficient hydraulic fracturing leaves valuable resources in the ground which may be extracted later at potentially higher financial and environmental cost. These two scenarios have billion-dollar development implications as well as significant environmental implications, as each scenario leads to added emissions and land footprint. Understanding of the hydraulic fracturing geometry, which informs the well spacing, is vital to addressing this optimization problem and is the focal point of the HFTS program (both HFTS-1 project in the Permian Midland, and HFTS-2 project in the Permian Delaware, https://netl.doe.gov/node/6840).

Funded by the US Department of Energy (US-DOE) through the National Energy Technology Laboratory (NETL) and managed by GTI Energy, the HFTS-1 project was a public private partnership involving multiple industry participants comprised of producing and service companies. The partnership leveraged industry funding and subject-matter expertise and facilitated immediate technology transfer leading to rapid adoption of learnings.

The test program spanned three different phases at three separate test sites with the first two sites operated by Laredo Petroleum and situated in the Midland Basin (Wolfcamp formation). The third site was operated by Devon Energy and located in the EagleFord Basin. While the first phase looked at primary stimulation, the second phase investigated huff n puff EOR using field gas injection, and the final phase looked at re-stimulation of producing wells using cemented liner refracturing. High degree of instrumentation at the three sites has enabled the collection of a research-quality dataset over the course of 9 years.

The comprehensive research datasets across the three phases of the project includes microseismic surveys, more than 1,200 ft of whole core drilled through hydraulically fractured reservoir, diagnostic formation injection tests (DFIT), fluid characterization, subsurface mapping tools such as ambient seismic monitoring, advanced logs such as perforation imaging techniques, geochemistry, downhole gauges, varying completion design tests, and advanced fiber optic surveys. These data were integrated and used to characterize hydraulic fracture geometry/ dimensions and resulting depletion profiles, leading to developing workflows to improve completion design and well spacing, and a better understanding of parent well depletion effects on child well performance. In addition, Impediments to EOR application using field gas injection in Midland Basin were identified and validated. Finally, with Phase 3 of the project, the use of liner refracturing as a tool to significantly enhance productivity of reservoir units was proven.

Project Data is publicly available on https://edx.netl.doe.gov/

The analysis and integration of the comprehensive HFTS-1 diagnostic datasets provide insights for optimal well placement and completions and improves our understanding about the effects of parent well depletion. This dataset can be used to blind test and develop subsurface

workflows for unconventional resources. It has already proven instrumental in updating numerical fracture modeling workflows to better mimic true subsurface fracture and proppant transport behavior. Key learnings from HFTS-1 can be applied to the environmentally prudent development of other unconventional plays. The collected cores and research quality dataset will be mined for many years to come and will lead to additional learnings and insights.

Published Art

Summary

With broad industry participation in the HFTS-1 project, various papers and articles have been published over the past few years. This section provides a listing of all such relevant articles and includes those by the project team and other HFTS consortium members, as well as published articles which have utilized HFTS-1 or interpretations dataset for their respective study.

Reference to publications

1. Campbell, W., et al. 2018. Natural and Hydraulic Fracture Density Prediction and Identification of Controllers. Presented at the SPE/AAPG/SEG Unconventional Resources Technology Conference, Houston, Texas. https://doi.org/10.15530/URTEC-2018-2934611.
2. Ciezobka, J., et al. 2018. Hydraulic Fracturing Test Site (HFTS) - Project Overview and Summary of Results. Presented at the SPE/AAPG/SEG Unconventional Resources Technology Conference, Houston, Texas. https://doi.org/10.15530/URTEC-2018-2937168.
3. Eisenlord, S., et al. 2018. Environmental Impact Analysis on the Hydraulic Fracture Test Site (HFTS). Presented at the SPE/AAPG/SEG Unconventional Resources Technology Conference, Houston, Texas. https://doi.org/10.15530/URTEC-2018-2900727.
4. Elliott, S. J., & Gale, J. F. W. 2018. Analysis and Distribution of Proppant Recovered from Fracture Faces in the HFTS Slant Core Drilled Through a Stimulated Reservoir. Presented at the SPE/AAPG/SEG Unconventional Resources Technology Conference, Houston, Texas. https://doi.org/10.15530/URTEC-2018-2902629.
5. Gale, J. F. W., et al. 2018. Hydraulic Fractures in Core from Stimulated Reservoirs: Core Fracture Description of HFTS Slant Core, Midland Basin, West Texas. Presented at the SPE/AAPG/SEG Unconventional Resources Technology Conference, Houston, Texas. https://doi.org/10.15530/URTEC-2018-2902624.
6. Kumar, A., et al. 2018. Surface Seismic Monitoring of Hydraulic Fracturing Test Site (HFTS) in the Midland Basin, Texas. Presented at the SPE/AAPG/SEG Unconventional Resources Technology Conference, Houston, Texas. https://doi.org/10.15530/URTEC-2018-2902789.
7. Maity, D., et al. 2018. Assessment of In-Situ Proppant Placement in SRV Using Through-Fracture Core Sampling at HFTS. Presented at the SPE/AAPG/SEG Unconventional Resources Technology Conference, Houston, Texas. https://doi.org/10.15530/URTEC-2018-2902364.
8. Maity, D. 2018. Microseismicity Analysis for HFTS Pad and Correlation with Completion Parameters. Presented at the SPE/AAPG/SEG Unconventional Resources Technology Conference, Houston, Texas. https://doi.org/10.15530/URTEC-2018-2902355.
9. Srivastava, K., et al. 2018. Formation of Complex Fracture Networks in the Wolfcamp Shale: Calibrating Model Predictions with Core Measurements from the Hydraulic

Fracturing Test Site. Presented at the SPE Annual Technical Conference and Exhibition, Dallas, Texas. https://doi.org/10.2118/191630-MS.

10. Stegent, N., & Candler, C. 2018. Downhole Microseismic Mapping of More Than 400 Fracturing Stages on a Multiwell Pad at the Hydraulic Fracturing Test Site (HFTS): Discussion of Operational Challenges and Analytic Results. Presented at the SPE/AAPG/SEG Unconventional Resources Technology Conference, Houston, Texas. https://doi.org/10.15530/URTEC-2018-2902311.
11. Tanner, W., et al. 2018. Interwell Communication Study of UWC and MWC Wells in the HFTS. Presented at the SPE/AAPG/SEG Unconventional Resources Technology Conference, Houston, Texas. https://doi.org/10.15530/URTEC-2018-2902960.
12. Wicker, J., et al. 2018. Using Stage Level Microseismic Analysis to Correlate and Ground Truth Cored Hydraulic Fractures. Presented at the SPE/AAPG/SEG Unconventional Resources Technology Conference, Houston, Texas. https://doi.org/10.15530/URTEC-2018-2937221.
13. Gale, J. F. W., et al. 2019. Natural Fracture Characterization in the Wolfcamp Formation at the Hydraulic Fracture Test Site (HFTS), Midland Basin, Texas. Presented at the SPE/AAPG/SEG Unconventional Resources Technology Conference, Denver, Colorado. https://doi.org/10.15530/urtec-2019-644.
14. Huang, J., et al. 2019. Numerical Modeling of Well Interference Across Formations at the Hydraulic Fracturing Test Site. Presented at the 53rd U.S. Rock Mechanics/Geomechanics Symposium, New York City, New York. ARMA-2019-1995.
15. Li, T., et al. 2019. Analysis and Interpretations of Pressure Data from the Hydraulic Fracturing Test Site (HFTS). Presented at the SPE/AAPG/SEG Unconventional Resources Technology Conference, Denver, Colorado. https://doi.org/10.15530/urtec-2019-233.
16. Morris, J. P., et al. 2019. Multiscale Geomechanical Analysis of the Hydraulic Fracturing Test Site. Presented at the 53rd U.S. Rock Mechanics/Geomechanics Symposium, New York City, New York. ARMA-2019-2069.
17. Wang, S., et al. 2019. Learnings from the Hydraulic Fracturing Test Site (HFTS) #1, Midland Basin, West Texas - A Geomechanics Perspective. Presented at the SPE/AAPG/SEG Unconventional Resources Technology Conference, Denver, Colorado. https://doi.org/10.15530/urtec-2019-1570.
18. Ciezobka, J., et al. 2020. Overview of Hydraulic Fracturing Test Sites (HFTS) in the Permian Basin and Summary of Selected Results (HFTS-I in Midland and HFTS-II in Delaware). https://doi.org/10.15530/urtec-2020-1544.
19. Fu, W., et al. 2020. Simulating Tightly Spaced Swarming Hydraulic Fractures at Field Scale Using an Upscaling Approach. Presented at the 54th U.S. Rock Mechanics/Geomechanics Symposium, virtual. ARMA-2020-1044.
20. Fu, W., et al. 2020. Developing Upscaling Approach for Swarming Hydraulic Fractures Observed at Hydraulic Fracturing Test Site Through Multiscale Simulations. Presented at the SPE Hydraulic Fracturing Technology Conference and Exhibition, The Woodlands,

Texas. https://doi.org/10.2118/199689-MS.

21. Kumar, A., et al. 2020. Integrated Analysis of Tracer and Pressure-Interference Tests to Identify Well Interference. SPE J. 25 (04): 1623–1635. https://doi.org/10.2118/201233-PA.
22. Maity, D., & Ciezobka, J. 2020. A Data Analytics Framework for Cored Fracture Imaging and Novel Characterization Workflow - Application on Samples from Hydraulic Fracturing Test Site HFTS in the Midland Basin. Presented at the SPE Hydraulic Fracturing Technology Conference and Exhibition, The Woodlands, Texas. https://doi.org/10.2118/199754-MS.
23. Salahshoor, S., et al. 2020. Stage-Level Data Integration to Evaluate the Fracturing Behavior of Horizontal Wells at the Hydraulic Fracturing Test Site (HFTS): An Insight into the Production Performance. Presented at the SPE/AAPG/SEG Unconventional Resources Technology Conference, virtual. https://doi.org/10.15530/urtec-2020-3058.
24. Salahshoor, S. 2020. Analysis and Interpretation of Multi-Source Data at the Hydraulic Fracturing Test Site: A Data-Driven Approach to Improve Well Performance Evaluation in Heterogeneous Formations. Presented at the SPE/AAPG/SEG Latin America Unconventional Resources Technology Conference, virtual. https://doi.org/10.15530/urtec-2020-1560.
25. Weijermars, R., et al. 2020. Hydraulic Fracture Propagation Paths Modeled using Time-Stepped Linear Superposition Method (TLSM): Application to Fracture Treatment Stages with Interacting Hydraulic and Natural Fractures at the Wolfcamp Field Test Site (HFTS). Presented at the 54th U.S. Rock Mechanics/Geomechanics Symposium, virtual. ARMA-2020-1996.
26. Fu, W., et al. 2021. Developing Upscaling Approach for Swarming Hydraulic Fractures Observed at Hydraulic Fracturing Test Site through Multiscale Simulations. SPE J. 26 (05): 2670–2684. https://doi.org/10.2118/199689-PA.
27. Kumar, A., et al. 2021. Machine Learning Applications for a Qualitative Evaluation of the Fracture Network in the Wolfcamp Shale Using Tracer and Completion Data. Presented at the SPE/AAPG/SEG Unconventional Resources Technology Conference, Houston, Texas. https://doi.org/10.15530/urtec-2021-5159.
28. Liu, X., et al. 2021. Learnings on Fracture and Geomechanical Modeling from the Hydraulic Fracturing Test Site in the Midland Basin, West Texas. presented at the SPE/AAPG/SEG Asia Pacific Unconventional Resources Technology Conference, virtual. https://doi.org/10.15530/AP-URTEC-2021-208377.
29. Maity, D., & Ciezobka, J. 2021. Digital Fracture Characterization at Hydraulic Fracturing Test Site HFTS-Midland: Fracture Clustering, Stress Effects and Lithologic Controls. Presented at the SPE Hydraulic Fracturing Technology Conference and Exhibition, virtual. https://doi.org/10.2118/204174-MS.
30. Maity, D., & Ciezobka, J. 2021. Systematic Comparison of Proppant Placement in SRV Along Two Fractured Wells at the Hydraulic Fracturing Test Site: A Case Study from

Midland Basin. Presented at the SPE/AAPG/SEG Unconventional Resources Technology Conference, Houston, Texas. https://doi.org/10.15530/urtec-2021-5190.

31. Nakagawa, S., et al. 2021. Chemically Induced Reduction of Fracture Closure for Shale Fractures Containing Sub-Monolayer Proppant. Presented at the 55th U.S. Rock Mechanics/Geomechanics Symposium, virtual. ARMA-2021-1602.
32. Weijermars, R., & Wang, J. 2021. Microseismicity and Dry Shear-Slip in the Stimulated Rock Volume During Fracture Treatment in Shale Wells: Analyzing Data from the Hydraulic Fracture Test Site (Permian Basin) With the Linear Superposition Method (LSM). presented at the 55th U.S. Rock Mechanics/Geomechanics Symposium, virtual. ARMA-2021-1808.
33. Xiong, W., et al. 2021. Hydraulic Fracturing Geochemical Impact on Fluid Chemistry: Comparing Wolfcamp Shale and Marcellus Shale. Presented at the SPE/AAPG/SEG Unconventional Resources Technology Conference, Houston, Texas. https://doi.org/10.15530/urtec-2021-5524.
34. Joseph, M., et al. 2022. An Investigation of Candidate Mechanisms for Hydraulic Fracture Swarming through High-Fidelity Numerical Modeling. Presented at the SPE Hydraulic Fracturing Technology Conference and Exhibition, The Woodlands, Texas. https://doi.org/10.2118/209126-MS.
35. Liu, G., et al. 2022. Multi-Level of Fracture Network Imaging: A HFTS Use Case and Knowledge Transferring. Presented at the SPE/AAPG/SEG Unconventional Resources Technology Conference, Houston, Texas. https://doi.org/10.15530/urtec-2022-3723466.
36. Sabbagh, R., & Bhattacharya, S. 2022. Integrated 3D seismic and petrophysical workflow to predict elastic and geomechanical properties in the Wolfcamp Formation: A case study from the Midland Basin, Texas. Presented at the SEG/AAPG International Meeting for Applied Geoscience & Energy, Houston, Texas. https://doi.org/10.1190/image2022-3745871.1.
37. Zoback, M., et al. 2022. Lithologically-Controlled Variations of the Least Principal Stress with Depth and Resultant Frac Fingerprints During Multi-Stage Hydraulic Fracturing. Presented at the SPE/AAPG/SEG Unconventional Resources Technology Conference, Houston, Texas. https://doi.org/10.15530/urtec-2022-3722883.
38. Brinkley, K., et al. 2023. Redefining Recoverable Reserves in the Eagle Ford: Refracs and Infill Development Lessons Learned from the Hydraulic Fracturing Test Site 1 (HFTS) Phase 3. Presented at the SPE Hydraulic Fracturing Technology Conference and Exhibition, The Woodlands, Texas. https://doi.org/10.2118/212340-MS.

Background

Introduction

As already mentioned, the test program was divided into three distinct phases. A brief overview of the three phases is highlighted in Table 1. While the first phase of the project was primarily looking at optimizing hydraulic fracturing process and minimizing the environmental impact of frac operations, the second phase investigated the potential for huff n puff EOR using field gas in the Midland Basin. The final phase of the project investigated the potential for cemented liner refracturing of existing wells as a means for significant production uplift and recovery factors from shale wells.

Table 1: HFTS-1 phase highlights.

Phase	Location	Operator	Test	Diagnostics
1	Reagan Co, TX	Laredo	Fracture optimization	Logs, microseismic, seismic, core through well, environmental monitoring, proppant log, reservoir pressure monitoring
2	Reagan Co, TX	Laredo	Huff n puff EOR	0.25 bcf injected field gas, ambient imaging, seismic, fracture modeling, core through well, proppant log, reservoir pressure monitoring
3	DeWitt Co, TX	Devon	Cemented liner refrac	Advanced FO diagnostics as well as pressure monitoring, core through well, perforation imaging, proppant log

The basic idea behind the HFTS projects has been to develop strong public-private research initiatives which can leverage public and private funding and technical expertise to address the complexities of sustainably developing stacked pay resources.

Test Sites

The HFTS-1 Phase 1 field test site was in the Permian Midland Basin in Reagan County, Texas (Figure 1) and is operated by Laredo Petroleum. The eleven-horizontal well package consisted of six upper Wolfcamp wells (SUGG-A-171 3SU, 4SU, 5SU, 6SU, 7SU, 8SU) and five middle Wolfcamp wells (SUGG-A-171 4SM, 5SM, 6SM, 7RM, 8SM). The new producing wells were landed in various Wolfcamp horizons and have lateral lengths of about 10,000 ft. All the Phase 1 project wells were drilled and ready prior to the project initiation. The lateral sections of the wells are spaced about 660 ft apart within the same horizon and a 330 ft lateral separation between wells within the development unit (chevron pattern). The new slant core well was

drilled and is positioned between the 6SU and 6SM laterals (Figure 1 right panel). The vertical section of one of the wells was used as pilot hole used to characterize the reservoir. The slant well which was drilled after all wells were stimulated and was used to collect whole cores through the created fractures. It was also instrumented with pressure and temperature gauges to monitor reservoir depletion during production. Open hole logs were acquired in many of the wells including quad combo and image logs.

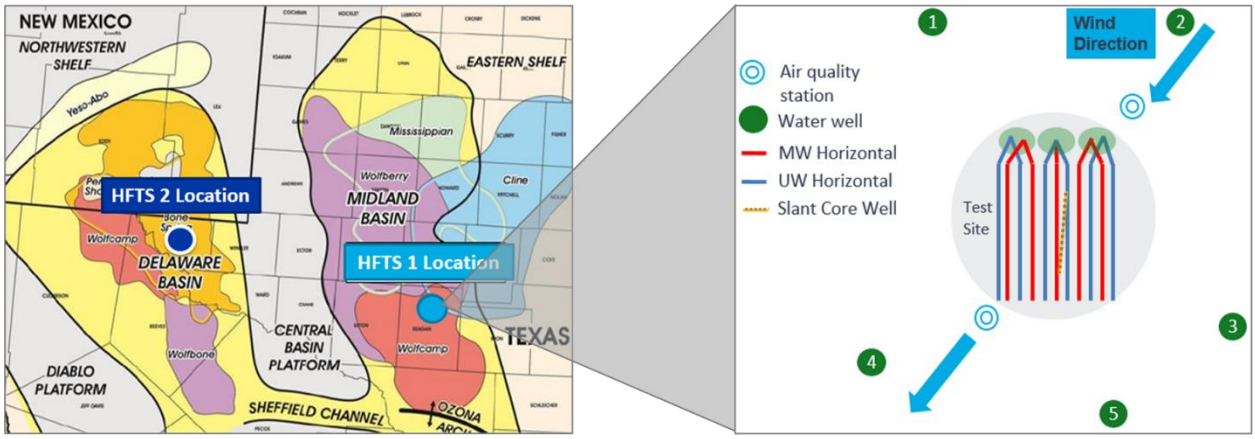


Figure 1: Location of HFTS 1 (Loving County Texas). Right insert is a plan view of 11 horizontal wells, as well as the slant core well. Air and water quality monitoring locations are also highlighted.

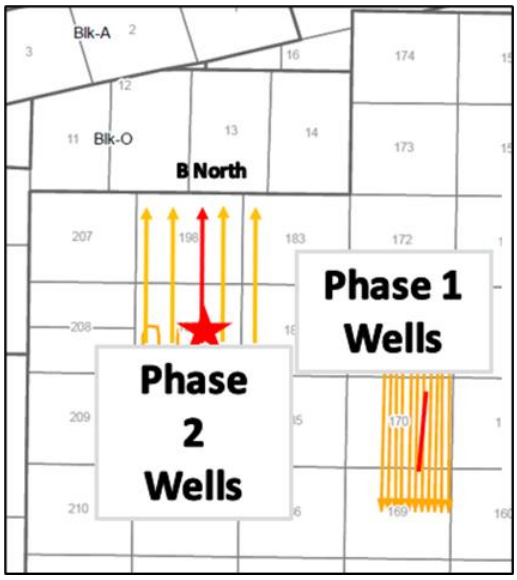


Figure 2: Phase 2 location relative to Phase 1 wells in Reagan Co, Texas.

The HFTS Phase 2 site was located proximal to the Phase 1 site in Reagan County, Texas. Figure 2 highlights the location relative to the Phase 1 wells as shown in Figure 1. The site had significant instrumentation, including bottom hole pressure gauges in multiple horizontal and vertical observation wells. Baseline datasets including past production and completion logs were provided as part of the project. Fiber optic injection and production logging using wireline deployment was also tested at the site. A total of 0.25 bcf of field gas was injected over a period of 2 months' time. However, even after pressure stabilization, a miscibility pressure of 4425 psi was not able to be reached and no discernable improvement in production was observed. All the observed data suggested that the injected gas quickly spread through the field with multiple offset well breakthroughs including wells more than a mile away from the injector.



Figure 3: Phase 3 location in DeWitt Co, Texas hosted by Devon Energy.

The Phase 3 test site was in DeWitt County, Texas targeting the EagleFord Shale formation (Figure 3). The aim of this phase of the program was to answer the key question: Can new, previously undrained reservoir be identified within a wellbore, and successfully contacted with new infill stimulation technology to boost production and improve recoveries? Liner technology was utilized to seal-off existing perforations, then re-perforate in-between and fracture stimulate through new perforations. Finally, the aim was to quantify the economic viability of infill stimulation using liner refrac, potential added resource that could be achieved, and environmental benefits by reducing the need for new wells.

Project structure

The HFTS-1 project was managed by GTI with DOE being the primary sponsor and NETL administering and managing the project for DOE and performing specific research. In addition to project management, GTI was also responsible for project budget, performing specific research including proppant analysis, data integration, benefit analysis, and industry outreach to solicit industry membership and technology transfer.

The test site host, Laredo, was responsible for managing day-to-day field operations of the test site, including management of vendors and subcontractors for field and laboratory work. In addition to hosting the test site, Laredo also provided a large background dataset including many nearby wells as well as extensive petrophysical and core data and geological models for the site. Laredo and Core Labs also hosted multiple project workshops both on site in Texas as well as virtually.

Multiple technical subcommittees were created to provide technical input and direction for specific areas of the project. The subcommittees comprise members from DOE/NETL, GTI Energy, the test site host, and all the industry members. Each subcommittee was headed by a chair (or co-chairs) leading the subcommittee. The chairs provided guidance on specific items based on input from the subcommittee to the Technical Advisory Group, which then made decisions regarding the direction of the overall research program.



Figure 4: HFTS sponsors and participants.

Industry membership comprised of 15 producing and service companies shown in Figure 4, who provided cost sharing to the project in the form of cash or in-kind contributions. The technical HFTS-1 program was designed by GTI Energy and experts from the industry through multiple workshops and meetings. Initial planning also included identification of technology and knowledge gaps and research needed for minimization of environmental impacts and improved efficiency of hydraulic fracturing.

Introduction

Laredo Petroleum offered a field site for the project in August 2015 which was finalized for this phase of the project. The site included eleven horizontal wells (10,000' horizontal laterals) drilled through the Upper and Middle Wolfcamp formation in the Permian Basin. In addition, multiple vertical wells in proximity were used as observation wells. Some of the high-level activities and observations at this site are listed next.

Two open-hole logs (image and quad combo) were run in horizontal laterals. A vertical pilot hole was drilled through the Wolfcamp Formation and quad combo and image logs were run in the pilot hole as well. 57 rotary side wall cores were recovered along with 50 core vault side wall cores. Diagnostic fracture injections tests were conducted in the pilot hole to better understand the frac gradient and stress conditions downhole in the reservoir. Cross-well seismic surveys were completed between three wells on test site prior to and post-hydraulic fracturing operations. Two diagnostic fracture injections tests were conducted in multiple wells. Water and air samples were collected prior to, during, and post-hydraulic fracturing operations. 400+ fracture stages were completed in the 11 wells and monitored using multi-well microseismic arrays. Radioactive and chemical tracers used in the stimulation program to understand fracture growth. Colored proppant markers were also used in two wells close to the slant core observation well to validate proppant transport behavior.

The slant core well (SCW) was drilled at 81 degrees through stimulated rock volume. 595 ft of core was recovered from this well (437 ft of continuous core in the Upper Wolfcamp and 158 ft of continuous core in the Middle Wolfcamp). Pressure gauges were installed in slant core well to monitor pressure drawdown during production. Core description was completed by multiple teams, and results were incorporated into a final core description report and analysis is presented later in this report as well. Two main sets of natural opening-mode fractures filled with calcite cement were identified trending broadly NE-SW and WNW-ESE. A total of eleven faults were identified, all within the Upper Wolfcamp formation. In all, more than seven hundred total fractures (natural and induced) were identified in the core.

Fracture modeling studies were conducted. In addition, sludge collected from core barrels was analyzed for proppant as a precursor to the development of proppant logging technique (developed by GTI Energy). Results provide a detailed subsurface proppant distribution every three feet for the entire cored interval. Proppant size and concentration was quantified as well as the amount of natural fracture cements, providing an indication of natural fractures. Proppant scraped from fractures of core was also independently analyzed to detect proppant quantity and color using a separate workflow. All identified hydraulic fractures were mapped in high resolution using benchtop 3D Laser scanning technique. The entire core was slabbed and analyzed including a complete geologic description of the slabbed core. Multiple multi-pad systematic pressure interference tests including all the test wells were conducted.

Overview of results

In the next few sub-sections, the report will summarize some of the major observations and results followed by a deep dive into some of the specific studies conducted as part of the Phase 1 project activities.

Coring Through the Stimulated Reservoir Volume (SRV)

The SCW was designed to collect whole core through the SRV both above and below the adjacent producing wells from which the hydraulic fractures would originate. Placement of cored intervals and methodology is described in Trowbridge et al., 2017 and Courtier et. al., 2018. In the Upper Wolfcamp, approximately 450 ft of continuous core was recovered, representing about sixty vertical feet of the fractured reservoir at 89 horizontal feet from the nearest completion stage. The Upper Wolfcamp core placement is shown in Figure 5A. An additional 158 ft of core was recovered in the Middle Wolfcamp formation at 135 horizontal feet from the nearest completion stage and showed less fracturing than the Upper Wolfcamp portion. Once at surface, gamma ray logging was conducted to identify the presence of radioactive tracers pumped during the completion of the horizontal wells. Radioactive tracers were not detected neither during the core-logging, nor within sampling of drill cuttings. Cut-ends of the 3-foot core sections were photographed to document current core state prior to laboratory transport.

The SCW trajectory enabled the collection of core with varying lateral distance from the adjacent producing wells providing insights into both the vertical and horizontal fracture geometries. Figure 5A shows an example of the SCW trajectory with respect to the offset producing horizontal wells. During drilling operations cuttings samples were collected every five feet to obtain additional proppant and lithology information along the path of the cored interval. Mass spectrometry data collected during operations was analyzed with the intent of assessing reservoir compartmentalization and hydraulic fracture identification via gas character and species variation, which did not yield any fundamental insights. Once coring was completed, the curve and lateral section of the SCW were logged utilizing a quad-combo logging suite, including an image log (oil-based mud imager). The log data and additional information collected while drilling, specifically the image log, were used to supplement the core data and aid fracture analysis in sections of the lateral where core was not obtained. After logging, the well was cased, cemented, and multiple isolated gauges were installed to monitor pressures at select intervals within the producing wells and target formations. These gauges along with additional pressure gauges placed in producing horizontals and select legacy wells were monitored for pressure changes during production timeframes.

CT scans of the core before removal from the barrels assisted in determining the integrity of the core as well as the best methodology for extracting core from the barrels. Several methodologies of core extraction were tested, as maintaining a pristine condition was critical for the physical fracture description. The least intrusive approach to maintaining the condition of the core and fractures as close to original was via cutting the core barrel along its length on both sides to then exposing the core for study (referred to as clam-shell methodology). Core was stored (un-slabbed) within the half-barrel to maintain original features (Figure 5B). CT scans were utilized to differentiate in-situ (natural and hydraulic) fractures from fractures created while removing the core from the barrels. The recovered core captured hundreds of hydraulic and natural fractures and in many cases captured the interaction of a hydraulic fracture with a natural fracture. Comprehensive hydraulic and natural fracture characterization was performed by consortia-led specialized teams upon core extraction. The process of identifying the fractures is described by Gale, 2018. Figure 5C shows a hydraulic fracture cutting across a natural fracture with a slight offset. Documented SCW hydraulic fracture

frequency and complexity is considered to exceed current industry technology with respect to hydraulic fracture modeling and simulation technology. Results from the SCW, subsurface proppant distribution, and insights from other acquired data sets is providing the basis for the research team to visualize and describe the physical parameters of subsurface hydraulic fracturing process.

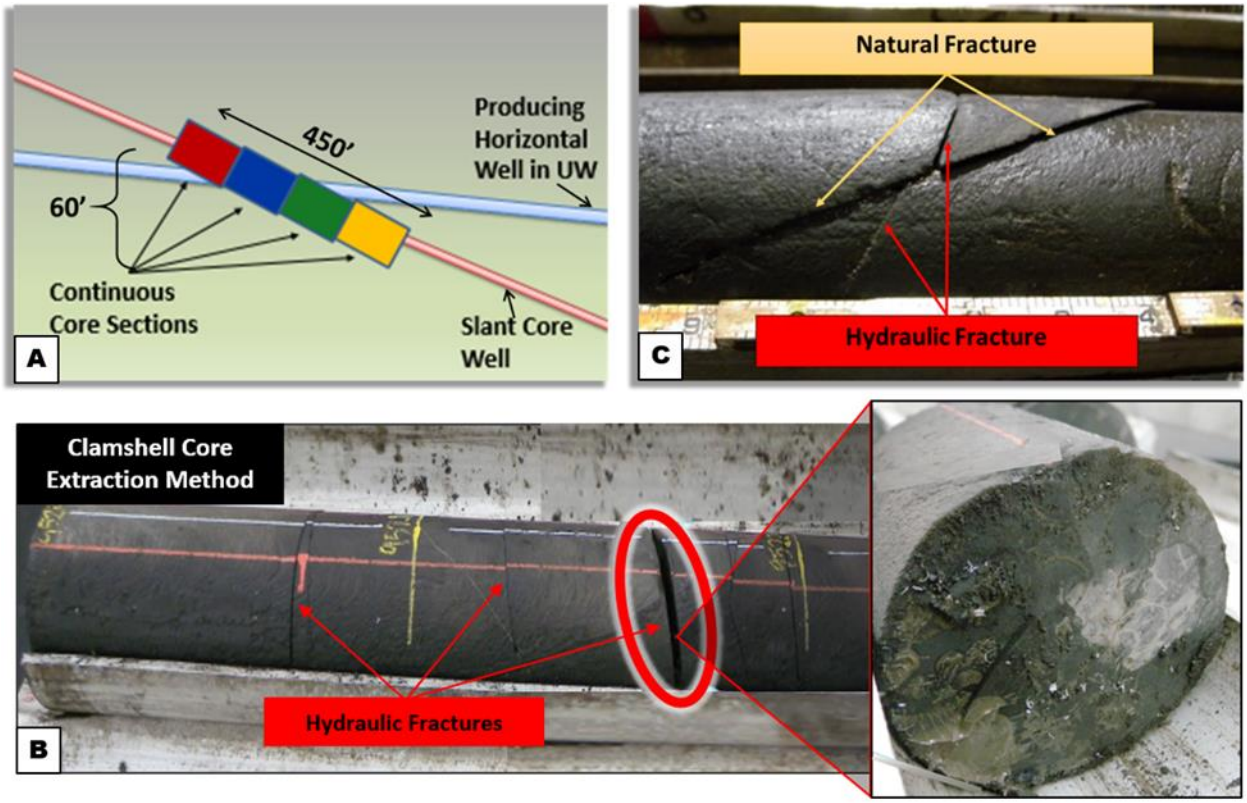


Figure 5: A) Depiction of continuous core sections collected adjacent to the stimulated producing Upper Wolfcamp well. B) Whole core interval after clamshell core barrel extraction method. Hydraulic fracture plane shown in right panel. C) Example of a hydraulic fracture cutting a natural fracture captured in the core.

Proppant Analysis

The recovered core provided a unique opportunity not only to capture hydraulic and natural fractures, but also to capture material contained within the fractures (Elliott et. al., 2018). Since proppant was pumped during the fracturing slurry in the immediate adjacent wells, it was anticipated that proppant would be discovered in the collected whole core within hydraulic fractures. Following core extraction, sludge residue from coring operations within the core barrels including drilling mud, rock cuttings, proppant and aluminum shavings from the clam-shell process was recovered. A sample was collected and catalogued by depth interval for each 3-foot section of the cut core for analysis (Figure 6 left panel). Most of the sludge was located on the exterior of the core, and within the core barrel itself (Maity et. al., 2018).

Determining proppant distribution within the SRV after hydraulic stimulation was a primary objective of the consortium. Ensuring accurate and reliable proppant detection protocols within the interval of the experimental slant core well was therefore of paramount importance. Detailed sampling procedures of proppant and associated residues was undertaken on all fracture faces, the exterior core surface, and within the core sleeves. Samples were processed following comprehensive cleaning and preparation procedures. Dried, segmented, and weighed samples were then scanned using high-resolution transparency imaging. Imaged

samples were processed using an automated image processing workflow to detect all identifiable particles of interest, including proppant, natural calcite, and shale (Figure 6, right panel).



Figure 6: Oily sludge in jar collected from core. After washing, proppant and other particles can be identified and quantified in count, shape, size, color, etc.

Lateral and vertical distribution of proppant has been documented via proprietary workflows developed by the consortia, which, incorporated with other available data, is anticipated to improve proppant distribution modeling and simulation technologies (Maity, D, et. al., 2018). To identify the origin of hydraulic fractures and proppant located within the SCW, over twenty unique chemical oil and water tracers were pumped during completion operations, as well as colored proppant. In order to detect the radioactive, oil and water tracers, an extensive fluid sampling and well logging program was employed in most newly drilled producing wells and some pre-existing offset wells.

Water Quality

Water for hydraulic fracturing operations was supplied from local water wells as well as treated, produced water. Monitoring of water quality in five landowner-owned water wells within 5,000 ft of HFTS provided insights into any potential impact of unconventional oil and gas operations. There was no detectable communication between the shallow Edward-Trinity Plateau reservoir and deeper hydrocarbon bearing zones activated by stimulation and production efforts. Levels of methane and BTEX remained at "non-Detectable" levels and there was no increase in constituents related to hydraulic fracture fluids from February 2015 through January 2017. (Eisenlord et al., 2018)

While supplying water for hydraulic fracturing operations, an increase in total dissolved solids and conductivity in the water wells was detected. There were no changes in total organic carbon or other oil and gas indicators. These anomalies are attributed to the drawdown of the local water supply for hydraulic fracturing efforts and the subsequent influx of water to the water reservoir from more saline regions. This portion of the aquifer was identified as a "priority groundwater management area" by the Texas Water Development Board and is less likely to assimilate large changes in volumes quickly. The total dissolved solids and

conductivity levels remained within normal ranges for the aquifer. When sampled six weeks after initial production, water quality had returned to baseline. Microseismic and tilt meter surveys further indicate hydraulic fractures did not grow into freshwater zones.

Air Quality

Air quality data gathered at HFTS indicates that hydraulic fracturing and production of the eleven test wells did not affect local air quality (Eisenlord et al., 2018). Methane, particulate matter (PM 10), VOCs, and NOx were measured 1,000 ft upwind and 1,000 ft downwind from the HFTS site. Upwind measurements were subtracted from downwind to account for emissions occurring near the test site unrelated to HFTS activities. Data was acquired before stimulation to serve as an air quality baseline. The data presented is the change in constituent concentrations from the baseline monitoring, using 12-hour averages over 72 hours of measurement. Deviation from baseline at each time point is presented in Figure 7. The same air sampling techniques were used to measure air quality at the closest city, downtown Midland, to provide an urban reference point. As shown in Figure 7, hydraulic fracturing and production operations did not alter air quality 1,000 ft from the well pad. Air quality on site is like Midland, TX. Benzene and Toluene concentrations were elevated during flowback operations but did not approach the concentrations the National Institute for Occupational Safety and Health (NIOSH) limits for health concerns. No differences were found to be statistically significant.

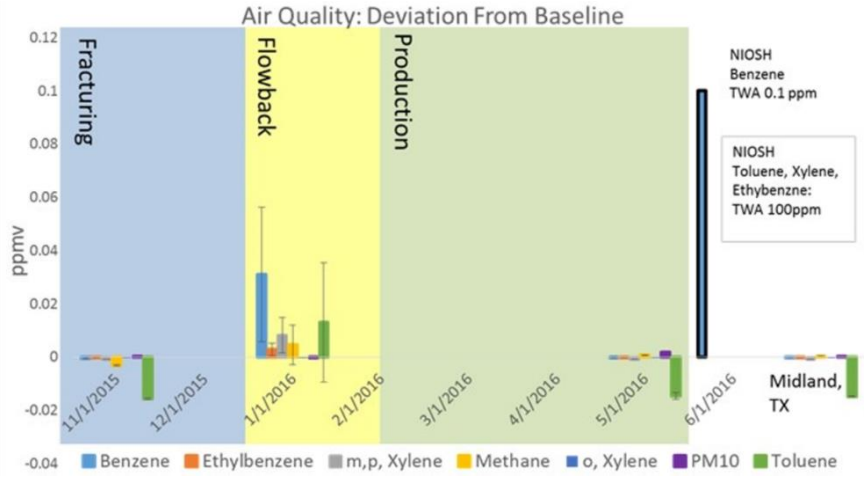


Figure 7: Air quality results from HFTS site near Midland TX. The data shown is the deviation from baseline air quality before HFTS operations began.

Variable Rate Fracturing (VRF)

Most hydraulic fracturing designs in shale utilize a predetermined fluid pump rate, which once achieved is held constant throughout the treatment, excluding situations when surface pressure limitations or other conditions prohibit it. The HFTS has undergone successful testing of a new patented method (Ciezobka & Salehi, 2017) of pumping hydraulic fracture treatments where the fluid pump rate is rapidly changed from the predetermined maximum rate to a significantly lower rate, and then rapidly increased back to original maximum rate. The rapid changes in the fluid flow rate, or a rate pulse, temporarily produces a pressure pulse of hundreds to thousands of psi (Figure 8). This pulse propagates in the wellbore from the surface to the perforations. If the created pulse pressure (p) is combined with existing bottom-hole pressure and is higher than perforation breakdown pressure, previously un-opened

perforations will open and create initiate new fractures. Real time analysis of both the perforation efficiency as well as downhole pressure response using modeling methods allowed for careful design and implementation of these rate fluctuations.

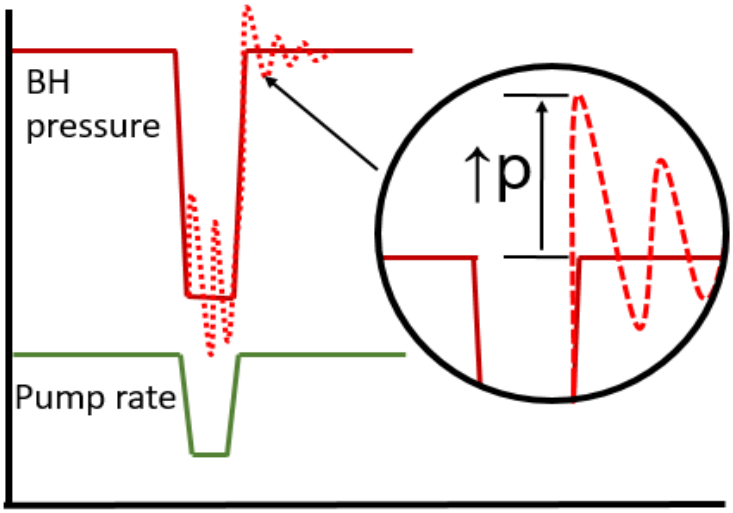


Figure 8: Example of a rate pulse and the resulting pressure pulse created with Variable Rate Fracturing.

The rate pulses were executed throughout each fracture stage, including during the pad and slurry portions of each stage. The rate pulses in the pad are critical to increasing the number of open perforations which in turn, create additional hydraulic fractures, improving connection to the shale reservoir matrix immediately near the well. Newly drilled and completed offset wells were used to baseline the VRF test well. Production was compared to the offset wells which did not include variable rate fracturing and had similar completion designs. The average production increase for the VRF test well after 14 months on production outperformed four adjacent wells with same or higher proppant loading (Figure 9).

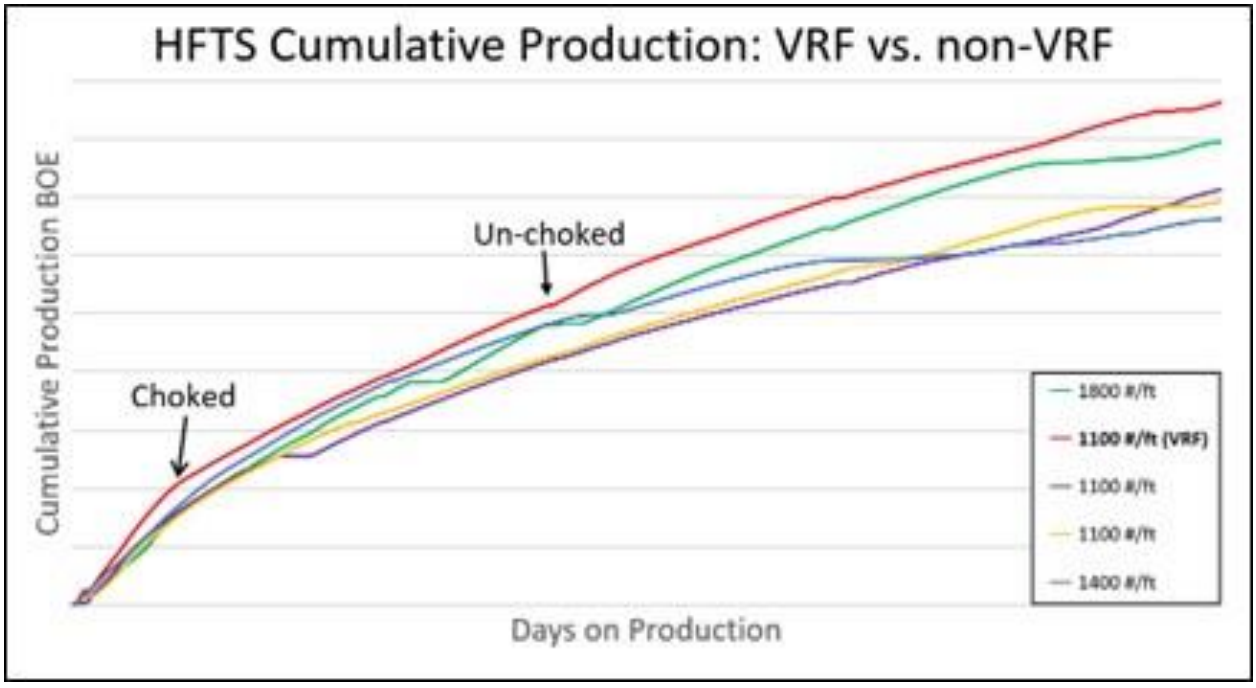


Figure 9: VRF well performance uplift relative to offset wells. Proppant loading is noted in the legend.

Tracer Results

During completion of the horizontal wells, oil-based, water-based, and radioactive tracers were

pumped to measure communication during the initial production period. Fluid samples were analyzed periodically through the first two years of production and showed limited hydraulic communication between the Upper and Middle Wolfcamp producing reservoirs with the amount of communication decreasing over time. (Wood et. al., 2018)

Microseismic

The hydraulic fractures observed and described in the SCW correlate to regions of intense microseismic activity. Analyzing time-series Kernel Density Estimate (KDE) maps of microseismic events across multiple stages within the HFTS shows a consistent trend of heelward migration of microseismic event density throughout the treatment of multiple stages (Fairfield et. al., 2018). The time series KDE maps also provide an indication of which specific perforation cluster is active at a given time, which in turn can be associated with the hydraulic fracture behavior observed in the SCW. Areas of increased event density within time-series KDE maps correlate with cored intervals containing independently documented high-certainty hydraulic fractures along with proppant packs with colored sand traced to a nearby stage. Changes in microseismic signature are also correlated with changes in pump rates and pressures during treatment. Correlations such as this along with the use of KDE maps show that microseismic event density can provide insight into hydraulic fracture density and complexity around a stimulated well (Fairfield et. al., 2018).

Geocellular Earth Modeling

All available geological and geophysical information was incorporated into proprietary geomodels used to understand the placement of horizontals and data collected in three-dimensional space. The geomodel was based on a structural model that incorporates all formation and zone tops in addition to depth converted seismic horizons. The petrophysical information from the vertical wells was propagated utilizing trends with acoustic impedance. The resulting geomodel properties had a resulting vertical cell height of five feet. The geomodel provides a basis to integrate all key reservoir and mechanical property data enabling interpretation and hydraulic fracture and production simulations.

Predictive Analytics Natural and Hydraulic Fracture Modeling

Natural and hydraulic fracture quantification and descriptions in combination with a comprehensive log suite acquired over the same interval on the SCW facilitates development of nonlinear multivariate analytical workflows to determine a predicted response of natural and hydraulic fracture intensity based on measured reservoir properties. This provides high quality geomodel inputs for a discrete fracture network (DFN) utilized in hydraulic fracture modeling and reservoir simulation. Given challenges typically associated in developing dependable DFN's, predictive analytics derived DFN's based on fracture quantification from core studies provides higher confidence in understanding how DFN's affect well performance. Additionally, characterizing the fracture complexity of the hydraulic fracture network provides insights into production impacts and can enhance decision making processes behind future completion design scenarios. (Campbell et. al., 2018).

Conclusions

Results outlined in this section comprise a high-level summary of select aspects of HFTS

consortium work, at various stages of completion. While tremendous empirical insights into hydraulic fracturing have been achieved, results presented here represent a mere sample of the anticipated total research and knowledge that will follow over time.

A priori studies of hydraulic fracturing from core provide a compelling data set to compare commonly applied hydraulic fracturing concepts and models. Early results indicate the understanding of hydraulic fracture behavior will advance because of these new data, serving to benefit future stimulated horizontal wells in the Permian Basin and other shale reservoirs. The objective behind the extensive HFTS data collection and interpretation effort is to optimize fracturing of horizontal wells leading to safe, practical, and economic development of unconventional resources.

Site-specific results from the HFTS Phase 1 include:

1. Observed hydraulic fractures in the core appear in varying densities and can display highly complex interactions and geometries, which are considered beyond current industry hydraulic fracture simulation technology.
2. Natural fractures can be reactivated and impact the complexity of the hydraulic fracturing (Gale et. al., 2018).
3. The Upper Wolfcamp reservoir demonstrates five times more combined fractures (hydraulic, natural and combinations thereof) versus the Middle Wolfcamp formation (Gale et. al., 2018). Future completion designs could be adjusted to account for the varying levels of fracture quantity and complexity to maximize resource recovery in formations with varying rock properties.
4. Proppant sampling studies indicate proppant is distributed within complex geometries, at varying concentrations, within limited vertical extent and at higher concentrations near wellbore. The majority of sampled proppant is located proximal to perforation clusters and toward the toe-direction of the perforation cluster and well.
5. Vertical proppant distribution is measured to be a small percentage of the recorded microseismic cloud height at the core intersection with the hydraulic volume. The core well indicates low fluid viscosity and fracture complexity limits vertical proppant transport (Maity, 2018).
6. Variable rate fracturing provides an uplift to production by improving perforation efficiency without adding additional cost.
7. Water and air quality studies over the HFTS site demonstrate safe and environmentally sound practices were always employed with no statistically significant detrimental impacts measured. Specifically, no connection between shallow aquifers and Permian reservoirs was observed.
8. Limited communication from fluid tracers is observed between wells in the Upper Wolfcamp and Middle Wolfcamp formations.
9. Predictive analytics workflows can be leveraged to reliably predict occurrence of both hydraulic and natural fractures based on measured reservoir properties.

The next few sections of this report provide a compilation of specific data collection and

studies conducted as part of the Phase 1 project. These will discuss both microseismic and surface seismic monitoring, core characterization work, proppant analysis, tracer studies, etc. to name a few.

Core fracture description of the HFTS Phase 1 slant core

Authors: Julia F. W. Gale, Sara J. Elliott, and Stephen E. Laubach

Abstract

Objectives and Scope: The geometry and extent of the hydraulic fracture network produced during well stimulation are usually not well known. Indirect methods such as microseismic monitoring may provide information on the network but are not definitive. For this reason, the Hydraulic Fracture Test Site project was designed to recover core from a stimulated volume, where the core provides direct information about the hydraulic fractures. Here we present the methods and some results from a fracture description of the HFTS slant well (Sugg A 171 6TW), where core was taken through a stimulated reservoir.

Methods: The examination was done on whole 4-inch diameter core prior to slabbing, with the core contained within an aluminum tube. A CT scan of the core was made available. We developed criteria for distinguishing between hydraulic, natural, drilling-induced and core-handling fractures by examining the orientation and surface features of all fractures.

Results: More than 700 fractures total were found in 600 ft. of core, including hydraulic fractures, two sets of calcite-sealed natural fractures, drilling-induced and core-handling fractures. Hydraulic fractures were found to be most abundant in the section of the core that was closest to the stimulated wells.

Significance: The benefits from an experiment of this type are: 1) Hydraulic fractures are observed directly, allowing fracture density and spatial distribution to be quantified. 2) Twist hackles on hydraulic fracture surfaces may provide information about the direction of fracture propagation. 3) The degree to which natural, sealed fractures have been reactivated may be assessed. 4) Proppant distribution in the fractures can be examined. 5) Details of the observed hydraulic fracture network can be used to verify, or provide input data for, models of hydraulic fracture growth and proppant distribution. 6) The findings can provide ground truth for indirect diagnostic techniques such as microseismic monitoring. 7) Fractures in core and image log can be compared and used in calibrating other horizontal image logs.

Introduction

Knowledge of the extent and geometry of hydraulic fracture (HF) networks in unconventional reservoirs is generally limited. Operators instead rely on indirect observation of HF growth through comparisons with mine-back experiments, tracking microseismic activity (e.g., Fisher & Warpinski, 2012), on modeled HF growth processes, and on replicating HF growth and interaction with weak planes in geomechanical experiments (e.g., Lee et al., 2016).

While these techniques provide many useful insights, verification of results by direct observation of hydraulic fractures is needed, and the best method to achieve this is to take core through intervals that have been hydraulically fractured. Previous studies adopting this method examined HFs in tight gas sandstones including Warpinski et al. (1993) and Branagan et al. (1996) in the DOE MultiWell site in Colorado, and Fast et al. (1994) in Lost Hills Field, California. Raterman et al. (2017) reported a direct sampling experiment in the Eagle Ford Formation, but in that case, there were very few natural fractures. The Hydraulic Fracture Test Site (HFTS) project described here acquired six cores comprising four continuous cores in the

Upper Wolfcamp and two continuous cores in the Middle Wolfcamp in the LAREDO SuggA 171 6TW slant well, located in the Midland Basin, Reagan Co., West Texas. In this case there are abundant calcite-filled natural fractures. Courtier et al. (this volume) provide background on the wider project, whereas this paper presents a systematic fracture description for the six cores from the slant well. We characterize natural, drilling-induced, and hydraulic fractures in the slant core, documenting the extent of reactivation of sealed natural fractures and bedding planes.

Slant core: acquisition, handling, and preparation for analysis

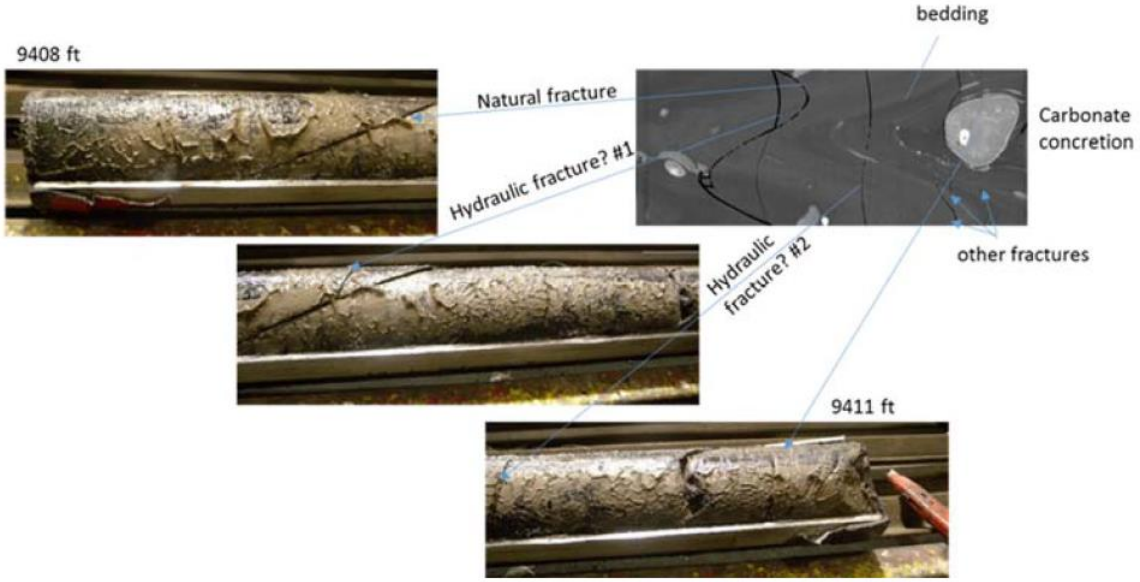


Figure 10: The core is left whole while the aluminum tube is bisected and opened to reveal core ("clamshell" method). Example test on section 9,408–9,411 ft, where the core has several fractures. Top right is the CT scan for this 3 ft section.

Locations of cores along the well selected to optimize the chances of capturing hydraulic fractures from two nearby stimulated wells (6SM and 6SU). Approximately 600 ft of core was recovered: ~400 ft in four continuous cores from the Upper Wolfcamp and ~200 ft in two continuous cores from the Middle Wolfcamp. The cores were encased in aluminum tubing to minimize break-up along fractures. CT scans of the core were made at CoreLab prior to core observation and the zero datum for the CT scan was marked on the core ends. The CT scans proved invaluable for mapping fractures in the core, with clear imagery of lithology changes, bedding, sealed natural fractures, and open fractures. They provided a ready 3D inventory of fractures for documentation purposes, and any fractures caused by core handling after the CT scans were done, or that were the result of core desiccation, could be identified as such by comparison of the CT scan with our direct observation. A further benefit of having the CT scan ahead of removing the core from the aluminum tubes was that we were able to anticipate the amount of fracturing and likely fragility of each 3-ft section. This knowledge was used to test three methods for removing the core from the tube for observation, while preserving the fracture features, and to decide whether to slab the core.

Method 1: the aluminum tube only was cut in a "clam shell", with a 50:50 cut subparallel to bedding (Figure 10). Fractures were easily examined after the drilling mud had been scraped off. Core pieces could be taken out and replaced, and the aluminum tube could be replaced once examination was complete. Damage to core was minimized using this method. Once the

analysis was done, the whole assembly (core and tube) was put back together and secured with shrink wrap for storage. This method was found to be the best of the ones tested.

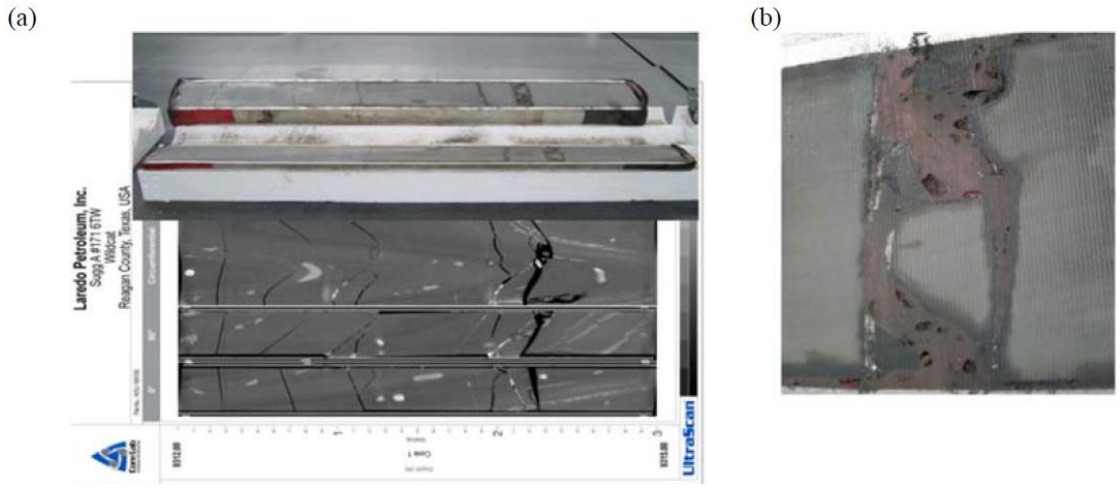


Figure 11: (a) CT scan and photograph of slabbed core from 9,312 to 9,315 ft measured depth (MD). This core section has multiple breaks and was treated with red epoxy prior to slabbing. (b) In places the force of introducing epoxy (red material) had widened existing fractures from their original width of 1–2 mm to around 1 cm.

Method 2: two 2 ft sections were stabilized with red-stained epoxy prior to slabbing (Figure 11). The sections that were epoxied (9,312–9,315 and 9,375–9,376.2 ft) and then slabbed subparallel to bedding were stabilized, but the fracture surfaces are no longer visible (Figure 11a). Although this technique prevents further breakup of the core, it is the least desirable option because inspection of the fracture surfaces is essential for determining fracture origin. Also, introduction of epoxy had widened some of the fractures considerably (up to 1 cm), so the geometry now observed is not the true, original fracture geometry (Figure 11b). No further sections were epoxied.

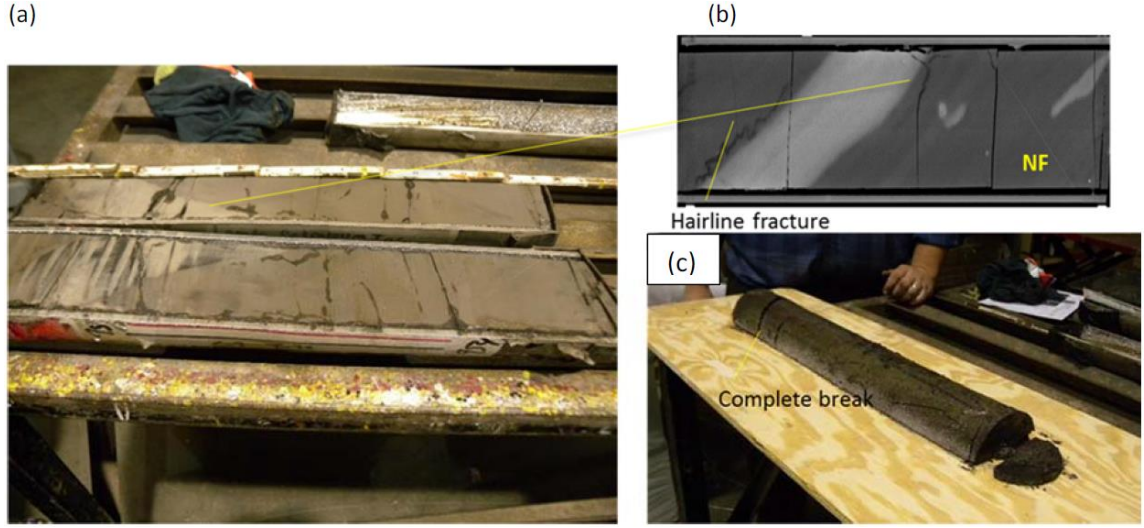


Figure 12: Core section from 9,539 to 9,541 ft. (a) Slabbed section inside aluminum tube. (b) Slice through CT scan of this interval. Pale carbonate layer and can be seen in whole core (a). Fracture face cannot be observed without removing core from tube. (c) Core has been removed from tube and inverted on the bench. The act of slabbing and removing core from the tube has generated a new complete break, the beginnings of which is visible as partial hairline fracture on CT scan.

Method 3: the core was slabbed in the sleeve with no stabilization (Figure 12a). The CT scan (Figure 12b) showed that this short section from 9,539 to 9,541 ft had several fractures in it. Once cut open, even with a 50:50 cut, the pieces of core could not easily be taken out of the

halved tube and had to be turned out on the bench for observation of fracture faces. This activity resulted in new breaks being created in the core (Figure 12c), and it was decided that slabbing, even with the core in the tube, was too damaging and should not be done prior to fracture description.

Systematic Description Methodology

The systematic description for fractures includes information on depth, orientation, aperture and fill of natural fractures, length and height, morphology and surface features, presence of proppant pack, information on faults, and an assessment of fracture origin, together with a measure of certainty of interpretation. This paper summarizes the descriptive methods and results.

Depth and Number

Fracture depths were reported by measured depth (MD) at the up-hole limit for the fracture. Each fracture is uniquely identifiable by the 3 ft core section and a fracture number.

Orientation

Fracture orientations were measured by Busetti and Farrell (unpublished HFTS report) and integrated with our fracture descriptions. We performed a qualitative check that orientations were consistent with our interpretation, using the CT-scan to aid in identification and description. Bedding is clear in most sections due to variation in carbonate content of adjacent beds (Figs. 1-3). In a few locations, the bedding dip azimuth and core axis become close to parallel because of changes in bedding orientation. Bedding undulates around concretions as well.

Aperture and fill

Fracture width (kinematic aperture) is the wall-to-wall distance measured normal to the fracture including mineral fill and any opening. For intact fractures in the slant core that are mostly less than 1 mm wide, we used a ruler (comparator) with calibrated, logarithmically graduated widths marked for comparison with fracture kinematic aperture (Ortega et al., 2006). The measurements are thus binned according to the marked widths. For parted fractures, the thickness of cement on walls is measured and reported as a minimum aperture. If filled, the mineral cement type was identified, and the completeness of fill noted as a percentage.

Length and height

Most fractures continue beyond core boundaries, meaning that length and height data cannot be obtained. If a fracture terminates within the core, the nature of the termination can be interpreted, for example, a gradual taper to the tip or an abrupt termination at a lithology change, a bedding plane, or another fracture. For fractures completely contained within the core, the length or height was recorded.

Morphology and surface features

Fractures may be planar, curviplanar, or irregular. Surface markings include slickensides, plumose structure, twist hackles, and arrest lines. Some fractures have remarkably smooth faces, others are rough and irregular. We use this difference to distinguish between fractures that formed under large confining stress in the subsurface (HFs or drilling induced fractures)

from those formed during core retrieval or handling.

Fracture origin

Each fracture is described and classified, together with an uncertainty indicator—sure, probable, and best guess. The sure category is reserved for natural fractures in which cement could be seen or for hydraulic fractures in which a thick proppant pack or proppant patches are present. Otherwise, most hydraulic fractures are classed as probable, given the uncertainty as to whether they could be drilling induced. Best guess, the least-certain classification, is made based on a combination of features such as orientation, morphology, and surface features.

Fracture Description and Criteria for Fracture Classification

Each of the fracture types are described and we outline criteria used to differentiate them, and to identify natural fracture reactivation. The different fracture types are presented in chronological order of formation: natural, drilling induced, hydraulic, core handling.

Natural fractures

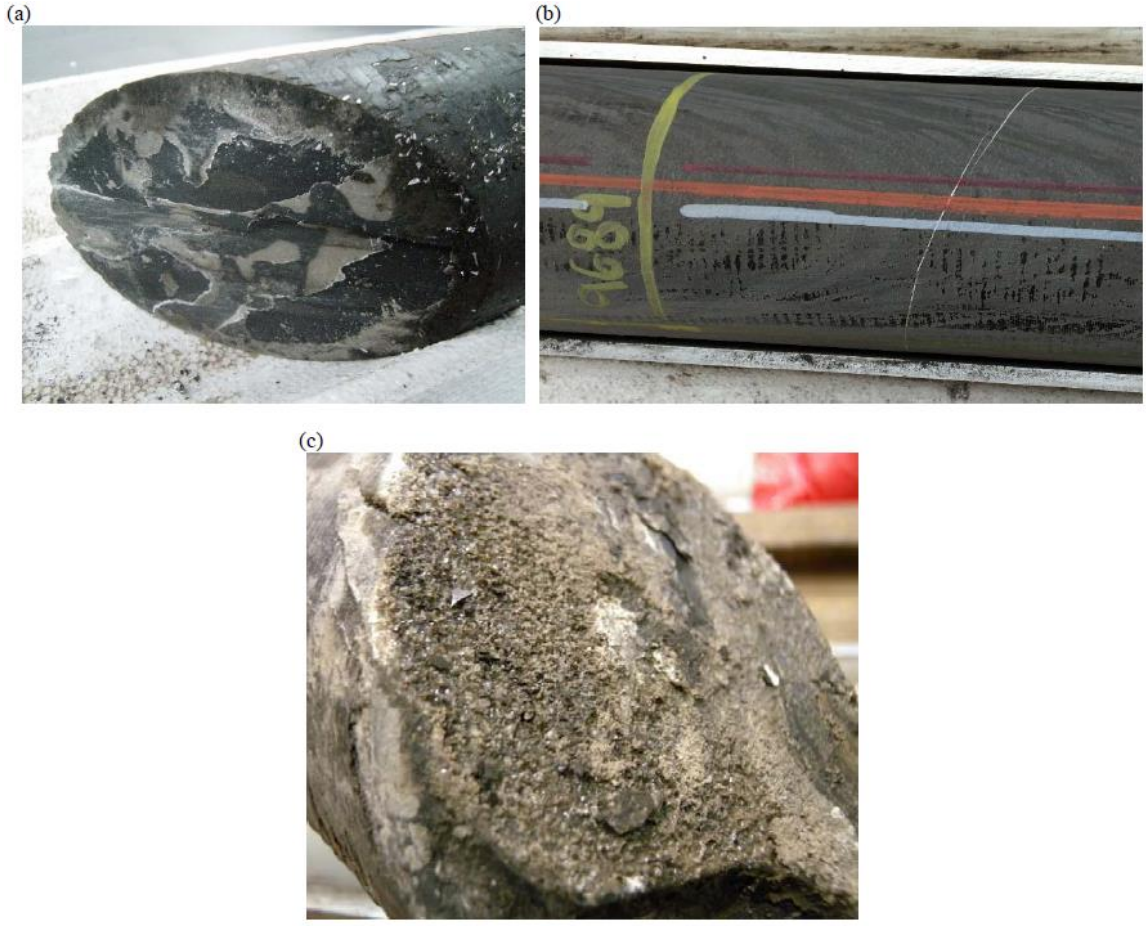


Figure 13: Natural fractures in the slant core. (a) Parted, Set 1 fracture with patchy calcite on fracture face, 9,365.10 ft. MD. (b) Intact, Set 2 composite fracture, 9,689.35 ft. MD; there are three segments, the middle segment is offset up-hole from the other two by a few millimeters. Slight deviation of the fracture path at the tips indicates stresses ahead of the tips were modified by the presence of the approaching neighbor. (c) Euhedral calcite crystals on fracture face at 9,292.8 ft indicating this fracture was open in the subsurface.

Two main sets of natural opening-mode fractures filled with calcite cement are present: Set 1 trends broadly NE-SW (Figure 13a, Figure 14a) and Set 2 trends WNW-ESE (Figure 13b, Figure 14b), both with steep dips. These natural fractures are identified primarily based on calcite

mineral fill. Fractures may be fully sealed and intact, partly sealed and intact (with original fracture porosity) or may be parted (Figure 13a). In the latter case, cement can be seen on the fracture wall(s).

This cement can be subtle and present as a patchy veneer on one or both surfaces. In some fractures positive cement identification is challenging—dried drilling mud can also resemble a pale cement veneer. The mud reacts with dilute HCl (owing to carbonate entrained in the mud) so that an acid-drop test cannot be used to identify cement. A small chip from such a fracture surface at the end of one core was imaged and examined using SEM-based EDS. The material on the surface proved to be dried drilling mud. Where positive identification of cement is not possible, orientation is a useful indicator of fracture origin, but it is not definitive by itself. In one location (9,292.8 ft in Core 1) a Set 1 natural fracture has euhedral calcite cement on the surface, indicating it was open in the subsurface (Figure 13c). We did not measure the kinematic aperture because the fracture is now parted, but estimate it was > 1 mm wide.

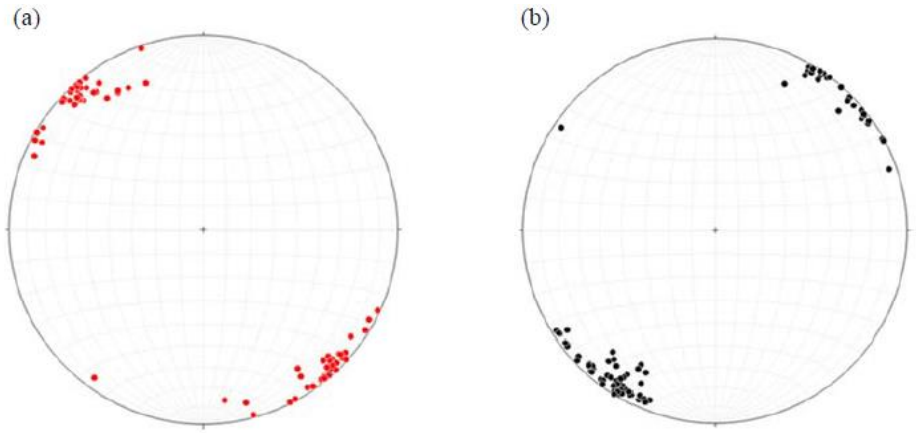


Figure 14: Lower-hemisphere stereograms of poles to calcite-filled natural fractures. (a) Set 1, (b) Set 2. Data from ConocoPhillips analysis.



Figure 15: Calcite-filled fractures associated with concretions. Some fractures are internal to concretions stopping at boundaries (IF). Others develop in shale surrounding concretions (SC) and most likely develop as result of strain localization around concretion. Example from Core 4 at 9,667 ft.

The natural, calcite-filled fractures in this well are typical of fractures in shale, occurring as narrow, composite groups typically less than 1 mm wide (c.f. those described by Gale et al., 2014 and references therein). The smallest are only a few centimeters in length and height, and the largest are perhaps 1 m or so long and high (but continue out of the core). Some are bed

bound. There are minor occurrences of other natural-fracture types, including those internal to concretions and those related to deformation around concretions (Figure 15).

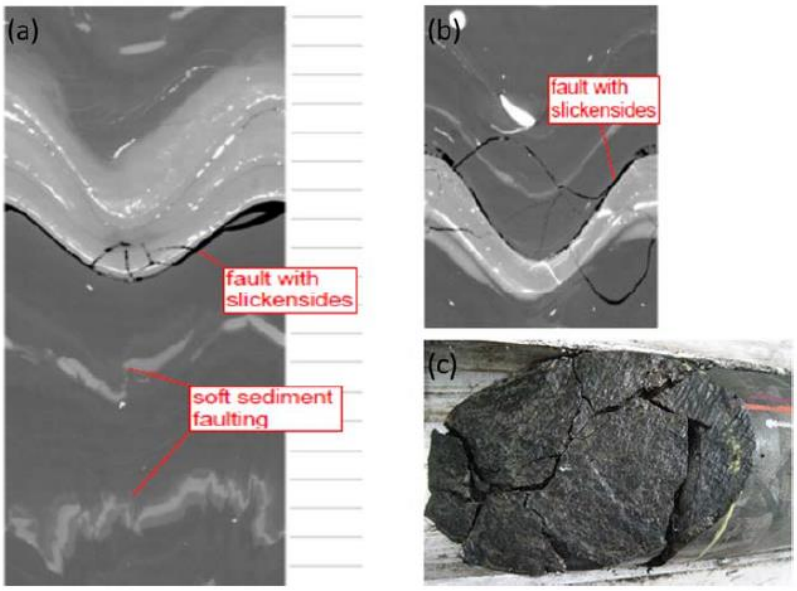


Figure 16: Faults in Core 4 at 9,675–9,681 ft MD. (a) CT scan of faulting and soft-sediment deformation (9,678–9,681 ft). (b) CT scan of fault in c, which has oblique slickensides.

Natural, bedding-parallel fractures are uncommon, occurring only around a few concretions, and we did not observe any "beef" (Cobbold et al., 2013). The core orientation and roughness of the outer surface, however, are not optimal for seeing narrow (< 1 mm-wide), bed-parallel fractures. Also, such fractures are challenging to distinguish from carbonate laminae on the CT scan. A few concretions have fractures on both margins with both calcite and pyrite fill, and there are also a few examples of pyrite-filled fractures internal to concretions. Other fractures in different orientations, filled with calcite and pyrite and having width to length aspect ratios that are generally greater than those for the Set 1 and Set 2 fractures, are present in a few locations, mostly in Core 4 close to faults. There are two types of fault: early, soft-sediment deformation faults (Figure 16a) and later, moderately dipping structures with oblique slip indicated by slickensides on the fault walls (Figure 16a–c). In the fault at 9,675.65 ft MD in Core 4, dip azimuth 22.5°/dip 57.4°, the slickensides suggest normal and dextral components of oblique slip. Some have a small amount of calcite cement. There are a total of 11 faults in the Upper Wolfcamp, 7 of them in Core 4, but none was observed in the Middle Wolfcamp.

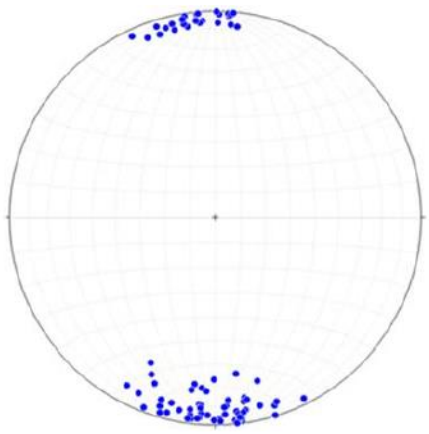


Figure 17: Lower-hemisphere stereogram of poles to hydraulic fractures. Data from ConocoPhillips analysis; n = 321.

Hydraulic fractures

Many barren, core-normal fractures are present, broadly trending E-W, which is subparallel to S_{Hmax} in this part of the Midland Basin (Lund Snee et al., 2016). Hydraulic fractures, present possibly as large planes of varying complexity, have been intersected in a singular location by the core. Thus, we only see a small snapshot of each fracture. Features on the fracture surfaces, such as twist hackles and plumose markings developed at the time of fracturing and are not related to the drilling process; they do not originate near the core margin and are not core symmetric. We identified 341 hydraulic fractures in the Upper Wolfcamp cores and 58 in the Middle Wolfcamp, totaling 399. The stereogram plotted for poles to the 321 measurable hydraulic fractures reveals an approximately 40° spread of dip azimuth, which may reflect local stress variations or branching geometries (Figure 17).

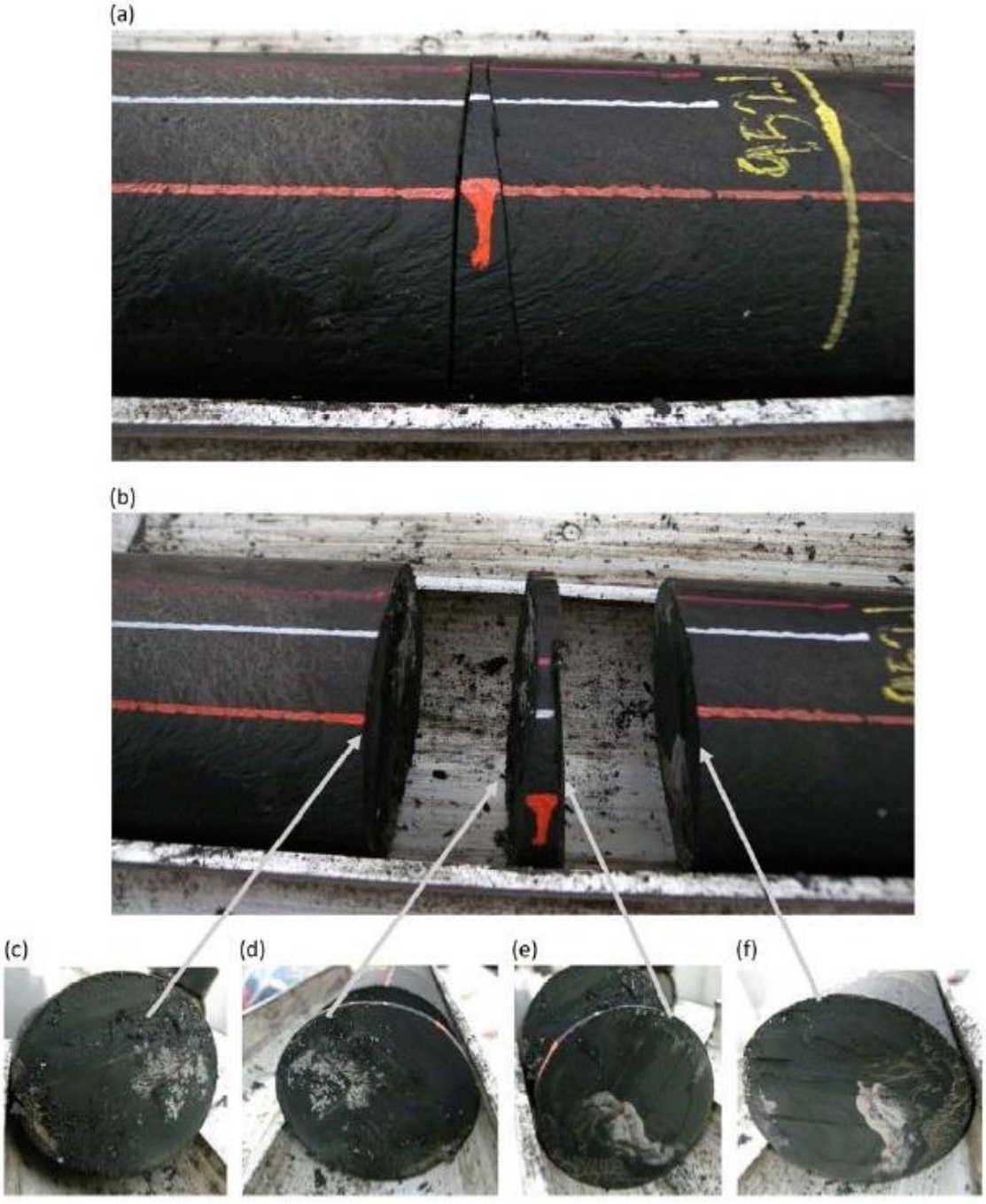


Figure 18: Hydraulic-fracture doublet indicating propagation to the west (orange mark = core top). (a) Whole core with two nonparallel fractures. (b) Core pieces pulled apart. (d–f) Fracture faces in b. (f) Example from Core 3 just above 9,521 ft.

Commonly, two to three hydraulic fractures (HFs) occur per 3 ft section, although some sections have many more (e.g., nine HFs in 9,520–9,523 ft) and some have none, including the four sections from 11,634 to 11,645 ft. Many are single planar breaks with smooth surfaces, and some have a stepped geometry (Figure 18). In other cases, two or more breaks are closely spaced, suggesting bifurcation. Clusters of two to four core-normal fractures in the space of a few centimeters are a common occurrence and may be multiple hydraulic-fracture strands (Figure 18). In rare cases, bifurcation is captured in the core and can be used to infer the direction of hydraulic-fracture growth.

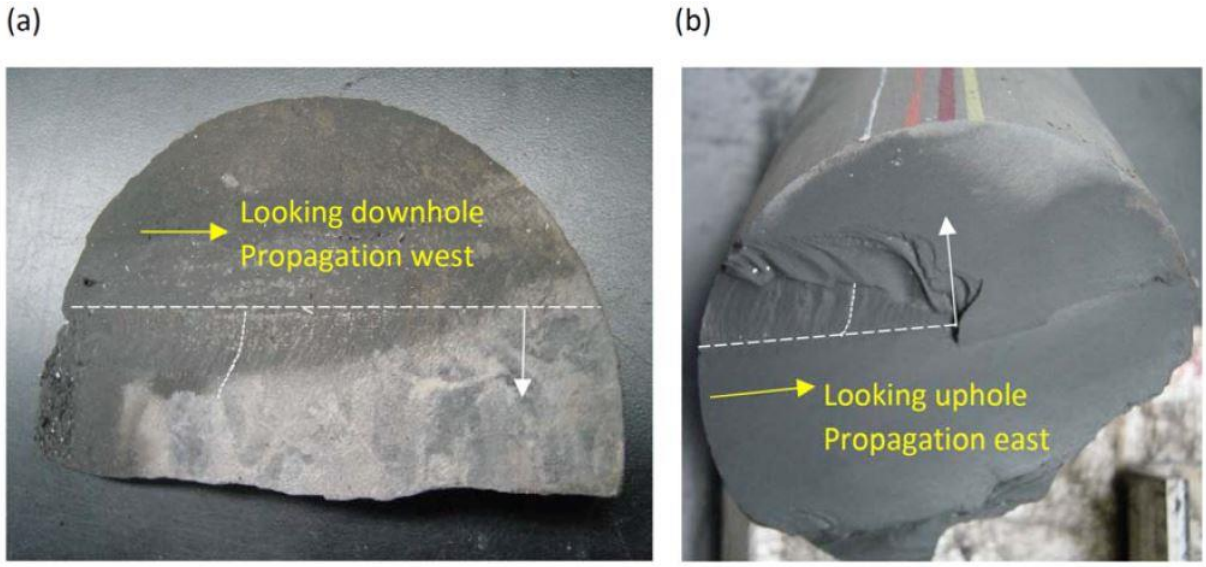


Figure 19: Examples of twist hackles (TH). Dashed line = initiation plane. Local direction of growth is normal to that line (white arrow). Overall fracture propagation direction given by yellow arrow. (a) 9,435 ft in Upper Wolfcamp; view downhole. TH initiate at pyrite layer. Propagation down and west. (b) 11,678.5 ft in Middle Wolfcamp; view uphole. TH initiate at bedding plane. Propagation up and east.



Figure 20: Example of twist hackles with anomalous orientation. At 9,372.45 ft, looking downhole, hackles suggest downward propagation. Twist-hackle asymmetry suggests overall propagation is to the east (left in photo).

In addition to bifurcation, surface markings such as twist hackles may be used to determine local propagation direction of the fracture (Figure 19). Twist hackles initiating at mechanical layer changes are orthogonal to the layer and gradually taper out away from the point of initiation. These may be used to indicate the local direction of hydraulic-fracture propagation. In some cases, it may be possible to determine wider-scale lateral propagation based on asymmetry of twist-hackle steps. Multiple examples of twist hackles occur in the slant core,

some suggesting local upward propagation, others downward, some large-scale eastward propagation and some westward.

Some twist hackles have apparently anomalous geometries, however, in that the inferred propagation direction is not consistent with the relative positions of the nearest stimulation well and the slant well. At 9,372.45 ft in Core 1, for example, twist hackles initiate off bedding and suggest local downward propagation (Figure 20). Twist-hackle asymmetry suggests that overall propagation is to the east, but the 6SU well is below and to the east of the slant core at this location and hydraulic fractures would therefore be expected to grow up and to the west.

Hydraulic fractures with proppant pack



Figure 21: Sand pack in a hydraulic fracture at 9,488.90 ft in Upper Wolfcamp. (a) 3 ft section of core with location of sand pack figured in b at base of section, where two HFs are in proximity—termed a doublet. Slightly uphole is a complex in which a hydraulic fracture interacts with a Set 2 natural fracture (Figure 17). (b) Detail of doublet. (c) Face of fracture at 9,488.9 ft looking uphole.

There are three locations where hydraulic fractures contain a sand (proppant) pack: at 9,459.9 ft, 9,488.85 ft, and 9,561 ft, all of which lie within the more intensely fractured interval in the Upper Wolfcamp. These examples are shown in detail (Figure 21, Figure 22, Figure 23). The sand pack at 9459.9 ft occurs as patches on the fracture face (Figure 21c). Notably, there is no drilling mud present, which is taken to indicate the sand was in place prior to drilling. The thickest sand pack occurs at 9488.85 ft (Figure 22). The fracture here is branched and the pack is present in each strand. The total complex is approximately 1-cm thick. In both these cases the HF is complex and branched. The third sand pack location is at a concretion (Figure 23). Where HFs encounter concretions, fractures become complex, and the concretions are shattered. The sand is visible in the fracture at the uphole end but can also be seen in some of the other breaks. A piece of the sand pack appears to have been pushed out of the fracture

(Figure 23a)—it was sampled, and the remainder left intact. The CT scan shows a bright signal in the fractures and in the concretion, which is likely to be pyrite (Figure 23b). The dark-gray signal of proppant noted in Figure 22a is not apparent, possibly being obscured by the pyrite.

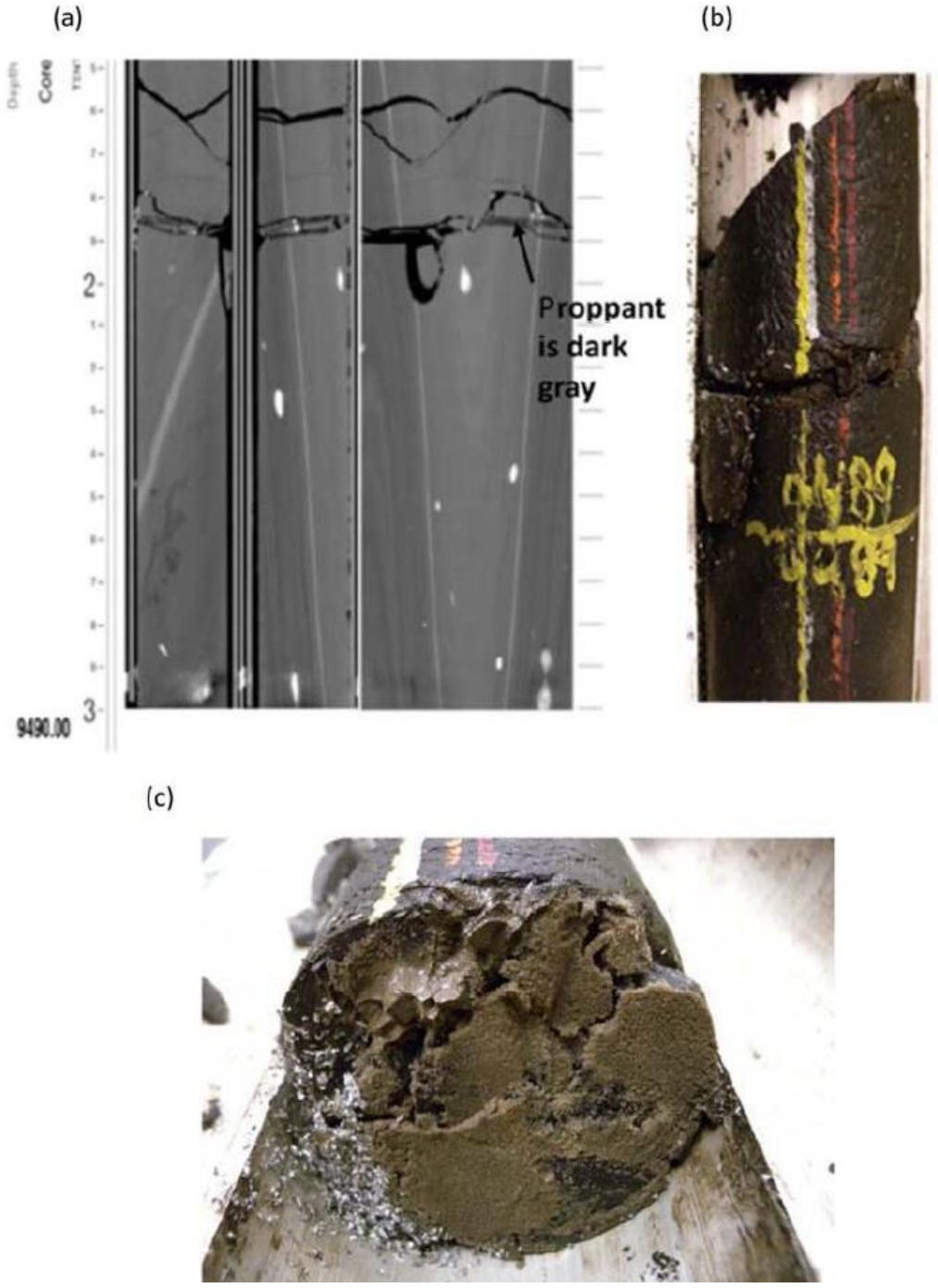


Figure 22: Sand pack in a complex hydraulic fracture at 9,488.85 ft in Core 3. (a) CT scan of fracture; proppant dark gray. (b) Intact core; fracture complex approximately 1 cm wide. (c) Sand pack viewed uphole with core piece below fracture removed. Sand has since been removed for analysis. Hydraulic fractures at this location have complex geometry that may have favored trapping of sand pack.

In several other locations there are patches of sand in hydraulic fractures. Some of these occur close to where the main proppant packs are located, whereas others occur away from the packs. The case at 9,458.8 ft is of interest because it is also an apparent interaction between a hydraulic fracture and a natural fracture (Figure 24). A similar occurrence is at 9,488.55 ft.

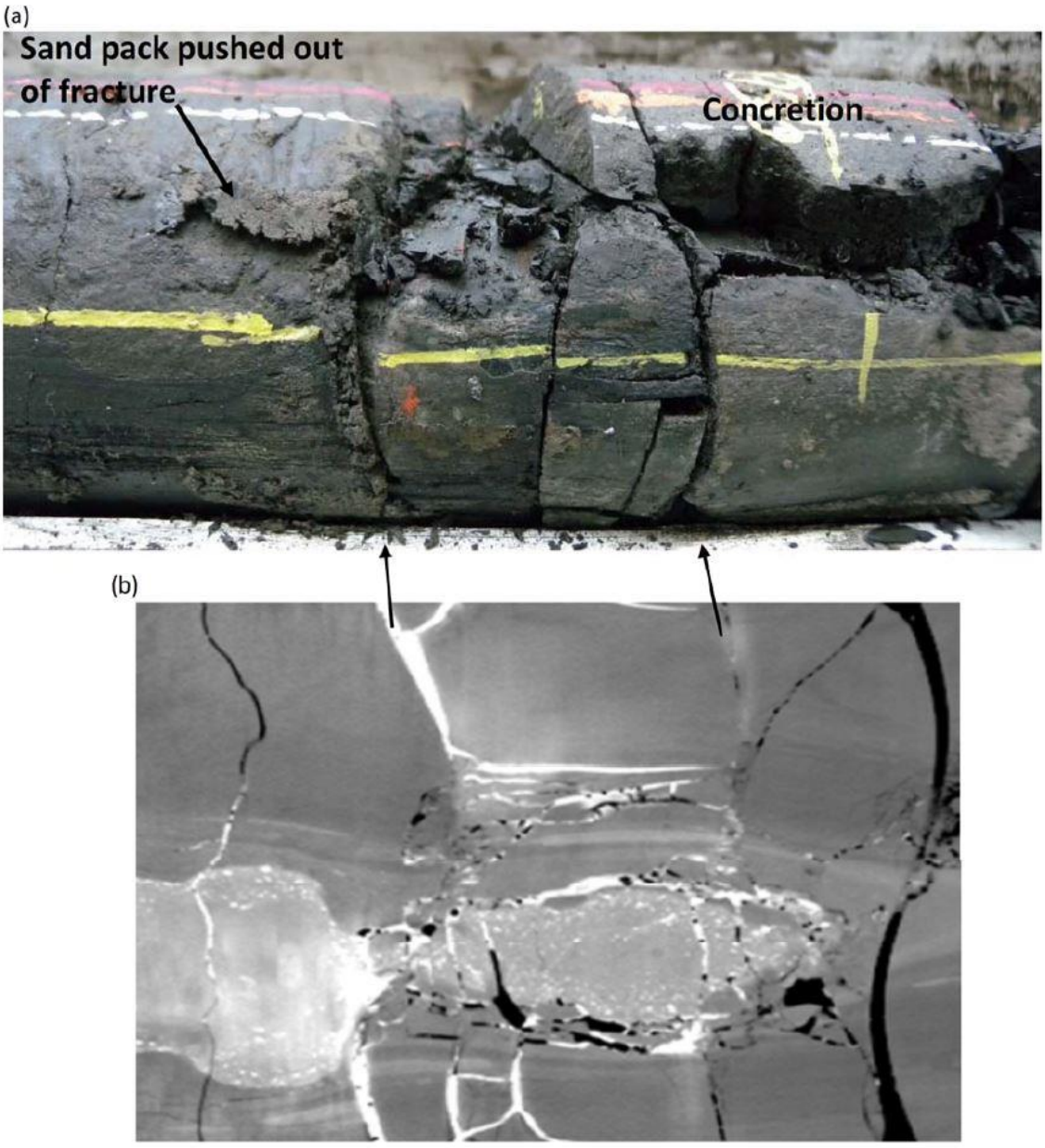


Figure 23: Sand pack in complex hydraulic fracture adjacent to concretion at 9,561.7 ft in Core 3. (a) Sand on outer surface of core with multiple breaks visible. (b) CT circumferential scan.

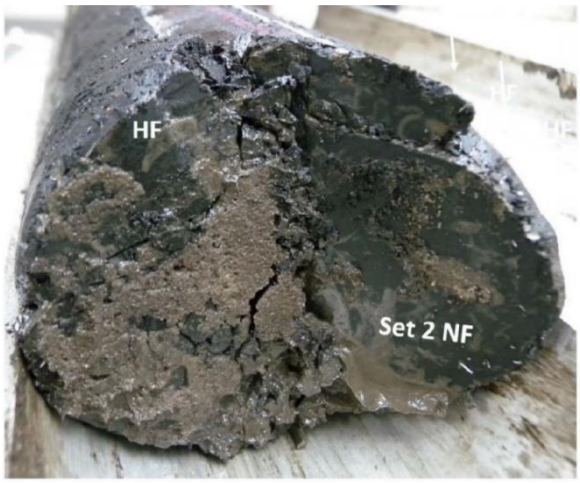


Figure 24: Possible interaction between HF and Set 2 natural fracture (NF) at 9,458.8 ft. (a) View of uphole face with thick sand patches on HF surface and some on NF face. We did not observe cement on face of NF; it was interpreted as such based on their orientation. At this location (out of view) an intact Set 1 NF also occurs with cement, although crosscutting relations were not clear.

Hydraulic fractures reactivating weak planes, such as bedding or natural fractures.

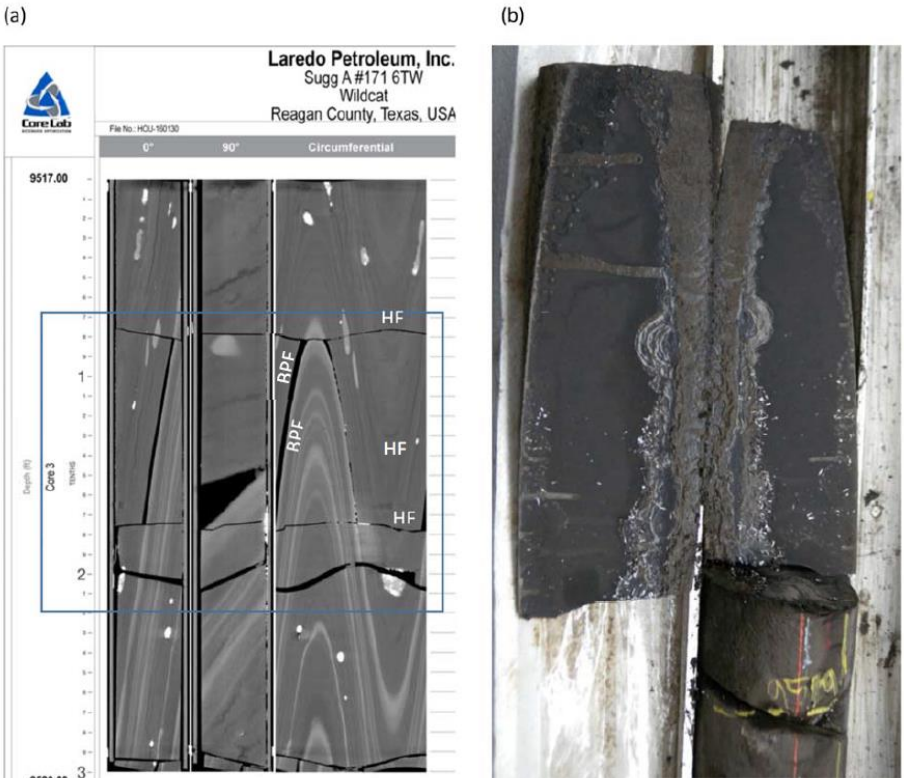


Figure 25: (a) CT scan of section with bed-parallel fracture (BPF) bounded by two hydraulic fractures (HF). (b) Photograph of bed-parallel fracture surfaces, which are smooth and planar. Drilling mud has partly invaded at the margins.

Breaks occur along some of the natural fractures and bedding planes, but the reason they are broken (reactivated) is not easy to determine. The mechanism for reactivation could be hydraulic fracturing, drilling, core retrieval stress, or core handling. For planes reactivated during hydraulic fracturing possible indicators include

(1) Bedding-plane breaks connected to a hydraulic fracture (hard linked) (Figure 25). These are smooth and planar, compared to other bed-parallel breaks, which are stepped and rough. Non-connected bed-parallel fractures could open as a result of a pressure front associated with hydraulic fracturing, and in this case would not be hard linked.

(2) Hard-linked, reactivated breaks should have some proppant in them, which is the case in the example in Figure 24, showing that proppant can travel around the angle between the hydraulic and reactivated fracture.

Drilling-induced fractures (from drilling the slant well)

Drilling-induced fractures are mostly at a high angle to the well bore and parallel to SHmax, as for hydraulic fractures. In horizontal or slant wells, drilling-induced fractures can be confined to the core top. In other cases, in which the weight-on-bit has increased significantly, breaks can occur along the bedding, with petal shapes extending outward to the core margin (Figure 26a). Induced fractures commonly have indications of breakage points within the core (e.g., core-rimming, plumose markings, and sharp points at the core margin), and they tend to be approximately core-symmetric, curviplanar (saddle shaped) (Figure 26b), or irregular. Surface markings can form, no matter the mechanism. For natural and hydraulic fractures, the markings would have no relation to core margins, barring coincidence. For drilling-induced and core

handling fractures plumose markings may emanate from a point source within the core. Some proppant grains may also be present, having been brought in with the drilling mud, but proppant will not be present as a sand pack. Drilling can also cause natural fractures or other weak surfaces to break. Differentiating these from reactivation caused by hydraulic fracturing is difficult.

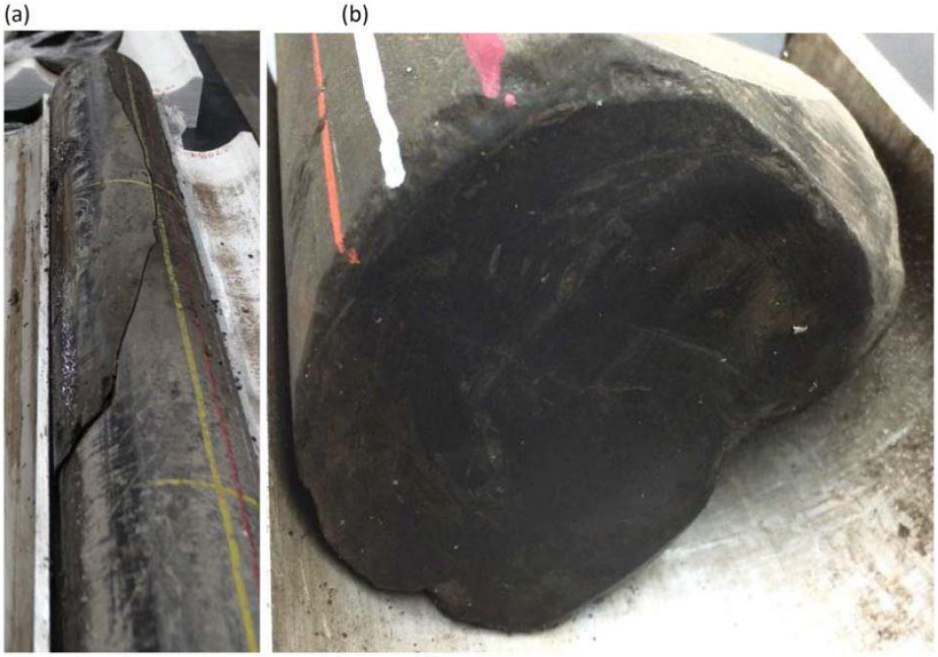


Figure 26: Drilling-induced fractures. (a) Petal centerline shape at 9,391 ft viewed looking downhole. (b) Irregular, saddle-shaped fracture at 11,564 ft.

Core recovery and handling



Figure 27: Likely core recovery fracture at 9,634 ft. Irregular surface with a sharp point (p), suggesting the break initiated within the core.

Core recovery causes vertical-stress release, commonly creating breaks parallel to bedding in vertical cores. In this slant well, there are very few examples of this, and where they do occur it is at the core margin close to another break. Breaks can also occur during core recovery as the core is retrieved around the bend at the well heel. This damage was most likely mitigated by the aluminum tube. Sharp points on the fracture face are commonly produced in core during flexural breaking, and in rotary-drilled sidewall cores can be used to identify way up (Laubach and Doherty, 1999). An example is shown from 9,634 ft (Figure 27).

Damage can also occur during sawing into sections, transportation, and other handling up to the point of CT scan acquisition. In these cases, surfaces are rough and fresh, but some drilling mud is usually present (Figure 28a). These fractures are present in the CT scan. New fractures created as a result of handling/desiccation after CT scan acquisition are not present in the CT scan. These surfaces are fresh breaks and have no drilling mud.



Figure 28: (a) Likely core-handling fracture at 9,479.6 ft. Irregular surface with some drilling mud splatters. (b) Post-CT scan break at 9,346.8 ft. It is irregular with a rough surface and has no drilling mud inside.

Fracture Distribution

The spatial organization of fractures along the core is heterogeneous. Most 3 ft intervals contain hydraulic fractures, with some present in clusters of up to 9 fractures in a single 3 ft interval, but some intervals have none. In the Middle Wolfcamp there are two 12 ft long intervals and several other > 3 ft intervals with no HFs. The intensity of HFs increases in the middle part of the Upper Wolfcamp cores, where the slant well came closest (~ 100 ft) to the 6SU stimulated well. The HF intensity represents a combined effect of distance from stimulation and propensity to fracture. The distribution of different fracture types along the length of the cores is shown in Figure 29.

Discussion

Systematic description of the 6TW slant cores revealed hydraulic fractures, natural fractures, drilling-induced fractures, and core-handling breaks, and criteria developed for distinguishing these potentially have wider application to other similar datasets. Raterman et al. (2017)

observed hydraulic-fracture doublets and triplets in their Eagle Ford study and interpreted them as being the result of HF branching at mechanical interfaces. We see similar features (Figure 18), and the slant core also captured some branch points, although the reason branching occurs is not clear. No consistent relationship with interfaces of mechanically different layers occurs, for example, and many examples of single planar HFs do not branch at such interfaces.

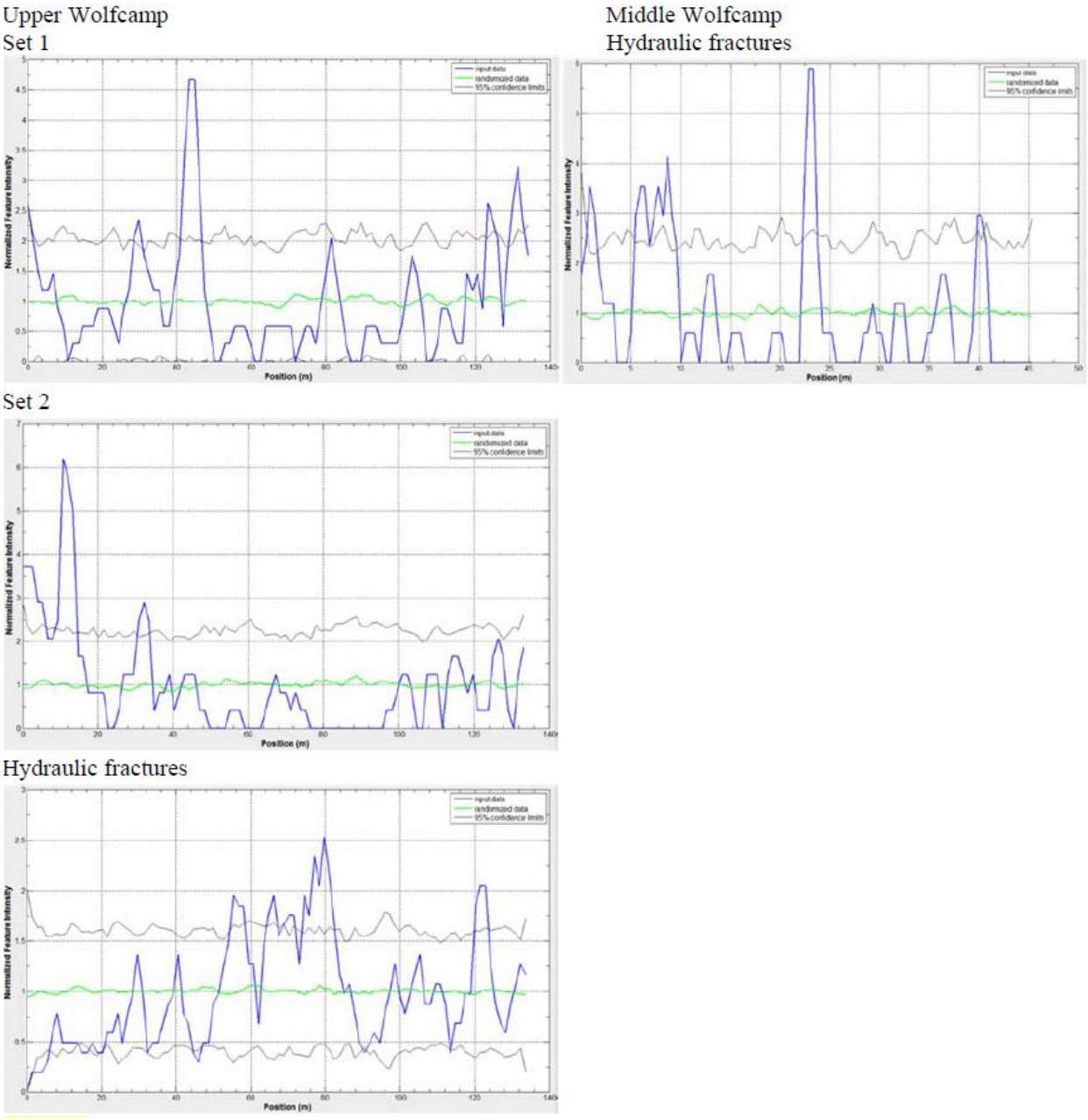


Figure 29: Distribution of different fracture types along the length of the cores for Upper Wolfcamp (left) and Middle Wolfcamp (right).

If the location of the hydraulically fractured wells relative to the slant well is known, the direction of propagation should be predictable and can be compared with observations. For the Upper Wolfcamp, because the hydraulically fractured well (6U) crosses the slant well and lies to the east of it, Cores 1, 2, and part of 3 are above the 6U well. In these cores, hydraulic fractures should propagate upward and to the west, whereas the lower part of 3 and Core 4 are below the 6U, and fractures should propagate downward, although still to the west. In the Middle Wolfcamp, hydraulic fractures would have propagated up from the 6M toward the east.

Although some observations are consistent with these predicted propagation directions, we observed some anomalies. Surface markings on fractures in outcrop (e.g., Cobain et al., 2015) show that both upward and downward propagation directions can occur in proximity within a single fracture plane (Figure 30). Our observations in the slant core may come from both upper and lower twist-hackle (fringe) zones. The lateral propagation direction, however, should be determinable from asymmetry of twist hackles (Figure 30) or from branching. A possible explanation for anomalous, inferred propagation directions is that the premise that fractures always propagate away from the well bore may not be correct. If some fractures initiated away from the well bore, then they may propagate laterally in opposing directions at the same time. A further, systematic analysis of all propagation-direction indicators in the slant core might illuminate the apparent anomalies in inferred propagation direction.

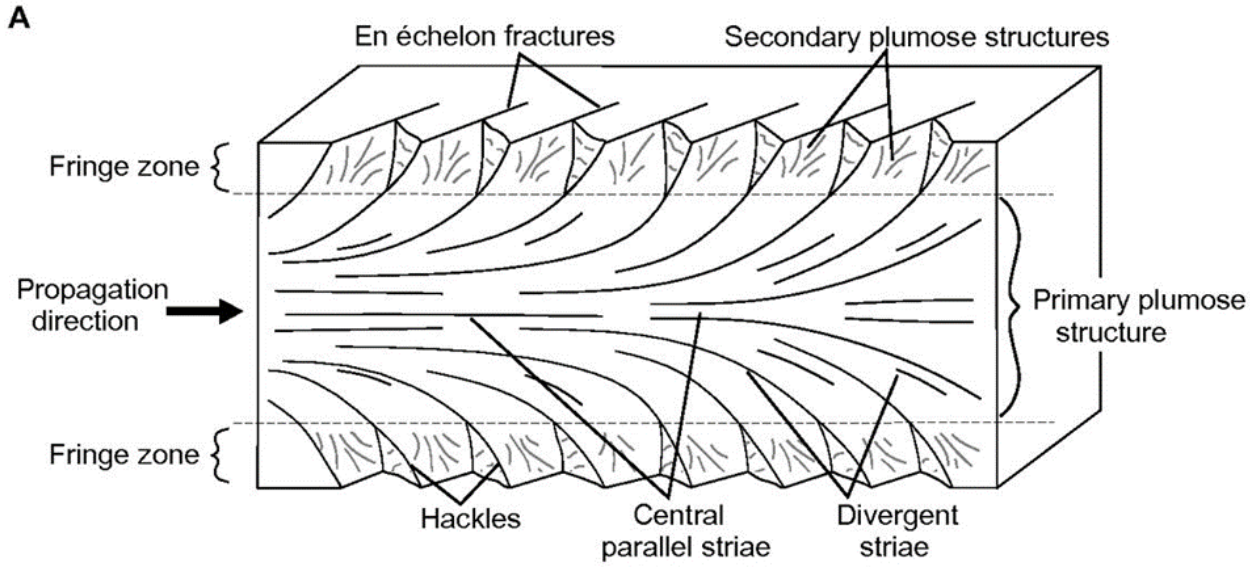


Figure 30: Diagram of plumose structure on a joint surface (from Cobain et al. (2015), their figure 6A). Note local direction of propagation indicated by twist hackles is up at the top and down at the base.

It is well established that geologic discontinuities, including natural fractures, can be reactivated during hydraulic fracture treatments, even when sealed with mineral cements (e.g., Dahi-Taleghani and Olson, 2011; Gale et al., 2014). Laboratory experiments in which a propagating crack interacts with a cement-filled natural fracture reveal the controlling factors that determine whether the hydraulic fracture arrests, diverts, or terminates against the natural fracture are the angle of approach and the thickness of the natural fracture (Lee et al., 2015). In this study we noted that whereas some of the natural fractures are reactivated, many remain intact (Figure 13b). The natural fractures in Set 1 are favorably oriented for reactivation and are mostly less than 1 mm wide, yet commonly they are not reactivated.

At the scale of a fracture stimulation, fracture patterns and in situ stress can be highly variable, even though the broad tectonic pattern may be consistent over hundreds of miles. Site-specific evaluation of natural fractures and in situ stress is therefore necessary. The many aspects of interest include the bifurcation and clustering of hydraulic fractures, and reactivation of preexisting discontinuities in the host rock. We envisage further analysis of this dataset yielding more information about growth of the hydraulic-fracture network. This information can then be used to better plan future wells and potentially provide additional information about the stimulated reservoir volume.

Conclusions

In the 6TW well, over 700 fractures, comprising hydraulic fractures, calcite-filled natural fractures, drilling-induced fractures, and core-handling breaks in approximately 600 ft of slant cores, were described, although fractures are not evenly distributed along the length of the cores. Hydraulic fractures may be distinguished from drilling-induced fractures based on morphology and surface markings. Natural fractures contain calcite cement, and they are mostly intact. Only two natural fractures were open in the subsurface prior to stimulation; they are now parted, but euhedral calcite crystals are present on the faces. Only a few bedding-parallel breaks were observed, and there is no beef.

The potential benefits of this project include verification of theoretical ideas/models of hydraulic-fracture growth of the well in question, as well as insights into the complexity (or otherwise) of the hydraulic-fracture system. Moreover, opportunities for a better understanding of microseismicity and/or aseismic fracture growth through comparison of microseismic event locations versus hydraulic-fracture paths abound.

Natural and Hydraulic Fracture Density Prediction and Identification of Controllers

Authors: Whitney Campbell, Joe Wicker, and James Courtier

Abstract

Discrete Fracture Networks (DFN's) incorporated into hydraulic fracture modeling and reservoir simulation are typically constructed and calibrated to all available high-quality natural fracture data from image logs and core, which results in an extremely limited calibration data set. To extrapolate these data over large areas, more broadly sampled data sets, such as discontinuity-related 3D seismic attributes are often used. Broad spatial trending methodologies can potentially misrepresent natural fracture systems through over-reliance on seismic attributes that are commonly influenced by noise. The Hydraulic Fracture Test Site (HFTS) provides a rare insight of the subsurface natural fracture network and controlling factors on fracture distribution from a mechanical and lithological standpoint. They physical occurrence of hydraulic fractures and their interaction and relationship to preexisting natural fractures can be predicted using analytical models. Such model outputs can be applied to provide higher confidence when developing DFN's.

Introduction

The Hydraulic Fracture Test Site (HFTS) Phase 1 is in Reagan County, TX (Figure 31). Understanding subsurface controls and operational impacts on natural and hydraulic fracture development is a primary objective of the HFTS and the focus of this paper. It should be noted that the analytical workflow described here utilizes measured rock parameters versus fluid and other engineering parameters which vary during the completion job.

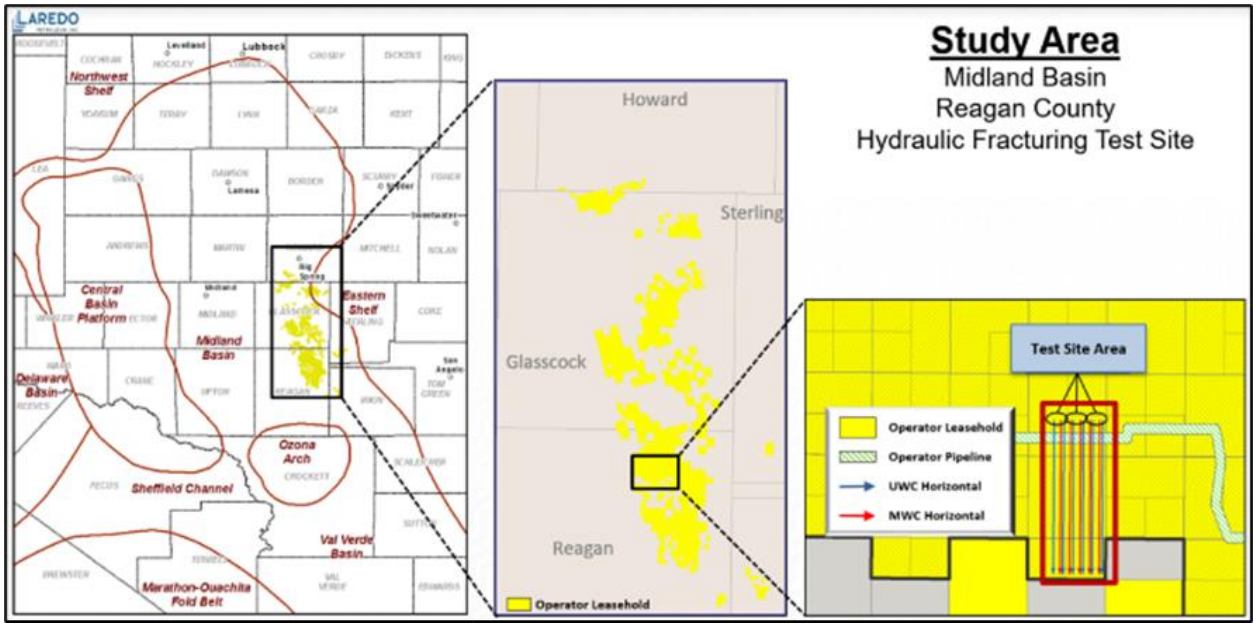


Figure 31: HFTS Phase 1 area located in core of Laredo's leasehold. Modified from Trowbridge et al., 2017.

The HFTS operation involved drilling and completing 11 horizontal wells, recompleting 2 existing horizontal wells, and drilling a slant well to collect a low-angle core at 82 degrees inclination, drilled at a closest approach of 89' from an Upper Wolfcamp (UWC) well and 135' from a Middle Wolfcamp (MWC) well (Figure 32). Along with the slant core, an extensive well data set was collected, including open-hole logs, microseismic, cross-well seismic, pressure

data, oil, water and proppant tracers, geochemical data (oil fingerprinting), and fiber coil production logs (Figure 33). The slant core fracture analysis (Gale, et al., 2018) and other interpreters make up the fundamental calibration data set for the analytical model discussed in this paper.

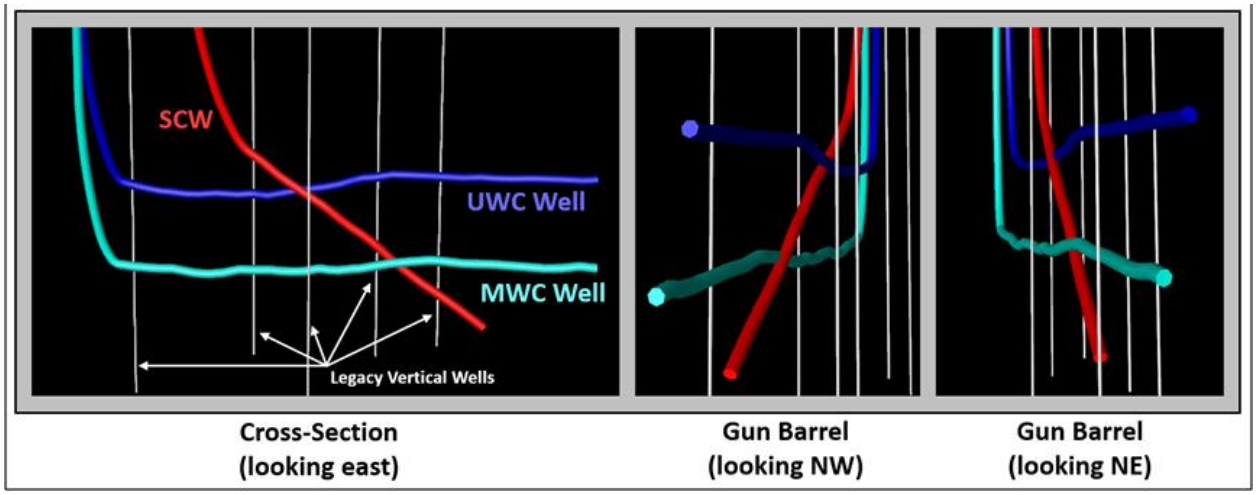


Figure 32: Schematic diagram showing Slant Core Well (SCW) position relative to the most proximal Upper and Middle Wolfcamp horizontal wellbores (UWC and MWC, respectively) as well as the most adjacent legacy vertical wells. All horizontal wells in the test site area were drilled from North to South including the SCW. The SCW trajectory comes within 89 ft of the UWC wellbore and 135' of the MWC well.

Discrete Fracture Network (DFN) models are commonly used during the development of unconventional reservoirs to understand the complexity of fracture geometries and how varying completion designs and spacing impact production. Extensive rock layering is common within the Wolfcamp formation (Figure 34) and can be observed from macro- to microscale (Suarez-Rivera et al., 2016). Outcrop, whole core, and laboratory-based hydraulic fracture testing show that highly layered rocks contain weak interfaces which induce step-over fractures during the hydraulic stimulation of a well, do not remain open and connected after pumping, and reduce the connected hydraulic fracture network (Suarez-Rivera et al., 2016). The Slant Core Well (SCW) provides a rare opportunity to observe and ground truth documented hydraulic and natural fracture networks as well as placed proppant (Courtier et al., 2017).

Data collection

The recovered core from SCW totals 595.4' and was collected in 6 core runs. Cores 1-4 represent the UWC while cores 5 and 6 represent the MWC. Placing the SCW as close as possible to producing wellbores provided the highest possibility of encountering hydraulic fracture networks. Three-dimensional geomodels as well as microseismic interpretations assisted in placement of the slant core wellbore (Courtier et al., 2017; Trowbridge et al., 2017, Fairfield et al., 2018). An extensive open hole log suite was acquired after the coring process from the total depth of the SCW to the intermediate casing point.

Prior to removing the core from the core barrel, CT scans were performed on the core to differentiate in-situ fractures from fractures induced by core barrel extraction. The CT scans allow visible observation of sealed and open fracture networks, bedding planes, and lithological changes and boundaries (Figure 35). A comprehensive fracture description on the SCW was compiled by integrating fracture interpretations from three separate sources. For more information on the methodology of fracture interpretation refer to Gale et al. (2018).

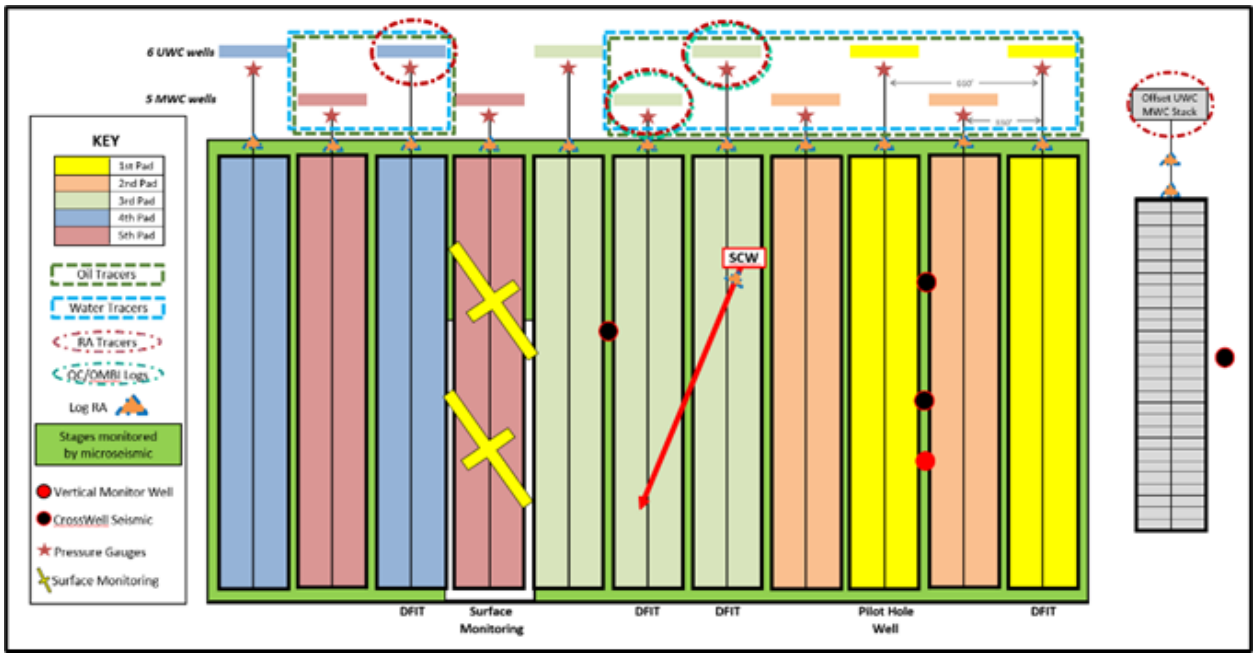


Figure 33: Schematic showing location of slant core well (SCW) relative to HFTS well package. 6 horizontal wells in the Upper Wolfcamp (UWC) and 5 horizontals in the Middle Wolfcamp (MWC). Order of operations: Drill 11 horizontal wells; recomplete 2 legacy vertical wells and complete 11 new horizontals with pressure monitors, microseismic monitors, cross-well seismic, and downhole logging; run tracers and fiber coil production logs; monitor post-frac pressure; drill and core slant well. Modified from Courtier et al., 2017.



Figure 34: Relative stratigraphic position of formations within the Lower Permian system.

Multivariate Analytics

Non-linear multivariate analytics (NLMVA) is conducted after all relevant data is collected to determine relationships between fractures, lithologies, fluid saturations, and mechanical properties derived from well logs.

Initial data requirements for the NLMVA models include direct fracture measurements (Gale et al., 2018), lithological indicators including gamma ray, resistivity, and mineralogical abundances, as well as mechanical properties such as Young's Modulus, Poisson's Ratio, stress gradient, and density (Figure 36a). A boxcar function (Weisstein, 2013) is applied to the fracture logs to calculate a 10' moving average and is then used as the primary response variable in analytical modeling (Figure 36b). A 10' moving average value was chosen after testing multiple

sensitivities to obtain a valid data set for prediction.

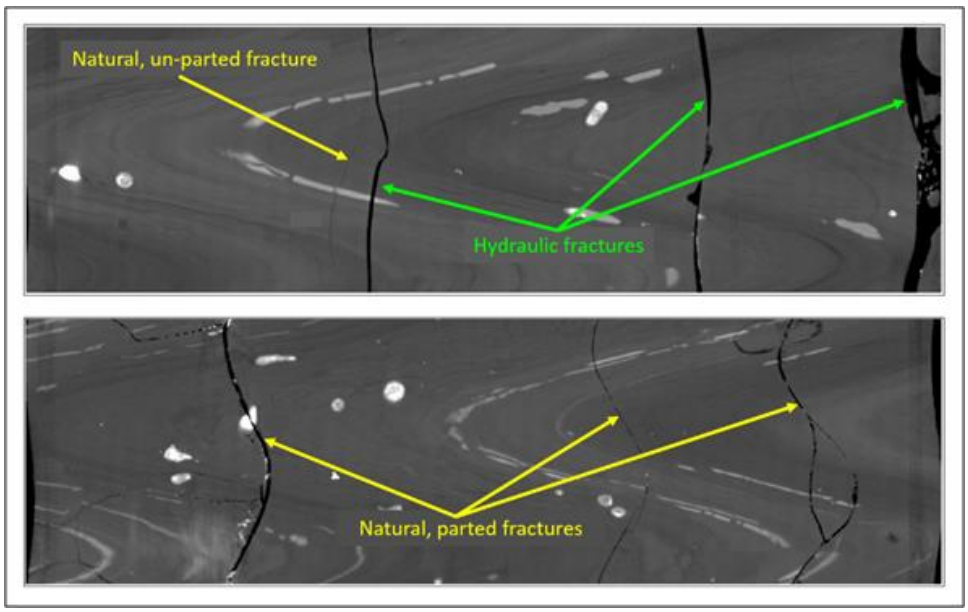


Figure 35: CT scan images of the SCW. Each image displays 3 ft of core. Hydraulic and natural fracture interpretations are noted. Two main sets of natural fractures are identified and are primarily classified based on calcite mineral fill. Hydraulic fractures are quantified as large planes of varying complexity that have been intersected by the core (Gale et al., 2018).

Comparison between three fracture interpretations is performed on the moving average values to ensure consistency between analyses. This allows the highest confidence interpretation to be utilized as the response variable for all predictive modeling. Next, all the input variables are sampled at a 10' moving average. All available log parameters are initially evaluated as input variables to determine the most significant prediction variables. The input variables are then evaluated through multivariate collinearity to remove redundant data and ensure only unique, non-related variables are utilized during modeling workflows. During the collinearity analysis, ambiguous input variables are removed in favor of input variables that correlate to direct fracture measurements, lithology, or mechanical properties (Wicker et al., 2016). For example, gamma ray was retained as an input variable versus bound water volume and clay content to avoid repetition. After retained variables are ranked by significance, model sensitivities and a predicted response is produced, and N-fold cross validation is performed to corroborate model results at 10-fold. All solutions are created based on a biased solution utilizing full order search. Finally, the models are run again utilizing geomodel and seismic inputs to produce 3D predictions of natural and hydraulic fracture intensities.

Analytical models are then developed to analyze natural fractures and hydraulic fractures separately. Initially, 30 input variables are tested in the natural fracture model (NFM) with the natural fracture intensity being the response variable (Figure 37a, Figure 37b). Variable significance rankings and relative model sensitivities are shown in Figure 37a. After testing multivariate collinearity, 12 unique variables are retained for modeling. Variables are ranked by significance and sensitivity (Figure 37c) and a predicted response log is generated and displayed against the measured fracture log in Figure 37e. The relationship between the four most significant independent variables and the response variable is investigated to analyze changes to the predicted response variable. The NFM result is used as an input in the hydraulic fracture model (HFM).

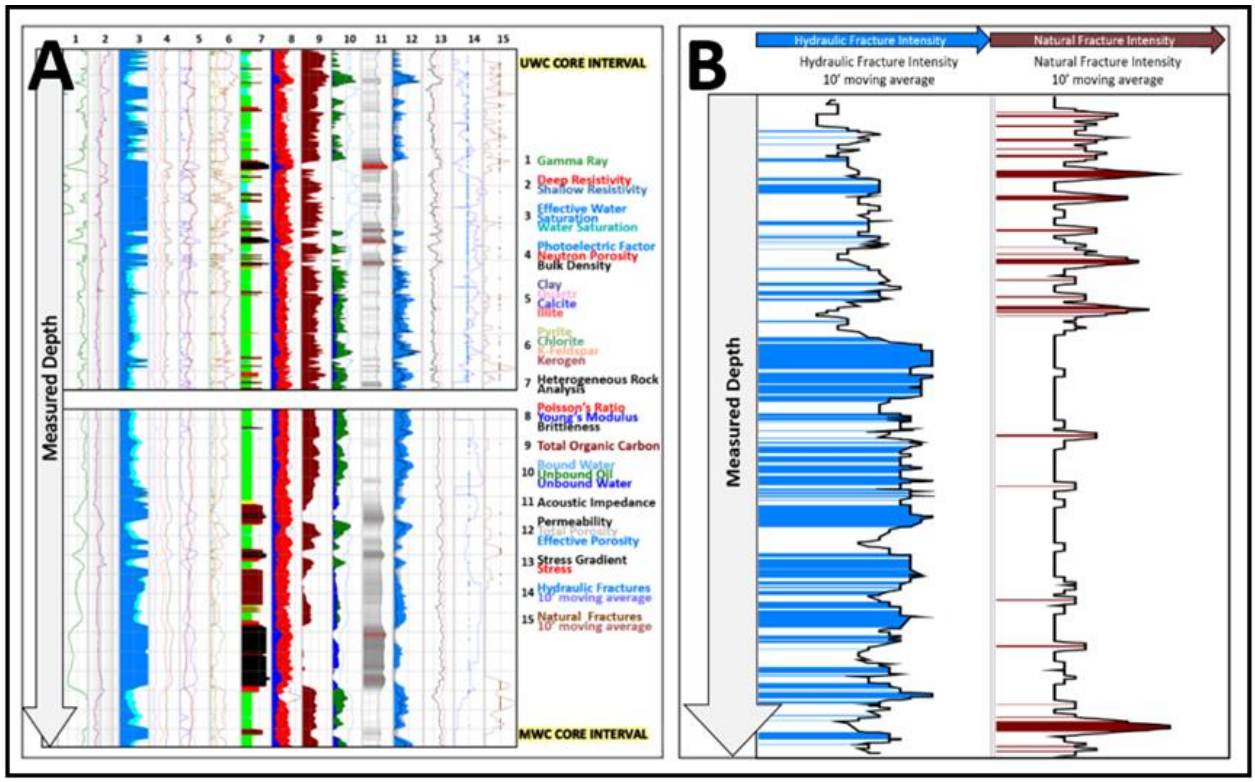


Figure 36: A) Well log tracks displaying fracture measurements over the cored intervals, lithological information, and mechanical properties. Several log tracks contain multiple logs. Log track key is shown on right and color coded by log curve color. B) Hydraulic fracture density log in blue and natural fracture density log in brown filled to 10' moving average curve (black line). Logs displayed represent the upper cored interval.

The HFM analyzes 33 total variables (Figure 38a, Figure 38b). As with the NFM, variables are ranked by significance and model sensitivity (Figure 38a). After collinearity, 18 variables remain in model as unique attributes (Figure 38c, Figure 38d). Final variables ranked by significance with model sensitivities are shown in Figure 38c. Finally, a predicted response log is generated to visually compare the actual hydraulic fracture density with the predicted hydraulic fractures (Figure 38e).

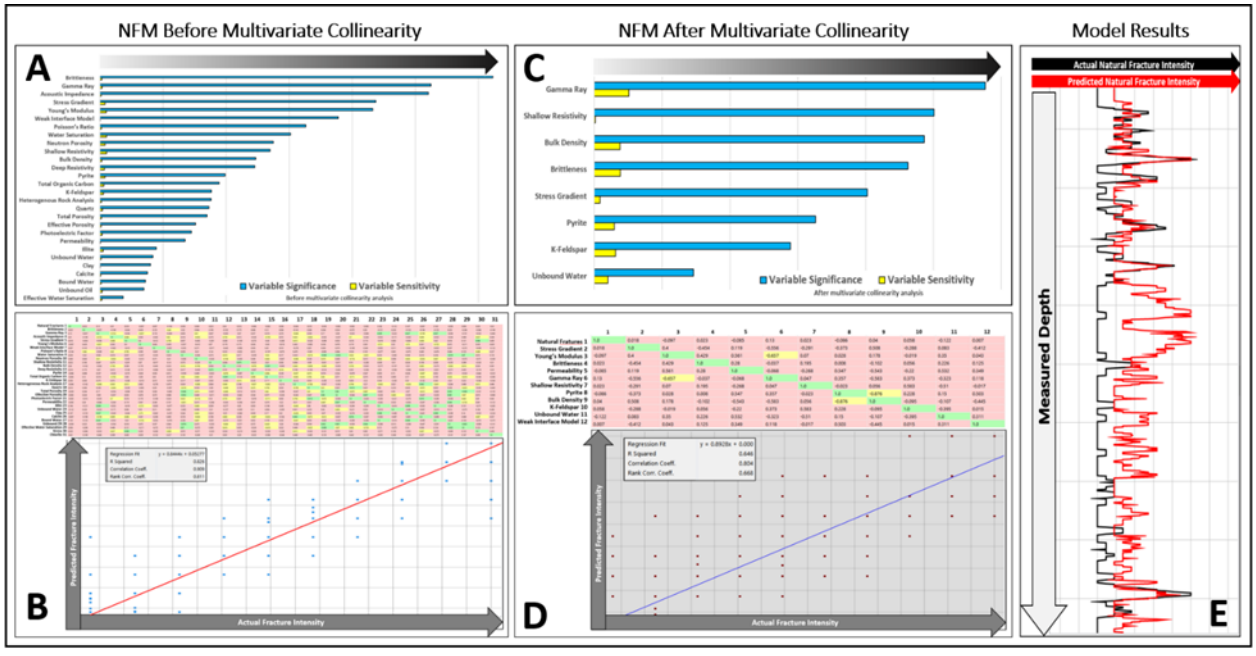


Figure 37: A) Natural Fracture Model (NFM) with initial 31 variables ranked by significance. B) Data correlation table (above) contains natural fracture intensity, brittleness, gamma ray, acoustic impedance, stress gradient, Young's modulus, weak interface model properties, Poisson's ratio, water saturation, neutron porosity, shallow resistivity, bulk

density, deep resistivity, pyrite, total organic carbon, k-feldspar, heterogeneous rock analysis, quartz, total porosity, effective porosity, photoelectric factor, permeability, illite, unbound water, clay, calcite, bound water, unbound oil, effective water saturation, stress, and chlorite. 422 samples were initially evaluated. Actual versus predicted plot (below) shows a correlation coefficient of 0.909. C) Final variables evaluated within NFM after collinearity analysis. Variables are ranked by significance (blue) with model sensitivities shown in yellow. D) NFM after collinearity analysis leaves 12 variables retained in the model. Data correlation table (above) contains natural fracture intensity, stress gradient, Young's Modulus, brittleness, permeability, gamma ray, shallow resistivity, pyrite, bulk density, k-feldspar, unbound water, and weak interface model properties. 422 samples were evaluated to understand which variables are most significant and have the highest model sensitivity. Actual versus predicted plot (below) shows a correlation coefficient of 0.804. E) NFM predicted versus actual log responses. The actual natural fracture density is shown with black curve. Predicted natural fracture density shown in red.

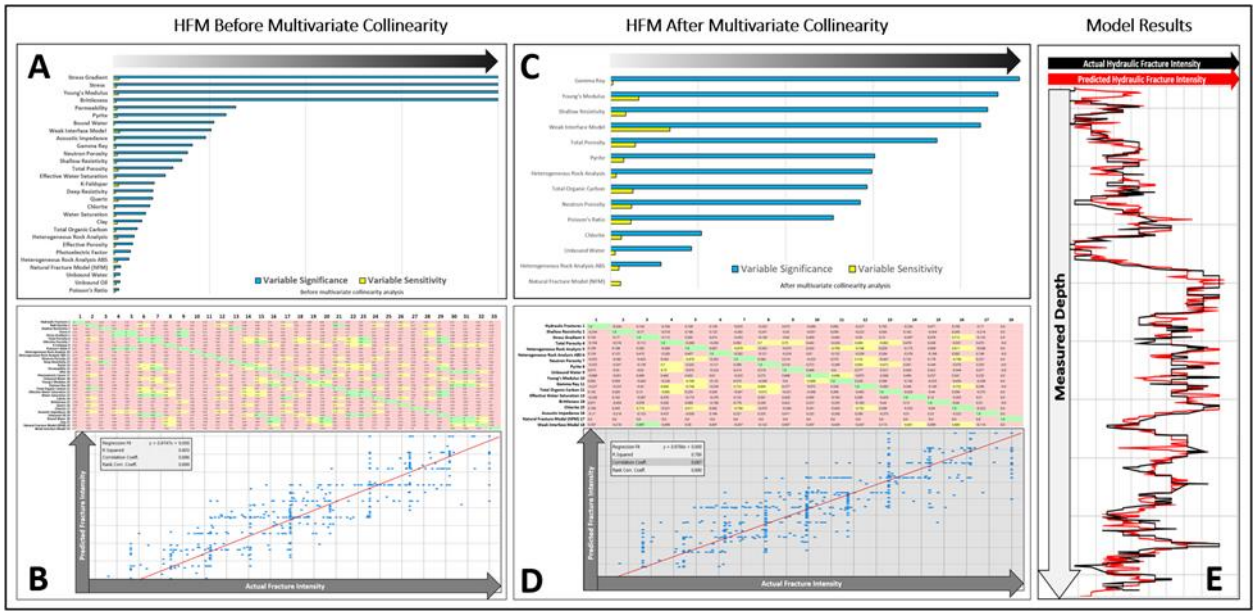


Figure 38: A) HFM with initial 33 variables ranked by significance. B) Data correlation table (above) contains hydraulic fracture intensity, bulk density, shallow resistivity, stress, stress gradient, total porosity, effective porosity, k-feldspar, Poisson's ratio, heterogeneous rock analysis (HRA), HRA absolute value, neutron porosity, deep resistivity, pyrite, permeability, illite, photoelectric factor, unbound water, Young's modulus, gamma ray, total organic carbon, effective water saturation, water saturation, calcite, brittleness, quartz, chlorite, acoustic impedance, unbound oil, bound water, clay, NFM model results, and the weak interface model results. 874 samples were initially evaluated to understand which variables are most significant and have the highest model sensitivity. Actual versus predicted plot (below) shows a correlation coefficient of 0.896. C) HFM significant variables with model sensitivities after collinearity analysis. D) HFM with final 18 variables. Data correlation table (above) contains shallow resistivity, stress gradient, total porosity, heterogeneous rock analysis and absolute value, neutron porosity, pyrite, unbound water, Young's Modulus gamma ray, total organic carbon, effective water saturation, brittleness, chlorite, acoustic impedance, NFM results, weak interface model results. Actual versus predicted plot (below) shows a correlation coefficient of 0.887. E) HFM predicted versus actual log responses. The actual hydraulic fracture density is shown with black curve. Predicted hydraulic fracture density shown in red.

Results

Utilizing the workflow described above, the NFM produced a correlation coefficient of 0.804 and the HFM resulted in a correlation coefficient of 0.887. The final product is a log-based prediction of the natural and hydraulic fracture density (Figure 39). The 3D prediction of the natural and hydraulic fracture intensities is limited to the vertical and lateral resolution of the geomodel.

The highest-ranked significant controllers in the NFM are gamma ray, shallow resistivity, bulk density, and brittleness (Figure 40). Gamma ray displays a positive linear increase in predicted natural fractures. Shallow resistivity ranks as the second most significant impact on natural fracture density and shows natural fractures to be the least abundant in samples with very low or very high resistivity. There is a small range of bulk density values in the sample population

that show increased natural fracture intensity. Model samples with mid-range brittleness index values contain the lowest abundance of natural fractures. These measurements are interpreted to be higher clay content shale, which is less prone to having natural fractures in the system. Thus, the lithological variation in the formation is the dominant controller on the natural fracture intensity development. The NFM prediction error is impacted by intervals of increased hydraulic fracture intensity (Figure 41) which could be caused by interpretation issues distinguishing natural from hydraulic fractures. The NFM provides no direct indication of aperture, fracture length, or orientation due to lack of measurements to calibrate the model.

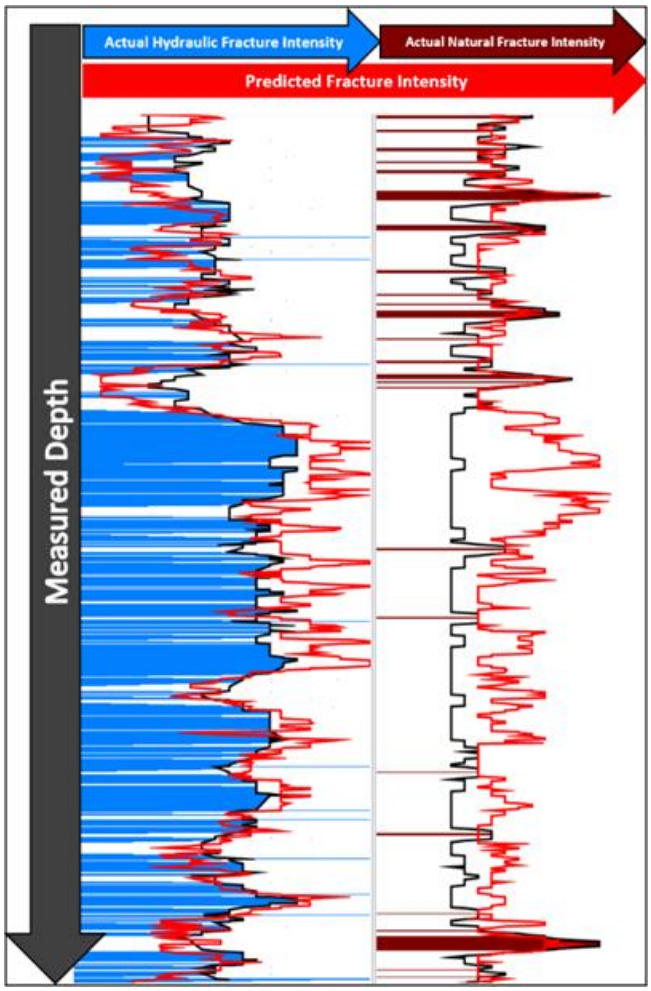


Figure 39: Final model results. HFM on the left. Black curve represents the calculated 10' moving average and is filled with blue showing interval intensity. NFM on the right. 10 ft moving average curve in black is filled with brown showing natural fracture density. The red curve on each log track shows the predicted response results from the NLMVA.

The most impactful attributes on the HFM are gamma ray, Young's Modulus, shallow resistivity, and weak interface model response. Cross plots of these four variables are shown in Figure 41. Results show that predicted hydraulic fracture intensity has a positive relationship with gamma ray and Young's Modulus. A negative trend is observed with shallow resistivity and the number of weak interfaces. These results imply that hydraulic fractures have increased intensity in organic-rich shale sequences.

Discussion and Model Utility

NLMVA provides a robust methodology to evaluate and determine dominant parameters that control the occurrence and distribution of natural and hydraulic fracture intensity. Results from

one NLMVA model can be leveraged and integrated as an independent variable in subsequent models.

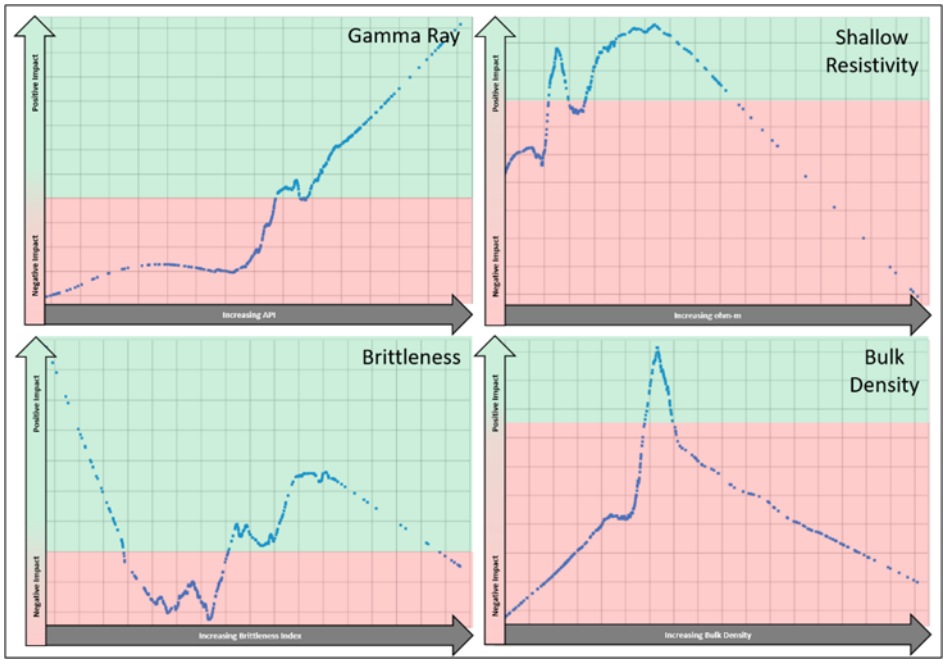


Figure 40: Impact of four most significant variables on natural fracture intensity.

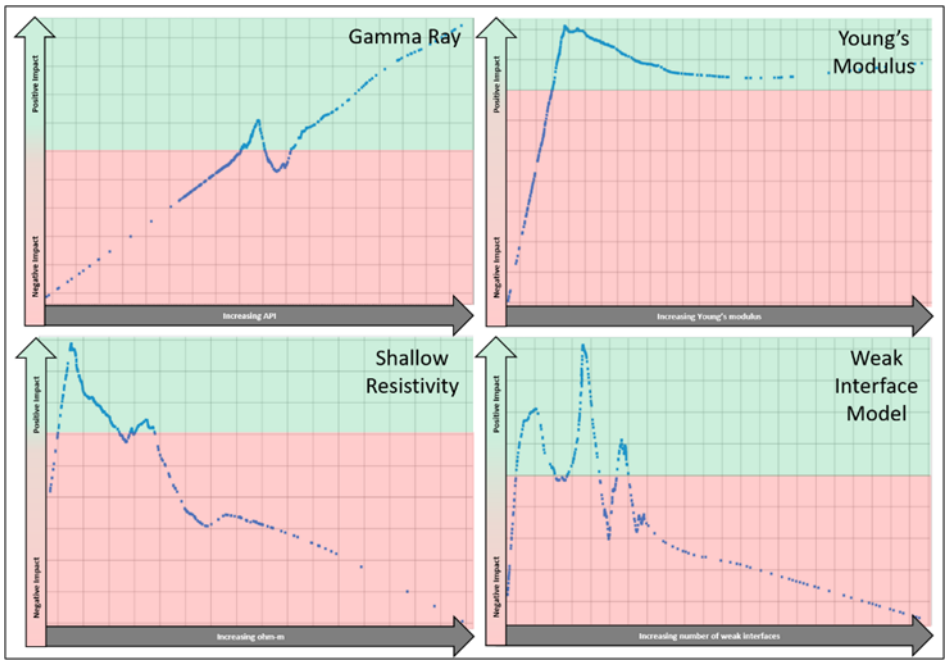


Figure 41: Impact of four most significant variables on hydraulic fracture intensity.

NLMVA results demonstrate that the combination of lithological, mechanical, and fluid saturation properties impacts the physical location of natural fractures and influences the position of hydraulic fracture intensities. Attributes that exhibit high correlation coefficients in the analytical model include rock type, brittleness, stress, and the presence of weak interfaces. Weak interfaces are interpreted to contribute to the closure of hydraulic fractures after pumping has ceased which limits the wellbore-reservoir connectedness (Suarez-Rivera et al., 2016).

Hydraulic fracture density within the HFM can be predicted with a high degree of certainty when the NFM results are used as input variables during modeling. This is essential for

understanding the economic impact that complex fracture networks have on well performance and can be included as a consideration in future well planning for target landing zone and completion design. An increased volume of natural fractures decreases the accuracy of the hydraulic model.

The utility of this model prediction is to better constrain the modeled DFN's for hydraulic fracture modeling and reservoir simulation. Additionally, these models can also be leveraged to place natural and hydraulic fracture networks into geomodels to sample horizontal well locations and to understand the relative impact on horizontal well production.

Future model improvements

Future studies include identifying the relationship between fluid viscosity during treatment and in-situ stress to determine net impact on fracture network complexity. Additionally, understanding the impact that varying the completion rates and screen out times has on the model could lend valuable insights. Well package spacing could also have a strong impact on fracture intensity considering there is a positive correlation between fracture intensity and distance to adjacent wellbores.

Conclusions

Utilizing the comprehensive fracture counts and analysis of the SCW at the HFTS, analytical modeling provides a predicted response of natural and hydraulic fracture intensity to use as a high confidence variable in 3D reservoir modeling of DFN's and population as three-dimensional properties with geomodels. Geomodel properties do not have an analog for natural fracture intensity, so populating this variable within geomodels can provide a higher understanding of how fracture intensity impacts well performance.

Downhole Microseismic Mapping

Authors: Neil Stegent, and Cody Candler

Abstract

The United States Department of Energy co-funded a joint industry project (JIP) in the Midland basin of Texas. The project was conducted in the Wolfcamp formation to better understand the relationships among horizontal lateral placement, production interference between laterals, effectiveness of completion sequences, and hydraulic fracture geometry in unconventional reservoirs. Downhole microseismic data was acquired from more than 400 fracturing stages during the completion project to better understand the generated hydraulic fracture geometries.

Eleven horizontal wells were drilled in the upper Wolfcamp (UW) and middle Wolfcamp (MW) formation in the Permian Basin. The 10,000 ft laterals were drilled in a chevron pattern to help improve inter-well fracture communication and maximize hydrocarbon recovery. The completions sequences were planned to restrain fracture height growth upward into a lower-pressure zone using a combination of zipper fracturing and simultaneous fracturing operations. Downhole microseismic monitoring was used to record more than 95% of the planned fracture stages. Downhole tiltmeters were also used to validate upward fracture height growth. Multiple geophone arrays, both vertical and horizontal, were used during this completion; this paper discusses coordination between maintaining completion efficiency and obtaining microseismic data. Additionally, this paper highlights the completion challenges associated with collecting diagnostic data along with results and findings.

Introduction

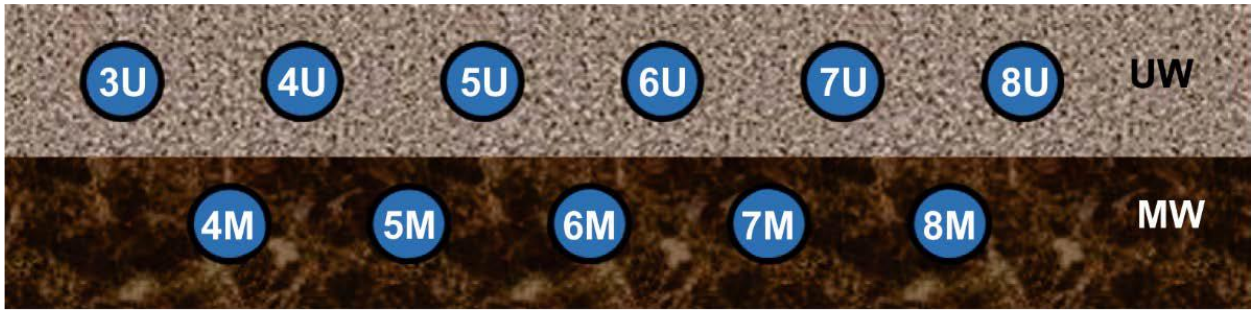


Figure 42: Illustration of chevron well pattern (end view).

The project primarily consisted of 11 horizontal wells drilled in the UW and MW formation in the Midland basin of West Texas. The wells were drilled in a chevron pattern (Figure 42) ~660 ft apart laterally and ~450 ft apart diagonally. This configuration can also be called a "wine-rack" or simply a "staggered" pattern. A 5 1/2-in. steel casing was cemented along the entire length of each lateral monobore well. Multiple drilling rigs were used to accomplish this task, and the wellheads resided on three separate physical pads to expedite the drilling process as well as accentuate the completion strategy with multiple fracture spreads. The subsurface laterals were drilled between existing vintage vertical wellbores, most of which were completed in multiple horizons ranging from the Cline to the Spraberry formation.

The Wolfcamp formation is a combination of quartz and calcite with typical clay content in the 15 to 40% range. It contains thin limestone layers that lie between the UW and lower

Wolfcamp (LW) formation and tend to function as weak fracture barriers between the two intervals. The Wolfcamp formation contains natural fractures and matrix permeability in the nano-darcys. The entire Wolfcamp formation section primarily lies between the Spraberry/Dean and the Canyon/Strawn formations. The UW formation is approximately 350 ft thick with an approximately 0.51-psi/ft reservoir pressure gradient and a permeability range of 200 to 800 nano-darcys. The MW formation is approximately 250 ft thick with a slightly higher reservoir pressure gradient (0.53 psi/ft) and a permeability range like the UW formation. The Spraberry formation, which lies above the UW formation, tends to be normally pressured or can be slightly higher than the normal reservoir pressure gradient (0.48 psi/ft). The reduction in reservoir pressure results in lower minimum horizontal in-situ formation stress; consequently, fractures tend to extend upward from the UW into the Spraberry formation. This phenomenon has been observed by other operators in the basin and is well documented in the literature (Staples et al, 2015; Mickey & Monson, 2013).

Microseismic Fracture Mapping Project Objectives

Microseismic data provide engineering knowledge for future field developments in this project area as well as in similar unconventional systems. Understanding hydraulic fracture generation in shale reservoirs can help enable the design and execution of effective fracturing stages that significantly contribute to increased hydrocarbon recovery. Improved design and execution could thereby reduce the number of future wells drilled, reduce resource requirements for fracturing, minimize or eliminate potential environmental impacts, and reduce energy input and cost.

The primary fracture mapping objectives during this project were as follows:

- Determine the extent of reservoir coverage from the hydraulic fractures.
- Measure fracture or fracture network geometry (i.e., height, length, and width) and azimuth.
- Characterize, if possible, the relationship between time (i.e., injected volume) and created fracture half-length and height.
- Identify and determine the extent of any interaction with the following:
    - Large-scale, pre-stressed natural geological features.
    - Previously produced or stimulated offset vertical wells.
- Evaluate the effectiveness and impact of the following on overall fracture geometry:
    - Laterals drilled in the UW and MW using a chevron pattern.
    - Zipper fracturing sequence and timing between stages.
    - Completing the UW wells before the MW wells.
    - Different numbers of fracture initiation points per fracturing stage.
- Use downhole microdeformation monitoring to determine the shallowest depth at which fractures could have propagated.

- Examine the microseismic data relative to the slant well core intervals.

Project Plan and Setup

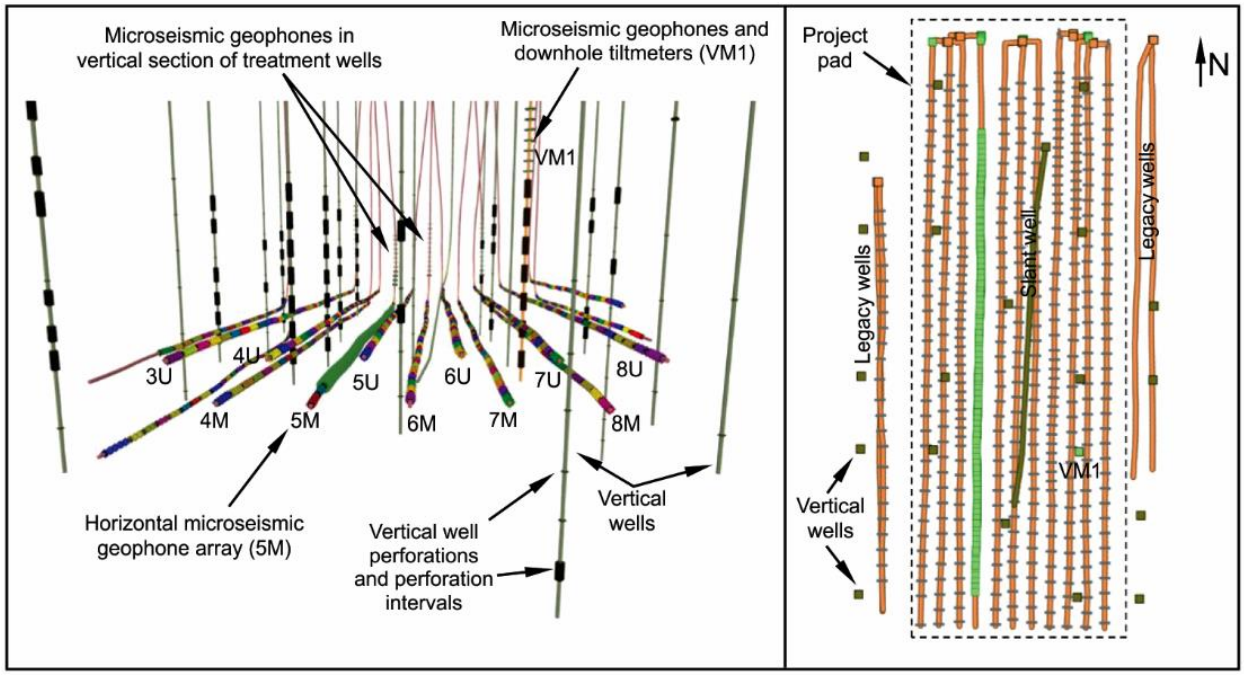


Figure 43: Three-dimensional (3D) and two-dimensional (2D) views of the subsurface project wells.

Downhole microseismic mapping (MSM) data was obtained to better understand the hydraulic fracture systems generated and the hydrocarbon contribution of the natural fracture system of the source rock reservoir. Dual arrays of geophones were used throughout the completion process to acquire the data. Figure 43 shows the subsurface configuration of all the project wells, with the 11 horizontal wells in the center being the primary test wells. A downhole hybrid array of geophones and tiltmeters was installed in a vertical well (VM1) that was in the southeast quadrant of the project pad. The downhole tilts independently measured potential upward fracture growth into the upper Spraberry formation. Downhole tiltmeters measure the actual microdeformation of the rock generated from a hydraulic fracture which is different from the shear events that are measured with microseismic technology. The bottom of the vertical geophone toolstring array was approximately 1,550 ft above the shallowest lateral. Typically, the array would be installed closer to the formation being fractured. However, because all the available vertical wellbores had existing perforations, which needed to be plugged back to minimize background noise, Well VM1 was selected because it would allow for the deepest deployment of the vertical geophone array. A second geophone array was tractored into the horizontal lateral of Well 5M and was repositioned during the completion process to remain close to the current treatment application. MSM data acquisition was divided into three phases to accommodate repositioning of geophone arrays (in the vertical wellbores) and maintain high-quality data. The vertical section of some of the horizontal treatment wells was also used for geophone arrays during the different completion phases. Next, we discuss the MSM quality assurance (QA) process.

MSM Quality Assurance

The key QA components of this analysis are the position of the tools and the accuracy of calculations and/or inversions. These two factors can influence the accuracy of the results and

ultimately provide a better understanding of the created fracture geometry.

Table 2: Completion order, fracturing stages monitored, and observation wells.

Phase No.	Treatment Well (Total Stages)	Observation Wells					
		5M Horizontal	5M Vertical 1	5M Vertical 2	6M	3U	Vertical Monitor Well
1	5U (37)	1 through 32		33 through 37			1 through 37
	6U (37)	1 through 32		33 through 37			1 through 37
	6M (37)	1 through 28		29 through 37			1 through 37
	8U (37)	1 through 37					1 through 37
	7U (43)	1 through 37		38 through 43			1 through 43
2	3U (37)	1 through 31	32 through 37				1 through 37
	4U (46)	1 through 29	30 through 46				1 through 46
	8M (37)	1 through 34	35 through 37				1 through 37
	7M (49)	1 through 29	30 through 49				1 through 49
3	4M (37)				1 through 37	1 through 37	
	5M (37)				1 through 37	1 through 37	

The first QA key component is the position of the tools used to map the project. Ideally, the array should be deployed as near to the target as possible, in both distance and depth, to minimize error and increase the signal-to-noise ratio (SNR). All treatment and observation laterals were landed in either the UW or MW with a parallel lateral spacing for wells at approximately the same TVD of 600 ft. The 11 wells were divided among three pads. The observation wells used during this project included the following:

- Well, 5M, which is located between the Well 4U and 5U laterals.
- Well, 3U, which is the westernmost lateral of the three treatment pads, with Well 4M directly east of it.
- Well, 6U, which is between the Well 5U and 4U laterals.
- Vertical monitor well, located approximately equidistant (at 100 ft) from Wells 7U and 7M.

Table 2 shows the location of the monitor wells relative to the completion wells along with the monitored fracturing stages.

A dual-receiver-array configuration was used throughout this project by means of four different toolstrings:

- An eight-level fracture-mapping hybrid receiver array (16 double-stacked microseismic tools and eight tiltmeters).
- An 18-tool, 12-level horizontal receiver array.
- Two 24-tool, 12-level vertical arrays.

The hybrid array in Well 170P recorded data during all stages of the first two pads. To complete the dual-array configuration for these pads, a horizontal array was placed in the nearby Well 5M. An optimum listening distance was achieved by moving the array heel-ward during the Pad 1 and 2 completions as the stages of each zipper fracturing sequence progressed. The array in Well 5M was pulled to a vertical position during the heel-most stages of all wells in Pads 1 and 2, except for the Well 8U completion. All Well 8U stages were monitored by means of a horizontal array position. After the completion of Pad 2, the array in Well 5M was removed. Pad 3 (Wells 5M and 4M zipper fracturing) was monitored using two vertical arrays—one deployed in Well 6M and one in Well 3U.

All vertical arrays were positioned above the treatment laterals because the vertical observation well was previously produced at multiple intervals across the Wolfcamp, Dean, and Spraberry formations, and the vertical arrays placed in the treatment laterals could only be lowered to just above the kickoff point within the vertical portion of the laterals. The bottom tool for the hybrid array was located at the top of the Spraberry formation, which was an ideal position for the tiltmeters because any extension into the Spraberry would be detected. While the other vertical arrays were not in an optimal position, they were reasonably close to the treatment wells and within the target zone. Therefore, increased event location uncertainty resulting from toolstring positioning is probable but not extensive.

The bottom tools of the vertical array placed in Wells 4M, 6M, and 5M were at approximately the same TVD, with Wells 4M and 6M in the middle of UW 1 and Well 5M at the top of UW 2. A shallower toolstring position was required for the vertical array in Well 3U because of its slightly shallower landing depth. For this array, the bottom tool resided near the base of the lower Spraberry 3L.

Individual microseismic nodes of 5.03-in. length and 2.50-in. diameter were composed of six OYO DS-250 15-Hz geophones—two X, two Y, and two Z—to internally stack the signal for single-channel data. Receivers were double stacked (i.e., two sondes per level) to enhance the SNR, decrease attenuation, improve hodogram linearity, and clarify phase arrival times. To obtain the total tilt vector, each tiltmeter contained two orthogonal sensors clamped between the microseismic tools on the same wireline. The arrays were configured using a varying number of flexible interconnects (30 m in length) depending on the number of levels in the toolstring (each level had one interconnect between it and the next level). The temperature limit of a DS-250 array is 275°F. Because the highest static temperature in the monitor well was well below this threshold, there were no tool failures caused by temperature restrictions. Microseismic data was sampled at 0.25 ms intervals and microdeformation data every 4 seconds.

During deployment, geophones rotate freely according to the localized torque. While the Z-axis of each sonde is aligned with the wellbore, the X and Y components can face in any direction perpendicular to each other. Tool orientation, or the direction of each tool component, is based on calibration points, as recorded by the array. Calibration points are audible events with known points of origin, such as an early event, a perforation shot, a string shot, a tubing-conveyed perforating (TCP) shot, a correlated surface vibe shot, or other mechanical source that produces a series of recordable P- and/or S-waves. During this project, the toolstring was oriented using perforation shots. Perforation-timing boxes were clamped to the perforation wireline and recorded the change in voltage during perforation detonation, thus providing a known calibration origin point in space and time. By calculating the compressional particle motion direction and angle from these events to a tool, the actual geophone locations were confirmed. Because the tiltmeters were coupled to the microseismic tools on the same wireline, they could be oriented at the same time using the same method.

Microseismic Velocity Model Optimization

The second key QA component is the accuracy of the velocity model used to analyze the microseismic data set. Anisotropic modeling [i.e., 3D vertical transverse isotropy (VTI)

modeling] was used to accurately locate microseismic events produced from the three pad stimulations. With five components per layer, VTI modeling results in a more accurate Earth model of the area. This project used four VTI velocity models, each comprising 22 layers, in which the velocities delineate obvious changes in rock properties with depth (Figure 44).

It was initially developed with operator-provided Thomsen parameters, dipole sonic, and gamma ray data from an offset well. A forward modeling algorithm was used to calculate travel times and ray paths between grid points and the monitoring tools for every grid point in the model. This allowed each event to be located based on its P- and S-wave arrival times. Model optimization was accomplished by lowering the time residuals and minimizing the distance error between a known location and the inverted location. This model was optimized by analyzing the P- and S-wave arrival times of the stage perforation shots at the array. In conjunction with perforation timing, a very fast simulated annealing (VFSA) inversion algorithm was applied during post-processing until the time residuals and locations improved. Time residuals for most of the data matched the picked arrivals reasonably well. However, inconsistencies were greater for events located farther from the array or shallower than the wellbore because of a lack of reliable calibration points in these areas. Overall, the final time residuals fell within an acceptable range.

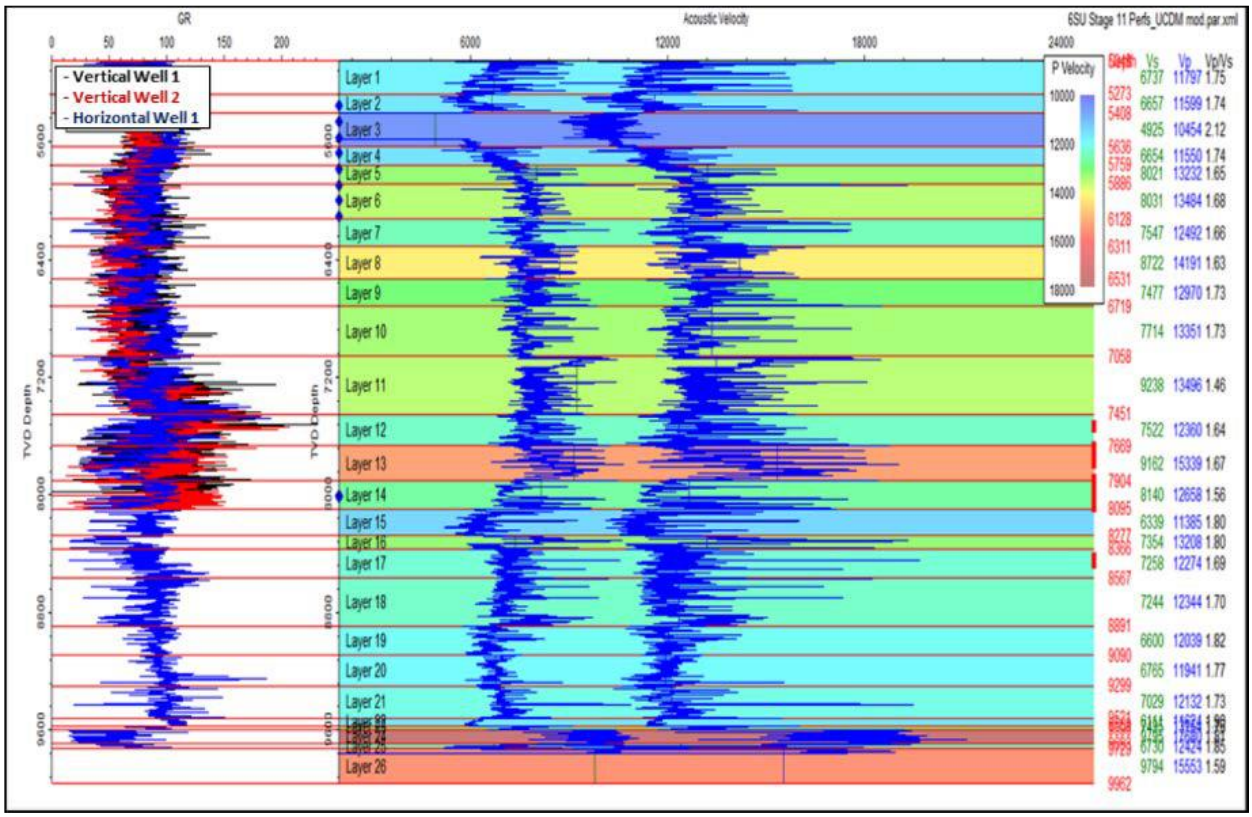


Figure 44: Final VTI Velocity Model 1 used during Phase 1 and 2 stages.

Microseismic Data Quality

The overall quality of the microseismic data is moderate. Results include a final total of 128,405 events for all stages monitored—an increase of 30% over the real-time count of 4,271 events. Tiltmeters in the hybrid array functioned properly; therefore, any microdeformation activity at or above the bottom tilt tool would have been detected.

The microseismic event SNR ranged from 0 to 108, and microseismic events of average

magnitude were imaged up to 4,500 ft from the toolstring. The point of crossover between the detection limit and the size of the largest events is considered the maximum viewing distance (Figure 45). With longer distances, events should be of higher magnitude to be detected by the microseismic tools. The detection limit is inversely proportional to the noise level, increasing with lower ambient noise and decreasing with increasing noise levels. Background noise levels averaged approximately 1,800 nV, which is considered average. Figure 46 shows typical background noise levels during pumping.

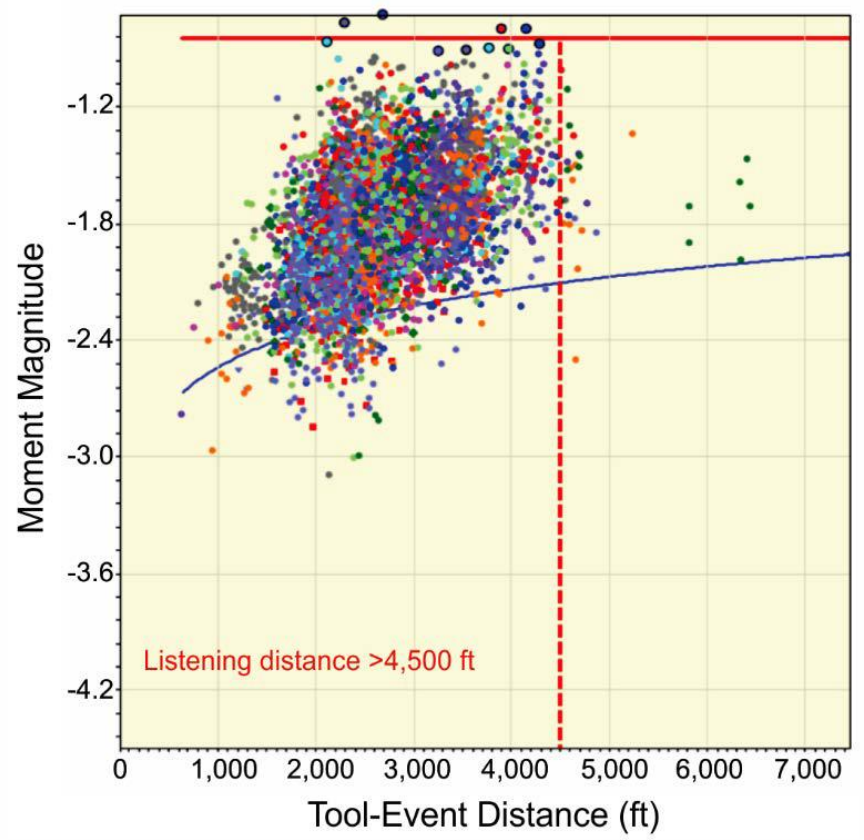


Figure 45: Listening distance.

Event-location error was calculated using 2D modeling, which consisted of three error "directions"—azimuth, radius (tool-to-event distance), and depth (elevation). The greatest component of uncertainty for the operator's pads is depth, with an average error of 49 ft. The average azimuthal uncertainty is 33 ft, and the average radial uncertainty is 47 ft. The depth error component was the largest of the three directions during this project because the vertical receiver arrays were placed well above the depth of the treatment laterals. Using vertical arrays that straddle the treatment lateral depths can minimize the error. Azimuthal error chords are displayed radially around the observation well as lateral error arcs, as they reflect the variations and uncertainties in the azimuth between the array and the microseismic events. Both distance- and depth-error bars associated with an event become longer as the time residual misfit increases. The size of the depth-error bar depends not only on the picked P- and S-wave arrival times but also on the relative position of the microseismic toolstring to the event location. Ideally, geophones should be located above and below the event location and as near to the target depth as possible to minimize depth error and increase the SNR.

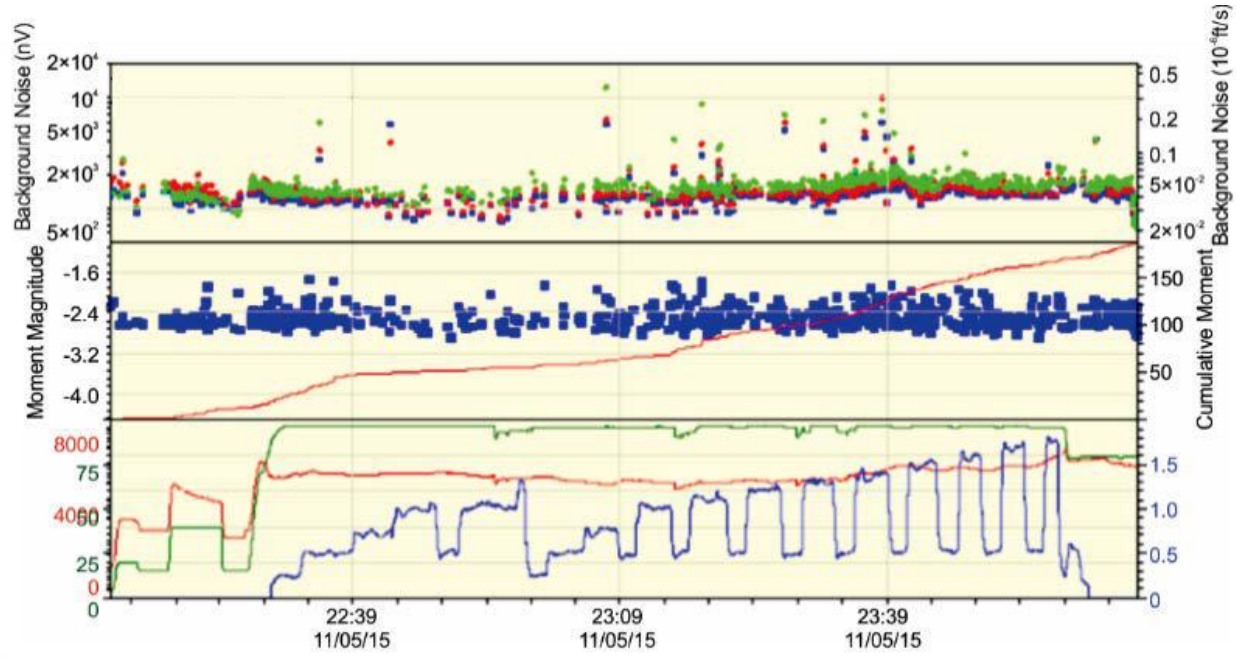


Figure 46: Typical background noise levels.

Prior wells and geophone setup

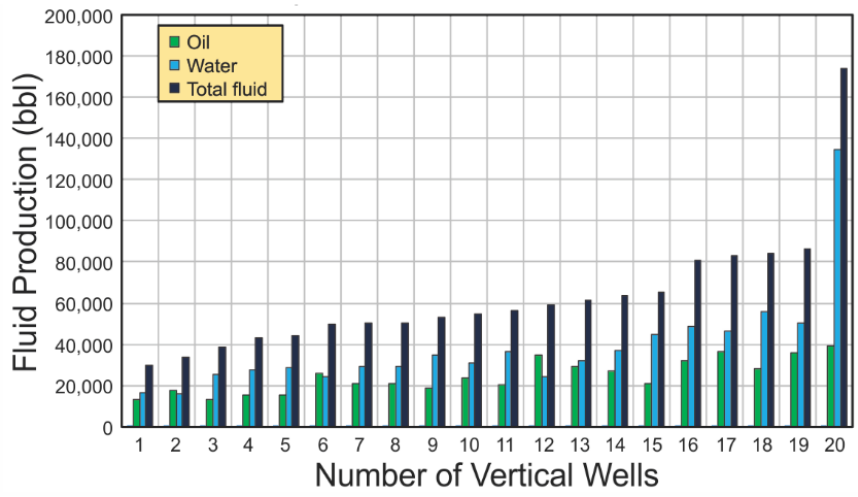


Figure 47: Offset well production (vertical wells).

Previously produced vertical wells are dispersed throughout the project well locations. Figure 47 shows the publicly recorded cumulative produced volumes of the offset active wells when the 11 wells were completed. A reduction in reservoir pressure also decreases the in-situ stress in each formation, which can influence the fracture geometry. Depletion can result in asymmetric fracture development and affect fracture containment. Determining the location of areas that might be affected by pressure drawdown is an important consideration during the microseismic data evaluation. Figure 48 shows a map view of the project area and illustrated historic drainage area.

Approximately 434 fracturing stages were monitored using a dual-array configuration on most of the completions. To maximize the listening distance, the arrays were moved throughout the project completion process. A fracture-mapping hybrid array, which has both MSM geophones and downhole tilt tools configured in the same tool string, was positioned in Well VM1 (vertical). A second horizontal MSM array was deployed into Well 5M (horizontal). Most stages were monitored from this horizontal array, and the array was pulled into the vertical section for

the later-stage completions. The last pad well was monitored using two downhole microseismic vertical receiver arrays. Tiltmeters in the hybrid array were fully functional for the duration of the hybrid array use in Well VM1. The bottom tiltmeter was located approximately 1,550 ft above the highest landed treatment lateral and did not detect sufficient microdeformation for a quantifiable diagnostic analysis. Figure 49 shows the monitoring setup.

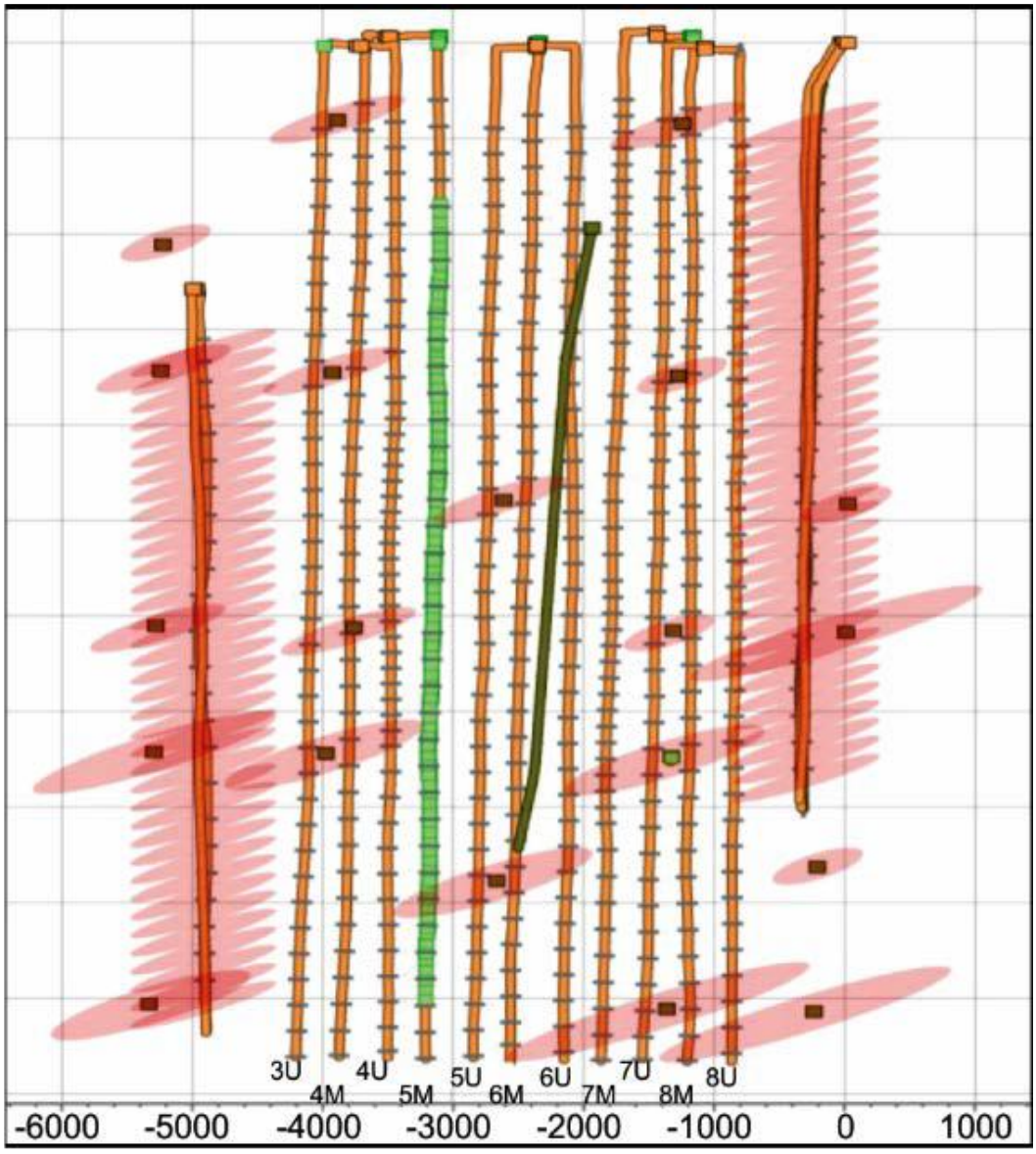


Figure 48: Project wells and existing wellbores (drainage patterns are shown for illustration only).

Well Completion and Fracturing Sequence

Before the completion of the 11-well pad, two offset legacy (parent) wells, located to the east of the project wells, were refractured to repressurize the reservoir (i.e., increase the reservoir stress) and minimize the generation of asymmetric fractures from the development (child) wells. Courtier et al. (2018) discuss the refracturing results.

All 11 wells were completed in a similar manner with a high-rate water fracturing treatment containing a friction reducer and a low concentration of surfactant. In addition, a friction reducer breaker was included. The injection rate was designed for 95 bbl/min on both the UW and LW completions.

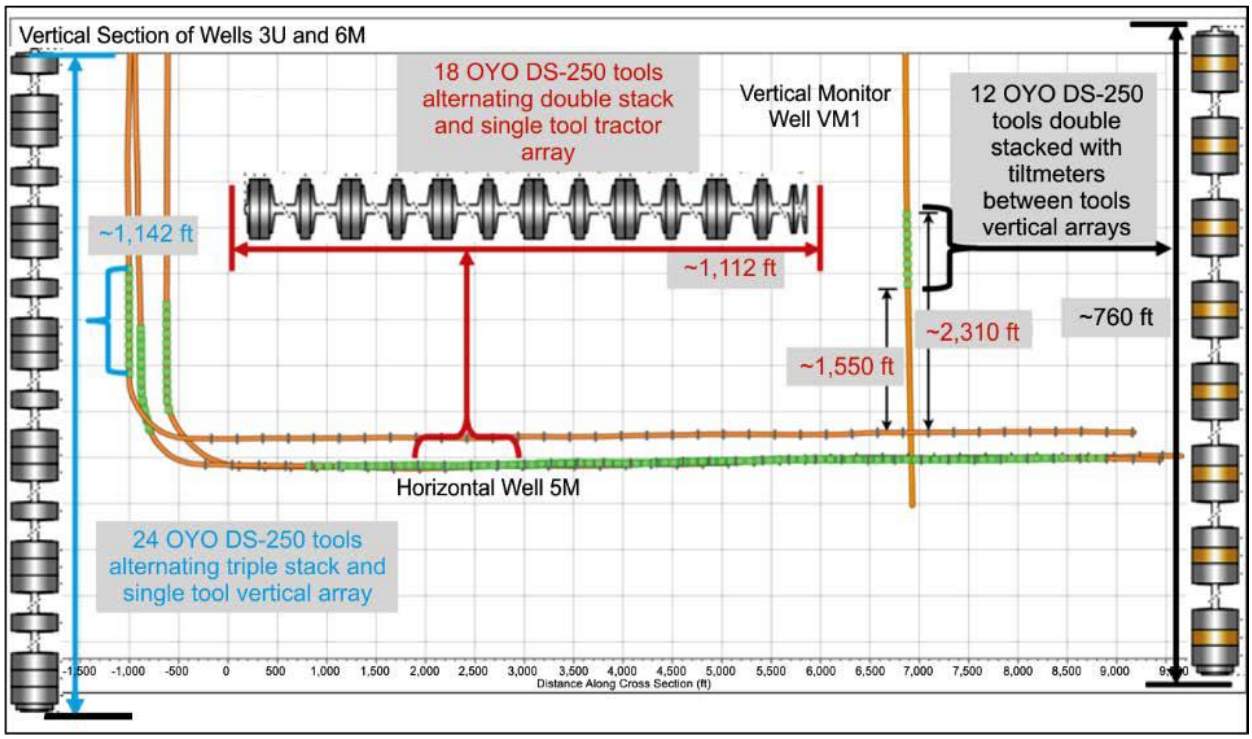


Figure 49: Geophone and tiltmeter arrays.

During the design phase, testing of some high- viscosity fluid systems was considered, but it was decided that because of the project complexity, it would be extremely difficult to make significant conclusions based on the completion fluid type. The number of fracturing stages per wellbore ranged from 37 to 49 and spanned ±200 ft/stage. A total of 434 fracturing stages was performed in less than 7 weeks. The number of fracture entry points also alternated between three and five perforation clusters per fracturing stage over a 1 ½ ft interval. Perforation cluster design varied (number of entry points, spacing between clusters, etc.) on some of the wells to determine the effect of cluster spacing and number of entry points during the completion. A 40/70-mesh proppant was pumped at a total volume equivalent to 1,100 lbm/ft of lateral completed per stage on most wells; however, several wells were completed with proppant volumes equivalent to between 1,400 and 1,800 lbm/ft of lateral completed per stage. Such configurations and fluid systems are typical for the Wolfcamp formation completions in the basin.

A zipper fracturing completion strategy was applied on the 11-well pad using two fracturing crews. Because the in-situ stress decreases between the Spraberry and Wolfcamp formations, the completions were sequenced to minimize upward fracture growth by completing the UW wells before the MW wells. This completion sequence was designed to contain the fracture height development in the MW by increasing the stress in the UW during the completions process. The completion design was also intended to maximize the effective stimulated area of fracture contact or the stimulated reservoir volume (SRV) (Mayerhofer er al, 2008).

The completion plan development required a significant amount of time-consuming complex operational pre-fracture planning and field coordination by the operator and service companies collaborating. Many man-hours were necessary to develop and revise the completion sequence (Figure 50).

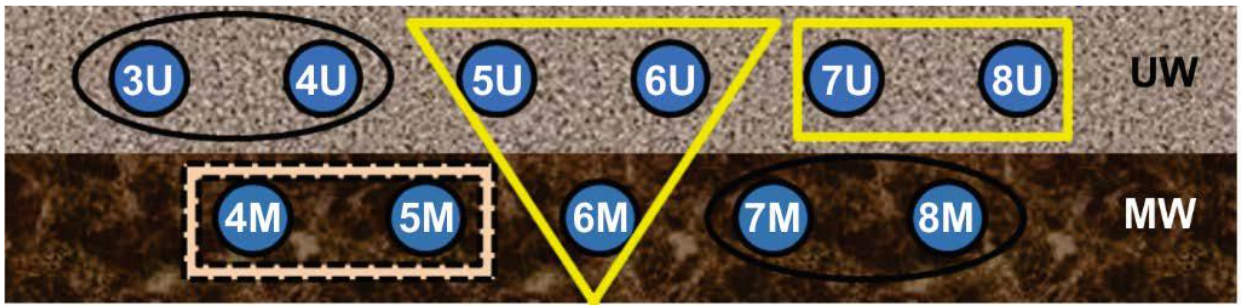


Figure 50: Zipper fracturing completions sequence: Phase 1 (Fracturing Crew 1), Wells 7U and 8U (yellow square); Phase 1 (Fracturing Crew 2), Wells 5U, 6U, and 6M (yellow triangle); Phase 2 (Fracturing Crew 1), Wells 7M and 8M (black oval); Phase 2 (Fracturing Crew 2), Wells 3U and 4U (black oval); Phase 3 (Fracturing Crew 2), Wells 4M and 5M (black dotted square).

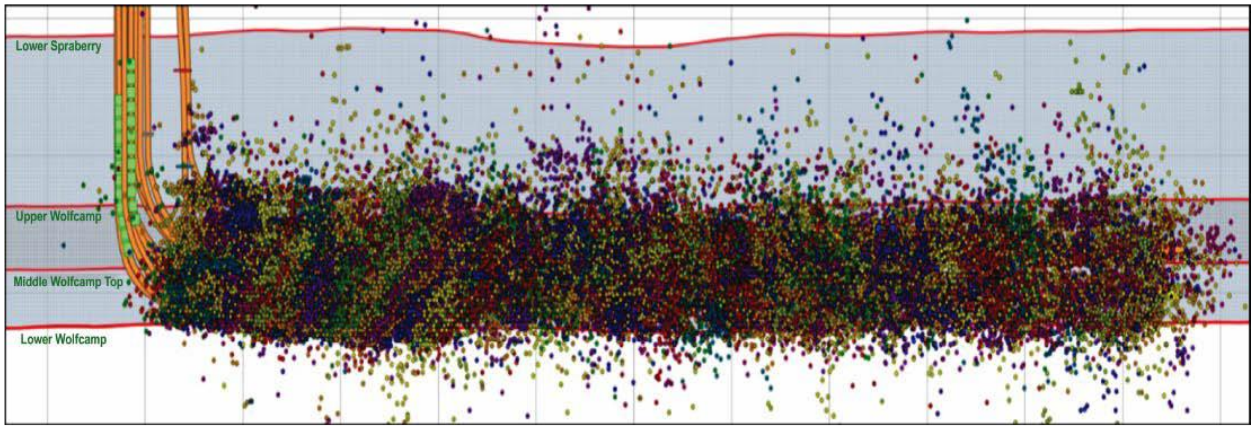


Figure 51: Side view of all real-time microseismic events (colored by fracturing stage).

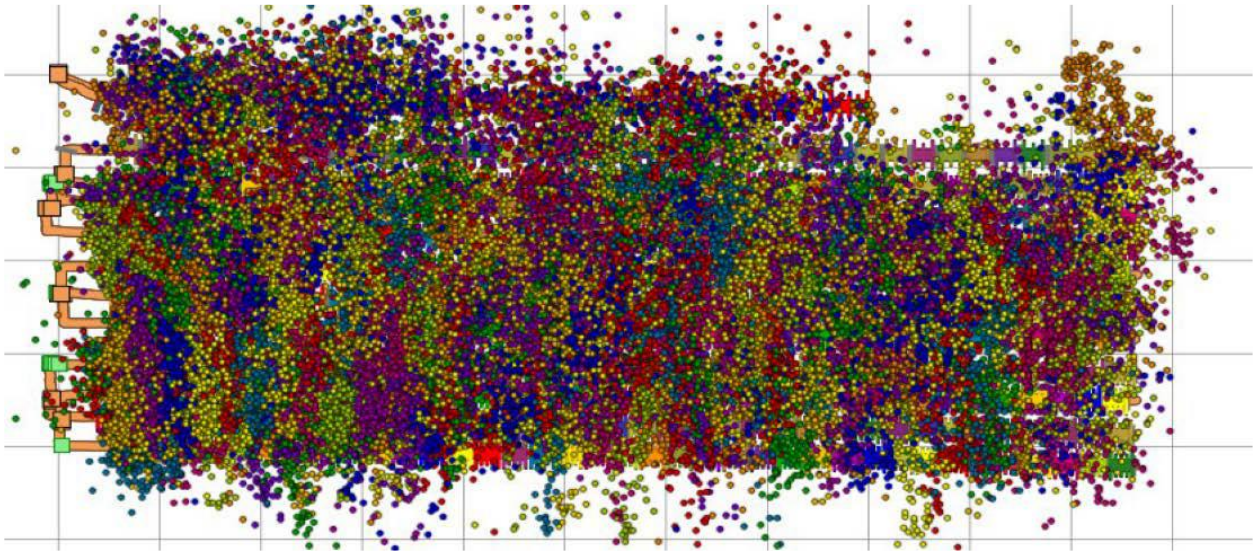


Figure 52: Map view of all real-time microseismic events (colored by fracturing stage).

The sequencing of the zipper fracturing completion was one of the most efficient and effective project components. Some wells were completed by sequentially completing the first five fracturing stages on one well before beginning the zipper fracturing sequencing on the neighboring lateral, while other sets of wells were completed using alternating sequencing between wells at the beginning of the completion process. An expectation of this design of experiment (DOE) was implemented to determine whether a noticeable difference, with respect to the microseismic measurements, could be correlated to the development of complexity during stimulation. The real-time downhole MSM clearly indicated that the target reservoirs were well stimulated (Figure 51 and Figure 52). Figure 53 shows moderate-to-high fracture

height containment in the higher stressed MW horizon with minimal growth up into the UW. The operator of the properties used careful planning with regards to the lateral landing depths of the wells and used in-depth reservoir understanding to improve the likelihood of a successful completion.

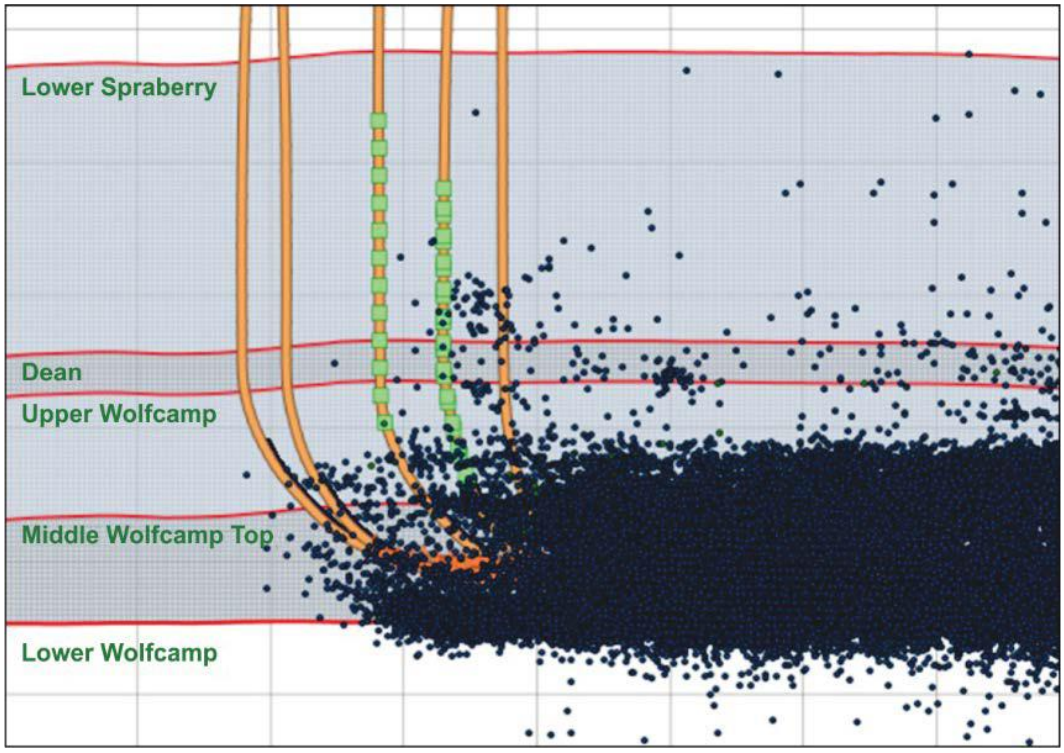


Figure 53: Side view of fracture height in the MW formation (color by formation).

Microseismic Monitoring (MSM)

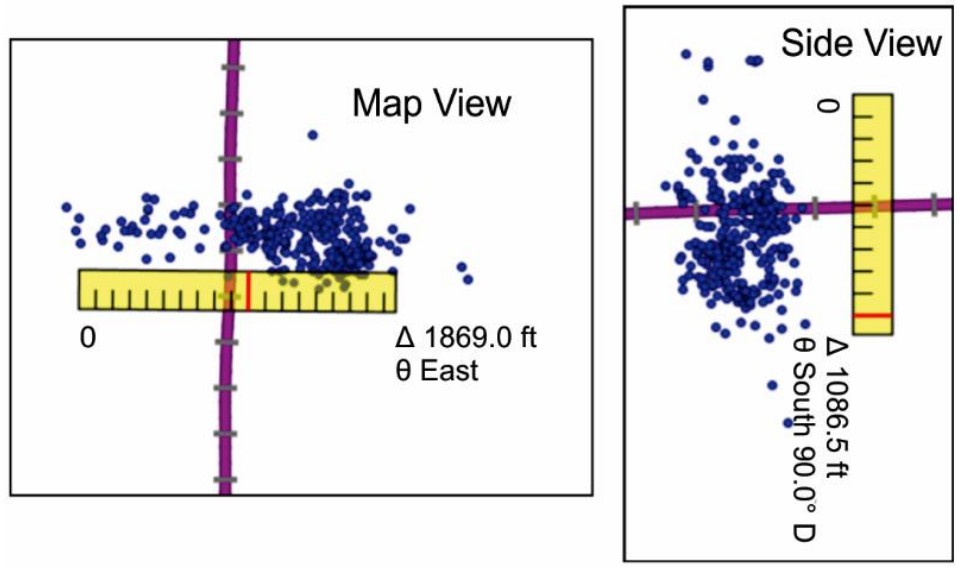


Figure 54: Example of fracture geometry (fracture length and height).

Downhole MSM of the project was an involved process that required significant planning and coordination. Multiple vertical wellbores were dispersed throughout the 11-well pad, but only one well was suitable for use as a monitor well for the downhole geophones. To minimize background noise in a monitor well, all open perforations should be isolated with a bridge plug so there is only non-perforated pipe for the geophone monitoring. Existing perforations can produce gas bubbles, which result in high background noise that can interfere with the

geophone's ability to detect the microseismic events. In addition to the vertical geophone arrays, a horizontal array was deployed in a horizontal well in the middle of the pad (Figure 47). The geophones were tractored into the well and then pulled back toward the heel during the offset well completions. This horizontal array was continually positioned directly across from the offset completion interval to help minimize the listening distance, reduce uncertainty, and minimize the observation well bias of the microseismic activity. The multiple-array setup always provided excellent coverage across most of the pad and delivered high-quality results. Figure 54 shows an example of one fracturing stage, which provides some insight into the fracture geometry generation. Created fracture half-lengths of more than 900 ft and total fracture heights of 1,000 ft were observed. Fracture event clouds greater than 500 ft wide were also observed during some fracturing stages. This is not the effective propped fracture geometry but most likely closer to the created SRV.

Representative Fracture Geometry from MSM

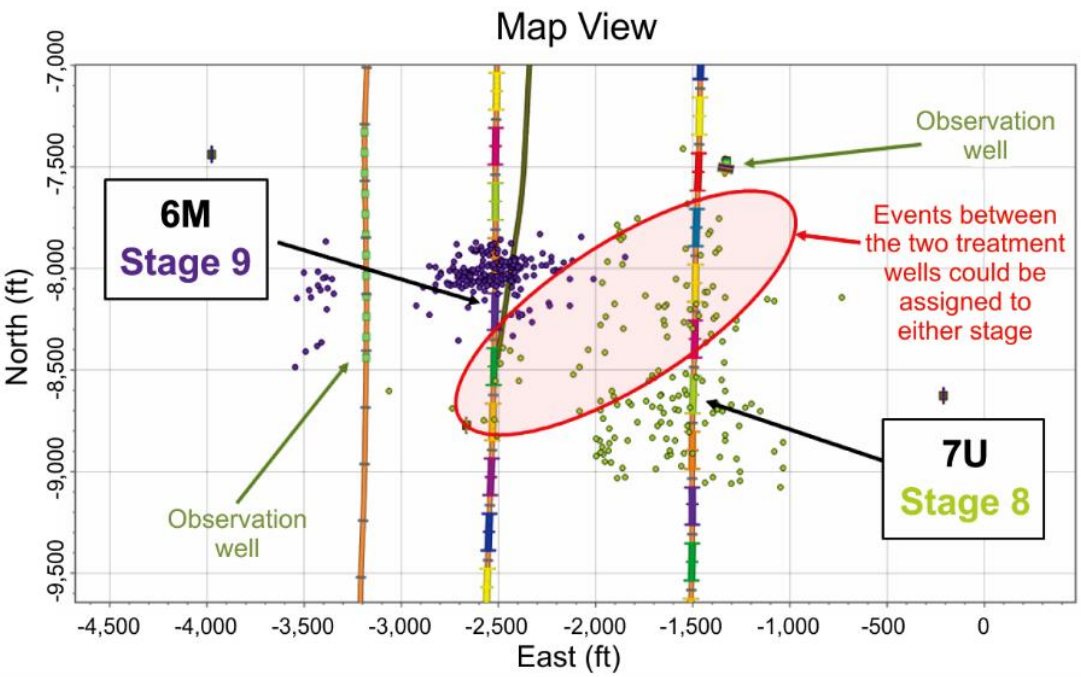


Figure 55: Map view of MSM events from simultaneously stimulated stages on Wells 6M and 7U.

Typical fracture geometry is based on the results of representative stages, which were minimally affected by artifacts of the measurement (Warpinski, 2009; Cipolla et al., 2011) and exhibit high data confidence. Some stages were not considered representative because they were pumped simultaneously with another stage; therefore, events attributed to those stages could be associated with their respective co-stimulated stage. Figure 55 shows such an example. The MSM events (in the red oval) were located between the two treatment wells and could be assigned to well because the completions were conducted during the same time period (two fracturing crews). Manual separation of the events was the only option at the time of the study, which extended the time necessary to deliver the final analysis. New processing techniques and algorithms have since been developed to address complex data sets acquired during multiwell zipper fracturing completions and have significantly decreased the post-completion processing time.

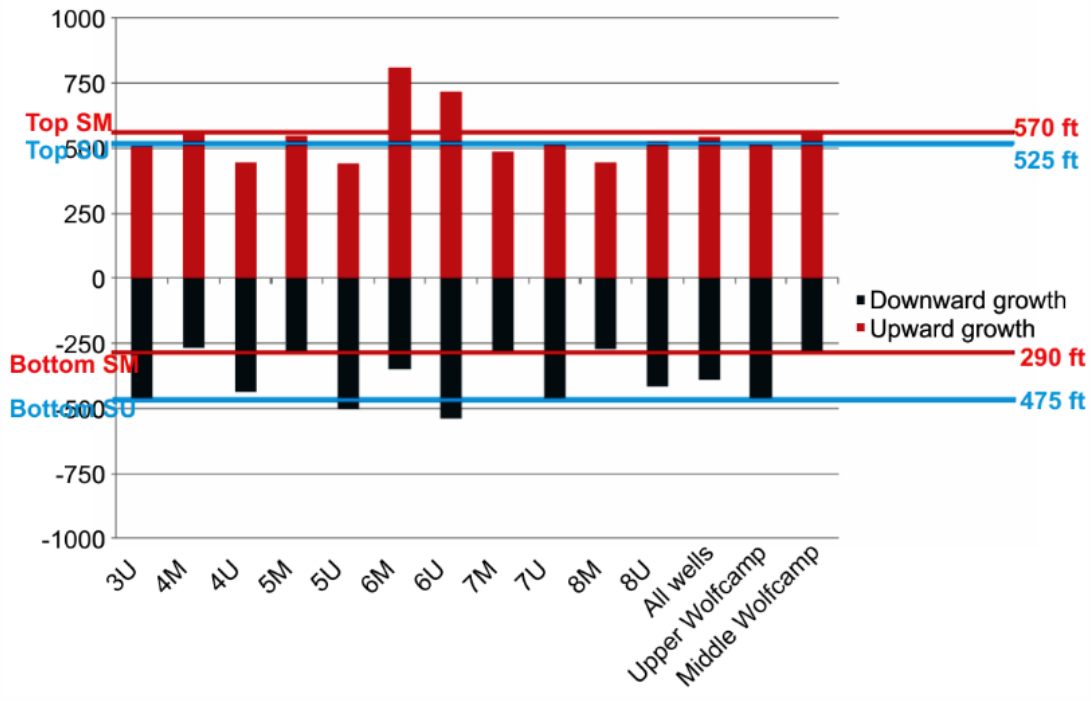


Figure 56: Average MSM height growth for all wells.

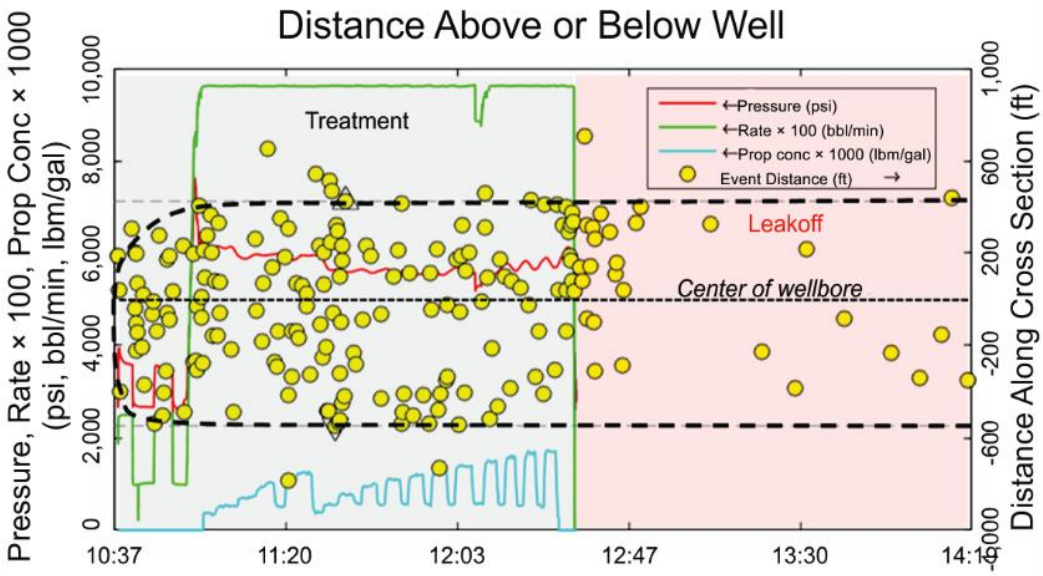


Figure 57: Example of typical fracture height and time relationship, well 5U.

Vertical coverage for the UW laterals extends from the top of the LW to the lower Spraberry formation but based on the principles of Stokes' law and the use of low-viscosity fluid, proppant distribution beyond the Dean formation is not expected. For the MW wells, fractures extend from the top of the LW to the top of the lower Spraberry formation, although as with the UW laterals, the low-viscosity fluid selection suggests upward proppant placement was likely confined to the top of the LW formation. Therefore, proppant presumably was not distributed into the lower Spraberry and Dean layers. Some LW stages extended farther downward into the LW formation, and proppant was probably able to reach these depths. Figure 56 shows the average height growth for each lateral relative to the perforation depth, respectively. The maximum fracture height was typically reached early during treatments according to the microseismic analysis. This relationship is consistent across all the project wells. Figure 57 and Figure 58 provide examples of the typical time/growth relationship for an

UW and MW well, respectively.

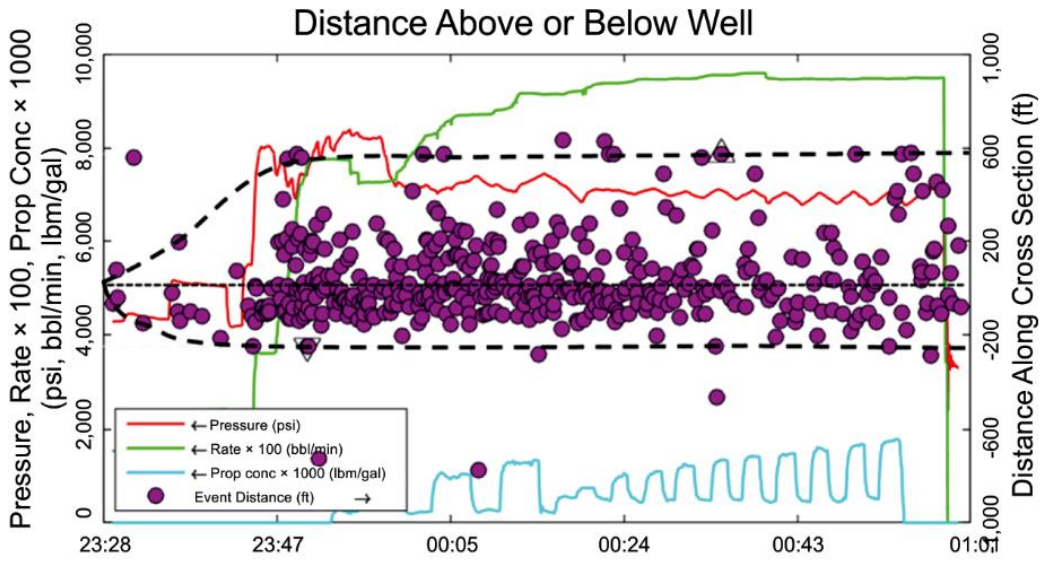


Figure 58: Example of typical fracture height and time relationship, well 7M.

Perforation Cluster Design Comparison

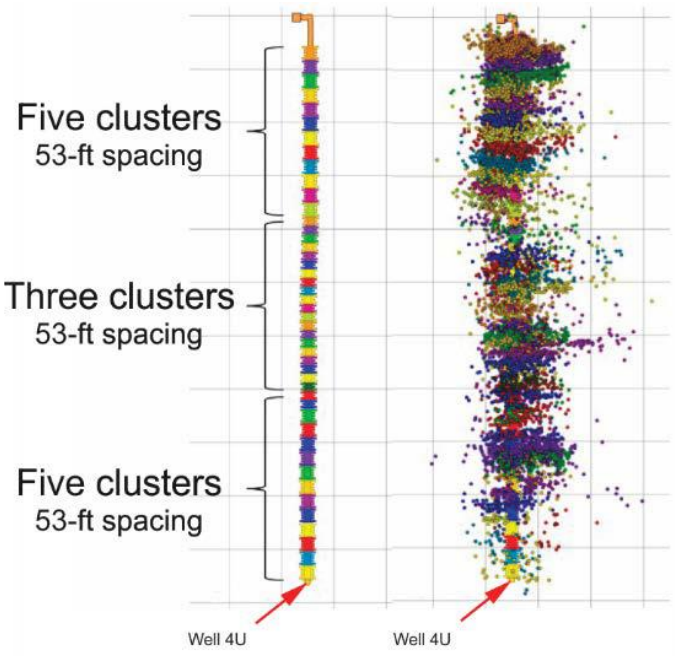


Figure 59: Perforation design and resulting fracture geometry on Well 4U.

Cluster count per stage varied between three vs. five clusters (entry points) per stage, and cluster spacing varied at 53 or 90 ft along the Well 4U and 7U laterals to determine whether these factors affected the created fracture geometry. Microseismic results can provide insight on additional far-field effects, such as azimuth and geometry measurements, but near-wellbore (NWB)-related conclusions, such as cluster efficiency and fluid distribution, are often indeterminate or have a low degree of certainty because of the inherent limitations of event location near the wellbore and measurement artifacts. A NWB monitoring technology, such as fiber optics, can provide real-time temperature and acoustic measurements, which can provide accurate NWB fluid distribution. Based on the acquired microseismic data, the varying perforation cluster count and spacing had no discernible effect on the fracture geometry of the

test wells vs. the standard completions on the other wells in the study. Figure 59 and Figure 60 show an example, in which fracture growth behavior and resulting geometry appear similar across the entire Well 4U lateral and are independent of the cluster design and number of entry points. While this is also likely true for the Well 7U lateral, the location of the MSM observation wells relative to the cluster design variations prevents a more definitive conclusion. Figure 61 shows the Well 7U microseismic data and cluster design variation points.

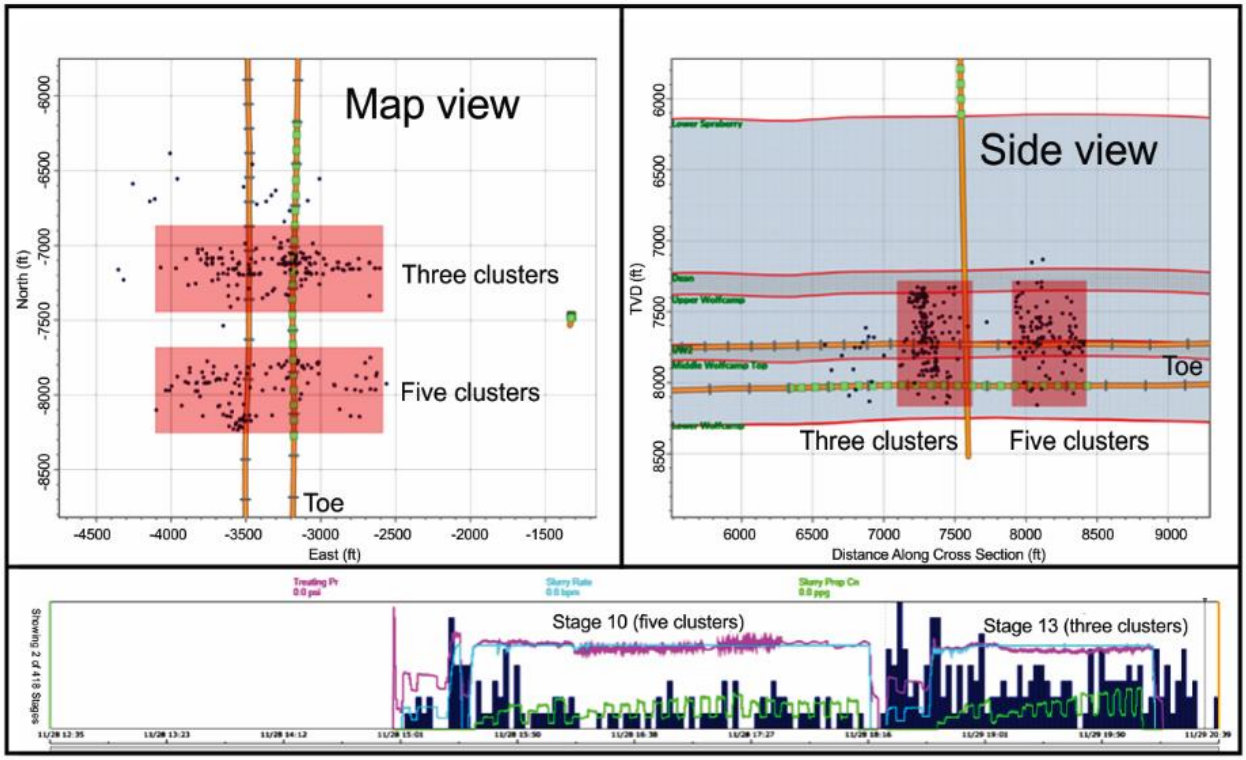


Figure 60: Comparison of Well 4U Stage 10 (five clusters) and Stage 13 (three clusters).

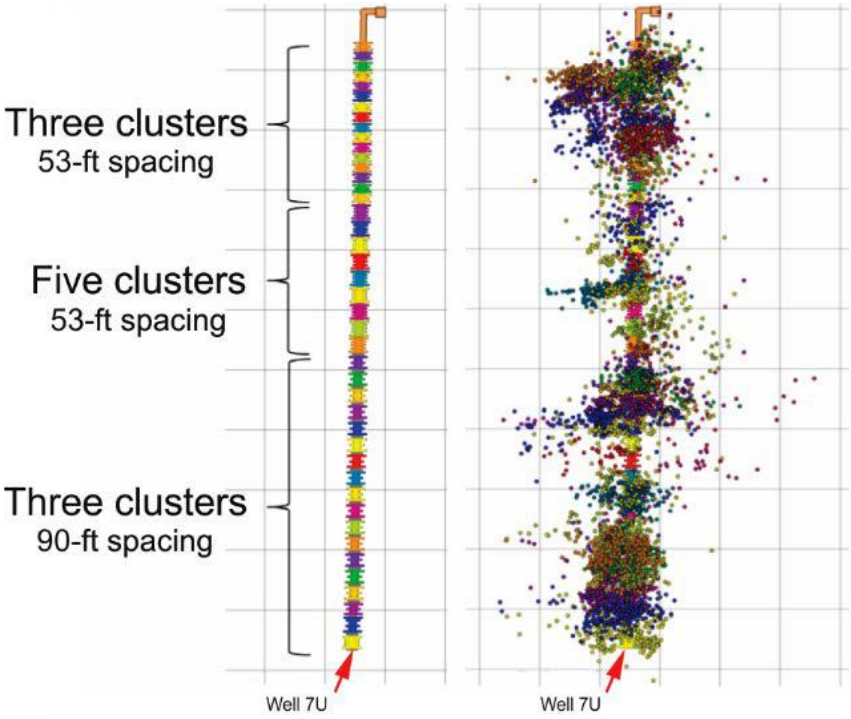


Figure 61: Well, 7U perforation design and resulting fracture geometry.

Fracture Azimuth and Complexity

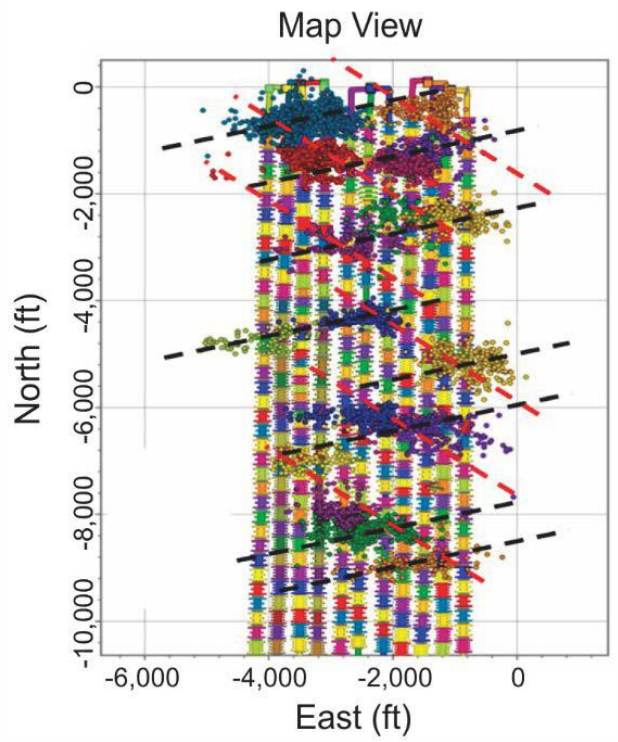


Figure 62: Map view of primary (black) and secondary (red) azimuths of selected project stages.

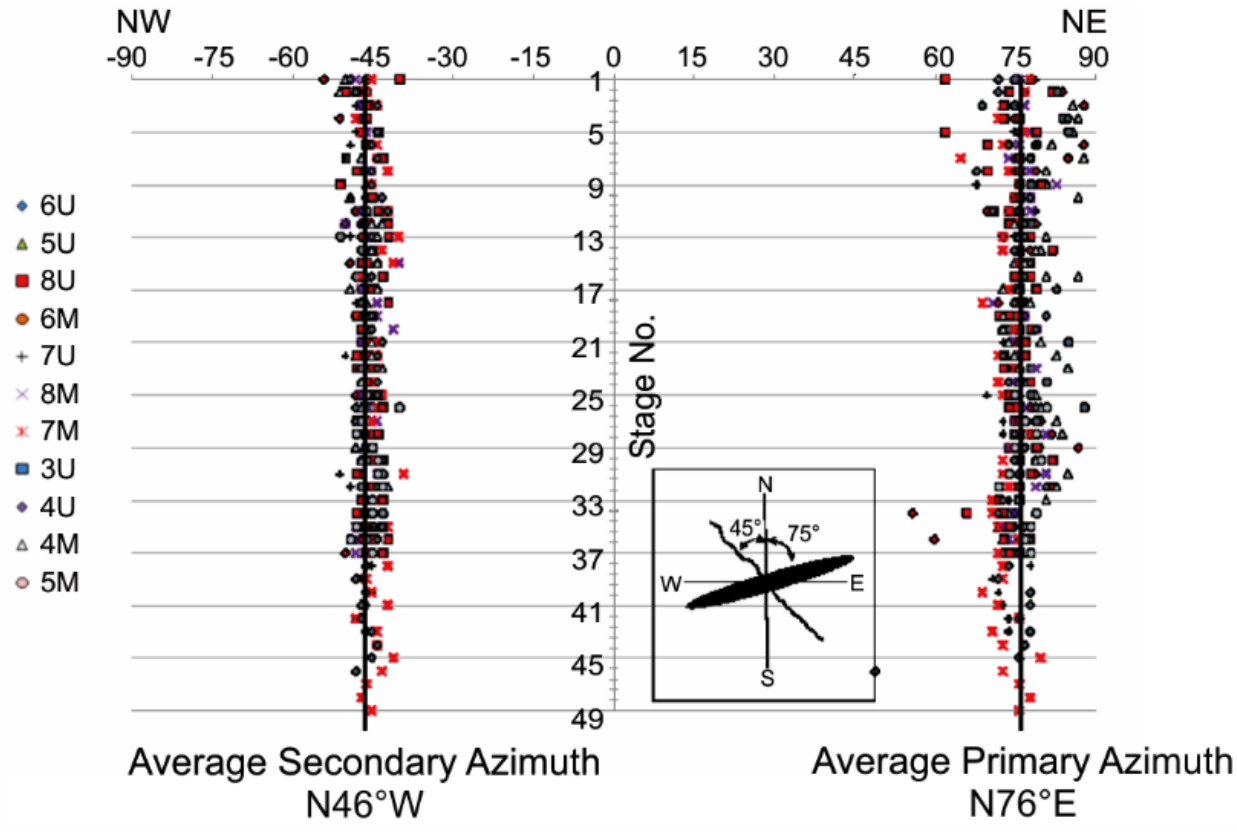


Figure 63: Primary and secondary fracture azimuths for all stages.

Figure 62 shows the primary and secondary azimuths for select stages. Figure 63 shows charted azimuth measurements for all stages of the 11 wells. The primary fracture azimuth is consistent among all wells and at N76°E is oblique to the north-south lateral orientation. Most stages of the 11 wells have a clear, strong secondary azimuth of approximately N46°W and a relatively wide event-cloud width of 535 ft (Figure 64), which in conjunction suggest an overall

moderate degree of fracture complexity was induced. Given the pervasive presence of the secondary azimuths and their rapid population after treatments began a small differential between the degree of the maximum and minimum principal horizontal stress directions in this region is likely. This would allow fractures to readily propagate along the minimum stress trend. During some stages, the primary azimuth displays a more east-west direction, and no discernible secondary azimuth is observed (Figure 65). For these stages, complexity is probably low, although it is possible some slight NWB complexity is present.

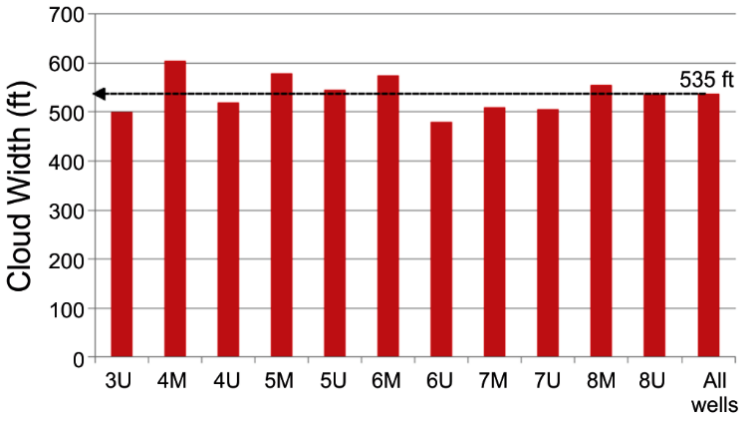


Figure 64: Average event-cloud width measurements for all wells.

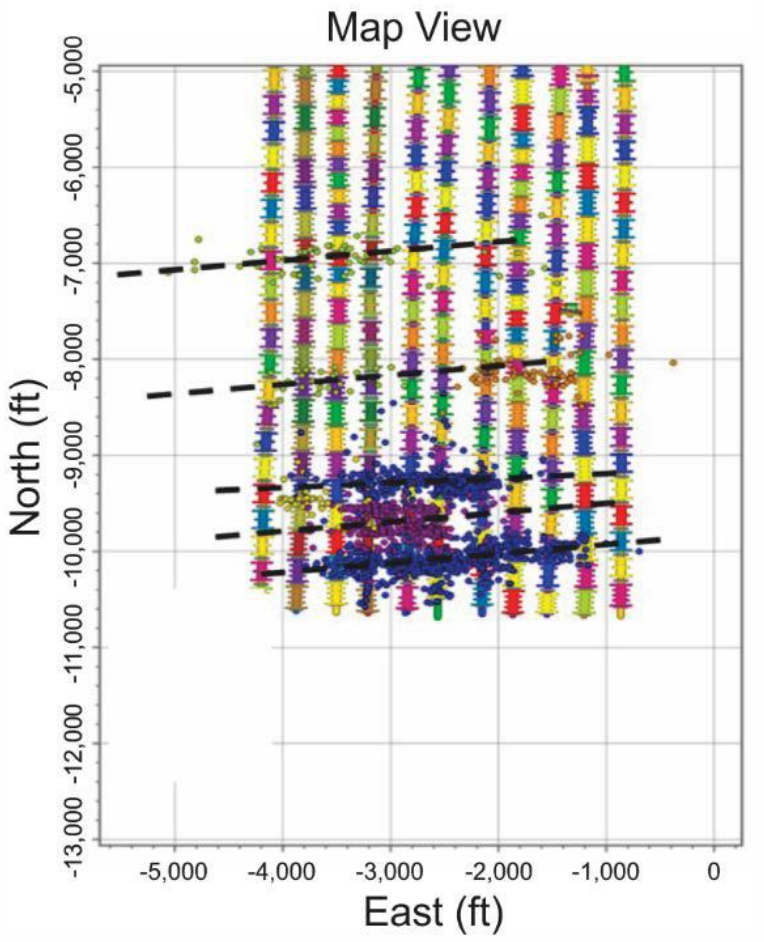


Figure 65: Map view of low complexity stages.

Completing the UW wells before the MW laterals might have affected certain aspects of the stimulation. Slightly wider event clouds were measured for the MW wells, and fracture

gradients were generally higher during the MW stages compared to the UW stages (Figure 66). These findings might be associated with the MW fractures interacting with the previously created fractures of the UW project wells, although it is possible stress-shadowing occurred between MW stages, as heel-ward cloud movement accompanied the increased fracture gradients during most stages of this well (Figure 67, Stage 6 blue MSM events). Toe-ward microseismic activity between stages could be caused by leaking fracturing valves or continued microseismicity caused by leak off from the previous fracturing stage (Figure 67, yellow MSM events overlapping Stage 4).

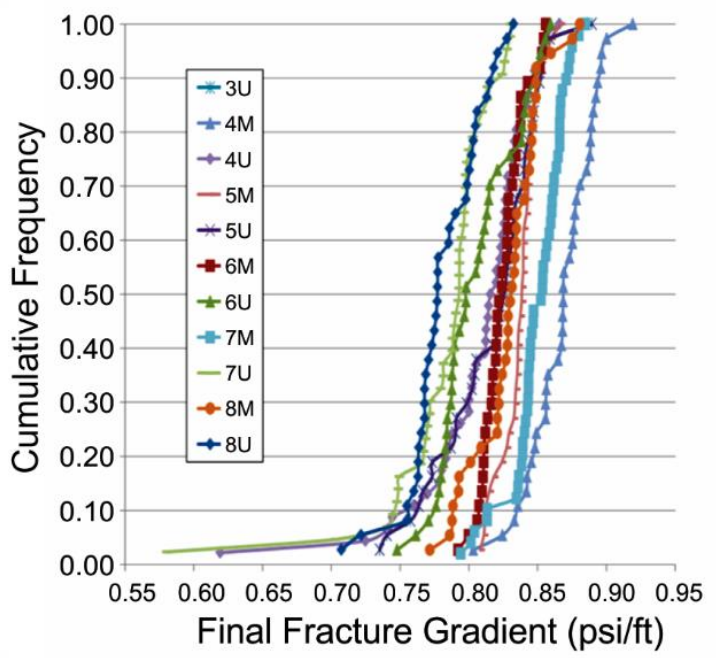


Figure 66: Final fracture gradients, all wells.

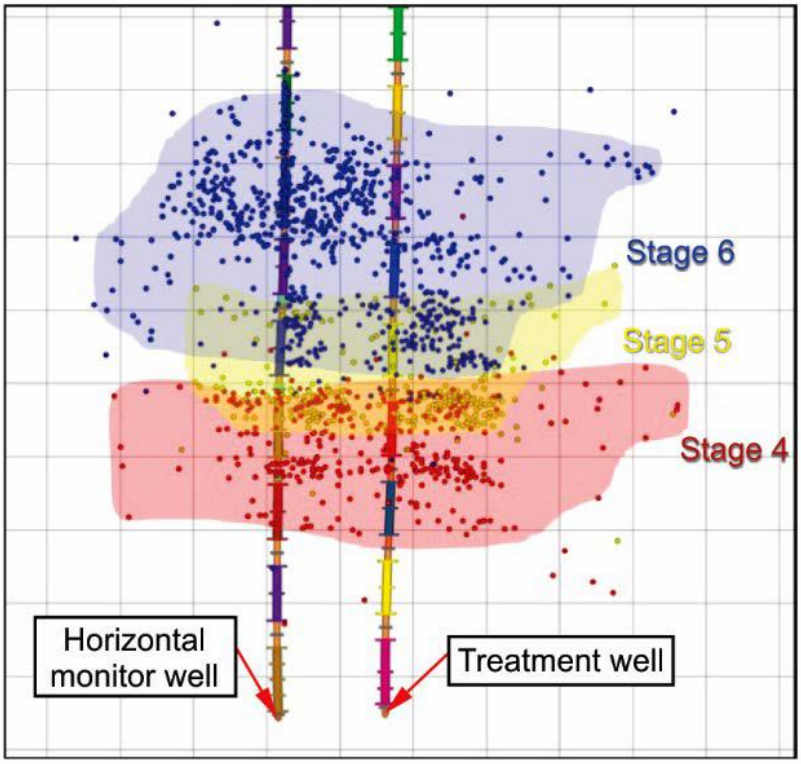


Figure 67: Interaction between adjacent stages, Well 5U Stages 4, 5, and 6.

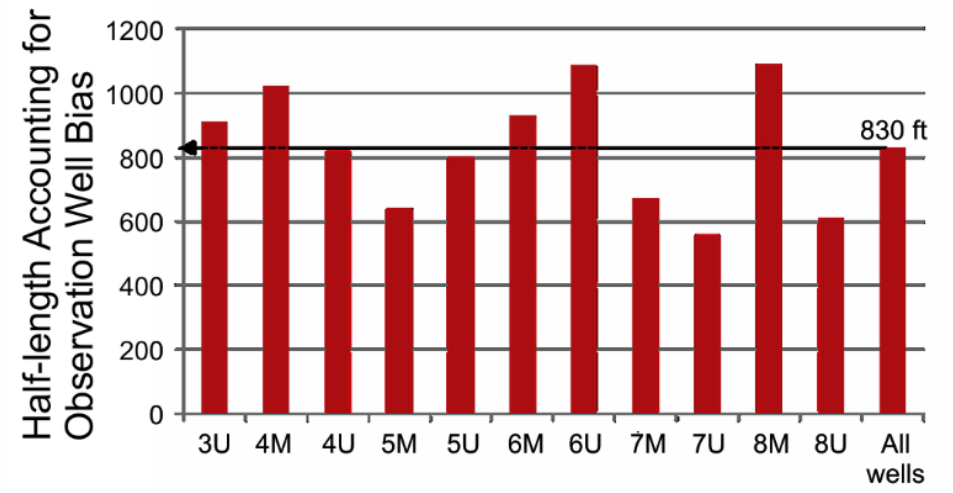


Figure 68: Average fracture half-length (ft) per well.

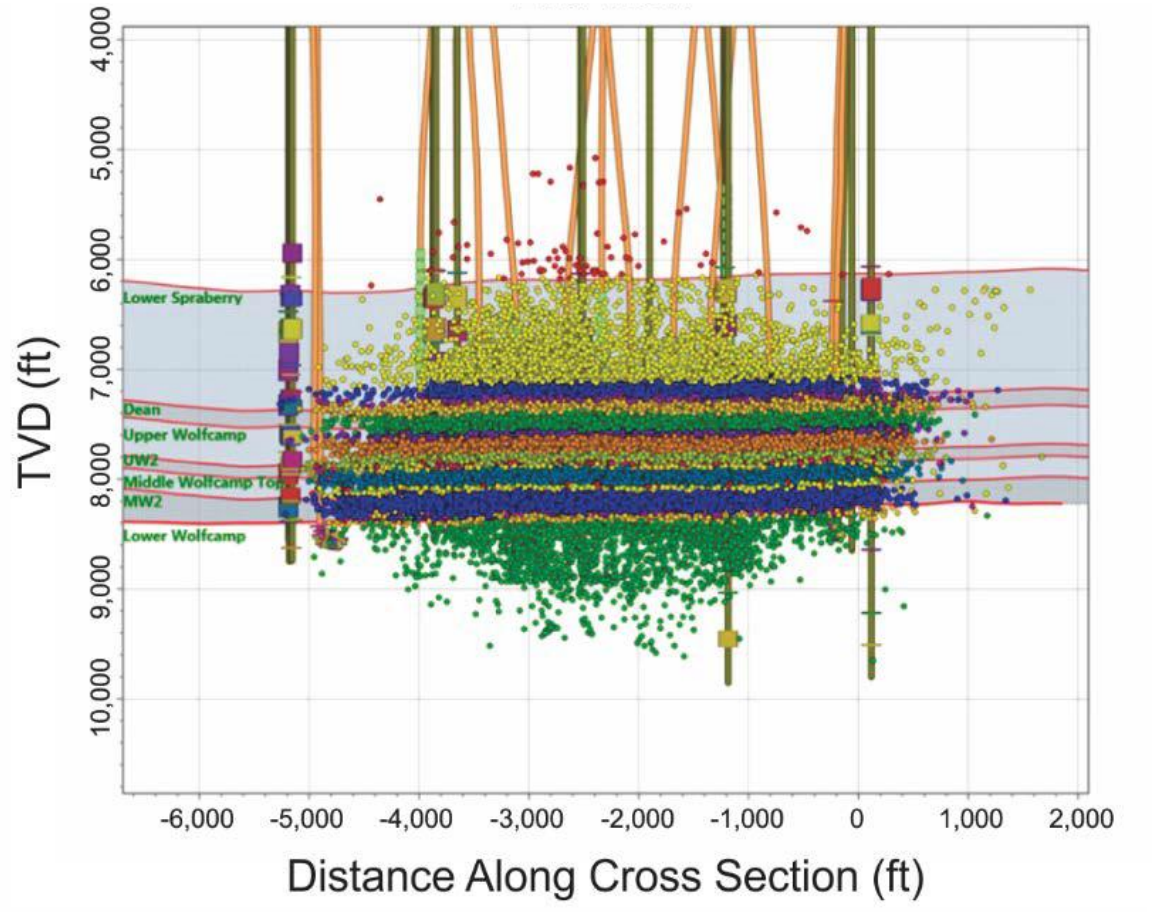


Figure 69: End view (gun barrel view) of all stages colored by formation.

Fracture half-lengths for the 11 wells range from 555 to 1,090 ft, with an average of 830 ft (Figure 68). Similar fracture extension exists between most formations, from the Dean to the bottom of the MW 2, but shorter fracture lengths in the LW and upper portion of the lower Spraberry are present (Figure 69). The maximum fracture half-length appears to have been reached approximately 60 minutes after the injections began. Only incremental growth was observed beyond this period. Figure 70 and Figure 71 show an example of this relationship for an UW and MW well.

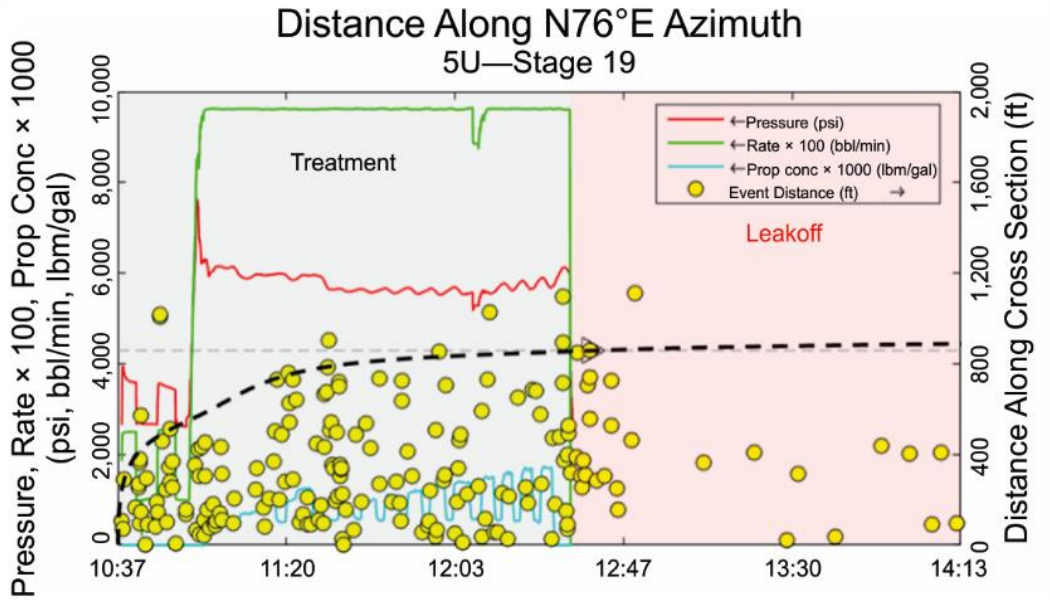


Figure 70: Example of fracture length and time relationship, Well 5U Stage 19.

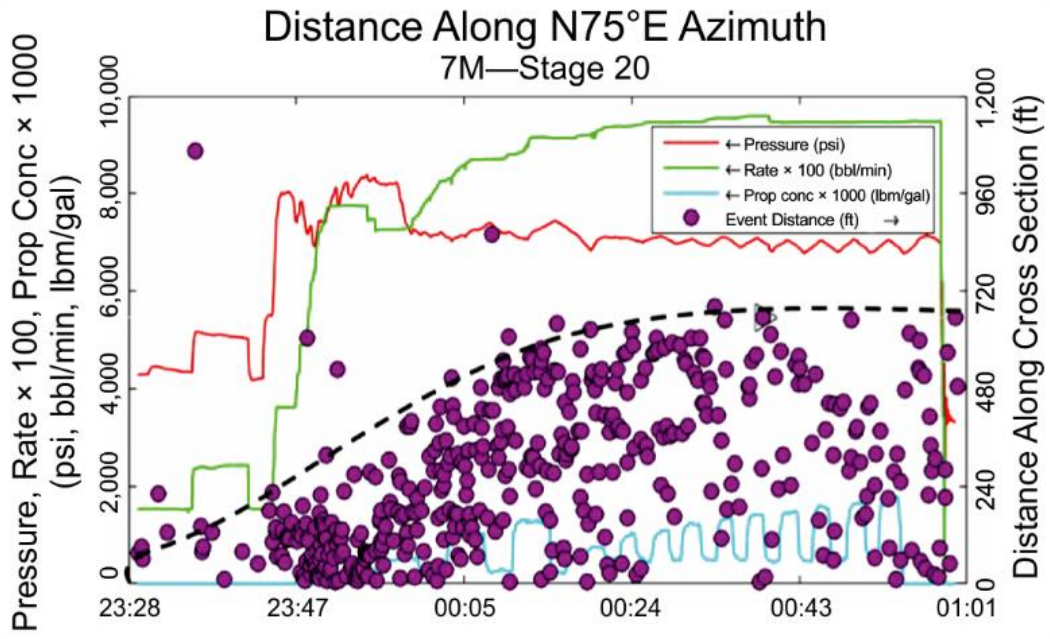


Figure 71: Example of fracture length and time relationship, Well 7M Stage 20.

Downhole Deformation Measurements (Tiltmeters)

The vertical monitor geophone array included a hybrid string of downhole tiltmeters (Wright et al., 1998; Warpinski et al., 2014; Fisher et al., 2011). The bottom of this toolstring was located approximately 1,500 ft above the uppermost lateral completion. The downhole tiltmeters were not intended to measure fracture height because the tools did not straddle the completion zone but were instead used to measure whether a hydraulic fracture extended upward past the toolstring array. The results showed only the lowermost tiltmeter indicated slight deformation of the reservoir rock during the completion (measured in microradians). This indicates that the hydraulic fractures generated during the completion did not propagate upward past the tiltmeter array. This means a hydraulic fracture was generated somewhere below the toolstring, which caused small vertical rock deformation at the leading edge of the upward growing fracture.

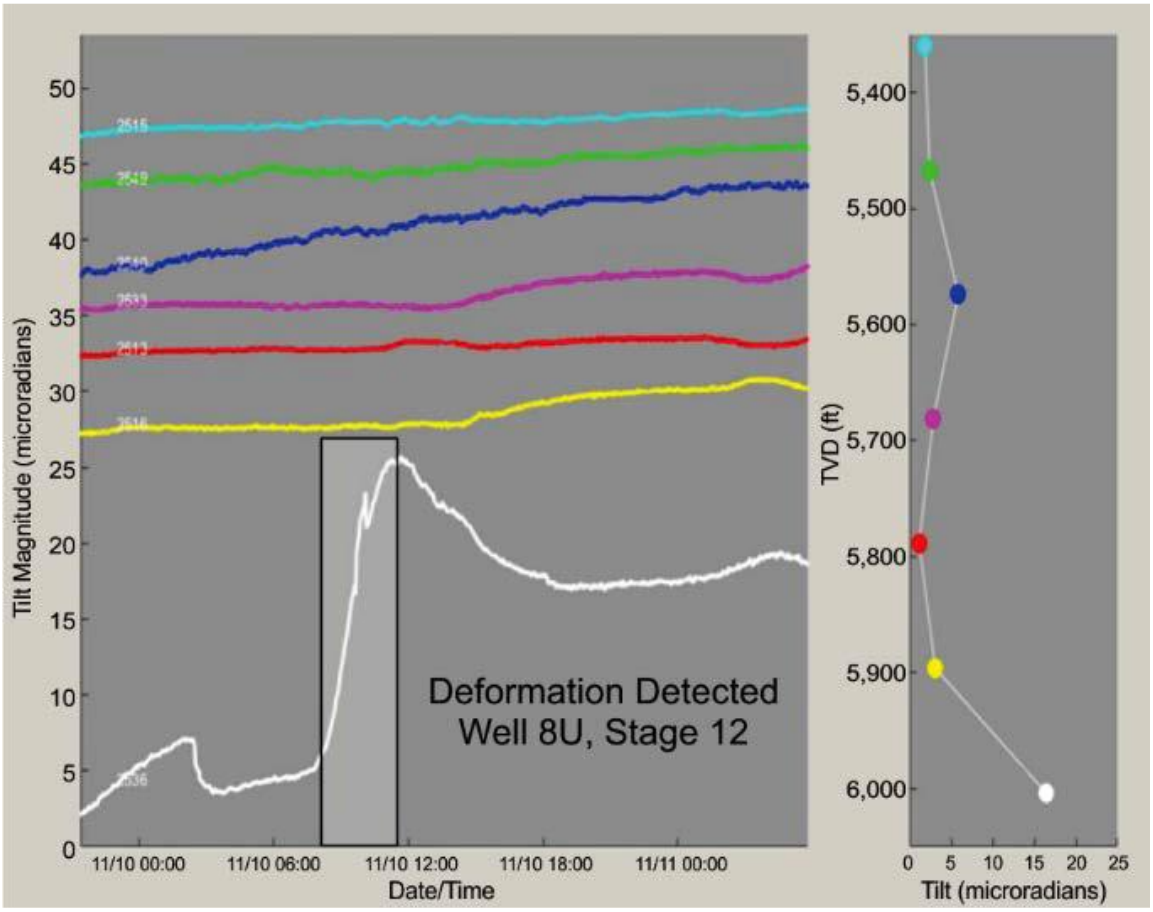


Figure 72: Deformation detected during Well 8U Stage 12.

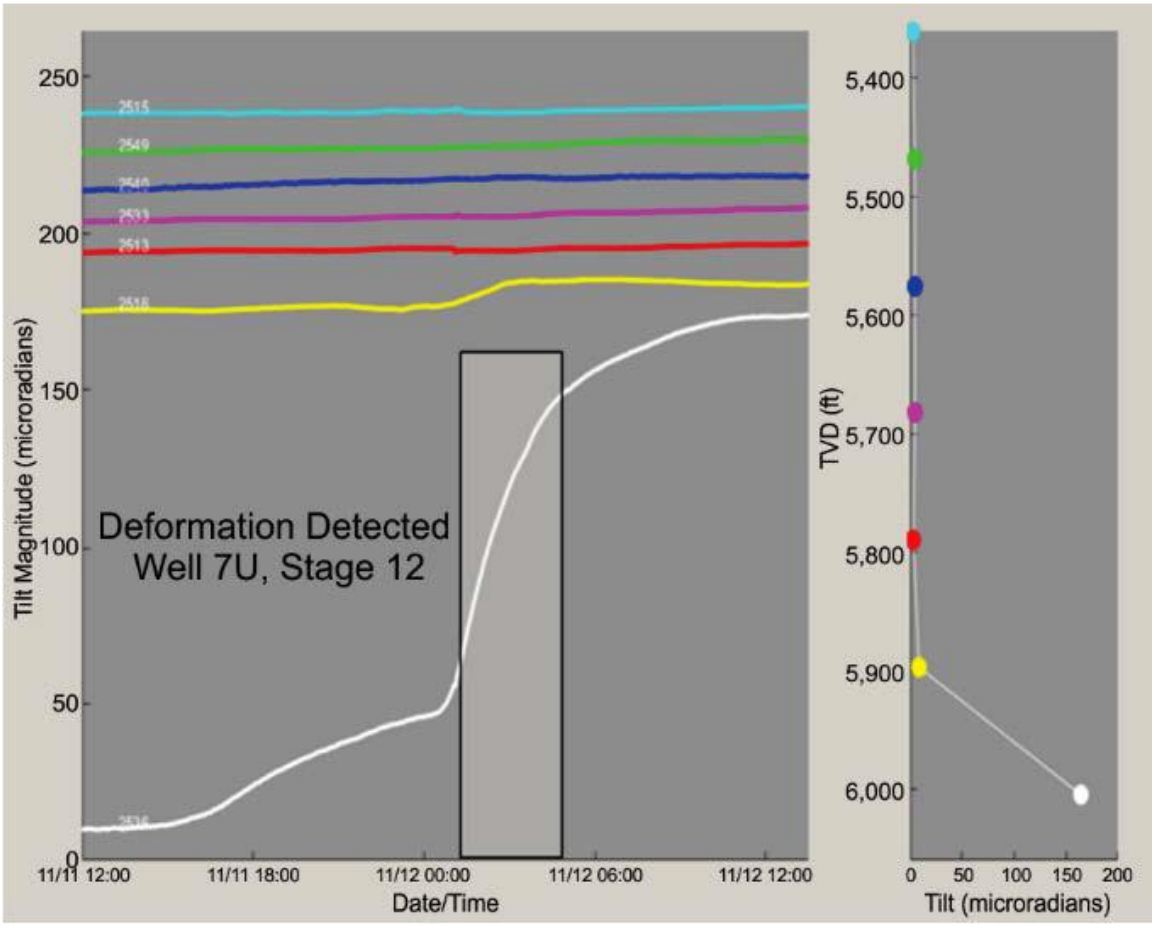


Figure 73: Deformation detected during Well 7U Stage 12.

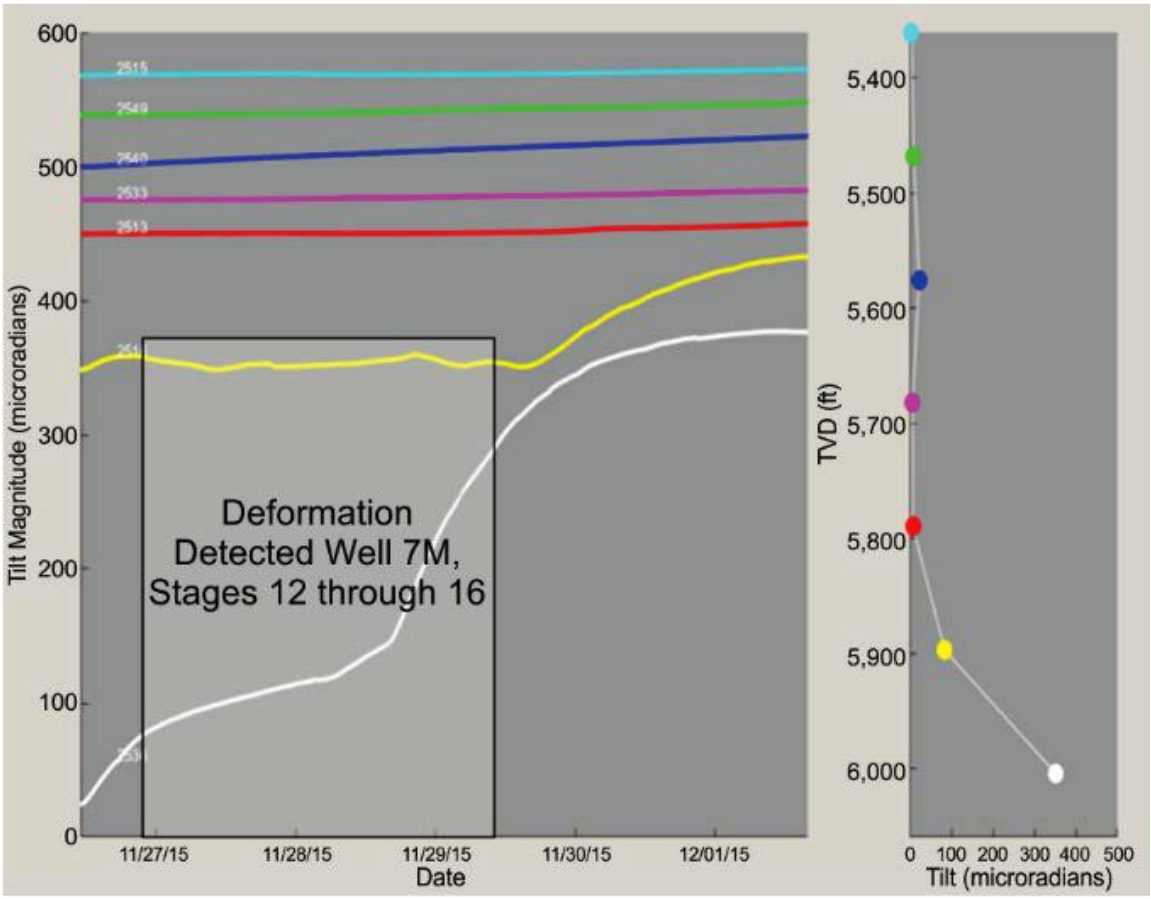


Figure 74: Deformation detected during Well 7M Stages 12 through 16.

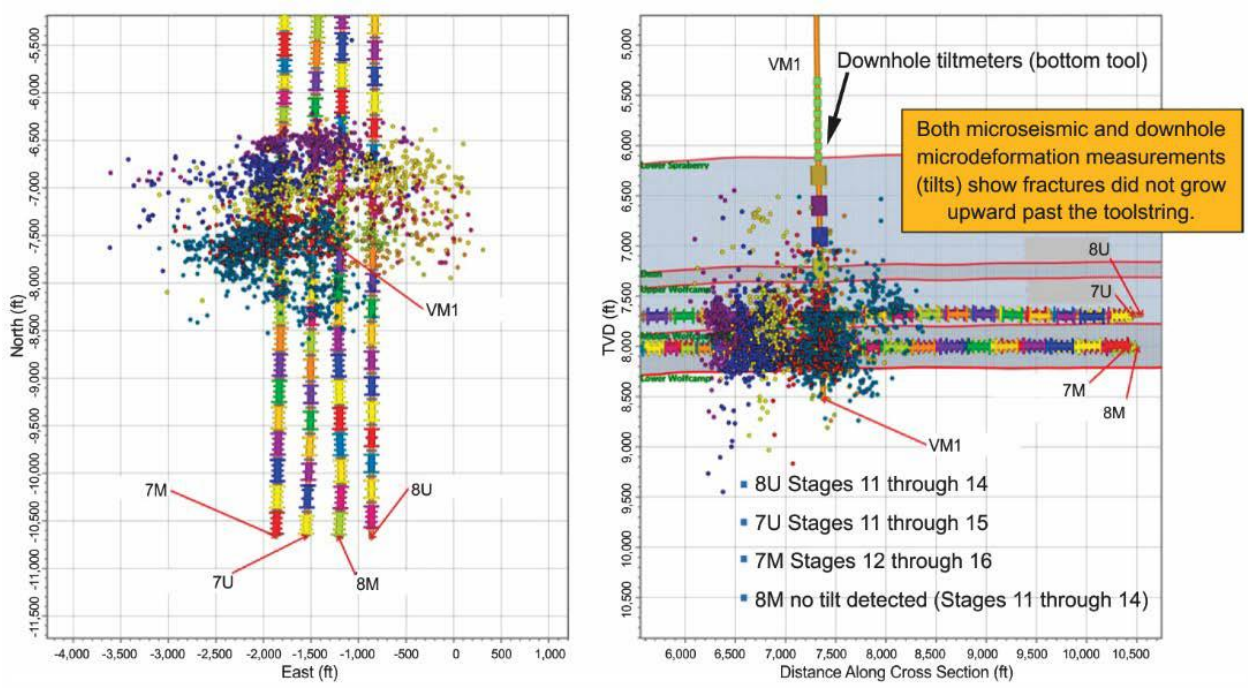


Figure 75: Correlating microseismic measurements during tiltmeter deformation detection.

The tiltmeter records the magnitude of deformation (tilt) in microradians. It was concluded that the hydraulic fracture was somewhere below the tool's true vertical depth (TVD) and did not extend to a shallower depth beyond the array. Recorded responses are shown in Figure 72, Figure 73, and Figure 74, in which the lowest tiltmeter is displayed in white. Figure 75 shows the correlated microseismic results from these stages, which support the downhole

microdeformation conclusions.

MSM Data Relative to the "Slant Well" Post-Fracturing Whole Core

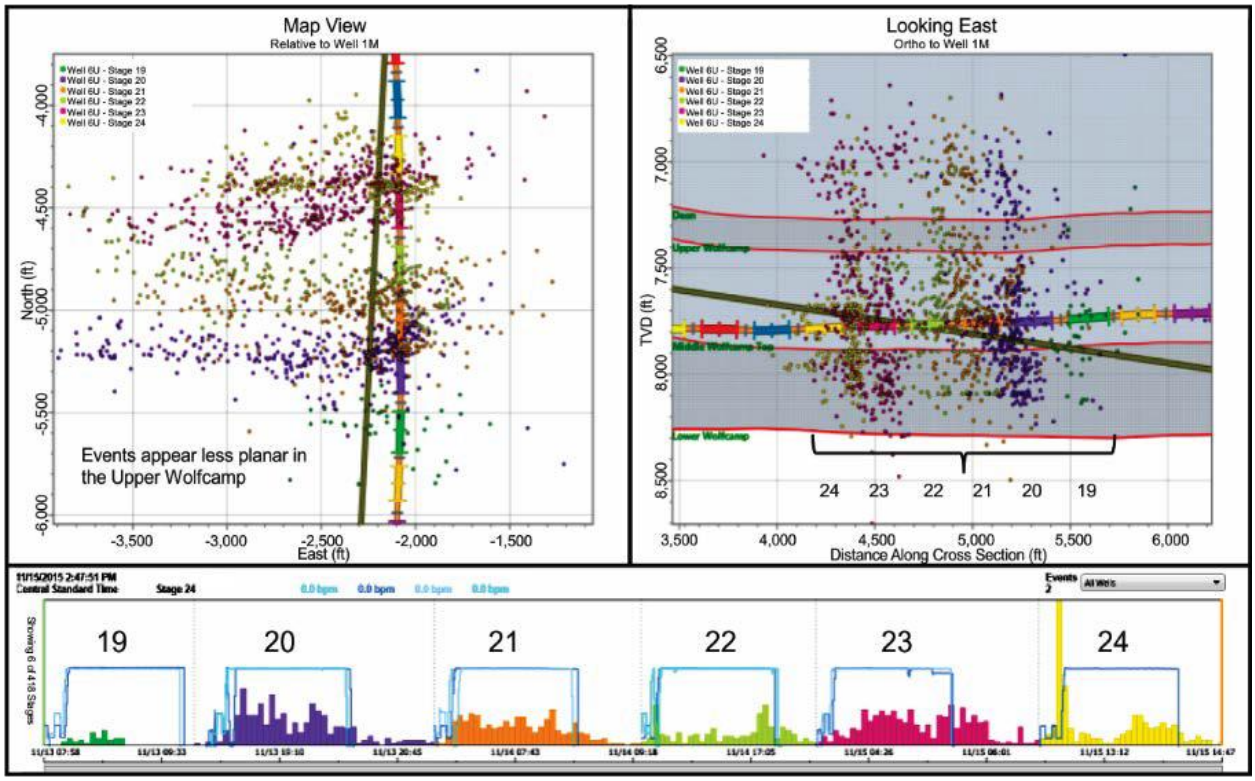


Figure 76: Core cut along Well 6SW adjacent to Well 6U Stages 19 through 24.

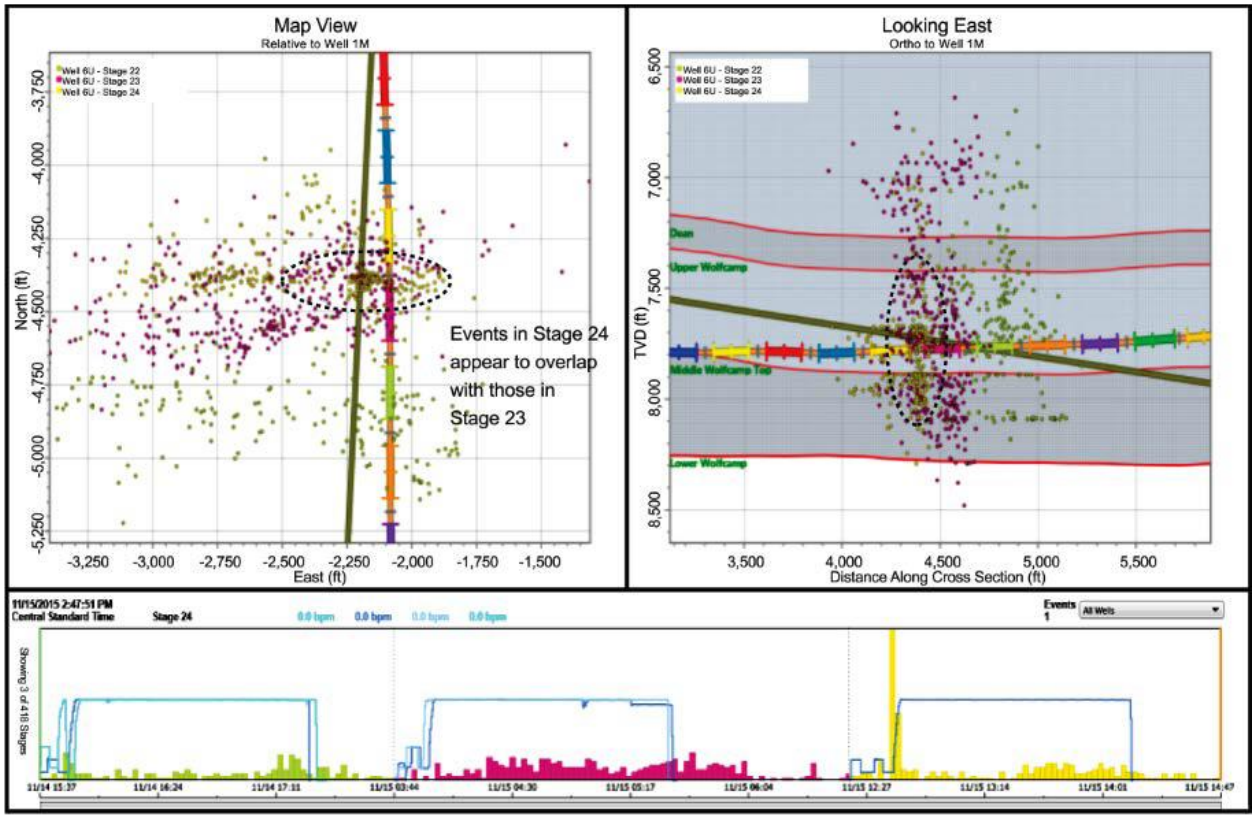


Figure 77: Core cut along Well 6SW interval adjacent to Well 6U Stages 22 through 24.

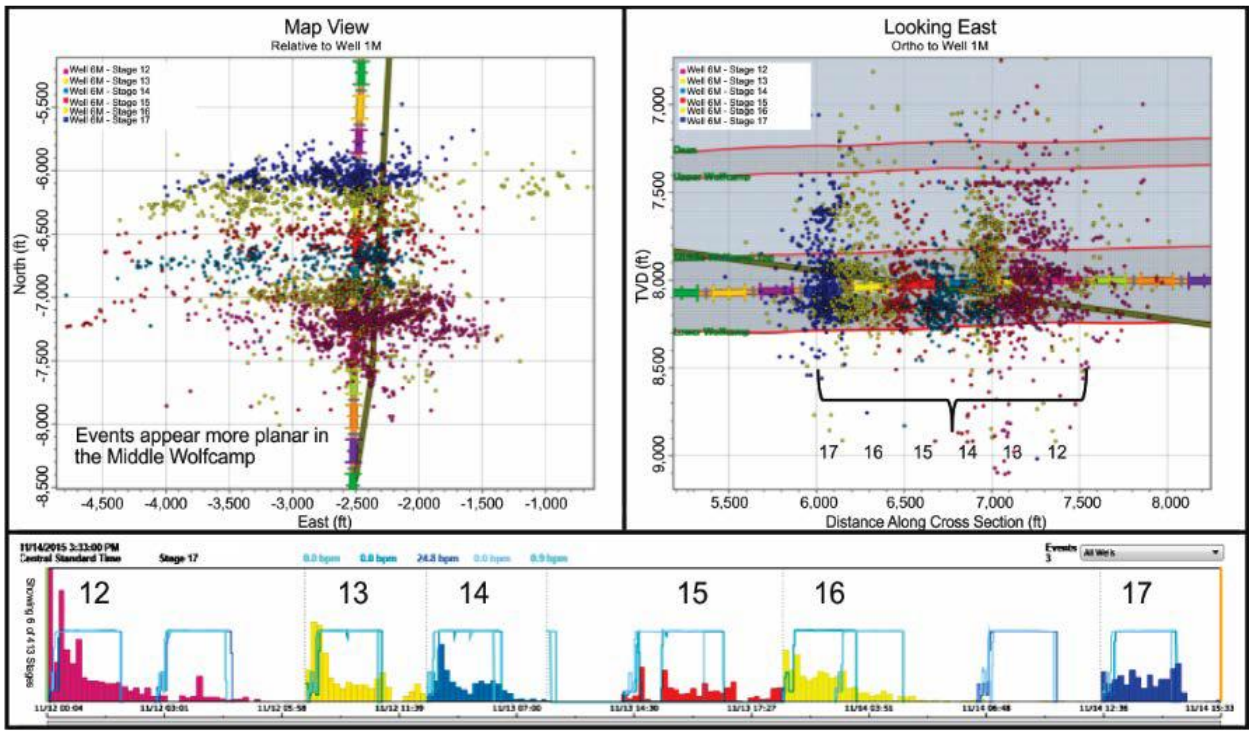


Figure 78: Core cut along Well 6SW interval adjacent to Well 6M Stages 12 through 17.

Two sections of openhole core were cut in Well 6SW (slant well) after the completion of the pad wells to provide a TVD/measured depth (MD) reference to previously recorded Well 6U and 6M events. As has been mentioned in the introduction, approximately 400 ft of core was cut adjacent to Stages 22 through 24 of Well 6U, and another 200 ft of core was cut across from Well 6M along Stages 14 and 15. Events from these stages can then be compared to the known TVDs along the two core locations of the 6SW slant core well to further characterize fracture growth.

Results indicate that the UW events are less planar and more dispersed than the MW events. The slight decrease in planar growth could be caused by the lithological properties in the UW. It is possible that there is a higher concentration of natural fractures in the UW vs. MW. Induced stresses related to the completion sequencing (UW wells stimulated before the MW wells) could have also contributed to the differing growth pattern. Figure 76, Figure 77, and Figure 78 show the microseismic results from Well 6U Stages 22 through 24 and Well 6M Stages 14 and 15 vs. the adjacent core cuts along Well 6SW.

Observations and Conclusions

The following conclusions are a result of this work.

- Fracture geometry is relatively consistent for all 11 wells; however, some localized differences might exist (offset production, interaction with previous fractures, etc.).
- Primary fracture azimuth is N76°E and secondary azimuth is N46°W.
- A moderate overall degree of complexity with additional exposed surface area in the secondary direction was likely achieved.
- Hydraulic fractures did not extend vertically upward beyond the downhole tiltmeter array (~1,500 ft above the UW laterals).

- Additional fracture complexity was possibly the result of back-to-back completions (zipper fracturing) and stress-shadowing effects.
    - Constructive interaction existed between stimulations.
    - Fractures in the LW were relatively contained because of UW completion.
- Generally, most of the fractures appear symmetric or show slightly asymmetric fracture growth (because of vertical offset production).
- Timing between completion sequencing does not appear to make a difference (based solely on microseismic data) if the completion:
    - Begins immediately with alternating stages between wells (zipper fracturing).
    - Begins by pumping the first five stages on one well and then alternating stages (zipper fracturing).
- The optimum number of perforation clusters per stage and cluster spacing was indeterminate, based on only the microseismic data, because of:
    - Difficulty establishing a baseline for the DOE.
    - Microseismic measurement artifacts.
    - Completion interval variations (UW and LW).
- NWB diagnostics (fiber optics) are necessary to determine NWB fluid distribution and cluster efficiency.

Using microseismic frequency-magnitude distributions from hydraulic fracturing as an incremental tool for fracture completion diagnostics.

Authors: Debotyam Maity, and Jordan Ciezobka

Abstract

Microseismic measurements are becoming increasingly routine with many large, pad scale hydraulic fracturing programs particularly in the prolific unconventional shale basins of North America. Spatial and temporal frequency-magnitude distributions or 'b-value' measurements can provide useful information, which can help with hydraulic fracturing diagnostics as well as design. In this study, we discuss the significant differences in the seismicity distributions in the upper and middle Wolfcamp formations at the Hydraulic Fracturing Test Site located in the Midland Basin, a sub-basin of the Permian. We validate observed seismicity behavior in relation to other reservoir properties of interest, including 3D seismic derived attributes and petrophysical data. The in-situ stress state has a significant bearing on b-value, and we validate this using various observations. We correlate observed microseismicity with available 3D seismic data. We see significant impact of in-situ discontinuities and rock brittleness on the microseismicity distributions. We also look at hydraulic fracturing treatment data, specifically, injection pressure, and tie it with variations in microseismicity during pumping. Our results extend the usefulness of microseismic b-value as a tool for fracturing treatment diagnostics during or post hydraulic fracturing operations. The analysis of microseismic b-value as shown in this study provides a template for future applications where microseismic surveys are available. It can be a significant value-add to traditional microseismic surveys with minimal computational and other resource requirements.

Introduction

Hydraulic Fracturing Test Site (HFTS) is a collaborative research project between the industry and the United States Department of Energy. The test site is in the Midland portion of the Permian Basin (Figure 79a). The HFTS study involves a comprehensive testing and diagnostics program piggybacked on routine hydraulic fracturing operations performed on an eleven-well pad in the Wolfcamp Shale formation (Perry et al., 2017; Ciezobka et al., 2018). These wells are extended horizontal laterals drilled from north to south and the estimated orientation of maximum horizontal in-situ stress is orthogonal to the well orientations. The unique feature of the test site is a single experimental slant core well. We used it to acquire more than 500 ft of through fracture cores from both the upper Wolfcamp and middle Wolfcamp formations (Figure 79b and Figure 79c). These two reservoir units will be henceforth referred to as UWC and MWC formations respectively. Alternately, these zones are also referred to as Wolfcamp A and Wolfcamp B formations in other studies on Permian Basin. As seen in Figure 79, wells W1 through W6 are in the UWC formation and wells W7 through W11 are in the MWC formation. The wells have been drilled and completed in a chevron pattern. The average lateral separation between the wells within the same formation is approximately 660 ft and the vertical separation between wells within the two formations is approximately 300 ft.

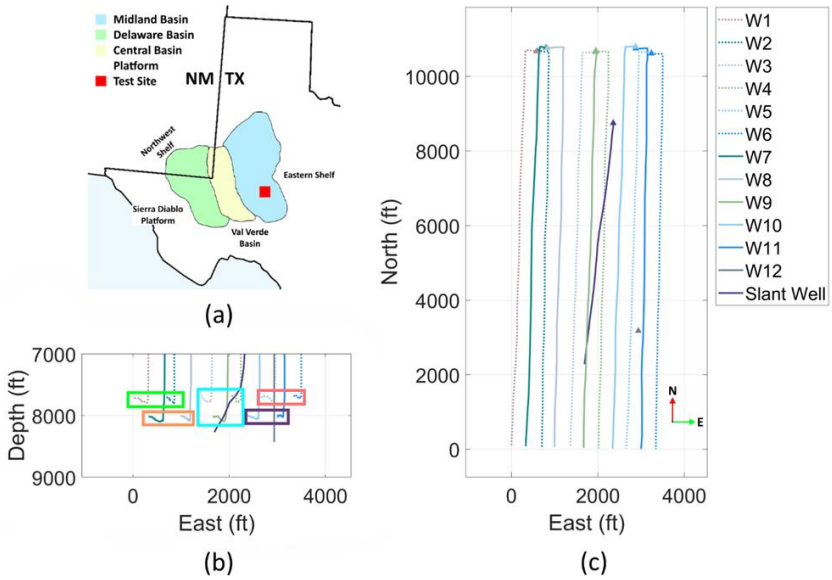


Figure 79: Test site well schematic showing the (a) test site location, (b) gun-barrel view looking north, and (c) map view looking down. We indicate all the wells hydraulically fractured as part of the experiments. The slant well was used to acquire through fracture core samples (Gale et al., 2018; Maity et al., 2018) and a vertical well W12 was used in microseismic monitoring. The colored box inserts in (b) highlight the wells that were fractured together in the zipper fracturing sequence (Table 3).

The core description (Gale et al., 2018) and proppant distribution within the fractured zone (Maity et al., 2018) provide significant insights into the fracturing behavior. In addition, the HFTS study includes various other datasets and measurements of interest. These include baseline 3D seismic data and comprehensive petrophysical logs (such as spectral gamma, compensated neutron, cross dipole sonic, micro-resistivity image logs, etc. for multiple wells). Apart from geomechanical studies and petrography, other datasets collected include an extensive oil and water tracer study, downhole pressure monitoring, multiple pre- and post-fracturing cross-well seismic surveys, comprehensive core testing based on more than 100 sidewall cores, micro diagnostic formation injection tests, tilt-meter surveys, oil based micro-imager (OBMI) logs, etc.

A comprehensive microseismic monitoring program involving a downhole as well as a surface microseismic survey were used at the test site. Our analysis uses data from the downhole geophone arrays. A maximum of two arrays were deployed in the horizontal laterals or alternatively, either in the vertical well, W12, within the area of interest, or in the vertical section of one of the completed horizontal well laterals. The placement is guided by the wells and stages being completed to reduce both the source to receiver separation as well as to minimize the need for frequent changes in array deployment between fracture stages. In addition, use of the two arrays allows for reduced uncertainty in estimated microseismic source parameters. The microseismic record generated by the fracturing program for this 11 well pad is exhaustive with data from approximately 380 treatment stages collected over more than 45 days. In all, almost 150000 microseismic events were processed and located with a majority being identified using waveform data from both the arrays. Overall, the average microseismic event density per stage for this pad is around 350 and the average moment magnitude is around -2. In Table 3, we show the zipper fracturing completion sequence followed for these wells. The fracturing program is split into three phases. For each phase, the location of the downhole arrays is also specified (see Figure 79 for relative location of wells). The dual receiver

array configuration uses four geophone strings (two each for phase 1 & 2). Table 3 highlights the fracturing sequence. Cells of identical color represent wells fractured together using zipper fracturing technique. Fracture sequencing includes wells that were switched after each stage was fractured as well as wells switched after five stages were fractured in each of the wells in sequence. Stegent and Candler (2018) provide a more detailed description of the monitoring array deployment, geophone tool-string details, fracturing sequence, and processed microseismic data.

Table 3: Completion sequence for various wells in the pad. Also, highlighted are the corresponding observation wells and number of stages with available microseismic data: modified from Stegent & Candler (2018). The colors represent wells fractured in each zipper fracturing sequence and correspond with rectangles in Figure 79b.

Phase #	Treatment well (total stages)	Formation	Observation wells						stages with data
			W8	W8	W8	W9	W1	W12	
1	W3 (37)	UWC	1 to 32		33 to 37			1 to 37	37
	W4 (37)	UWC	1 to 32		33 to 37			1 to 37	37
	W9 (37)	MWC	1 to 28		29 to 37			1 to 37	37
	W6 (37)	UWC	1 to 37					1 to 37	37
	W5 (43)	UWC	1 to 37		38 to 43			1 to 43	43
2	W1 (37)	UWC	1 to 31	32 to 37				1 to 37	37
	W2 (46)	UWC	1 to 29	30 to 46				1 to 46	46
	W11 (37)	MWC	1 to 34	35 to 37				1 to 37	37
	W10 (49)	MWC	1 to 29	30 to 49				1 to 49	49
3	W7 (37)	MWC				1 to 37	1 to 37		13
	W8 (37)	MWC				1 to 37	1 to 37		13

Microseismic phase arrivals and amplitudes are regularly used to invert for hypocentral source locations and magnitudes. While these and other relevant source parameters can provide valuable information, another useful parameter is the relationship between the moment magnitudes and the frequency of earthquakes in both time and in space. Gutenberg & Richter (1944) first proposed the power law model for seismicity, i.e., frequency magnitude distribution (FMD). The slope parameter 'b', henceforth referred to as 'b-value', provides statistical characteristics of magnitude distribution for any seismic catalog. The general power-law relationship has been validated for hundreds of catalogs, at the laboratory, regional as well as teleseismic scales (Utsu, 1999; Wang et al., 2000; Gerstenberger et al., 2001; Wiemer & Wyss, 2002; Amitrano, 2003; Scholz, 2015). Many recent studies have used b-value variations as a means for better understanding of the hydraulic fracturing operations (Vermylen & Zoback, 2011; Wessels et al., 2011; Sil et al., 2012; Roche et al., 2015). A significant influence on b-value is the source environment, i.e., the tectonic setting and the prevalent in-situ stress state.

Regions dominated by activation of relatively large faults generally show a b-value close to 1, which is indicative of higher in-situ differential stress. During earthquake swarms, values closer to and higher than 2 are possible indicating a relatively larger proportion of smaller earthquakes in the microseismic catalog. In the context of injection induced seismicity, similar distinction in observed b-value has been correlated with prevalence of "wet" and "dry" microseismic events (Maxwell et al., 2015). Furthermore, recent laboratory experiments have validated the effect of differential stress on seismicity behavior with higher stress anisotropy generating more planar fracturing behavior (Maxwell et al., 2017).

At various seismicity scales, b-value has been correlated with the in-situ state of geomechanical stress. As a natural extension, studies have tied the tectonic stress regime with the observed b-value distribution. A seminal work on validating this idea was by Schorlemmer et al. (2005). Others, such as Grob & van der Baan (2012) have expanded on this idea and applied it to an unconventional reservoir setting. The hypothesis is that a value less than 1 indicates a compressive regime (reverse faulting or fracture closure). In contrast, a value close to 1 characterizes a strike slip regime, and a value higher than 1 indicates normal faulting stress state. Since b-value represents the calculated slope from the FMD, this idea makes intuitive sense. In a normal faulting stress regime, slip occurs easily as the rock fabric is extended under pressure. This should cause relatively smaller seismic emissions. In a compressive tectonic regime, upon pressurization, the fault or fracture faces close, and it is harder for them to slip. Under such situations, there is an expectation for larger seismic emissions since the elastic strain buildup before energy release through rupture can be significant. From rock mechanics, we know that there is a direct correlation between effective differential stress and the resulting elastic deformation. Thus, with a compressive stress state, we expect much higher strain and consequently a higher differential stress when compared with a strike-slip, or an extensional stress state. Using acoustic emissions in laboratory setting, Liakopoulou-Morris et al. (1994) has identified a proportional relationship between differential stress and b-value. Using similar rock failure experiments, Wang et al. (2000) has identified a strong relationship between b-value and crack densities as well as crack size distributions. Using field observations, Vermylen (2011) has proposed a direct relationship between b-value and in-situ stress estimates. At the teleseismic scale, Scholz (2015) has shown an inverse relationship between b-value and differential stress based on multiple catalogs and earthquake sequences. Many recent studies (Kratz et al., 2012; Bao and Eaton, 2016; Lei et al., 2017) have also identified the impact of faults on spatial b-value distributions.

In summary, in terms of statistical expression, we expect high b-values in areas under relatively smaller differential stress. Disregarding the thermal effects on rock failure, these areas are also more susceptible to tensile rock failure. On the other hand, presence of large faults or areas under higher differential stress should show lower b-value distributions. Based on the high-resolution microseismic event catalog obtained by processing of available data, we carry out a comprehensive analysis of FMD parameter, i.e., b-value distribution in space and time for the HFTS study area. The aim is to understand variability in observed seismicity and its relationship with the UWC and MWC reservoirs. Apart from a deeper analysis of relationship between microseismicity and in-situ rock properties, the purpose is to investigate correlations between hydraulic fracture treating pressures, and b-value variability during fracturing.

Method

As introduced earlier, Gutenberg & Richter (1944) first proposed a power-law relation between the frequency of occurrence and magnitude of seismicity. The Gutenberg-Richter law is defined as follows:

$$N = 10^{a - bM} \quad (1)$$

Here, N is the number of events having magnitude ≥ M while parameters a, and b are constants, which define the total seismicity and relative activity within the region or time-period defined by the catalog. Since this is a simple power-law relationship, it is possible to estimate the value of parameter 'b' or b-value by simply plotting the frequency of occurrence against the magnitudes of events. However, due to the limitations of instrumentation, clamping issues, source to receiver separation, and other constraints, microseismicity associated with smaller deformations may remain undetected. This manifests as an apparent b-value roll-off at relatively lower magnitudes when plotted as per Eq. 1. A similar behavior might also occur at the higher end of the magnitude distribution. To get an accurate estimate of the b-value slope, a magnitude cut-off is applied (magnitude of completeness, M_C) to discard events with very low magnitudes. This allows removal of incomplete portion of the catalog such that only magnitudes higher than MC are used in b-value calculations. We use maximum likelihood method (Fisher, 1950) to calculate the fit of the distribution. As suggested, seismic events smaller than MC are discarded in the fitting process. There are various methods for estimating M_C and the choice can influence the calculated slope significantly. We also use a maximum magnitude cut-off, which is particularly useful for smaller catalogs. Since smaller datasets tend to show higher uncertainties (Figure 80), when looking at microseismicity for each fractured stage individually, we only use catalogs with at least 200 microseismic events.

For a comprehensive look at the spatial FMD, b-value parameter is computed for the microseismic data for each hydraulic fracture stage separately. In addition, it is also calculated based on a three-dimensional grid distribution within the target reservoir. The magnitude cut-off (M_C), as defined earlier, is identified using a goodness of fit approach. To evaluate the goodness of fit, we use a measure of difference between the observed and a synthetic FMD distribution. The initial estimate for the synthetic distribution is based on the estimation of Gutenberg-Richter parameters using the entire catalog with magnitudes higher than the minimum magnitude M_m. For a distribution with mean moment magnitude, $\bar{M}$. The formal equation to estimate b-value (Fisher, 1950) is given by:

$$b_{MLE} = \frac{1}{\ln(10)\,(\bar{M} - M_m)} \quad (2)$$

The use of maximum likelihood allows for small variances and relatively smaller changes with addition of newer data in a statistical sense. We estimate the confidence limits using standard deviation defined by Shi and Bolt (1982):

$$\sigma(b_{MLE}) = 2.3b_{MLE}^2\sqrt{\frac{\sum_{i=1}^{N}(M_i - \bar{M})}{N(N-1)}} \quad (3)$$

Here, M_i denotes the individual magnitudes, and N is the total size of the catalog. Using the estimates of Gutenberg-Richter parameters (b, a, and M_m), a synthetic distribution of magnitudes is generated such that the distribution fits the power law model. A difference measure between the actual and synthetic data is calculated as follows (Wiemer & Wyss, 2002):

$$R(a, b, M_m) = 100\left(1 - \frac{\sum_{M_m}^{M_M}|B_i - S_i|}{\sum_i B_i}\right) \quad (4)$$

Here, B_i and S_i represent the observed and synthetic event count in each magnitude bin of the corresponding distribution. Parameter M_M represents the maximum magnitude observed in the catalog.

With each successive iteration, the minimum magnitude Mm is increased such that the catalog shrinks but the goodness of fit (100 - R) rises until it reaches a maximum as shown in Figure 81c. M_C is chosen as the magnitude where the power law model provides the most accurate prediction of the overall FMD. This corresponds with the maximum on the goodness of fit curve (Figure 81b). Unlike teleseismic catalogs, most catalogs associated with hydraulic fracturing show a maximum goodness of fit measure that is less than 90%. Poor fit could be a result of smaller catalogs, or where the observed FMD is highly curved or is bimodal and the relatively simple power law model fails to fit the data accurately. This phenomenon can be traced to spatial or temporal inhomogeneities in seismicity. An example of such inhomogeneity could be the presence of significant earthquake swarms driven by physical processes in-situ. Apart from M_C used for b-value calculation, a higher magnitude cut-off is evaluated based on best fit with minimized error (L2-norm).

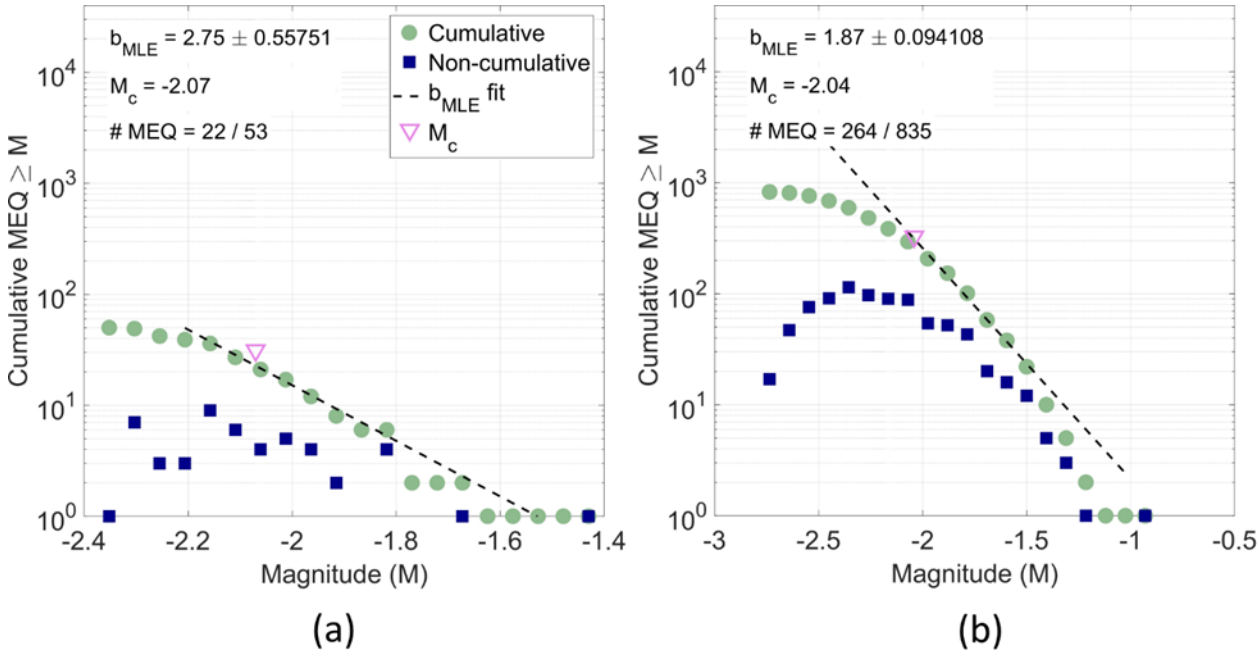


Figure 80: Cumulative frequency-magnitude distribution of events for two selected hydraulically fractured stages at HFTS. We can clearly see the higher uncertainty for (a) due to low event count compared to (b) which has a higher

event count and lower uncertainty band (Eq. 3). The magnitude of completeness (M_C) for both stages is similar, but the calculated slope of the distribution varies significantly.

For spatial b-value calculations, we use a grid search approach. Each grid cell has a lateral spacing of 200 ft and a vertical spacing of 300 ft. The grid size is selected based on available microseismic event density within the test site area. This is key since each grid cell should have adequate microseismicity for relatively accurate b-value estimation with high confidence (low σ). In addition, we select the vertical spacing based on the average vertical separation between the UWC and MWC formations in the test site area.

We also interpret 3D seismic properties for comparative analysis with spatial b-value distribution. Discontinuities within the seismic volume are mapped by generating ant-track volumes (Basir, et al., 2013; Ngeri, et al., 2015). There are various seismic attributes widely used for fault detection. These include semblance (or variance), dip, curvature, etc. to name a few (Chopra & Marfurt, 2007). Seismic workflows can generally also include various enhancements to allow for better interpretation of structural discontinuities. Examples include dip steering (Tingdahl & de Groot, 2003; Chopra & Marfurt, 2007; Santosh et al., 2013; Maity and Aminzadeh, 2015), and frequency filtering (Chopra et al., 2010), etc. among others. Ant tracking is an Ant Colony Optimization method (Dorigo & Stutzle, 2004), which is used to enhance detection of discontinuities within the seismic volume.

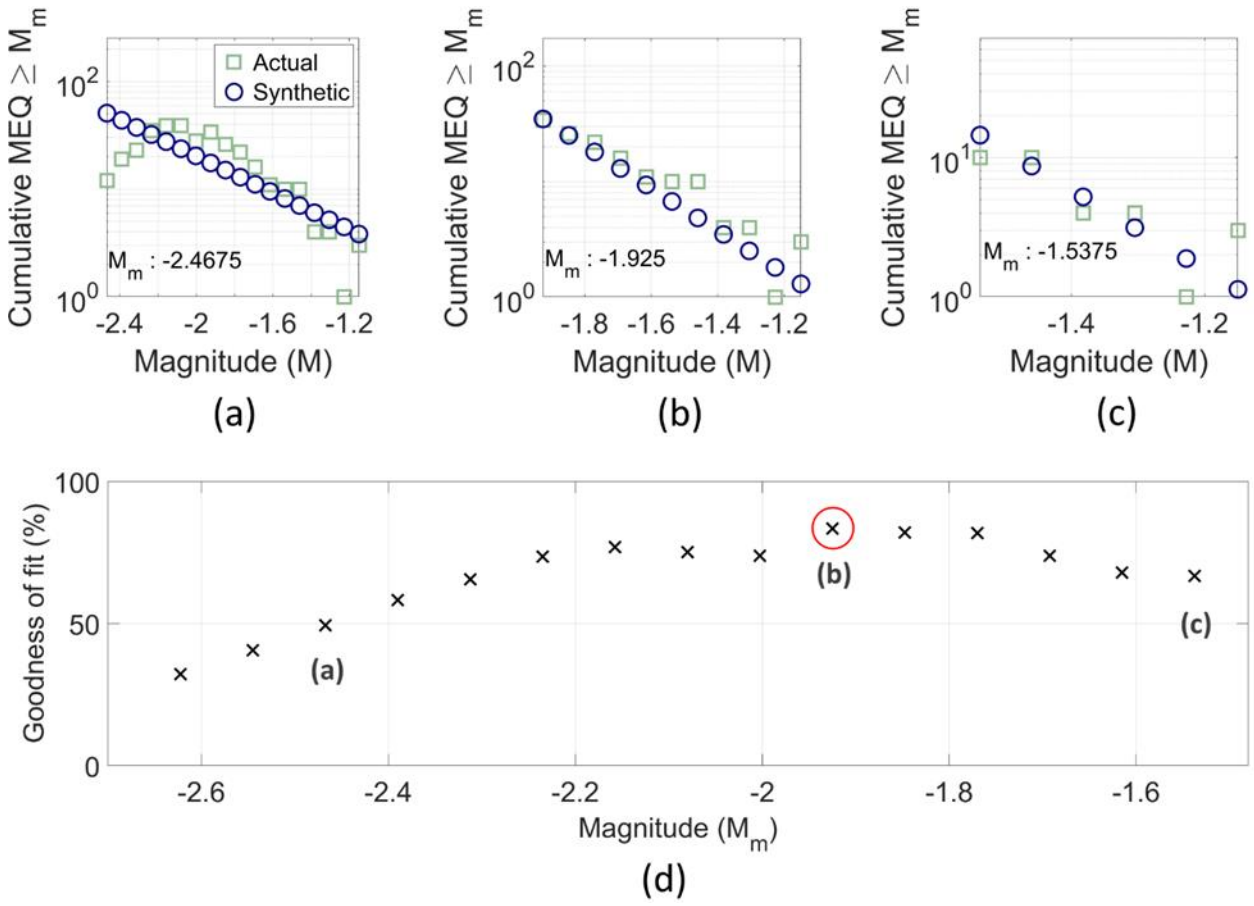


Figure 81: Estimation of magnitude of completeness using goodness of fit approach for microseismic catalog data from a randomly selected hydraulic fracturing stage at HFTS. The synthetic fits to the actual catalog are shown in subplots (a), (b) and (c) for three arbitrary values of Mm. The goodness of fit as a function of Mm is shown in subplot (d). The

selected data fit instances from subplots (a), (b) and (c) are highlighted in subplot (d). The selected M_C is highlighted in subplot (d). For this case, we find the best fit to be 83.4%.

A typical first step towards seismic classification of faults and fractures is the application of appropriate frequency filter to extract relevant frequencies. From the filtered data, two discontinuity features are generally calculated and used as inputs for ant-tracking algorithms, namely, variance and chaos attributes. Variance is an edge method to measure the similarity or coherency of waveforms within lateral and vertical windows. Chaos is a measure of lack of organization in dip and azimuth. Generally, edge-detection and edge-enhancement is applied before variance or chaos calculation and subsequent ant tracking. Variance is useful in mapping discontinuities in seismic data that relate to faulting and stratigraphy (Pigott et al., 2013). It is useful in delineating faults, large fractures, channel edges, unconformities and sequence boundaries. Chaos can detect chaotic structures within seismic data thus highlighting positions of reflector disruptions. It can be used to distinguish sediment facies, fault zones, angular unconformities, channel bodies and possible zones of fractures (Pigott et al., 2013). In this paper, we use variance-based ant tracks to identify significant discontinuities within the reservoir.

The other seismic attribute we use is the rock brittleness index. Brittleness defines the characteristic behavior of rocks to break upon application of stress, without undergoing any significant deformation. Both geomechanical well logs as well as 3D seismic derived geomechanical models can be used to identify brittleness variations within the reservoir. The relative elastic behavior of rocks is defined by the elastic rock properties, i.e., bulk modulus, shear modulus and Young's Modulus. Rock stiffness or Young's Modulus is a relevant property of interest since it is believed to govern the hydraulic fracturing behavior. Various measures of brittleness have been defined in the past such as measures using Young's Modulus and density (Sharma and Chopra, 2014) and those, which consider effective stress and fracture toughness (Hu et al., 2016). We use a model based on Rickman et al. (2008) which calculates brittleness index (BI) using dynamic Young's Modulus and Poisson's ratio. The model used is defined as follows:

$$BI = \frac{100}{2}\left(\frac{E - E_{min}}{E_{max} - E_{min}} + \frac{\nu - \nu_{min}}{\nu_{max} - \nu_{min}}\right) \qquad (5)$$

Here, we use both the Young's Modulus, E, and Poisson's Ratio, ν, as indicators of brittleness. The elastic properties can be calculated from instantaneous shear and compressional wave velocities and are modeled using an elastic inversion workflow, which generally also includes calibration with petrophysical measurements (Varga et al., 2012). While the use of this or similar brittleness measures may be error prone, we use this attribute for comparative analysis to see if there is any correlation with microseismicity distribution obtained independently.

To calculate variations in seismicity FMD parameters with time, we specify a sliding time window of 5 minutes and calculate b-value for all the events that occur within that time window. This includes microseismicity within the stimulated zone as well as events out of zone. Since the implicit assumption is that all the seismicity within the specified window is associated with the same geologic system, interpretations need to be adequately qualified. Examples of a similar geologic system will include a system of faults or clastic rock with significant natural

fractures. Since typical microseismicity associated with fluid injection includes triggering of far-field seismicity, other systems can affect the calculated b-value distribution. Thus, the calculated FMD must be understood as a composite measure of the complexity in geology or other factors driving variations in spatial seismicity behavior. We move the selected time window by small increments to prevent any occurrence of significant outliers in the distribution.

To understand time-variant seismicity, we also look at the completion parameters the hydraulic fracturing treatment pressure, which indicates changes in fracturing based on fluctuations in net pressure behavior. Nolte and Smith (1981) proposed a technique to interpret hydraulic fracturing behavior using net pressure. The power law model guiding the propagation of hydraulic fractures (Perkins & Kern, 1961; Nordgen, 1972) is defined as follows:

$$p_{net} \propto t^{e} \tag{6}$$

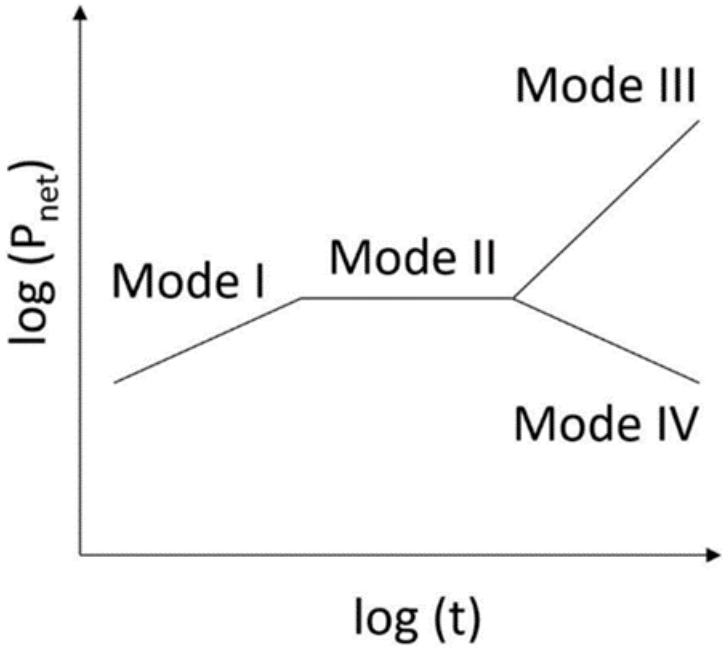


Figure 82: Diagnostic Nolte-Smith interpretation guide depicting fracture propagation modes. From Britt et al. (1994).

Where p_{net} defines the net fracturing pressure at time t since the initiation of fracturing. Parameter e, or the Nolte-Smith exponent, defines the slope of net pressure curve. Using dimensional analysis, Nolte and Smith predicted that fracture propagation could follow a predefined mode based on slope of the net fracturing pressure. The modes include confined height with unrestricted extension (Mode I), constant height growth (Mode II), restricted extension (Mode III), and unstable height growth (Mode IV). Figure 82 shows the impact of these propagation modes on net fracturing pressure. Pirayesh et al. (2013) proposed a modified method called "moving reference point" approach which considers the intermittent nature of fracture propagation as well as natural and hydraulic fracture interactions during fracturing of shale formations (Soliman et al., 2014; Maity, 2015). The reference time t_i indicates the time at which fracture growth initiates. In order to account for multiple growth periods, t_i must be reset for each of these periods. The derivative approach used is as follows:

$$(t - t_i)\frac{\partial p}{\partial t} = e(p - p_i) \quad (7)$$

The exponent e can be calculated using measured pressure at varying times and does not require an estimate of the fracture closure pressure normally needed for net pressure calculations.

Result: hydraulic fracture stage data

The maximum likelihood estimate method used for b-value calculation requires a significant range of magnitudes within the catalog for reasonable estimation of fit ($\Delta M \geq 3$). Hydraulic fracturing operations seldom generate large magnitudes unless there is moderate to large fault activation associated with the injection of fracturing fluid or if the geophones are in proximity of stages being fractured. Thus, resulting microseismic catalogs may not provide significant magnitude range. The range of observed magnitudes for various wells in the study area is shown in Figure 83a. We see that for a few wells, the observed magnitude range is well below the threshold for reasonable maximum likelihood estimation. In order to validate the b-value estimates using the maximum likelihood method, we compare the results with the least squares error approach of finding slope (Marzocchi & Sandri, 2003). The regression fit between the calculated b-values for hydraulically fractured stages using both the maximum likelihood and the least square error approach is shown in Figure 83b. They show a very good correlation and a near unit slope.

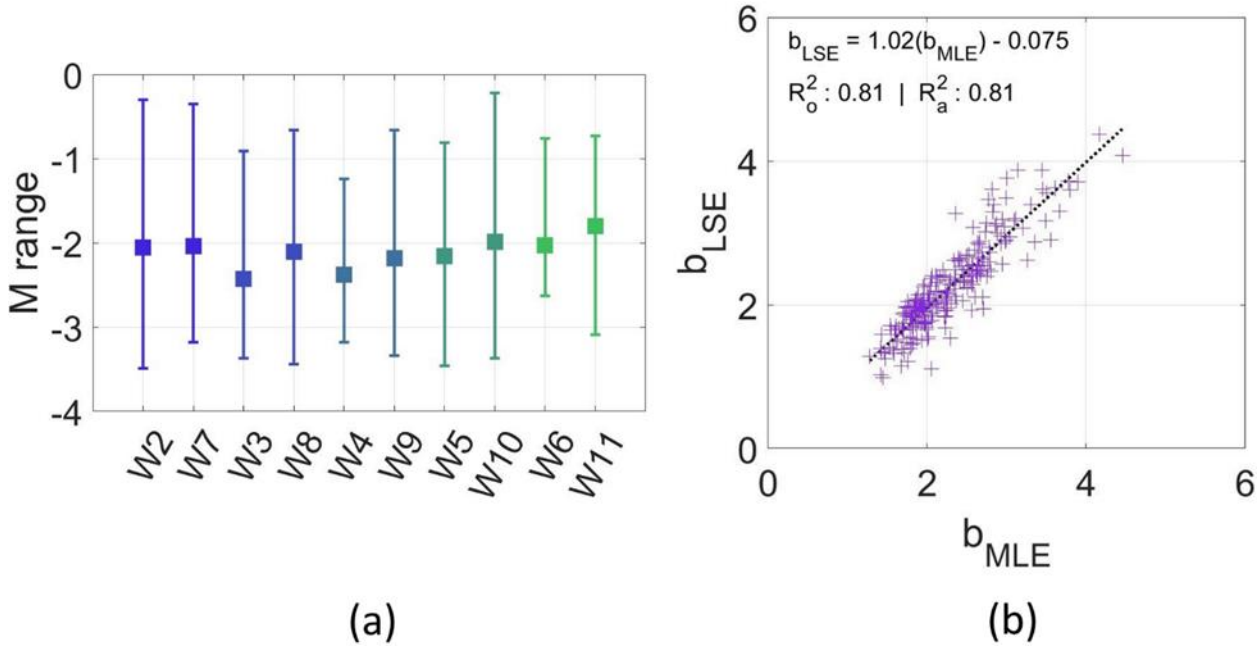


Figure 83: Applicability of maximum likelihood estimate for catalogs from test site: (a) observed magnitude range for various HFTS study wells and (b) comparison between b-value calculated for various catalogs using both the maximum likelihood and the least square error estimates. We did not observe any microseismic event of significant magnitude.

M_C, or the magnitude below which the catalog is incomplete, is an artifact of recording constraints with the source to receiver separation being a key driver for observed variations. We expect M_C to be directly proportional to this separation, i.e., the ability of the array to identify smaller magnitude events diminishes at larger array distances. This is the primary reason for the observed roll-off at lower magnitudes in most seismic catalogs. To validate this,

we find the separation between the geophones and the hydraulic fracturing stages (mid-point of the perforated interval) for the wells at the site (Figure 84a). Here the distance measure is the average of distance of each stage from all geophones associated with that stage. The range in Figure 84a provides the observed maximum and minimum average separation for a particular stage of a well. We consider three wells (W7, W8, W11) for which, the average distance to the two geophone arrays is similar, and the available range of separation is significant (approximately 2000 ft). We compare the stage wise M_C distribution for their microseismic catalogs and their dependence on the average distance measure (Figure 84b). The impact of source to receiver separation on catalog M_C is clearly observed based on data from these three selected wells.

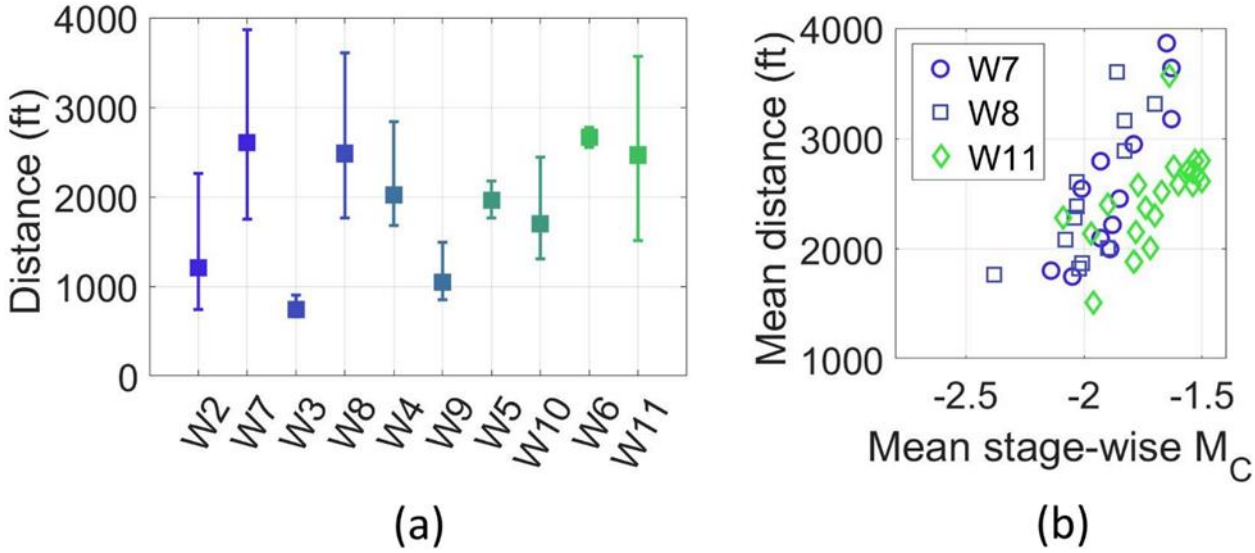


Figure 84: Impact of microseismic survey design (source to receiver separation) on catalog quality: (a) source to receiver distance for various wells and (b) stage-wise M_C behavior for three selected wells compared with the mean source to receiver distance for corresponding stages.

Stage wise FMD analysis for ten wells from the HFTS study shows a reasonable positive correlation between b-value distribution and the instantaneous shut in pressure (ISIP) for corresponding stage (Table 4). ISIP is the final injection pressure during fracturing corrected for the frictional pressure drop within the system, i.e., the pressure drops across the wellbore and the perforations. Since hydraulic fracturing operations are designed such that, the fracture propagates in the direction of maximum horizontal stress (S_{Hmax}) and opens against the minimum horizontal stress (S_{Hmin}), ISIP is regularly considered a proxy measure for the in-situ S_{Hmin} as the pumping terminates (Hickman and Zoback, 1983). Based on geomechanical studies, we know that the test site is governed by a normal faulting stress regime where the vertical stress (S_V) dominates, i.e., $S_V > S_{Hmax} > S_{Hmin}$. Thus, a positive correlation between b-value and measured ISIP suggests an inverse relationship with in-situ differential stress ($S_V - S_{Hmin}$).

Table 4: Ordinary and adjusted coefficients of determination for b-value vs. ISIP data for various UWC and MWC wells from HFTS study.

Well	**W2**	**W3**	**W4**	**W5**	**W6**	**W7**	**W8**	**W9**	**W10**	**W11**
R_o^2	0.39	0.18	0.18	0.12	0.31	0.76	0.72	0.25	0.27	0.44

R_a^2	0.37	0.15	0.14	0.06	0.26	0.73	0.69	0.24	0.25	0.41

However, it is noted that ISIP is a subjective interpretation, and therefore, it is not a reliable estimate for S_{Hmin}. At best, it provides a reasonable upper bound estimate for its value. Moreover, impact of stress shadowing on ISIP calculations is a known phenomenon (Dohmen et al., 2014). Some of the biggest outliers in the observed correlations (Table 4) are close to the toe end of the wells and some of the best fits are identified towards the heel end. The latter is highlighted in the very high correlations observed for wells W7 and W8 for which we only have data available for the heel-side fracture stages (Table 3). This makes intuitive sense since even with pronounced stress shadow effect the most significant impact should be observed for stages towards the toe end and the effect should stabilize after the first few stages. The impact could be significant enough to cause local stress reversals, which in turn may have an impact on the observed seismicity.

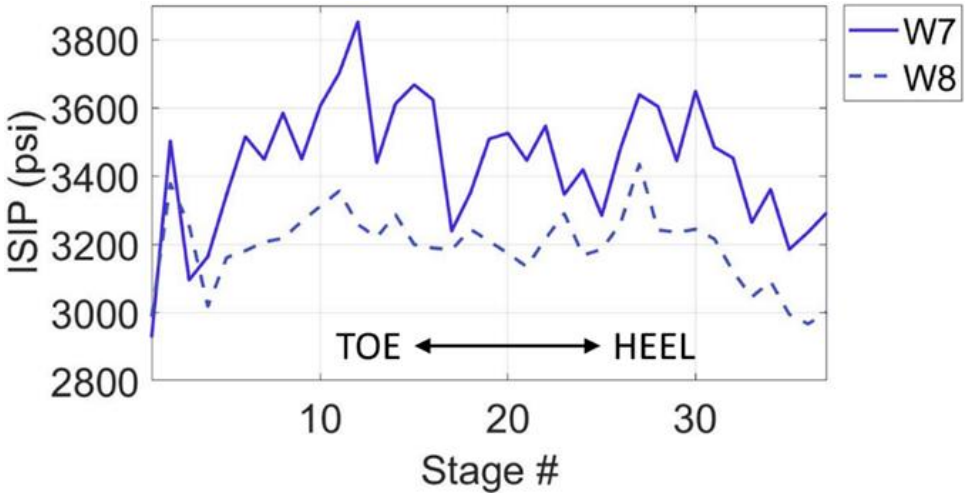


Figure 85: Variation in ISIP with stage (toe to heel) for wells W7 and W8. The stress shadow effect and resulting gradual rise in ISIP can be seen towards the toe section. Local stress reversal is evident, particularly for well W7.

The actual ISIP data from wells W7 and W8 are shown in Figure 85. The stress shadow effect is obvious with the gradual increase in stress towards the toe section of the wells. The gradual drop in ISIP values towards the heel end of the stages indicates relatively lower stresses, which correspond with increasingly lower b-values. Stress modeling work has shown that a true convergence behavior may not always manifest since stress shadowing is a complex function of fracture spacing design, mechanical rock properties and prevalent in-situ stress state (Nagel et al., 2013). Thus, many factors can influence the observed ISIP behavior and consequently, any analysis, which makes use of ISIP values as a proxy for in-situ stress estimation, should be used carefully. Finally, depending on the geomechanical stress state, there can be significant out of zone growth between various reservoir units. This can significantly affect observed seismicity, which can be spatially spread out (100's or even 1,000's of ft). ISIP is a near-wellbore measurement at best and therefore, comparisons should be avoided while making interpretations.

Overburden stress estimation

In-situ geomechanical model definition includes pore pressure, unconfined or uniaxial compressive strength (C_0), and magnitude and orientation of three principal stresses (vertical stress, S_V; minimum horizontal stress, S_{Hmin}; and maximum horizontal stress, S_{Hmax}). Calibrated

pore pressure and overburden stress models are provided by the operator for this study. Pore pressure is usually measured using leak-off or extended leak-off tests while the overburden stress is estimated by integrating density log measurements for the overburden with depth, z. In particular, the overburden stress is calculated as:

$$S_V(z) = g\sum_{0}^{z}\rho(z) \tag{8}$$

S_{Hmin} is estimated based on the core triaxial tests and sonic and density log measurements at the pilot well (W6) using elastic rock property estimates. C_0 is critical for constraining maximum horizontal stress (S_{Hmax}). Dynamic Young's modulus values identified using triaxial testing of core plugs is correlated with C_0. The correlation is then used to estimate C_0 with depth based on derived Young's Modulus values from dipole sonic measurements, i.e., the P- and S-wave sonic velocities. The Young's Modulus is defined as:

$$E = \rho V_S^2 \frac{3V_P^2-4V_S^2}{V_P^2-V_S^2} \tag{9}$$

Since no breakouts are observed based on the available image logs from multiple wells within the study area, we use the method proposed by Barton et al. (1988) to estimate limit for S_{Hmax}. For application of failure criteria based on frictional faulting theory, we use a coefficient of sliding friction of 0.6. Past studies have shown that high carbonate concentrations can lead to higher coefficient values while higher shale and hydrocarbon concentrations can cause lower frictional coefficients (Sone & Zoback, 2013). Therefore, this assumption may not be accurate across the entire Wolfcamp interval. The constraints for S_{Hmax} for breakouts are defined as follows:

$$S_{Hmax} = \frac{(C_o+2P_P+\Delta P+\sigma^{\Delta T})-SH_{min}(1+2\cos 2\theta_b)}{1-2\cos 2\theta_b} \tag{10}$$

In this model, ΔP is the difference between the mud weight and the pore pressure, and $2\theta_b = \pi - w_b$ where w_b is the observed breakout angle. Since we do not observe any identifiable breakouts based on the image logs, w_b is estimated to be 0^0. C_0 is calculated based on the identified correlation with Young's Modulus from core analysis as described earlier.

We observe reasonably good correlation between the Young's Modulus and C_0 estimated from petrophysical data with values from tri-axial core testing. Based on the available S_{Hmax} and S_{Hmin} values for given depths of interest we predict a normal faulting stress regime by mapping stresses onto stress polygons. The maximum uncertainty in the stress estimation is with S_{Hmax} values, which in turn has a significant impact on the stress transformations acting on any fracture or fault face. However, since most of the pre-existing fractures are near vertical, even relatively large errors in S_{Hmax} estimates do not affect the final analysis as shared in this paper significantly.

Result: spatial variations

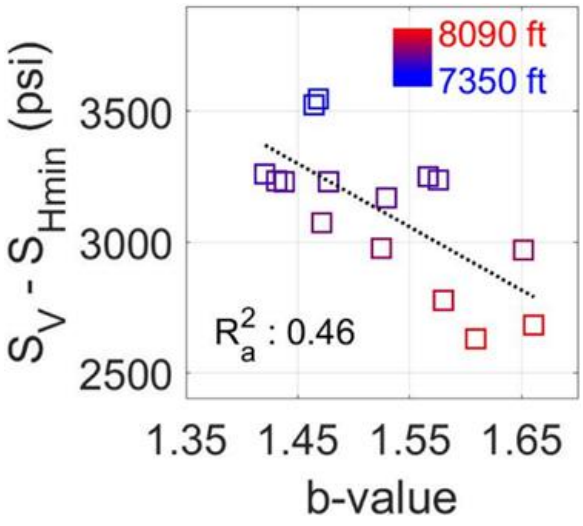


Figure 86: Relationship between b-value calculated in depth and in-situ differential stress along pilot well W6.

To validate stress dependence on b-value, we look at its variation with depth close to the pilot well, W6. If we compare differential stress with average b-values identified close to well W6, we see an inverse correlation (Figure 86). Here, the overburden stress is estimated based on the density log as highlighted in previous section. Unlike earlier discussion on spatial b-value calculation using grid definition, in this case, we consider all recorded microseismicity within a lateral distance of 2000 ft from the pilot well with vertical sampling at 50 ft.

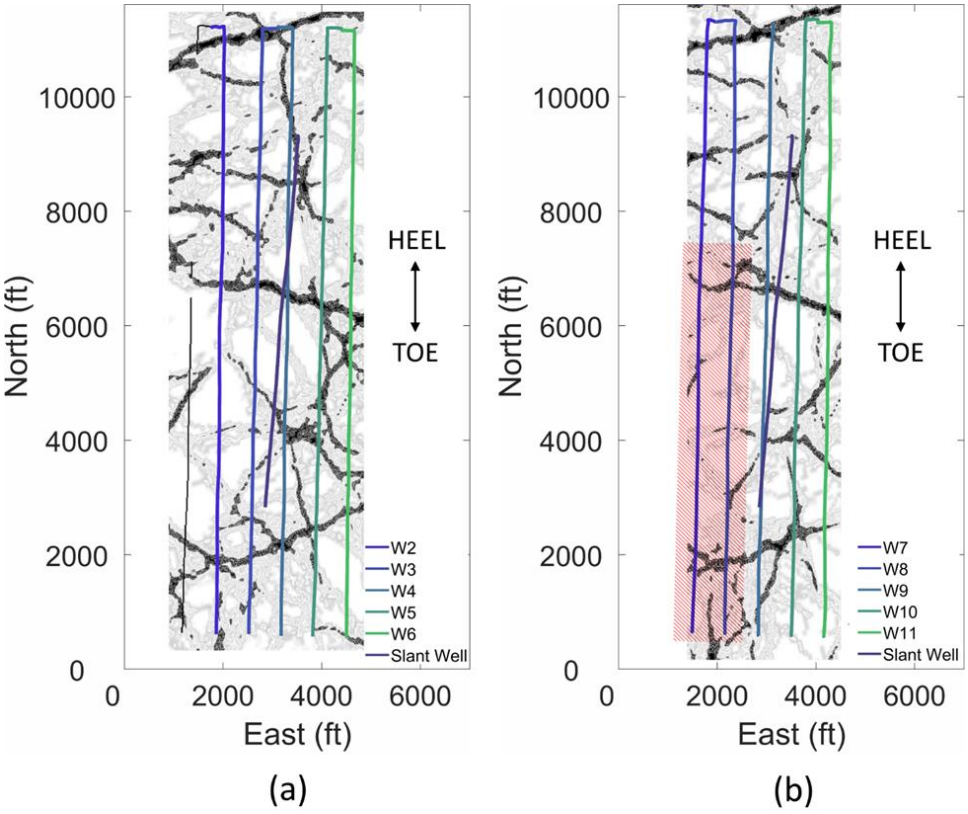


Figure 87: Ant-track (variance) attribute highlighting potential discontinuities within (a) UWC and (b) MWC formations close to the hydraulically fractured wells. Section identifying stages where microseismic data is unavailable is highlighted in (b).

Faults are one of the most significant structural drivers for seismicity as they can have a significant impact on in-situ stress distribution. Moreover, shear failure along large faults lead to lower b-values due to higher proportion of large magnitude events. Fault damage zone

fracture mechanics suggests a gradual decay in fracture density away from the main fault (Johri et al., 2014). This would suggest that close to the location of significant discontinuities (with propensity for large shear mode failure); the b-value should be small. However, as we move away from these discontinuities, the tendency for tensile or opening mode failure is higher and consequently, the b-value should be higher. The discussion can be extended from faults towards much broader distributed deformation mechanisms associated with various types of fracture, structural deformations or fault corridors. Ogata et al. (2014) shared conceptual models for various types of deformation structures in sand-shale successions. The results, based on outcrop analysis again suggests localized nature of deformation close to faults and highly distributed nature of deformation associated with folds in shales (Stephenson et al., 2018). These deformation structures could be associated with the subsurface discontinuities.

To identify locations of significant discontinuities and deformation in-situ, we use the available 3D seismic survey. The seismic variance attribute is used to calculate ant track volumes for both the UWC and the MWC formations. The expectation is that the location if these lineaments should have a significant influence on the hydraulic fracturing behavior within the reservoir. In Figure 87, we see a map view of the identified variance derived ant-tracks along with the UWC and MWC wells of interest. Location of the slant core well is also indicated. For wells W7 and W8, we do not have any microseismicity available for a significant number of toe end stages and corresponding area is highlighted in Figure 87b.

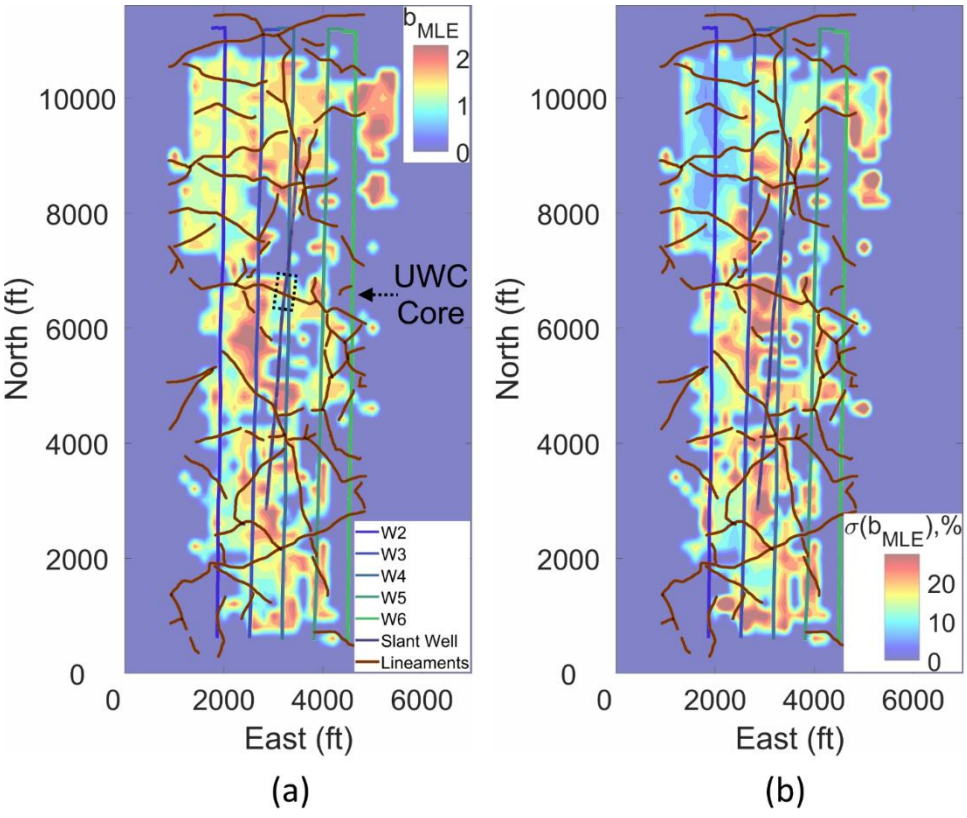


Figure 88: Map view of UWC wells showing distribution of (a) b-value and (b) associated uncertainty measure. Major identified lineaments from ant track discontinuity maps (Figure 87a) are superimposed on top. Dotted insert shows the approximate location of cored section along the slant well.

A cursory study suggests that there is significant variability in density of lineaments along UWC and MWC wells, the heel sections for both the formations show much higher density of identified discontinuities compared with the middle sections. The toe sections also show

higher density of lineaments in general, but not as high as the heel sections. Furthermore, a distinct difference between the heel side and the toe side lineaments is in their strike orientations. The lineaments on the heel side seem to strike close to S_{Hmax} direction compared with the toe side where many of the lineaments strike closer to S_{Hmin} direction. This is principally true for the western half of the pad, in particular, along wells W2 through W4 in UWC formation and wells W7 through W9 in MWC formation. To understand any correlation between calculated b-value distribution across the two formations and the discontinuities identified using ant-tracks, we extract all significant lineaments from the ant-track volumes and plot these lineaments on top of the b-value maps. A map view of the distribution and overlaid lineaments for UWC formation in shown in Figure 88. In Figure 89, we show a similar representation for MWC formation. The mapping has been value limited for a maximum b-value of 2.5 to minimize impact of outliers on visualization of the data. The uncertainty distributions (Figure 88b and Figure 89b) provide a quick indication of locations where b-value distributions could be subject to significant errors. In most situations, this is a result of smaller microseismic event count available for the corresponding grids. For all other locations with high confidence (low σ), a careful look at the distribution of b-value close to the identified lineaments shows that in many instances, the b-value is relatively lower (approximately range-bound: $1 \leq b \leq 1.75$). In particular, the direction of lineament (N-S vs. E-W) seems to influence observed seismicity distribution. Areas where most lineaments are trending proximal to E-W orientation show lower b-value distributions (north-west section of the pad).

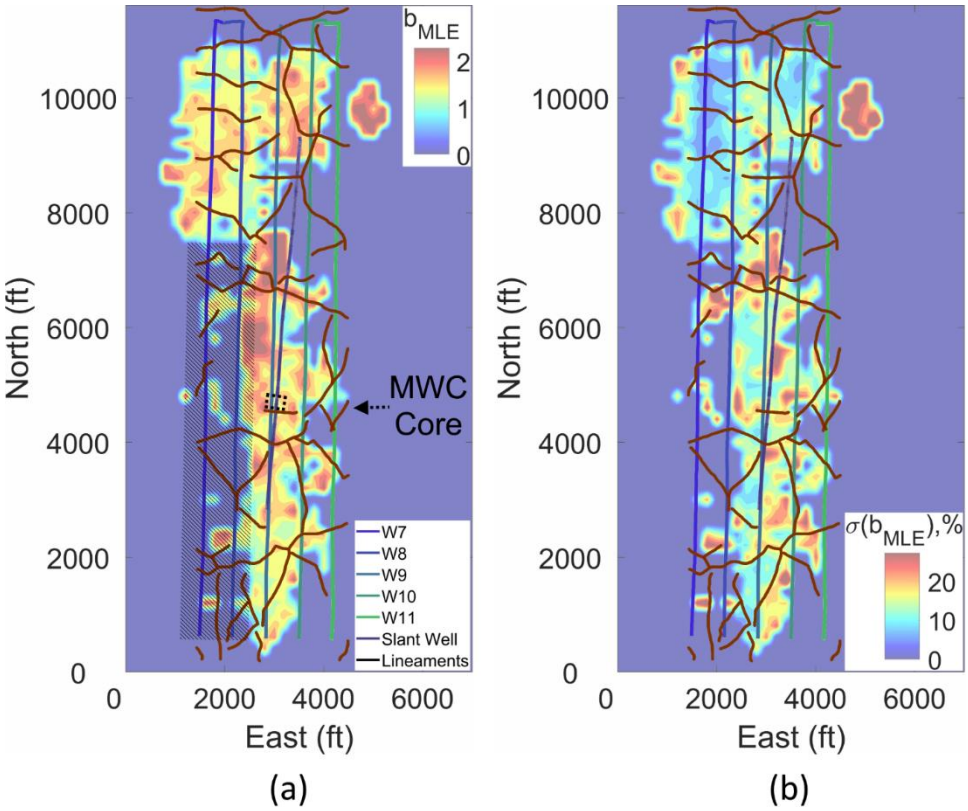


Figure 89: Map view of MWC wells showing distribution of (a) b-value and (b) associated uncertainty measure. Major identified lineaments from ant track discontinuity maps (Figure 87b) are superimposed on top. Section identifying stages where microseismic data is unavailable is highlighted in (a). Dotted insert shows the approximate location of cored section along the slant well.

These observations can be tied with the theory of distributed deformation mechanisms associated with faults, folds or other structural features as discussed earlier. Analysis of

fractures along the slant core well (Gale et al., 2018) suggests that for the cored sections, the UWC formation has a much higher density of pre-existing natural fractures compared with the MWC formation. From the reported fracture description, on average, UWC core shows 0.6 fractures/ ft while MWC core shows 0.2 fracture/ ft. A closer look at the location of these two cores suggests that this observed difference is likely a function of proximity of significant faults close to the UWC core and no such proximal discontinuity close to the location of the MWC core (Figure 88a and Figure 89a). Gale et al. (2018) also identifies 12 faults of various types in the UWC core and no faults within the MWC core. Large discontinuities, such as faults and large fractures, can see relatively large slip failure through stress perturbations causing larger microseismic moment magnitudes and consequently lower b-value distributions. Moreover, in the presence of significant natural fracturing and a propagating hydraulic fracture, we expect significant near- and far-field shear or mixed mode failures to occur. This is driven by stress changes transmitted through the rock matrix or pressure front propagation into pre-existing natural fractures I relative proximity of propagating hydraulic fractures. In areas with sparse natural fractures density, the probability of similar shear failure on pre-existing planes of weakness should drop significantly. Moreover, based on the in-situ stress state, a relatively higher proportion of fractures in the UWC formation seem to be critically stressed when compared with the MWC formation (discussed later). This suggests that in general, there should be much more shear activation of natural fractures associated with the UWC formation when compared with the MWC formation. We calculate the average b-value considering all evaluated grid points by limiting the grid selection such that the standard deviation (σ) at any grid point considered is 15% or lower. We observe an average b-value of 1.04 for the UWC formation and 1.27 for the MWC formation.

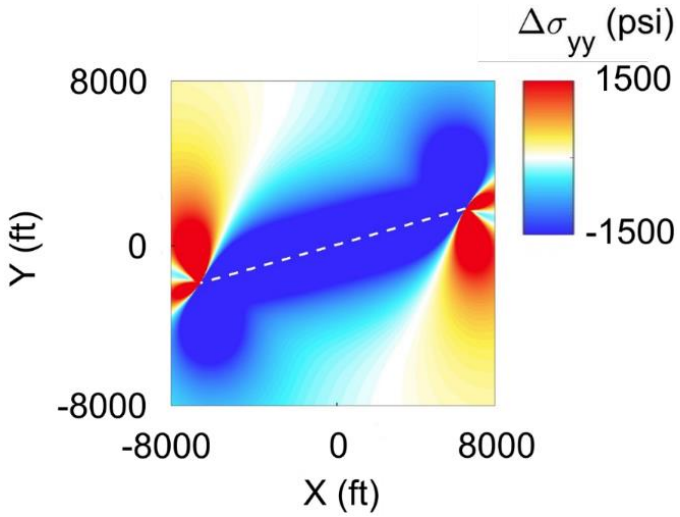


Figure 90: Normal stress change due to strike-slip failure along defined vertical fault plane, modeled for a linear displacement of approximately 3.3 ft. The stress change is modeled along the direction of S_{Hmin}.

An alternative approach to interpret the observed distribution for lower b-value and presence of discontinuities is by considering the nature of these discontinuities. As discussed earlier, the orientation of S_{Hmax} is almost E-W trending, and most of the identified discontinuities towards the heel side of the pad from Figure 87 seem to fall within ± 30^0 of S_{Hmax} orientation. This is a strong indication that these discontinuities are associated with strike-slip faulting. This is even though the current stress state seems to be normal faulting. General fracture azimuths from image logs also shows a similar distribution. Independent studies at other locations within the

Permian Basin validates this observation (White et al., 2014). The presence of larger number of such discontinuities towards the heel end of the pad compared with the toe end suggests significant stress variations may be possible along these features, which can guide how the rocks fail when stressed. As an example, consider an elastic half space with a single fault plane oriented E30^{0}N with S_{Hmax} along E-W orientation. If we assume that the fault fails in strike slip, the in-situ deformation and changes in the original stress state can be calculated (King et al., 1994). The modeled stress change along NS orientation is shown in Figure 90. Here, the dislocation solution defined by Okada (1992) is used. The region in lateral proximity of the fault planes sees a dramatic reduction in stress with the fault slip causing a significant drop in S_{Hmin}. While these failures may have happened in the geologic past, if we assume that some of the residual stress perturbations from such deformations remain within the reservoir, there should be higher differential stress in these zones. Consequently, we would expect to see larger microseismic events and a relatively lower b-value distribution. These lineaments likely represent multiple secondary echelon faulting (Gale et al., 2018). Thus, the stress variations should be much more complex. However, the basic observations should still hold. Evidence of significant stress buildup has been observed at this test site based on geomechanical logs from the UWC formation (Maity, 2018).

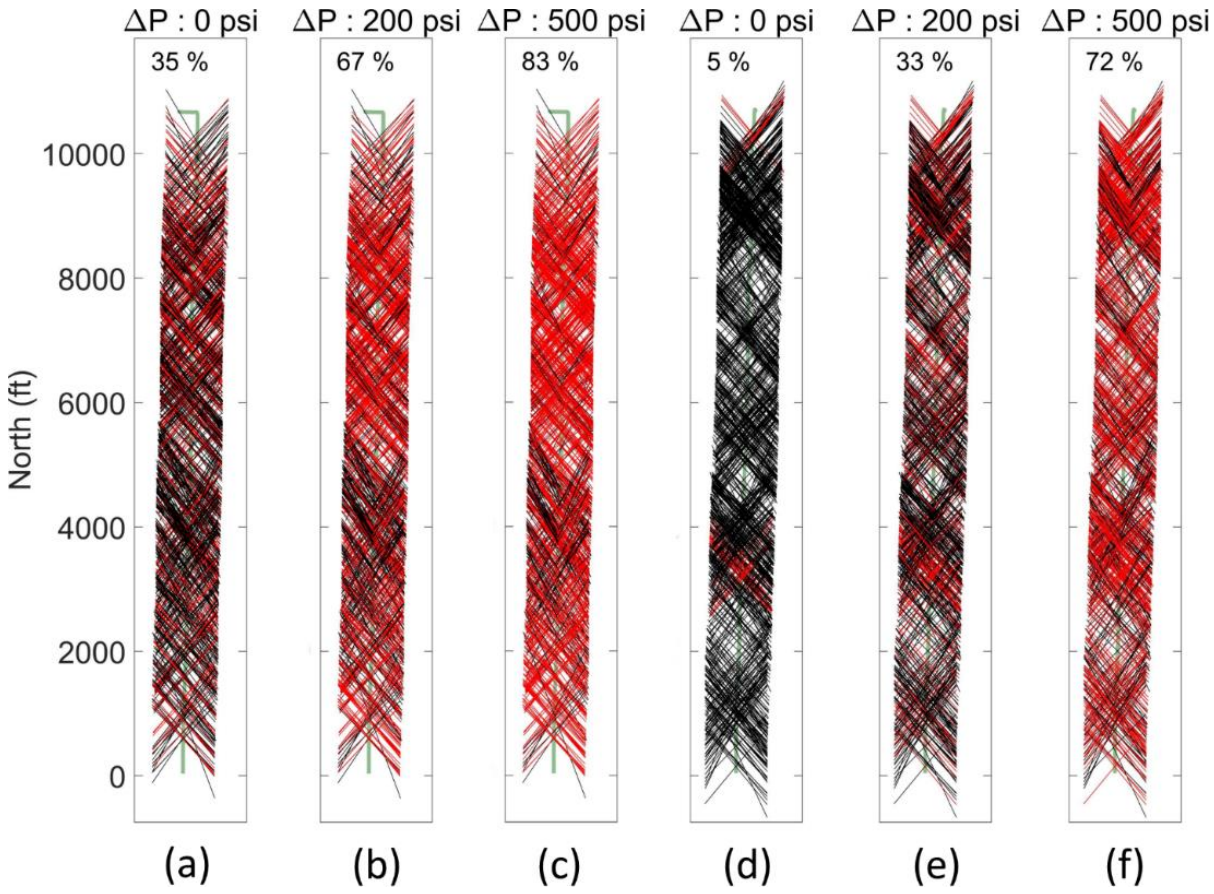


Figure 91: Based on stress models for UWC and MWC formations, critically stressed natural fractures for well W4 landed in UWC formation at (a) no pressurization, (b) 200 psi pressurization, and (c) 500 psi pressurization; and for well W9 landed in MWC formation at (d) no pressurization, (e) 200 psi pressurization, and (f) 500 psi pressurization. The percentage values reported in each panel represents the proportion of critically stressed fractures compared with the total fractures for that well at specified pressurization. The critically stressed fractures are highlighted in red.

There is significant difference in the state of in-situ stress between the UWC and the MWC formations. In general, we find MWC formation to be at a lower differential stress compared

with the UWC formation. In other words, the fracture gradient increases as we move from upper to the middle formation (Xu et al., 2015; Maity, 2018). This causes out of zone microseismicity and has a significant impact on the behavior of naturally fractured rock under elevated pore pressures during fracturing. As an example, consider wells W4 and W9. As part of the HFTS study, we collected OBMI logs for these two wells prior to initiating any hydraulic fracturing. Thus, the interpreted fractures from these logs are essentially pre-existing natural fractures at the corresponding wellbore locations. Using our stress model and Mohr-Coulomb failure criteria with a coefficient of sliding friction value of 0.6. We identify whether these fractures are critically stressed, and the pore pressure perturbation required for remaining fractures to become critically stressed. In Figure 91, we show this response to pressurization. We can see the original state (Figure 91a and Figure 91d) as well as the perturbed state for identified fractures based on the stress profile for UWC and MWC formations. For the UWC well, we interpret 35% of the identified fractures to be critically stressed before injection begins. A pressurization of 200 psi results in 67% of the fractures to become critically stressed and prone to failure. On the other hand, for the MWC well, we interpret only 5% of the identified fractures to be critically stressed before injection. A pressurization of 200 psi results in 33% of the fractures to become critically stressed. Even with a pressurization of 500 psi, there is an 11% difference in the number of critically stressed fractures between the two formations. A pressurization of 500 psi is a conservative estimate of the degree of pressure change occurring at many portions of the stimulated reservoir during typical fracturing operations. While these results are driven by various assumptions, the general trend behavior suggests that the variations in in-situ stress state between the UWC and MWC formations should manifest in variable fracture activation behavior. The stress models are based on triaxial stress testing of sidewall rotary cores under varying confining pressures and petrophysical measurements. Based on response to pressurization, more shear activations are expected for well W4 compared with well W9. Thus, the b-values close to well W4 in the UWC formation is expected to be comparatively lower.

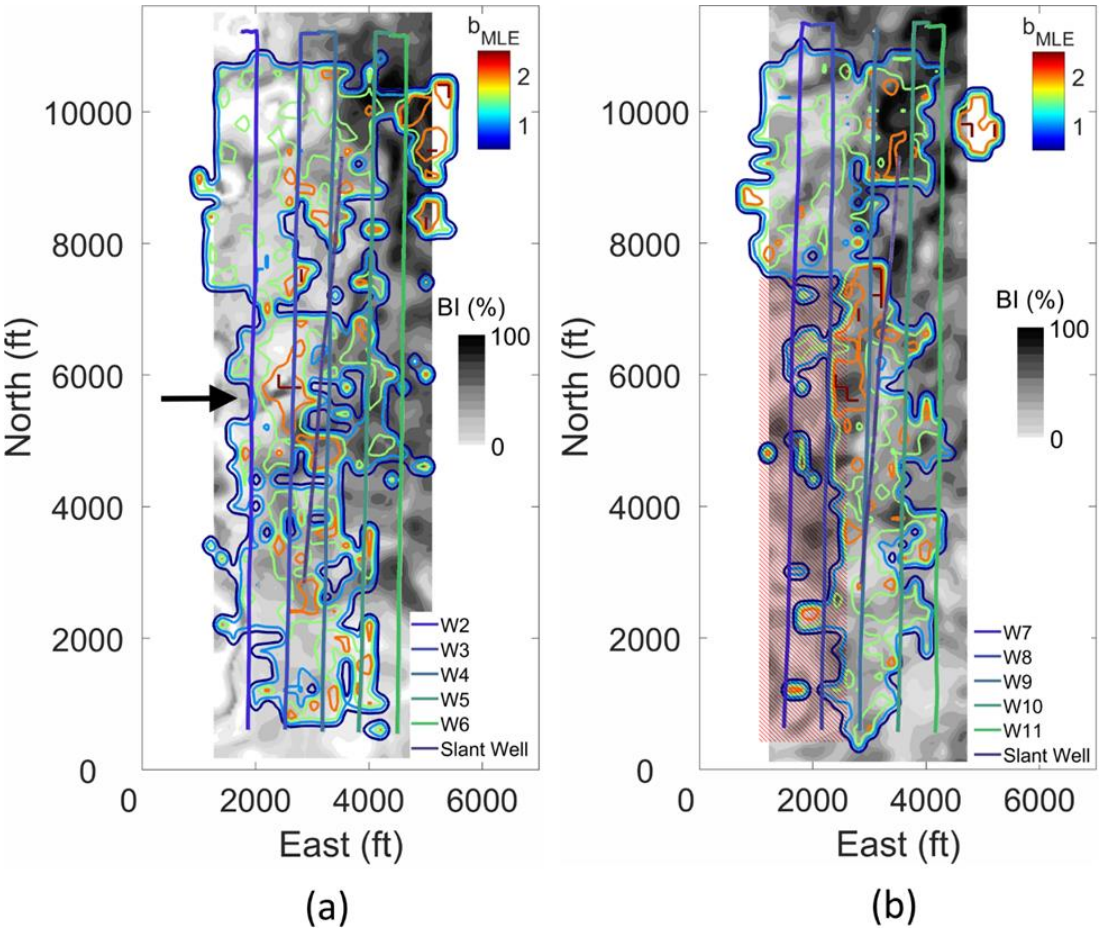


Figure 92: 3D Seismic derived brittleness compared with microseismic derived spatial b-value distribution for (a) UWC and (b) MWC wells. There seems to be a good correlation between areas showing high brittleness and areas with high b-values and vice versa. The areas with significant mismatch between these two properties generally show higher uncertainty (σ). The black arrow highlights one such location in UWC formation. Section identifying stages where microseismic data is unavailable is highlighted in (b).

Finally, consider the zones, which show very high b-value distribution in Figure 88 and Figure 89. For areas with high b-values (b-value >> 1), we can assume a relative dominance of tensile or mode I fractures associated with hydraulic fracturing. In these zones, the microseismicity should have a complex three-dimensional distribution. Inverse relationship between confining stress and b-value has already been demonstrated (Figure 86). Moreover, experimental results show that rock behavior becomes more ductile with increasing confining pressures (Amitrano, 2003). Thus, we expect a positive correlation between areas with high b-value and brittle zones. For the test site, these two parameters are compared in Figure 92. In general, we see a positive correlation between these two parameters towards the heel end and the toe end of the pad. The strongest correlation can be observed towards the NW end of the pad, which is seemingly ductile and may be subject to very high stress anisotropy. Locations with significant mismatch such as the one shown in Figure 92a also show high standard deviation (σ) as seen in Figure 88b and Figure 89b.

Result: temporal variations

While a comprehensive analysis of all fracture stages is beyond the scope of this paper, we select four stages from different wells and interpret specific behavior from observed seismicity and hydraulic fracturing treatment data collected in the field. In Figure 93, we show these four examples and henceforth, we will call them stages A, B, C and D. We can clearly see varying

FMD behavior with time and these can be interpreted based on spatio-temporal distribution in seismicity and fracturing pressure behavior. Stages A and B (Figure 93a & Figure 93b) show no abrupt out of zone seismicity growth. However, the vertical spread of observed seismicity is almost twice for Stage A compared to Stage B indicating significant out of zone fracture growth. For stages C and D (Figure 93c and Figure 93d), abrupt out of zone growth can be observed (pointers). Stages C and D are associated with MWC wells, and the seismicity seems to extend within the UWC formation, which is vertically separated by approximately 300 ft from the MWC formation. As mentioned earlier, we know that in the Wolfcamp formation, the pore pressure and stress gradients decrease significantly, as we go from the MWC to the UWC formation (Figure 88). This can result in significant out of zone growth routinely observed for wells completed within these formations. While out of zone growth is common for many of the fractured stages, the distinct abruptness noted in Figure 93c and Figure 93d suggests rapid onset of significant hydraulic diversion. Depending on nature of such growth, there could be potential issues of post fracturing inter-zonal connectivity between these zones creating stimulated yet stranded sections within the reservoir. Next, we look at the net fracturing pressure data to identify specific behavior, which can help explain these observations.

Connectivity issues post hydraulic fracturing operations can occur since initially, apart from the tensile hydraulic fractures, connected fracture fairways comprise of existing natural fractures, which may open through shear or mixed mode failure including aseismic slip. Apart from natural fractures, further complexity is introduced through potential failure along thin layer bed boundaries common in clastic formations. The resulting flow pathways are prone to localized proppant pinch-outs, which may allow fluid to pass through but restrict proppant movement (Maity et al., 2018). As the pumping ends and the pressure drops, fracture closure occurs. Unpropped areas beyond significant pinch-out zones are unlikely to contribute towards productivity of corresponding fracture stages. This behavior is likely governed my multiple factors, including local lithology, in-situ stress, their surface asperities when open, as well as complexity in fracture connectivity patterns. Such complex propagation behavior has been observed in cores where hydraulic and natural fractures are present (Gale et al., 2018; Maity et al., 2018).

To understand net pressure behavior, we use the modified Nolte-Smith approach using "moving reference point" proposed by Pirayesh et al. (2013) for our analysis. Figure 94 shows results from modified net pressure analysis for data from the same four stages shown in Figure 93.

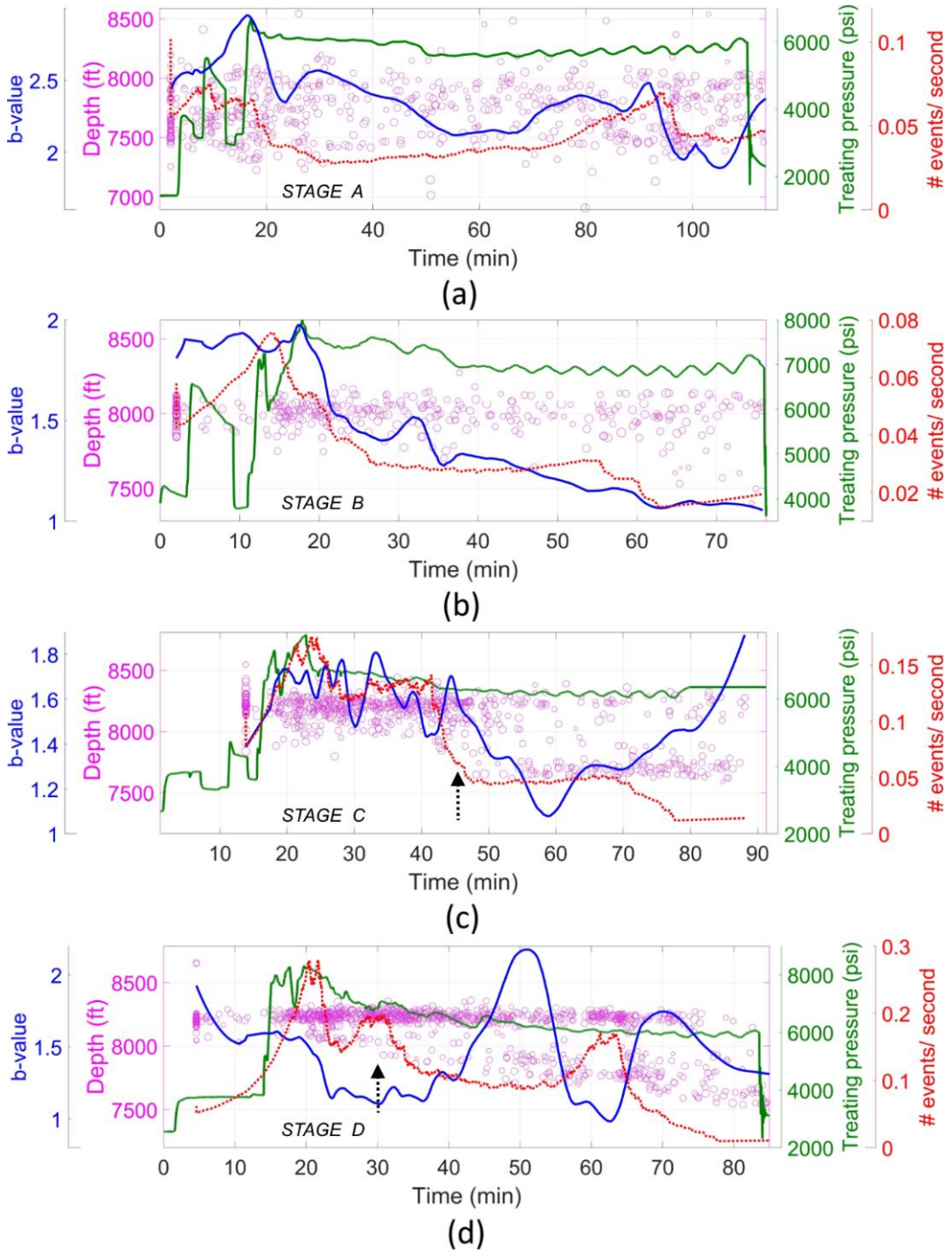


Figure 93: Temporal distribution showing b-value, rate of occurrence, distribution of seismic events with depth and fracturing treatment pressure for four stages: (a) stage A, (b) stage B, (c) stage C, and (d) stage D.

Specifically, the variation in Nolte-Smith exponent is shown with time. There is considerable difference in the behavior of the exponent for stages A and B (Figure 94a and Figure 94b) compared with stages C and D (Figure 94c and Figure 94d). For Stages C and D, we observe significant periods where exponent curve is negative. As discussed earlier, this could indicate rapid height growth into a lower closure stress zone (UWC formation) which is also observed in the microseismicity distribution. In addition, sections where we see negative slope corresponds with low b-value distribution from trends shown in Figure 93. This makes intuitive sense since the UWC formation is at a higher differential stress (Figure 86) which should cause larger magnitude microseismic events.

Since the slope of the net pressure curve is calculated using changing reference time, the estimated value of the exponent also varies significantly with time. However, we can observe some general trend behavior in their distribution. First, we consider stage A in the UWC formation. High values close to unit slope corresponds with mode III fracture growth (Figure 82). This indicates restricted growth of fracture causing increased fracture pressure and width. We know that excessive height growth or interaction with natural fractures can create such situations since it tends to increase the overall fluid loss area and dehydrate the slurry. While microseismicity distribution with depth shows significant vertical height growth into the underlying MWC formation, relatively high b-value distribution throughout pumping (b-value > 2) suggests fracture growth forming a complex three-dimensional network of fractures. No abrupt out of zone growth suggests that the height growth is not rapid and abrupt, such as behavior associated with sudden activation of connecting faults or fractures between zones. Rather, it is a continuous process associated with complex fracturing.

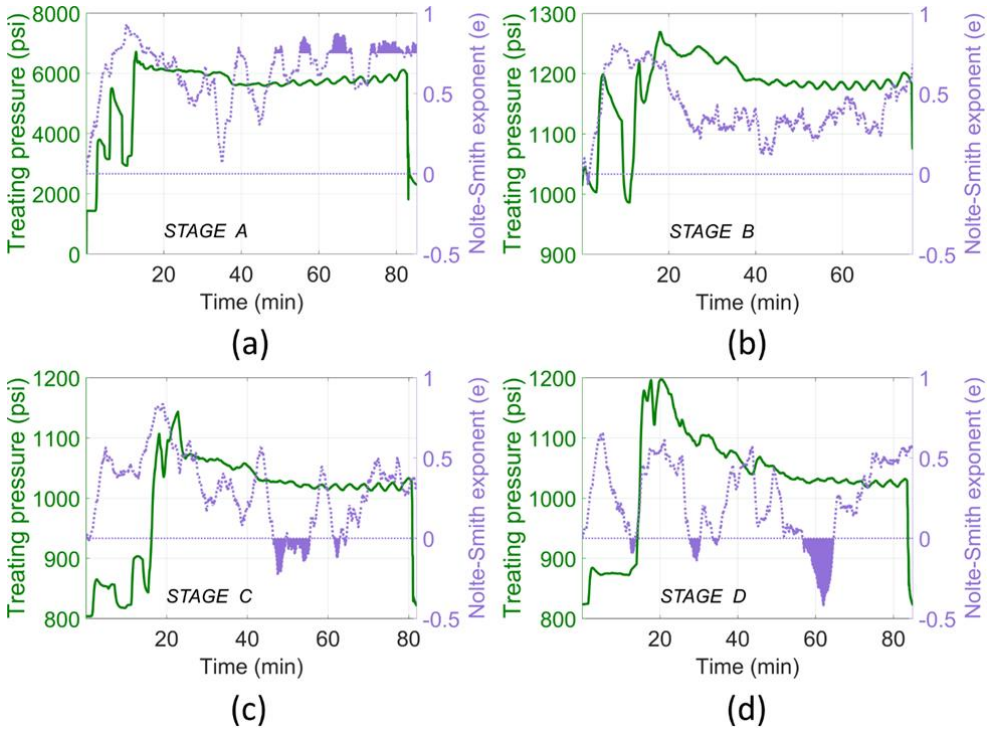


Figure 94: Nolte-Smith exponent 'e' based on fracturing treatment pressure for stages in Figure 93: (a) stage A, (b) stage B, (c) stage C, and (d) stage D. For stage A, there are significant portions of the treatment where the value is close to unit slope as shown by the shaded regions. For stage B, the value of the slope is approximately 0.3 for most of the treatment. For stage C and stage D, we see significant negative distribution of slope highlighted by the shaded regions.

For stage B, which is a MWC completion, the exponent stays range bound between 0.1 and 0.5 for much of the pumping with an average value of approximately 0.3. This is a classical fracture growth scenario where the net treating pressure continuously increases with time and the injection rate and fracture height remain relatively constant. The vertical height growth from microseismicity distribution suggests that the fracture height remains almost constant throughout pumping barring approximately 10 minutes before pumps are shut-in at the end of the fracturing. A significant difference between stage A and stage B is the local reservoir setting as observed from the discontinuities from ant track volumes (Figure 87). In Figure 95, the location of the stages and the relevant ant-track attribute distribution close to these two stages are shown. Stage A is in a part of the reservoir with significant discontinuities, which

propagate in depth while for stage B, the local reservoir seems to be devoid of any significant discontinuities.

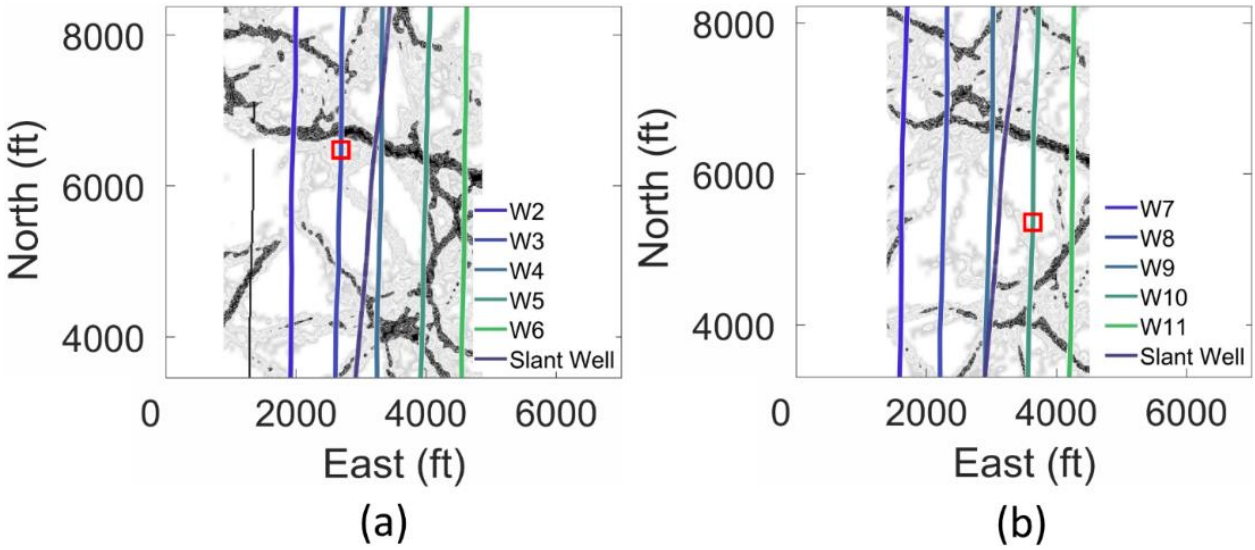


Figure 95: Distribution of 3D seismic derived ant-tracks close to (a) stage A in well W3 and (b) stage B in well W10. The locations of stages are identified by the red inserts.

When we consider stages C and D in the MWC formation, we observe signs of unstable height growth based on the observed microseismicity distribution. Moreover, growth initiation is abrupt and happens at approximately 45 minutes for stage C and around 30 minutes for stage D (Figure 94c & Figure 94d). This corresponds with the observations from microseismicity distribution (Figure 93c & Figure 93d) where the height growth into the lower closure stress zone happens at around the same time. Finally, a significant negative growth is observed at around 60 minutes for stage D. This corresponds with a significant rise in event density out of zone as well as some additional height growth. We hypothesize that at those relevant points in time where abrupt out of zone growth begins; a barrier is crossed such that the fluid encounters the lower stress UWC formation. Since the fracturing pressure is higher than the in-situ minimum stress within UWC formation, accelerated fracture growth and fluid infiltration occurs. The higher differential stress should cause larger slip failures leading to larger moment magnitudes of associated microseismic events. With these features connecting various reservoir units, once open, they can allow pressure and hydraulic communication between the two zones. The impact on FMD distribution, i.e., low b-value can be observed for stages C & D.

The relationship between the calculated b-value variation and microseismic event density is not uniform (Figure 93). The low b-values are likely not a data quality artifact, i.e., they are not a result of relatively large catalog size. Thus, provided the confidence measure for calculated b-value is reasonably high, the values should be usable for any analysis and interpretations that are made.

Discussion

We have looked at various ways in which microseismicity FMD can be used as a diagnostic tool for hydraulic fracturing operations, both independently, as well as in combination with other information. However, it is pertinent that we discuss the potential pitfalls in our analysis. Microseismic catalog size, quality as well as magnitude distribution affects the uncertainty associated with b-value analysis. Recent studies (e.g., Jiao et al., 2014) have suggested the use

of alternate moments for magnitude prediction and the impact of choice of moments on the calculated b-values. Errors in microseismic magnitude and location estimates can occur due to improper adjustments for attenuation, error in geophone locations from lack of accurate well directional surveys, inaccurate velocity models, limitations of inversion algorithms, etc. Moreover, variance for b-value estimation increases with decreasing number of events in the catalog or with a narrower range of magnitudes within the catalog. Examples for this include stages that are at a significant distance from monitoring arrays or stages, which show severe distance-magnitude thresholding (Grob & van der Baan, 2016). When conducting spatial analysis, the uncertainties associated with the inversion workflow for moment magnitudes and hypocentral locations are carried forward. With 3D seismic data, accurate time to depth migration and good seismic ties using careful calibration with well logs is necessary. Resolution mismatch between the 3D seismic and other data such as petrophysical logs and microseismicity also need to be considered. Various brittleness measures and their relative accuracy in predicting behavior of rocks under stress is relevant and has a significant impact on any interpretations. We use surface pressure measurements for our net pressure analysis. This may be acceptable since proppant concentration is moderate for these fracturing treatments (< 2 pounds per gallon of fluid). However, when analyzing fracturing pressures for understanding variations in net pressure with treatment time, it is better if measured bottom-hole pressure is used instead of surface pressure readings. This removes the effect of suspended proppant within the fluid column, since proppant significantly alters the fluid rheology and measured surface treating pressures.

Conclusion

In this case study from the Permian Basin, we have demonstrated the validity and use of microseismic b-value distributions as a useful tool for hydraulic fracturing completion diagnostics. Moreover, when used with other independent datasets, such as 3D seismic data or hydraulic fracturing treatment parameters, it can provide useful insights into the fluid behavior within the subsurface and its interaction with the in-situ rock. We have demonstrated b-value to be a good indicator of in-situ stress state based on microseismic monitoring of multiple hydraulically fractured wells at the HFTS. Seismic attributes such as ant track derived discontinuity and brittleness are found to be useful in validating the spatial distribution of seismicity FMD at the test site. We have shown the utility of using temporal variations in b-value distribution to help identify the relative dominance of different failure mechanisms associated with fracturing operations. When combined with hydraulic fracturing pressures, we can identify corresponding fracture growth behavior, understand the driving mechanism behind observed behavior and predict the overall effectiveness of hydraulic fracturing stimulation. Moreover, such studies can prove useful in redesigning hydraulic fracturing completion design strategies, such as changes in well spacing, and they can help identify the need for alternate landing zones.

Using stage level microseismic analysis to ground truth cored hydraulic fractures.

Authors: James Courtier, Ryan Fairfield, Stacy Trowbridge, Tammy Campbell, and Shawn Lee

Abstract

The Hydraulic Fracture Test Site in Reagan County, Texas contains a valuable dataset to correlate the occurrence, position, and frequency of microseismic events in relation to physical observations of hydraulic fractures taken from a low-angle whole core acquired immediately adjacent and after a modern hydraulically fractured horizontal well within the Upper & Middle Wolfcamp formations. Microseismic event density maps visualized through time locate concentrations of microseismic activity in relation to independently documented hydraulic and naturally occurring fractures. Microseismic activity observed over the duration of a single completion stage at the closest proximity to the cored interval demonstrates conformity and correlation with the presence of hydraulic fractures. Changes in microseismic signature are also correlated with changes in pump rates and pressures throughout treatment. A positive correlation was found between the high certainty hydraulic fractures observed in the core and areas of highest microseismic density in the stage of the neighboring horizontal nearest to the Upper Wolfcamp cored interval of the slant well, demonstrating that microseismic density can be a reliable indicator of hydraulic fracture density and complexity around the stimulated well. Given caveats often cited with microseismic acquisition, processing and interpretation, this study provides a ground truth example and insights into the degree of accuracy microseismic can offer as a technology in discerning the efficacy of modern completions.

Introduction

The Hydraulic Fracture Test Site (HFTS) in Reagan County, Texas consists of 11 horizontal development wells in the Wolfcamp Formation along with two preexisting Wolfcamp wells which were refractured on the eastern side of the package (Figure 96) (Courtier et al, 2016; 2017). The primary objective of the HFTS throughout the course of testing was to evaluate subsurface controls and operational impacts on hydraulic fracture geometry and completion efficiency, with one of the main undertakings of the project involving the drilling and coring of a slant well between two of the completed wells in the package to determine the presence and distribution of hydraulic fractures and proppant.

Analysis of the core in conjunction with downhole microseismic data provides unique insight into the representation of fracture propagation and proppant distribution from nearby stages with microseismic events recorded via downhole arrays. Through careful analysis of the density of the microseismic events and viewing the animation of events together with the pump schedule, relationships can be ascertained between the concentration and behavior of microseismic events, and the hydraulic fractures and proppant identified within the slant core. It is the intention of this paper to ground truth these data through empirical observations involving best-certainty hydraulic fractures noted in the core with kernel density estimate maps of microseismic events.

Since the main subject of this paper is relating the microseismic to fractures identified within the Sugg A 171 6TW slant well core (6TW), the focus from this point forward will be primarily on analyzing the microseismic of the Sugg A 171 6SU Upper Wolfcamp well (6SU) to the east and lesser so the 6SM Middle Wolfcamp well (6SM) to the west. In particular, the focus will be

largely on the stages immediately adjacent to the cored locations of the 6TW slant core well - Stages 23-24 in the 6SU.

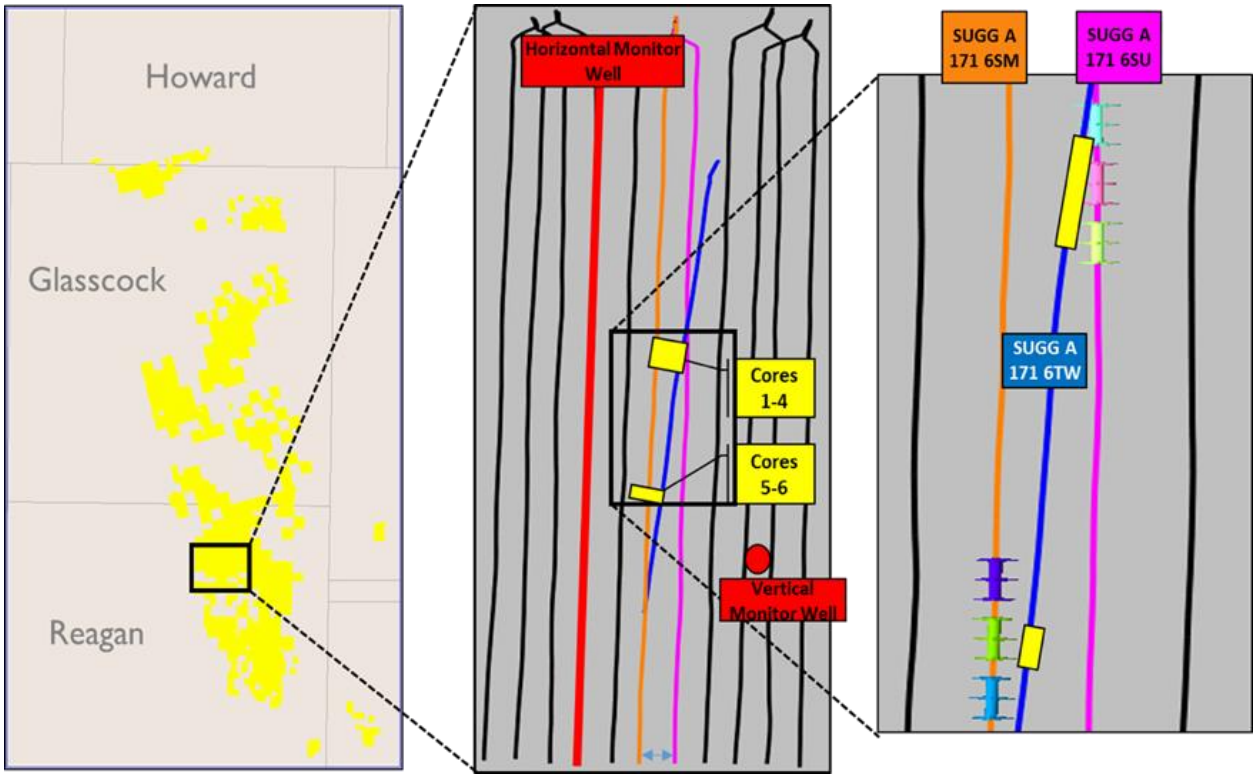


Figure 96: Whole core were successfully obtained in 4 separate runs (Core 1-4) in the Upper Wolfcamp portion of the slant well after the 6SU and 6SM wells were completed. Core segments 5-6 were collected in the Middle Wolfcamp for a total of 594 ft of whole core. Downhole microseismic data were also collected throughout the completion of these wells.

The Sugg A 171 6SU and Sugg A 171 6SM are two of eleven wells drilled during the HFTS study. These wells were triple zipper fracked along with the Sugg A 171 5SU well directly west of the 6SM with alternating stages in the three wells sequentially stimulated from the toe to heel by completing a stage on one well before moving to complete a stage on an adjacent well. The completion utilizes 100 mesh proppant pumped during the first 25 minutes of the stage completion before transitioning to 40/70 mesh proppant 30 minutes into the treatment. Varying colors of proppant were pumped in discrete stages, with the intention of correlating a particular-colored proppant associated with a specific stage, with its physical presence traced within the core.

Application of Microseismic

During completion, real-time microseismic data was acquired for the entire HFTS package in order to monitor the efficiency of the refrac treatment on the two parent wells east of the package, evaluate the impact of completion design variations chosen for the wells, and ensure all chosen designs were effectively stimulating the reservoir as reflected in the real-time microseismic events. The data were acquired over all the test wells and geophone monitor locations were moved several times throughout the completion of the pad as the frac moved from east to west, in order to mitigate monitor bias and accurately map event locations (Stegent et. al, 2018). During stimulation of the 6SU and 6SM wells, geophones were in one vertical well to the east of the 6SU and in one horizontal Wolfcamp well 660 ft to the west of the 6SM.

Microseismic data subsequently went through iterative processing to constrain event locations, magnitudes, and confidence, however, the real-time microseismic was still highly valuable in gaining insight into the behavior of the stimulated reservoir during treatment.

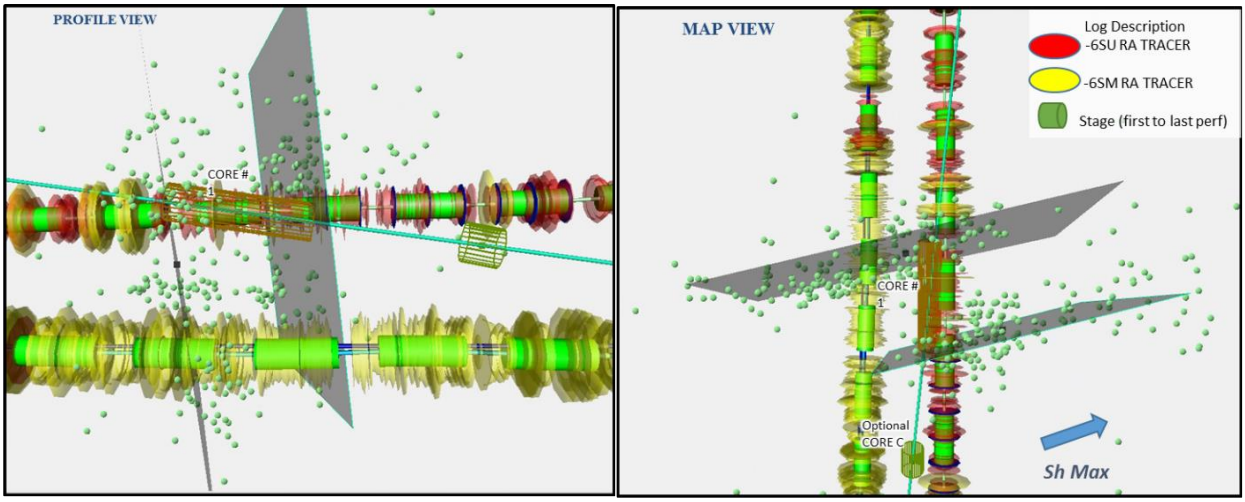


Figure 97: Image of the two "fracture planes" identified by planar microseismic event clouds which were used to alter planned core location to better intersect with both planes and thus increase likelihood of encountering hydraulic fractures.

Real-time microseismic in the vicinity of the planned coring location was thoroughly analyzed and used to determine final coring locations within the slant well. Three nearest stages between the 6SU and the slant well and three nearest stages between the 6SM and the slant well were prioritized to undergo a higher degree of processing. Prior to analysis of real-time processed microseismic, coring locales of the slant well were based on the closest encounter to the neighboring horizontals, lithology contacts, and the hypothesized hydraulic volume extents at the time. Processed microseismic of the stages nearest to the planned location of the slant core revealed a high density microseismic cloud in Stages 23 of the 6SU that formed two fracture planes and passed slightly above the planned coring interval (Figure 97).

With this information. the coring interval near the 6SU was extended, increasing the coring footage along the closest encounter to the 6SU and adjusted to intersect microseismic planar event fields and increase the probability of encountering hydraulic fractures within the core. This allowed the slant core to also pass through a high microseismic density zone near the 6SM. The utilization of real-time, processed microseismic events to adjust coring intervals within the slant well increases confidence in encountering hydraulic fractures and potential proppant within the core prior to the slant well being drilled. Subsequently, the slant core well was drilled at an 82-degree angle between the 6SU and 6SM chevron spaced wells. The closest encounters of the slant well to the neighboring horizontals occurred when it passed within 89 ft of stage 23 on the 6SU well and within 135 ft of stage 15 on the 6SM well.

Classification of hydraulic fractures in the core

Whole cores were successfully obtained in 4 separate runs (Core segments 1-4) in the Upper Wolfcamp portion of the slant well after the 6SU and 6SM wells were completed. Core segments 5-6 were collected in the Middle Wolfcamp for a total of 594 ft of whole core. All extracted core was analyzed inch by inch to catalog the presence of fractures and their distinguishing features (Gale et al, 2018). Fracture origin interpretations were made as to

whether the fractures were natural intact, natural reactivated, hydraulic, drilling induced, core handling induced, connection break, fault or bed parallel natural. The fracture origin observations were classified according to the certainty of identification: sure, probable or best guess. Only "Sure" hydraulic fractures were utilized, hereafter referred to as "best-certainty". It was also noted where proppant was found and whether colored proppant was found.

Application of KDE plots

Kernel Density Estimate (KDE) maps provide a way to estimate the probability density function of a group of microseismic events (Fairfield et al., 2018). To illustrate the application of KDE maps, the following example is presented. In Core 2, two proppant packs were found that align with perforation clusters on the nearby Stage 23. The 6TW core fracture analysis shows hydraulic fractures present in this range with orange/red colored sand. This colored sand was pumped from Stage 23. A single microseism intersects with Core 2 at ~9,458′ md during Stage 23 within a few feet of the colored sand filled hydraulic fractures. However, the microseismic positioning error on this event is +/- 16′ N/S, +/- 18′ E/W and +/- 36′ depth. This error in microseismic positioning makes it impossible to state unequivocally that a specific microseismic event is directly attributable to a hydraulic fracture or proppant pack in a 4" diameter core. However, when taking the representative cloud of events and KDE maps created with those events, we can assume that those areas under the intensely colored portion of the KDE anomaly are areas of highest energy and thus highest statistical likelihood of being hydraulically fractured.

Results

Microseismic events of varying density intersect the 6TW wellbore from stages 15-29 of the 6SU, however the cored intervals cover only cover portions of Stages 22-24. The fracture planes on stage 23 are estimated to be oriented at N77° E and 80° S. Regional compressive stress direction was estimated to be 75° x 255°. When creating KDE maps of the microseismic event clusters throughout time and viewing the animation coincident with the pump data, Stage 23 at the 15-minute mark prior to onset of completion pressure shows far field activity away from the wellbore (Figure 98a). At the 26–30-minute mark, the concentration of microseismic events abruptly snaps to the wellbore precisely when the ramp up in pressure begins, indicating that rock is being fractured, thus generating microseismic events (Figure 98b). At the 36-minute mark, the KDE maps show an area of microseismic event density centered over Core 2 which then migrates to the heel of the stage and stays over Core 1 for the remainder of the stage (Figure 98c). The concentration of the microseismic around the heelward perf correlates to a part of Core 1 where high certainty hydraulic fractures were identified. Similarly, on Stage 24, at the 20-minute mark, the activity snaps to the same Core 1 area of the slant well where high certainty hydraulic fractures were cataloged and the activity remains there throughout the stage, growing outward in an E-W trend (Figure 98d).

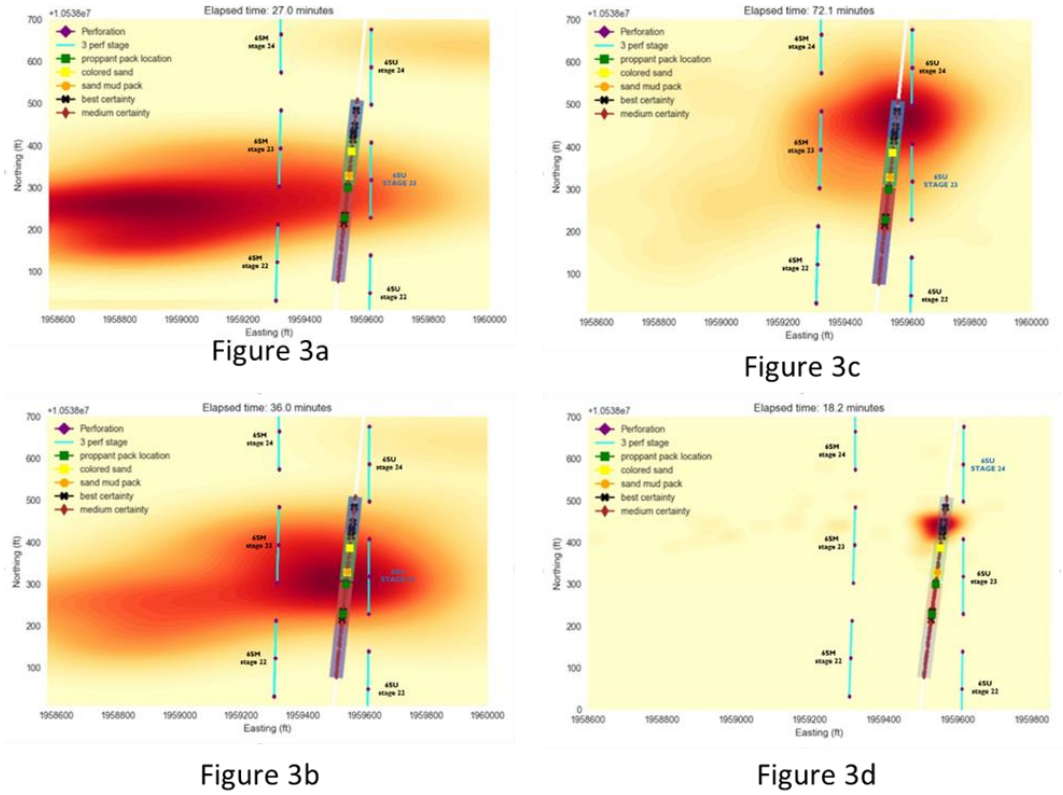
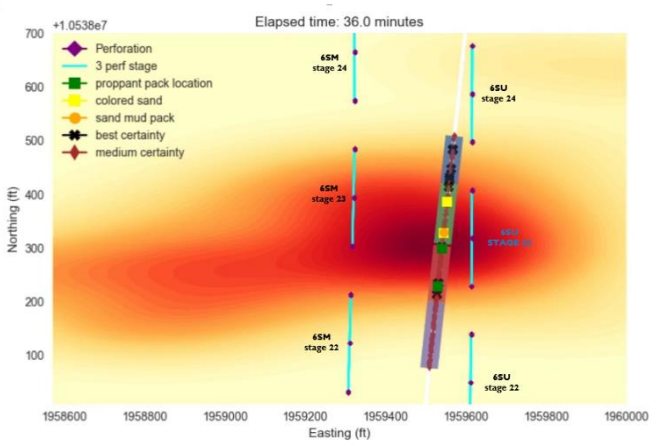


Figure 98: Evolution of KDE microseismic anomalies over stages 23 and 24 on the Sugg A 171 6SU. (a) shows the far field events present in the data prior to ramp up of casing pressure, the events snap to a location intersecting a proppant pack with colored sand linked to Stage 23 in (b), later in the treatment, (c), the anomaly migrates to the heel of the stage over an area of high certainty hydraulic fractures and remains there for the duration of the treatment. Early in Stage 24 the anomaly reoccupies the same location over Core 1 as in the previous stage.

Discussion

a)



b)



Figure 99: 36 minutes into the treatment of Stage 23, a high-density cloud of microseismic events gathers around the core intervals 2 and 3 in the same location a large proppant pack, b), and was seen in the core. The microseismic concentration at 36 minutes into treatment of the stage likely is showing the fracture network that emplaced the proppant encountered in the Slant Core.

Early in the treatment of Stage 23, the KDE cloud starts over Core 2 where the proppant packs and colored sand were encountered (Elliott et. al., 2018). A statistically significant KDE trend extends through the location of the proppant packs. It is assumed that the proppant packed fractures and colored sand pumped from Stage 23 are placed at that time (Figure 99). As the microseismic migrates toward the heel and coalesces over Core 1, the high certainty hydraulic

fractures observed in the core are being created at this time. When overlaying the microseismic events of Stage 23 on a geocellular model, a high calcite interval can be seen arresting the presence of microseisms and thus acting as a fracture barrier. (Figure 100a, Figure 100b) Interestingly, no high certainty fractures were cataloged in Cores 5-6 near the 6SM. This may be since the core is roughly 46′ further away from the closest 6SM stage than that of Core 2 and its closest stage (Stage 23) on the 6SU.

Conclusions

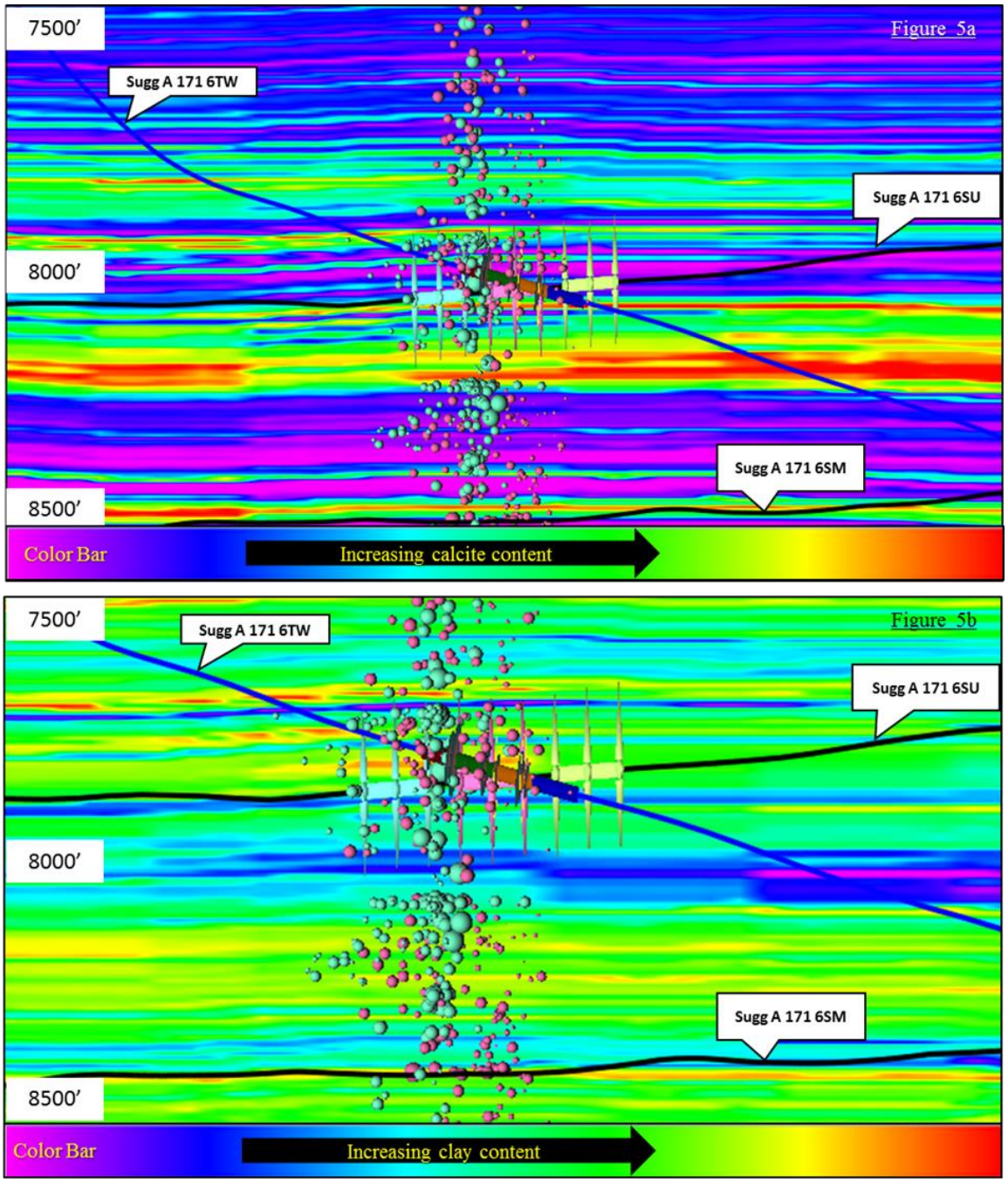


Figure 100: Proprietary geocellular model of calcite volume. (b): Proprietary geocellular model of clay volume. On both figures, notice the arresting of events in the center of the figure coinciding with elevated calcite/lower clay volume. The cyan microseismic events are from Stage 24, purple events are Stage 23.

Real-time microseismic was successfully utilized to optimize the likelihood of encountering hydraulically induced fractures during the coring of the slant well. Microseismic used in conjunction with additional geological and engineering parameters is an invaluable tool for

well spacing optimization and assessing efficiency of completion design. Time series maps of microseismic event density show strong conformance with cored intervals containing not only independently documented, high certainty hydraulic fractures but also proppant packs with colored sand traced to a nearby stage. Changes in microseismic signature are also correlated with changes in pump rates and pressures throughout treatment. These positive correlations along with the use of KDE maps demonstrate that microseismic event density can be a reliable indicator of hydraulic fracture density and complexity around the stimulated well. Given caveats often cited with microseismic acquisition, processing and interpretation, this study provides ground truth examples and insights into the degree of accuracy microseismic can offer as a technology in discerning the effectiveness of modern completions.

Using stage level microseismic analysis to gain insight into fracture efficiency and completion effectiveness.

Authors: Ryan Fairfield, Iris Haihong Wang, James Courtier, Danny Gray, and Shawn Lee

Abstract

Microseismic event density heat maps at sequential time intervals during the treatment of individual completion stages have been developed to better understand fracture behavior on a stage level. Animating these heat maps through time on a single stage provides fascinating visual insights into the dynamic sequencing of populations of events, event timing and their likely genesis, providing a new way of visualizing and interpreting microseismic data sets. This technique leverages heat-map benefits, excluding microseismic event clusters that may obscure or skew statistical analysis of the event densities, thus allowing for more accurate assessment of geologic features, stimulated rock volume, near-field concentration of events due to varying cluster spacing, fracture efficiency and stress shadowing. Far-field microseismic events prior to ramp up of treatment pressure are clearly indicated from this technique that cannot be observed with standard heat maps with certain completion designs. Unambiguous changes in microseismic event character from these far-field pre-ramp up events to those near-field events occurring at the onset of pressure are also observed. Applying a stage-by-stage approach on packages of wells and different locations provides robust statistical conclusions pertaining to reservoir behavior during well completion.

Introduction

The objective of drilling and completion design is to produce the maximum volume of hydrocarbons per dollar invested. During well placement and completion design, engineers have several basic questions that require evaluating hydraulic fracture stimulations or treatment (Maxwell S., 2014). These include: What is the primary fracture orientation? How far away from the well will the fracture grow? How much upward and downward height growth will occur? What is the best injection volume, rate, and pressure? How many fracture stages should be used and where? How many fracture initiation points (i.e., casing perforations) per stage will be required and where? Are there preexisting fracture zones of faults that can influence the fracture? What is the best spacing between wells?

Microseismic data can be interpreted to answer these questions directly, and it can be integrated with other measurements, such as physical whole core, subsurface geocellular models and other data to answer the remainder. This study provides an innovative way of visualizing and interpreting microseismic data sets, assisting in answering several the above questions.

A multi-well spacing test and fracturing project with an associated extensive data acquisition program across two Wolfcamp zones was undertaken within the Midland Basin in Reagan County, Texas (Figure 101) (Courtier et al., 2017) The key component of the program included a high quality microseismic acquisition, providing insight into hydraulic fracture efficiency and completion effectiveness; also included was a high-angle slant core, providing a rare opportunity to contrast and ground-truth documented hydraulic fractures and associated placed proppant with data sets and hydraulic fracturing models frequently applied during the development of unconventional reservoirs. (Fairfield et al., 2018). Individual wells included

variations in completion design including stages with 3 and 5 perforation clusters per stage, proppant loading amounts varying from 1,100, 1,400 and 1,800 pounds per foot, along with variations in pump schedules. The comprehensive microseismic data set provides a technology to assist in understanding how variances in completion style affect the generated hydraulic fractures.

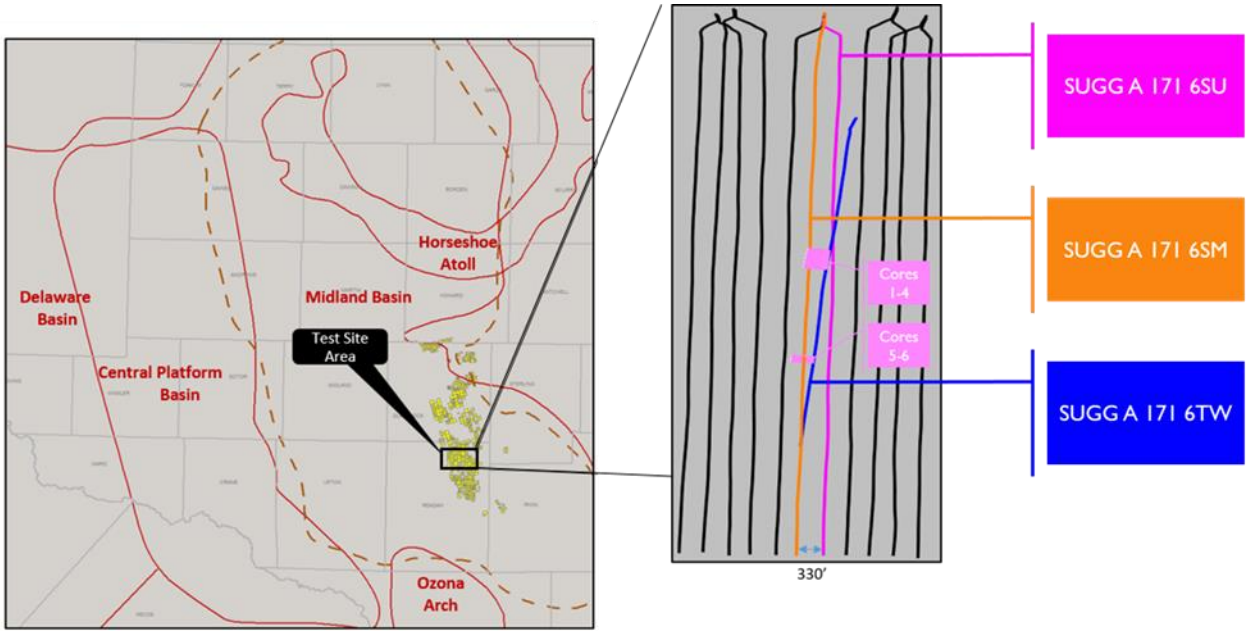


Figure 101: Location view map.

Method

Microseismic events are associated with naturally occurring or artificially induced fracture movements (Maxwell S., 2014). In order to identify large-scale trends within the data, heat maps and Kernel Density Estimation (KDE) maps are generated showing two-dimensional views of all microseismic events for each well.

Stacked Heat Maps

The Stacked Heat Map technique leverages benefits from Trowbridge S. (2017), providing an overall assessment of the stimulated rock volume. It involves calculating the X, Y, and Z (SSTVD) coordinates of the center of each fracture stage that has microseismic data. Since one of the main objectives is to find a consistent and reliable method to quantify fracture geometries, normalization of acquisition design variations and determination of other variables such as landing zone, completion design and multi-well versus single-well pad is required. Plotting histograms with associated percentile cutoffs of previously calculated Delta X, Delta Y, and Delta Z values is a key step in normalizing variability between data sets.

For improved comparison across the dataset, microseismic data is filtered by magnitude, setting the minimum magnitude to a value of -2.75. The 25th, 50th, and 75th percentiles of each microseismic property (Delta X, Delta Y, and Delta Z) are recorded from the histograms. To obtain average fracture half-length values, the percentiles of all microseismic events east and west of the wellbore are plotted and recorded separately. The same method is used for Delta Y and Delta Z. These percentile values are then used to calibrate heat maps with the calculated geometries from the histogram analysis.

The workflow described above has allowed for the assignment of specific values for approximate microseismic fracture lengths and heights which can then be used to compare with a variety of geologic and engineering variables. A leading objective of the microseismic geometry quantification workflow is its application as a calibration tool with hydraulic fracture modeling (Maxwell et al., 2016). Critically, this assumption considers areas of highest microseismic event density to be equivalent to areas of highest fracture complexity around the wellbore.

Kernel Density Estimation (KDE) Maps

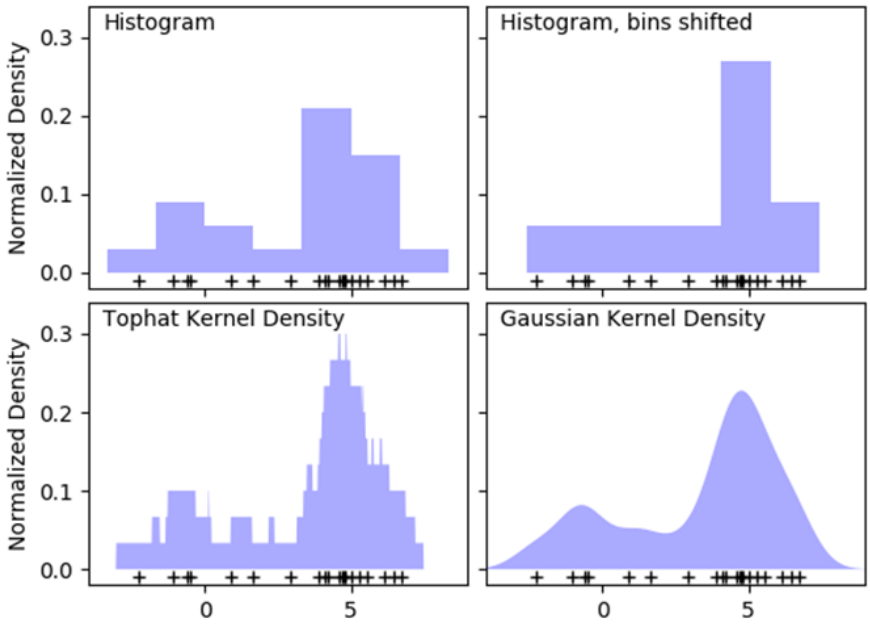


Figure 102: Comparison of the histogram vs. KDE (scikit-learn.org)

Kernel density estimation (KDE) is a non-parametric way to estimate the probability density function of a random variable. KDE addresses a fundamental data smoothing problem where inferences about the population are made, based on a finite data sample. (Parzen, 1962). KDE is an extension of the histogram (Figure 102). Histogram is a popular method of estimating the probability density function (PDF); however, the disadvantage lies in the following three aspects:

A. The probability density function is not a smoothed function.
B. It is greatly influenced by the width of the subinterval (i.e., each bin), and the displayed histogram result may be completely different if we take different bin size for the same raw data.
C. The histogram only shows up to two dimensions. Data cannot be displayed effectively if it has more dimensions.

Figure 102 shows two different KDE algorithms. In many cases, Gaussian KDE are used more often. Aside from the KDE algorithm, the bandwidth of the kernel is a parameter which exhibits a strong influence on the resulting estimate. To illustrate its effect, we take a simulated random sample from the standard normal distribution (plotted at the blue spikes in Figure 103 on the horizontal axis). The gray curve is the true density (a normal density with mean 0 and variance 1). In comparison, the red curve is under-smoothed since it contains too many spurious data artifacts arising from using a bandwidth h=0.05, which is too small. The green curve is over-

smoothed since using the bandwidth h=2 obscures much of the underlying structure. The black curve with a bandwidth of h=0.337 is optimally smoothed since its density estimate is close to the true density (Buch-larsen, 2005).

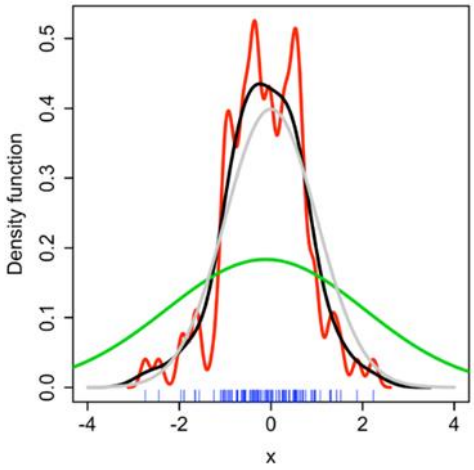


Figure 103: Kernel density estimate (KDE) with different bandwidths of a random sample of 100 points from a standard normal distribution. Grey: true density (standard normal). Red: KDE with h=0.05. Black: KDE with h=0.337. Green: KDE with h=2.

In summary, KDE can be used to accurately estimate a pdf of any univariate data set and is broadly implemented across other fields and disciplines, including, obtaining crime statistics; finding road or utility lines that affect towns or wildlife habitats; predicting risk of stocks. This paper describes how KDEs are used to develop microseismic heat maps, providing a more accurate and technically valid visualization methodology of microseismic event density.

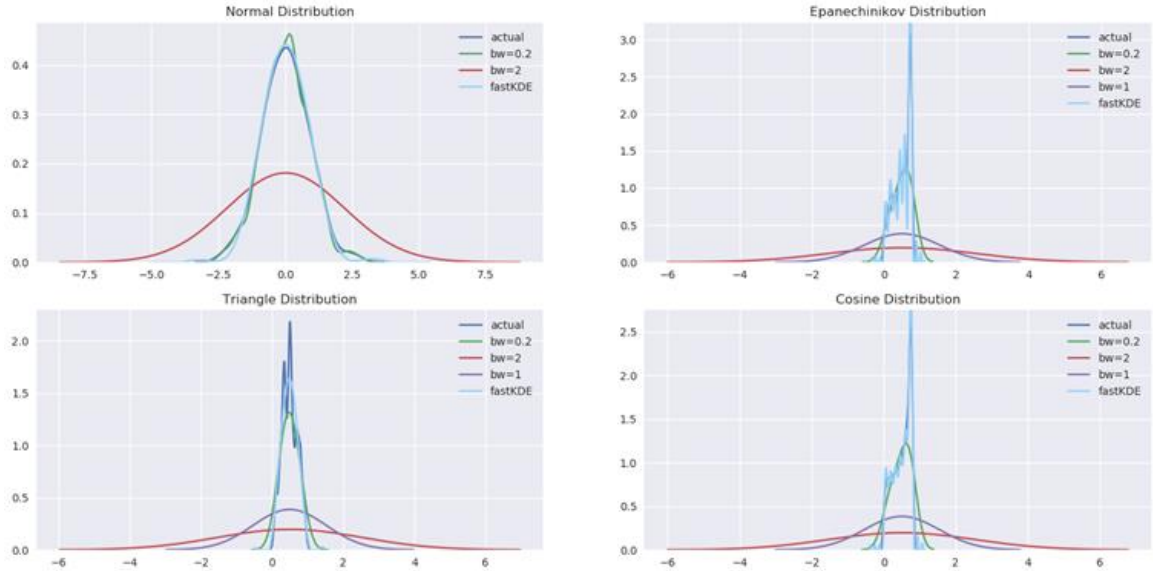


Figure 104: Kernel density estimate (KDE) algorithm comparison.

An advanced proprietary KDE algorithm, termed "fastKDE" was developed during this study in order to provide an implementable tool for the purposes of analyzing microseismic heat maps through time, to estimate the pdf, versus a Gaussian model. The fastKDE algorithm converges on the optimal kernel and bandwidth selection without having to make assumptions about the distribution itself. The algorithm uses a non-uniform Fourier transform to approximate the actual empirical characteristic function. Figure 104 shows the algorithm tested on different

distributions with examples of fastKDE verses various KDE algorithm with varying bandwidth. The fastKDE (cyan line) appears to be superior, being closest to the actual data (blue line).

This paper describes Gaussian KDE results, with a comparative example of fastKDE, given the recency of algorithm development. Animations of KDE maps can be generated through time of the microseismic event distribution throughout the treatment of single stages. A time window of approximately 10 minutes is typically chosen as the time interval between heat maps but varies based on changes in event frequency throughout the course of the stage. Creating displays for a given time window provides the possibility of following the behavior and concentration of the microseismic events and thus interpreted fracture network development during the treatment of every stage. The technique of animating microseismic heat maps through time provides additional valuable technical insights versus a single summary heat map for a single stage or an entire well.

Results

Comparing the stacked heat map versus KDE time-series maps over a single stage 23, indicates that KDE time-series maps provide far more details and greater insight into interpreted hydraulic fracture behavior during a single stage (Figure 105).

The generation of time-series microseismic KDE heat maps reveals valuable dynamic insights into the interpreted behavior of hydraulic fractures during treatment of an individual stage, including:

- How fracturing responds to changes in treatment.
- How fracturing develops spatially in terms of near and far proximity to the wellbore.
- How fracturing interacts with prior and subsequent treated stages.

Analyzing time-series KDE maps across multiple stages in several wellbores within the Hydraulic Fracture Test Site (HFTS) shows a consistent trend of heelward migration of microseismic event density throughout the treatment of multiple stages. 6SU Stage 23 is a prime example of this type of behavior, showing disperse microseismic around the wellbore during early treatment (Figure 105, Stage 23, 9 minutes) followed by a distinct shift to the heel cluster about 40 minutes into treatment where the microseismic activity takes place for the remainder of the stage. This behavior suggests the frac of the previous stage pressured the reservoir proximal to the toe-cluster and influenced fractures generated in stage 23 to migrate preferentially to the untreated heel portion of the completion stage. This is interpreted as an example of the effects of stress shadowing.

A related observation is the behavior of the microseismic in subsequent Stage 24 in the 6SU. KDE higher density regions within the time series heat maps show the majority of microseismic activity throughout the treatment of the stage migrating toward the toe perf cluster of the stage, almost in the exact location the activity was focused on stage 23 (Figure 106). This correlated heat map activity between successive stages suggests that the fractures from stage 23 may have reactivated a natural fracture network or a plane of weakness, causing the fractures from both stage 23 and 24 to preferentially concentrate within that zone. Furthermore, all microseismic events around this zone show approximately the same strike and dip and remain relatively confined in a single plan growing away from the wellbore with time, possibly indicating a small fault zone or weakness that promoted fracture growth.

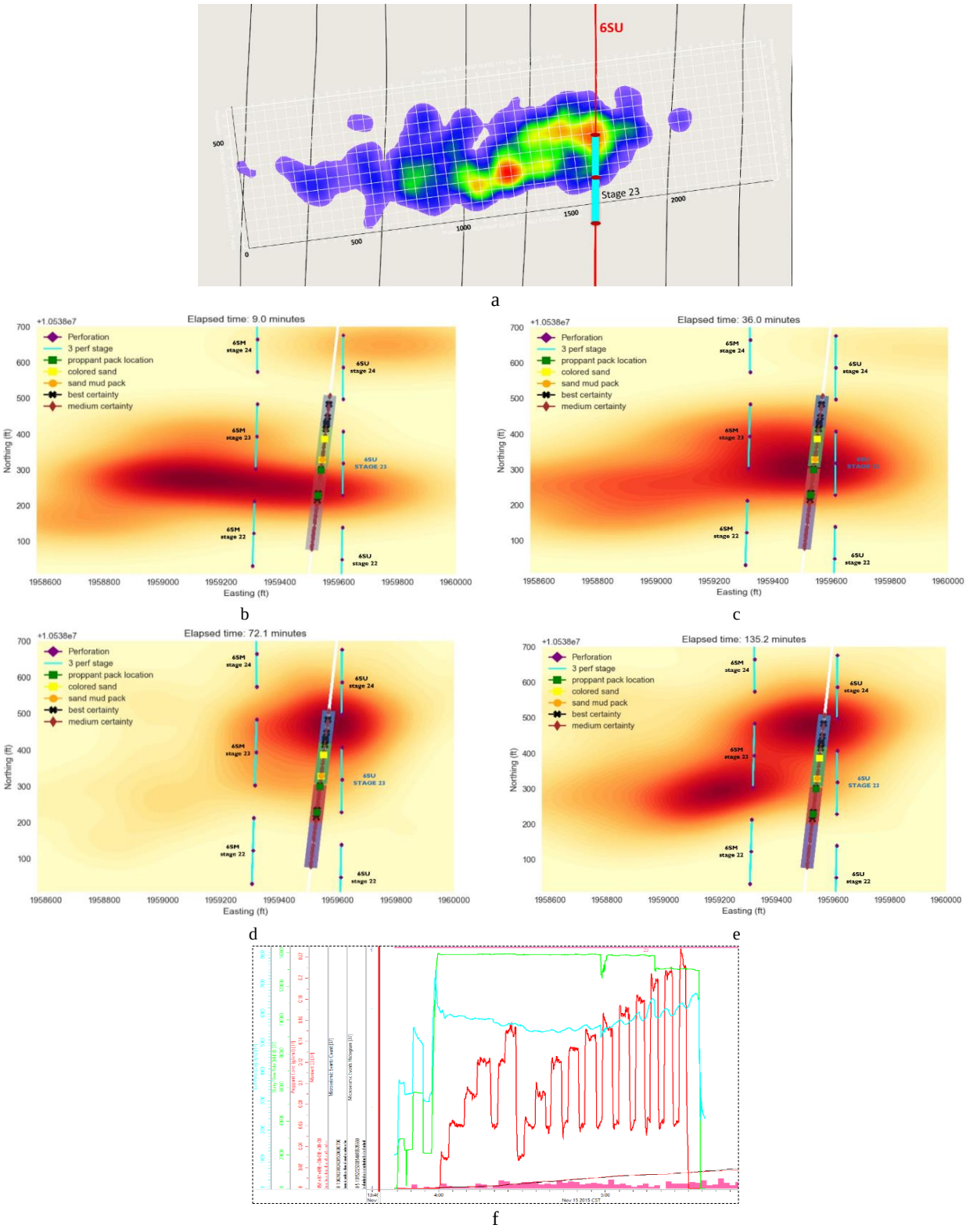


Figure 105: Evolution of Gaussian KDE microseismic time series map view over Stage 23. (a) Stacked heat map over stage 23. (b) KDE map shows elapsed time at 9 minutes into pump schedule. Microseismic events have initial far field event in the beginning of completion. (c) Ramp up at 15 minutes but microseismic event cloud jump to wellbore not until around 36 minutes. (d) Later event cloud jumps back to wellbore at 72 minutes. (e) Heelward extent towards end stage (elapsed time 135 minutes) could be the effect of stress shadowing. (f) Pump schedule over Stage 23.

Far-field microseismic events prior to ramp-up in pump rates are also observed in stage 24 (Figure 106). These occur at 600 to 1,000 ft from the wellbore before pressure build up. Immediately following ramp-up of pump rates, slurry and proppant concentration at 18

minutes elapsed time the microseismic event density rapidly returns to near-well bore vicinities.

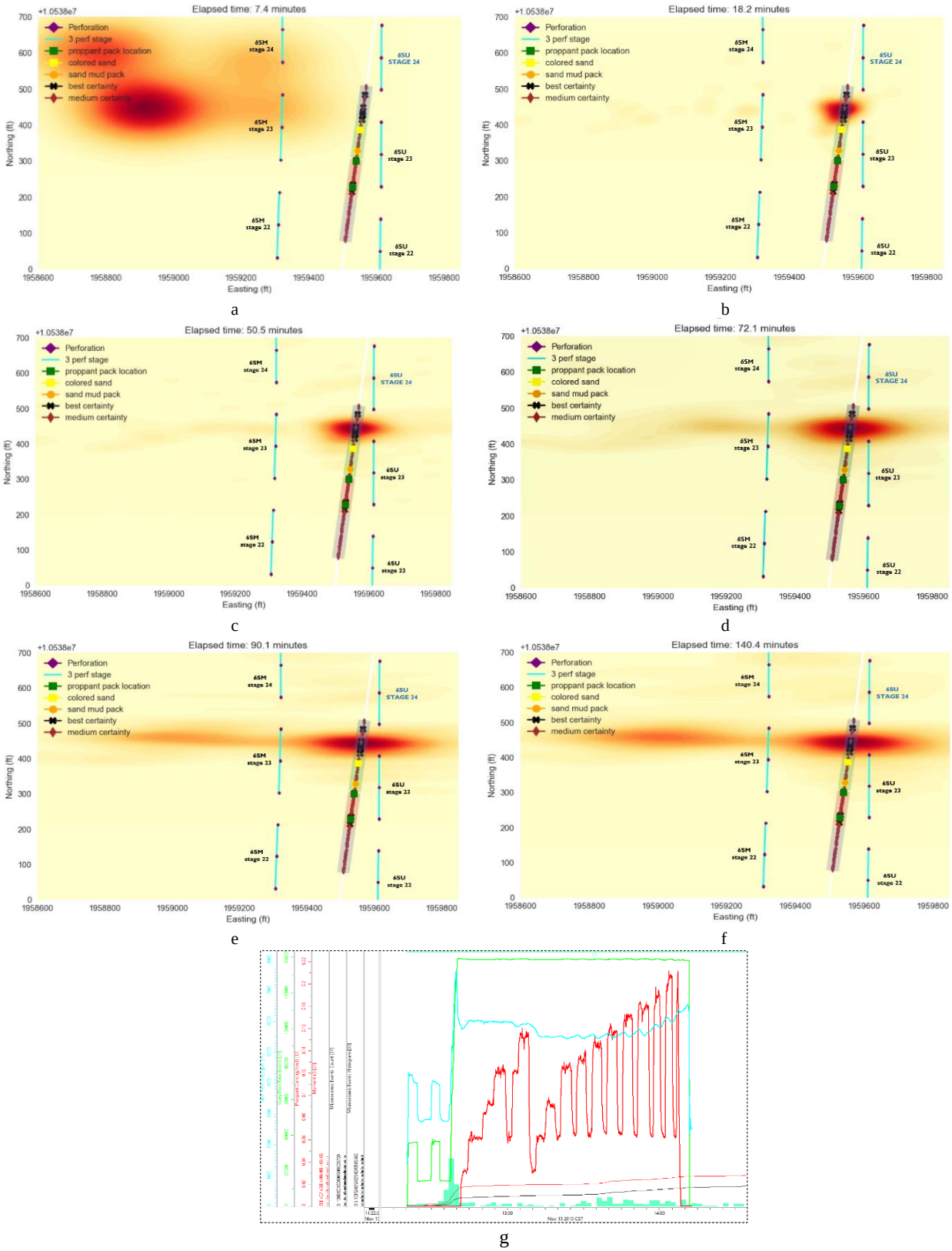


Figure 106: Evolution of Gaussian KDE microseismic time series map view over Stage 24. (a) KDE map shows microseismic event cloud at elapsed time ~8 minutes. Far-field microseismic event occurred prior to ramp up. (b) Microseismic event cloud snap back to the wellbore, right after pumping at elapsed time 18 minutes. Later in the treatment, Figure c to f, the microseismic event migrates toward the toe perf cluster of the stage throughout the

reminder treatment of the stage 24. It indicates the 2nd and 3rd perf which are close to the heel of the stage 24, were not efficient. (g) Pump schedule over stage 24.

While analysis of offset operations reveals no obvious activity in the area associated with far-field microseismic activity for this discrete stage, this cannot be completely ruled out. Observations of similar far-field microseisms on multiple completion stages of a similar completion design, indicates this to be a recurring phenomenon, versus anomalous observations associated with a discrete stage.

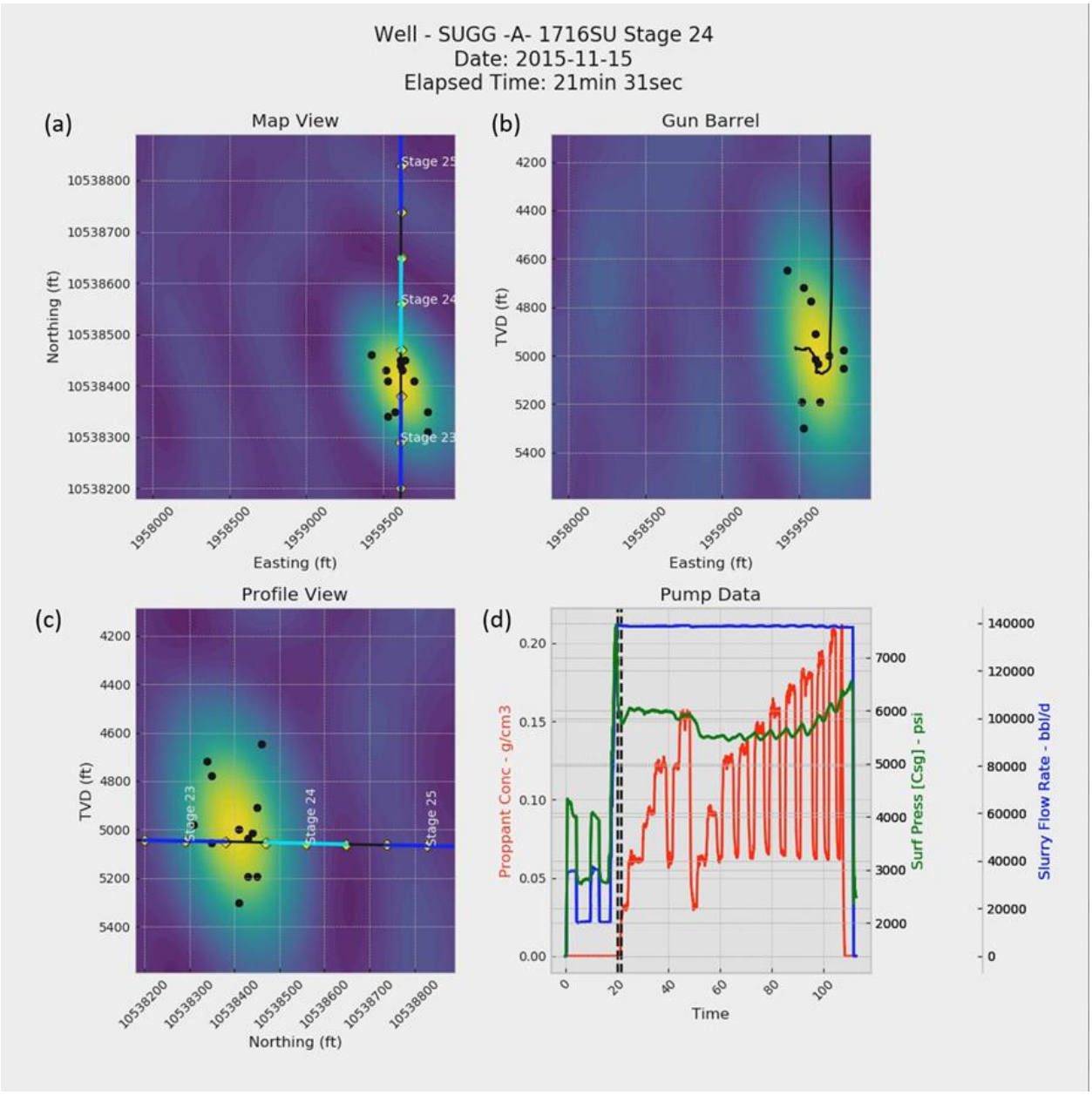


Figure 107: fastKDE time series heat map at elapsed time 21 minutes 31 second over stage 24; black dots show the actual microseismic events. (a) Map view. (b) Gun barrel view. (c) Profile view. (d) pump schedule over stage 24.

The slant core shows hydraulic fractures related to microseismic activity (Fairfield et al., 2018). The time series KDE map also gives us an indication of what perf of cluster has been activated (Figure 106, toe perf).

The fastKDE technique takes microseismic magnitude into consideration, versus the Gaussian KDE technique. The magnitude describes the strength of an event and tells us about the dynamics of the fracturing processes (Baig & Urbancic, 2010). The fastKDE time series map

allows generating most representative interpretation of probability density function utilizing the microseismic event and magnitude (Figure 107).

Discussion

Higher permeability systems within the reservoir such as natural fractures and weak interfaces between bedding plans (Campbell et al., 2018)) appear responsible and effective at moving completion fluids at lower pump rates, proppant concentrations and pressures to far-field wellbore locations and triggering microseisms on critically stressed rock.

The 6SU displays initial far-field events during in the beginning of individual completion stages (Figure 106). This hypothesis could be more scientifically accurate if we integrate microseismic with other supplementary datasets (such as geocellular model, natural fault/fracture analysis, petroleum system model, etc.) to ensure the most representative interpretation of fracture networks created throughout treatment.

Conclusions

- Utilizing time series heat maps allows greater insight into interpreted hydraulic fracture behavior during a single stage, furthering knowledge from investment placed into this technology to assist in future completion designs and field development decisions.
- KDE time-series mapping shows dynamic behavior over the total time elapsed during a single completion stage.
- Despite location errors, directionality of where events are occurring can be identified, which demonstrates non-uniform cluster efficiency and an interpretation of different perf clusters active at different times.
- Long-distance microseismic appears to occur early and when pump-rates are low.
- Legacy 90 ft cluster spacing completion designs show a heel-ward bias towards the end of an individual completion stage, an evidence of stress shadowing.
- The probability density function strongly influences the appearance of microseismic intensity within heat maps. Gaussian KDEs provide a more smoothed appearance versus the fastKDE approach. More work is needed to understand the relative merits and drawbacks of both methods.

Surface seismic Monitoring at HFTS Phase1

Authors: Abhash Kumar, Kevin Chao, Richard Hammack, and William Harbert

Abstract

Low-frequency seismic events of long duration were recorded by a surface array of 48, 3-component geophones during the fracture stimulation of two offset horizontal wells in the Middle Wolfcamp Formation (8,000-8,100 ft. below the geophone array) at the Hydraulic Fracturing Test Site (HFTS) in Reagan County, TX. Each recorded event was approximately 5-10 seconds long, with no clear first wave arrival; the seismic energy was largely visible on the vertical component suggesting that the events are dominated by P waves. A finite temporal moveout was observed across the seismic network in event arrival times indicating a causal relationship with the local source of deformation. The low-frequency seismic events observed in this study can be distinguished from the more commonly known microseismic events by their: 1) emergent waveform, 2) lack of clear P wave and S wave arrivals, 3) longer duration (few seconds), and 4) lower-frequency energy content (10-60 Hz). Previous researchers have observed similar low-frequency, long duration events in conjunction with the hydraulic fracturing of hydrocarbon reservoirs and have referred to them as long-period, long-duration (LPLD) events in the literature. LPLD events may be important to a comprehensive understanding of fracture stimulation because these events are thought to represent: 1) movement along pre-existing discontinuities such as bedding planes and fractures/faults, 2) deformation of ductile rocks with high clay content, and 3) the jerky tensile opening of hydraulic fractures. LPLD events resulting from slow shear-slip on faults and fractures of relatively larger dimension or rupture in the clay rich rock are collectively referred to as slow-slip seismicity, which was first observed in tectonic and volcanic settings, areas with high pore pressure like hydraulically fractured reservoirs. Because LPLDs are thought to represent deformation mechanisms not captured by microseismic analysis (which dominantly indicate shear failure of brittle rock), we believe that incorporating LPLD events into a new methodology for delimiting stimulated reservoir volume might improve predictions of well production.

Introduction

Hydraulic fracturing is an advanced exploration technique to efficiently extract significant volumes of oil and natural gas from organic-rich shale and tight gas reservoirs, which are naturally low permeability rocks. This involves the injection of large amount of fluid, typically water, in the reservoir rock that increases fluid pressure in the pore spaces and alters the stress condition of the rock significantly. This sudden change in the stress condition is strong enough to create new fractures in the rock or stimulates slip along the pre-existing fractures. Creating new fractures or inducing slip along multiple pre-existing fractures, both results into a marked increase in the interconnectivity of pore spaces in the certain volume of rocks and enhance the flow of oil and gas within the stimulated volume that were originally trapped in the isolated pores (Warpinski et al., 2008). The deformation along pre-existing faults and the opening of new fractures is likely recorded as microseismic events during hydraulic fracturing treatment. The distribution of microseismic earthquakes is traditionally used as a proxy to estimate the

stimulated reservoir volume (SRV) (Vermylen & Zoback, 2011). For the most part, this correlation between SRV and microseismicity is still inconclusive in the literature, with evidence both in support of and against the practice (Wilson et al., 2016 and Sicking et al., 2013 respectively).

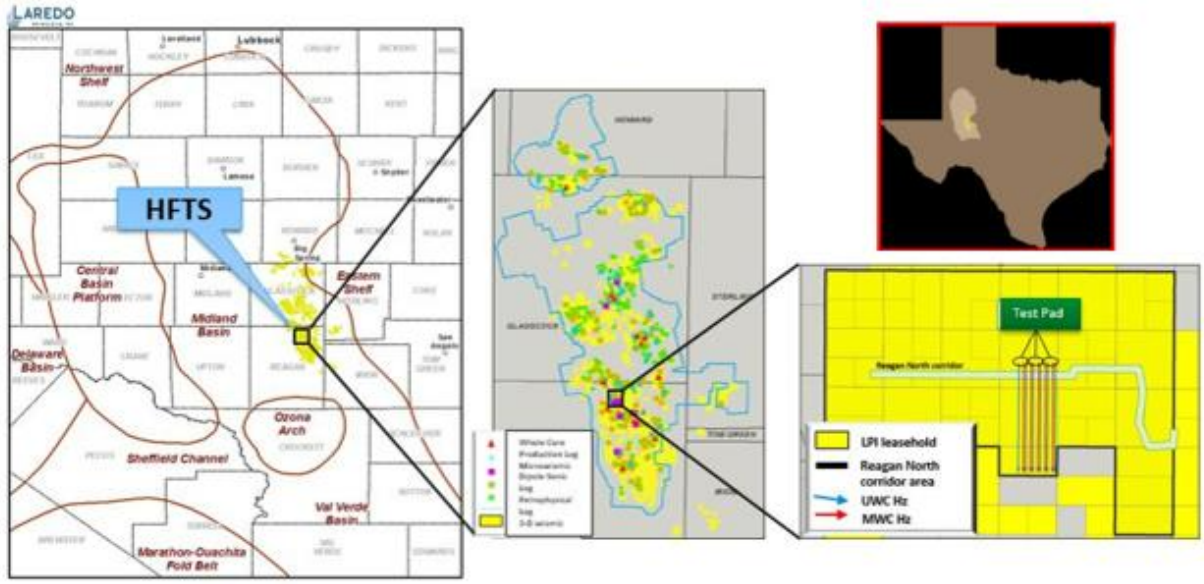


Figure 108: Index maps showing the location of the Hydraulic Fracturing Test Site (HFTS) within the Midland Basin in Reagan County, Texas. Maps provided by Laredo Petroleum, Inc. (LPI) and Gas Technology Institute (GTI Energy).

Even after 80 years of operational history of hydraulic fracturing technology, a clear understanding of complex fracturing processes of unconventional reservoir is still lacking. The response of a shale reservoir to hydraulic stimulation has been reported to be extremely variable among different fracturing locations. For efficient extraction of oil and natural gas, it is extremely important to get an accurate estimate of the stimulated reservoir volume. However, a simple energy balance calculation suggests that the combined energy released from all microseismic earthquakes during hydraulic fracturing is a small portion of the total input energy, supplied to the reservoir rock in the form of injected fluid (Boroumand & Eaton, 2012). This suggest that the SRV, calculated using microseismic earthquakes alone that represent a small portion of the total injected energy, is perhaps an underestimated portion of the actual reservoir volume that get stimulated during hydraulic fracturing. The difference in the total input and output energy suggests some alternate mechanism of deformation in the reservoir rock during hydraulic fracturing that need to be considered to account for the energy difference and get more accurate estimate of the SRV. In recent studies of hydraulic fracturing treatment in the Barnett, Marcellus and Eagle Ford Shale, evidence of low-frequency events, with drastically different seismic signature (frequency, amplitude, time duration) than traditional microseismic earthquakes, have been found (Das & Zoback, 2011; Kumar et al., 2016, 2017; Hu et al., 2017). Each of these events had significant concentration of energy in the low frequency band (10-80 Hz) that persist for long duration of time (between 10-100 seconds) and quite different from traditional microseismic events that are much higher in frequency (>100 Hz) and lasts for less than a second. These low frequency (or long period) earthquakes are proposed to be associated with slow rate of slip along pre-existing fractures that are unfavorably oriented in the

ambient stress field or caused by tensile opening and resonance of fluid filled cracks (Das & Zoback, 2011; Zoback et al., 2012; Hu et al., 2017).

In this study, we identified low frequency events of long-time duration in the surface seismic data collected during hydraulic fracturing of the two laterals in the Middle Wolfcamp formation (Figure 108). These long period long duration (LPLD) events show significant concentration of energy in the 10-60 Hz frequency range with duration times of 5-10 s. Waveform signature of these low frequency events show highly emergent phase arrivals and are like LPLD events reported in the previous studies (Das & Zoback, 2011; Eaton et al., 2013; Kumar et al., 2016, 2017; Hu et al., 2017). For the observed LPLD events, we noticed dominant concentration of the seismic energy in the form of P-wave that are more clearly recorded on the vertical component of the geophone array. This dominance of P-wave energy is like the LPLD events previously observed in the Eagle Ford Shale in NE Mexico and likely indicates similar source characteristics for the low frequency events identified in the current study.

Data and Field description

The surface seismic data used in the current study was acquired from the Hydraulic Fracturing Test Site (HFTS, Figure 108), which is a joint government/industry research partnership intended to improve reservoir characterization and maximize hydrocarbon recovery from horizontal wells landed in the Upper and Middle Wolfcamp Formations in the Midland Basin, Reagan County, Texas. At HFTS, microseismic monitoring, cross-well seismic tomography, fluid and proppant tracers, and pressure monitoring were used to determine the extent and complexity of hydraulic fracture networks, and the resultant reservoir and inter-well communication, both vertically and horizontally as different fracture treatments were tested. The unique feature of HFTS is the slant core well which extracted core from hydraulically fractured zones of the Upper and Middle Wolfcamp for a comprehensive examination of natural and hydraulic fractures, including propped fractures. However, the scope of this paper is limited to the examination, analysis, and interpretation of low-frequency, long-duration waveforms recorded by a surface array of 48, three component geophones during the hydraulic fracturing of two horizontal Middle Wolfcamp wells (SUGG-A-171 4SM and 5SM) at approximately 8,000 ft.-depth. This site comprises 11 horizontal wells, including six Upper Wolfcamp wells and five Middle Wolfcamp wells. The nine other HFTS wells had been hydraulically fractured prior to the time of surface seismic recording but plug drill out and flowback operations at HFTS wells did not commence until after the recording of data from the surface seismic array was completed. Dawson Geophysical Company installed two arrays of 24, 3C-geophones each above SUGG-A-171 5SM to record seismic waveforms during the fracture stimulation of SUGG-A-171 4SM and 5SM (Figure 109). Each array consisted of 24 GS-One 3C geophones (Geospace Technologies) spaced 220 ft apart; for each array, 20 geophones were deployed in a magnetic north-south direction (353.5° azimuth) with four geophones deployed orthogonally, intersecting the 20- geophone line at its midpoint. The Geospace Technologies GS-One 3C geophones have natural frequency of 10 Hz and sensitivity of 85.8 V/m/s with <0.1 percent distortion. The horizontal wells SUGG-A-171 4SM and 5SM have lateral lengths of 10,261 ft (18,495 ft. total depth) and 10,213 ft. (18,484 ft. total depth), respectively. Wells 4SM and 5SM were stimulated during December 9 – 21, 2015 using conventional plug and perf

operations with simple zipper sequencing (4SM stage 1, 5SM stage 1, 4SM stage 2, 5SM stage 2, etc.). However, each well was treated using separate frac plans as detailed in Table 5 below.

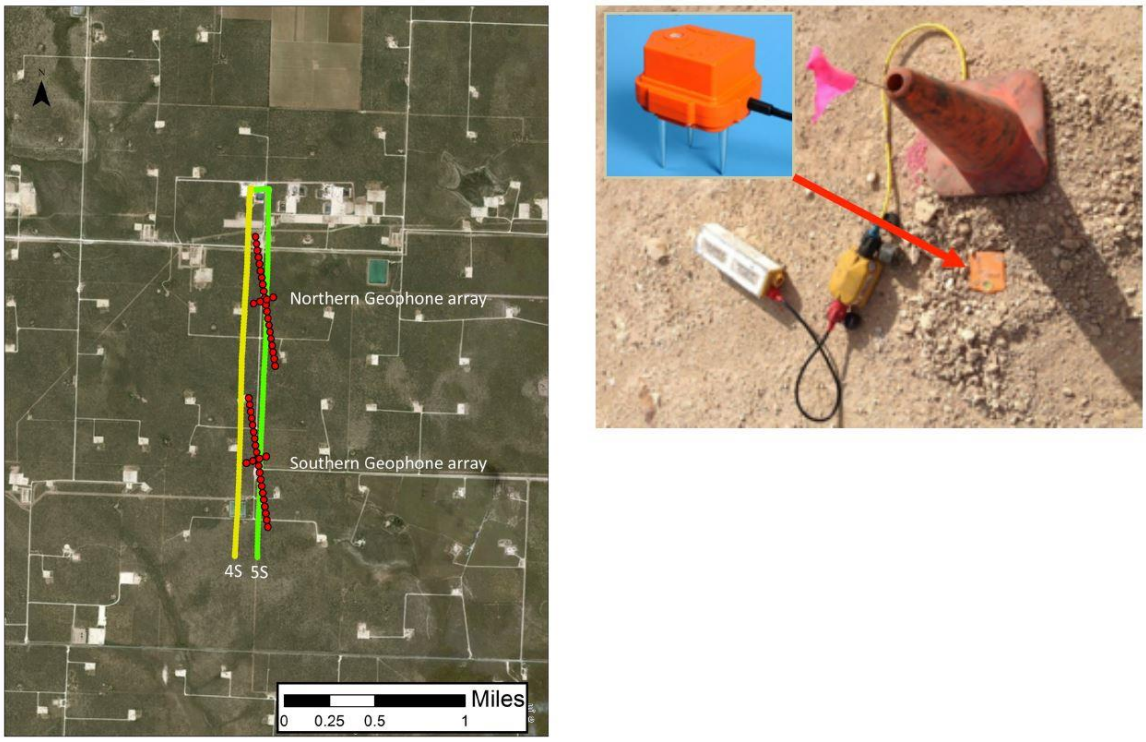


Figure 109: Map view of two arrays of 3C geophones (red dots) that recorded seismic waveforms during the fracture stimulation of two Middle Wolfcamp wells (4S and 5S) located about 8,000 ft. below the geophone arrays. Each array consisted of 24 GS-One 3C geophones spaced 220 ft.-apart; for each array, 20 geophones were deployed in a magnetic north-south direction (353.5° azimuth) with four geophones deployed orthogonal, intersecting the 20-geophone line at its midpoint. The picture at right shows a geophone deployment at the HFTS site where the GSOne 3C sensor is buried with only its top surface showing above ground.

Table 5: Treatment design for the two Middle Wolfcamp wells

Parameter	4SM	5SM
Stages	1-37	1-37
Stage Length (ft)	224	188
Perf. Clusters/Stage	5	3
Cluster Length (ft)	1.5	1.5
Shots Per Foot (SPF)	6	6
Total Fluid (bbl)	15,185	9,440
100 mesh (lb)	100,010	81,100
40-70 mesh (lb)	397,465	221,055
Proppant Placed (lb/ft)	1,774	1175
Rate (bbl/min)	96.1	95.5
Pressure (psi)	6,215	6,230
Fracture Gradient (psi/ft)	0.86	0.83

Methods

We use Antelope software to create a continuous seismic database for the surface seismic data collected during hydraulic fracturing of wells 4SM and 5SM. In a comprehensive search of low frequency events, we manually inspected the seismic waveform recorded during first five days of fracturing. We filtered seismic waveform in multiple frequency range of 10-40 Hz, 10-60 Hz, and 10-80 Hz to facilitate the search of low frequency events and reduce the masking effect of high frequency noise. We observed the best coherent and clear arrivals between stations in the 10-40 Hz frequency range. Due to limited frequency response of surface geophones, we are unable to find any seismic signal below 10 Hz. We identified 203 discrete seismic events with waveform characteristics like LPLD events previously observed at other fracturing sites. These events are characterized by highly emergent waveforms with no impulsive phase arrivals. We observed significant concentration of seismic energy in the 10-40 Hz frequency range for these LPLD like events with event duration of 5-10 seconds. The seismic energy of the observed low frequency events is dominantly visible on the vertical component and like the LPLD events previously observed during hydraulic fracturing in the Eagle Ford Shale in NE Mexico (Hu et al., 2017).

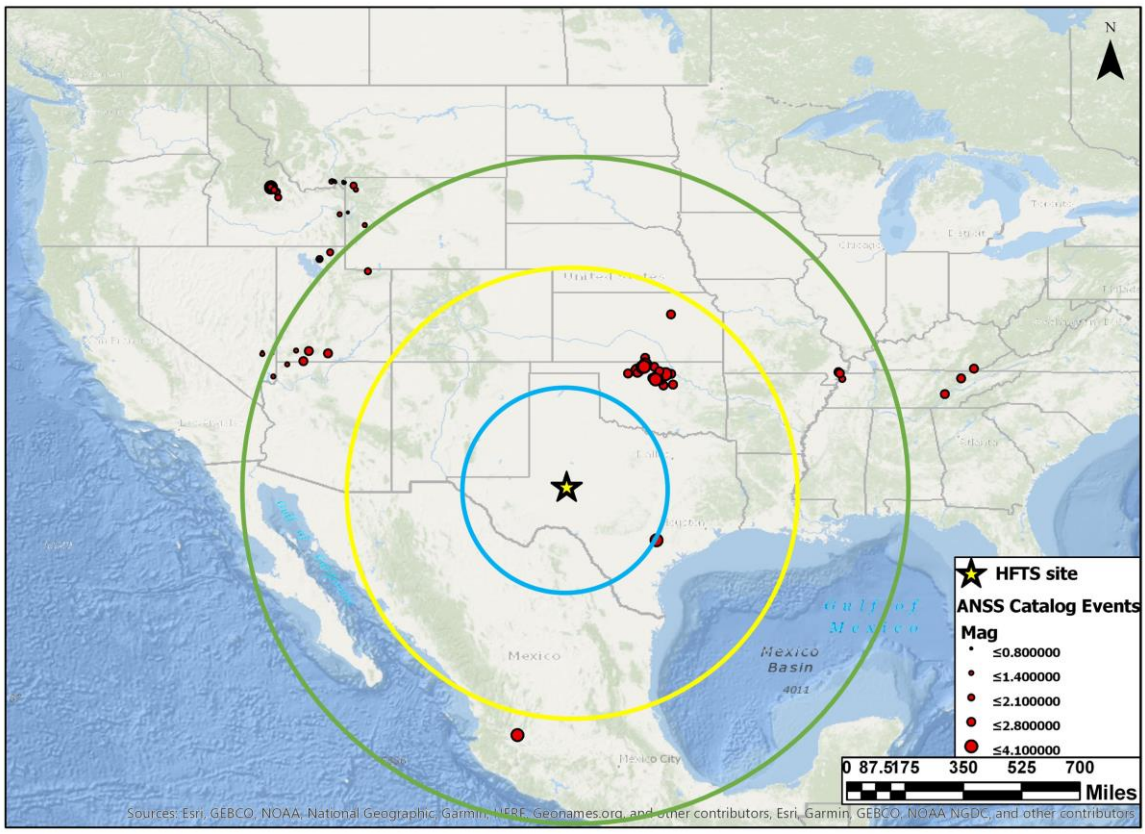


Figure 110: Map showing the location of regional events (solid red dots) reported in the ANSS catalog during the fracturing of horizontal wells in Reagan County. The blue, yellow and green circles drawn on the map have a radius of 500 km, 1,000 km, and 1,500 km respectively.

It is critical to rule out the possibility of misinterpreting any regional or distant seismic events of tectonic origin as local LPLD events. As highlighted in recent studies (Caffagni et al., 2015; Zecevic et al., 2016), both large magnitude regional events reported in the earthquake catalog and smaller magnitude distant events (smaller than the detection threshold of standard earthquake catalogs) not listed in the standard earthquake catalogs are potential pitfalls for identifying and characterizing LPLD events due to their overlapping frequency content and emergent waveform characteristics. We investigated the ANSS (Advance National Seismic System) Composite Catalog for regional seismicity to avoid any obvious misinterpretation of large regional events, listed in the national catalog, as LPLD events. We searched for regional events within 500km radius surrounding our study area (blue circle, Figure 110) and found temporal overlap with 9 regional events reported in the ANSS catalog. We progressively increased our search radius to 1,000km and 1,500km (yellow and green circles in Figure 110) and found one more regional event that temporally overlapped with our observed LPLD events.

This suggests that either the remaining 193 events are small magnitude regional events below the detection threshold of standard catalogs, or they are local earthquakes near our seismic network. To rule out the possibility of mispicking small magnitude regional events as local earthquakes, we examined the waveform data from a nearby station of the United States National Seismographic Network (USNSN), less than 120 miles from our study area (red prism, Figure 111). The distance between the USNSN station and hydraulic fracturing site is such that the USNSN station is neither in the immediate vicinity of the study site to be able to record similar observations (related to hydraulic fracturing) as the local geophone array nor extremely

far away to be unable of recording small magnitude non-catalog regional events surrounding the study area. Of 194 non-catalog events, we found temporal correlation with 21 events in the USNSN data that we excluded from our list of observed LPLD events. For the remaining 173 LPLD events that are missing from both regional catalog and nearby station of the USNSN, we stacked the waveform of the vertical component of each station and calculated the spectrogram of the stacked waveform to analyze the dominant frequency content of the signal.

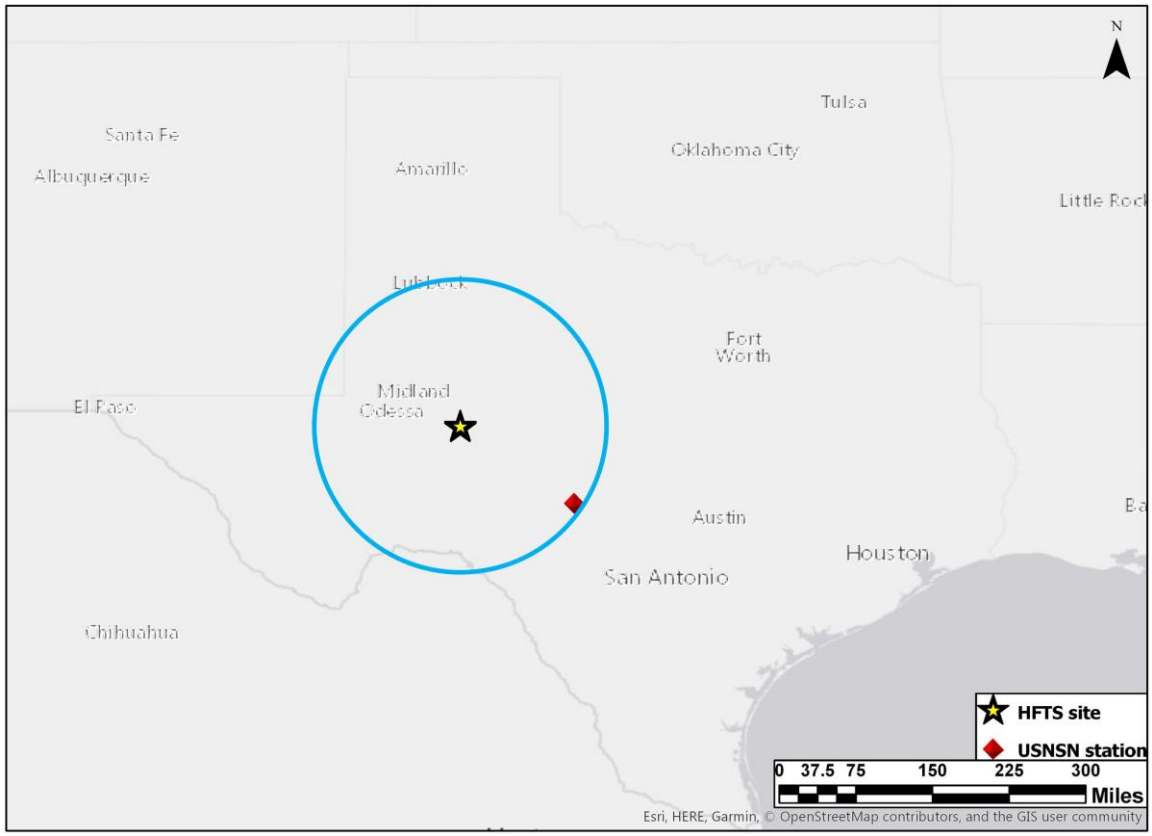


Figure 111: Map showing the location of nearby station from the United States National Seismographic Network (red pyramids) used for waveform comparison with LPLD events recorded at Reagan County site (yellow star). The circle (blue) drawn on the map has a radius of 120 miles.

Results and Discussions

Oil and natural gas combined is a key source of energy, meeting more than half of the world's energy requirements. Recent advances in hydraulic fracturing technology that helped unlocking the domestic source of oil and natural gas has started contributing significantly to the nation's current energy supply and it has opened the door for country's energy independency. However, with the continuous growth in population, the energy requirements are increasing constantly, therefore, it is of utmost importance to optimize the production of oil and natural gas during hydraulic fracturing to meet with the country's growing energy needs. A detail understanding of the response of shale reservoir to hydraulic fracturing is critical from the perspective of improved hydrocarbon production. Additionally, the knowledge of shale response is important for the selection of fluids, rate and volume of injected fluids to maximize the extent of fracturing (Moos et al., 2011). It has been a longstanding assumption that microseismic events are the wholesome representative of deformations that the rock undergoes during hydraulic fracturing. However, recent studies at several hydraulic fracturing

sites have highlighted the significance of non-brittle deformation and ensuing low frequency events that are potentially triggered by increased fluid activity and subsequent pore pressure changes.

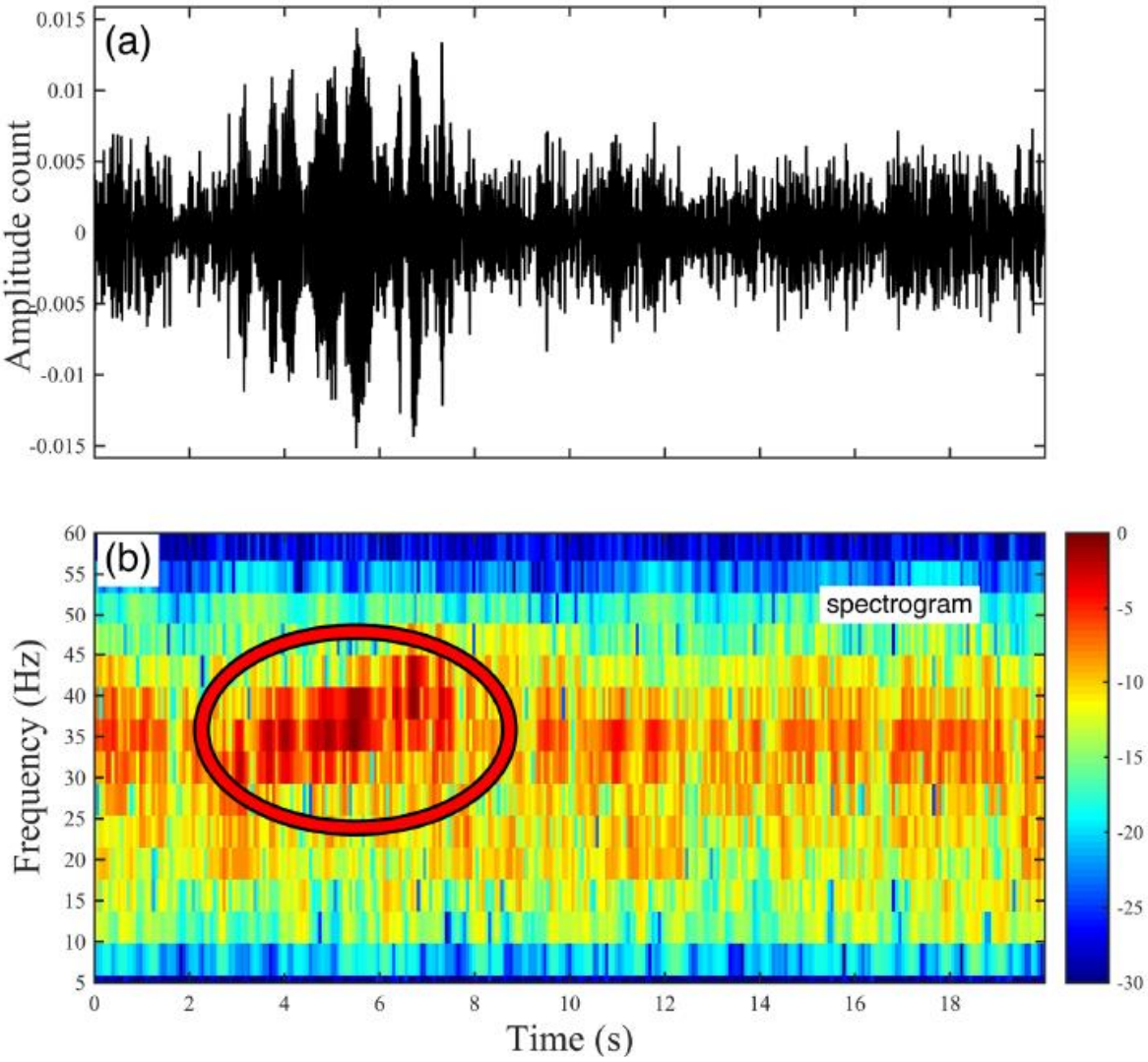


Figure 112: Stacked waveform (panel-a) and spectrogram (panel-b) of a long duration event identified during hydraulic fracturing of one of the toe stages. Color scale shows amplitude in decibel, with warmer colors corresponding to higher amplitude.

We found record of multiple low frequency events of long-time duration during hydraulic fracturing of the two horizontal Middle Wolfcamp wells in the Midland basin portion of Texas. Our detailed analyses of the surface seismic data in three different frequency range of 10-40 Hz, 10-60 Hz, and 10-80 Hz revealed large numbers of low frequency events in the 10-40 Hz frequency range. We inspected the spectrogram of individual low frequency events and found distinct flares of energy in the frequency range of ~10 to 40 Hz, with occasional spikes up to 50 Hz (Figure 112). Comparison of spectrograms of low frequency events recorded in this study with the LPLD events previously reported from the Barnett Shale (Das & Zoback, 2011) and Eagle Ford Shale (Hu et al., 2017) revealed significant similarity in the waveform characteristics with slightly differing frequency content. The minor differences observed in the spectral content of LPLD events could be linked to the difference in geomechanical properties of the rock among various sites, variable treatment strategies (pump schedule, fluid content,

proppant concentration, proppant size) and their local effect on rocks deformation characteristics among other hydraulic fracturing sites.

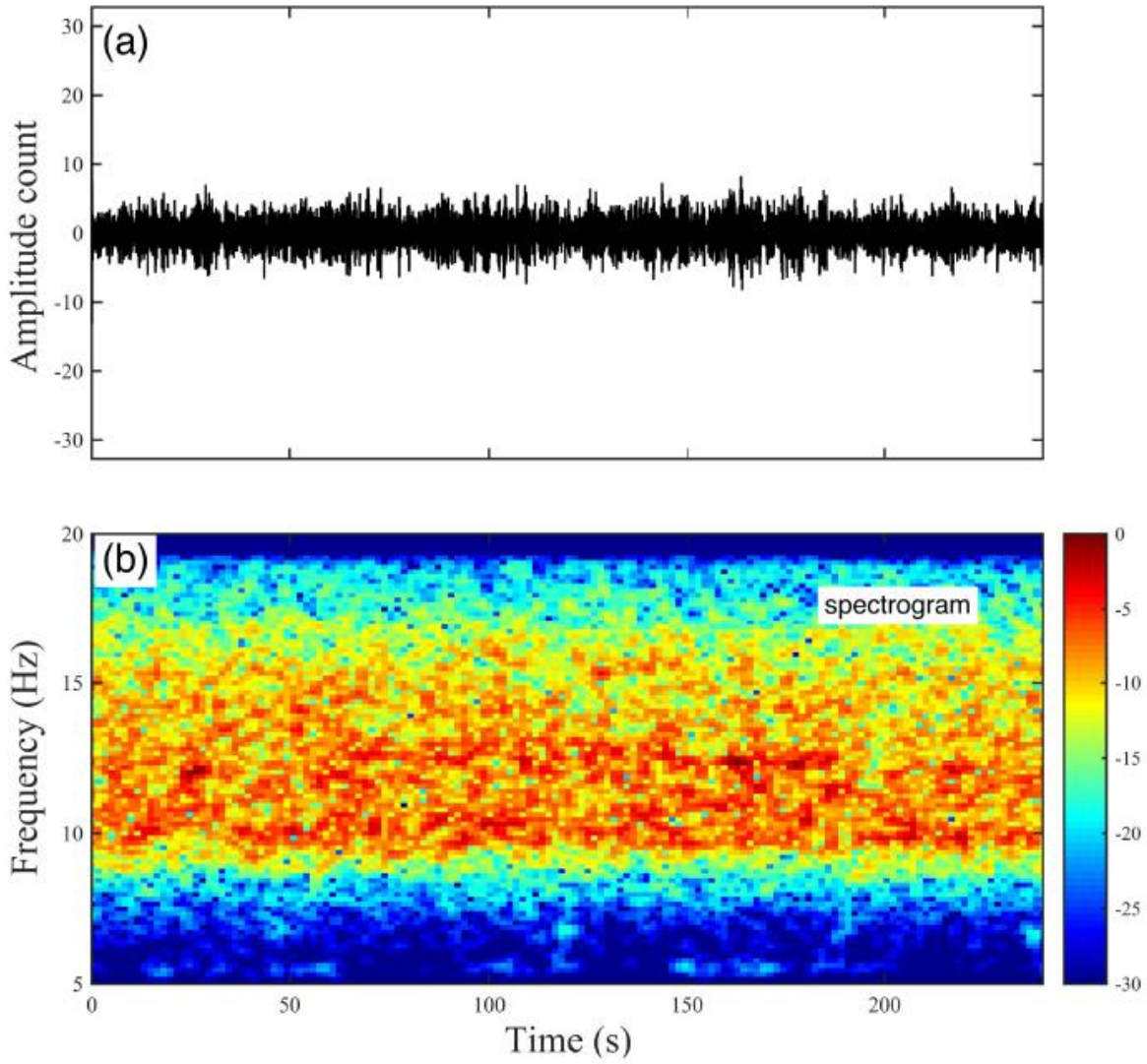


Figure 113: Seismic waveform (panel a) and spectrogram plot (panel b) of United States National Seismographic Network (USNSN) data recorded for similar timeframe as LPLD event observed in the current study and shown in Figure 112.

We thoroughly checked ANSS composite earthquake catalog and data from nearby station of USNSN to avoid any obvious misinterpretation of large regional events listed in the national catalog or small magnitude events missing from the catalog, as LPLD events. From our final list of 173 LPLD events, we selected some high quality LPLD events with high signal to noise ratio and analyzed 4-minute records of USNSN data spanning the arrival times of selected LPLD events. We found no indication of small magnitude events during the relevant time intervals at USNSN station (Figure 113). The waveform and spectrogram of USNSN data does not show any observable change in the amplitude level or frequency content throughout the time window and look like a uniform record of background noise. This agrees with the expectation that if the LPLD events are genetically linked to small-scale rock deformation triggered by hydraulic fracturing then there should be no corresponding record of such local deformation and associated LPLD events at distant (or regional) station. The absence of time-correlative signal from the USNSN data is a key observation and it strongly suggests a local source of

deformation for the causality of LPLD events identified in the current study rather than small magnitude regional earthquakes not listed in the standard catalogs.

The seismograms of observed LPLD events have much larger concentration of seismic energy on the vertical component (left panel, Figure 114). Fundamentally, the recorded energy on the vertical component is proportional to the energy released at the earthquake source in the form P-wave. This dominance of P-wave signal in our observed LPLD events is like seismic tremors recorded in the volcanic region (McNutt et al., 1992) and observed LPLD events in the Eagle Ford Shale in NE Mexico (Hu et Al., 2017). This is particularly different from the seismic characteristics of LPLD events observed in the Barnett Shale that had larger contribution from S-wave energy (Das & Zoback, 2011). Earlier, Aki et al. (1977) proposed a model for the source mechanism of volcanic tremor and magma transport through the volcanic conduit that highlighted the role of jerky opening of fluid filled cracks as the source of seismic tremors.

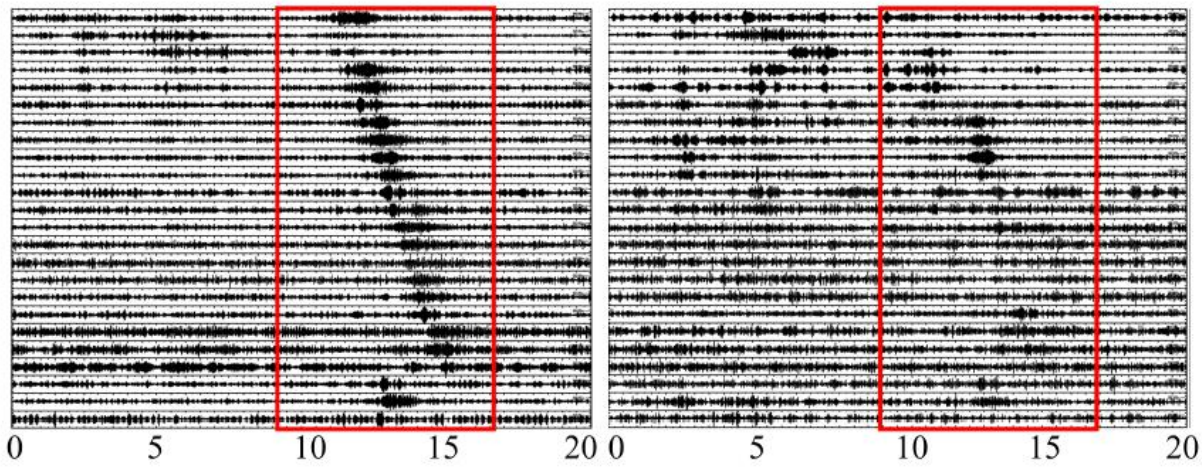


Figure 114: Filtered seismograms of vertical (left panel) and horizontal (right panel) components showing the record of LPLD event. Red rectangle marks the time interval of observed LPLD event.

On a similar note, Hu et al. (2017) suggested both jerky opening and resonance of fluid cracks as the source of observed LPLD events during hydraulic fracturing of the Eagle Ford Shale. We believe that our observed LPLD events and their seismic signals are probably linked to the tensile opening of fluid filled cracks that are triggered by increased fluid activity during fracturing. Hu et al. (2017) used the location of LPLD events to mark the transport of hydraulic fluids with crack propagation. As a continuation of our current study, we envision to determine the location of LPLD events and utilize them to obtain an improved estimate of the spatial extent of tensile fractures that is difficult to determine solely from the high frequency microseismic observation. This improved knowledge about the tensile fractures and associated rock deformation during hydraulic fracturing would be helpful for accurate estimation of stimulated reservoir volume that would further aid into optimizing the production of hydrocarbon from shale reservoir.

Conclusion

We present new evidence on the presence of LPLD events during horizontal drilling of the Middle Wolfcamp Shale wells in Reagan County of Texas. We used surface seismic data collected through a monitoring network of 48, 3-component geophones placed over the footprint of one of the two horizontal wells being stimulated in the study area. LPLD events

identified in this study show a tremor like waveforms with highly emergent phase arrivals dominated by P-wave signal and are like other long duration events previously identified in the Eagle Ford Shale. We noticed a significant concentration of energy in the low frequency band of 10-40 Hz for these long duration events (persist up to 5-10 s). These low frequency events are uniquely recorded by the local geophone array with no temporal overlap from regional earthquakes or data from the nearby seismic network, suggesting that these LPLD events are not the attenuated signal from distant earthquakes. We believe that our observed LPLD events are caused by local deformation in the rock and most likely reflect the tensile opening of fluid filled cracks, triggered by increased fluid activity during hydraulic fracturing.

Interwell Communication Study at HFTS Phase 1

Authors: Tanner Wood, Richard Leonard, Chad Senters, Chris Squires, and Matthew Perry

Abstract

The focus of this paper is to examine the water, oil and proppant communication between wells at the Hydraulic Fracturing Test Site (HFTS) in the Permian Basin. Unique tracers were employed during the stimulation of the HFTS pad in conjunction with many additional diagnostic technologies to evaluate interwell communication, fracture behavior, proppant transport and reservoir drainage.

Water and oil chemical tracers were utilized on four Upper Wolfcamp (UWC) and four Middle Wolfcamp (MWC) horizontal wells on the HFTS pad. Each traced well was divided into three or four uniquely traced segments. The segments consisted of consecutive stage groupings that were stimulated with the same water and oil tracers. During the production phase of the project, oil and water samples from a combined total of 33 horizontal and vertical wells were analyzed for the presence of the tracers from the eight wells. Additionally, proppant tracers were employed in the stimulation of two UWC and one MWC horizontal well. After all the wells were completed, a spectral gamma ray log was run on each well to identify the proppant coverage, cluster efficiency, near-wellbore (NWB) fracture behavior and/or any proppant communication that occurred.

The results of this project provide a better understanding of the fluid and hydrocarbon communication that is taking place between and within the UWC and MWC wells over an initial short-term period as well as the long term. Additionally, the target zone, stimulation design, production methodology and stimulation sequencing are discussed so that comparisons could be made with other diagnostic data from this project.

The insights from this two-year study highlight the continued need to optimize completion designs, even while targeting different benches of the same formation. Additionally, future fracture modeling and design criteria can be enhanced with the hydraulic fracture and propped fracture heights and half-lengths determined from fluid and proppant communication to the offset wells.

Introduction

The hydraulic fracturing test site (HFTS) is in Reagan County, Texas. The site is comprised of multiple wells, both vertical and horizontal, in the Wolfcamp formation and is operated by Laredo Petroleum. The Wolfcamp formation is a hydrocarbon-producing zone in the Permian Basin (Figure 115). Located in West Texas and extending into the southeast portion of New Mexico, it is primarily a basinal structure. Covering the Midland, Delaware and Central Platform sub-basins (Scotia Howard Weil, 2014; Schwartz et al., 2015), it varies in thickness depending on location, with some areas exceeding 2,000 ft.

The HFTS focused on understanding the hydraulic fracturing process, in particular fracture propagation and well spacing and how these processes vary with changes in lithology (Upper vs Middle Wolfcamp) and completion design. This paper highlights the inter-well communication observed between the 11 newly completed horizontal wells and 22 existing vertical and horizontal wells in the UWC and MWC through the evaluation of proppant, frac

fluid and hydrocarbon tracers. In addition, the conclusions of this paper will highlight the completion effectiveness across three of the newly completed horizontals, as well as an evaluation of frac fluid and hydrocarbon recovery trends across the section. Figure 116 below highlights the wellbore positioning of the 11 newly completed horizontal wells and the drilled but not completed traverse well (6TW). The traverse well was intended to be drilled as near as possible to both the 6U and 6M wells, with the goal of intersecting the created fracture networks in both formations.

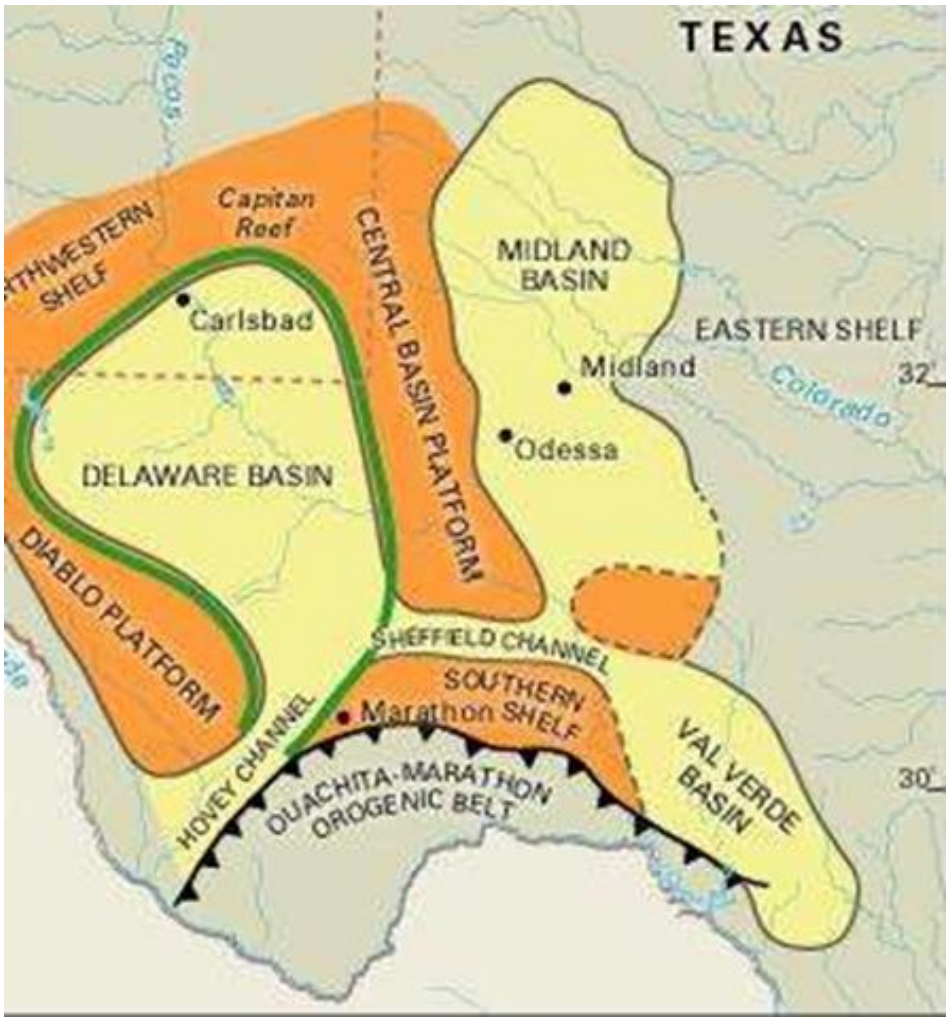


Figure 115: Permian Basin (source: Encyclopedia Britannica).

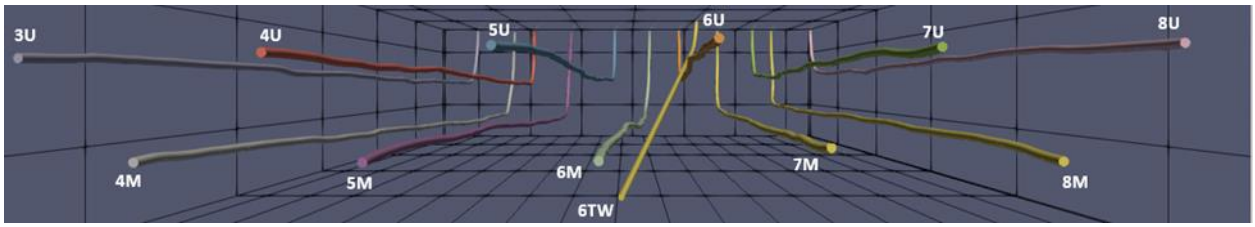


Figure 116: Wellbore positioning and spacing of the 12 newly drilled wells in the HFTS.

Methods

To evaluate near-wellbore completion effectiveness and any potential interwell proppant communication, proppant tracers were utilized in only three of the 11 newly drilled horizontal wells. Proppant tracing utilizes three distinct low-level gamma-emitting sources: Iridium-192 (red), Scandium-46 (yellow), Antimony-124 (blue). They are pumped primarily throughout the proppant-laden portion of the stimulation treatment (Fisher et al., 1995; Reis et al., 1996). A

spectral gamma-ray log was run to identify near-wellbore proppant placement of each individual tracer. This diagnostic technology was utilized to evaluate unstimulated perf clusters, proppant coverage across the lateral, as well as cluster and stage spacing. In addition, spectral gamma-ray logging of untraced offset wells was used to identify proppant communication and transport between wells (Warren et al., 2016).

The 4U, 6U and 6M wells were selected to be proppant traced. All stages were traced in each of the wells with a single isotope unique to that well: 4U – Antimony (blue), 6U – Iridium (red), 6M – Scandium (yellow) (Figure 117). Selecting these wells was primarily based on their proximity to the traverse well and allowed for a comparison of the same frac design in a UWC and MWC. Additionally, it provided a comparison of a 3-cluster 90' spacing design to that of a higher density 50' cluster spacing design within the same UWC bench. Immediately following the completion/drill-out of the 11 horizontal wells and the drilling of the traverse well, each of the wells was logged with a spectral gamma-ray tool to determine near-wellbore proppant placement.

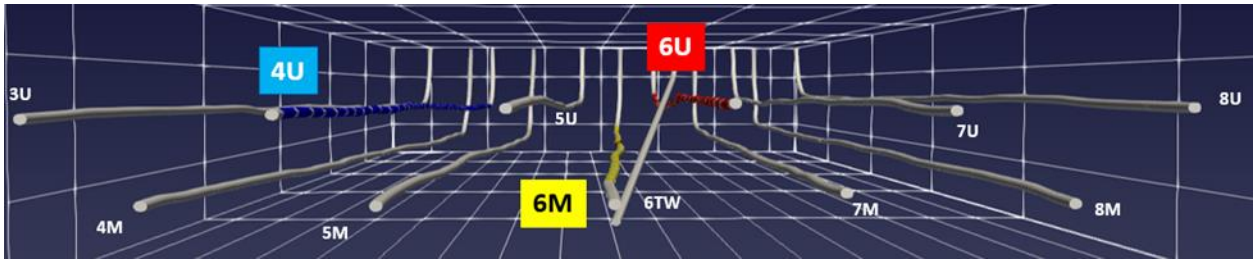


Figure 117: Proppant traced wells highlighted with corresponding tracer color utilized.

In addition to proppant tracing and spectral gamma ray logging, 8 of the 11 new horizontal wells utilized both frac fluid and hydrocarbon chemical tracers (Figure 118). Frac fluid tracers are injected during the pad and proppant-laden fluid at a set concentration. The frac fluid tracers are chemical compounds designed to remain in the frac fluid as it is produced to surface. Water samples are then collected at surface and analyzed with gas chromatography/mass spectrometry techniques to determine the concentrations of frac fluid tracer in the water. Untraced offset wells are sampled for the presence of the frac fluid tracers injected in a traced offset well for interwell frac fluid communication analysis (Asadi et al., 2008; King et al., 2011; Leonard et al., 2007).

Liquid oil tracers are injected as a slug in the early portion of the proppant-laden fluid during the hydraulic fracture treatment. Like the frac fluid tracers, unique oil tracers are utilized across multiple segments of the lateral. As oil is produced at surface, samples are collected and analyzed in a similar fashion to the frac fluid tracers. These diagnostics are used to evaluate oil production along the lateral as well as interwell oil communication (Warren).

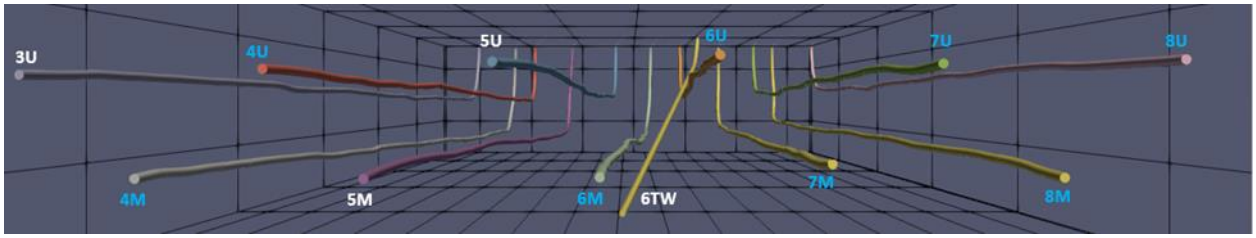


Figure 118: 3U, 5M, 5U and 6TW wells labeled in white were not traced.

The 3M, 5M and 5U were selected as the only wells to not be traced. The rest of the wells were either divided into thirds or fourths with each segment of the lateral receiving its own unique frac fluid and oil tracer as displayed in Figure 119 below. Fluid sampling data in this paper cover a two-year timespan, December 2015 thru December 2017.

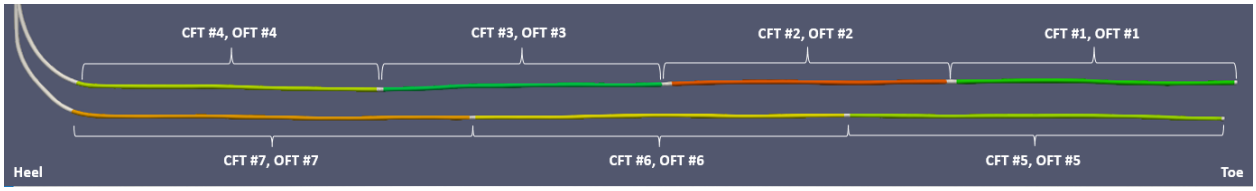


Figure 119: Break down of oil (OFT) and frac fluid (CFT) tracer injection intervals for 3 and 4 segment wells.

Results

Analysis of the spectral gamma-ray logging on the three proppant-traced wells showed an overall high degree (>80%) of cluster efficiency across all three wells and relatively low near-wellbore coverage. Near-wellbore coverage is calculated by creating a ratio of the total lateral length where proppant tracer counts were detected to the total lateral length. The 6U well, completed with 270' stages utilizing three clusters per stage and a proppant concentration of 1,100 lb per lateral ft, exhibited a cluster efficiency of 91% and a near-wellbore coverage of 63%. An example stage is shown in Figure 120. This stage exhibits a relatively even distribution of tracer counts amongst the three perf clusters with minimal inter-cluster growth and gaps with no near-wellbore tracer counts. The 6M well, located in the MWC bench, was completed with the same design and showed similar results to that of the 6U. Overall cluster efficiency was 90% and total near-wellbore coverage was 73%, highlighting a slight improvement in inter-cluster growth and overall near-wellbore proppant placement. Figure 121 shows an example stage from the 6M well. The 4U well utilized a slightly larger design than the 6U/6M wells of 1,800 lb per lateral foot. In addition to the larger proppant volume, two different perforating schemes were tested in this well. The toe and heel portions of the lateral utilized 5 clusters at 50' spacing and the middle portion of the well utilized 3 clusters at 50' spacing. The resulting spectral gamma-ray log showed no loss in cluster efficiency (92%) compared to the 6U and 6M wells and an improvement in near-wellbore coverage to 86%. Figure 122, Figure 123 below highlight both a five cluster and three cluster stage in the 4U well.

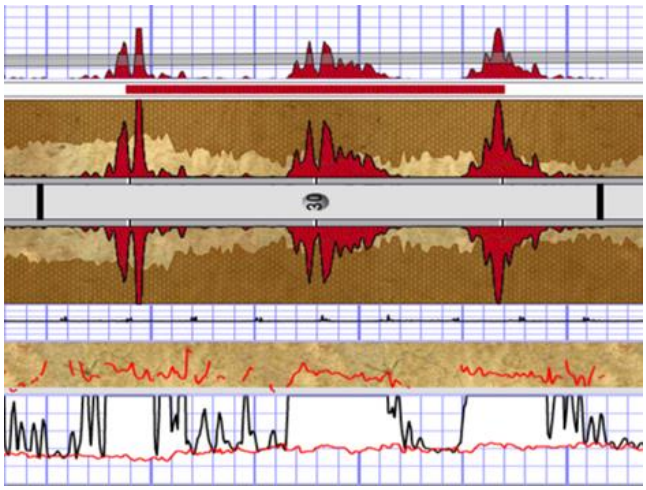


Figure 120: 6U well, stage 30.

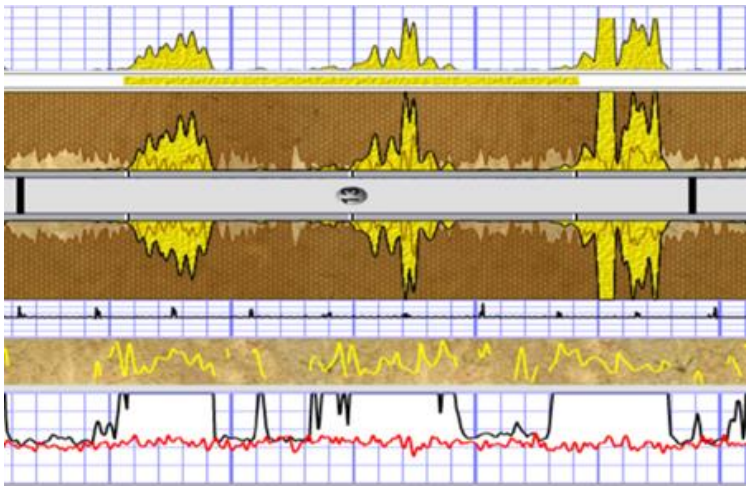


Figure 121: 6M well, stage 13.

Analysis of the offset horizontal well logs showed that five of the nine offset wells detected proppant communication from at least one of the traced wells. The 7U, 7M, 8U and 6TW wells did not reveal any proppant tracer communication. A comparison of the total tracer counts in all the offset wells reveals that the 5U had the highest tracer counts. All three proppant traced wells communicated with four offset wells. In addition, proppant tracer from the 6M well showed the highest counts in the offset wells. No proppant tracers were detected during the drilling or logging of the 6TW well.

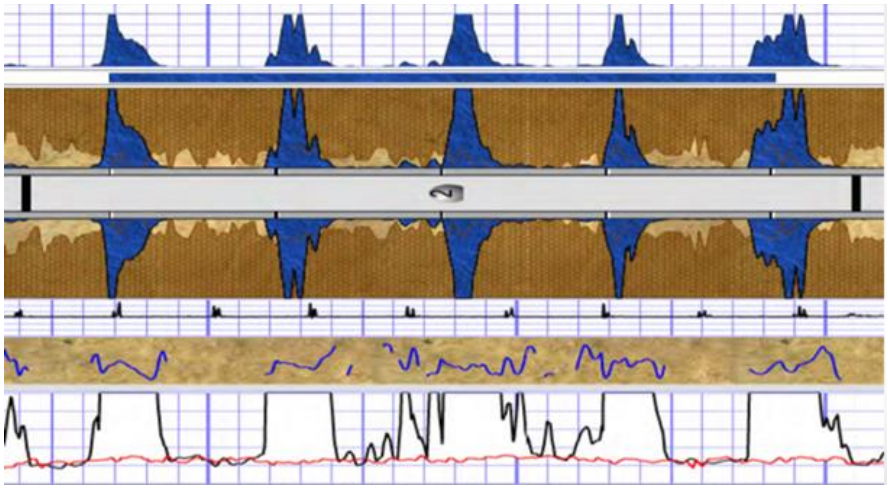


Figure 122: 4U well, stage 2 – 5 cluster design.

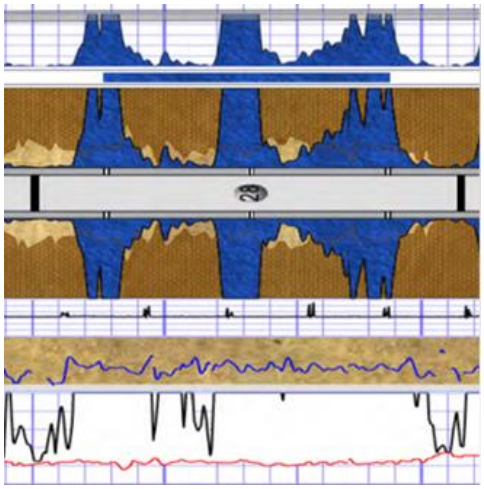


Figure 123: 4U well stage 28 – 3 cluster design.

Results from two years of flowback sampling indicate a high degree of both oil and water tracer communication amongst all the newly completed horizontal wells in the HFTS and 17 of the 21 earlier completed horizontal and vertical wells. Initial results from flowback sampling show that all traced wells sustained hydraulic communication with at least one offset horizontal well. A comparison of treatment well frac fluid recoveries to offset well recoveries revealed that the MWC wells had a significantly higher degree of lateral and vertical hydraulic communication than the UWC wells. Analysis of the frac fluid communication shows a noticeable contrast in the magnitude, duration and total number of communicating segments between the UWC and MWC wells. The MWC wells have a higher degree of communication amongst wells in the same horizon. The UWC wells exhibit less communication amongst wells in the same horizon. The MWC wells indicate more vertical communication up to UWC wells than the reverse. These trends have continued through two years of sampling with all traced wells indicating hydraulic communication with at least one offset well.

			Sampled Wells																	
		Units	Norm. ppb															Norm. ppb	%	
	Segment	Tracer	#1U	#2M	#3U	#4M	#4U	#5M	#5U	#6M	#6U	#6TW	#7M	#7U	#8M	#8U	#1RM	#1RU	Tracer Total Communication	% Frac Fluid Recovered in Offsets	% Frac Fluid Recovered from Treatment Well
Traced Well																					
#4M	1	CFT A	3.9	4.1	4.9	11.2	3.2	2.1	0.9	1.5	0.4	0.0	0.7	0.1	0.2	0.0	0.0	0.0	22.0	65%	34%
	2	CFT B	7.4	13.5	3.8	8.8	2.2	2.6	0.9	2.3	0.4	0.0	1.4	0.2	0.5	0.0	0.1	0.0	41.9	83%	17%
	3	CFT C	6.6	4.5	4.8	9.9	3.5	2.8	1.5	2.0	0.6	0.0	1.2	0.1	0.4	0.0	0.1	0.0	28.3	74%	26%
#4U	1	CFT D	0.1	0.0	0.4	0.0	2.4	0.0	0.2	0.0	0.0	0.0	0.0	0.0	0.0	0.0	0.0	0.0	0.7	24%	76%
	2	CFT E	0.8	0.1	1.1	0.1	4.6	0.0	0.7	0.1	0.1	0.0	0.0	0.0	0.0	0.0	0.0	0.0	2.9	38%	62%
	3	CFT F	0.2	0.9	0.9	0.2	4.0	0.1	0.5	0.1	0.0	0.0	0.0	0.0	0.0	0.0	0.0	0.0	3.0	43%	57%
#6M	1	CFT G	0.4	3.1	0.2	2.4	0.4	2.4	2.7	4.1	3.2	0.0	3.8	1.0	3.2	1.0	0.1	0.0	23.8	85%	15%
	2	CFT H	0.0	1.0	0.0	0.8	0.0	1.2	1.1	3.5	1.9	0.0	1.8	0.2	1.2	0.0	1.4	0.0	10.7	75%	25%
	3	CFT I	0.1	2.8	0.0	0.7	0.0	1.1	0.8	2.0	1.0	0.0	1.2	0.1	0.8	0.0	1.1	0.1	10.0	83%	17%
	4	CFT J	0.0	0.0	0.0	0.0	0.0	0.1	0.6	1.5	0.3	0.0	0.4	0.0	0.1	0.0	0.0	0.0	1.5	49%	51%
#6U	1	CFT K	0.0	0.3	0.0	0.0	0.0	0.0	0.5	0.2	3.5	0.0	0.2	1.8	0.0	0.0	0.0	0.0	3.0	47%	53%
	2	CFT L	0.0	0.0	0.0	0.0	0.0	0.0	0.2	0.0	2.5	0.0	0.0	0.0	0.0	0.0	0.0	0.0	0.3	11%	89%
	3	CFT M	0.0	0.0	0.0	0.0	0.0	0.0	0.5	0.2	2.1	0.0	0.1	0.2	0.0	0.0	0.0	0.0	1.0	33%	67%
	4	CFT N	0.0	0.0	0.0	0.0	0.0	0.0	0.0	0.0	1.7	0.0	0.0	0.0	0.0	0.0	0.0	0.0	0.0	1%	99%
#7M	1	CFT O	0.0	0.0	0.0	0.0	0.0	0.0	0.1	2.1	2.1	0.0	4.4	2.4	3.4	0.8	0.0	0.0	10.9	71%	29%
	2	CFT P	0.0	0.0	0.0	0.1	0.0	0.4	0.6	2.7	4.5	0.0	4.7	3.4	4.5	1.7	1.4	0.4	19.8	81%	19%
	3	CFT Q	0.0	0.0	0.0	0.0	0.0	0.3	0.5	4.8	3.4	0.0	7.5	2.7	8.1	0.4	1.2	0.1	21.6	74%	26%
	4	CFT R	0.0	0.0	0.0	0.0	0.0	0.0	0.0	0.7	0.8	0.0	2.3	0.7	1.6	0.0	0.0	0.0	3.8	63%	37%
#7U	1	CFT S	0.0	0.0	0.0	0.0	0.0	0.0	0.0	0.0	0.0	0.0	0.0	1.2	0.0	0.1	0.0	0.0	0.1	5%	95%
	2	CFT T	0.0	0.0	0.0	0.0	0.0	0.0	0.0	0.0	0.3	0.0	0.0	1.6	0.1	0.7	0.0	0.0	1.1	40%	60%
	3	CFT U	0.0	0.0	0.0	0.0	0.0	0.0	0.0	0.0	0.0	0.0	0.0	1.4	0.0	0.3	0.0	0.0	0.3	18%	82%
	4	CFT V	0.0	0.0	0.0	0.0	0.0	0.0	0.0	0.0	0.0	0.0	0.0	1.3	0.0	0.6	0.0	0.0	0.6	31%	69%
#8M	1	CFT W	0.6	1.7	0.1	0.1	0.2	0.0	0.0	0.9	0.9	0.0	2.0	2.6	6.3	3.6	0.7	0.1	13.5	68%	32%
	2	CFT X	0.6	3.3	0.0	0.4	0.0	0.7	0.2	1.6	0.8	0.0	1.9	1.7	3.9	2.3	4.5	1.0	18.9	83%	17%
	3	CFT Y	0.3	2.1	0.0	0.0	0.0	0.2	0.4	2.3	1.4	0.0	3.4	4.5	6.5	3.4	4.3	3.6	25.8	80%	20%
#8U	1	CFT Z	0.0	0.0	0.0	0.0	0.0	0.0	0.0	0.0	0.0	0.0	0.0	0.5	0.1	4.3	0.0	0.1	0.7	14%	86%
	2	CFT AA	0.0	0.0	0.0	0.0	0.0	0.0	0.0	0.0	0.0	0.0	0.0	0.0	0.0	2.1	0.1	0.7	0.9	29%	71%
	3	CFT BB	2.5	0.1	0.0	0.0	0.0	0.0	0.0	0.0	0.0	0.0	0.0	1.0	0.2	2.9	0.4	3.4	7.6	72%	28%
	# Samples Taken From Well		44	44	45	47	48	51	41	54	51	0	58	49	50	54	46	49			
	Sample Dates	12/24/15 - 10/12/17																			
			Communication Tiers: Significant / Moderate / Minimal																		

Figure 124: Frac fluid communication matrix for the HFTS horizontal wells.

Figure 124 summarizes the normalized time-weighted average tracer recoveries for both treatment and offset wells through the entire two years of sampling. The traced wells are listed vertically down the left column and the sampled wells are listed horizontally across the top. The time-weighted average of the treatment well recoveries are highlighted in gray cells within the matrix. Offset communication from these wells is shown in the cells on each side of the treatment well recovery. The offset well recoveries are shaded based on the extent of communication from the treatment well to the offset wells. The categories of communication within the matrix include significant, moderate and minimal communication. Significant communication for this project occurs when offset well recoveries exceed 50% of the treatment well recovery. Moderate communication is from 10%-49%, and minimal communication is when the offset recoveries show less than 10% of the treatment wells' recoveries over the same time period. The two columns on the right side of the chart indicate the percentage of tracer returns detected in the traced and offset wells. A distinct contrast is noticed between the UWC and MWC wells based on this metric. As mentioned earlier, all frac fluid traced segments of the MWC wells exhibit greater total frac fluid tracer recoveries in offset wells. Whereas only one traced segment on an UWC well shows a similar trend. The 6TW well was never completed or

produced, thus no fluid samples were collected from the well. Analysis of rehydrated mud from the coring of the 6TW well indicates the presence of frac fluid tracers from the 6U well.

Looking closer at the individual wells, the 6M well demonstrates the highest magnitude of communication both in terms of concentration of frac fluid tracers detected in offsets as well as the frequency of communication with offset wells. This well utilized the smaller proppant loading and wider cluster spacing. Conversely the 7U well shows the least amount of frac fluid communication to offsets wells. The 4U well received the least amount of communication of all the horizontal wells and the 6U well the most. In a similar trend to the other UWC wells, most of the offset communication to the 6U was from the nearest offsetting MWC wells staggered below. The 4U and 4M wells are the only two wells to utilize the larger 1,800 lb per lateral ft design, and there are no significant increases in hydraulic communication when compared to other horizontal wells utilizing the smaller proppant volume.

Oil tracer communication highlights similar trends to that of the frac fluid tracers. However, the overall oil tracer recovery in offset wells was significantly less both in terms of magnitude and duration. Initial oil sampling indicates that all newly completed horizontal wells had oil communication with at least one offset well. Through 11 months, only eight of the 16 horizontal wells are exhibiting communication, with no significant communication as defined above. Figure 125 shows the normalized time-weighted average of hydrocarbon tracer recoveries in both treatment and offset horizontal wells over the two years of sampling. In a fashion like the frac fluid tracers, there is a strong trend between the magnitude and extent of communication based on the bench of the well. The MWC wells showed more communication both laterally as well as vertically when compared to UWC wells. On an individual well basis, results indicate that the 4M well has the most oil communication with offset wells. Conversely the 6U well shows the least amount of oil tracer recovery in offset wells. These results are more consistent with the frac size variations, with the 4M utilizing the largest design and the 6U the smallest.

				Sampled Wells																		
			Units	Norm. ppb																Norm. ppb	%	
		Segment	Tracer	#1U	#2M	#3U	#4M	#4U	#5M	#5U	#6M	#6U	#6TW	#7M	#7U	#8M	#8U	#1RM	#1RU	Tracer Total Communication	% OFT Recovered in Offsets	% OFT Recovered from Treatment Well
Traced Well	#4M	1	OFT A	0.6	1.2	0.7	33.6	0.9	3.4	7.7	0.0	0.1	0.0	0.0	0.5	0.5	0.0	0.0	0.0	15.7	32%	68%
		2	OFT B	0.0	1.2	0.0	43.0	0.4	4.5	0.0	214.1	0.0	0.0	0.5	0.0	0.0	0.0	0.0	0.0	220.7	84%	16%
		3	OFT C	0.0	0.0	0.0	35.3	0.5	7.6	0.0	0.0	0.0	0.0	0.0	0.0	0.6	0.0	0.0	0.0	8.7	20%	80%
	#4U	1	OFT D	0.0	0.0	0.4	1.4	34.9	0.0	0.0	0.0	0.0	0.0	0.0	0.0	0.0	0.0	0.0	0.0	1.9	5%	95%
		2	OFT E	0.0	0.0	0.6	1.0	24.5	0.0	0.0	0.0	0.0	0.0	0.0	0.0	0.0	0.0	0.0	0.0	1.6	6%	94%
		3	OFT F	0.0	0.0	0.0	1.3	33.3	0.0	0.0	0.0	0.0	0.0	0.0	0.0	0.0	0.0	0.0	0.0	1.3	4%	96%
	#6M	1	OFT G	0.0	0.0	0.1	0.0	0.0	0.3	0.3	43.4	0.8	0.0	2.5	0.0	0.3	0.0	0.0	0.0	4.3	9%	91%
		2	OFT H	0.0	0.0	0.1	0.0	0.0	0.3	0.0	56.0	0.4	0.0	3.4	0.0	0.5	0.0	0.0	0.0	4.7	8%	92%
		3	OFT I	0.0	0.0	0.1	0.0	0.0	0.1	0.0	37.2	0.0	0.0	2.8	0.0	0.3	0.0	0.0	0.0	3.2	8%	92%
		4	OFT J	0.0	0.0	0.0	0.0	0.0	0.1	0.0	19.5	0.0	0.0	1.3	0.0	0.3	0.0	0.0	0.0	1.8	8%	92%
	#6U	1	OFT K	0.0	0.0	0.0	0.0	0.0	0.0	0.0	0.0	14.2	0.0	0.1	0.0	0.0	0.0	0.0	0.0	0.1	1%	99%
		2	OFT L	0.0	0.0	0.0	0.0	0.0	0.0	0.0	0.0	10.0	0.0	0.0	0.0	0.0	0.0	0.0	0.0	0.0	0%	100%
		3	OFT M	0.0	0.0	0.0	0.0	0.0	0.8	0.0	0.5	24.9	0.0	0.0	0.0	0.0	0.0	0.0	0.0	1.3	5%	95%
		4	OFT N	0.0	0.0	0.0	0.0	0.0	0.0	0.0	0.6	19.4	0.0	0.0	0.0	0.1	0.0	0.0	0.0	0.8	4%	96%
	#7M	1	OFT O	0.0	0.0	0.0	0.0	0.0	0.0	0.0	2.9	0.2	0.0	42.6	0.1	1.2	0.1	0.0	0.0	4.5	9%	91%
		2	OFT P	0.0	0.0	0.0	0.0	0.0	0.0	0.0	0.5	0.0	0.0	52.7	0.1	1.1	0.7	0.0	0.0	2.4	4%	96%
		3	OFT Q	0.0	0.0	0.1	0.0	0.0	0.1	0.0	0.0	0.0	0.0	46.6	0.1	1.6	0.0	0.0	0.0	1.8	4%	96%
		4	OFT R	0.6	0.0	0.2	0.0	0.0	0.3	0.0	0.1	0.4	0.0	72.8	0.5	2.8	1.2	1.6	0.0	7.7	10%	90%
	#7U	1	OFT S	0.0	0.0	0.0	0.0	0.0	0.0	0.0	0.0	0.0	0.0	0.0	27.5	0.0	0.9	0.1	0.0	1.0	4%	96%
		2	OFT T	3.9	8.2	3.1	0.0	4.3	2.5	0.0	0.0	4.0	0.0	0.0	20.2	2.2	3.1	0.0	0.0	31.4	61%	39%
		3	OFT U	0.0	0.0	0.0	0.0	0.0	0.0	0.0	0.0	0.2	0.0	0.0	18.9	0.0	0.0	0.0	0.0	0.2	1%	99%
		4	OFT V	0.0	0.1	0.0	0.0	0.0	0.0	0.0	0.0	0.0	0.0	0.0	7.2	0.0	0.2	0.0	0.0	0.2	3%	97%
	#8M	1	OFT W	0.0	0.0	2.2	0.0	0.0	0.0	0.0	0.0	0.0	0.0	2.8	0.0	38.2	0.3	0.0	0.0	5.3	12%	88%
		2	OFT X	0.0	0.6	0.0	0.0	0.0	0.0	0.0	0.0	0.0	0.0	4.7	0.1	48.6	0.1	0.4	0.0	5.9	11%	89%
		3	OFT Y	0.0	0.0	0.0	0.0	0.0	0.0	0.0	0.0	0.1	0.0	1.8	0.0	20.9	0.0	3.2	1.5	6.6	24%	76%
	#8U	1	OFT Z	0.0	0.0	0.0	0.0	0.0	0.0	0.0	0.0	0.0	0.0	0.0	0.9	0.0	32.8	0.9	0.9	2.6	7%	93%
		2	OFT AA	0.0	0.0	0.0	0.0	0.0	0.0	0.0	0.1	0.0	0.0	0.0	0.0	0.0	14.9	1.0	0.9	2.0	12%	88%
		3	OFT BB	0.7	0.0	0.9	0.0	0.0	0.0	7.2	0.0	0.0	0.0	0.3	4.1	0.6	37.0	1.8	6.1	21.7	37%	63%
	# Samples Taken From Well			28	33	42	46	47	51	9	51	50	0	52	50	50	52	49	52			
	Sample Dates		12/26/15 - 10/12/17																			
																				Communication Tiers	Significant	Moderate	Minimal

Figure 125: Oil communication matrix for the HFTS horizontal wells.

Discussion

A comparison of interwell communication between the three tracer types shows that frac fluid communication across the section is far more prevalent than for both the proppant and oil tracers. Oil tracer communication is more prevalent than proppant communication, however, all three diagnostics exhibit the same general trend in interwell communication. The MWC is responsible for the most communication overall. In addition, attributing differences in interwell communication to any one factor is difficult due to the total number of variables involved in the completion process (frac design variations, well location within the section, completion order, etc.).

Also, included in this study but not highlighted in this paper are two previously completed horizontal wells in the UWC and MWC benches. More information on these wells can be found in Courtier et al. (2016). These wells were refractured for fracture hit protection refracs prior to the completion of the HFTS horizontal wells. Both refractured wells did receive oil and frac fluid tracer communication, but most of the communication was limited to the immediate offset wells, the 8SU and 8SM. Analysis of the direction and magnitude of the communication from the 8U and 8M wells indicates that their frac fluid shows a higher degree of communication to the refractured wells than to the newly fractured 7U/M wells that were offset in the opposite direction. This trend was like the oil tracer results for the 8U well, however, the 8M well showed a higher degree of oil communication back to the newly fractured 7M well.

Conclusions and Recommendations

- Proppant tracer results indicate a high degree of cluster efficiency can be obtained through the three-cluster 90’ spacing design, however, it left behind a larger percentage of unstimulated rock.
- Stimulated rock coverage increased through a higher density, five-cluster, 50’ spacing perf scheme without sacrificing perf cluster efficiency.
- Proppant tracers show similar near-wellbore proppant placement when applying the same completion strategy to both the Upper and Middle Wolfcamp benches.
- Proppant, frac fluid and oil tracers all exhibited interwell communication.
- Interwell communication within MWC wells is significantly higher than communication within UWC wells.
- Vertical communication is greater from MWC wells to the UWC wells.
- Communication results were consistent for all three tracer types.
- The frac fluid communication observed, while stronger in magnitude early, continued through two years of flowback sampling.
- Most of the oil communication observed through hydrocarbon tracers disappeared by the end of the first year of sampling.
- Communication was significantly different for the Upper and Middle benches even though the completion designs were the same.
- A need exists to further optimize completion designs and/or well spacing by not only formation, but also by each bench within the formation.

Proppant Transport at HFTS 1 Phase 1 site

Authors: Debotyam Maity, and Jordan Ciezobka

Summary

We collected more than 500ft of through fracture core in the upper and middle Wolfcamp formations in the Permian Basin. As part of core characterization, we analyzed the core sludge samples for presence of proppant and natural calcite particles. Apart from sample preparation and imaging, we designed and developed a novel image processing workflow to detect and classify the particles. We used the observations from the identified particle distribution within the stimulated rock volume to understand proppant transport behavior. We used relative distributions of smaller 100 mesh and larger 40/70 mesh proppant particles to interpret proppant placement in relation to perforation clusters. Finally, we used the relative distribution of particles to understand the interaction between natural and hydraulic fractures. We observe that stress variations and the degree of natural fracturing has a bearing on local proppant screen-out behavior. Smaller 100 mesh proppant seems to dominate at larger lateral offsets from the hydraulically fractured wells. We also observe indications of heel side bias based on lateral proppant distribution. We share our workflow for particle detection and classification, which can serve as a template for proppant analysis in future if significant through fracture cores are collected in similar field experiments.

Introduction

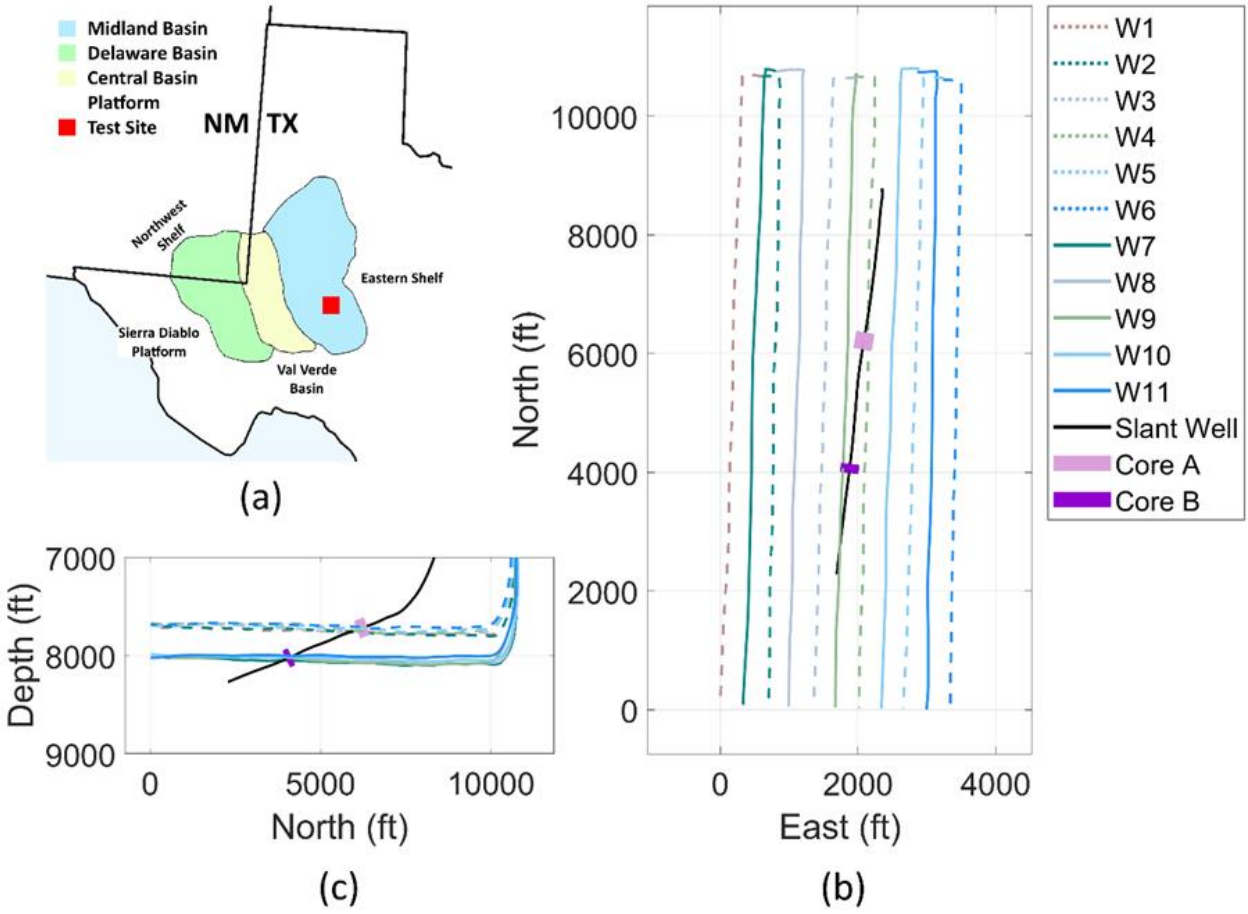


Figure 126: Location of test site along with the Schematic view of the UWC (dotted curves) and MWC (solid curves) wells at HFTS; (a) test site location, (b) map view, (c) section view.

Table 6: Description of cores, depths and sample numbers from HFTS slant core well. Depths reported are the measured depths along the well.

Core	Layer	Starting Depth (ft)	Final Depth (ft)	Number of Samples
1	Upper Wolfcamp	9276	9365	32
2	Upper Wolfcamp	9366	9478	41
3	Upper Wolfcamp	9482	9588	39
4	Upper Wolfcamp	9590	9716	46
5	Middle Wolfcamp	11525	11559	12
6	Middle Wolfcamp	11600	11684	43

Permian Basin Province is a major unconventional shale play spread over the western part of Texas and southeastern part of New Mexico. The two major lobes of the basin, namely the Delaware and the Midland basins, are separated by a tectonically uplifted basement rock known as the Central Basin Platform. Basin stratigraphy consists of thick Permian and Pennsylvanian sections with siliceous mudrocks interbedded with carbonate packstone/ wackestone and calcareous mudrocks (Hamlin & Baumgardner, 2012). The Wolfcamp formation is generally subdivided into four separate reservoir zones, which are defined by slightly differing lithology. These also guide the landing points for various horizontal wells that are drilled in the basin. The Hydraulic Fracturing Test Site (HFTS) is in the eastern part of Midland Basin, between Central Basin Platform and the Eastern Shelf. The test wells for this study are in Reagan County, Texas. It involves an 11 well, multi pad hydraulic fracturing project in two of the Wolfcamp reservoir zones (Perry et al., 2017; Ciezobka et al., 2018). The project team collected and analyzed significant data at this site including micro–Diagnostic Formation Injection Tests, advanced open-hole logs, 110 side wall cores, complete core analysis including petrophysics, geomechanical analysis and petrography imaging, chemical tracers, microseismic surveys, tilt-meter surveys, bottom-hole pressure data, multiple pre- and post-treatment cross-well seismic surveys, etc. (Courtier et al., 2017). We collected and studied more than 500ft of through fracture cores from both the upper Wolfcamp (UWC) and the middle Wolfcamp zones (MWC) as highlighted in Table 6. In Figure 126, we show the relative locations of the 11 horizontal wellbore laterals as well as the slant core well. The individual core barrels contain sludge material from drilling, coring and core handling operations. In this study, the aim is to analyze these core sludge samples carefully to detect and quantify the presence of proppant and natural calcite or other naturally occurring mineral particles from the subsurface rocks. The basic premise behind the study is the idea that some of the proppant particles present within the hydraulic fractures in the core will extrude out from the fractures and into the core barrel upon depressurization and general core handling. The same also holds true for any cemented natural fracture provided the fracture breaks to release some of the calcite and other mineral particles. Finally, hydraulic fractures, where present, can also hold naturally occurring mineral cements, which are transported by the fracturing fluid as it interacts with natural fractures during fracture propagation and growth.

In total, we collected and cataloged two hundred and thirteen core sludge samples by scraping material from the interior of the core barrel sleeves and the exterior of the cores. Table 6 shows the distribution of these samples across the UWC and MWC formations. We note that the UWC

cored interval comprised of one hundred and fifty-eight core sludge samples spread over approximately 440 ft. On the other hand, the MWC cored interval is much shorter with fifty-five core sludge samples spread over approximately 159 ft. We also note that barring a few exceptions such as core end members, each core sample is from a 3 ft core tube. However, the actual sludge samples varied significantly in volume, weight and consistency. The largest sample weighed 587 gm and the smallest sample weighed 7.5 gm. Using microscopic observations, we found significant material including drilling mud, shale particles, aluminum shavings (from the process of cutting of the core barrels to retrieve the cores), natural calcite and various other mineral particles in smaller quantities within these samples.

Sample Preparation

Depending on the consistency and size of the sample, we add one to four tablespoons of concentrated liquid or powdered detergent to each sample jar along with a small volume of water. The sample jar is vigorously agitated, and then set to soak for 4 to 24 hours. We re-agitate the sample and pour the material over a stainless steel 200 mesh USA standard 8" diameter sieve. In the sieve, we again agitate the sludge in a warm water bath using a soft bristle paintbrush. If needed, we add more detergent to emulsify and remove the oil. We continue this process until the water flow through the sieve is clear and the shale particles do not clump together. We then wet sieve the washed sludge over a stack of three USA standard sieves: 20 mesh, 120 mesh, and 200 mesh. We place this stack of sieves in a vented 80^0C oven for 20 to 40 minutes or until the sample gets dry. Once the dry sample is ready, the size fractions are weighed, recorded, and stored. We only analyze the sample collected within mesh 20 and 120 screens for proppant concentration. This range is selected as it covers the size range of the proppant used in the stimulation of the offset producing wells, i.e., 40/70 and 100 mesh silica sand. The mass of the recovered sample between mesh 20 and 120 sieves varies significantly from as little as 0.2 gm to as much as 15 gm. Therefore, we use a sub-sampling technique using a riffler to reduce the overall sample size used for analysis but still provide proppant concentrations and size distributions representative of the whole sample. A riffler splits a sample in half without biasing on particle weight or size. After multiple iterations, we can reduce each sample to two to four approximately 0.25 gm to 0.5 gm sub-samples depending on the original sample weight. We widely spread each sub-sample over a transparent sheet and image it is using a high-resolution transparency scanner. In transparency scanning, the sample is imaged by capturing the light that passes through the particles. This effectively images the shale and aluminum pieces as extremely dark objects that are easily classifiable. In the next section, we describe how we process each image.

Method

We have developed a novel approach involving image processing, analysis and machine learning to detect and classify the proppant as well as possible natural calcite particles from the scanned images of the samples obtained from the core barrels. Since particles of interest are essentially spherical in shape (barring some which have a rough, irregular surface features), we use a Circular Hough Transform (CHT) for particle detection from within the images. Before we apply CHT, we extract the edges of all objects within the image using any standard edge detection algorithm (Umbaugh, 2010). While an in-depth look into how a Hough transform works is beyond the scope of this paper, in the next section, we provide a basic outline of the

algorithm. For a more detailed understanding of CHT and its implementation, we suggest for further reading: Atherton & Kerbyson, 1995; Atherton & Kerbyson, 1999; and Yuen et al., 1990.

Introduction to circular Hough Transform

A Hough transform is a feature extraction technique that is used to identify imperfect instances of objects (circular shapes for this problem) using a voting procedure. Hough transform can be used to determine the parameters of a circular object when several points that fall on the perimeter of that object are known. A circle located within the image can be described in parametric form using its location and radius as follows:

$$x = a + R\cos\theta \,, \quad (1)$$

$$y = b + R\sin\theta \quad (2)$$

Here angle θ sweeps from 0^0 through 360^0 such that the evaluated points (*x, y*) trace the perimeter of the circular shape. Since the radius of the object is an unknown parameter, the locus of points (*x, y*) in parameter space fall on the surface of an inverted, right angled, virtual cone with apex at (*x, y, 0*). The parameter triplet (*a, b, R*) will correspond with the accumulation cell where the largest number of cone surfaces intersect. In practice, an accumulator matrix is introduced for this purpose. Since the parameter space is 3D, the accumulator matrix is also 3D. We iterate over all possible values for radii in pixels. Note that the values for possible particle size are range bound based on our criteria as per the mesh sizes of interest. For each iteration, we divide the parameter space into "buckets" using a grid and produce an accumulator matrix according to the grid. The element in the accumulator matrix denotes the number of "circles" in the parameter space that is passing through the corresponding grid cell. To start with, all the elements in the matrix are initialized to zero. Then for each "edge" point in the original space, we can formulate a circle in the parameter space and increase the voting number of the grid cell through which the circle for the corresponding radii is passing through. We note that the voting is for each pixel location and for each radii. Once all iterations are complete, we get a 3D accumulator matrix with votes. Finally, we find the local maxima within the accumulator matrix. The positions of the local maxima correspond to the locations with high votes in parameter space or potentially, to centers of the circular objects in the original space. In addition, the value of the maxima can be used as an indication of how circular the detected object is.

Attribute definition

For computational efficiency and parallelization, we divide the scanned image into smaller sub-sections for easier handling. We apply CHT on the individual sub-section and all potential candidate objects are identified. For each of the identified objects, we calculate various attributes to identify whether the object is a possible proppant, natural calcite particle, or other miscellaneous material. These attributes include "darkness", "hue", "entropy", "translucence", etc. to name a few. We then use these attributes to classify the corresponding particles by using a ranking scheme, which serves as the first classification estimate. The ranking scheme is designed to rank possible proppant and calcite objects positively and other particles negatively.

Attributes define various features and properties, which characterize the proppant, natural calcite and other miscellaneous particles as, obtained and subsequently imaged from the core sludge samples. Some of the attributes used for this classification problem are defined below. Note that the feature space can be expanded by adding other morphological or textural attributes.

a. Hue is computed using the color spectrum of the object after removing pixel elements outside its boundary. For proppant and smaller calcite particles, the images generally have high bluish hue and very low reddish hue. This is because sand particles tend to transmit more of the blue spectrum due to absorption of other frequencies within white light. Since absorption is also influenced by particle size, larger particles tend to be darker. Some aluminum and shale particles tend to show reddish hue close to their outer edges, which are imaging artifacts. The size dependence of hue is important. Specifically, the image is broken down into its component color channels (Red, *R*; Green, *G*; & Blue, *B*). Mathematically, for darker parts of the object image (identified to be areas where the mean value from all three channels is less than 200 based on 8-bit decimal coding), hue is defined as:

$$H\ (i,j)\ =\ maximum\ (G\ (i,j) - R\ (i,j);\ B\ (i,j) - R\ (i,j))$$

(3)

Here indices *i*, and *j* represent the exact pixel location within the image. The blue and red hue attributes are calculated as either the maximum or minimum of the hue map, i.e., *Max. Hue = max* (*H*) and *Min. Hue = min* (*H*).

b. Dark objects are discarded as potential shale/ aluminum particles. The identified object is converted from an RGB image into a monochromatic image (red channel data is selected). Next, five darkness measures are calculated and are used as classification features. If *A* represents the red channel data vector for pixels identified to be corresponding to object in question, then:

$$D1\ =\ quantile\ (A, 0.2)$$

(4)

$$D2\ =\ quantile\ (A, 0.1)$$

(5)

$$D3\ =\ quantile\ (A, 0.01)$$

(6)

$$D4\ =\ 1/standard\ deviation\ (A)$$

(7)

$$D5\ =\ maximum\ (A)$$

(8)

Comparatively, if attribute values *D1* and *D5* are the same, the particle is likely not proppant since it is too dark. A high value for *D4* can indicate a particle that is likely not proppant because they tend to have significant hue or translucence, resulting in larger standard deviation measure.

c. Large proppant particles tend to be roundish in shape with relatively smooth edges [particularly at 40-70 mesh size range]. Smaller particles may contain sharp edge effects

due to proppant crushing. However, even if they are not perfectly round, they do have roundish and relatively smooth edges. The maximum of the 3D accumulator array for the corresponding object detected using CHT is used as measure of roundness (Kimme et al., 1975).

d. Sand particles are expected to be translucent when imaged under transparency. In the images, the translucence shows as light bands within the identified objects. These bands depend on particle size, cleanliness, and mineralization or crystal structure. To calculate translucence, a cut-off is used to bin the light and the dark sections separately. Translucence is calculated as the fraction of pixels falling within the lighter sections compared to the total pixel count within the object in question.

e. While roundness provides an indication of particle circularity, it may fail to provide an accurate value depending on accuracy of the predicted object radius from the original CHT run. In order to get an indication of objects with sharp edges, the variation of "white ratio" with azimuthal (θ) shifts is used. For objects that have non-circular shapes, there is a tendency for the search space to show up significant lighter zones influenced by the image background (white). They are a strong indicator of non-circular objects, which may have been misclassified proppant. The attribute is defined as:
$EWR1 = (Continuous\ \theta > white\ threshold)/ 2\pi$
(9)

f. Smaller particles are hard to characterize in general and should be classified as natural calcite barring any additional available information due to resolution limits of imaging. Size of the object is identified based on original CHT algorithm that provides an estimate for radius of any detected object.

g. Entropy is calculated for a grayscale map of the original object image. The zone outside of the actual particle is trimmed and the value for the remaining data (within the object radius) is calculated using the normalized histogram counts of the relevant image intensity data binned from 0 to 255 (8-bit color encoding). The entropy, which is a measure of textural variance, is calculated as:
$\boldsymbol{Entropy} = -\sum_{i=0}^{255} NP_i \times log_2 NP_i$
(10)
Here, *NP* represents the normalized histogram counts and the values are summed for entire scale.

We use a simple ranking algorithm to get the first estimates of particle type. The particles are classified into three separate classes, namely "proppant", "natural calcite or cement", and "others" based on the calculated ranks. The ranking scheme is as follows:

a. Calculate various attributes.
b. Initialize rank as zero.
c. Check if object is too dark – adjust rank upwards if false.
d. Check if object is too dark and it is large – adjust rank downward if true.
e. Check if blue hue is significant but red is not and the particle is reasonably large – adjust rank upwards if true.
f. Check if red hue is significant but blue is not, and particle is very dark – adjust rank downwards if true.

g. Check if particle size is too small – adjust rank downward if true.
h. Check if object shows significant translucence but is slightly dark – adjust rank upwards if true.
i. Check object extremity white distribution and see if significant white zones exist – adjust rank downwards if true.
j. Check object extremity white distribution variance and see if value is small – adjust rank downwards if true.
k. Check entropy and see if value is small – adjust rank downwards if true.

In place of the ranking scheme highlighted above, a simple classifier may also be used for initial classification. However, for any supervised method to work, training requires significant population of object examples that will be hard to generate using visual object classification. An alternative method could be the use of unsupervised classification techniques. Once the ranks have been calculated, a k-means clustering algorithm is used to segment particles into three classes of interest (Kanungo et al., 2002). For further discussion on attributes, consider Maity et al. (2018).

Based on the ranking, we carry out a visual analysis to identify obvious classification errors. We rectify any identified errors by manually reclassifying the particles. However, we cannot use his approach for the entire image, as it is very time consuming. We use a supervised machine learning approach to resolve the classification problem. An artificial neural network-based classifier is trained using the classified particles (see classification section) for subsequent use. The selected data must be adequately representative so that the trained classification model is applicable for other core samples. Another advantage of using machine learning is the class memberships or likelihood values, which indicates how robust the classification is. We can also use them later during the quality control (QC) process.

Classification using machine learning.

A machine learning approach using artificial neural nets is used for the classification problem. The entire classifier is implemented within MATLAB environment using relevant MATLAB toolboxes. We use a supervised feed forward network with backpropagation to train the node weights and biases. The network is divided into the input, hidden, and output layers made up of computational nodes. The nodal connections are defined by weights and activation functions. For our three-class classifier, the outputs are defined by a three-element vector with the element corresponding to the true class type set to '1' and all other elements set to '0'. Network training involves optimizing the weights and the biases of the network based on mean square error measure. Available data is divided into three separate datasets, i.e., training, validation and the test sets. The training data is applied to the feed forward network and the network weights and biases are updated using the Levenberg-Marquardt optimization (Levenberg, 1944; Marquardt, 1963). Bayesian Regularization is used to reduce bias and variance of the network by minimizing the linear combination of squared errors and weights (MacKay, 1992). Network training is terminated when the classification error with the validation dataset has saturated. Specifically, this is achieved by setting a cut-off of twenty continuous training epochs with no reduction in classification error for the validation dataset to cease training. One epoch represents a single instance of inputs being sent through the network and subsequent network update based on the training results.

The choice of a robust dataset is key to design of a good classifier. The dataset should encompass various possible types of particles with varying attribute ranges. To achieve this, various sections of the scanned image are analyzed to find areas with high proppant, calcite or other particle counts based on the initial ranking and clustering. Since the ranking is never completely accurate, a manual reclassification is generally necessary to make sure that the selections are accurate for training. However, the availability of a "first guess" classification based on the ranks makes the training data preparation easier and less time consuming. Apart from actual scan sections of prepared subsurface samples, controlled test samples prepared in the lab using sourced proppant, natural calcite and aluminum shavings are also imaged and classified for use as training data. This is done to have significantly large training population and good quality control. Having larger training datasets also helps reduce variance and reduces impact of sampling or other subjective errors. We use a minimum of 2,000 sample objects with defined attributes for network training. Since we use supervised learning, care is taken to reduce both bias and variance in our results. Reducing the size of the layers is the easiest approach towards reducing overfitting or variance. However, while reducing dimensionality reduces variance, the opposite is true for bias where the hypothesis maps poorly to the training data (underfitting).

We conduct network optimization studies using 10-fold cross-validation for both the network hidden layer size as well as the selected attributes for classification. While the final hidden layer is designed with eight nodes, all the originally defined attributes are used without feature trimming due to lack of interdependence. Once the optimal feature space and other network hyper-parameters are optimized, the classifier is re-run to validate that the results are reasonably accurate. Our tests have shown that other classifiers such as optimized support vector machine or k-nearest neighbor classifier can provide reasonably good results. Therefore, the use of artificial neural nets for classifier design is not critical to the actual results, i.e., the particle size fraction distributions obtained for all the core samples.

Two relevant approaches applied in this study are highlighted in the subsequent discussion. The first is the use of manual QC procedure, which is used to update size fraction counts based on observable classifier errors. This step is not a requisite for classification, but it provides a reasonably quick understanding of classifier performance for a given sample being processed. The steps for manual QC adjustments are as follows:

a. Complete automated detection and classification of objects within the original sample image.
b. Select an image sub-section for QC. Selections are made based on presence or absence of identified objects and their relative counts. Check each identified object within selected sub-sections.
c. For miss-classification or missed objects, make necessary changes including addition, removal or correction of objects as proppant, natural calcite or other material.
d. Based on corrections, adjust the relative distribution of various size fractions of both proppant and natural calcite particles for sub-section being quality-controlled.
e. For all other sub-sections for that sample, recalculate the size fractions based on the adjustments made in the quality-controlled sub-section. For this, we use the adjustment

fractions from the QC process and the overall object count within each sub-section. The correction is defined as:

$$CP_{i,j} = \frac{P_{i,j}^{final}}{P_{i,j}^{initial}} \quad (11)$$

$$P_{k,j}^{final} = \left[\frac{n_k}{n_i}\right] \times CP_{i,j} \times P_{k,j}^{initial} \quad (12)$$

In these definitions, *CP* indicates the correction for particle type for a particular scan sub-section *i* and for a particular size fraction *j*. *P* represents the total count of relevant particles for scan section and size fraction. It is evaluated as either the final count (after QC) or the initial count (prior to QC). Index *k* represents another sub-section where the correction is to be applied. Parameter *n* indicates the total particle density for the corresponding scan sub-section.

f. Based on the updated size fractions from each scan sub-section upon application of corrections, the final size fractions for the entire image are updated to give the post QC size distributions.
g. Steps b through f are repeated for other sub-sections as necessary.
h. The final size fractions are compared with the classification results. If the distributions are significantly different, a new classifier may be necessary.

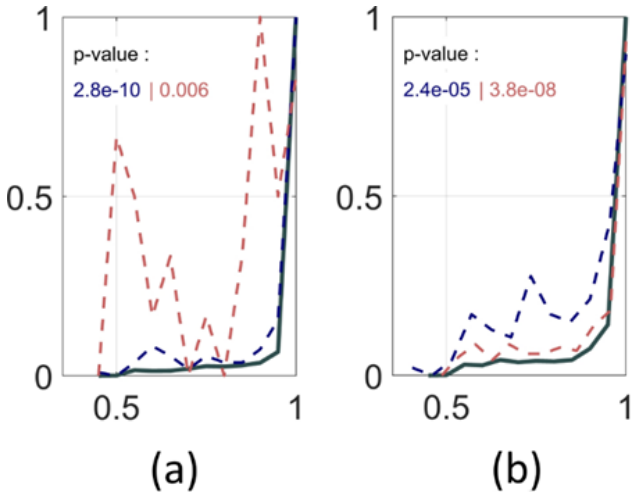


Figure 127: Classifier confidence comparison for (a) proppant and (b) natural calcite. The training data results for the model are shown with the solid line and the dotted lines show results for two separate datasets where the model is applied.

If a new classifier is defined, it is added on to the classifier ensemble as highlighted in Figure 129. The second method used to check the requirement of a new classifier is by comparing the classifier confidence distributions for a given sample. The confidence values are calculated automatically by the classification workflow as the class output values. In Figure 127, we show the comparison between the confidence distributions obtained when the model is trained (using training data) and the confidence distributions from application on example datasets. Note that for the first dataset (blue curve); the distributions for both proppant and natural calcite particles are very similar. However, for the second dataset (red dotted curve), the distribution for proppant particles varies significantly (p-value is relatively higher from chi-squared test). A significant difference in confidence distributions as shown here can be another

indicator that the classifier performance is poor, and a new classifier might be better. There is an added advantage of using this approach as it allows rapid evaluation of classifier performance in a relativistic sense without having to know the exact solution, i.e., the true particle distribution assuming that the classifier is showing poor performance. This approach is also useful in selecting the most appropriate classifier for application on a new dataset from the available classifier ensemble.

Workflow validation

We conducted several tests to validate this workflow. These include controlled tests for proppant, calcite, shale and aluminum discrimination, size fractions, and attribute selection. In Figure 128, we share results from controlled tests to characterize the particle types. We note that the trained classification model can predict the particle types relatively accurately. The exclusion of shale or aluminum particles is very precise. However, there is some residual uncertainty when it comes to identification of proppant vs. calcite or other mineral particles which tend to show proppant like behavior when imaged using either reflective or transparency scanning (see attribute definition section).

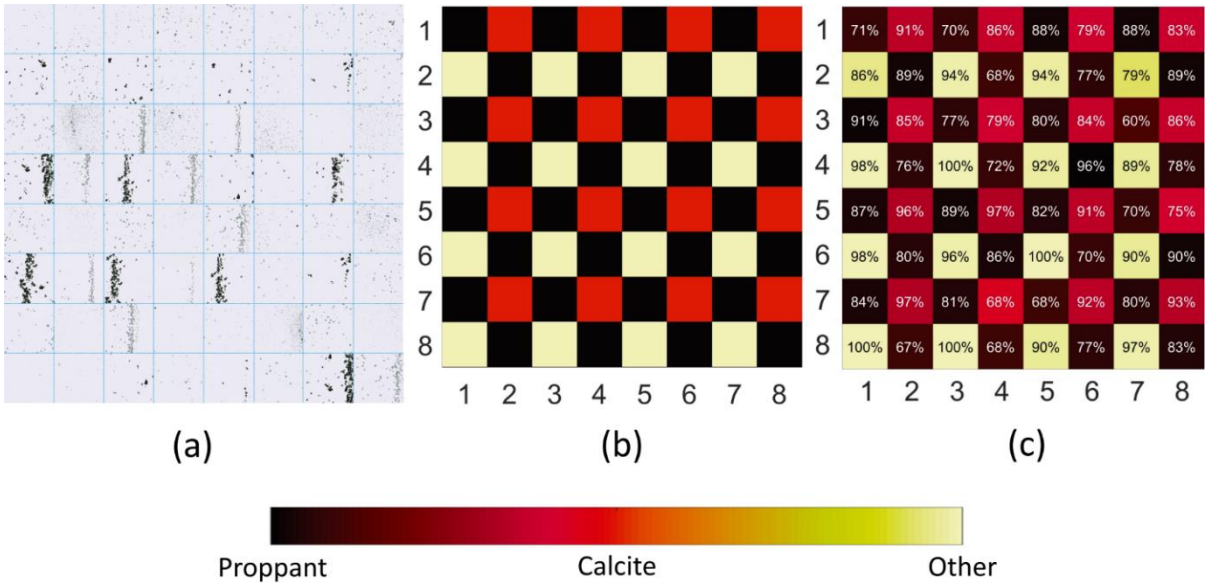


Figure 128: Results from controlled classification tests showing samples distributed within a segregated matrix (a) with particle type populating each grid highlighted in (b) and results from the classification workflow in (c). The percentage values in (c) are that of particles identified accurately in relation to the particle type populating a particular grid cell.

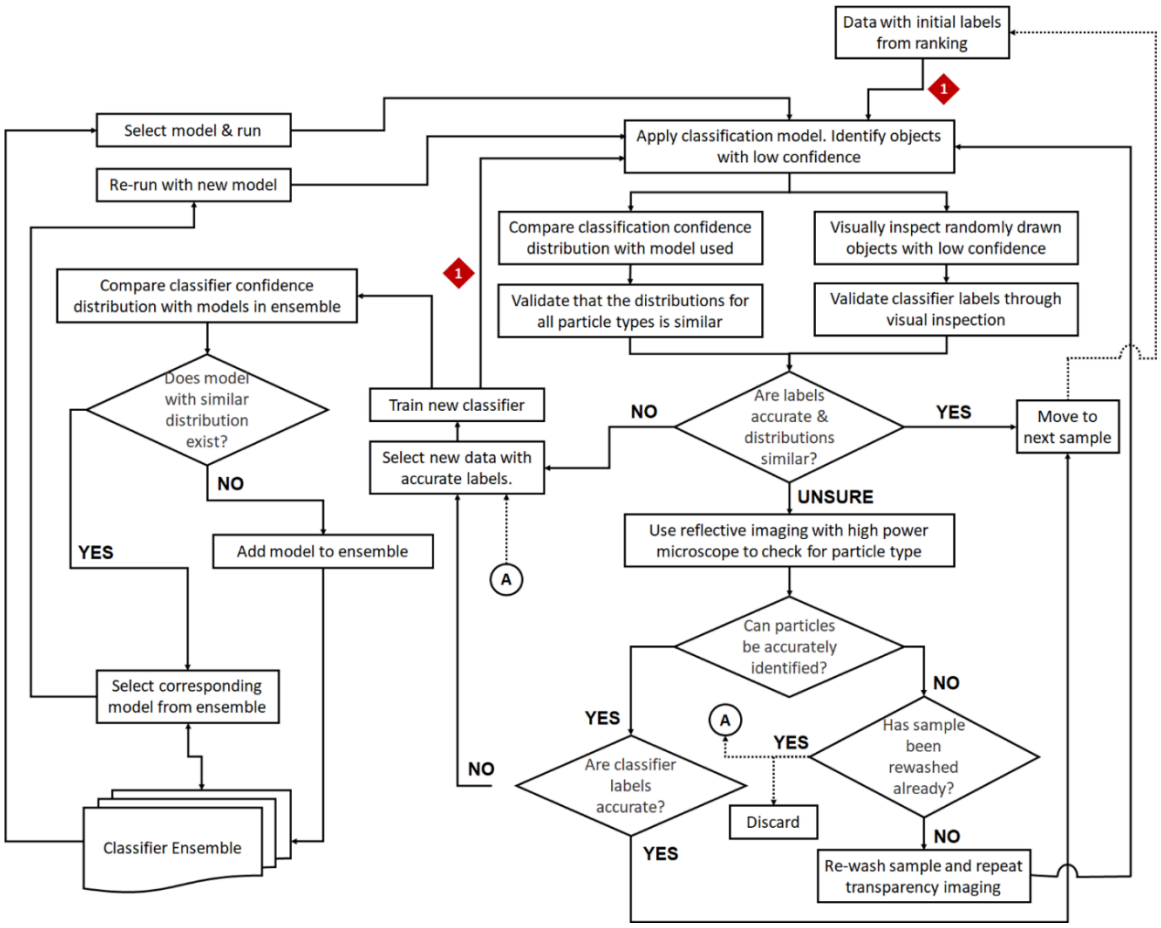


Figure 129: Classification and QC workflow to inspect and validate classifier results for proppant & calcite detection and classification. The first connectors are indicated.

The QC process is instrumental in verifying whether the available classifier models are working for the core sample and if so, is there any need for improvement. In Figure 129, we outline the QC steps within the ambit of the classification workflow, which include a step to create a classifier ensemble and adjustment of size fraction populations based on changes made through human intervention. The ensemble provides a library of classifiers that can be applied based on sample features. It also precludes the need for repeated classifier training whenever a new type of sample is encountered provided similar samples have been classified earlier and relevant models are available in the ensemble.

We generate results after each run and post QC process to get complete tabulation of all size fractions from identified proppant and natural calcite distribution. We test multiple sub-samples from the same core tube for repeatability and accuracy. This acts as an additional validation step before we tabulate these numbers for further analysis. Once the identified objects are classified as proppant or otherwise, they can be used to estimate the relative size distribution within the imaged sample. This involves transforming the size information of all detected particles from pixels to microns. Since scanned image resolution is known before hand, this is easily done using the following transformation: $R_m = R_p \times 25400/DPI$. R_m is the size of particle in microns, R_p is the size of object in pixels and DPI is the native resolution of the scanned image being processed. Once the sizes have been transformed into microns, they can be further characterized into mesh sizes of interest. The mapping from microns to mesh dimensions is trivial within expected limits of accuracy, which is inherent with any size distribution based on physical mesh screens.

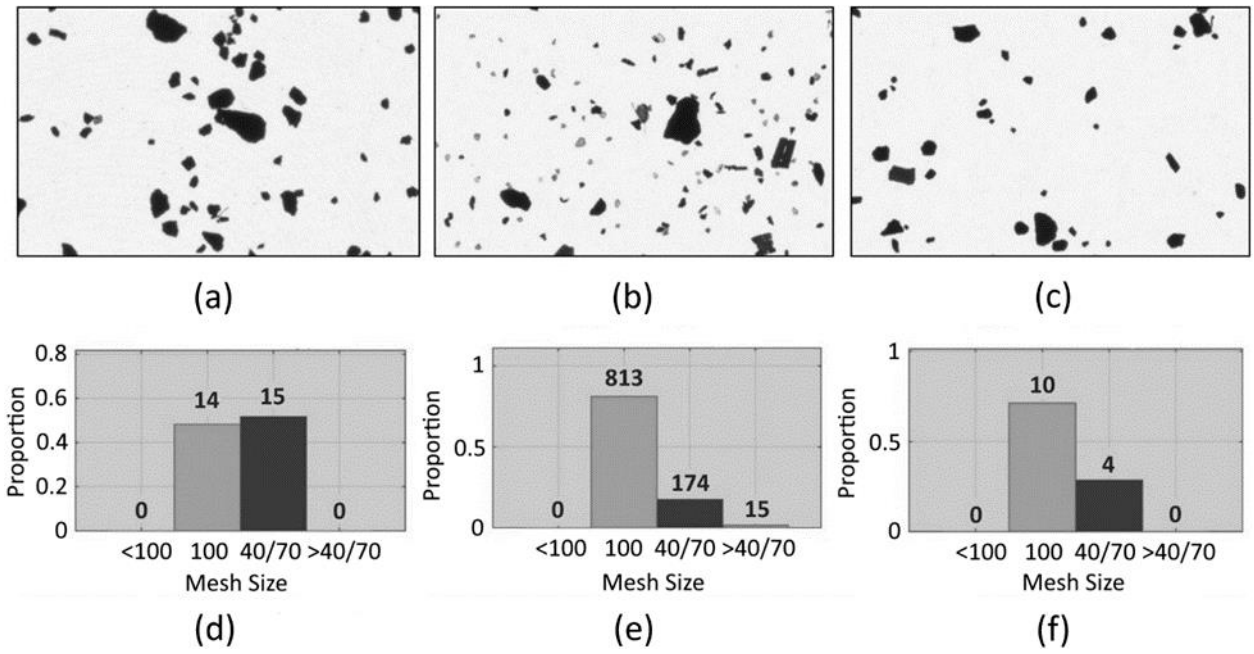


Figure 130: Sample scan sub-section images from Core 3 at depths (a) 9,570ft, (b) 9,573ft and (c) 9,576ft. Corresponding size distributions are shown in (d), (e) and (f). The number on each bar indicates total proppant particles of the corresponding mesh size fraction identified by classification workflow in the samples referenced in (a), (b) and (c). We observe significant proppant in the middle core tube but negligible proppant in the straddling tubes.

The final size fractions are representative of the sub-sample associated with the scanned image. In order to get a more accurate estimate of total particles of interest within the sample, we normalize the numbers to account for the total sample weights with the assumption that the imaged and analyzed sub-sample is a true representation of the original sample extracted from the core. Since the process is repeated over a significant number of scan sub-sections of varying particle densities, this assumption is reasonable to make. As part of the QC process described in Figure 129, we conduct frequent blind comparison with microscopically imaged samples to validate the observed classification results. As an example, we tested a few samples from core tubes in sequence and validated minimal to no mixing between corresponding core samples. In Figure 130, we highlight one such example where results from analysis of three core tubes in sequence from the UWC formation are shown. Note that while the sample in the middle has significant proppant identified through our workflow, the samples from upstream and downstream of this core do not show any significant proppant or natural calcite counts.

In-situ stress model definition

In-situ geomechanical model definition includes pore pressure, unconfined or uniaxial compressive strength (C_0), and magnitude and orientation of three principal stresses (vertical stress, S_V; minimum horizontal stress, SH_{min}; and maximum horizontal stress, SH_{max}). For the study, the producer provided the calibrated pore pressure and overburden stress models. SH_{min} is estimated based on the core triaxial tests and sonic and density log measurements from the pilot well (W6) by using elastic rock property estimates. C_0 is critical for constraining maximum horizontal stress (SH_{max}). Static Young's modulus values identified using triaxial testing of core plugs is correlated with C_0. The correlation is then used to estimate distribution of C_0 with depth using dynamic Young's Modulus values from dipole sonic measurements. Since we observe no breakouts based on the available image logs from multiple wells within the study area, we use the method proposed by Barton et al. (1988) to estimate limit for SH_{max}. For

application of failure criteria based on frictional faulting theory, the coefficient of sliding friction of 0.6 is used. We do note that past studies have shown that high carbonate concentrations can lead to higher coefficient values while higher shale and hydrocarbon concentrations can cause lower frictional coefficients (Sone & Zoback, 2013). Therefore, this assumption may not be accurate across the entire cored depth interval. The constraints for SH_{max} for breakouts are defined as follows:

$$SH_{max} = \frac{(C_o + 2P_P + \Delta P + \sigma^{\Delta T}) - SH_{min}(1 + 2\cos 2\theta_b)}{1 - 2\cos 2\theta_b} \quad (13)$$

In this model, ΔP is the difference between the mud weight and the pore pressure, and $2\theta_b = \pi - w_b$ with w_b being the breakout angle. Since we do not observe any identifiable breakouts, w_b is taken to be 0^0. C_0 is calculated based on the identified correlation with Young's Modulus from core analysis.

We do observe reasonably good correlation between the Young's Modulus and C_0 estimated from petrophysical data with values from tri-axial core testing. Based on the available SH_{max} and SH_{min} values for given depths of interest we predict a normal faulting stress regime by mapping stresses onto stress polygons. The maximum uncertainty in the stress estimation is with SH_{max} values, which in turn has a significant impact on the stress transformations acting on any fracture or fault face. However, since most of the pre-existing fractures are near vertical, even relatively large errors in SH_{max} estimates do not significantly affect the final analysis as shared in this paper.

Results

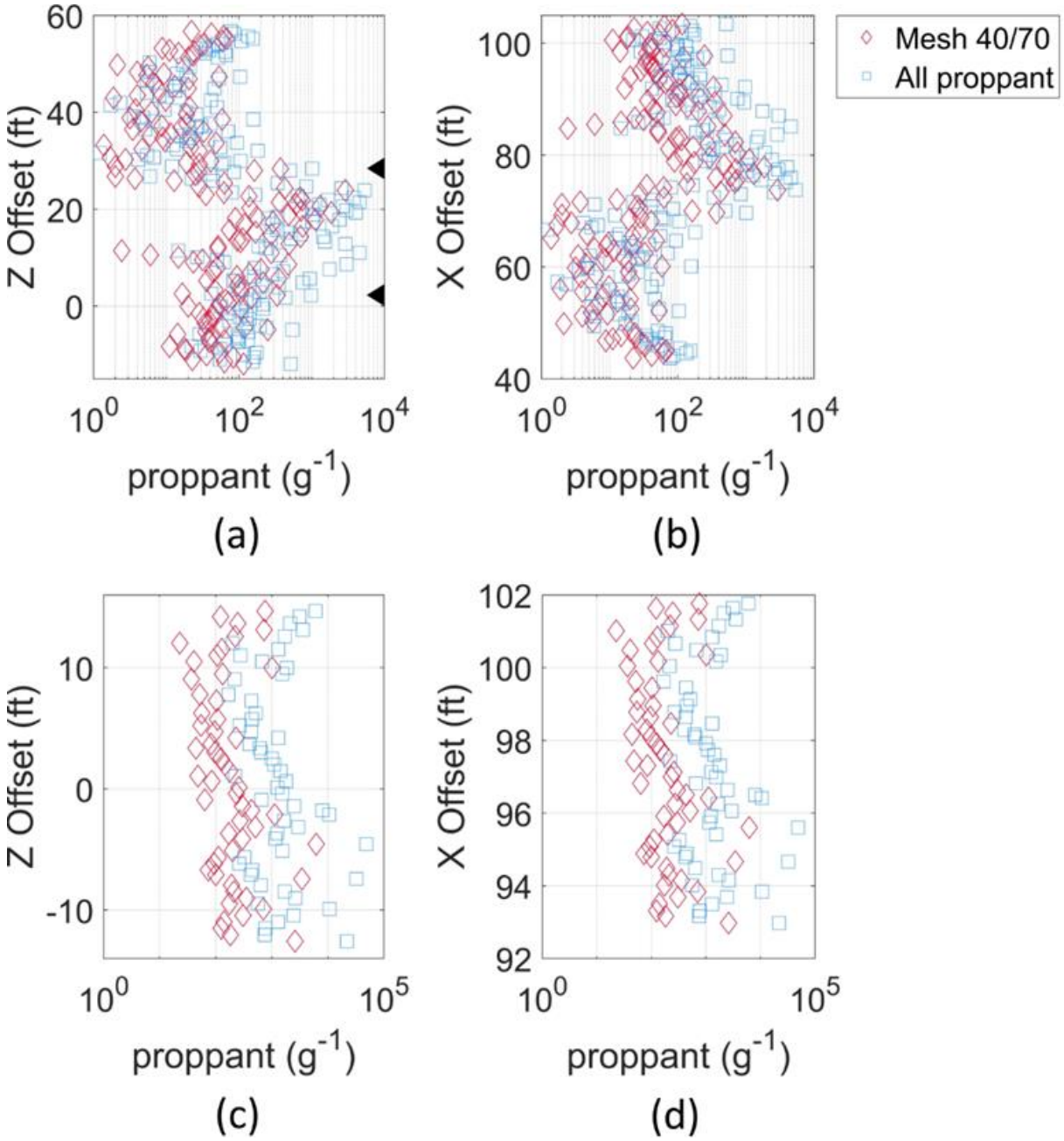


Figure 131: Lateral and vertical variation of proppant particles: (a) vertical variation in UWC, (b) Lateral variation in UWC, (c) Vertical variation in MWC and, (d) Lateral variation in MWC.

Based on analysis of cores as identified in Table 6, we have identified significant proppant and natural calcite particles across both the UWC and the MWC cores. However, due to the length of core available in the UWC formation, UWC core provides a much better understanding of overall distribution of proppant particles as well as natural calcite particles when compared with the MWC core. The UWC core covers approximately 75ft of vertical sampling compared with approximately 25ft for the MWC core. Similarly, the UWC core is situated at a lateral offset of approximately 75ft, on average, compared with approximately 95ft, on average, for the MWC core. In Figure 131, we see the vertical and lateral offset of proppant particles in the UWC and the MWC cores based on the results of classification workflow as applied on all the available samples from Table 6. The vertical and lateral offsets identified in the plots are relative to the locations where the offset well laterals are vertically nearest to the slant core well. This crossover is identified as the location where the slant core well is at the same vertical depth as the average vertical depth of the nearby hydraulically fractured well lateral while only

considering the wellbore length that corresponds with the lateral variation of the core well. From Figure 126, for the UWC cored interval, the nearest well is W4 and for the MWC cored interval, the nearest well is W9. In Figure 131, the actual proppant particle distribution reported on the horizontal axis gives the total proppant count scaled to the sample weight, i.e., *Norm. Count = Count/Sample Weight in grams*.

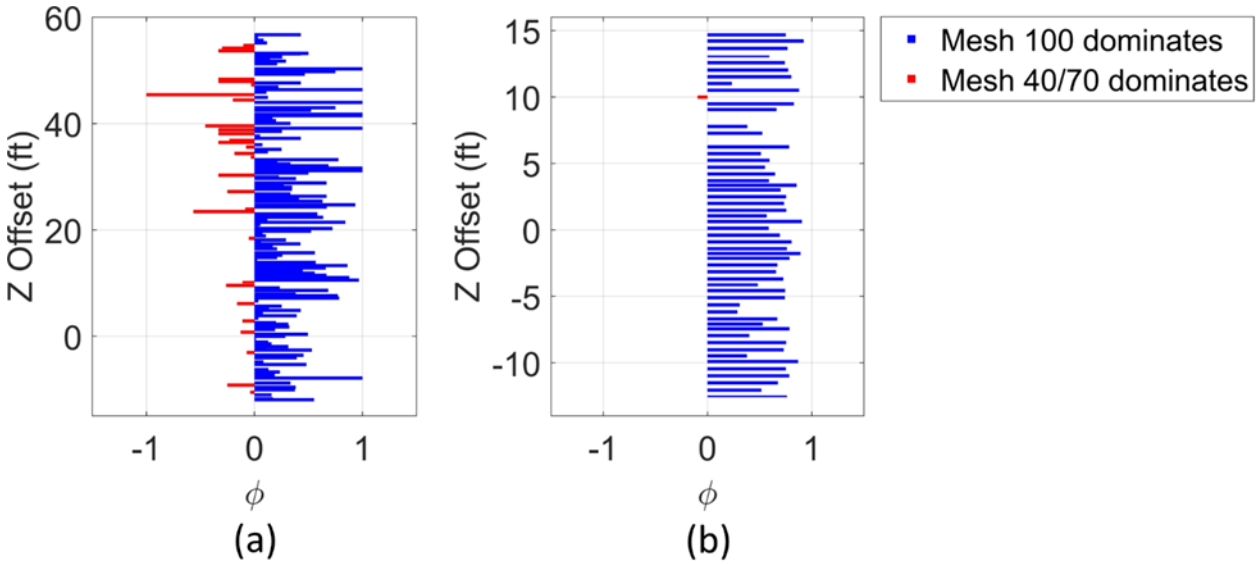


Figure 132: Relative size distribution of identified proppant particles: (a) UWC cored interval and, (b) MWC cored interval. For most of cored interval, mesh 100 size fraction dominates.

As we move downhole along the cored well towards the toe, the UWC core gradually moves away from well W4, while in the MWC formation, cored section gradually moves towards well W9. Based on the vertical proppant particle distribution observed from the UWC core data, we find that most of the proppant is limited in depth to approximately a 25 ft vertical spread close to the nearby, completed well lateral, W4 (Figure 131a, black arrowheads). Moreover, UWC core has similar distributions of mesh 100 and mesh 40/70 proppant, though mesh 100 is generally more prevalent compared to mesh 40/70. On the other hand, we see significantly larger proportion of mesh 100 proppant in MWC core compared to mesh 40/70. In addition, for the UWC core, most of the proppant particle distribution seems to be concentrated within a section of the core that is about 70 ft to 80 ft away from the nearby well. The depth interval where most of the proppant particles seem to be concentrated falls above the well cross-over point, where the slant core well comes nearest to the nearby, hydraulically fractured well, W4. We see a much higher concentration of proppant at a few sample locations ($> 10^4$) for the MWC core when compared to the UWC core ($< 10^4$). The difference is approximately an order of magnitude, particularly when we consider the distribution of smaller mesh size 100 proppant. For both the UWC and the MWC cored sections, barring a few instances, smaller mesh size dominates when compared with the mesh size 40/70 proppant. In Figure 132, we highlight this relative distribution of size fractions for clarity. To calculate the relative size fraction, ϕ, we use the following relation:

$$\phi = \frac{Mesh\ 100\ concentration - Mesh\ 40/70\ concentration}{Total\ proppant\ concentration} \quad (14)$$

Though we do see some general trends in the proppant distribution, locally, it is highly erratic with sudden jumps and drops. Some cored samples show minimal proppant while others show

significant proppant (Figure 130). The larger proportion of smaller mesh proppant within the MWC core could be a function of the lateral separation of the core from the nearby well W9 when compared with the lateral separation of the core from well W4. Based on particle size difference, we expect mesh 100 proppant, which is pumped initially, to travel further out into the reservoir. Larger mesh 40/70 proppant is pumped in later during the treatment and should be distributed relatively closer to the completed perforations along the hydraulically fractured well. Only at the larger lateral offsets, we see significantly higher mesh 100 proppant count compared to mesh 40/70 proppant count. We see evidence for this from the UWC distributions in Figure 131a, and Figure 131b. Another contributing factor could be the difference in degree of natural fracturing within these two zones. In this area, core analysis has shown UWC formation to be much more naturally fractured compared to MWC formation. This observation is further strengthened by tracer data, which also indicates much more communication associated with the MWC wells compared to the UWC wells. In Table 7, we provide a brief outline of the UWC and MWC behavior based on the observed fracture distribution within the cored section and tracer data analysis. For the tracers, we report the average number of wells with observed tracers across a given formation based on sampling over six months after completion of fracturing operations. Being more naturally fractured, we expect more complex fracture growth during hydraulic stimulation in UWC formation, which can reduce the fracture growth laterally away from the wells (Warpinski & Teufel, 1987; Daneshy, 2009). Since UWC hydraulic fractures interact a lot more with natural fractures, there are more opportunities for proppant to screen-out locally due to loss in the carrying capacity of fracturing fluid (Gale et al., 2018).

Table 7: Comparison between core fracture description and tracer results for UWC and MWC formations. Communication data is based on tracer study within the study area (Wood et al., 2018). In the two rows, we report average numbers for wells within the two formations where we introduced tracers, i.e., the average number of wells in said formations where we observed oil or water tracers.

Tracer introduced in Formation	Natural fracture density (1/ft)	Oil tracer (average number of UWC wells receiving tracer)	Oil tracer (average number of MWC wells receiving tracer)	Water tracer (average number of UWC wells receiving tracer)	Water tracer (average number of MWC wells receiving tracer)
UWC	0.62	2.75	2	2	2.25
MWC	0.23	4	3.5	5.5	4

We also investigated the distribution of identified calcite particles across the core as identified by our classification workflow. The distribution is shown in Figure 133. Figure 133a shows the relative distribution of proppant vs. natural calcite in the UWC cored section and Figure 133b shows the relative distribution in the MWC cored section. To calculate the relative particle type distribution, χ, we use the following relation:

$$\chi = \frac{Total\ proppant\ concentration - Total\ calcite\ concentration}{Total\ proppant\ concentration + Total\ calcite\ concentration} \quad (15)$$

We do need to mention that apart from general classification errors with our workflow, the particles classified as natural calcite could be other mineral particles that are semi-translucent

and can sometimes show other attributes that makes them appear like proppant particles. Moreover, this identified calcite population may not be associated with natural fractures in their entirety as there could be calcite presence from carbonates, particularly concretions as well as debris flows which are common in Permian Basin. On average, we see a lot more identified natural calcite along the UWC core compared to the MWC core. Some of this calcite should be a result of coring through cemented fractures or concretions as well as fractures breaking during coring or core handling operations. A significant portion of identified calcite could be due to activation of fractures during stimulation as well as transport of some of the calcite as entrained material along with hydraulic fracturing fluid. For the UWC core, we can identify three distinct zones of interest, which show variations in relative proppant and calcite distributions. These zones will be discussed in detail later in this paper. The proppant distribution is further analyzed in relation to geology and petrophysics in the next section.

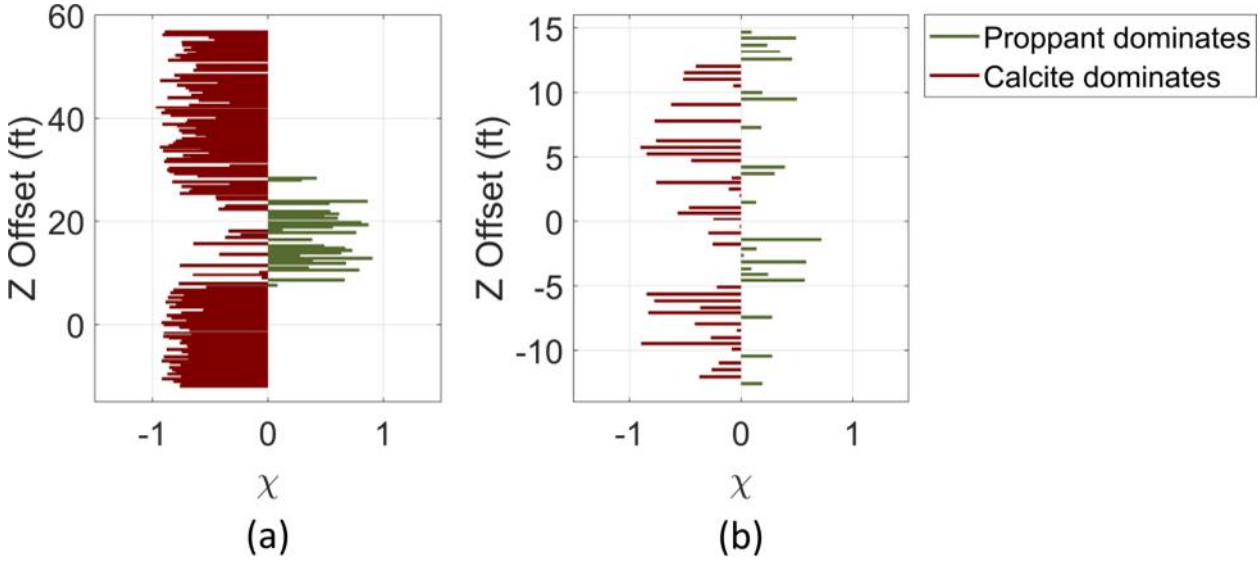


Figure 133: Relative proppant vs. natural calcite distribution: (a) UWC core, and (b) MWC core.

Correlation with petrophysical logs

The sporadic nature of proppant distribution with depth, including localized peaks, suggests local geologic, fracture or stress related variations and other complexities might be influencing where we observe jumps of proppant and natural calcite distributions along the cored interval. As an example, fracture complexity can be governed by the localized stress distribution within the rock. Presence of bed boundaries and stress anisotropy or varying mechanical properties of proximal beds can cause complexity in fracture growth (Wright et al., 1999; Weijers et al., 2005; Suarez-Rivera et al., 2013). In Figure 134, we share an example of such complexity from the cored interval as well as the corresponding sample image sub-section for reference. In order to understand if there is an identifiable correlation between the in-situ stress state and the observed proppant distribution, we map the identified proppant distribution against measured and modeled petrophysical properties of interest. For the UWC cored interval, we highlight the petrophysical properties in Figure 135, and for the MWC interval, in Figure 136. Almost all the high proppant concentration zones appear close to carbonate bed boundaries or where there is significant change in stress.

Based on computed tomography scans of the cores as well as extensive core description, we know that we have complex fracturing across thin lamina or beds, particularly associated with

carbonate layers and concretions. One possible explanation for observed proppant distribution could be that some of the proppant tends to be deposited where complex fracturing and local stress contrasts create possible avenues for localized screening of proppant from the fracturing fluid stream. However, this does not imply that there is no proppant transport beyond these localized "proppant hot spots". However, this does lead to questions and has implications regarding proppant placement efficiency.

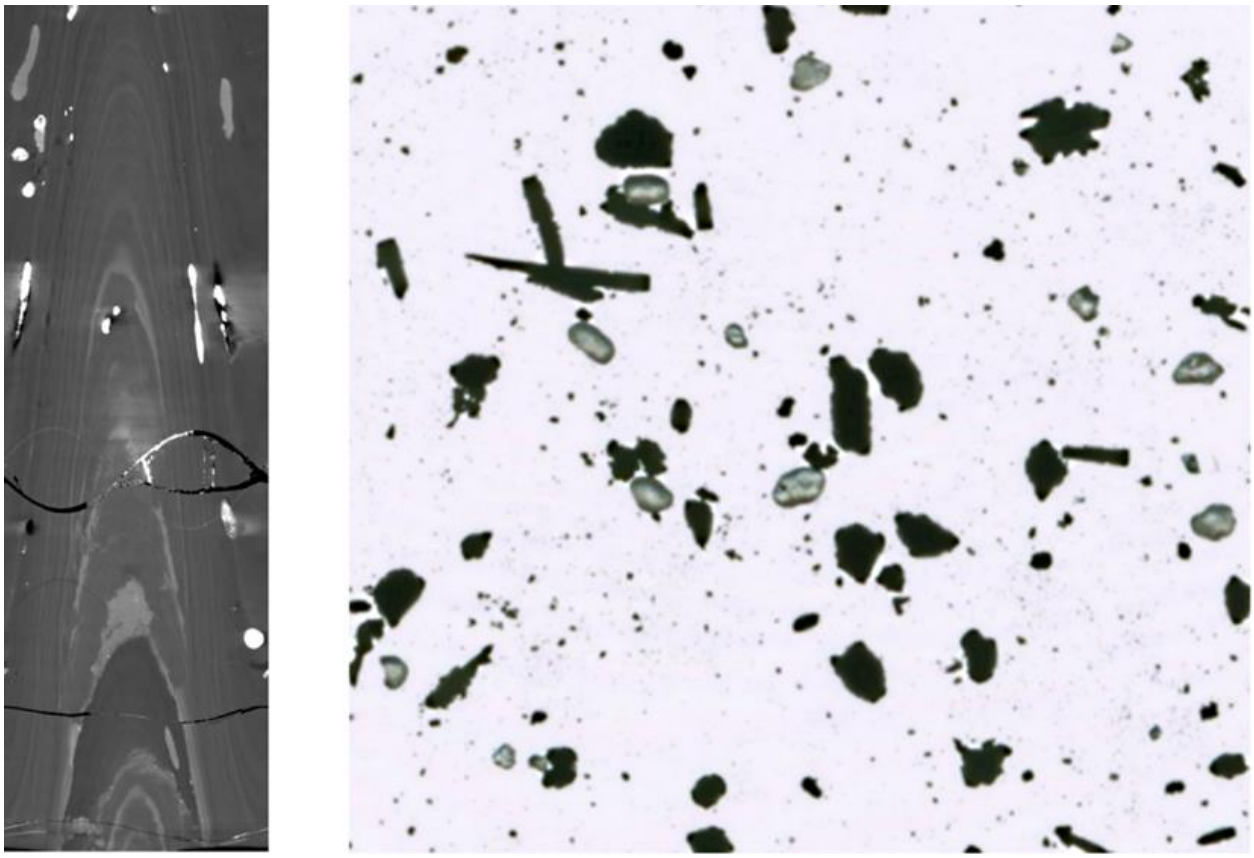


Figure 134: Example of fracture complexity from core # 3 at 9,460ft. The computed tomography scan of the intact core is shown in (a) and snapshot of the core sludge sample from processing is shown in (b).

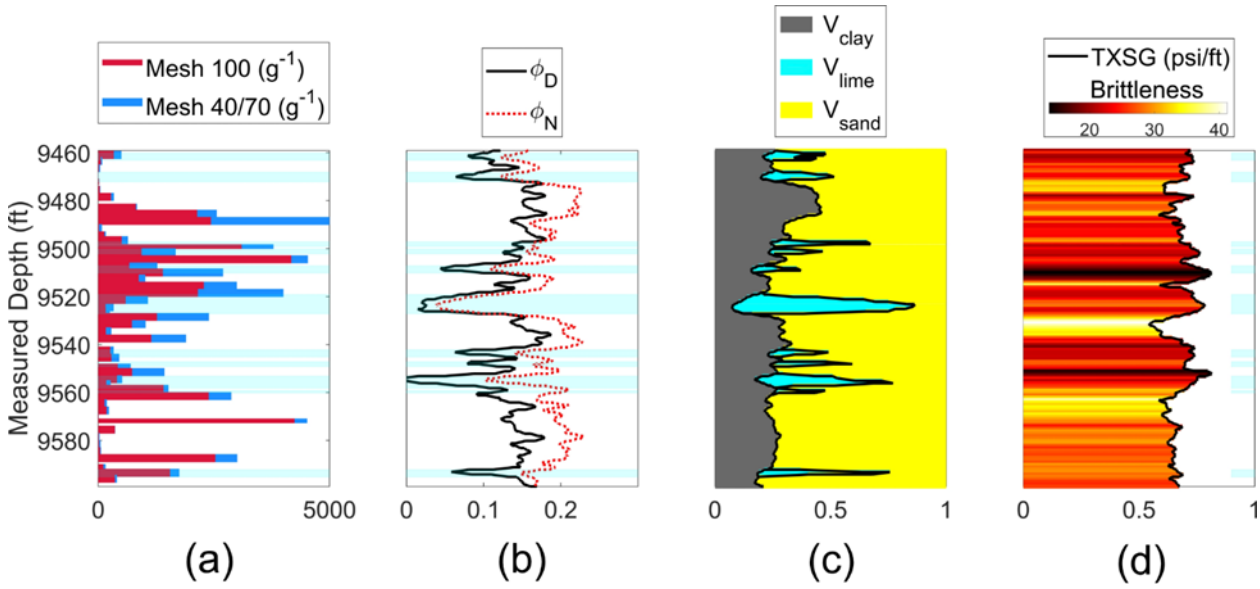


Figure 135: Proppant distribution correlated with petrophysical measurements for a part of the UWC cored interval: (a) proppant distribution, (b) porosity, (c) rock type and (d) in-situ stress gradient with brittleness. The aquamarine-colored bands in (a), (b) and (d), highlight the locations with significant carbonate layers as seen in (c). Only the depth horizon with significant identified proppant is shown.

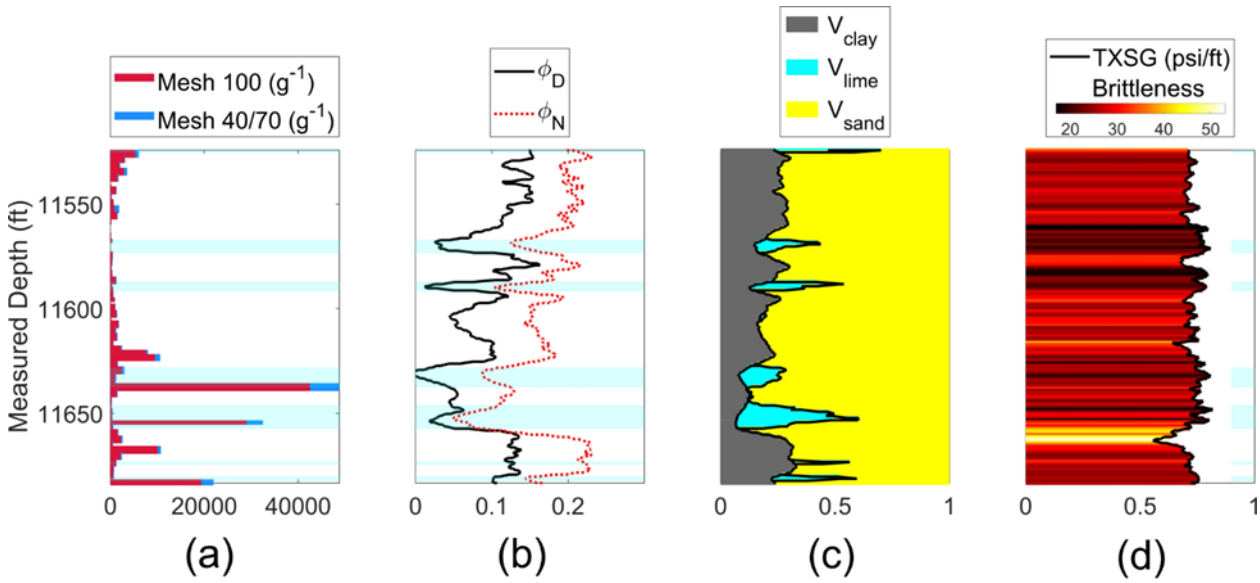


Figure 136: Proppant distribution correlated with petrophysical measurements for the MWC cored interval: (a) proppant distribution, (b) porosity, (c) rock type and (d) in-situ stress gradient with brittleness. The aquamarine-colored bands in (a), (b) and (d), highlight the locations with significant carbonate layers as seen in (c).

Cursory analysis of microseismic monitoring data for completed laterals well W4 and W9 show microseismic event distributions spreading around ± 500ft in depth across the hydraulically fractured wells at the test site (Trowbridge et al., 2017; Maity 2018). This raises questions as to how far the propped and connected fractures extend beyond the wellbore as well as the distribution of unconnected stimulated zones within the reservoir. Better sampling with additional cores or use of tagged proppant may provide an answer.

Interaction between natural and hydraulic fractures.

We compare the results from the proppant distribution analysis shared in this study with the fracture distribution along the cored interval (Gale et al., 2018). Fracture description indicates significant hydraulic fracture density within both the cores. The observed frequency seems

reasonable considering recent core and petrophysical studies, which have validated the presence of significant hydraulic fracture density away from the perforation clusters (Raterman et al., 2017). In our analysis, we restrict ourselves to the upper core with the most coverage in depth. The aim is to identify significant changes in fracturing behavior in relation with the proppant distribution. The average distribution of fractures identified from core description is compared with observed proppant and natural calcite counts in Figure 137. The higher the particle markers, the larger the type count for that particular core sample relative to other samples. In addition, the size of the particle markers represents the prevalence of that specific particle type compared to the total particle count observed in that sample. The total particle count for calcite is not a reliable estimate because not all calcite particles are present within the screened sample. However, it serves as a good indicator of relative distributions if we assume that the bigger natural calcite fragments will lead to much higher concentration of calcite particles within the studied size fraction range due to natural or handling related comminution. We can clearly identify three sections of interest along this cored interval that show distinct behavior in terms of fractures as well as proppant and natural calcite distributions. We classify these as sections A, B & C in Figure 137.

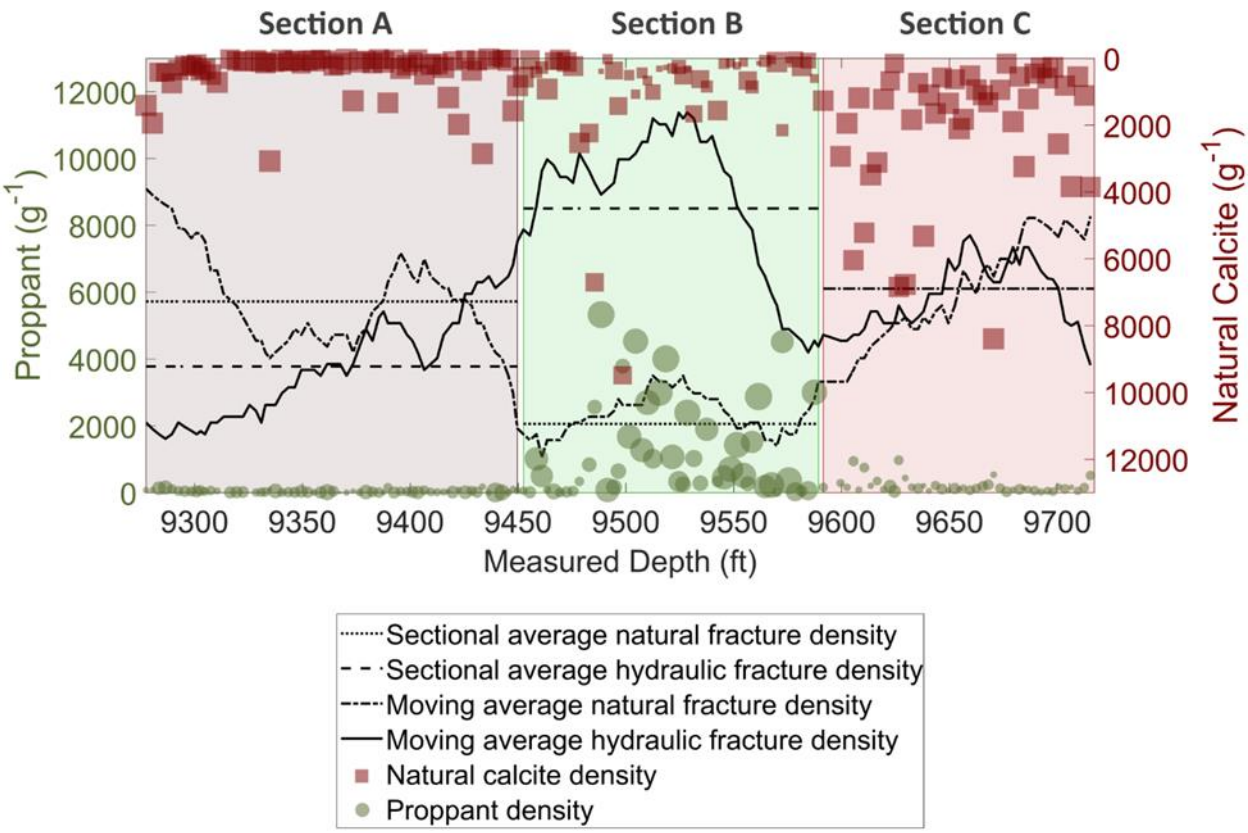


Figure 137: Distribution of average natural and hydraulic fractures compared with distribution of identified proppant and natural calcite count along the UWC cored section. Note that the average fracture densities are relative and not scaled as per the vertical axes.

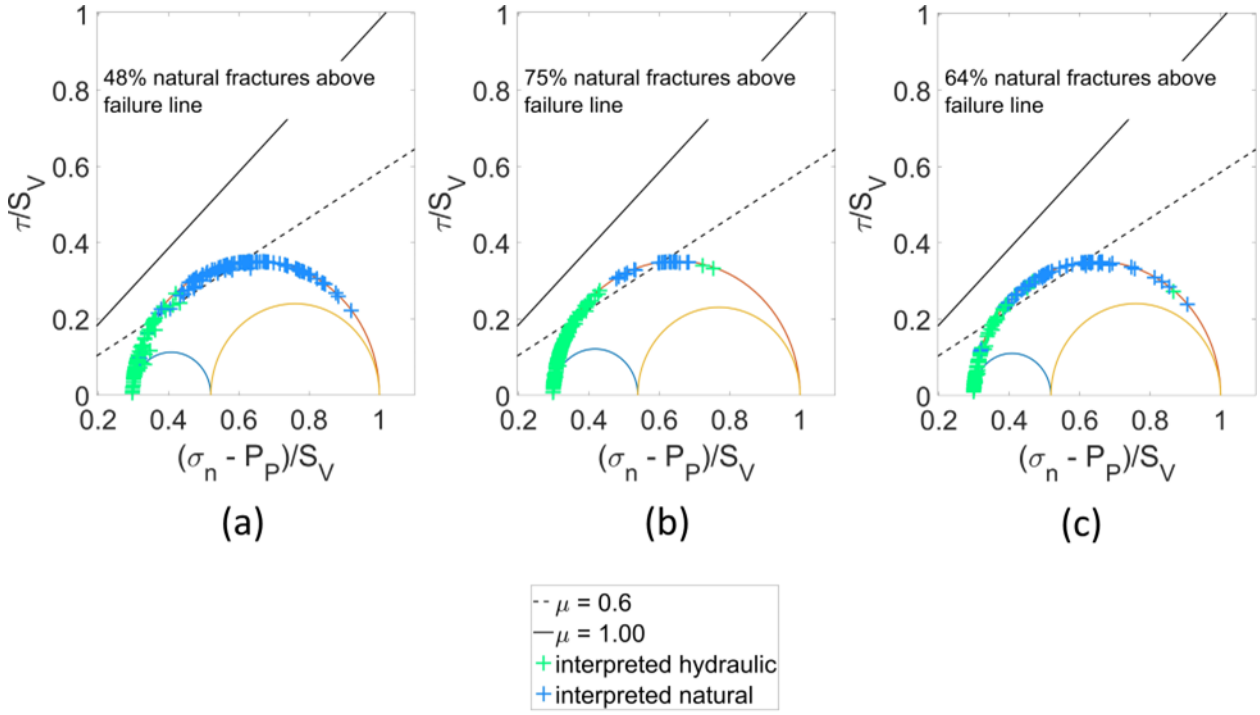


Figure 138: Geomechanical state of fractures: (a) section A, (b) section B and (c) section C as highlighted in Figure 137. The percentage fractures reported are those that fall strictly above the Mohr-Coulomb failure line for coefficient of friction of 0.6.

Based on the identified fractures, section A has relatively low hydraulic fracture density, high natural fracture density and some calcite though isolated and intermittent in nature. On the other hand, section B has very high hydraulic fracture density and relatively low natural fracture density. Section C has high natural fracture density. For section C, the hydraulic fracture density in low in comparison with section B and high in comparison with section A. One way to explain the proppant distribution is based on relative fracture densities in these zones. Section C has more hydraulic fractures compared to section A but similar natural fracture density. In section C, this may cause, in a relative sense, more interactions between them during fracturing. In section B, we see the highest proppant concentrations observed for the entire core and the highest hydraulic fracture density as well. Since there are significant differences in depth as well as the fractures as we move across the cored interval, the geomechanical state of the fractures is a relevant consideration. Relevant data from pilot well (W5) is used to constrain the in-situ stresses. Details of the stress modeling approach are shared in the stress model definition section for reader's interest.

Based on the stress model and fracture properties identified along the cored interval, Mohr diagrams representing fractures from the three sections (section A, B & C) are shown in Figure 138. Results indicate that within section A, approximately 52% of the natural fractures are stable. This compares with approximately 25% for section B and approximately 36% for section C. Based on the state of stress of the fractures, a larger proportion of natural fractures in section B and section C may have been open during the geologic history of the reservoir. Thus, due to lack of flow and calcite deposition, there should be a lower proportion of natural fractures in section A with calcite when compared to section B and section C. In addition, this should cause fewer reactivations of fractures in section A during hydraulic fracturing operations. This explanation fits with the observed distribution of natural calcite from Figure 137. However, sampling biases or subjective errors in fracture description cannot be ruled out.

Correlation with perforation clusters.

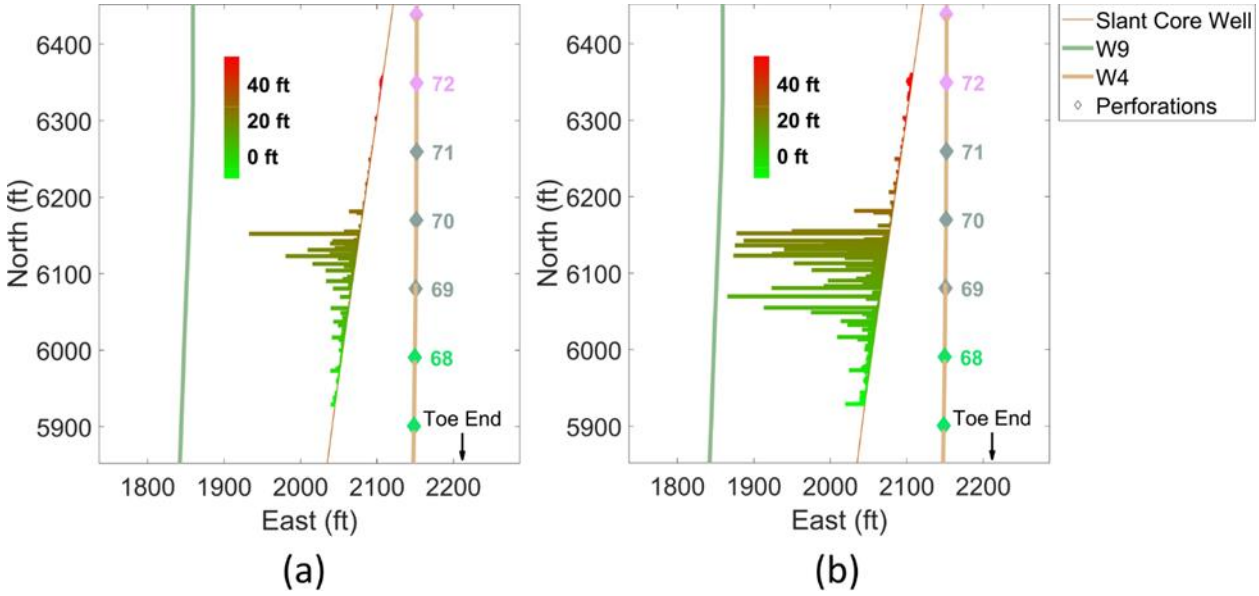


Figure 139: Map view of the hydraulically fractured wells W4 in UWC and W9 in MWC formations. The relative proppant count distribution identified along the cored interval is highlighted using bars along the well for two size fractions: (a) mesh 40/70 distribution and (b) mesh 100 distribution. The clusters are colored similarly for the same stage (e.g., clusters 69, 79 and 71 belong to the same stage). The bars are colored according to the average vertical offset from well W4.

The map view of the UWC well nearest to the core, i.e., well W4, and the identified proppant distribution is shown in Figure 139. The horizontal bars represent relative values along the slant core well. While the size of the bars indicates the relative proppant count within the samples, the color indicates the depth offset of the sampling point relative to the nearby lateral. For reference, we also highlight the perforation clusters along well W4. Various studies have reported flow bias based on monitoring of flow from perforations after hydraulic fracturing or based on fluid flow into the perforations during hydraulic fracturing (Gustavo at al., 2016; Wheaton et al., 2016).

From Figure 139, we do see some evidence of possible heel side bias in the observed proppant count distribution with the mesh 40/70 size fraction, i.e., the relative proppant count is much higher for the middle cluster compared to the toe cluster. However, this is not so clear with the mesh 100 size fraction. Slurry transport along perforated interval is governed by complex flow phenomenon. With transport efficiency issues, it can be expected that during initial phases of fracturing, most of the proppant will preferentially flow towards the toe end. However, as treatment progresses, the flow rates in the toe clusters drop causing screening out and reduced or negligible proppant transport from the toe clusters (Wu et al., 2017). As per design, the mesh 100 proppant is pumped at the very beginning of hydraulic fracturing. Its tendency to screen out is much lower compared to mesh 40/70 proppant particles due to relatively smaller size (Ngameni, 2016). Therefore, we might be seeing higher mesh 100 concentration along cluster 69 due to the initial proppant placement (Figure 139b). Another possible explanation for the apparent bias could be the decreasing lateral separation as we go from cluster 69 to cluster 70. In Figure 139a, we see higher proppant concentrations close to cluster 70 compared to the toe cluster 69. With cluster 71, the core is at a significant height above the lateral and this may have caused a lack of any significant proppant zones close to the heel side

cluster. However, based on fracture description and analysis of the actual core (Gale et al., 2018), there is still significant hydraulic fracture count observed in this part of the cored interval. Greater lateral as well as vertical coverage can provide a much more constrained solution regarding proppant distribution behavior close to the fractured clusters and stages. Thus, in future tests, the coring experiments will be appropriately designed for better coverage.

Conclusions

In this study, we highlight a comprehensive analysis of proppant particle distribution obtained from through fracture cores. We have shared a robust sample preparation and analysis workflow, which provides a means for systematic analysis of core samples for both proppant as well as natural calcite particles. Based on the identified particle counts, we developed proppant and calcite logs for the entire core. Our broad observations and conclusions follow:

- For the UWC formation, we identified significant proppant particles approximately 25 ft in vertical proximity of the nearby hydraulically fractured well (W4) at a lateral offset of approximately 80ft.
- Hydraulic and natural fracture interactions or their presence do not necessarily lead to high proppant concentration or high natural calcite concentration in the corresponding core sludge samples.
- Locally, proppant distribution in depth seems to be governed by stress contrast and changes in lithology. Consequently, the distribution is likely a function of complexity generation at layer boundaries during fracture propagation. The presence of arrest features is thought to be instrumental in allowing proppant accumulation during flow.
- Natural calcite distribution may be governed by the degree of cementation associated with the fractures along with presence of significant hydraulic fracturing nearby and their interactions. This can also result in flushing out of some of the natural calcite as the fluid moves through the fractures and sweeps and erodes any cement from the exposed fracture face.
- As we move away from the treatment well laterally, the smaller proppant size fraction (mesh 100) dominates to a significant degree. This is observed both within the UWC core (mesh 100 vs. mesh 40/ 70 distribution towards the toe end cluster) as well as in comparison with the MWC core (larger lateral offset compared with the UWC core on average).
- There may be some heel-side dominance in terms of proppant distribution along the completed stages for the UWC cored interval.

Proppant Analysis from Fracture Faces to Study Trapping and Crushing Behavior

Authors: Sara J Elliott, and Julia F. W. Gale

Summary

Since 1949 sand proppant has been used to increase efficacy of hydraulically fractured treatments by preventing fractures from closing after well depressurization, and yet many questions remain regarding the behavior and distribution of proppant in the subsurface. To this end, we quantified the amount of recovered proppant in open fractures within a slant core drilled through hydraulically fractured Wolfcamp Shale. We then addressed basic questions regarding proppant behavior in the subsurface in order to improve understanding of hydraulic fracture growth and patterns. For example, where is the proppant found; in hydraulic fractures, in reactivated natural fractures, or is it transported into drilling-induced fractures during recovery? Is there variation along the length of the examined core? Do most proppant grains remain whole or tend to get crushed? To answer these questions, we collected all material from every open fracture within ~600 ft of core (407 samples), which consisted of drilling mud, aluminum shavings from the core barrel, shale and lithic fragments, calcite, and potentially sand proppant (both plain and colored resin-coated grains) pumped during the hydraulic fracturing of adjacent wells. We then washed, sieved, weighed, and imaged all samples for quantitative image analysis. Proppant packs 0.5-1 cm thick were found in two locations where there is complex fracture geometry, but there was no evidence of proppant embedment on fracture faces. In-situ sand patches were found on a few fracture faces, mostly in fractures proximal to the big proppant packs. Pumped proppant was 40/70 and 100 mesh (149-420 µm), yet the majority of recovered proppant ranges from 63-250 µm. Retrieved samples were labeled with respect to a master fracture database where fractures were identified in the core and on CT scans of each 3 ft interval, allowing us to code them as either hydraulic fracture, natural reactivated fracture, or drilling/recovery induced fracture. From this we were able to not only quantify the amount of proppant within each fracture, but also analyze the distribution of grains among different fracture types, as well as trace base versus colored grains. Samples labeled as hydraulic fractures contain variable amounts of proppant, and the distribution of retrieved proppant, especially the larger size fractions, mirrors the proximity of the slant core to the hydraulic fracture treatment wells. Ultimately, almost all fractures contain at least some proppant in the smallest size fraction, however the extent to which this was introduced during the core drilling process is still unknown.

Introduction

Hydraulic fracture treatments use on average about 100,000 lbs. of proppant, with larger stimulations exceeding 5 million lbs. (Montgomery & Smith, 2010). Plain sand is by far the most common proppant used, although premium proppants, e.g., ceramic beads and resin-coated sands, are thought to be crushed less frequently than typical sand, so most treatments in the United States utilize a mix of proppant types (Patel et al., 2014). Investigating proppant distribution in hydraulic fracture treatments is important for understanding the propped fracture network, which is not necessarily the same as the network of fractures created, and in turn the flow behavior during flowback and production. Near-wellbore proppant detection is common practice but understanding where proppant is located farther away from the well is

also necessary for optimizing well spacing, completion design, and production. Recent advances in modeling (e.g., Dontsov & Peirce, 2015), as well as innovative techniques such as remote imaging of proppant in the subsurface using electromagnetic (EM) field data (Palisch et al., 2016; Palisch et al., 2018) have had increasing success in both predicting and determining proppant locations after treatment. However, there are still significant problems with models due to myriad assumptions about the process including Newtonian fluid, laminar flow, linear-elastic rock behavior (ignoring poro-elastic effects), and simplified fracture geometry. EM field studies require the injection of specialty, electrically conductive proppants instead of plain sand. Here, we conduct one of the first attempts at physically recovering and quantifying injected proppant from parted fracture breaks within a slant core drilled through hydraulically fractured Upper and Middle Wolfcamp Shale, in the Midland Basin, Reagan Co., West Texas. The study is part of the wider HFTS project (Courtier et al., 2018). The material collected from each open fracture consists of oil-based drilling mud, aluminum shavings from the core barrel, shale fragments, calcite and other lithic particles, and potentially base and colored proppant that was pumped during the hydraulic fracturing of adjacent wells. In addition to quantifying the total amount of proppant present in each fracture, we have semi-quantitatively analyzed the amount of base (plain sand) versus colored resin-coated sand grains to diagnose the pumping stage linked to specific fractures. We note that a separate discussion on proppant distribution using core barrel scrapings has been discussed in the previous section.

Methods

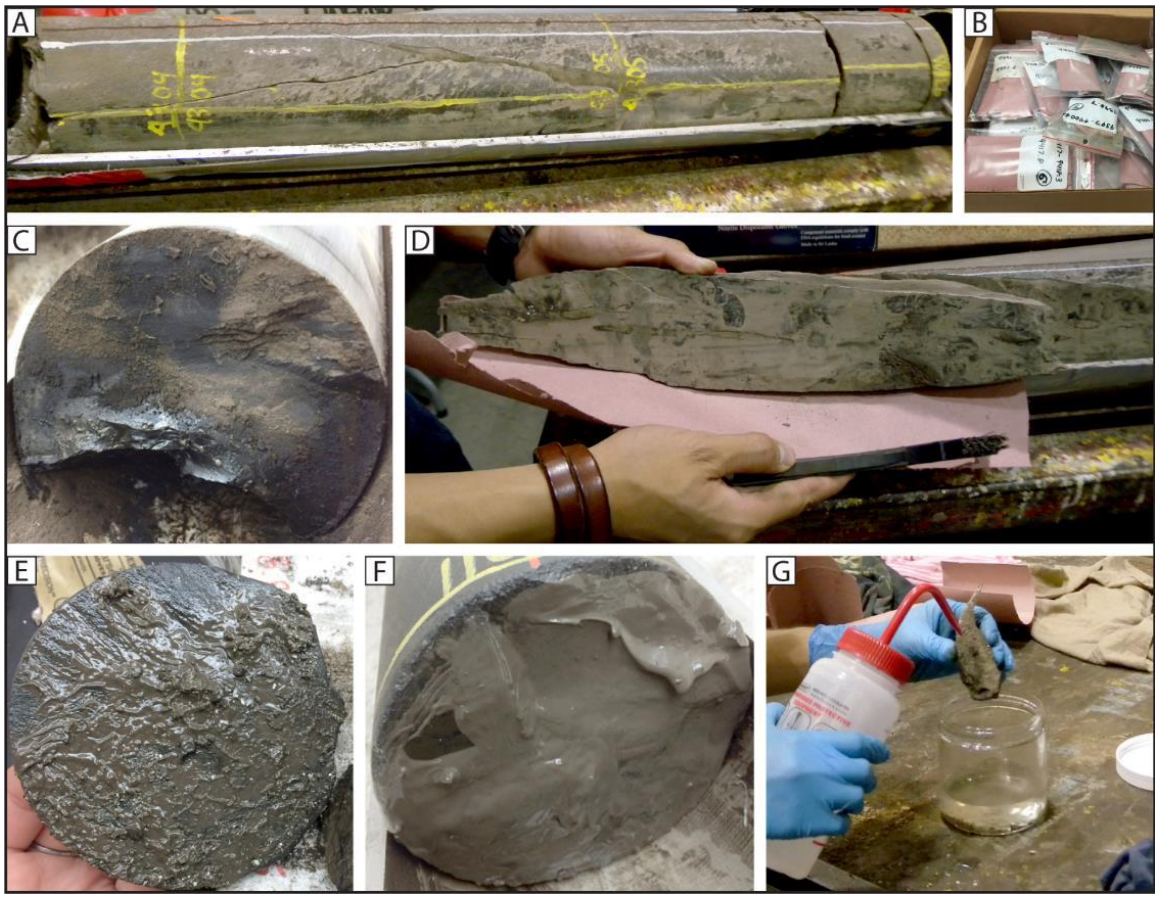


Figure 140: Fracture face sample collection from core. (A) Example 3 ft interval of core before sampling. (B) Samples bagged to be transported to Bureau of Economic Geology labs. (C) Example of a dry fracture face. (D) Brushing method of dry fracture faces using paper and brushes. (E-F) Example of rough and/or wet fracture faces that were either scraped with heavy duty paper or rinsed with water into jars (G).

Depending on the fracture surface features (planar, curviplanar or irregular with twist hackles, arrest lines etc.) and the amount of drilling mud present, we either scraped the fracture faces with durable construction paper, or washed all material into bags or jars to be brought back to UT-BEG labs for processing (Figure 140). A master fracture database for all 600 ft of core (in six core segments) is described by Gale et al. (2018) and we used this to code all proppant samples based on fracture type; hydraulic, natural reactivated, or drilling-/recovery-induced fracture.



Figure 141: Cleaning and sieving of fracture face samples. (A-C) Bagged and jarred samples were rinsed into a detergent bath and cleaned with paint bushes. (D-E) When no oily mud remained, samples were wet-sieved into 4 size fractions: >500 µm, 250-500 µm, 120-250 µm, and 63-120 µm. (F-G) Fractionated samples were then put into separate containers where excess water, clumps of paper fibers, and floating aluminum shavings were removed with a pipette, followed by air-drying.

Samples were put through a vigorous washing process to remove drilling mud (Figure 141). Each sample bag or jar was thoroughly rinsed with water into a detergent bath, and then was stirred with a soft-bristled paint brush to physically clean the material. For many samples this process was repeated multiple times until no apparent traces of oily mud remained. Samples were then thoroughly rinsed to remove soap and wet-sieved into 4 size fractions: >500 µm, 250-500 µm, 120-250 µm, and 63-120 µm, with all material <63 µm removed. After separation by sizes, a pipette was used to remove excess water, clumps of paper fibers, and floating aluminum shavings, and then the samples were left to air dry.

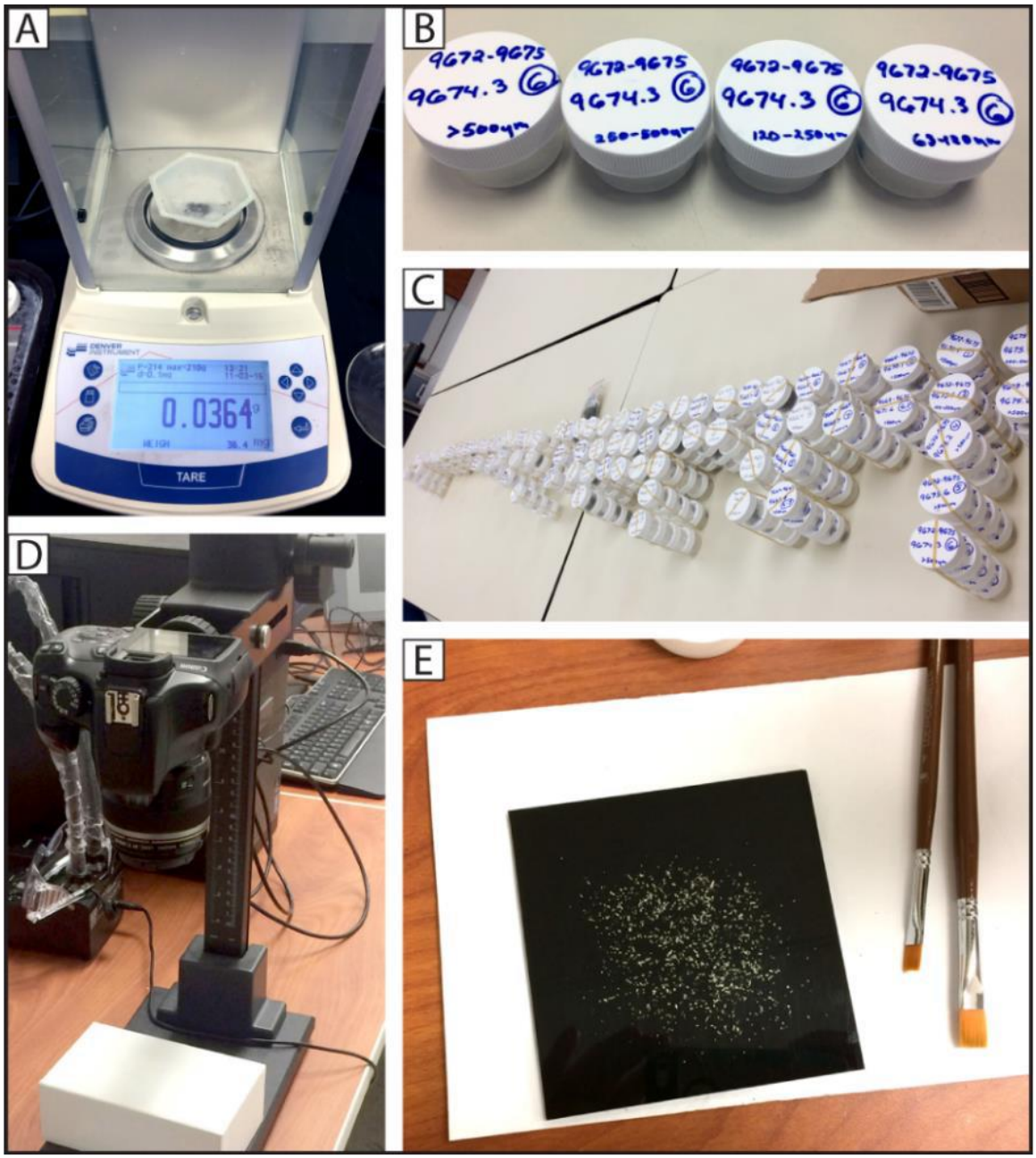


Figure 142: Weighing and imaging of fracture face samples. (A-C) Each fractionated size was weighed on a high-precision balance and then put into labeled tubs. (D-E) Samples were laid out in monolayers on a black background to be imaged with a macro lens attached to a mounted DSLR camera.

When dry, each size fraction of each sample was weighed on a high-precision balance scale. All material was then imaged in monolayers on a black background using a DSLR macro lens in order to capture such small particles at full resolution (Figure 142). The digital camera settings

were such that darker material like shale fragments blended into background, while lighter sand, calcite, and aluminum appear bright. This step results in 0-45 images per fraction per sample. Images were first prepared in two different ways using Photoshop® levels (Figure 143). The first preparation was for total particle counts, where white and midtone levels were brightened till all particles were visible. The second preparation was for proppant counts only, so the white level was brightened until proppant stood out, and the black level was darkened until most other material disappeared into background. This made image thresholding easier and accurate.

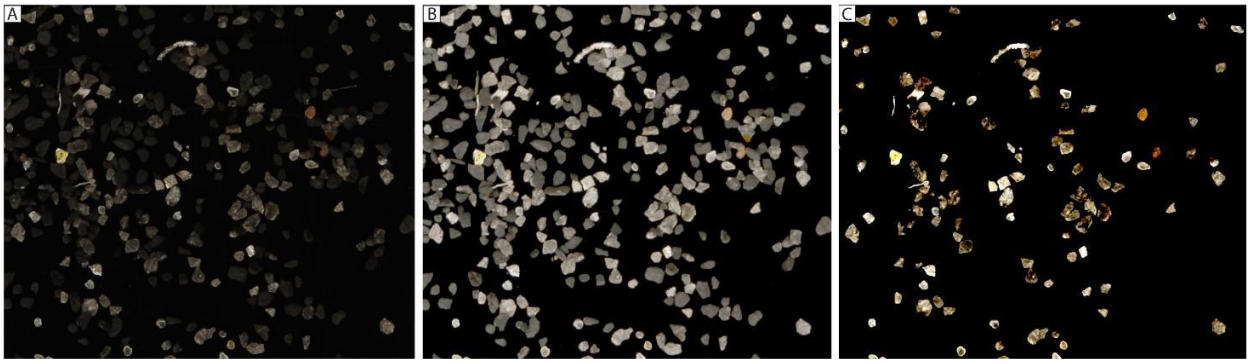


Figure 143: Photoshop image preparation. (A) Original image from DSLR. (B) Modified image with all particles lightened for total count. (C) Modified image with darker particles removed and proppant, calcite, and/or aluminum highlighted.

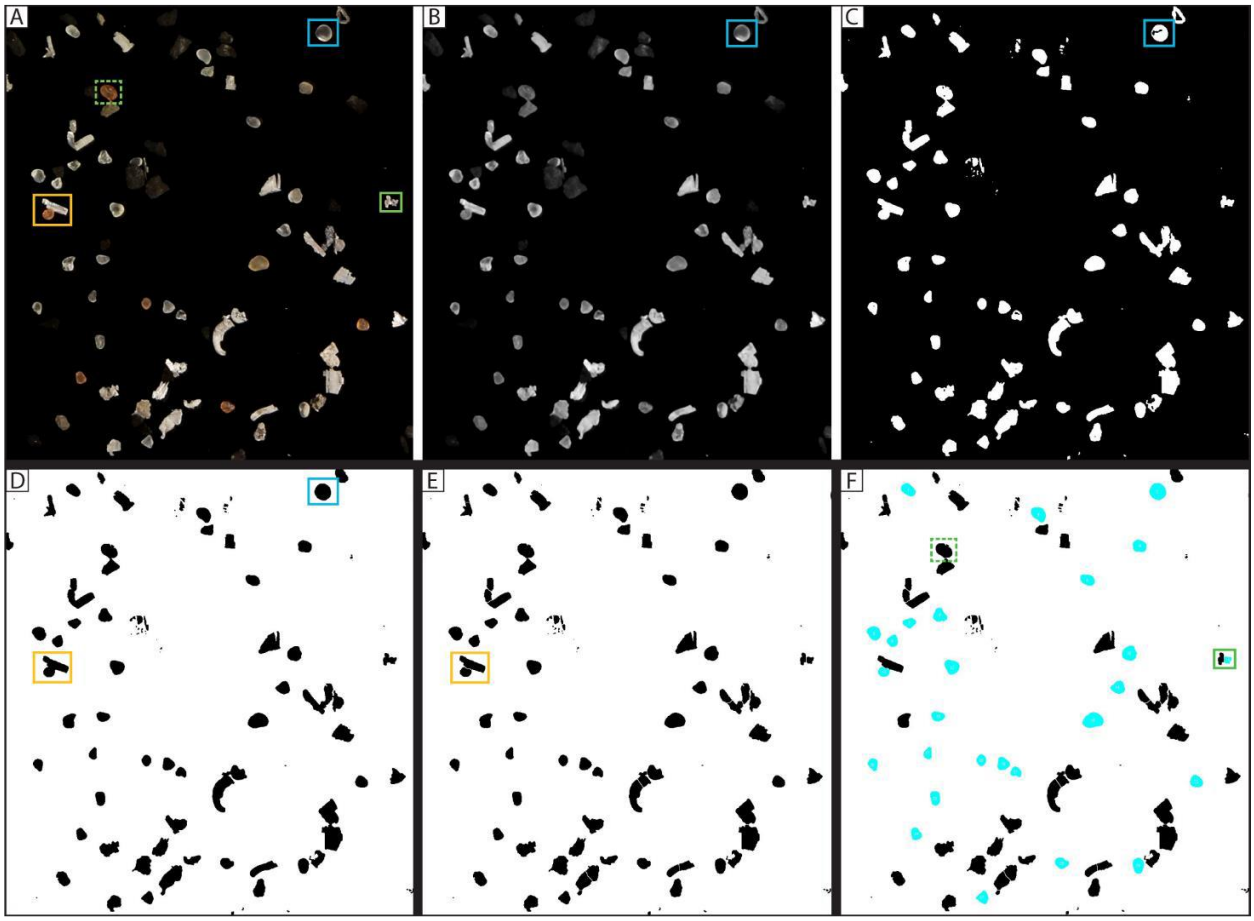


Figure 144: Image analysis protocol, depth 9,487.9, 250-500 µm size fraction. (A) Sample image contains base and red proppant, shale, and aluminum. (B) Conversion to 8-bit with a 2 px median smoothing. (C) Thresholding of bright particles only, ignoring shale. (D) LUT inversion with holes filled. Blue box from A-D shows example of proppant with darker interior and bright perimeter needing infill after thresholding. (E) Watershed algorithm applied to touching

particles. Orange box in D shows proppant touching aluminum, which is then separated in E. (F) Proppant counts based on circularity, which exclude angular calcite and elongate aluminum. Green boxes in A and F show automation error which counted a piece of aluminum (solid box) and excluded a red proppant (dashed box). In larger size fractions error is negligible, whereas in smaller size fractions error is ~5% underestimated by automation.

Image analysis was performed using FIJI® to determine both total material present and abundance of proppant in each size fraction within each fracture sample.

Image analysis protocol (Figure 144) for proppant counts consisted of:

- Changing each image to 8-bit and applying a median smoothing filter dependent on edge pixel size (1 px for 63-120 µm and 120-250 µm, 2 px for 250-500 µm, and 3 px for >500 µm).
- Conservatively thresholding the image to only capture bright particles and then inverting the LUT so particles were black on a white background.
- Applying the "fill holes" action because proppant tended to have a darker interior and brighter perimeter.
- Applying a Watershed algorithm to separate borders of touching particles.
- Setting "analyze particles" parameters to only count particles of a certain size (pixel2, depending on the size fraction) and circularity (0.83-0.90, also depending on the sizes being analyzed) to exclude angular calcite and elongated aluminum, and then applying a "count mask" to the image to get a minimum proppant count.

For total particle counts, protocol was the same except the images were thresholded to include all visible particles, rather than only bright objects. To estimate error, manual counting of proppant grains was compared to the automated analysis, and for the 250-500 µm and >500 µm sizes the error is negligible, whereas for the two smaller size fractions the error is ~5%, resulting in a minimum estimate of proppant abundance by automated counting.

Results & Discussion

While collecting samples from the core, the occurrence of any in situ sand patches, colored grains, and thick proppant packs was noted. We saw no evidence of embedment (dimpling) on fracture faces, however, proppant packs 0.5-1 cm thick were found in two locations with complex fracture geometry (Figure 145A), and a few other fractures contained undisturbed sand patches on the fracture face (Figure 145B). The lack of drilling mud in these fractures reinforces our interpretation that the sand was in place in the subsurface prior to drilling. All proppant packs/patches were found in the Upper Wolfcamp cores. Between cores 5 and 6 in the Middle Wolfcamp, a large proppant pack was encountered, the drilling rig jammed, and 5% sand was observed in mud loggers' samples. We interpret this to have been a proppant pack in a fracture, but it was not preserved because there is 5 ft of missing core between Cores 5 and 6 where it would have been located.

Pumped proppant was 40/70 and 100 mesh (149-420 µm), yet the majority of recovered proppant is in the two smallest size fractions, especially the 63-120 µm. Originally, we hypothesized that the size discrepancy between pumped and recovered proppant could be due to widespread grain crushing of the larger sand within the subsurface, but inspection of the smallest size fraction from samples indicates that this is not necessarily the case. Some grain crushing is observed, but the majority of small proppant recovered is rounded (Figure

146). Thus, it appears that most of the recovered proppant is 100 mesh base, possibly because the pumped proppant contained a much larger size range than was indicated by the standard mesh size.

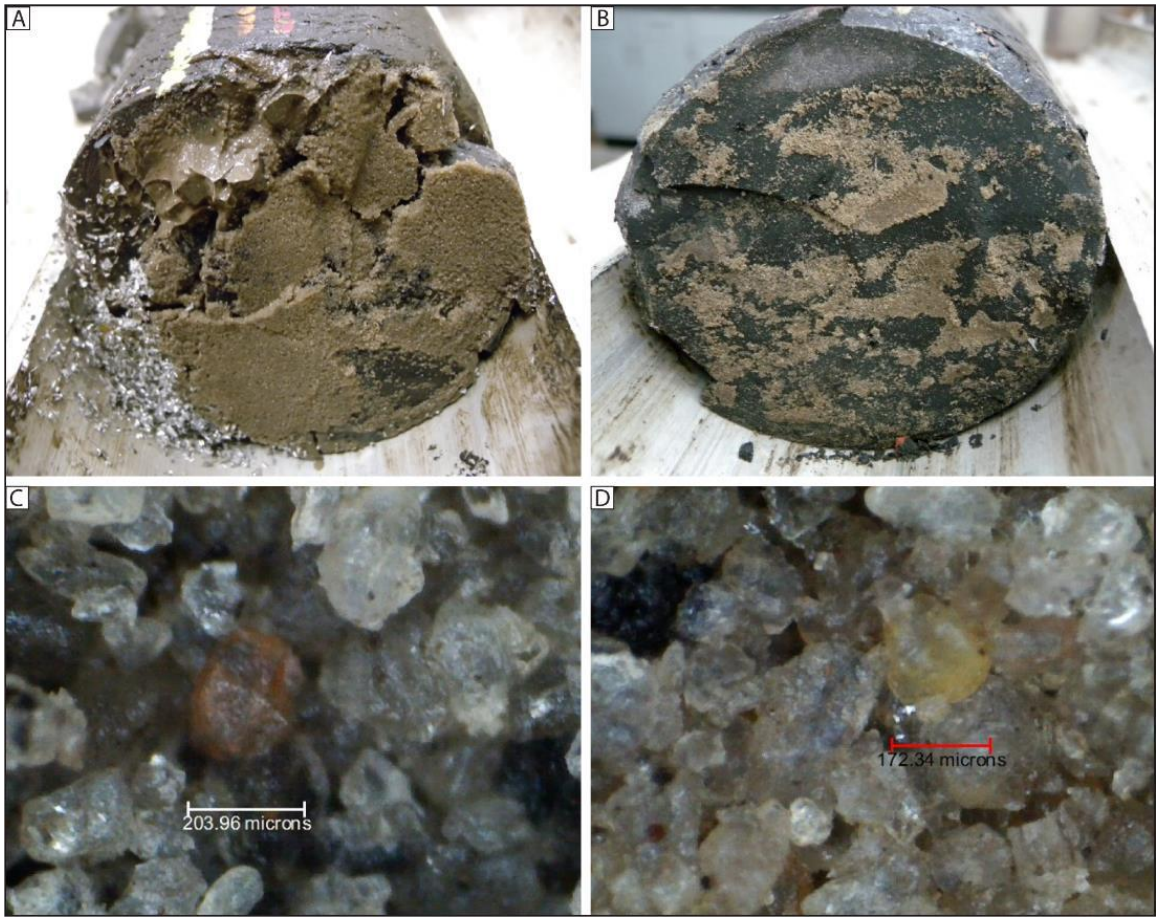


Figure 145: (A) Complex hydraulic fracture with 1 cm sand pack and (B) hydraulic fracture with thinner sand patches. (C) Base along with potential red proppant and (D) potential yellow proppant measured in situ before sample collection.

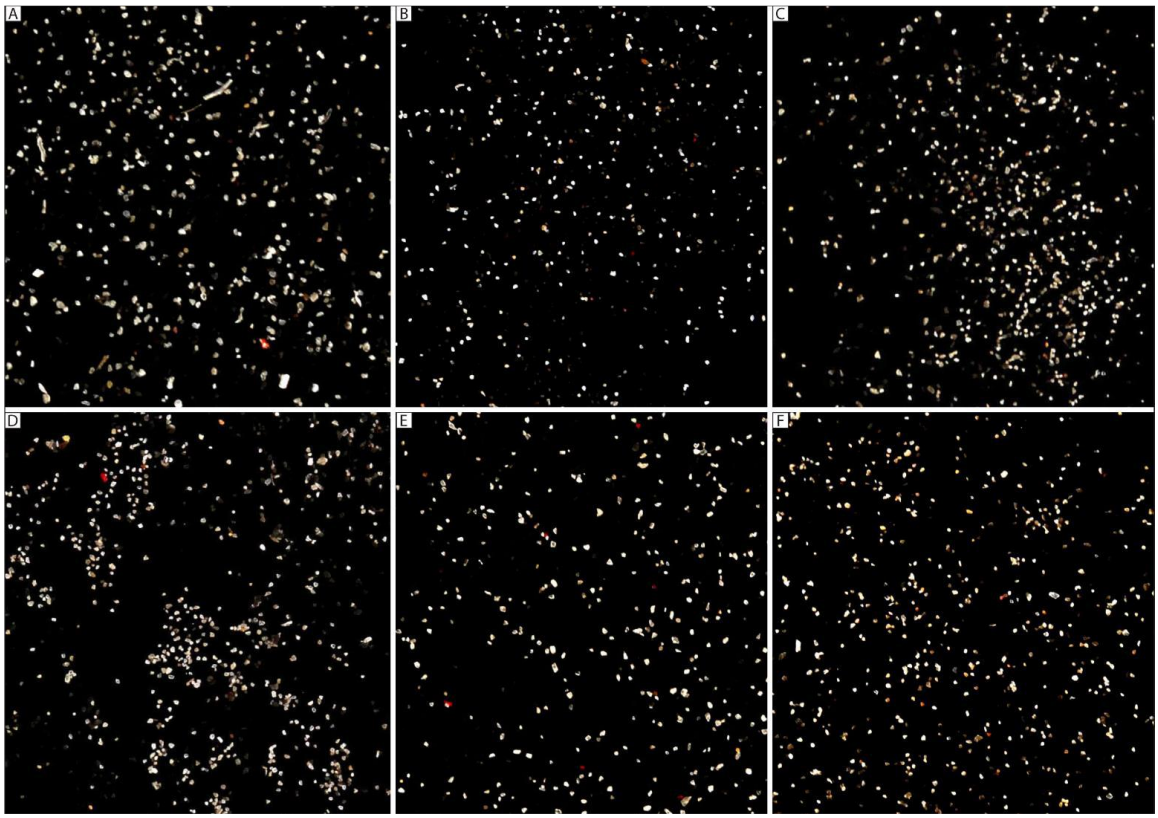


Figure 146: Randomly chosen examples of 63-120 µm, we observe rounded particles across all 6 core examples highlighted showing minimal grain crushing. Upper Wolfcamp: (A) 9,380.2 ft, (B) 9,478.2 ft, (C) 9,514.9 ft, & (D) 9,709.7 ft. Middle Wolfcamp: (E) 11,534.1 ft & (F) 11,661.4 ft.

Furthermore, some of the pumped 40/70 mesh included grains coated in colored resins. Different colors had been pumped in different stages in the adjacent wells. We noted all recovered colored grains (red, yellow, green, and blue) to diagnose the pumping stage linked to specific fractures. However, there are some significant challenges with diagnosing colored versus base proppant, and so this aspect of the project was done in a semi-quantitative manner only.

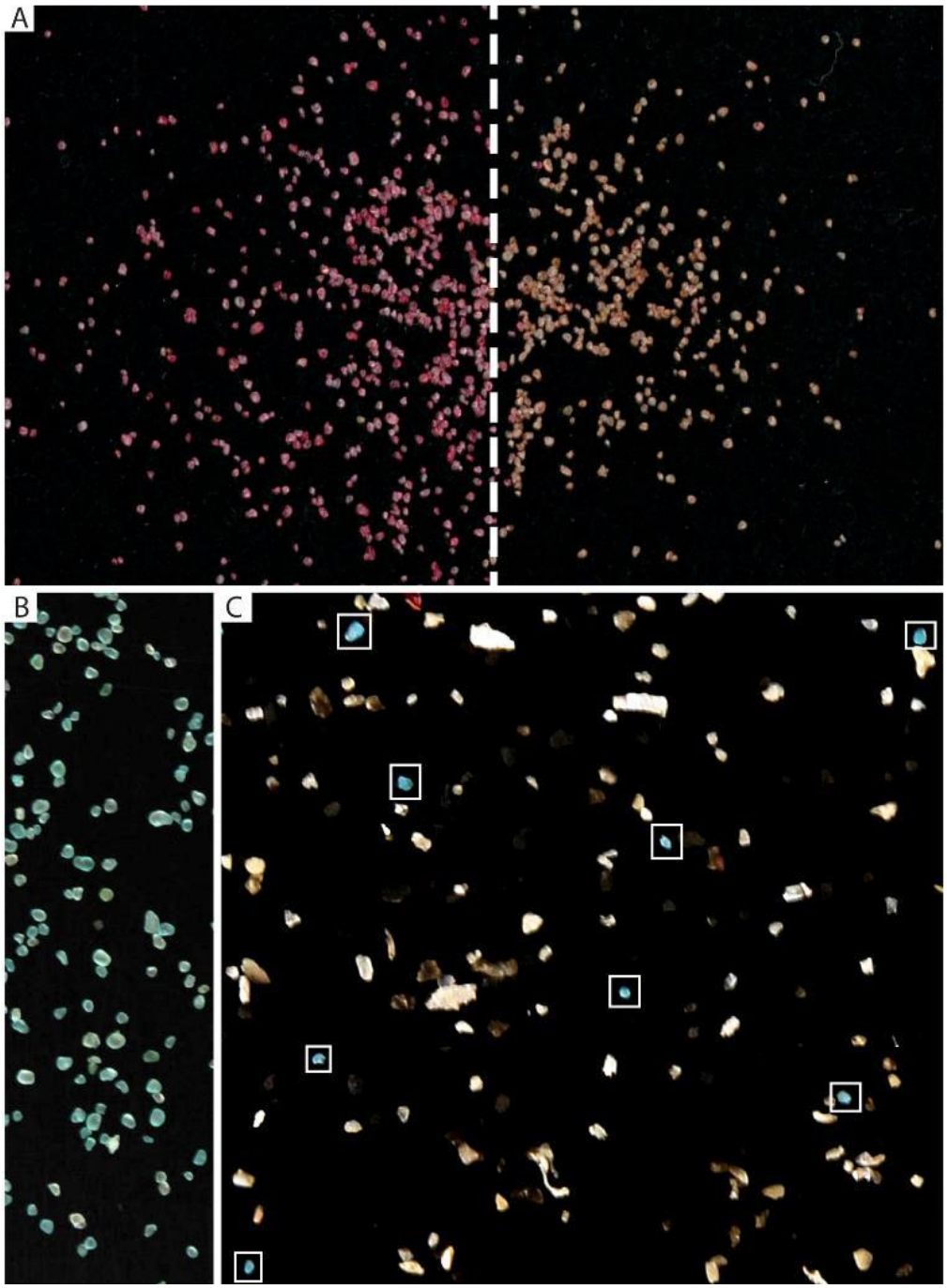


Figure 147: Examples of resin-coated sand changing colors due to high temperatures and pressures. (A) Red resin-coated sand before autoclaving (left) and after (right). (B) Fresh blue resin-coated proppant imaged with a macro lens. (C) Blue proppant recovered from fracture face at 11,683.6 ft has a more sky-blue appearance versus the greenish tinge of the unpumped blue proppant from (B).

Problems for interpreting the colored particles include:

- There are pink and yellow grains within the 100-mesh base. SEM EDS (elemental X-ray energy dispersive spectroscopy) revealed that many of the 100 mesh base grains have Fe-oxide deposits on the surface giving them a reddish or yellowish color.
- In a separate study (GTI sludge analysis, Maity et al., 2018) autoclaving of fresh red resin-coated proppant in the lab showed that under high pressure-temperature conditions, the resin itself changes color to a more orange/yellow hue (Figure 147A). This pronounced temperature effect was consistently observed over multiple sample

tests. Based on these results, we can assume the other pumped colors changed in hue from fresh as well.

For these reasons, colored proppant within the imaged samples was categorized as either base, red, yellow, blue, or green, where blue likely included some green grains and vice versa, and some of the oxidized base grains were potentially counted as red or yellow and vice versa. Colored proppant was manually visually estimated in a very conservative manner from each image, giving the minimum estimate of any colored proppant found (Figure 148). The blue/green proppant occurs in discreet fracture samples; however, the red and yellow proppant are usually found together in the smallest size fraction of almost every sample indicating potential mixing within the core barrels.

Conclusions

A total of 407 fracture faces were sampled along ~600 ft of slant core retrieved from hydraulically fractured Upper and Middle Wolfcamp Formation. Retrieved samples were labeled with respect to the fracture descriptions and coded according to fracture type: hydraulic fracture, natural reactivated fracture, or drilling/recovery induced fracture. From this we were able to not only quantify the amount of proppant within each fracture, but also analyze the distribution of grains among different fracture types. Samples labeled as hydraulic fractures contain variable amounts of proppant, and the distribution of retrieved proppant, especially the larger size fractions, mirrors the proximity of the slant core to the hydraulic fracture treatment wells. Proppant packs 0.5-1 cm thick were found in 2 hydraulic fracture locations with complex fracture geometry in the Upper Wolfcamp, and a few other fractures had in situ sand patches on fracture faces. These tended to occur near proppant packs.

Increased proppant abundance was also found near the end of Core 5/beginning of Core 6 in the Middle Wolfcamp where a large proppant pack was encountered when drilling but was not recovered in the core. Thus, persistent proppant accumulation seems determined by the complexity of the fracture(s), e.g., the amount of arrest features present. Pumped proppant was 40/70 (base and colored) and 100 mesh (149-420 µm), yet the majority of recovered proppant is in the 63-120 µm and 120-250 µm fractions. Proppant grains in the two larger size ranges are mostly found in and around the proppant packs, as well as where the slant core came closest to the treatment wells. Image analysis has low error versus manual counting, so it is a viable method for analyzing the particles recovered. Ultimately, all sampled fractures contain at least some proppant, however the extent to which the proppant (especially the smallest size fraction) was introduced during the core drilling process is unknown. This is one of the first attempts at physically recovering and quantifying injected proppant from parted fracture breaks within a stimulated reservoir, and the results are significant in terms of understanding and predicting future proppant distribution during hydraulic fracturing.

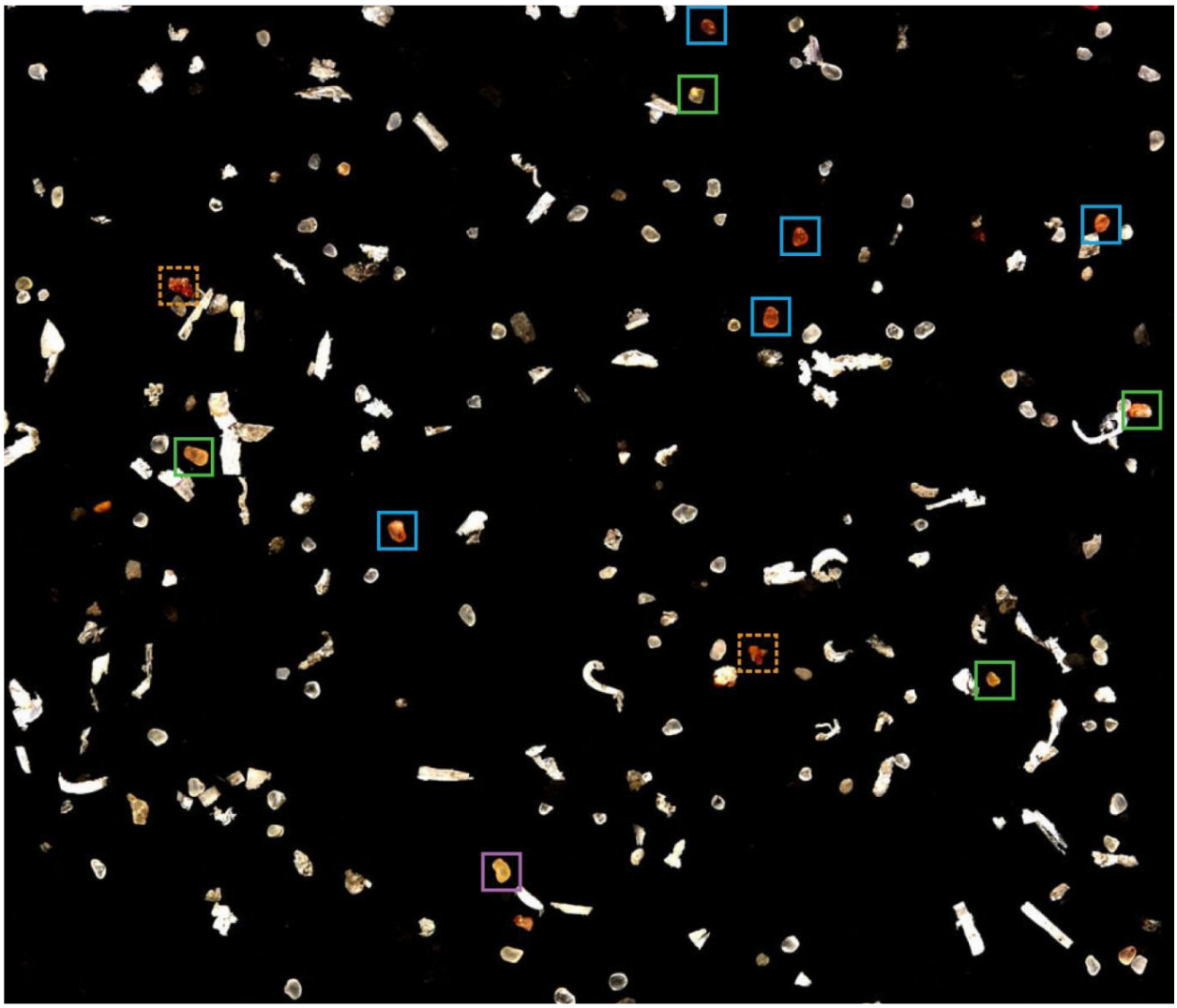


Figure 148: Part of 250-500 µm image from depth 9485.9 illustrating difficulty of characterizing colored proppant after retrieval from the subsurface. Clear-to-white base proppant is abundant and obvious. Blue boxes are red proppant. Purple box is yellow proppant. Green boxes are grains that could be either oxidized base, faded red or yellow proppant. Dashed orange boxes are examples of other colored particles found within samples that are not proppant.

Well Interference Diagnosis through Integrated Analysis of Tracer and Pressure Interference Tests

Authors: Ashish Kumar, Puneet Seth, Kaustubh Shrivastava, Ripudaman Manchanda, and Mukul M Sharma

Abstract

In ultra-low permeability reservoirs, communication between wells through connected fractures can be observed through tracer and pressure interference tests. Understanding the connectivity between fractured horizontal wells in a multi-well pad is important for infill well drilling and parent-child well interactions. Inter-well tracer and pressure interference tests involve two or more fractured horizontal wells and provide information about hydraulic fracture connectivity between the wells. In this work, we present a workflow based on combining the analysis of tracer and pressure interference data to obtain the degree of interference between fractured horizontal wells in a multi-well pad.

We analyze well interference using tracer (chemical tracer and radioactive proppant tracer) and pressure data in an 11-well pad in the Permian Basin. Changes in pressure and tracer concentration in the monitor wells were used to identify and evaluate interference between the source and monitor wells. Extremely low tracer recovery and weak pressure response signify the absence of connected fractures and suggest that interference through matrix alone is insignificant. Combined tracer and pressure interference data suggest connected fracture pathways between the communicating wells. The degree of interference can be estimated in terms of pressure response times and tracer recovery. An effective reservoir model was used to simulate pressure interference between wells during production. Simulation results indicate that well interference observed during production is primarily due to hydraulically connected fractures.

Combined tracer and pressure interference analysis provides a unique tool for understanding the time dependent connectivity between communicating wells, which can be useful for optimizing infill well drilling, well spacing and fracture sizing in future treatment designs.

Introduction

In conventional reservoirs, well interference tests have been widely used to gather information about inter-well communication and reservoir permeability. In such high permeability reservoirs, well interference has been well studied and is based on pressure diffusion in the reservoir. However, in unconventional reservoirs, due to the ultra-low permeability of the reservoir, pressure diffusion through the reservoir rock is negligible as compared to the elastic response and pressure diffusion through the fracture network. This renders traditional well interference techniques based on pressure diffusion through the reservoir inapplicable.

Horizontal wells drilled in ultra-low permeability reservoirs need to be hydraulically fractured to be economical. Hydraulic fracturing is generally done in multiple stages along the length of the horizontal portion of the well. Over the years, the size of these fracture treatments has increased substantially. Massive hydraulic fracturing treatments are being pumped to increase the productivity from these ultra-low permeability reservoirs. An increase in the amount of fluid and proppant pumped will lead to the creation of longer fractures. In the presence of

natural fractures these hydraulic fractures can form complex fracture networks (Fisher et al., 2002; Weng et al., 2011; Shrivastava & Sharma, 2018). In a multi-well pad, the hydraulic fracture network of a well can intersect with networks from other wells resulting in frac-hits (Sardinha et al., 2014). With increasing size of frac jobs and the size of the created fractures, the probability of interaction between multiple wells has increased. Wells in a pad are more likely to be connected through a hydraulically conductive fracture pathway. These conductive fracture pathways can lead to interference between wells and can be diagnosed using data collected in the field. Chemical tracer, RA tracer, microseismic data and pressure data are the most common forms of data that can help in detecting the interference between wells.

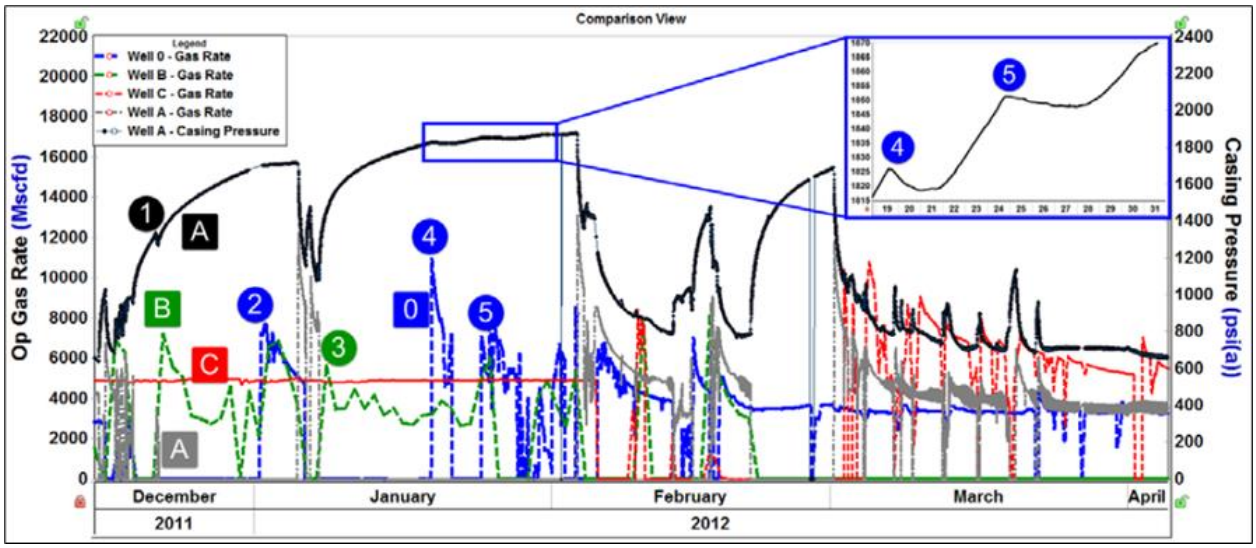


Figure 149: Pressure interference between Well 0 and well A, no interference between Well 0 and Well B (Awada et al., 2015)

Pressure interference tests in fractured horizontal wells have been used to understand the interference between wells (Sardinha et al., 2014; Awada et al., 2015; Dawson & Kampfer, 2016; Roussel & Agrawal, 2017). These tests involve two or more fractured horizontal wells (source and monitor wells) and provide information about hydraulic fracture connectivity (or lack thereof) between the wells. Pressure interference tests during production involve monitoring the pressure changes at the monitor well in response to rate changes at the source well. If sudden rate changes (shut-ins or restarts) in the source well cause a change in the pressure profile of the monitor well, we can infer that the source and monitor well are interfering as shown in Figure 149 (Awada et al., 2015).

Fracture connectivity between wells is reflected in fluid and tracer transport in a fractured reservoir. Chemical fluid tracers have been used to evaluate the extent of fracture communication with offset wells (Mulkern et al., 2010), estimating fracture volume between well pairs (Leong et al., 2015), and diagnosing fracture wellbore connectivity (Kumar & Sharma, 2018). However, fracture connectivity can change due to fracture closure because of in-situ stress changes during flowback and production (Seth et al., 2018). Due to fracture closure over time, well interference is time dependent and only analyzing fluid tracer can lead to erroneous conclusions. Fracture connectivity is a function of proppant distribution during stimulation. Radioactive proppant tracers (sand coated with radioactive materials) can provide information about the proppant distribution around wellbores (Liang et al., 2016). Combining fluid tracer

data with proppant tracer data provides useful information on fracture connectivity between wells.

Tracer communication, both chemical and radioactive, was used to diagnose the interference between fractured horizontal wells (Manchanda et al., 2014). In their study, Manchanda et al. (2014) describe a scenario in which the tracer communication between two wells is observed. Their analysis concludes that the tracer travels between two wells and is observed in the wells but is not observed in a well in the middle. They conclude that this is caused by the sequencing of fractures in the pad (Manchanda & Sharma, 2013). Zipper fracturing the two wells causes the tracer to migrate via open fracture networks and hence is not observed in the middle well since the network of fractures in the middle well closed over time. This impact of stimulation sequence and the extent, onset and duration of interference observed is discussed in more detail in this work using a new data set obtained at the Hydraulic Fracturing Test Site (HFTS).

Field Information, Observations and Analysis

At the HFTS, chemical fluid tracer, radioactive proppant tracer and pressure interference data was collected by Laredo Petroleum for 11-wells in the Permian Basin.

Well Configuration and Stimulation Sequence:

The well configuration is shown below using a gun-barrel view (Figure 150). The upper layer (Upper Wolfcamp) comprises six wells (UWC1-UWC6) separated by 660 ft and the lower layer (Middle Wolfcamp) has 5 wells (MWC1-MWC5) spaced 660 ft apart. The vertical distance between the UWC and MWC layers is 325 ft, and the wells in the lower layer are chevroned 330 ft horizontally offset to UWC wells. The well stimulation sequence is shown in Figure 151. The 8 wells were zipper fractured in pairs. The remaining 3 wells were zipper fractured as a triplet. The text under the arrows represents the order of stimulation with ZF-1 being the first well-pair stimulated and ZF-5 being the last. More information about the wells can be found in Courtier et al. (2017).

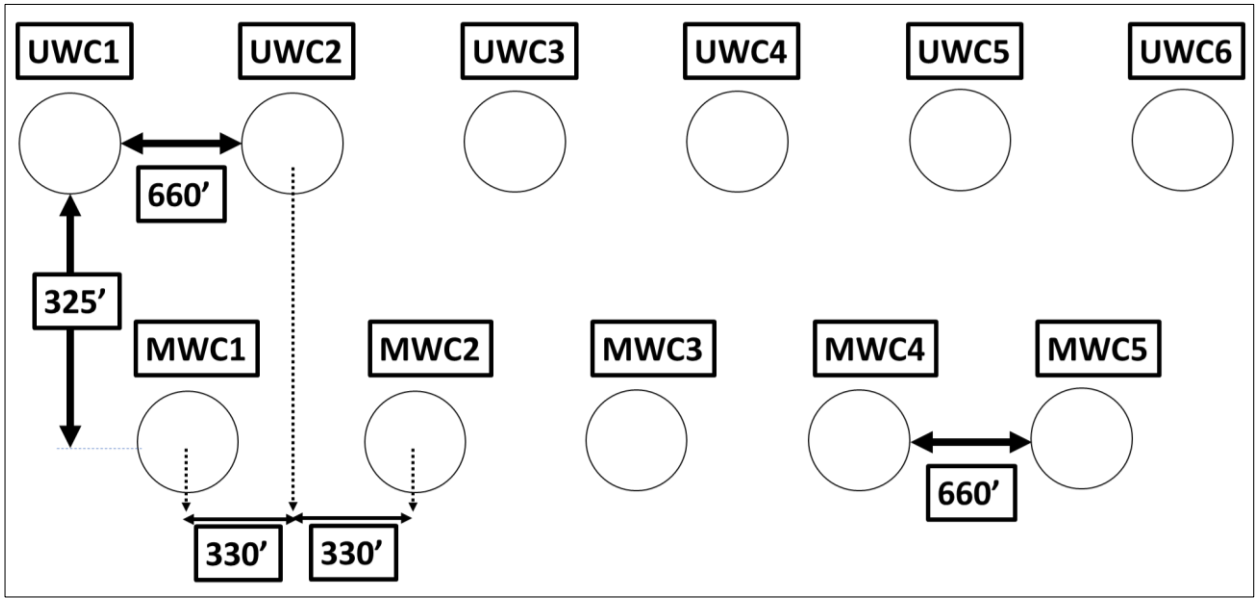


Figure 150: Well configuration showing UWC and MWC wells (circles) using gun-barrel view. MWC wells are 325 ft deeper and chevroned 330 ft horizontally offset to UWC wells.

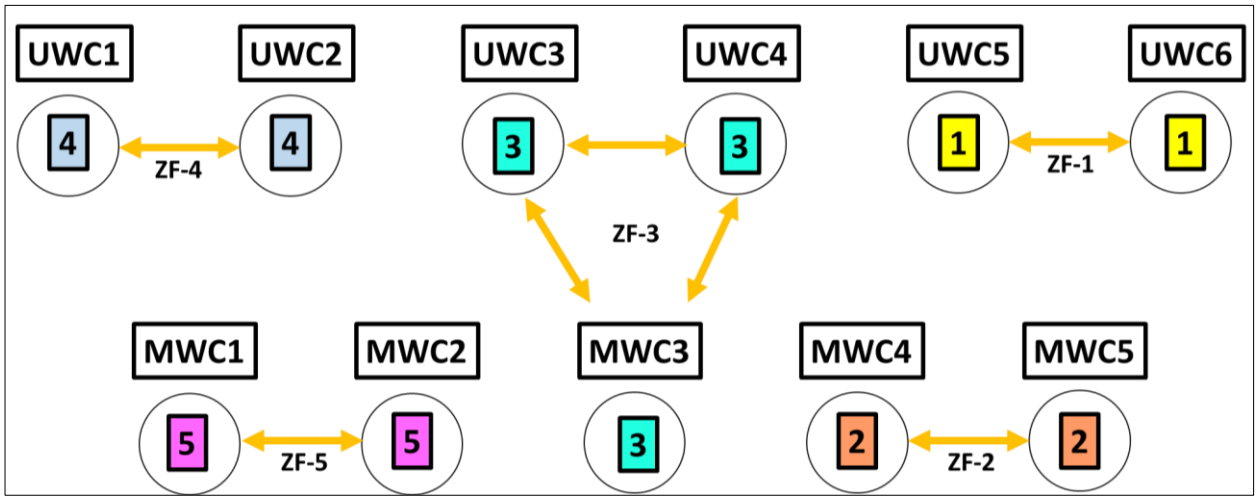


Figure 151: Well stimulation sequence, ZF denotes zipper fracturing.

Fluid Tracer Test Analysis:

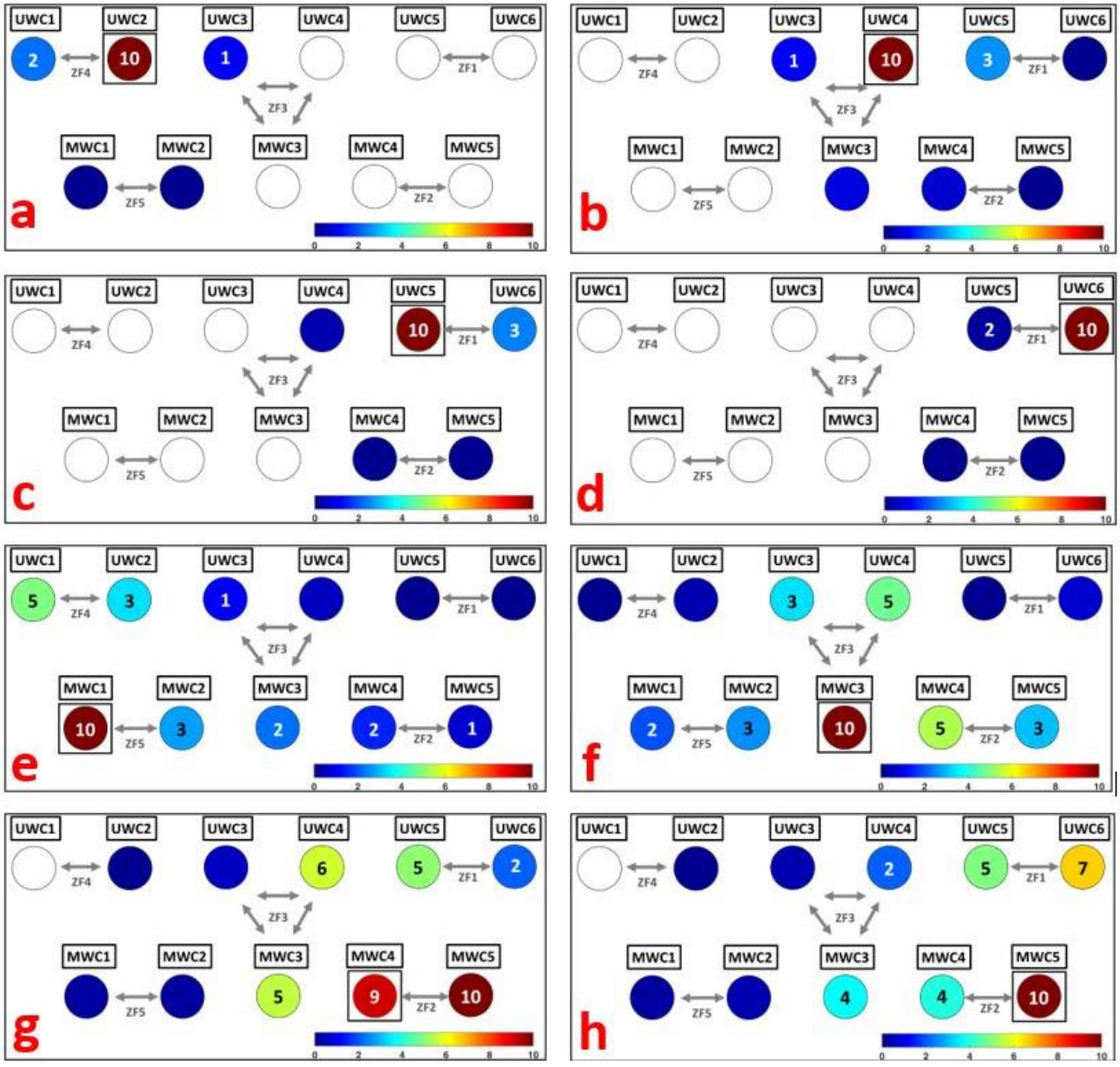


Figure 152: Water soluble chemical tracer analysis during flowback/production. Each sub-figure represents an inter-well tracer test with tracer injected in a well (enclosed by a square) and observed at all wells. The numbers on the well (and the color) represents the normalized tracer concentration at that well (high numbers indicate more tracer observed).

Water soluble chemical fluid tracers were injected in 8 of the 11 wells. All stages in a well were clubbed and divided into three/four zones, and a unique tracer was injected in each zone. Tracer injected at a well can be observed at other offset wells, and the concentration of each tracer was monitored versus time at all wells. We computed the average tracer concentration at each well during the first three months of flowback/production. This average tracer concentration at each well was normalized on a scale of integer values (0 to 10) based on the minimum and maximum tracer concentration observed. Figure 152 shows a summary of these averaged fluid tracer results for all wells using a gun-barrel view. Each sub-figure represents an inter-well tracer test for a specific tracer injected in a well (enclosed by a square) and normalized tracer concentration observed at all the wells. The numbers (and the color) on the well represent the normalized tracer concentration at that well during flowback. White color at a well represents that the tracer was not recovered at that well.

Important observations based on fluid tracer analysis:

- Tracer injected at well UWC4 has a higher concentration at wells UWC5, UWC6, MWC4, MWC5 as compared to wells UWC1, UWC2, MWC1 and MWC2 (Figure 152b). Similar examples are shown for tracer injected at well UWC5 (Figure 152c) and MWC3 (Figure 152f). These observations suggest that more fluid tracer is recovered from previously fractured wells. This is because fluid travels easily through the preexisting fracture network from previous stimulations. In certain cases, connectivity between all previously fractured wells is observed (Figure 152e). This indicates that the previously created fracture network can extend thousands of feet away from the wellbore, at least during the early life of the well.
- It is also observed that zipper fractured wells show better tracer communication. This may be since the time between two successive fractures created in the two zippered wells is short and the induced unpropped fractures have not closed over this short time. These zipper fractured wells can potentially create comingled fracture networks. This network can allow chemical tracer to travel between the zippered wells.

Proppant Tracer (Radioactive Tracer) Tests Analysis:

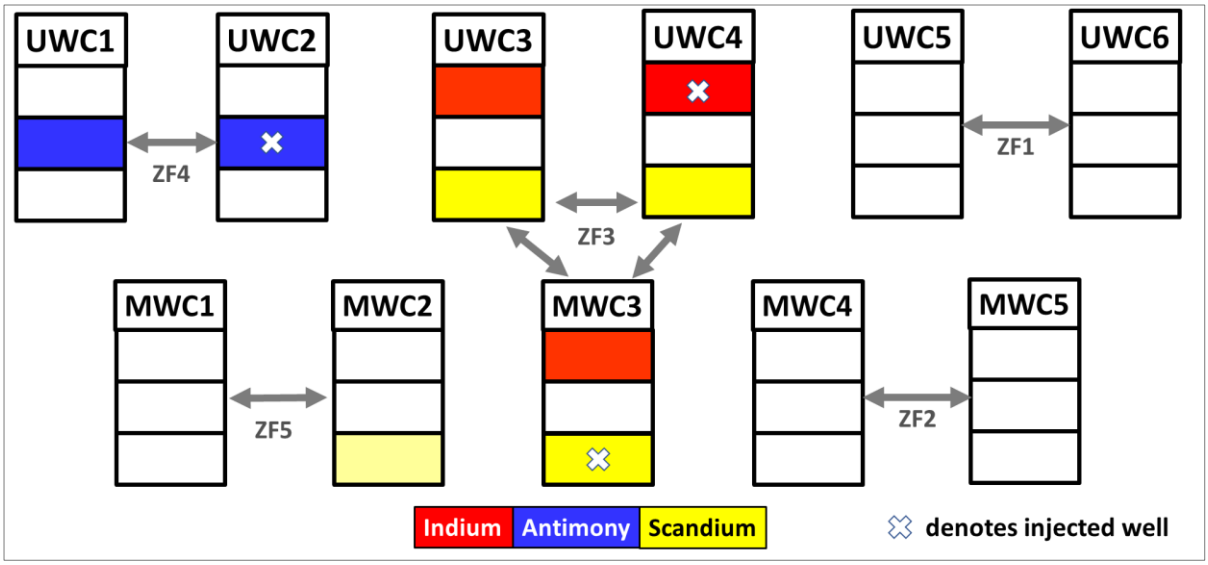


Figure 153: Proppant communication between wells based on radioactive tracer (Red: Indium; Blue: Antimony; Yellow: Scandium) presence at each well. Cross mark denotes the well where the RA tracer was injected.

Radioactive (RA) tracers were pumped in wells UWC2, UWC4 and MWC3. These wells along with offset wells were logged to determine the proppant distribution around the wells. Figure 153 shows the RA tracer distribution at each well. Red, blue and yellow colors represent Indium, Antimony, and Scandium RA tracers respectively.

Important observations based on RA tracer analysis:

- RA tracers have a higher propensity to stay close to the wellbore as compared to fluid tracer. This is because RA tracers are tagged on the proppant and proppant generally does not travel as far as the fluid.
- Wells that are zipper fractured show better communication than adjacent wells that were previously fractured. We postulate that this is due to the time dependent closure of induced unpropped fractures (Manchanda et al., 2014). For example, Well UWC3 was fractured and shut-in for ~15 days before UWC2-UWC1 were zipper fractured. The RA tracer from well UWC2 did not show up near well UWC3 because the fracture network created by the stimulation of well UWC3 had probably closed before the stimulation of well UWC2 was started.
- During the zipper fracturing of wells UWC-3, UWC-4, and MWC-3 we see that the proppant tracer injected in MWC3 is observed in UWC3 and UWC4. This indicates transport of proppant between the Middle Wolfcamp and Upper Wolfcamp during fracturing and suggests that the frac barrier between the two formations is ineffective in containing fractures created in the middle Wolfcamp wells.
- Proppant tracer from previous stimulations is observed in newly stimulated wells. This indicates the creation of at least a few long, dominant fractures.

Pressure Interference Tests Analysis:

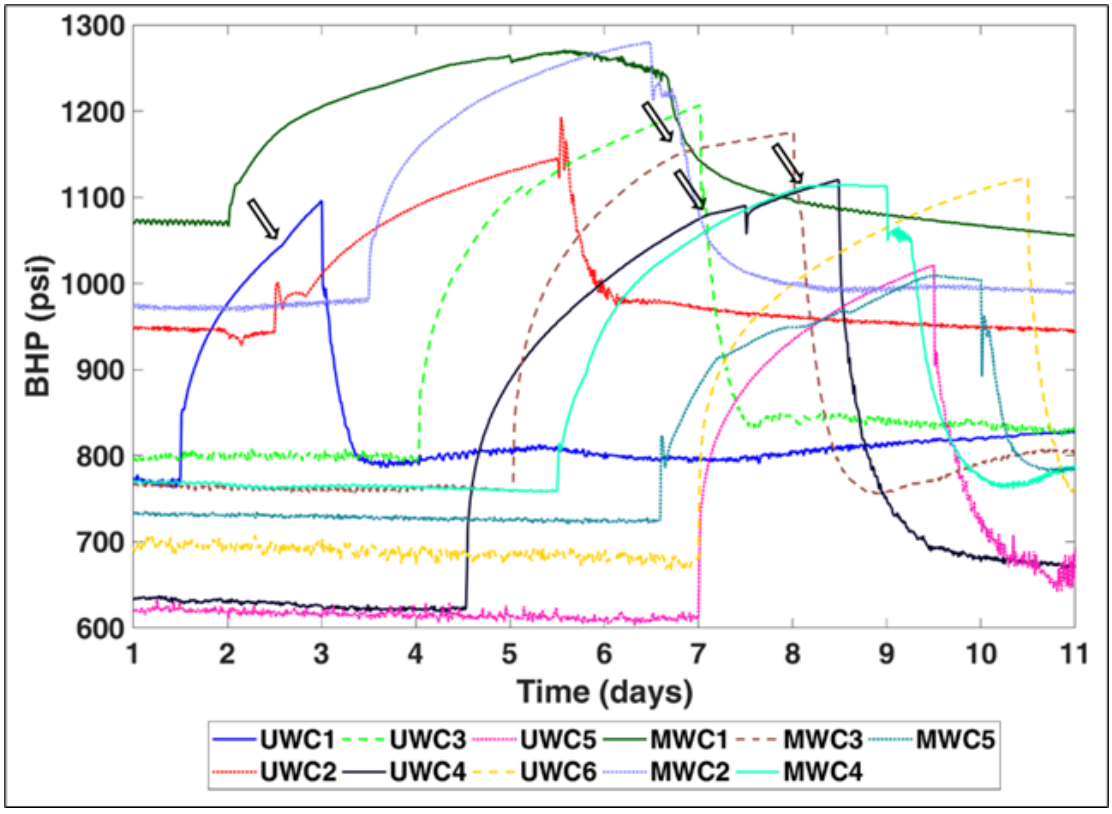


Figure 154: Bottomhole pressure monitored in 11 wells during pressure interference testing. Arrows in the figure represent pressure interference events.

Pressure interference tests were conducted by Laredo Petroleum approximately eight months after production was commenced. Bottomhole pressure gauges were used to record high resolution pressure data for all wells during pressure interference testing. The pressure response observed in all the wells is shown in Figure 154. As seen in Figure 154, sudden rate changes (shut-in or restarts) in source wells causes a change in the pressure build-up response at the monitor wells. Field data shows interference between well pairs UWC1-UWC2, UWC3-UWC4, MWC2-MWC3 and MWC3-MWC4. Figure 155 illustrates the pressure interference between wells UWC3-UWC4. Approximate travel time for the pressure pulse to reach the monitor well is defined as the response time. Response time can also be interpreted as the time-lag following a sudden rate change in the source well, after which the pressure build-up profile at the monitor well changes. Figure 156 summarizes the pressure interference observed between UWC and MWC wells. Green arrows represent a clear interference observed, while yellow arrows represent possible communication. The numbers beneath the arrow represent response time. A lower response time signifies stronger communication between wells. The response time observed for all the field cases that show pressure interference was in the range of one to two hours.

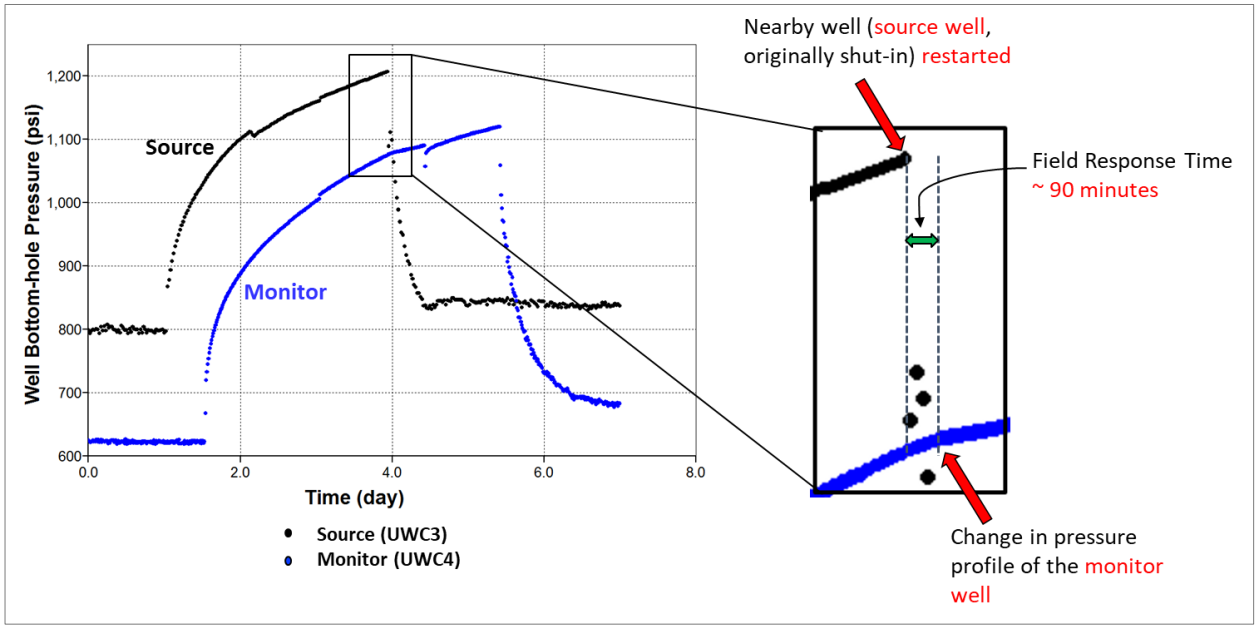


Figure 155: Pressure interference between the source (UWC3) and monitor (UWC4) well, as the source well is restarted.

Here are some of the important observations we made based on pressure interference test analysis:

- Wells that show RA tracer (proppant) communication (UWC1-UWC2 and UWC3-UWC4) are much more likely to show pressure communication with each other in the same layer. This indicates that the propped fractures remain open and are, therefore, primarily responsible for pressure communication.
- Pressure communication (after ~200 days of production) is not directly correlated with the interference obtained from inter-well fluid tracer data. This indicates that the hydraulically conductive fracture pathways created during stimulation may close during production.
- Pressure interference (after ~200 days of production) between Upper and Middle Wolfcamp is not observed even for zipper fractured wells even though strong fluid

tracer and proppant tracer (radioactive) exchange is observed. This indicates post fracturing closure of connected pathways. A possible reason for such loss of connectivity may be due to formation of disconnected proppant banks between layers (Shrivastava & Sharma, 2018).

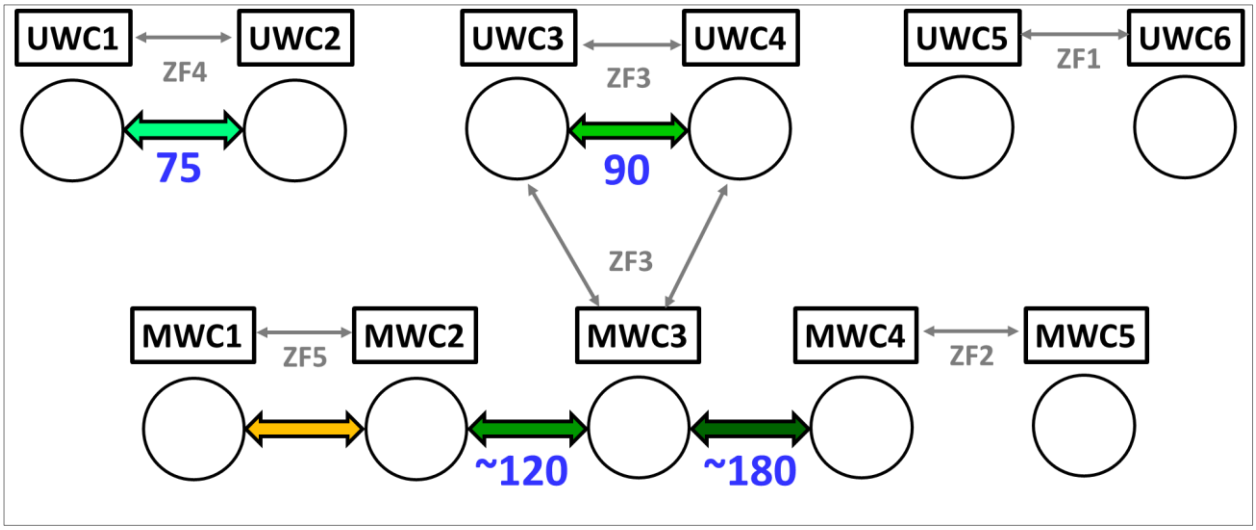


Figure 156: Summary of pressure interference test. Arrows represent interference between well pairs and the corresponding number is the response time in minutes.

Modeling and Sensitivity Analysis

The objective of this analysis is to study the impact of fracture geometry and reservoir properties on the pressure response observed at the monitor well. An effective model (Figure 157) was developed to capture the pressure interference between fractured wells during production, which might have been in communication through a complex network of fractures.

The impact of model parameters - Overlap (L_o), Offset (d), Matrix Permeability (K_m) and Induced-Unpropped (IU) Fracture Permeability (K_{iu}) on the pressure response observed at the monitor well is analyzed (forward model shown in Figure 158). The propped fractures from the source and monitor well are assumed to have infinite conductivity, and they are connected by an IU fracture having finite conductivity. Response time (T_r) is defined as the time taken for the pressure at the monitor well to change by 0.1 psi.

For sensitivity analysis, we first simulate a case where the source well starts producing at a constant rate and we observe the pressure changes at the monitor well in response to production from the source well considering different matrix permeability values (Figure 159). In this case, the propped fractures are not connected by IU fractures. Simulation results indicate that production from the source well lowers the pressure at the monitor well, and even in the highest matrix permeability case (1μD) at an offset of 18 ft between the fractures, a change of 0.1 psi at the monitor well takes ~ 9 hours, so T_r ~ 9 hours. (Figure 159a). This suggests that in unconventional reservoirs, if the source and monitor well fractures are not hydraulically connected, pressure changes at the monitor well due to hydraulic pressure diffusion are negligible. However, in field pressure interference scenarios during production, we observe that the response time is of the order of a few minutes (Figure 155). This suggests that there is a hydraulic connection between the propped fractures through an induced unpropped fracture (activated natural fracture/plane of weakness).

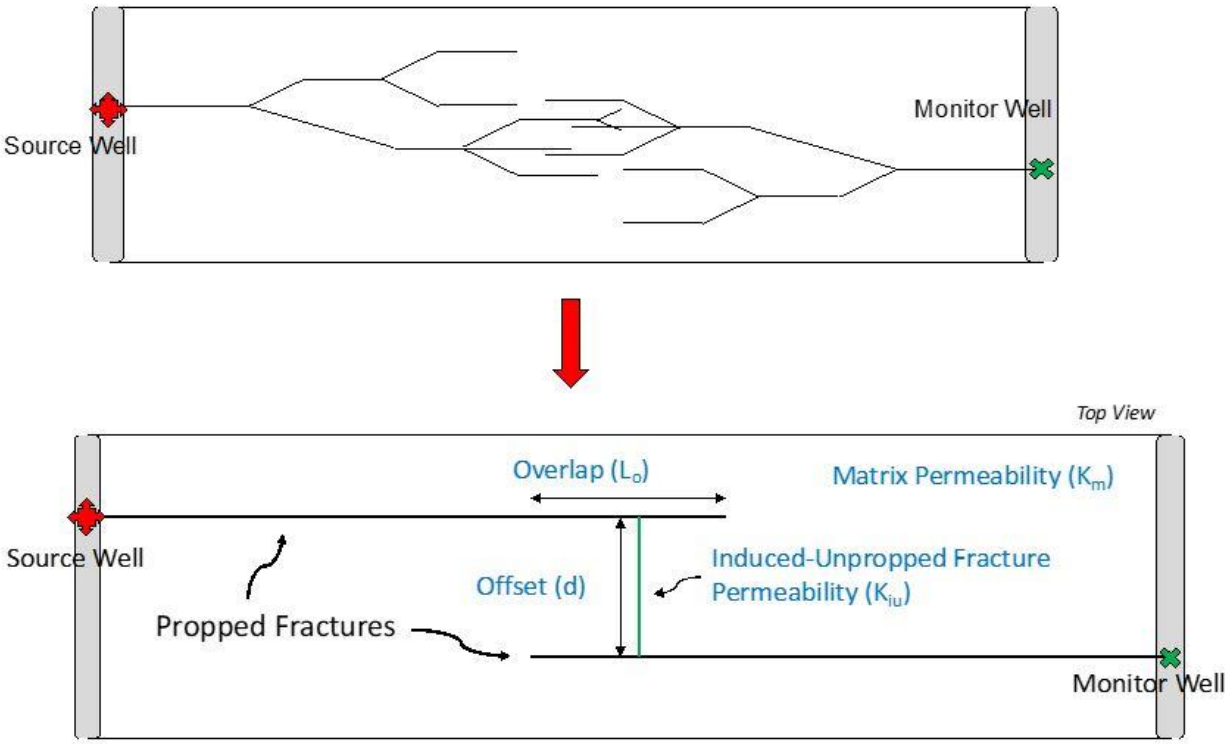


Figure 157: Effective model to capture the pressure interference between fractured wells during production.

For the same case, with the propped fractures not connected, we analyzed the impact of Overlap (L_o), Offset (d) and Matrix Permeability (K_m) on the Response Time (T_r). We observed that d and K_m dominate the T_r at the monitor well (Figure 159b, Figure 159c). Increasing d increases T_r, whereas increasing K_m decreases T_r (Figure 159b, Figure 159c). The overlap between the propped fractures (L_o) does not have a significant impact on Tr, which agrees with our assumption that propped fractures have infinite conductivity (Figure 159d).

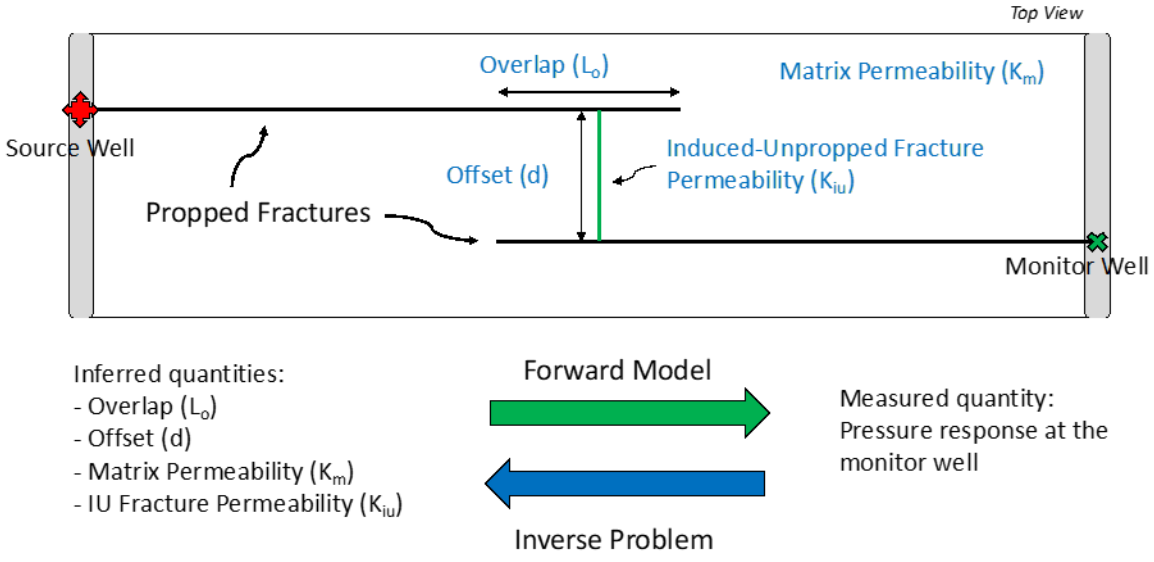


Figure 158: Forward model and the inverse problem.

The effective model was then applied to estimate effective model parameters (d, K_m and K_{iu}) by history matching the pressure response observed at the monitor well (UWC4).

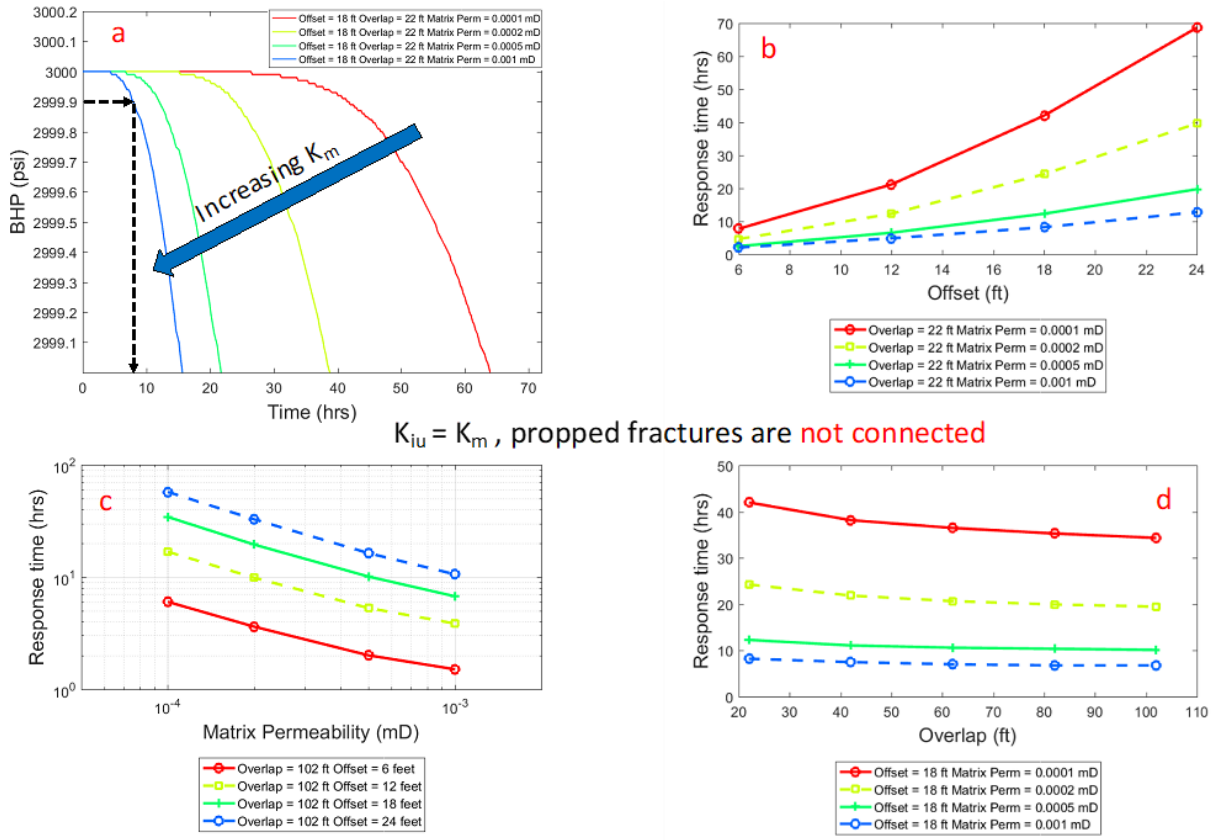


Figure 159: a) Pressure response at the monitor well due to production from the source well, b) Response Time as a function of offset between the propped fractures, c) Response Time as a function of matrix permeability, d) Response Time as a function of the overlap between the propped fractures.

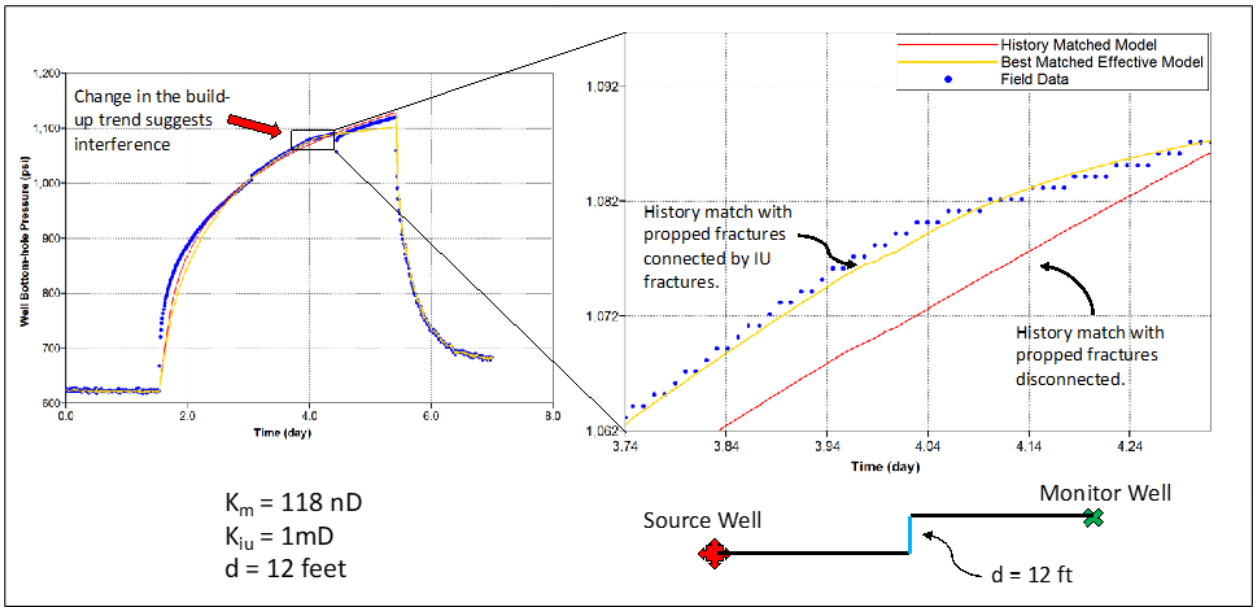


Figure 160: History match of the simulation with field data. Pressure interference captured when propped fractures are hydraulically connected by IU fractures.

Field data shows that restarting the source well changes the monitor well pressure build-up profile. When the source well (originally shut-in) is restarted, the rate of pressure build-up at the monitor well decreases. The response time observed in the field was found to be ~ 90 minutes (Figure 155).

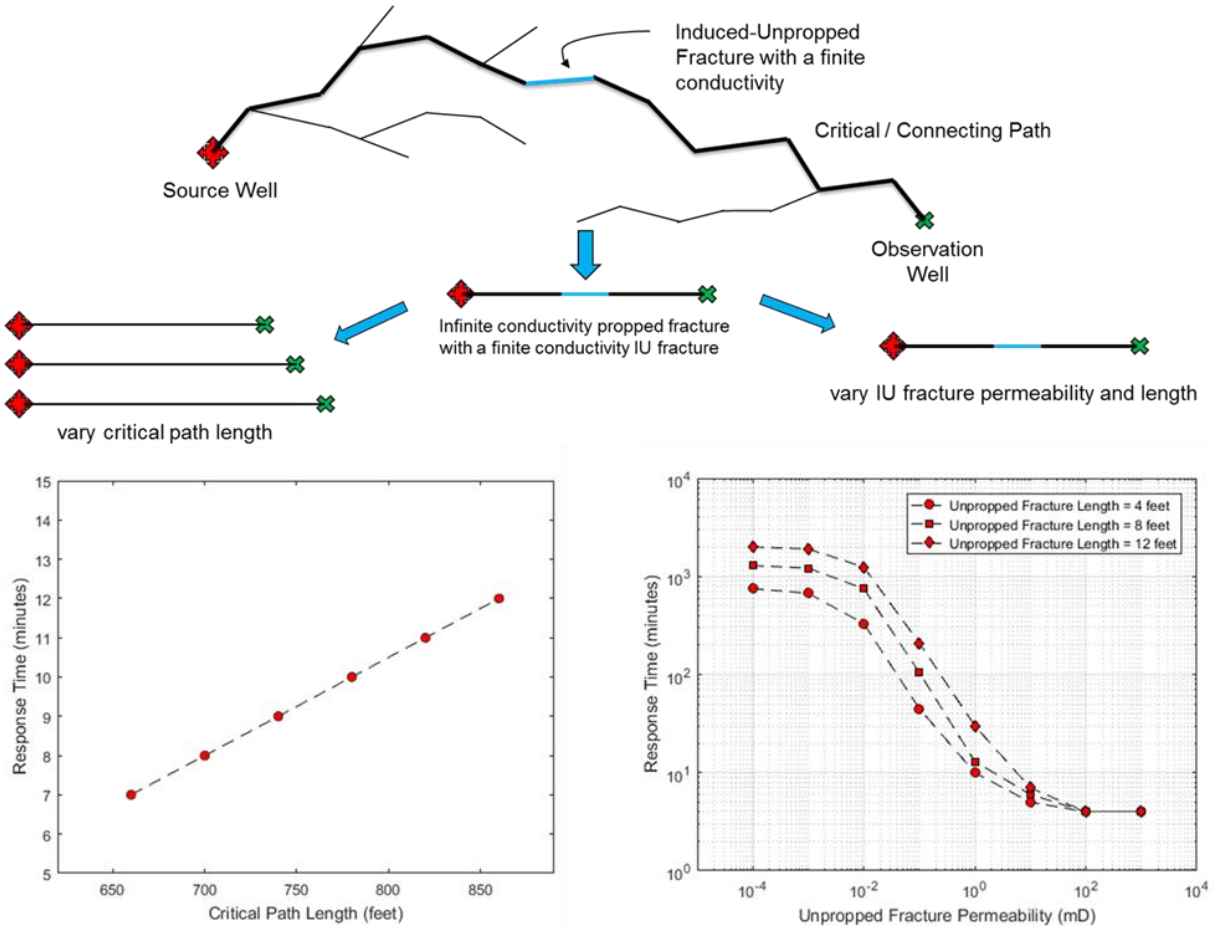


Figure 161: Sensitivity study to analyze the impact of length of the critical path, IU fracture permeability and IU fracture length on Response Time (T_r).

Upon history matching the pressure build-up profile in the monitor well with field data, the effective model parameters were estimated, and pressure interference was captured when the propped fractures in the source and monitor well were connected by an IU fracture with K_{iu} = 1mD (Figure 160). The estimated effective model parameters were K_m = 118 nD, K_{iu} = 1mD, d = 12 ft.

The hydraulic connection between the source and monitor well observed in the field, can be represented by a critical path that is composed of propped hydraulic fractures (having infinite conductivity) originating from the source and monitor wells which are connected by segments of induced-unpropped fractures having finite conductivity (Figure 161). To analyze the impact of the length of the connecting/critical path, and the length and permeability of the IU fractures on T_r observed at the monitor fracture, an additional sensitivity study was performed. The study indicates that the length of the connecting path does not have a significant impact on T_r, with every 100 ft length increment of the connecting path changing T_r by only ~ 1-2 minutes (Figure 161). On the other hand, changes in permeability and length of the IU fracture change T_r at the monitor well by several orders of magnitude as can be seen in Figure 161.

Summary

This work provides an integrated analysis of pressure interference with fluid and proppant tracer for a multi-well pad. Fluid tracer transport between the wells shows a clear connection between the created fracture networks originating from multiple wells during the hydraulic fracturing process. These channels (fracture network) can provide pathways for the fluid to

escape to regions near pre-fractured wells. As the path of connectivity is expected to have a reduced width (due to fluid leak-off in the preexisting fracture network and pressure drop across tortuous pathways) the likelihood of the proppant transport in these regions is small. This can lead to generation of unpropped fracture networks. Unpropped fracture closure is evident from the absence of pressure communication between the wells after a few months of production. During pressure interference testing, the pressure in the fracture network is well below the far field stresses. This makes it unlikely for the closed fracture networks to reopen and regain lost connectivity. In addition, the pressure connectivity is observed to be strong between the wells that exhibited exchange of proppant tracer. It is observed that this proppant exchange is very likely to happen between zipper fractured wells. This signifies the comingled nature of the fracture network generated during the zipper fracturing process. The creation of this commingled fracture network should be accounted for while deciding on well spacing and infill well drilling for zipper fractured wells, as the network between zipper fractured wells is more likely to be propped and contributing to production. It is also observed that zipper fracturing between different layers does not result in pressure connectivity, indicating the disconnected nature of the fracture networks (after production) despite the comingled nature of the IU fracture network. It is possible that proppant settling plays an important role in inducing this behavior. This work enhances our understanding of the geometry of the fracture network and clearly shows dynamic fracture closure due to production. Well pressure interference can, therefore, be useful for deciding the locations of infill wells and well spacing.

Conclusions

Conclusions based on Fluid and Proppant Tracer Tests

- Fluid tracers travel much further than the proppant tracer. Fluid tracer recovery at multiple offset wells indicates frac-hits during stimulation.
- Fluid tracer recovery is higher at previously fractured wells. This is because fluid can travel more easily through the preexisting fracture network.
- Zipper fractured wells show better communication between each other as compared to adjacent wells that were previously fractured. This is most likely due to the closure of induced unpropped fractures resulting from the time delay between the creation of fractures in previously fractured wells.
- Proppant tracer exchange between Middle and Upper Wolfcamp is observed during zipper fracturing. This suggests that the frac barrier layer between the two formations allows fracture breakthrough from middle Wolfcamp wells.
- Proppant tracer from previous stimulations in newly stimulated wells indicates the creation of at least a few long, dominant fractures.

Integrating Pressure Responses with Tracer Responses

- In a layer, wells that show proppant tracer exchange are much more likely to show pressure communication with each other. This pressure communication can be due to the propped fractures that remain open at the time of pressure interference testing.

- Interference obtained from inter-well water tracer data does not correlate with inter-well pressure communication observed after ~200 days of production. This indicates the possibility of induced unpropped fracture closure during this period of production.
- Connectivity between the Upper and Middle Wolfcamp wells as indicated by strong fluid tracer and proppant tracer exchange is not observed during pressure interference testing (after ~200 days of production). This indicates the possibility of post fracture closure of connecting fracture pathways between the two layers due to proppant settling. This further validates the existence and importance of IU fractures (Sharma & Manchanda, 2016)

Conclusions based on Pressure Interference Modeling

- In low-permeability reservoirs, pressure interference due to reservoir fluid pressure diffusion is insignificant.
- Simulation results indicate that in the absence of hydraulic connectivity between the source and monitor wells, response time is of the order of a few days.
- Any change observed in the pressure response at the monitor well during production is due to hydraulic connectivity between the source and the monitor well (through IU or propped fractures).
- Sensitivity studies show that during production, the pressure response at the monitor well is highly influenced by SRV permeability, induced-unpropped fracture conductivity, offset between fractures, and is least affected by fracture overlap.
- Pressure interference observed during stimulation is most often a result of an elastic response induced by the propagation of the fracture.

Environmental Impact Analysis on the Hydraulic Fracture Test Site (HFTS Phase 1)

Authors: Sarah Eisenlord, Thomas Hayes, and Kent Perry

Abstract

Objective

The Hydraulic Fracture Test Site (HFTS) provided a platform to test new extraction and production techniques and technologies to understand fracture geometry and increase the efficiency of shale hydrocarbon production. Eleven test wells were drilled in the Upper and Middle Wolfcamp formations, hydraulically fractured, and produced. Air quality, groundwater quality, and produced water chemistry and microbiology were monitored through the duration of the field experiment and one year into production.

Methods

BTEX, methane, VOCs, SO_x, NO_x, and PM10 were measured 1,000 ft up-wind and 1,000 ft down-wind of the HFTS experiment before operations began, during hydraulic fracturing, flowback, and several months into production to evaluate operational impact on local air quality. The underlying Edward-Trinity Plateau aquifer was monitored using 5 groundwater wells within 2 miles of the HFTS pad; BTEX, methane, petroleum hydrocarbons, and a comprehensive suite of anions and metals were analyzed from samples taken before operations began, during hydraulic fracturing, flowback, and one year after production. Water produced from 3 of the 11 HFTS wells was analyzed for chemical and microbiological properties 1.5 years into production.

Observations

There was no significant impact to air quality from HFTS operations, although elevated BTEX concentrations were measured 1,000 ft away from the well-pads during the flowback period. We detected no migration of hydrocarbon or fracture fluid chemical migration into the Edward-Trinity Plateau aquifer. Source waters used for hydraulic fracturing contained naturally occurring high concentrations (~500 ppm) of sulfate. Rapid microbially induced corrosion was detected in several wells, leading to biocide dosing. Microbiological populations were significantly altered by biocide treatment but continued to increase in population size six months after application.

Significance

After hydraulic fracturing, detailed chemical and microbiological analysis provides evidence for microbiologically mediated sub-surface transformations of supplied sulfate and organic carbon into sulfides. This report discusses air quality, water quality, and produced water analytical results for the HFTS experiment and further implications for the unconventional oil and gas industry.

Introduction

Hydrocarbons derived from shale deposits in the United States are poised to become instrumental in our energy independence and a clean energy future. These resources are projected to constitute over 38% of the national hydrocarbon energy portfolio by 2040. The Permian Basin is the largest petroleum-producing basin in the United States and has produced

a cumulative 28.9 billion barrels of oil and 75 trillion cu ft. of gas. Currently, nearly 2 million barrels of oil a day are being produced from the basin. Constant innovations in horizontal drilling and hydraulic fracturing technologies are increasing shale hydrocarbon production efficiency and minimizing environmental impact.

Sustainable production of these resources requires a clear understanding of the potential environmental impacts arising from shale development as well as effective strategies for managing risks to the public health and the environment (Small, et al., 2014). Several reviews in the literature have identified various areas of risk and have discussed pathways of potential impacts to the environment (Small et al., 2014; USEPA, 2016; Clark et al., 2013). About public opinion and regulatory interaction, significant concerns have been raised over the environmental impacts of shale development on groundwater and ambient air receptors. These concerns arise from an awareness of the large amounts of water that are handled and of the substantial mechanized equipment (e.g., diesel driven pumps) and high pressures that are employed in shale well field development.

Economic recovery of shale resources is dependent on the pressurized injection of large volumes of chemically treated water to hydraulically fracture the shale and alter its permeability through the generation of extensive fracture networks. As horizontal wells become longer and fracture treatments more complex, water use and management needs will increase. The practice of produced water recycling and re-use substantially decreases the industry's reliance on fresh water sources and disposal needs yet may introduce new and unforeseen risks to infrastructure integrity and formation productivity through the re-introduction of sub-surface tolerant microorganisms. Biogeochemical processes carried out by microorganisms in the deep subsurface has been of much interest to microbiologists and geochemists since shale hydrocarbon extraction began to expand in the United States (Magot et al., 2000; Roling et al., 2003; Voordouw et al., 2009; Mohan et al., 2013; Daly et al., 2016; Lipus et al., 2017).

There is widespread evidence of microbial growth with complex metabolic abilities in shale petroleum reservoirs across the United States (Magot et al., 2000; Galperin et al., 2011; Gaspar et al., 2014; Daly et al., 2016). Potential microbial mechanisms include (1) increased methane production from microbially produced hydrogen and carbon dioxide or acetate, (2) biodegradation of crude oil, (3) biomass accumulation leading to bio-plugging of fractures or surface equipment, (4) iron sulfide deposition decreasing permeability, (5) corrosion of steel well infrastructure, and (6) production of sour gas. Despite the potential impacts, little is known about the function, activity, and controls of microorganisms in hydraulically fractured shale. Key questions remain regarding the introduction and proliferation of microorganisms in the subsurface, mechanisms for mitigating deleterious impact, and how production operations influence the subsurface environment regarding microbial activity.

The aim of this study was to conduct careful measurements of constituents of concern in ambient air and groundwater strata proximal to shale gas well construction, completion, and production associated with the HFTS in the Permian Basin, Texas. The environmental monitoring program focused on determining the condition of the groundwater and ambient air before, during, and after critical shale well actions that were performed at the HFTS.

Additionally, the research presented in this report is aimed to illuminate microbial population dynamics in fracture fluids, produced water (over one year of production) and treated, recycled produced water all at the HFTS. The HFTS experiment was designed to test new extraction and production techniques and technologies aimed at increasing the efficiency of shale hydrocarbon production. Eleven test wells were drilled in the Wolfcamp Formation, hydraulically fractured, and produced. This study examines the microbiological populations in three of the eleven wells.

Description of the Hydraulic Fracture Test Site

Situated about 55 miles southeast of Midland, Texas, the HFTS, comprised of oil and gas assets owned and operated by Laredo Petroleum, is in the Northeast quadrant of Reagan County near the northern boundary of the county (Figure 162). The test site included eleven wells; six horizontal wells drilled into the Upper Wolfcamp play and five horizontal wells drilled into the Middle Wolfcamp in a chevron pattern. Five groundwater wells, within a 2-mile radius of the drill pads, supply the site with water necessary for hydraulic fracturing from the Edward-Trinity Plateau aquifer. Laredo owns and operates an on-site facility for produced water recycling and re-use.

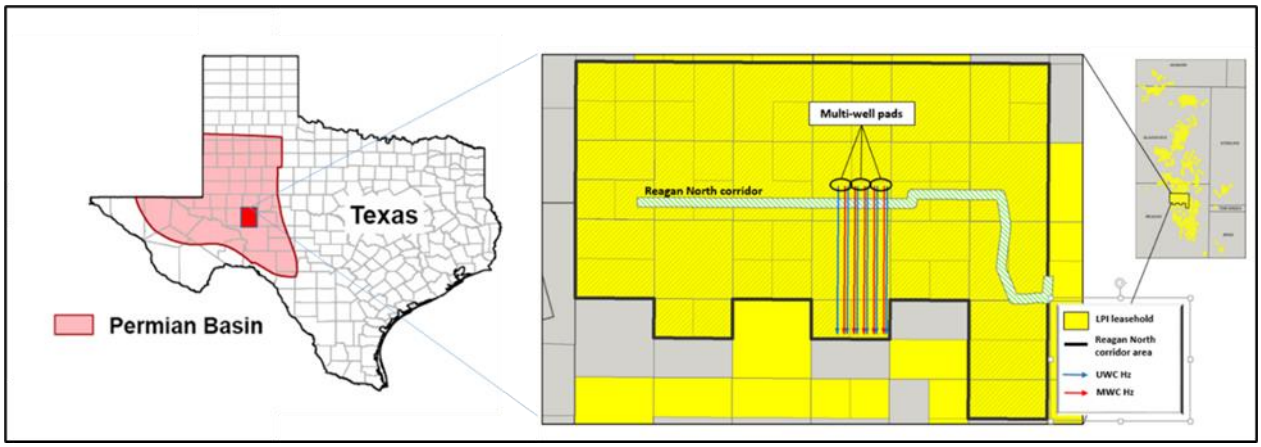


Figure 162: Location of the Hydraulic Fracture Test Site in Reagan, Texas, USA.

Methods

Groundwater Monitoring

Five groundwater wells were sampled throughout the HFTS experiment to measure the impact of development activities on groundwater reserves. Water was collected at five time points: (1) baseline (before hydraulic fracturing), (2) during hydraulic fracturing, (3) during flowback, (4) six months into production, and (4) one year into production. The wells ranged 350 to 740 ft deep. Water was collected directly from the well head using the direct fill method. The list of parameters measured at each sampling point and the methods used are given in Table 8. TOC and BTEX were analyzed at Test America in Northwest Chicago, IL, all other analyses were conducted at the Gas Technology Institute in Des Plaines, IL (GTI).

Air Quality Analysis

The air monitoring effort was designed to determine the effect of shale development operations on the quality of ambient air at ground level and at distances proximal to shale energy well pads.

A Vantage Pro2 (Davis Instruments) measured the prevailing wind direction and speed during the experiment to determine placement of air sampling equipment 1,000 ft upwind and 1,000 ft downwind of the center HFTS pad. Samples for BTEX and Methane were collected with a 6L Summa Can with 24-hour valving, volatile organic carbon (VOC), hydrogen sulfide, and PM10 were detected with direct read data loggers (RaePPB, ToxiRae Pro and TSI Dustrak DRX 8533 respectively). Samples for nitrogen dioxide and nitric oxide measurement were taken with a pump and treated sorbent tube for visible absorption spectrophotometry. Sampling occurred at four time-points for 72 consecutive hours. Time points are (1) baseline (before hydraulic fracturing), (2) during hydraulic fracturing, (3) during flowback, and (4) three months into production. The sampling was repeated in Midland, TX at one 72-hour time-point in May for comparative analysis.

Table 8: Parameters and Methods for Groundwater Quality Analysis at the HFTS.

Parameter	Sample Preservation	Standard Method	Instrumentation	Comments
General Chemistry				
pH	Ice	EPA 9040	Electrometric Equipment	Suitable for water analysis
Total Dissolved Solids	Ice	SM18 2540 C	Gravimetric Apparatus	Standard USEPA Method
Specific Conductance	Ice	EPA 120.1	Self-Contained Conductivity Meter	Standard USEPA Method
Alkalinity	Ice	SM18 2320 B	Titration Equipment	21st Ed. Standard Methods (2015)
Organic Compounds				
Total Organic Carbon	Sulfuric Acid	EPA 415.1	Combustion and Infrared Detection	Provides the concentration of total organics as Carbon.
Dissolved Methane	Sulfuric Acid	EPA RSK SOP 175	Gas Chromatography with thermal conductivity, flame ionization or electron capture detector	Uses purge and trap sample preparation procedures.
Volatile Organic Compounds	Hydrochloric Acid	EPA 8260B or 8021B	Gas Chromatography with Mass Spectroscopy or Photoionization and Flame Ionization Detection	Benzene, Toluene, Ethylbenzene, Xylenes
Inorganic Species				
Cations	Nitric Acid	EPA 200.7	Inductively Coupled Plasma Emission Spectroscopy	As, Ba, B, Cd, Ca, Cr, Cu, Fe, Pb, Mg, Mn, Ni, K, Na, Zn
Anions	Ice	EPA 300.0	Ion Chromatography	Chloride, Fluoride, Sulfate, Nitrate
		EPA 9030B (modified)	Distillation / Ion Chromatography	Total Sulfide

Produced Water Chemistry and Microbiology

The overall purpose of the effort to characterize waters associated with the hydraulic fracturing and production at the HFTS was to obtain information of value for long-term produced water management (including reuse) and to gain some insight into possible transformations that may have implications for production, corrosion, and sour gas generation.

The scope of this effort included the collection of samples from:

- Three open top water impoundments that stored freshwater and recycled produced water for hydraulic fracturing operations; sampled weekly for five consecutive weeks.
- Fracture fluids (an 80/20 mix of fresh and recycled produced water) mixed with fracture treatment chemicals; sampled on the first, sixth, and final day of hydraulic fracturing of three wells.
- A time series of produced water samples to characterize the produced water from three selected shale wells. Sampling occurred at days 0, 1, 5, 14, 36, 90, 210, 365, and 550 days following the initial release of flowback water.

More than 10 million gallons of fracture fluids was injected while stimulating each of the shale wells. Post stimulation, the wells were shut in and fracture fluids were held downhole for about six weeks before the initiation of flowback release and production.

Water chemistry sampling and analyses for produced water were identical to the groundwater sampling with the addition of microbiological analyses (Table 8). Water for microbiological analyses was collected in two 1L sterile Nalgene bottles and kept cold at 4°C until overnight shipment on ice to GTI within 4 days of collection. Water samples were vacuum filtered through 0.2um PES filters upon arrival and filters were immediately frozen at -80°C until DNA extraction.

Microbial DNA was extracted from the frozen filters with an optimized protocol using the MP Biomedicals FastDNA Spin Kit for Soil DNA Extraction Kit. Extracted DNA was quantified with the Qubit (ThermoFisher), and aliquoted for archive, qPCR analysis, and 16S rRNA gene sequencing. Quantitative PCR (qPCR) was conducted at GTI on 1:10 dilutions of extracted DNA according to the NACE TM0106-2006 and TM0212-2012 standards. Genes targeted with qPCR include 16S RNA to estimate total Bacteria, and functional genes for sulfate reduction, methane production, and nitrate reduction.

Results and Discussion

Groundwater Quality

Table 9: Groundwater Quality Results during the HFTS Experiment

		Baseline		HF		Flowback		6 Months		1 Year	
Parameter	Units	Range	Median	Range	Median	Range	Median	Range	Median	Range	Median
pH	-	7.96-8.23	8.06	7.60-8.01	7.64	7.63-7.98	7.84	7.44-7.63	7.6	7.69-7.99	7.82
Alkalinity	mg/L as $CaCO_3$	188-217	193	185-292	209	183-210	192	184-195	194	179-207	189
Total Dissolved Solids	mg/L	370-722	484	670-1950	844	290-703	443	490-850	635	320-600	445
Specific Conductivity	µS/cm	631-928	762	854-2870	1390	478-1060	722	691-1050	752	373-772	460
Total Organic Carbon	mg/L	0.41-2.20	0.71	0.43-0.96	0.46	0.23-2.3	0.25	0.47-0.69	0.54	0.48-1.10	0.64
Benzene	mg/L	-	<0.00050	-	<0.00050	-	<0.00050	-	<0.00050	-	<0.00050
Toluene	mg/L	-	<0.00050	-	<0.00050	-	<0.00050	-	<0.00050	-	<0.00050
Ethylbenzene	mg/L	-	<0.00050	-	<0.00050	-	<0.00050	-	<0.00050	-	<0.00050
Xylenes	mg/L	-	<0.001	-	<0.001	-	<0.001	-	<0.001	-	<0.001
Methane	mg/L	0.00030-0.00109	0.00047	0.00016-0.00103	0.00037	0.00018-0.00063	0.00019	0.00031-0.00086	0.00064	0.00010-0.00072	0.00035
Cations Above 0.5 mg/L											
Sodium	mg/L	23.1-67.5	42	29.6-233	128	22.7-85.1	63.3	34.2-88.9	43.2	30.2-66.9	33.9
Calcium	mg/L	60.3-90.8	69.9	75.3-108	76.7	56.8-157	70.3	57.8-77.7	60.5	41.6-72.5	60.3
Magnesium	mg/L	30.1-49.6	42	31.1-56.4	47.2	26.9-81.2	36.8	27.8-43.7	35	25.9-38.4	34
Potassium	mg/L	3.9-7.2	4.1	4.0-10.8	7.4	0.3-54.7	4.6	3.8-5.6	4.4	5.1-6.9	5.6
Iron	mg/L	0.2-3.9	0.5	0.2-2.0	0.8	0.2-8.8**	5.8	0.8-4.2	0.8	0.8-12	0.8
Anions Above 0.5 mg/L											
Chloride	mg/L	21.8-52.2	28.9	26-614	71	8.0-33.8	16	22.8-49.4	29.8	26.7-49.6	30.6
Nitrate	mg/L	19.7-24.2	22.6	2.7-17.9	12.2	8.3-13.9	10.6	18.7-24.8	20.2	0.1-20.3	18
Sulfate	mg/L	68.6-254	135	145-390	247	65-185	89	102-246	125	67.4-235	125
Fluoride	mg/L	1.2-1.6	1.5	1.5-2.1	1.5	0.1-0.9	0.7	-	<1	1.1-1.6	1.3

Overall, the data from the groundwater monitoring indicates there was little impact on groundwater quality measured because of HFTS operations. The data presented in Table 9 show that during the baseline and throughout the sampling campaign, the quality of the groundwater remained high quality, suitable for residential use. Generally, the water was low in total dissolved solids at median values less than 800 mg/L. Calcium concentrations ranged from 22.7 to 157 mg/L, concentrations greater than 60 mg/L categorized the groundwater as "hard". The ratio of sodium and calcium/ magnesium cations was sufficient to maintain the sodium absorption ratio (SAR*) at values well below 6, which makes the water highly suitable for irrigation of crops. Only five of the fifteen metals sought after in the analyses of the water samples were consistently present in concentrations over 0.5 ppm. The five cations (sodium, calcium, magnesium, potassium, and iron) that were greater than 0.5 ppm are included in Table 9.

Organic compounds were low in all water samples taken at all sampling times from the five-groundwater wells. Total organic carbon remained less than 1 mg/L and the sentinel compounds for impact from shale wells including benzene, toluene, and ethylbenzene that remained less than 0.5 ppb, and xylenes that remained less than 1 ppb. Median values for methane, the most mobile compound of interest in subsurface strata, remained below 1 ppb providing evidence that no mass transfer of constituents from the shale strata or the producing wells to the overlying groundwater aquifer was occurring.

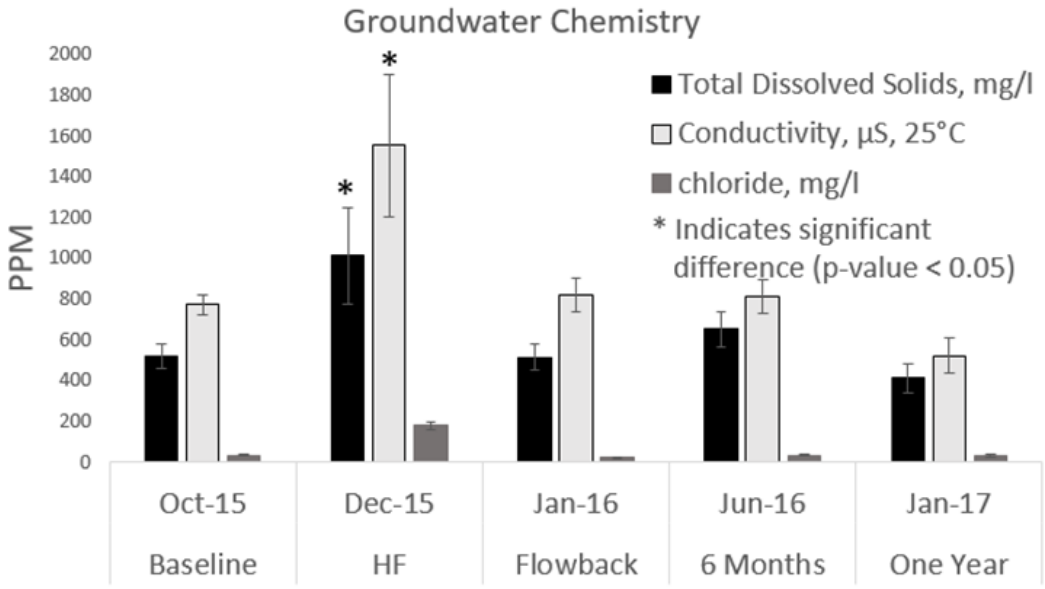


Figure 163: Groundwater Salinity Changes during HFTS Experiment.

Significant, measurable changes were observed with two parameters – total dissolved solids (TDS; p-value < 0.01) and conductance (p-value < 0.01) – during one time period, hydraulic fracturing (Figure 163). The median value for TDS increased by about 75% from 484 to 844 mg/L from the baseline to the hydraulic fracturing time period; subsequently, median TDS values recovered to baseline levels in the 1 to 10 months that followed. Even at the elevated salinity levels, median TDS levels remained less than 850 mg/L, far below the level of TDS (3,000 mg/L) that defines the highest record TDS from the Edward-Trinity Plateau aquifer (Anaya & Jones, Texas Water Development Board, 2009). The median value for conductance among the five-groundwater wells showed an increase from 762 to 1,390 µS/cm from the Baseline to the Hydraulic Fracturing stage, and subsequently recovered to Baseline values.

The impact on salinity of the groundwater was detectable only during the stage of operations when hydraulic fracturing of the 11 wells was being performed and large volumes of water were being withdrawn from the local aquifer to provide water for hydraulic fracturing. Since the rise of salinity was not accompanied with any trace of methane or BTEX, it is unlikely that the measured rise in salt in the groundwater was due to water infiltration from the shale strata or from the shale well structures. Preparation for hydraulic fracturing operations involved the pumping of tens of millions of gallons from the groundwater wells into the open top impoundments. Extensive pumping of the wells likely caused considerable drawdown of the aquifer which could have promoted the infiltration of water from lower portions of the aquifer that may have had a higher salinity level. This mechanism is further supported by the rapid return of TDS and conductance levels to baseline values in water samples upon cessation of large withdrawals. Salinity increases in wells due to drawdown is a phenomenon that has been described elsewhere (USEPA, 2016). Additionally, downhole deformation measurements conducted by Haliburton with three arrays of tiltmeters at the test site found no microcosmic events were detected shallower than 6,000 ft true vertical depth, several thousand feet below the deepest reaches of the Edward-Trinity Plateau aquifer.

Air Quality

Air monitoring results of the HFTS field experiment during the four phases of activity, including baseline and Midland TX sampling events, are summarized in Table 10. Table 10 presents average concentrations (12 or 24 hour) for each parameter, calculated from both upwind and downwind measurements. Upwind and downwind measurements were combined due to the lack of a constant wind direction for each 72-hour sampling effort and the limitation of having only two monitoring stations per sampling. Therefore, this data represents the concentrations of key air quality parameters 1,000 ft away from the oil and gas development site, HFTS. Not included in this table were constituents that were consistently not detected: nitrogen dioxide, nitric oxide and hydrogen sulfide. It should be noted, no nitrogen oxide or nitrogen dioxide was detected at the sampling locations at any of the sampling time points, most notably during hydraulic fracturing when multiple diesel engines were running to pressurize fluids for hydraulic fracturing. This indicates the methods deployed may have been inadequate to accurately measure all emissions at the HFTS field site. Regardless, the data collected are presented and discussed below.

Nearly all air-monitoring parameters measured during fracturing and during the production phases were lower or comparable to the HFTS baseline values, the Midland baseline, and literature values for the DFW and Fort Worth measurements (Rich et al., 2011; Bunch et al., 2014). PM-10 values were not detected in the high quantities expected during hydraulic fracturing from to truck traffic and sand loading. HFTS operations used high quality filters on all silica proppant silos to prevent particulate matter pollution, and the installation and use of water, gas, and oil pipelines across the Laredo facility limited truck traffic during this time period. The highest 24-hour average of PM 10 was measured during production, at 5.23 mg/m3, OSHA acceptable levels for 8-hour time weighted average is 15 mg/m3.

Table 10: Air Quality Results for HFTS Experiment.

Background	Units	Average	Max	Min	Std error
Benzene	ppb	0.478	0.570	0.380	0.034
Ethylbenzene	ppb	0.206	0.550	0.000	0.127
Toluene	ppb	15.53	56.00	0.390	10.51
Xylenes	ppb	0.752	1.800	0.000	0.394
Methane	ppm	2.720	3.000	2.500	0.192
PM 10	mg/m3	0.786	2.320	0.014	0.594
VOC	ppb	68.33	205.0	0.000	52.93
Fracturing	Units	Average	Max	Min	Std error
Benzene	ppb	0.487	0.000	1.100	0.194
Ethylbenzene	ppb	0.000	0.000	0.000	0.000
Toluene	ppb	0.390	0.000	0.870	0.148
Xylenes	ppb	0.000	0.000	0.000	0.000
Methane	ppm	2.700	2.300	3.200	0.144
PM 10	mg/m3	0.062	0.013	0.107	0.018
VOC	ppb	46.42	1.000	153.5	24.57
Flowback	Units	Average	Max	Min	Std error
Benzene	ppb	16.29	0.230	82.00	13.30
Ethylbenzene	ppb	1.583	0.000	7.900	1.290
Toluene	ppb	14.76	0.180	73.00	11.82
Xylenes	ppb	4.588	0.000	22.00	3.560
Methane	ppm	15.50	10.00	32.00	4.491
PM 10	mg/m3	0.004	0.001	0.012	0.002
VOC	ppb	853.6	333.5	1377	226.9
Production	Units	Average	Max	Min	Std error
Benzene	ppb	0.400	0.000	1.200	0.400
Ethylbenzene	ppb	0.000	0.000	0.000	0.000
Toluene	ppb	0.983	0.000	2.600	0.815
Xylenes	ppb	0.000	0.000	0.000	0.000
Methane	ppm	3.500	3.200	3.700	0.153
PM 10	mg/m3	1.777	0.010	5.230	1.727
VOC	ppb	7.667	3.500	10.00	2.088
Midland	Units	Average	Max	Min	Std error
Benzene	ppb	0.327	0.000	0.540	0.166
Ethylbenzene	ppb	0.000	0.000	0.000	0.000
Toluene	ppb	0.860	0.640	1.000	0.111
Xylenes	ppb	0.000	0.000	0.000	0.000
Methane	ppm	3.100	2.700	3.300	0.200
PM 10	mg/m3	0.060	0.023	0.097	0.021
VOC	ppb	25.17	65.00	2.500	19.98

Median and average concentrations of BTEX, total VOCs, and methane are displayed in the bar charts of Figure 164. Average values for BTEX, VOCs and methane for the hydraulic fracturing and production phases were either less than or comparable to the HFTS Baseline and Midland air monitoring values. BTEX, VOC and methane concentrations during the flowback phase were substantially greater in magnitude in terms of average and median values than the air monitoring results obtained from the baseline, fracturing, and production phases, as well as from the Midland location. This difference was not significant when analyzed with ANOVA for BTEX (p-value=0.18), VOC (p-value=0.92), or methane (p-value=0.52).

Overall, our limited air monitoring effort indicates the HFTS experiment had a minimal impact on concentrations of key pollutants related to oil and gas development. The concentrations of BTEX, Methane, and VOCs 1,000 ft. from the well pad increased during the flowback period. The concentrations of BTEX measured at HFTS were orders of magnitude lower than the OSHA

limits for worker safety exposure. The authors acknowledge the improper comparison between our 12-hour average data and OSHA's 8-hour averages; however, the merit of the compassion is relevant as the highest recorded 12-hour HFTS concentrations of benzene (82 ppb) are several orders of magnitude below OSHA's 8-hour limits (1,000 ppb). If mitigation is deemed necessary, granular sorbents (such as granular activated carbon) would likely be effective and economical in the control of BTEX and VOCs emitted from frac tank vents.

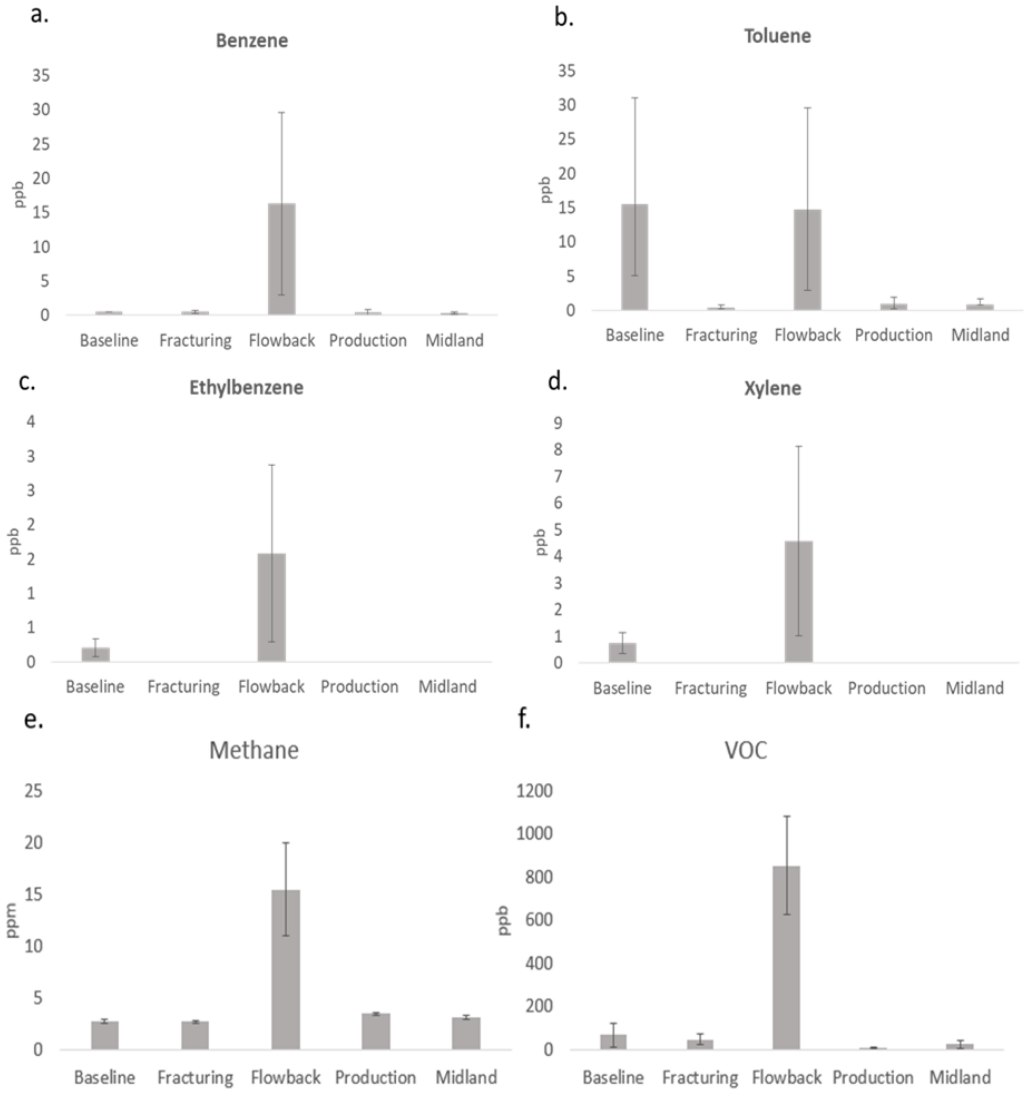


Figure 164: BTEX, Methane, and VOC 12-hour Averages during HFTS Experiment.

Water Characterization

Characterization data on the composition of the impoundment water used for hydraulic fracturing are shown in Table 11. Impoundment water includes two freshwater impoundments and one recycled produced water impoundment known as the Poseidon tank. Fracture fluids were a mixture of fresh and recycled produced water (80/20), samples were obtained after chemical mixing before proppant addition and pressurization at the first, sixth, and final day of hydraulic fracturing. Hydraulic fracturing of each well occurred over 12-13 days. All impoundments and the fracture fluids themselves were of normal alkalinities at pH levels ranging 6.2 – 8.3. Impoundment water had total organic carbon (TOC) concentrations of about 1-2 mg/L, fracture fluids around 150 mg/L. The salinity of the freshwater impoundments showed a modest level around 2,000 to 5,000 mg/L of TDS, while the water from the Poseidon

storage unit exhibited more than 20 times that ionic strength (75,000 to over 100,000 mg/L); salinity of all the impoundments was comprised mostly of sodium and chloride.

Table 11: Characteristics of Impoundments that Store Water for Hydraulic Fracturing at the HFTS.

Parameter	Freshwater Impoundment*		Poseidon Impoundment**		Fracture Fluids***	
	Range	Median	Range	Median	Range	Median
pH	8.03-8.3	8.17	6.64-7.03	6.81	6.28-7.08	6.66
TDS, mg/L	1,790-3,800	2,580	75,400-104,000	98,500	3,370-25,300	21,700
Conductivity, µS/cm	1,460-5,270	3,790	13,000-69,100	47,850	4,960-29,500	18,200
Alkalinity, mg/L as $CaCO_3$	143-183	177	236-383	344	114-190	178
Total Organic Carbon, mg/L	1.97-5.4	2.2	0.4-1.1	0.98	87-180	150
Chloride, mg/L	149-1,380	793	730-1,380	1,220	1,310-13,800	12,200
Nitrate, mg/L	6.7-15.1	13	<1	<1	2-11	8
Sulfate, mg/L	340-650	494	185-310	230	342-570	490

** Freshwater Impoundment: Six samples obtained and analyzed per impoundment (2).*

*** Treated Produced Water (Saline Water) Impoundment: Six samples taken and analyzed.*

**** Fracture Fluids: Fracture fluids after mixing and chemicals added to Impoundment water. Three samples per well were taken and analyzed.*

Sulfate which has a high potential of biotransformation is present in all the impoundment and fracture fluids at substantial concentrations. Sulfate can be converted to sulfide (e.g., H_2S) through the action of sulfate reducing bacteria. Sulfate in freshwater impoundments was present at around 500 mg/L, while the recycled produced water impoundment had a median value of around 230 mg/L; an 80/20 mixture of freshwater to saline would result in sulfate levels of over 400 mg/L in streams used for the hydraulic fracturing operations. With the introduction of 10 million gallons of fracture fluids containing 400 mg/L of sulfate, it is likely that more than 16.5 tons of sulfate was introduced into the subsurface during the completion of each shale well; at this level of mass input of sulfur to the subsurface, it becomes important to understand the degree to which sulfate is involved in biological processes that result in accelerated corrosion (i.e. microbial influenced corrosion or MIC), the microbial production of sour gas (i.e. H_2S), or the deposition of iron sulfides. Another compound with potential for biotransformation is nitrate which can be converted to nitrogen through the action of denitrifying bacteria. Nitrate levels in the freshwater impoundments showed median values of over 12 mg/L, though even higher levels of nitrate could be possible if completion operations involved the use of nitric acid for cleaning.

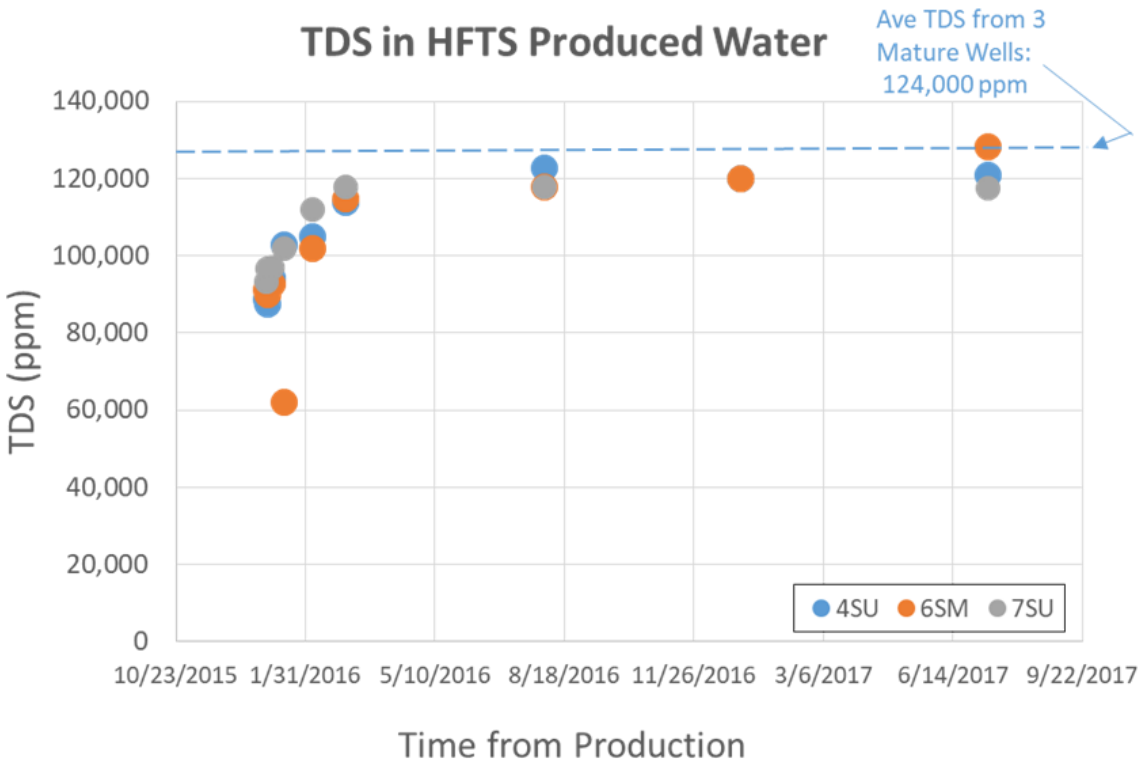


Figure 165: Total Dissolved Solids with Time in Produced Waters Collected from the Three Shale Wells at the HFTS.

Quantitative PCR of the 16S rRNA gene (an estimation of total Bacteria (BA)) in surface impoundments and fracture fluids revealed fresh water bacterial concentration to be around $1x10^4$ 16S rRNA gene copies per mL in freshwater impoundments and concentrations up to $1x10^8$ 16S rRNA gene copies per mL of water in the Poseidon impoundment. The differences in BA concentration are expected as Poseidon water is recycled produced water that is stored in open top pits without anti-microbial treatment. Drill out muds, used for drilling out the fracture plugs, also contained a high concentration of bacteria, averaging $1x10^7$ copies per mL. Bacteria ranged in concentration from $6x10^4$ to $5x10^7$ 16S gene copies per mL in fracture fluids over the course of 12-14 days of hydraulic fracturing. This moderate to high concentration of bacteria introduced to each well during hydraulic fracturing has been documented in other cases (Struchtemeyer & Elshahed, 2011) and is recognized as a significant source of potentially metabolically active microorganisms to the subsurface.

Upon initiation of flowback approximately six weeks after hydraulic fracturing, substantial increases in salinity are documented in the produced water (Figure 165). Also indicated in this graph is the level of average TDS levels measured in produced water obtained from three mature shale wells operating in the Wolfcamp formation for three years with an average of 124,000 mg/L TDS; this was done to show the levels of salinity that are reached as a result of long-term saturation of downhole minerals and mixing with formation water.

At many shale wells monitored in the Marcellus and in the Barnett plays, profiles of salinity measurements in flowback waters that are released within a few days following hydraulic fracturing show an initial TDS level that is less than 20% of the ultimate saturation concentration (Hayes, 2009; Hayes & Severin, 2012). The profiles of the monitored wells of HFTS, however, were quite different; the plot of Figure 165 shows that the initial flowback water stream had TDS levels of about 90,000 mg/L TDS, more than 75% of the ultimate saturation level of 120,000 mg/L. This was likely due to the relatively longer contact time (6

weeks) that the flowback water had with formation mineral materials that allowed the water to come closer to salt saturation before the initiation of flowback water release.

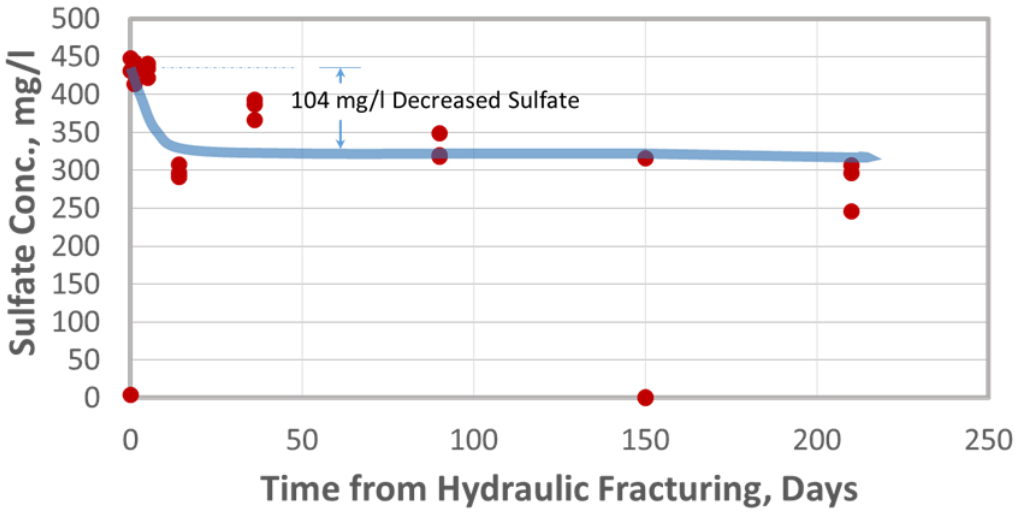


Figure 166: Sulfate Vs. Time in Produced Waters Collected from Three Wells Selected for Sampling at the HFTS.

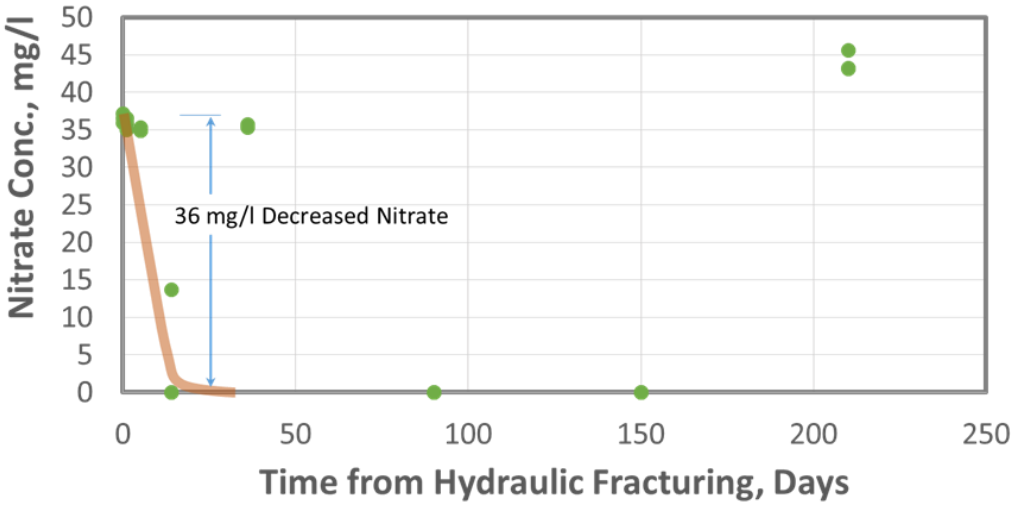


Figure 167: Nitrate Vs. Time in Produced Waters Collected from the Three Wells Selected for Sampling at the HFTS.

As modest increases in salts were observed in the flowback and produced water collected from each of the three sampled shale wells, decreasing concentrations in other constituents were noted that indicated possible dilution and transformational actions were taking place in the downhole environment. Plots of sulfate, nitrate and total organic carbon (TOC) with time following the initiation of release of flowback/produced water are shown in Figure 166, Figure 167 and Figure 168, respectively. Over the initial 14-day interval, sulfate concentrations were decreased from approximately 422 mg/L down to 318 mg/L, a 104 mg/L reduction (Figure 166). In the same period, nitrate concentrations fell from 36 mg/L to 0 mg/L (Figure 167). Simultaneously, soluble organics measured as total organic carbon (TOC) showed a decrease of approximately 36 mg/L in the flowback during the first 14 days as seen in Figure 168.

These observed changes suggest the occurrence of microbial-mediated transformations where the oxygen content of nitrate and sulfate is used to convert organic compounds to carbon dioxide and subsequently to methane. One group of microorganisms, the denitrifying bacteria, can utilize nitrate to oxidize organic compounds to carbon dioxide while reducing nitrate to nitrogen gas (Brock, 1970). Another group of microbes, sulfate reducing bacteria

(SRBs), can utilize sulfate to oxidize organic compounds to carbon dioxide while reducing sulfate to hydrogen sulfide (Stumm and Morgan, 1981). Methanogens present in the formation are then able to generate methane from the microbiologically produced carbon dioxide.

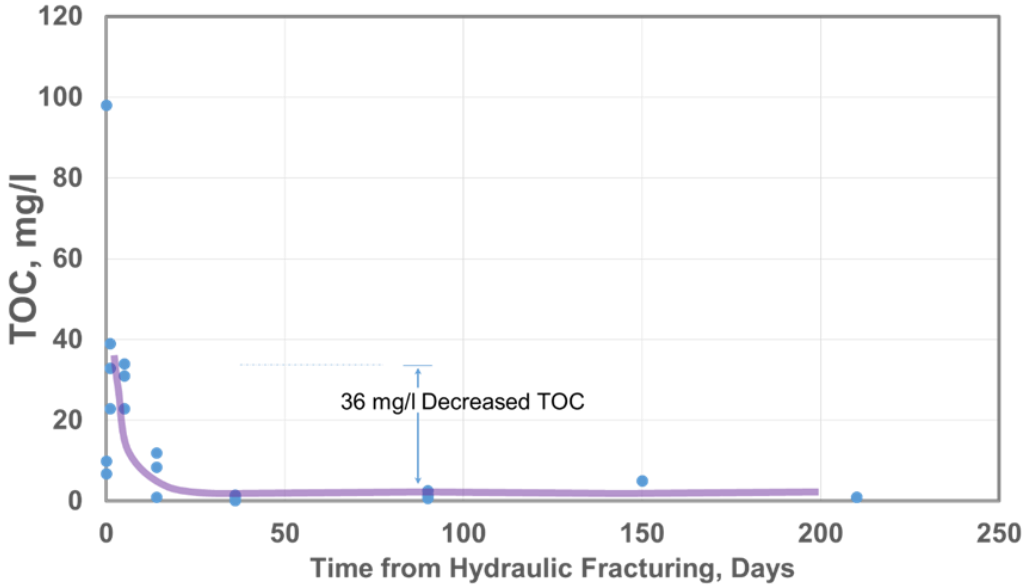


Figure 168: Total Organic Carbon Vs. Time in Produced Waters Collected from Three Wells at the HFTS.

Table 12: Average Copies / mL of Bacteria (BA), Sulfate Reducing Bacteria (SRB), Denitrifying Bacteria (DNB), and Methanogens (Meth) over 550 of Production at the HFTS.

		Average copies / mL in Produced Water			
ID	**Date**	**BA**	**SRB**	**DNB**	**Meth**
PW0	**12/31/2015**	1.13E+05	1.29E+01	3.31E+02	2.70E+04
PW1	**1/1/2016**	3.25E+07	3.91E+01	7.58E+02	3.08E+03
PW6	**1/5/2016**	6.96E+05	3.73E+02	1.78E+01	7.69E+03
PW14	**1/14/2016**	1.46E+07	1.12E+02	1.37E+02	3.76E+03
PW36	**2/5/2016**	5.34E+07	1.73E+03	4.95E+01	2.31E+04
PW90	**3/2/2016**	1.56E+07	9.62E+02	4.09E+00	2.89E+03
PW210	**8/2/2016**	6.57E+04	4.54E+02	3.70E+00	6.34E+02
PW365	**12/30/2016**	9.51E+05	8.14E+03	2.31E+00	8.24E+03
PW550	**6/30/2017**	3.41E+06	1.68E+03	9.61E+00	4.31E+03

Average bacteria concentration, as measured by qPCR in all three wells over the first year and a half of production is shown in Table 12 along with sulfate-reducing bacteria (SRB), denitrifying bacteria (DNB), and methanogen (Meth) concentrations. Total bacterial populations peaked at $1.3x10^8$ 16S genes per mL after 36 days of production in well 6SM, the lowest measured concentration of bacteria to date is $1x10^4$ 16S genes per ml after 210 days of production in well 4SU. Concentrations of SRB increased over the first year and a half of production and concentrations of DNB decreased in time with the decline in nitrate concentrations. Methanogens were detected in moderate concentration throughout the lifetime of the well. The deleterious effect of microbiological activity was witnessed within three months of production, when unplanned downtime was necessary to replace tubing in one of the wells

due to extensive microbially induced corrosion (MIC). Within 6 months of production, biocide treatment was necessary in all 11 wells.

Metagenomic sequence (16S rRNA gene) analysis revealed consistent, increasing populations of sulfur cycling microorganisms including *Arcobacter,* which form filamentous sulfur mats (Wirsen, 2004) aiding in bacterial attachment to rocky surfaces with high fluid flow. Also found were *Archaeoglobus*, which are sulfate reducing archaea with optimal growth at 83°C, commonly found in oilfield systems with the ability to reduce sulfate to sulfide with the oxidation of complex carbon polymers, several types of sulfate-reducing bacteria including *Desulfonatronum, Desulfovibrio, Desulfomondaceae, Desulfonatronovibrio, Desulfovermiculus, Desulfobacteraceae*, and a large persistent population of *Halanaerobium*. *Halanaerobium* are fermentative bacteria often found in produced water, which feed on ethylene glycol, a common additive to fracture fluids. These bacteria produce hydrogen, which is then a primary source of energy for the SRB and Methanogens. *Halanaerobium* also reduce thiosulfate to hydrogen sulfide. The microbiological data and observed microbiological action of MIC support the theory of microbiological transformation of sulfate in the stimulated reservoir volume (SRV).

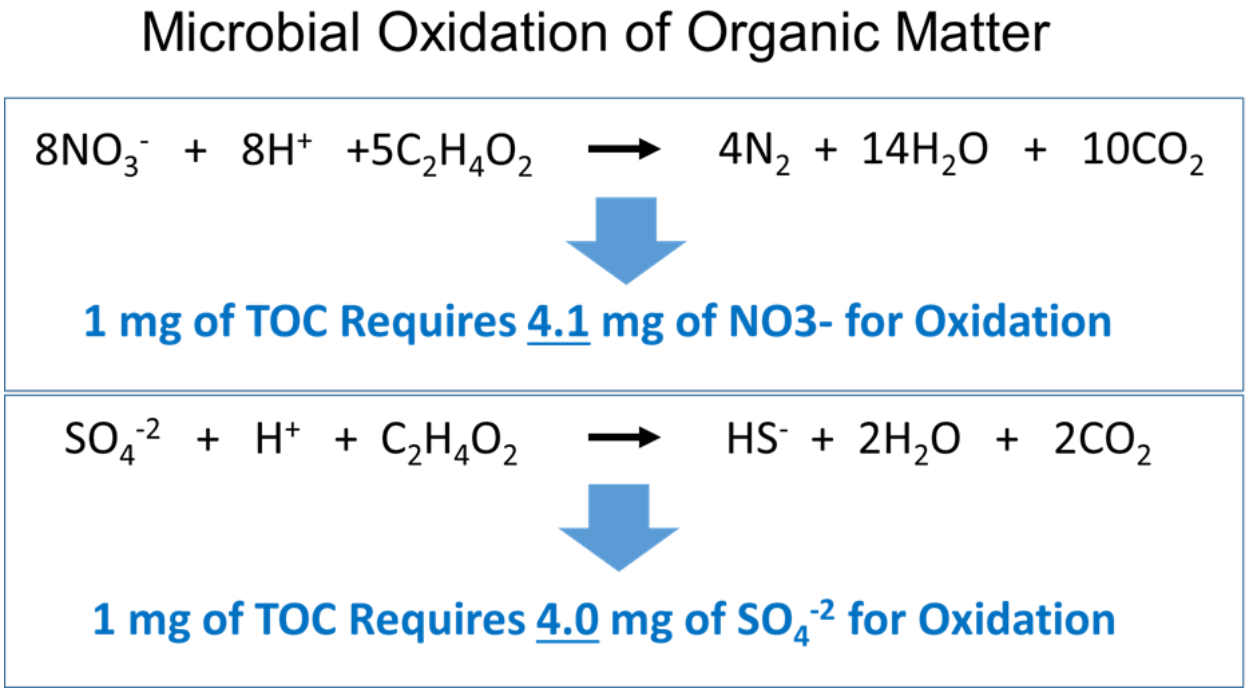


Figure 169: Balanced Equations Describing the Microbial Oxidation of Organic Matter Using Nitrate and Sulfate.

When organic matter is not available for conversion by microbial communities, both sulfate and nitrate are stable and persist in the subsurface aquatic environment, as evidenced by groundwater composition data in many areas of Texas as well as in the baseline groundwater composition data for the five wells adjacent to the HFTS facility. In the case of the groundwater wells adjacent to the HFTS location, Table 9 shows values for sulfate and nitrate at about 65-390 mg/L and 0.1-25 mg/L, respectively, which persist at these levels in the aquifer environment; this is due to the low activity of key microbial communities in the aquifer (i.e. denitrifiers and SRBs) and the very limited availability (i.e. low concentration) of total organic carbon (at 2 mg/L or less). When the same water is blended with chemicals and injected downhole during hydraulic fracturing, the soluble organic carbon rises significantly to levels

that may possibly stimulate introduced or *in-situ* microbial communities to utilize sulfate and nitrate to convert (oxidize) some or all the soluble carbon to produce carbon dioxide.

If the availability of soluble organic carbon is key to the microbiological reduction of nitrate and sulfate, then the oxygen equivalent of the TOC consumed should be roughly matched to the oxygen equivalent of the nitrate and sulfate that was remove from solution during the same period. Balanced equations that describe denitrification and sulfur reduction using organic matter are shown in Figure 169, using acetic acid as the example of organic matter that is oxidized. Between the two types of oxidation that occur (denitrifying and sulfur reducing), one milligram of TOC requires roughly four milligrams of nitrate or sulfate to achieve complete conversion of the organic compound to CO_2.

When these stoichiometric conversion factors are considered along with the concentration reductions during the first 14 days of flowback release, it appears that the decreased concentration of TOC in the downhole water in terms of oxygen equivalent is close in value to the oxygen equivalent of sulfate and nitrate consumed during this same period. This is shown in a comparison of oxidant and TOC conversion shown in Figure 170 where the loss of soluble TOC (oxygen equivalent) came within 3% of the consumption of nitrate and sulfate in terms oxygen equivalents. This would indicate that the drop in soluble TOC is due to oxidation using nitrate and sulfate. More important, this would strongly suggest that the oxidative transformations of TOC utilizing sulfate and nitrate are mediated by microbial consortia in the downhole environment.

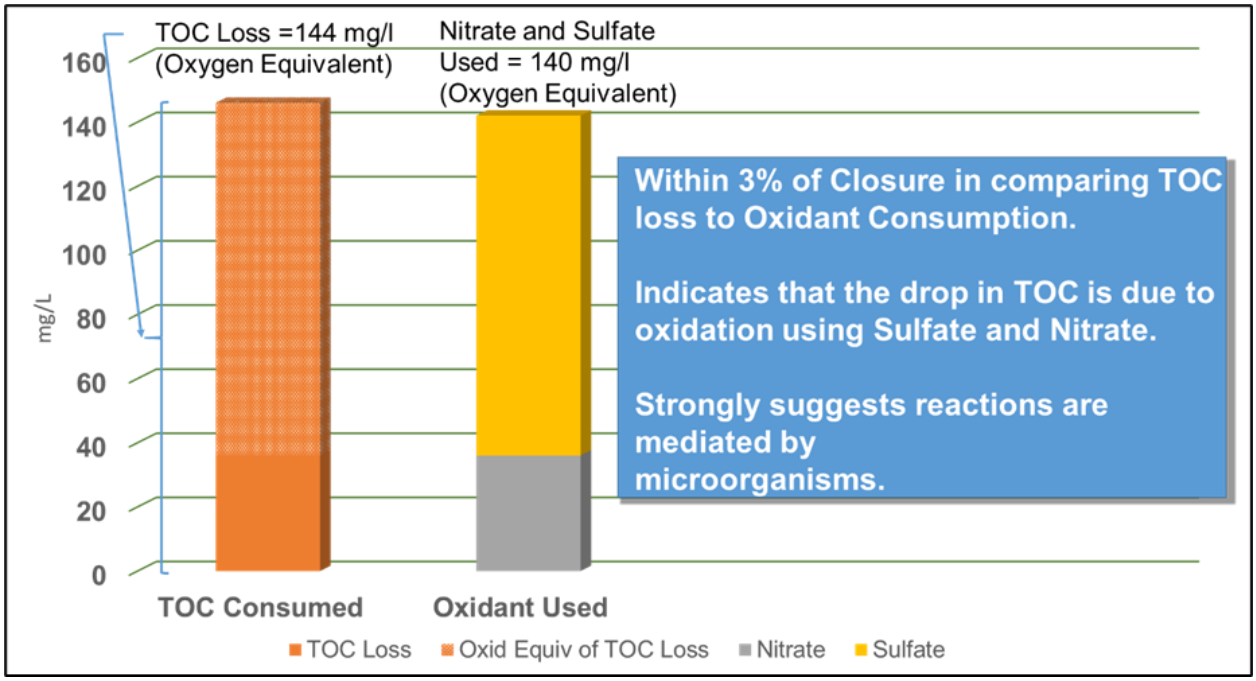


Figure 170: Comparison of Oxidant and TOC Conversion in the Downhole Aquatic Environment During the Initial 14 Days of Flowback Release.

If the concentrations in the produced water samples are indicative of the levels of TOC, sulfate and nitrate in the SRV (with a total initial volume of 10 million gallons per completed well), then mass flow calculations show that within two weeks following the release of flowback about 1.5 tons of TOC was converted to CO_2 through the action of microbes with the concomitant reduction of 1.5 tons of nitrate to nitrogen gas and 4.2 tons of sulfate to sulfide

amounting to about 1.4 tons. While the nitrogen gas is inert, the formation of over a ton of sulfide from sulfate conversion could potentially be problematic in terms of corrosion, deposition, or sour gas formation. If all the 104 mg/L of transformed sulfate was converted to soluble sulfide and distributed in the formation, the resultant concentration of soluble sulfide would be at least 30 mg/L as HS^-.

The results of sulfide analysis of all flowback and produced water samples, however, show soluble sulfide levels at below detection (< 1 mg/L). This is likely due to the presence of soluble iron at concentrations of 15 to 170 mg/L in the downhole aquatic environment; at these concentrations, iron levels at the pH level of the produced water (pH 7.5 to 8.0) may be sufficient to precipitate the sulfide as ferrous sulfide, thereby reducing soluble sulfide concentrations to below 1 mg/L. A similar observation of low sulfide (<1.2 mg/L) in the presence of 25-200 mg/L of iron has also been described in another study where produced waters were characterized at 19 locations in the Marcellus Shale (Hayes, 2010) and in the Barnett Shale (Hayes & Severin, 2012). Sulfide may also be complexed with metals associated with the well corrosion materials and be rapidly generated in biofilms involved with microbiologically influenced corrosion experienced in all 11 wells during the HFTS experiment.

Alternative transformations which could occur in the subsurface, attributing to a decrease in measurable sulfate include the formation of calcium sulfate or barium sulfate scale. However, levels of Ca in produced water increased from 1,900ppm to 2,410ppm over the year and a half of production. Ba concentration was low, between non-detect and 2.5mg/L over the year and a half of production. Therefore, we do not have strong evidence of Ca or Ba reacting with sulfate to create scale at a large enough scale to lead to the marked decline in sulfate in PW over time.

Microbial Control

Biocides are used in the oil and gas industry to prevent the breakdown of fracture fluid chemicals, microbiologically induced corrosion, sour gas production, and decreased formation permeability due to biofilm. Our microbiology results indicated high concentrations of bacterial populations were introduced into the wells and persisted in the subsurface, up to 550 days after production. The detrimental impact of biofilms was observed on site as corrosion failures, and potentially through decreased production rates due to microbiological transformation of sulfate to iron sulfide deposits. Biocides were used at HFTS twice: once to pre-treat fluids used for hydraulic fracturing and six months into production to mitigate the impact of corrosive microbiological activity on downhole equipment including tubing and gauges.

Two factors likely contributed to the establishment of viable microbial communities in the subsurface. First, recycled produced water used for hydraulic fracturing was not treated to adequately kill all microorganisms before hydraulic fracturing, as communicated by Laredo operations. Recycled produced water at the HFTS was treated with chlorine dioxide, a strong oxidizing biocide, and stored in impoundment tanks before being mixed with fresh water, fracturing fluid chemicals and sand, and then injected into the reservoir. This introduced living, thermo- and halo-tolerant, biofilm promoting organisms into the SRV. Secondly, the wells were shut in for a period of six weeks after hydraulic fracturing. Post-fracture biocide treatments are found to be most successful when flowback occurs within 24 hours of hydraulic fracturing

(Struchtemeyer & Elshahed, 2012). The shorter residence time of fracturing fluids limits the amount of time for cell – surface interactions required for anaerobic biofilm growth and proliferation. Once established however, biofilms are notoriously difficult to remove from the formation and steel surfaces, so produced water microbiology must be monitored and managed.

In November and early December 2016, wells were taken offline and shut in for 12 hours for biocide treatment after microbiologically influenced corrosion was observed on tubing and pressure gauges. Approximately 55 gallons of B-1203, a Glutaraldehyde/ Didecyldimethylammonium Chloride blend, was pumped downhole. Gluteraldehyde binds to cell's amine groups, killing microorganisms by inhibiting the transport of essential nutrients. Didecyldimethylammonium chloride, is a quaternary ammonium compound, otherwise known as "quats". Quats are added to glutaraldehyde biocides for their ability to disrupt cell membranes and grant access for amine binding. Quaternary compounds are most effective on Gram positive cell membrane structure. Sequencing results of produced water revealed the majority or organisms growing in the reservoir since the early days of production were Gram negative.

The qPCR results from samples taken one month after biocide application indicate bacteria concentrations have remained steady or increased in some wells (Table 12). The persistence of high concentrations of bacterial DNA in the subsurface indicates an incomplete kill job in these wells. Although live vs. dead tests were not conducted for these samples, consistent and increased population concentrations sampled over time with quantitative methods indicates populations are alive and sustaining growth in the SRV. Furthermore, the sequencing of DNA in samples taken days after the biocide treatment indicate the subsurface population is now dominated by Gram negative organisms, and organisms with natural defenses to quats such as double membranes or protective sheaths around the cell body. There are strategies for enhancing biocide effectiveness against Gram negative bacteria (Denyer & Maillard, 2002), which can be determined based on fracturing fluid and formation chemistry.

Incomplete kill jobs from biocide treatments are common in the unconventional oil and gas industry (Gaspar et al., 2014). Chemically, quaternary ammonium compounds work best in soft water, with calcium concentrations below 60 mg/L. The ground water introduced to the reservoir during hydraulic fracturing at HFTS was only moderately hard (Ca = 75 mg/L), however the produced water has Ca >2,000 mg/L. The biocide treatment in November introduced 55 gallons of B-1203 to a reservoir containing considerably hard water, likely compromising the biocide effectiveness. Microbial response to biocide choice and duration for fracturing fluids to be in contact with the formation, indicate operation activities do have an influence on ultimate subsurface microbiological community structure and activity.

Conclusions

In consideration of the monitoring results obtained by this evaluation effort, the following summary conclusions are drawn:

- Application and testing of advanced technologies of drilling, completion and production at the HFTS facility did not result in lasting deterioration of groundwater. In the monitoring of groundwater before and during each phase of operation, no

evidence of migration of methane, benzene, toluene, ethylbenzene, xylenes or total organic carbon (TOC) was detected.

- The temporary rise in median salinity of the groundwater measured at the five groundwater wells (increasing from about 500 mg/l to 800 mg/l) was likely due to the infiltration of water from deeper portions of the aquifer of higher salinity during the fracturing phase when extensive pumping (amounting to tens of millions of gallons) could have caused groundwater drawdown of each of the five wells. The effect was short termed: dissolved solids returned to baseline TDS levels within 50 days.
- Air monitoring measurements conducted at the HFTS including VOC, PM-10, benzene, toluene, ethylbenzene, total xylenes, and methane indicate that nearly all phases of HFTS operations (except for flowback collection) had no discernable impact to air quality when compared to the baseline HFTS samples, monitoring conducted in downtown Midland, and to literature values from other urban locations in Texas. It is recognized that there are some limitations to the sampling protocol.
- The collection and storage of initial produced water released from each well (flowback) does result in measurable release of VOCs and BTEX to the atmosphere; however, near-site air quality values for BTEX are less than 10% of OSHA limits for worker safety (8-hour exposure) and the short-term nature of the flowback collection phase limits local residential exposure to air emissions. If needed, however, these small emissions can be economically controlled through engineering controls (adsorbents) applied to frac tank vents.
- Delaying flowback release by 6 weeks following the completion of each well provided contact time for the injected fluids to equilibrate with downhole materials and causes higher salinities to be measured in early flowback samples. Upon release, median TDS levels in flowback water were measured at around 90,000 mg/l in the first day of release increasing to a plateau of 120,000 mg/l in about 3 months, close in value with the salinity of produced waters generated from mature wells of nearby Wolfcamp shale well fields.
- As salinity in the flowback increased with time, concentrations of several constituents decreased simultaneously, the nature of which strongly pointed to the likelihood of substantial microbial mediated transformations of hydrocarbons and oxidants. Within the first 14 days following initial release of flowback, TOC decreased by 95% while nitrate decreased by 100% (mediated by denitrifier microbial populations) and sulfate (initially present at over 420 mg/l) decreased by 24% (mediated through the action of sulfate reducing bacteria). The measured TOC loss was in stoichiometric balance with nitrate and sulfate consumption: The oxygen equivalents of TOC oxidized to CO2 were within 3% of the measured losses of sulfate and nitrate oxygen equivalents in the flowback at 14 days. Chemical data is supported by quantitative microbiological analysis of denitrifier and sulfate reducing bacteria.
- If the changes in concentration in the flowback water samples were indicative of the 10 million gallons of injected water, more than 1.4 tons of sulfide could have been generated in place in the fractured shale. The non-detect levels of soluble sulfide measured in the flowback water samples together with the presence of excess soluble iron point to the substantial formation of iron sulfide precipitate. More than 3.8 tons of

ferrous sulfide precipitate may have formed along the lateral of each horizontal well. This in-place precipitate may later move toward the horizontal well bore as water is removed and may over time mechanically impede the movement of fluids and gases from a horizontal well and become a factor in overall well performance. More research will be needed to determine the fate of sulfide and management approaches to prevent deleterious effects on well performance.

- All 11 wells experienced microbiologically influenced corrosion within six months of production. Subsequent biocide application was not adequate to limit microbial growth and activity. Biocide dosing decreased the population of methane producing bacteria; however, it did not substantially reduce overall bacterial populations sizes or the relative abundance of sulfate reducing bacteria. The biocide used targeted Gram-positive bacteria and works optimally in soft water (<60 mg/L Ca). At the time of biocide treatment bacterial populations were composed of primarily Gram-negative organisms with a Ca concentration over 2,000 mg/L.

Introduction

For the Phase 2 EOR field pilot study, a new set of horizontal wells were selected by the project members. The selected wells were approximately one mile to the NW of Phase 1 experiment wells. The EOR wells had an updated completion design to reflect learnings from Phase 1. The site included a central injector/producer to test cyclic gas injection, offset by horizontal and vertical wells used to monitor gas movement during injection in the reservoir. Significant events and field activities completed as part of this project are listed next.

Multiple vertical wells at the site had to be secured in order to restrict vertical gas movement through existing perforations. Bottomhole pressure gages were installed in five offset wells to monitor gas movement. Prior to actual EOR test, a second slant core well was drilled and cored next to the injector and a total of 260 ft of through fracture core was recovered and comprehensively analyzed like the first core in Phase 1, including CT scans, fracture description, laser scans, and proppant analysis. The slant core well was logged with quad combo and water-based image log was also acquired. Three discrete pressure gages were installed to monitor far-field pressure across the injector/ producer well.

Prior to the actual injection program, well interference test was performed across the EOR test site to assess interwall communication. The actual test involved gas injection using field gas with the help of a custom high-pressure compressor as well as post injection production tests (huff and puff test). Surface passive seismic surveys were conducted during low- and high-pressure portions of gas injection. Pressure Volume Temperature (PVT) analysis on injected gas and reservoir fluids were conducted to understand the phase behavior of injected fluids under reservoir conditions. Core flow experiments were also conducted. Extensive 3D reservoir simulation studies were conducted to understand cyclic gas injection at this site and reconcile actual field observations. Finally, a field test to clean up Permian produced water using Membrane Distillation technology was also completed (Appendix E).

Literature Review on the Application of Enhanced Oil Recovery in Shale formations

Intensive research has been conducted on proving the efficiency of different EOR methods for various shale formations over the past two decades. However, field tests on this topic are still limited because developing an EOR test plan means risking the return of investment for operators. Therefore, to implement any EOR technique in a field, a wide-ranging theoretical and laboratory experiments are needed to support the economics of re-investing. Also, the complicated phase behavior of fluid system inside the matrix of shale formation adds to the complexity of designing a successful EOR technique.

The most common successful EOR technique for tight formations, covered in the literature as of today, are natural gas and CO_2 injection using huff n puff procedure. Application of surfactants has been addressed in some studies did not receive much attention from the industry due to the relatively slow rate of recovery in their process. We will summarize some of these previous studies plus their significant results and conclusions in this section.

Gas/ CO_2 Huff n Puff

The ability of a formation to contain the high pressure injected gas near the wellbore, contact of the wellbore with maximum volume of the productive zone within the formation, and the

appropriate well spacing to minimize the hydraulic commination between the wells are the three most important factors in determining the success of a huff n puff practice (Konopczynski & Dowlatabad, 2018).

The effect of fracture density and miscibility on the effectiveness of CO_2 huff n puff is addressed by (Ding et al., 2019; Jia et al., 2019). The experimental results of this study showed that the existence of fractures reduces the sweep efficiency of the injected fluid, and a larger number of cycles is required to improve the oil recovery. Also, first contact miscibility is proven to be more efficient that the multi-contact miscibility.

Sheng (2017) has summarized the results of several huff n puff and gas injection field pilot studies showing that for the formations with the permeabilities above 1 mD, where injectivity is not an issue, gas injection projects were successful. However, for the tight formations with permeabilities in the nano-Darcy range, gas or CO_2 huff n puff should outperform the gas flooding, if it is properly designed in terms of soaking time, injection rates, injection pressure, and well spacing.

Surfactant injection/ Huff n Puff

Many surfactants are often added to the fracturing fluid for different purposes other than EOR. In the past decade, the application of surfactants for EOR in tight and shale formations was introduced because of its higher feasibility compared to the waterflooding and water huff n puff in ultra-low permeability formation (Sheng, 2017).

Surfactant application in changing the wettability and interfacial tension of the reservoir fluid-rock system has been addressed through numerous laboratory studies on formation cores (Yang & Wadleigh, 2000; Weiss & Xie, 2007; Shuler et al., 2011; Neog & Schechter, 2016; Bidhendi et al., 2019). The challenge of surfactant application in field studies is the uneconomical slow rate of oil recovery through the large volume of matrix through spontaneous imbibition which makes its unpractical (Mattax & Kyte, 1962; Kazemi et al., 1992; Babadagli, 2001; Sheng, 2017). Therefore, in many cases, surfactant huff n puff is paired with re-fracturing process to speed up the imbibition and provide a significant uplift to the re-fracturing economics. Alternatively, soaking after fracturing would make the application of surfactant a more feasible option.

Biological EOR

Another mechanism to improve the wettability of the system towards one that is favorable to the enhancement of production is the use of enzymes. Application of enzymes in reducing oil viscosity, interfacial tension, and wettability alteration is addressed in several studies (Harris & McKay, 1998; Liu & Zhang, 2011; Jabbar et al., 2015; Sookprasong et al., 2016; Rahayyem et al., 2019). In most of these studies, commercially available enzyme mixtures were used and proved to be efficient in improving oil recovery. The notable point about enzymes is that they act as a catalyst and will not be consumed during the process which makes them durable and their impact everlasting in the formation (Nasiri, 2011). Moreover, enzymes are globular proteins and are eco-friendly which minimizes any adverse long-term impact on the formation rock.

Feng et al. (2007) explains the mechanism of oil-rock bond breaking using enzymes by affecting the wettability of the rock and reducing the surface tension to release the oil from

pore walls. Khusainova et al. (2015) performed contact angle measurement using image analysis on the enzymes showing that enzymes can change the adhesion behavior of the oil-enzyme-rock system, showing that enzyme can "push away" the oil from rock surface and allow it to flow. Several experimental studies demonstrate the impact of enzymes on improving oil recovery in both laboratory and field samples. Most of these studies, however, are focused on conventional formations and limited work is available on the application of enzymes in tight formations. A recent study by (Salahshoor et al., 2019) proposes the applicability of enzymes for EOR practices in shale and tight formations through a series of laboratory experiments using spontaneous imbibition. This study proved the potential of obtaining an additional 20% of oil recovery by using enzyme on the Woodford shale samples.

The majority of EOR pilot studies and simulation models are conducted on the three main U.S. shale formations: Bakken, Eagle Ford, and Wolfcamp. Below, this report will highlight some of the important studies on EOR application in these major shale formations.

Bakken Formation

Todd & Evans (2016) summarized the outcome of about seven different EOR field pilot studies over the course of eight years. Despite different locations, performing operator, and injection techniques used in these studies, early gas breakthrough is reported as a common issue in all of them. Increased hydraulic connectivity of the wells is recognized as the main cause of gas breakthrough and ease of injectivity. Most of the pilots did not exhibit any increase in the production and in those who did, the increase was minimal.

Pu & Hoffman (2014) studied water-alternating gas and CO_2 huff n puff simulation models for the Bakken formation and concluded that the success of these methods is tied to the permeability of the reservoir. Simulation of cyclic CO_2 injection in Bakken done by (Yu et al. (2014) introduced gas injection rate, number of injection cycles, and huff and puff period as the dominant factors controlling efficiency of CO_2 injection in Bakken.

Wang et al. (2010) studied the injection potential of CO_2 in Bakken formation and compared different injecting schemes including continuous CO_2 injection, huff n puff CO_2 injection, waterflooding and CO_2 flooding, and the injection of mixed gases. In their simulation of the field, continuous CO_2 injection worked better than huff n puff. Sheng & Chen (2014) noted this conclusion regarding the better performance of CO_2 flooding compared to the huff n puff practice is due to the using a permeability of 2.5 mD and 0.04 mD which are not in the ultra-low ranges.

Application of chemicals and surfactants in altering the wettability of the formation rock towards a water-wet system in order to improve the oil recovery is investigated in several laboratory studies. Most of these studies are conducted using spontaneous imbibition mechanisms on the formation core samples saturated with the native crude and repeatedly reported improvements in the oil recovery (Chen et al., 2000; Yang & Wadleigh, 2000; Weiss & Xie, 2007; Berry et al., 2009; Abbasi Asl et al., 2010; Shuler et al., 2011).

The Elm Coulee field pilot study was started in early 2009 to test CO_2 huff n puff in the Bakken formation. Upon completion of the first cycle by injecting about 45 million cubic feet of CO_2 with a soak time of 64 days, the well was opened to production. After a rapid increase in the

production for eight days, the oil rate declined rapidly and by 30 days it was not flowing any longer (Sorensen & Hamling, 2016).

Schmidt & Sekar (2014) reported the results of a continuous immiscible gas injection (350 Mscfd and 1000 Mscfd) through one horizontal injector that was perpendicular to nine horizontal producers. The average decline rate of the producing wells changes from 20% prior to injection to 15% after the injection, increasing the total produced oil from about 135 bbl/d to 295 bbl/d. They determined the key factor in the success of this project was the injector to producer well ratio (1:9) which made the project economically justifiable.

Eagle Ford Formation

Simulation studies on the performance of EOR huff n puff in the Eagle Ford agree that injection of field gas causes improvement in the incremental oil recovery. Injection patterns including the injection pressure, injection/production time, and composition of the injected gas are determined to be the most influential factors on the success of an EOR huff n puff. Transport in the natural or hydraulic fractures is known as the dominant oil recovery mechanism in Eagle Ford and well interference has a significant negative impact on the efficiency of gas injection (Atan et al., 2018; Ganjdanesh et al., 2019; Wang & Yu, 2019).

Based on these studies, gas injection huff n puff tends to be inefficient in the case of extreme leakage of the injected gas to the neighboring wells which will prevent gas containment and achieving miscibility condition. In these cases, enrichment of the gas might allow producing a higher drawdown during the production cycle and help with the recovery; yet, it has not been studied.

Sharma et al. (2018) tested the application of surfactant and huff n puff methane injection on gas condensate recovery from Eagle Ford core samples. The results show that surfactant can alter the wettability of the formation rock and improve the gas condensate recovery from the fractures. Huff n puff methane experiment also demonstrated significant recovery of the gas condensate both near the fractures and inside the matrix. In conclusion, huff n puff was introduced as a more efficient recovery method for the ultra-low permeability gas condensate reservoir.

Morsy et al. (2013) introduced waterflooding through imbibition mechanism as an alternative EOR potential approach for Eagle Ford shale. Experimental results of this study showed a higher recovery of oil from the Eagle Ford cores using distilled water (19%) spontaneous imbibition compared to the brine solution (12%). These results were approved by numerical simulation of the experiment as well.

EOG Resources was one of the first operators who performed a successful gas huff n puff EOR in the Eagle Ford formation leading to an uplift of 30% to 70% in total oil recovery. However, little is known about the technical details of this pilot study (Rassenfoss, 2017; Hamdi et al., 2018).

Data from seven different EOR pilot projects implemented by different operators in three distinct counties show that all these tests used hydrocarbon gas for huff n puff, however, the composition of gas was different for each of these studies. The overall results of these studies

were very encouraging and all of them demonstrated a considerable increase in the incremental oil recovery as a result of cyclic injection (Hoffman, 2018).

Results of a multi-well pilot study of gas huff n puff in the Eagle Ford is reported by (Carlsen et al., 2019) in which one the wells were getting injected with gas and the other offset wells (with spacing of around 500 ft) were shut-in during the soak time of the huff n puff cycle. Despite the shutting in, the injected gas was observed in offset wells both during the soak time and during the production cycle. The start date of the first cycle is reported as early 2018 followed by injection cycles of 2-3 months. This study concluded that multi-contact miscibility is not relevant to the huff n puff application and the recovery efficiency of a huff n puff depends on the pressure difference between the saturation pressure of the fluid and pressure within rock pieces, the greater the pressure difference, the better oil recovery.

Wolfcamp Formation

Phan et al. (2018) studied the lithologic and geomechanical controls that impact CO_2 huff n puff in Wolfcamp. Their study improved efficiency of CO_2 in enhancing oil recovery given sufficient soaking time and increasing number of injection cycles. Their sensitivity analysis conducted on several well-spacing and gas injection cycles showed that early gas breakthrough in the offset wells is unavoidable and small well-spacing results in poor injection performance.

Liu et al. (2018) conducted a Constant Composition Expansion (CCE) test on a sample of reservoir fluid (separator oil recombined with separator gas with a GOR value observed during the production prior to falling below bubble point). Swelling test was performed on the reservoir fluid using CO_2 with increasing CO_2 concentration. MMP test was performed on the reservoir fluid using C1, produced field gas (from separator), and CO_2 using RSA (Rising Bubble Apparatus). RSA is a fast and simple alternate to the slim-tube test. Results show that methane did not show first contact miscibility; same story or the separator gas. CO_2 got miscible almost immediately after contacting oil, indicating that first contact miscibility was achieved.

Core flooding was conducted in a HPHT core holder for investigating the cyclic injection of different gases by recording the amount of collected oil at the end of each cycle. Highest recovery was achieved in the first cycle getting lower towards the sixth (and last) cycle. Cycle 7 was to small, so 6 was considered the final point. After each cycle, the effluent fluid composition was analyzed using GC showing that:

- Most light HCs (less than C16) were recovered in the first two cycles while heavier components appeared towards the end of cycles (lighter HCs get vaporized first).
- CT scan of the core after CO_2 injection is compared with the CT scan prior to the injection to visualize how CO_2 changes the oil saturation profiles in the rock (could be done using NMR too).
- CO_2 was the most efficient solvent.

In an experimental study of surfactant induced wettability alteration in Wolfcamp (Neog & Schechter, 2016) Wolfcamp core samples were saturated and aged (4 months under reservoir temperature) with the native crude followed by contact angle and IFT measurements. Spontaneous imbibition was the main experimental method coupled with CT imaging to

visualize the imbibition process. 5 different surfactants were tested to evaluate their effectiveness. Contact angle experiment confirmed that the native wettability of Wolfcamp shale is intermediate wet which was altered to water-wet after the imbibition test using surfactant. The recovery of oil from the pores was confirmed through comparison of the CT scan images of the core before and after the experiment.

Similar experiments and results were also presented by Zhang et al. (2019). Their conclusions were supported by numerical simulations of the core scale and field scale surfactant-imbibition model as well.

Spontaneous imbibition for improving the wettability and enhancing the recovery using different chemicals and surfactants is addressed in several other studies for the Wolfcamp shale in Permian basin (Alvarez et al., 2017, Alvarez et al., 2018).

In an experimental/Field study on Surfactant EOR in Wolfcamp by Haliburton (Jones et al., 2016), Weak Emulsifying Surfactant (WES) was used for recovering oil to create short lived oil-in-water emulsion.

The following is the experimental process used to select an effective surfactant: the formation rock is crushed and screened to 100 size mesh, then packed in a column and saturated with formation oil at Res. Temperature. Fracturing fluid containing different surfactants is passed through the column twice. The first pass extracts free oil, and the second pass extracts the trapped oil.

A group of 163 wells in the Wolfcamp formation were studied in a field test. 43 of them used WES while 120 didn't (in the fracturing fluid). Accounting for all completion (horizontal displacement, proppant, lithologies) and production (GOR, artificial lift) factors affecting the well performances and normalizing data to mitigate their impact, WES treated well showed better performance. This study suggested that WES added to benefits by:

1- mobilizing the trapped oil in the pores by affecting surface/interfacial tensions.

2- Adding an uplift to the non-treated wells who had hydraulic communication with the treated wells (frac hits).

Field results were significantly better than the lab results (19% additional recovery in the field). The hypothesis for explaining this is that the hydraulic communication in the field/ effect of fractures created an uplift.

In another experimental/Field study of chemical (Surfactant) EOR in Permian (Bidhendi et al., 2019), both core and formation fluids sample were taken from Wolfcamp A, Wolfcamp B, and Sprayberry formation. Spontaneous imbibition tests were carried out to evaluate the surfactants efficiency. Captive bubble method was used to measure the contact angle before and after chemical treatment. IFT of crude oil samples with brine and chemical solutions were also measured using spinning drop tensiometer proving that IFT decreases in the presence of surfactant.

A set of microfluidic devices were also used to visualize the process of imbibition in the matrix as a result of wettability changes. This experiment showed that under static no-flow conditions, solution mostly imbibes into finest channels and not much into the main channel. However,

under dynamic conditions the solution enters the main channel we well (through imbibition). It also showed that oil was produced in all direction including against gravity using chemicals for wettability alteration and imbibition improvement.

In the field trial for 2 Wolfcamp A wells in Delaware basin, a specific volume of the selected surfactant was added to the completion fluid for each stage of fracturing. After completion the well did not go through additional shut in and was online immediately after. Evaluating performance after 180 days, the oil rate was increased about 39% above the average type-curve for the area and 14% above the Delaware basin type curve. This study proposed wettability and IFT alteration as the key for enhancing oil recovery in Permian.

Jin et al. (2019) presented a field pilot of microbial huff n puff in Wolfcamp Permian. Fracture containment and restriction of flow path between the nanopores cause reduction of flow, blockage of the nanochannels by heavier hydrocarbons and contaminates the effective SRV. Microbial EOR was implemented in this study on a fractured well (twenty stages of frac). 500 bbls microbial nutrients were added to the water and injected down the well using water delivery pump (1 day). The well was shut-in afterwards for a period of seven days then was placed backed on production. The production uplift after 180 days was 81%. Field results further confirmed that the assumption of SRV containment was valid.

In conclusions, it is evident from the literature that molecular diffusion is a key factor in investigating the oil and gas interaction under high pressure in porous media consisting of a low-permeability matrix and a dense network of fractures. To improve the understanding of miscibility, phase behavior, and flow behavior of oil-gas-water system under the compositional and pressure changes during both injection and production, diffusion flow factors must be thoroughly studied.

Laboratory works have shown great success in improving the oil recovery from core samples through gas or surfactant/ biosolvent solution injection. However, most of these samples are taken from the pure matrix neglecting the added complexity of mechanisms due to the induced fracture in the formation. Up scaling the over-optimistic laboratory results to the potential recovery expected in the field scale has been the biggest challenge of the industry to debate large scale field implementation of any potential technique.

Most of the proposed EOR methodologies require long soaking time of the injected fluid which is contradictory to the real field operation expectations by requiring shut-ins of the wells for a long period of time. Any proposed technique that eliminated the need for loss of production for a period, has been better received to be field-tested from the industry. This makes continuous injection methods and techniques combined with the fracturing/re-fracturing work more appealing in terms of the economic feasibility (Fragoso et al., 2018).

Background Information on Enhanced Oil Recovery (EOR) from Hydraulically Fractured Reservoir Using Cyclic Gas Injection

Miscible gas flooding is a recovery technique controlled by the mass transfer happening in the formation when miscibility develops between the gas and reservoir oil (Lake et al., 2014). Miscibility as defined in the physical condition occurs when two fluids can mix in all proportions without the development of an interface (Clark et al., 1958). Miscibility can either be achieved at first contact of the injected fluid with the native fluid (first-contact miscibility) or

be developed as the native fluid is continuously mixed with the injected fluid (multiple-contact miscibility). Miscibility is sensitively controlled by the injection and mixing pressure, intermediate hydrocarbon content of the reservoir oil and reservoir temperature. The gases historically used in the field application of miscible gas injection vary widely based on the accessibility and economics. In most cases, various hydrocarbon gases are cheap and easily accessible which makes them the most popular gases being used currently in the US (Dao et al., 2005). Sheng (2017) has summarized the results of several huff n puff and gas injection field pilot studies showing that for the formations with the permeabilities above 1 mD, where injectivity is not an issue, gas injection projects were successful. However, for the tight formations with permeabilities in the nano-Darcy range, gas or CO_2 huff n puff should outperform the gas flooding, if it is properly designed in terms of soaking time, injection rates, injection pressure, and well spacing.

Cyclic gas injection or "huff n puff" is proven to be the most effective method for applying miscible gas injection EOR in the hydraulically fractured low-permeability reservoirs. The ability of a formation to contain the high pressure injected gas near the wellbore, contact of the wellbore with maximum volume of the productive zone within the formation, and the appropriate well spacing to minimize the hydraulic commination between the wells are the three most important factors in determining the success of a huff n puff practice (Konopczynski & Dowlatabad, 2018). The effect of fracture density and miscibility on the effectiveness of CO_2 huff n puff is addressed by (Gao et al., 2019, Tsau et al., 2019). The experimental results of this study showed that existence of fractures reduces the sweep efficiency of the injected fluid, and a larger number of cycles is required to improve the oil recovery. Also, first contact miscibility is proven to be more efficient that the multi-contact miscibility.

Simulation studies on the performance of EOR huff n puff in Eagle Ford agree that injection of field gas causes improvement in the incremental oil recovery. Injection patterns including the injection pressure, injection/production time, and composition of the injected gas were determined to be the most influential factors on the success of an EOR huff n puff. Transport in the natural or hydraulic fractures is known as the dominant oil recovery mechanism in Eagle Ford and well interference has a significant negative impact on the efficiency of gas injection (Ajayi et al., 2018, Yu et al., 2019, Wang & Yu, 2019). Based on these studies, gas injection huff n puff tends to be inefficient in the case of extreme leakage of the injected gas to the neighboring wells which will prevent gas containment and achieving miscibility condition. In these cases, enrichment of the gas might allow producing a higher drawdown during the production cycle and help with the recovery; yet, it has not been studied.

Todd & Evans (2016) summarized the outcome of about seven different EOR field pilot studies over the course of eight years. Despite different locations, performing operator, and injection techniques used in these studies, early gas breakthrough is reported as a common issue in all of them. Increased hydraulic connectivity of the wells is recognized as the main cause of gas breakthrough and ease of injectivity. Most of the pilots did not exhibit any increase in the production and in those who did, the increase was minimal. EOG Resources was one of the first operators who performed a successful gas huff n puff EOR in the Eagle Ford formation leading to an uplift of 30% to 70% in total oil recovery. However, little is known about the technical

details of this pilot study (Rassenfoss, 2017, Hamdi et al., 2018). Results of a multi-well pilot study of gas huff n puff in Eagle Ford is reported by (Carlsen et al., 2019) in which one the wells were getting injected with gas and the other offset wells (with spacing of around 500 ft) were shut-in during the soak time of the huff n puff cycle. Despite the shutting in, the injected gas was observed in offset wells both during the soak time and during the production cycle. The start date of the first cycle is reported as early 2018 followed by injection cycles of 2-3 months. This study concluded that multi-contact miscibility is not relevant to the huff n puff application and the recovery efficiency of a huff n puff depends on the pressure difference between the saturation pressure of the fluid and pressure within rock pieces, the greater the pressure difference, the better the oil recovery. Data from seven different EOR pilot projects implemented by different operators in three distinct counties show that all these tests used hydrocarbon gas for huff n puff, however, the composition of gas was different for each of these studies. The overall results of these studies were very encouraging and all of them demonstrated a considerable increase in the incremental oil recovery as a result of cyclic injection (Hoffman, 2018).

Overview of the Project Objectives & Results

The main objective of the Phase II of HFTS project was to design and perform a huff n puff gas EOR experiment in the Midland Basin by leveraging HFTS data and results in order to:

- Demonstrate through a field experiment the effectiveness of cycling gas injection ("huff-n-puff") as a potential EOR technique for increasing oil and gas recovery from the Wolfcamp shale in the Midland Basin. The gas came from nearby Targa gas processing facilities resulting in the added benefit of the field gas being sequestered rather than flared to the atmosphere.
- Evaluate the impact of the pre-existing fracture networks on the containment of the injected gas above the pre-determined miscibility pressure. Results of this study showed that existence of fractures reduces the sweep efficiency of the injected fluid, and a larger number of cycles is required to improve the oil recovery. Early gas breakthrough in offset wells is reported as the main challenge in achieving and establishing the minimum miscibility pressure. Increased hydraulic connectivity of the wells is recognized as the main cause of gas breakthrough, ease of injectivity, and rapid pressure loss. Most of the involved wells did not exhibit any increase in the production and in those who did, the increase was minimal.
- Determine the optimum composition of the injected gas, number of injection cycles, ideal soaking time and operational conditions by compiling pertinent inventory of engineering and geological characterization through laboratory studies, simulations, and field data acquisition.

Field Operations

Executive Summary

The Phase II EOR experiment was executed in two parts: laboratory testing and full-scale field testing of the natural gas huff-and-puff which also involved geological characterization and reservoir simulation of the area of study. Laredo Petroleum and GTI performed an EOR field pilot near the original Hydraulic Fracturing Test Site (HFTS). History matching and reservoir

simulations to estimate the required volume of gas for pressurizing gas was conducted. Slim tube/PVT tests and swell experiments were carried out to determine the minimum miscibility pressures, measure constant composition expansion and oil viscosity after each addition, and understand contribution of swelling and viscosity reduction. Acoustic activities were also monitored in the area to observe and analyze fracture network connectivity and impact on gas injection by comparing the pre-injection and post-injection activities between the involved wells.

The field pilot resulted in injecting over 280 MMscf of natural gas into a previously fracture-stimulated well to produce additional oil through a miscible gas injection process utilizing the huff-and-puff method. Injection pressures and natural gas compositions were selected to maintain pressure in the reservoir below fracturing pressure but above the determined miscibility pressure. In the first cycle, 15 Mscf of gas was injected at the rate of above 3.5 Mscf/d and the initial tubing pressure of 1,000 psi and pressure was closely monitored to assure the maximum injection bottom-hole pressure remained under 4,700 psi to avoid re-fracturing. Injection was stopped after 20 days due to operational issues with the compressor and the compressor was replaced. Once replaced, injection restarted at a rate of 4 followed by 5 Mscf/d. The injection was supposed to continue until the bottom hole pressure built up to above the minimum miscibility pressure of 3,500 psi before the well was placed back on production. Early gas breakthrough in offset wells led to shutting in multiple offset producers for the purpose of pressuring up the reservoir. Shut-ins included 7 horizontal offset wells: Sugg-E-197 198 6NU, 3NU, 3SU, 4SU, 5SU, Sugg-E184 1NU, 1NM, and one vertical well: Sugg-E-197H. Observing an increase of gas production in the 3 other wells including Sugg-E-197 198 1NU, Sugg E-5 and Sugg 184E more than 1 mile away from the injector, while the pressure at the injector was far below the MMP, led to ceasing the injection due to the un-economic state of shutting-in multiple wells and increased gas production in the others. On May 31, 2019, after about 14 weeks and injection of over 280 MMscf of natural gas, the injection was stopped, and injection/production logs were obtained using a fiber optic cable deployed in carbon-fiber rod.

To better evaluate the effectiveness of cycling gas injection in increasing oil and gas recovery from the Wolfcamp shale, diagnostic data were collected during the cyclic gas injection and afterwards to monitor post-injection production performance of pilot wells as part of the field execution of the experiment. Laboratory experiments including black oil study, MMP slim tube analysis, swell testing and core flooding experiments were also performed to determine PVT behavior and de-couple the impact of pre-existing hydraulic and natural fractures from the injected & native fluid flow and phase behavior.

A slant core was collected from a deviated well drilled offset to the injector to provide physics-based explanations for the observations from the gas injection pilot by proving direct observations for characterizing the fracture network.

Field Demonstration

Laredo Petroleum provided a few options for the location of the EOR pilot and after evaluating all possible options based on various criteria including age of wells, interference with adjacent wells, completion type, landing point, and facilities access, a group of test wells located about 1 mile to the northwest of the original HFTS wells were selected for the EOR pilot. Figure 171

shows the location of the selected wells for the EOR pilot as well as other vetted test site options.

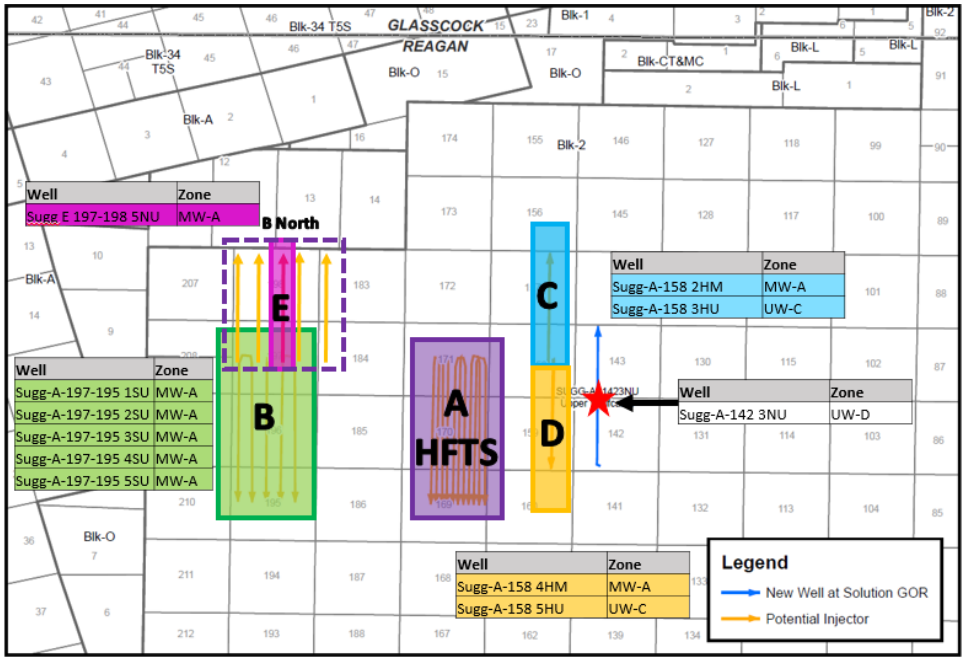


Figure 171: Location of EOR test wells and other potential test locations.

In Figure 171, the dashed purple box shows the location of the EOR test site, and the solid pink box shows the injector well, which is the Sugg E 197-198 5NU. This is a north facing 7,500-foot horizontal well drilled though the upper Wolfcamp formation. Adjacent to it are other horizontal wells also drilled in the north direction. B-North (EOR test site) geological variations from area A (original Hydraulic Fracturing Test site) include being more distal to shelf deposition, having slightly higher carbonate content, middle Wolfcamp zone A is about 200' deeper. Similar structure, similar stress orientation, similar lithology, and similar fracture

gradient was observed for these two test sites.

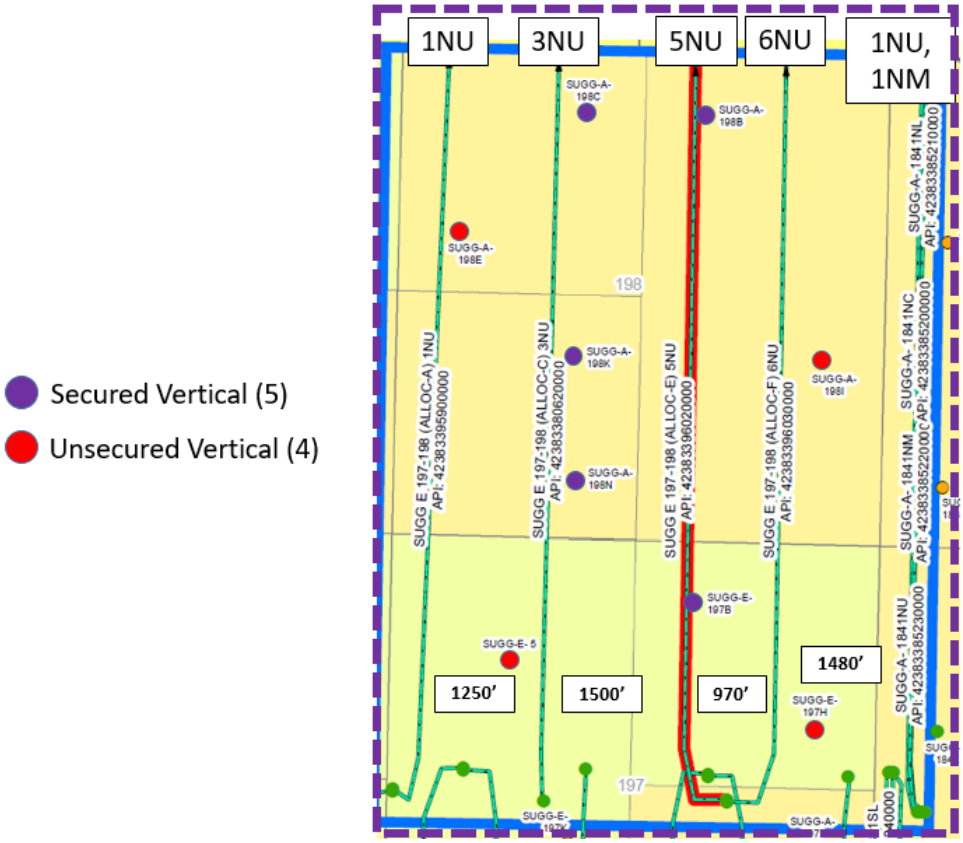


Figure 172: Plan view of EOR test site showing the horizontal injector and monitor wells, and vertical wells.

Figure 172 shows a more detailed layout of the wells in the EOR field pilot. The middle well (highlighted in red) is the injector used to inject the miscible gas. The green wells, two wells to the left (west) and the three wells to the right (east), were used to monitor gas breakthrough. In between the horizontal wells multiple vertical wells were available that some of which were instrumented for observation of the extent of the injected gas plume. Other vertical in the test area were plugged at strategic depths to ensure no gas communication in the wellbore between various producing zones. Table 13 is the completion summary of the pilot horizontal wells shown in Figure 172. Highlighted in pink is the selected injector whose production performance was the best among all pilot options.

Test wells were prepared for the EOR experiment by upgrading the tubing in the injector well and installation of bottom-hole pressure and temperature gauges in the offset monitor wells. Gas delivery system was also modified and prepared for the compressor installation. Other activities related to instrumentation included land surveys for the deployment of passive surface seismic/microseismic arrays to monitor acoustic emissions during gas injection and production cycles.

Table 13: Completion summary of the EOR pilot wells; injection well is highlighted.

Name	Sugg E 197-198 1NU	Sugg E 197-198 3NU	Sugg E 197-198 5NU	Sugg E 197-198 6NU	Sugg A 184 1NU
Lateral Length (ft)	7577	7473	7371	7439	7192
No. of Stages (#)	28	28	27	27	27
Clusters Per Stage (#)	5	3	5	5	3
Stage Length (ft)	271	267	273	276	266
No. of clusters (#)	140	84	135	135	83
Fluid per Foot (bbl/ft)	71	35	56	56	35
Proppant per Foot (lbs/ft)	2406	1125	1822	1809	1178
Rate (bpm)	95	93	96	96	92

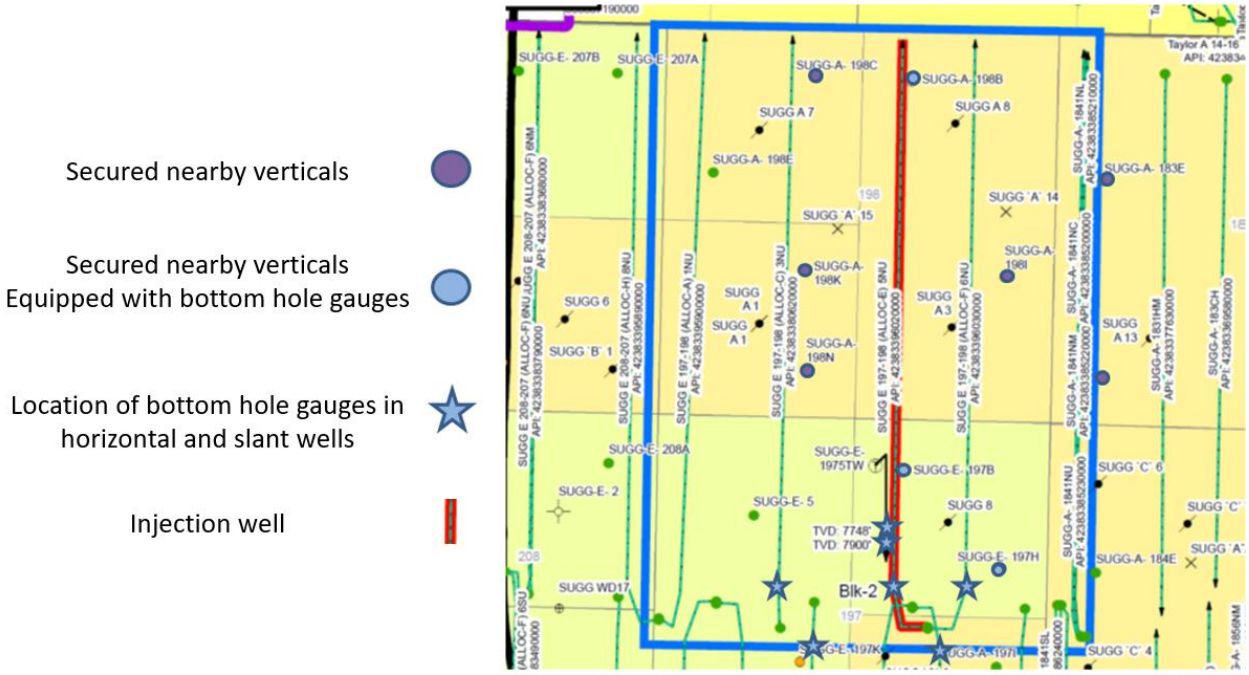


Figure 173: Plan view of EOR test site showing the horizontal, vertical, and slant wells as well as the location of BHP gauges.

Figure 173 shows the detailed configuration of all involved wells, horizontal and vertical, in addition to the location of pressure/temperature gauges.

As shown in Figure 173, one slant core well (SUGG E 197 5TW equipped with two bottom hole gauges) was drilled offset to the injector (SUGG E 197-198 5NU equipped with one bottom hole gauge) to monitor oil saturation before, during, and after each injection cycle.

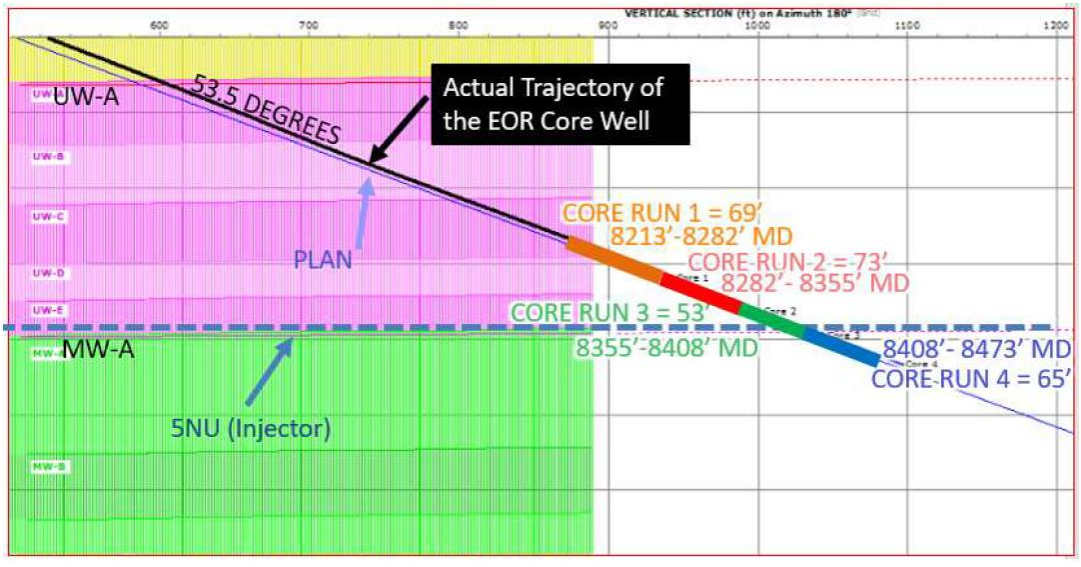


Figure 174: Trajectory of the Second Slant Core Well. Run #1: Cut 69' with 100% recovery; Run #2: Cut 73' with 99.5% recovery (72.65'); Run #3: Cut 53' with 99.4% recovery (52.7'); Run #4: Cut 66' with 100% recovery (65.9').

Figure 174 shows the trajectory of the slant core well in relation to the injector. In total, 260 ft of SRV core from the Middle Wolfcamp formation was recovered as summarized in Figure 174.

Field Tests & Results

Gas Injection



Figure 175: Pressure and Rate data in the injector well during gas injection.

Low pressure gas injection was initiated on February 14, 2019. An injection rate of more than 3.5 million scf/d at an initial tubing pressure of about 1,000 psi was achieved. A few hours after injection, the compressor faced operational issues, including electrical and mechanical component failures. After repeated attempts to resolve the issues and multiple re-starts, a decision was made on March 6, 2019, to replace the low-pressure compressor. At this point, about 15 million scf of gas was already injected through several attempted injections with the initial low-pressure compressor, as shown in Figure 175. Limited pressure buildup was also obtained as indicated by the orange arrow.

Upon replacement of the compressor, a sustained rate of 4 followed by 5 Mscf/day was achieved. Maintaining the injection, pressure and gas rates raised in the offset SUGG E 197-198 6NU producing well. After two temporary shut-ins of the 6NU well, the significant increase in the gas production led to the decision for permanently shutting-in the this well on March 20, 2019. The estimated amount of injected gas production from 6NU well prior to shut-in was about 75% of the total gas injected into the injector ,5NU. Figure 176 represents the sequence of these events on the rate/pressure vs date graphs.

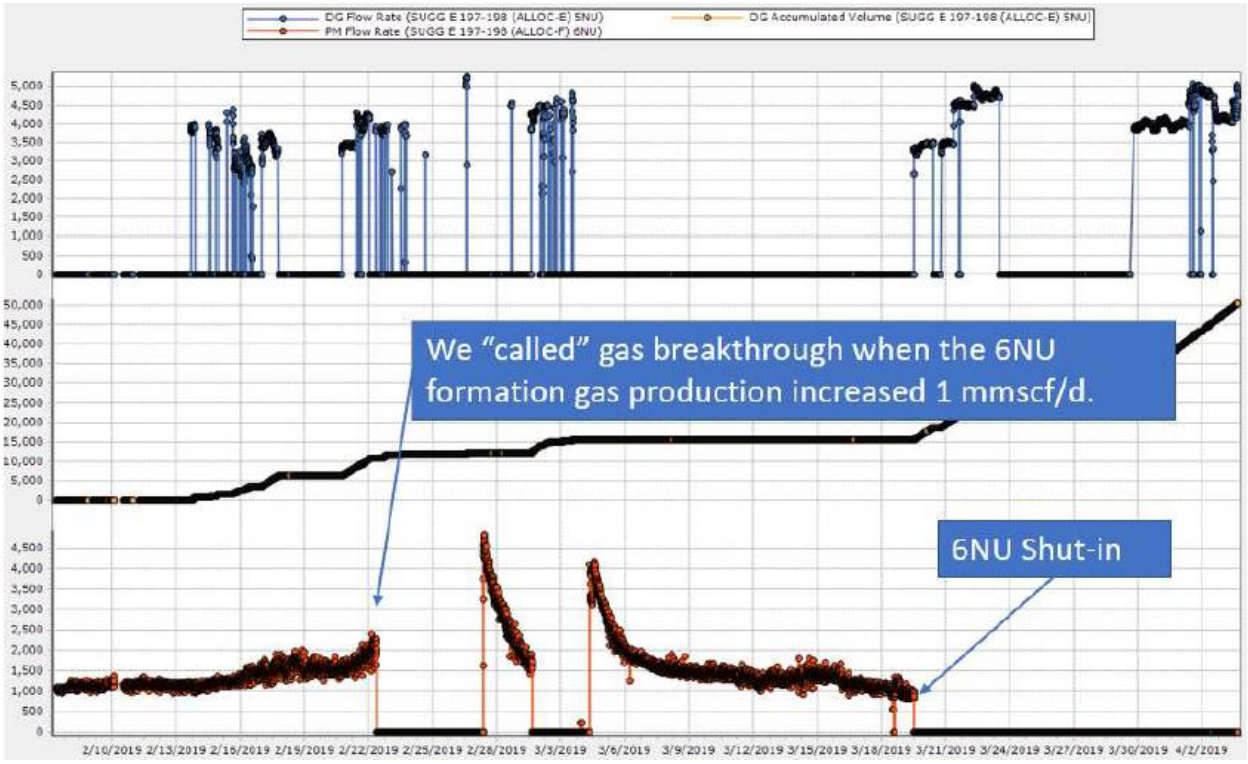


Figure 176: Produced gas rates in the 6NU well. Once the gas rate increased by 1000 mcf, the well was shut in.

Gas breakthrough to the nearby wells continued by observing significant pressure increase in SUGG E 197H, an adjacent vertical well to the of injector as shown in Figure 173. 197H well was successfully secured causing a short pause in the gas injection process. Shortly after, many of the offset wells had to be shut in due to a significant increase in gas production which overwhelmed the gathering and processing facilities. In total, 7 well had to be shut in as a result of the excessive increase in the gas production and pressure build-up. Three other wells also experienced increase in gas production but were not shut based on the decision made by involved parties. The configuration of these wells is shown in Figure 177.

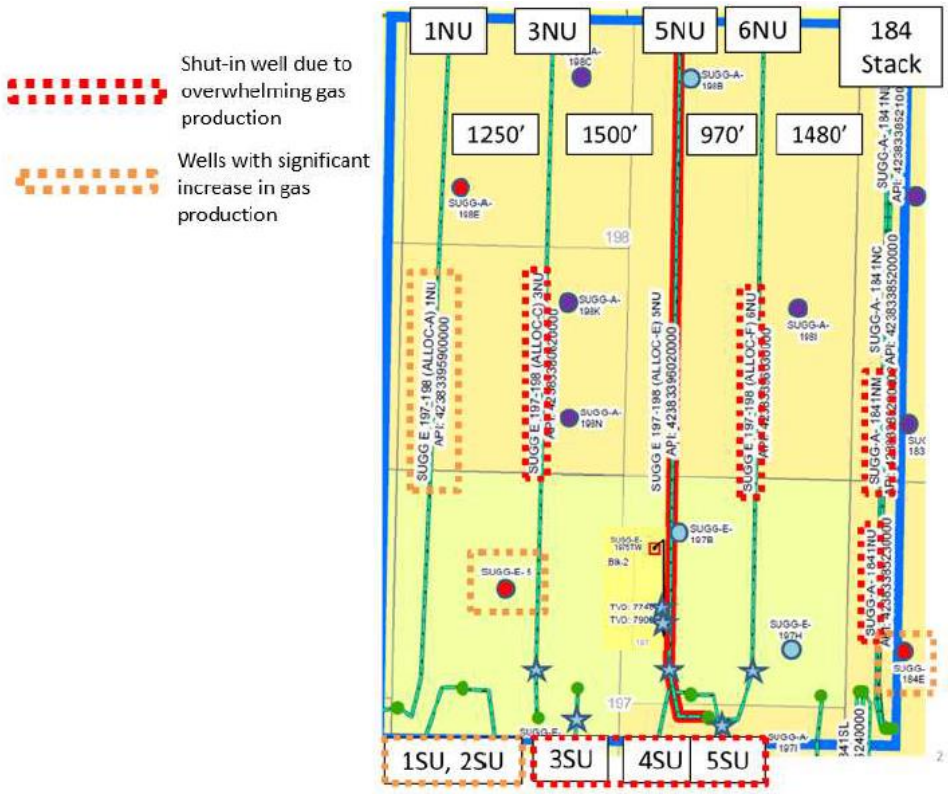


Figure 177: EOR pilot well layout indicating wells which were shut in due to the severity of their increased gas production (red dashed boxes) and the wells with increased gas production that were not shut in (Orange dashed boxes).

The increasing number of wells needed to be shut in and the observed excessive gas production in several other wells, indicated that gas expansion across the hydraulically fractured field was faster and broader than the field operational capacity. In order to build up the downhole pressure above the predetermined miscibility pressure, in a decent amount of time, an extensive range of well shut-ins were required. The significant business impact of continuing the gas injection experiment on the test-site host led to the decision of terminating the experiment and stopping gas injection on May 31, 2019, 45 days after the initial injection. Over this period of injection, over 280 MMscf was approximately injected in total as shown in the Figure 178. An injection and production log using a fiber optic cable deployed in a carbon-fiber rod was ran into the well after concluding the injection for further data collection.

Post Injection Data Monitoring

All wells that were shut-in during the gas injection were returned to production in June 2019. An assessment of individual horizontal well production performance before and after gas injection is summarized below:

- Sugg A 197-195 5SU (South of 5NU injector) experienced a significant increase in the gas production during the gas injection in the 5NU which led to the well's shut-in. No significant increase in oil production was observed after bringing this well back to production. Also, oil production followed its original decline trend after the gas injection. Gas decline, despite a brief elevation right after returning to production, continued to follow the trend shown before the injection. Water production did not exhibit any significant changes throughout the experiment. Figure 179 illustrates all

these observations for Sugg A 197-195 5SU, which is indicated by a black star on the field's layout map.

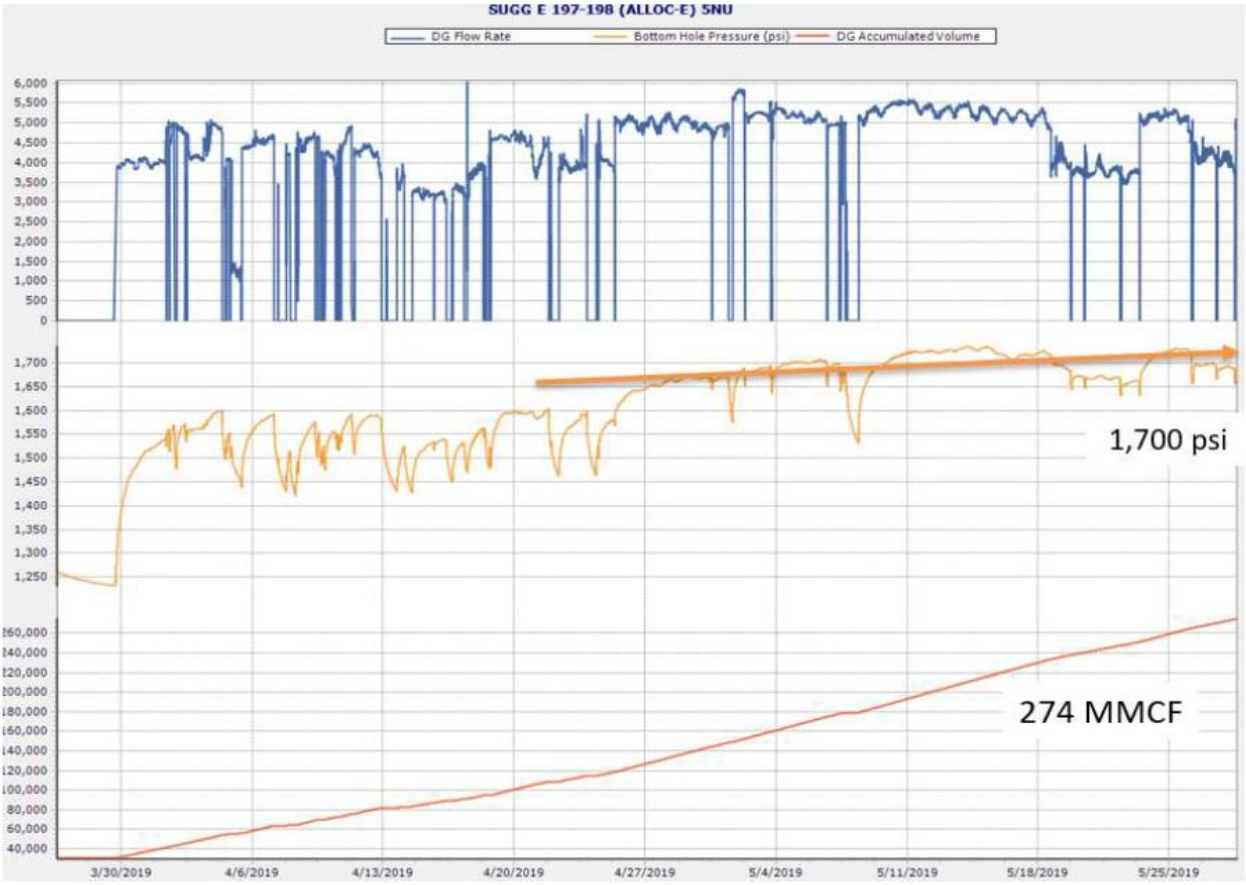


Figure 178: Gas injection timeline in the 5NU well showing the cumulative injected gas plot at the bottom.

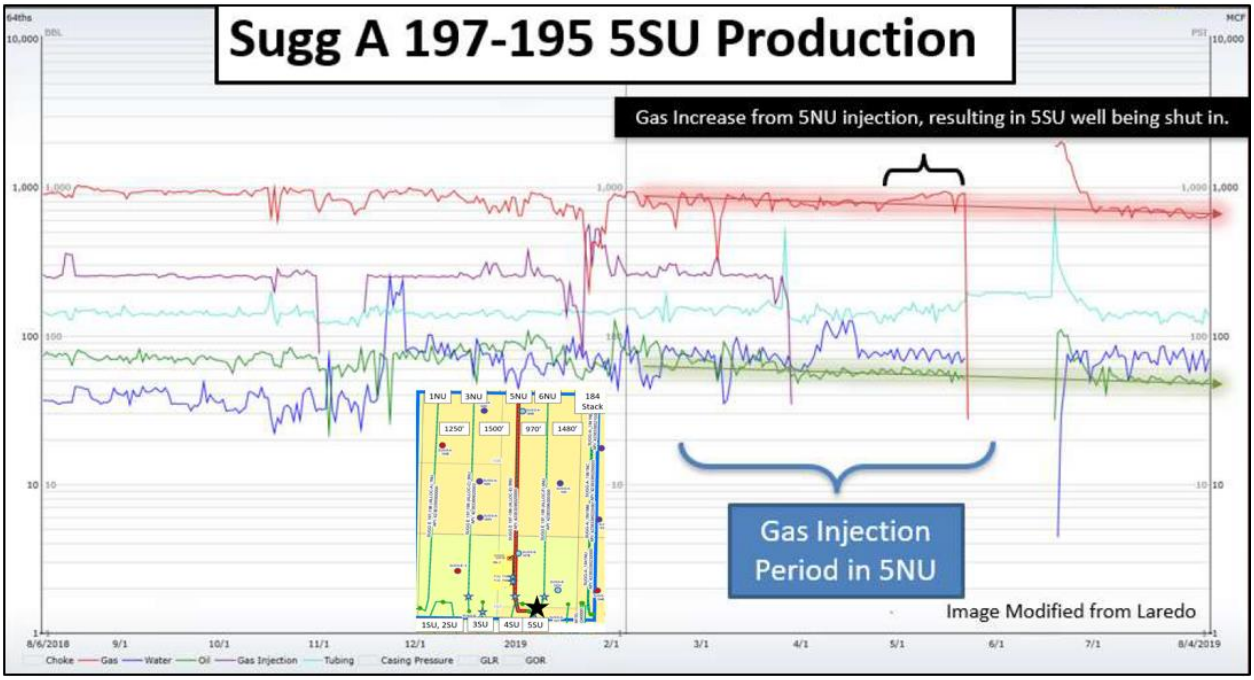


Figure 179: Production profile showing decline trends for Sugg A 197-195 5SU before and after gas injection.

- Sugg A 197-195 4SU (South of 5NU injector) experienced a significant increase in the gas production during the gas injection in the 5NU, leading to the well's shut-in. No significant increase in oil production was observed after bringing this well back to production. Also, oil production followed its original decline trend after the gas

injection. Gas production exhibited a sharp elevation right after returning to production then continued to follow original decline trend as before injection. Water production did not exhibit significant changes throughout the experiment. Figure 180 illustrates these observations for Sugg A 197-195 4SU which is indicated by star on the layout map.

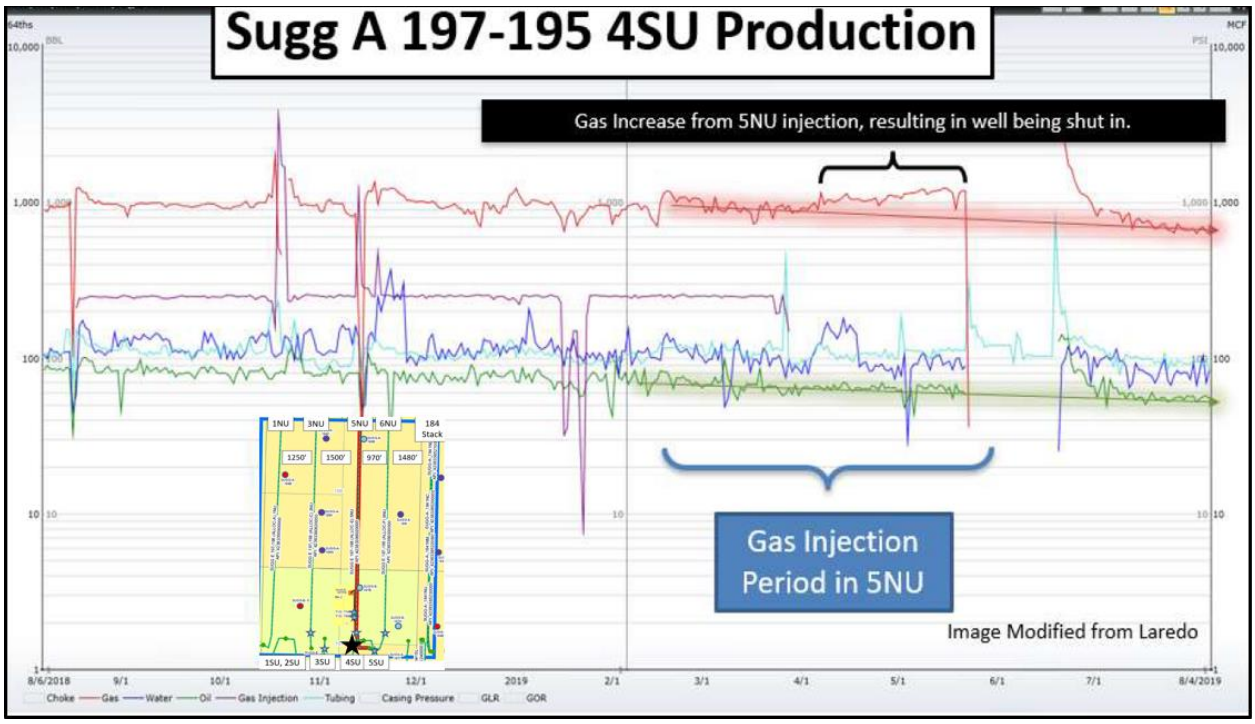


Figure 180: Production profile showing decline trends for Sugg A 197-195 4SU before and after gas injection.

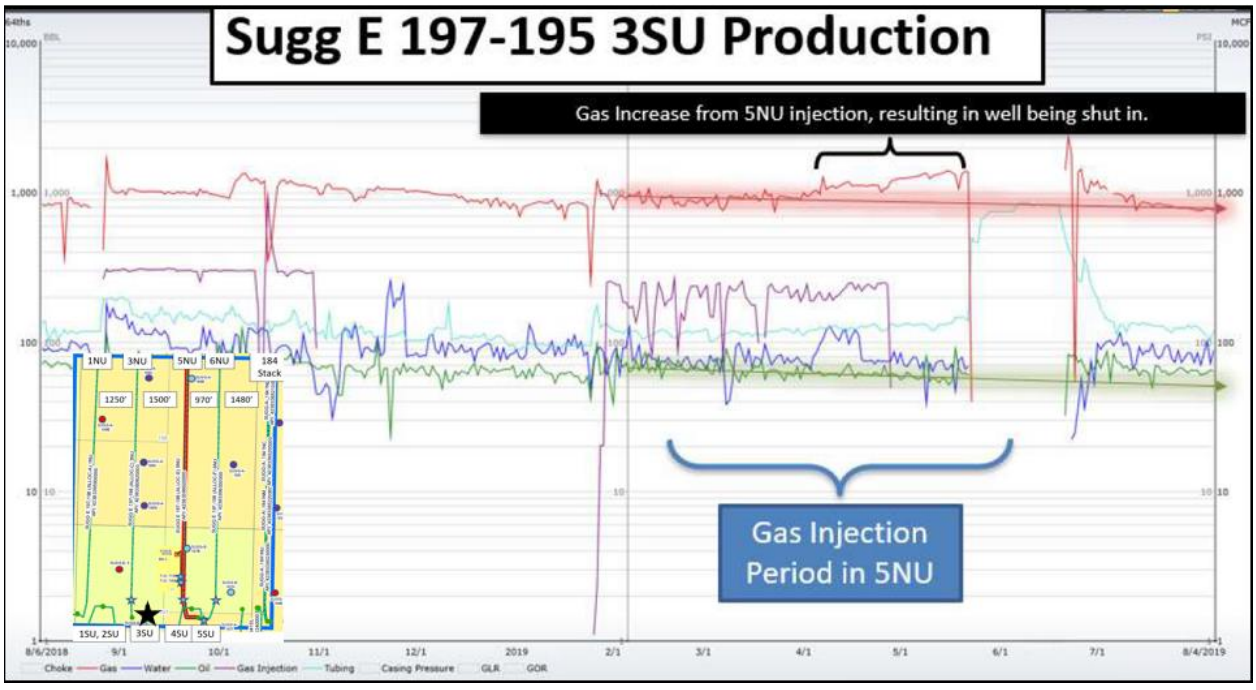


Figure 181: Production profile showing decline trends for Sugg A 197-195 3SU before and after gas injection.

- Sugg A 197-195 3SU (South of 5NU injector) experienced a significant increase in the gas production during the gas injection in the 5NU, leading to the well's shut-in. About 10 bbl/day increase in the oil production was observed after bringing this well back to production. Also, oil production followed its original decline trend after the gas injection. Gas production exhibited a sharp elevation right after returning to production

then continued to follow the original decline trend as before the injection. Water production exhibited a slight increase right after getting well back into production. Figure 181 illustrates all these observations for Sugg A 197-195 3SU which is indicated by a black star on the field's layout map.

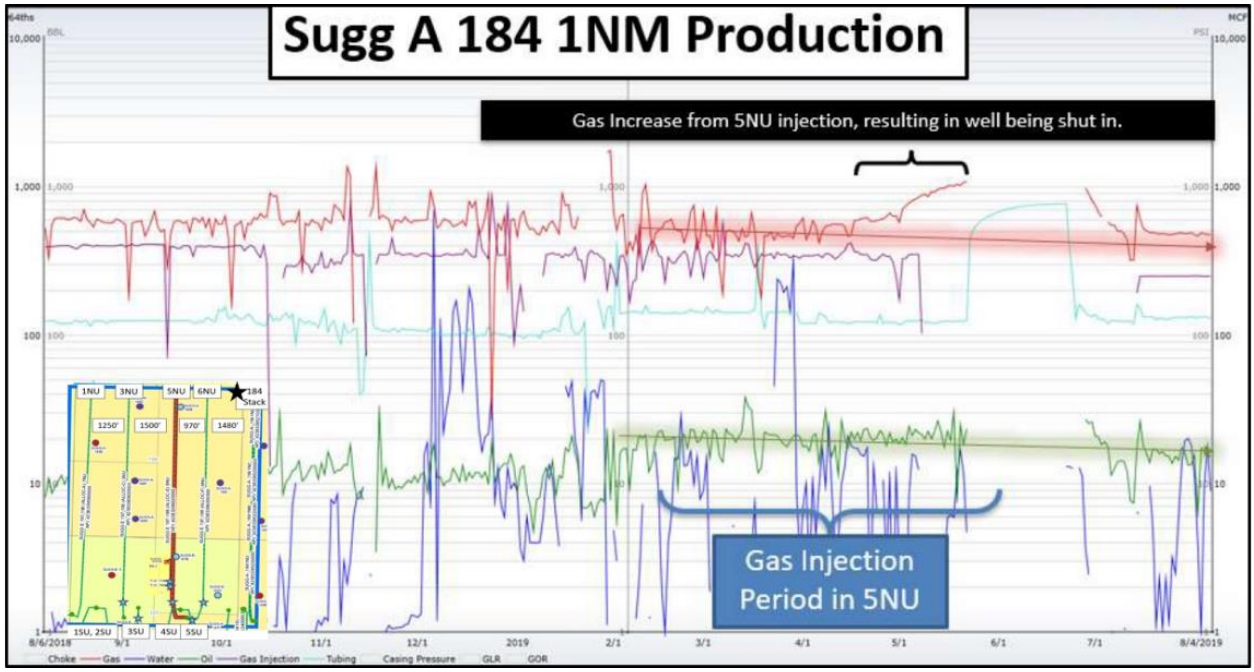


Figure 182: Production profile showing decline trends for Sugg A 184 1NM before and after gas injection.

- Sugg A 184 1NM (north facing well, east of 5NU injector) experienced a significant increase in the gas production during the gas injection in the 5NU, leading to the well's shut-in. No significant increase in oil production was observed after bringing this well back to production. Also, oil production followed its original decline trend after the gas injection. Gas production exhibited a sharp elevation right after returning to production then continued to follow the original decline trend as before the injection. Water production did not exhibit any significant changes throughout the experiment. Figure 182 illustrates all these observations for Sugg A 184 1NM which is indicated by a black star on the field's layout map.
- Sugg A 184 1NU (north facing well, east of 5NU injector) experienced a significant increase in the gas production during the gas injection in the 5NU, leading to the well's shut-in. No significant increase in oil production was observed after bringing this well back to production. Also, oil production followed its original decline trend after the gas injection. Gas production exhibited a sharp elevation right after returning to production then continued to follow the original decline trend as before the injection. Water production exhibited a slight increase right after getting well back into production. Figure 183 illustrates all these observations for Sugg A 184 1NU which is indicated by a black star on the field's layout map.
- Sugg A 197-198 3NU (north facing well, west of 5NU injector) experienced a significant increase in the gas production during the gas injection in the 5NU, leading to the well's shut-in. No significant increase in oil production was observed after bringing this well back to production. Also, oil production followed its original decline trend after the gas injection. Gas production exhibited a sharp elevation right after returning to production

then continued exhibiting an elevated decline trend compared to before the injection. Water production did not exhibit any significant changes throughout the experiment. Figure 184 illustrates all these observations for Sugg A 197-198 3NU which is indicated by a black star on the field's layout map.

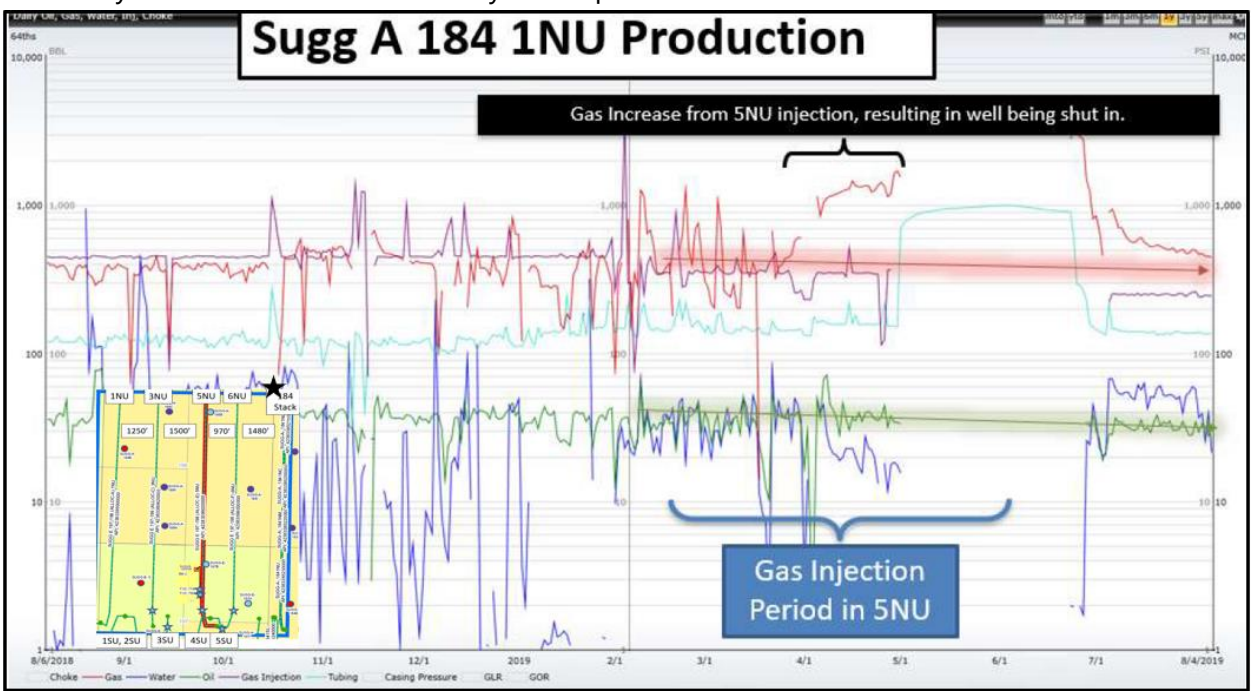


Figure 183: Production profile showing decline trends for Sugg A 184 1NU before and after gas injection.

after stopping the injection (Figure 187). Also, no significant change was observed in the production performance of the wells.

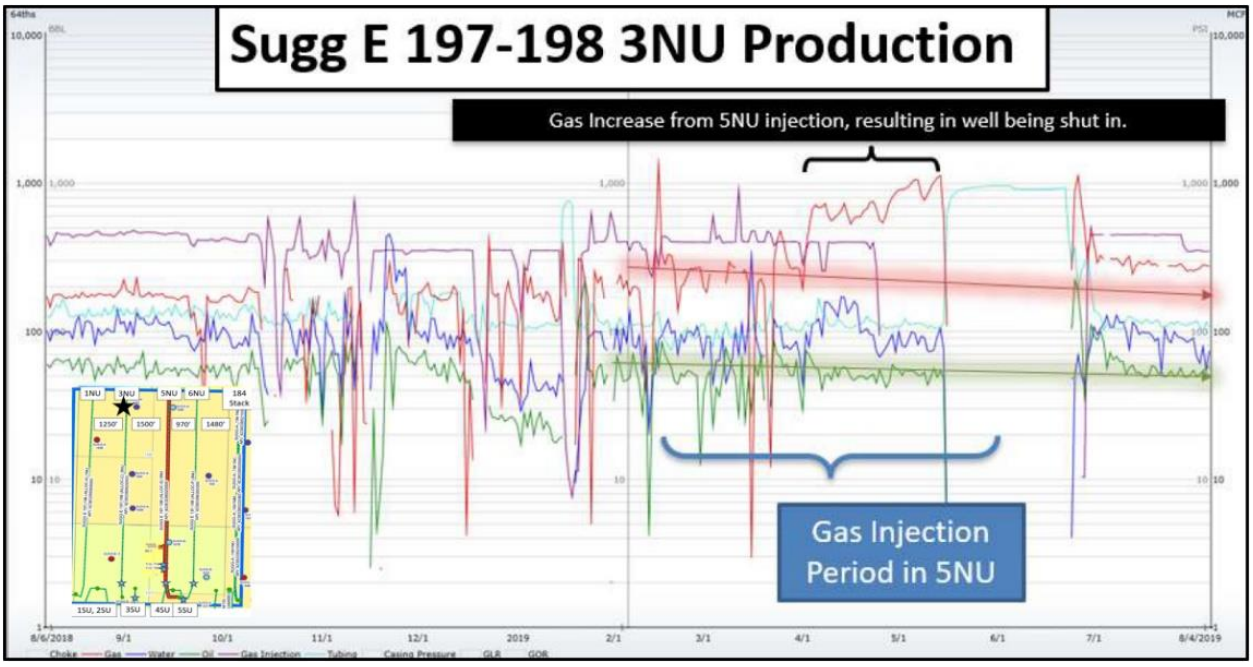


Figure 184: Production profile showing decline trends for Sugg A 197-198 3NU before and after gas injection.

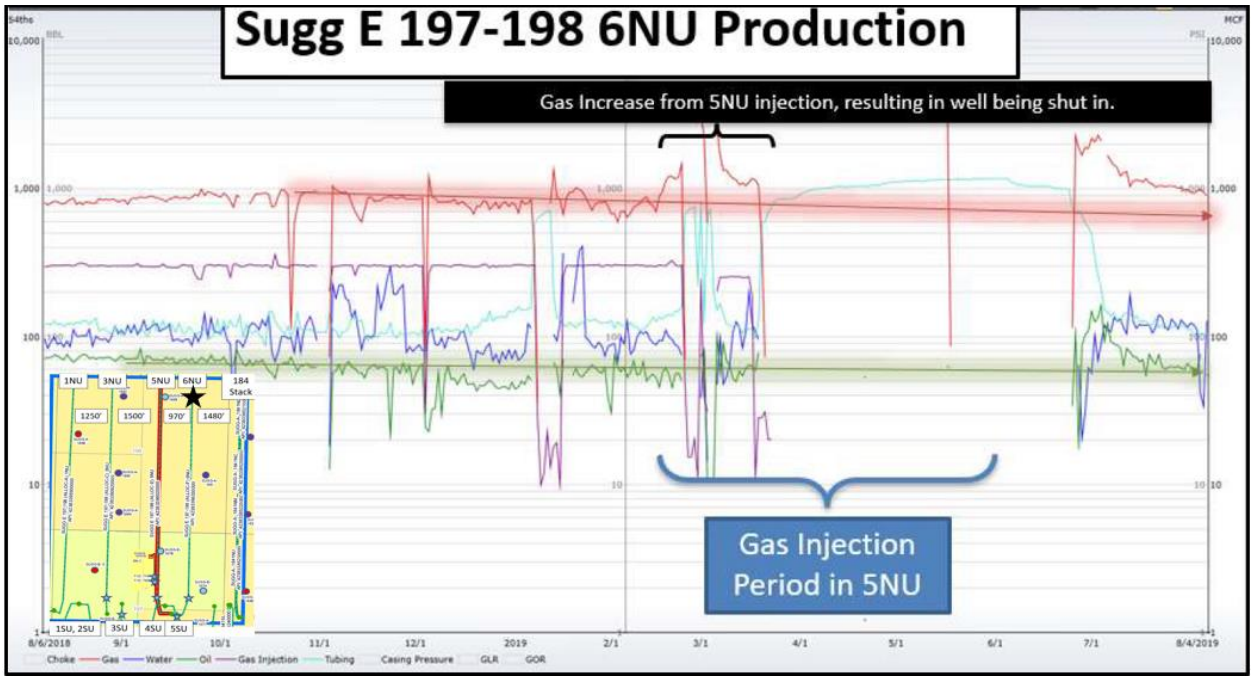


Figure 185: Production profile showing decline trends for Sugg A 197-198 6NU before and after gas injection.

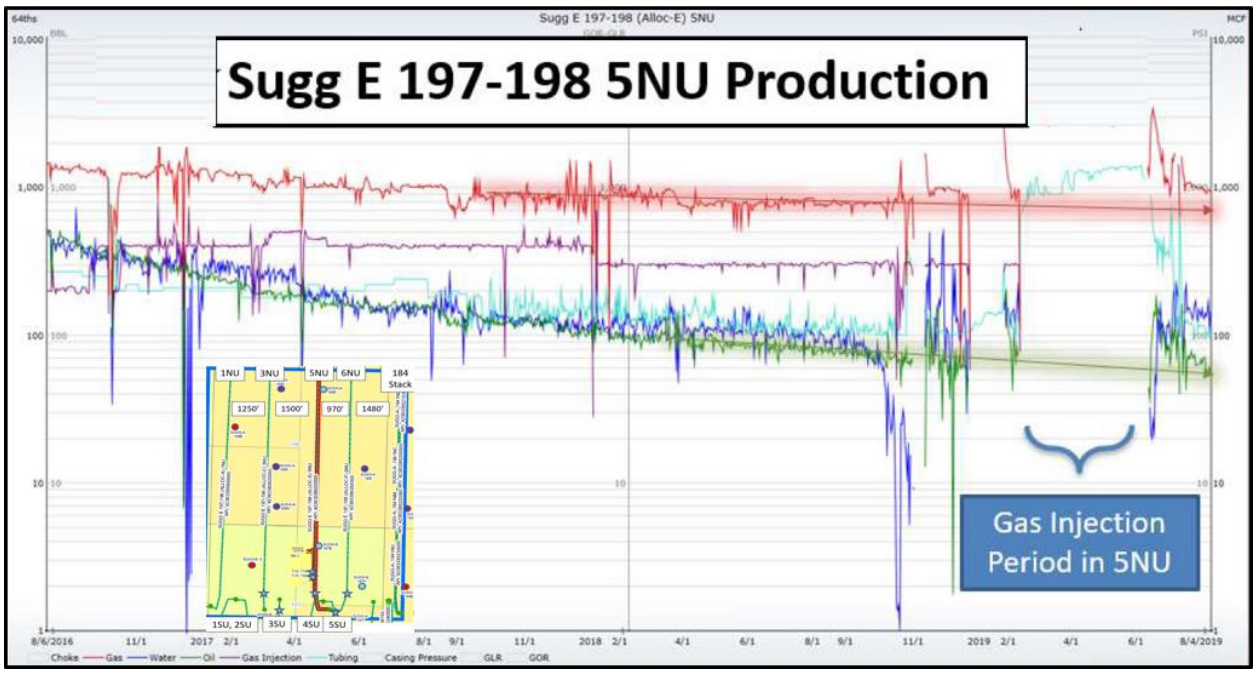


Figure 186: Production profile showing decline trends for Sugg A 197-198 5NU (injector well) before and after gas injection.

- Sugg A 197-198 6NU (north facing well, east of 5NU injector) experienced a significant increase in the gas production during the gas injection in the 5NU, leading to the well's shut-in. No significant increase in oil production was observed after bringing this well back to production. Also, oil production followed its original decline trend after the gas injection. Gas production exhibited a sharp elevation right after returning to production then continued exhibiting an elevated decline trend compared to before the injection. Water production did not exhibit any significant changes throughout the experiment. Figure 185 illustrates all these observations for Sugg A 197-198 6NU which is indicated by a black star on the field's layout map.

- Sugg A 197-198 5NU (gas injection well) did not show any significant increase in oil production after bringing this well back to production. Also, oil production followed its original decline trend after the gas injection. Gas production exhibited a sharp elevation right after returning to production then continued exhibiting an elevated decline trend compared to before the injection. Water production exhibited a slight increase right after getting well back into production. Figure 186 illustrates all these observations for Sugg A 197-198 5NU which is indicated by the red line on the field's layout map.

Monitoring of the production and bottom hole pressure data continued in the test field until the end of 2019 to assess any potential long-term impact of the gas injection on the test site wells. Observation showed that all wells went back to their original downhole pressure behavior.

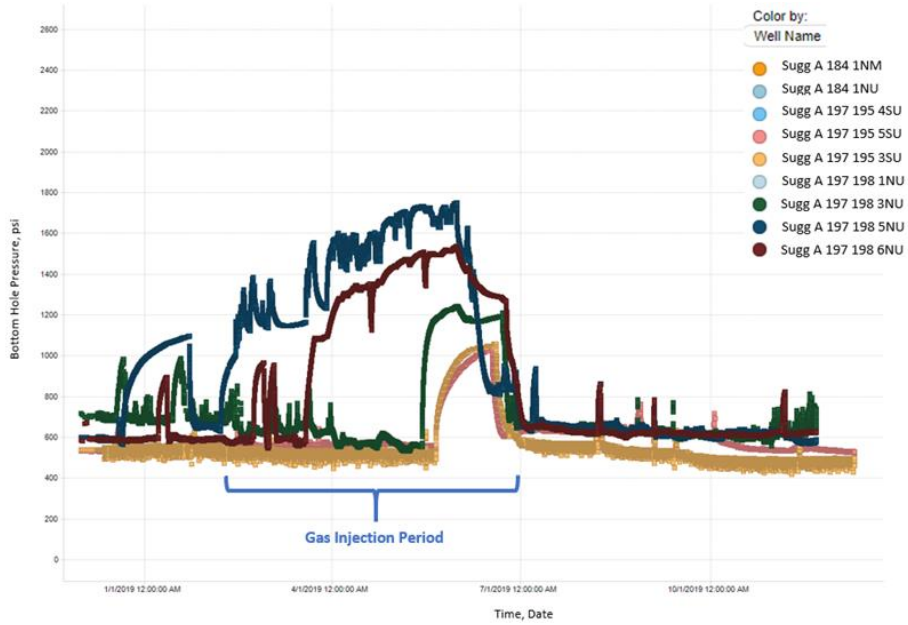


Figure 187: Pressure drawdown profile of the test site wells showing bottom hole pressure responses before and after injection.

Data Compilation

Background Data

Geology

Figure 188 shows the structure map of the HFTS1 phase I (area A) and phase II (Area B), comparing the geological similarities and differences between these two areas. Shown in the geological earth model, the B North area (EOR test site) has similar structure, lithology, stress orientation, and fracture gradient to the original HFTS area except that it is more distal to the shelf, about 200' deeper, and has slightly higher carbonate content.

PVT

Considering the stratigraphic sequence and identified genetic depositional sequences, fluid samples taken from SUGG A 132 3NU, an offset well to the east of EOR test wells, were recommended as representative samples for PVT characterization. This well was still on solution GOR and in the early production stage which made it an ideal candidate to collect a representative sample of the reservoir fluid. Figure 189 shows the location of this well (red star) compared to the EOR test wells (B North).

These samples were used for the following analysis:

- Black oil study
- MMP slimtube on injection gas (with 1,250 BTU Targa gas)
- Swell experiment with injection gas
- Multiple contact experiments with injection gas at different pressures
- MME slimtube with injection gas and condensate (if required)

Details of the results and discussions on these PVT tests are provided in the next section.

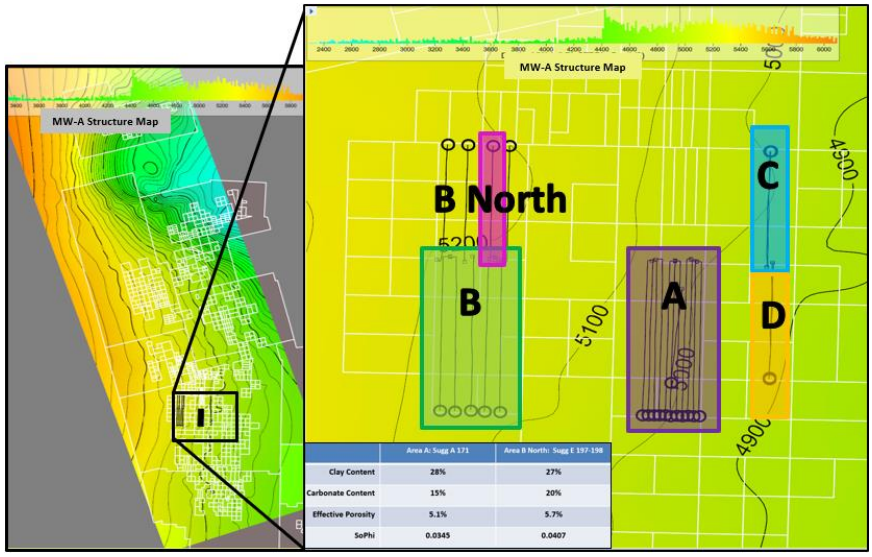


Figure 188: Geology variations and similarities between the two areas A (HFTS Phase I) and B-North (HFTS EOR phase) by Laredo.

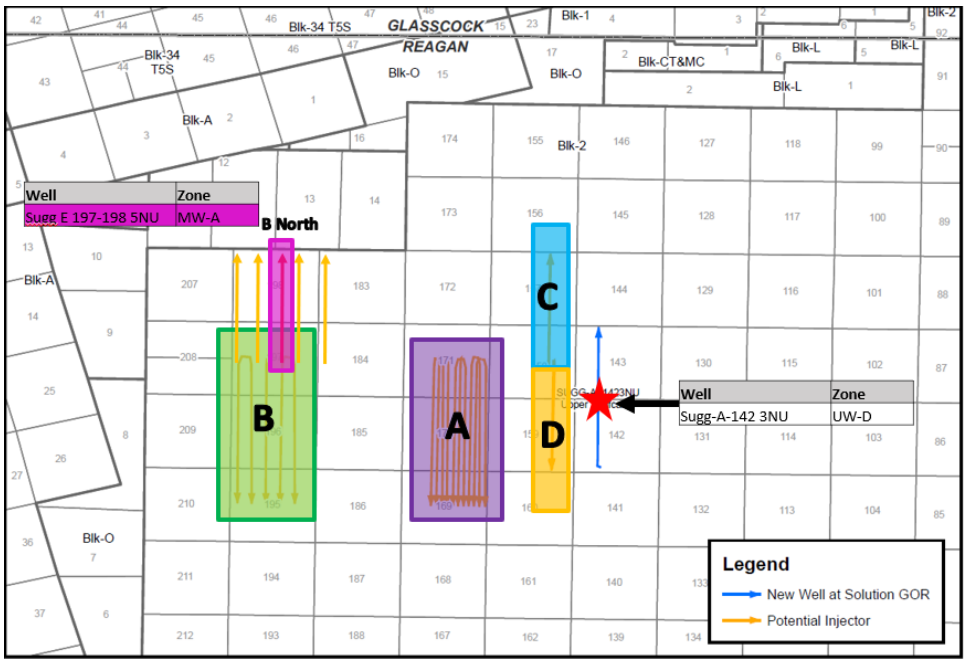


Figure 189: Location of this SUGG A 142 3NU well (indicated by the red star) compared to the EOR test wells (B North).

Acquired Data

Lab data acquisition consisted of collecting the PCT (Pressure-Composition-Temperature) experimental data besides slant core data. Field data acquisition consisted of collecting downhole pressure and temperature from HFTS both Phase 1 and Phase 2 (EOR) horizontal producing wells and the slant core well. The production data form Phase 2 EOR wells, including

recording of an interference test and a flush production test in the 5NU injector, were also collected.

Shortly after stopping gas injection, a service vendor (Zibel) ran a carbon fiber rod deployed in fiber optic cable in the wellbore up to the depth of about 9,449 ft in the injector well. At this depth, the fiber covered the last 5 fracture stages closest to the heel of the well. On June 4th, recording of the geothermal gradient data in the well began. Next day with the fiber still in the well, gas injection resumed in order to determine the gas injection points (perforations) as part of the injection profiling. Injection was then again stopped to record the temperature responses in the well. To analyze the production distribution, a series of well shut-ins during production was implemented to assess the location of fluid entry. Table 14 shows the sequence of events for both the injection and production log.

Table 14: Operations timeline for the fiber optic injection profiling/production allocation monitoring on the Sugg A 197-198 5NU

	Laredo		Sugg E 197-198 5NU		Begin Sensing Program	6/4/19 9:00 PM
	Sequence Number	Operation	Duration (hrs)	Start Time	End Time	5NU
		Run 1 - RIH (while shut in)	8	6/4/19 1:00 PM	6/4/19 9:00 PM	CLOSED
Injection	1	Geo Thermal Shut-In	4	6/4/19 9:00 PM	6/5/19 1:00 AM	CLOSED
Injection	2	Injection	12	6/5/19 1:00 AM	6/5/19 1:00 PM	OPEN
Injection	3	Stable Injection Shut-In	24	6/5/19 1:00 PM	6/6/19 1:00 PM	CLOSED
Injection	4	Run 1 - POOH (Pull up to 7,130')	2	6/6/19 1:00 PM	6/6/19 3:00 PM	CLOSED
Flow Allocation	5	Run 2 - RIH (while flowing)	2	6/6/19 3:00 PM	6/6/19 5:00 PM	OPEN
Flow Allocation	6	Production	4	6/6/19 5:00 PM	6/6/19 9:00 PM	OPEN
Flow Allocation	7	Shut-In	4	6/6/19 9:00 PM	6/7/19 1:00 AM	CLOSED
Flow Allocation	8	Production	4	6/7/19 1:00 AM	6/7/19 5:00 AM	OPEN
Flow Allocation	9	Shut-In	4	6/7/19 5:00 AM	6/7/19 9:00 AM	CLOSED
Flow Allocation	10	Production 3	4	6/7/19 9:00 AM	6/7/19 1:00 PM	OPEN
Flow Allocation	11	Run 2 - POOH (while flowing)	5	6/7/19 1:00 PM	6/7/19 6:00 PM	OPEN

Based on the DTS data shown in Figure 190, in the measured interval, a significant amount of gas penetrated the heel-most fracture stage (stage 27) as well as stage 25. Stages 23, 24, and 26 seemed to receive less gas. This is a qualitative assessment as full well coverage was not obtained by the fiber optic cable. However, this data does support the gas injection experiment since three south facing wells were shut in (due to high gas production) were in the vicinity of the injector's heel portion. Figure 191, shows the DTS profile during the production profiling in SUGG A 197-198 5NU. As shown in this figure, the heel-most stages (25 to 27) seemed to receive more gas during the production and then, they went back to the "cooling" behavior which indicates receiving less gas. The production allocation log also approves that much of the production in the measured interval comes from the heel stages, mostly from stage 27 with some contributions from the other stages. Figure 192 displays the DAS response from the fiber and the qualitative fluid allocations to individual clusters. While there seems to be some fluid inflow from all perforation clusters in the fracture stages which were monitored, there are clusters with significantly higher production contribution. When separating gas production from total fluid inflow, the results are comparable to the qualitative fluid inflow analysis. Stage 27 indicates high gas production contribution, which compares favorably to the injection log. Once the production log was completed the fiber was pulled out of the well and injector well was put on production.

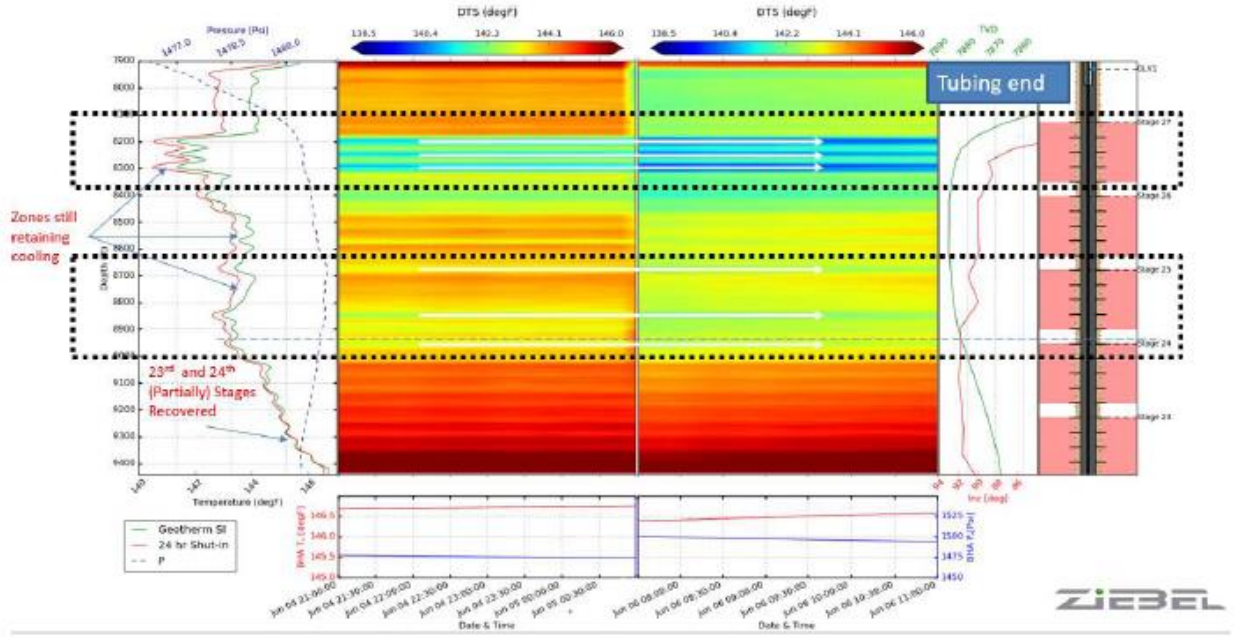


Figure 190: Results from fiber optic injection profiling monitoring using Distributed Temperature Sensing (DTS).

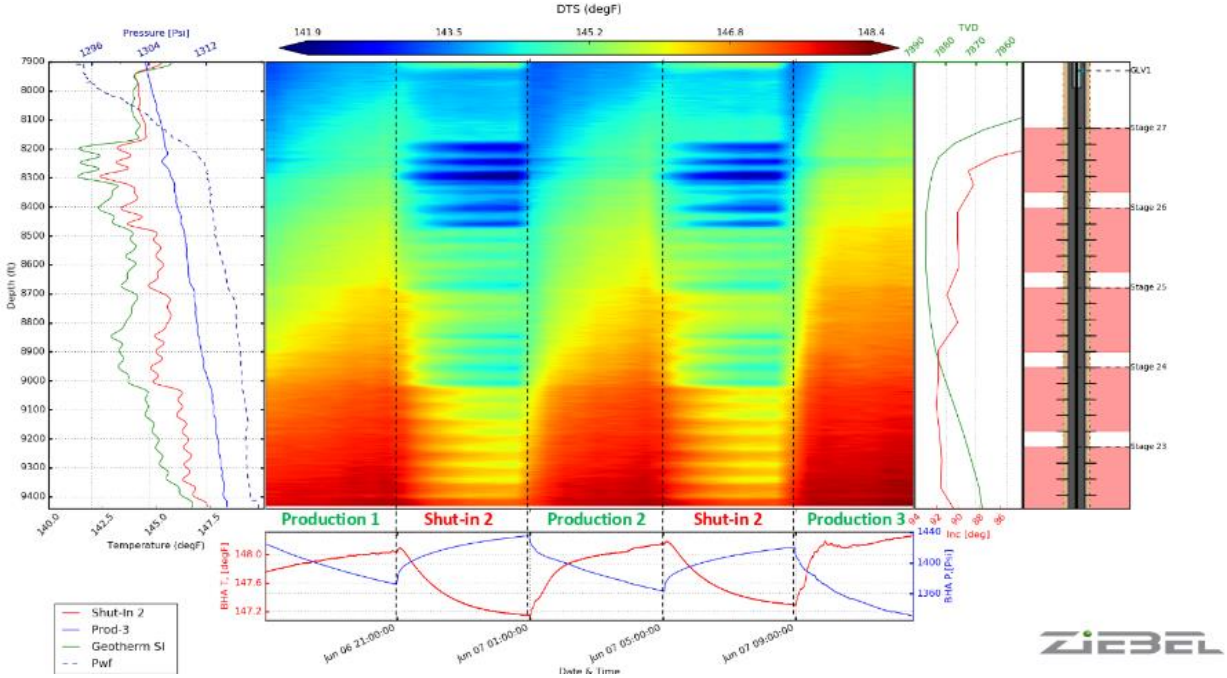


Figure 191: Results from fiber optic production profiling using Distributed Temperature Sensing (DTS).

Ambient Reservoir Monitoring (ARM) deployed an array of surface geophones to monitor the low-pressure gas injection in order to capture recurring acoustic emissions (activity) from the transmissive parts of the subsurface as they respond to changes in fluid pressure and stress. The high-pressure surface injection monitoring began on May 27, 2019, and continued until June 6, 2019, as shown in Figure 194. The fiber optic injection/production logging operations was also conducted simultaneously during this time frame which is shown is Figure 194.

Analyzing the recurrent acoustic activities, images of the activity volumes and active fracture volumes were generated by ARM for both low- and high- pressure injection as well as the pre- and post- injection periods. An example of these images is presented in Figure 195. Images show the hydraulically conductive pathways that fluid injections and produced fluids follow through the reservoir.

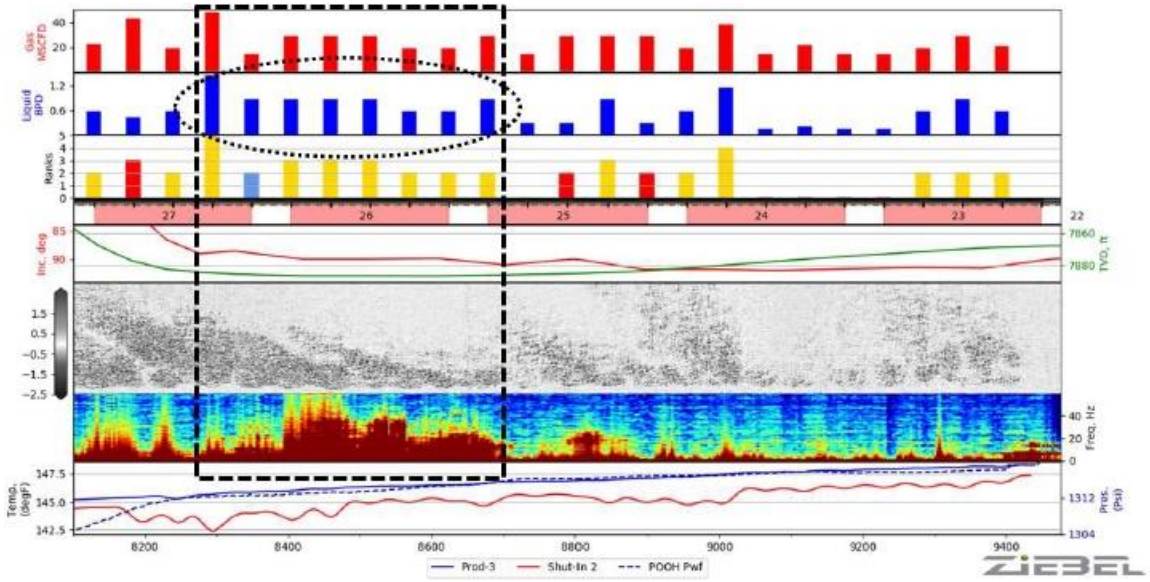


Figure 192: Results from fiber optic production allocation monitoring using Distributed Acoustic Sensing (DAS).

The acoustic activity volumes for the low-pressure gas injection (February 13 and 17, 2019) showed that the direct connection of the Sugg E 197-198 5NU and 6NU horizontal well tracked in the vicinity of the SUGG-E 197B vertical well. Activity levels showed an identifiable correlation with the gas production increase on 6NU prior to shutting in this well. The activity volumes from May to June 2019 (both high pressure injection and production monitors) exhibited consistent activity between the heels of the SUGG-E 197/198 North and South laterals. However, insignificant acoustic activity was observed near the center of the 5NU wellbore during the second monitoring period.

Populated 2D and 3D activity volumes are shown in the Figure 196 and Figure 197 respectively, representing the active fracture volumes in the area of study.

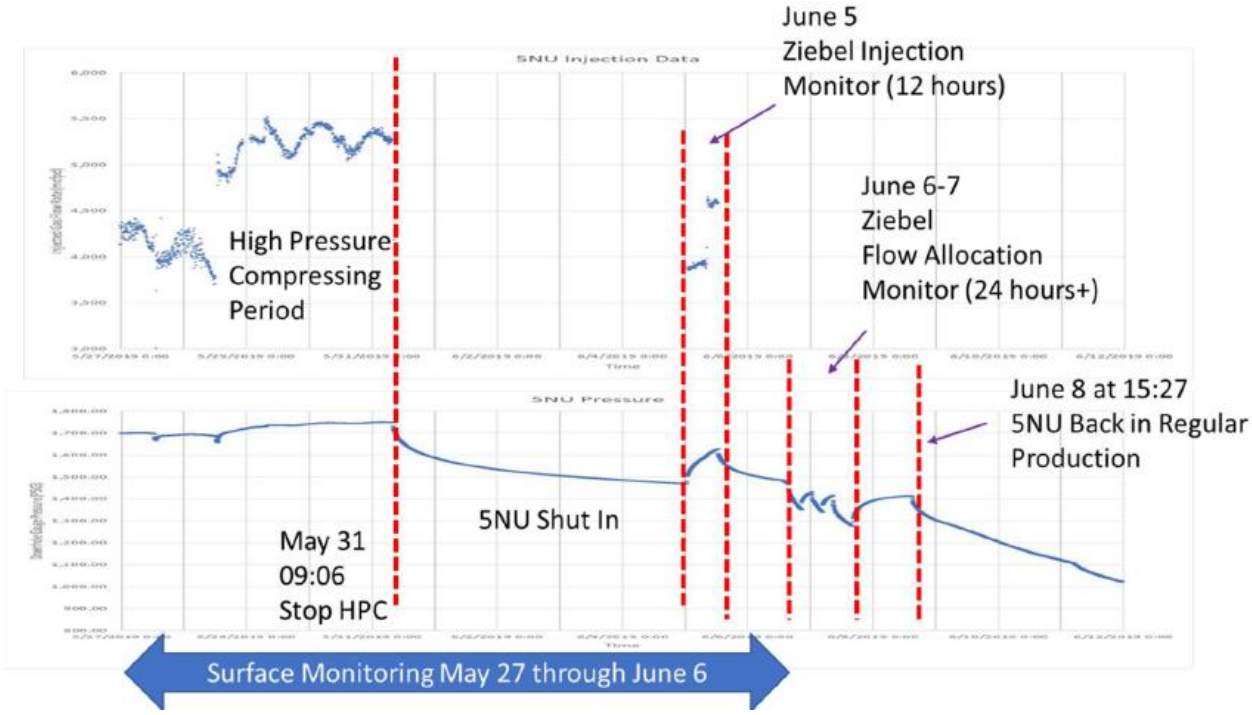


Figure 193: Gas injection rate (top) and bottom-hole pressure (bottom) in the 5NU during acoustic response monitoring and injection/production logging.

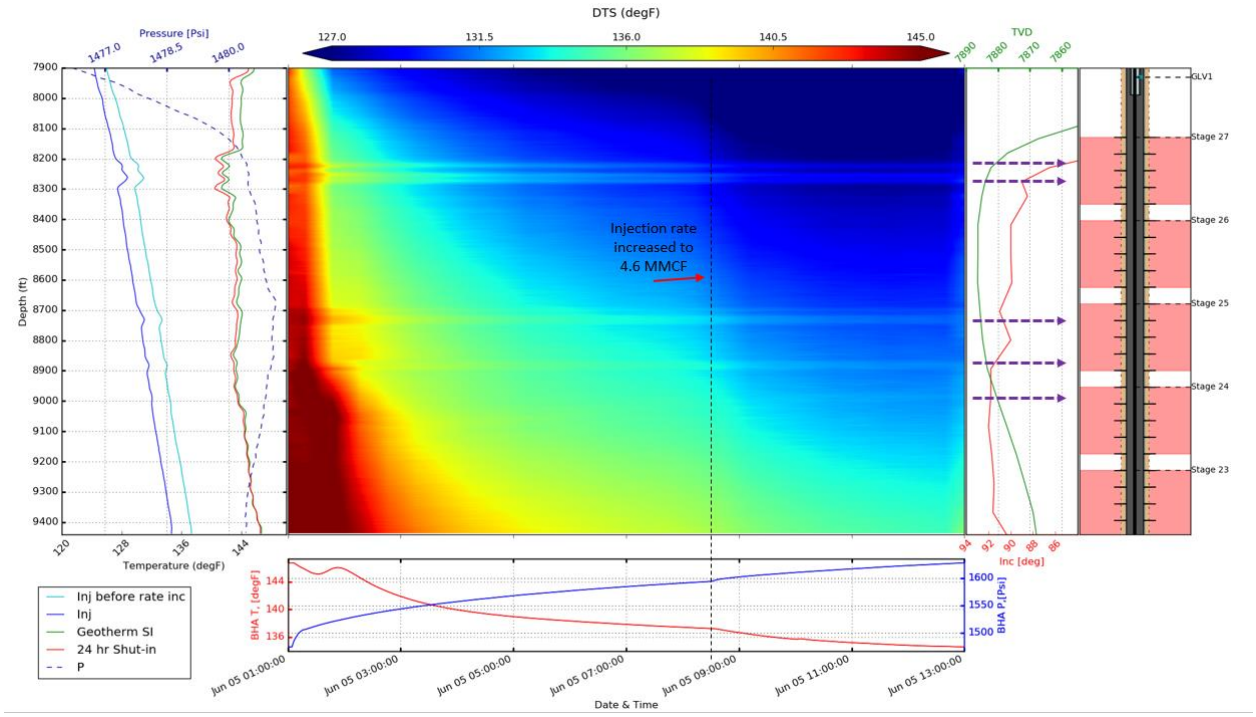


Figure 194: DTS pressure and temperature monitoring in Sugg E 197-198 5NU showing that the "hot spots" during injection are in the middle of stage 27 and stage 25 with the south end of stage 24.

Overall, a considerable agreement between DTS results (by Ziebel) and the acoustic activity volumes recorded at the surface (by Ambient Reservoir Monitoring) was observed showing that:

- All the vertical wells in the study area intersect the fracture network within the Upper Wolfcamp and tie directly to the closest horizontal wellbores.
- The induced fractures from the horizontal fracs preferentially went towards the existing vertical wells, establishing zones of higher hydraulic conductivity.
- The persistent acoustic activity around the vertical wellbores clearly indicated that fluids have moved towards the wellbore during normal production activities.
- Vertical communication between the Wolfcamp and Spraberry around the vertical wells was also observed, showing that these vertical wells likely provide preferential conduits for fluids and/or pressure due to the increased conductivity.

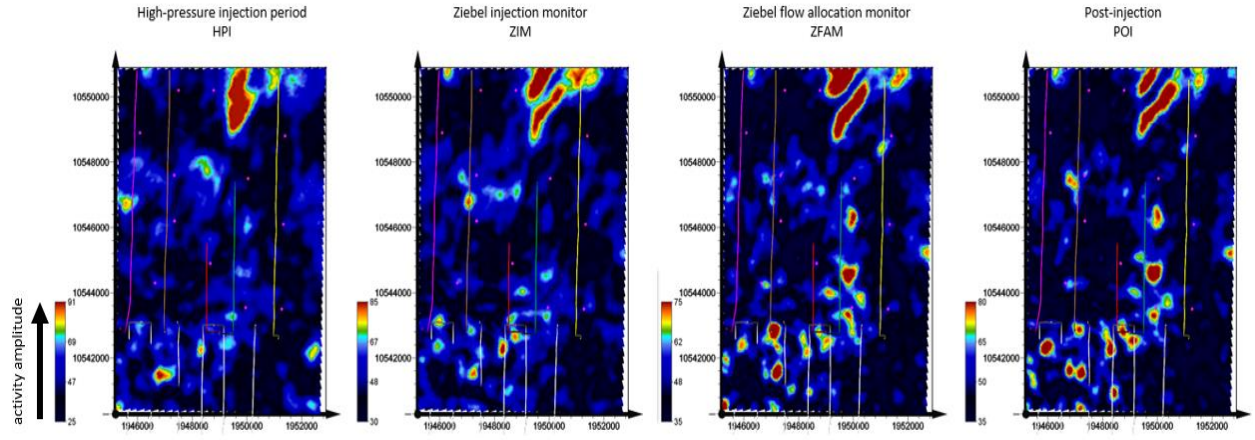


Figure 195: Acoustic activity volumes near 5NU horizontal well during HP injection and post-injection.

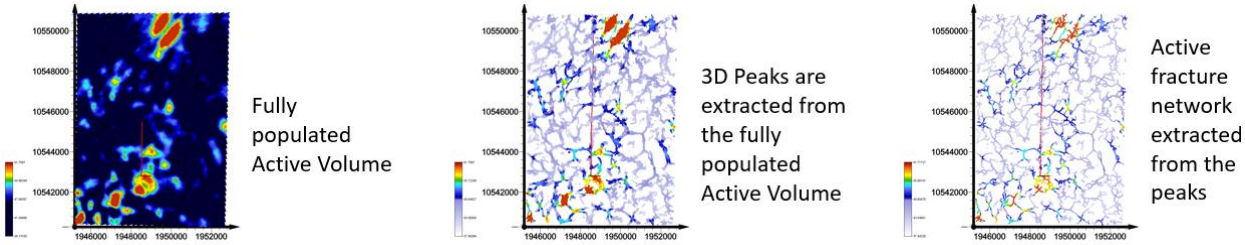


Figure 196: Fully populated active volumes in Sugg E 197-198 5NU horizontal well (depth viewed from above).

Core Laboratories performed PCT experiments on using the fluid samples collected from a relatively new offset well to the EOR test site, Sugg A 142 3NU.

Separator gas was heated above sampling temperature to ensure that vaporization of condensate and the opening pressure is measured. After heating, the separator gas was checked for free liquid and the air content was measured. Also, the bubble point of the separator liquid was measured and the amount of free water in the separator liquid besides the water content in the oil was determined. Summary of the analyzed samples is provided in Table 15.

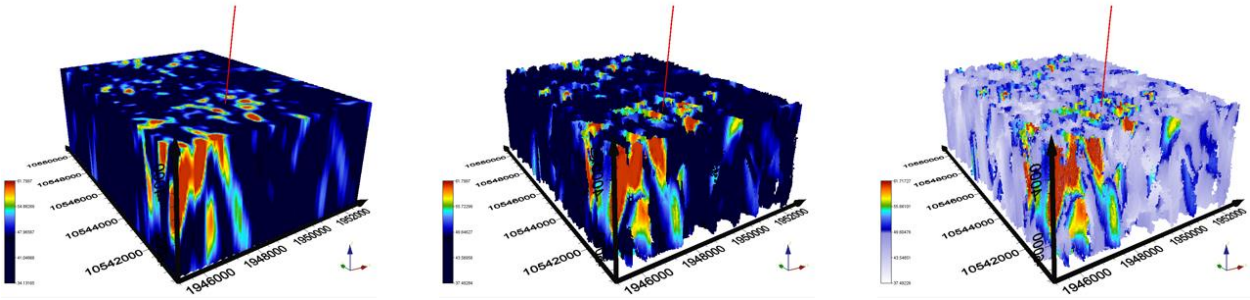


Figure 197: Fully populated 3D active volumes in Sugg E 197-198 5NU horizontal well (the red line) viewed from the SW.

Experimental & Modeling Studies

Laboratory Tests & Results

After QC, the separator samples were recombined with the resulting reservoir fluid composition (Table 16) and standard PVT testing was performed. Results of these PVT experiments are summarized in

Table 17.

A Constant Composition Expansion (CCE) experiment was also performed in order to measure the compressibility factor of the synthetic injection gas (composition provided in Table 18). Figure 198 shows the Z-factor plot obtained from this experiment.

In order to simulate the process of cyclic gas injection in the laboratory, swelling gas experiment was performed by Corelab. The swelling test consists of several gas injections. In this study, it was performed with 6 gas additions to the reservoir fluid while measuring saturation pressure, relative volume, and density at each stage. Table 19 summarizes the results of this 6-stage swelling test and Figure 199 and Figure 200 provide the graphs of saturation pressures at different mole percentages of the injection gas.

Table 15: Summary of the samples that were analyzed, and quality controlled by CoreLab.

Summary of Samples Received

Separator Gas Samples

Sample Number	Cylinder Number	Sampling :- Pressure (psig)	Sampling :- Temp. (°F)	Laboratory opening: Pressure (psig)	Laboratory opening: Temp. (°F)	Liquid Drained (cm3)	Air Content (Mole%)
201704143-01	2C607	115	68	120	170	0	6.00
201704143-02	KA123823	115	68	126	170	0	0.03
201704143-03	KA126347	115	68	122	170	0	0.13
201704143-04	KA072622	115	68	125	170	0	0.04
201704143-05	KA123824	115	68	119	170	0	0.13
201704143-06	KA123791	115	68	121	170	0	0.05
201704143-07	KA123826	115	68	125	170	0	0.07
201704143-08	KA058831	115	68	126	170	0	0.10
201704143-09	KA058832	115	68	122	170	0	0.08

Separator Liquid Samples

Sample Number	Cylinder Number	Sampling :- Pressure (psig)	Sampling :- Temp. (°F)	Laboratory Bubble point:- Pressure (psig)	Laboratory Bubble point:- Temp. (°F)	Water Recovered (cm3)	Sample Volume (cm3)	Water Content wt%
201704143-10	2ML073	116	64	95	64	1	3602	0.06
201704143-11	2ML071	116	64	92	64	1	3589	0.20
201704143-12	2ML051	116	64	91	68	1	3510	0.19
201704143-13	2ML070	116	64	89	65	2	3559	0.36
201704143-14	2ML072	116	64	88	71	105	3265	0.07
201704143-15	2ML060	116	64	87	66	2	3493	0.15

Table 16: Analysis of the reservoir fluid composition by CoreLab.

Reservoir Fluid Composition

Component	Mole %
Hydrogen	0.000
Hydrogen Sulphide	0.000
Carbon Dioxide	0.270
Nitrogen	0.790
Methane	39.780
Ethane	9.470
Propane	9.160
i-Butane	1.030
n-Butane	4.460
Neo-Pentane	0.000
i-Pentane	1.360
n-Pentane	2.040
Hexanes	2.410
M-C-Pentane	0.980
Benzene	0.180
Cyclohexane	0.610
Heptanes	2.770
M-C-Hexane	1.090
Toluene	0.300
Octanes	2.910
E-Benzene	0.280
M/P-Xylene	0.330
O-Xylene	0.300
Nonanes	1.770
1,2,4-TMB	0.150
Decanes	1.980
Undecanes Plus	15.580
Total	100.00

Table 17: Analysis of the reservoir fluid properties by CoreLab.

Properties at Working Pressure & Temperature

Reservoir Pressure	8,500	psig at 161 °F
Density	0.6970	g/cm3
FVF (from MSF)	1.434	Pres bbl/stb
Viscosity	0.489	cP
Compressibility	7.138	Δϖολ/ϖολ/Δπσι ξ 106

Properties at Saturation Pressure & Temperature

Saturation Pressure	2,635	psig at 161 °F
Density	0.6543	g/cm3
FVF (from MSF)	1.528	Psat bbl/stb
Viscosity	0.326	cP

Flash Comparison

Experimental Procedure	GOR (SCF/stb)	Gas Gravity	API at 60 °F	FVF (Psat bbl/stb)
Multi-Stage Separator Test	1027	0.905	43.3	1.528
Reservoir Fluid Single-Stage Flash	1,122	1	40.4	1.609
Differential Liberation at Reservoir Temperature	1,174	1.150	39.2	1.648

Table 18: Analysis of the synthetic and injection gas composition by CoreLab.

	Component	Synthetic Gas Mol%	Injection Gas Mol%
H2	Hydrogen	0.00	0.00
H2S	Hydrogen Sulphide	0.00	0.00
CO2	Carbon Dioxide	0.52	1.07
N2	Nitrogen	2.39	3.15
C1	Methane	77.52	58.40
C2	Ethane	9.91	14.00
C3	Propane	6.13	12.70
iC4	i-Butane	0.67	1.83
nC4	n-Butane	1.73	4.73
iC5	i-Pentane	0.32	1.08
nC5	n-Pentane	0.38	1.29
C6	Hexane	0.43	1.75
	Totals:	100.00	100.00

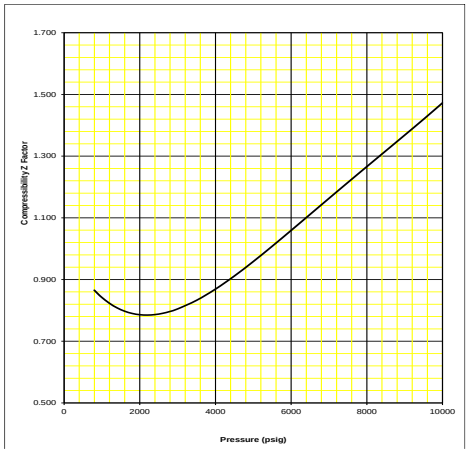


Figure 198: Gas compressibility factor (Z-factor) of gas as a function of pressure.

Table 19: Summary of the swelling gas experiment conducted by CoreLab at 157°F.

Solubility Swelling Test Data

Gas Addition Stage	Cumulative Mole % Injection Gas Relative to Moles of Original Fluid	Cumulative Mole % Injection Gas Percent of Total Fluid Moles	Saturation Pressure (psig)		Relative Volume (1)	Gas-Oil Ratio Relative to Original Fluid at Bubble Point (Scf/bbl)	Density at Saturation Pressure (g cm-3)
0	0.00	0.00	2635	Pb	1.0000	0	0.6543
1	25.00	20.00	3581	Pb	1.1236	269	0.6206
2	66.67	40.00	4739	Pb	1.3406	718	0.5737
3	100.00	50.00	5371	Pb	1.5102	1076	0.5473
4	122.23	55.00	5733	Pb	1.6295	1315	0.5307
5	150.01	60.00	6201	Pd	1.7642	1614	0.5173
6	185.72	65.00	6850	Pd	1.9325	1999	0.5041

(1) Pb = Bubble point. Pd = Dew point.
(2) Volume at saturation pressure relative to original reservoir fluid.

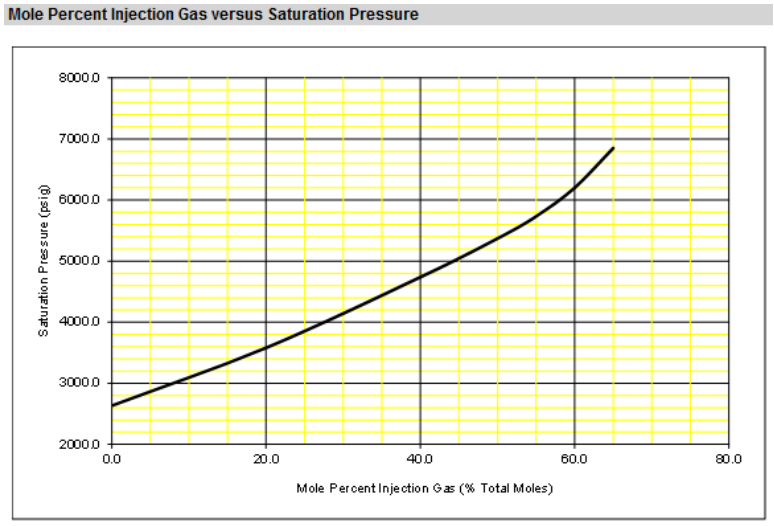


Figure 199: Variations in saturation pressures as a function of gas injection mol%.

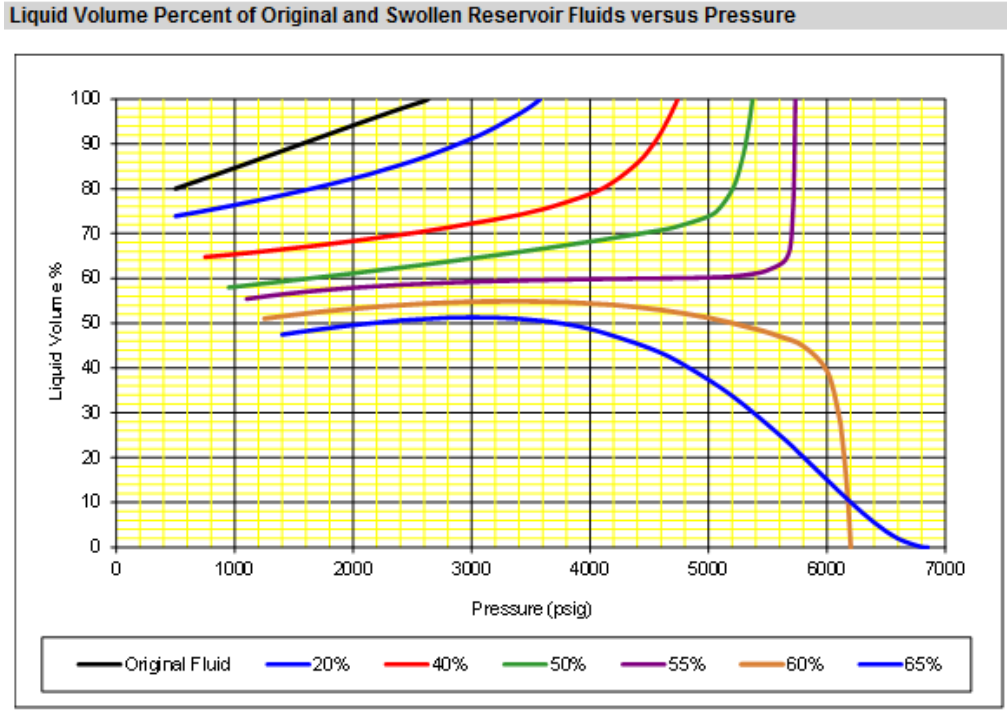


Figure 200: Liquid volume drop-out as a function of pressure.

In order to identify the minimum miscibility pressures for the injection gas and native reservoir fluid, a slim tube experiment was performed, and results are provided below in the Figure 201.

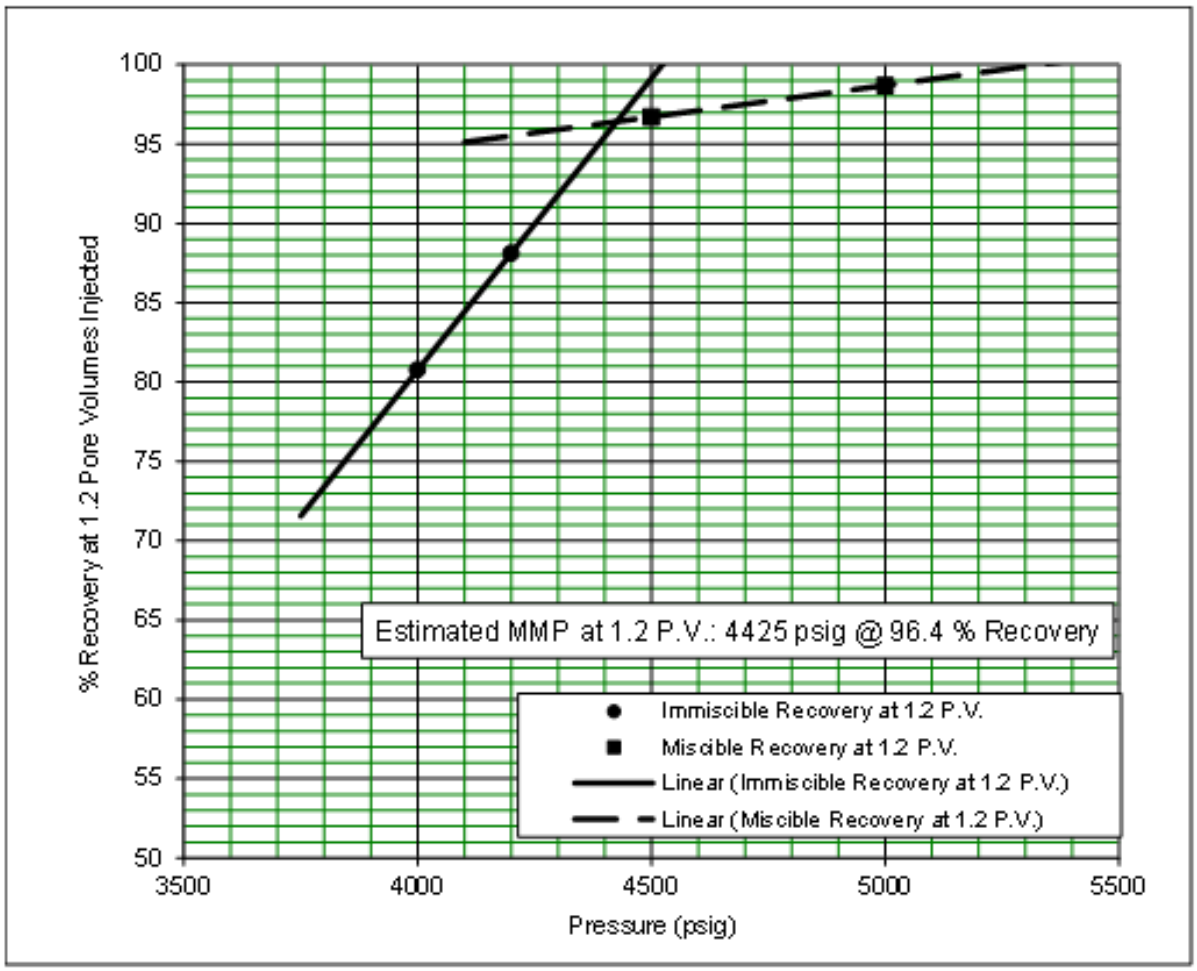
Equation of State estimates of the required MMP for the gas injection (field gas composition) showed a desirable pressure of 4,500 psi. The MMP experiment, as shown in the Figure 201, also showed MMP of 4,425 psig which was congruent with the EOS results.

Simulation Results

Summary of Packed Column Displacement Data at 157°F

Displacement Pressure psig	Cumulative Oil Recovery at 1.00 P.V. Injected (volume%)	Cumulative Oil Recovery at 1.20 P.V. Injected (volume%)	Total Oil Displaced (volume%)
4000	78.56	80.76	82.82
4200	85.44	88.12	90.01
4425	**Interpolated Minimum Miscibility Pressure (96.4% recovery at 1.2 P.V.)**		
4500	93.12	96.70	96.71
5000	95.48	98.69	98.82

Packed Column Recovery at 1.2 P.V. as a Function of Pressure



MMP interpolation method from Yellig and Metcalf, 1980.

Figure 201: Slim tubes study to determine the MMP.

A dual porosity model with hydraulic fracturing was built by Nitec to simulate the gas injection process in the EOR field. This simulation model was built upon the original Geo-model developed by Laredo by making some adjustment including:

- Upscaling the original Geo-Model in the vertical direction.
- Downscaling the original Geo-Model in horizontal directions.
- Translating the PVT data from a 17-component model into an extended black oil table.
- Inputting the perforation and hydraulic fracturing data to start the life of each well.
- Inputting the production data to control the wells by liquid rates for history matching.

The generated model was evaluated by achieving a reasonable accuracy in the history matching of the production data which assured that underlying flow mechanisms are well understood in the model. Figure 202 represents this good match as explained.

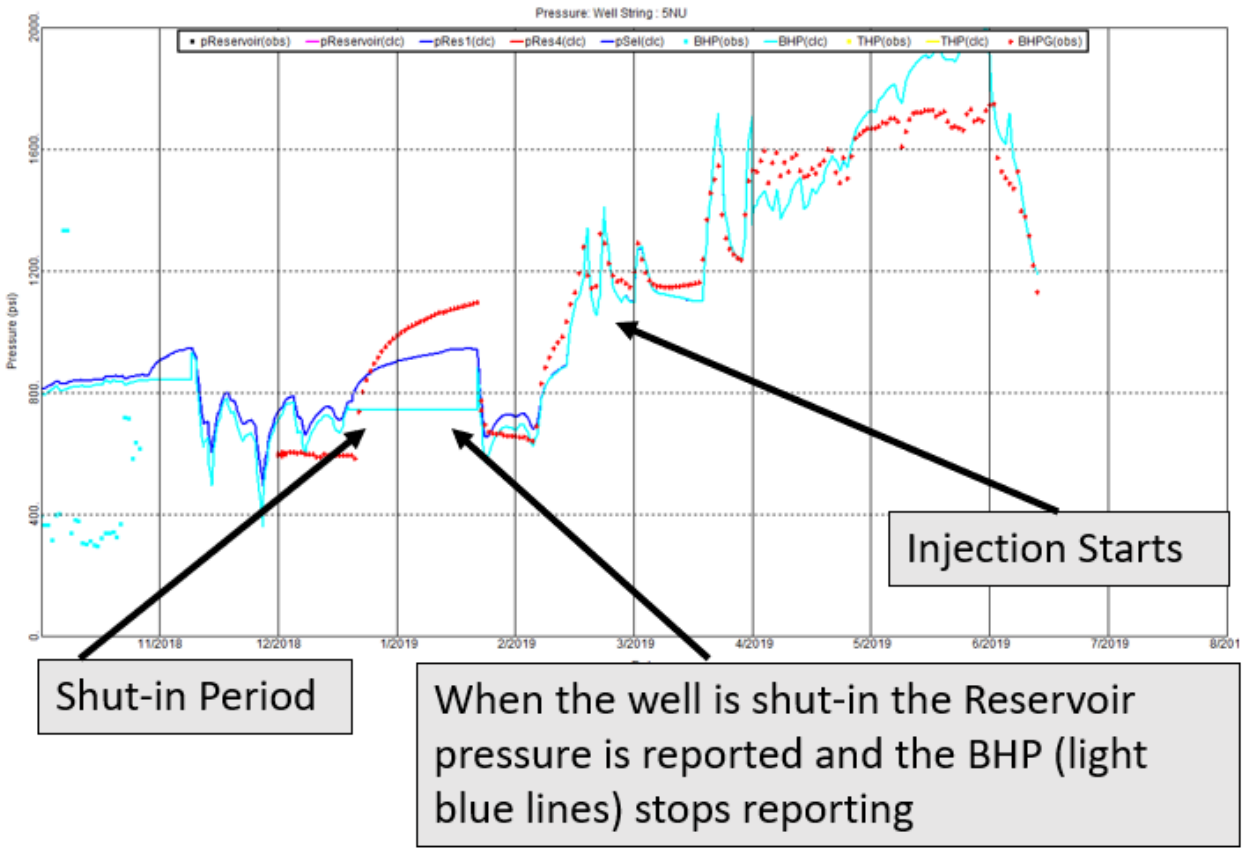


Figure 202: Pressure match for the well Sugg E 197-198 5NU. Dark blue line is simulated reservoir pressure; light blue line is simulated BHP; and dark red dots are the gauge pressures.

The simulated model showed that there is a larger cloud of enhanced permeability region around each of the main hydraulic fractures that is too small for a significant liquid production but can act as a pathway for gas (Figure 203). This region with an estimated permeability of roughly 0.001-0.01 mD in the regions known as the secondary and tertiary SRV. The secondary SRV is the area between the clusters that is not propped and the tertiary SRV is the area outside of the main clusters that represents unpropped hydraulic fractures. Note that the main (primary) SRV is the area around the clusters that is propped and contributes easily to the flow of liquid. Also, it should be noted that the permeability of the unfractured region (matrix) was

set to 0.00015 mD and is very small. Figure 204 shows the main, secondary, and tertiary SRV on the drainage profile of a hydraulic fracture compared to the native matrix.

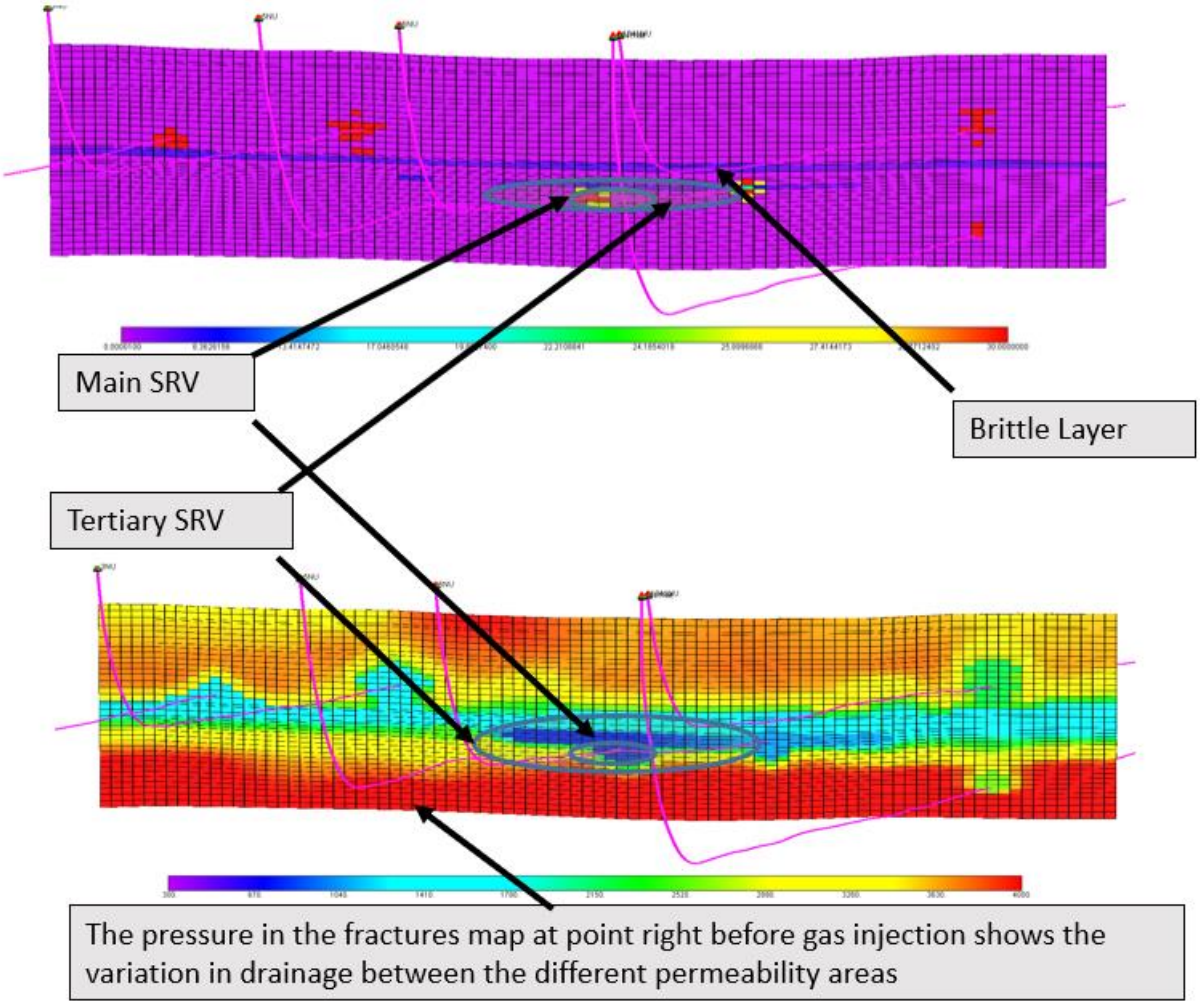


Figure 203: Regions with enhanced permeability around the hydraulic fracture (top) and the pressure distribution within the fracture (bottom).

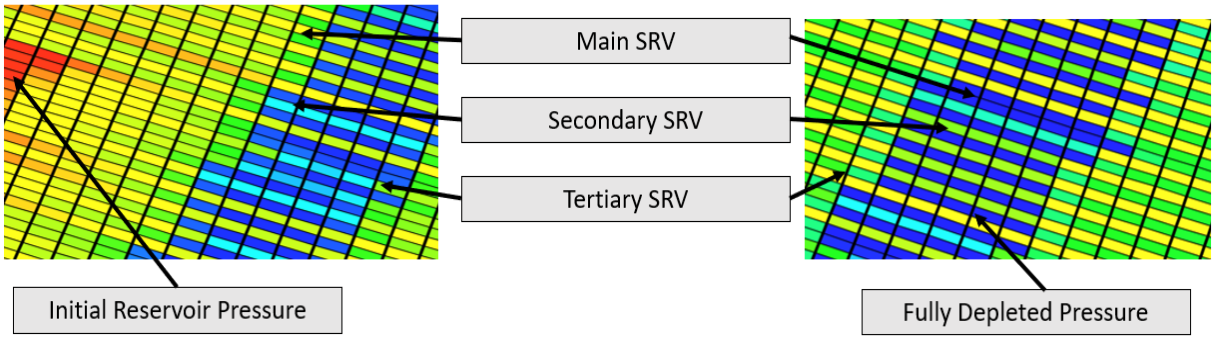


Figure 204: The drainage profile showing different SRV areas around the fracture. Colors represent the pressure (red being the highest pressure) in the matrix (left) and in the fracture (right).

Simulation results for the gas injection scenario in the model explained above led to the following observations:

- All horizontal wells included in the model showed a gas hit eventually.
- There was minimal pressure increase in the wells further away from the gas hits.
- It was not clear if it was the background natural fractures or the hydraulic fractures that facilitated the gas transfer.

In order to make conclusions about the best gas injection scenario, several other injection cases were also tested to accommodate comparison of the field pilot with other potential cases. Table 20 summarizes all the different gas injection scenarios simulated by Nitec using the same model.

Table 20: Summary of all different gas injection simulation cases ran by Nitec. BHP limits of 3500 psia set for all injection cases.

Cases
1. 5NU injected with 20 MMCFPD for 2 months. 2 weeks of shut-in. Production for 3 months. 3NU and 6NU are closed right away.
2. 5NU injected with 3000 BOWPD for 1 months. 6 weeks of shut-in. Production for 3 months. 3NU and 6NU are closed right away.
3. 5NU injected with 3000 BOWPD for 1 months. 5NU injected with 20 MMCFPD for 1 months 2 weeks of shut-in. Production for 3 months. 3NU and 6NU are closed right away.
4. 5NU injected with 5 MMCFPD for 2 months. 2 weeks of shut-in. Production for 3 months. 3NU and 6NU inject 3000 BOWPD during 5NU's gas injection. Other wells are shut.
5. 5NU injected with 5 MMCFPD for 2 months. 2 weeks of shut-in. Production for 3 months. 3NU and 6NU inject 3000 BOWPD during 5NU's gas injection. Other wells are shut.
6. 5NU, 3NU, and 6NU are shut-in for 2.5 months. Production for 3 months. (base case)
All cases will be compared to 6 (base case)

Results showed that the production performance improves when water is injected into the neighboring wells with low gas injection into 5NU. But the neighbors see significant production reduction due to flowing back water. Therefore, the base case remains as the best-performing gas injection scenario in term of potential improvement in the oil recovery (Figure 205).

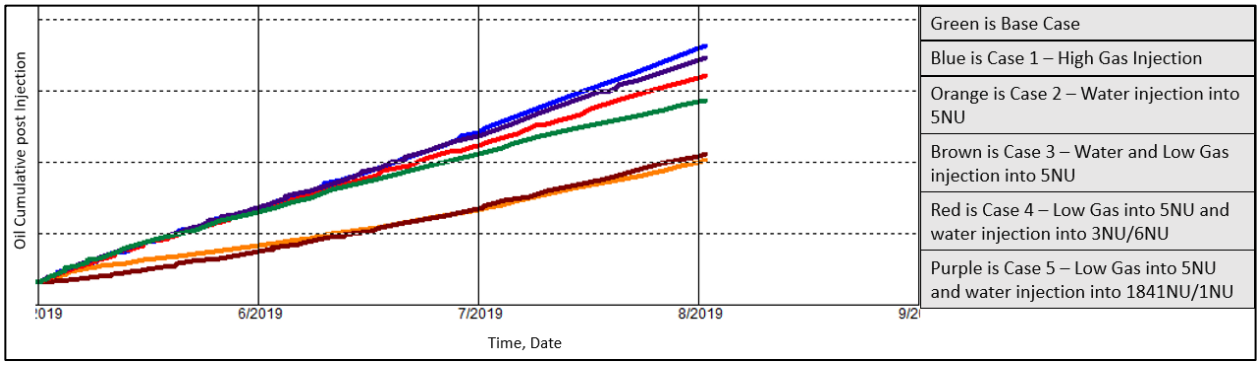


Figure 205: Comparing gas injection performance predictions for the scenarios outlined in the Table 20.

Above discussion illustrates that gas could be injected into the 5NU and see a good pressure build up at a 20 MMscf/d injection rate, while 3NU and 6NU are shut in. 1NU and 184 1NU would see the gas but keeping them as pressure sinks allows controlling the gas direction.

Water injection into the offset wells for keeping them pressurized did not seem to be effective. In this model, water showed to be choking the well's oil rate once they come back online. Also, in the field application water may not have the proper chemistry and cause permanent damage to the matrix of rock. However, water did show any sign of movement into the neighbors of the gas being injected despite what gas did.

New Findings/Lessons Learned

Field observation proved that the fracture network around the injector well SUGG E 197-198 5NU was leakier than what was observed in the model. It is also showed that a more complex

communication path exists around the wellbore and between the hydraulically fractured wells than the way the model handled it in the simulation which only handled this by adding brittle layers. It is also evident that the injected gas not only went towards the offset horizontal wells but also penetrated vertically to where it really did not do much good.

Because of numerical problems, simulation runs were done with a black oil table which limited the production improvement into the oil swelling as the primary impact of the gas injection on oil production. However, in the field implementation, other mechanisms such as oil vaporization into the gas phase and miscibility could add to the upside effect.

The pre-injection fracture map from the data recorded during Sugg E 197-198 5NU injection and production shows a very similar fracture network to the acoustic recurrent activity map produced from all the other volumes. This is an indicator that the injected gas and/or fluid pressure front has indeed followed the pathways that were already open before the gas injections began. Therefore, due to the fast expansion of the injected gas within a widely distributed fracture network which prevented achieving the high pressure required for miscibility of the injected gas, enrichment of the gas for lowering the required miscibility pressure needed to be further investigated as an alternate solution.

Introduction

The aim behind Phase 3 of the HFTS project was to answer a key question regarding re-stimulation. Can new, previously undrained reservoir be identified within an existing wellbore, and successfully contacted with new infill stimulation technology to boost production and improve recoveries? In addition, to improve our understanding of how new fractures grow in the presence of existing SRV, and changes in drainage. Finally, to quantify the economic viability of infill stimulation, potential added resource that could be achieved, and the environmental benefits by reducing the need for new wells. The scope of work is highlighted next.

- Identify candidate infill stimulation.
- Well Drill/core offset horizontal observation well, log, install permanent gauges & fiber, measure existing depletion, monitor frac growth, and measure changes in depletion achieved.
- Diagnose perf clusters in candidate well; recomplete with liner; perforate and re-stimulate.

The conceptual illustration of the test is highlighted in Figure 206. The aim behind the observation well is to understand inter-well fracture communication and understanding the development of SRV during the re-stimulation and infill stimulation of the parent wells.

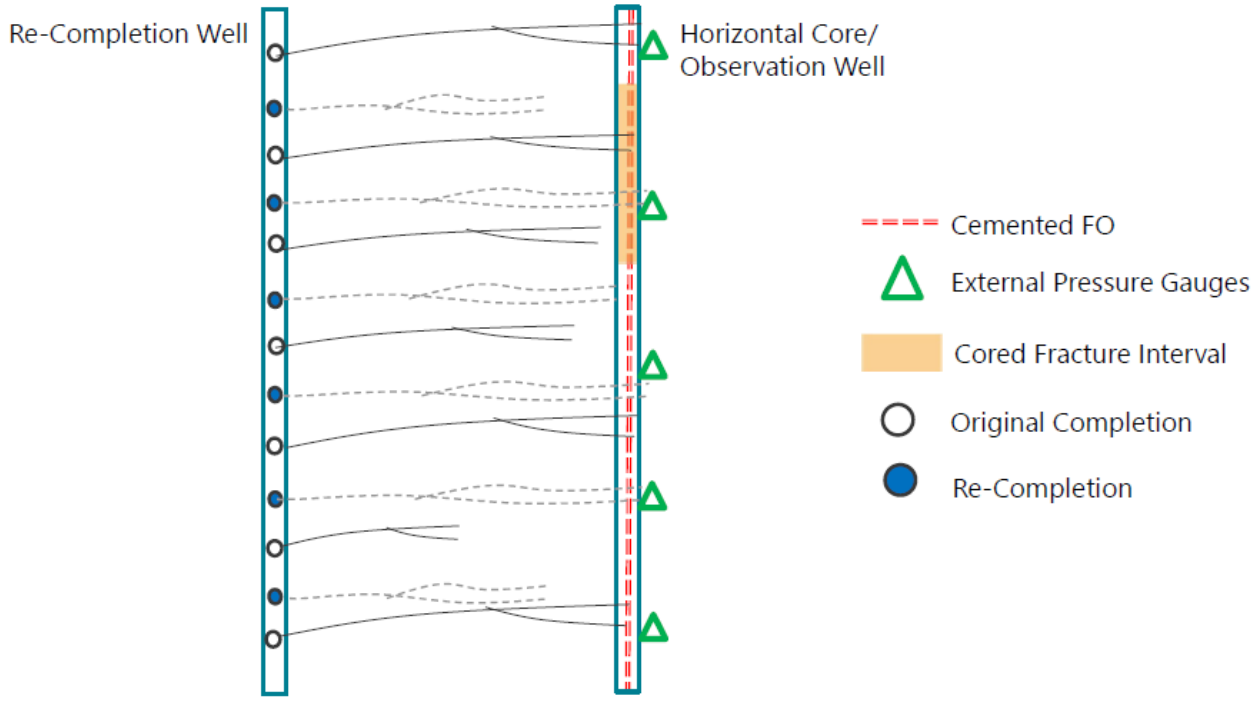


Figure 206: Conceptual illustration of the test program as planned.

Background

The HFTS-1 Phase 3 project site was located at the northern border of DeWitt County in Texas targeting the Eagle Ford formation. The reservoir is in a black oil window with a gas oil ratio of approximately 1,500. The project site hosted 10 parent wells. As part of this project, one horizontal observation well was planned along with 2 refracturing candidate wells and three Lower Eagle Ford infill wells at various spacings ranging from 440 ft to 750 ft. Prior to the refrac program, the operator, Devon Energy, removed production equipment, cleaned out, and

installed a cemented liner in two legacy Eagle Ford wells. The project involved significant operational and data acquisition program as follows:

- Petrophysical Logs: Included USIT to measure cement bond effectiveness around fiber and casing pressure gauges which allowed for areas of potential concern/lower data quality to be identified prior to analysis. Additional petrophysical logs along multiple selected wells.
- Pre/Post Refrac Perf Imaging: Classify both initial and post refrac perforation erosion, frac fluid entry points, and efficiency across wellbore.
- Horizontal Core between two recompleted wells with 420 ft of whole core through SRV: Observation of hydraulic fractures (core description) in conjunction with image log data. Also, 3D laser scans of all hydraulic fracture faces collected.
- Proppant Log: Mud return samples during drilling are collected and analyzed for proppant distribution.
- Image Log: Identify faults, natural fractures, and existing hydraulic fractures.
- Stimulation program: A total of sixty-eight new fracture stages were treated as part of the refrac program in two pre-existing wells (Zgabay 3H and Zgabay 5H). In addition, three new infill wells were also fracture stimulated.
- Time Lapse Geo Chemistry: Oil samples periodically collected to characterize produced fluids (oil &/or water) and understand drainage source area.
- Oil and Water Tracer: Understand offset stimulation overlap along with time period/ length of interaction.
- Sealed Wellbore Pressure Monitoring: Ability to quantity and characterize hydraulic fracture interference, geometries, and efficiencies across multiple landing zones.
- Interference Testing: Original and repeat testing with workflow utilizing permanent and temporary downhole pressure gauges and fibers to quantify conductive interaction of wellbores.
- External Casing Pressure Gauges: Allows for pressure data to be collected along both vertical and horizontal sections of observation well to understand levels of depletion and hydraulic fracture geometry impacts.
- Permanent Fiber: Allows for DAS, DTS, Stain and Pressure data to be collected consistently down wellbore, detail will allow for recompletion and redevelopment interference to be better understood.
- Temporary Fiber: A temporary fiber optic cable was deployed in adjacent horizontal well and data was analyzed for monitoring re-frac treatments.

The project location and wells along with identified refracturing and infill wells are highlighted for reference in Figure 207. This also highlights the degree of complexity associated with this reservoir unit with multiple wells in proximity of each other.

Post the project planning phase, observation logs, such as perforation mapping in existing re-frac candidate well were conducted. Project execution started in October 2021 with drilling operations and actual refracturing and infill completions were conducted in January and February 2022 spread of approximately 45 days. Drill out operations began in February 2022. Initial production started on March 14, 2022, followed by regular operational data monitoring

including post stimulation interference testing. Figure 208 highlights the project timeline for Phase 3 project.



Figure 207: Project location along with observation, refrac, and new infill wells.

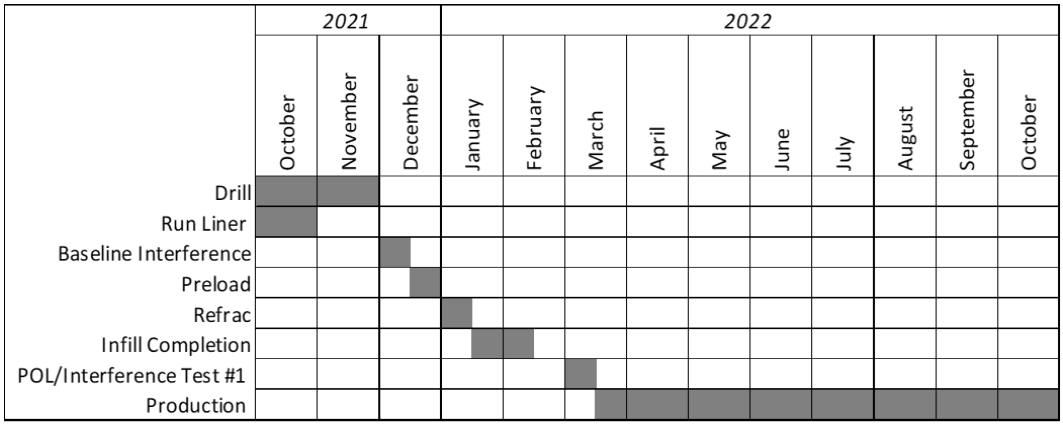


Figure 208: Project timeline.

Four infill wells were drilled as part of the Zgabay development. An image log was run along Zgabay 14H and only partial data was successfully recovered (down-log 9,690 ft to 14,175 ft and up-log 12,245 ft to 17,800 ft partial data due to caliper failure). Gamma ray, Neutron and Sonic logs were collected along the 14H lateral. However, density tool failure caused caliper failure on image log. Coring program along this well involved 420 ft of horizontal core. Routine core testing as well as fracture descriptions were performed on this core prior to slabbing and core characterization. Figure 209 highlights some of the core testing results including HC indicators, fractures from CT scans as well as cuttings samples from Zgabay 14H.

External casing gauges and fiber was run on Zgabay 14H well. However, the DPATS fiber installation failed and only the DTS/ DAS fibers and gauges were operational during the monitoring phase of the project. For the refracturing wells, after cleaning out the well, 4-inch liners were installed on the Zgabay 3H and Zgabay 5H refrac wells. Perforation imaging was captured post refracturing on Zgabay 5H over stages 3 through 22. A 3-day base interference test was conducted once all the downhole gauges were actuated in Zgabay 14H (December 27, 2021) during which fiber and pressure gauge data was collected and analyzed. Prior to fracturing operations, offsetting wells were pre-loaded for pressurization with data was

collected and analyzed during Zgabay 4H preload. Next, the refrac wells (Zgabay 3H and Zgabay 5H) were fracture stimulated (1/14/2022 through 1/29/2022). In Zgabay 3H, data shows 2,250 PPF (pounds per foot) of proppant placement and 54.5 PPF of fluid placement. In Zgabay 5H, data shows an average sand placement of 2,000 PPF and average fluid placement of 53 PPF.

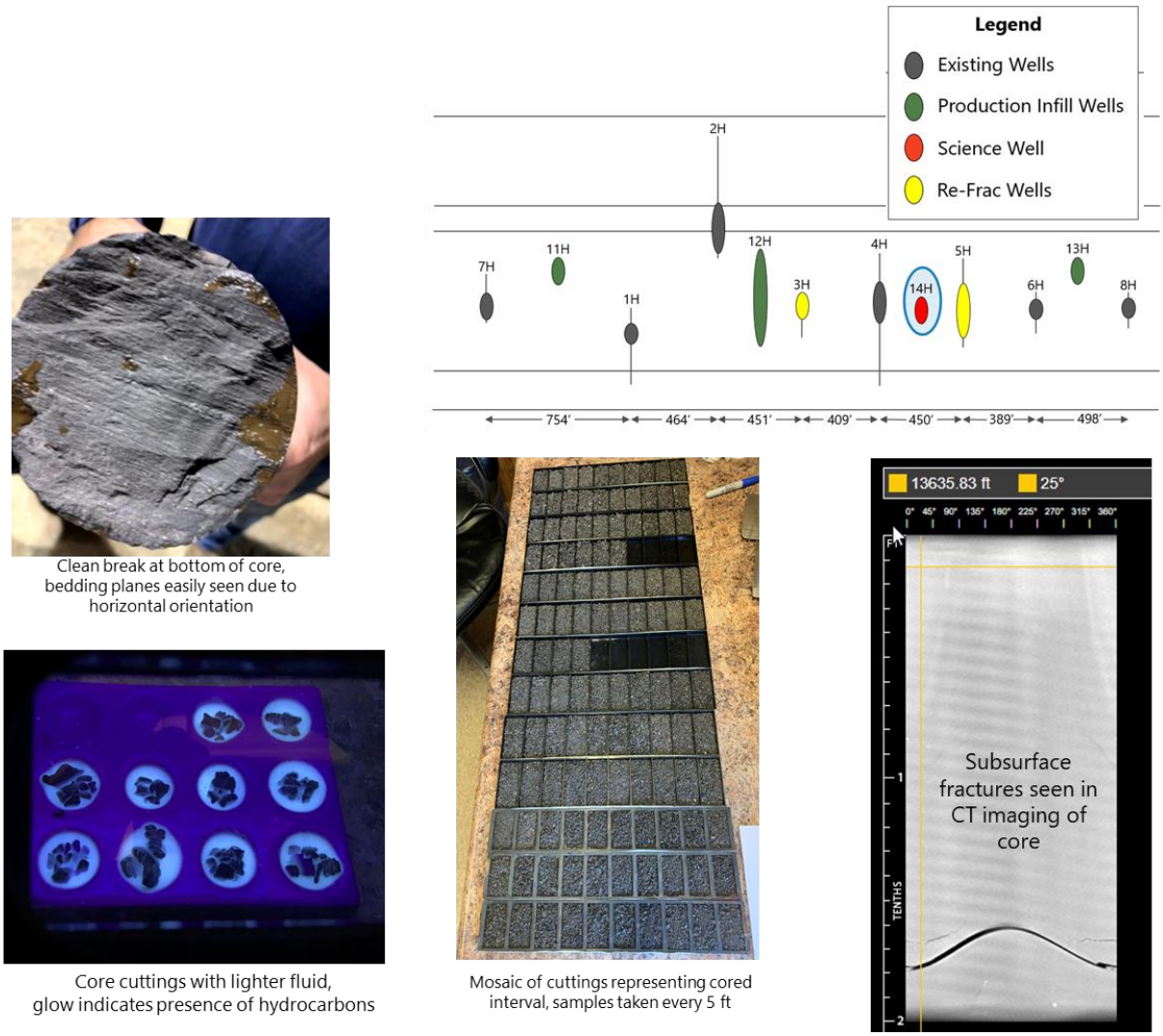


Figure 209: Core testing examples for Zgabay 14H.

During Zgabay 3H and Zgabay 5H refrac, 14H permanent fiber and pressure gauges were leveraged. A temporary fiber was conveyed in Zgabay 12H during refrac period to collect additional cross-well strain data. Zgabay 11H and 13H infills were used as sealed wellbore monitors. The program was designed to evaluate several stage/cluster level designs. Figure 210 highlights the perforation design for the liner refracturing program. The summary of completion design followed for the refrac wells is highlighted in Table 21.

With respect to infill wells (Zgabay 11H, 12H and 13H), operationally, zipper pattern was used across Zgabay 11H, 12H and 13H wells. The design details used for the infill wells are broadly, 3,000 pounds per foot treatments, high viscosity friction reducer treatments were used with 200 ft stage spacing and 20 ft cluster spacing with 3 shots per foot. The sequence of stage completions is highlighted in Figure 211. The colors indicate the sequence of the zipper as implemented. Again, the permanent gauges and fiber in Zgabay 14H were leveraged for

observations. Throughout the fracturing program, high resolution (1 minute) pressure data was collected across deployed gauges.

A3 refrac									
Stage	clusters	perf friction	cluster spacing	stage length	cum gpi	stage prop	stage fluid	prop/cluster	fluid/cluster
1	7	low	15	105	113	300000	6000	42857	857
2	7	low	15	105	233	300000	6000	42857	857
3	7	low	15	105	353	300000	6000	42857	857
4	7	low	15	105	473	300000	6000	42857	857
5	7	low	15	105	593	300000	6000	42857	857
6	7	low	15	105	713	300000	6000	42857	857
7	7	low	15	105	833	300000	6000	42857	857
8	1	low	15	15	863	75000	1500	75000	1500
9	12	low	15	180	1058	487500	9750	40625	813
10	12	low	15	180	1253	487500	9750	40625	813
11	12	low	15	180	1448	487500	9750	40625	813
12	12	low	15	180	1643	487500	9750	40625	813
13	12	low	15	180	1838	487500	9750	40625	813
14	12	low	15	180	2033	487500	9750	40625	813
15	1	low	15	15	2063	75000	1500	75000	1500
16	22	low	10	220	2293	575000	11500	26136	523
17	22	low	10	220	2523	575000	11500	26136	523
18	22	low	10	220	2753	575000	11500	26136	523
19	22	low	10	220	2983	575000	11500	26136	523
20	22	high	10	220	3213	575000	11500	26136	523
21	22	high	10	220	3443	575000	11500	26136	523
22	22	high	10	220	3673	575000	11500	26136	523
23	1	high	15	15	3703	75000	1500	75000	1500
24	7	high	15	105	3823	300000	6000	42857	857
25	7	high	15	105	3943	300000	6000	42857	857
26	7	high	15	105	4063	300000	6000	42857	857
27	7	high	15	105	4183	300000	6000	42857	857
28	7	high	15	105	4303	300000	6000	42857	857
29	7	high	15	105	4423	300000	6000	42857	857
30	1	high	15	15	4453	75000	1500	75000	1500
31	12	high	15	180	4648	487500	9750	40625	813
32	12	high	15	180	4843	487500	9750	40625	813
33	12	high	15	180	5038	487500	9750	40625	813
34	12	high	15	180	5233	487500	9750	40625	813
35	12	high	15	180	5428	487500	9750	40625	813
36	12	high	15	180	5623	487500	9750	40625	813
37	12	high	15	180	5810	520000	9750	40625	813

A5 refrac									
Stage	clusters	perf friction	cluster spacing	stage length	cum gpi	stage prop	stage fluid	prop/cluster	fluid/cluster
1	7	low	20	140	150	400000	8000	57143	1143
2	7	low	20	140	310	400000	8000	57143	1143
3	7	low	20	140	470	400000	8000	57143	1143
4	7	low	20	140	630	400000	8000	57143	1143
5	7	low	20	140	790	400000	8000	57143	1143
6	1	low	20	20	830	100000	2000	100000	2000
7	12	low	20	240	1090	650000	13000	54167	1083
8	12	low	20	240	1350	650000	13000	54167	1083
9	12	low	20	240	1610	650000	13000	54167	1083
10	12	low	20	240	1870	650000	13000	54167	1083
11	12	low	20	240	2130	650000	13000	54167	1083
12	1	low	20	20	2170	100000	2000	100000	2000
13	22	low	12	264	2446	690000	13800	31364	627
14	22	low	12	264	2722	690000	13800	31364	627
15	22	low	12	264	2998	690000	13800	31364	627
16	22	high	12	264	3274	690000	13800	31364	627
17	22	high	12	264	3550	690000	13800	31364	627
18	22	high	12	264	3826	690000	13800	31364	627
19	1	high	20	20	3866	100000	2000	100000	2000
20	7	high	20	140	4026	400000	8000	57143	1143
21	7	high	20	140	4186	400000	8000	57143	1143
22	7	high	20	140	4346	400000	8000	57143	1143
23	7	high	20	140	4506	400000	8000	57143	1143
24	7	high	20	140	4666	400000	8000	57143	1143
25	1	high	20	20	4706	100000	2000	100000	2000
26	12	high	20	240	4966	650000	13000	54167	1083
27	12	high	20	240	5226	650000	13000	54167	1083
28	12	high	20	240	5486	650000	13000	54167	1083
29	12	high	20	240	5746	650000	13000	54167	1083
30	12	high	20	240	6006	650000	13000	54167	1083
31	12	high	20	240	6256	650000	13000	54167	1083

Figure 210: Refrac well perforation design.

Table 21: Completion design summary for Zgabay 3H and Zgabay 5H refrac wells.

Active Well	Stages Monitored	Total Proppant (lbs)	Average Proppant per Stage (lbs)	Total Slurry Vol (bbls)	Average Slurry Vol per Stage (bbls)	Average Rate (BPM)	Average Pressure (psi)
3H	36	12,464,911	389,528	334,772	9,299	56	8,494
5H	32	12,214,885	436,246	353,308	11,041	56	8,578
excludes single cluster stages							

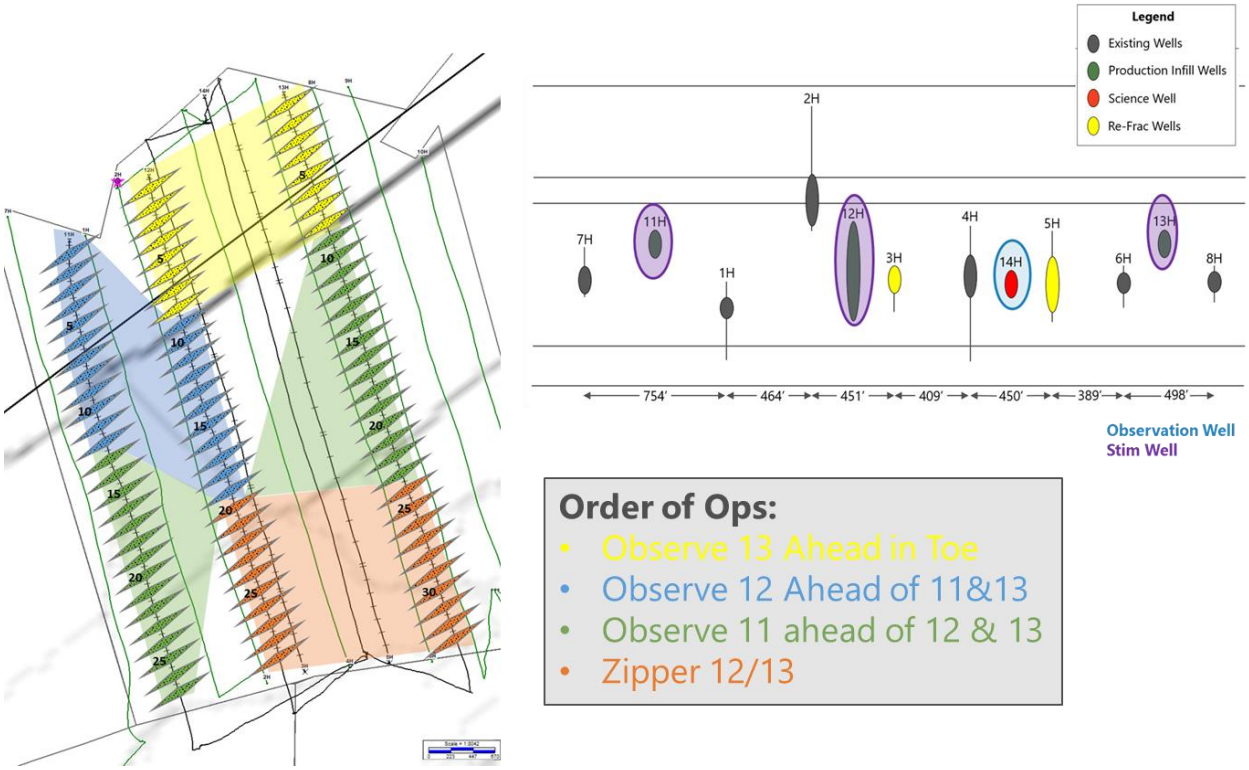


Figure 211: Operational summary at Zgabay unit during infill operations.

Upon completion of the stimulation program, a production interference test was performed. A staggered well opening approach was used for the refrac as well as the new infill wells. Prior to flowback, downhole pressure gauges were installed in neighboring Zgabay 1H, Zgabay 2H and Zgabay 6H well laterals. Apart from gauge data collection as well as response on the downhole fibers, time lapse geochemistry data was sampled as well. Figure 212 shows the production interference test plan for this unit prior to production monitoring.

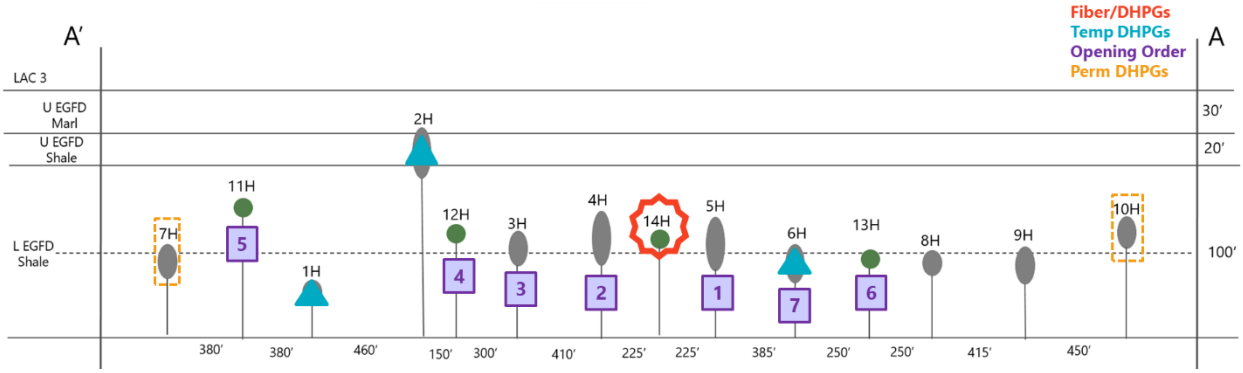


Figure 212: Production interference test plan with POP (Put On Production) sequence.

Sealed wellbore pressure monitoring (SWPM)

Various wellbores were used for SWPM analysis during the fracture stimulation of Zgabay 3H and Zgabay 5H refrac wells. Specifically, Zgabay 11H, 12H, 13H and 14H were used for refrac monitoring using the SWPM technique. VFR (Volume for first response) analysis is shared next.

VFR Analysis

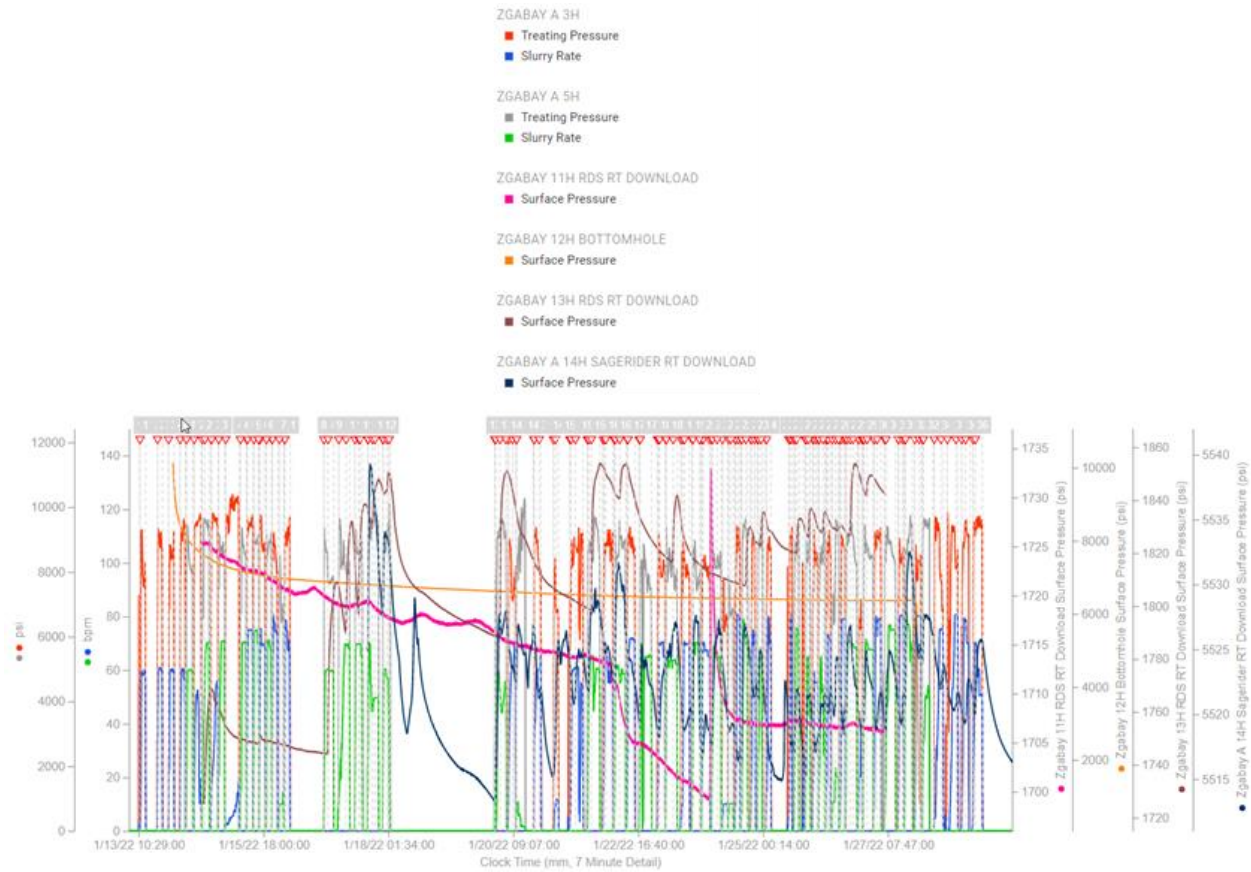


Figure 213: SWPM - Zgabay 3H/ 4H active wells with Zgabay 11H, 12H, 13H, 14H monitor wells.

Using volume for first response or VFR, one can understand communication between fracturing stages and nearby monitored wellbores where SWPM is being used. Figure 213 highlights the monitored pressure response in various wells during Zgabay 3H and Zgabay 4H fracturing operations.

From VFR analysis, hydraulic fracture half lengths can be calculated for various fracture stages during the stimulation program. Figure 214 compiles all the calculated fracture half lengths from the VFR analysis for the two refrac wells as cumulative distributions. Note that the half lengths are calculated using the Shapiro Equation (Shapiro & Dinske, 2009).

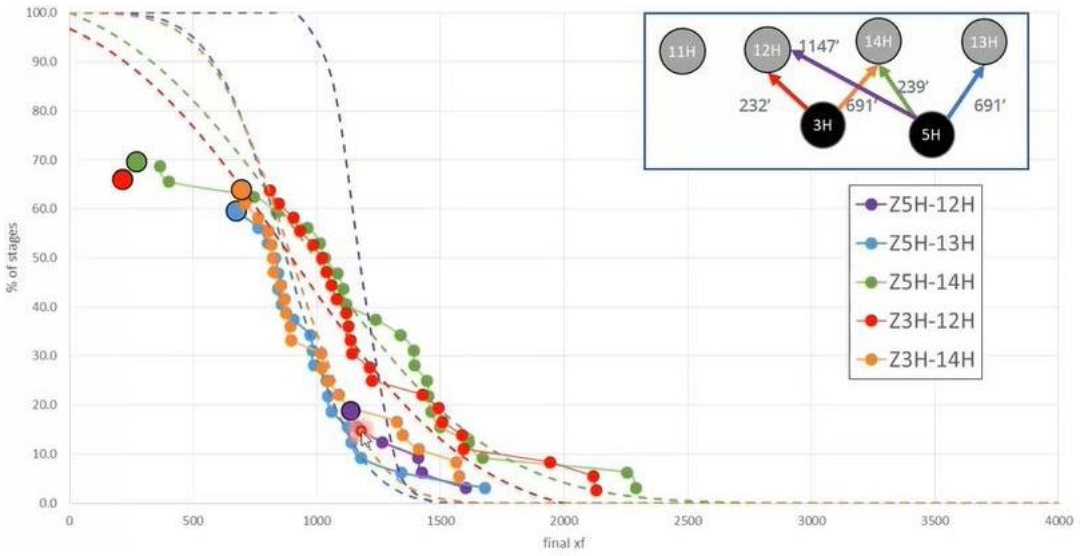


Figure 214: Hydraulic interaction plot indicating estimated fracture half lengths associated with various fracture Zgabay 3H and 5H refrac stages. We see good overlap between VFR response and the distance of these observation wells from the correpesponding refrac wells.

Table 22: Zgabay 3H SWPM summary (15 ft cluster spacing).

Stage details		Perforation details						3H to the 14H (Avg. on Azimuth 691')							
Stages	Stage Count	Perfs	Perf Friction	Perf Friction (psi)	Clusters	Stage Length (ft)	Average Slurry Volume per Stage (bbls)	Responses to 14H	High confidence Responses	Average on-Azimuth distance (ft)	Average VFR (bbls)	Avg VFR/Avg Stage Vol. %	Normalized VFR (bbls/cluster)	Avg Growth Rate (ft2/bbl)	Avg Frac Half-Length (ft)
7,14,21,29*	4	6,12,24,24	1554	1554	1	30	2415	3	3	697	2415	100%	2415	653	708
2-6	5	77	292	292	7	125	7045	2	2	716	2408	34%	344		
22-28	7	35	2305	2305	7	125	7670	6	5	690	4630	60%	661	347	875
8-13	6	72	500	500	12	200	10512	6	4	687	6024	57%	502	251	912
30-36	7	36	2071	2071	12	200	12160	7	7	710	6403	53%	534	281	1025
15-17	3	66	476	476	22	260	14950	2	2	671	5309	36%	241	290	1185
18-20	3	44	1782	1782	22	260	12814	3	3	663	2277	18%	104	630	1596
Total/Avg	**35**						**9299**	**29**	**26**	**691**	**4613**			**583**	**1053**

Table 23: Zgabay 5H SWPM summary (20 ft cluster spacing).

Stage details		Perforation details					5H to the 13H (Avg. on Azimuth 691')							
Stages	Stage Count	Total Perfs	Perf Friction (psi)	Clusters	Stage Length (ft)	Average Slurry Volume per Stage (bbls)	Responses to 13H	High confidence Responses	Average on-Azimuth distance (ft)	Average VFR (bbls)	Avg VFR/Avg Stage Vol. %	Normalized VFR (bbls/cluster)	Avg Growth Rate (ft2/bbl)	Avg Frac Half-Length (ft)
7,14,21,27***	4	18,18,24,24	130	1	~30	2775	1	1	670	2703	97%	2703	521	678
2-6	5	77	446	7	155	9028	2	2	755	5258	58%	751	557	1220
22-26	5	35	1837	7	155	7538	5	5	669	4627	61%	661	317	858
8-13	6	72	369	12	260	12444	6	6	702	6276	50%	523	251	1024
28-32	5	36	2007	12	260	15097	2	2	648	5847	39%	487	228	1131
15-17	3	66	476	22	300	17533	2	2	702	6350	36%	289	254	1192
18-20	3	44	1782	22	300	15792	1	1	687	11695	74%	532	127	856
Total/Average	31					11041	19	19	691	5795			361	1016

Since VFR can also be calculated from fiber response, VFR picks from fiber were compared with VFR picks from the SWPM analysis (Figure 216). A strong positive correlation was observed between the two responses, and they align along the 1:1 slope as a validation. Table 22 and Table 23 highlight the summary observations from SWPM analysis for the two refrac wells.

Finally, SWPM data can be useful in monitoring for probable fracture reactivations based on the slope of the pressure curves. Figure 215 shows an example of a stage which had signals from possible reactivation as well as new fracture arrival as well. Table 24 shows a snapshot of the interpretation including stages were new fractures as well as reactivated fractures were observed in Zgabay 14H during re-stimulation of Zgabay 3H stages. Interpreted fracture lengths are also highlighted.

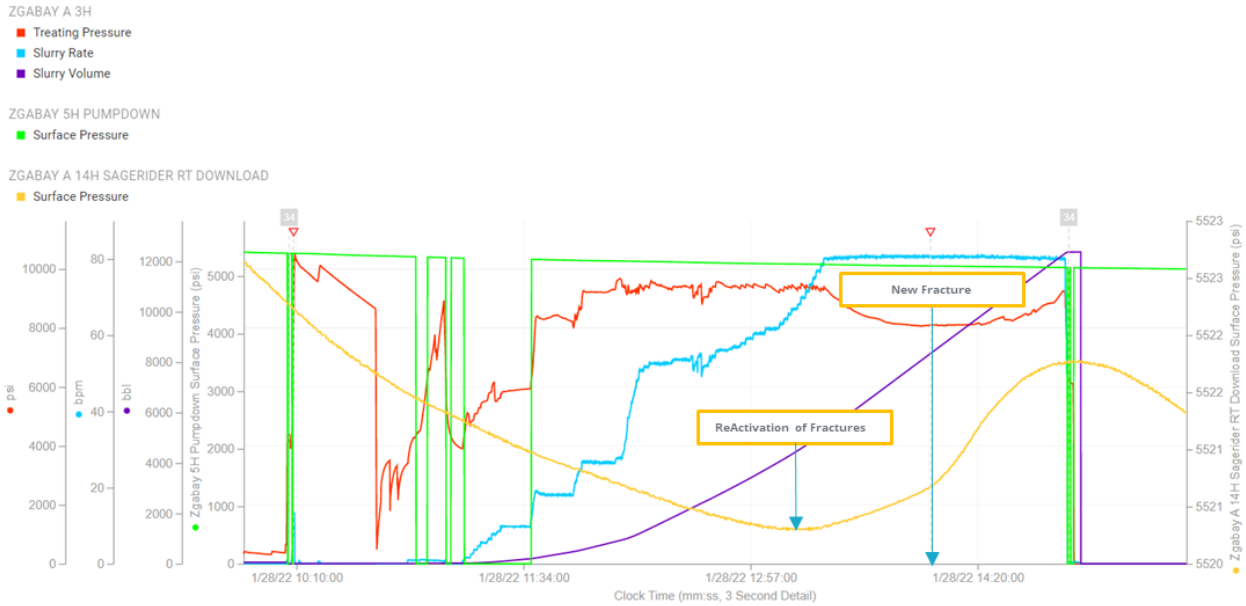


Figure 215: Zgabay 3H stage 34 to Zgabay 14H response. New fracture as well as probable fracture reactivation are highlighted.

Table 24: Reactivation vs. new fracture arrivals in Zgabay 14H (Zgabay 3H active)

Monitor Well	Active Well	Stage	VFR Start Time (datetime)	VFR End Time (datetime)	VFR Start Vol (bbl)	VFR End Vol (bbl)	VFR (bbl)	VFR Confidence	Fracture Reactivation	New Fracture	Pressure at Response (psi)	Final Pressure (psi)	ΔP Increase (psi)	Well Distance (ft)	Frac Growth Rate (ft^2/bbl)	Frac Lengths
Zgabay 14H	Zgabay 3H	1	01/13/22 11:01:39		0		7,080							734		
Zgabay 14H	Zgabay 3H	2	01/13/22 18:50:28		0		7,404							707		
Zgabay 14H	Zgabay 3H	3	01/13/22 23:50:12		7		7,584							719		
Zgabay 14H	Zgabay 3H	4	01/14/22 04:54:10		0		7,175							710		
Zgabay TH	Zgabay 3H	5	01/14/22 11:09:45		0		6,510							704		
Zgabay 14H	Zgabay 3H	6	01/14/22 18:40:20		0		6,545							729		
Zgabay 14H	Zgabay 3H	7	01/15/22 01:10:30		0		2,369							731		
Zgabay 14H	Zgabay 3H	8	01/15/22 10:36:48		0		11,089							721		
Zgabay 14H	Zgabay 3H	9	01/15/22 16:05:36		0		10,555							710		
Zgabay 14H	Zgabay 3H	10	01/15/22 21:46:20		1		10,503							699		
Zgabay 14H	Zgabay 3H	11	01/16/22 03:18:10		0		9,936							699		
Zgabay 14H	Zgabay 3H	12	01/20/22 06:59:30	01/20/22 08:43:59	4	4,966	4,963	3	Probable		5,523.3	5,523.7	0.4	692	303.10	1,021
Zgabay 14H	Zgabay 3H	13	01/20/22 18:18:59	01/20/22 20:40:32	3	7,328	7,324	3	Probable		5,521.2	5,522.0	0.8	681	198.82	803
Zgabay 14H	Zgabay 3H	14	01/21/22 02:57:00	01/21/22 03:52:04	101	388	287	2	Probable	Yes	5,517.2	5,525.6	8.4	686	5,155.47	1,410
Zgabay 14H	Zgabay 3H	15	01/21/22 10:18:48	01/21/22 12:45:30	0	6,850	6,850	1		Yes	5,521.2	5,525.0	3.8	674	208.51	1,047
Zgabay 14H	Zgabay 3H	16	01/22/22 00:58:12	01/22/22 02:19:20	8	3,776	3,768	1	Probable		5,523.0	5,525.1	2.1	667	370.89	1,322
Zgabay 14H	Zgabay 3H	17	01/22/22 11:40:04		2		13,533							639	94.76	639
Zgabay 14H	Zgabay 3H	18	01/23/22 01:12:19	01/23/22 02:09:46	12	2,127	2,114	1	Probable		5,518.1	5,523.8	5.7	644	616.41	1,562
Zgabay 14H	Zgabay 3H	19	01/23/22 11:40:22	01/23/22 13:16:38	55	2,967	2,913	1	Probable		5,518.6	5,520.5	1.9	661	461.81	1,348
Zgabay 14H	Zgabay 3H	20	01/23/22 20:42:45	01/23/22 21:33:31	1	1,806	1,805	2	Probable		5,516.9	5,520.0	3.1	684	812.43	1,678
Zgabay 14H	Zgabay 3H	21	01/24/22 06:10:54		0		1,299							671	1,087.89	671
Zgabay 14H	Zgabay 3H	22	01/24/22 11:46:59	01/24/22 13:20:46	1	5,157	5,156	1		Yes	5,516.0	5,517.1	1.1	679	281.19	869
Zgabay 14H	Zgabay 3H	23	01/24/22 18:48:21	01/24/22 20:26:32	1	5,343	5,342	1	Possible	Yes	5,521.3	5,522.4	1.1	673	266.33	762
Zgabay 14H	Zgabay 3H	24	01/25/22 01:36:03		0	3,595	7,139							697	213.54	697
Zgabay 14H	Zgabay 3H	25	01/25/22 11:41:40	01/25/22 12:55:04	1	3,595	3,594	3		Yes	5,517.4	5,518.0	0.6	688	414.02	823
Zgabay 14H	Zgabay 3H	26	01/25/22 22:16:22	01/25/22 23:51:26	0	4,094	4,093	1	Probable	Yes	5,517.1	5,518.4	1.3	683	357.71	895
Zgabay 14H	Zgabay 3H	27	01/26/22 04:12:56	01/26/22 05:22:58	0	3,029	3,029	1	Possible		5,520.1	5,522.2	2.1	712	525.84	1,088
Zgabay 14H	Zgabay 3H	28	01/26/22 10:26:02	01/26/22 12:17:59	3	6,568	6,567	1		Yes	5,518.5	5,520.6	2.1	704	236.98	815
Zgabay 14H	Zgabay 3H	29	01/26/22 18:36:40	01/26/22 20:13:16	42	2,457	2,415	1	Probable		5,518.4	5,519.4	1.0	708	652.51	708
Zgabay 14H	Zgabay 3H	30	01/27/22 01:29:25	01/27/22 02:54:07	3	4,920	4,917	1	Probable		5,518.8	5,521.9	3.1	700	313.13	1,142
Zgabay 14H	Zgabay 3H	31	01/27/22 12:22:57	01/27/22 14:10:47	0	7,040	7,040	1		Yes	5,519.6	5,521.7	2.1	693	214.14	823
Zgabay 14H	Zgabay 3H	32	01/27/22 19:45:39	01/27/22 21:39:09	0	8,234	8,233	1		Yes	5,524.4	5,525.4	1.0	688	180.41	855
Zgabay 14H	Zgabay 3H	33	01/28/22 04:23:46	01/28/22 07:23:18	1	7,315	7,315	1	Probable	Yes	5,522.0	5,523.8	1.8	691	204.72	875
Zgabay 14H	Zgabay 3H	34	01/28/22 10:09:19	01/28/22 14:03:02	5	8,341	8,336	1	Probable	Yes	5,520.7	5,521.8	1.1	733	202.62	893
Zgabay 14H	Zgabay 3H	35	01/28/22 16:38:31	01/28/22 18:23:22	2	6,053	6,052	1		Yes	5,519.3	5,522.7	3.4	733	278.50	1,017
Zgabay 14H	Zgabay 3H	36	01/28/22 21:33:42	01/28/22 22:41:42	1	2,928	2,927	2		Yes	5,520.2	5,525.4	5.2	730	572.32	1,573

Some key observations are as follows:

- Out of the total 272 stage-well pairs that were evaluated, 107 responses were observed. Very few responses were observed in the wells that were furthest away from the refrac wells.
- The 7-cluster high perf friction design has shown the highest cluster efficiency followed by the 12 cluster designs and lastly, the 22 cluster designs.
- The 7-cluster design with high perf friction (both Zgabay 3H to 14H and Zgabay 5H to 13H) had a VFR/cluster of 661 bbls and a fracture half-length of approximately 850 ft.
- There is good agreement between fiber and SWPM VFR's.

Single clusters data (calibration stages) suggest that pumping at least 20 bpm and pumping in the range of 3.5 to 4.5 bbls/ft/cluster is required to see a response in offset observation wells (distance in ft is between the active and monitor well along the fracture azimuth).

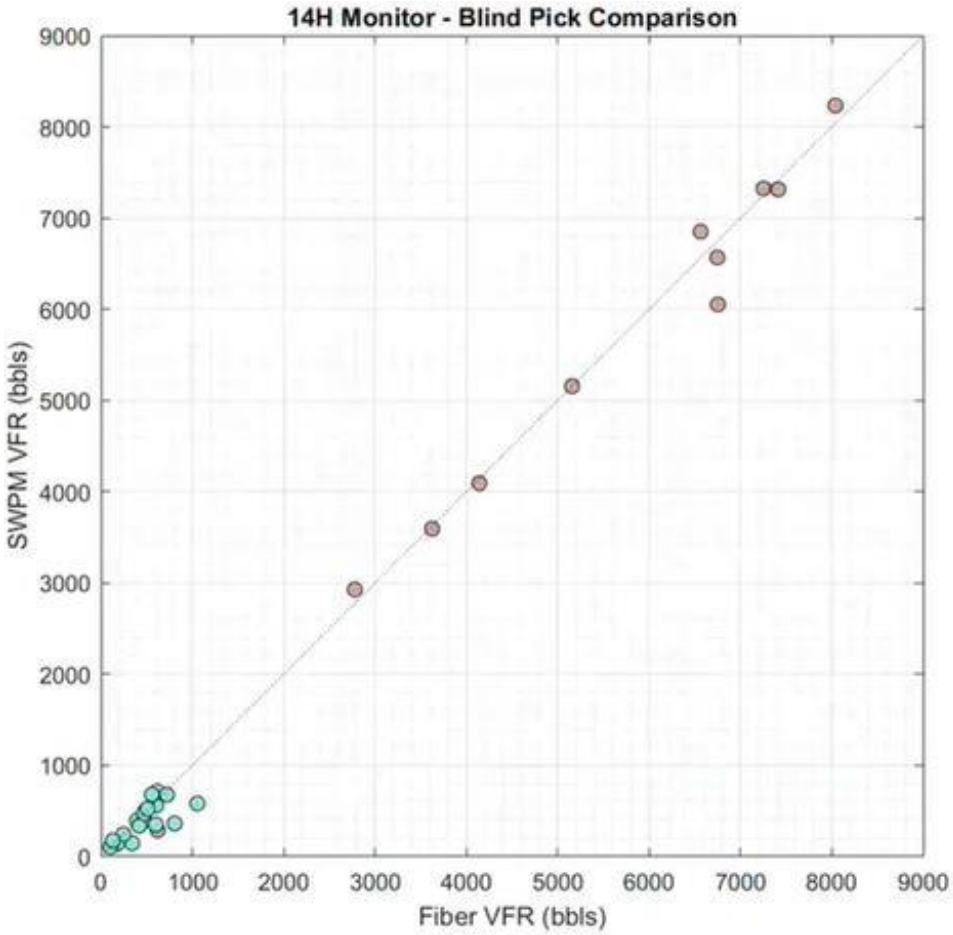


Figure 216: VFR response comparison. Red dots indicate Zgabay 3H response & blue dots indicate 5H response at 14H.

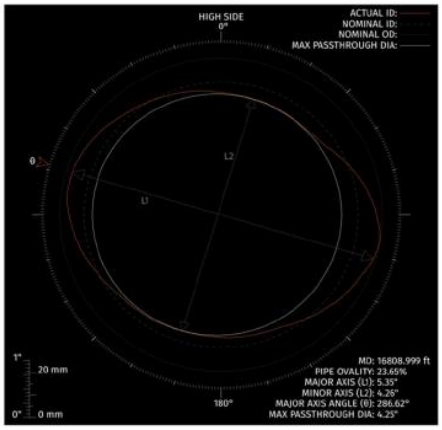
Pre- and Post-refracturing perforation efficiency

In order to better understand the perforation and cluster level efficiencies, and to contextualize post refracturing stimulation effectiveness, perforation imaging was conducted in Zgabay 5H treatment well using high resolution acoustic imaging techniques. This allowed mapping of both casing deformation and perforation erosion profiling along the well. This logging run was repeated after refracturing to understand the perforation efficiency post stimulation along the newly perforated sections.

Pre-refracturing perforation imaging

As an overview of this study, on October 4, 2021, DarkVision scanned Zgabay 5H well to perform a pre-fracture perforation analysis. The DarkVision tool was able to scan from the 6th cluster of stage 3 to the top of the perforated portion of the well. Out of the 690 expected perforations in the scanned depth range, 403 perforations were identified and measured, while 242 were identified but not measured due to plugging, for a total of 645 or 93%. The remaining 45 perforations were fully obscured. Significant deformation in the casing was observed in this well (Figure 217). Specifically, as one moves into deeper sections of the well, the ovality increases significantly and a maximum of 26% is observed at a depth of approximately 17,000 ft. This does create limits on maximum tool diameters that can be accommodated within the casing and require specific changes to the re-fracturing operations design including choice of guns, plug types and locations, etc.

Depth (ft)	Ovality (%)	Max Passthrough Dia. (Inches)
11011.9	0	4.65
11967.2	4	4.56
12298.9	5	4.52
13527.3	8	4.47
14026.7	17	4.30
15326.7	15	4.26
16389.7	19	4.30
16710.4	24	4.20
16808.9	24	4.25
17017.0	26	4.25



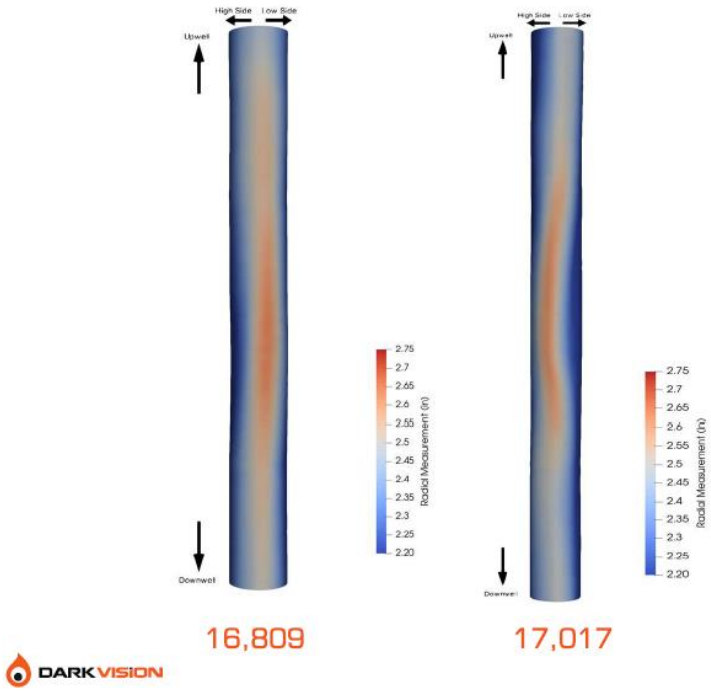


Figure 217: Observed ovality along Zgabay 5H during perforation imaging.

Figure 218 below shows an overall view of perforation areas for all the fractured perforations inspected. This is an overview of the relative sizes of the measured perforations with respect to depth and phase. We note that in the original treatment, we had 6 perforations per cluster with 0.42" entry hole diameter (EHD). Perforation mapping suggests that most of the perforations are oriented low (57%) and high (16%) followed by those with E-W orientation. A clear influence of orientation on charge performance (EHD) is also observed. Figure 219 highlights the perforation erosion as a function of depth.

Some stages show heel side bias whereas other stages tend to show toe side bias. However, this is not random and there is a systematic transition in bias as one goes from toe of the well towards the heel stages of the well. To more clearly differentiate the stages with heel bias and toe bias, Figure 220 plots the slope of the trendlines from the area erosion plot for each stage in the well. Units of the plot are percent increase per foot. Negative values indicate a heel side bias and positive values indicate a toe side bias.

As shown in Figure 220, most stages show a heel side bias. Stages with a bias of more than 0.15%/ft slope are classified as having a toe side bias and stages with a bias less than -0.15%/ft are classified as having a heel side bias. Stages with a bias that falls between those values are classified as having an even distribution. Using these classifications, the relationship between perforation efficiency and cluster efficiency can be arrived at. Perforation efficiency is the percent of perforations in a stage that eroded more than 20% in area. Cluster efficiency is the percent of clusters in a stage where at least one perforation in that cluster eroded more than 20% in area.

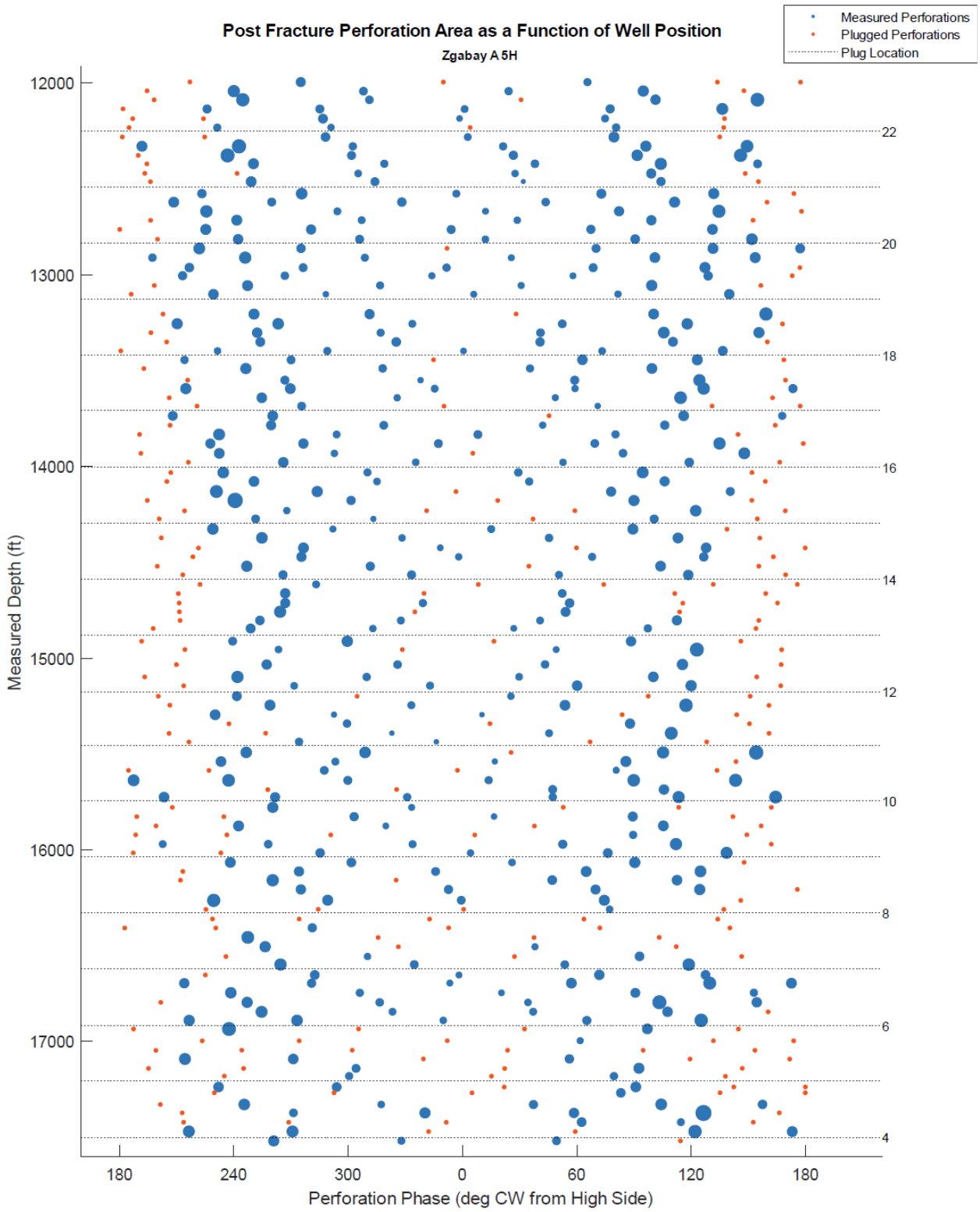


Figure 218: Perforation area as a function of well position along Zgabay 5H well.

The perforation vs. cluster efficiency behavior (Figure 221) is consistent with independent observations. By the nature of cluster design, depending on number of perforations shot per cluster, cluster efficiency tends to be lot higher compared to perf efficiency (Maity & Ciezobka, 2023). Stages with no bias show a higher cluster efficiency. Also, there seems to be a slight toe side bias in observed erosion per stage. On the other hand, when data from all stages were considered and one looks at erosion at the cluster level, a heel side bias is seen. Also, considering depth offset of plugs as surveyed when set vs. where they were observed during imaging was found to be less than ±10 ft. Considering some general observations, the perforation area increase varies from a minimum of 0%, to a maximum of 96%, with a mean of

3%. However, this is with reference to the perforation size based on the charge specifications of the original completions.

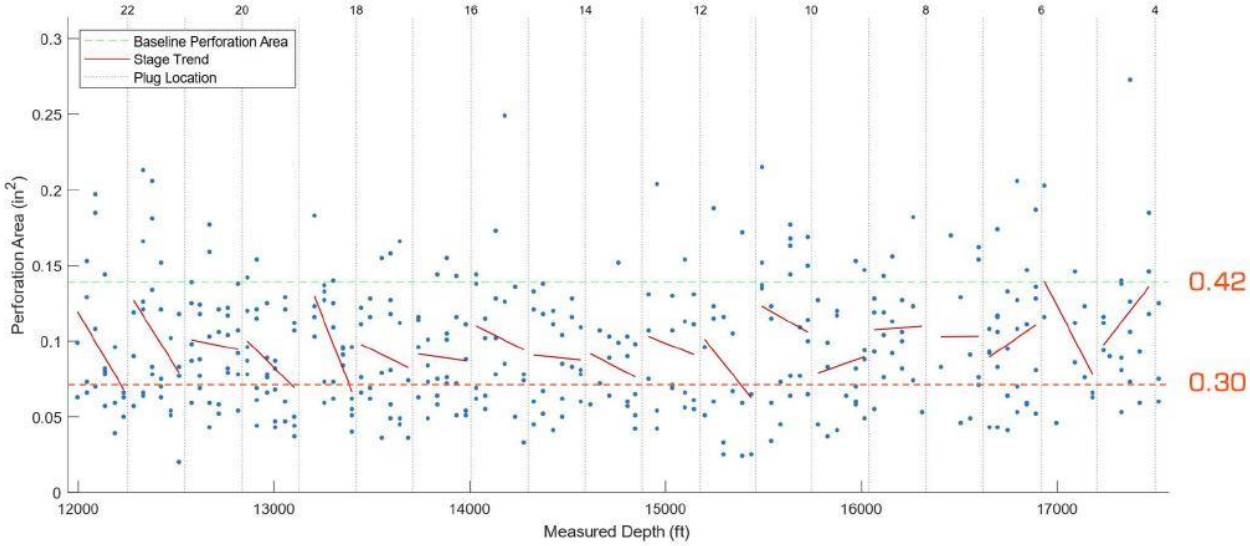


Figure 219: Perforation are as a function of depth along Zgabay 5H. The vertical lines indicate plug depth and red lines show erosion trend line.

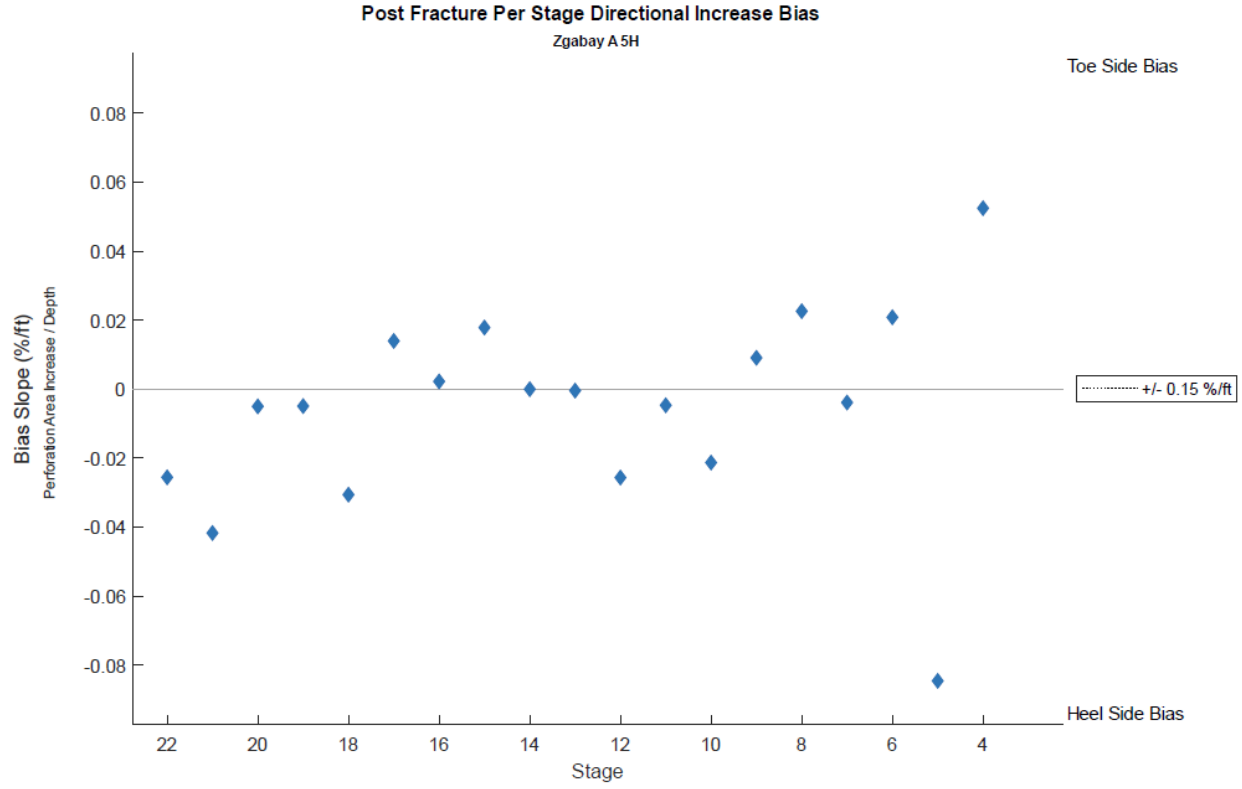


Figure 220: Observed pre-refracturing per stage directional increase in bias.

At the stage level, a heel side bias was seen when it comes to perforation erosion. Overall, the well shows a toe side bias in erosion. Looking downhole, the right side was observed to have eroded slightly more (15%) when compared to the left side. Using a 20% erosion threshold, 19% of the clusters can be considered efficient. No evidence of casing damage was found at the observed plug depths. Finally, two of the clusters were observed to be shot through a connection.

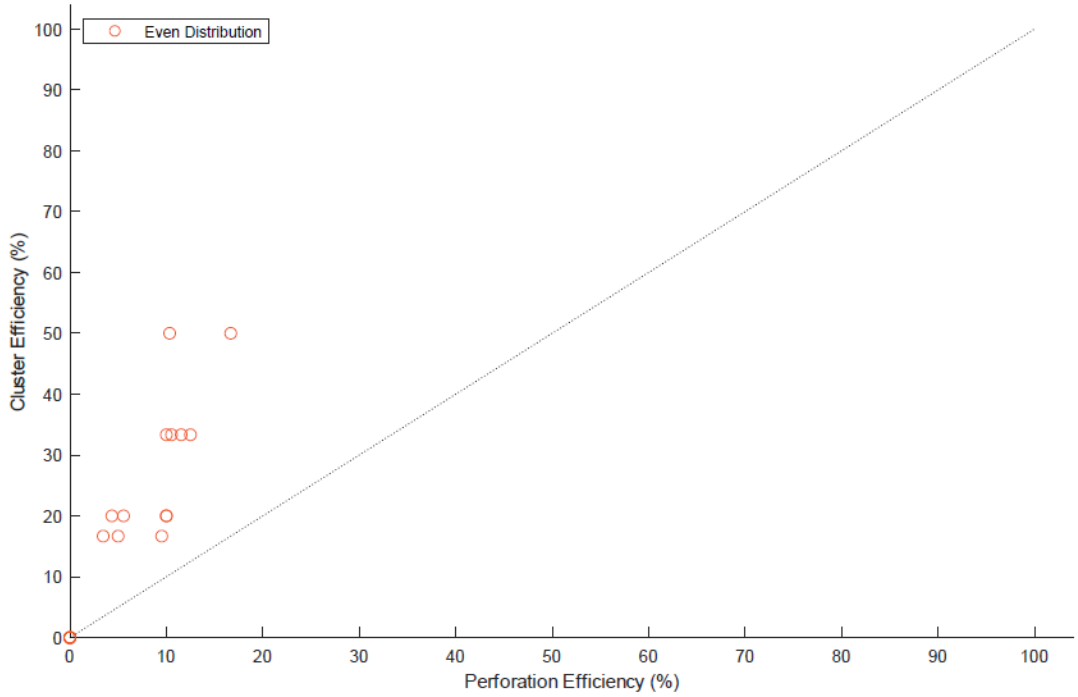


Figure 221: Cluster vs. perforation efficiency for observed perforations in Zgabay 5H before refracturing.

Post-refracturing perforation imaging

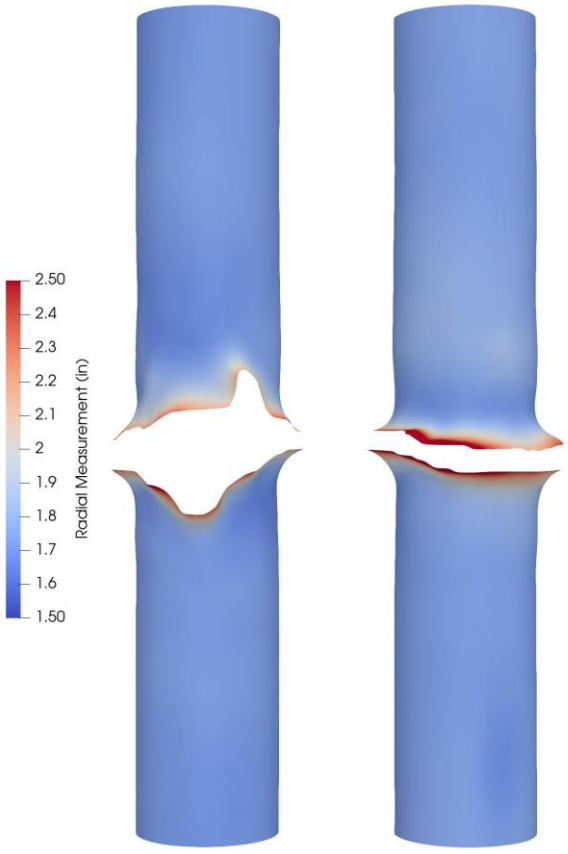


Figure 222: Parted casing observed in the well could have been due to a frac hit from in-fill fracturing operations at the site.

On March 12, 2022, DarkVision scanned Zgabay 5H well to perform a post-fracture perforation analysis. The tool was able to scan from the 1st cluster of Stage 9 to the top of the perforated portion of the well. Based on the original stage design, a total of 1183 perforations were expected in the scanned depth range. After identifying several stage discrepancies, the total of

expected perforations was amended to 1,170. Of these, 920 perforations were identified and measured, while 196 were identified but not measured due to plugging, for a total of 1,116 or 95%. 47 perforations were missed due to lack of data. 7 perforations were not detected, potentially due to charges not being loaded in the perforating gun. 64 of the expected 72 calibration perforations were measured, and the remaining 8 were identified but not measured due to plugging. Interestingly, a parted casing was observed at 16,849 ft as shown in Figure 222.

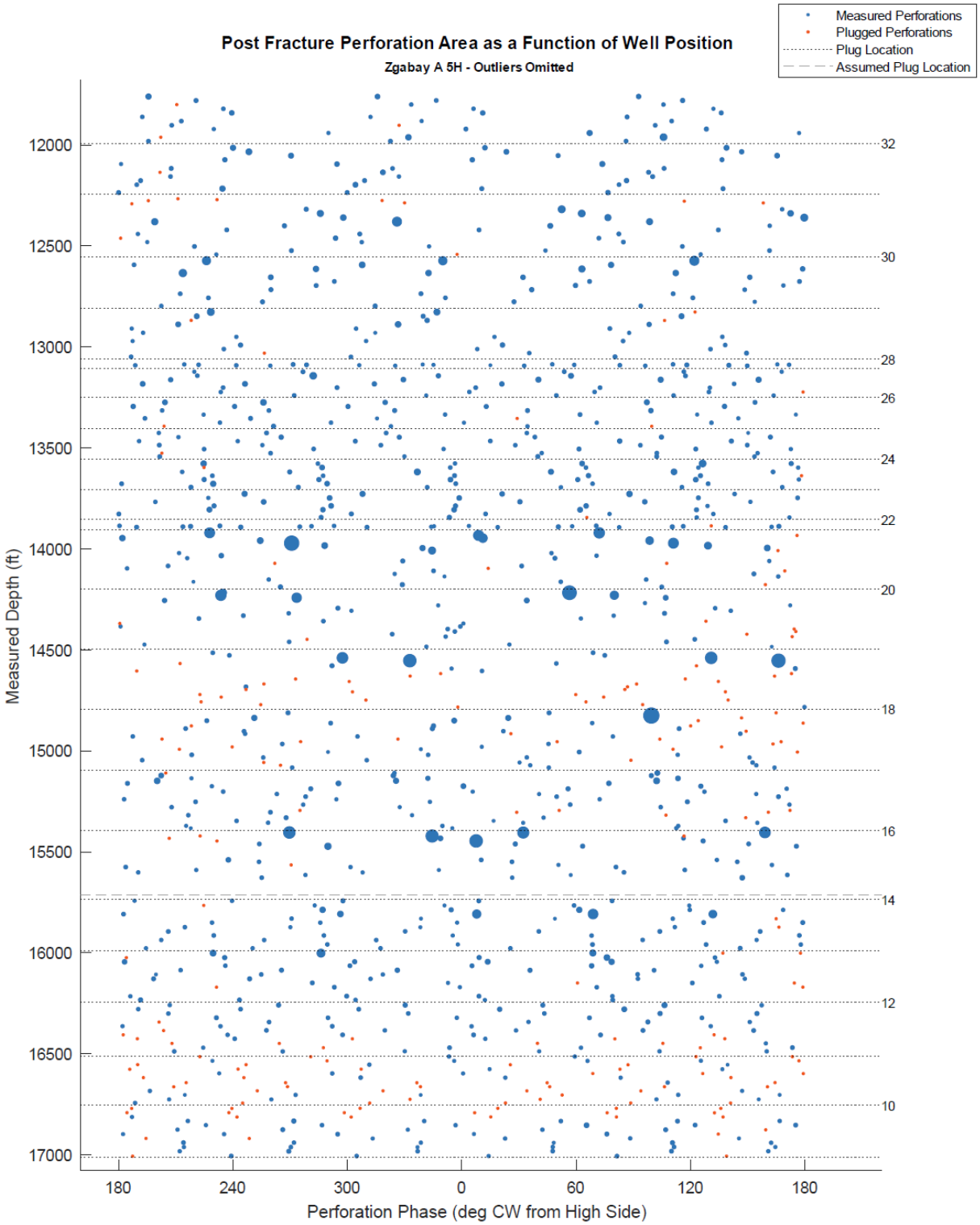


Figure 223: Post refracturing perforation area as a function of well position in Zgabay 5H. Note that outliers have been omitted in this display.

Based on the intensity data gathered by the tool close to the liner packers, no evidence of erosion was observed, and the packers appear to be in good condition at the time of the logging run. Additionally, two perforations (stage 17, cluster 21, perforation #1 and stage 19, cluster 18, perforation #2) show above normal erosion and were not used for any analysis and interpretation. Figure 223 shows the overall view of all the perforations inspected, with these two outliers omitted. At approximately 15,700 ft, an assumed plug location is indicated where no obvious plug markings were observed with the tool. We clearly see fewer plugged perforations and significant sections where perforations did take significant fluid when compared to the original completions (Figure 218)

Throughout the logged fractured stages, nine different stage designs were implemented, varying by cluster configuration and charge used to perforate the well. Figure 224 illustrates the perforation erosion over all the inspected fractured stages, on a per stage basis, specifically, perforation area versus measured depth, with outliers omitted. Each stage is divided by vertical lines indicating plug depth. The erosion trend for the stage is shown in red. Stages not scanned in their entirety have trendlines omitted.

To more clearly differentiate the stages with heel bias and toe bias, Figure 225 below plots the slope of the trendlines from the area erosion plot for each stage in the well, with outliers omitted. Units of the plot are percent increase per foot. Negative values indicate a heel side bias and positive values indicate a toe side bias. As shown in Figure 225, with outliers omitted, most stages show a heel side bias.

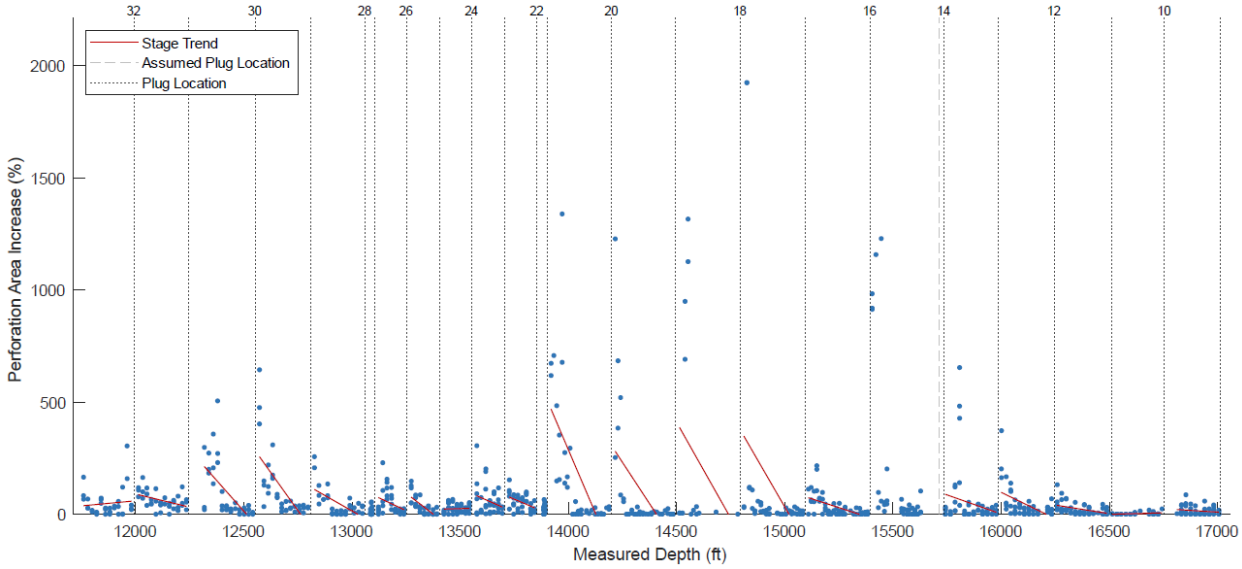


Figure 224: Post refracturing perforation area increase as a function of depth. Outliers have been removed.

As already discussed in the previous section where pre-refracturing results were discussed, stages with a bias of more than 0.15%/ft slope are classified as having a toe side bias and stages with a bias less than -0.15%/ft are classified as having a heel side bias. Stages with a bias that falls between those values are classified as having an even distribution. Using these classifications, the relationship between perforation efficiency and cluster efficiency can be displayed. Perforation efficiency is the percent of perforations in a stage that eroded more than 20% in area. Cluster efficiency is the percent of clusters in a stage where at least one perforation in that cluster eroded more than 20% in area.

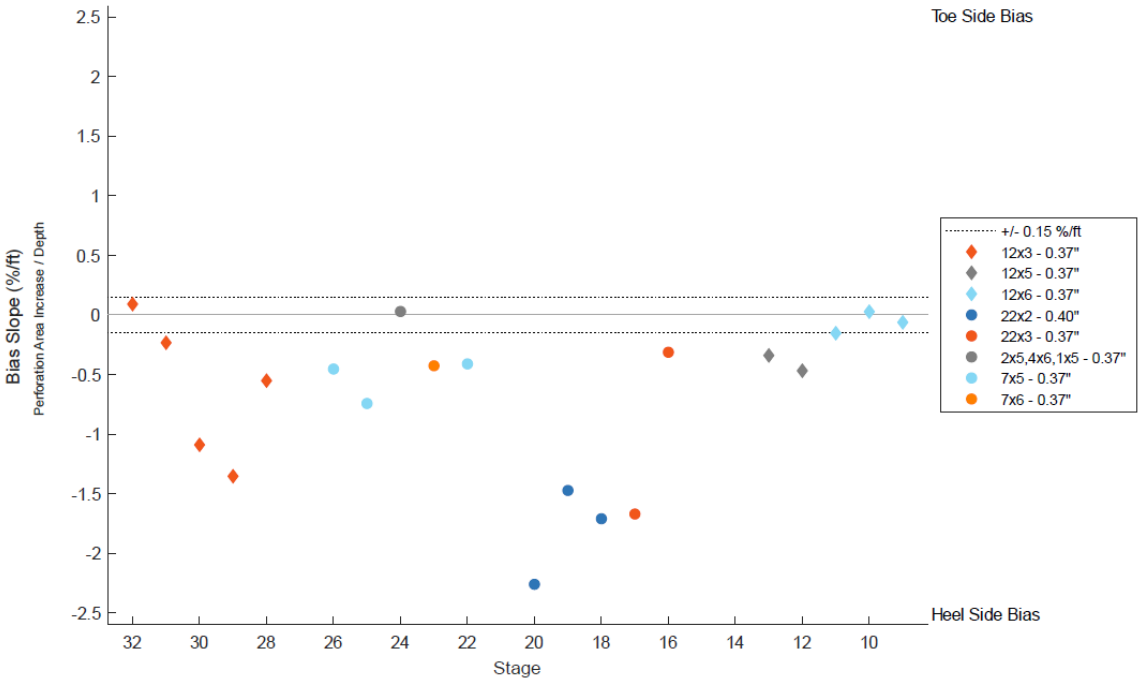


Figure 225: Post fracture per stage directional increase bias in Zgabay 5H post refracturing.

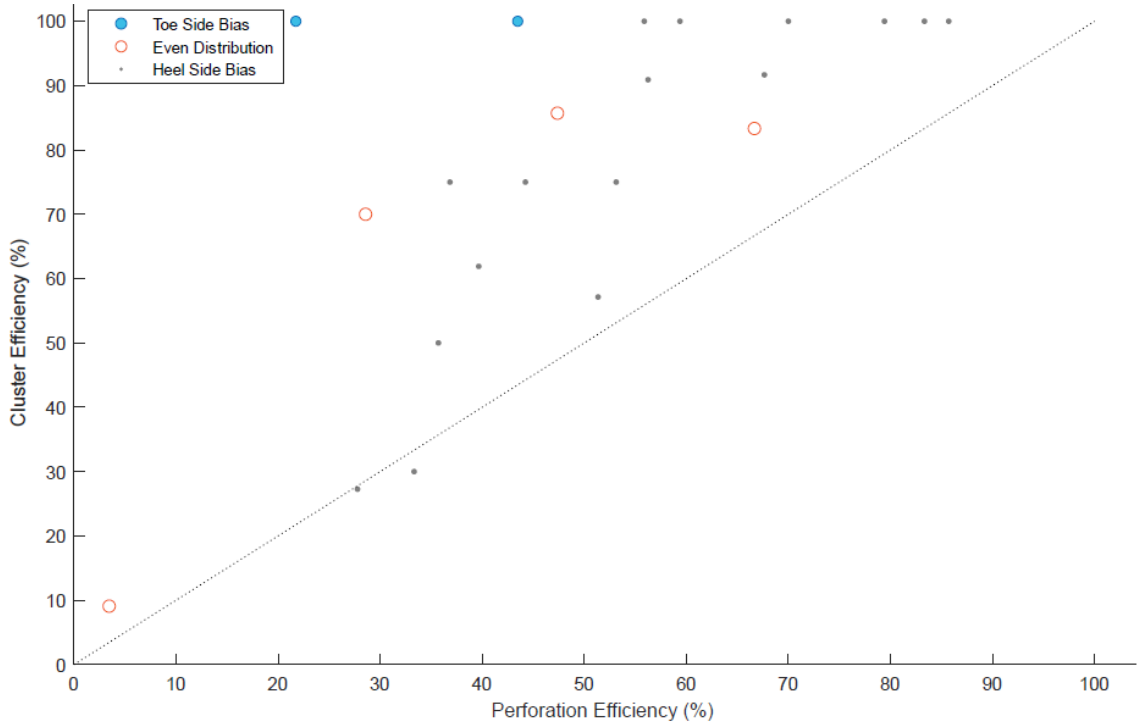


Figure 226: Cluster vs. perforation efficiency for observed perforations in Zgabay 5H after refracturing.

It was noted that with more limited entry designs and with larger number of clusters in general used for the restimulation (Figure 225), compared to the older parent completions which had 6 clusters per stage, the correlation between the perforation and the cluster efficiency is skewed towards the 1:1 slope line. This makes intuitive sense as higher cluster counts and aggressive limited entry suggests fewer perforations per clusters. The fewer perforations per cluster there are, the closer the efficiency distribution is to the unitary slope line which corresponds with clusters having single perforations (Maity & Ciezobka, 2023). Also, technically, cluster efficiency cannot be lower than perforation efficiency and the outlier values observed are a function of the arbitrary nature of defining these parameters.

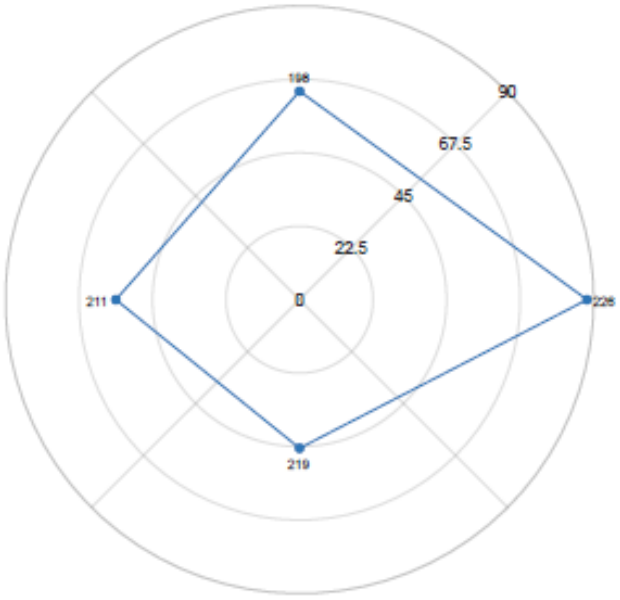


Figure 227: Mean post refracturing area increase vs. phase range. Right perforation (when looking from top) seems to have eroded more (57%) compared to left perforations. Also, the high side seems to have eroded 40% more compared to low side.

With the outliers omitted, stages with a toe side bias show a higher cluster efficiency. When one looks at perforation erosion statistics on a per stage basis, a heel side bias was observed. By calculating the mean perforation erosion by quadrant or phase of the shots, the impact of phasing on the perforation erosion characteristics can be understood. Figure 227 demonstrates the post re-fracturing perforation area increase as a function of phase range. Analyzing for plugged perforations, in terms of likelihood, the low side perforations are more likely to be plugged followed by the right and left perforations and the high perforations are least likely to be plugged.

Impact of re-frac and in-fill fracs on SRV

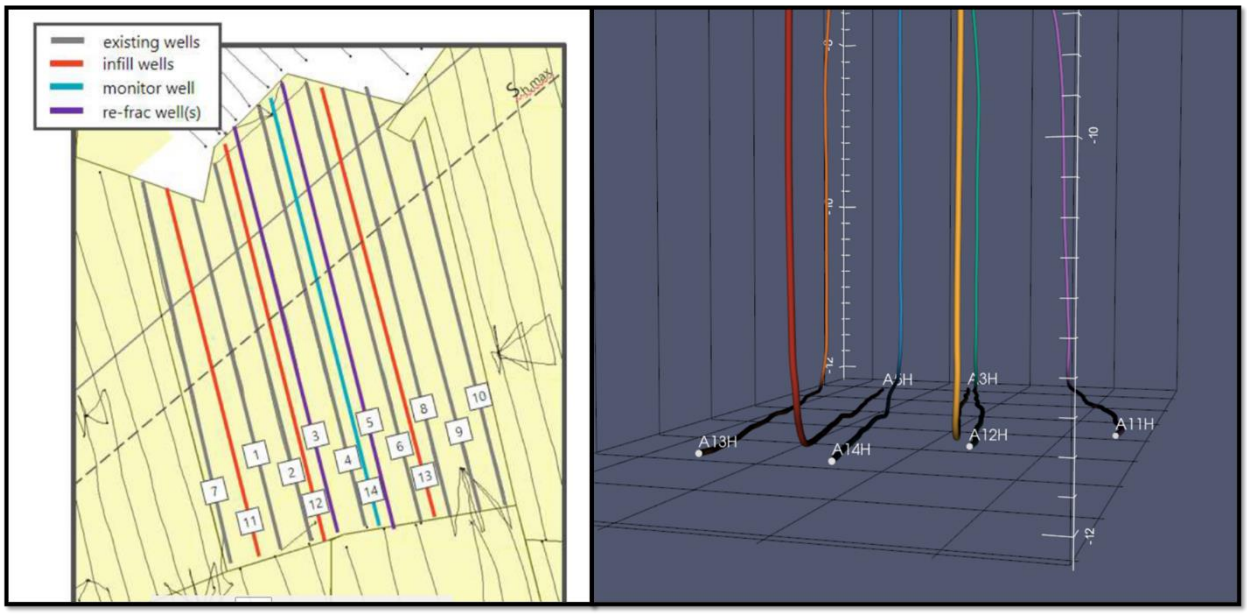


Figure 228: Wells (LHS: map view and RHS: gun-barrel view) at the test site.

The Phase 3 test site provides a permanently installed downhole fiber in a horizontal observation well which was used to monitor various operations at the test site. These include

baseline measurements, cross-well response with pre-load operations in Zgabay 4H, re-frac monitoring, in-fill monitoring, POP interference monitoring, choke interference monitoring and finally, flowback monitoring. These allow for qualitative evaluation of pre-existing SRV (from primary completions) as well as from refracturing and in-fill fracturing operations at the site. Figure 228 highlights the refrac wells (Zgabay 3H and 5H), preload well (Zgabay 4H) and infill wells (Zgabay 11H, 12H and 13H). Table 25 highlights the progression of operations and the cross-well strain data acquired as part of the analysis. This section will discuss major observations from cross-well fiberoptic strain monitoring during various phases as mentioned and conclusions that can be drawn from those observations regarding the fracture system or SRV around the 14H observation well as it evolves over time.

Evolution 1 [Pre-pump baseline measurements]

Data collected during the three days for baseline mapping show stable temperature profiles and stable baseline Raman and Rayleigh signals. These recordings were precursor to operational recordings to validate the fiber installation, data quality and baseline values for in-situ conditions at Zgabay 14H prior to any fracturing operations.

Evolution 2 [Zgabay 4H pre-load]

During the preload operations, significant region of change with notable strain response in the Zgabay 14H monitor well was observed. To map strain change, Rayleigh frequency shift is used (Ugueto et al., 2021). Specifically, multiple positive strain features were identified, and these defined a significant region of change associated with the Zgabay 4H primary fractures (SRV). Furthermore, these primary features correlate strongly with proppant distribution and interpreted propped fracture corridors along Zgabay 14H lateral. Dominant strain change observed during the preload was within 15,000’ to 17,500’ MD along the observation well.

Table 25: Zgabay 14H measurement phases from Neubrex.

Name	Target	Neubrex acquisition	
		start	end
Evolution 0	Fiber installation	Dec 7, 21 03:38	Dec 7, 21 19:30
Evolution 1	Baseline measurements	Dec 27, 21 22:32	Dec 31, 21 14:00
Evolution 2	Crosswell response from pressure preload in offset A4H	Jan 4, 22 17:40	Jan 6, 22 20:00
Evolution 3	Re-frac monitoring	Jan 12, 22 16:00	Jan 29, 22 8:00
Evolution 4	In-fill monitoring	Jan 31, 22 08:15	Feb 18, 22 21:22
Evolution 5	POP interference monitoring	Mar 14, 22 20:00	Mar 21, 22 18:40
Evolution 6	Choke interference monitoring	Apr 1, 22 23:20	Apr 5, 22 08:20
Evolution 7	Flowback monitoring	May 31,22 23:18	Jun 7, 22 11:20

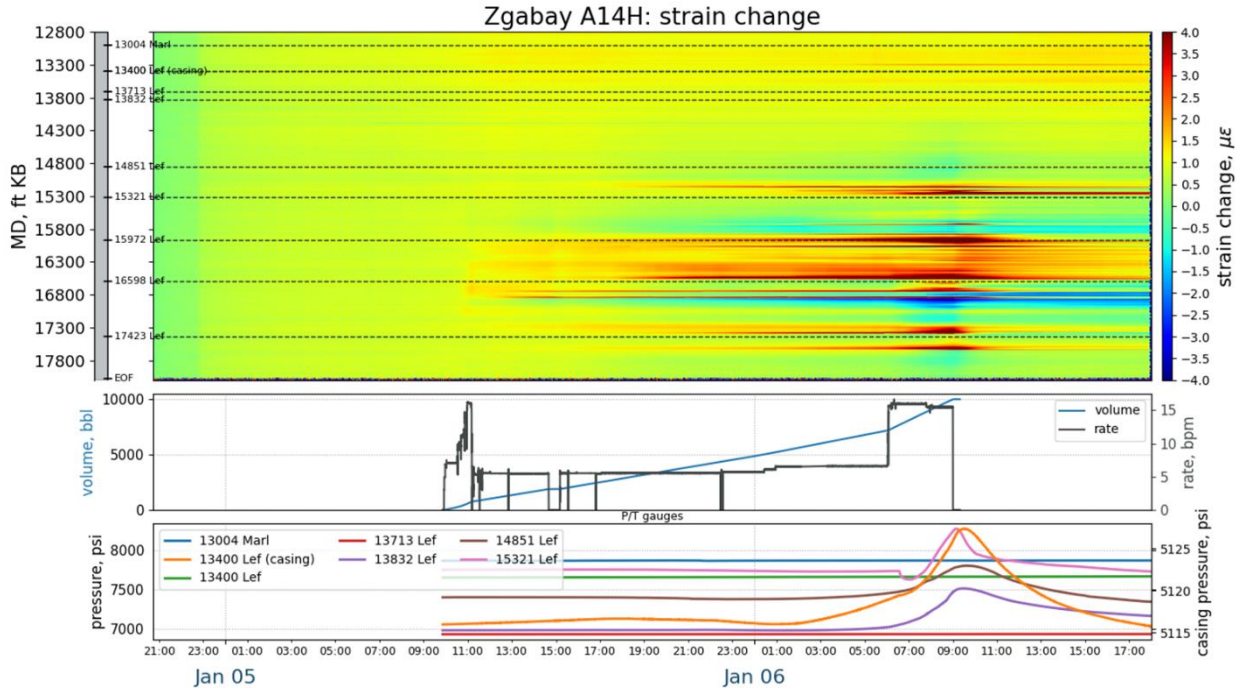


Figure 229: Zgabay 4H preload strain change response at Zgabay 14H. Pressure gauge locations are identified using dotted inserts.

Figure 229 highlights the preload vs. various gauges within the Zgabay 14H observation well and the strain change response in the fiber. Maximum strain change was observed to coincide with maximum injection during the preload. Strain change rate during this period highlights fracture corridors which were further validated using observed fracture corridors from proppant log analysis. Figure 230 shows the strain change rate and an example of definable communication zones with Zgabay 4H.

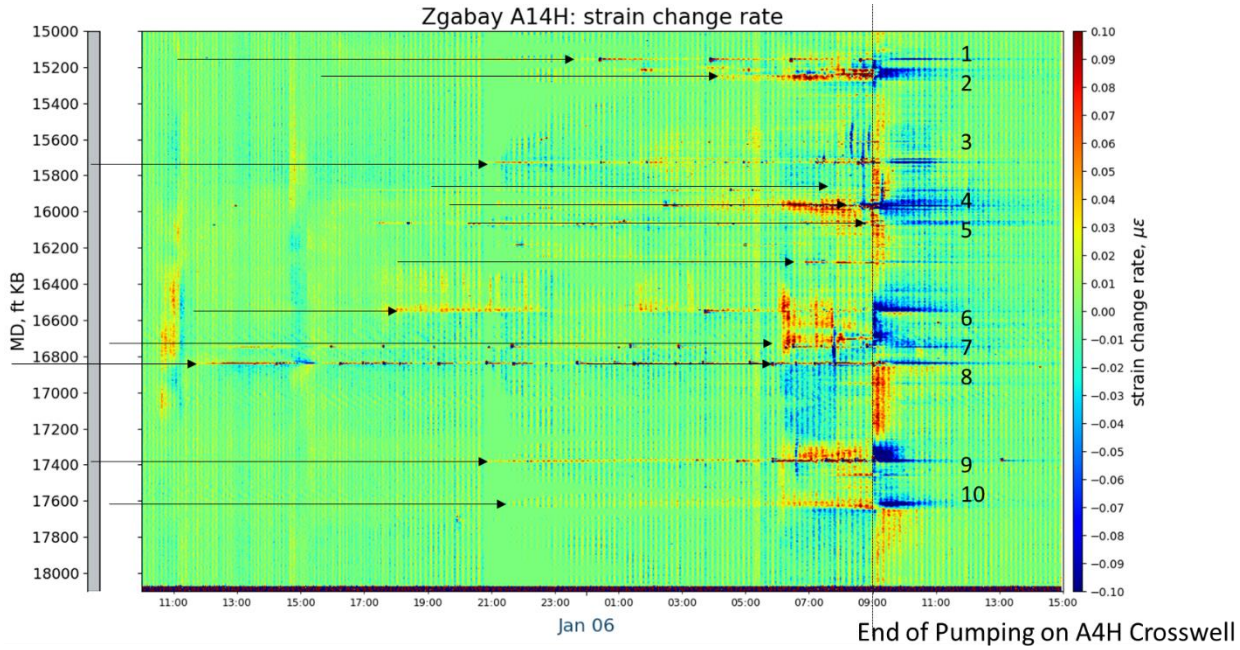


Figure 230: Rayleigh frequency shift, strain change rate along Zgabay 14H with definable communication zones.

Evolution 3 and 4 [re-frac and in-fill frac]

Observations during Zgabay 3H and Zgabay 5H refracturing as well as during Zgabay 11H, Zgabay 12H and Zgabay 13H in-fill fracturing were measured during a one-month period from January 13th through February 19th, 2022. Figure 231 highlights the strain change response

observed in Zgabay 14H during these operations. Partial cable failure was observed during the later portions of the infill refracturing operations. Specifically, 1,559 ft of single mode fiber in toe of the monitor well was lost. The strain monitoring limit is 16,521 ft MD whereas the new DTS fiber limit is at 16,704 ft MD. Fortunately, this happened after the corresponding infill stages in Zgabay 11H, 12H and 13H wells were already fracture stimulated. The toe-to-heel vs. heel-to-toe directions of the re-fracs and infill fracturing match the direction of stimulation treatment followed as part of this project.

Careful analysis of the strain change response can be used to understand new fracture domains associated with various stages fracture stimulated during this project. However, to understand the perturbation they may have caused and longer-term drainage characteristics, it becomes necessary to understand the strain response during cross well interference, for example during POP sequence as wells are brought online or during shut-in, which will be discussed later. Comparing the RFS strain change behavior post the re-fracs and post the in-fill fracturing can provide insights into how the SRV proximal of the Zgabay 14H evolved during this project. Since the wells are still shut-in, strong negative strain change response can be used as a proxy indication for significant fracture zones communicating with the nearby wells which were fracture stimulated. This is because pressure pumping liquid into these fractures pushes the fiber apart creating a negative strain change response. Figure 232 and Figure 233 show the strain change response after the re-fracs (blue trace) and after the in-fill stimulation (red trace). Perturbed and communicating zones can be visually identified and associate them with either the re-fracs or new in-fill fracturing operations.

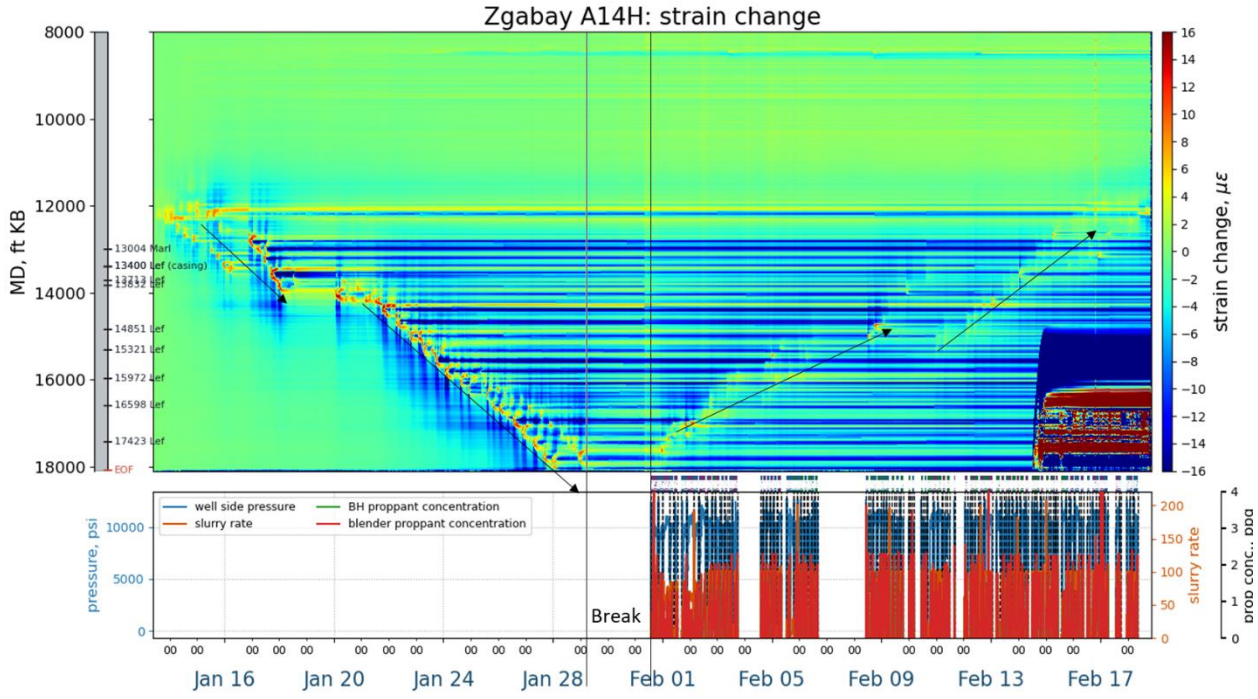


Figure 231: Zgabay 14H RFS DSS strain change during fracturing operations.

Discriminating between the response from the two fracturing programs can be observed as a divergence with a pronounced negative strain change response after the in-fill program vs. the in-situ strain change distribution after the re-frac program. Specifically, where time lapse RFS strain feature differences occur, this is evidence for presence of fracture corridors resulting from infill frac operations. Moreover, if time lapse RFS strain features overlap, then this could

indicate a reoccupation along existing fracture fabric within the SRV. Final assessment suggests that about 70% of the strain fabric detected at Zgabay 14H was placed in / around Zgabay 14H monitor well during zipper refrac of Zgabay 3H and Zgabay 5H. Furthermore, about 30% of strain fabric detected at Zgabay 14H appears to have been placed during infill frac period where the zipper frac wells were farther "outboard" than the refrac wells on either flank of Zgabay 14H (i.e., Infill wells were farther away than refrac wells).

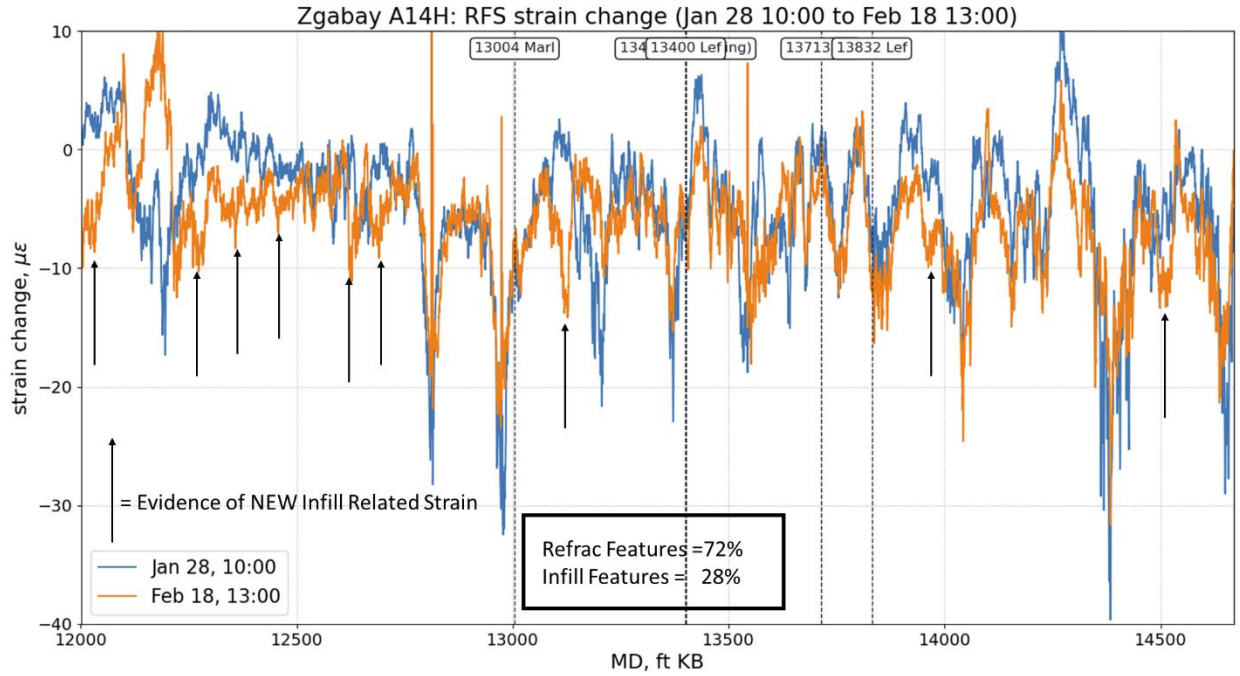


Figure 232: Strain change after refrac and after infill fracturing periods from 12,000 ft to 14,650 ft.

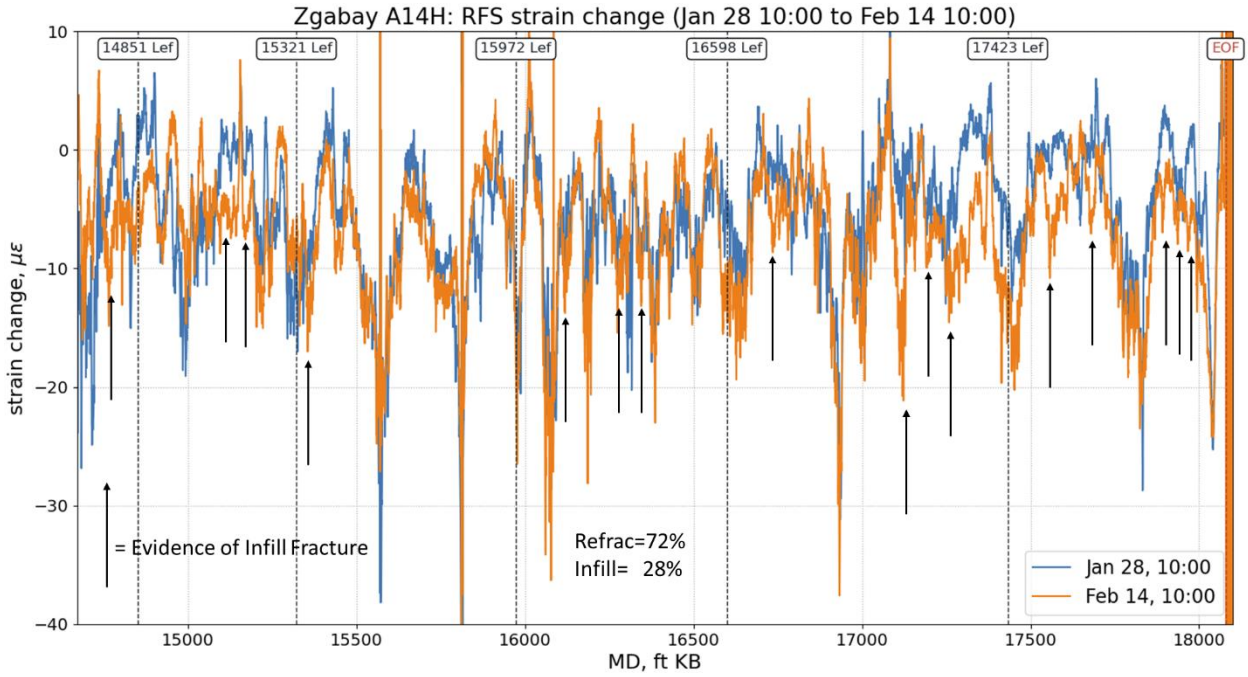


Figure 233: Strain change after refrac and after infill fracturing periods from 14,650 ft to 18,000 ft.

In terms of refrac cluster spacing, Zgabay 3H and Zgabay 5H had 15 ft and 20 ft cluster spacing on average barring a few stages with tighter cluster spacing. Stage lengths were in the range of 125 ft to 300 ft. Most of the strain change features observed far field at Zgabay 14H location seem to be clustered and spaced at 100's of feet, i.e., a similar spacing as the re-frac stage

lengths. If the original fracturing treatments are considered, the separations observed with the strain change rate features observed during Zgabay 4H preload operations (Figure 230), also ranged from 100 ft to 200 ft.

It is also noted that the cross-well frac hits observed during this phase of monitoring correlate very strongly with the pressure observed in the observation well. The pressure response in the casing was monitored using the permanently installed gauges and a strong correlation of pressure with the frac hits observed in the fiber as poroelastic effect due to fracture tip tensional effects was observed. Similar effects can also be observed with the temperature changed based on the DTS data, though to a much smaller degree.

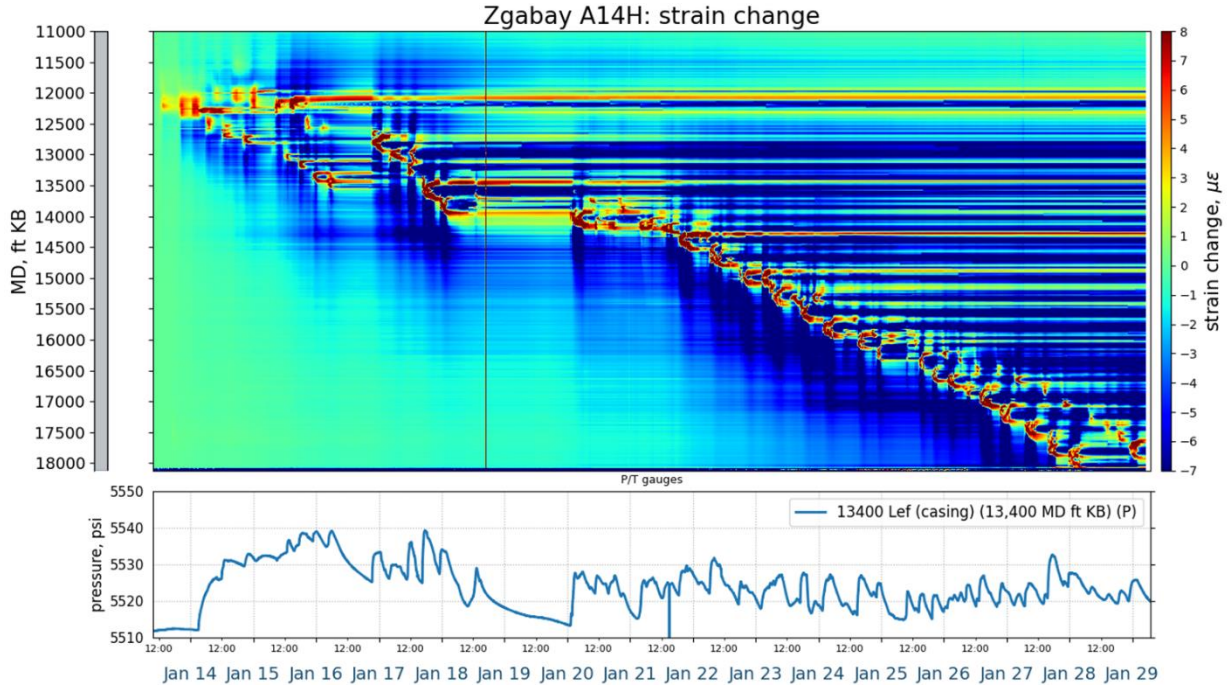


Figure 234: Strain change during refrac with Zgabay 14H casing pressure measured at 13,400' in Lower EagleFord.

Evolution 5 and 6 [POP and flowback monitoring]

Table 26 highlights the POP order following the fracturing operations. Specifically, refrac wells were put on production first followed by the infill wells Zgabay 12H, Zgabay 13H and Zgabay 13H. Finally, the parent well Zgabay 6H was opened followed by the rest of the wells in the development. The fiber data was captured and processed between March 14th and March 21st, 2022, with a total of 7,008 traces. It is important to note that strain change rate is useful in mapping short term divergences but does not reflect the gradual changes in signal very well. While other techniques may be developed, such as using larger time windows to calculate strain change, accumulated strain may be another way of analyzing the strain change data during the POP phase to detect gradual changes in response. This is highlighted in Figure 235 where alternating bands of positive and negative cumulative strain change (red vs blue end of the spectrum) with depth can be seen. The loss of fiber at the bottom section of the wellbore as well can also be clearly seen.

Figure 236 highlights the strain change response during refrac, infill and parent well flowback operations. Since with flowback, strong negative strain signals (compressional) to highlight conductive fracture corridors are expected, one can use the strain change observations to make these interpretations. It is noted that the negative strain magnitudes are much greater

than positive strain features. Moreover, negative strain features are much more isolated and distinct compared to the positive strain features. This suggests presence of distinct conductive fracture pathways where individual corridors may have multiple conductive hydraulic fractures clustered together. This ties with actual field based hydraulic fracture mapping from prior HFTS phases where clustering behavior of hydraulic fractures have been observed (Maity & Ciezobka, 2021). It is also noted that the overall magnitude of positive as well as negative strain increases from heel to toe for Zgabay 14H fiber. This divergence is clear from Figure 236.

Table 26: Zgabay wells POP order followed during monitoring.

Date	3/14/2022	3/15/2022	3/16/2022	3/17/2022	3/18/2022	3/19/2022	3/20/2022	3/21/2022	3/22/2022
Well Name	Day 1	Day 2	Day 3	Day 4	Day 5	Day 6	Day 7	Day 8	Day 9
5H	Baseline	POP							
4H	Baseline		POP						
3H	Baseline			POP					
12H	Baseline				POP				
11H	Baseline					POP			
13H	Baseline						POP		
6H	Baseline							POP	
7H									POP
1H									POP
2H									POP
8H									POP
9H									POP
10H									POP

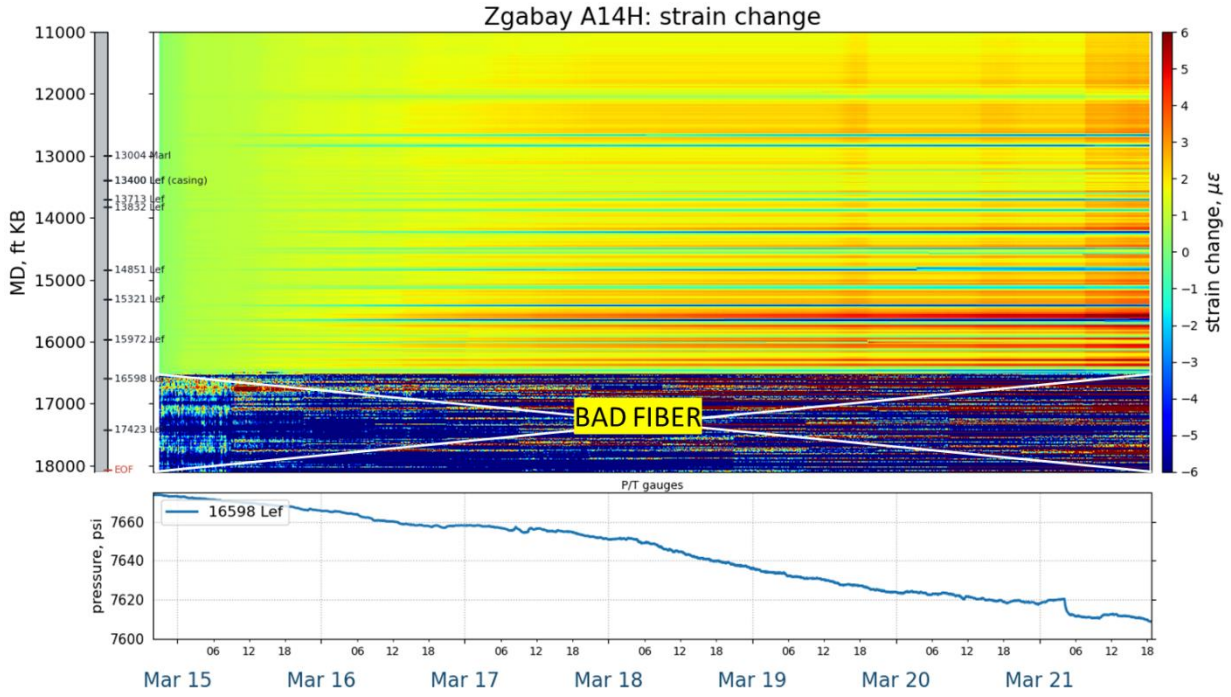


Figure 235: Accumulated RFS strain change waterfall during Evolution 5 monitoring.

In terms of vertical communication, it is interesting to note that significant strain change peaks above the horizontal zone of the Zgabay 14H monitor well were not observed. This is despite significant overlap of nearby infill and refrac lateral sections of wells at this test site as seen in Figure 228.

The clustering behavior is clearly observed when these negative strain responses along the fiber are carefully looked at. Figure 237 shows a zoomed in view of one such section with two negative strain peaks, each peak with its own sub-peaks clustered within. This provides an estimate of how far apart these strain features are both within and in-between the clusters. The

inter-corridor negative strain peaks separation ranges from 130 ft to 270 ft. The clustering length within these features is within 10's of feet. While the separation can vary over a wide range, it seems to be in line with the stage length between clusters in proximal wells which were either refrac or infill completions. This would suggest that for many of these stages, there is likely one or maybe two dominant conductive fracture corridors associated with the parent well clusters which are interacting during flowback operations. Moreover, the observed clustering is likely associated with multiple clusters of parent-well stages which are dominant within that stage. This makes intuitive sense since some of the stages had very aggressive limited entry designs with short cluster spacing (10 ft) and multiple stage clusters (7 to 22) which can create poor cluster level efficiencies as has been observed in prior HFTS projects (For example, with HFTS-2, Delaware Basin by Zakhour et al., 2021).

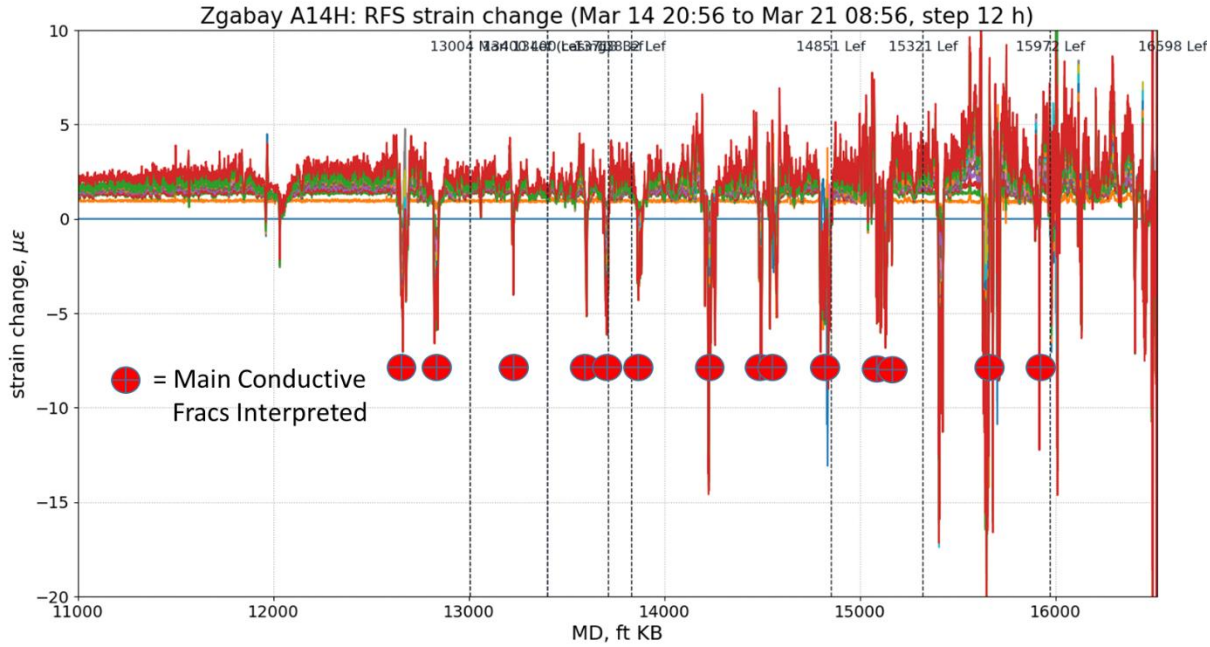


Figure 236: Time lapse strain profiles during refrac-infill and parent well flowback operations. Negative strain change indicates compression in fiber due POP (green trace)/ flowback (red trace) operations.

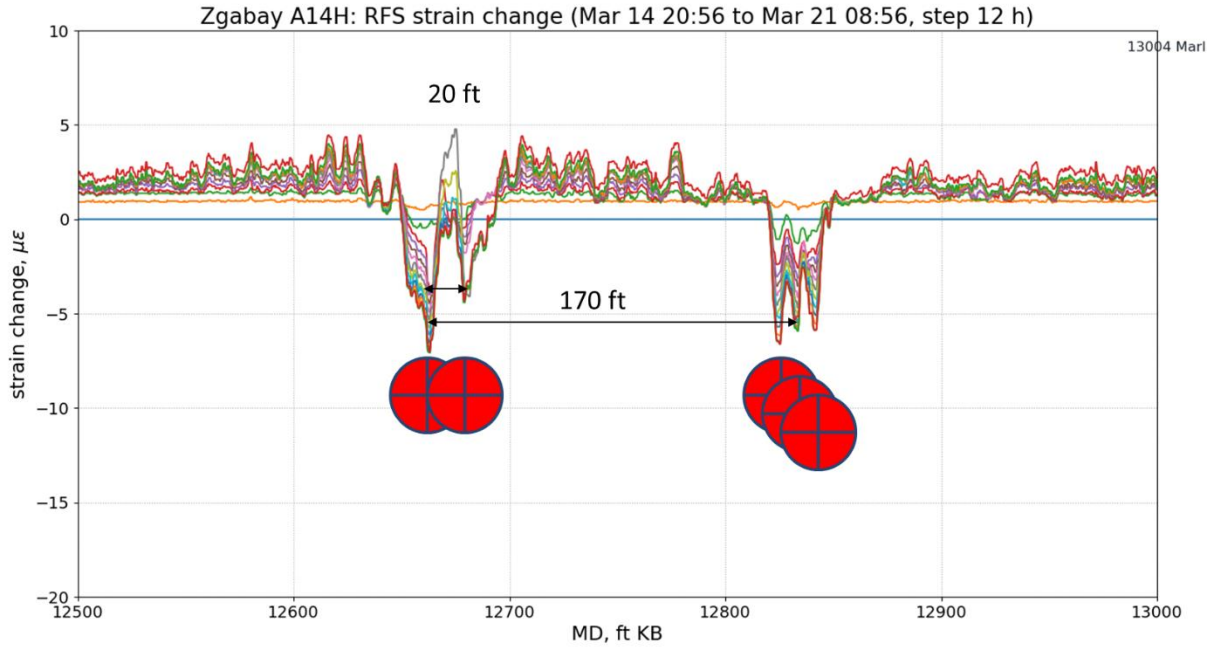


Figure 237: Examples of conductive fracture clustering within each conductive corridor.

Integrated analysis

With the various phases of well operations and crosswell strain monitoring at the observation well, it becomes possible to map the existing and newly developed communicating fracture corridors along the monitoring wellbore. Generally, good spatial correlation was observed between what are interpreted as active conductive fracture strain features based on dynamic strain change as detected on the permanent fiber of the Zgabay 14H monitor well during POP flowback and strain features observed during Zgabay 4H preload, Zgabay 3H and 5H refrac and Zgabay 11H, 12H and 13H infill frac operations. The project had original fracture corridors from the primary completions followed by the refrac and the infill completions. In terms of SRV coverage, within the horizons of interest, some interesting observations were made. Firstly, despite multiple stimulations including the primary and secondary (refrac and infill) programs, there are sections along the interval at the observation lateral along Zgabay 14H where no discernable communicating fracture corridor was seen. In some cases, these likely poorly communicating zones can extend up to 400 ft. There can be various factors at play here, including variations in rock properties or stress effects associated with geologic setting, evolving propped fracture network, or near wellbore conditions. However, it is instructive to measure approximate number of hydraulic fracture corridors in communication across different points in time at the monitored well to get a semi-quantitative sense of the SRV at the end of the operations. On average, the separation of such communicating corridors is approximately 150 ft.

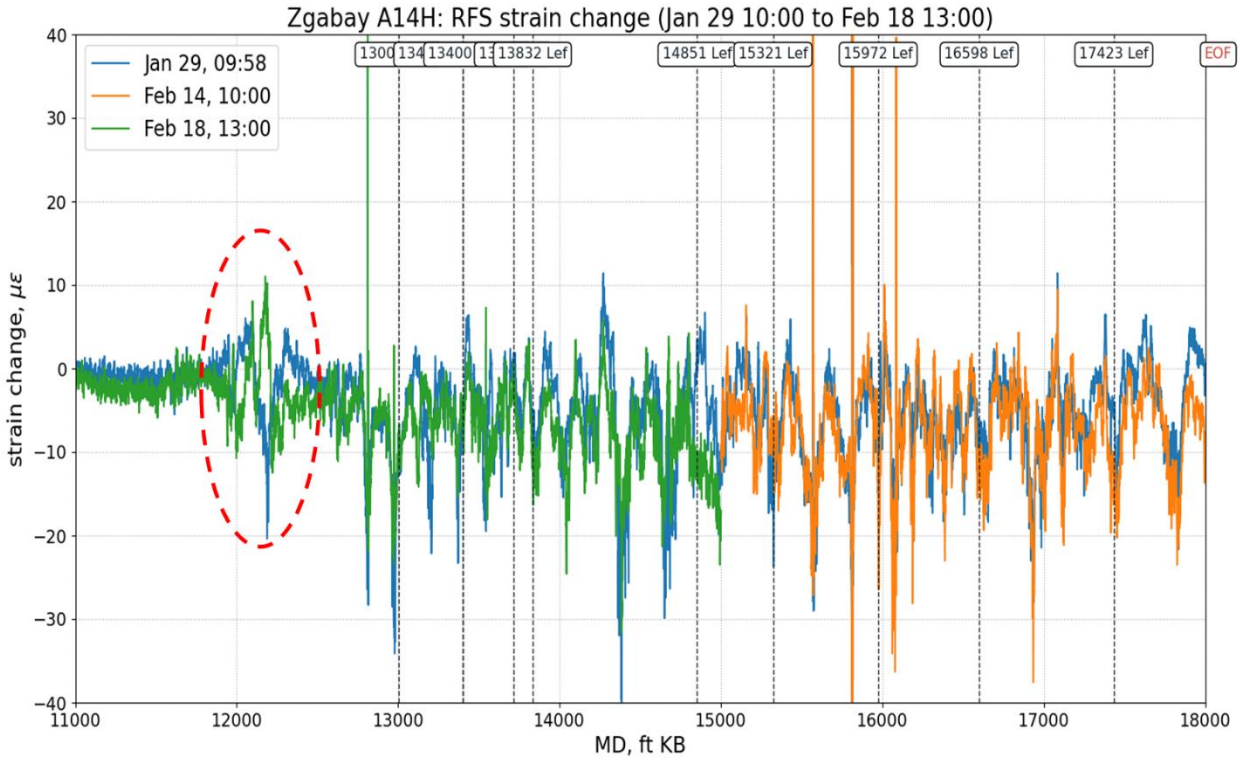


Figure 238: RFS strain change before and after the refrac and infill operations. Example of strain reversal is noted for reference.

Another notable observation is the reversal of strain change direction, i.e., positive to negative and vice versa as one goes from end of refrac to end of infill monitoring. This provides an indication of evolving stress state within the SRV where initially, there may have been an opening and intersecting fracture during refrac (compressional effect on fiber) but during infill,

there may have been new proximal fractures which invert the stress profile and create tensional effects on the fiber in the shadow zone associated with the new fracture corridors intersecting the instrumented well. Figure 238 shows an example of such a reversal for reference. It is also noted that a lot of the post refrac and post infill cumulative strain features identified during POP operations correlate spatially with where a strain response due was seen to Zgabay 4H preload operations. This suggests that even though the target was to try a new SRV generation with the refrac and infill operations, a significant portion of the new treatment is likely getting redirected into fracture corridors associated with the primary completions. However, the new strain field at the end of the operations dies suggesting that there is a significant increase in the communicating fracture corridors far-field at the instrumented well which is a direct result of the efficacy of the secondary fracturing operations at this site.

Mapping pre-existing and new fracture network

Prior to any fracturing operations, the drilling of Zgabay 14H monitoring well lateral provided ample opportunity to map existing fracture corridors at this site. This was done using multiple techniques and consolidation and integration of results from these independent methods provide a useful mapping of the pre-existing SRV at the Zgabay 14H monitoring well location. Four of these sets of observations include downhole pressure gauges, permanently installed fiberoptic observations, proppant log along the lateral, and finally, sealed wellbore pressure monitoring. This section will discuss some of these datasets and related observations, as well as integrated analysis to validate the in-place SRV prior to any restimulation of in-fill stimulation. Specifically, it demonstrates the drainage zones as identified based on these independent observations. The site itself is highly complex due to presence of large number of pre-existing wells as well as multiple new in-fill wells as well as refrac wells. Figure 239 highlights some of this complexity in a gun barrel representation of the wells at the test site along with the targeted Lower Eagle Ford shale horizon.

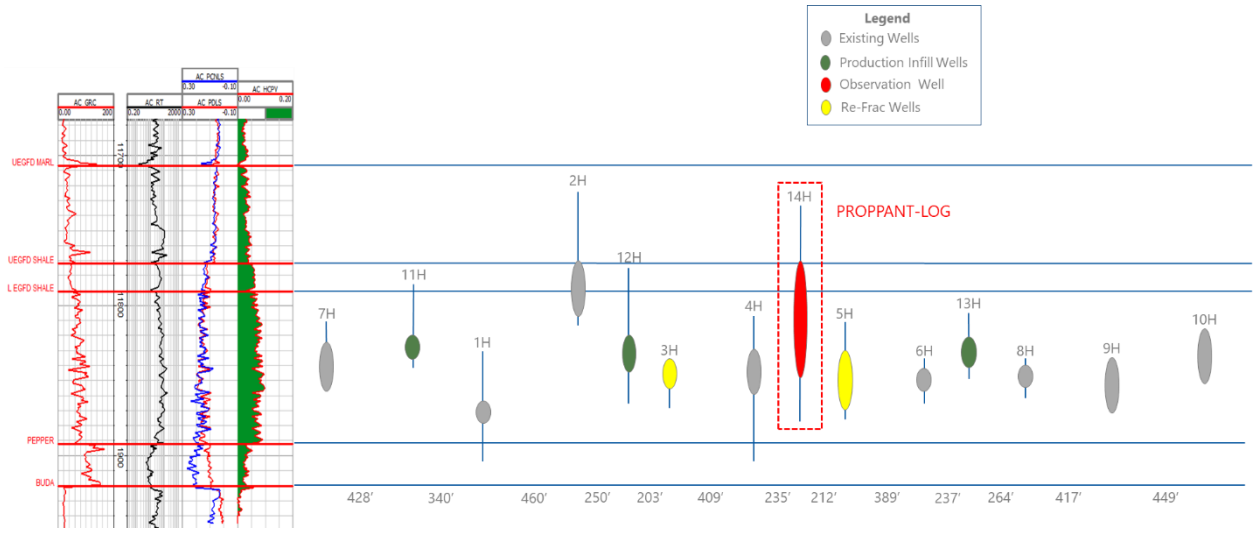


Figure 239: Test site including well representations showing site complexity.

As can be inferred, one can expect significant pre-existing complexity from parent stimulations (10 parent wells).

Proppant log

Proppant logging has been developed as part of the HFTS projects and successfully implemented at the HFTS-2 site in Delaware Basin. Figure 240 shows the basic workflow highlighting the processing applied on drilling mud return samples to generate the log (Maity & Ciezobka, 2022).

The log (Figure 241) shows that most of the proppant seems to be within the cored interval but that's not strictly true. It is noted that higher sampling rates do cause more high peaks being sampled through the log. However, there are large peaks both before and after the cored interval as well.

Two dominant sampling rates (10 ft sampling interval along the cored section and 30 ft sampling interval for rest of the well) were used in this study. Some gaps in sampling also observed. It is instructive to analyze the particle size distribution of observed proppant sand in mud return samples. Much larger fraction of material falling outside the size range of material pumped was observed. This could be due to multiple reasons. Specifications for pumped sand, significant crushing, dominance of tails as one moves far-field as influenced by proppant transport mechanisms (larger/ heavier proppant settling first), etc. Some of these impacts have been observed in other HFTS test sites and validated as well (Maity et al., 2018).

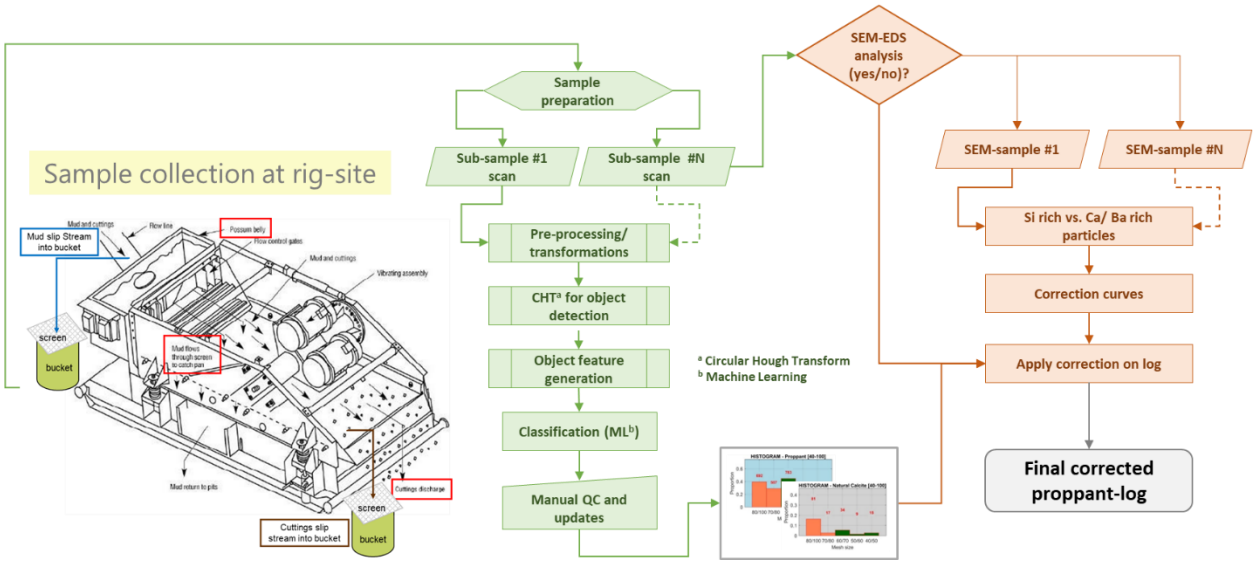


Figure 240: Proppant-log workflow.

Figure 242 shows the log data mapped with the lateral and vertical offset from various proximal parent wells. It is noted that the first significant peak in the proppant data is observed close to where the Zgabay 2H lateral crosses the Zgabay 14H observation lateral in depth. Furthermore, significant peaks are seen when Zgabay 3H, Zgabay 4H and Zgabay 5H cross Zgabay 14H lateral. Observations are in line with Midland and Delaware basin observations where majority of the observed proppant was found proximal of the sampled wells (in depth). Also, lateral proppant transport of at-least 1,000 ft is observed from Zgabay 2H. At HFTS-2 site, lateral proppant transport of at-least 2,300 ft had been observed. It should be noted that large variation between proppant loads across sections could also be a function of completion design.

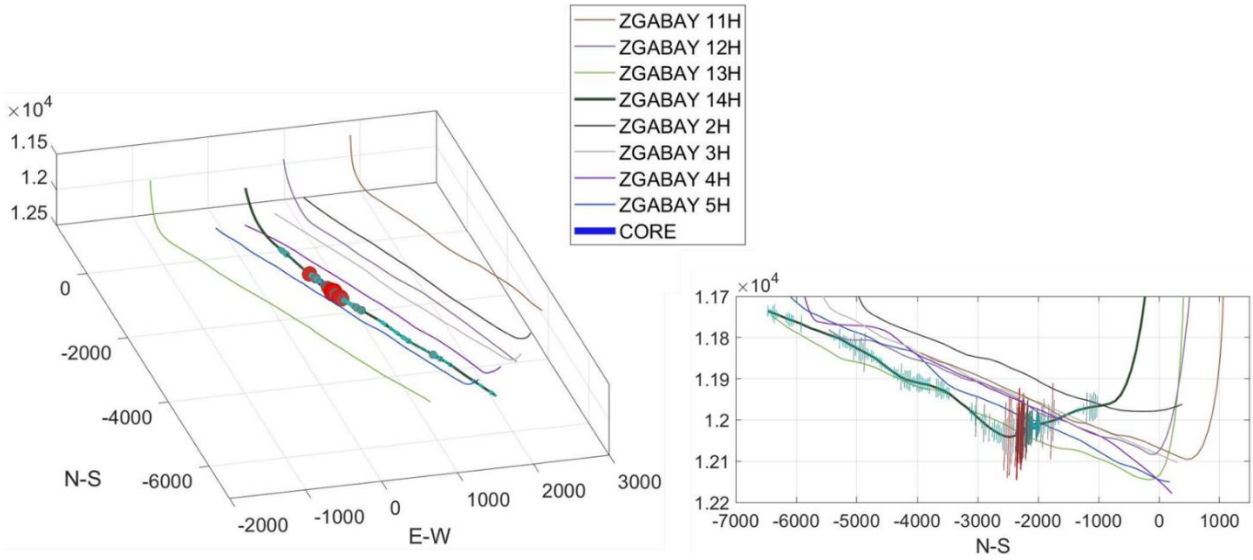


Figure 241: 3D visualization of proppant-log output.

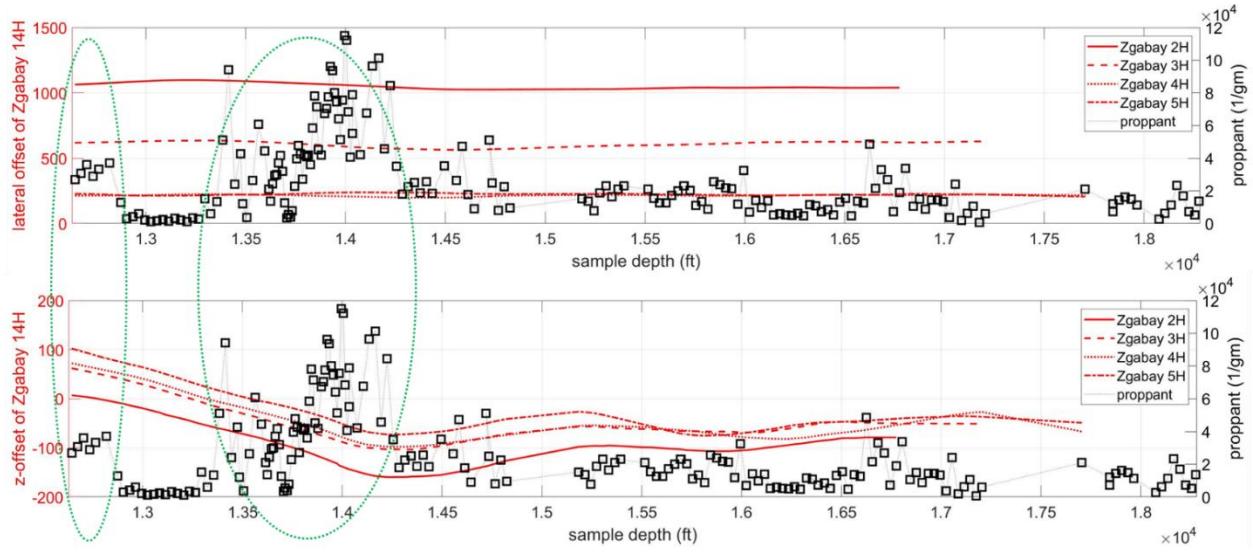


Figure 242: Proppant log response relative to offset from parent wells.

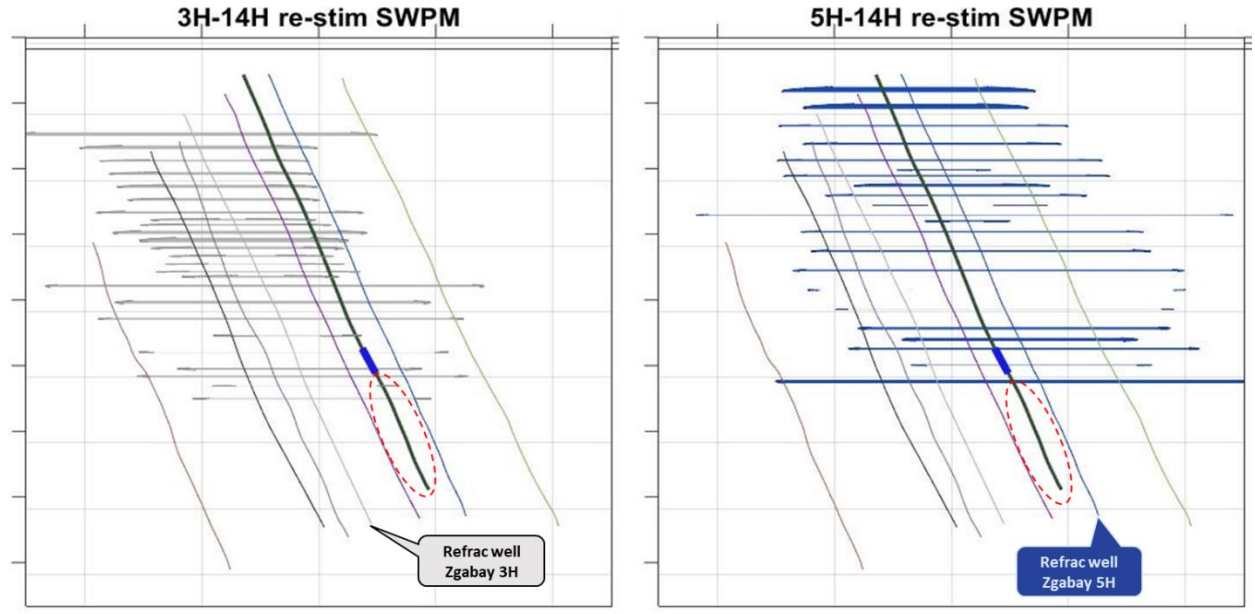


Figure 243: Sealed wellbore pressure monitoring results with interpreted fractures. Red indicates lack of communication.

Sealed wellbore pressure monitoring (Olson et al, 2023) was used to monitor treatments in proximal Zgabay 3H and Zgabay 5H restimulation program (Figure 243). There were some other more broader observations from the SWPM analysis which have been shared earlier. Specifically, a total of 272 fracture stages were evaluated using this method with a total of 107 responses. In some of the furthest monitor wells limited response was observed, specifically, with Zgabay 11H (1,400 ft from Zgabay 3H and 2,277 ft from Zgabay 5H), only 3 responses were observed and with Zgabay 13H, no response as observed (1,610 ft from Zgabay 3H). The 7-cluster high perf friction design showed highest cluster efficiency followed by the 12-cluster design and the 22-cluster design showed the lowest cluster efficiency. From SWPM, for both these wells, limited fracture height growth was interpreted along the heel end of the observation well, Zgabay 14H, which is shallower and at a significant vertical offset from these two refrac wells (Figure 244).

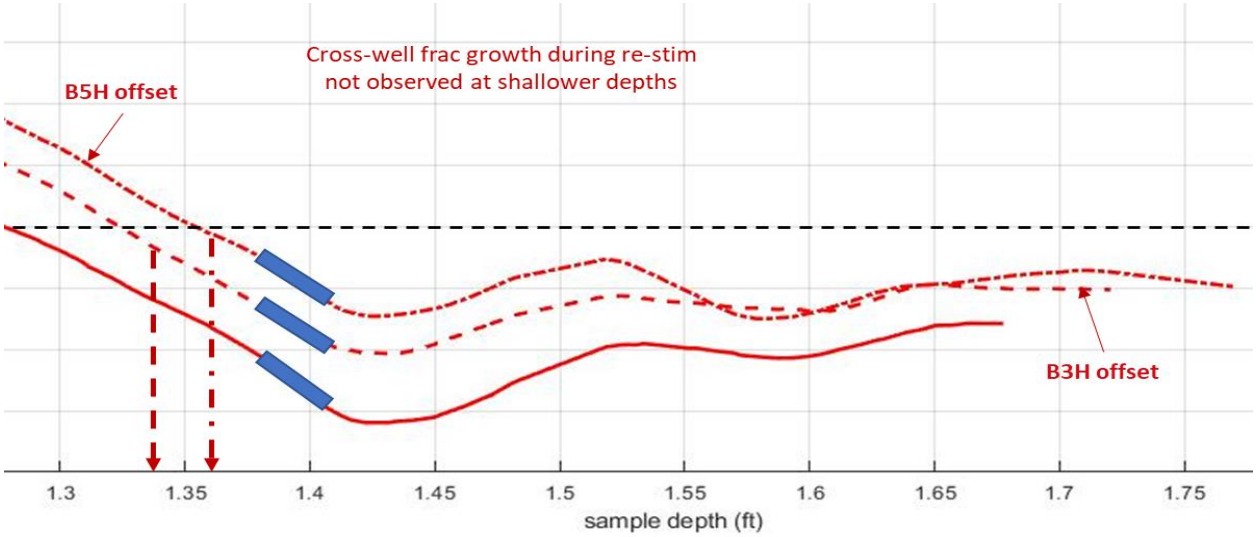


Figure 244: Side view showing relative location of Zgabay 14H, Zgabay 3H and Zgabay 5H laterals. We observe limited fracture height growth above 60 to 70 ft vertically during restimulation or 3H and 5H wells (Figure 243).

It is noted that Zgabay 4H reload operations must be looked at in the context of the relative well orientations and position. Specifically, Zgabay 4H and Zgabay 14H monitoring well is oriented in opposing directions (north to south vs. south to north). As mentioned, during preload, the highest interaction was observed towards the heel of the preload well indicating the full lateral length along the 4H preload well may not be charging (Figure 245).

Various derived attributes, such as relative particle size can be useful in further interpretation of the observed proppant distribution. Specifically, let us consider the beta (β) attribute defined as follows:

$$\beta_i = SF \times \frac{C_{125-150} + C_{150-175}}{C_{100-125} + C_{125-150} + C_{150-175}} \quad (1)$$

Here SF indicates a scaling factor which can be used to normalize counts and the $C_{XXX\text{-}YYY}$ indicates identified proppant particle counts for any given size range in microns. Figure 246 shows distribution of β attribute which provides indication of proppant source from more distant source towards the heel end and more proximal proppant source towards the toe end of the identified depth interval. Specifically, the red section shows abundance of smaller proppant particles whereas the green interval shows relatively higher counts of larger

proppant particles. Similarly, the relative dominance of proppant particles in samples can be used as an indicator of proppant presence. Alpha (α) parameter is defined as follows:

$$\alpha_i = \frac{\text{Number of proppant particles}_i}{\text{Number of other mineral particles}_i} \quad (2)$$

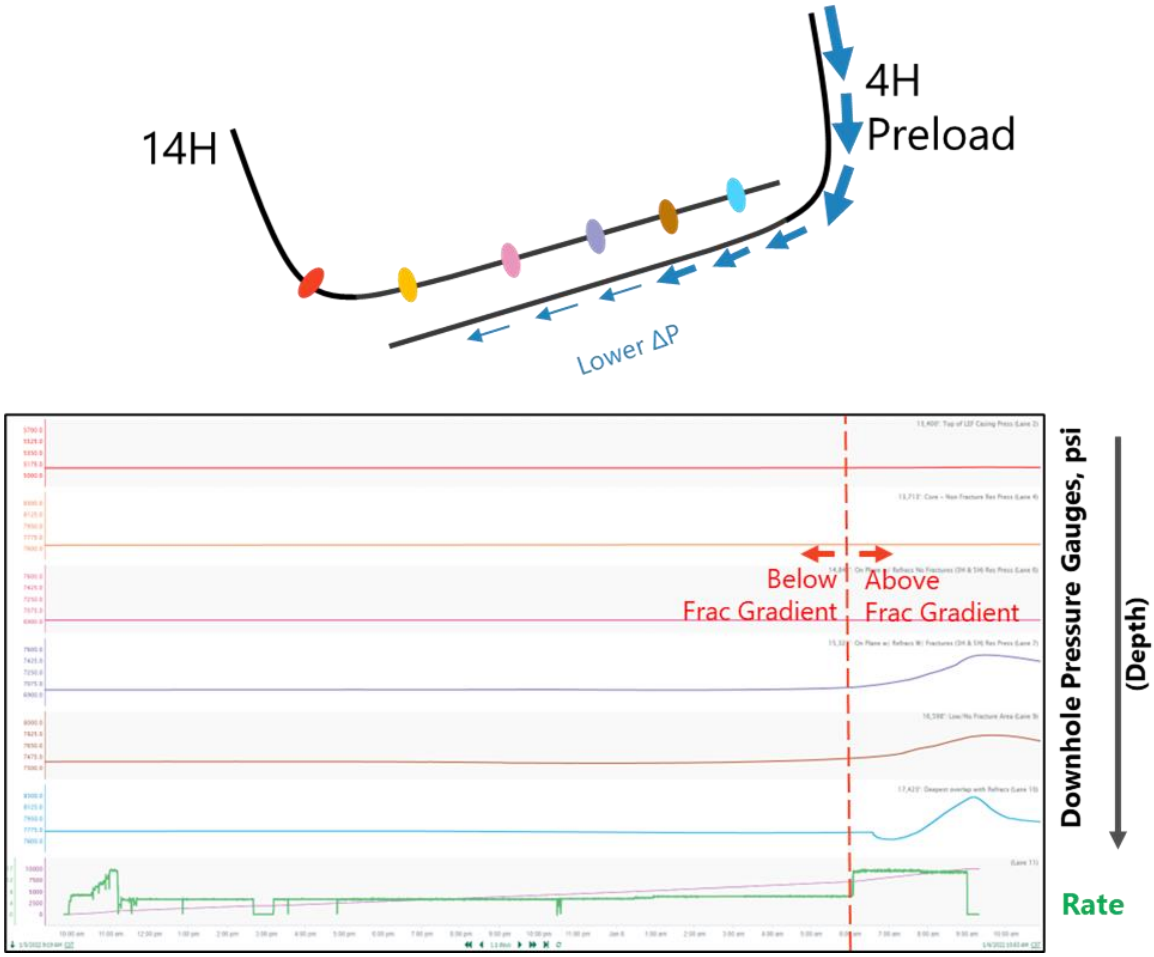


Figure 245: Preload operations - high level observations (pressure response above and below fracture gradient during preload operations showing stronger response in the heel vs. the toe. Offset pressure changes, i.e., parent fracture network growth is only observed above fracture gradient.

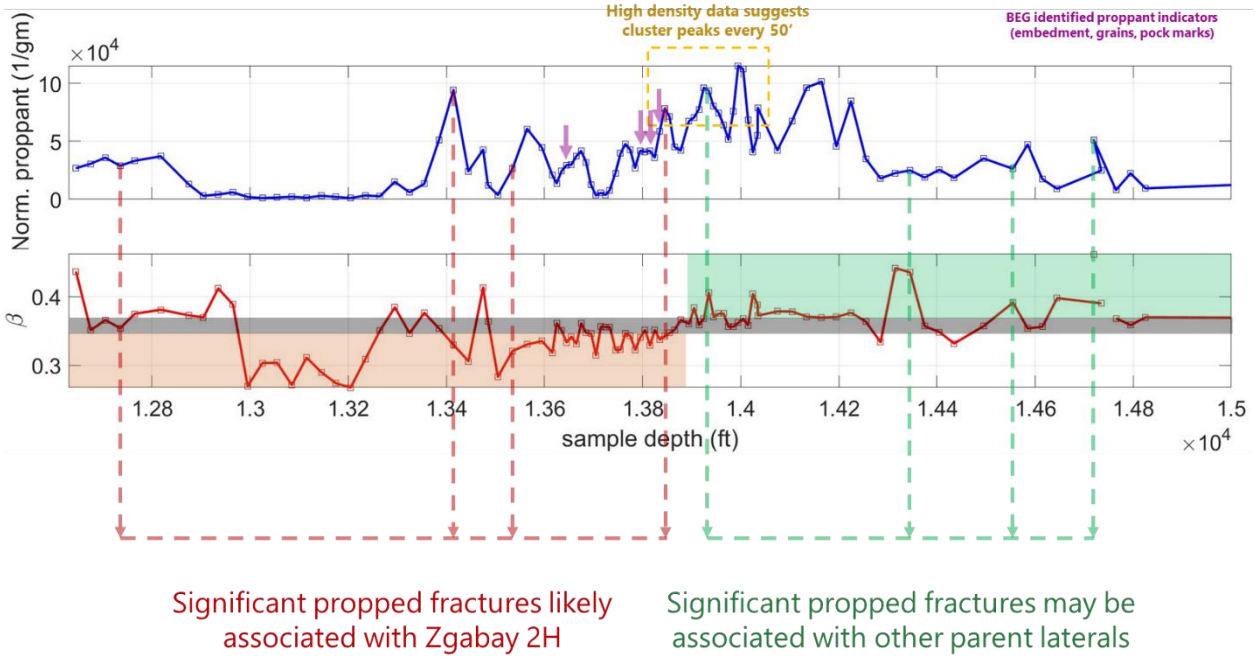


Figure 246: Using derived attributes (β) to interpret proppant source.

Figure 247 shows the distribution of α attribute which provides a better indication of location of propped fracture corridors when compared to the normalized proppant-log.

These observations remain valid despite the specific observations around 4H preload conditions made earlier since cross well SWPM results further validate our interpretations.

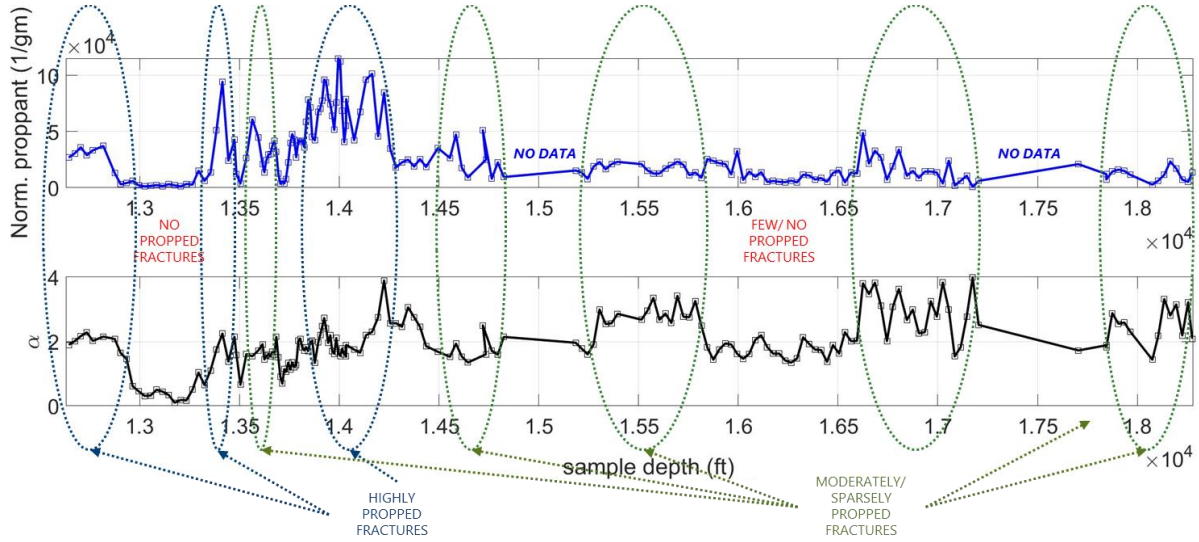


Figure 247: Using derived attributes (α) to interpret propped fracture corridors.

The log suggests two sections with lack of significant propped fracture corridors from this interpretation (Figure 247). It is noted that there are a few no data sections due to lack of any samples collected for the log along those sections. Sections with significant proppant and sections with low proppant counts but proppant dominance can be clearly observed. Sparsely propped fracture zones likely have relatively more smoother fractures compared to sections with larger proppant concentrations observed from the log distribution (Maity & Ciezobka, 2021). The oldest wells are 9+ year old vintage. Even some of the newer parents are 5+ year old vintage. So, significant drainage was expected to have occurred within the SRV around Zgabay 14H monitoring well.

Core integration

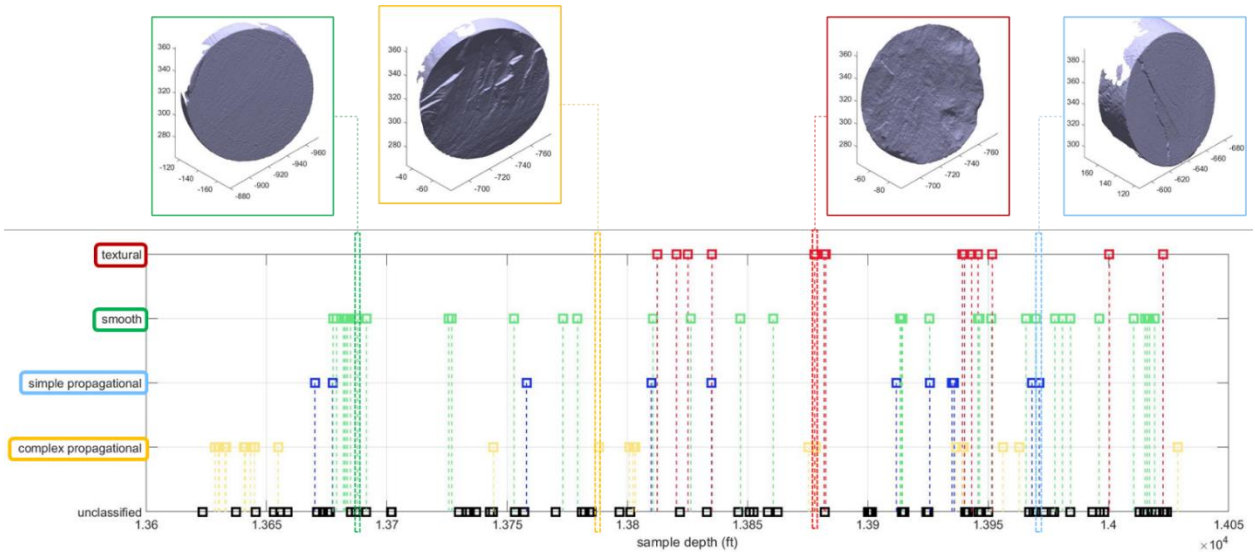


Figure 248: Roughness based fracture classification for hydraulic fractures in HFTS-1 Phase 3 core. Reds highlight fractures where textural roughness dominates, greens highlight very smooth fractures, blues indicate presence of simple propagational features whereas yellows highlight complex propagation artifacts.

As already mentioned, 420 ft of core was also captured along the observation well and this core was carefully characterized for fractures as well as for rock properties by teams from BEG, Core Labs, Devon Energy among others. Another study was conducted was to carry out digital fracture characterization of the core to better understand fracture morphology and grain size distribution. Like other cores in the past phases of HFTS projects, many hydraulic fractures were extremely smooth and flat whereas some fractures are very rough. Rough fractures tend to show propagational effects or have textural roughness. Figure 248 provides automated classification results for fracture morphology and example fractures to validate the classification.

Figure 249 highlights the variation in roughness measures (Maity & Ciezobka, 2020) along the cored interval for each individual hydraulic fracture as interpreted by BEG. Of significance is the absence of hydraulic fractures along significant sections of the cored interval and the occurrence of hydraulic fractures in clusters. This observation is broadly in line with older cores analyzed for HFTS-1 project. This clustering behavior can be quantified by using secondary fracture parameters which are intrinsically connected to hydraulic fracture propagation behavior (Maity & Ciezobka, 2021). Figure 250 provides a quantitative analysis of said clustering at the HFTS-1 Phase 3 site based on fracture roughness characteristics. Specifically, clustering with an inter-cluster separation of approximately 25 to 30 ft was observed. There may be some overlap of significant gaps in hydraulic fracture distribution as already mentioned but this spacing is consistent across the entire cored interval.

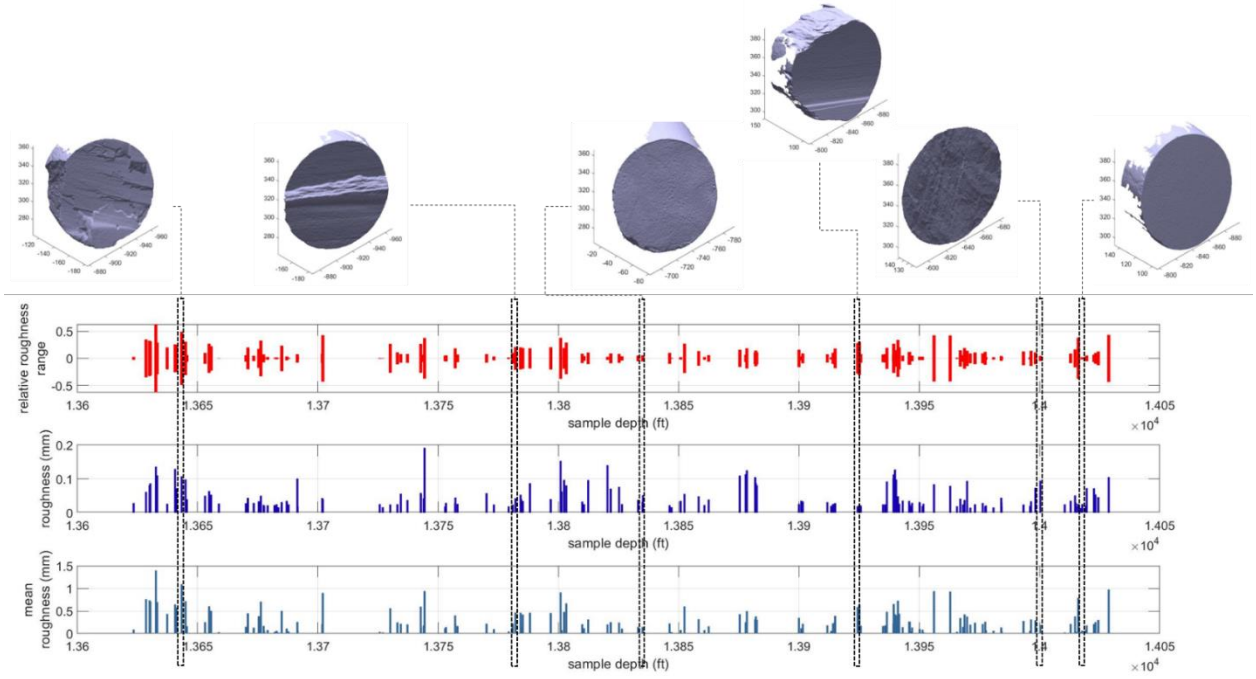


Figure 249: Fracture roughness measure along the cored interval along Zgabay 14H for identified hydraulic fractures.

The original completions in the nearby parent wells (Zgabay 4H and Zgabay 5H) had 50 ft perforation cluster spacing. In the hydraulic fracture clustering at Zgabay 14H, a cluster spacing of 25 to 30 ft was observed. Thus, there was a 1:2 correlation between cluster spacing in

nearby parent wells and fracture cluster spacing in the sampled location. Since both the wells (Zgabay 4H and Zgabay 5H) are almost at the same lateral offset from the observation well (Figure 242), this suggests that broadly speaking, each individual cluster is generating a single fracture cluster far field at this side. Now this single cluster could have 10's of hydraulic fractures, way more than the six perforations which each of these clusters typically had based on their completion design. Thus, it is possible to assign individual clusters far-field to specific clusters in either the Zgabay 4H or Zgabay 5H parent well based on the regional stress state in this reservoir.

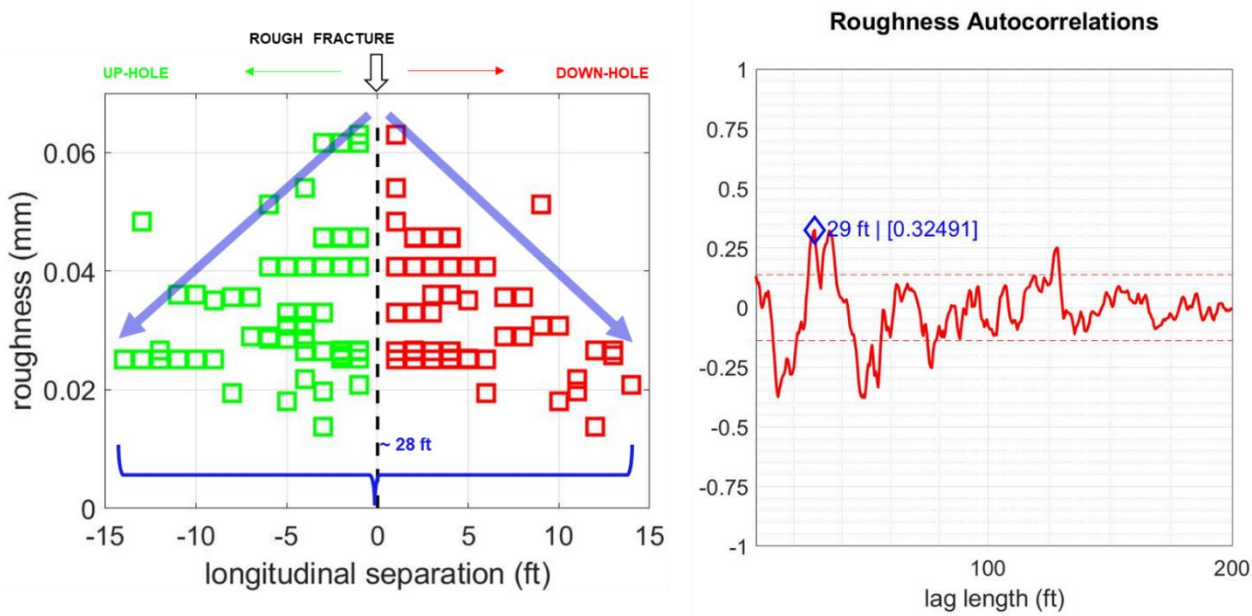


Figure 250: Fracture clustering at HFTS-1 Phase 3 site. The figure on the left highlights the gradual rise and fall in roughness observed along the core, likely governed by stress effects. The confidence boundaries in the figure on the right are for asymptotic normal distribution of coefficients using Pearson's correlation coefficient.

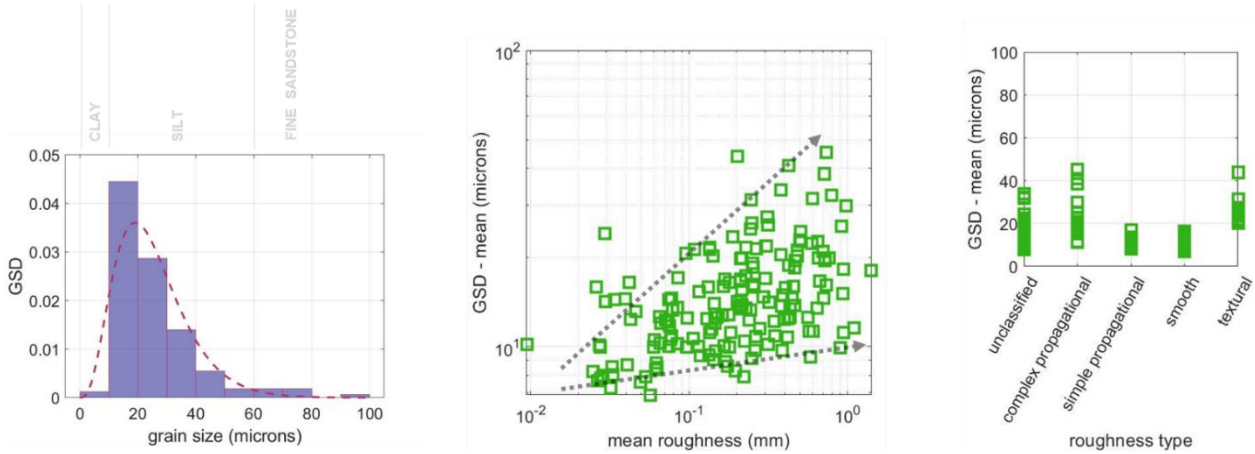


Figure 251: Grain size distribution (GSD) interpreted from digital fracture surface maps. Notice that rocks with more quartz (larger GSD) tend to have higher roughness (complex propagational or textural roughness).

Figure 251 highlights the calculated grain size distribution from the high-resolution laser scans of the fracture surfaces. In general, a positive correlation between mean roughness and mean grain size distributions can be seen. This makes intuitive sense as sections with rock having larger particle sizes would tend to be rougher due to presence of more fracture propagation artifacts as well as general textural roughness characteristics. Finally, the impact of stresses and lithology on the fracture properties can be clearly observed and how that in turn impacts the

proppant distribution that were observed at the sampled locations. Specifically, as observed in the past from HFTS-1 (Phase 1/ EOR) and HFTS-2 cores, fracture complexity is observed when there have been significant transitions in rock properties, i.e., proximal to or across bed boundaries. Thus, formations with multiple inter-bedded layers can create complex fracturing which can have a significant impact on fracture propagation but more importantly, on proppant transport and distribution. Specifically, when there are interbedded quartz rich or carbonate rich zones, one tends to find hydraulic fractures with very high textural roughness characteristics. Figure 252 highlights examples of such sections along the core at the HFTS-1 Phase 3 site. Locally rough fracture generation can in turn be tied back to the stress contrast associated with these bed boundaries. It is instructive to try and tie the observed variations in rock properties and its consequent impact on fracture properties and distribution to the observed proppant distribution along this cored interval. These observations are broadly like earlier observations from Phase 1, Phase 2-EOR and HFTS-2 cores. Specifically, a strong positive correlation was seen between observed proppant distribution along this interval and the broader distribution of hydraulic fracture density along the core (Figure 253). Similarly, at the local scale as well, a strong correlation was seen between fracture roughness values and proppant distribution (Maity & Ciezobka, 2021).

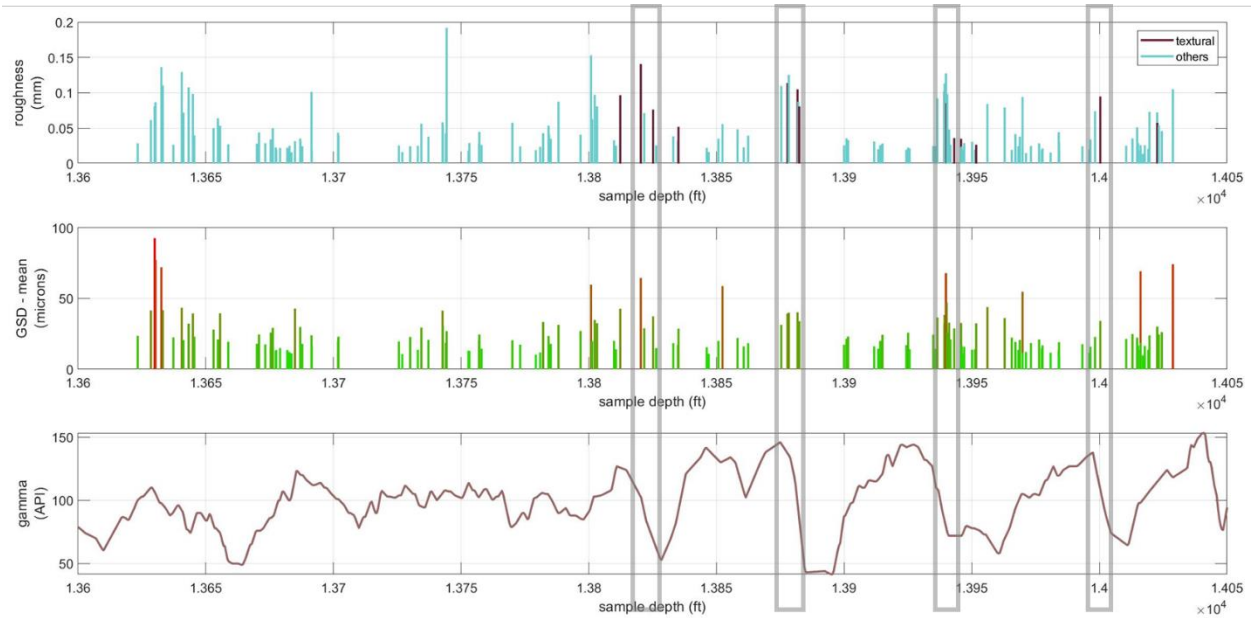


Figure 252: Comparison of gamma ray log vs. fracture roughness including basic type classification of textural roughness vs. others. Highlighted sections indicate quartz or carbonate rich zones and hydraulic fractures with textural roughness.

Crosswell strain response during proximal well operations can provide indication of where there may be inter-well communication. Due to the baseline structural setting of the reservoir, it can be safely assumed that most of the observed communication is likely associated with communicating propped fracture corridors. One of the nearest parent well to the observation lateral is Zgabay 4H. Preload operations (Evolution 2 [Zgabay 4H pre-load]) in this well were monitored using the installed fiber in Zgabay 14H. Figure 254 shows the fiber response in Zgabay 14H as well as proppant log traces superimposed in depth to highlight various propped fracture zones along the observations well and their communication with Zgabay 4H. There were highly propped zones which were observed from the proppant log along the shallower depths. However, lack of fiber response suggests that these zones are likely not connected to Zgabay 4H. This observation is in line with core analysis from earlier HFTS-1

cores as well as from HFTS-2 core where propped fractures were not observed at significant heights above the treatment wells suggesting limited proppant height growth.

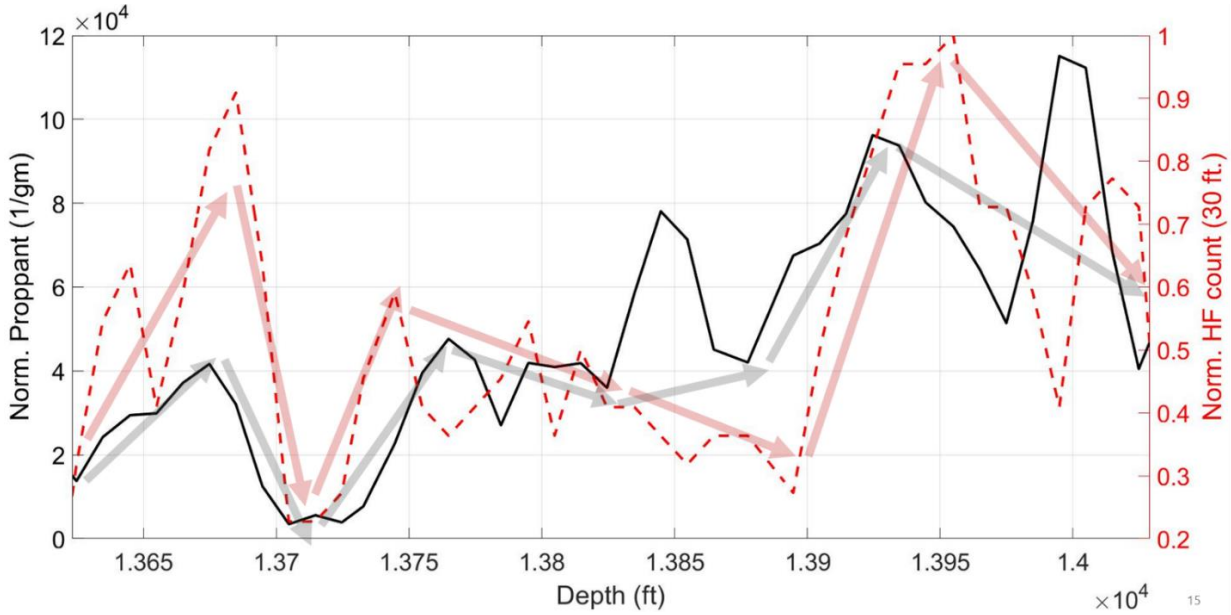


Figure 253: Hydraulic fracture density (distribution) compared with proppant distribution along cored interval.

Integrated analysis with DSS strain response

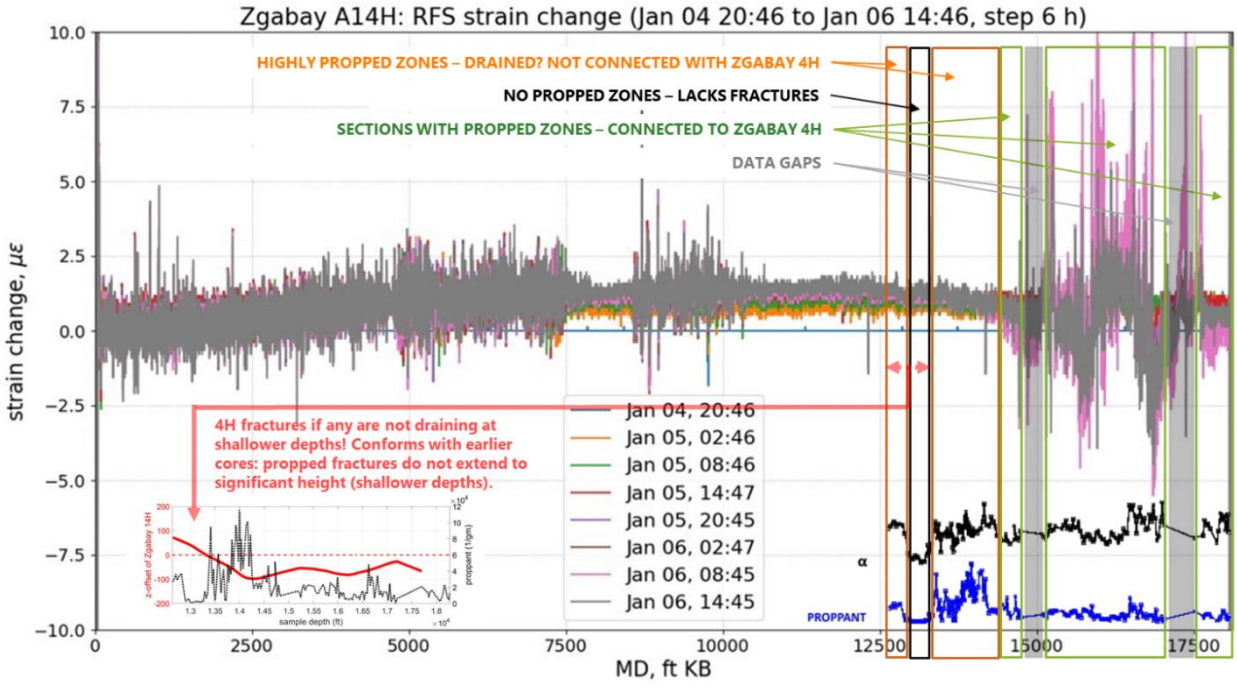


Figure 254: Observed communication observed broadly along various sections of the monitoring well lateral during Zgabay 4H preload operations.

Thus, the propped zones as marked with orange in Figure 254 highlights non communicating fracture corridors, likely associated with another parent well which is laterally further away from the observation well compared to Zgabay 4H. This further validates the interpretation presented in Figure 246. Sections where significant strain response was not seen generally corresponds with sections where multiple fracture corridors had been interpreted earlier based on proppant log distribution. However, to better analyze for any correlation, one needs to carefully look at the strain response and the log along this section of the observation lateral,

specifically, 15,000 ft and deeper. Figure 255 shows the log data superimposed along the strain response observed along this interval.

It should be noted that there is a strong correlation between all observed strain change rate perturbations which can be correlated to opening and subsequent communication through fracture corridors followed by closure at the end of preload operations with peaks in proppant log distribution which can be interpreted as fracture corridors (Figure 255). This is even though the two have varying sampling resolutions (order of magnitude difference). Note that there are other proppant peaks observable from the log distribution. Most of these peaks not showing corresponding strain change response are likely associated with other proximal wells in the pad (Zgabay 5H). This provides validation for use of this logging approach as a way of mapping the near wellbore SRV. If systematically applied on all new infill wells, infill completions can be optimized to better target the unstimulated rock and prevent inefficiencies in refracturing or infill fracturing programs due to fracture hits or diversions.

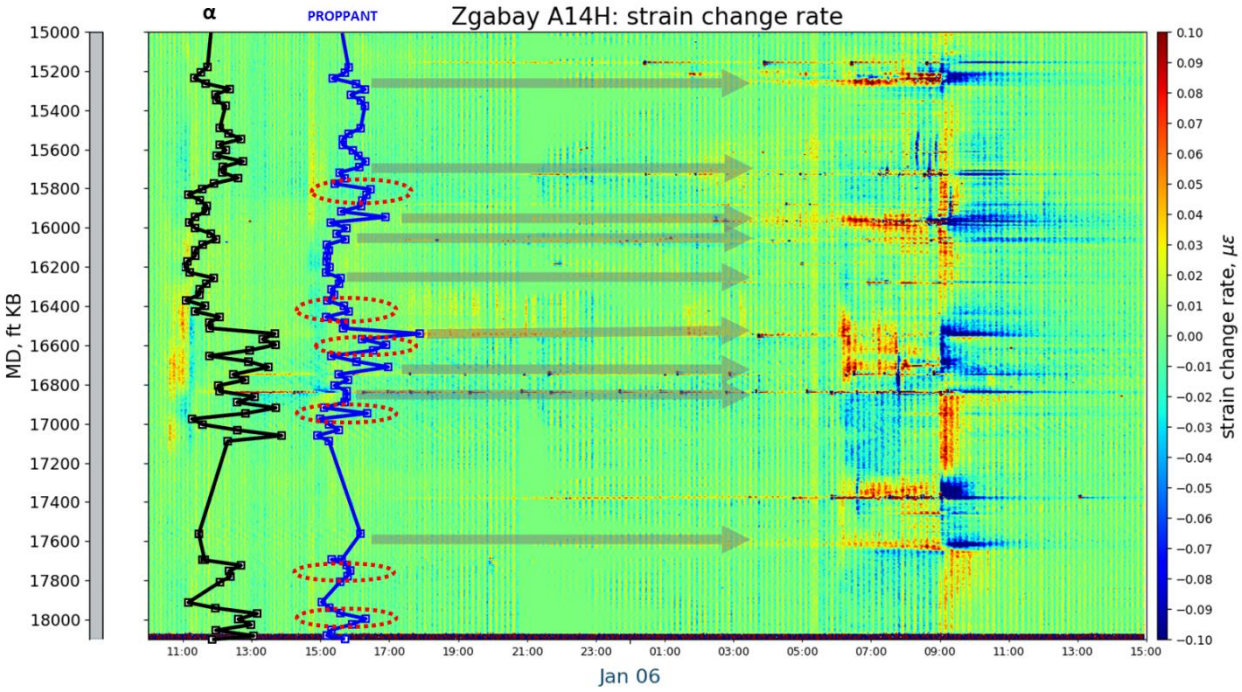


Figure 255: DSS strain change rate snapshot measured along Zgabay 14H fiber during Zgabay 4H preload operations. Proppant log attributes are overlayed for reference.

Integrated analysis with pressure gauges

Additionally, permanently installed pressure gauges along the monitoring well allow us the understand the pressure drawdown behavior prior to any major fracturing operations (Figure 256). Gauges showing significant drawdown can be seen to align with sections with significant identified propped fracture corridor. In the same vein, the two gauges showing limited to no drop in pressure aligns with sections where either no propped fractures are seen a or a section with propped fracture corridor which may have drained significantly. This is because these fractures were identified to be likely associated with Zgabay 4H clusters which is of 9+ year old vintage and would have already drained significantly resulting in negligible pressure response. It is also instructive to look at these gauge responses individually in a bit more detail (Figure 257). Specifically, since these locations are within the lower Eagle Ford formation, the pressures can be checked, particularly in gauges along the cored interval, and see how their response

compared with the proppant and hydraulic fracture distribution that were observed within the core.

As was observed, the gauge showing the lowest Eagle Ford pressure (6,336 psi at 13,400 ft) highlighted in purple corresponds with one of the highest peaks in the proppant distribution whereas the gauge showing a very high pressure reading (7,603 psi at 13,713 ft) corresponds with a location with little to no proppant. Thus, at 13,400 ft depth, likely there had been significant drainage tied to identified propped zone associated with wells other than Zgabay 4H. On the other hand, at 13,713 ft depth, lack of significant drainage is likely associated with local unpropped zone. Thus, proppant-log, at high resolution, can distinguish between specific proximal sections very well in terms of propped zone productivity behavior. The observed unpropped section at 13,713 ft also shows no hydraulic fractures, i.e., unfractured rock based on the analysis of the core itself (Figure 258). Specifically, for three sampling points in our proppant log, very small proppant counts were seen indicating lack of propped fractures. These correlate with the 13,705 to 13,725 ft interval with no hydraulic fractures as already mentioned.

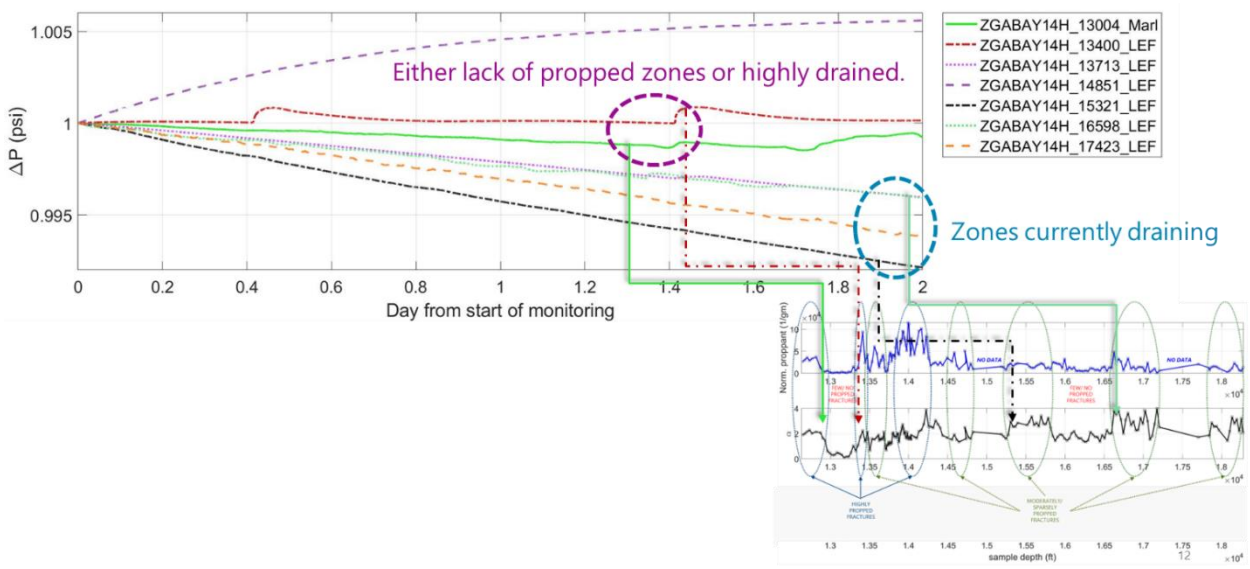


Figure 256: Pressure drawdown observed at various depths along the Zgabay 14H monitoring well.

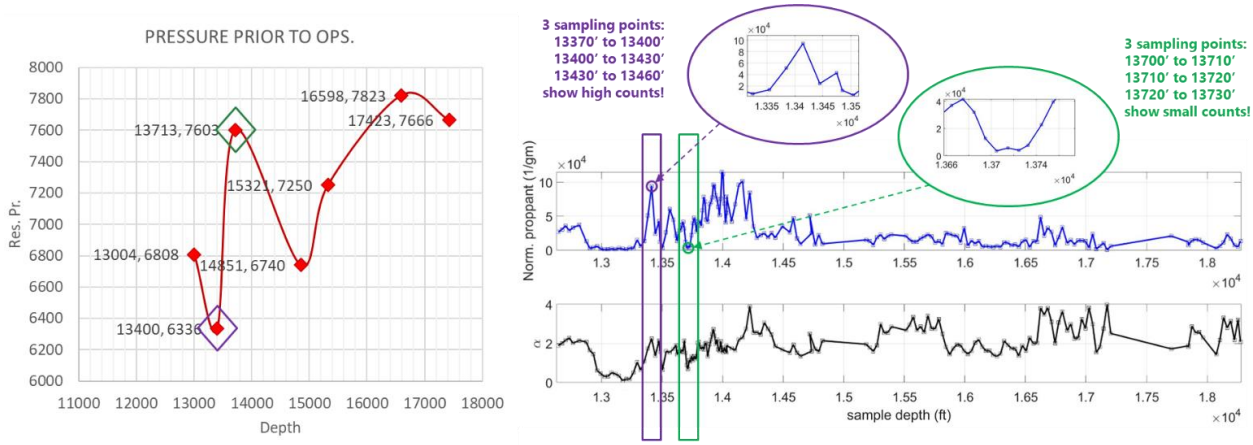


Figure 257: Pressure gauge readings prior to refracturing/ infill fracturing operations. We note responses are being directly correlated to propped zones as interpreted from the log.

These independent datasets allow for validation of proppant log as a tool to understand existing SRV at the location being sampled during drilling and along with other independent observations, such as using fiberoptic DSS measurements, allow for mapping drainage and inter-well communication behavior within the development unit. An example of such interpretation for SRV and propped fracture zones is presented in Figure 259 using the proppant log interpretation. Yellow sections highlight areas where there was not significant pre-existing fracture corridors associated with parent wells.

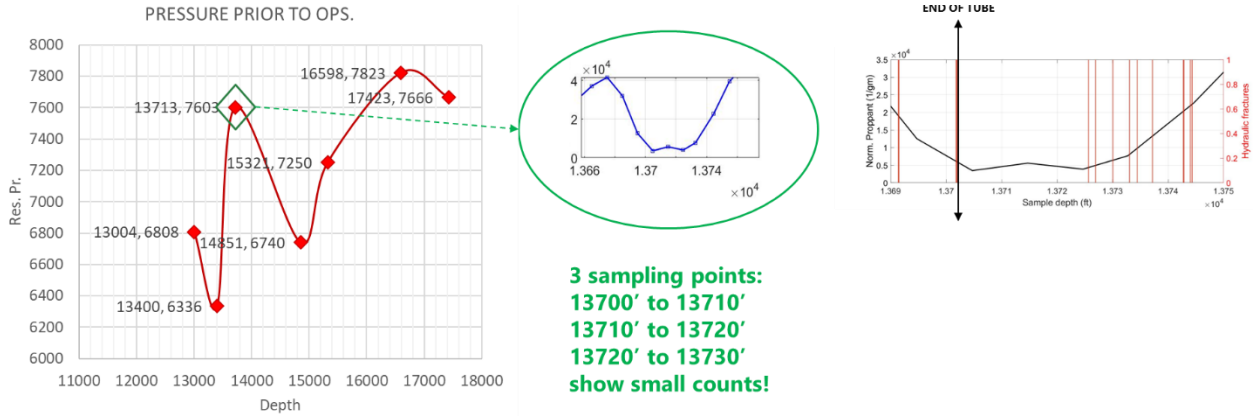


Figure 258: Lack of hydraulic fractures (core characterization, BEG) correlates with lack of propped zones from proppant log and high reservoir pressure (lack of drainage).

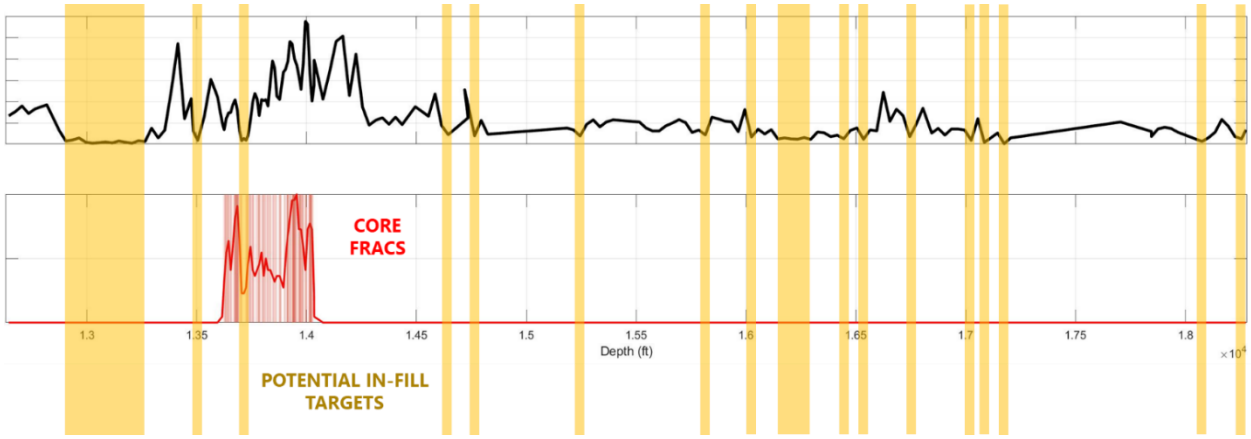


Figure 259: Identification of potential targets for infill fracturing guided by proppant log.

While Zgabay 14H is not optimally landed as an in-fill, Figure 259 highlights how the proppant-log can be used to identify and map under-stimulated sections and potentially minimize the impact of fracture corridors by tailoring infill stimulation.

Proppant log: value proposition and other considerations

While placing fractures during re-stimulation is quite intuitive, optimizing spacing for fractures in in-fill wells is a significant challenge. Geometric stage designs and completions can divert significant proppant laden slurry into previously stimulated rock causing wasted resources, potential frac hit issues, and detrimental effects on existing well productivity. Proppant-log can help add drilling locations and provide quantitative reserves uplift by identifying under-stimulated zones and quantifying stranded reserves. Adding reserves in a depreciating asset is key since there are few other organic ways to add on reserves and these are either limited in scope or already scoped and accommodated (such as adding acreage or pay zones). Provided there is good sampling and depth control, proppant-log can be a key indicator for propped

sections at the drilled location. It can serve as a useful tool to design fractures for in-fill wells to prevent fluid diversion through existing fracture corridors.

From a technical standpoint, sampling rates as high as 90 ft has been found to be adequate in understanding pre-existing propped fracture zones at both the HFTS-2 (Delaware site) as well as the HFTS-1 Phase 3 Eagle Ford site. This provides for a relatively cheap tool to improve completions, particularly when the legacy parent completions have higher cluster spacing. This is a fail-safe logging tool, equally applicable in harsher environments with higher temperature and pressure conditions where traditional logging tools have higher propensity to fail. Furthermore, it is significantly easier and cheaper to acquire compared to traditional wireline logging tools. It requires minimal personnel training and importantly, it does not impinge on normal wellsite operations. Even in complex environments with 10's of wells, proppant-log has demonstrated its ability to predict propped and unpropped zones and these have been tied back to pressure response (drainage behavior) and core at multiple sites.

In terms of designing the logging run, mud system, fluid properties and sample size are key parameters. Both spot and composite sampling have been tested and found to work well. The key requirement is to be consistent with sampling technique and protocols to reduce subjective errors. At higher sampling rates (for example, 10 ft to 20 ft), there were enough resolution to map fracture zones and corridors at in-fill sampling locations. This can allow highly targeted in-fill stimulation optimization or advanced diagnostics. Sampling rates can be fine-tuned depending on number of parent well laterals expected to impact the stimulation zone and the completion designs such as cluster spacing used on those parent completions. Lower sampling rates should be adequate for most older vintage designs with higher cluster spacing unless there are many proximal parent laterals potentially impacting in-fill SRV. Sampling rate can be easily modified along the wellbore with higher rates along zones of interest.

Fiberoptic crosswell monitoring during refrac operations.

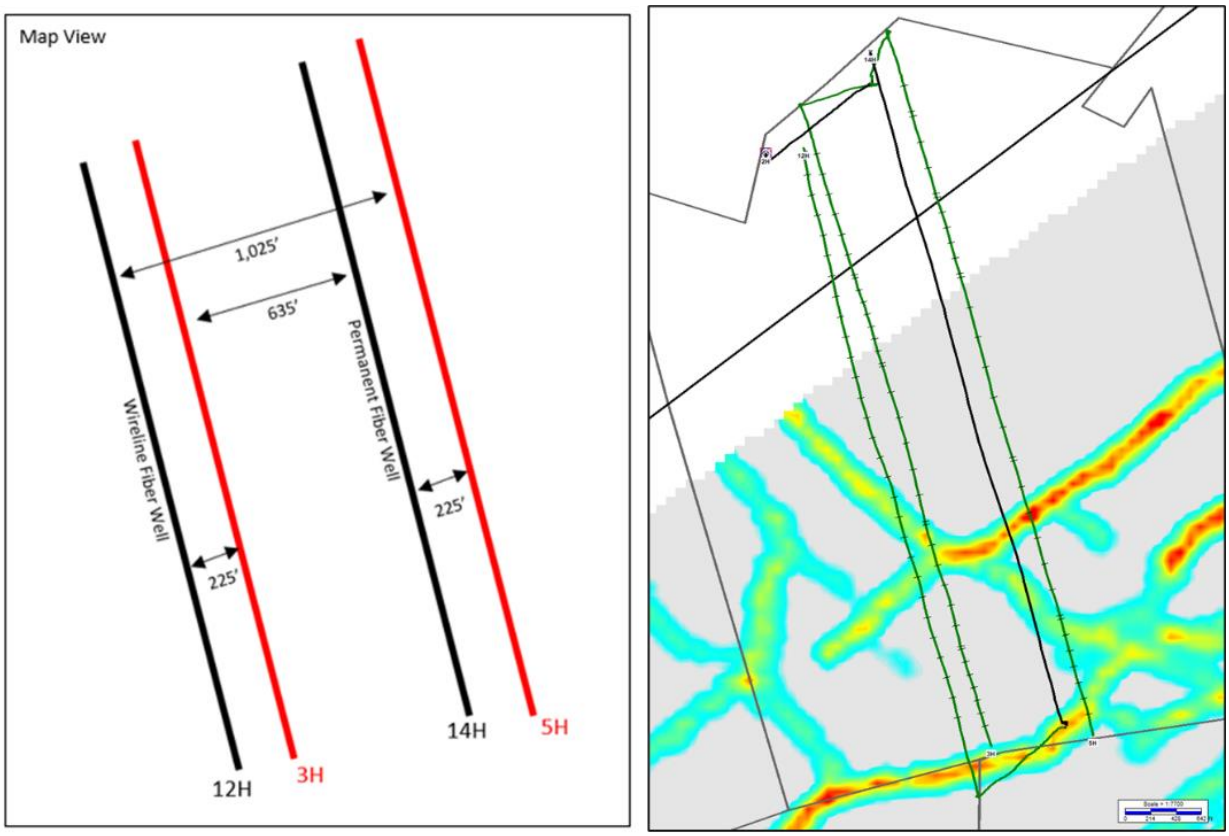


Figure 260: Instrumented wells (black) and known geologic features.

The permanent fiber in Zgabay 14H and a temporary fiber deployed in Zgabay 12H were used to monitor the refrac operations in Zgabay 3H and Zgabay 5H wells. There were some geologic features at the unit which are highlighted based on the available discontinuity volume in Figure 260.

There are some basic assumptions that need to be considered while making interpretations with crosswell fiberoptic strain measurements. Specifically, there could be fracture growth bias either towards or away from the monitoring well which impacts interpretation. Fracture growth without frac-hits cannot be interpreted and as such cause significant uncertainty. There could be indirect fracture interactions, particularly longitudinally close to and along the wellbore. Finally, there may be variable fracture height growth from individual clusters or preferential growth below and above the monitoring fiber, which will impact the observed number of fracture arrivals far-field. Both intersecting and non-intersecting fracture interactions can be interpreted as well as possible fracture reactivations based on the strain response patterns (Shahri et al., 2021). Specifically, during fracture interceptions, a tensional process zone stress (heart shape) leading the fracture tip was seen. The strain transition goes from compression to tension followed by compression. The fracture closing signature is narrow and relatively intense. During fracture reactivation, a tensional process zone leading the fracture tip with strain transition going from compression to tension followed by compression was seen. The downhole pressure data provides validation with muted response in case of reactivations. Finally, during non-intersecting fracture interactions (Zhang et al., 2020), there is a wide in-depth fiber extension signature spanning 100's – 1,000 ft. Double-lobe fiber extension signature that is wide in depth was observed. As a validation, there is no pressure gauge derivative response during such interactions.

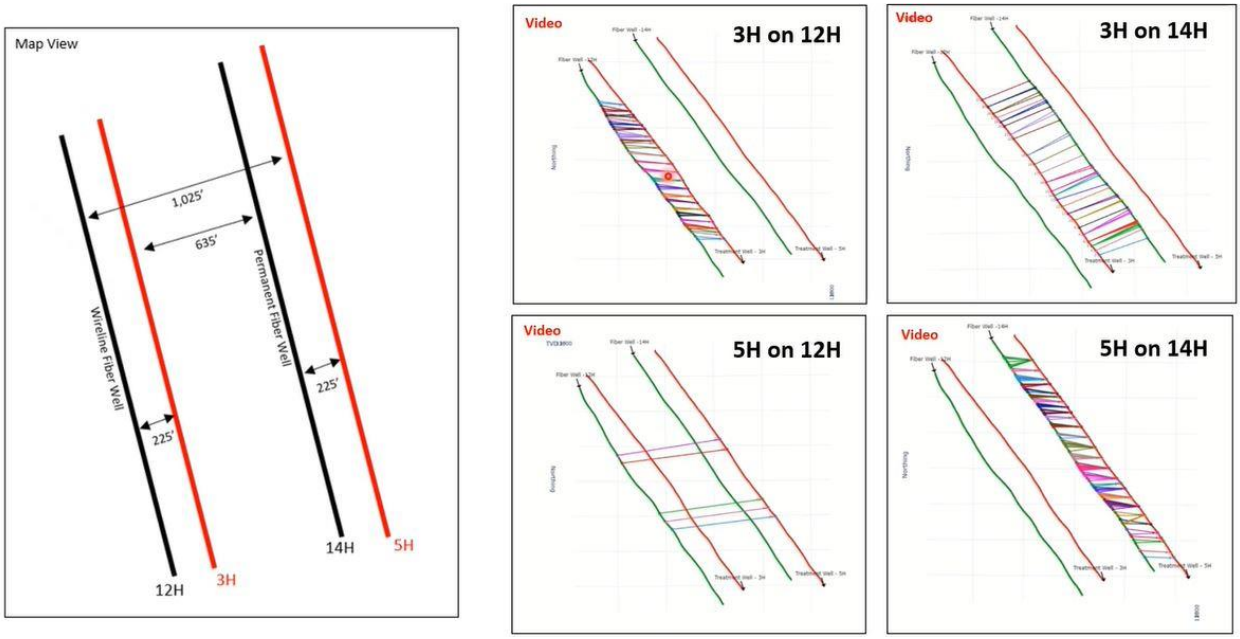


Figure 261: Mapped fracture interceptions along the Zgabay 12H and Zgabay 14H fibers during refracturing operations.

Mapped fracture interceptions along the fibers during the re-stimulation are highlighted in Figure 261. Based on these interceptions, cluster efficiencies can be calculated for various fracture stages (Figure 262). Based on the observations, high perf friction 7-cluster stages seem to perform the best but for other designs (12 or 22 clusters) high perf friction designs underperform compared to low perf friction designs. A major observation based on various designs used in the study is highlighted in Figure 263 for reference. Specifically, higher cluster count stages do not have a higher fracture interception rate in the nearby observation wells when compared to stages with lower cluster counts.

In order to better understand the fracture corridors and understand gaps or overlaps in fracture corridors associated with the refrac wells as observed in the observation well fibers, the project looked at the actual interceptions as well as the induced strain on the fiber in the identified fracture corridors. Figure 264 and Figure 265 highlight the identifiable overlaps and gaps in the fracture coverage due to the two refrac treatments in Zgabay 3H and 5H wells. Fracture corridor analysis suggests that there are areas of prior stage fracture corridor restimulation as well as significant gaps in stimulation. With respect to the strain distribution, more induced strain variability (unevenness) was seen during 22-cluster stages. The percentage of induced strain within new fracture corridors was used to understand overlap with prior stage fracture corridor (Figure 273). On average, about 13% of the induced strain occurs in the prior stage fracture corridor. The low perforation friction 22 cluster design induces the least strain in the prior stage fracture corridor. In general, more clusters (longer stage lengths) seem to limit prior stage activation.

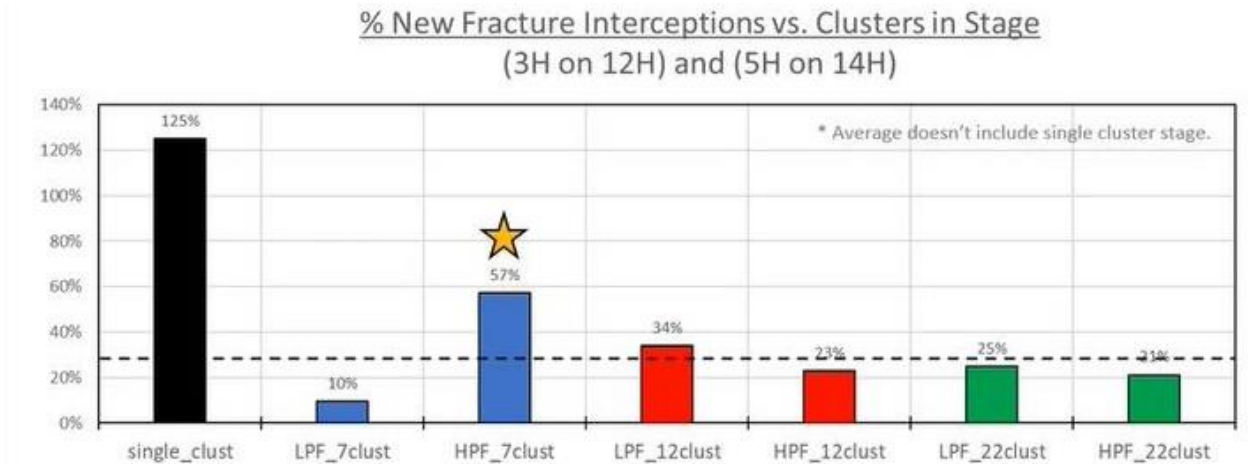


Figure 262: Cluster efficiency observations from crosswell response.

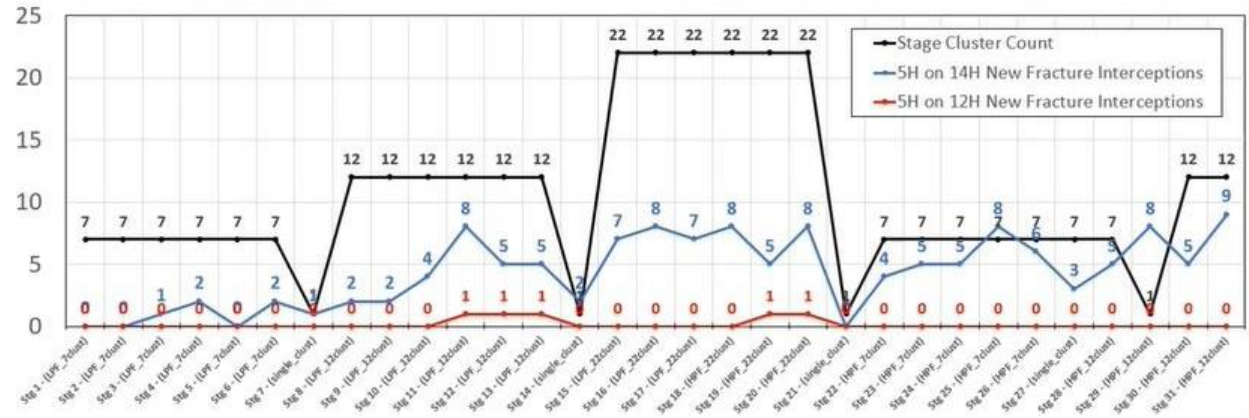


Figure 263: Fracture interception morphology with cluster counts vs. new fracture interception far-field.

Average fracture orientations can be interpreted by considering fracture propagation from center of cluster stages to the center of the observed strain event in the instrumented fiber (Figure 266). Fracture corridors can also be interpreted to understand both gaps as well as overlaps in fracture corridor as one moves from strain response (top and bottom extent of the identified strain corridors) associated with one fracture stage to the next. Exact definition of the corridors can be defined by the start of stage (ball seat during pumping), start of next stage or one hour after stage end (whichever is earlier), and finally, top and bottom of closure signatures.

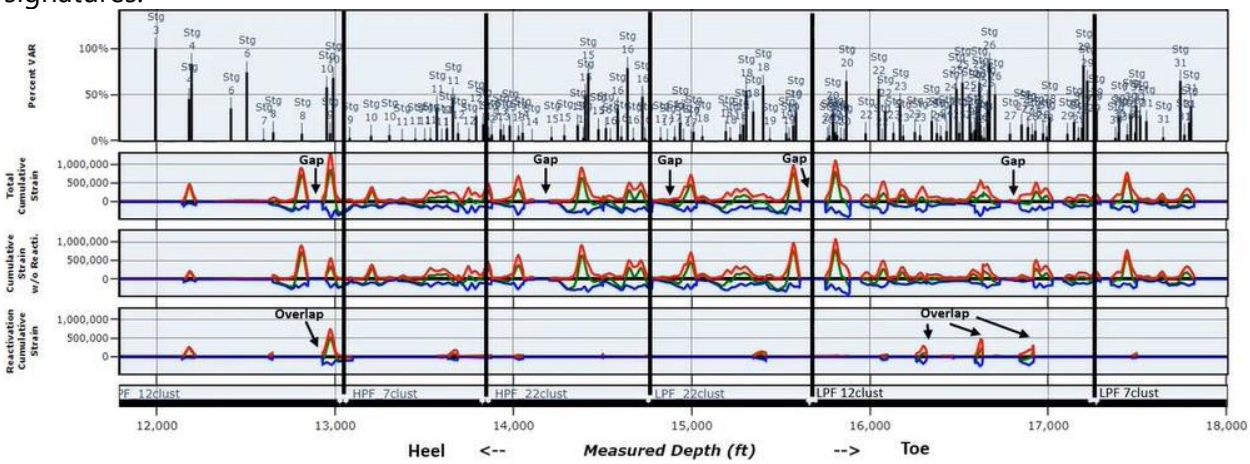


Figure 264: Zgabay 5H on Zgabay 14H fracture corridor analysis.

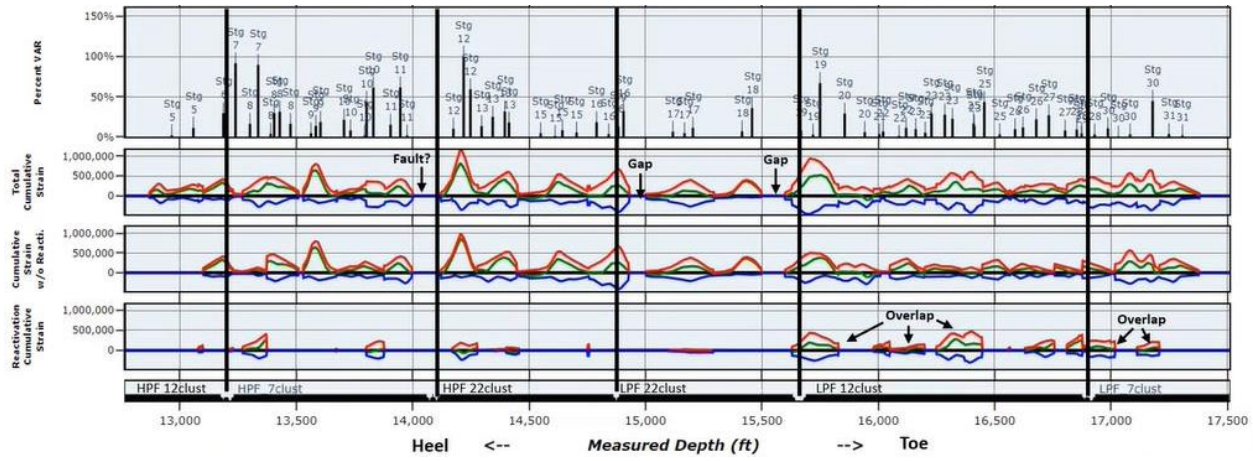


Figure 265: Zgabay 3H on Zgabay 12H fracture corridor analysis.

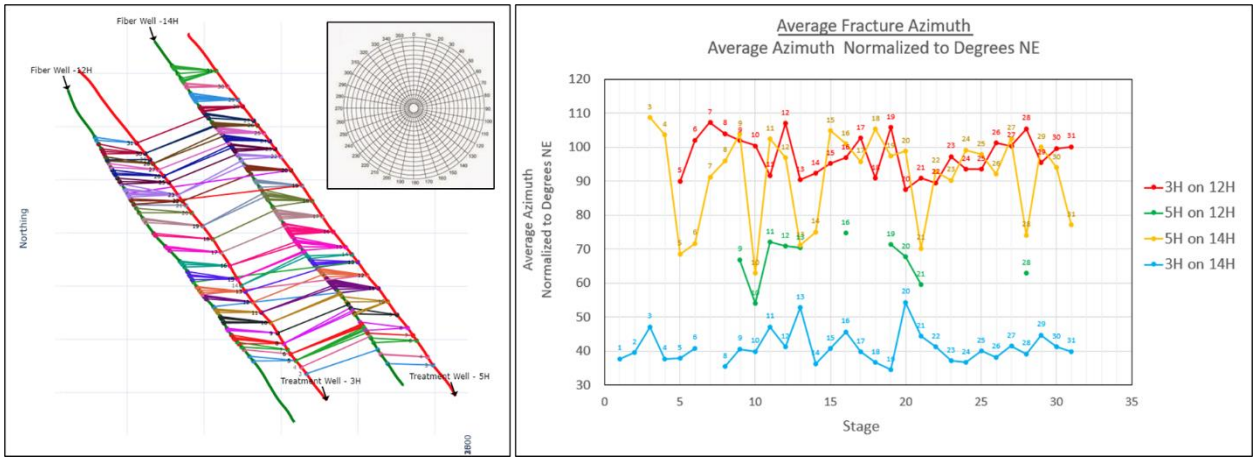


Figure 266: Interpreted fracture azimuth across re-stim stages.

Figure 267 highlights the interpreted fracture corridor for an example stage (Zgabay 3H stage 9 observed in Zgabay 14H). Total extensional strain observed in the interpreted corridors is summarized in Figure 268. Similarly, fracture corridor widths were tabulated based on proposed methodology shared earlier to get statistical distribution for various observation (fiber) and treatment (refrac) well pairs. The new fracture corridors are expected to be smaller (or same dimension) as the total fracture corridor. On average, larger fracture corridors were observed at the proximal fiber whereas relatively smaller fracture width at larger lateral offsets from the treatment wells.

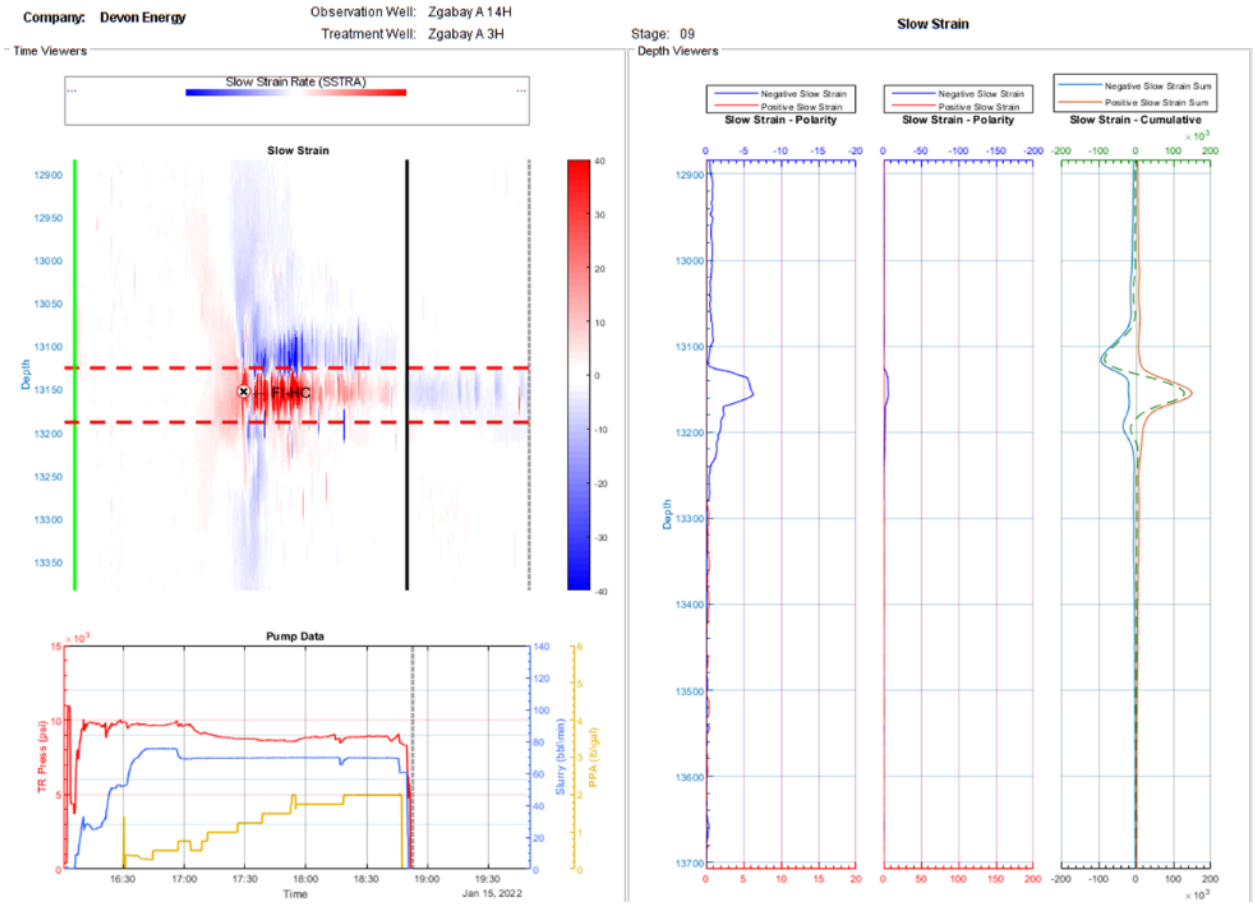
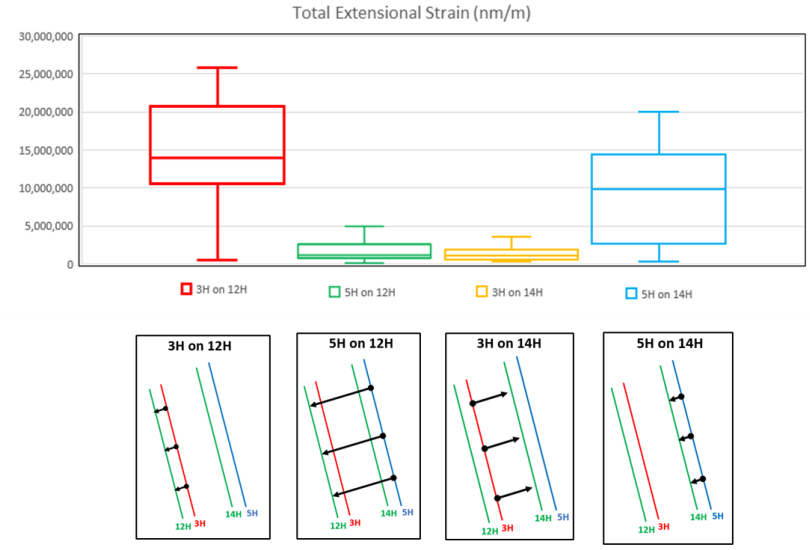


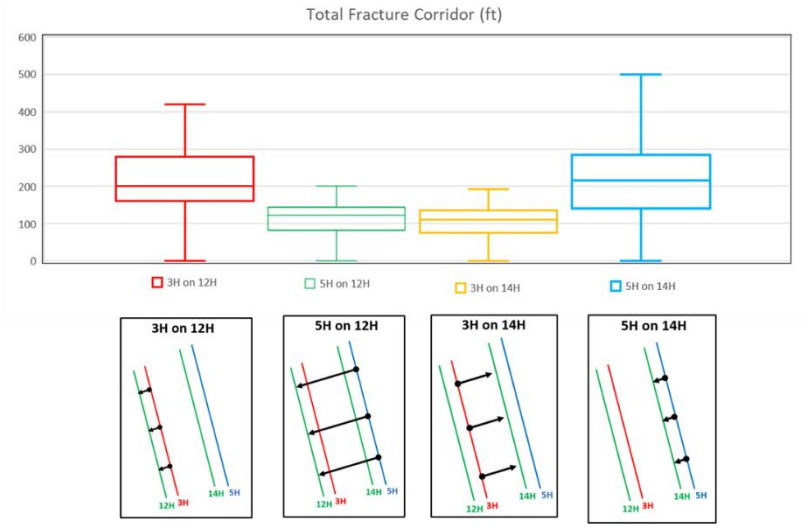
Figure 267: Fracture corridor interpretation for a sample stage. Note that we would consider prior stage reactivation when evaluating the corridor width. However, non-interception is not included in evaluating the corridor.



	3H on 12H	5H on 12H	3H on 14H	5H on 14H
Average (ft)	14,410,338	1,707,040	1,407,327	9,586,193
Standard Deviation (ft)	6,909,523	1,515,283	1,106,104	6,165,351
CV	0.48	0.89	0.79	0.64

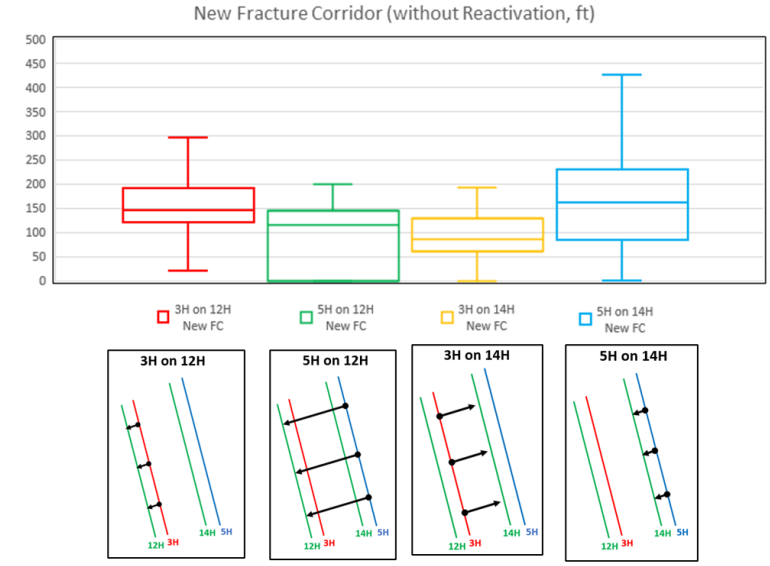
Figure 268: Total observed extensional strain (Stage-wise) across identified fracture corridors for various well pairs.

Figure 271 and Figure 272 highlight examples of significant gap in fracture corridors or overlap in fracture corridors based on the crosswell strain interpretation.



	3H on 12H	5H on 12H	3H on 14H	5H on 14H
Average (ft)	221	113	105	221
Standard Deviation (ft)	95	59	43	120
CV	0.43	0.52	0.41	0.54

Figure 269: Total interpreted fracture corridor summary statistics.



	3H on 12H	5H on 12H	3H on 14H	5H on 14H
Average	141	93	87	168
Standard Deviation	84	72	48	109
CV	0.59	0.77	0.55	0.65

Figure 270: New fracture corridor statistics (total without reactivation).

The skewness of the corridors was observed using cumulative extensional strain observations. Figure 274 highlights the observed skewness by completion design. Note that positive skewness means a heel-side bias away from the prior stage fracture corridor. On average, nearly all designs showed major heel side bias away from prior stage fracture corridor. The 7-cluster stage designs may reduce the heel-side bias, but the benefit may not be significant.

In conclusion, there was some degree of non-uniformity in the refrac stimulation with significant stimulation gaps, particularly with the 22-cluster designs. The 7-cluster high perf friction design seems to outperform and the 22 cluster designs seem to underperform. The lower cluster designs also tend to limit heel-side bias. Finally, stress transmissibility is significantly reduced due to pore-pressure depletion prior to stimulation. This is observed by

mapping the transmitted stress or normalized cumulative strain as a function of distance from the fracture face and fitting an exponential decline curve to the data.

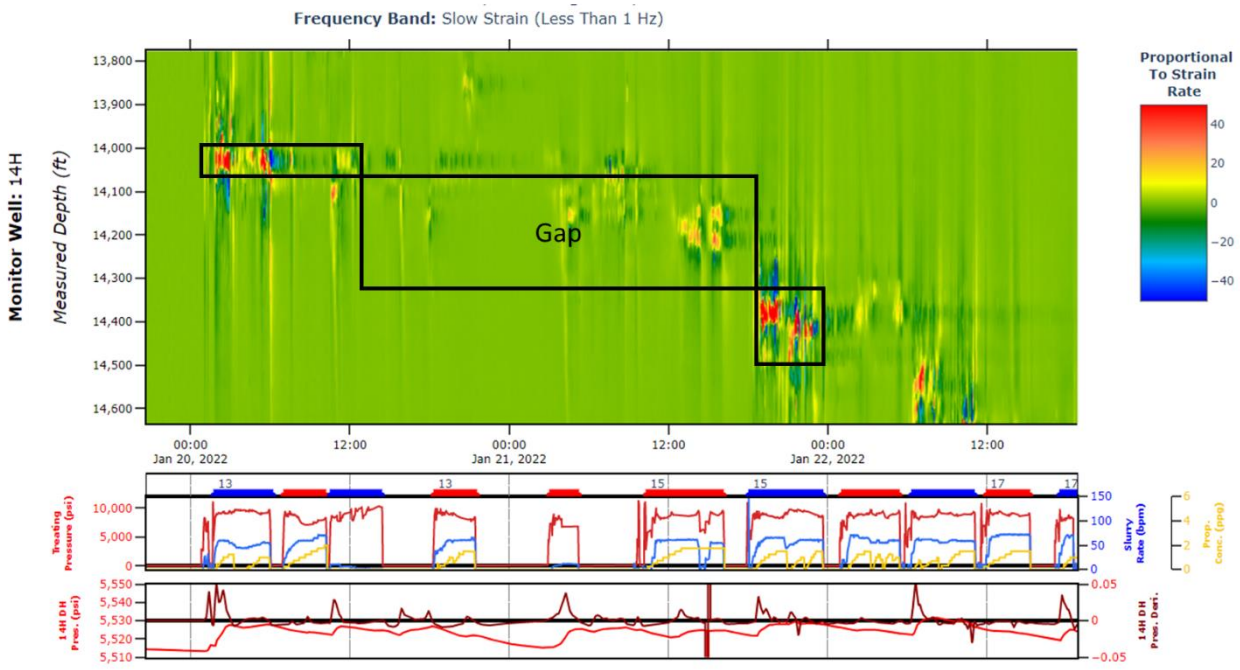


Figure 271: Interpreted fracture corridor gap (Zgabay 5H stage 20 on Zgabay 14H).

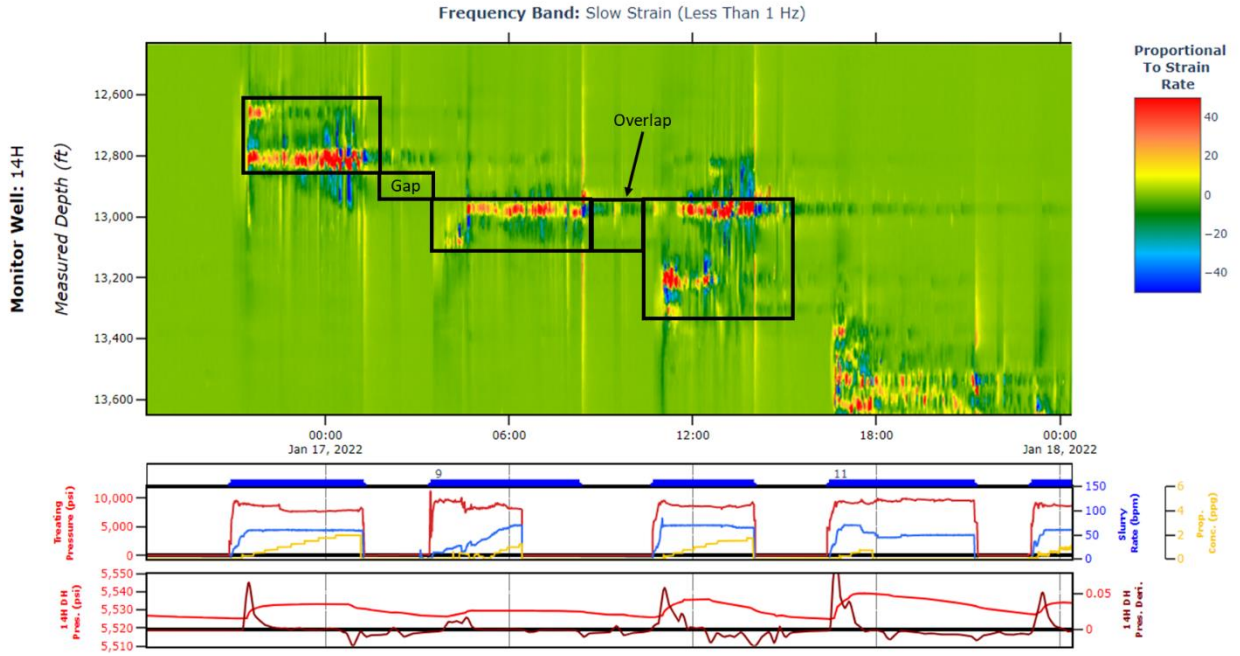


Figure 272: Interpreted fracture corridor overlap (Zgabay 5H stage 10 on Zgabay 14H).

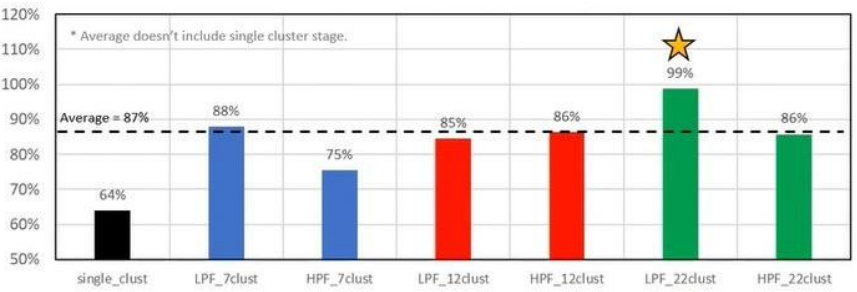


Figure 273: Percent of total extensional strain in new fracture corridor only (nm/ m) for both Zgabay 3H to 12H and Zgabay 5H to 14H observations.

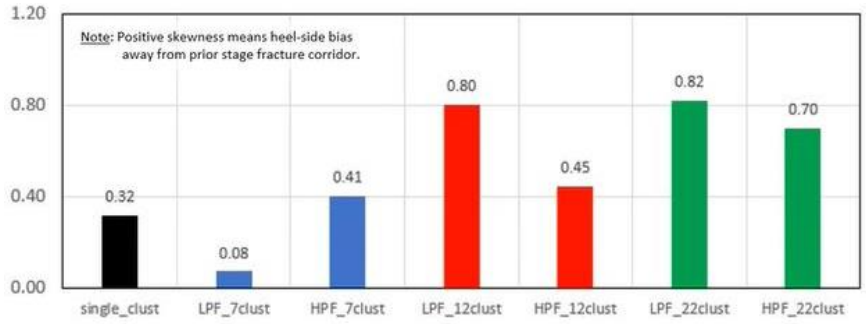


Figure 274: Skewness of new fracture corridor cumulative extensional strain for the two refrac wells.

Refrac and new infill production response

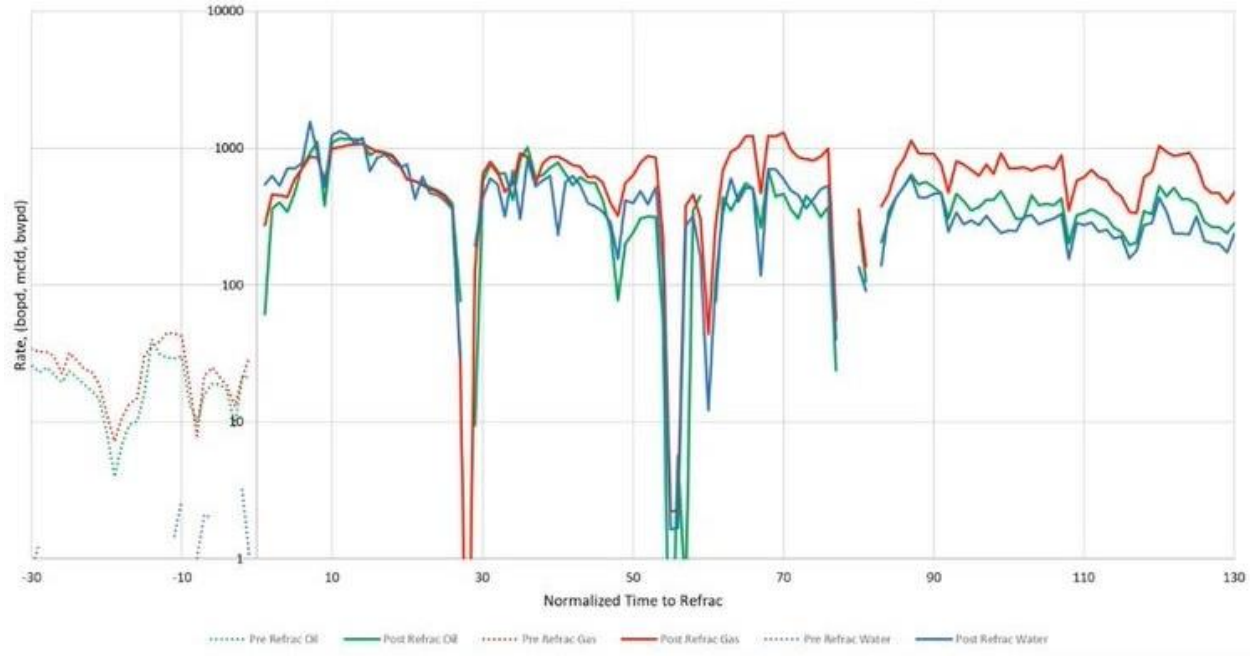


Figure 275: Zgabay 3H well production before (dotted) and after (solid) refrac operations.

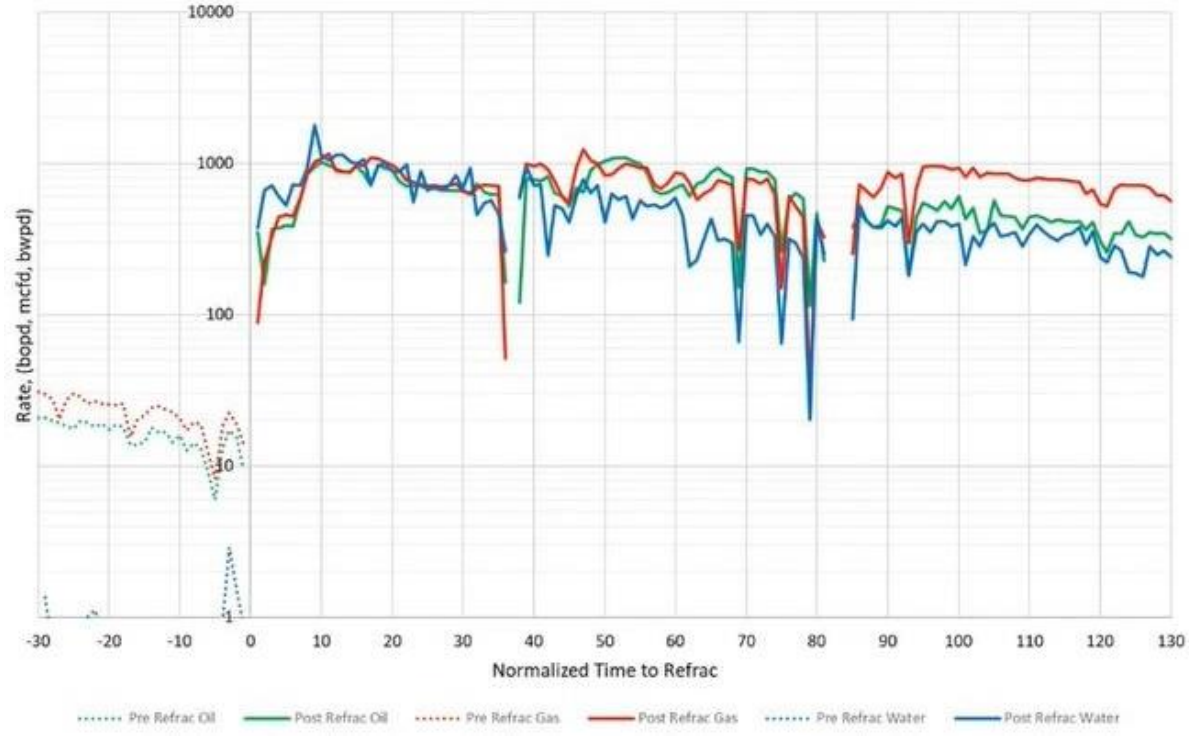


Figure 276: Zgabay 5H well production before (dotted) and after (solid) refrac operations.

This final section looks at the production response post the refrac and infill operations. For the two refrac wells, significant order of magnitude uplift in hydrocarbon production was observed. Figure 275 and Figure 276 highlight the observed incremental production from Zgabay 3H and Zgabay 5H refrac wells. Specifically, within the first 3 months of production post the refracturing operations, Zgabay 3H observed rates of 300 bpd of oil, 600 mcfd of gas, and 250 bpd of water. Zgabay 5H observed rates of 350 bpd of oil, 600 mcfd of gas, and 250 bpd of water production. This suggests significant uplift in overall well productivity post refrac operations and the observed uplift is sustained for significant period creating considerable positive impact on NPV.

The infill program saw three new infill wells at this unit. Production over the first three months for Zgabay 11H was observed at 500 bpd of oil, 850 mcfd of gas, and 125 bpd of water. Zgabay 12H observed on average 400 bpd of oil, 800 mcfd of gas, and 150 bpd of water production. Finally, Zgabay 13H observed 600 bpd of oil, 1200 mcfd of gas, and 200 bpd of water production on average.



Figure 277: Zgabay A unit wells (non-infill or non-refrac wells) showing production before and after operations.

Also post these operations, the non-refrac, non-infill well production was observed to go back up to the original pre-operation rates suggesting limited to know impact on baseline productivity of the unit before the refrac operations (Figure 277).

References

1. Abbasi-Asl, Y., et al. 2010. Mechanistic Modeling of Chemical Transport in Naturally Fractured Oil Reservoirs. Presented at the SPE Improved Oil Recovery Symposium, Tulsa, Oklahoma. https://doi.org/10.2118/129661-MS

2. Aki, K., et al. 1977. Source mechanisms of volcanic tremor: Fluid-driven crack models and their application to the 1963 Kilauea eruption. Journal of Volcanology and Geothermal Research, 2, 259-287. https://doi.org/10.1016/0377-0273(77)90003-8.

3. Alvarez, J. O., et al. 2017. The Impact of Surfactant Imbibition and Adsorption for Improving Oil Recovery in the Wolfcamp and Eagle Ford Reservoirs. Presented at the SPE Annual Technical Conference and Exhibition. San Antonio, Texas. https://doi.org/10.2118/187176-MS.

4. Alvarez, J. O., et al. 2018. The Impact of Surfactant Imbibition and Adsorption for Improving Oil Recovery in the Wolfcamp and Eagle Ford Reservoirs. SPE Journal 23 (06): 2103-2117. https://doi.org/ 10.2118/187176-PA.

5. Amitrano, D. 2003. Brittle-ductile transition and associated seismicity: Experimental and numerical studies and relationship with the b value. Journal of Geophysical Research: Solid Earth, 108 (B1): 2044. https://doi.org/10.1029/2001JB000680.

6. Anaya, R., & Jones, I. 2009. Groundwater Availability Model for the Edwards-Trinity (Plateau) and Pecos Valley Aquifers of Texas: Texas Water Development Board Report 373. (103 pages).

7. Asadi, M., et al. 2008. Post-Frac Analysis Based on Flowback Results Using Chemical Frac-Tracers. Presented at the International Petroleum Technology Conference, Kuala Lumpur, Malaysia. http://dx.doi.org/10.2523/IPTC-11891-MS.

8. Atan, S., et al. 2018. The Viability of Gas Injection EOR in Eagle Ford Shale Reservoirs. Presented at the SPE Annual Technical Conference and Exhibition. Dallas, Texas. https://doi.org/10.2118/191673-MS.

9. Atherton, T. J., & Kerbyson, D. J. 1995. Circle detection using Hough transform filters. Presented at the 5th International Conference on Image Processing & its Application, Edinburgh, UK. https://doi.org/10.1049/cp:19950683.

10. Atherton, T. J., & Kerbyson, D. J. 1999. Size invariant circle detection. Image and Vision Computing, 17: 795-803. https://doi.org/10.1016/S0262-8856(98)00160-7.

11. Awada, A., et al. 2015. Is That Interference? A Workflow for Identifying and Analyzing Communication Through Hydraulic Fractures in a Multi-Well Pad. Presented at the Unconventional Resources Technology Conference, San Antonio, Texas. https://doi.org/10.15530/URTEC-2015-2148963.

12. Babadagli, T. 2001. Scaling of Cocurrent and Countercurrent Capillary Imbibition for Surfactant and Polymer Injection in Naturally Fractured Reservoirs. SPE Journal 6 (04): 465-478. https://doi.org/10.2118/74702-PA.

13. Baig, A., & Urbancic, T. 2010. Magnitude Determination, Event Detectability, and Assessing the Effectiveness of Microseismic Monitoring Programs in Petroleum Applications. CSEG Recorder, 35 (2).

14. Bao, X. & Eaton, D. W. 2016. Fault activation by hydraulic fracturing in western Canada. Science, 354 (6318): 1406-1409. https://doi.org/10.1126/science.aag2583.

15. Barton, C. A., et al. 1988. In-situ stress orientation and magnitude at the Fenton geothermal site, New Mexico, determined from wellbore breakouts. Geophysical Research Letters, 15 (5): 467-470. https://doi.org/10.1029/GL015i005p00467.

16. Berry, S. L., et al. 2009. Improved Oil Recovery from Combining Well Stimulation with Novel Surfactant Technologies. Presented at the SPE Annual Technical Conference and Exhibition. New Orleans, Louisiana. https://doi.org/10.2118/124215-MS.

17. Barton, C. A., et al. 1988. In-situ stress orientation and magnitude at the Fenton geothermal site, New Mexico, determined from wellbore breakouts. Geophysical Research Letters, 15 (5): 467-470. https://doi.org/10.1029/GL015i005p00467.

18. Basir, H. M., et al. 2013. Multi-attribute ant-tracking and neural network for fault detection: a case study of an Iranian oilfield. Journal of Geophysics and Engineering, 10 (1): 015009. https://doi.org/10.1088/1742-2132/10/1/015009.

19. Bidhendi, M. M., et al. 2019. A Set of Successful Chemical EOR Trials in Permian Basin: Promising Field and Laboratory Results. Presented at the SPE/AAPG/SEG Unconventional Resources Technology Conference. Denver, Colorado. https://doi.org/10.15530/urtec-2019-881.

20. Boroumand, N., & Eaton, D. 2012. Comparing energy calculations - Hydraulic fracturing and microseismic monitoring. Presented at the 74th EAGE Conference and Exhibition. http://dx.doi.org/ 10.3997/2214-4609.20148187.

21. Branagan, P. T., et al. 1996. Characterization of a remotely intersected set of hydraulic fractures: results of intersection well No. 1-B GRI/DOE Multi-Site Project. Presented at the SPE Annual Technical Conference and Exhibition, Denver, Colorado. https://doi.org/10.2118/36452-MS.

22. Britt, L. K., et al. 1994. Hydraulic Fracturing in a naturally fractured reservoir. Presented at the SPE International Petroleum Conference and Exhibition, Veracruz, Mexico. https://doi.org/10.2118/28717-MS.

23. Brock, T. 1970. Biology of Microorganisms. Prentice Hall, Inc. Englewood, NJ. pp. 486-487.

24. Buch-Kromann, T., et al. 2005. Kernel density estimation for heavy-tailed distributions using the Champernowne transformation. Statistics. 39 (6): 503–518. Buch-Kromann, Tine and Nielsen, Jens Perch and Guillen, Montserrat and Bolancé, Catalina, Kernel Density Estimation for Heavy-Tailed Distributions Using the Champernowne Transformation (January 2005). Available at SSRN: https://ssrn.com/abstract=704903 or http://dx.doi.org/10.2139/ssrn.704903.

25. Bunch, A.G., et al. 2014. Evaluation of Impact of Shale Gas Operations in the Barnett Regions on Volatile Organic Compounds and Potential Health Risks. Science of the Total Environment, 468-469: 832-842. https://doi.org/10.1016/j.scitotenv.2013.08.080

26. Caffagni, E., et al. 2015. Regional seismicity: A potential pitfall for identification of long-period long-duration events. Geophysics 80 (1): A1-A5. https://doi.org/10.1190/geo2014-0382.1.

27. Campbell, W., & Wicker, J. 2018. Natural and Hydraulic Fracture Density Prediction and Identification of Controllers. Presented at the SPE/AAPG/SEG Unconventional Resources Technology Conference, Houston, Texas. https://doi.org/10.15530/URTEC-2018-2934611.

28. Carlsen, M., et al. 2019. Compositional Tracking of a Huff-n-Puff Project in the Eagle Ford. Presented at the SPE/AAPG/SEG Unconventional Resources Technology Conference. Denver, Colorado. https://doi.org/10.15530/urtec-2019-539.

29. Chen, H. L., et al. 2000. Laboratory Monitoring of Surfactant Imbibition Using Computerized Tomography. Paper presented at the International Petroleum Conference and Exhibition. Villahermosa, Mexico. https://doi.org/10.2118/59006-MS.

30. Chopra, S., & Marfurt, K. J. 2007. Seismic Attributes for Prospect Identification and Reservoir Characterization: Society of Exploration Geophysicists and European Association of Geoscientists and Engineers.

31. Chopra, S., & Marfurt, K. J. 2007. Volumetric curvature attributes add value to 3D seismic data interpretation. The Leading Edge, 26 (7): 856-867. https://doi.org/10.1190/1.2756864.

32. Ciezobka, J., & I., Salehi. 2017. Hydraulic fracturing system and method. U.S. Patent 9,581,004 issued February 28, 2017.

33. Ciezobka, J., et al. 2018. Hydraulic Fracturing Test Site (HFTS) – Project Overview and Summary of Results. Presented at the Unconventional Resources Technology Conference (URTeC). Houston, Texas. https://doi.org/10.15530/URTEC-2018-2937168.

34. Cipolla, C. L., et al. 2011. A Practical Guide to Interpreting Microseismic Measurements. Presented at the North American Unconventional Gas Conference and Exhibition, The Woodlands, Texas. https://doi.org/10.2118/144067-MS.

35. Clark, C., et al. 2013. Hydraulic Fracturing and Shale Gas Production: Technology, Impacts, and Regulations. USDOE Office of Scientific and Technology Information, Oak Ridge, TN. Report No. ANL/EVS/R-12/5.

36. Cobain, S. L., et al. 2015, Indicators of propagation direction and relative depth in clastic injectites: implications for laminar versus turbulent flow processes: GSA Bulletin, 127: 1816–1830. https://doi.org/10.1130/B31209.1.

37. Cobbold, P. R., et al. 2013, Bedding-parallel fibrous veins (beef and cone-in-cone): worldwide occurrence and possible significance in terms of fluid overpressure, hydrocarbon generation and mineralization. Marine and Petroleum Geology, 55: 250–261, https://doi.org/10.1016/j.marpetgeo.2013.01.010.

38. Courtier, J., et al. 2016. Legacy Well Protection ReFrac Mitigates Offset Well Completion Communications in Joint Industry Project. Presented at the SPE Liquids-Rich Basins Conference – North America, Midland, Texas. https://doi.org/10.2118/181767-MS.

39. Courtier, J., et al. 2017. Best Practices in Designing and Executing a Comprehensive Hydraulic Fracturing Test Site in the Permian Basin. Presented at the SPE/AAPG/SEG Unconventional Resources Technology Conference. Austin, Texas. https://doi.org/10.15530/URTEC-2017-2697483.

40. Courtier, J., & Ciezobka, J. 2018. Hydraulic fracture test site—project overview and summary of results. Presented at the SPE/AAPG/SEG Unconventional Resources Technology Conference, Houston, Texas. https://doi.org/10.15530/URTEC-2018-2937168.

41. Courtier, J., et al. 2018. Using Stage Level Microseismic Analysis to Investigate Correlate and Ground Truth Cored Hydraulic Fractures. Presented at the SPE/AAPG/SEG Unconventional Resources Technology Conference, Houston, Texas, USA. https://doi.org/10.15530/URTEC-2018-2937221.

42. Dahi-Taleghani, A., & Olson, J. E. 2011. Numerical modeling of multistranded-hydraulic-fracture propagation: Accounting for the interaction between induced and natural fractures. SPE Journal, 16: 575–581. https://doi.org/10.2118/124884-PA.

43. Daly, B., et al. 2016. Microbial metabolisms in a 2.5km deep ecosystem created by hydraulic fracturing in shales. Nature Microbiology, 1: 16146. https://doi.org/10.1038/nmicrobiol.2016.146.

44. Daneshy, A. A. 2009. Factors Controlling the Vertical Growth of Hydraulic Fractures. Presented at the SPE Hydraulic Fracturing Technology Conference (HFTC), The Woodlands, Texas. https://doi.org/10.2118/118789-MS.

45. Das, I., & Zoback, M. D. 2011. Long period long duration seismic events during hydraulic fracture stimulation of a shale gas reservoir. The Leading Edge, 30 (7): 778–786. https://doi.org/10.1190/1.3609093.

46. Dawson, M., & Kampfer, G. 2016. Breakthrough in Hydraulic Fracture & Proppant Mapping: Achieving Increased Precision with Lower Cost. Presented at the SPE/AAPG/SEG Unconventional Resources Technology Conference. https://doi.org/10.15530/URTEC-2016-2432330.

47. Denyer, S. P., et al. 2002. Cellular impermeability and uptake of biocides and antibiotics in Gram-negative bacteria. Journal of Applied Microbiology Symposium Supplement, 92: 35S-45S. https://doi.org/10.1046/j.1365-2672.92.5s1.19.x.

48. Ding, M., et al. 2019. Experimental study on CO_2-EOR in fractured reservoirs: Influence of fracture density, miscibility and production scheme. Journal of Petroleum Science and Engineering, 174: 476-485. https://doi.org/10.1016/j.petrol.2018.11.039.

49. Dohmen, T., et al. 2014. Measurement and Analysis of 3D Stress Shadowing Related to the Spacing of Hydraulic Fracturing in Unconventional Reservoirs. Presented at the SPE Annual Technical Conference and Exhibition, Amsterdam, Netherlands. https://doi.org/10.2118/170924-MS.

50. Dontsov, E. V., & Peirce, A. P. 2015. Proppant transport in hydraulic fracturing: crack tip screen-out in KGD and P3D models. International Journal of Solids and Structures, 63: 206-218. https://doi.org/10.1016/j.ijsolstr.2015.02.051.

51. Dorigo, M. & Stutzle, T. 2004. Ant Colony Optimization: MIT Press.

52. Eaton, D., et al. 2013. Broadband microseismic observations from a Montney hydraulic fracture treatment, northeastern British Columbia. CSEG Recorder 38 (3): 45–53.

53. EIA: International Energy Outlook 2017. Report No. IEO2017. U.S. Energy Information Administration: 55.

54. EIA: Drilling Productivity Report. 2017. U.S. Energy Information Administration.

55. Eisenlord, S., & Hayes, T. 2017. Microbiological Analysis of Hydraulic Fracture Test Site (HFTS) Operations. Final Report. Gas Technology Institute, Des Plaines, IL.

56. Eisenlord, S., & Hayes, T. 2018. Environmental Monitoring of the Hydraulic Fracture Test Site (HFTS). Presented at the SPE/AAPG/SEG Unconventional Resources Technology Conference, Houston, Texas, USA. https://doi.org/10.15530/URTEC-2018-2900727.

57. Elliott, S., & Gale, J. 2018. Analysis and Distribution of Proppant Recovered from Fracture Faces in the HFTS Slant Core Drilled Through a Stimulated Reservoir.

Presented at the SPE/AAPG/SEG Unconventional Resources Technology Conference, Houston, Texas. https://doi.org/10.15530/URTEC-2018-2902629.

58. Fairfield, R., et al. 2018. Using Stage Level Microseismic Analysis to Gain Insight into Fracture Efficiency and Completion Effectiveness. Presented at the SPE/AAPG/SEG Unconventional Resources Technology Conference, Houston, Texas. https://doi.org/10.15530/urtec-2018-2937228.

59. Fast, R. E., et al. 1994. Description and analysis of cored hydraulic fractures—Lost Hills field, Kern County, California, in Society of Petroleum Engineers. SPE Production and Facilities, 9(2): 107–114. https://doi.org/10.2118/24853-PA.

60. Feng Q., et al. 2007. EOR Pilot Tests with Modified Enzyme in China. Presented at the EUROPEC/EAGE Conference and Exhibition, London, U.K. https://doi.org/10.2118/107128-MS.

61. Fisher, R. A. 1950. Contributions to mathematical statistics. New York: Wiley.

62. Fisher, K., et al. 1995. A Comprehensive Study of the Analysis and Economic Benefits of Radioactive Tracer Engineered Stimulation Procedures. presented at the SPE Annual Technical Conference and Exhibition, Dallas, Texas. http://dx.doi.org/10.2118/30794-MS.

63. Fisher, M. K., et al. 2002. Integrating Fracture Mapping Technologies to Optimize Stimulations in the Barnett Shale. Presented at the SPE Annual Technical Conference and Exhibition, San Antonio, Texas. https://doi.org/10.2118/77441-MS.

64. Fisher, K., & Warpinski, N. 2012. Hydraulic fracture height growth: real data, in Society of Petroleum Engineers, SPE Production and Operations 27(1): 8-19. https://doi.org/10.2118/145949-PA.

65. Fragoso, A., et al. 2018. An Investigation on the Feasibility of Combined Refracturing of Horizontal Wells and Huff and Puff Gas Injection for Improving Oil Recovery from Shale Petroleum Reservoirs. Presented at the SPE Improved Oil Recovery Conference, Tulsa, Oklahoma. https://doi.org/10.2118/190284-MS.

66. Friedrich, M., & Monson, G. 2013. Two Practical Methods to Determine Pore Pressure Regimes in the Spraberry and Wolfcamp Formation in the Midland Basin. Presented at the Unconventional Resources Technology Conference, Denver, Colorado. https://doi.org/10.1190/urtec2013-258.

67. Gale, J. F. W., et al. 2014. Natural fractures in shale: a review and new observations. AAPG Bulletin, 98 (11): 2165–2216. https://doi.org/10.1306/08121413151.

68. Gale, J. F. W., et al. 2018. Hydraulic Fractures in core from stimulated reservoirs; Core fracture description of the HFTS slant core, Reagan Co., Midland Basin, Texas.

SPE/AAPG/SEG Unconventional Resources Technology Conference, Houston, Texas. https://doi.org/10.15530/URTEC-2018-2902624.

69. Galperin, K. 2011. Review of microbial processes in the near-surface environment and their implications for the chemical fingerprinting of hydrocarbon fuels, Environmental Forensics: Taylor & Francis.

70. Ganjdanesh, R., et al. 2019. Gas Injection EOR in Eagle Ford Shale Gas Condensate Reservoirs. Presented at the SPE/AAPG/SEG Unconventional Resources Technology Conference. Denver, Colorado. https://doi.org/10.15530/urtec-2019-987.

71. Gaspar J., et al. 2014. Microbioal dynamics and control in shale gas production. Enviornmental Science and Technology, 1 (12): 465-473. https://doi.org/10.1021/ez5003242.

72. Gallegos, T. J., et al. 2015. Hydraulic Fracturing in the U.S. AGU Water Resources: AGU.

73. Gerstenberger, M., et al. 2001. A systematic test of the hypothesis that the b value varies with depth in California. Geophysical Research Letters, 28 (1): 57-60. https://doi.org/10.1029/2000GL012026.

74. Grob, M., & Van Der Baan, M. 2012. Statistical analysis of microseismic event characteristics helps monitor in-situ stress changes. Presented at the 21st Canadian Rock Mechanics Symposium, Edmonton, Canada. https://doi.org/10.1190/1.3663403.

75. Grob, M. & Van Der Baan, M. 2016. Influence of acquisition geometry on event cloud asymmetry and on b-value analysis. CSEG Recorder, 41 (5): 30-35.

76. Gutenberg, R. & Richter, C. F. 1944. Frequency of earthquakes in California. Bulletin of the Seismological Society of America, 34 (4): 185-188. https://doi.org/10.1785/BSSA0340040185.

77. Hamdi, H., et al. 2018. Huff-N-Puff Gas Injection Performance in Shale Reservoirs: A Case Study From Duvernay Shale in Alberta, Canada. Presented at the SPE/AAPG/SEG Unconventional Resources Technology Conference. Houston, Texas. https://doi.org/10.15530/URTEC-2018-2902835.

78. Hamlin, H. S., & Baumgardner, R. W. 2012. Wolfberry (Wolfcampian-Leonardian) deep-water depositional systems in the Midland Basin—Stratigraphy, lithofacies, reservoirs, and source rocks: Bureau of Economic Geology, The University of Texas at Austin: Report of Investigations No. 277.

79. Hayes, T. D. 2010. Sampling and Analysis of Water Streams Associated with the Development of Marcellus Shale Gas. Final Report to the Marcellus Shale Coalition: Gas Technology Institute, Des Plaines, IL.

80. Hayes, T. D., & Severin, B. F. 2012. Barnett and Appalachian Shale Water Management and Reuse Technologies: RPSEA Report No. 08122-05.FINAL.2.

81. Hayes, T. D., & Severin, B. F. 2012. Characterization of Flowback Waters from the Marcellus and the Barnett Regions: RPSEA Report No. 08122-05.09.

82. Harris, R. E., & McKay, I. D. 1998. New Applications for Enzymes in Oil and Gas Production. Presented at the European Petroleum Conference. The Hague, Netherlands. https://doi.org/10.2118/50621-MS.

83. Hickman, S. H., & Zoback, M. D. 1983. The interpretation of hydraulic fracturing pressure-time data for in-situ stress determination. In Hydraulic Fracturing Measurements: National Academy Press, Washington D. C.

84. Hoffman, B. T. 2018. Huff-N-Puff Gas Injection Pilot Projects in the Eagle Ford. presented at the SPE Canada Unconventional Resources Conference, Calgary, Alberta. https://doi.org/10.2118/189816-MS.

85. Hu, Y., et al. 2016. A Novel Model of Brittleness Index for Shale Gas Reservoirs: Confining Pressure and Pore Pressure Effect. Presented at the AAPG Annual Convention and Exhibition. Calgary, Canada. https://doi.org/10.2118/176886-MS.

86. Hu, H., et al. 2017. Long-period long-duration seismic events during hydraulic fracturing: Implications for tensile fracture development. Geophysical Research Letters. 44 (10): 4814-4819. http://dx.doi.org/10.1002/2017GL073582.

87. Jabbar, M., et al. 2015. Application of Enzyme EOR in a Mature UAE Offshore Carbonate Oil Field. Presented at the Abu Dhabi International Petroleum Exhibition and Conference. Abu Dhabi, UAE. https://doi.org/10.2118/177688-MS.

88. Jia, B., et al. 2019. A review of the current progress of CO_2 injection EOR and carbon storage in shale oil reservoirs. Fuel, 236: 404-427. https://doi.org/10.1016/j.fuel.2018.08.103.

89. Jiao, W., et al. 2014. The matter of size: On the moment magnitude of microseismic events. Geophysics, 79 (3): KS31-KS41. https://doi.org/10.1190/geo2013-0194.1.

90. Jin, X., et al. 2019. Field Pilots of Unconventional Shale EOR in the Permian Basin. Presented at the SPE/AAPG/SEG Unconventional Resources Technology Conference. Denver, Colorado. https://doi.org/10.15530/urtec-2019-506.

91. Johri, M., et al. 2015. A scaling law to characterize fault-damage zones at reservoir depths. AAPG Bulletin, 98 (10): 2057-2079. https://doi.org/10.1306/05061413173.

92. Jones, M., et al. 2016. Case Study: Successful Applications of Weak Emulsifying Surfactants in the Wolfcamp Formation of Reagan County, TX. Presented at the SPE

Liquids-Rich Basins Conference - North America. Midland, Texas. https://doi.org/10.2118/181771-MS.

93. Kanungo, T., et al. 2002. An efficient k-means clustering algorithm: analysis and implementation. IEEE Transactions on Pattern Analysis and Machine Intelligence, 24 (7): 881-892. https://doi.org/10.1109/TPAMI.2002.1017616

94. Kazemi, H., et al. 1992. Analytical and Numerical Solution of Oil Recovery From Fractured Reservoirs With Empirical Transfer Functions (includes associated papers 25528 and 25818). SPE Reservoir Engineering 7(02): 219-227. Paper Number: SPE-19849-PA.

95. Khusainova, A., et al. 2015. Study of wettability of calcite surfaces using oil–brine–enzyme systems for enhanced oil recovery applications. Journal of Petroleum Science and Engineering, 127: 53-64. https://doi.org/10.1016/j.petrol.2014.12.014.

96. Kimme, C., et al. 1975. Finding circles by an array of accumulators. Communications of the ACM, 18 (2): 120-122. https://doi.org/10.1145/360666.360677.

97. King, G. C. P., et al. 1994. Static stress changes and the triggering of earthquakes. Bulletin of the Seismological Society of America, 84 (3): 935-953. https://doi.org/10.1785/BSSA0840030935.

98. King, G.E., & Leonard, R. S. 2011. Deciphering Chemical Tracer Results in Multi-Fractured Well Backflow in Shales: A Framework for Optimizing Fracture Design and Application. Presented at the SPE Hydraulic Fracturing Technology Conference, The Woodlands, Texas. http://dx.doi.org/10.2118/140105-MS.

99. Konopczynski, M., & Dowlatabad, M. M. 2018. Improving the Performance of EOR in Unconventional Oil Reservoirs Using Advanced Completion Technology. Presented at the SPE Improved Oil Recovery Conference. Tulsa, Oklahoma. https://doi.org/10.2118/190260-MS.

100. Kratz, M., et al. 2012. Identifying Fault Activation in Shale Reservoirs Using Microseismic Monitoring during Hydraulic Stimulation: Source Mechanisms, b Values, and Energy Release Rates. CSEG Recorder, 37 (6): 20-28.

101. Kumar, A., et al. 2016. Surface seismic monitoring of hydraulic fracturing activity in Pennsylvania and West Virginia. Presented at the SPE/AAPG/SEG Unconventional Resources Technology Conference, San Antonio, Texas. https://doi.org/10.15530/urtec-2016-2435574.

102. Kumar, A., et al. 2017. Long-period, long-duration seismicity observed during hydraulic fracturing of the Marcellus Shale in Greene County, Pennsylvania. The Leading Edge, 36 (7): 580-587. https://doi.org/10.1190/tle36070580.1.

103. Kumar, A., & Sharma, M. M. 2018. Diagnosing Fracture-Wellbore Connectivity Using Chemical Tracer Flowback Data. Presented at the SPE/AAPG/SEG Unconventional Resources Technology Conference. https://doi.org/10.15530/urtec-2018-2902023.

104. Laredo, Nitec, ARM, Ziebel, CorLab, & GTI: Weekly and final presentation updates.

105. Laubach, S. E., & Doherty, E. 1999. Oriented drilled sidewall cores for natural fracture evaluation. Presented at the SPE Annual Technical Conference and Exhibition, Houston, Texas. https://doi.org/10.2118/56801-MS.

106. Lee, H. P., et al. 2015. The interaction of propagating opening mode fractures with preexisting discontinuities in shale. Journal of Geophysical Research: Solid Earth, 120: 169–181. https://doi.org/10.1002/2014JB011358.

107. Lei, X, et al. 2017. Fault reactivation and earthquakes with magnitudes of up to Mw4.7 induced by shale-gas hydraulic fracturing in Sichuan Basin, China. Scientific Reports, 7 (1): 7971. https://doi.org/10.1038/s41598-017-08557-y.

108. Leonard, R. S., et al. 2007. Barnett Shale Completions: A Method for Assessing New Completion Strategies. Presented at the SPE Annual Technical Conference and Exhibition, Anaheim, California. http://dx.doi.org/10.2118/110809-MS.

109. Leong, Y., et al. 2015. Estimation of Fracture Volume Between Well Pairs Using Deuterium Tracer. Presented at the SPE Annual Technical Conference and Exhibition, Houston, Texas. https://doi.org/10.2118/174832-MS.

110. Levenberg, K. 1944. A Method for the Solution of Certain Non-Linear Problems in Least Squares. Quarterly of Applied Mathematics, 2: 164-168. https://doi.org/10.1090/qam/10666.

111. Liakopoulou-Morris, F., et al. 1994. Microseismic properties of a homogeneous sandstone during fault nucleation and frictional sliding. Geophysical Journal International, 119 (1): 219-230. https://doi.org/10.1111/j.1365-246X.1994. tb00923.x.

112. Lipus, V., et al. 2017. Prdominance and metabolic potential for halanaerobium in produced water from hydraulically fractures marcellus shale wells. Applied and Environmental Microbiology, 83 (8): e02659-16. https://doi.org/10.1128/AEM.02659-16.

113. Liu, H., & Zhang, Z. 2011. Biology Enzyme EOR for Low Permeability Reservoirs. Presented at the SPE Enhanced Oil Recovery Conference, Kuala Lumpur, Malaysia. https://doi.org/10.2118/144281-MS.

114. Liu, S., et al. 2018. Laboratory Investigation of EOR Techniques for Organic Rich Shales in the Permian Basin. Presented at the SPE/AAPG/SEG Unconventional Resources Technology Conference. Houston, Texas. https://doi.org/10.15530/URTEC-2018-2890074.

115. Lund Snee, J. E., & Zoback, M. D. 2016. State of stress in Texas: implications for induced seismicity. Geophysical Research Letters, 43: 10208–10214, https://doi.org/10.1002/2016GL070974.

116. MacKay, D. J. C. 1992. Bayesian interpolation. Neural Computation, 4 (3): 415-447. https://doi.org/10.1162/neco.1992.4.3.415.

117. Magot M., et al. 2000. Microbiology of petroium reservoirs. Antonie van Leeuwenhoek, 77(2): 103-116. https://doi.org/10.1023/a:1002434330514.

118. Maity, D., & Aminzadeh, F. 2015. Novel fracture zone identifier attribute using geophysical and well log data for unconventional reservoirs. Interpretation, 3 (3): T155-T167. https://doi.org/10.1190/INT-2015-0003.1.

119. Maity, D. 2015. Correlating Pressure with Microseismic to Understand Fluid-Reservoir Interactions During Hydraulic Fracturing. Journal of Sustainable Energy Engineering, 3 (2): 127-142. https://doi.org/10.7569/JSEE.2015.629506.

120. Maity, D. 2018. Microseismicity Analysis for HFTS Pad and Correlation with Completion Parameters. Presented at the SPE/AAPG/SEG Unconventional Resources Technology Conference (URTeC). Houston, Texas. https://doi.org/10.15530/URTEC-2018-2902355.

121. Maity, D., et al. 2018. Assessment of In-Situ Proppant Placement in SRV Using Through- Fracture Core Sampling at HFTS. Paper presented at the SPE/AAPG/SEG Unconventional Resources Technology Conference, Houston, TX. https://doi.org/10.15530/URTEC-2018-2902364.

122. Maity, D., & Ciezobka, J. 2020. A Data Analytics Framework for Cored Fracture Imaging and Novel Characterization Workflow - Application on Samples from Hydraulic Fracturing Test Site HFTS in the Midland Basin. Presented at the SPE Hydraulic Fracturing Technology Conference and Exhibition, The Woodlands, TX. https://doi.org/10.2118/199754-MS.

123. Maity, D., & Ciezobka, J. 2021. Digital Fracture Characterization at Hydraulic Fracturing Test Site HFTS-Midland: Fracture Clustering, Stress Effects and Lithologic Controls. Presented at the SPE HFTC Conference and Exhibition, virtual. https://doi.org/10.2118/204174-MS.

124. Maity, D., & Ciezobka, J. 2022. Novel Proppant Logging Technique for Infill Drilling of Unconventional Shale Wells. SPE Reservoir Evaluation & Engineering, 25 (3): 641-654. https://doi.org/10.2118/209790-PA.

125. Maity, D., & Ciezobka, J. 2023. Understanding near-field fiberoptic observations in the context of completion designs, fracturing effectiveness, and drainage characteristics. A case study from the hydraulic fracturing test site (HFTS-2) in Delaware basin. Gas Science & Engineering, 112. https://doi.org/10.1016/j.jgsce.2023.204929.

126. Manchanda, R., & Sharma, M. M. 2013. Time-Delayed Fracturing: A New Strategy in Multi-Stage, Multi-Well Pad Fracturing. Presented at the SPE Annual Technical Conference and Exhibition, New Orleans, Louisiana. https://doi.org/10.2118/166489-MS.

127. Manchanda, R., et al. 2014. Time-Dependent Fracture-Interference Effects in Pad Wells. SPE Production & Operations, 29(4): 274–287. https://doi.org/10.2118/164534-PA.

128. Marquardt, D. W. 1963. An algorithm for least-squares estimation of nonlinear parameters. Journal of the Society for Industrial and Applied Mathematics, 11 (2): 431-441. https://doi.org/10.1137/0111030.

129. Marzocchi, W. & Sandri, L. 2003. A review and new insights on the estimation of the b-value and its uncertainty. Annals of Geophysics, 46 (6): 1271-1282. https://doi.org/10.4401/ag-3472.

130. Mattax, C. C., & Kyte J. R. 1962. Imbibition Oil Recovery from Fractured, Water-Drive Reservoir. Society of Petroleum Engineers Journal, 2(02): 177-184. https://doi.org/10.2118/187-PA.

131. Maxwell S. C. 2014. Microseismic Imaging of Hydraulic Fracturing: Improved Engineering of Unconventional Shale Reservoirs, SEG.

132. Maxwell, S. C., et al. 2015. Differentiating Wet and Dry Microseismic Events Induced During Hydraulic Fracturing. Presented at the SPE/AAPG/SEG Unconventional Resources Technology Conference (URTeC). San Antonio, Texas. https://doi.org/10.2118/178585-MS.

133. Maxwell, S. C., et al. 2017. Acoustic Emission Geomechanics and Seismic Energy Budgets of Laboratory Hydraulic Fracturing. Presented at the Geoconvention meeting, Calgary, Canada.

134. Mayerhofer, M. J., et al. 2008. What is Stimulated Rock Volume? Presented at the SPE Shale Gas Production Conference, Fort Worth, Texas. https://doi.org/10.2118/119890-MS.

135. McNutt, S. R. 1992. Volcanic tremor, in Encyclopedia of Earth System Science, 4: 417–425. Academic Press, San Diego, California.

136. Mohan, A. M., et al. 2013. Microbial communities in flowback water impoundments from hydraculic fracturing for recovery of shale gas. FEMS Microbiology Ecology, 86 (3): 567-580. https://doi.org/10.1111/1574-6941.12183.

137. Montgomery, C. T., & Smith, M. B. 2010. Hydraulic fracturing: history of an enduring technology. Journal of Petroleum Technology, 62 (12): 26-40. https://doi.org/10.2118/1210-0026-JPT.

138. Moos, D., et al. 2011. Predicting shale reservoir response to stimulation in the upper Devonian of West Virginia. Presented at the SPE Annual Technical Conference and Exhibition, Denver, Colorado. http://dx.doi.org/10.2118/145849-MS.

139. Morsy, S., et al. 2013. Waterflooding in the Eagle Ford ShaleFormation: Experimental and Simulation Study. Presented at the SPE Unconventional Resources Conference and Exhibition-Asia Pacific. Brisbane, Australia. https://doi.org/10.2118/167056-MS.

140. Mulkern, M. E., et al. 2010. Fracture Extent and Zonal Communication Evaluation Using Chemical Gas Tracers. presented at the SPE Eastern Regional Meeting, Morgantown, West Virginia. http://doi.org/10.2118/138877-MS.

141. Nagel, N. B., et al. 2013. Evaluation of Stress Changes Due to Multi-Stage Hydraulic Fracturing – Consideration of Field Results. Presented at the ISRM International Symposium – Eurorock 2013, Wroclaw, Poland.

142. Nasiri, H. 2011. Enzymes for Enhanced Oil Recovery (EOR), The University of Bergen.

143. Neog, A., & Schechter, D. S. 2016. Investigation of Surfactant Induced Wettability Alteration in Wolfcamp Shale for Hydraulic Fracturing and EOR Applications. Presented at the SPE Improved Oil Recovery Conference. Tulsa, Oklahoma. https://doi.org/10.2118/179600-MS.

144. Ngameni, K. L. 2016. Proppant transport in horizontal wellbores using fresh water. MS thesis. Colorado School of Mines, Golden, Colorado.

145. Ngeri, A. P., et al. 2015. Ant-tracker attributes: An effective approach to enhancing fault identification and interpretation. IOSR-JVSP, 5 (6): 67-73.

146. Nolte, K., & Smith, M. 1981. Interpretation of Fracturing Pressures. Journal of Petroleum Technology, 33 (9): 1767–1775. https://doi.org/10.2118/8297-PA.

147. Nordgren, R. P. 1972. Propagation of a Vertical Hydraulic Fracture. SPE Journal, 12 (4): 306-314. https://doi.org/10.2118/3009-PA.

148. Obara, K. 2002. Nonvolcanic deep tremor associated with subduction in southwest Japan. Science, 296: 1679–1681, https://doi.org/10.1126/science.1070378.

149. O'Brien, T. A., et al. 2016. A fast and objective multidimensional kernel density estimation method: fastKDE. Computational Statistics and Data Analysis, 101: 148–160. https://doi.org/10.1016/j.csda.2016.02.014.

150. O'Brien, T. A., et al. 2014. Reducing the computational cost of the ECF using a nuFFT: A fast and objective probability density estimation method. Computational Statistics and Data Analysis, 79: 222–234. https://doi.org/10.1016/j.csda.2014.06.002.

151. Ogata, K., et al. 2014. Fracture corridors as seal-bypass systems in siliciclastic reservoir-cap rock successions: Field-based insights from the Jurassic Entrada

Formation (SE Utah, USA). Journal of Structural Geology, 66: 162-187. https://doi.org/10.1016/j.jsg.2014.05.005.

152. Okada, Y. 1992. Internal deformation due to shear and tensile faults in a half-space. Bulletin of the Seismological Society of America, 82 (2): 1018-1040. https://doi.org/10.1785/BSSA0820021018.

153. Olson, K., et al. 2023. Sealed Wellbore Pressure Monitoring (SWPM) and Calibrated Fracture Modeling: The Next Step in Unconventional Completions Optimization. Presented at the SPE Hydraulic Fracturing Technology Conference and Exhibition, The Woodlands, TX. https://doi.org/10.2118/212367-MS.

154. Ortega, O. J., et al. 2006, A scale-independent approach to fracture intensity and average spacing measurement. AAPG Bulletin, 90 (2): 193–208. https://doi.org/10.1306/08250505059.

155. Palisch, T., et al. 2016. Recent advancements in far-field proppant detection. Presented at the SPE Hydraulic Fracturing Technology Conference, The Woodlands, Texas. https://doi.org/10.2118/179161-MS.

156. Palisch, T., et al. 2018. Far-Field Proppant Detection Using Electromagnetic Methods: Latest Field Results. SPE Production & Operations, 33 (3): 557-568. https://doi.org/10.2118/184880-PA.

157. Parzen, E. 1962. On Estimation of a Probability Density Function and Mode. The Annals of Mathematical Statistics. 33 (3): 1065-1076. https://doi.org/10.1214/aoms/1177704472.

158. Patel, P. S., et al. 2014. Analysis of US hydraulic fracturing fluid system and proppant trends. Presented at the SPE Hydraulic Fracturing Technology Conference, The Woodlands, Texas. https://doi.org/10.2118/168645-MS.

159. Perkins, T. K., & Kern, L. R. 1961. Widths of Hydraulic Fractures. Journal of Petroleum Technology, 13 (9), 937-949. https://doi.org/10.2118/89-PA.

160. Perry, K., et al. 2017. The Hydraulic Fracture Test Site (HFTS) a West Texas Research Experiment for New Hydraulic fracturing Technology in the Wolfcamp Formation. Presented at the IGU Research Conference. Rio de Janeiro, Brazil.

161. Phan, T. N., et al. 2018. Lithologic and Geomechanical Control on CO_2 Huff-n-Puff Enhanced Oil Recovery Processes Using Integrated Modeling Framework in Wolfcamp. Presented at the SPE/AAPG/SEG Unconventional Resources Technology Conference. Houston, Texas. https://doi.org/10.15530/URTEC-2018-2901346.

162. Pigott, J. D., et al. 2013. First order seismic attributes for clasticseismic facies interpretation: Examples from the East China Sea. Journal of Asian Earth Sciences, 66: 34-54. https://doi.org/10.1016/j.jseaes.2012.11.043.

163. Pirayesh, E., et al. 2013. Make Decision on the Fly: A New Method to Interpret Pressure-Time Data during Fracturing – Application to FracPack. Presented at the SPE Annual Technical Conference and Exhibition, New Orleans, Louisiana. https://doi.org/10.2118/166132-MS.

164. Pu, W., & Hoffman, B. T. 2014. EOS Modeling and Reservoir Simulation Study of Bakken Gas Injection Improved Oil Recovery in the Elm Coulee Field, Montana. Presented at the SPE/AAPG/SEG Unconventional Resources Technology Conference. Denver, Colorado. https://doi.org/10.15530/URTEC-2014-1922538.

165. Rahayyem, M., et al. 2019. Enzyme Enhanced Oil Recovery EEOR: A Microfluidics Approach. Presented at the SPE Middle East Oil and Gas Show and Conference. Manama, Bahrain. https://doi.org/10.2118/195116-MS.

166. Rassenfoss, S. 2017. Shale EOR Works, But Will It Make a Difference? Journal of Petroleum Technology, 69 (10): 34-40. https://doi.org/10.2118/1017-0034-JPT.

167. Raterman, K. T., et al. 2017. Sampling a stimulated rock volume: an Eagle Ford example. Presented at the SPE/AAPG/SEG Unconventional Resources Technology Conference, Austin, Texas. https://doi.org/10.15530/URTEC-2017-2670034.

168. Reis, J. C., et al. 1996. Measuring Hydraulic Fracture Width Behind Casing Using Radioactive Proppant. Presented at the SPE Formation Damage Control Symposium, Lafayette, Louisiana. https://doi.org/10.2118/31105-MS.

169. Rickman, R., et al. 2008. A practical use of shale petrophysics for stimulation design optimization: All shale plays are not clones of the Barnett Shale. Presented at the SPE Annual Technical Conference and Exhibition, Denver, Colorado. https://doi.org/10.2118/115258-MS.

170. Roche, V., et al. 2015. Statistical characteristics of microseismic events and in-situ stress in the Horn River Basin. Presented at GeoConvention, Calgary, Canada.

171. Roling, W. F. M., et al. 2003. The microbiology of hydrocarbon degradation in subsurface petroleum reservoirs: perspectives and prospects. Research in Microbiology, 154 (5): 321-328. https://doi.org/10.1016/S0923-2508(03)00086-X.

172. Roussel, N. P., & Agrawal, S. 2017. Introduction to Poroelastic Response Monitoring - Quantifying Hydraulic Fracture Geometry and SRV Permeability from Offset-Well Pressure Data. Presented at the SPE/AAPG/SEG Unconventional Resources Technology Conference, Austin, Texas. http://doi.org/10.15530/URTEC-2017-2645414.

173. Salahshoor, S., & Fahes, M. 2018. Experimental Investigation of the Effect of Pore Size on Saturation Pressure for Gas Mixtures. Presented at the SPE Annual Technical Conference and Exhibition. Dallas, Texas. https://doi.org/10.2118/191399-MS.

174. Salahshoor, S., et al. 2018. A review on the effect of confinement on phase behavior in tight formations. Journal of Natural Gas Science and Engineering, 51: 89-103. https://doi.org/10.1016/j.jngse.2017.12.011.

175. Salahshoor, S., & Fahes, M. 2018. Experimental and Theoretical Investigation of the Confinement Effect on Gas Properties in Nano-Scale Porous Media. Presented at the SPE/AAPG/SEG Unconventional Resources Technology Conference. Houston, Texas. https://doi.org/10.15530/URTEC-2018-2902592.

176. Salahshoor, S., et al. 2019. Experimental Investigation on the Application of Biological Enzymes for EOR in Shale Formations. Presented at the SPE/AAPG/SEG Unconventional Resources Technology Conference. Denver, Colorado. https://doi.org/10.15530/urtec-2019-1117.

177. Santosh, D., et al. 2013. An integrated approach for faults and fractures delineation with dip and curvature attributes. Presented at the 10th biennial international conference and exposition on petroleum geophysics, Kochi, India.

178. Sardinha, C. M., et al. 2014. Determining Interwell Connectivity and Reservoir Complexity Through Frac Pressure Hits and Production Interference Analysis. Presented at the SPE/CSUR Unconventional Resources Conference – Canada, Calgary, Alberta, Canada. https://doi.org/10.2118/171628-MS.

179. Saurez-Rivera, R., et al. 2016, Optimizing Lateral Landing Depth for Improved Well Production. Presented at the SPE/AAPG/SEG Unconventional Resources Technology Conference, San Antonio, Texas. https://doi.org/10.15530/URTEC-2016-2460515.

180. Schmidt, M., & Sekar, B. K. 2014. Innovative Unconventional EOR-A Light EOR an Unconventional Tertiary Recovery Approach to an Unconventional Bakken Reservoir in Southeast Saskatchewan. Presented at the 21st World Petroleum Congress, Moscow, Russia.

181. Scholz, C. H. 2015. On the stress dependence of the earthquake b value. Geophysical Research Letters, 42 (5): 1399-1402. https://doi.org/10.1002/2014GL062863.

182. Schorlemmer, D., et al. 2005. Variations in earthquake-size distribution across different stress regimes. Nature, 437 (7058): 539-542. https://doi.org/10.1038/nature04094.

183. Schwartz, K. M., et al. 2015. Pay Distributions and Basin Architecture of the Wolfcamp Shale in the Delaware Basin. Presented at the SPE/AAPG/SEG Unconventional Resources Technology Conference, San Antonio, Texas. http://doi.org/10.2118/178613-MS.

184. Seth, P., et al. 2018. Hydraulic Fracture Closure in a Poroelastic Medium and its Implications on Productivity. Presented at the 52nd U.S. Rock Mechanics/ Geomechanics Symposium, Seattle, Washington.

185. Shahri, M., et al. 2021. High Fidelity Fibre-Optic Observations and Resultant Fracture Modeling in Support of Planarity. Presented at the SPE Hydraulic Fracturing Technology Conference and Exhibition, virtual. https://doi.org/10.2118/204172-MS.

186. Shapiro, S. A., & Dinske, C. 2009. Fluid-induced seismicity: Pressure diffusion and hydraulic fracturing. Geophysical Prospecting 57: 301-310. https://doi.org/10.1111/j.1365-2478.2008.00770.x.

187. Sharma, R. K., & Chopra, S. 2015. Determination of lithology and brittleness of rocks with a new attribute. The Leading Edge, 34 (5): 936-941. https://doi.org/10.1190/tle34050554.1.

188. Sharma, M. M., & Manchanda, R. 2015. The Role of Induced Un-propped (IU) Fractures in Unconventional Oil and Gas Wells, Presented at the SPE Annual Technical Conference and Exhibition, Houston, Texas. https://doi.org/10.2118/174946-MS.

189. Sharma, S., et al. 2018. A Comparative Experimental Study of Huff-n-Puff Gas Injection and Surfactant Treatment in Shale Gas-Condensate Cores. Energy & Fuels 32 (9): 9121-9131. https://doi.org/10.1021/acs.energyfuels.8b01816.

190. Sheng, J. J. 2017. Critical review of field EOR projects in shale and tight reservoirs. Journal of Petroleum Science and Engineering 159: 654-665. https://doi.org/10.1016/j.petrol.2017.09.022.

191. Sheng, J. J., & Chen, K. 2014. Evaluation of the EOR potential of gas and water injection in shale oil reservoirs. Journal of Unconventional Oil and Gas Resources 5: 1-9. https://doi.org/10.1016/j.juogr.2013.12.001.

192. Shi, Y., & Bolt, B. A. 1982. The standard error of the magnitude-frequency b value. Bulletin of the Seismological Society of America, 72 (5): 1677-1687. https://doi.org/10.1785/BSSA0720051677.

193. Shrivastava, K., & Sharma, M. M. 2018. Mechanisms for the Formation of Complex Fracture Networks in Naturally Fractured Rocks. Presented at the SPE Hydraulic Fracturing Technology Conference and Exhibition, The Woodlands, Texas. https://doi.org/10.2118/189864-MS.

194. Shrivastava, K., & Sharma, M. M. 2018. Proppant Transport in Complex Fracture Networks. Presented at the SPE Hydraulic Fracturing Technology Conference and Exhibition, The Woodlands, Texas. https://doi.org/10.2118/189895-MS.

195. Shuler, P. J., et al. 2011. Chemical Process for Improved Oil Recovery From Bakken Shale. Presented at the Canadian Unconventional Resources Conference, Calgary, Alberta, Canada. https://doi.org/10.2118/147531-MS.

196. Small, M.J., et al. 2014. Risk and Risk Governance in Unconventional Shale Gas Development. Environmental Science & Technology, 48: 8289-8297. https://doi.org/10.1021/es502111u.

197. Rich, A., et al. 2014. An Exploratory Study of Air Emissions Associated with Shale Gas Development and Production in the Barnett Shale. Journal of the Air and Waste Management Association, 64 (1): 61-72. https://doi.org/10.1080/10962247.2013.832713.

198. Sicking, C., et al. 2013. Permeability field imaging from microseismic. Geophysical Society of Houston Journal, 3: 11–14. http://doi.org/10.1190/segam2012-1383.1.

199. Sil, S., et al. 2012. Analysis of b value from Barnett Shale microseismic data. Presented at the 74th EAGE Annual International Conference and Exhibition, Copenhagen, Denmark. http://doi.org/10.3997/2214-4609.20148490.

200. Soliman, M. Y., et al. 2014. Analysis of fracturing Pressure Data in Heterogeneous Shale Formations. Hydraulic Fracturing Journal, 1 (2), 8-13.

201. Sone, H., & Zoback, M. D. 2013. Mechanical properties of shale-gas reservoir rocks — Part 2: Ductile creep, brittle strength, and their relation to the elastic modulus. Geophysics, 78 (5): D393-D402. http://doi.org/10.1190/geo2013-0051.1.

202. Sookprasong, P. A., et al. 2016. Leveraging Biotechnological Innovation for Improved Oil Production in Shale Formations: A Case Study. Presented at the SPE Asia Pacific Hydraulic Fracturing Conference, Beijing, China. https://doi.org/10.2118/181829-MS.

203. Sorensen, J. A., & Hamling, J. A. 2016. Historical Bakken Test Data Provide Critical Insights on EOR In Tight Oil Plays. The American Oil & Gas Reporter.

204. Staples, E., et al. 2015. Exploration Through Early Appraisal of the Horizontal Wolfcamp Play in the Ozona Area, Southern Midland Basin. Presented at the SPE/AAPG/SEG Unconventional Resources Technology Conference, San Antonio, Texas. https://doi.org/10.15530/URTEC-2015-2154046.

205. Stegent, N. A., & Candler C. 2018. Downhole Microseismic Mapping of More Than 400 Fracturing Stages on a Multiwell Pad at the Hydraulic Fracturing Test Site (HFTS): Discussion of Operational Challenges and Analytic Results. Presented at the SPE/AAPG/SEG Unconventional Resources Technology Conference, Houston, Texas. https://doi.org/10.15530/URTEC-2018-2902311.

206. Stephenson, B., et al. 2018. Origin, Detection, Involvement in Hydraulic Stimulation and Consequences for Field Development of large-scale Structural Lineaments in the Marcellus and Duvernay plays. Presented at the SPE/AAPG/SEG Unconventional Resources Technology Conference (URTeC). Houston, Texas. https://doi.org/10.15530/urtec-2018-2902874.

207. Struchtemeyer C., & Elshahed, M. 2011. Bacterial communities associated with hydraulic fracturing fluids in thermogenic natural gas wells in North Central Texas, USA. FEMS Microbial Ecology, 81(1): 13-25. https://doi.org/10.1111/j.1574-6941.2011.01196.x.

208. Struchtemeyer C., & Elshahed, M. 2012. A crittical assessment of the efficacy of biocides used during the hydraulic fracturing process in shale natural gas wells. International Biodeterioration & Biodegradation, 71: 15-21. https://doi.org/10.1016/j.ibiod.2012.01.013.

209. Stumm, W., & Morgan, J. J. 1981. Aquatic Chemistry. John Wiley & Sons, Inc., Hoboken, NJ. (pp 458-461).

210. Suarez-Rivera, R., et al. 2013. Understanding the Effect of Rock Fabric on Fracture Complexity for Improving Completion Design and Well Performance. Presented at the International Petroleum Technology Conference (IPTC), Beijing, China. https://doi.org/10.2523/IPTC-17018-MS.

211. Saurez-Rivera, R., et al. 2016. Optimizing Lateral Landing Depth for Improved Well Production. Presented at the SPE/AAPG/SEG Unconventional Resources Technology Conference, San Antonio, Texas. https://doi.org/10.15530/URTEC-2016-2460515.

212. Tingdahl, K. M., & de Groot, P. F. M. 2003. Post-stack-dip- and azimuth processing. Journal of Seismic Exploration, 12 (2): 113-126.

213. Todd, H. B., & Evans, J. G. 2016. Improved Oil Recovery IOR Pilot Projects in the Bakken Formation. Presented at the SPE Low Perm Symposium, Denver, Colorado. https://doi.org/10.2118/180270-MS.

214. Trowbridge, S., et al. 2017, Application of Microseismic to Assess Hydraulic Fracture Behavior in Relation to Completion Design and Landing Zone. Paper presented at the SPE/AAPG/SEG Unconventional Resources Technology Conference, Austin, TX. https://doi.org/10.15530/URTEC-2017-2674376.

215. Ugueto, G. A., et al. 2016. Perforation Cluster Efficiency of Cemented Plug and Perf Limited Entry Completions; Insights from Fiber Optics Diagnostics. Presented at the SPE Hydraulic Fracturing Technology Conference, the Woodlands, Texas. http://dx.doi.org/10.2118/179124-MS.

216. Ugueto, G. A., et al. 2021. New Fracture Diagnostic Tool for Unconventionals: High-Resolution Distributed Strain Sensing via Rayleigh Frequency Shift during Production in Hydraulic Fracture Test 2. Presented at the SPE/AAPG/SEG URTeC, Houston, TX. https://doi.org/10.15530/urtec-2021-5408.

217. Umbaugh, S. E. 2010. Digital Image Processing and Analysis: Human and Computer Vision Applications with CVIPtools, second edition. Boca Raton, Florida: CRC Press.

218. USEPA. 2016. Hydraulic Fracturing for Oil and Gas: Impacts from the Hydraulic Fracturing Water Cycle on Drinking Water Resources in the U.S. Report No. EPA-600-R-16-236Fa.

219. Utsu, T. 1999. Representation and Analysis of the Earthquake Size Distribution: A Historical Review and Some New Approaches. Pure and Applied Geophysics, 155: 509-535. https://doi.org/10.1007/s000240050.

220. Vanderplas J., scikit-learn.org, Simple 1D Kernel Density Eastimation

221. Varga, R., et al. 2012. Seismic inversion in the Barnett Shale successfully pinpoints sweet spots to optimize well-bore placement and reduce drilling risks. Presented at the SEG Annual Meeting, Las Vegas, Nevada. https://doi.org/10.1190/segam2012-1266.1.

222. Vermylen, J., & Zoback, M. D. 2011. Hydraulic fracturing, microseismic magnitudes, and stress evolution in the Barnett Shale, Texas, USA. Presented at the SPE Hydraulic Fracturing Technology Conference, The Woodlands, Texas. https://doi.org/10.2118/140507-MS.

223. Voordouw, G., et al. 2009. Sulfide remediation by pulsed injection of nitrate into a low temperature Canadian heavy oil reservoir. Environmental Science and Technology, 43 (24): 9512-9518. https://doi.org/10.1021/es902211j.

224. Wang, Y., et al. 2000. Numerical simulation of rock failure and earthquake process on mesoscopic scale. Pure and Applied Geophysics, 157: 1905. https://doi.org/10.1007/PL00001067.

225. Wang, L., & Yu, W. 2019. Gas Huff and Puff Process in Eagle Ford Shale: Recovery Mechanism Study and Optimization. Presented at the SPE Oklahoma City Oil and Gas Symposium, Oklahoma City, Oklahoma. https://doi.org/10.2118/195185-MS.

226. Wang, X., et al. 2010. Assessment of CO_2 Flooding Potential for Bakken Formation, Saskatchewan. Presented at the Canadian Unconventional Resources and International Petroleum Conference, Calgary, Alberta, Canada. https://doi.org/10.2118/137728-MS.

227. Warpinski, N., & Teufel, L. W. 1987. Influence of Geologic Discontinuities on Hydraulic Fracture Propagation. Journal of Petroleum Technology, 39 (2): 209-220. https://doi.org/10.2118/13224-PA

228. Warpinski, N. R., et al. 1993, Examination of a cored hydraulic fracture in a deep gas well: Society of Petroleum Engineers SPE Production & Facilities, 8 (3): 150–158. https://doi.org/10.2118/22876-PA.

229. Warpinski, N. R., & Mayerhofer, M. J. 2008. Stimulating Unconventional Reservoirs: Maximizing Network Growth While Optimizing Fracture Conductivity. Journal of Canadian Petroleum Technology, 48 (10): 39-51. https://doi.org/10.2118/114173-PA.

230. Warpinski, N. R. 2009. Microseismic Monitoring: Inside and Out. Journal of Petroleum Technology, 61 (11): 80-85. https://doi.org/10.2118/118537-JPT.

231. Warpinski, N. R., et al. 2014. Integrating Fracture Diagnostics for Improved Microseismic Interpretation and Stimulation Modeling. Presented at the Unconventional Resources Technology Conference, Denver, Colorado. https://doi.org/10.15530/URTEC-2014-1917906.

232. Warren, M. N., et al. 2016. Wolfcamp Completions: Lessons Learned through the Implementation of Completion Diagnostics to Optimize Existing Drilling and Stimulation Practices. presented at the SPE Annual Technical Conference and Exhibition, Dubai, UAE. https://doi.org/10.2118/181679-MS.

233. Weijers, L., et al. 2005. Developing Calibrated Fracture Growth Models for Various Formations and Regions across the United States. Presented at the SPE Annual Technical Conference and Exhibition, Dallas, Texas. https://doi.org/10.2118/96080-MS.

234. Weil S. H. 2014. The "New" Horizontal Permian Basin, New Orleans, Louisiana: Howard Weil.

235. Weiss, W. W., & Xie, X. 2007. Oilfield Surfactants Improve Recovery via Imbibition. Presented at the International Symposium on Oilfield Chemistry, Houston, Texas. https://doi.org/10.2118/106402-MS.

236. Weisstein, E. W. 2013. Boxcar Function. From MathWorld-A Wolfram Web Resource. http://mathworld.wolfram.com/BoxcarFunction.html.

237. Weng, X., et al. 2011. Modeling of Hydraulic-Fracture-Network Propagation in a Naturally Fractured Formation. SPE Production & Operations, 26 (4): 368-380. https://doi.org/10.2118/140253-PA.

238. Wessels, S., et al. 2011. Identifying fault activation during hydraulic stimulation in the Barnett shale: source mechanisms, b values, and energy release analyses of microseismicity. Presented at the SEG Annual Meeting, San Antonio, Texas. https://doi.org/10.1190/1.3627478.

239. Wicker, J., et al. 2016. Multivariate Analytics of Seismic Inversion Products to Predict Horizontal Production in the Wolfcamp Formation of the Midland Basin. Presented at the SPE/AAPG/SEG Unconventional Resources Technology Conference, San Antonio, Texas. https://doi.org/10.15530/URTEC-2016-2449798.

240. Wheaton, B., et al. 2016. A Case Study of Completion Effectiveness in the Eagle Ford Shale Using DAS/DTS Observations and Hydraulic Fracture Modeling. Presented at the SPE Hydraulic Fracturing Technology Conference, the Woodlands, Texas. http://doi.org/10.2118/179149-MS.

241. White, T., et al. 2014. Fault and Fracture Characterization From an Integrated Subsurface and Seismic Dataset: Impact on Well Performance of the Wolfcamp Shale, Midland Basin, West Texas. Presented at the SPE/AAPG/SEG Unconventional Resources Technology Conference (URTeC). Denver, Colorado. http://doi.org/10.15530/urtec-2014-1934166.

242. Wiemer, S., & Wyss, M. 2002. Mapping spatial variability of the frequency-magnitude distribution of earthquakes. Advances in Geophysics, 45: 259-302. http://doi.org/10.1016/S0065-2687(02)80007-3.

243. Wilson, T., et al. 2016. Interrelationships of Marcellus Shale gas production to frac-induced microseismicity, interpreted minor faults and fractures zones, and stimulated reservoir volume, Greene County, Pennsylvania. Interpretation 4: T15-T30. http://doi.org/10.1190/INT-2015-0045.1.

244. Wood, T., et al. 2018. Inter-well communication study of UWC and MWC wells in the HFTS. Presented at the SPE/ AAPG/ SEG Unconventional Resources Technology Conference, Houston, Texas. https://doi.org/10.15530/URTEC-2018-2902960.

245. Wright, C. A., et al. 1999. Understanding Hydraulic Fracture Growth: Tricky but Not Hopeless. Presented at the SPE Annual Technical Conference and Exhibition (ATCE). Houston, Texas. https://doi.org/10.2118/56724-MS.

246. Wright, C. A., et al. 1998. Downhole Tiltmeter Fracture Mapping: Finally Measuring Hydraulic Fracture Dimensions. Presented at the SPE Western Regional Meeting, Bakersfield, California. https://doi.org/10.2118/46194-MS.

247. Wu, C., et al. 2017. Proppant Distribution among Multiple Perforation Clusters in a Horizontal Wellbore. Presented at the SPE Hydraulic Fracturing Technology Conference, the Woodlands, Texas. https://doi.org/10.2118/184861-PA.

248. Xu, S., & Zoback, M. D. 2015. Analysis of Stress Variations with depth in the Permian Basin Spraberry/ Dean/ Wolfcamp Shale. Presented at the 49th U.S. Rock Mechanics/Geomechanics Symposium. San Francisco, California.

249. Yang, H. D., & Wadleigh, E. E. 2000. Dilute Surfactant IOR - Design Improvement for Massive, Fractured Carbonate Applications. Presented at the SPE International Petroleum Conference and Exhibition in Mexico, Villahermosa, Mexico. https://doi.org/10.2118/59009-MS.

250. Yu, W., et al. 2014. Simulation Study of CO_2 Huff-n-Puff Process in Bakken Tight Oil Reservoirs. Presented at the SPE Western North American and Rocky Mountain Joint Meeting, Denver, Colorado. https://doi.org/10.2118/169575-MS.

251. Yuen, H. K., et al. 1990. Comparative study of Hough transform methods for circle finding. Image and Vision Computing, 8: 71-77. https://doi.org/10.1016/0262-8856(90)90059-E.

252. Zakhour, N., et al. 2021. HFTS-2 Completions Design and State-of-the-Art Diagnostics Results. Presented at the SPE/AAPG/SEG Unconventional Resources Technology Conference, Houston, Texas. https://doi.org/10.15530/urtec-2021-5242.

253. Zecevic, M., et al. 2016. Questioning the Existence of Hydraulic Fracturing-Induced LPLD Events in a Barnett Shale, Texas, Microseismic Dataset. Presented at the Sixth EAGE Workshop on Passive Seismic, 2016: 1-5. http://dx.doi.org/10.3997/2214-4609.201600004.

254. Zhang, F., et al. 2019. Experimental and Numerical Studies of EOR for the Wolfcamp Formation by Surfactant Enriched Completion Fluids and Multi-Cycle Surfactant Injection. Presented at the SPE Hydraulic Fracturing Technology Conference and Exhibition. The Woodlands, Texas. https://doi.org/10.2118/194325-MS.

255. Zhang, Z., et al. 2020. Fiber Optic Strain Monitoring of Hydraulic Stimulation: Geomechanical Modeling and Sensitivity Analysis. Presented at the SPE/AAPG/SEG Unconventional Resources Technology Conference, virtual. https://doi.org/10.15530/urtec-2020-2648.

Appendix A: Phase 1 Fracture Characterization by BEG

Research Entity: Bureau of Economic Geology, The University of Texas at Austin

Final Report, March 24, 2017

Prepared by Julia F. W. Gale

Research by Julia F. W. Gale, Sara J. Elliott, John Z. Li, and Stephanie Forstner

Acknowledgement:

This material is based upon work supported by the Department of Energy under Award Number DE-FE0024292.

Disclaimer:

This report was prepared as an account of work sponsored by an agency of the United States Government. Neither the United States Government nor any agency thereof, nor any of their employees, makes any warranty, express or implied, or assumes any legal liability or responsibility for the accuracy, completeness, or usefulness of any information, apparatus, product, or process disclosed, or represents that its use would not infringe privately owned rights. Reference herein to any specific commercial product, process, or service by trade name, trademark, manufacturer, or otherwise does not necessarily constitute or imply its endorsement, recommendation, or favoring by the United States Government or any agency thereof. The views and opinions of authors expressed herein do not necessarily state or reflect those of the United States Government or any agency thereof.

Project findings covered in this report.

LAREDO_SuggA171_6TW Slant Well Fracture Characterization: Systematic Description

A systematic fracture description was accomplished for the six cores (four continuous in the Upper Wolfcamp and two continuous in the Middle Wolfcamp) from the Sugg 171 6TW Slant Well over the summer of 2016 at CoreLab and was completed August 18th, 2016. The completed description spreadsheet for all cores has been uploaded to the project website. The orientation data collected by ConocoPhillips have been integrated with the Bureau of Economic Geology (BEG) fracture descriptions, and each fracture is described and classified together with an uncertainty indicator. This report explains the methodology and summarizes the key findings.

LAREDO_SuggA171_6TW Slant Well Fracture Characterization: Systematic Description Methodology

Slant core: acquisition, handling, and preparation for analysis

Recommendations for locations of cores along the wells were deliberated at length during conference calls in early 2016 and during the project workshop in Tulsa (Feb 4, 2016), taking all new data into account to provide the best chance for the slant core to capture hydraulic fractures from two nearby wells (6SM and 6SU). BEG participated in these discussions and recommendations. Drilling of the six cores was successful, with 600 ft of core being recovered.

CT scans were made by CoreLab prior to core observation. These were high quality and invaluable for mapping fractures in the core. All fractures in the core were compared with those seen in the CT scan so that any fractures caused by core handling after the CT scans were done, or that were the result of core desiccation, could be identified as such. The CT scans provide clear imagery of lithology changes, bedding, sealed natural fractures, and open fractures. Most 3-ft intervals contain fractures, but some intervals do not. The spatial organization of fractures along the core is therefore heterogeneous and is analyzed in this report.

Considerable effort was spent in deciding on the best methods for handling core. The priority was clearly defined as an understanding of the hydraulic fracture system and its potential interaction with natural discontinuities, natural fractures in particular.

Three methods were tested:

(1) The aluminum sleeve was cut in a "clam shell", a 50:50 cut subparallel to bedding (Fig. 1).

(2) Two 2-ft sections were stabilized with red-stained epoxy prior to slabbing (Fig. 2).

(3) The core was slabbed while in the aluminum sleeve but without epoxy stabilization (Fig. 3).

Method 1

Only the aluminum sleeve was cut, core fractures being revealed and held in place somewhat by the sleeve. Once the analysis was done, the whole assembly (core and sleeve) was put back together and secured with shrink wrap for storage. This method was found to be the best of the ones tested.

The 3-ft section tested, from 9,408 to 9,411 ft (Fig. 1), contains a natural fracture and several hydraulic fractures. The natural fracture, which is steeply dipping, contains calcite cement, and the hydraulic fracture appears to be diverted along it for approximately 1 cm before reverting to its original path. This relationship can also be seen in the CT-scan image and is consistent with behavior seen in laboratory experiments in which a propagating crack interacts with a cement-filled natural fracture (Lee et al., 2015). In these cases, whether the hydraulic fracture arrests, diverts, or terminates against the natural fracture is determined by the angle of approach and the thickness of the natural fracture. The cement thickness on the natural fracture in this section is less than 1 mm. The carbonate concretion at the bottom of this 3-ft section could not easily be seen in the core because of the challenge of observing composition and texture on the rough, outer surface of the whole core. The outline of the concretion could be discerned using the CT scan as a guide.

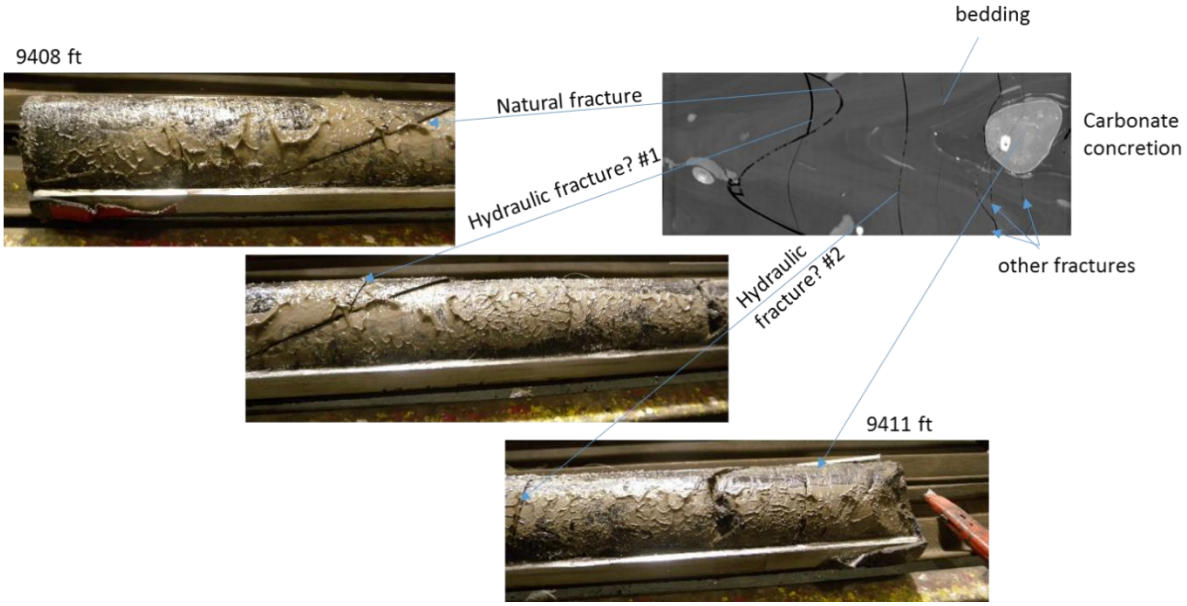


Figure 1. Core is left whole while aluminum sleeve is bisected and opened to reveal core (so-called "clam-shell" method). Example first tested on section between 9,408 and 9,411 ft, where core has several fractures. Fractures were easily examined after drilling mud had been scraped off. Core pieces could be taken out and replaced, and aluminum sleeve could be replaced once examination was complete. Damage to core was minimized using this method.

Method 2

The sections that were epoxied (9,312–9,315 and 9,375–9,376.2 ft) and then slabbed subparallel to bedding were stabilized, but the fracture surfaces are no longer visible (Fig. 2a). Although this technique prevents further breakup of the core, it is the least desirable option because inspection of the fracture surfaces is essential for determining fracture origin. Also, introduction of epoxy had widened some of the fractures considerably (up to 1 cm), so the geometry now observed is not the true, original fracture geometry (Fig. 2b). We decided that no further sections should be epoxied.

Method 3

In this method the core was slabbed in the sleeve with no stabilization (Fig. 3). The CT scan showed that this short section from 9,539 to 9,541 ft had several fractures in it. Once cut open, even with a 50:50 cut, the pieces of core could not easily be taken out of the halved sleeve and had to be turned out for observation of fracture faces. This activity resulted in new fractures

being created in the core (Fig. 3). The team therefore decided that slabbing, even with the core in the sleeve, was too damaging and should not be done for most of the core. A few intervals that are of critical interest from a sedimentological standpoint may be slabbed in the future, after a full fracture description has been completed. We strongly recommend that we preserve most of this core as whole core for a better understanding of the fractures and for teaching. A core of this kind is rare and has tremendous value. Slabbing can introduce breaks and will present practical problems for how to show the core halves together in the future. Preservation in the aluminum sleeve remains the best option for maintaining it for future inspection and reducing degradation.

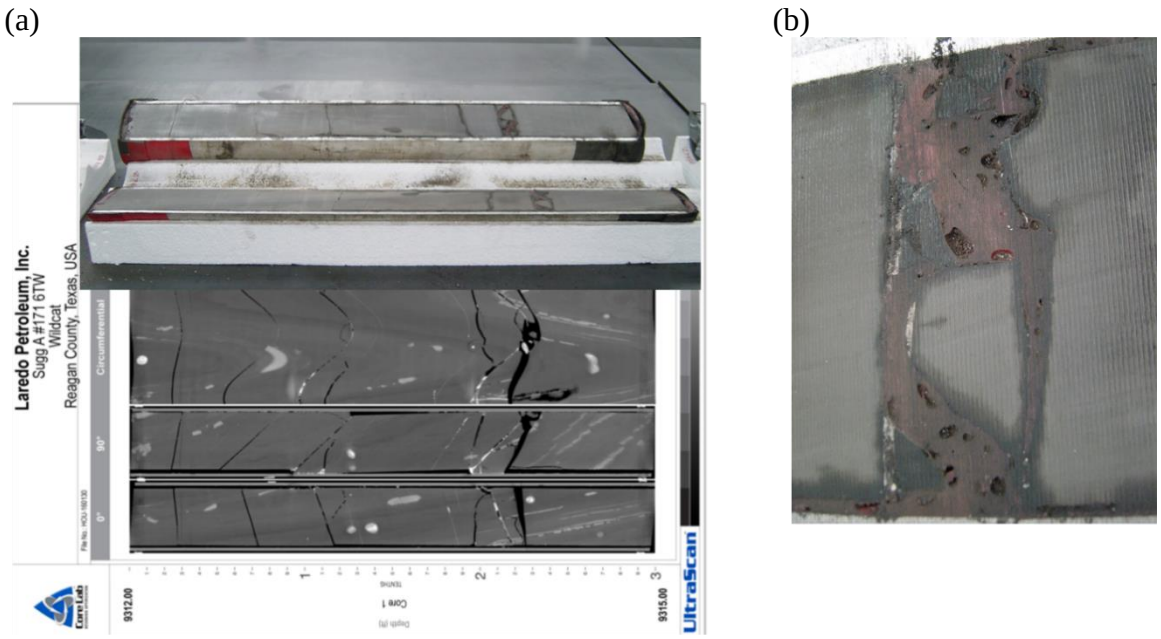


Figure 2. (a) CT scan and photograph of slabbed core from 9,312 to 9,315 ft measured depth (MD). This core section has multiple breaks and was treated with red epoxy prior to slabbing. (b) Force of introducing epoxy (red material) had widened existing fractures from 1 to 2 mm to around 1 cm in places.

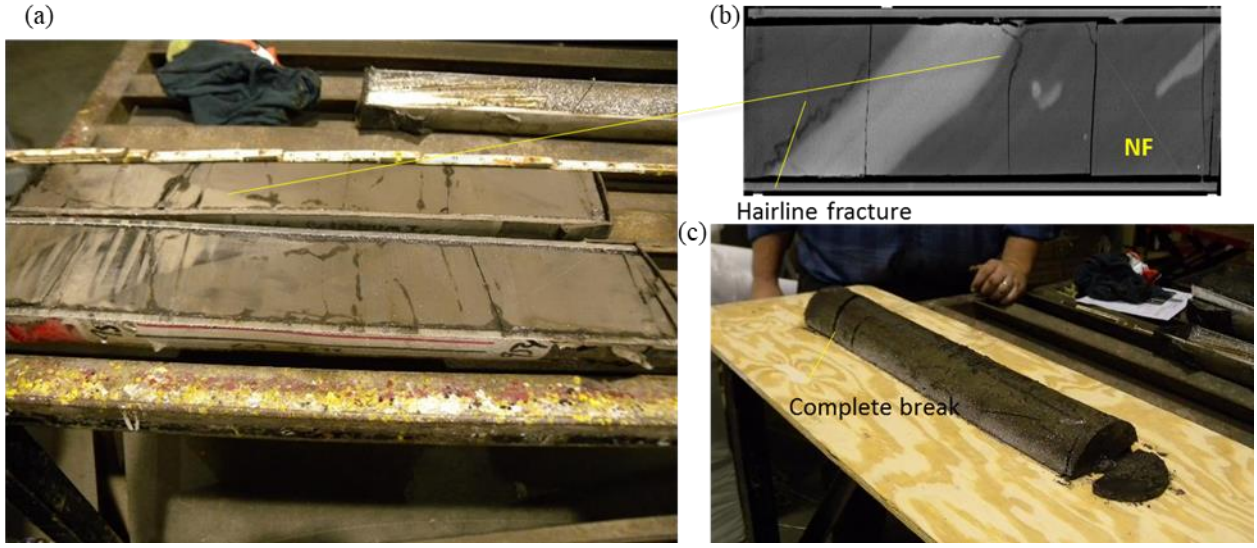


Figure 3. Core section from 9,539 to 9,541 ft. (a) Slabbed section inside aluminum sleeve. (b) Slice through CT scan of this interval. Pale layer is carbonate and can be seen in whole core in a. Fracture faces cannot be observed without removing core from sleeve. (c) Core has been removed from sleeve and inverted on the workbench. The act of slabbing and removing core from sleeve has generated new break, which is visible as partial hairline fracture on CT scan.

Slant core: proppant analysis

A protocol for collecting sludge from each core section was developed. Sludge comprises drilling mud, rock fragments, aluminum shavings, and possible proppant. The aluminum sleeve was scraped out and sludge scraped off the core exterior. Scrapings for each 3-ft section were stored together in a glass jar and Ziploc plastic bag and sent to GTI, where they are being analyzed for proppant. Separately, during core analysis, all open fractures were scraped or washed to collect any proppant. These samples are currently at BEG, where they are being analyzed. The full report on proppant analysis will be provided at a later date, when analysis is finished. This step was not part of the original project deliverables but was regarded as being necessary for the best chance at detecting proppant and associating it with particular fractures. The work will require further modest funding to complete; a proposal and budget are being prepared for consideration.

Results—spreadsheet format

The systematic description for fractures in all cores is presented in spreadsheet format. Each spreadsheet for the core description shows information on depth, orientation, lateral and vertical extent, morphology and surface features, presence of proppant pack, aperture and fill of natural fractures, information on faults, and an assessment of fracture origin, together with a measure of certainty of interpretation (Fig. 4). Fractures are reported by depth interval (3-ft core sections). The color coding provides a visual impression of the occurrence of hydraulic fractures, natural fractures of different sets, and faults (Fig. 5). Notes on each provide additional information about interpretation of the fracture.

Fracture descriptions are organized so that each core is reported in a separate worksheet within the Master Fracture Description Excel spreadsheet. The format for each core is the same. Here we provide a brief explanation of the methodology and terminology used under the column headers.

CORE 4 — Proppant analysis separate — Observer name: Julia Gale, Sara Elliott — 17 Me

Orientations measured from core by ConocoPhillips (given to 1 dp) — Core diameter: tated (some intervals were test slabbed)

Depth and number				Orientation		Extent	Morphology & Surface features			Proppant	Aperture and fill				Faults		Fracture origin		
3 ft interval measured depth range (ft)	Fracture measured depth of upper terminus (ft, to nearest 0.05 ft)	Fracture number BEG	Fracture number ConocoPhillips	Fracture dip	Fracture dip direction	Termination of tips (upper and lower)	Fracture shape	Fracture surface characteristics	Local propagation direction from twist hackles or bifurcation	Proppant found or embedded?	Kinematic aperture (mm)	Mineralization type in fractures	Mineral character	Completeness of filling (%)	Sense of displacement and amount	Rake of slickensides relative to horizontal looking downdip	Fracture origin	Certainty of fracture origin	Notes
						MS= at mudstone	P = planar	SL = Slickensides		NA not applicable -	WM = wall missing	Q= quartz	B = blocky, subhedral	> unknown			N = natural (color for Set 1)	S = sure	
						OC= out of core	C = curved	PL = plumose		fracture not open	HL=hair line	cc = calcite	F = fibrous	) cement seen			NR natural reactivated (color for Set 2)	P = probable	
						GT= gradual taper	I=regular	TH = twist hackles			P = parted	D= dolomite	D=Drusy		N = normal		HF = hydraulic fracture	BG = best guess	
						AB= abrupt at bedding plane	PS - planar stepped	AL = arrest lines				G = gypsum	A=Amorphous		R = reverse		D= drilling induced		
						AF= abrupt at fracture	PSp planar spiral					B = bitumen	V = veneer		S= strike slip		CH = core handling induced		
						NA= no info available		S=smooth				CL=clay	ind = indeterminate		O= oblique		CB = connection break		
						BS= at bedding slip surface		R = rough				none			ind = indeterminate		F = Fault		
																	BP = Bed-parallel natural		
																	N = natural fracture (color for pre Set 1)		
																	N = natural fracture (color for N-S)		
																	NO FRACTURES		
9590-9593	9590.05	–	429	89.5	213.9	upper OC lower OC	P					none					HF	BG	This
	9590.05	1 a, b	430	87.5	132.3	upper OC lower OC	P				0.62	cc	B	100			N	S	Set 1
	9590.45	2	431	84.7	20.9	upper OC lower OC	P	S TH	down			none					HF	P	Twist
	9591.60	3	–			upper GT lower GT	P				0.14	cc	B	100			N	S	Set 1

Figure 4. Screen shot of header and first 3-ft section of Core 4 fracture description. This core is over 100 ft long.

Depth and number

Cores are cut into intervals, mostly 3 ft, some 2 or 1 ft, and some at nonstandard lengths owing to core breakage or termination. The core description is set out so that each interval has a block— the measured depth (MD) range is given in Column A. For our description, the MD is the uphole limit, whereas ConocoPhillips analysts Seth Busetti and Helen Farrell (COP) recorded the MD at which the fracture crosses their green datum line (core top). Fracture

identification numbers were recorded differently. We numbered fractures 1 through X for each section, whereas COP numbered their fracture picks sequentially from 1 to 707. In both cases, some fractures were added after the numbers had been created following further inspection. We numbered additions as fractions, such as 2.5, depending on location relative to other fractures, or as 2a, 2b, etc., if they appeared related to a main fracture. COP have some out of sequence numbers in their analysis that reflect the order that they numbered them. Both numbers are shown in the spreadsheets for cross-referencing. Most of the fractures recognized are common to both data sets, but both studies identified fractures not recorded by the other team. These are marked with —.

Orientation

Numbers in the orientation columns were provided by COP. We did not independently measure fractures, although we performed a qualitative check that numbers were consistent with our interpretation. There are a few sections in Core 4 (9,628–9,634 ft and 9,655–9,667 ft) in which the orientation given by COP does not match our interpretation of fracture set. In these locations, bedding is not easily discernable, and we think it likely that the green datum line used by COP is on the base of the core rather than the top. In these sections (indicated in red numbering on the spreadsheets), orientations are likely to be rotated by 180° from where they should be. For drilling-induced and hydraulic fractures at a high angle to the well bore, the error is not significant, but for natural fractures, it would need correcting.

The CT-scan datum is not consistent relative to the bedding tops. In this way, the two cross sections in the CT panels are misleading because they do not necessarily represent the bed-parallel and vertical sections they are designed for. In some cases, the datum is on the top (orange and yellow lines close together), in some cases the datum is close to the base (orange and yellow lines on opposite sides of the core), and in others the datum is in between the top and base. Using the CT scan will therefore require corrections for the bedding tops. In a few places, however, the bedding dip and core axis become close because of either well-bore undulation or change in bedding orientation. Bedding undulates around concretions as well. The dip meter on the image log should be used to discern whether the changes are associated with the bedding. Also, the drillers' report should show any well-bore deviation, which will have to be combined for orientation corrections.

For direct measurement from core, the challenge is to find the top and to know the well plunge, although complications from the CT scan can be avoided. The image log can help also, where concretions are present. The practicality of handling some of the less-clean breaks and broken-up sections is a greater difficulty.

Lateral and vertical extent

Lateral and vertical extent refers to the length and height of fractures. Most fractures continue beyond core boundaries, and for these we use the label OC (out of core). If the fracture terminates within the core, we distinguish between abrupt termination at a lithologic change, bedding plane or another fracture, and a gradual taper. Both upper and lower terminations are recorded. For fractures contained within the core, the length or height is recorded in the notes column.

Morphology and surface features

The fracture may be planar, curviplanar, or irregular. The surface markings, which include slickensides, plumose, twist hackles, and arrest lines, are described in detail in the results section. A broad appraisal of rough versus smooth for the face can help in distinguishing breaks that occurred under considerable confining stress in the subsurface, versus those made during core retrieval or handling.

Proppant

The main proppant analysis is not yet complete and will be reported separately. In this column (in red), the occurrence of sand patches, colored grains, and thick proppant packs is noted.

Aperture and fill

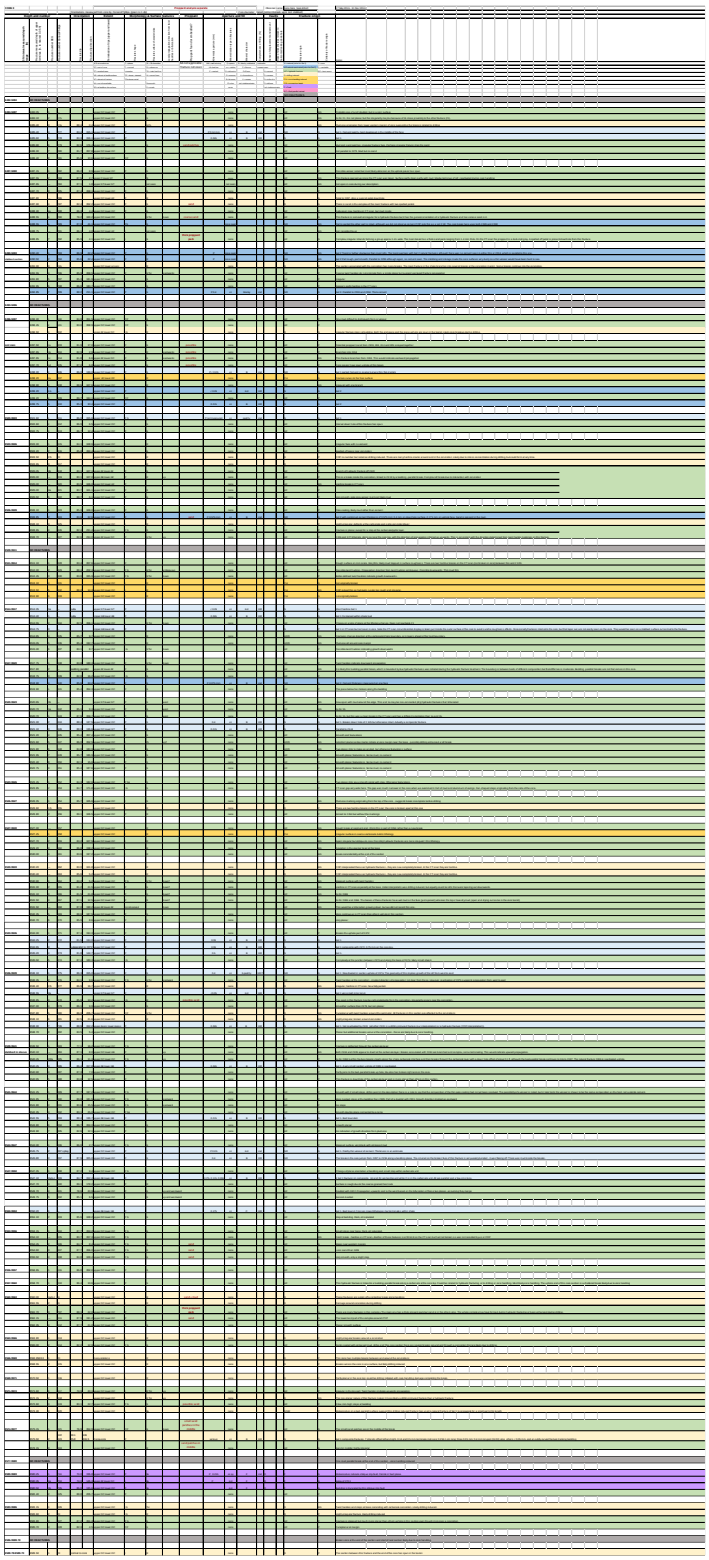


Figure 5. Core 3 description panel. Full scale in App. A. Hydraulic fractures, green; natural fractures, blue; drilling-induced and core-handling fractures, yellow; and faults, pink. This scale gives a sense of fracture-type distribution.

Fracture width (kinematic aperture) is the wall-to-wall distance measured normal to the fracture and which includes mineral fill and the opening. For intact fractures in the slant core that are mostly less than 1 mm wide, we used a comparator to measure the aperture—a ruler with calibrated widths already marked so that fracture width can be compared, and measurements thus binned. For parted fractures, we can measure thickness of the cement on walls and report it as a minimum aperture.

If filled, the mineral cement type is noted. In the slant well, the dominant mineral is calcite, with some minor pyrite. The crystal habit is also noted, with most fractures having a blocky/subhedral texture. We did not observe fibrous fills. A very few fracture fills have a drusy habit, suggesting some original fracture porosity. Many fracture faces have a pale-gray coating, which is described as a veneer; it can be difficult to tell a calcite veneer from a thin layer of mud in some places. The completeness of fill is given as a percentage. Where attributes cannot be quantified or observed, the term indeterminate is used. Not seen means that the attribute was expected based on other features but could not be seen.

Faults

The sense of displacement, and orientation of slickensides on the fracture surface are recorded where possible.

Fracture origin

Each fracture is described and classified, together with an uncertainty indicator—sure, probable, and best guess. We reserved the sure category for natural fractures in which cement could be seen or for hydraulic fractures in which a thick proppant pack or proppant patches are present. Otherwise, most hydraulic fractures are classed as probable, given the uncertainty as to whether they could be drilling induced. Best guess, the least-certain classification, is made on the basis of a combination of features such as orientation, morphology, and surface features. Details of the reasoning are given in the Notes column.

Summary of Results and Criteria for Fracture Classification

Here we outline criteria, developed in collaboration with Helen Farrell and Seth Busetti (ConocoPhillips), that we used to classify different fracture types and to identify mechanisms of reactivation. In some cases, classification and mechanisms are equivocal. In the fracture-description spreadsheets we use a three-tier measure of uncertainty for each classification: sure, probable, and best-guess.

Possible fracture types in chronological order of formation:

Natural fractures

We identified two main sets of natural opening-mode fractures filled with calcite cement, trending broadly NE-SW (Figs. 6a, 7a) and WNW-ESE (Figs. 6b, 7b), both with steep dips. Natural fractures are identified primarily based on calcite mineral fill. Fractures may be sealed and intact, may be partly sealed and intact (original fracture porosity), or may be parted (Fig. 6a). In the latter case, cement can be seen on the fracture wall(s). This cement can be subtle and present as a patchy veneer on one or both surfaces. In one location (9,292.8 ft in Core 1) a Set 1 natural fracture has euhedral calcite cement on the surface, indicating it was open in the subsurface (Fig. 6c). We did not measure the kinematic aperture because the fracture is now parted, but estimate it was > 1 mm wide. Some rounded grains were seen under a binocular microscope between the angular crystals. We interpreted these as possible proppant caught up in the irregular surface. It is not known if these were introduced during hydraulic fracturing or drilling.

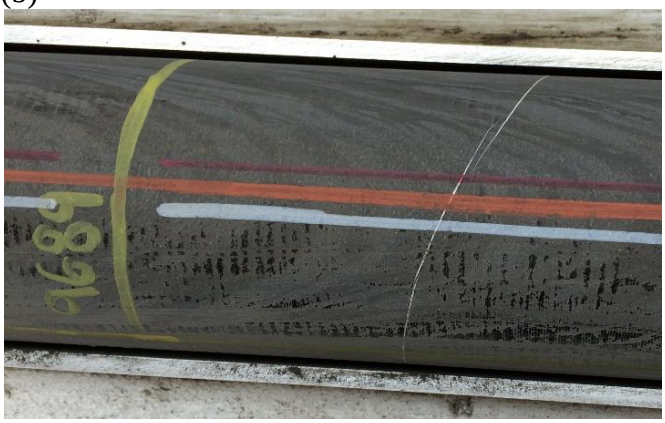
In some fractures positive cement identification is challenging—dried drilling mud can also resemble a pale cement veneer. The mud reacts with dilute HCl (owing to carbonate entrained

in the mud) so that an acid drop test cannot be used to identify cement. A small chip from a fracture surface at the end of one core was imaged and examined using SEM-based EDS. The veneer proved to be dried drilling mud in this case. Where positive identification of cement is not possible, orientation is a useful indicator of fracture origin, but it is not definitive by itself.

(a)



(b)



(c)



Figure 6. Natural fractures. (a) Parted, Set 1 fracture with patchy calcite on fracture face, 9,365.10 ft. MD. (b) Intact, Set 2 composite fracture, 9,689.35 ft. MD; three segments, middle segment is offset uphole from the other two by a few millimeters. Deviation of the paths at the fracture tips indicates stresses ahead of the tips were modified by the presence of the approaching neighbor. (c) Euhedral crystals on fracture face at 9,292.8 ft.

The natural, calcite-filled fractures in this well are typical of fractures in shale, occurring as narrow, composite groups typically less than 1 mm wide. The smallest are only a few centimeters in length and height, and the largest are perhaps 1 m or so long and high (but continue out of the core). Some are bed bound. In future work we plan to analyze aperture-size distributions of the different sets; this information can be helpful in modeling natural-fracture distribution, which may be needed as input for some hydraulic-fracture models that take into account the interaction of hydraulic fractures and discontinuities in the reservoir, such as bedding planes, opening-mode fractures, and faults. There are minor occurrences of other natural-fracture types, including those internal to concretions and those related to deformation around concretions (Fig. 8).

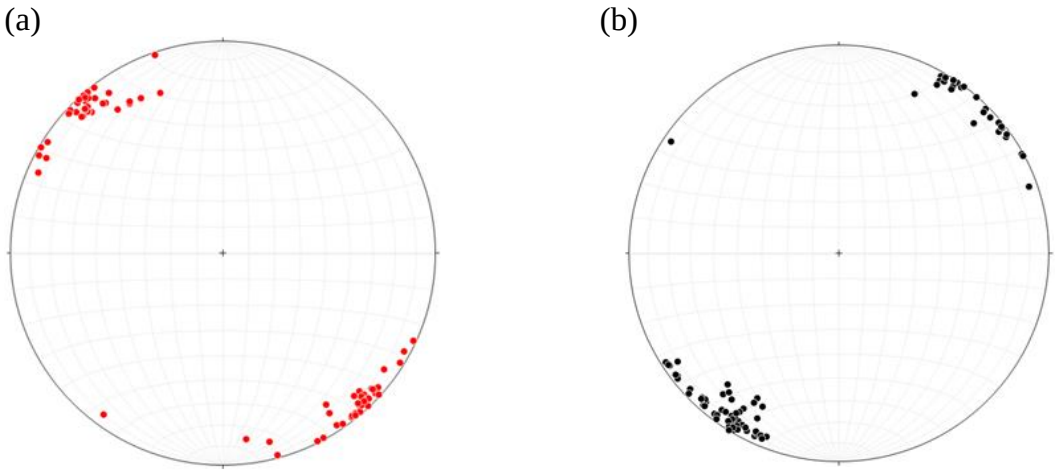


Figure 7. Lower-hemisphere stereograms of poles to calcite-filled natural fractures. (a) Set 1. (b) Set 2. Data from ConocoPhillips analysis.

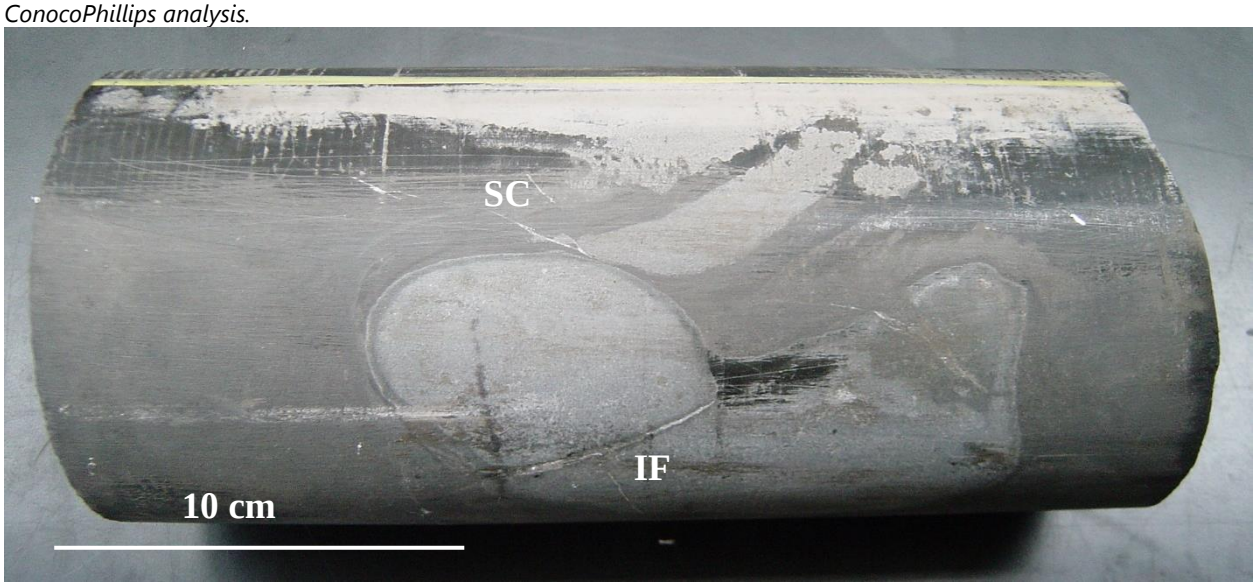


Figure 8. Calcite-filled fractures associated with concretions. Some fractures are internal to concretions stopping at boundaries (IF). Others develop in shale surrounding concretions (SC) and most likely develop as result of strain localization around concretion. Example from Core 4 at 9,667 ft.

Natural, bedding-parallel fractures are uncommon, occurring only around a few concretions. The core orientation and roughness of the outer surface, however, are not optimal for seeing narrow (< 1-mm-wide), bed-parallel fractures filled with calcite. Also, such fractures are challenging to distinguish from carbonate laminae on the CT scan. A few concretions have fractures on both margins with both calcite and pyrite fill, and there are also a few examples of pyrite-filled fractures internal to concretions. Other fractures in different orientations, filled with calcite and pyrite and having width:length aspect ratios that are generally higher than those of the Set 1 and Set 2 fractures, are present in a few locations, mostly in Core 4 close to faults.

There are two types of fault: early, soft-sediment deformation faults (Fig. 8a) and later, moderately dipping structures with oblique slip indicated by slickensides on the fault walls (Fig. 8a–c). In the fault at 9,675.65 ft MD in Core 4, dip azimuth 22.5°/dip 57.4°, the slickensides suggest normal and dextral components of oblique slip. Some have a small amount of calcite cement. There are a total of 11 faults in the Upper Wolfcamp, 7 of them in Core 4, but none was observed in the Middle Wolfcamp.

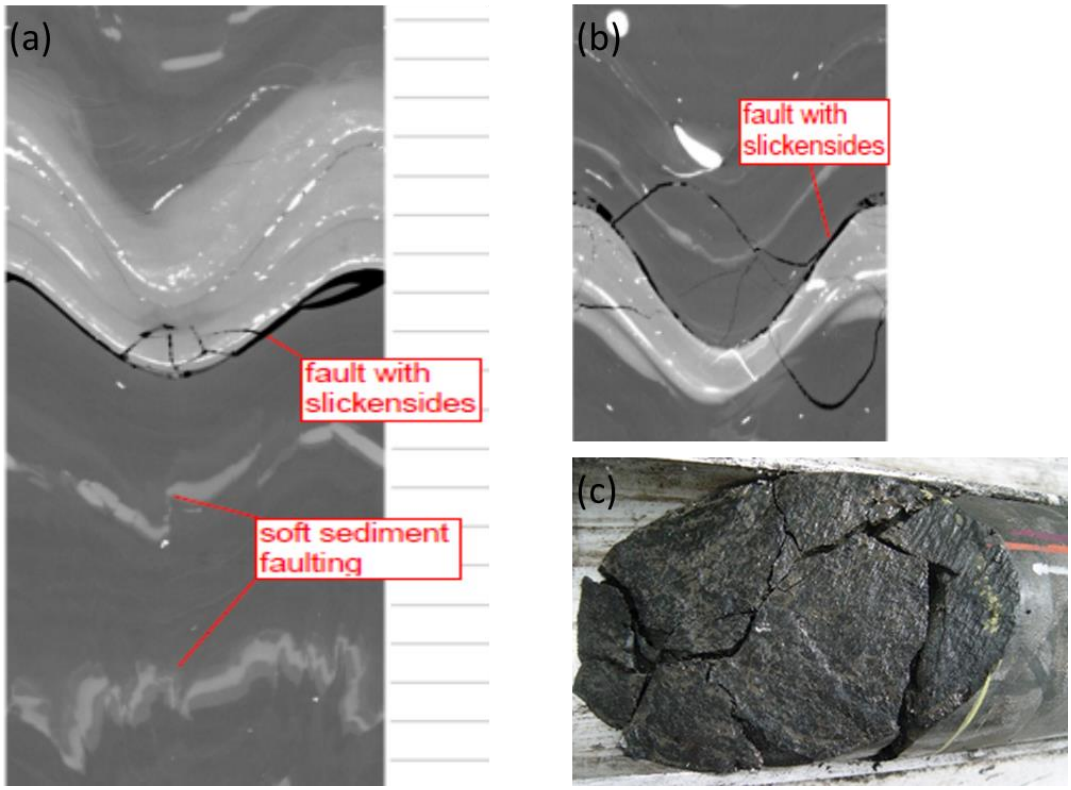


Figure 8. Faults in Core 4 at 9,675–9,681 ft MD. (a) CT scan of faulting and soft-sediment deformation (9,678–9,681 ft). (b) CT scan of fault in c, which has oblique slickensides.

Hydraulic fractures

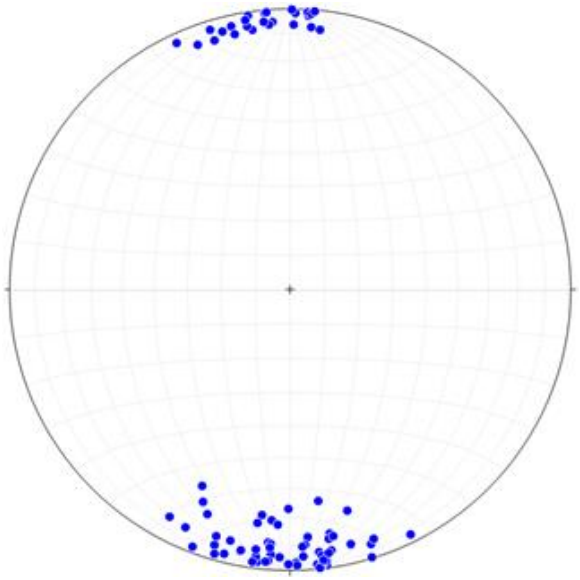


Figure 9. Lower-hemisphere stereogram of poles to hydraulic fractures. Data from ConocoPhillips analysis; n = 321.

A large number of barren, core-normal fractures are present, broadly trending E-W, which is subparallel to SHmax in this part of the Midland Basin. Hydraulic fractures are large planes of varying complexity that have been intersected by the core. Features on the fracture surfaces, such as twist hackles and plumose markings developed at the time of fracturing, are not related to the drilling process; they do not originate near the core margin and are not core symmetric. We identified 323 hydraulic fractures in the Upper Wolfcamp cores and 51 in the Middle Wolfcamp, totaling 374. COP identified 321 measurable hydraulic fractures; the stereogram plotted from their data reveals an approximately 40° spread of dip azimuth, which may reflect local stress variations (Fig. 9).

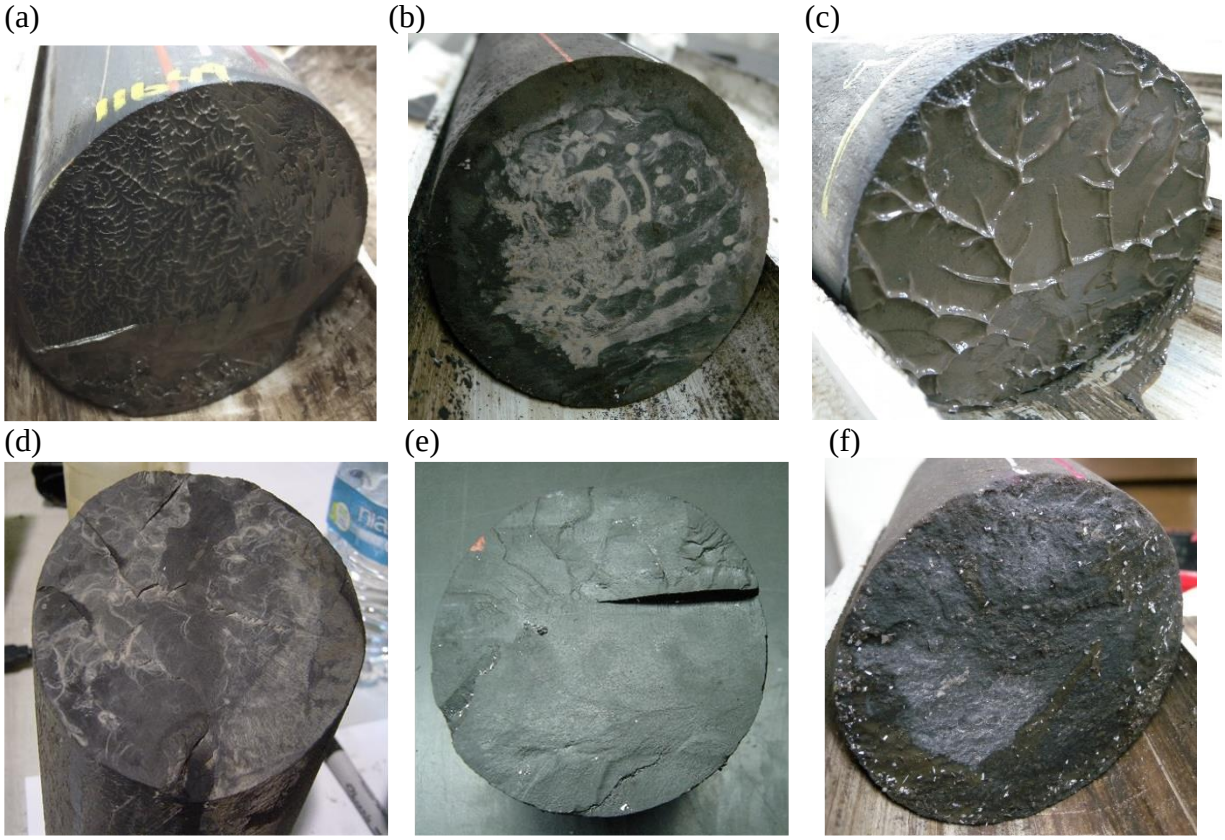


Figure 10. Surface character of hydraulic fractures at time of core description. Measured depth is given for each. (a) 11,649 ft, smooth face with one step and wet mud. (b) 9,522.75 ft, smooth, planar, featureless face with dried mud in center and wet mud around perimeter. (c) 9,565 ft, smooth, planar surface with thick drilling mud and no obvious sand. Note that this fracture is just 3.3 ft below the complex at 9,561.70 ft that has thick proppant sand pack (Fig. 14). (d) 9,287.5 ft, stepped, somewhat irregular face. (e) 9,398.5 ft, partly smooth face with one large step. (f) 9,527.7 ft, somewhat irregular face in coarser carbonate layer.

Commonly two to three hydraulic fractures (HFs) occur per 3-ft section, although some sections have many more (e.g., nine HFs in 9,520–9,523 ft) and some have none, including the four sections from 11,634 to 11,645 ft. Many are single planar breaks with smooth surfaces, sometimes with a stepped geometry (Fig. 10). In other cases, two or more breaks are closely spaced, suggesting bifurcation. Clusters of two to four core-normal fractures in the space of a few centimeters are a common occurrence and may be multiple hydraulic-fracture strands. In rare cases, bifurcation is captured in the core (Fig. 11) and can be used to infer the direction of hydraulic-fracture growth.

In addition to bifurcation, surface markings such as twist hackles may be used to determine local propagation direction of the fracture (Fig. 12). Twist hackles initiating at mechanical layer changes are orthogonal to the layer and gradually taper out away from the point of initiation. These may be used to indicate the direction of hydraulic-fracture propagation. Multiple examples of twist hackles can be found in the slant core, some suggesting upward propagation, others downward.

Note that both upward and downward propagation can occur in close proximity, depending on the location the core intersects the fracture plane (Fig. 13). The lateral propagation direction, however, should be determinable from the asymmetry of the twist hackles (c.f., Fig. 13). If the location of the hydraulically fractured wells relative to the slant well is known, the direction of propagation should be predictable and can be compared with observations. For the Upper Wolfcamp, the hydraulically fractured well (6SU) crosses the slant well at around

9,510 ft MD (in Core 3) and lies to the east of it, so Cores 1, 2, and part of 3 are above the 6SU. In these cores, hydraulic fractures should propagate upward and to the west, whereas the lower part of 3 and Core 4 are below the 6SU, and fractures should propagate downward, although still to the west. In the Middle Wolfcamp, hydraulic fractures would have propagated up from the 6SM toward the east.

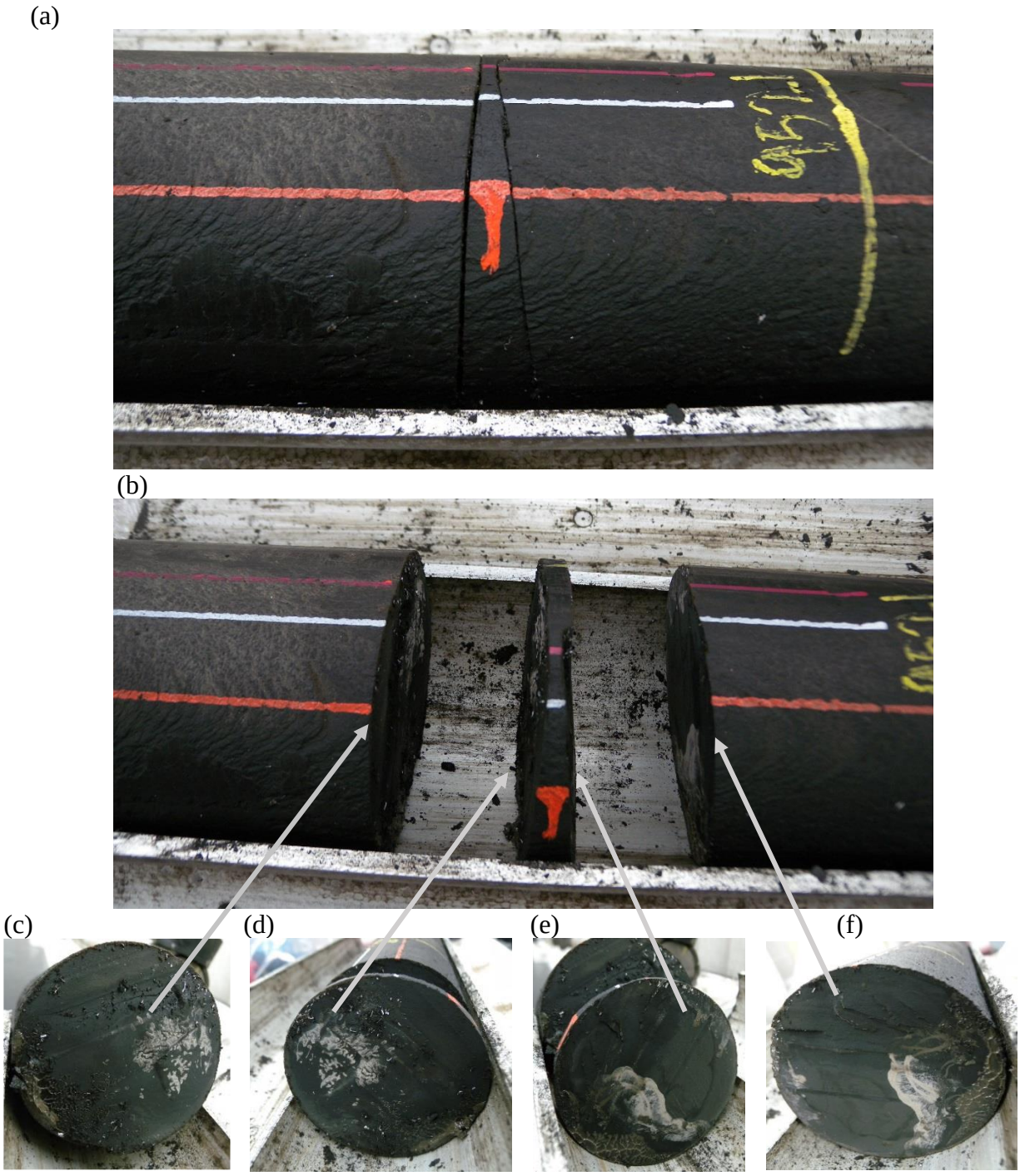


Figure 11. Hydraulic-fracture doublet indicating propagation to the west (orange mark = core top). (a) Whole core with two nonparallel fractures. (b) Core pieces pulled apart. (d–f) Fracture faces in b. (f) Example from Core 3 just above 9,521 ft.

Some examples of twist hackles have anomalous orientations. At 9,372.45 ft in Core 1, twist hackles initiate off bedding and suggest local downward propagation (Fig. 14). Twist-hackle asymmetry suggests that overall propagation is to the east, but the 6SU is below and to the east at this location. Hydraulic fractures would therefore be expected to grow up and to the west. A possible explanation is that the premise that fractures always propagate away from the

well bore may not be correct. If fractures initiate away from the well bore because of stress perturbation driven by hydraulic fracturing, then they may propagate laterally in opposing directions at the same time. We propose further, systematic analysis of all propagation-direction indicators in the slant core in an effort to explain the apparent anomalies in inferred propagation direction.

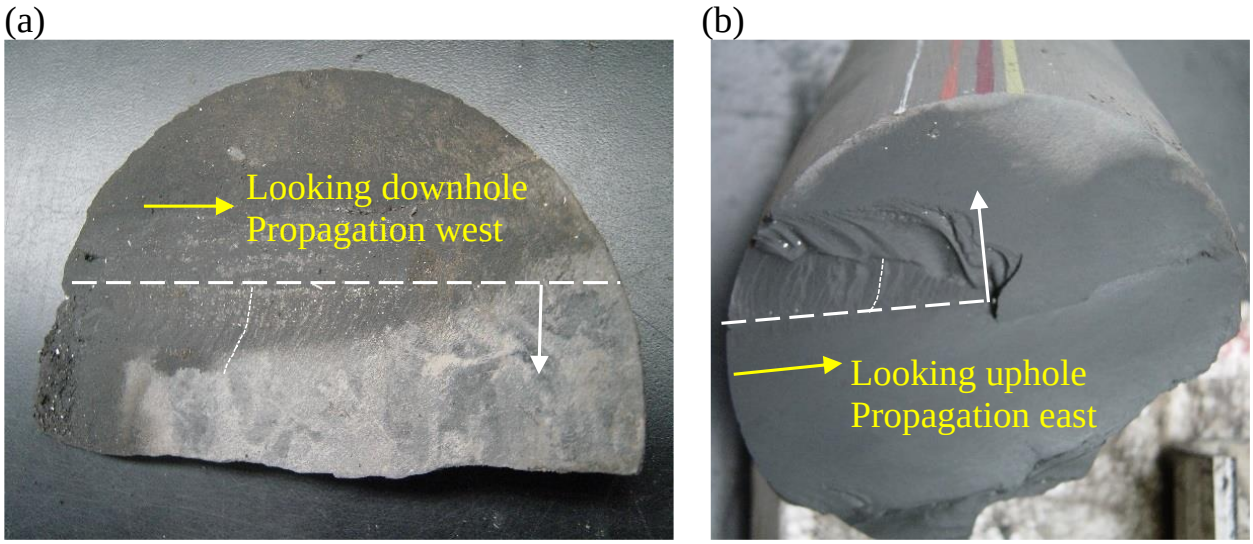


Figure 12. Examples of twist hackles (TH); plane at which they initiate shown with dashed line. Local direction of growth is normal to that line (white arrow). Overall fracture propagation direction given by yellow arrow. (a) 9,435 ft in Upper Wolfcamp; view downhole. TH initiate at pyrite layer. Propagation down and west. (b) 11,678.5 ft in Middle Wolfcamp; view uphole. TH initiate at bedding plane. Propagation up and east.

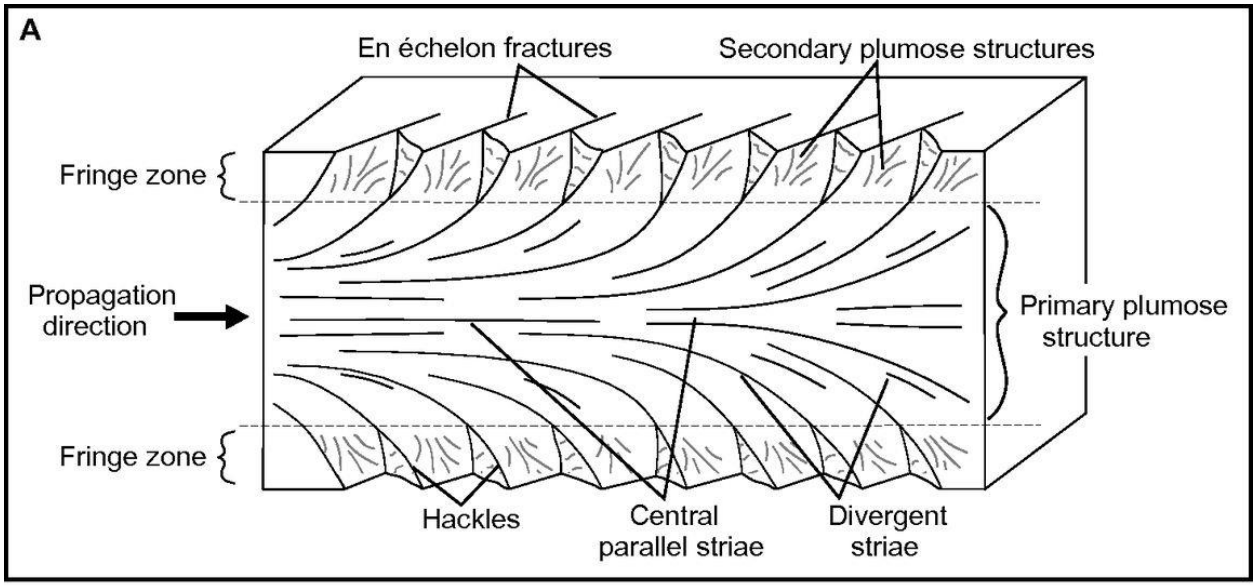


Figure 13. Diagram of plumose structure on a joint surface. Note local direction of propagation indicated by twist hackles is up at top and down at base. In some cases, it may be possible to determine lateral propagation on the basis of asymmetry of twist-hackle steps. Diagram from Cobain et al. (2015), their figure 6A.

There are three locations where hydraulic fractures contain a sand (proppant) pack: at 9,459.9 ft, 9,488.85 ft, and 9,561 ft, all of which lie within the more intensely fractured interval in the lower part of Cores 2 and 3. These examples are shown in detail in the accompanying figures (Figs. 15–17).

Where core-normal fractures encounter concretions, fractures become complex, and the concretions are shattered. The third location where a sand pack occurs is at a concretion (Fig. 17). The sand is visible in the fracture at the uphole end but can also be seen in some of the

other breaks. A piece of the sand pack appears to have been pushed out of the fracture—it was sampled, and the remainder left intact. The CT scan shows a bright signal in the fractures and in the concretion, which is likely to be pyrite. The dark-gray signal of proppant noted in Figure 16 is not apparent, possibly being obscured by the pyrite.



Figure 14. Example of twist hackles with anomalous orientation. At 9,372.45 ft, looking downhole, hackles suggest downward propagation. Twist-hackle asymmetry suggests overall propagation is to the east (left in photo).

Hydraulic fractures with proppant pack

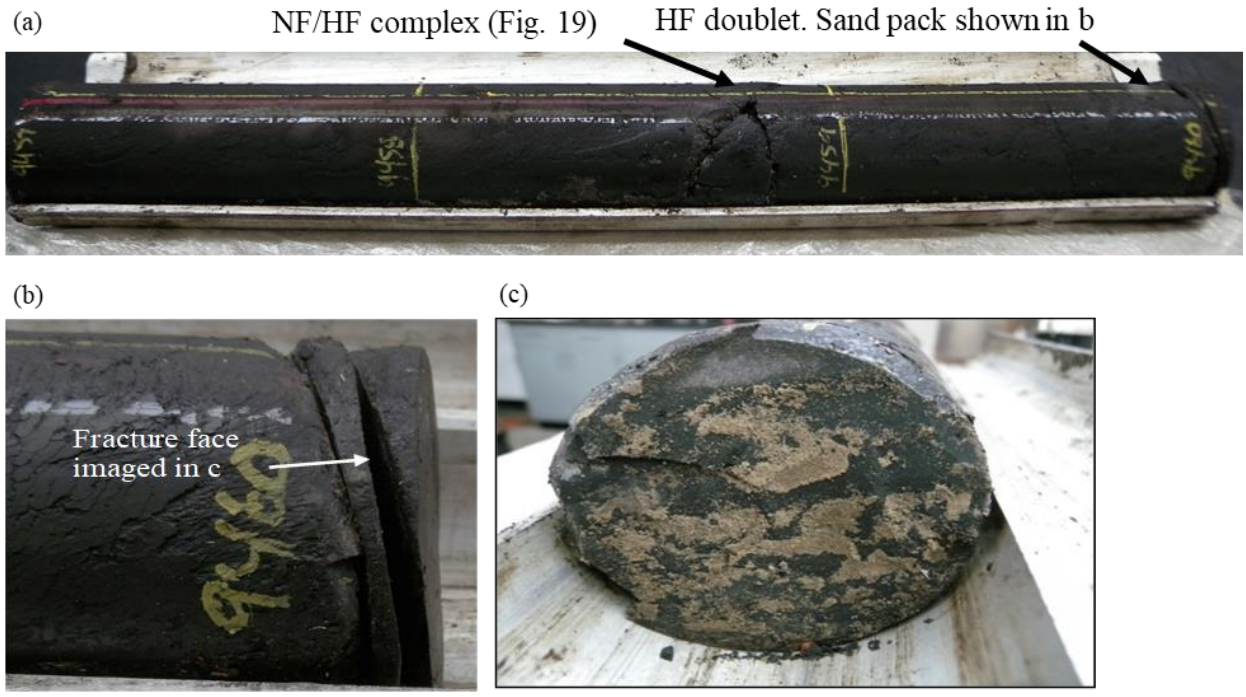


Figure 15. Sand pack in a hydraulic fracture at 9,488.90 ft in Core 3. (a) 3-ft section of core with location of sand pack figured in b at base of section, where two HFs are in proximity—termed a doublet. Slightly uphole is a complex in which a hydraulic fracture interacts with a Set 2 natural fracture. See Figure 19. (b) Detail of doublet. (c) Face of fracture at 6,488.9 ft looking uphole.

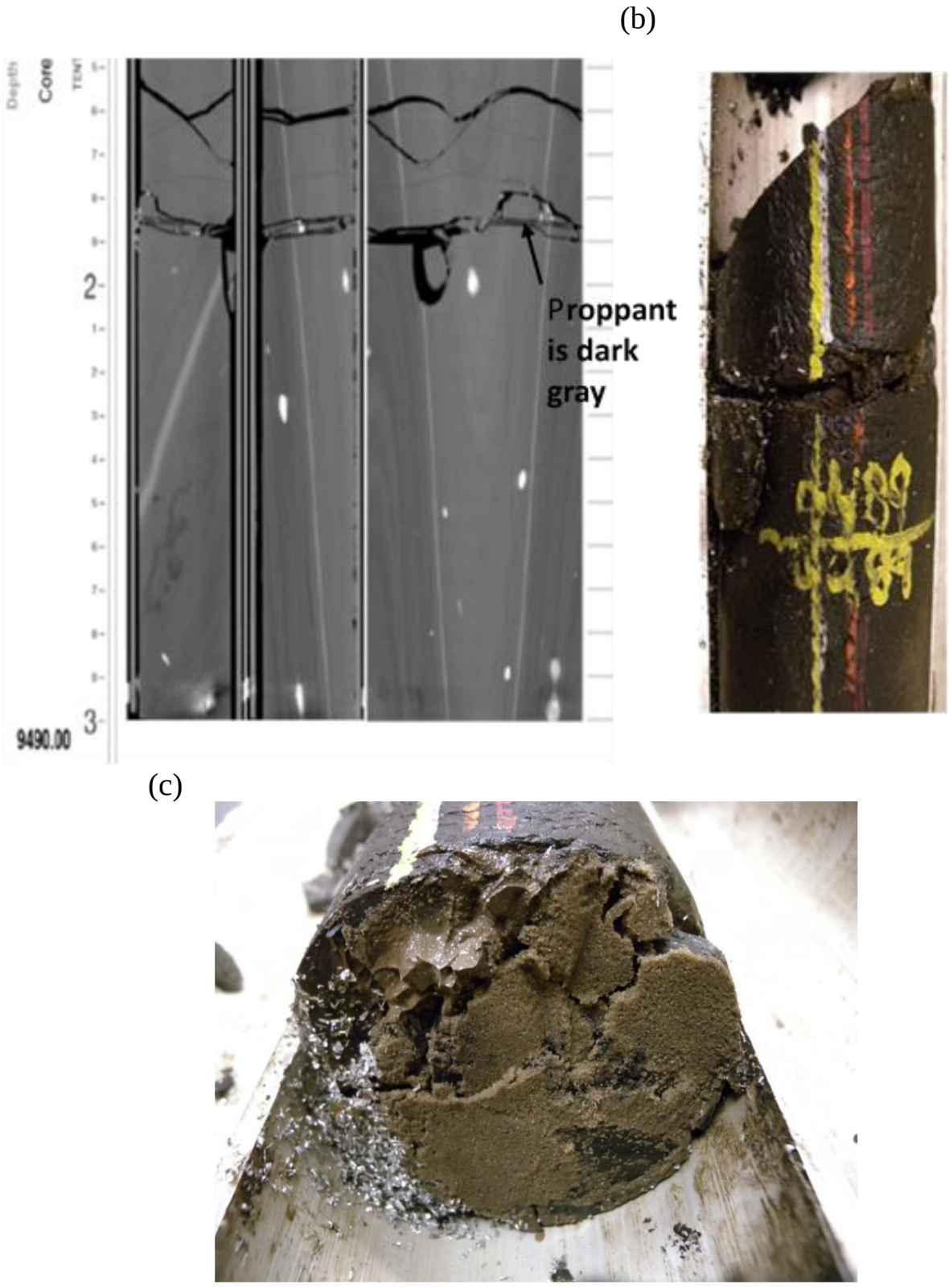
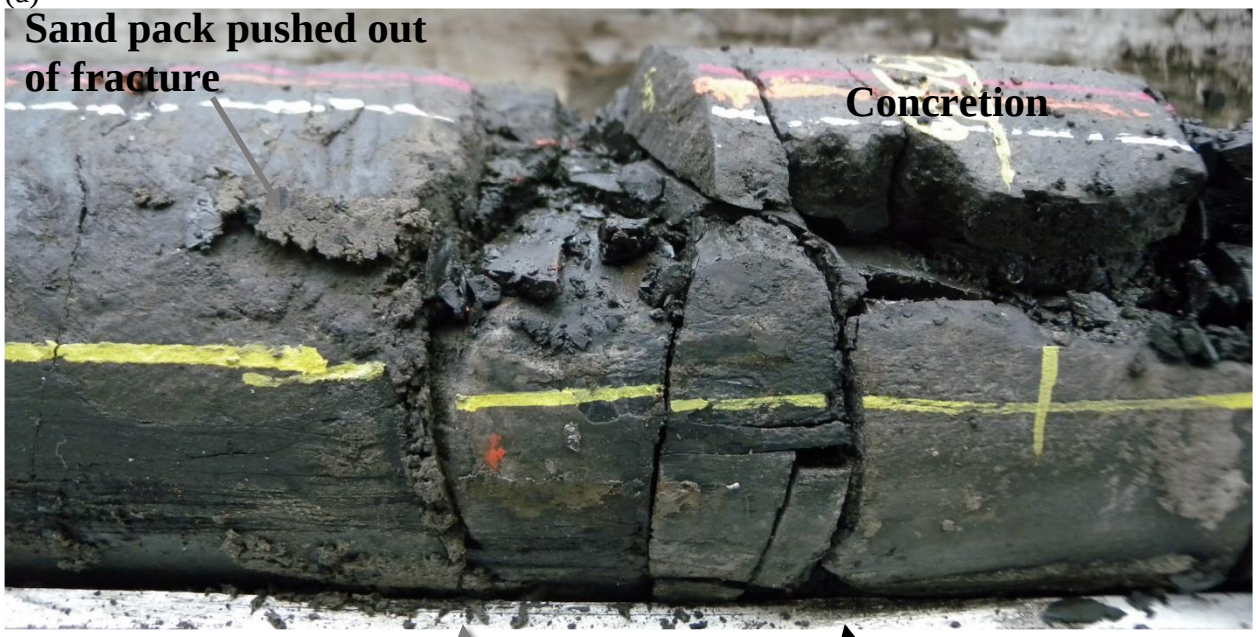


Figure 16. Sand pack in a complex hydraulic fracture at 9,488.85 ft in Core 3. (a) CT scan of fracture; proppant dark-gray. (b) Intact core; fracture complex approximately 1 cm wide. (c) Sand pack viewed uphole with core piece below fracture removed. Sand has since been removed for analysis. Hydraulic fractures at this location have complex geometry that may have favored trapping of sand pack.

In several other locations there are patches of sand in hydraulic fractures. Some of these occur close to where the main proppant packs are located, whereas others occur away from the packs. The case at 9,458.8 ft is of interest because it is also an apparent interaction between a hydraulic fracture and a natural fracture (Fig. 18). A similar occurrence is at 9,488.55 ft.

(a)



(b)

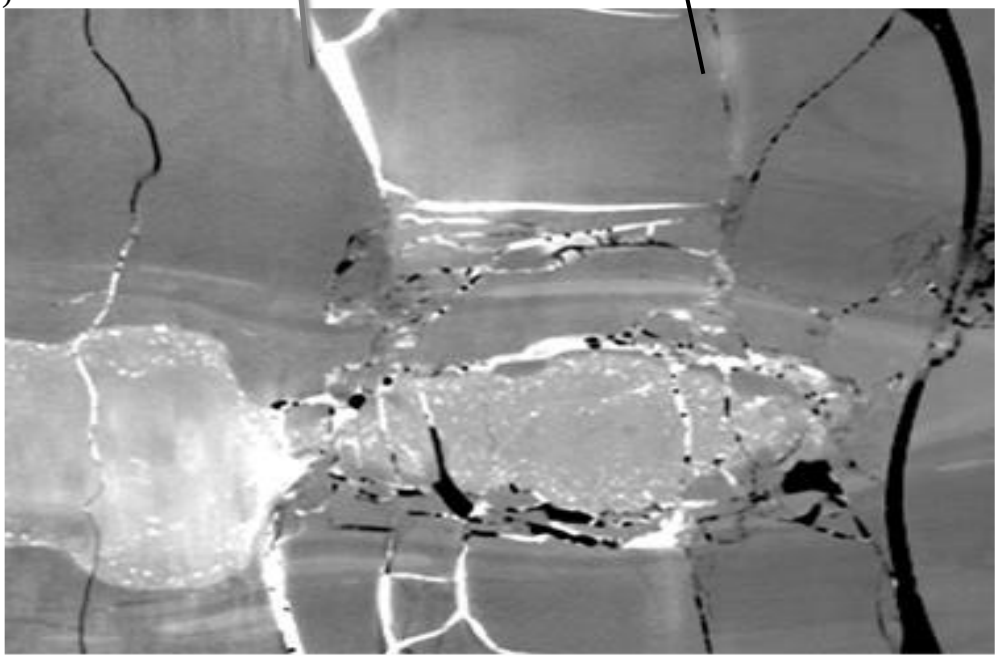


Figure 17. Sand pack in complex hydraulic fracture adjacent to concretion at 9,561.7 ft in Core 3. (a) Sand on outer surface of core with multiple breaks visible. (b) CT circumferential scan.

Hydraulic fractures reactivating weak planes, such as bedding or natural fractures.

Breaks occur along some of the natural fractures and bedding planes, but the reason they are broken (reactivated) is not easy to determine. The mechanism for reactivation could be hydraulic fracturing, drilling, core retrieval stress, or core handling. For planes reactivated during hydraulic fracturing possible indicators include

(a) Bedding-plane breaks connected to a hydraulic fracture (hard linked) (Fig. 19). These are smooth and planar, as compared with other bed-parallel breaks that are stepped and rough. Nonconnected bed-parallel fractures could pop open because of a pressure front associated with hydraulic fracturing, and in this case would not be hard linked.

(b) Hard-linked, reactivated breaks perhaps should have some proppant along them, which is the case in the example in Figure 18, showing that proppant can travel around the angle between the hydraulic and reactivated fracture.

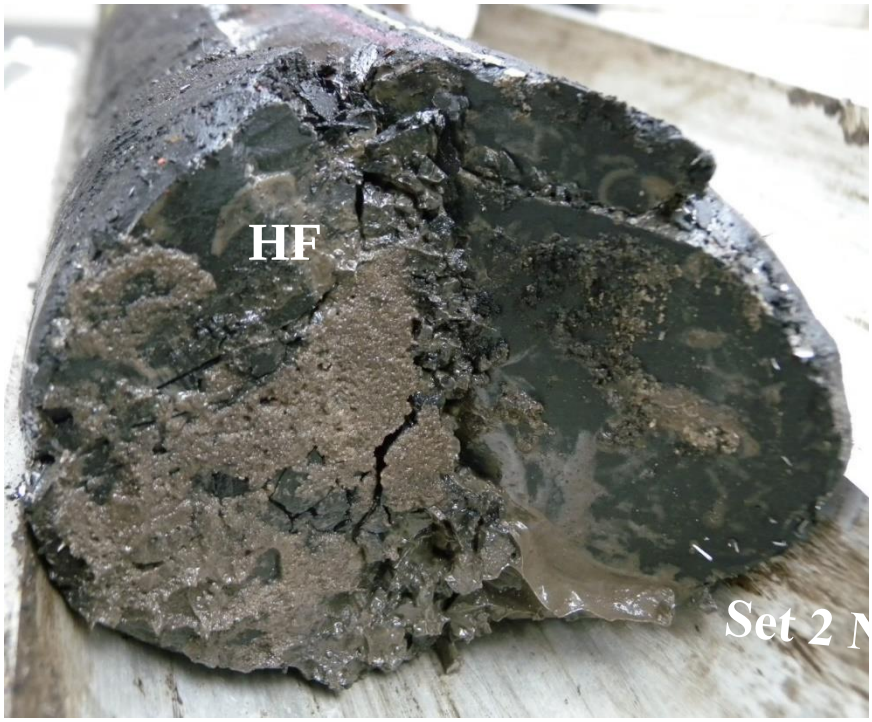


Figure 18. Possible interaction between HF and Set 2 natural fracture (NF) at 9,458.8 ft. (a) View of uphole face with thick sand patches on HF surface and some on NF face. We did not observe cement on face of NF; it was interpreted as such on the basis of orientation. At this location (out of view) an intact Set 1 NF also occurs with cement, although crosscutting relations were not clear.

(a) (b)

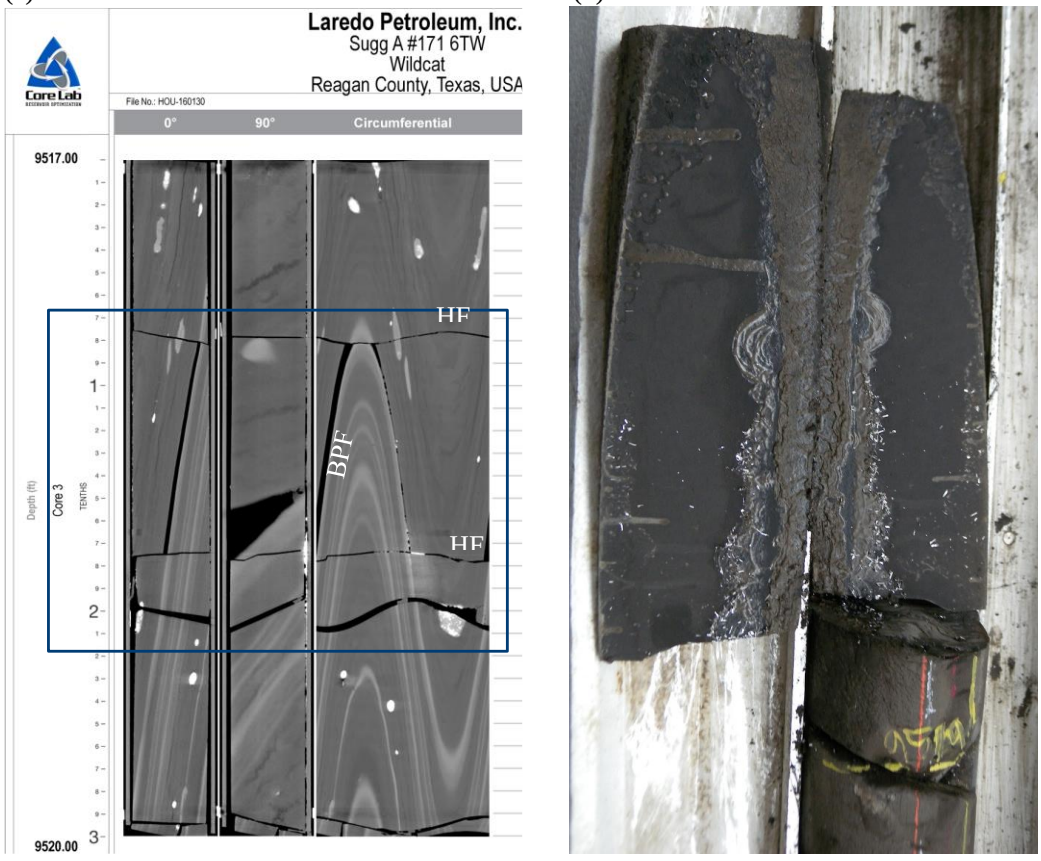


Figure 19. (a) CT scan of section with bed-parallel fracture (BPF) bounded by two hydraulic fractures (HF). (b) Photograph of bed-parallel fracture surfaces, which are smooth and planar. Drilling mud has partly invaded at the margins.

Drilling-induced fractures (from drilling the slant well)

Drilling-induced fractures are mostly at a high angle to the well bore and parallel to SHmax, as for hydraulic fractures. In horizontal or slant wells, drilling-induced fractures can be confined to the core top. In other cases, in which the weight on bit has increased significantly, breaks can occur along the bedding, with petal shapes extending outward to the core margin (Fig. 20a). Induced fractures commonly have indications of breakage points within the core (e.g., core-rimming plumose markings, sharply pointed raises at the core margin, called tangs), and they tend to be approximately core-symmetric, curviplanar (saddle shaped) (Fig. 20b), or irregular. Surface markings can form, no matter the mechanism. For natural and hydraulic fractures, the markings would have no relation to core margins (barring coincidence). For drilling-induced fractures and core handling plumose markings may emanate from a point source. Some proppant grains may also be present, having been brought in with the drilling mud, but proppant will not be present as a sand pack. Drilling can also cause natural fractures or other weak surfaces to break. Differentiating these from reactivation caused by hydraulic fracturing is difficult.

(a) (b)



Figure 20. Drilling-induced fractures. (a) Petal centerline shape at 9,391 ft viewed looking downhole. (b) Irregular, saddle-shaped fracture at 11,564 ft.

Core Recovery

Core recovery causes vertical-stress release, commonly creating breaks parallel to bedding in vertical cores. In this slant well, not many examples of this occur, and where they do occur it is at the core margin close to another break. Breaks can also occur during core recovery as the core is retrieved around the bend at the well heel. This damage was most likely mitigated by the aluminum sleeve. Tangs are commonly produced in core during flexural breaking, and in rotary-drilled sidewall, cores can be used to identify way up (Laubach and Doherty, 1999). An example is shown from 9,634 ft (Fig. 21).



Figure 21. Likely core recovery fracture at 9,634 ft. Irregular surface with a tang (t), suggesting the break initiated within the core.

Damage during sawing into sections and transportation and other handling up to point of CT scan.

Surfaces are rough and fresh, but some drilling mud is present (Fig. 22a). These fractures are present in the CT scan.

Fractures created because of handling/desiccation after CT scan.

New fractures are created that are not present in the CT scan. The surfaces are completely fresh, with no mud.



Figure 22. (a) Likely core-handling fracture at 9,479.6 ft. Irregular surface with some drilling mud splatters. (b) Post-CT scan break at 9,346.8 ft. It is irregular with a rough surface and has no drilling mud inside.

Proppant analysis

Material on the surface of each fracture was collected with the aim of analyzing it for proppant. This collection was done using stiff paper and soft brushes. Fracture surfaces were photographed prior to the surface material being taken. We have looked for evidence of proppant embedment but have found none, even on surfaces where we have found sand. Pressure drawdown from the hydraulically fractured wells was probably insufficient by the time the slant core was taken to cause fracture closure and embedment.

The protocol for analysis of the scraped material was developed by our trying a selection of different solvents and surfactants on small quantities of sludge retrieved from the aluminum sleeves. Dish- washing soap and fabric conditioner have been found to be most effective, and they are cheap and do not require use of a fume hood. The different materials in the scrapings can then be wet-sieved to separate them; most coarse shale pieces and aluminum swarf are retained on a 500-micron sieve. Sand and finer shale pieces then fall into 200- to 500-, 120- to 200-, and 63- to 120-micron size ranges. We have also obtained samples of the colored proppants that were pumped in the different stages, which can be used for comparison with the sand seen in the fractures. A systematic analysis of all the scraped samples has begun. We have developed a protocol for this analysis also, in terms of measuring (weighing) the different sized fractions and using image analysis techniques to determine amounts of proppant. Probably 750- to 1,000 samples will be analyzed. We will compare results with the sludge analysis from each of the 3-ft sections of core to be done by GTI.

Use of results for modeling

Dr. Mukul Sharma and students (UT) are using results described in this report and in Appendix A in geomechanical modeling of hydraulic fracture growth. There are many aspects of interest, in particular the bifurcation and clustering of hydraulic fractures and the possible reactivation of preexisting discontinuities in the host rock. We envisage that further analysis of this dataset will yield more information about growth of the hydraulic fracture network. This information can be used to better plan future wells and could potentially provide additional information about the stimulated reservoir volume.

References

1. Cobain, S. L., Peakall, J., and Hodgson, D. M., 2015, Indicators of propagation direction and relative depth in clastic injectites: implications for laminar versus turbulent flow processes: GSA Bulletin, v. 127, p. 1816–1830; doi: 10.1130/B31209.1

2. Laubach, S. E., and Doherty, E., 1999, Oriented drilled sidewall cores for natural fracture evaluation: Society of Petroleum Engineers, Formation Evaluation and Reservoir Geology, SPE Paper 56801, p. 793–800.

3. Lee, H. P., Olson, J. E., Holder, J., Gale, J. F. W., and Myers, R. D., 2015, The interaction of propagating opening mode fractures with preexisting discontinuities in shale: Journal of Geophysical Research: Solid Earth, v. 120, no. 1, p. 169–181, http://doi.org/10.1002/2014JB011358.

Appendix B: Phase 2 Fracture Characterization by BEG

Research Entity: Bureau of Economic Geology, The University of Texas at Austin

Final Report HFTS EOR Fracture Description, June 21, 2019

Prepared by Julia F. W. Gale

Research by Julia F. W. Gale, Sara J. Elliott

Introduction

We summarize results for fracture description and proppant analysis of the Sugg E 197 5TW Slant Well cores. The background and methods for fracture description and proppant analysis were described in the final reports for Phase 1 of the HFTS project (Gale et al., 2017, 2018). We do not repeat the previously developed methodologies here and attach the Phase 1 reports for reference (Appendix A). Any new or different methodologies are described here.

Fracture Description

Fractures in all four of the 5TW cores were characterized, described, photographed and orientations measured. Fracture orientations were measured with cores lying flat on a bench using an iPad with a GeoID application (Fig. 1) and then corrected for magnetic declination (~4°E at the place of measurement in CoreLabs, Houston), and finally rotated into their in-situ orientations. Rotations and plotting of stereograms were done using Richard Allmendinger's free 'Stereonet' software available at:

http://www.geo.cornell.edu/geology/faculty/RWA/programs/stereonet.html.



Figure 1. Measurement of structures and rotational correction, and iPad with GeoID measurements.

Compiled fracture data spreadsheets for cores 1–4 is uploaded to the project Google Drive site, together with labeled photographs of the fractures in the cores, which are cross referenced to fracture identification numbers in the spreadsheets. Photographs are organized in folders for each 3 ft core section. Photographs of fractures are labeled with the unique fracture identification number, and whether the face is uphole (U) or downhole (D). The stereograms of fracture orientations (Fig. 2), also with fracture ID numbers, are also provided as .stnt files (compatible with 'Stereonet' software). Orientations are separated by core and presented as planes in lower hemisphere stereographic projections. Raw measurements and corrected measurements are in the data tables.

Key findings from fracture description and proppant analysis

We documented a total of 431 fractures in the 5TW cores. Some fractures have additional, subsidiary breaks, particularly at the apices of core pieces where the tips are weak. These small breaks are commonly, although not always, parallel to bedding. In most cases we labeled these with letter 'a' after the main fracture number, e.g., #167 and #167a. These are mostly described in the notes column in the spreadsheet. Hydraulic fractures, and two main sets of natural fractures were identified. These fracture types, including their orientations, are like those seen

in the HFTS 6TW well. There are some differences in other aspects of the fracture population in the 5TW well. The key findings are as follows:

1) Hydraulic fractures are present through all 4 cores, but the intensity varies. Typically, hydraulic fractures tend to be clustered, with doublets and bifurcations and in some cases the fracture tip is contained in the core. There are a total of 129 hydraulic fractures distributed thus:

Core 1: 30 in 69 ft (mean 0.43 fracs/ft)

Core 2: 57 in 73 ft (mean 0.78 fracs/ft)

Core 3: 23 in 53 ft (mean 0.43 fracs/ft)

Core 4: 20 in 66 ft (mean 0.30 fracs/ft)

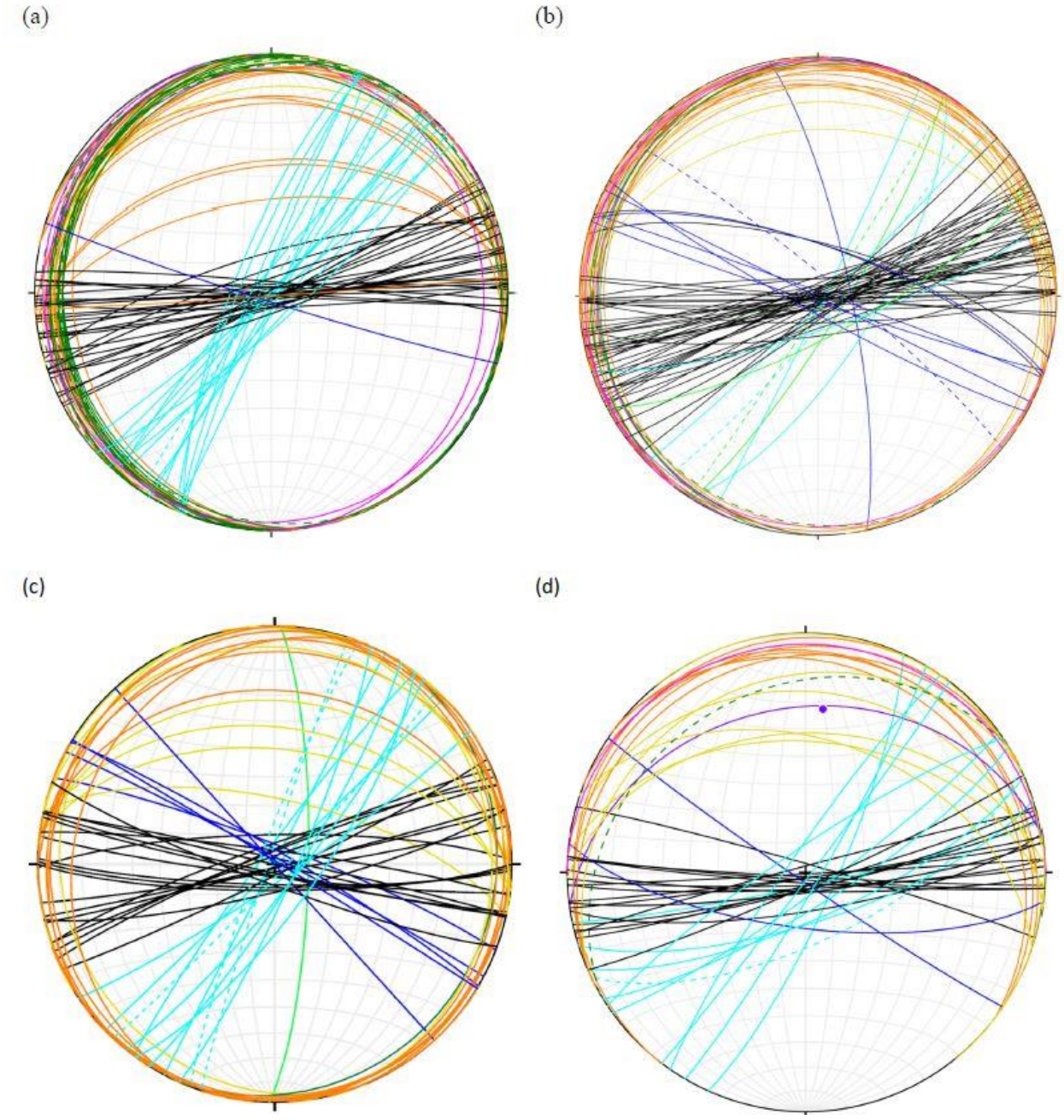


Figure 2. Lower hemisphere equal angle projection of fracture planes (a) Core 1, (b) Core 2, (c) Core 3, and (d) Core 4. Hydraulic fractures = black; Set 1 natural fractures = light blue; Set 2 natural fractures = dark blue; bed-parallel fractures = pink; faults = mauve; unassigned natural fractures = light green; drilling induced fractures = mustard; core

handling breaks = orange; bedding plane = green. Dashed planes are those that have been interpreted as hydraulic fracture reactivation. The mauve circle in (d) is the orientation of slickensides on the fault.

The data show the greatest abundance is in Core 2, least in Core 4, and similar abundance in Cores 1 and 3. As in the 6TW cores, hydraulic fractures are remarkably smooth and planar. Some have twist hackles, which can be used to infer propagation direction. Hydraulic fractures with twist hackles are a consistent proportion of the total in Cores 1-3 but are less common in Core 4. Distribution is as follows: Core 1: 11 of 30 (37 %); Core 2: 19 of 57 (33%); Core 3: 10 of 23 (43%); Core 4: 3 of 20 (15%)

2) Two sets of subvertical, calcite-filled fractures, like those in the 6TW cores, are present: Set 1 strike NE-SW and Set 2 strike WNW-ESE. Both sets have sealed and parted fractures. Set 1 fractures: 18 in Core 1, of which 7 are parted; 6 in Core 2 of which 3 are parted; 13 in Core 3 of which 8 are parted; 17 in Core 4 of which 11 are parted. Set 2 fractures: Core 1 has 1 sealed; 7 in Core 2 of which 1 parted; 6 in Core 3 of which 2 parted; 3 in Core 4 of which 1 parted. There are 13 bed-parallel natural fractures mostly in Cores 1 and 2 (3 in 6TW). We observed one thrust fault in Core 4, dipping 32• to the north, with well-developed slickensides and fibrous calcite plunging to the north in this plane. This was the only fault seen. Minor soft sediment deformation is present in several places, most notably in Cores 3 and 4.

3) A major difference between the 5TW and the 6TW is the large number of parted bed-parallel fractures in the 5TW: 37 in Core 1, 29 in Core 2, 23 in Core 3, and 22 in Core 4. There were very few in the 6TW. They are colored a bright green in the spreadsheets, with shading indicating the interpreted reason for parting. The challenges with interpreting the cause of bed-parallel fracture opening are addressed in the Discussion section. Broadly, we used the following criteria based on the morphology of the fracture plane and the degree of roughness of the surface:

- Smooth and planar: Hydraulic Fracture
- Smooth with shear: Drilling Induced
- Rough and irregular: Core Handling

4) The number of drilling-induced fractures identified, per foot of core, in the 5TW (65/261 = 0.25 fractures/ ft) is greater than found in the 6TW (91/600 ft = 0.15 fractures/ft). In the 5TW there are 7 in Core 1, 11 in Core 2, 21 in Core 3, and 26 in Core 4. In the first part of Core 3 and in parts of Core 4 there are several irregular, but smooth and core-symmetric breaks almost normal to the core axis. At these depths (~8355–8375 ft) there are coarse carbonate layers, which may have affected the way the core failed during drilling; core fails normal to the core axis in massive, coarse, carbonate layers. In the shaly intervals it is possible the orientation of bedding relative to the well-favored drilling reactivation along bedding planes. Shading indicates the structure has reactivated.



Table 1. Fracture description, Core 1.

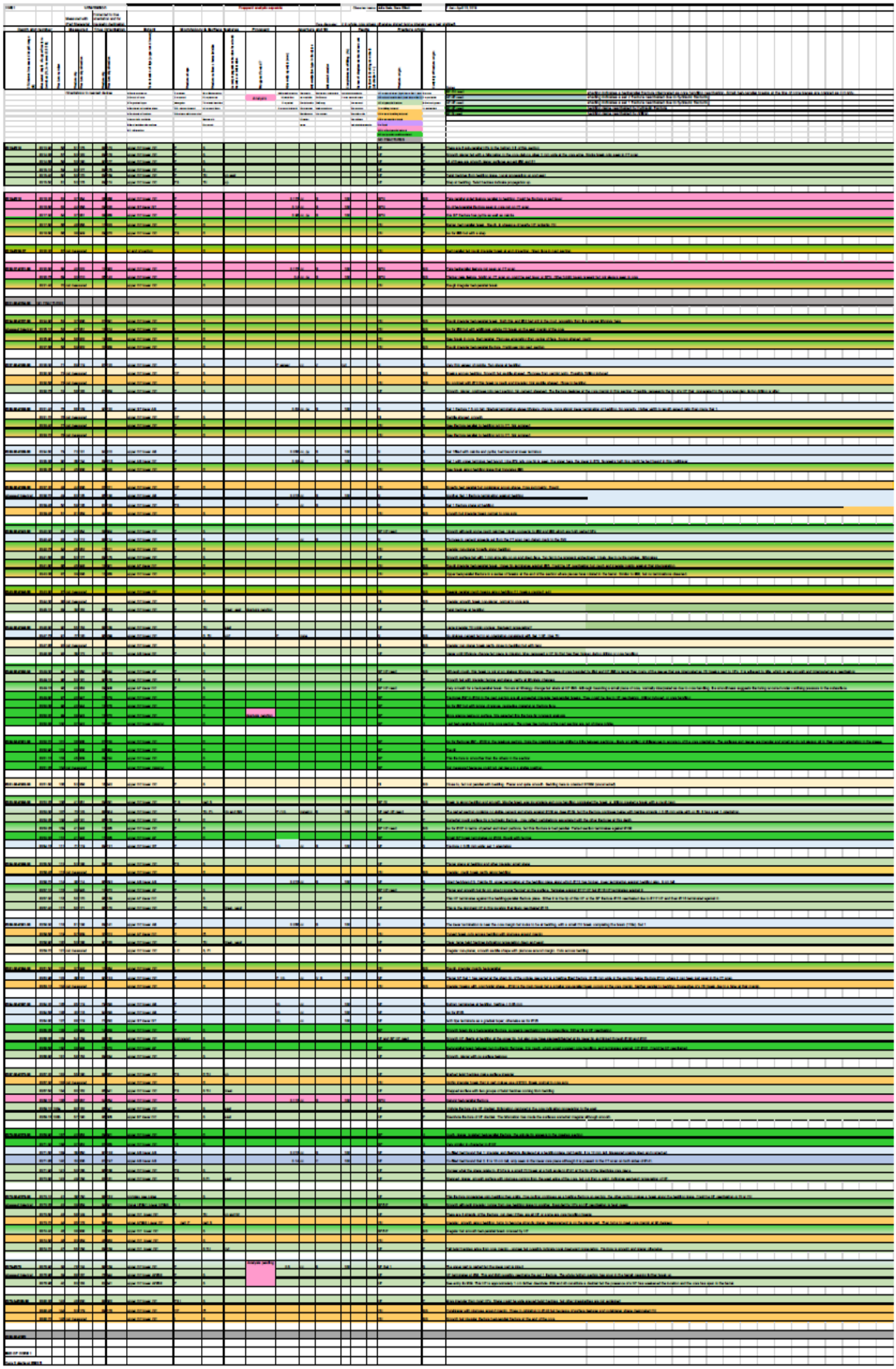


Table 2. Fracture description, Core 2.

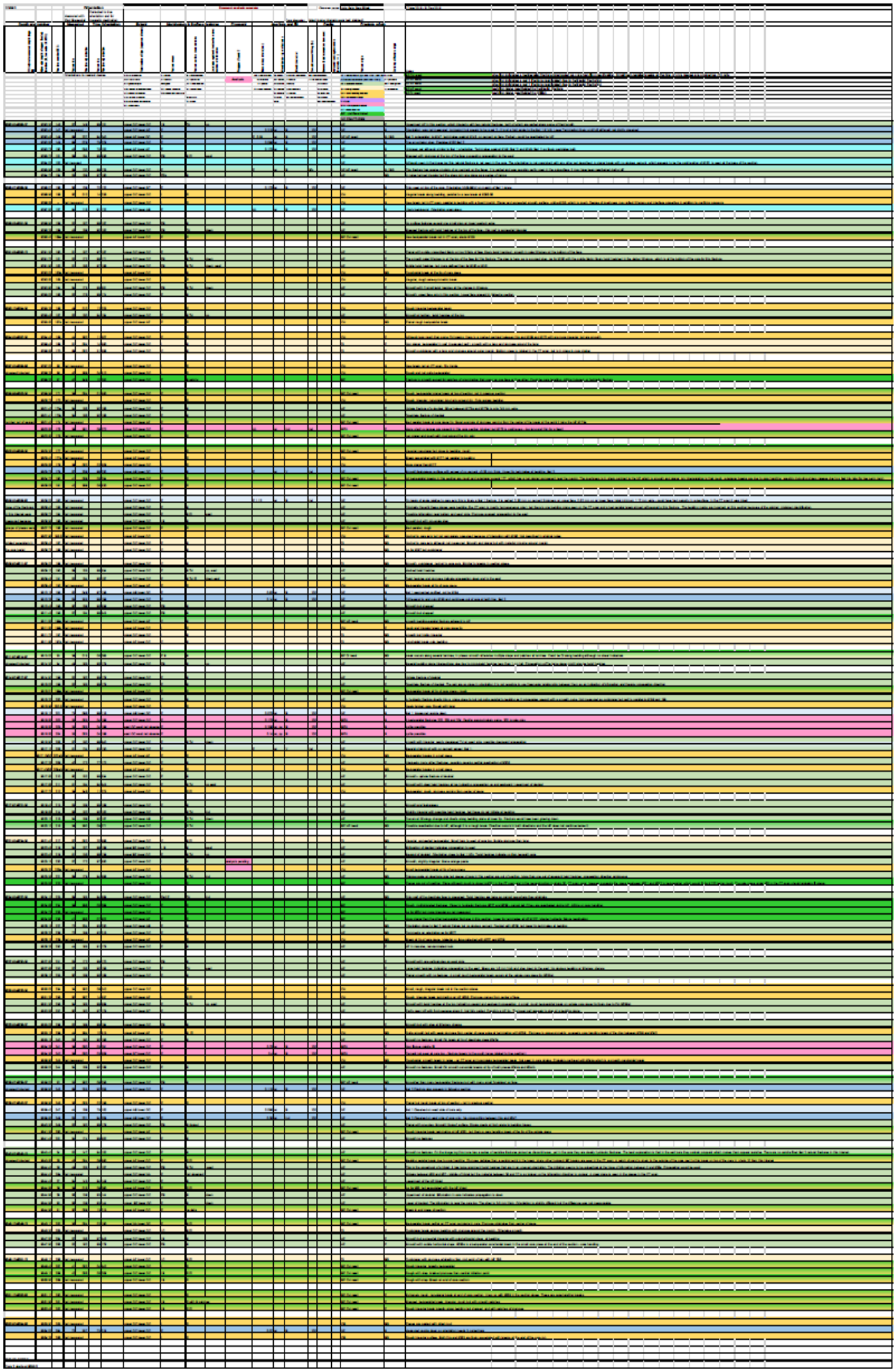


Table 3. Fracture description, Core 3.

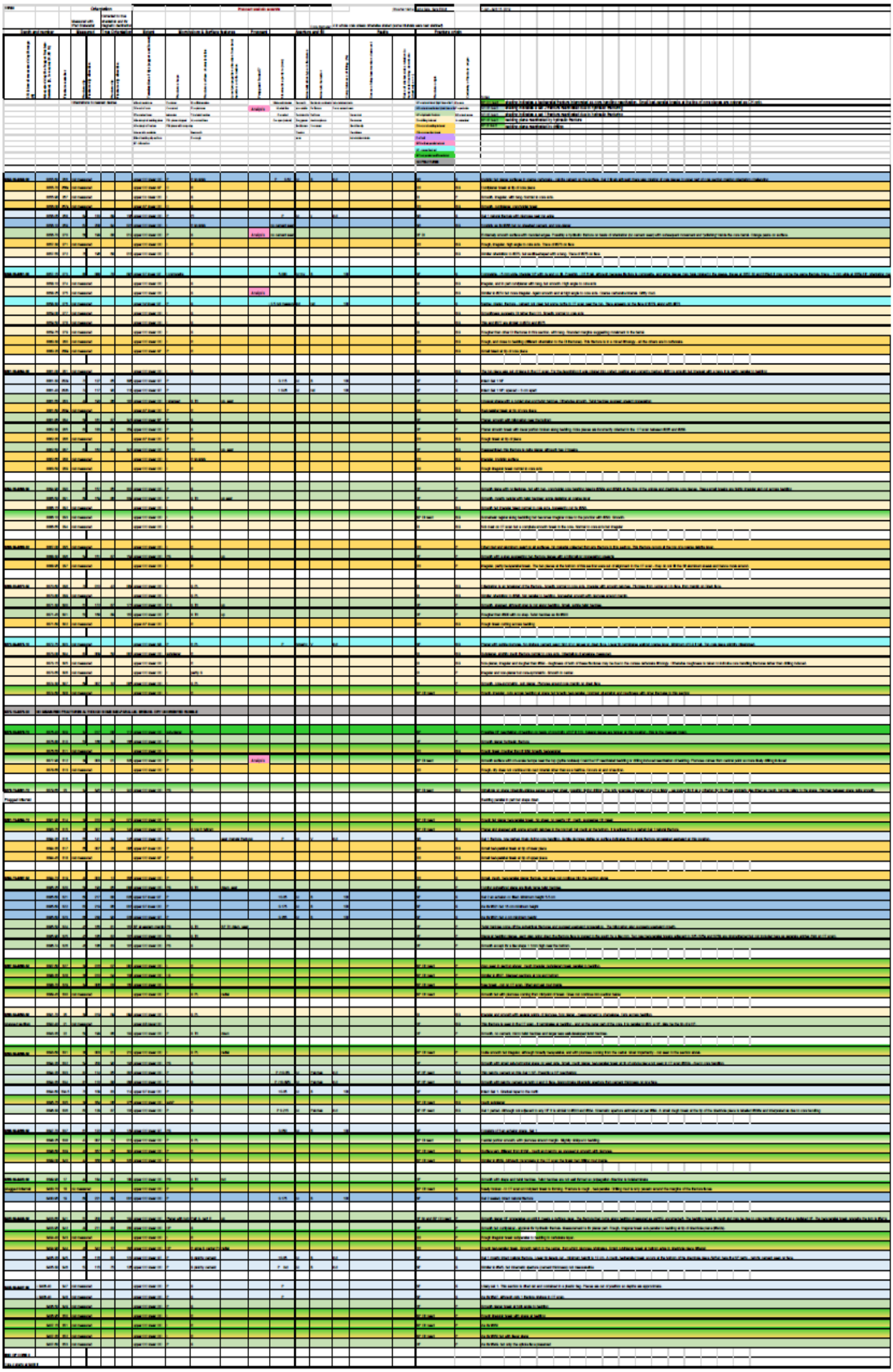
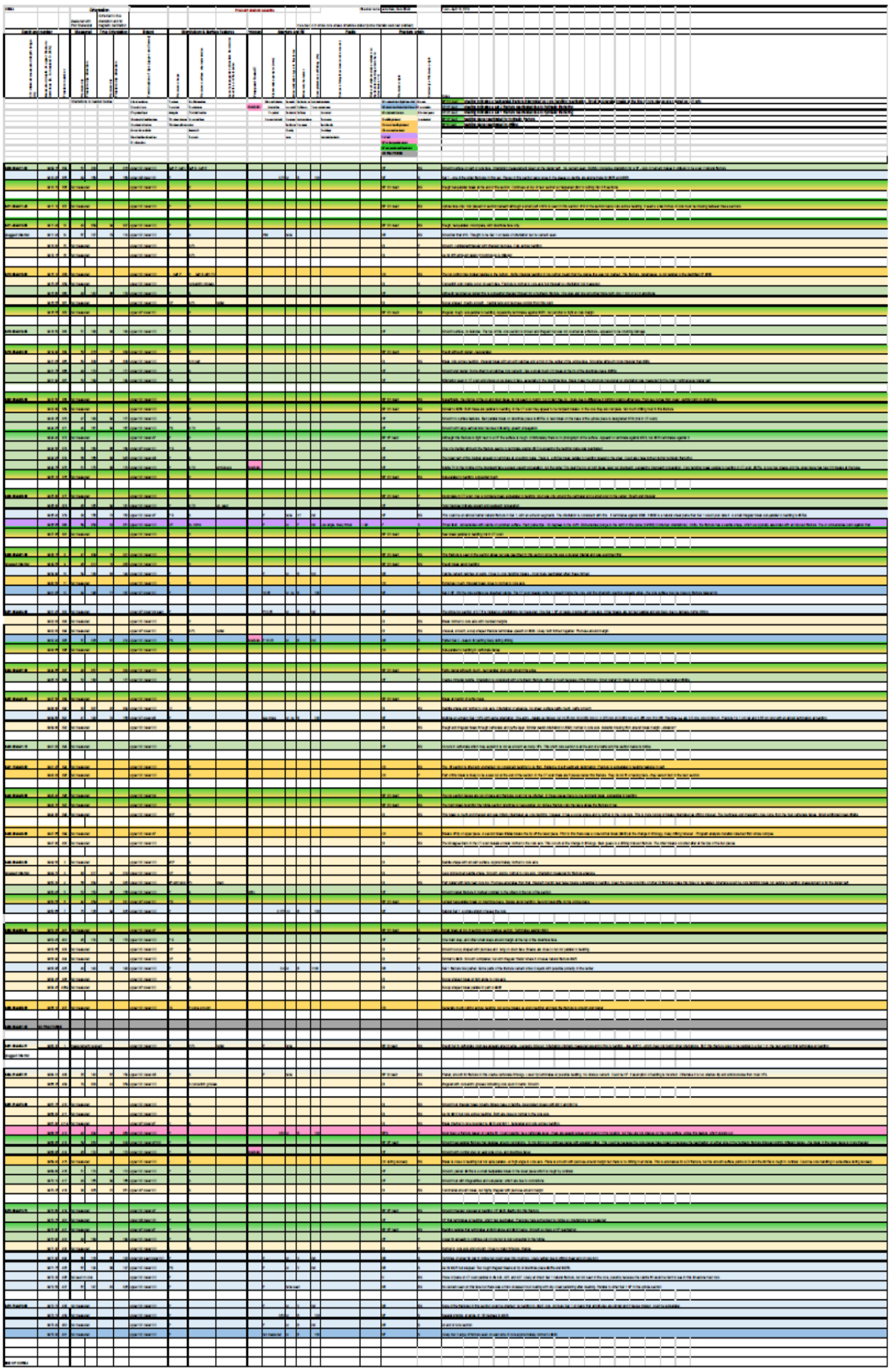


Table 4. Fracture description, Core 4.



5) Fracture orientations are similar to those found in the 6TW cores: hydraulic fractures strike broadly E-W, set 1 natural fractures strike NE-SW, and Set 2 natural fractures strike WNW-ESE. All three are subvertical. Core handling fractures are commonly subhorizontal, parallel to bedding, as are some drilling-induced fractures, but many drilling-induced fractures dip moderately to the north and are normal to the core axis.

Tables 1-4 are images of the fracture description spreadsheets. Colors give an impression of the types of fractures present. We used the same color scheme as for the 6TW with the addition of a bright green for bed parallel fractures, and shaded coloring for reactivated fractures, many of which start as a bedding plane. The shading convention we use is that the original plane is the color at the top, with the cause of reactivation being represented by the color at the bottom. Here we present a systematic description of the fracture types, with example photographs and references to particular fractures. The color key is as follows:

Hydraulic Fractures

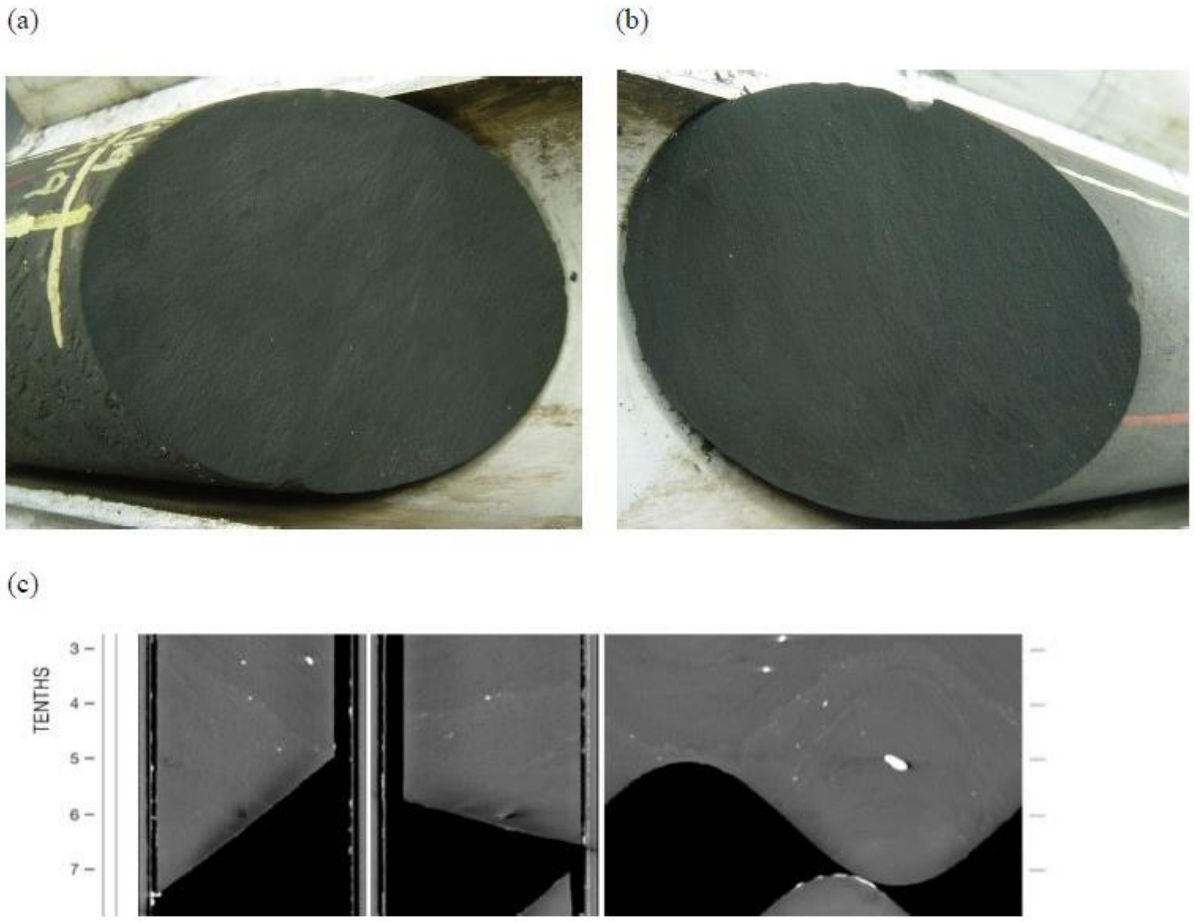


Figure 3. Hydraulic fracture at 8418.5 ft (a) downhole and (b) uphole faces. (c) CT scan of uphole piece and hydraulic fracture (lower piece had rotated in the sleeve), which cuts through the paler gray lithology only.

Many hydraulic fractures are remarkably planar, smooth, and featureless (Fig. 3). The example shown cuts through relatively homogeneous rock with no obvious lithology change in the CT scan (Fig. 3c). Similar fractures were seen in the 6TW cores. Yet others have twist hackles on surfaces, particularly when the hydraulic fracture cuts through different lithologies (Fig. 4). Propagation direction may be inferred from twist hackles, bifurcation, and plumose structure. The directions are variable as with the 6TW core. Hydraulic fractures tend to occur in clusters (Fig. 5). Some 3ft sections have none, others have a single, and others have up to 6. They are

most common in Core 2, least common in Core 4, and intermediate numbers occur in Cores 1 and 3 (see summary point 1).

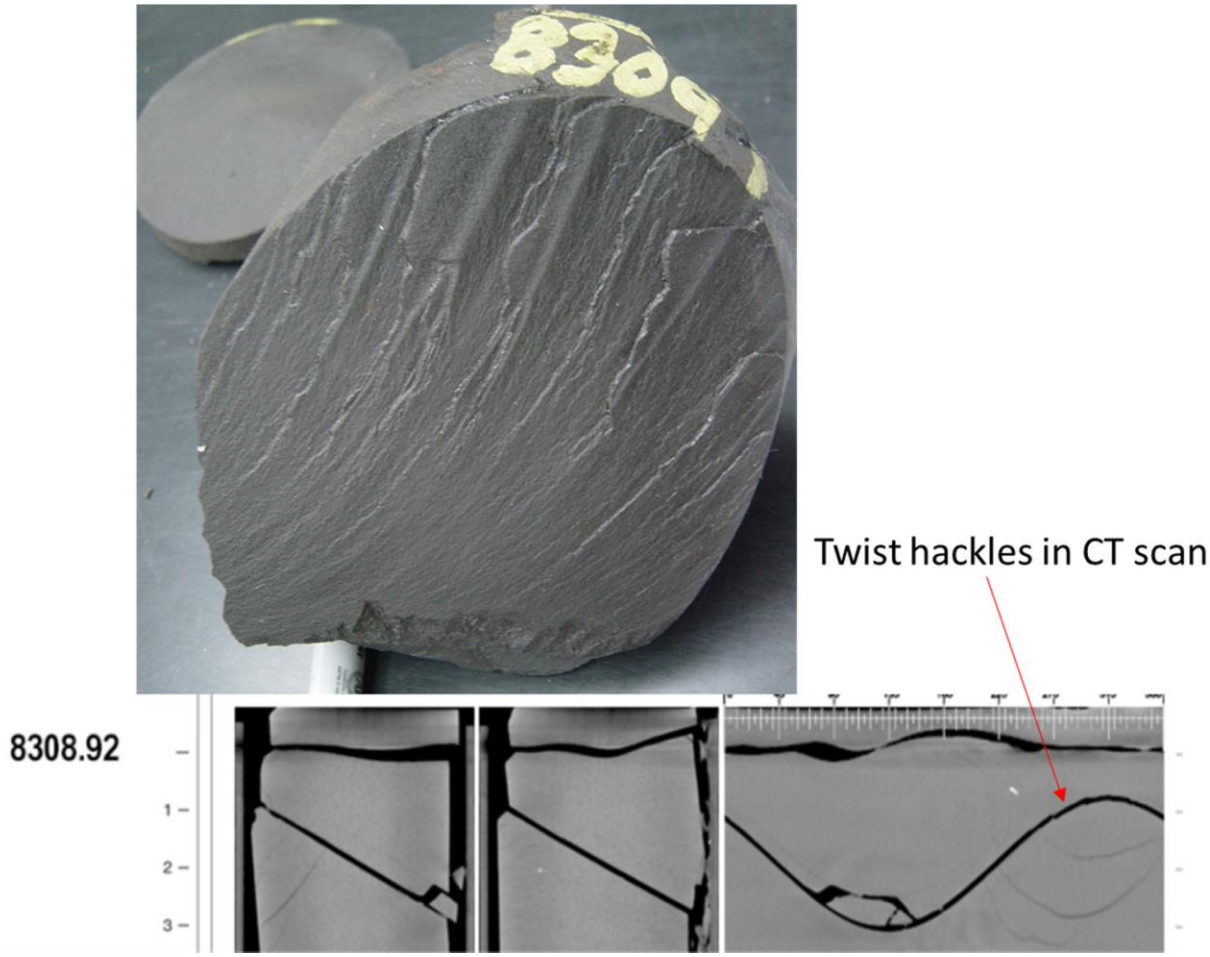


Figure 4. Twist hackles on uphole hydraulic fracture face, #190 in Core 2 at 8,309 ft. Note twist hackles can be seen in the CT scan as well.



Figure 5. Cluster of 6 hydraulic fractures in the 3 ft section at the top of Core 1. (a) whole core, (b) CT scan of section.

In the coarse carbonate debrites hydraulic fractures can be rough and somewhat irregular, but they retain their orientation, which is approximately normal to bedding (Fig. 6). The debrites are most common at the top of core 3 and through core 4, although they occur throughout the section.

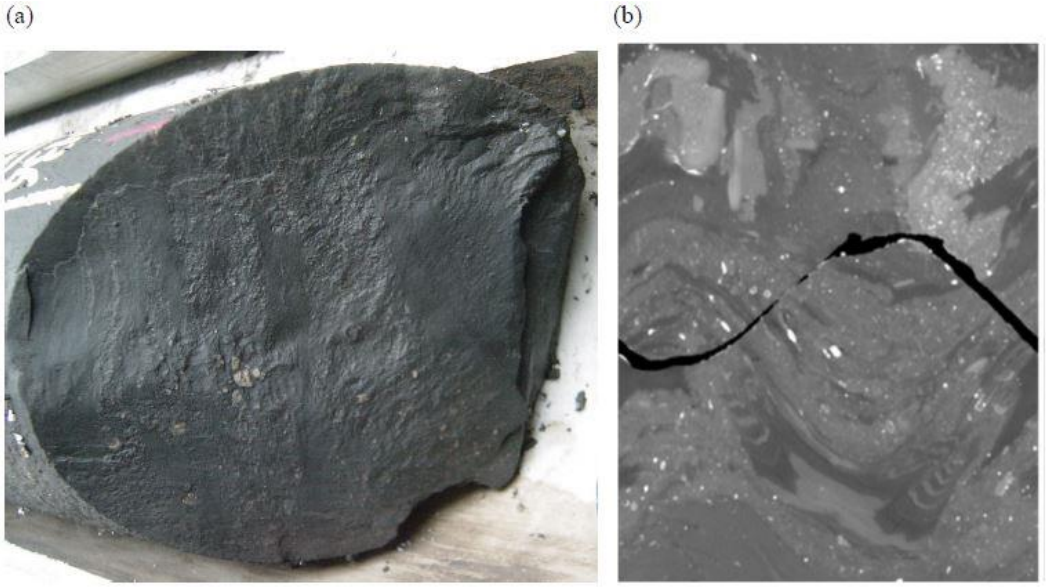


Figure 6. Hydraulic fracture cuts through coarse carbonate debrite at 8435.7 ft in Core 4 (a) downhole face (b) CT scan of this fracture. Note bedding in the debrite.

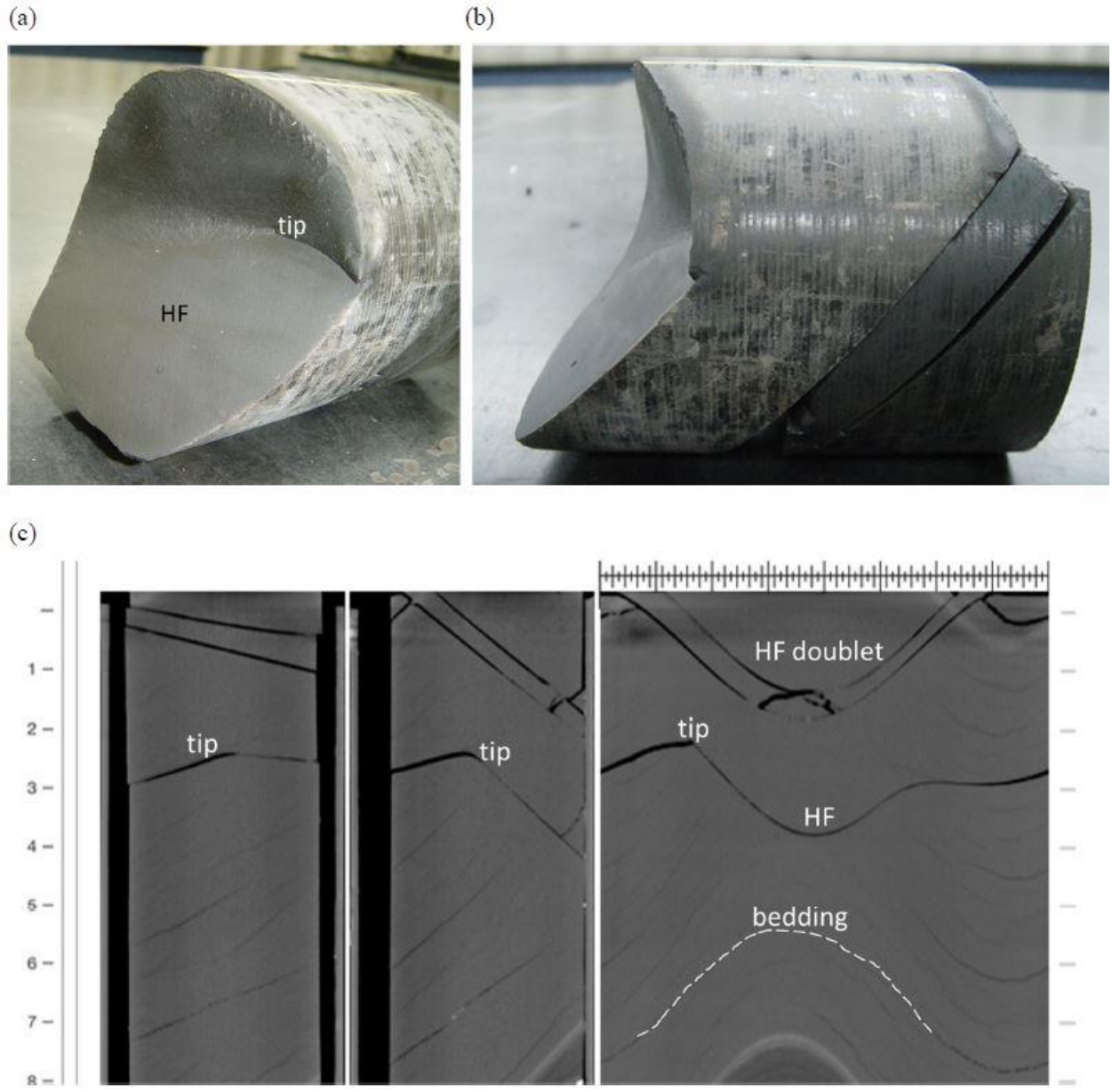


Figure 7. (a) Hydraulic fracture tip at 8315.25 ft in Core 2 (fracture #200), (b) lateral view of (a) also showing a hydraulic fracture doublet to the right (uphole), (c) CT scan of interval with bedding and the doublet indicated.

There are a two examples of hydraulic fractures that deviate within the core. In the first example, at 8315.25 ft in Core 2 (fracture #200), a smooth, planar, hydraulic fracture turns almost orthogonal to itself (Fig. 7a). Part of the turn is a gradual curve, and another part shows a sharp change in angle. The part of the fracture past the tip (upper part of Fig. 7a) does not quite follow bedding, and is smooth like the main, planar part of the hydraulic fracture. There is no obvious change in lithology that could be the cause for the turn, but we note that just a couple inches uphole there is a hydraulic fracture doublet (Fig. 7b, c). It is possible this doublet caused a perturbation in the stress field ahead of fracture #200, causing it to deviate. Also possible is that the hydraulic fracture terminates at the tip, and that the remaining smooth deviation occurred during drilling.

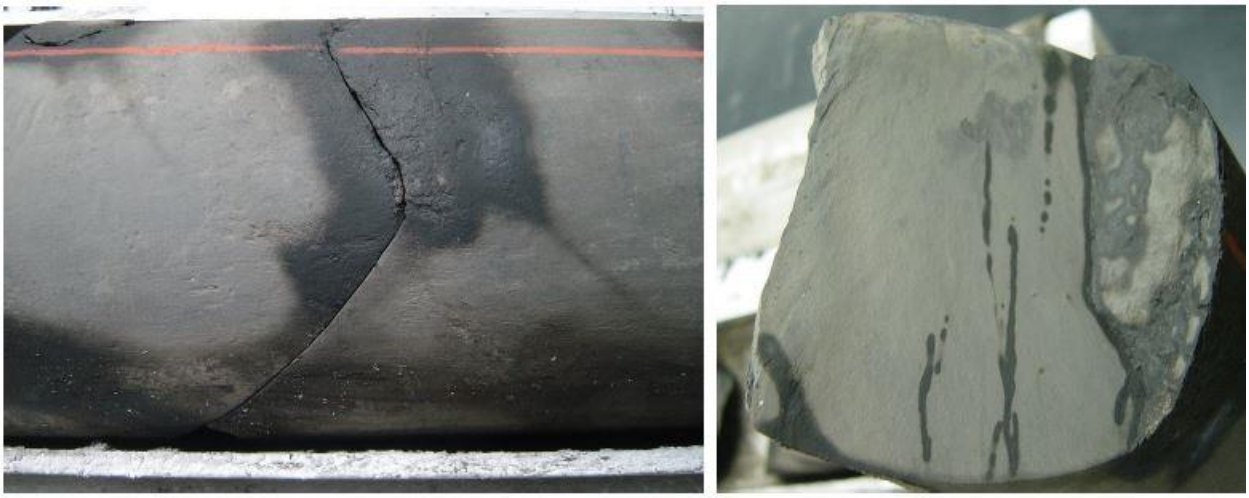


Figure 8. Fracture #34 at 8403.65 ft in Core 3. (a) Side view of core (orange line is top, north to the right): the lower part
of the fracture is planar and has a typical orientation for a hydraulic fracture (HF). The upper part turns sharply at a pyritous layer (PL). (b) Upper face of fracture: the smooth hydraulic fracture (S) contrasts with the rough surface of the bed-parallel break after the turn (R).

In a second example, fracture #34 is smooth, but the upper tip reaches a course, pyritic layer and then turns into a rough, bedding-plane break (Fig. 8). Our favored interpretation, based on the roughness of the bed-parallel break, and the contrast between this example and the previous one, is that the tip of the hydraulic fracture was sampled in the core, but subsequently core handling resulted in further, irregular propagation to the core margin, broadly along the bedding. We note, however, that it is possible that the whole fracture was formed during hydraulic fracturing, and that the reason the bed-parallel break is rough is because of the pyrite nodules in the shale. In this case, we have a rare example of a hydraulic fracture propagating along bedding.

Planes reactivated during HF.

A few examples of bedding-plane reactivation have been identified. At 8469 ft in Core 4 the break is notable for its smooth surface and deviation of the break around small concretions (Fig. 9). Note the asymmetry of the deviation, away from the hydraulic fracture (Fig. 9b). The bedding plane appears to be reactivated on both sides of the hydraulic fracture. Although in the CT scan the pieces are seen to have moved the core pieces can be fitted back together indicating no diversion at the bedding plane (Fig. 9c). This example is in marked contrast to a common geometry seen in all four cores where a core handling break occurs along bedding, breaking off the tips of core pieces adjacent to hydraulic fractures (Figs 9 d, e). In these cases,

the core handling break is rough, which contrasts sharply with the smooth surface of the hydraulic fracture.

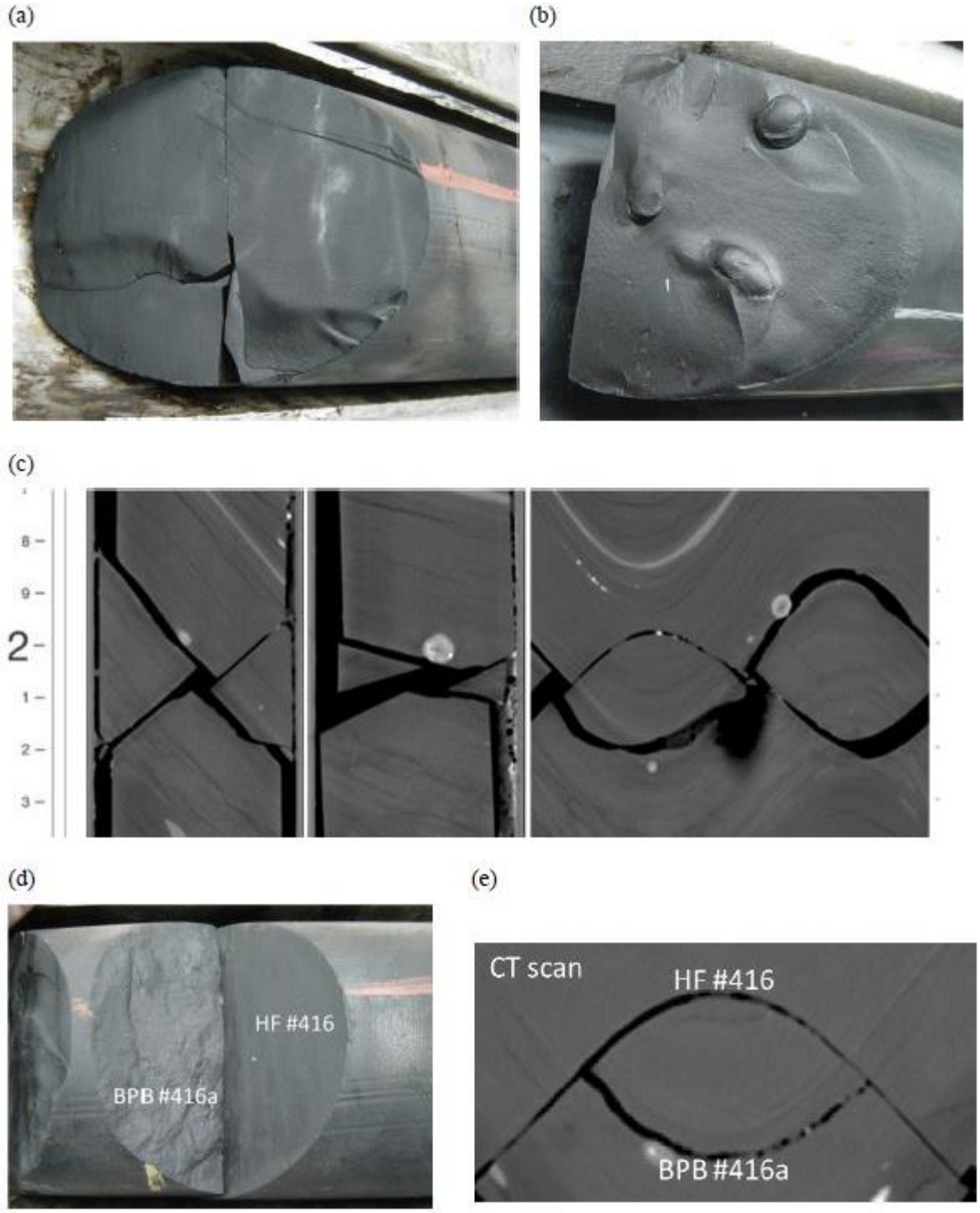


Figure 9. (a) Hydraulic fracture #414 and (b) bed-parallel reactivation #413 at 8469 ft in Core 4. (c) CT scan from this depth showing both fractures. Note the concretion nodules in both the core photo and CT scan. (d) Smooth hydraulic fracture with rough bed-parallel break at tip of downhole core piece, (e) CT scan of (d).

Natural Fractures, Sets 1 and 2, bed-parallel, others.

Set 1 fractures are the most numerous natural fracture type (Fig. 10). There are 18 in Core 1, of which 7 are parted; 6 in Core 2 of which 3 are parted; 13 in Core 3 of which 8 are parted; and 17 in Core 4 of which 11 are parted. They have NE-SW subvertical orientations and are all less than 1 mm in kinematic aperture. Very few show any indication of being open in the subsurface; #405 appears to have some porosity in the center between fracture cement linings

on each wall (Fig. 10). We interpreted 6 as being reactivated by hydraulic fracturing. In the example in Figure 10c the fracture plane is in the orientation for Set 1, but with no obvious cement (although a veneer could be present). Other intact Set 1 fractures in this orientation are present in the same 3ft core interval. It is adjacent to a hydraulic fracture.

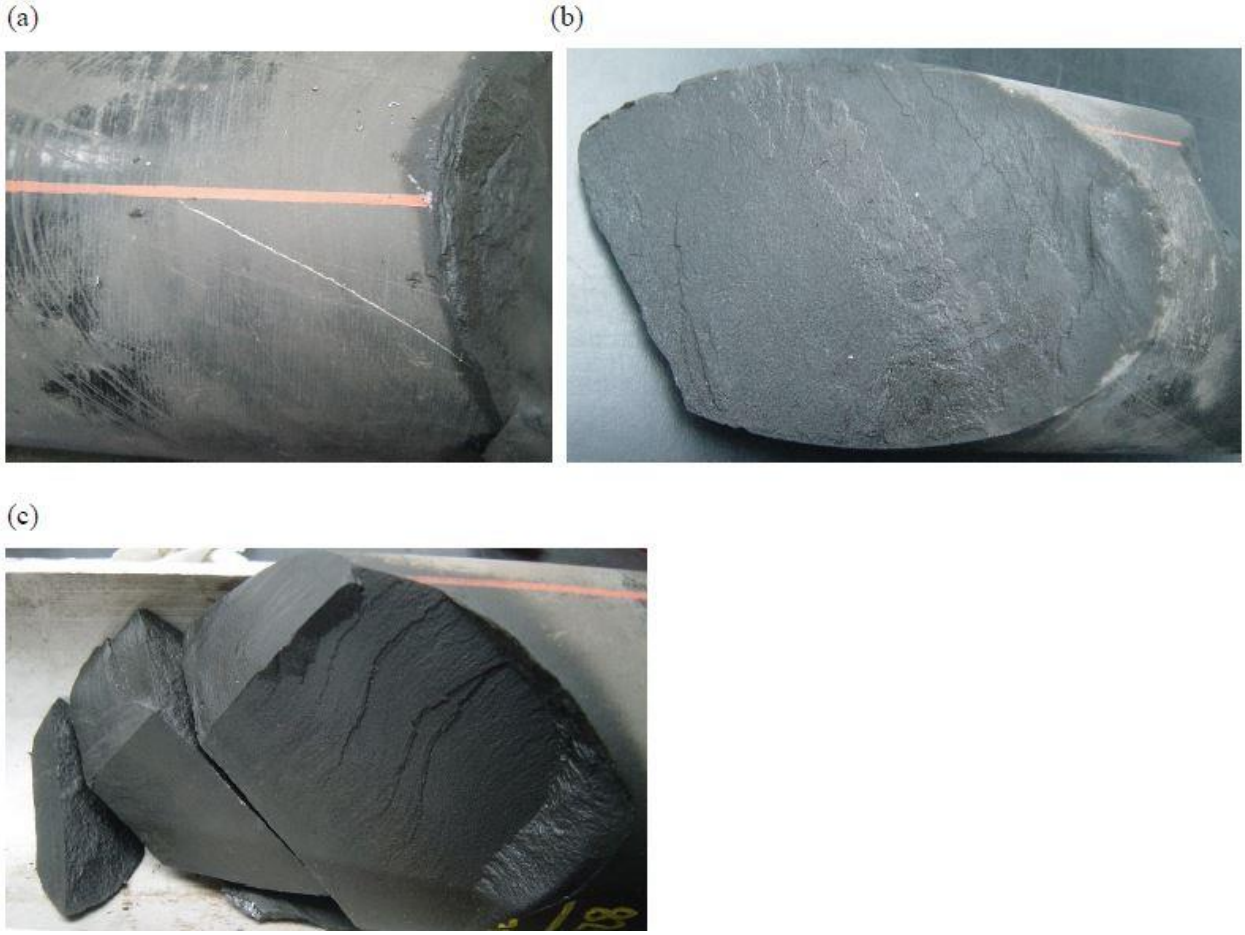


Figure 10. Set 1 natural fractures. (a) Intact fracture #114, 0.215 mm wide at 8256.7 ft in Core 1 (b) Parted fracture #10,
from 8429.9 ft in Core 4, possibly reactivated during core handling, (c) Fracture #107 from 8253 ft in Core 1, reactivated by hydraulic fracture #108, seen obliquely at top left of photo.

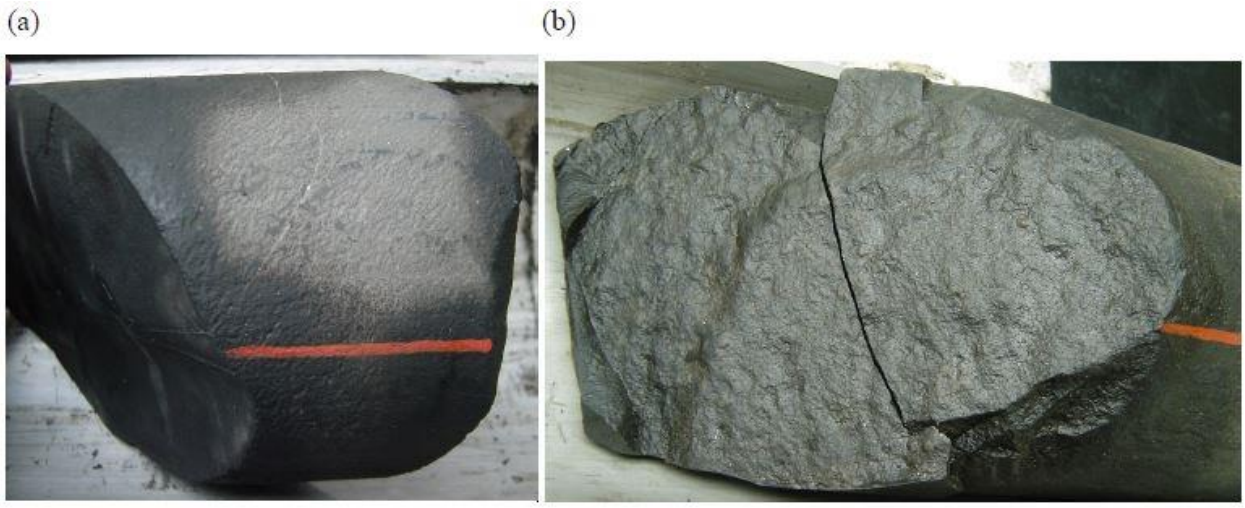


Figure 11. Set 2 natural fractures (a) En echelon segments #321, 322 and 323 sealed with calcite at 8385.6 ft in Core 3, (b) Parted fracture #266 in coarse carbonate at 8355.6 ft in Core 3. The calcite cement is present as a veneer on the surface, which is rougher than most natural fractures.

Set 2 fractures are much less common: there is 1 sealed example in Core 1; 7 in Core 2 of which 1 is parted; 6 in Core 3 of which 2 are parted; 3 in Core 4 of which 1 is parted (Fig. 11). These also are less than 1 mm wide and do not show indication of having been open in the subsurface. In most cases where these calcite-filled fractures cut shale they are readily seen in the core and in the CT scan because of the contrast between the calcite cement and the shale host rock. Where they occur in carbonate intervals they can be challenging to identify because of the lack of contrast between cement and host rock composition. The example in Figure 11b is of a Set 2 fracture in coarse carbonate. Orientation, while a useful guide, is not always conclusive because orientation ranges of natural fractures and hydraulic fractures (designated Sure or Probable) overlap (Fig. 2). As with other natural fractures most have one or both tips out of the core so length and height cannot be measured. Many in both sets occur in groups of en echelon segments (Fig. 11a). There are 13 bed-parallel natural fractures mostly in Cores 1 and 2, compared to only 3 in the 6TW well.

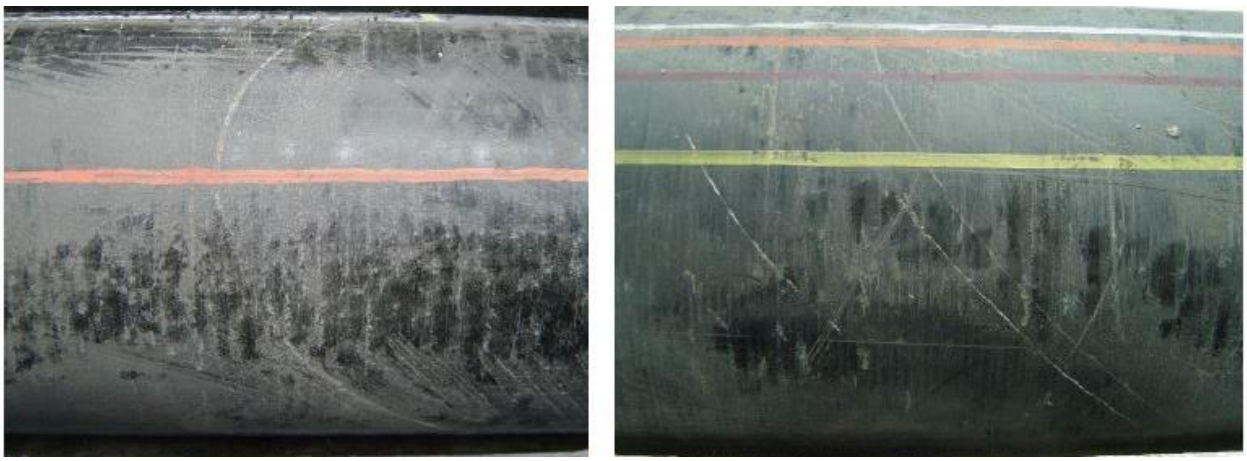


Figure 12. Two examples of bed-parallel, calcite filled fractures (a) #69 from 8220.75 ft in Core 1, (b) #202 from 8316.5 ft in Core 2.

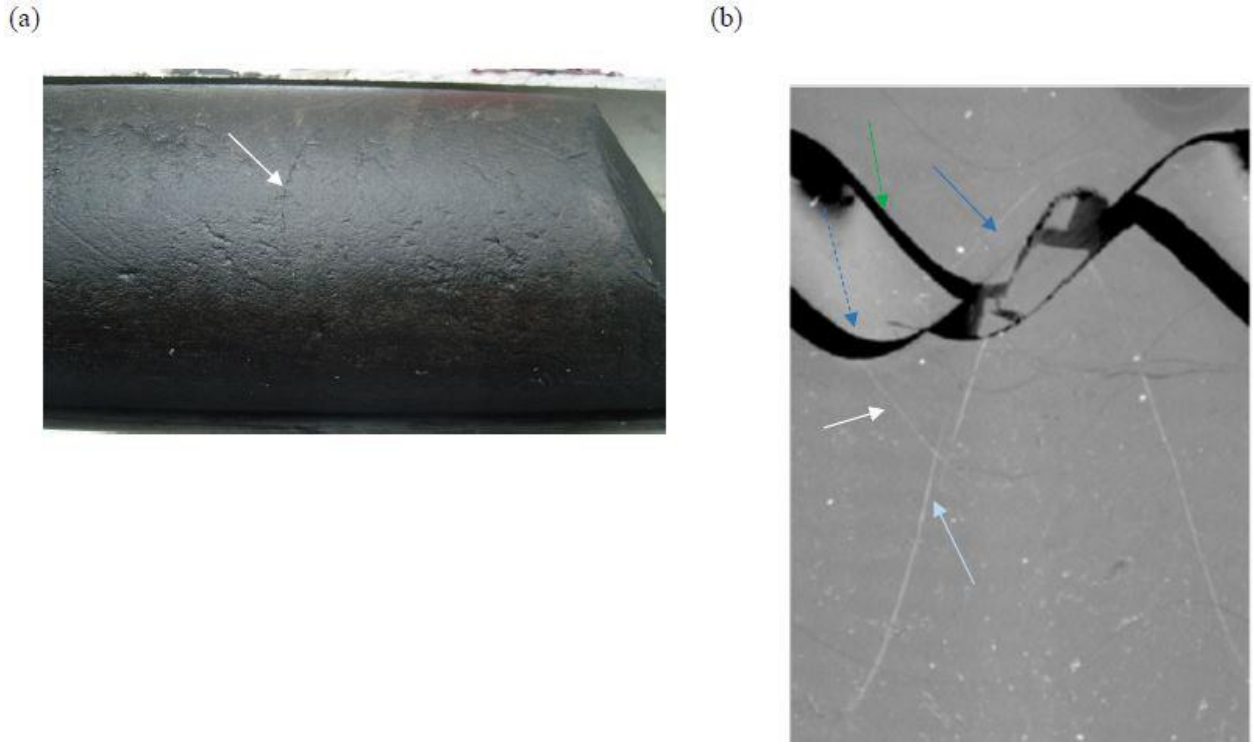


Figure 13. Undifferentiated fractures at 8282-8282 ft. (a) trace of 0.175 mm wide fracture #150 on the core surface (arrow). (b) CT scan of same interval showing #150 undifferentiated (white arrow), #149 set 1 (light blue arrow), #147

set 2 (dark blue arrow) and #146 hydraulic fracture (green arrow). The dashed blue arrow is #148, which is interpreted as a Set 2, reactivated during hydraulic fracturing.

They are challenging to distinguish from thin carbonate laminae. The criteria we used were consistent width, planar margins, calcite fill with a blocky appearance (no fibrous 'beef' was seen), and lack of other particles in the fill. Examples are shown in Figure 12; we only identified sealed examples although it is possible a few bedding parallel breaks occur along this fracture type. We did not observe crosscutting relationships between Sets 1 and 2, nor with the bed-parallel fractures. The only timing information observed was for the undifferentiated fractures seen at the top of Core 2 (Fig. 13). There, fracture #150, which is a sealed, 0.175 mm- wide, calcite filled fracture, terminates against #148 (Set 2) and #149 (Set 1) so likely postdates both (Fig. 13).

Faults

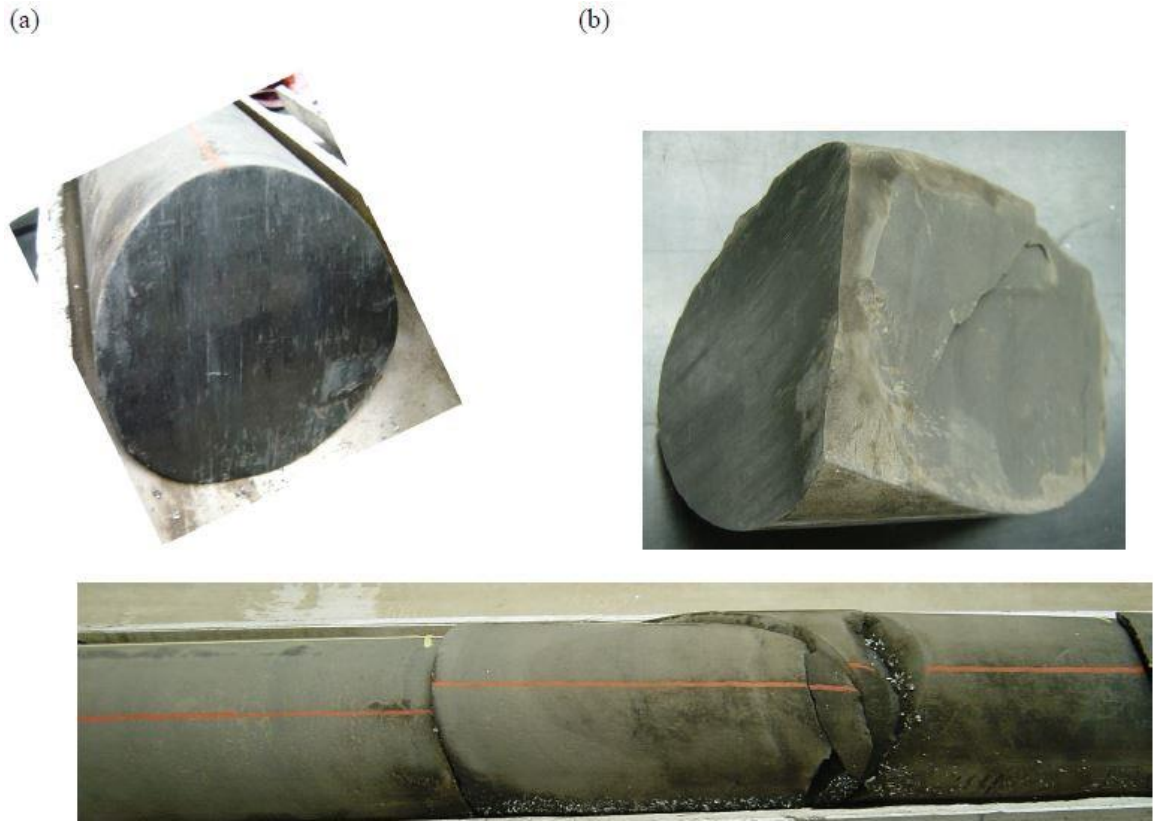


Figure 14. Thrust fault #380 at 8427 ft in Core 4. (a) downhole face with slickensides (b) Uphole face and barren Set 1 fracture #379 terminating at fault. (c) Thrust close to yellow tick mark at 8,427 ft & Set 1 fracture #379 uphole of that.

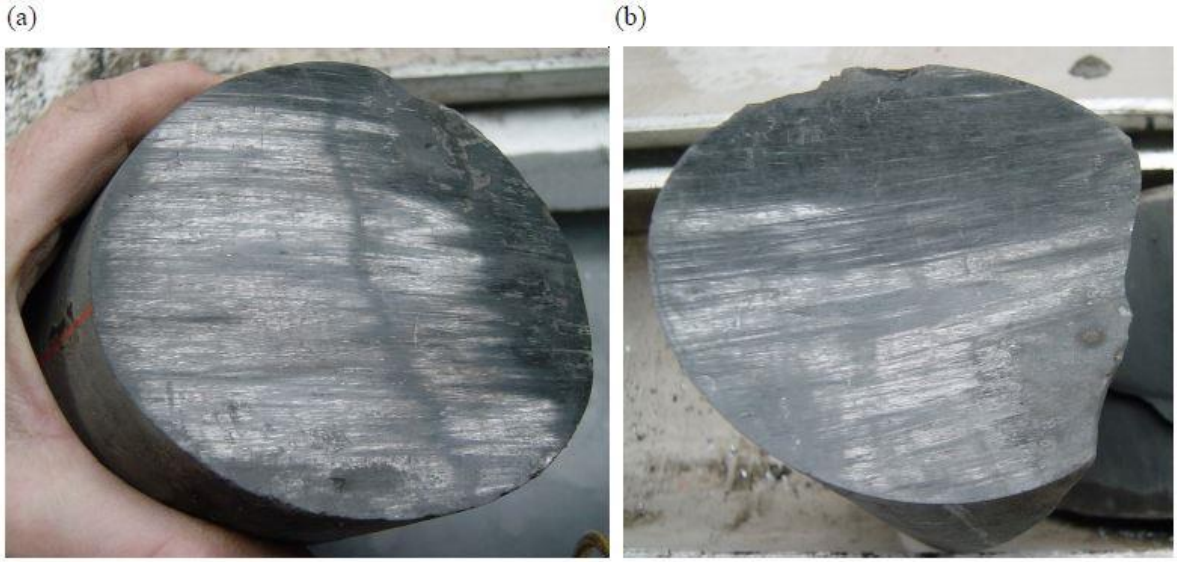


Figure 15. The sheared, highly polished surface of fracture #380 (a) downhole face (b) uphole face.

A thrust fault (#380) occurs in Core 4 at around 8427 ft (Fig.14) dipping 32▪ to the north, with well-developed slickensides with associated calcite fibers plunging 32▪/006▪. This is the only fault observed in the core, although minor, soft sediment deformation with early faulting is present in several places, most notably in Cores 3 and 4. The saddle shape of the fault plane in the core is suggestive of a drilling induced fracture, but we do not favor this interpretation on the basis that no other fractures have these slickensided, polished surfaces (Fig 15), and that these polished surfaces (mirror planes) are recognized as faults in other cored shales, most notably the Marcellus Fm. where they occur as bedding-plane slip surfaces (Wilkins et al., 2014).

Drilling induced fractures

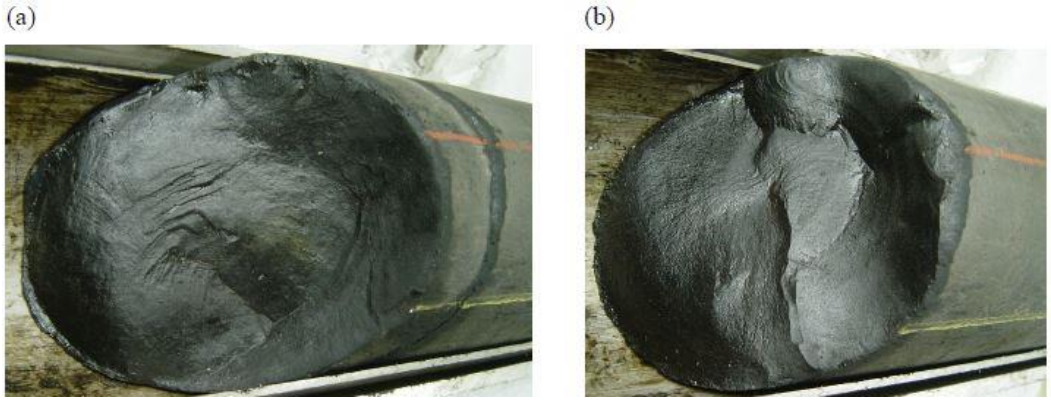


Figure 16. Downhole faces of (a) Fracture #15 & (b) Fracture #16 at ~ 8413 ft in Core 4. These two smooth, curvi-planar yet irregular breaks with plumose in multiple locations and orientation both cut across bedding. Uphole is to the left.

(a)



(b)

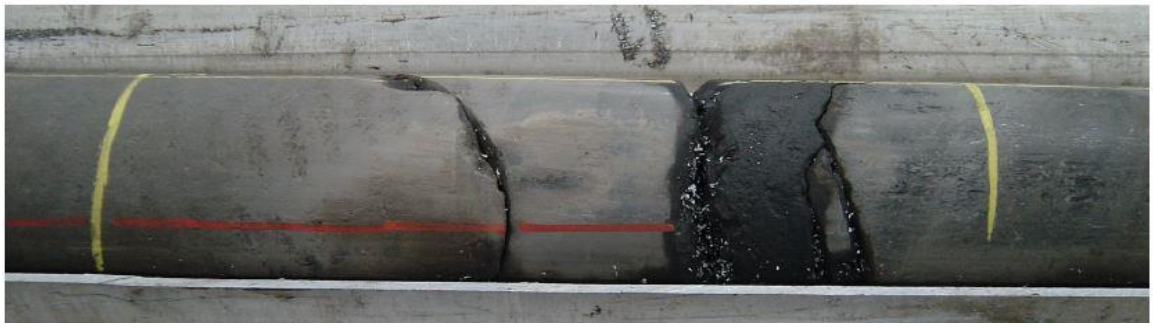


Figure 17. (a) Concentric spin marks on the uphole face indicate a drilling-induced break normal to the core axis (b) Core 4 at 8415.4 ft; the break in (a) is the middle fracture, #359. Fracture to the right (uphole) is a core handling break, #358, and the fracture to the left is a hydraulic fracture, #360.

Drilling induced fractures are identified from core-symmetric features occurring on smooth but irregular surfaces. Common features are plumose around the margin and breakoff tangs. Scoop shaped or saddled shaped morphologies also occur (Fig. 16)

At 8415.4 ft in Core 4 concentric spin marks on each face indicate a drilling induced break normal to the core axis (Fig. 17).

Planes reactivated during drilling.

There is one example, fracture #23, at 8379.65 ft in Core 3, of a shear fabric in the fracture plane (Fig.18). This is in a plugged interval. Bedding has reactivated in steps with striations slightly oblique to core axis trace on plane, which is consistent with shear along bedding during drilling.



Figure 18. Bedding parallel break with shear indicators. Fracture #23, at 8379.65 ft in Core 3.

Planes reactivated during CH.

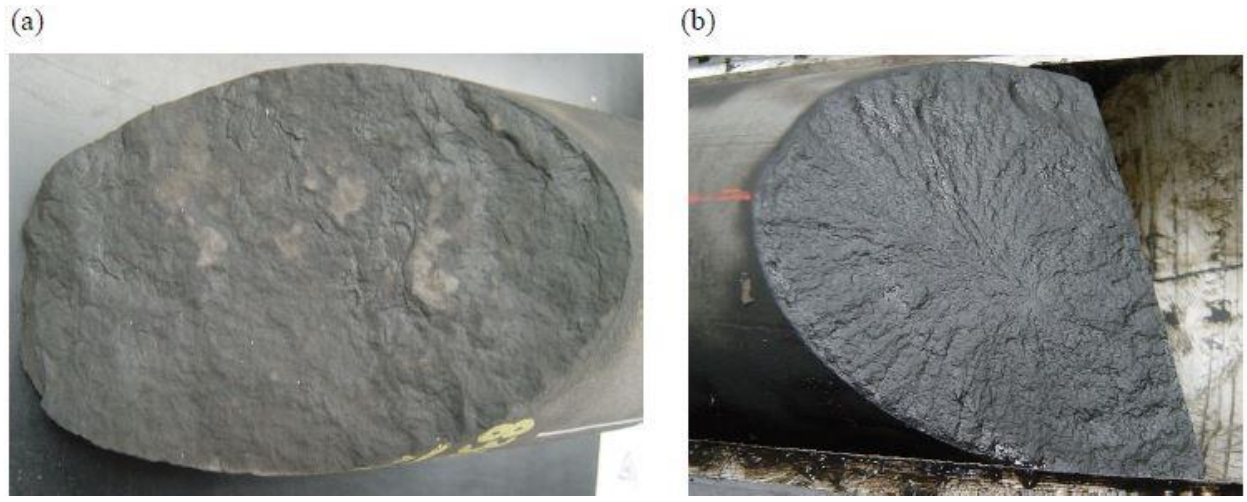


Figure 19. The photo is of #314, a rough, bed-parallel plane approximately 2 ft below Fracture #23. There is no shear, no nearby hydraulic fracture and the surface is rough and slightly irregular. The 'best guess' interpretation is that this is a break along bedding due to core handling.

Many bed-parallel breaks appear to have been caused by core handling (Fig. 19). They generally have rough surfaces although they can be quite planar (Fig. 19a). Others may step along different bedding planes or may be irregular. This category includes all the small 'tip of core piece' breaks that occur adjacent to throughgoing fractures of any kind (e.g., Fig. 9d). A few of these breaks have plumose surface markings from the center of the break (Fig. 19b).

Discussion of bed-parallel break interpretation

The difference in deviation of the two wells (~57° in the 5TW versus 80° in the 6TW) likely impacts the manifestation of drilling-induced fractures and core-handling breaks; the core is more likely to break along bedding in the 5TW than in the 6TW. In some cases, parted bed-parallel breaks could not be assigned a category. They might be reactivated during hydraulic fracturing, during drilling or during core handling. Core handling could include the rate of core retrieval to the surface. It is known that in vertical cores fast trip rates in low permeability rock can lead to multiple bed-parallel breaks ('poker chips'). The retrieval rate for the 5TW was variable for the different cores, some faster than for the 6TW, some slower. In other cases, the

designation is a 'best guess' made based on a criterion of roughness and irregularity of the plane. Fractures developing in the subsurface are likely to be more planar than those formed at the surface because they form under a substantial confining pressure. Differences in sedimentary fabrics, however, can affect planar vs rough fracture growth—finely laminated mudrock could lead to a more planar bed-parallel fracture than a massive, coarse carbonate debris flow. Firm classification is therefore not possible for many bed-parallel fractures, and most are assigned a 'Best Guess' uncertainty in the data spreadsheets.

Discussion of hydraulic fracture occurrence in the cores

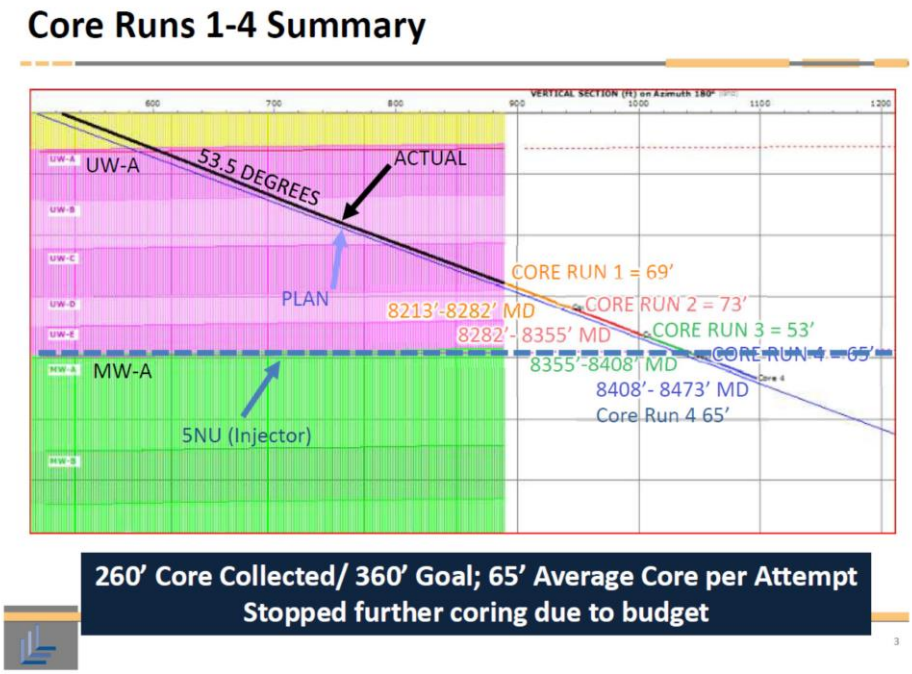


Figure 20. Slide from Laredo showing position of the 5TW cores relative to the 5NU well.

Hydraulic fracture intensity varies between cores and tends to be clustered. A comparison of the relative position of the 6TW cores against the 5NU injector well (Fig. 20) shows that the lowest intensity of hydraulic fractures, in Core 4, lies below the 5NU. The highest intensity is not in Core 3, which is closest to the 5NU, but in Core 2 some way above the 5NU. We also note the relatively high abundance of carbonate debrites in Cores 3 and 4, which may inhibit hydraulic fracture growth to some extent. The effect of positioning of perforation clusters, combined with lithological variation, on hydraulic fracture intensity would be a topic for further work.

Conclusions: fracture description

Examination of the 5TW cores and CT scans revealed 431 main fractures and multiple additional, small, subsidiary breaks. Orientations are broadly like those found in the 6TW well.

Hydraulic fractures, and two main sets of natural fractures were identified. These fracture types, including their orientations, are like those seen in the HFTS 6TW well. There are some differences in other aspects of the fracture population in the 5TW well.

Hydraulic fractures, striking approximately E-W, are present through all 4 cores but the intensity varies. The greatest abundance is in Core 2, least in Core 4, and similar abundances in Cores 1 and 3. Typically, hydraulic fractures tend to be clustered, with doublets and

bifurcations and in some cases the fracture tip is contained in the core. There are a total of 129 hydraulic fractures.

Core 1: 30 in 69 ft (mean 0.43 fracs/ft)

Core 2: 57 in 73 ft (mean 0.78 fracs/ft)

Core 3: 23 in 53 ft (mean 0.43 fracs/ft)

Core 4: 20 in 66 ft (mean 0.30 fracs/ft)

As in the 6TW cores, hydraulic fractures are remarkably smooth and planar. Some have twist hackles, which can be used to infer propagation direction. Hydraulic fractures with twist hackles make up a consistent proportion of the total in Cores 1-3 but are less common in Core 4. Distribution is as follows: Core 1: 11 of 30 (37 %); Core 2: 19 of 57 (33%); Core 3: 10 of 23 (43%); Core 4: 3 of 20 (15%)

There are two sets of subvertical, calcite-filled fractures, like those in the 6TW cores: Set 1 strike NE-SW and Set 2 strike WNW-ESE. Both sets have sealed and parted fractures. Set 1 fractures: 18 in Core 1, of which 7 are parted; 6 in Core 2 of which 3 are parted; 13 in Core 3 of which 8 are parted; 17 in Core 4 of which 11 are parted. Set 2 fractures:

Core 1 has 1 sealed; 7 in Core 2 of which 1 parted; 6 in Core 3 of which 2 parted; 3 in Core 4 of which 1 parted. There are 13 bed-parallel natural fractures mostly in Cores 1 and 2 (3 in 6TW). We observed one thrust fault in Core 4, dipping 32° to the north, with well-developed slickensides and fibrous calcite plunging to the north in this plane. This was the only fault seen. Minor soft sediment deformation is present in several places, most notably in Cores 3 and 4.

A major difference between the 5TW and the 6TW is the large number of parted bed-parallel fractures in the 5TW: 37 in Core 1, 29 in Core 2, 23 in Core 3, and 22 in Core 4. There were very few in the 6TW. Broadly, we used the following criteria based on the morphology of the fracture plane and the degree of roughness of the surface:

Smooth and planar: Hydraulic Fracture

Smooth with shear: Drilling Induced

Rough and irregular: Core Handling

The number of drilling-induced fractures identified, per foot of core, in the 5TW (65/261 = 0.25 fractures/ ft) is greater than found in the 6TW (91/600 ft = 0.15 fractures/ft). In the 5TW there are 7 in Core 1, 11 in Core 2, 21 in Core 3, and 26 in Core 4. In the first part of Core 3 and in parts of Core 4 there are several irregular, but smooth and core-symmetric breaks almost normal to the core axis. At these depths (~8355–8375 ft) there are coarse carbonate layers, which may have affected the way the core failed during drilling; core fails normal to core axis in massive, coarse, carbonate layers. In the shaly intervals it is possible the orientation of bedding relative to the well-favored drilling reactivation along bedding planes.

Laredo Sugg E 197 5TW Slant Well Proppant Analysis

Proppant Analysis Overview

In this part of the project, we undertook proppant analysis on a subset of the fractures (10 out of 431). The rationale behind sample selection is indicated in Table P1. During the core fracture

description, we looked for fractures that had any sign of sand. We did not observe sand packs or patches (unlike the 6TW). We did note some occurrences of an orange, paste-like substance with grains in a few fractures, or on the outside of the core in a few places near the end of Core 1, in Core 2, and at the beginning of Core 3. This potential sand slurry was imaged through a hand lens before disturbing (Figure P1), and the three fracture samples with this material were collected and analyzed. We also analyzed one of the more complex fracture networks and included samples from all 4 cores, from different lithologies, and those with various surface characteristics, e.g., smooth vs. twist hackles etc. (Figures P2-P5).

We collected, washed, sieved, weighed, imaged, and conducted image analysis and interpretation for the 10 selected samples using the protocols established and documented during Phase 1 of the HFTS project (Gale et al., 2017). The only differences in methodology here is that 1) a mild blue-hued white-balance correction was applied to the images before analysis in order to make any true red or yellow grains more apparent, and 2) with a data set this small it was feasible to spend more time manually editing the images before analyzing to remove any obvious aluminum. This additional editing ensured increased proppant count accuracy because during automated analysis elongate aluminum tends to get segmented by the watershed algorithm and then counted as numerous individual "grains."

Table P1. Proppant samples analyzed keyed to fracture numbers. Notes were made at the time of the fracture description. Samples were also eyeballed for proppant during cleaning and processing (stars); size indicates relative quantity of apparent proppant observed.

Core	Depth Interval	Fracture #	Fracture Type - Description	Notes Taken during Collection
	8276.0-8279.0	38	1/2 intact NF Set 1	
		39		
Core 1		40	HF doublet; reactivated part of #38	Messy complex
	8242.8-8245.8	89	HF - twist hackle at bedding	Gritty surface
	8248.8-8250.55	99	BP break - rough & irregular	Blobs of orange "paste" (sand slurry?) on surface
Core 2	8321-8324	220	HF - smooth, slightly irregular	Some orange "paste" on surface
	8355-8358	270	HF - Extremely smooth	Some orange "paste" on surface; in carbonate section
	8358-8361	275	DI - irregular break high angle to core, smooth	Gritty muddy surface; in carbonate section
Core 3	8376.2-8378.7	312	BP break - smooth w/ cm-scale pyrite nodules	Probably drilling-react. b/c of plumose in center, but could be HF-react.
	8422.3-8425.3	375	HF - face has 2 sets of twist hackles, 1 up 1 down	"Good candidate for propp"
Core 4	8431.3-8434.3	385	NF Set 2 - planar w/ stepped break & cc cement	One of the few open, collected Set 2's; probably drilling reactivated
	8467.3-8470.4	414	HF - smooth with curving step on east side	Possible BP reactivation next to it

Visible Sand After Washing

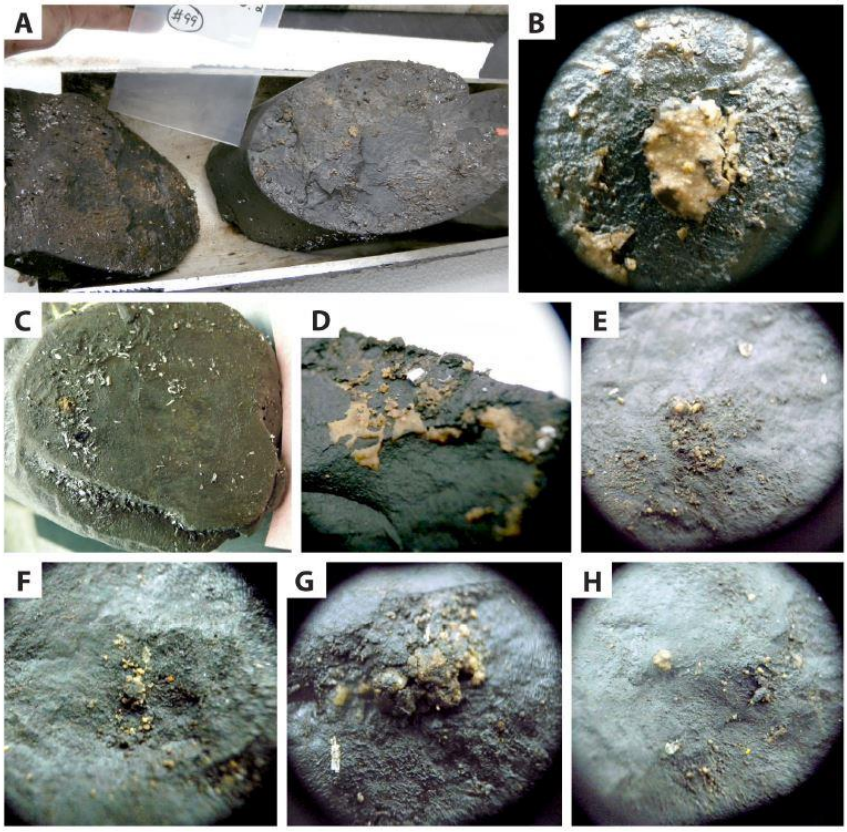


Figure P1. Orange paste material (potential sand slurry) found on certain fracture faces. A) Both fracture faces of BP #99. B) Closeup of orange substance through hand lens; can see larger red and yellow tinted grains. C) Fracture face of HF #270 with small area of orange paste. D) Closeup of various examples of the orange sandy material through hand lens on fracture BP #98. (E-H) Closeup of orange substance through hand lens on fracture HF #221. Large grains of sand are apparent, and in (F) can see red and yellow tinted grains as well.

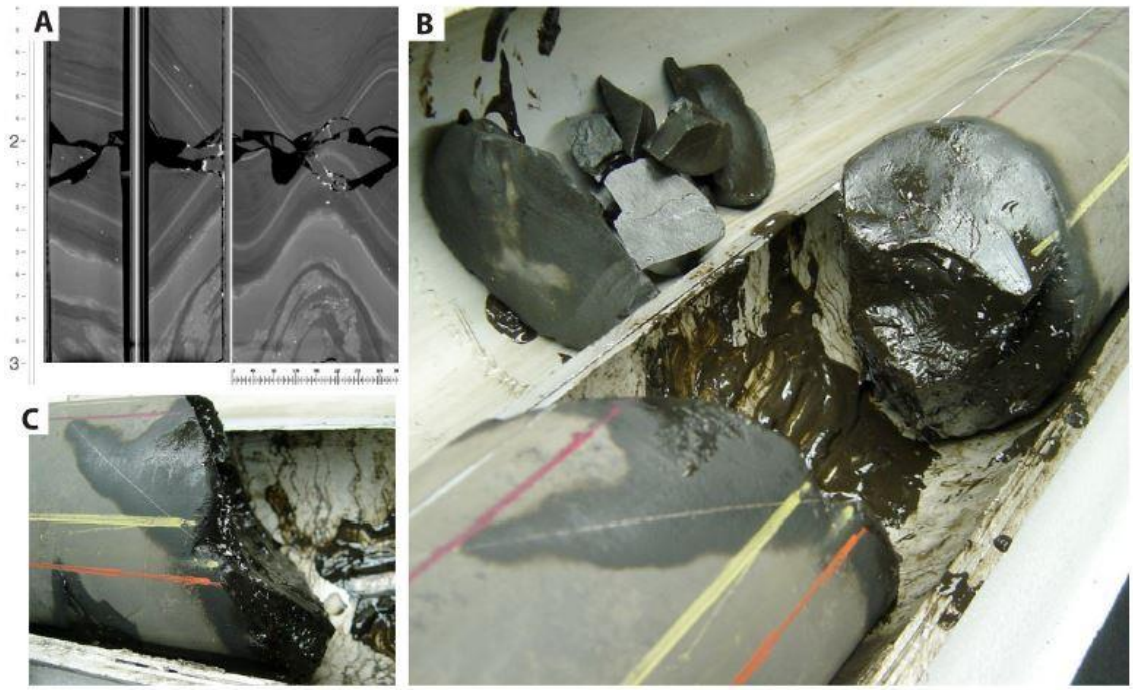


Figure P2. Hydraulic fracture doublet – reactivated set 1 natural fracture complex. A) CT scan of complex for reference. B) View uphole part way through cleaning/sample collection, the larger piece in the lid of aluminum tube is the shale "disc" between the doublets. C) View of #38 reactivated natural fracture showing that only part of it is now open while the rest is still intact.

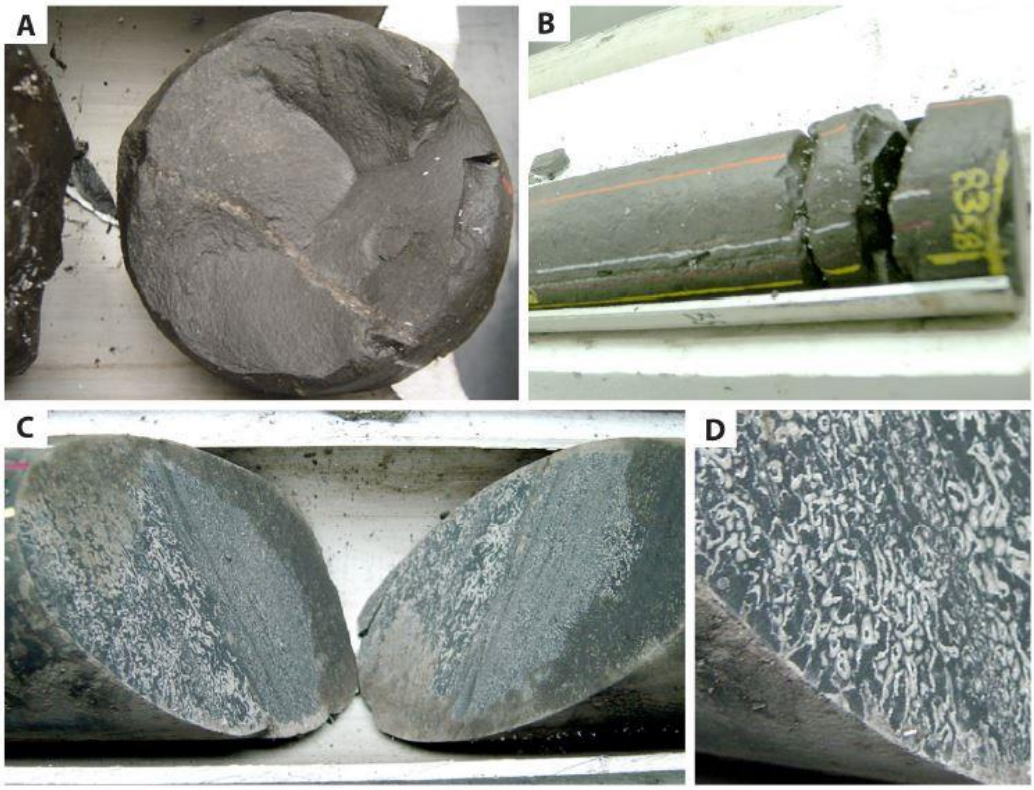


Figure P3. (A & B) Drilling induced break #275 nearly perpendicular across core axis. A large, intact, composite vein (#273) normal to the fracture face can be seen. (C) Both faces of drilling-reactivated natural set 2 fracture #385. (D) Close up of calcite cement on fracture face.



Figure P4. Bed Parallel Fractures. (A) Interval 8248.8-8250.55 showing that BP #99 is part of a set of similar breaks, all with the orange paste in and around them. (B) Downhole face of BP #99 showing rough irregular surface and gritty looking orange substance. (C) Downhole face of BP #312 with plumose structure emanating from center indicating that it's probably drilling-reactivated, although it could possibly be HF-reactivated. (D) Interval 8376.2-8378.7 showing seepage from bedding planes around #312, but none of the surrounding planes are fully broken.

A preliminary presentation of results was shared with the HFTS consortium in a conference call on June 12, 2019. Tables of results are archived on the Project Google Drive. Retrieved samples were labeled with respect to fracture descriptions and coded according to fracture type: hydraulic (HF), bed parallel (BP), natural reactivated set 1 or set 2 (NF), or drilling/recovery-induced fracture (DI). From this process, we quantified the amount of proppant within each fracture, and analyzed the distribution of grains among different fracture types.

Material collected, as for the 6TW cores, consists of drilling mud, aluminum shavings from the core barrel, shale and other lithic particles, calcite, and proppant that was pumped during the hydraulic fracturing of adjacent wells. The purpose of the work was to quantify the amount of proppant present in each fracture and investigate the proppant distribution along the core to the extent possible with such a limited data set. Ultimately the goal is to improve understanding of the propped fracture network, as well as hydraulic fracture growth and patterns.

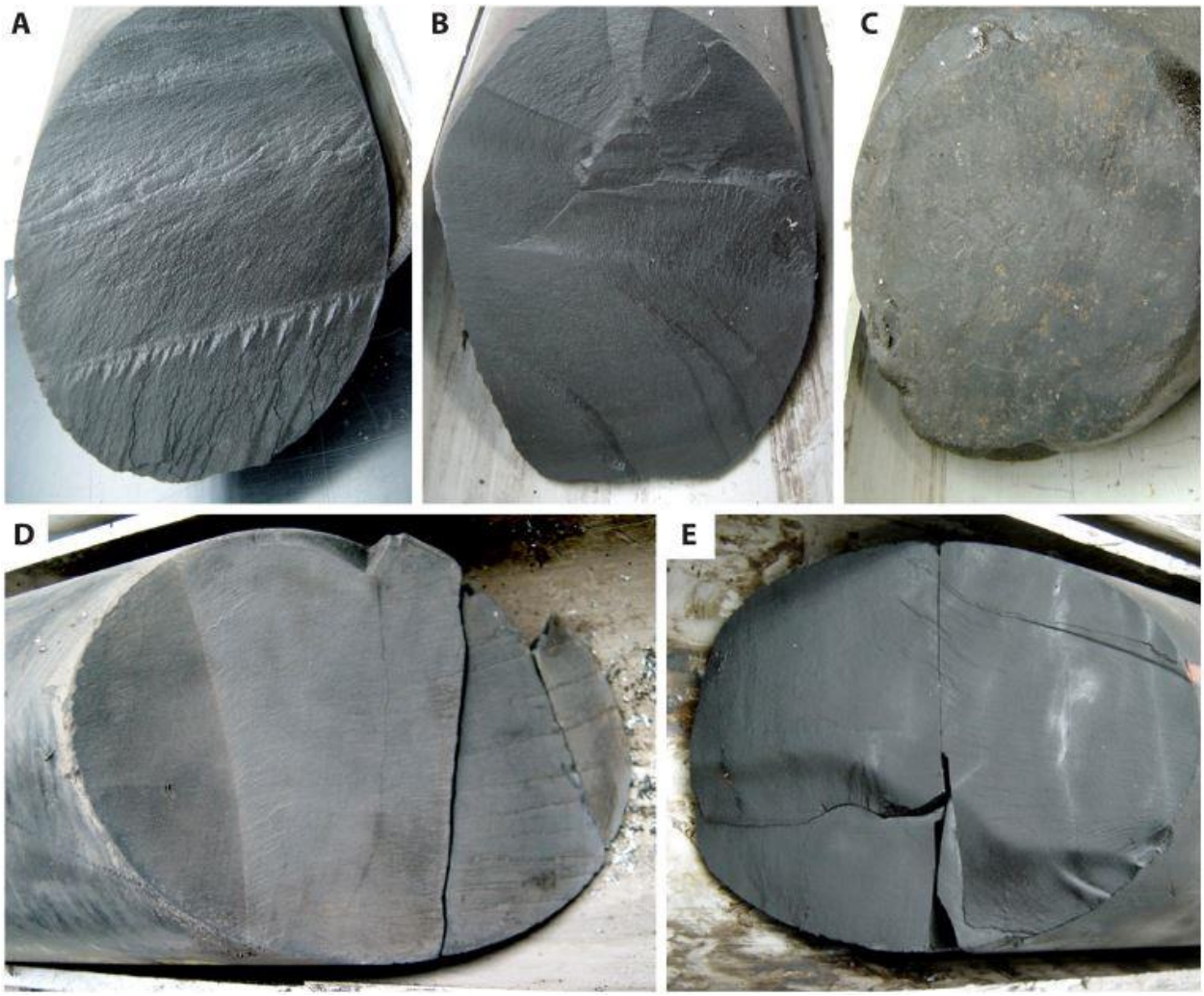


Figure P5. Single Hydraulic fractures chosen for proppant analysis. A) HF #89 (8242.8-8245.8 at 8285.1 ft) with twist hackles at bedding on part of the face. B) HF #220 (8321-8324 at 8323.1 ft) with a smooth, but slightly irregular face. C) HF #275 (8358-8361 at 8358.25 ft) with an extremely smooth, featureless face located in the coarser carbonate lithology. D) HF #375 (8422.3-8425.3 at 8424.65 ft) with multiple sets of twist hackles propagating different directions. E) HF #414 (8467.3-8470.4 at 8469 ft) with a curving step on the east side of the face. These hydraulic fractures contained variable amounts of proppant with (D) #375 containing the most and (B) #220 containing the least.

Key findings are:

1) Proppant was recovered from all 10 samples across all 4 cores, however there were not enough samples analyzed to categorize the proppant distribution. The sand grains found include some of the larger size fractions that were pumped; proppant ≥500 μm was recovered from 4 out of 10 samples. However, just like the 6TW slant core from Phase 1, the vast majority of recovered proppant (>99% for the 5TW) is ≤250 μm and not crushed suggesting it is mostly recovered 100 mesh base. No proppant packs or patches were found like those in the 6TW; however, some fracture faces contained an orange substance that potentially looked like small blobs of sand slurry. As with the 6TW slant core, there is always the chance that proppant could have been brought into fractures with the drilling mud.

2) The vast majority of recovered sand, as well as the largest size grains, were retrieved from the HF doublet – reactivated NF 1 complex (8276 -8279 ft, #38, 39, 40 at 8278.0 ft; Fig. P2). This appears to substantiate one of our main conclusions from the 6TW slant core: that HF doublet and triplet complexes have some of the best proppant trapping potential. In contrast, the drilling induced break across the core and the natural set 2 fracture, which is interpreted as being drilling-reactivated, contain the least amount of total material and proppant, indicating that this type of analysis is indeed capturing some in situ, fracture-specific signal of proppant placement and material trapping ability.

3) The next highest abundances of sand occurred in the HF with multiple sets of twist hackles on the face (8422.3-8425.3 ft, #375 at 8424.65 ft; Fig. P5) and the undifferentiated rough irregular BP break (8248.8-8250.55 ft, #99 at 8250.2ft; Fig. P4), indicating that fracture surface features affect proppant placement. BP #99 is also one of the three fractures analyzed with orange paste on the surface, and it contained the second highest amount of large sized proppant, with 5x more (279 grains >250 μm) than the next highest samples, which are both HFs (#270 with 56 grains and #414 with 51 grains >250 μm).

4) The next highest proppant abundance was found in the extremely smooth HF #270 located in the coarse carbonate unit, suggesting a possible lithologic control on proppant trapping in addition to fracture type and surface features. However, this is also one of the three orange paste samples, so further investigation of this hypothesis is needed with more samples analyzed.

5) In addition to the HF doublet complex, the individual hydraulic fracture samples generally contain the most recovered proppant (excepting BP #99) yet are still highly variable (between 3850 – 38691 grains).

6) All 10 samples contained red and yellow colored sand grains, even though no resin coated grains were pumped in the 5TW. From visual inspection, the overall proportion of colored grains versus clear or white is comparable among samples from this core, samples from the 6TW core, and DSLR-imaged samples of fresh 100 mesh base. This means that the majority of "colored proppant" was very likely overestimated in the 6TW colored-proppant analysis previously completed as part of HFTS Phase 1.

Results and Discussion

As previously stated, all fractures are designated a type and then color coded according to the master fracture Excel database explained above. The dry weights of all material recovered per sample, both by size fraction and sum total, are presented in Table P2. Based on weight data,

the least material was recovered from the DI break, followed by the NF Set 2, which is interpreted as being drilling-reactivated. This makes sense if both fractures were not actually open in the subsurface. On the other hand, the most material by far was recovered from the HF doublet-NF Set 1 fracture complex, which is unsurprising considering this is a combination of three fractures. The second highest volume of material was retrieved from the undifferentiated rough irregular BP break. Regarding hydraulic fractures, the recovered volumes of material are highly variable, ranging from ~100 to ~650 mg.

Table P2. Dry sample weights by size fraction (g) and total (mg).

Fracture Sample	Dry Weight (g)					Total Material (mg)	Fracture Type
	63-120 µm	120-250 µm	250-500 µm	≥500 µm	Total		
8276-8279_8278_**#38/39/40**	0.59054	0.32033	0.24450	3.06048	4.2159	4215.9	NF Set 1 + HF Doublet
8242.8-8245.8_8285.1_**#89**	0.03340	0.06862	0.12983	0.41513	0.6470	647.0	HF
8248.8-8250.55_8250.2_**#99**	0.06203	0.08727	0.14959	0.62265	0.9215	921.5	BP
8321-8324_8323.1_**#220/220a**	0.01440	0.02218	0.34980	0.18303	0.5694	569.4	HF
8355-8358_8356.7_**#270**	0.02425	0.01162	0.01189	0.05615	0.1039	103.9	HF
8358-8361_8358.25_**#275**	0.00418	0.00282	0.00319	0.00339	0.0136	13.6	Break across core
8376.2-8378.7_8377.9_**#312**	0.02079	0.02610	0.04697	0.28397	0.3778	377.8	BP
8422.3-8425.3_8424.65_**#375**	0.07024	0.03371	0.04311	0.08787	0.2349	234.9	HF
8431.3-8434.3_8432.4_**#385**	0.00641	0.00827	0.00852	0.02031	0.0435	43.5	NF Set 2
8467.3-8470.4_8469_**#414**	0.02152	0.01823	0.03371	0.27137	0.3448	344.8	HF

Table P3. Total particle counts per sample. Particles include shale fragments, calcite, aluminum shavings, and any proppant from the fracture face.

Fracture Sample	Particle Count #				Total Particle Count #	Fracture Type
	63-120 µm	120-250 µm	250-500 µm	≥500 µm		
8276-8279_8278_**#38/39/40**	315842	35182	4367	1262	356653	NF Set 1 + HF Doublet
8242.8-8245.8_8285.1_**#89**	18912	7833	2022	457	29224	HF
8248.8-8250.55_8250.2_**#99**	46295	11196	2405	470	60366	BP
8321-8324_8323.1_**#220/220a**	10319	2705	565	145	13734	HF
8355-8358_8356.7_**#270**	15118	1587	249	25	16979	HF
8358-8361_8358.25_**#275**	3253	495	58	10	3816	Break across core
8376.2-8378.7_8377.9_**#312**	17005	3481	903	142	21531	BP
8422.3-8425.3_8424.65_**#375**	49870	4750	826	150	55596	HF
8431.3-8434.3_8432.4_**#385**	6053	1330	166	17	7566	NF Set 2
8467.3-8470.4_8469_**#414**	16565	2602	585	144	19896	HF

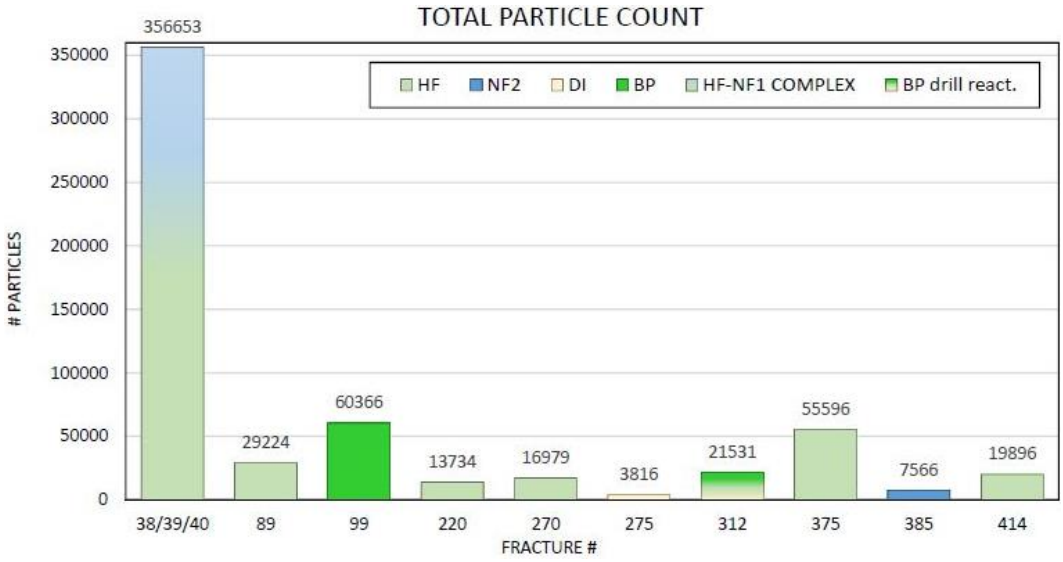


Figure P6a. Histogram of total retrieved particle abundance per sample color-coded by fracture type. The hydraulic fracture doublet-reactivated natural fracture complex has so much more material than all the other analyzed samples that the data is easiest viewed in log form on Figure P6b below.

Based on this limited data set, the analyzed fracture types span three order of magnitude: DI and NF 2 fractures contain 1000's of particles, HF and BP fractures contain 10,000's of particles, and fracture complexes contain 100,000's of particles.

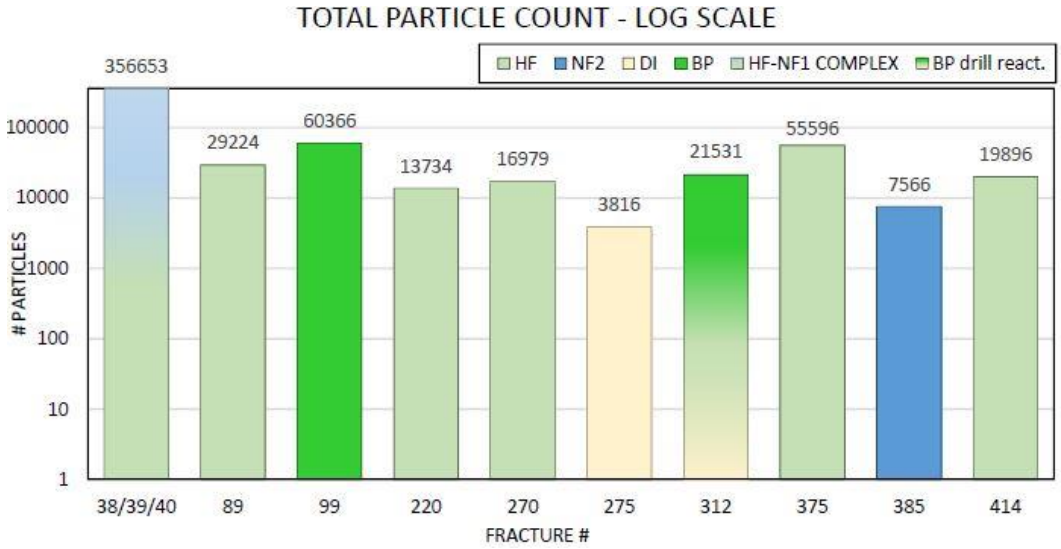


Figure P6b. Log scale histogram of total retrieved particle abundance per sample color-coded by fracture type. Samples spread across three orders of magnitude with the hydraulic fracture doublet-reactivated natural fracture complex boasting the most material and the drilling induced break containing the least.

Table P4. Proppant counts. Particles include shale fragments, calcite, aluminum shavings, and any proppant from the fracture face.

Fracture Sample	Proppant Count #				Proppant Total Count #	Fracture Type
	63-120 µm	120-250 µm	250-500 µm	≥500 µm		
8276-8279_8278_**#38/39/40**	252144	20114	953	33	273244	NF Set 1 + HF Doublet
8242.8-8245.8_8285.1_**#89**	4905	947	2	1	5855	HF
8248.8-8250.55_8250.2_**#99**	29677	5547	273	6	35503	BP
8321-8324_8323.1_**#220/220a**	3470	374	6	0	3850	HF
8355-8358_8356.7_**#270**	13168	1019	56	0	14243	HF
8358-8361_8358.25_**#275**	2754	223	6	0	2983	Break across core
8376.2-8378.7_8377.9_**#312**	7225	696	25	0	7946	BP
8422.3-8425.3_8424.65_**#375**	37476	1200	14	1	38691	HF
8431.3-8434.3_8432.4_**#385**	2628	403	7	0	3038	NF Set 2
8467.3-8470.4_8469_**#414**	10803	439	51	0	11293	HF

The recovered proppant abundance per sample, both by size fraction and total, are presented in Table P4. Proppant results are illustrated in two ways: color-coded by fracture type in Figures P7a & b and by size fraction in Figures P8a & b. Based on total proppant count data, fracture samples containing the least amount of sand were the DI break and the NF Set 2, which is interpreted as being drilling reactivated. Unlike the total particle count, the fracture containing the third least amount of proppant is the smooth slightly irregular HF #220. Just like with total volume and number of total particles, the HF doublet-NF set 1 fracture complex by far contains the most recovered proppant of any sample analyzed. This sample also contained most of the recovered larger sized proppant (>250 microns). The sample with the second largest amount of proppant is the HF #375, which has multiple sets of twist hackles on the fracture faces, and the third highest amount of proppant was retrieved from the rough irregular BP #99 fracture, which is one of the samples with the orange paste. Like total particle counts, the hydraulic fracture samples are extremely variable in their total proppant counts, ranging from 3850 – 38,691 proppant grains.

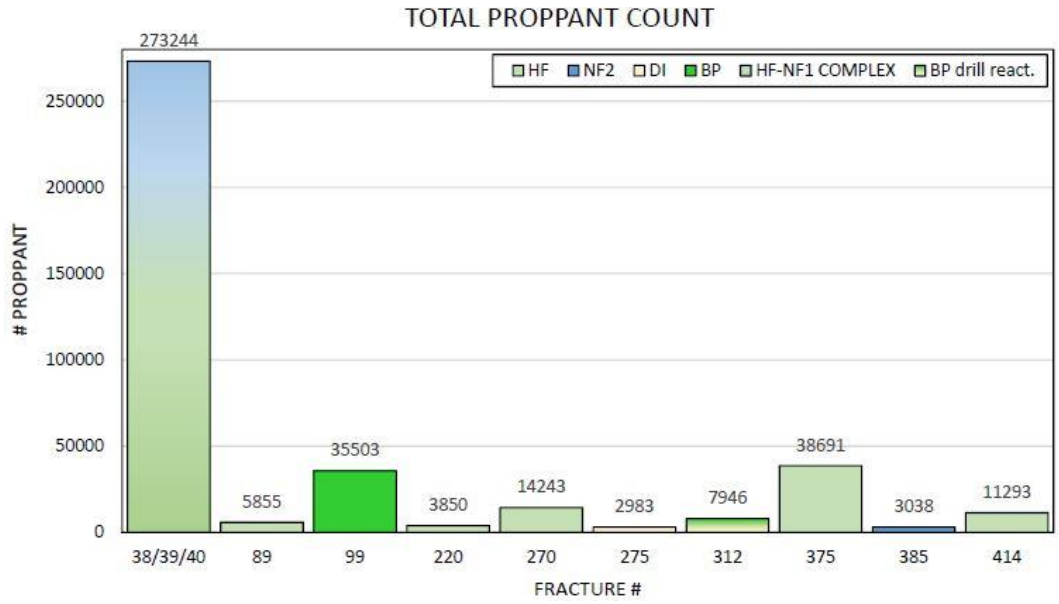


Figure P7a. Histogram of total retrieved proppant abundance per sample color-coded by fracture type. The hydraulic fracture doublet-reactivated natural fracture complex has so much more proppant than all the other analyzed samples that the data is easiest viewed in log form on Figure P7b below.

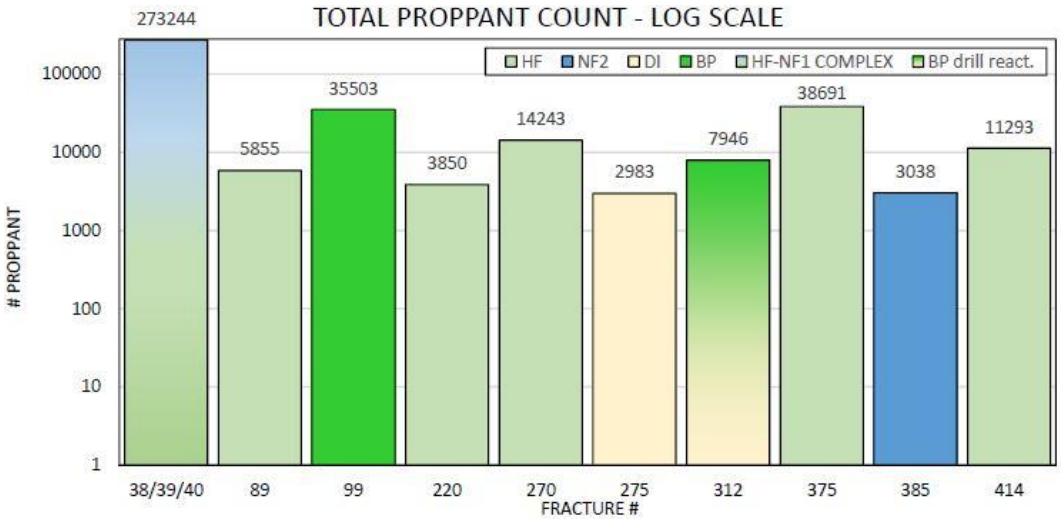


Figure P7b. Log scale histogram of total retrieved proppant abundance per sample color-coded by fracture type. Samples spread across three orders of magnitude with the hydraulic fracture doublet-reactivated natural fracture complex boasting the most material and the drilling induced break containing the least.

As with the total particle count, the sample total proppant count spans three orders of magnitude. The fracture complex #38, 39, 40 has 100,000's of sand grains, 3 out of 5 of the single HFs and the rough irregular BP contain 10,000's of proppant grains, and finally the drilling induced/reactivated features (e.g., the DI, the NF Set 2, and the BP #312) along with the remaining two HFs contain only 1000's of grains. It is possible that samples within this last category contain the "background" proppant abundance found in the drilling mud, while the others contain a true proppant network signal, but again more samples would need to be systematically analyzed to determine this.

The vast majority of recovered proppant is in the 63–120-micron range, even though persistent grain crushing is not observed, and most of these small sand grains appear rounded. It is possible that the smaller sand has significantly increased mobility versus the larger sand grains, which may just stay closer to the well.

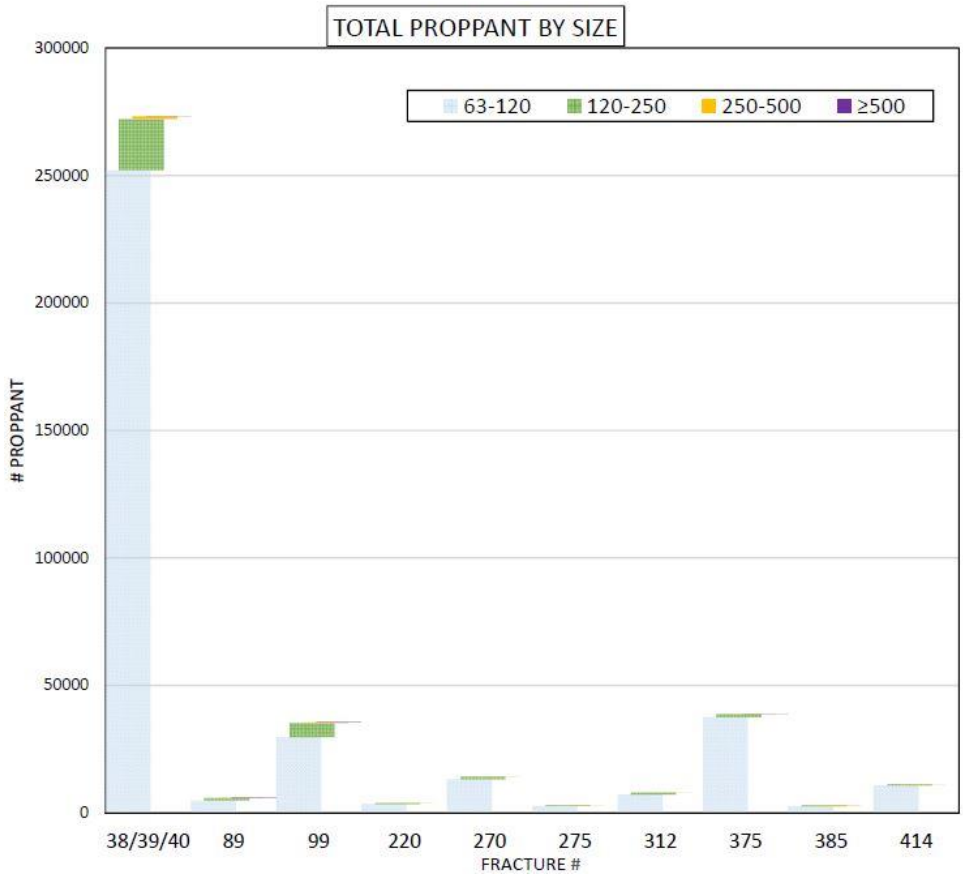


Figure P8a. Histogram of proppant abundance segregated into size fractions. The overwhelming abundance of small sand makes it nearly impossible to see the larger sand, thus it is extracted and shown separately on Figure P8b.

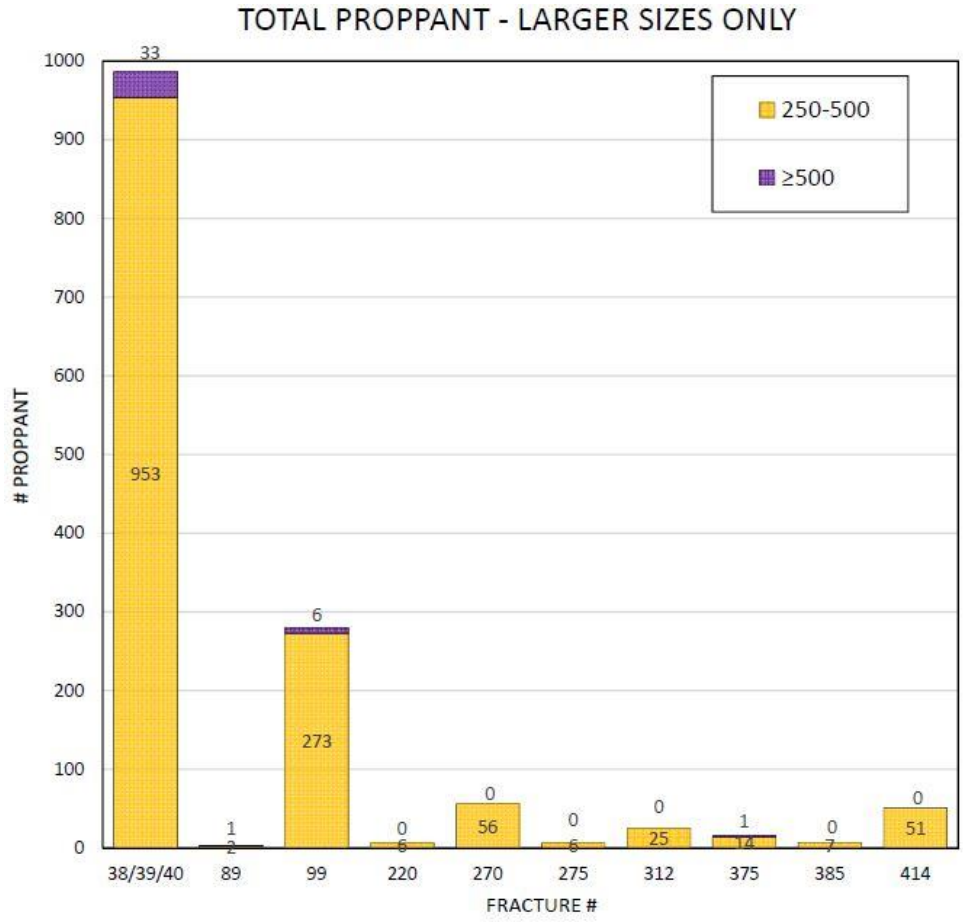


Figure P8b. Histogram of the two largest proppant size abundances. Fracture samples that contained the orange paste are #99, #220, and #270. Only 4 out of the 10 samples contained proppant >500 microns.

Using the total particle count and proppant count data per sample, we calculated the percentage of each sample that consisted of proppant, the percentage of each size fraction per sample that consisted of proppant, and the size distribution of the proppant across each sample (Table P5). Additionally, the size distribution of the total amount of recovered proppant across the whole sample suite is shown in Table P6. Nearly 92% of all recovered proppant is 63-120 microns, 7.8% is 120-250 microns, and less than 0.5% is >250 microns.

Table P5: Percentage of each sample that consisted of proppant, percentage of each size fraction of each sample that consisted of proppant, and the size distribution of the proppant of each sample calculated from total particle and proppant count data.

		% Sample that	% of Size Fraction that is Proppant				Proppant Size Distribution (%)				
Core	Sample	is Proppant	63-120	120-250	250-500	>500	63-120	120-250	250-500	>500	Fracture Type
CORE 1	8276-8279_8278_**#38/39/40**	**76.6**	79.83	57.17	21.82	2.61	92.28	7.36	0.35	0.01	NF Set 1 - HF Doublet Complex
	8242.8-8245.8_8285.1_**#89**	**20.0**	25.94	12.09	0.10	0.22	83.77	16.17	0.03	0.02	HF -1/2 twist hackle
	8248.8-8250.55_8250.2_**#99**	**58.8**	64.10	49.54	11.35	1.28	83.59	15.62	0.77	0.02	BP Break - rough/irreg
CORE 2	8321-8324_8323.1_**#220/220a**	**28.0**	33.63	13.83	1.06	0.00	90.13	9.71	0.16	0.00	HF - smooth, slight irreg
CORE 3	8355-8358_8356.7_**#270**	**83.9**	87.10	64.21	22.49	0.00	92.45	7.15	0.39	0.00	HF - very smooth
	8358-8361_8358.25_**#275**	**78.2**	84.66	45.05	10.34	0.00	92.32	7.48	0.20	0.00	DI
	8376.2-8378.7_8377.9_**#312**	**36.9**	42.49	19.99	2.77	0.00	90.93	8.76	0.31	0.00	BP Break - Drill react.
CORE 4	8422.3-8425.3_8424.65_**#375**	**69.6**	75.15	25.26	1.69	0.67	96.86	3.10	0.04	0.00	HF - full face twist hackles
	8431.3-8434.3_8432.4_**#385**	**40.2**	43.42	30.30	4.22	0.00	86.50	13.27	0.23	0.00	NF Set 2
	8467.3-8470.4_8469_**#414**	**56.8**	65.22	16.87	8.72	0.00	95.66	3.89	0.45	0.00	HF - smooth w/curving step

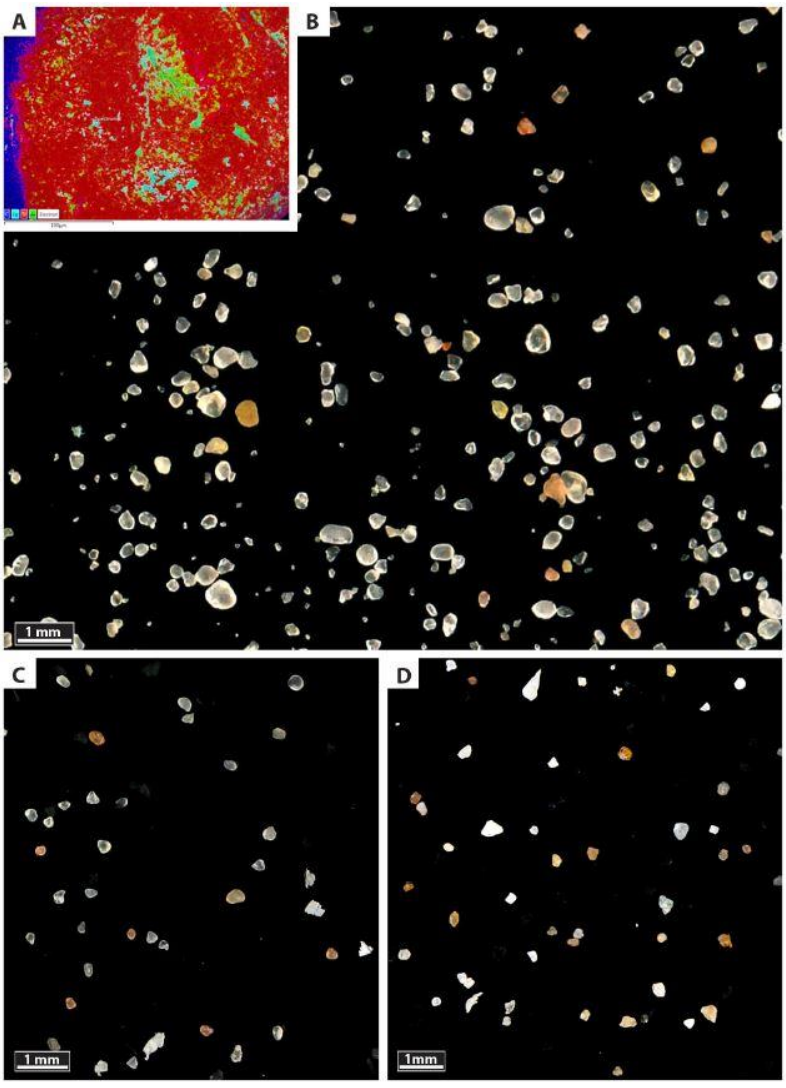


Figure P8. Comparison of colored grains among B) fresh 100 mesh base, C) 250–500-micron size fraction, fracture #4, 9487-9490 ft, SuggA171_6TW Slant Well, and D) 250-500 micron size fraction of the HF-NF set 1 fracture complex #38, #39, #40 from this 5TW core. The recovered "colored" grains are most likely just oxidized base. This is reinforced by inset (A) which shows Fe-oxidation (teal) and aluminum clays (green) on a recovered "red" proppant grain from SuggA171_6TW under SEM-EDS.

Table P6: Size distribution of the total amount of recovered proppant across the whole sample suite calculated from total particle and proppant count data. More than 99% of all retrieved proppant was <250 microns.

Total Recovered Proppant Size Distribution - All Samples (%)					
	63-120	120-250	250-500	>500	
	91.83	7.81	0.35	0.01	

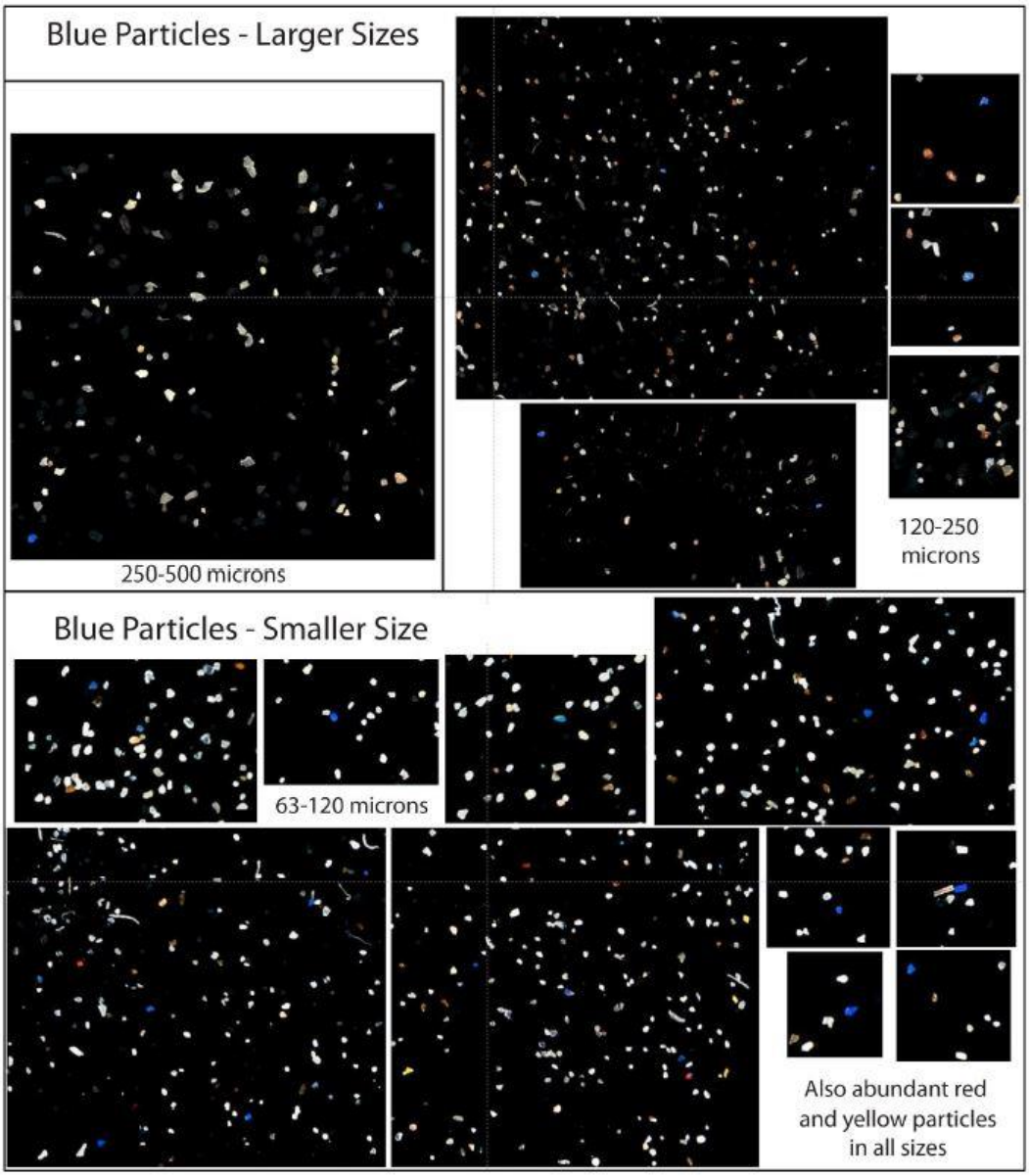


Figure P9. Fracture BP #99 (8248.8-8250.55 ft at 8250.2 ft) contains mysterious blue particles <500 microns that are sometime rounded but other times angular or elongate.

Comparing the visual inspection results obtained during sample processing (stars: Table P1) with the quantified proppant count data revealed that this preliminary method is generally accurate for an overall impression of proppant abundance, but that there are exceptions. For example, fracture #385 turned out to contain mostly calcite grains, not sand, even though with the naked eye the two materials look the same. Further, sample HF #414 contained one of the larger abundances of proppant, even though the sand was not readily apparent during cleaning.

It was recognized immediately that each of the 10 samples contained not only clear and white proppant, but also red and yellow grains just like samples from the 6TW core, even though no resin-coated sand was pumped in this 5TW core. Further inspection of the fresh 100 mesh base

along with samples from the 6TW core (Figure P8) suggest that the vast majority of red and yellow "colored proppant" counted in the 6TW was most likely just oxidized base grains.

In addition to copious red and yellow sand grains, the bed parallel fracture #99 (8248.8-8250.55 ft at 8250.2 ft) also contained mysterious blue particles which sometimes looked rounded and proppant-like, but at other times looked elongate or angular (Figure P9).

Summary

In this part of the project, we performed proppant analysis on a subset of the fractures (10 out of 430). We did not observe sand packs or patches (unlike the 6TW), but we did note some occurrences of an orange, paste-like substance (PB) with grains in a few fractures, or on the outside of the core in a few places near the end of Core 1, in Core 2, and at the beginning of Core 3. Samples analyzed include one of the more complex fracture networks, a drilling induced break, a reactivated natural fracture, 2 bed parallel breaks and 5 individual hydraulic fractures. These samples spanned all 4 cores, were from different lithologies, and had various surface characteristics, e.g., smooth vs. twist hackles etc.

1) Proppant was recovered from all 10 samples across all 4 cores, however there were not enough samples analyzed to categorize the proppant distribution. Proppant ≥500 μm was recovered from 4 out of 10 samples. The vast majority of recovered proppant (>99% for the 5TW) is ≤250 μm and not crushed suggesting it is mostly recovered 100 mesh base. No embedment was observed, and as with the 5TW slant core, there is always the chance that proppant could have been brought into fractures with the drilling mud.

2) The vast majority of recovered sand, as well as the largest size grains, were retrieved from the HF doublet – reactivated NF 1 complex. This appears to substantiate one of our main conclusions from the 6TW slant core: that HF doublet and triplet complexes have some of the best proppant trapping potential. In contrast, the drilling induced break and the drilling-reactivated natural set 2 fracture contain the least amount of total material and proppant, indicating that this type of analysis is indeed capturing some in situ, fracture-specific signal of proppant placement and material trapping ability.

4) A large amount of proppant was found in the extremely smooth HF #270 located in the coarse carbonate unit, suggesting a possible lithologic control on proppant trapping in addition to fracture type and surface features. However, this is also one of the three orange paste samples, so further investigation of this hypothesis is needed with more samples analyzed.

5) In addition to the HF doublet complex, the individual hydraulic fracture samples generally contain the most recovered proppant (excepting BP #99) yet are still highly variable (between 3850 – 38691 grains).

6) All 10 samples contained red and yellow colored sand grains, even though no resin coated grains were pumped in the 5TW. Likely this means that the majority of "colored proppant" was very likely overestimated in the 6TW proppant analysis previously completed as part of HFTS Phase 1.

References

1. Gale, J. F. W., Elliott, S.A., Li, J. Z. and Forstner, S., 2017, Laredo Sugg A 171 6TW slant well fracture characterization: systematic description. Final report for HFTS project, 26 p.
2. Gale, J. F. W., and Elliott, S. J., 2018, Fracture Spatial Organization and Proppant Analysis. Subcontract S5 for GTI Project No. 21686: Hydraulic Fracture Test Site (HFTS): Final Report Phase 2, 29p.
3. Wilkins, S. J., Mount, V., Mahon, K., Perry, A. and Koenig, J., 2014, Characterization and development of subsurface fractures observed in the Marcellus Formation, Appalachian Plateau, north-central Pennsylvania. AAPG Bulletin, v. 98, p. 2301–2345.

Acknowledgements

This project was funded as a subcontract under the Gas Technology Institute (GTI) NETL contract DEFE0024292. The project was coordinated by GTI, with Jordan Ciezobka providing project management. Laredo Petroleum assisted greatly with many aspects of data sharing and interpretation. CoreLabs staff handled logistics core layout and marking and provided the CT scans. Publication authorized by the Director, Bureau of Economic Geology, Jackson School of Geosciences, The University of Texas at Austin.

Appendix C: Phase 3 Eagle Ford Project Fracture Characterization by BEG

Research Entity: Bureau of Economic Geology, The University of Texas at Austin

Final Report HFTS EOR Fracture Description, June 30, 2022

Prepared by Julia F. W. Gale

Research by Julia F. W. Gale, Sara J. Elliott, Qiqi Wang, Stephen E. Laubach

Report Contents

Fracture descriptions of core from the ZYGBAY 14H well, cut in the Eagle Ford Formation in DeWitt County, Texas, are presented together with analysis of fracture spatial organization. Fracture description methods follow those used for previous HFTS slant core fracture descriptions and published in URTeC papers (Gale et al., 2018, 2019). The fracture description team for this project comprised: Julia Gale and Sara Elliott (BEG), with input from David Hull and Joe Comiskey from Devon Energy at an early stage when samples for the wider project were being selected. Analysis of data and contributions to the written report was done by Gale, Elliott, Qiqi Wang (Ph.D. student – spatial organization analysis), and Stephen Laubach (context and report review). Appendices and this report are stored on UTBOX, a secure site.

Core description was done at CoreLab in Houston, with logistics handled by Corey Rawlings and Conrad Erck. An in-person core workshop was held at Devon Energy labs, Oklahoma City on April 6th, 2022.

Fracture Description

Methods

We described, photographed, and measured orientations of fractures in whole core, prior to slabbing. Three continuous cores had been drilled, with the downhole direction opposite to the dip of bedding so that an optimal 6–8-degree angle between the core axis and bedding could be achieved. This angular relationship meant that bedding could be seen in the core, allowing the cores and thereby fractures to be oriented. The drilling report was used to calculate the deviation for different depth intervals along the length of the core so that corrections to orientation measurements could be made (Fig. 1).

A CT scan was done by CoreLab, and was used to help locate fractures, but because the core was collected and imaged in steel tubes, rock features such as bedding, and fractures were obscured for the most part (Fig. 2a). Core had been processed by CoreLab staff: cleaned, depth intervals marked, uphole indicated with red/white lines, and placed in boxes mostly in 2-ft, 4-in diameter sections. We examined the core for bedding and marked way up with an orange line (Fig. 2b). Sampled intervals were examined for fractures prior to sample selection (Fig. 2c). We note in some intervals there was a mismatch of labeled CT-scan depths and core depths; in these cases, all our depths were measured off the core.

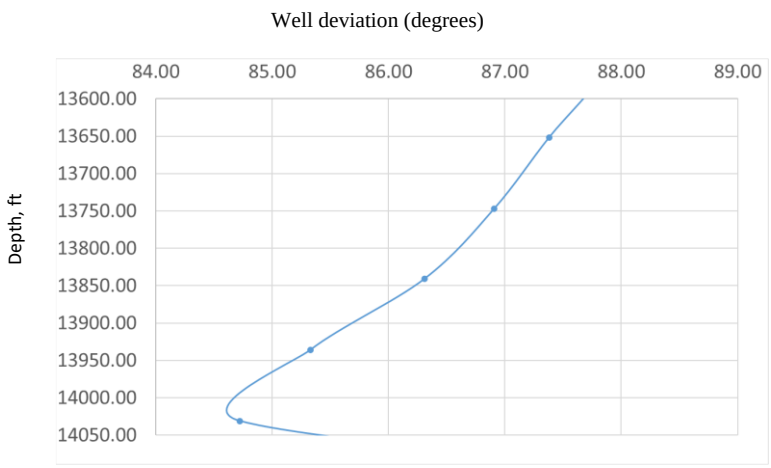


Figure 1. Core deviation angle in the Zgabay 14H, used to calculate corrections to fracture orientation measurements.

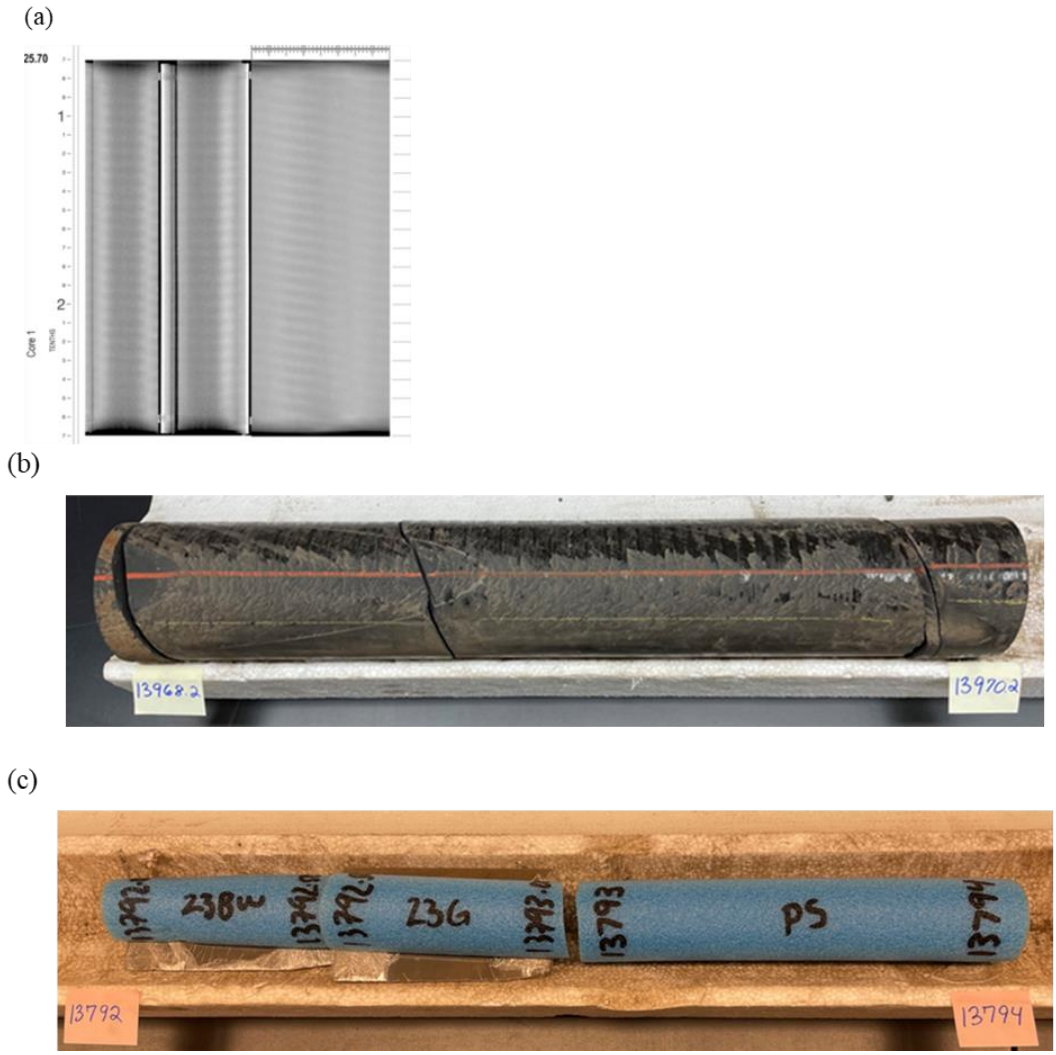


Figure 2. (a) Output from CT scan with vertical (left), horizontal (center) and circumferential images. In this case, from the top of Core 1, the steel tubes obscures geology and bedding cannot be seen. In this tube there were no fractures. (b) Orange line indicates the top of the core; bedding intersections with the core margin are clear in this example. (c) Samples taken by Devon Energy for this 2-ft interval, which was checked for fractures prior to sampling.

Fracture orientations were measured in the core using an iPad with a GeoID application and then corrected for magnetic declination and rotated into their in-situ orientations. Rotations and plotting of stereograms were done using Richard Allmendinger's free 'Stereonet' software available at: http://www.geo.cornell.edu/geology/faculty/RWA/programs/stereonet.html.

Proppant and proppant embedment were observed at several locations in this core. An analysis of three samples collected from fracture faces is included. Implications of these findings are discussed together with the fracture findings.

Results

Measured core depths are as follows: Core 1, 13616-13734.95 ft; Core 2, 13736-13883.4 ft; and Core 3, 13886-14038.5 ft. The total cored interval is 422.5 ft long, with minimal core missing at the junctions between the cores. In these 422.5 ft we interpreted 167 hydraulic fractures, 40 NE-SW striking natural fractures, 69 drilling-induced fractures, and 40 core-handling fractures. There are also small numbers of vertical fractures in other orientations, faults, and bed-parallel fractures. The distribution of the main groups of fractures along the length of the core is non-

uniform and we present a discussion section on quantification of fracture spatial distribution (Fig. 3).

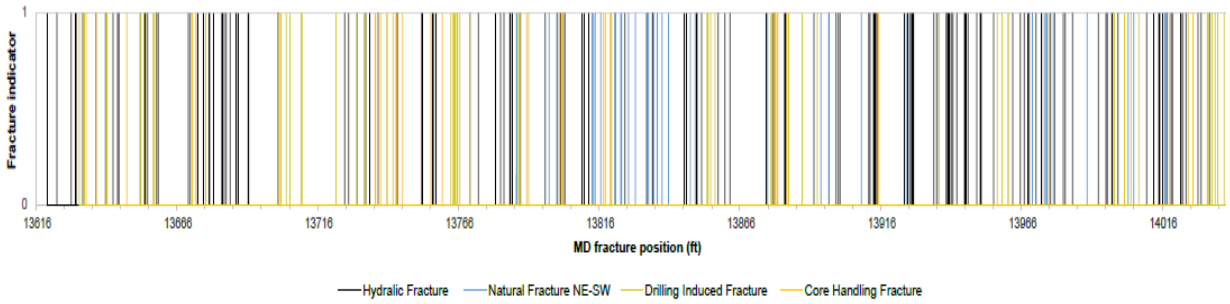


Figure 3. Fracture locations along length of cored interval. Plot includes hydraulic, drilling-induced, and core-handling fractures, and one set of natural fractures only; those examined for spatial organization. Colored by type – zoom for detail.

Fracture orientations are presented as great circles in stereograms, for each core (Fig. 4). In the top 21 ft of Core 1 there are six hydraulic fractures with anomalous orientations (Fig. 4a). Other than these six, hydraulic fractures are consistent in orientation, broadly striking NE-SW. The spread of strike directions is around 45°, which is comparable to that seen in the HFTS1 and HFTS2 datasets in the Wolfcamp Formation. Drilling-induced fractures and the dominant natural fractures also share this orientation. Structures that depart from this orientation include a set of subvertical WNW-ESE natural fractures, a few bed-parallel natural fractures, one occurrence of short, wide, en echelon veins, and one extensive bed-parallel shear plane at 13,899.40 ft in Core 3. Timing of these relative to the dominant natural fracture set and to each other has not been determined.

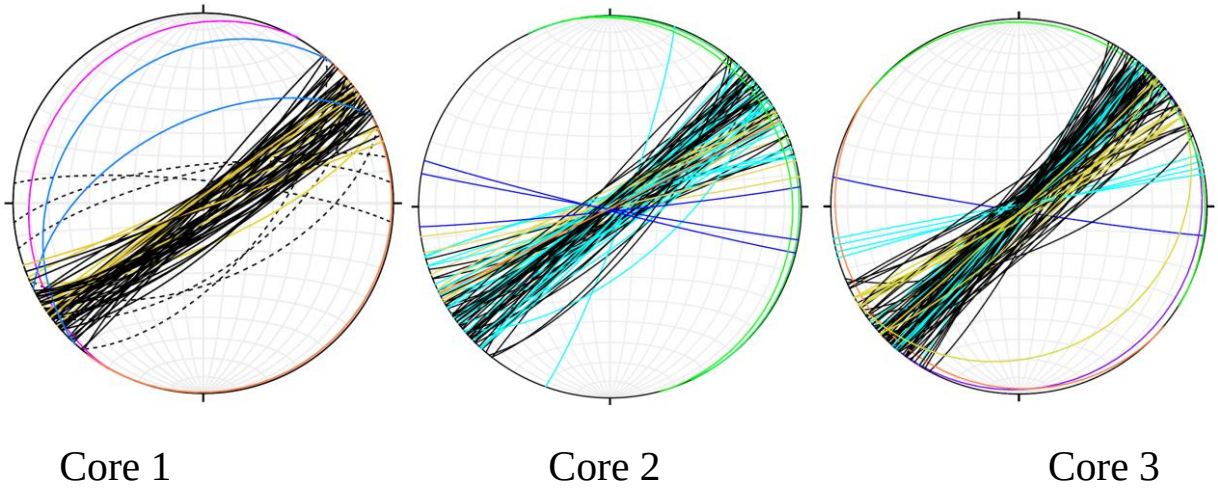
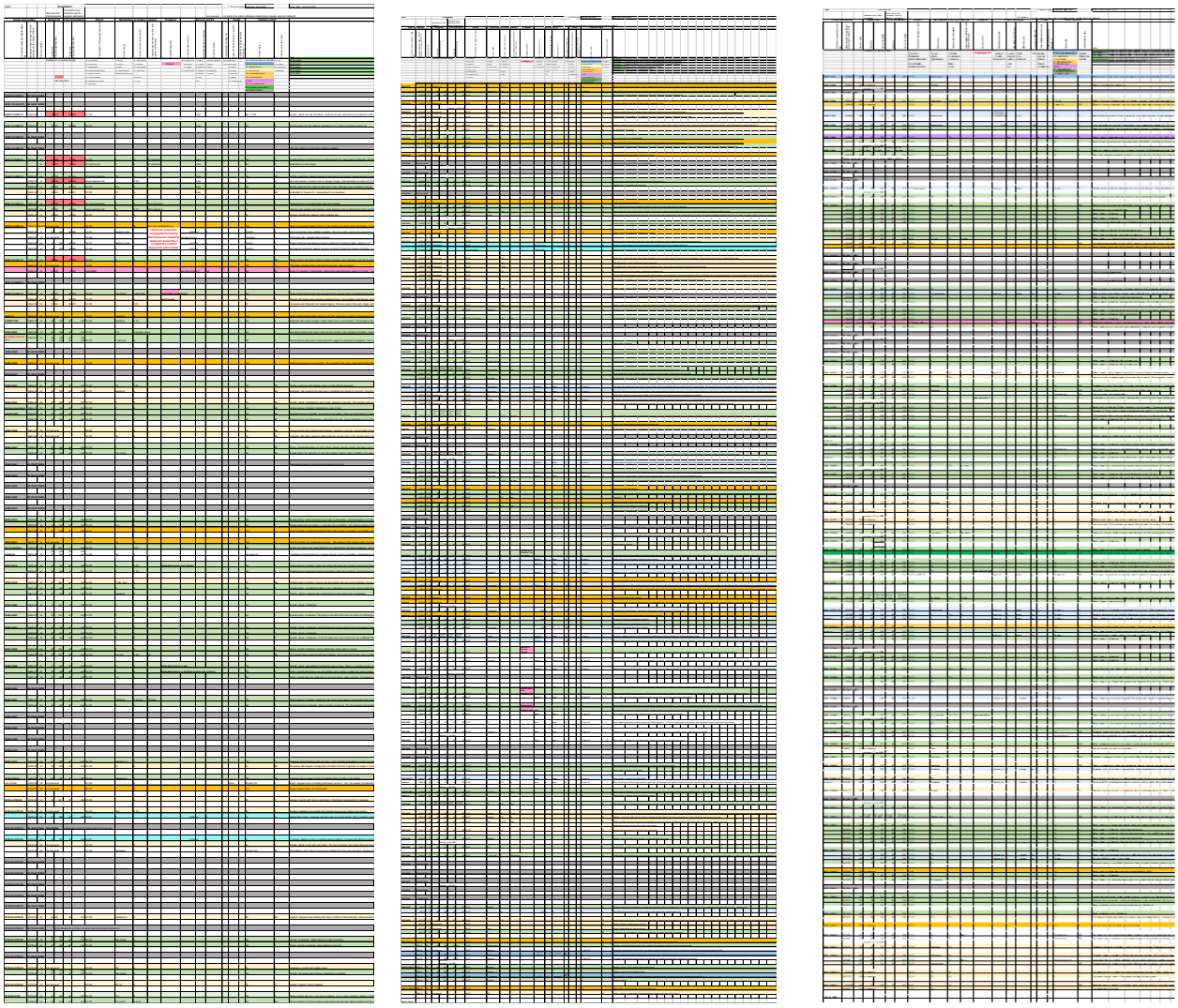


Figure 4. Lower hemisphere stereographic projections. Black = hydraulic fractures; blues = natural fractures; pink = bed parallel fractures; purple = faults; yellow = drilling induced fractures; orange = core handling fractures; green = bedding. Anomalous HF orientations in Core 1 = black dashed

Fracture description spreadsheets are provided in Appendix A. Images of the spreadsheets give an impression of the fracture types of present, by color (Fig. 5). Shading indicates reactivated fractures, for example, a Set 1 natural fracture reactivated by a hydraulic fracture would have light blue to mid green shading, with the descriptor "NFreactHF" in the ID column of the spreadsheet. We use a shading convention where the original fracture is the upper color, with the cause of reactivation being represented by the lower color. The tables in Figure 5 are presented at the same scale, which does not reflect the relative number of fractures in each.

The approximate number of fractures (some numbers represent groups in rubble) and core interval length are in the caption.



Core 1. Length 118.95 ft; n ~ 74 Core 2 Length 147.4 ft; n ~ 117 Core 3 Length 152.5 ft; n ~ 120

Figure 5. Images of the fracture description spreadsheets for the three cores. Original Excel spreadsheets in Appendix A. Legend for colors: light green = hydraulic fractures; blues = natural fractures; pink = bed parallel fractures; purple = faults; yellow = drilling induced fractures orange = core handling fractures; dark green = bedding.

Hydraulic Fractures

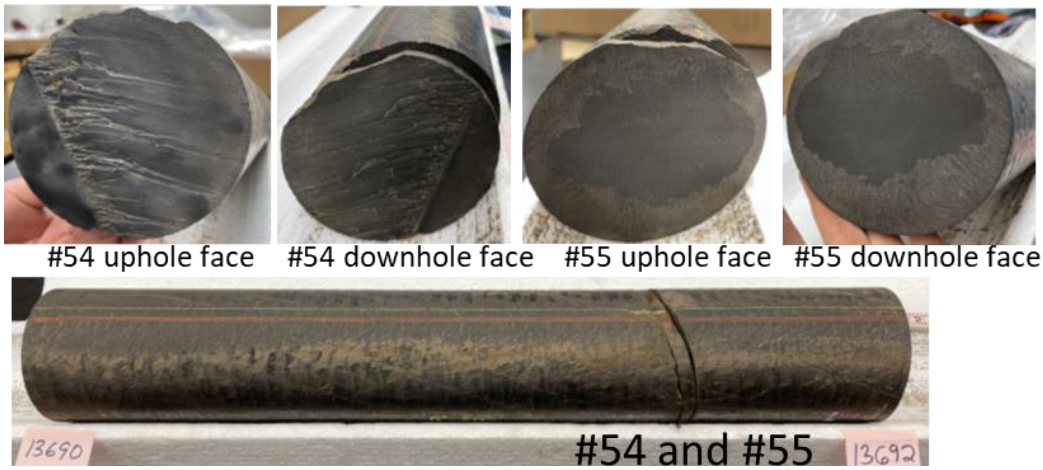


Figure 6. Hydraulic fracture doublet in Core 1 from 13,690 to 13,692 ft. Fracture #54 is the uphole fracture of the doublet and has twist hackles emanating from bedding. Fracture #55 is smooth and planar.

Overall, 167 hydraulic fractures were interpreted across the cored interval; 44 in Core 1; 46 in Core 2; 77 in Core 3. Given the different core lengths (Fig. 5) these numbers translate to average spacings of 2.7 ft (Core 1), 3.2 ft (Core 2), and 1.98 ft (Core 3). The average spacing, while giving a broad representation of fracture intensity, does not properly convey the spatial distribution. This is addressed in the discussion section of the report.

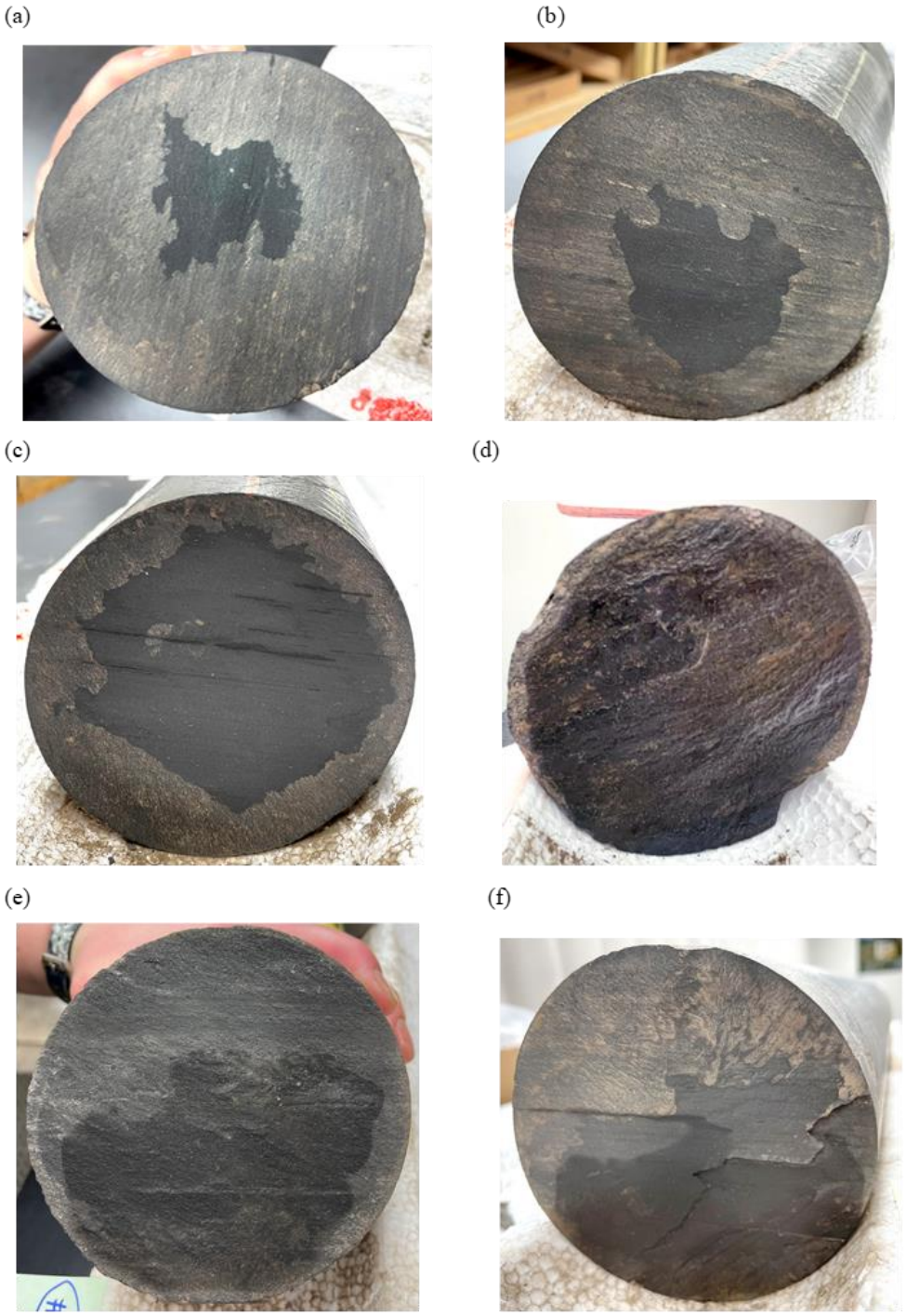


Figure 7. Hydraulic fractures: (a, b, c) Core 1, #47, #48 and #49 from 13682-84 ft. All three are planar, smooth, featureless, with drilling mud around the margins of the fracture face but absent from the center. (d) Core 2, #145 rough face in carbonate. (e) Core 3, laminated carbonate at 13939.30 ft, fracture #227 is subplanar with a somewhat rough surface, (f) Core 2 #106 at 13770.1 ft, irregular steps mostly along laminations.

There are several intervals 8 feet or more in length that have no fractures of any kind, and others that just have drilling/handling fractures. For example, Core 1: 13,660-13,670 (10 ft), 13,711.3-13,725.3 (14 ft); Core 2: 13,760-13,770 ft (10 ft), 13,813-13,821 ft (8 ft), 13,835-13,846

ft (11 ft), 13,864-13,874 ft (10 ft); Core 3: 13,915-13,924 ft (9 ft), from 14,030 ft to end of Core 3 (8 ft). These are depicted in grey (no fractures) or yellow and orange (drilling/handling) in the spreadsheets (Fig. 5).

Fracture doublets are present in the Zgabay 4H core, where two hydraulic fractures occur within a centimeter or so of each other but are typically not quite parallel. The example shown from Core 1 (Fig. 6) has one smooth, planar fracture, and one with twist hackles emanating from a bedding plane.

Many hydraulic fractures are smooth, planar, with no features, when cutting more homogeneous mudrock facies (Fig. 7a, b, c). In coarser grained carbonate facies or laminated facies, hydraulic fractures tend to have rougher and somewhat stepped surfaces (Fig. 7 d, e, f).

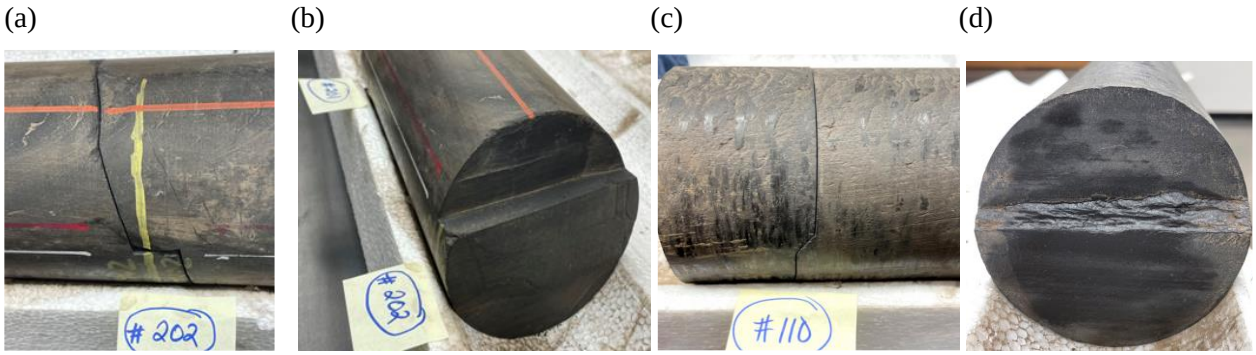


Figure 8. (a, b) Side and face view of hydraulic fracture #202 diverting along bedding for ~ 2 cm. (#202 at 13901.6 ft, Core 3); (c, d) Side and face view of step using multiple bedding planes (#110 at 13,782 ft, Core 2).



Figure 9. Effect of ash layer on hydraulic fracture propagation at 13967.55 ft in Core 3. Upper photo is looking downhole at fracture #252. The ash layer (ash) causes a small deviation in the fracture, which steps downhole by a few millimeters along the top of the bed. Bottom photo shows the deviation from the side; also shown is fracture #251, which also cuts the ash layer, but has no deviation.

Hydraulic fracture morphologies may be more complex than indicated in Figure 7. Small steps of a few millimeters are present on many faces, not always parallel to bedding laminations and likely have multiple origins. Larger steps (more than a few millimeters) with diversion of the hydraulic fracture along bedding are not common. In one example the step is along a single bedding plane (Fig. 8a, b), whereas in another case a series of mini steps along multiple bedding planes results in a step at 45° to the hydraulic fracture planes (Fig. 8c, d).

At 13967.55 ft (Core 3) a thick (~1 cm) pale colored layer extends 45.5 cm along the core length. Hydraulic fracture #251 cuts through this layer with no deviation, but #252 deviates along the top of the layer (Fig. 9).

Hydraulic fracture #248 at 13962.9 ft (Core 3) bifurcates into two branches (Fig. 10). A smooth plane on the upper and east side of the uphole face ends with a subvertical arrest line with twist hackles coming off the west side (westward growth) (Fig. 10a). Also, the main plane splits into two at a bedding plane, one on each side of the main plane (Fig. 10b). Because the piece between is now missing the impression is of 3 fractures but it is a bifurcation using bedding - see the 0-degree CT scan image (Fig. 10c). Growth direction is down for the bifurcation and to the west for the main plane in this case.

(a) (b) (c)

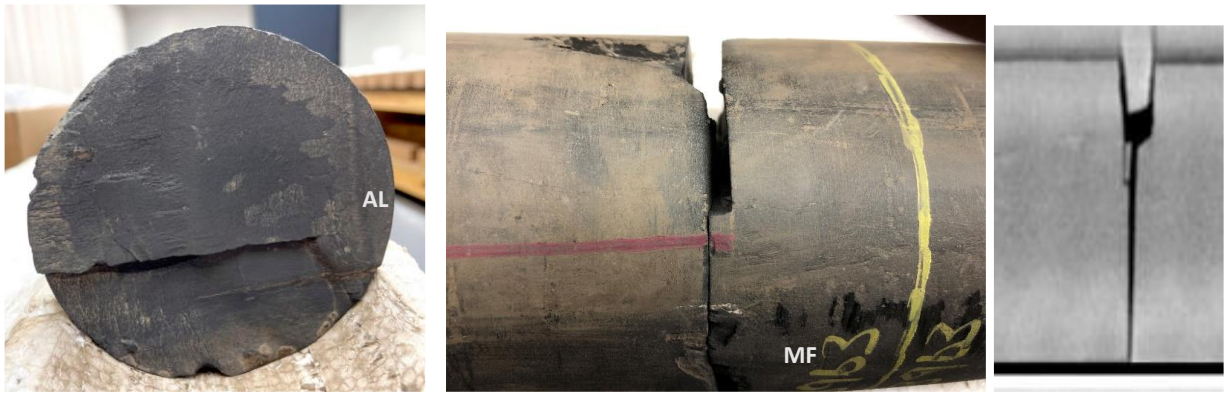


Figure 10. Bifurcation and diversion of hydraulic fracture #248 in Core 3 at 13962.9 ft. (a) View of uphole face; planar smooth in upper half with a vertical arrest line on west side (AL). Step diversion along bedding in lower part of face. (b) Side view of reassembled faces. Note the top in this photo is the bottom of the core. The smooth upper face is the main fracture (MF) and it branches into two at bedding. (c) CT scan image of fracture #248.



Figure 11. (a) Kinked hydraulic fracture at arrest line #22, Core 1, 13645.5 ft. (b) Plumose structure on hydraulic fracture #129 at 13803.25 ft in Core 2. (c) Hydraulic fracture #165 in Core 3 at 13,850.6 ft (smooth, planar) terminates within the core; the break is completed with a rough, hackled tang.

Some hydraulic fractures deviate in orientation without a step (kink). The kink can occur at bedding or along lines of intersection. In the case illustrated, the kink is a curved arrest line, with its asymmetry suggesting westward propagation (Fig. 11a). Features like hackles and plumose are common in the fractures and can indicate local propagation direction. For

example, fracture #129 shows plumose originating outside the core indicating westward propagation (Fig. 11b). There are cases where planar fracture terminates within core, with the break completing with a rough (hackled) surface at the base of the core indicating downward propagation (Fig. 11c).

Natural Fractures

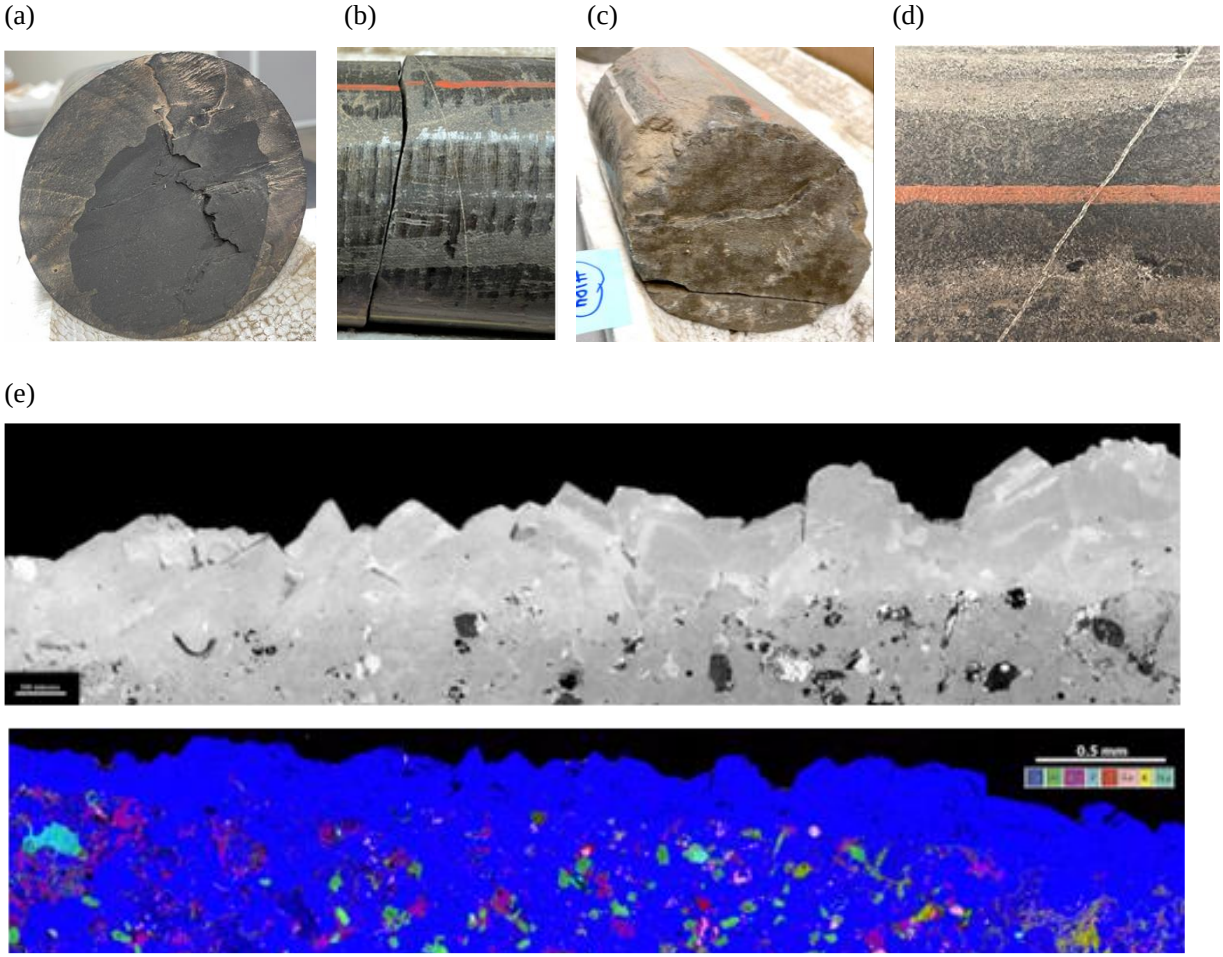


Figure 12. (a) Parted set 1 natural fracture #136 13814.55 ft (Core 2) with calcite veneer on surface. (b) Intact, 0.265 mm wide, calcite-filled Set 1 natural fracture #138 at 13816.55 ft (Core 2). (c) Parted Set 2 fracture #184 at 13879.50 ft (Core 2) with drusy calcite cement on face. (d) Intact, 0.75 mm Set 2 natural fracture #188 at 13882.2 ft, Core 2 that is mostly filled with calcite but retains some porosity. (d) Thin section images of fracture face #184: SEM CL (top) and EDS (bottom) showing euhedral zoned calcite crystals on fracture face.

Multiple subvertical, calcite-filled natural fractures are present. Most are parted with just a veneer of calcite cement on the surface (Fig. 12a), but several are intact, these being less than 1 mm wide. There is a notable cluster of NE-SW striking natural fractures (termed Set 1) in the middle of Core 2 beginning at 13813.55 ft; the first 3 fractures in the cluster are parted, but the fracture at 13816.55 ft is 0.265 mm wide, intact, and filled with calcite (Fig. 12b). In addition to this main cluster, natural fractures are present throughout Cores 2 and 3, and there are a couple at the bottom of Core 1. A second set trends approximately WNW-ESE (Set 2, dark blue in Fig. 3). Near the bottom of Core 2, fractures in this set have porosity (Fig. 12 c, d). Fracture #184 is parted but has drusy calcite on the walls indicating it was open in the subsurface (Fig.12 c, e). No cross-cutting relations between the different sets were observed. We note that a previous study in a slant cored well in the same county (Raterman et al., 2017) found no natural fractures.

The mechanism of parting is mostly unknown, although best guess interpretations are made where other structures such as hydraulic fractures, drilling-induced fractures, or core-handling fractures are nearby.

Bed-parallel fractures

Unequivocal, bed-parallel natural fractures are not common in the Zygabay 4H core. Distinguishing between calcite-filled natural fractures, thin-walled fossils, and stress-release breaks filled with calcite-rich drilling mud is challenging in the lab, even with hand lens or binocular microscope; all react with dilute HCl. We took a sample of possible bed-parallel fractures (#15) occuring at 13637.4 ft in Core 1. Examination of the sample using a confocal microscope and of a thin-section using a scanning-electron microscope, showed the features to be breaks packed with driling mud (Fig. 13).

(a) (b)

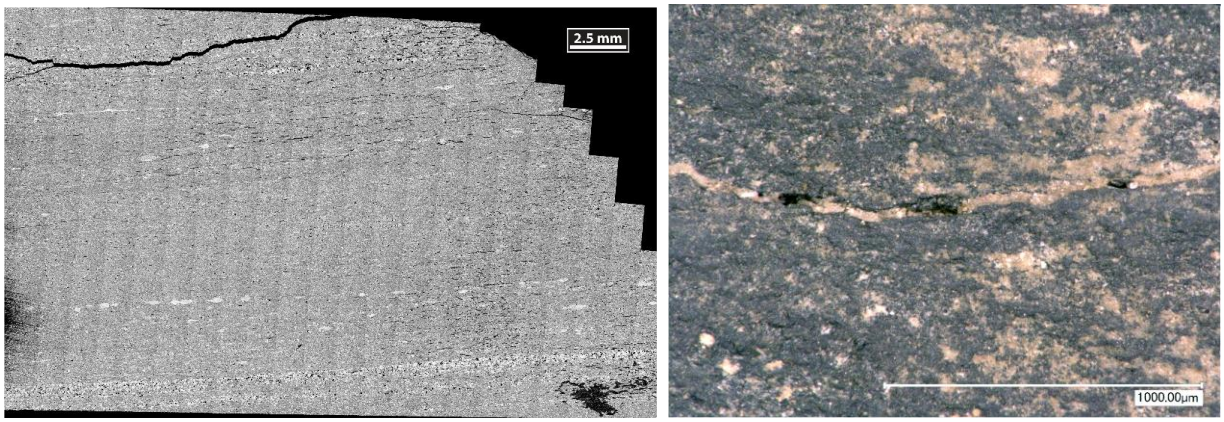


Figure 13. Sample of laminated host rock with bed-parallel breaks (on face of fracture #13). Microscopy shows no natural fractures; breaks are filled with mud. (a) SEM backscattered electron image, (b) stacked surface images of fracture face #13 with horizontal break. The pale material is drilling mud, which also fills surface irregularities.

The only example interpreted as an opening-mode; bed-parallel, natural fracture is at 13927.55 ft in Core 3; it was given an uncertainty rating of best guess (#221.5). It crosses the entire core width and is 15 cm long, tapering gradually up and down hole. It is superficially like the example in Figure 13, but is more continuous, although less than 0.05 mm wide, and is partly filled with amorphous calcite (Fig. 14). The hydraulic fracture cutting it shows no deviation.

(a) (b)



Figure 14. Bed-parallel natural fracture (a) Hydraulic fracture face #222, cut by bed-parallel fracture #221.5 (dashed line shows location; note orange marker for core top). Lines on the face at 45° are possibly drilling torque features, some line up with grooves on the core margin. (b) oblique view of #221.5 – indicated by the pen tip – showing the trace on the face and along the core margin. Core 3, 13927.55 ft

A natural, bed-parallel, shear plane with slickensides continues across two boxes at 13899.4 ft; minimum length 0.66 m since both termini are out of core. Well developed, consistently oriented slickensides are present across the whole face, slightly oblique to the trace of hydraulic fracture #200. Slickensides plunge 03°/066° (lying in the shear plane). The HF in the same location does not divert along the shear plane.

(a) (b)



Figure 15. (a) Bed-parallel shear plane #199 with slickensides (white arrow) in Core 3; upper terminus at 13899.4 ft. The hydraulic fracture #200 does not deviate along the shear plane. (b) View uphole showing face of #200, and trace of #199 on it. The saw cut at 13,900 ft is seen at the yellow depth marker behind the fracture face.

Unascribed natural fractures

At 13,707.2 ft and 13,709.55 ft in Core 1 there are unusual groupings of sigmoidal, en echelon, calcite-filled features. They could be local shear fractures, or possibly even fossil fragments, and are not seen elsewhere in the core. They were not measured. There are also two planar fractures, which have measured orientations different from those denoted as Set 1 or Set 2. These are termed unascribed fractures.

(a) (b)



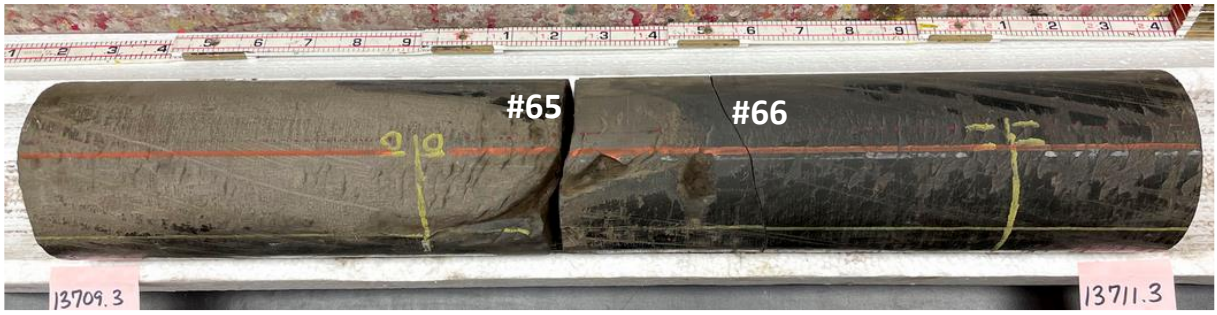
Figure 16. (a) Sigmoidal calcite filled structures at 13,707 ft in Core 1 on uphole face of saw cut between boxes 47 and 48. (b) Short planar fracture #63 seen on top of same face and on core margin; the orientation is not parallel to Set 1 or 2; powder blue in Fig. 4, Core 1 (dip azimuth 336°/ dip 55°).

Drilling induced and core handling fractures

Drilling-induced and core-handling fractures as described in Gale et al. (2018) are present in all three cores. We do not address them further here other than to note that distinction between

drilling-induced and hydraulic fractures and natural fracture with only a very thin veneer of calcite cement is challenging in this core because they are all subparallel. Reasons for individual fracture determinations are noted in the comments column in the fracture description spreadsheets.

(a)



(b)

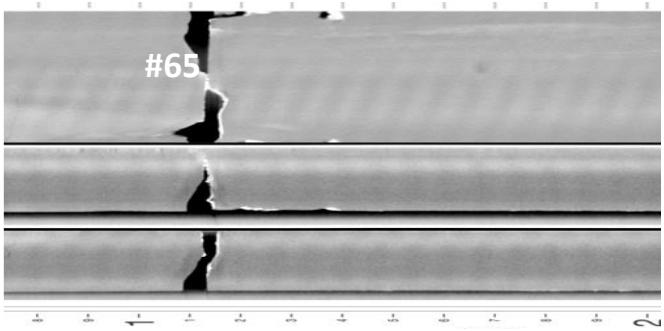
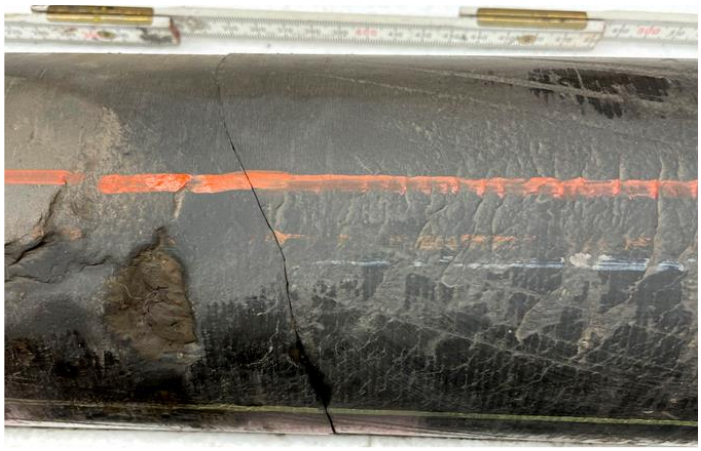


Figure 17. (a) Whole core from 13709.3 ft to 13711.3 ft in Core 1 showing fractures #65 and #66. (b) CT scan from same interval showing only #65 – #66 is not present.

An example of reasoning behind the interpretation for a complex break is given in Figure 17. At 13,710.45 ft in Core 1 there is a fracture (Fig. 17a) that is not visible in the CT scan (Fig. 17b). Absence in the CT scan is typically interpreted as a core handling fracture that formed after the CT scan was taken. However, the fracture is smooth and sub planar, with a tang. This is more typical of drilling-induced fractures. Our interpretation is an incipient drilling-induced fracture not detected on the CT scan that was reactivated during core handling.

(c)



(d)



Figure 17 contd. (c) Close view of trace of #66 on the core margin. (d) Downhole face of #66 showing planar smooth break across most of the face, but with a tang and twist hackles at top right. Core 1, 13710.45 ft.

We note that several of the saw cuts in Core 3 go through hydraulic fractures. This seemed an odd coincidence and at the time of description was taken to suggest there might be even

spacing (2 ft) of hydraulic fractures in this part of the core. The section on statistical analysis of fracture distribution addresses this question.

Proppant

Proppant embedment, pock marks left by proppant, and proppant patches were found in multiple hydraulic fracture locations along the length of the core: Core 1 fracture #s 16, 17, 40, 51, 52; Core 2 fracture #s 133, 149, 153, 155, 156; Core 3 fracture #s 230, 253, 270; occurrences are documented in the spreadsheets (Appendix A) and in the workshop poster (Appendix D). We did not find any full-face proppant packs. The first appearance (most uphole location) of proppant was in fractures #16 and #17 at 13639.7-13641.7 ft in Core 1.

We show examples in this report from Core 1, of proppant grains and pock marks in fracture #40 (Fig. 18a, b) and clusters of embedded grains making proppant patches in fracture #52 (Fig. 18c, d). In the latter case the patches tend to utilize weaknesses along bedding planes, making linear as well as more equidimensional patches (Fig. 18c).

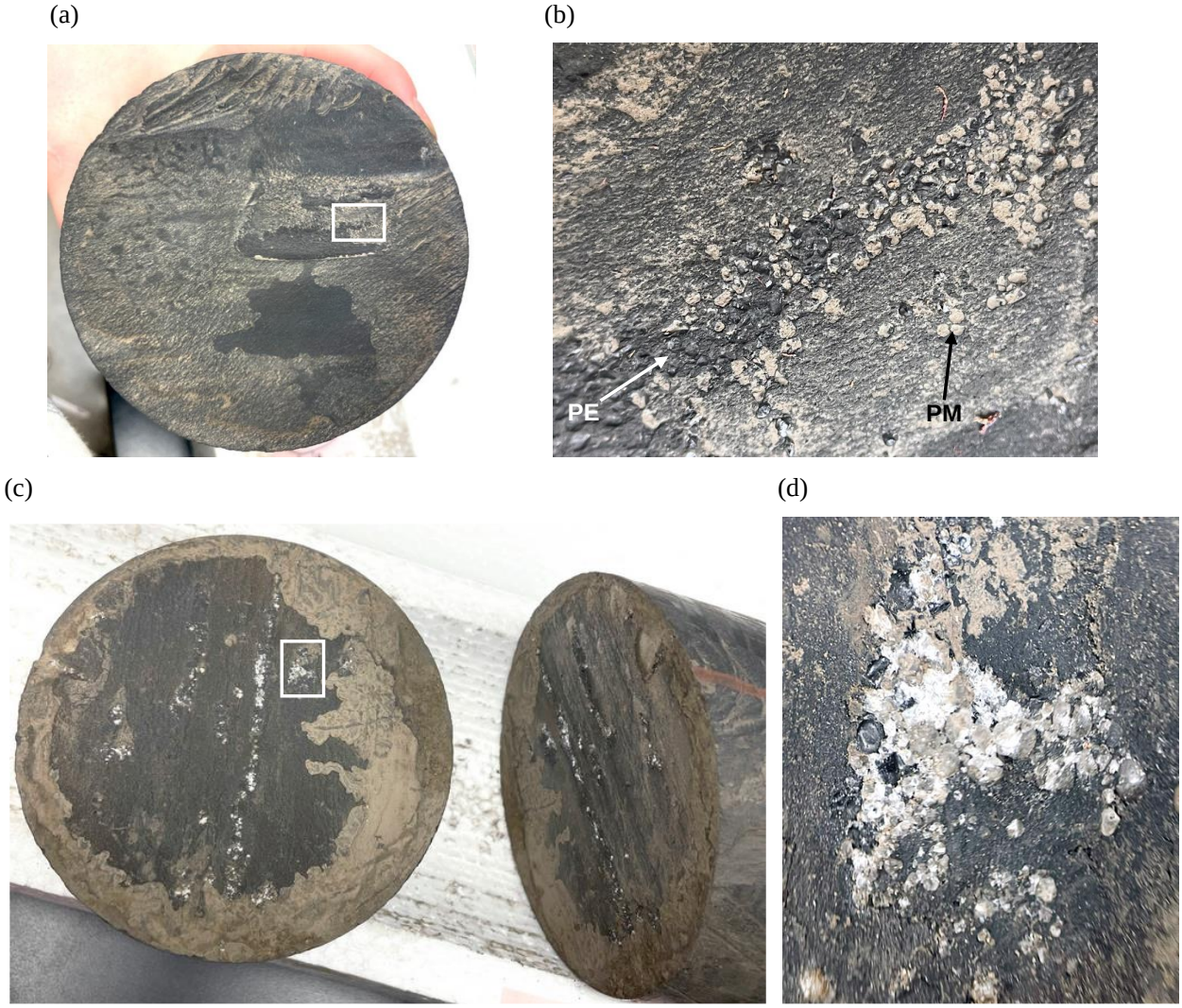


Figure 18. (a) Uphole face of fracture #40 with location of (b) proppant detail (box). (b) Proppant embedment (white arrow, PE, dark grains) and pale, mud-filled pock marks left by proppant grains (black arrow, PM). Long dimension of photo ~ 1.5 cm. (c) Uphole (left) and downhole (right) faces of fracture #52. Location of (d) = box. (d) Proppant grains embedded in the fracture face. The white powder is crushed proppant, the buff-colored powder is dried drilling mud. Long dimension of photo ~ 1.5 cm.

Proppant distribution is highly variable, even in adjacent hydraulic fractures. For example, in Core 2, in fracture #155, the proppant is piled up against a step on the face, whereas in #156 it

is distributed across the face. In Core 3, hydraulic fracture #253 has proppant, but the natural fracture right next to it, parted likely due to hydraulic fracturing, does not. Proppant was not observed in any natural fractures.

Semiquantitative analysis was done for proppant samples from fractures #16, #52, and #149. Most of the sand was in the 63-120 μm size range which is smaller than the nominal proppant mesh size pumped. This finding is similar to that for the proppant analyzed in the HFTS1 Wolfcamp slant core in the Midland Basin. In both cases the nominal 100 mesh pumped contains much smaller grains (c.f. Elliott et al., 2018). The proppant poster in Appendix D provides more details of proppant samples, with breakdown by size, and photographs of other locations where proppant was observed.

Statistical analysis of fracture distribution

We used a normalized correlation count (NCC) method to do a preliminary statistical analysis of the distribution of different fracture types. The method is fully explained in Marrett et al. (2018), and this paper includes a link to access the CorrCount software that we employ. The method is designed to quantify the spacing of fractures at different length scales and can be used to assess the degree of clustering of fractures or if fractures are more evenly spaced. Input data (blue curve in plots) consists of fracture spacings and apertures. Because of the range of orientations within each data set and the relatively small departure from a core-normal orientation for the fracture types analyzed, measurements are not corrected for obliquity to the core. Results are compared to a randomized, Monte Carlo type analysis of the fracture spacing data (green line in plots, with grey lines as 95% confidence limits).

Fracture distribution is shown on a fracture intensity plot and on NCC plots with both logarithmic and linear graduations of length scale. A logarithmic length scale is best for characterizing clustering patterns, whereas a linear length scale is best for characterizing anti-clustering/regularly spaced patterns. We show plots for all fractures and then separated by fracture type. We did not analyze the Set 2 or bed-parallel natural fractures because there are too few of them. Where fractures are reactivated, for example a natural fracture reactivated by hydraulic fracturing, the fracture is counted in both the natural and the hydraulic fracture data sets. Plotting variables used are indicated on each plot and where the count lies outside the 95% confidence limit envelope the area between the data and envelope is shaded light blue. Note that for the NCC plots, length scales more than half the total scanline length (> 65 m) are subject to edge effects and should be interpreted with caution.

<u>All fractures</u>

The plots for all fractures (Figs. 19a, b) lie mostly within the confidence limits. Peaks and troughs are small for the most part, except for the intensity peak at around 91 m (Fig. 19a) corresponding to approximately 13,914 ft in Core 2. At this location there are two adjacent intervals with 5 fractures each. Note there are many intervals with 0 fractures/meter. In the NCC plots (Fig. 19b, c) beyond a length scale of 3 meters the data lie between the confidence interval for a random distribution for the most part, and we interpret this as indicating the distribution is indistinguishable from random. At a length scale of approximately 2.5 m there is a small trough indicating fewer fractures spaced at 2.5 m than for a random distribution.

Between 0.1 m and 0.7 m (Fig. 19c) there are a series of small peaks indicating several length scales where spacings are more common than for a random distribution.

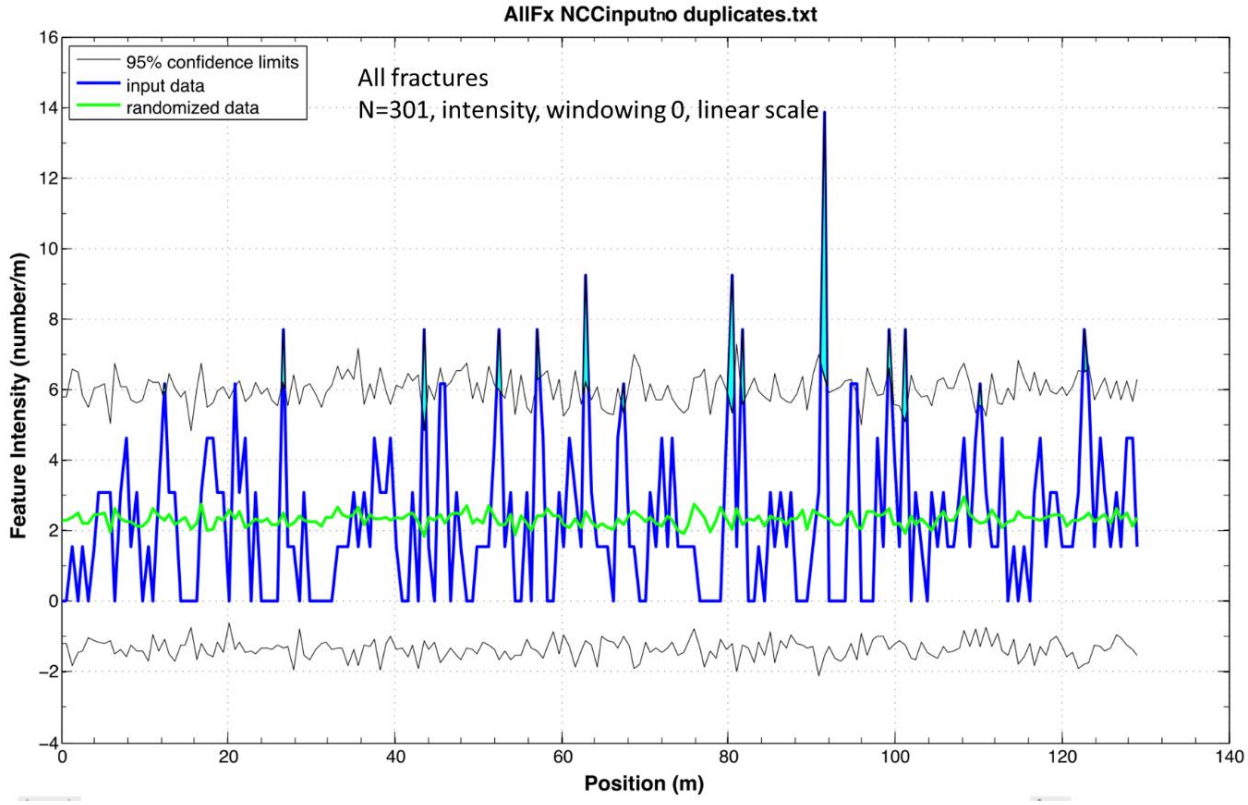


Figure 19a. Fracture intensity for all fractures

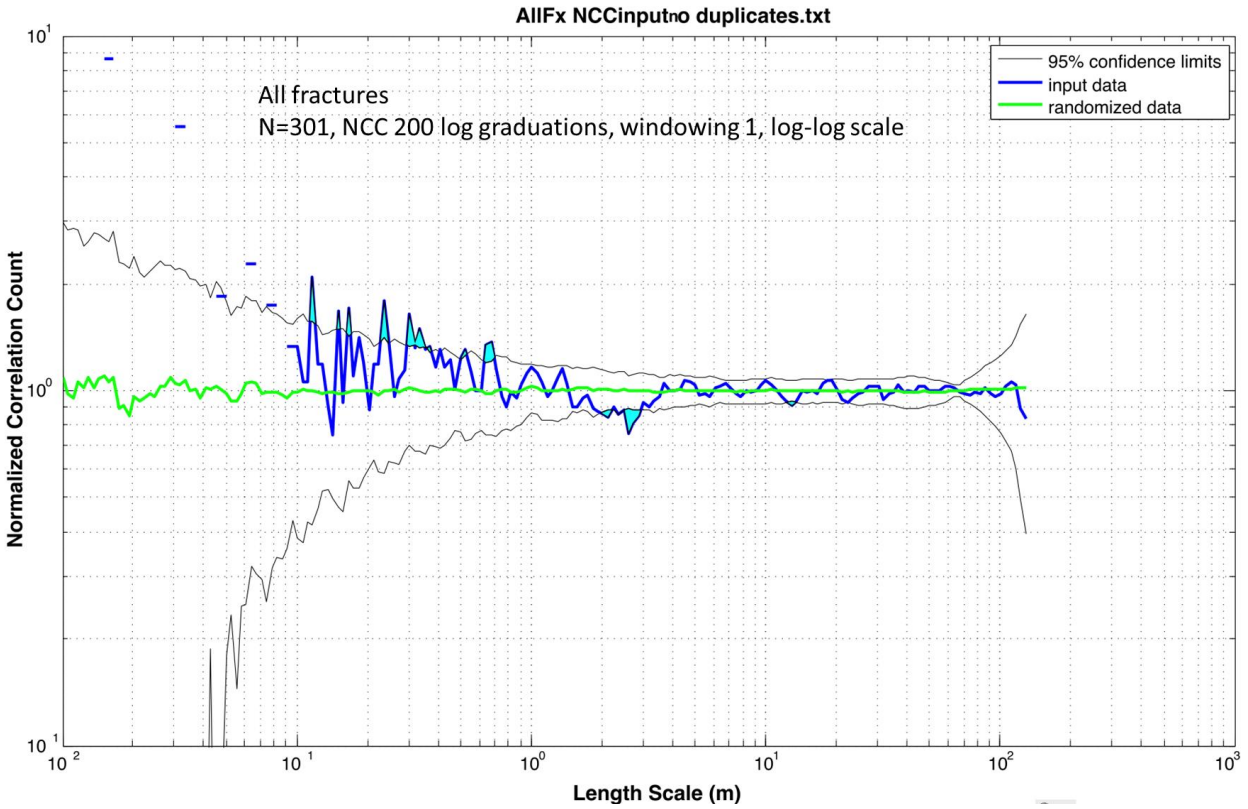


Figure 19b. NCC plot for all fractures, logarithmic length scale.

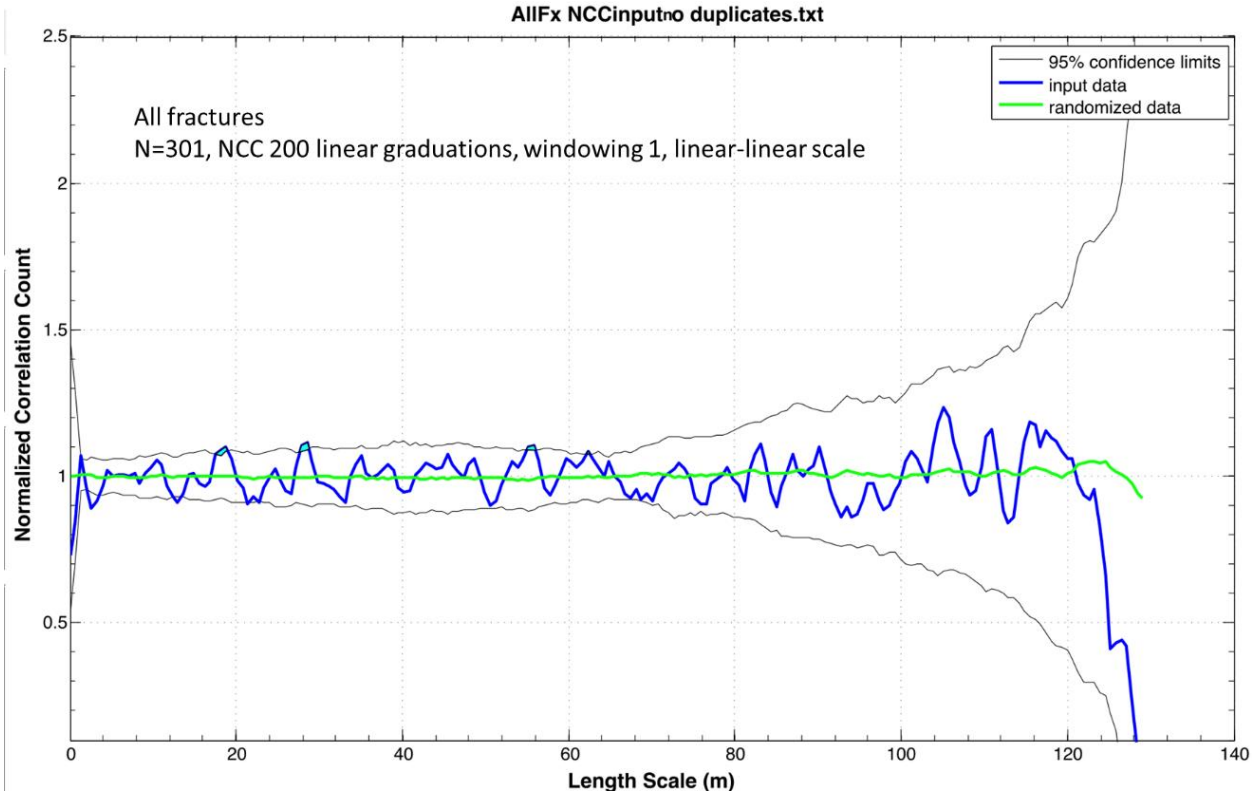


Figure 19c. NCC plot for all fractures, linear length scale.

Hydraulic fractures

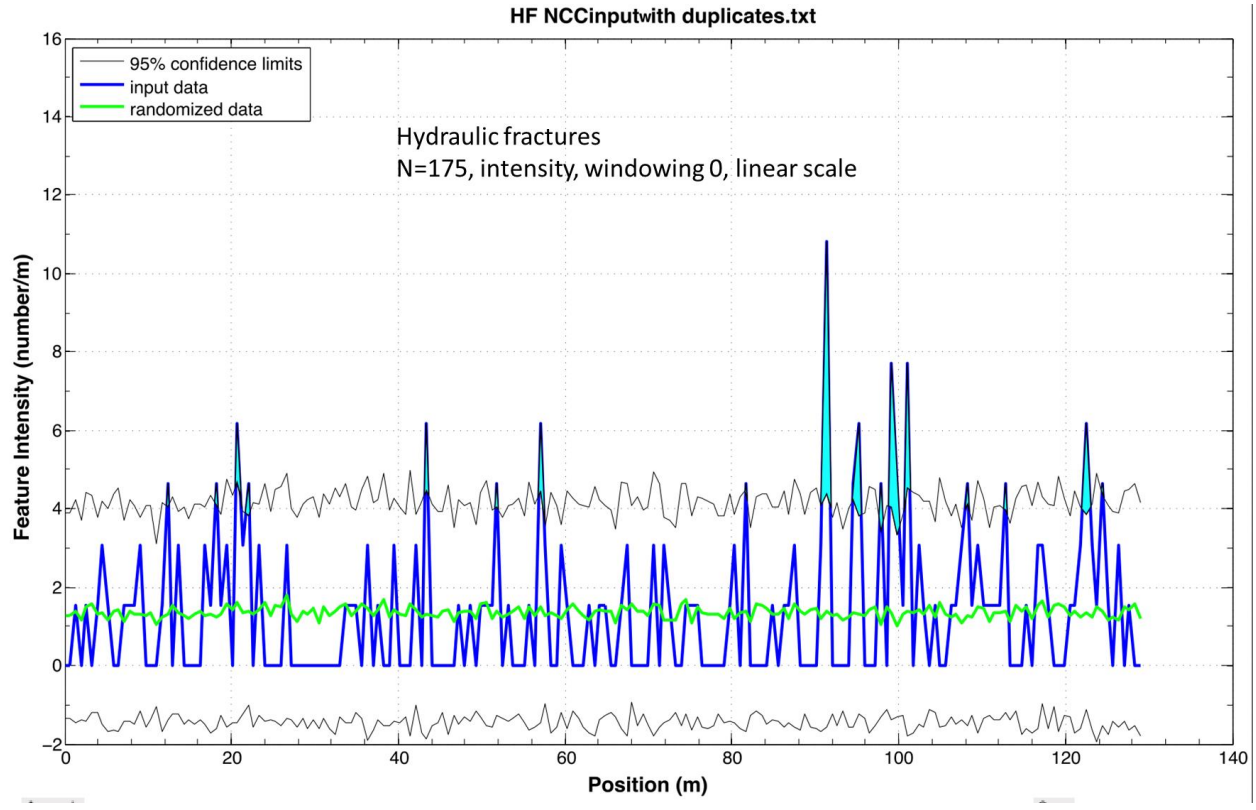


Figure 20a. Fracture intensity plot for hydraulic fractures.

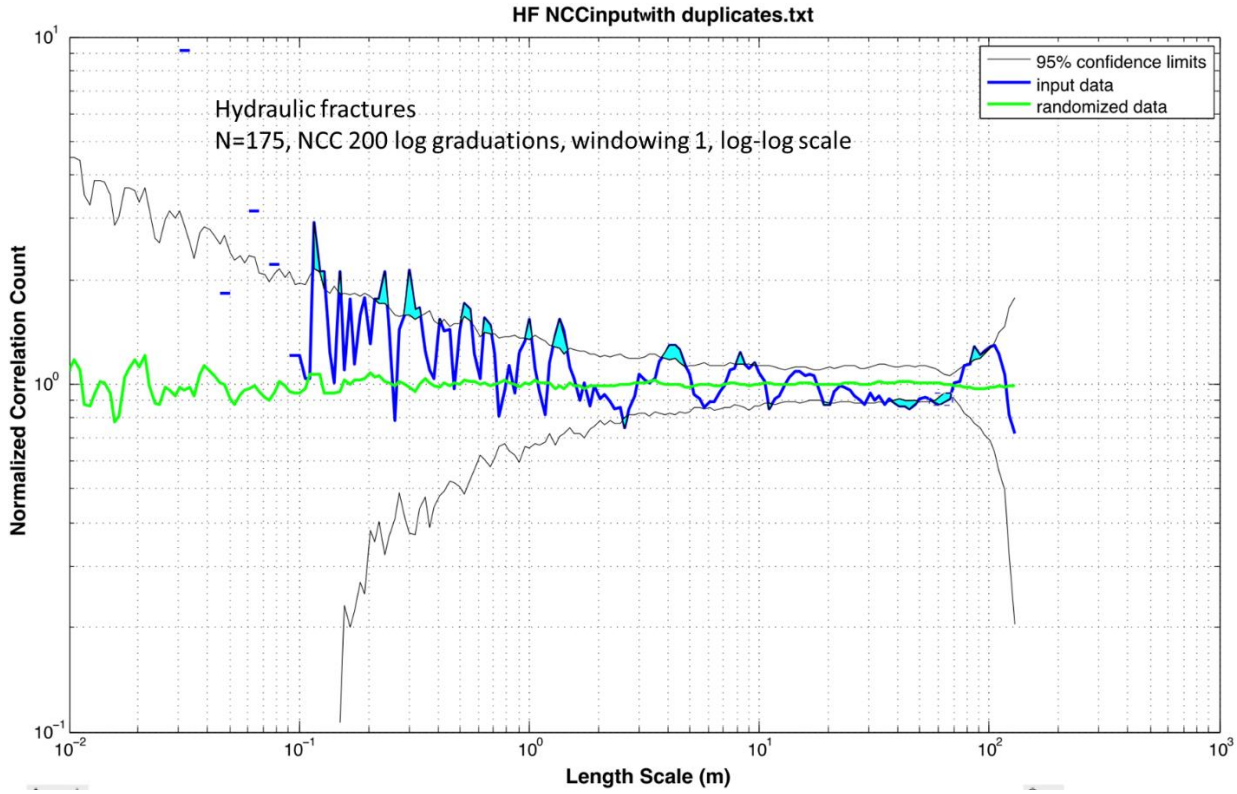


Figure 20b. NCC plot for hydraulic fractures, logarithmic length scale.

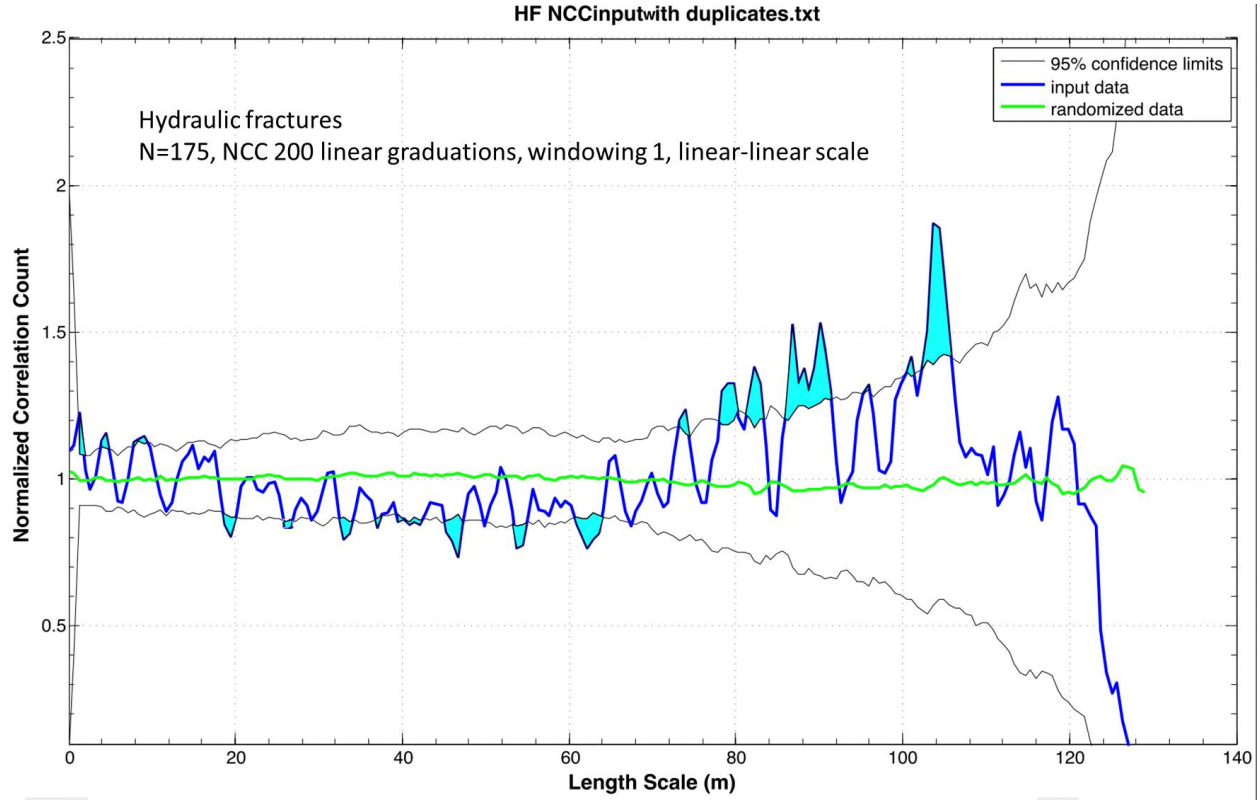


Figure 20c. NCC plot for hydraulic fractures, linear length scale.

Natural fractures striking NE-SW

The intensity plot for these fractures reflects the fact that none were observed in the first part of the core; they first appear at around 50 m in the plot (Fig. 21a) (13,780 ft, end Core 1). The peaks at 60 m in the plot reflect the cluster in the middle of Core 2 beginning at 13,813.55 ft. A further large peak occurs at 110 m in the plot. Intensities are lower than those for hydraulic fractures. The NCC log plot (Fig. 21b) shows a strong pattern that is commonly seen in natural

fractures. A section of the data curve at small length scales (< 15 m) lies above the random distribution curves but overall decreases with increasing length scale. At approximately 17 m length scale the blue data curve crosses the NCC=0 line, continuing with a trough and then peaking at ~45 and ~55 m (Fig. 21c).

Drilling-induced fractures

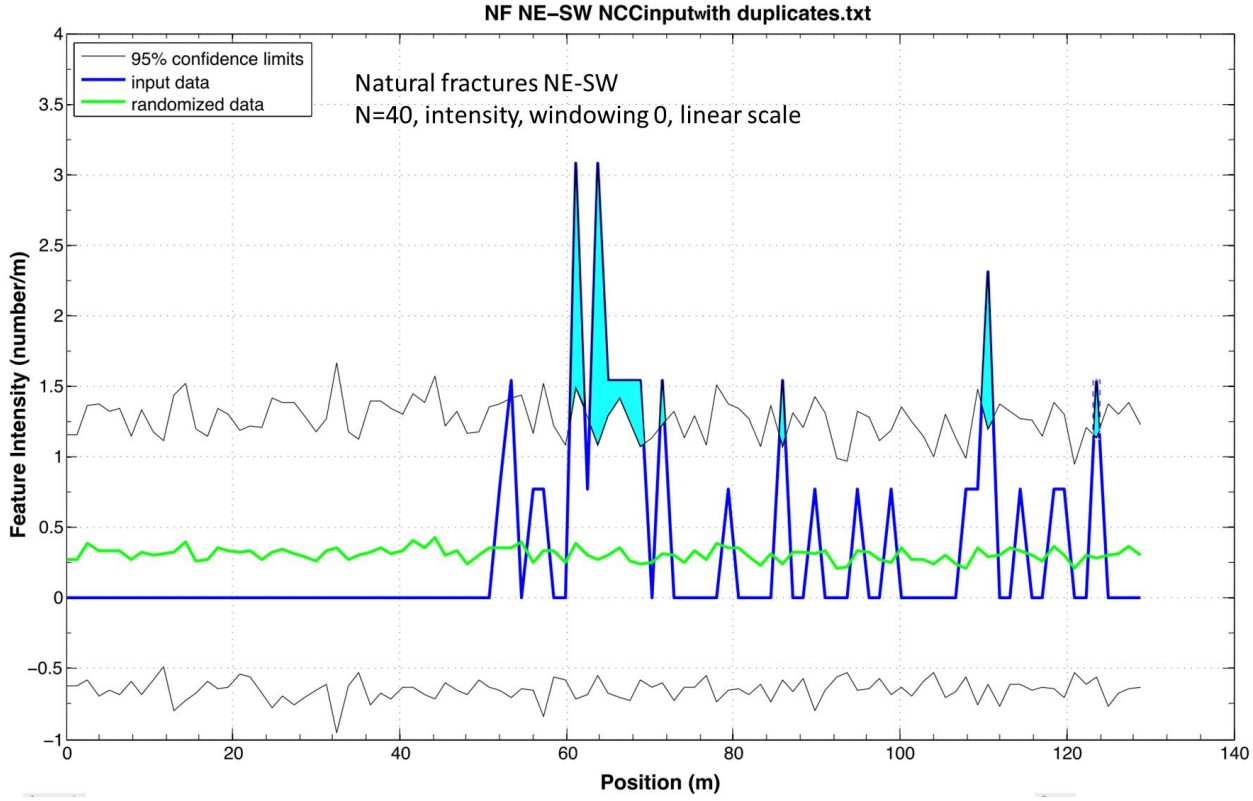


Figure 21a. Intensity plot for Set 1 natural fractures striking NE-SW

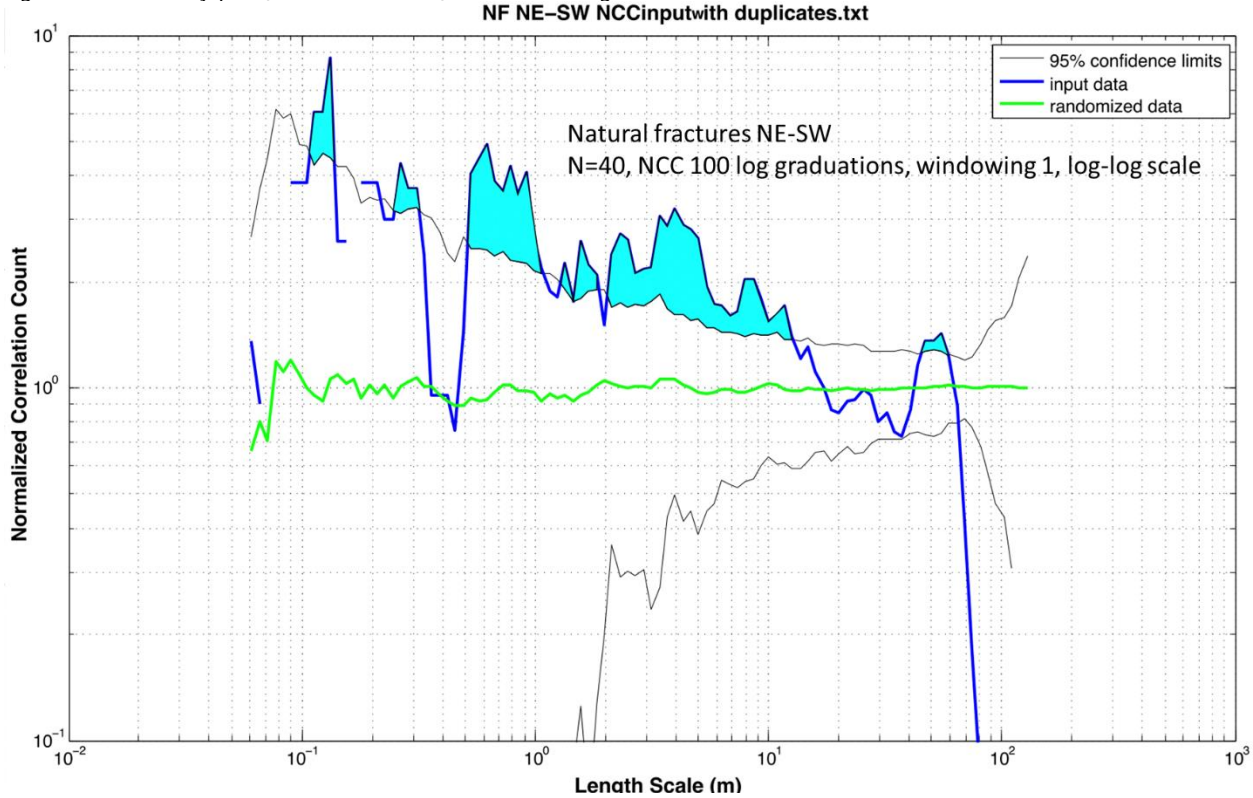


Figure 21b. NCC plot for Set 1 natural fractures striking NE-SW, with logarithmic length scale.

Fracture intensities for drilling-induced fractures are lower than for hydraulic fractures. There are several peaks indicating higher intensities, separated by intervals with no interpreted drilling-induced fractures (Fig. 22a). The NCC plot with logarithmic length scale shows several peaks at or below the 1-meter scale, with an absence of spacings between ~ 2 m and 6 m, and again between ~11 m and 18 m (Fig. 22b). There is a peak at 6-9 m. The peaks and troughs at length scales between 4 and 65 m seem to show some periodicity on the order of ~7-8m (~25 ft) (Fig. 22c). The curve above 65 m length scale is subject to edge effects.

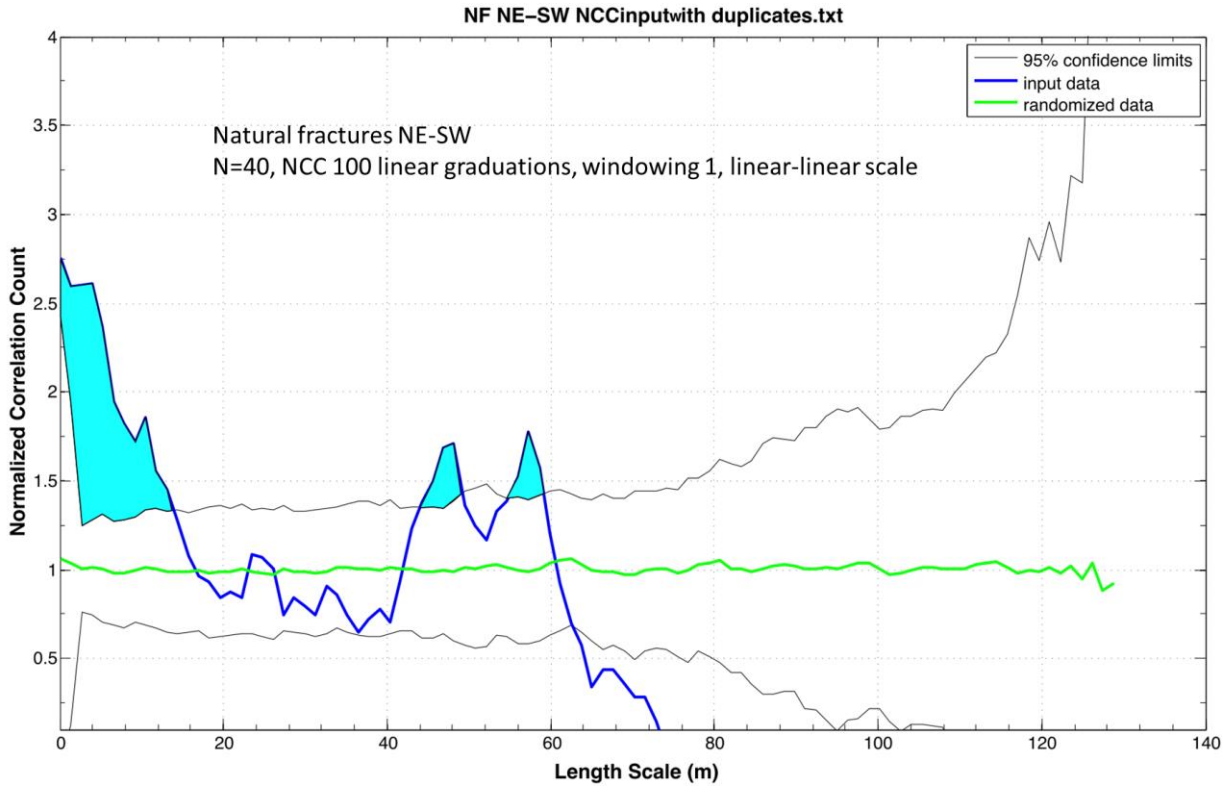


Figure 21c. NCC plot for Set 1 natural fractures striking NE-SW, with linear length scale.

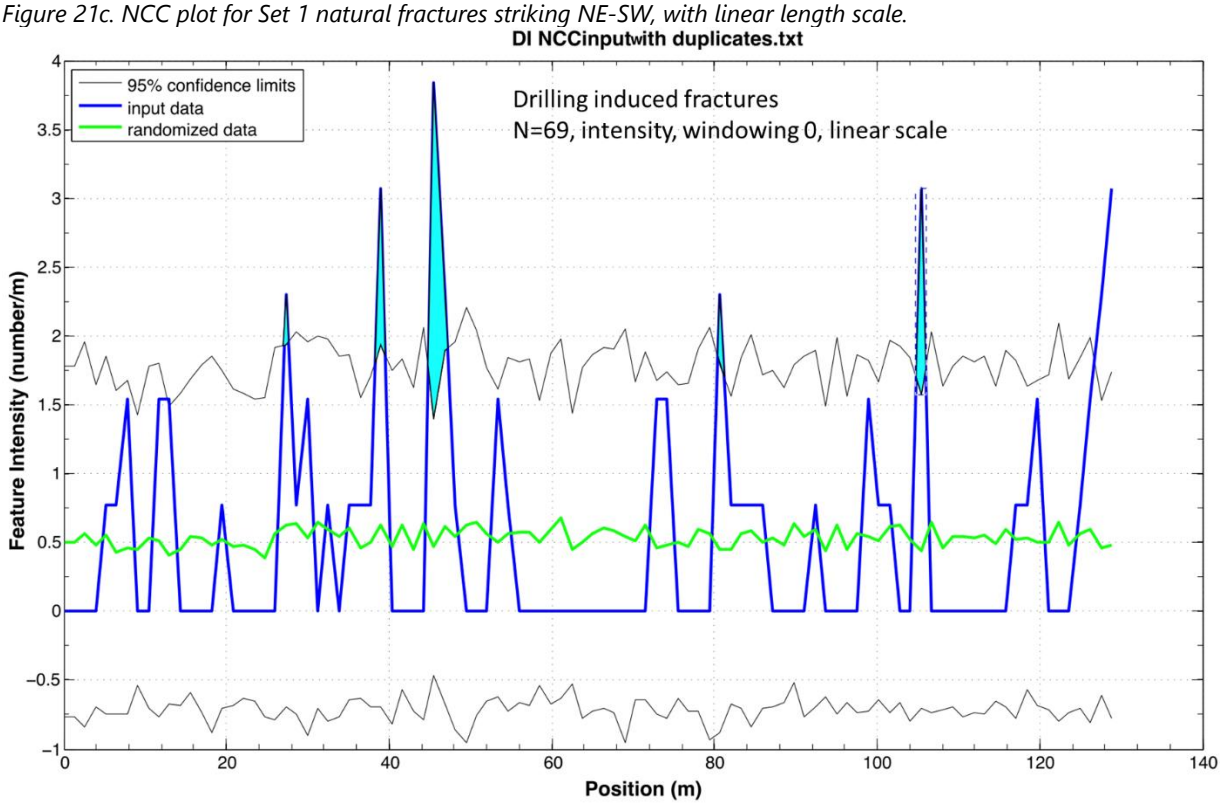


Figure 22a. Intensity plot for drilling-induced fractures

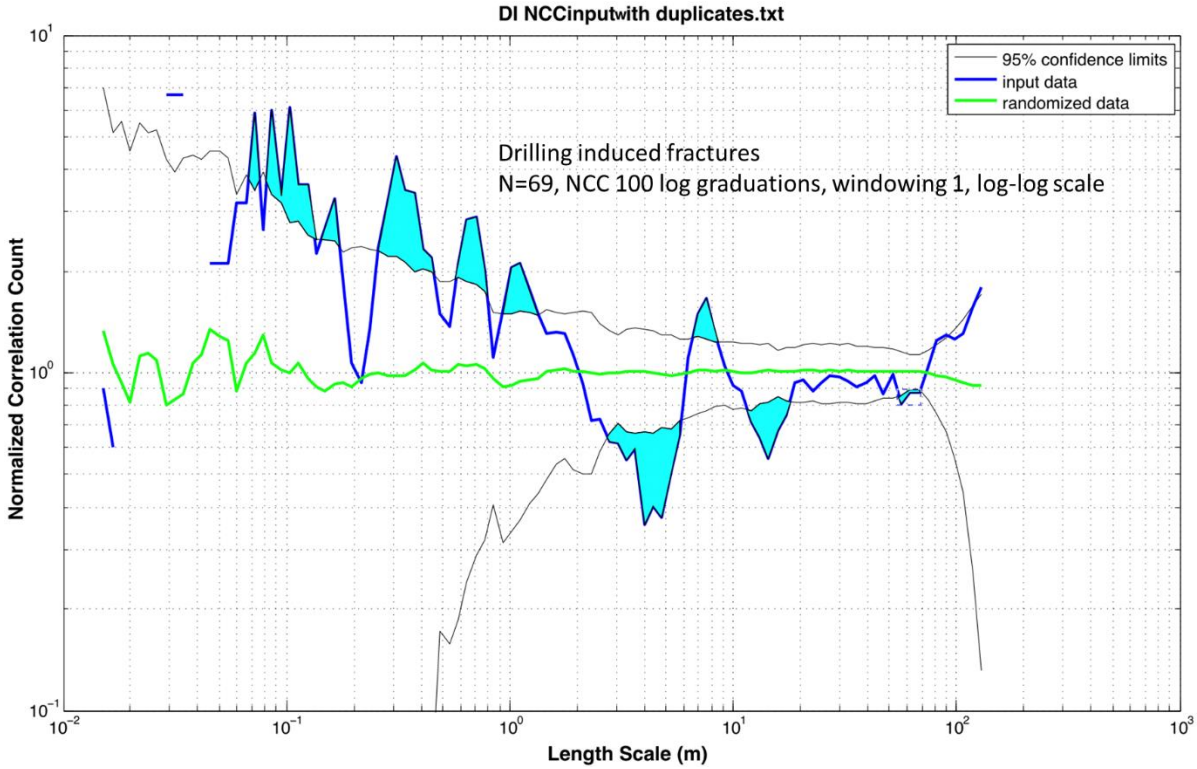


Figure 22b. NCC plot for drilling-induced fractures, logarithmic length scale.

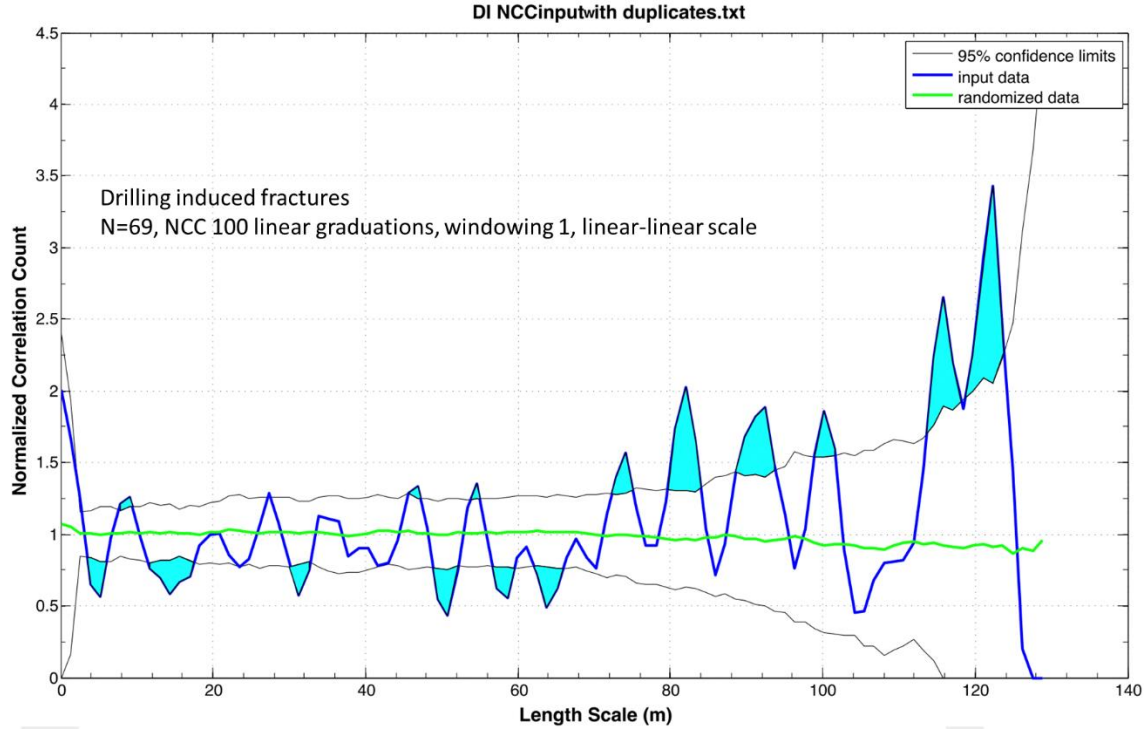


Figure 22c. NCC plot for drilling-induced fractures, linear length scale.

Core-handling fractures

Core-handling fracture intensity is the lowest of the fracture types plotted. There are peaks above random intensity and intervals with no fractures of this kind (Fig. 23a). The largest concentration of core-handling fractures is seen at 60-65 m (~13,816 ft), which is in the middle of Core 2. The pattern of spatial arrangement revealed by the NCC plots is like that for drilling-induced fractures, with several peaks at the small length scale (< 1 m), a trough from 1–4 m and a substantial peak at 5 m (Fig. 23b, c). Beyond 30 m length scale the NCC drops off steeply.

Discussion of fracture spatial organization analysis

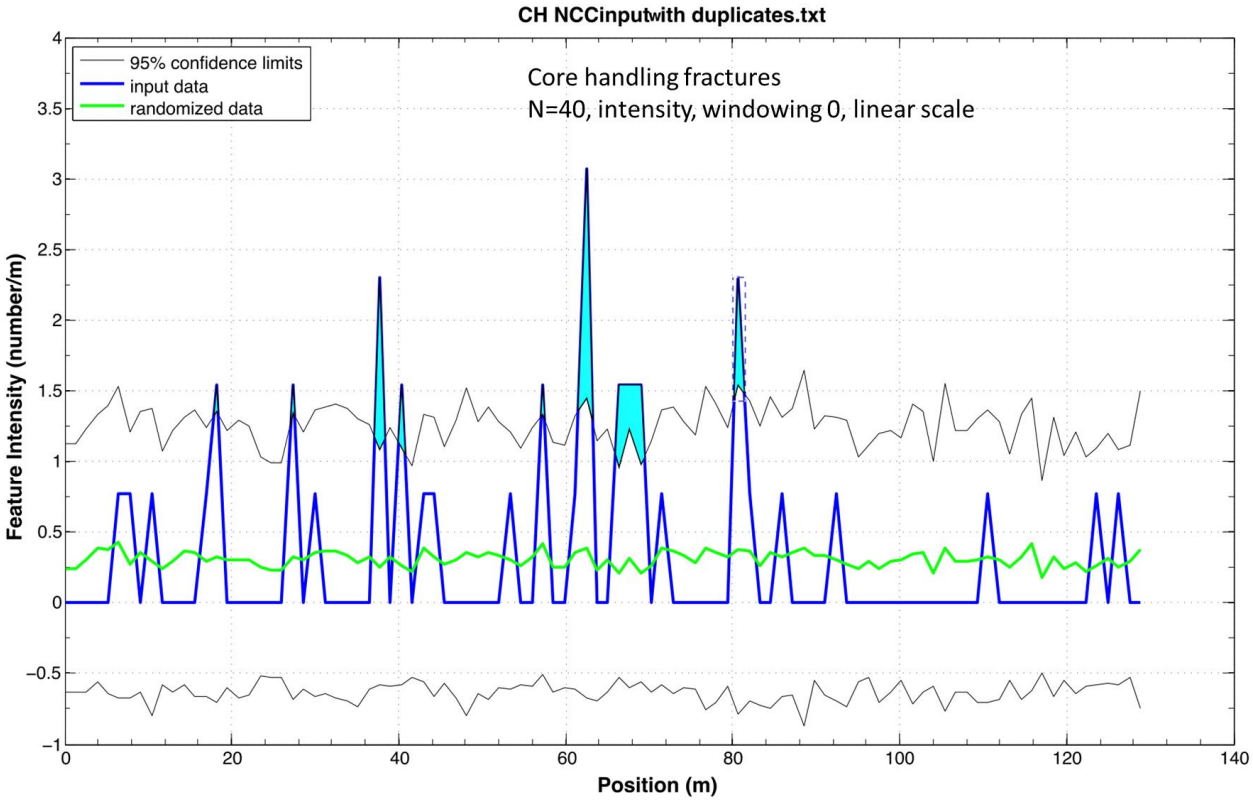


Figure 23a. Intensity plot for core-handling fractures

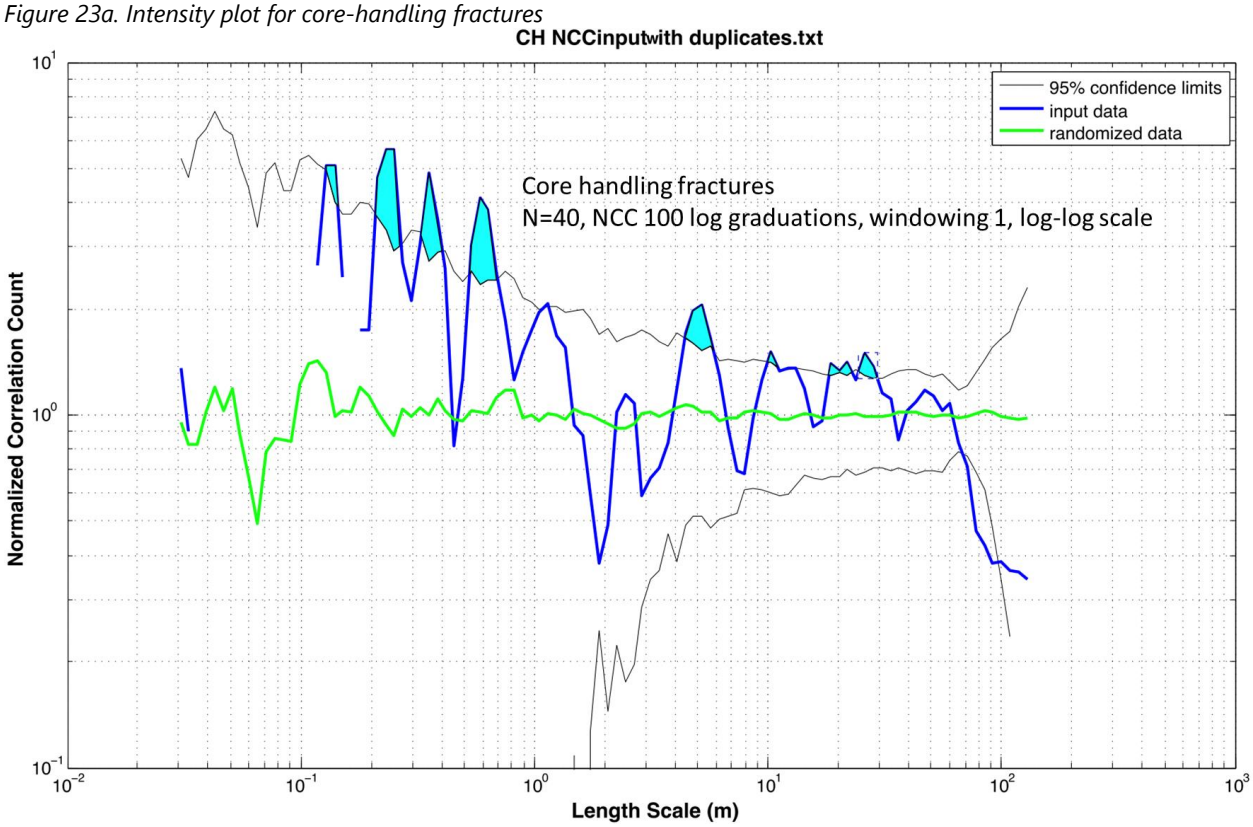


Figure 23b. NCC plot for core-handling fractures, logarithmic length scale.

Hydraulic fractures show weak log-periodic clustering at small length scales (< 1.5 m) which may be interpreted to reflect clusters of fractures, including the presence of fracture multiples such as doublets. The lack of spacings at the 1.5 –3.5 m length scale likely indicates gaps between hydraulic fracture clusters. The peak at 4 m (13 ft) is interpreted as dominant spacing between hydraulic fracture clusters, and there is another peak at 8 m which is likely a harmonic.

Overall, however, the data curve is mostly contained within the 95% confidence interval and thus is not strongly different from a random distribution. Natural fractures are not present in the first part of the core, but then follow a pattern of log-periodic clusters with width of ~17 m, and a cluster spacing of ~50 m. The lack of fractures in the first part of the core causes the steep drop in the curve beyond the 50 m length scale. The peak in intensity for these fractures coincides with a peak in intensity for the core-handling fractures. It is possible the core breaks more readily in the section with the most natural fractures.

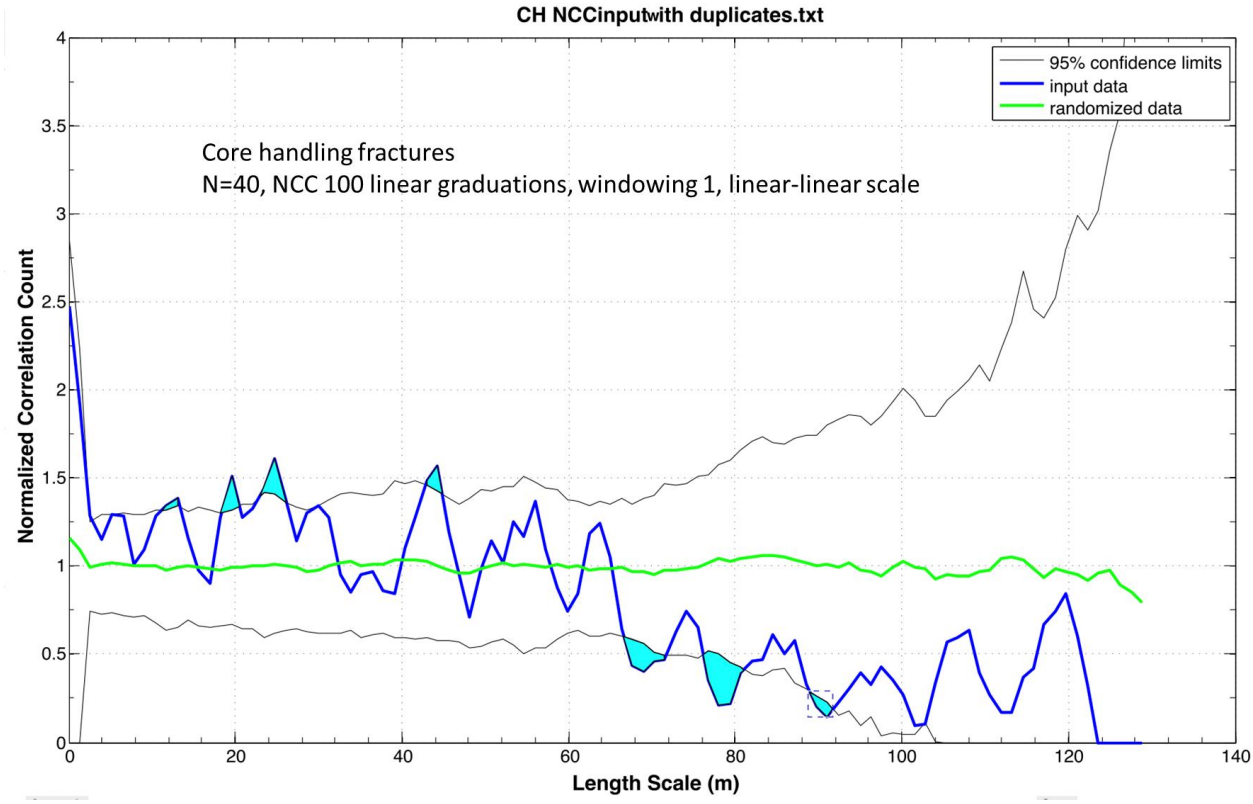


Figure 23c. NCC plot for core-handling fractures, linear length scale.

Drilling-induced fractures also show log-periodic clustering at length scales below 2 m. The dominant spacing at 7.5 m might reflect a mechanical drilling process. Core-handling fractures follow a similar but weaker pattern.

Discussion of aspects of fracture description findings

The observation that hydraulic fractures, drilling-induced fractures, and the dominant natural fractures share the same NE-SW strike orientation is no surprise - the stress field orientation here has been consistent since the Cretaceous (Laubach et al., 2004). The consequence for fracture description work is that orientation alone is insufficient as a criterion for designating fracture type because different fracture types have a common orientation. Criteria developed by Gale et al. (2018) were used to make distinctions between fracture types, and we note the greatest challenge was for hydraulic fractures and drilling-induced fractures.

The similarity in spread of strike orientations of hydraulic fractures in this project (~ 45°) and in the HFTS1 and HFTS2 projects in the Wolfcamp Formation is interesting. At first consideration the similarity in orientation spread might be interpreted as suggesting the mechanism for hydraulic fracture growth in the two situations is similar. However, the slant core in the Eagle Ford (this project) is ~250 ft away from the stimulated wells compared to 60-100 ft for the Wolfcamp projects. If we envisage a spreading network that would imply a tighter distribution

in the Eagle Ford at an equivalent distance. Moreover, there are two wells on each side of the Zgabay 4H that are presumed to have initiated HFs. Thirdly, the natural fractures are mostly parallel to hydraulic fractures in the Eagle Ford; reactivation along natural fractures would tend to result in a narrower distribution of orientations in this case.

Variation in lithology affects surface roughness and possibly orientation of hydraulic fractures. It would be useful to break out the orientations by lithology to determine if this is the case. The project facies review that was done for the project could be combined with the fracture description for this purpose in future work. Such a study could help improve understanding of the effect of lithologic variation on the propagation of the hydraulic fracture network, and potentially improve interpretation of microseismic data and fiber optic data.

A general observation we made during the fracture description work was that many parted fractures (both hydraulic and natural fractures) did not have much drilling mud in them; mud was typically only around the core margins (Fig. 7). We interpreted the lack of drilling mud to suggest strong pressure drawdown and closing of fractures before drilling. There was a multiyear gap between completion of the adjacent wells and acquisition of the Zgabay 4H core, which would allow time for this pressure drawdown to occur. The high degree of proppant embedment supports this hypothesis and is in marked contrast to the HFTS1 core in the Wolfcamp Fm. where there was no proppant embedment, and the core was drilled only a few months after the completions were done.

Several publications in the recent literature address the topic of the origin of microseismic double-couple events, making the case that the shear plane responsible for the event is along bedding rather than being subvertical (e.g., Tan et al., 2021 and references therein). We looked for evidence of shear along bedding adjacent to hydraulic fractures. We observed several bed-parallel partings adjacent to hydraulic fractures but found no evidence of shear caused by this mechanism. In the case of shear plane #199 (Fig. 15), the slickensides are near normal to the shear direction that would be predicted in Tan et al.'s model, so in this case they are unlikely to be due to hydraulic fracture #200, which cuts the shear plane. We note however, that the slant core represents a small sample from the reservoir and although our findings do not support the Tan et al. model they do not refute it either.

References

1. Elliott, S. J., and Gale, J. F. W., 2018, Analysis and distribution of proppant recovered from fracture faces in the HFTS slant core drilled through a stimulated reservoir. URTeC 2902629 presented at URTeC, Houston, TX 23-25th July, 2018.
2. Gale, J. F. W., Elliott, S. J., Li, J. Z. and Laubach, S. E., 2018, Hydraulic fractures in core from stimulated reservoirs: core fracture description of HFTS slant core, Midland Basin, West Texas. URTeC 2902624 presented at URTeC, Houston, TX 23-25th July, 2018.
3. Gale, J. F. W., Elliott, S. J., Li, J. Z., and Laubach, S. E., 2019, Natural fracture characterization in the Wolfcamp Formation at the Hydraulic Fracture Test Site (HFTS), Midland Basin, Texas (ext. abs.): Proceedings of the Unconventional Resources Technology Conference (URTeC), Denver, Colo., no. 644, 16 p., http://doi.org/10.15530/urtec-2019-644.

4. Laubach, S E., Olson, J.E. and Gale, J.F.W. 2004. Are open fractures necessarily aligned with maximum horizontal stress? Earth and Planetary Science Letters, 222(1), 191–195.
5. Marrett, R., Gale, J.F.W., Gómez, L.A. and Laubach, S.E. 2018. Correlation analysis of fracture arrangement in space. Journal of Structural Geology, 108, 16–33.
6. Raterman, K.T., Farrell, H.E., Mora, O.S., Janssen, A.L., Gomez, G.A., Busetti, S., McEwen, J., Davidson, M., Friehauf, K., Rutherford, J., Reid, R., Jin, G., Roy, B. and Warren, M. 2017. Sampling a stimulated rock volume: An Eagle Ford example: URTeC: 2670034 Unconventional Resources Technology Conference Austin, Texas, USA, 24-26 July 2017, p.937–954, https://DOI.org/10.15530/urtec-20172670034
7. Tan, Y., Wang, J., Rijken, M., Zhang, Z. Fang, Z., Wu, R., Lim, I., Chen N., and Liu, X. 2021. URTeC: 5296, Mechanism of microseismic generation during hydraulic fracturing – with evidence from HFTS 2 observations. Unconventional Resources Technology Conference, Houston, Texas, USA, 26-28 July 2021, 16 p. https://DOI.org/10.15530/urtec-2021-5296

Acknowledgements

This project was funded as a subcontract (No. S592 Amendment No. 5, phase three, Eagle Ford core description) under the Gas Technology Institute (GTI) DOE NETL contract DE-FE0024292. The project was coordinated by GTI, with Jordan Ciezobka providing project management. Devon Energy staff assisted with core logistics, data provision, and interpretation. CoreLab staff handled logistics, did the whole core CT-scan, core layout and marking. Publication authorized by the Director, Bureau of Economic Geology, Jackson School of Geosciences, The University of Texas at Austin.

Appendix D: Environmental Monitoring of the Hydraulic Fracturing Test Site (HFTS) Operations

Research Entity: GTI Energy

Final Report HFTS Environmental Monitoring, April 12, 2018

Prepared by Thomas Hayes and Sarah Eisenlord

Research by Thomas Hayes, Sarah Eisenlord, Karen Crippen, Alan Janos, Russ Bora, Yuliana Drobit, Brian Landreth

Legal Notice

This information was prepared by Gas Technology Institute ("GTI") for NETL-DOE.

Neither GTI, the members of GTI, the Sponsor(s), nor any person acting on behalf of any of them:

a. Makes any warranty or representation, express or implied with respect to the accuracy, completeness, or usefulness of the information contained in this report, or that the use of any information, apparatus, method, or process disclosed in this report may not infringe privately-owned rights. Inasmuch as this project is experimental in nature, the technical information, results, or conclusions cannot be predicted. Conclusions and analysis of results by GTI represent GTI's opinion based on inferences from measurements and empirical relationships, which inferences and assumptions are not infallible, and with respect to which competent specialists may differ.

b. Assumes any liability with respect to the use of, or for any and all damages resulting from the use of, any information, apparatus, method, or process disclosed in this report; any other use of, or reliance on, this report by any third party is at the third party's sole risk.

c. The results within this report relate only to the items tested.

Acknowledgment: "This material is based upon work supported by the Department of Energy under Award Number DE-FE0024292."

Disclaimer: "This report was prepared as an account of work sponsored by an agency of the United States Government. Neither the United States Government nor any agency thereof, nor any of their employees, makes any warranty, express or implied, or assumes any legal liability or responsibility for the accuracy, completeness, or usefulness of any information, apparatus, product, or process disclosed, or represents that its use would not infringe privately owned rights. Reference herein to any specific commercial product, process, or service by trade name, trademark, manufacturer, or otherwise does not necessarily constitute or imply its endorsement, recommendation, or favoring by the United States Government or any agency thereof. The views and opinions of authors expressed herein do not necessarily state or reflect those of the United States Government or any agency thereof."

Executive Summary

The successful expansion of shale development to predominance in the U.S. has been made possible through the rapid development of multiple advanced technologies such as directional drilling and hydraulic fracturing, that have been successfully deployed by many energy developers, natural gas field service providers, and engineering solution providers that comprise this new industry of innovation. Critical to this national effort are the on-going programs in research, development and in-field testing that are conducted as a result of government-industry partnerships. The HFTS-1 field demonstration project that is co-funded by the energy industry and NETL-DOE and focused on the testing of advanced drilling and completion techniques in the Upper and Lower Wolfcamp formations (Permian Basin) of Reagan County, TX, represents an important contributor to the national effort for the improvement of shale energy production as a low-cost, environmentally sustainable source of energy in the U.S. for the future. The field location for this effort is a shale well pad system

owned by Laredo Petroleum.

The approach used by GTI was to monitor the groundwater and ambient air in locations within 1,000 feet of the HFTS well field before HFTS activity, and during the HFTS operations of hydraulic fracturing, flowback collection and energy production. These measurements were taken to determine the overall level of environmental impacts of HFTS shale well development operations (including production) on the surrounding community as measured by the transport of key constituents of concern (e.g., benzene, ethylbenzene, toluene and total xylenes) to the ambient air and to groundwater wells that are proximal to the HFTS facility. This effort also included the characterization of flowback water (for three of the eleven shale wells of HFTS) within weeks following well completion and produced water generated during well production. Measurements associated with this work included determinations of cumulative water volumes generated and concentrations of constituents that are usually used to define the composition of flowback and produced water streams.

The major findings of this environmental monitoring effort were as follows:

1. **Minimal impact to ambient air quality**. Air monitoring measurements conducted at the HFTS including VOC, PM-10, benzene, toluene, ethylbenzene, total xylenes, and methane indicate that nearly all phases of HFTS operations (except for flowback collection) had no discernable impact to air quality when compared to the Baseline HFTS samples, to monitoring conducted in downtown Midland, and to literature values from other urban locations in Texas.

The collection and storage of initial produced water released from each well (flowback) results in a small, measurable release of VOCs and BTEX to the atmosphere; however, near-site air quality values for BTEX are less than 3% of OSHA limits for worker safety (8-hour exposure) and the short-term nature of the flowback collection phase limits residential exposure to air emissions.

2. **No measurable migration of methane and BTEX to groundwater**. There was no detection of migration of hydrocarbons or fracturing chemicals from the wellbore or from the shale strata to groundwater aquifers. In the monitoring of groundwater before and during each phase of operation, no evidence of migration of methane, benzene, toluene, ethylbenzene, total xylenes or total organic carbon (TOC) was detected. Field based tiltmeter measurement of hydraulic fracture height growth indicated no fracture growth into or near ground water sources.

3. **Minimal, temporary rise of TDS in groundwater aquifer followed by recovery**. The small, temporary rise in median salinity of the groundwater measured at the five groundwater wells (increasing from about 500 mg/l to 800 mg/l TDS) was likely due to the infiltration of water from neighboring aquifers of higher salinity occurring during the Fracturing Phase when pumping (amounting to tens of millions of gallons) could have caused groundwater drawdown of each of the five wells. The effect was short termed: dissolved solids returned to baseline TDS levels within 50 days.

4. **Normal characteristics of flowback composition and volume collection**. Flowback collection efficiencies amounted to approximately 25% of the 10 million gallons of water injected in each of the three HFTS wells monitored for produced water characterization over a period of 210 days following the initiation of flowback. Delaying flowback initiation by 6 weeks

following the completion of each well provided more contact time of the injected aliquot to equilibrate with downhole materials and causes higher salinities to be measured in early flowback samples. Initially, median TDS levels in flowback water were measured at around 90,000 mg/l in the first day of release increasing to a plateau of 120,000 mg/l in about 3 months, close in value with the salinity of produced waters generated from mature wells of nearby Wolfcamp shale well fields.

5. Changes measured in flowback composition point to biologically mediated transformations of organics, sulfate and nitrate in the deep subsurface. As salinity in the flowback increased with time, concentrations of several constituents decreased simultaneously, the nature of which strongly pointed to the likelihood of substantial microbiologically mediated transformations of hydrocarbons and oxidants. Within the first 14 days following initial release of flowback, TOC decreased by 95% while nitrate decreased by 100% (mediated by denitrifier microbial populations) and sulfate (initially present at over 420 mg/l) decreased by 24% (mediated through the action of sulfate reducing bacteria). The measured TOC loss was in stoichiometric balance with nitrate and sulfate consumption: The oxygen equivalents of TOC oxidized to CO2 were within 3% of the measured losses of sulfate and nitrate oxygen equivalents in the flowback at 14 days. In this project, sampling for microbial community characterization was closely coordinated with compositional sampling; microbial structure results are described in a separate report.

6. **Possible downhole formation of multiple tons of iron sulfide precipitates**. If the changes in concentration in the flowback water samples were indicative of the 10 million gallons of injected water, more than 1.4 tons of sulfide could have been generated in place in the fractured shale of each HFTS well. The non-detect levels of soluble sulfide measured in the flowback water samples together with the presence of excess soluble iron point to the substantial formation of iron sulfide precipitate. More than 3.8 tons of ferrous sulfide precipitate may have formed within the formation. This in-place precipitate may later move toward the horizontal well bore as water is removed and may over time mechanically impede the movement of fluids and gases from a horizontal well and become a factor in overall well performance. More research will be needed to determine the fate of sulfide and management approaches to prevent deleterious effects on well performance.

Introduction

Shale development has become an increasingly important source of oil and natural gas over the past decade; some have estimated that as of 2015, shale gas alone provides more than half of the natural gas supply North America — which would amount to over 14 tcf of natural gas per year representing more than $70 billion of revenue at current market prices (EIA, 2017). This has been made possible through the rapid development of multiple advanced technologies, such as directional drilling and hydraulic fracturing, that have been successfully deployed by many energy developers, natural gas field service providers, and engineering solution providers that comprise this new industry of innovation.

The shale gas plays of North America are numerous, shown in Figure 1, covering substantial areas of the Eastern, Southwestern, Northern, Southern, and Western states of the U.S.; vast areas of Canada have extensive shale gas plays as well. Development continues to move

forward at an aggressive pace; between 2011 and 2014, it is estimated that 25,000 to 30,000 new shale wells per year were drilled and completed with hydraulic fracturing in the U.S. (Gallegos, et al., 2015).

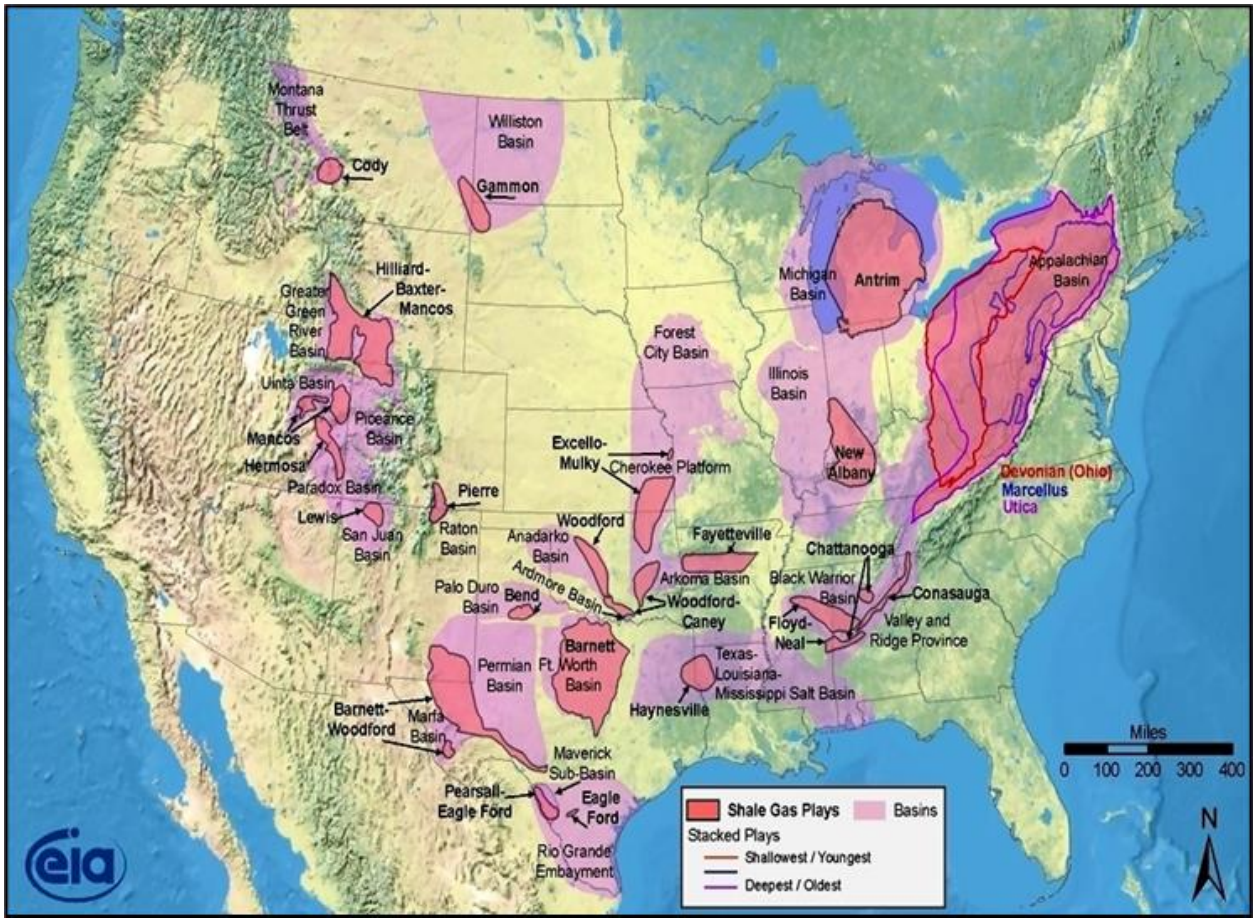


Figure 1: Shale Gas Regions of the United States.

As shale oil and gas emerges as one of the world's most abundant, affordable, and clean-burning sources of energy, sustainable growth in the development and production of these resources will require a clear understanding of the potential environmental impacts arising from shale development as well as effective strategies for managing risks to the public health and the environment (Small, et al., 2014). The manner in which risks to the public health and to the environment are described and quantified with regard to shale development is not without controversy; a number of reviews in the literature have classified various areas of risk and have discussed various pathways of potential impacts to the environment (including groundwater and ambient air) that need to be considered (Small, et al., 2014; USEPA, 2016; Clark, et al., 2013). About public opinion and regulatory interaction, significant concerns have been raised over the environmental impacts of the industry, particularly the effects of shale development on groundwater and ambient air receptors. These concerns arise from an awareness of the large amounts of water that are handled and of the substantial mechanized equipment (e.g., diesel driven pumps) and high pressures that are employed in shale well field development. There are multiple steps involved in the development and operation of shale wells; these steps include road and well pad construction, drilling the well, casing, perforating, hydraulic fracturing, completion, production, abandonment, and reclamation (RPSEA, 2012).

To date, most of the environmental concerns (real or perceived) associated with the

development of shale gas well fields stem from the management of large amounts of water associated with the early temporal steps associated with drilling, hydraulic fracturing, and completion shale wells; contamination of freshwater municipal aquifers; air emissions associated with these steps are also a concern. One promising direction for reducing environmental impact can potentially be realized through new approaches to shale well pad development. The same technological improvements that now allow up to 8-16 wells to be drilled and completed from a single well pad (versus 2-3 wells per pad ten years ago), while increasing energy production from each well (through advanced well construction and hydraulic fracturing design) may not only substantially improve the economics of energy production but can potentially reduce environmental impacts per unit of energy produced.

Though improvements in shale development are gradually reducing the environmental footprint of the industry, the nature of the shale industry remains one of a series of transient activities (i.e. well installations and completions) in highly dispersed locations that are often proximal to residential and urban areas. This means that much of the industry's activities are performed not only in remote areas but in locations that touch the lives of fellow citizens; drilling operations are observed from the windows of many urban homes, large shale gas water impoundments can often be clearly seen from cars passing by on highways and automobile drivers are increasingly aware of the heavy traffic of trucks carrying water to and from wells pass through neighborhoods. The property-owner stakeholder list now grows larger than the few ranchers in the countryside of conventional oil and gas operations. Many shale well pads may be fairly close to residential housing, which means that particular attention needs to be paid to the effects of shale well development on ambient air quality and groundwater security. Under this high visibility setting for shale well pad development, it will be even more important for the industry to conduct careful environmental sampling with meaningful measurements that quantify the impact of shale development on ambient air quality and on freshwater supplies.

The aim of this study was to conduct careful measurements of constituents of concern in ambient air and groundwater strata proximal to shale gas well construction, completion, and production associated with the Hydraulic Fracturing Test Site (Phase I) operated at the Laredo facility near Midland, TX. The environmental monitoring program focused on determining the condition of the groundwater and ambient air before, during and after critical shale well actions that were performed at the HFTS location for three shale wells; the study included efforts to obtain a good baseline of measurements before shale well pad construction followed by the monitoring of the same critical parameters following the initiation of well pad construction, completion, and operation activities. Finally, water associated with the hydraulic fracturing of three wells was characterized to gain insight into long term produced water management.

Objectives

The overall objective of this study is to determine the level of impacts of HFTS shale well development, operations and production on the surrounding community as measured by the transport of key constituents of concern to the ambient air and to groundwater wells that are proximal to the HFTS facility operated by Laredo. Specific objectives of this work include the following:

1. Determine the potential environmental impact of HFTS operations on groundwater.
2. Determine the potential impact of HFTS operations on air quality in locations proximal to the HFTS site.
3. Characterize waters associated with the hydraulic fracturing and production at the HFTS facility to obtain information of value for long-term produced water management.

Description of the HFTS Site

Situated about 55 miles southeast of Midland, TX, the hydraulic fracturing test site, owned and operated by Laredo Petroleum, is in the Northeast quadrant of Reagan County near the northern boundary of the county as shown in Figure 2. Rural in nature with a small population of 3,367 (according to the Year 2010 Census), the county and the immediate area containing the facility is sparsely populated containing less than three people per square mile. The Edward-Trinity Plateau Aquifer provides fresh water for this region.

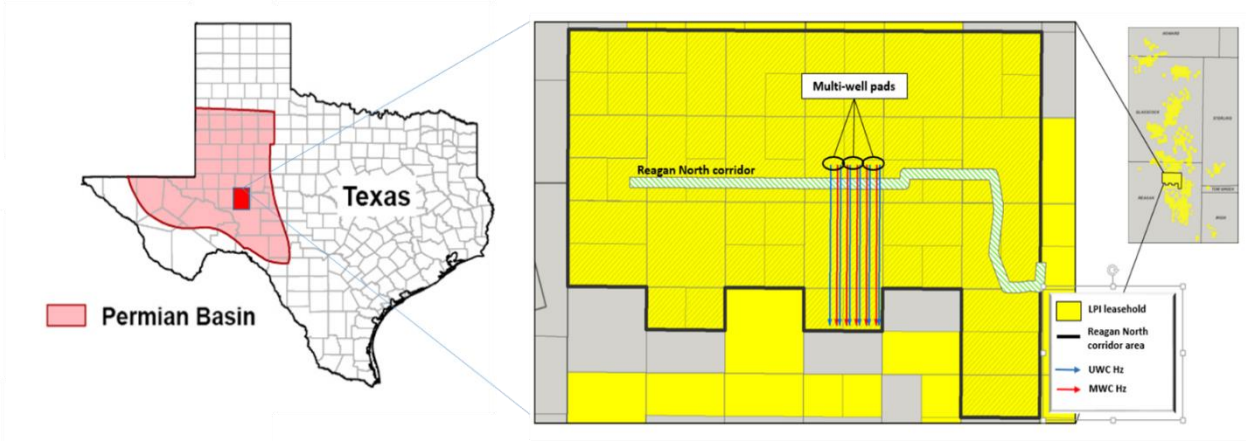


Figure 2: Location of the Hydraulic Fracturing Test Site.

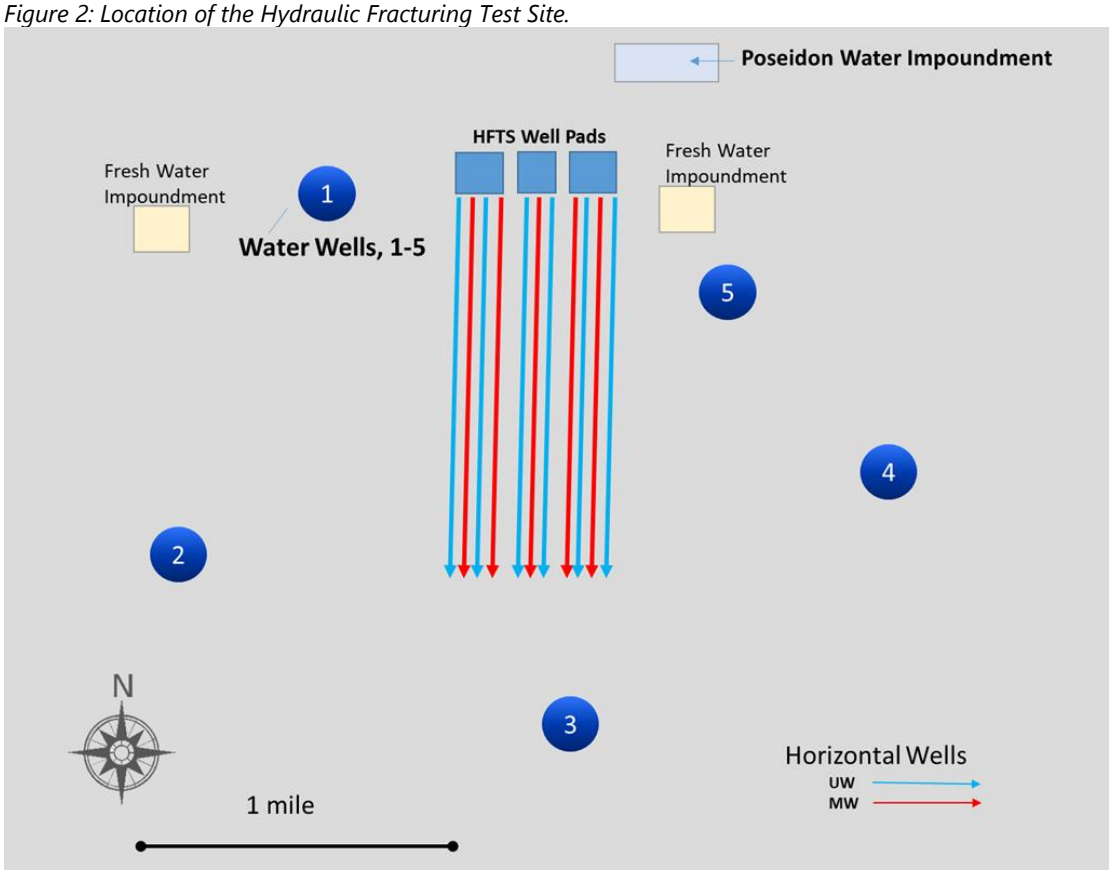


Figure 3: Layout of the Hydraulic Fracturing Test Site and Water Wells.

The HFTS facility itself is comprised of three well pads from which eleven horizontal wells were drilled during the HFTS1 project. A layout of the well pad system is shown in Figure 3. In this array, six horizontal wells were drilled into the Upper Wolfcamp Horizonal oil play (UW Hz) and five horizontal wells were drilled into the Middle Wolfcamp Horizonal oil play (MW Hz) as depicted in the figure. Also shown in this diagram are the five groundwater wells used to obtain the freshwater required for hydraulic fracturing. Water from the water wells was collected over a period of weeks and stored in several large impoundments with a maximum storage capacity of more than 80 million gallons. The impoundment structures were positioned in proximity to the well pad facility to facilitate easy delivery of water for creating the desired blends of freshwater, flowback, chemicals and proppant required for the successful performance of the hydraulic fractures at the Well Pad of the HFTS facility.

In the determination of environmental impact, the major activities of interest at HFTS included drilling, hydraulic fracturing, flowback water collection, and production with the concomitant generation of produced water.

Migration of constituents of interest to groundwater was of particular interest in the downhole activities of drilling and hydraulic fracturing, while impacts to ambient air were of interest for all four activity stages of the HFTS facility. Procedures that involved substantial handling of water supporting the main activities of HFTS included the following:

- Obtain large amounts (tens of millions of gallons) of freshwater from the five groundwater wells (Wells 1-5 shown in Figure 3) surrounding the facility and use the large water impoundments (including the Poseidon structure) for water staging that is needed for subsequent fracturing operations.

- During hydraulic fracturing, send a freshwater stream from the storage impoundments to the blending stage where water is mixed with chemicals and sand; this water blend is subsequently injected downhole under high pressure involving the operation of diesel-driven pumps that are key to the transport of water, chemicals, and proppant to the targeted subsurface shale strata.

- As the water is released from each completed well under pressure, collect the flowback water stream and store the flowback in frac tanks for subsequent treatment and reuse.

- In the production phase, collect and dispose of produced water that is co-produced with oil and natural gas from the HFTS wells.

- Large volumes of produced water are collected, treated, and stored on site in double lined impoundment ponds for use in subsequent stimulation operations.

All the above well pad development activities and water handling steps were considered when designing the approaches that were used to determine impacts to groundwater and ambient air associated with HFTS. Particularly, schedules for the frequency and timing of sampling of groundwater and ambient air were developed to allow comparisons of the conditions of the environment before and after major well pad development events. The descriptions of these approaches are discussed in more detail in the sections to follow.

Groundwater Monitoring

Methods and Approach

Table 1: Sampling Schedule for Groundwater Monitoring at the HFTS Facility.

Stage	Description of Activity	General Time Frame of Activity	Sampling Dates
Baseline	After drilling but before hydraulic fracturing of the 11 wells.	October 2015	10/12/2015
Hydraulic Fracturing	During the hydraulic fracturing of the 11 wells of the HFTS well pad.	November and December 2015	12/1/2015
Flowback	During the period when flowback water from the wells is collected.	January 2016	1/14/2016
Production	Beyond flowback and into the production period of the well pad.	Beyond March 2016	6/3/2016 1/4/2017

Table 2: List of Constituents and Analytical Methods for Groundwater

Parameter	Sample Preservation	Standard Method	Instrumentation	Comments
General Chemistry				
pH	Ice	EPA 9040	Electrometric Equipment	Suitable for water analysis
Total Dissolved Solids	Ice	SM18 2540 C	Gravimetric Apparatus	Standard USEPA Method
Specific Conductance	Ice	EPA 120.1	Self-Contained Conductivity Meter	Standard USEPA Method
Alkalinity	Ice	SM18 2320 B	Titration Equipment	21st Ed. Standard Methods (2015)
Organic Compounds				
Total Organic Carbon	Sulfuric Acid	EPA 415.1	Combustion and Infrared Detection	Provides the concentration of total organics as Carbon.
Dissolved Methane	Sulfuric Acid	EPA RSK SOP 175	Gas Chromatography with thermal conductivity, flame ionization or electron capture detector	Uses purge and trap sample preparation procedures.
Volatile Organic Compounds	Hydrochloric Acid	EPA 8260B or 8021B	Gas Chromatography with Mass Spectroscopy or Photoionization and Flame Ionization Detection	Benzene, Toluene, Ethylbenzene, Xylenes
Inorganic Species				
Cations	Nitric Acid	EPA 200.7	Inductively Coupled Plasma Emission Spectroscopy	As, Ba, B, Cd, Ca, Cr, Cu, Fe, Pb, Mg, Mn, Ni, K, Na, Zn
Anions	Ice	EPA 300.0	Ion Chromatography	Chloride, Fluoride, Sulfate, Nitrate
		EPA 9030B (modified)	Distillation / Ion Chromatography	Total Sulfide

The overall approach to measuring the impact of HFTS activities on groundwater involved the collection and analysis of samples obtained from the five existing wells surrounding the HFTS facility (i.e., Wells 1-5 of Figure 3) in accordance with a sampling schedule summarized in Table 1. Sampling of the five groundwater wells occurred after drilling of the wells before hydraulic fracturing for a baseline period, then during hydraulic fracturing, during flowback, and twice during production: 6 months and 1 year into production. All five of the wells draw freshwater from the Edward Trinity Plateau Aquifer to the HFTS operations.

The groundwater monitoring approach included the analysis of samples for constituents and parameters that could provide any early indication of impacts due to the transport of hydrocarbons into the groundwater table due to compromised well infrastructure, or communication between fresh water and hydrocarbon bearing zones. These methods allowed for the detection of the transport of inorganic constituents from adjacent aquifers due to drawdown of the aquifer in the weeks preceding hydraulic fracturing. The list of constituents measured, and the analytical methods used on the water samples are given in Table 2.

Water sampling was conducted by EnvrioClean Cardinal (Tulsa, OK). Groundwater wells were actively pumping water for a minimum of 24 hours before samples were taken. Water samples for general chemistry were collected in duplicate 500mL plastic bottles, samples for TOC were taken in triplicate in 40mL glass VOA vials with sulfuric acid preservative, total petroleum hydrocarbon samples were held in 1L amber glass containers, BTEX samples were taken in triplicate 40mL glass VOA vials with hydrochloric acid for preservation, samples for cation analysis were taken in duplicate in 500mL glass containers with nitric acid preservative. Samples for anion analysis were collected in 500mL plastic vials, preserved with ice and refrigeration. Samples were shipped to GTI on ice, within 4 days of collection. After which samples were stored in 4C refrigerators before analysis. GTI conducted general chemistry, dissolved methane, cation, and anion analysis. TOC and BTEX were analyzed at Test America in Northwest Chicago, IL. Well S-158 was offline after the third sampling period.

Results and Discussion

The results from the characterization of groundwater samples taken from the five wells surrounding the well pad are presented in Tables 3-7 and allow comparisons of the baseline period to the condition of the water during hydraulic fracturing, flowback and the first months of production. Examination of the data in these tables was used to determine the extent and nature of impact that the HFTS well pad development had on the overlying groundwater strata. Results for all the chemistry parameters of the groundwater wells at each sampling event are shown in Appendix Tables A3-A7. The elevated levels of dissolved solids in the groundwater negatively impacted detection limits reported; GTI's ICP sample introduction system was not optimized for handling dissolved solids at these concentrations and therefore instrument detection limits were raised.

Overall, the data from the groundwater monitoring clearly show that there was little impact on groundwater quality measured because of HFTS operations. In particular, examination of Tables 3-7 shows that during the baseline and throughout the sampling campaign, the quality of the groundwater remained high quality, suitable for residential use. Generally, the water was low in total dissolved solids at median values less than 800 mg/L (well below the 3,000

mg/L criterion for brackish aquifers), and the calcium concentrations at greater than 60 mg/L would cause the water to be categorized as "hard". The ratio of sodium and calcium/ magnesium cations was sufficient to maintain the sodium absorption ratio (SAR*) at values well below 6, which makes the water highly suitable for irrigation. Only five of the fifteen metals sought after in the analyses of the water samples were consistently present in concentrations over 0.5 ppm. The five cations (sodium, calcium, magnesium, potassium, and iron) that were greater than 0.5 ppm are included in Tables 3-7. Data for other heavy metals are found in Appendix tables A3 – A7.

Table 3: Summary of Chemical Characteristics of Groundwater Wells Sampled During the Baseline Stage.*

Parameter	Range	Median	Units
pH	7.96-8.23	8.06	-
Alkalinity	188-217	193	mg/L as $CaCO_3$
Total Dissolved Solids	370-722	484	mg/L
Specific Conductivity	631-928	762	µS/cm
Total Organic Carbon	0.41-2.20	0.71	mg/L
Benzene	-	<0.00050	mg/L
Toluene	-	<0.00050	mg/L
Ethylbenzene	-	<0.00050	mg/L
Xylenes	-	<0.001	mg/L
Methane	0.00030-0.00109	0.00047	mg/L
Cations Above 0.5 mg/L			
Sodium	23.1-67.5	42.0	mg/L
Calcium	60.3-90.8	69.9	mg/L
Magnesium	30.1-49.6	42.0	mg/L
Potassium	3.9-7.2	4.1	mg/L
Iron	0.2-3.9	0.5	mg/L
Anions Above 0.5 mg/L			
Chloride	21.8-52.2	28.9	mg/L
Nitrate	19.7-24.2	22.6	mg/L
Sulfate	68.6-254	135	mg/L
Fluoride	1.2-1.6	1.5	mg/L

* *Groundwater Wells 1-5.*

Organic compounds were low in all water samples taken at all sampling times from the five wells. Total organic carbon remained less than 1 mg/L and the sentinel compounds for impact from shale wells including benzene, toluene, and ethylbenzene that remained less than 0.5 ppb, and xylenes that remained less than 1 ppb. Even median values for methane (the most mobile compound of interest in subsurface strata) remained well below 1 ppb. Although it is recognized that methane from natural sources can impart levels at 1 mg/L (1000 ppb) or more in groundwater, it is notable that methane in the five wells that were sampled remained below 1 ppb throughout the entire monitoring campaign for all five groundwater wells, providing the strongest evidence that no mass transfer of constituents from the shale strata or the producing wells to the overlying groundwater aquifer was occurring. Even during the hydraulic fracturing stage of operations, no organic constituents were measured at levels greater than baseline concentrations as seen in the comparison of BTEX and methane concentrations of Table 3 (Baseline) with the values of Table 4 (Hydraulic Fracturing). Detailed methane concentration

data for each of the five groundwater wells are presented in Table A1 of the Appendix.

Table 4: Summary of Chemical Characteristics of Groundwater Wells Sampled During the Fracturing Stage.*

Parameter	Range	Median	Units
pH	7.60-8.01	7.64	-
Alkalinity	185-292	209	mg/L as $CaCO_3$
Total Dissolved Solids	670-1950	844	mg/L
Specific Conductivity	854-2870	1390	µS/cm
Total Organic Carbon	0.43-0.96	0.46	mg/L
Benzene	-	<0.00050	mg/L
Toluene	-	<0.00050	mg/L
Ethylbenzene	-	<0.00050	mg/L
Xylenes	-	<0.001	mg/L
Methane	0.00016-0.00103	0.00037	mg/L
Cations Above 0.5 mg/L			
Sodium	29.6-233	128	mg/L
Calcium	75.3-108	76.7	mg/L
Magnesium	31.1-56.4	47.2	mg/L
Potassium	4.0-10.8	7.4	mg/L
Iron	0.2-2.0	0.8	mg/L
Anions Above 0.5 mg/L			
Chloride	26-614	71	mg/L
Nitrate	2.7-17.9	12.2	mg/L
Sulfate	145-390	247	mg/L
Fluoride	1.5-2.1	1.5	mg/L

* *Groundwater Wells 1-5.*

In consideration of all stages of development of the HFTS well pad, measurable changes were observed only with two parameters – total dissolved solids (TDS) and conductance – which was evident in proceeding from the Baseline to the Hydraulic Fracturing Stage. These parameters are shown in the graph of Figure 4 across the 355-day monitoring of the five groundwater wells. In particular, the median value for TDS increased by about 75% from 484 to 844 mg/L from the Baseline into the weeks when the well pad was intensively involved in the hydraulic fracturing of the 11 horizontal wells at 51 days following the Baseline sample; subsequently, median TDS values recovered to Baseline levels in the 1.5 to 10 months that followed. Even at the elevated salinity levels, among all of the groundwater samples collected from Wells 1-5, median TDS levels remained less than 850 mg/L, far below the level of TDS (3,000 mg/L) that defines the highest record TDS from the Edward-Trinity Plateau aquifer (Anaya & Jones, Texas Water Development Board, 2009).

Similarly, the median value for conductance among the five groundwater wells showed an increase from 762 to 1,390 µS/cm from the Baseline to the Hydraulic Fracturing stage, and subsequently recovered to Baseline values within the 1.5 to 10 months that followed.

The above-described impact on salinity of the groundwater was detectable only during the stage of operations where hydraulic fracturing of the 11 wells was being performed. Since the rise of salinity was not accompanied with any trace of methane or BTEX, it is unlikely that the measured rise in salt in the groundwater was due to water infiltration from the shale strata or from the shale well structures. Preparation for hydraulic fracturing operations, however, did

involve the pumping of tens of millions of gallons from the groundwater wells into the impoundments that were used to provide freshwater for the development of the horizontal shale wells.

Table 5: Summary of Chemical Characteristics of Groundwater Wells Sampled During the Flowback Stage.*

Parameter	Range	Median	Units
pH	7.63-7.98	7.84	-
Alkalinity	183-210	192	mg/L as $CaCO_3$
Total Dissolved Solids	290-703	443	mg/L
Specific Conductivity	478-1060	722	µS/cm
Total Organic Carbon	0.23-2.3	0.25	mg/L
Benzene	-	<0.00050	mg/L
Toluene	-	<0.00050	mg/L
Ethylbenzene	-	<0.00050	mg/L
Xylenes	-	<0.001	mg/L
Methane	0.00018-0.00063	0.00019	mg/L
Cations Above 0.5 mg/L			
Sodium	22.7-85.1	63.3	mg/L
Calcium	56.8-157	70.3	mg/L
Magnesium	26.9-81.2	36.8	mg/L
Potassium	0.3-54.7	4.6	mg/L
Iron	0.2-8.8**	5.8	mg/L
Anions Above 0.5 mg/L			
Chloride	8.0-33.8	16.0	mg/L
Nitrate	8.3-13.9	10.6	mg/L
Sulfate	17-185	89	mg/L
Fluoride	0.1-0.9	0.7	mg/L

** Groundwater Wells 1-5.*

*** Eliminated an outlier of 206 mg/L of iron measured in a water sample from Well 5.*

Extensive pumping of the wells likely caused considerable drawdown of the aquifer which could have promoted the infiltration of water from neighboring aquifer(s) that may have had a higher salinity level. In other words, it is highly likely that the aquifer that provided the water for HFTS was in communication with neighboring aquifer(s) of greater salinity; the over-pumping of Wells 1-5 in the aquifer proximal to the HFTS site evidently caused the infiltration of water from adjacent saline aquifer(s) to enter the localized drawdown zones of each of the groundwater wells during the time of aggressive freshwater acquisition to supply the water impoundments for fracturing. This mechanism is further supported by the rapid return of TDS and conductance levels to baseline values in water samples upon cessation of large withdrawals of water from Wells 1-5. Salinity increases in wells due to drawdown is a phenomenon that has been described elsewhere (USEPA, 2016).

All these results, therefore, clearly indicate that there was no migration of fluids or gases bearing constituents of concern from the 11 horizontal wells developed at the HFTS facility to the underlying or adjacent groundwater strata; this was evident in the results from groundwater monitored from the baseline period through all operations and well into the first year of operation of the HFTS wells. Based on the groundwater monitoring data obtained during HFTS1 operations, there is no evidence of natural gas or produced water migration to

the groundwater aquifer. This is further supported by the downhole deformation measurements conducted by Haliburton with three arrays of tiltmeters at the test site. No microcosmic events were detected shallower than 6,000ft true vertical depth, several thousand feet below the deepest reaches of the Edward-Trinity Plateau aquifer.

Table 6: Summary of Chemical Characteristics of Groundwater Wells Sampled During the Production Stage in June 2016.*

Parameter	Range	Median	Units
pH	7.44-7.63	7.6	-
Alkalinity	184-195	194	mg/L as $CaCO_3$
Total Dissolved Solids	490-850	635	mg/L
Specific Conductivity	691-1050	752	µS/cm
Total Organic Carbon	0.47-0.69	0.54	mg/L
Benzene	-	<0.00050	mg/L
Toluene	-	<0.00050	mg/L
Ethylbenzene	-	<0.00050	mg/L
Xylenes	-	<0.001	mg/L
Methane	0.00031-0.00086	0.00064	mg/L
Cations Above 0.5 mg/L			
Sodium	34.2-88.9	43.2	mg/L
Calcium	57.8-77.7	60.5	mg/L
Magnesium	27.8-43.7	35.0	mg/L
Potassium	3.8-5.6	4.4	mg/L
Iron	0.8-4.2	0.8	mg/L
Anions Above 0.5 mg/L			
Chloride	22.8-49.4	29.8	mg/L
Nitrate	18.7-24.8	20.2	mg/L
Sulfate	102-246	125	mg/L
Fluoride	-	<1	mg/L

* *Groundwater Wells 1-5.*

Produced Water Characterization

The overall purpose of the effort to characterize waters associated with the hydraulic fracturing and production at the HFTS facility was to obtain information of value for long term produced water management (including reuse) and to gain some insight into possible transformations that may have implications for future impacts such as corrosion and sour gas generation. The scope of this effort included the collection of samples from three water impoundments that provided the freshwater and recycled produced water for hydraulic fracturing operations, fracture fluids once mixed with fracture treatment chemicals, and a time series of samples to characterize the produced water from three selected shale wells.

Among the water storage facilities, two impoundments were used to store freshwater and one impoundment (the Poseidon) was used to store treated recycled saline produced water. These sources of water were mixed in a ratio of 80% freshwater to 20% saline water to comprise an aqueous stream that was subsequently blended with chemicals and various grades of silica proppant for each of the hydraulic fracturing operations. More than 10 million gallons of fracture fluids was injected while completing each of the shale wells. In each of the completions, the wells were shut in and fracture fluids were held downhole for about six weeks

before the initiation of flowback release.

Table 7: Summary of Chemical Characteristics of Groundwater Wells Sampled During the Production Stage in January 2017.*

Parameter	Range	Median	Units
pH	7.69-7.99	7.82	-
Alkalinity	179-207	189	mg/L as $CaCO_3$
Total Dissolved Solids	320-600	445	mg/L
Specific Conductivity	373-772	460	µS/cm
Total Organic Carbon	0.48-1.10	0.64	mg/L
Benzene	-	<0.00050	mg/L
Toluene	-	<0.00050	mg/L
Ethylbenzene	-	<0.00050	mg/L
Xylenes	-	<0.001	mg/L
Methane	0.00010-0.00072	0.00035	mg/L
Cations Above 0.5 mg/L			
Sodium	30.2-66.9	33.9	mg/L
Calcium	41.6-72.5	60.3	mg/L
Magnesium	25.9-38.4	34.0	mg/L
Potassium	5.1-6.9	5.6	mg/L
Iron	0.8-12	0.8	mg/L
Anions Above 0.5 mg/L			
Chloride	26.7-49.6	30.6	mg/L
Nitrate	0.1-20.3	18.0	mg/L
Sulfate	67.4-235	125	mg/L
Fluoride	1.1-1.6	1.3	mg/L

* *Groundwater Wells 1-5.*

Methods and Approach

Three wells were selected to provide water samples for characterization of produced waters (i.e., flowback generated within weeks following well completion and produced water generated during well production). Two of the wells were in the Upper Wolfcamp (designated U) and one in the Middle Wolfcamp (designated M). The shale wells that were chosen for produced water sample collection are identified as 4-SU, 6-SM, and 7-SU. The hydraulic fracturing involved the pumping of 10 million gallons of water blended with chemicals (such as friction reducers, corrosion inhibitors, scale inhibitors and biocides) and with various grades of silica sand proppant into each well. The fracture fluids were sampled at the beginning, middle, and end of the 12-day hydraulic fracturing process at each well. Following hydraulic fracturing and after the fracture fluids were held in for about six weeks, produced water samples were taken at 0, 1, 5, 14, 36, 90, 210, 365, and 550 days following the initiation of release of the flowback water. Standard procedures were used to conduct sampling and analysis needed for the development of water characterization data. All sampling was performed by EnviroClean Cardinal (Tulsa, OK).

In the weeks surrounding hydraulic fracturing, samples were taken of the water contained in the three impoundments used as a source of fracture fluids for the HFTS well hydraulic fracturing; impoundments were sampled weekly, for five weeks between November 5th and December 7th 2015., Information from the fracture fluid and impoundment sampling and

analysis was of considerable valuable in the effort to understand the composition of flowback water, especially in the initial flowback samples obtained from the three selected shale wells. The list of constituents measured, and the analytical methods used on impoundment water samples are the same as used for the produced water; these methods are described in Table 8.

Table 8: List of Constituents and Analytical Methods for Produced Water and Impoundment Water.

Parameter	Preservation	Standard Method	Instrumentation	Comments
Microbiology				
DNA Analysis	Ice	NACE Standards TM0106-2006 and TM0212-2012	Qiagen qPCR Thermocycler, Illumina HiSeq Sequencer	Standard for qPCR and Sequencing
General Chemistry				
pH	Ice	EPA 9040	Electrometric Equipment	Suitable for water analysis
Total Dissolved Solids	Ice	SM18 2540 C	Gravimetric Apparatus	Standard USEPA Method
Specific Conductance	Ice	EPA 120.1	Self-Contained Conductivity Meter	Standard USEPA Method
Alkalinity	Ice	SM18 2320 B	Titration Equipment	21st Ed. Standard Methods (2015)
Organic Compounds				
Total Organic Carbon	Sulfuric Acid	EPA 415.1	Combustion and Infrared Detection	Provides the concentration of total organics as Carbon.
Total Petroleum Hydrocarbons	Ice	EPA 1664B	Gravimetric Apparatus	Involves Hexane Extraction
Volatile Organic Compounds	Hydrochloric Acid	EPA 8260B or 8021B	Gas Chromatography with Mass Spectroscopy or Photoionization and Flame Ionization Detection	Benzene, Toluene, Ethylbenzene, Xylenes
Inorganic Species				
Cations	Nitric Acid	EPA 200.7	Inductively Coupled Plasma Emission Spectroscopy	As, Ba, B, Cd, Ca, Cr, Cu, Fe, Pb, Mg, Mn, Ni, K, Na, Zn
Anions	Ice	EPA 300.0	Ion Chromatography	Chloride, Fluoride, Sulfate, Nitrate
		EPA 9030B (modified)	Distillation / Ion Chromatography	Total Sulfide

** TPH not determined for impoundment water.*

Water samples for general chemistry were collected in two 500mL plastic bottles, samples for TOC were taken in triplicate in 40mL glass VOA vials with sulfuric acid preservative, total petroleum hydrocarbon samples were held in 1L amber glass containers, BTEX samples were taken in triplicate 40mL glass VOA vials with hydrochloric acid for preservation, samples for cation analysis were taken in duplicate in 500L glass vials with nitric acid preservative. Samples

for anion analysis were collected in 500mL plastic vials, preserved with ice and refrigeration.

Sample analyses were performed by GTI and Test America of Northwest Chicago, IL. Test America, an independent analytical laboratory, provided the appropriate sample containers, preservatives and completed the analytical analyses for BTEX, total organic carbon, and total petroleum hydrocarbons. Test America is certified in Texas, West Virginia, and Pennsylvania. Data compilation and analysis was provided by the Gas Technology Institute. The list of constituents measured, and the analytical methods used on produced water, fracture fluids, and impoundment water samples are shown in Table 8. After collection, samples were kept cold at 4°C until overnight shipment on ice to GTI within 4 days of collection.

Optimization methods were taken to minimize matrix inference, dilutions were necessary due to the high levels of potassium and sodium in addition to viscosity and hydrocarbons.

Results and Discussion

Characterization data on the composition of the impoundment water used for hydraulic fracturing are shown in Table 9. Impoundment water includes two freshwater impoundments and recycled produced water in the Poseidon tank. Fracture fluids were a mixture of fresh and recycled produced water, samples were obtained after chemical mixing before proppant addition and pressurization. All impoundments and the fracture fluids themselves were of normal alkalinities at circum-neutral pH levels.

Impoundment water had total organic carbon concentrations of about 1-2 mg/L, fracture fluids around 150 mg/L. The salinity of the freshwater impoundments showed a modest level around 2,000 to 5,000 mg/L of TDS, while the water from the Poseidon storage unit exhibited more than 20 times that ionic strength (75,000 to over 100,000 mg/L); salinity of all the impoundments was comprised mostly of sodium and chloride.

Table 9: Characteristics of Impoundments that Store Water for Hydraulic Fracturing at HFTS.

Parameter	Freshwater Impoundment*		Poseidon Impoundment**		Fracture Fluids***	
	Range	Median	Range	Median	Range	Median
pH	8.03-8.3	8.17	6.64-7.03	6.81	6.28-7.08	6.66
TDS, mg/L	1,790-3,800	2,580	75,400-104,000	98,500	3,370-25,300	21,700
Conductivity, µS/cm	1,460-5,270	3,790	13,000-69,100	47,850	4,960-29,500	18,200
Alkalinity, mg/L as $CaCO_3$	143-183	177	236-383	344	114-190	178
Total Organic Carbon, mg/L	1.97-5.4	2.2	0.4-1.1	0.98	87-180	150
Chloride, mg/L	149-1,380	793	730-1,380	1,220	1,310-13,800	12,200
Nitrate, mg/L	6.7-15.1	13	<1	<1	2-11	8
Sulfate, mg/L	340-650	494	185-310	230	342-570	490

** Freshwater Impoundment: Six samples obtained and analyzed per impoundment (2).*
*** Treated Produced Water (Saline Water) Impoundment: Six samples taken and analyzed.*
**** Fracture Fluids: Fracture fluids after mixing and chemicals added to Impoundment water. Three samples per well were taken and analyzed.*

Sulfate which has a high potential of biotransformation is present in all the impoundment and fracture fluids at substantial concentrations, as shown in Table 9. Sulfate can be converted to sulfide (e.g., H2S) through the action of sulfate reducing bacteria. Sulfate in freshwater impoundments was present at around 500 mg/L, while the samples taken from the recycled produced water impoundment had a median value of around 230 mg/L; a 80/20 mixture of freshwater to saline would result in sulfate levels of over 400 mg/L in streams used for the hydraulic fracturing operations. With the introduction of 10 million gallons of fracture fluids containing 400 mg/L of sulfate, it is likely that more than 16.5 tons of sulfate was introduced into the subsurface during the completion of each shale well; at this level of mass input of sulfur to the subsurface, it becomes important to understand the degree to which sulfate is involved in biological processes that result in accelerated corrosion (i.e. microbial influenced corrosion or MIC), the microbial production of sour gas (i.e. H2S), or the deposition of iron sulfides. Another compound with potential for biotransformation is nitrate which can be converted to nitrogen through the action of denitrifying bacteria. Nitrate levels in the freshwater impoundments showed median values of over 12 mg/L, though even higher levels of nitrate could be possible if completion operations involved the use of nitric acid for cleaning. Following the pumping of the aqueous blend of impoundment water, chemicals, and sand, and following the six-week period in which this water mixture was held downhole in each of the shale wells, the production of water (flowback/produced water) was initiated, and data was recorded on the volumes of flowback water collected each day. Cumulative flows for the three wells are shown in the plots of Figure 5; these plots indicate that during the flowback period of 8 weeks, about 25-30% of the 10-million-gallon water aliquot introduced for the completions of each of the wells.

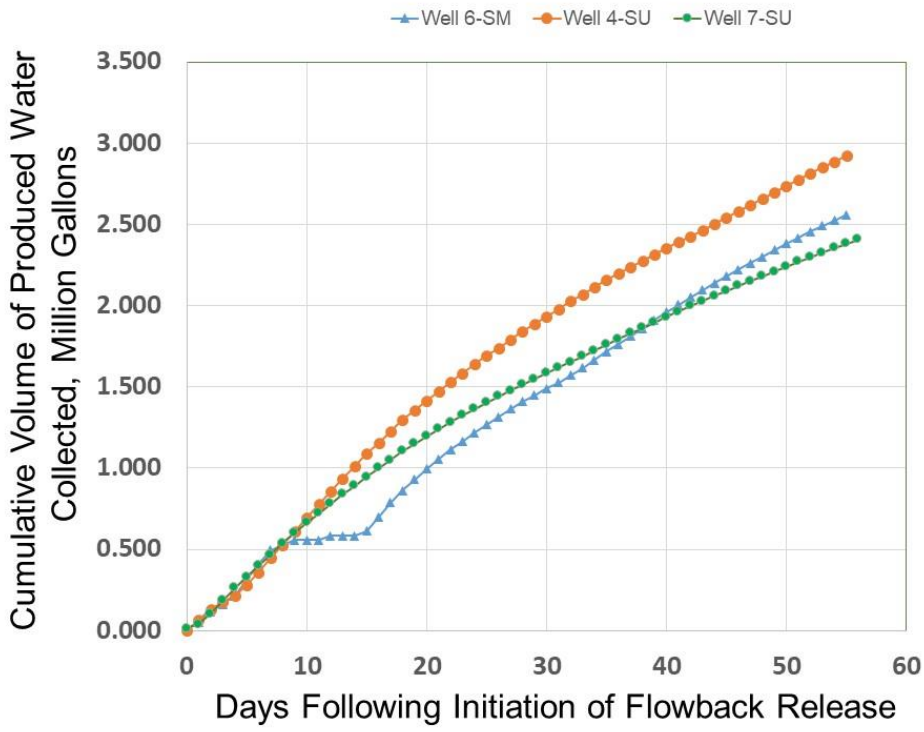


Figure 5: Cumulative Volumes of Produced Water Collected from the Three Shale Wells Selected for Sampling.

Results from the analysis of samples taken from the three shale wells selected for sampling have been tabulated. Measurements and determinations included the following: 1) General

Chemistry; 2) Organic Compounds; 3) Metals; and 4) Anions. Tables of these results are presented in Tables A8 to A13 of the Appendix.

Generally, upon initiation of flowback, substantial increases in salinity are noted in the produced water that is collected over the first few months of production. In the days following the initiation of flowback, total dissolved solids in the produced water increased with time as seen in the plot of all the TDS data points in Figure 6. Also indicated in this graph is the level of average TDS levels measured in produced water obtained from three mature shale wells operating in the Wolfcamp formation for several years; this was done to show the levels of salinity that are reached because of long-term saturation of downhole minerals and mixing with formation water. The TDS levels of long-term saturation produced waters from the three mature wells ranged from 120,000 to 128,000 mg/L with an average of 124,000 mg/L TDS.

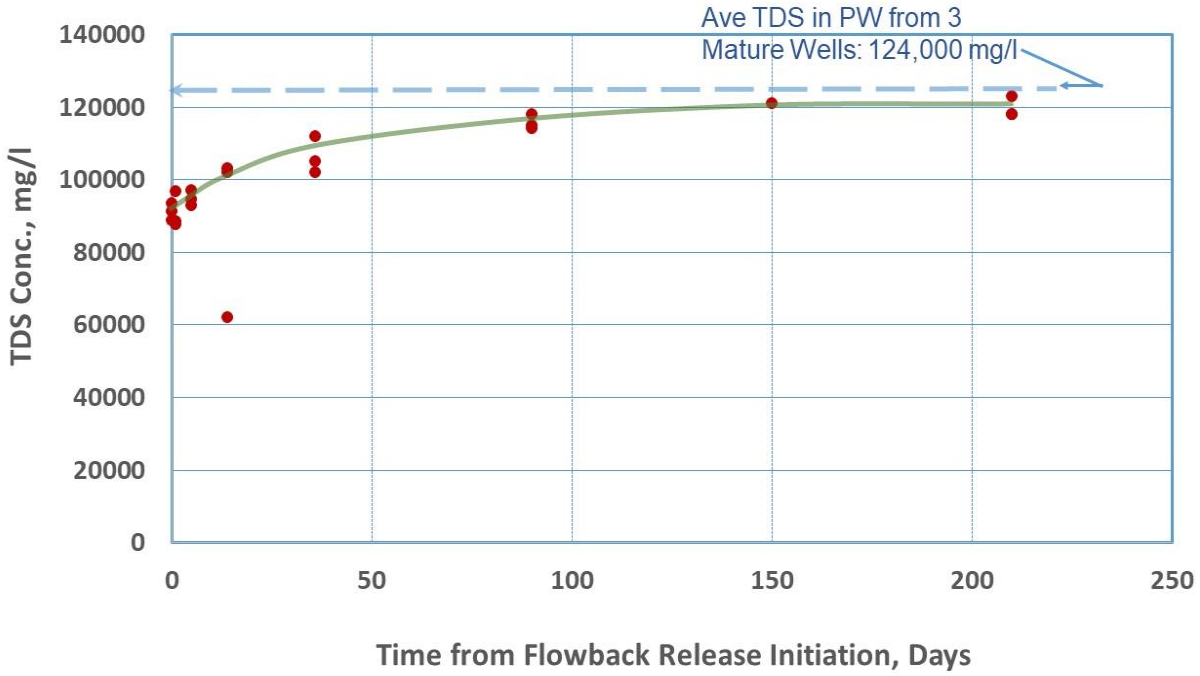


Figure 6: Plot of Total Dissolved Solids with Time in Produced Waters Collected from the Three Shale Wells Selected for Sampling.

At many shale wells monitored in the Marcellus and in the Barnett plays, profiles of salinity measurements in flowback waters that are released within a few days following hydraulic fracturing show an initial TDS level that is less than 20% of the ultimate saturation concentration (Hayes, 2009; Hayes and Severin, 2012). The profiles of the monitored wells of HFTS, however, were quite different than those from wells where flowback was released soon after completion; the plot of Figure 6 shows that the initial flowback water stream had TDS levels of about 90,000 mg/L TDS, more than 75% of the ultimate saturation level of 120,000 mg/L. This was probably due to the relatively longer contact time (6 weeks) that the flowback water had with formation mineral materials that allowed the water to come closer to salt saturation before the initiation of flowback water release.

As modest increases in salts were observed in the flowback and produced water collected from each of the three sampled shale wells, decreasing concentrations in other constituents were noted that indicated possible dilution and transformational actions were taking place in the downhole environment within the millions of gallons of injected and formation waters. Plots

of sulfate, nitrate, and total organic carbon (TOC) with time following the initiation of release of flowback/produced water are shown in Figures 7, 8 and 9, respectively; each of these constituents showed a substantial reduction over the first two weeks of flowback sampling. Over the initial 14-day interval, sulfate concentrations were decreased from approximately 422 mg/L down to 318 mg/L, a 104 mg/L reduction (see Figure 7). In the same period, nitrate concentrations fell from 36 mg/L to 0 mg/L (see Figure 8). Simultaneously, soluble organics measured as total organic carbon (TOC) showed a decrease of approximately 36 mg/L in the flowback during the first 14 days as seen in Figure 9.

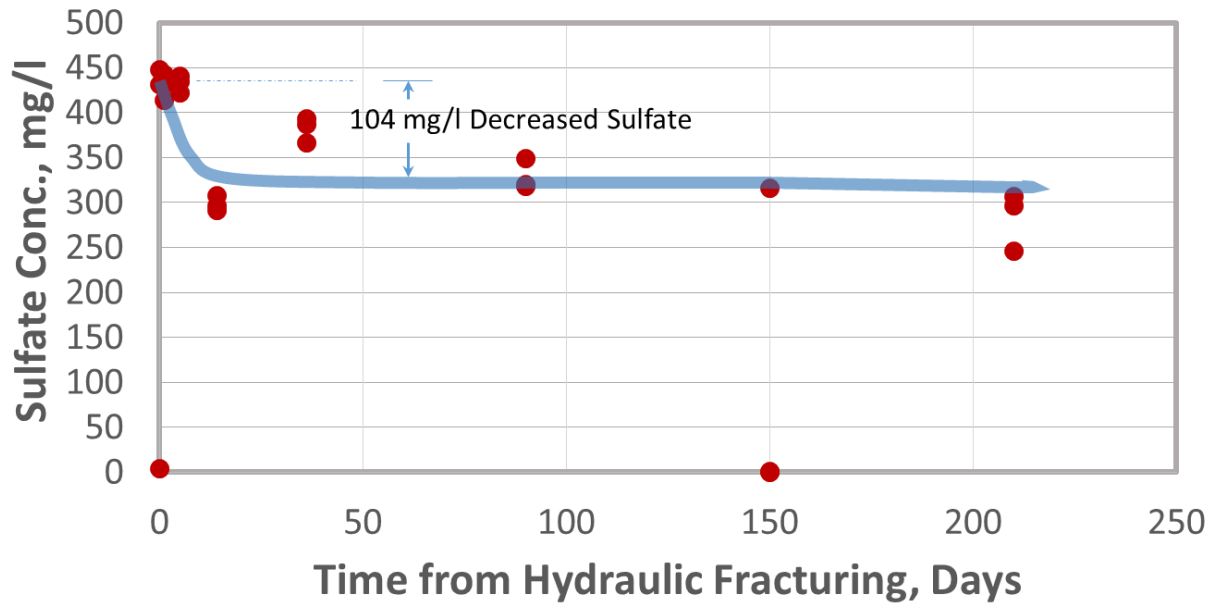


Figure 7: Plot of Sulfate Vs. Time in Produced Waters Collected from the Three Shale Wells Selected for Sampling.

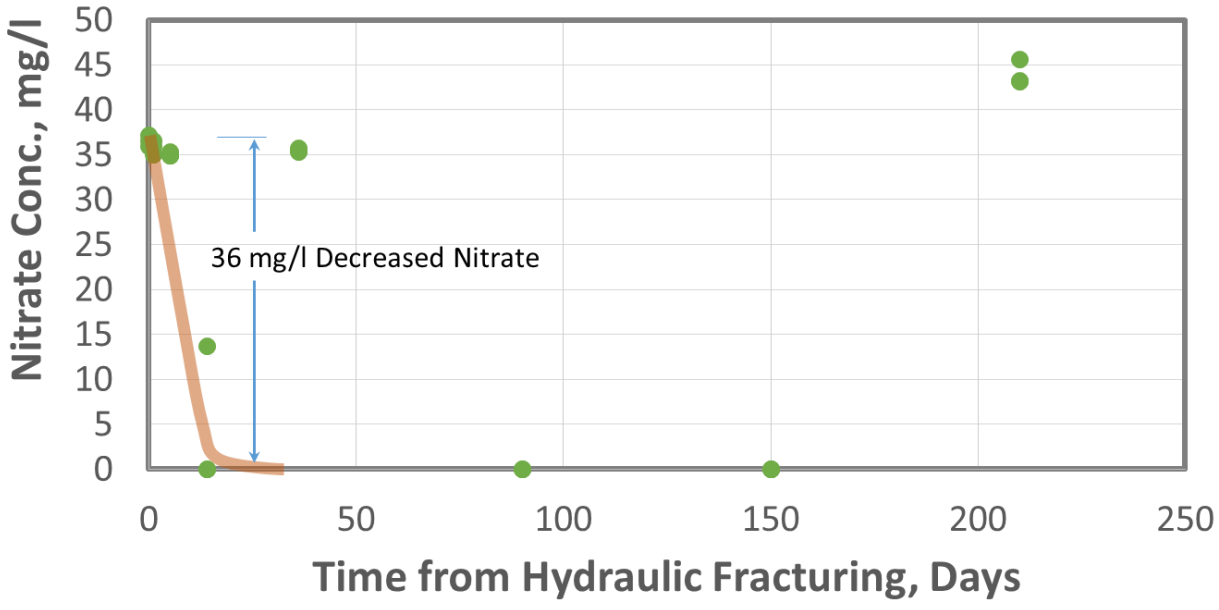


Figure 8: Plot of Nitrate Vs. Time in Produced Waters Collected from the Three Shale Wells Selected for Sampling

The plots of Figures 7-9 show that concentrations of sulfate, nitrate and soluble organic carbon all experienced substantial decreases within the same period. These observed changes suggest the occurrence of microbial-mediated transformations where the oxygen content of nitrate and sulfate is used to convert organic compounds to carbon dioxide and subsequently to methane. One group of microorganisms, the denitrifying bacteria, can utilize nitrate to

oxidize organic compounds to carbon dioxide while reducing nitrate to nitrogen gas (Brock, 1970). Another group of microbes, sulfate reducing bacteria (SRBs), can utilize sulfate to oxidize organic compounds to carbon dioxide while reducing sulfate to hydrogen sulfide (Stumm and Morgan, 1981). Methanogens present in the formation are then able to generate methane from the microbiologically produced carbon dioxide. When organic matter is not available for conversion by microbial communities, both sulfate and nitrate are stable and persist in the subsurface aquatic environment, as evidenced by groundwater composition data in many areas of Texas as well as in the baseline groundwater composition data for the five wells adjacent to the HFTS1 facility. In the case of the groundwater wells adjacent to the HFTS location, Table 3 shows baseline values for sulfate and nitrate at about 68-254 mg/L and 20-24 mg/L, respectively, which persist at these levels in the aquifer environment; this is due to the low activity of key microbial communities in the aquifer (i.e. denitrifiers and SRBs) and the very limited availability (i.e. low concentration) of total organic carbon (at 2 mg/L or less). When the same water is blended with chemicals and injected downhole during hydraulic fracturing, the soluble organic carbon rises to levels that may possibly stimulate introduced or in-situ microbial communities to utilize sulfate and nitrate to convert (oxidize) some or all the soluble carbon to produce carbon dioxide.

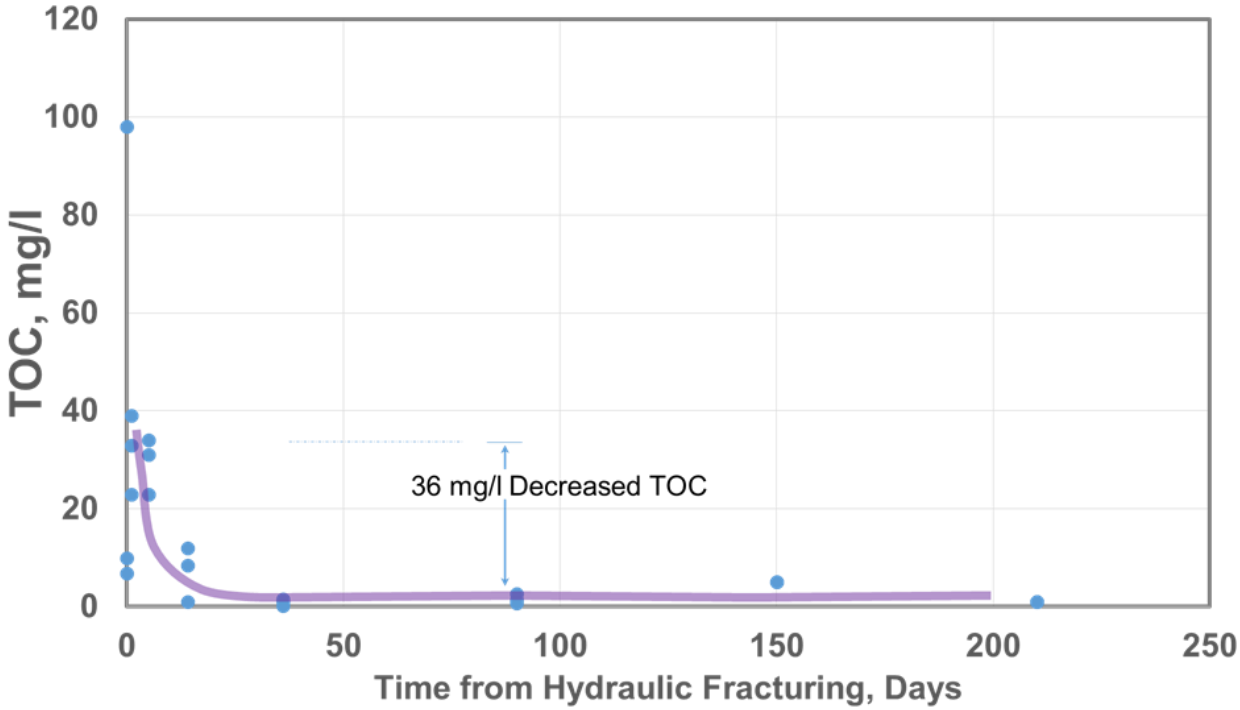


Figure 9: Plot of Total Organic Carbon Vs. Time in Produced Waters Collected from the Three Shale Wells Selected for Sampling

If the availability of soluble organic carbon is key to the reduction of nitrate and sulfate, then the oxygen equivalent of the TOC consumed should be roughly matched to the oxygen equivalent of the nitrate and sulfate that was remove from solution during the same period. Balanced equations that describe denitrification and sulfur reduction using organic matter are shown in Figure 10, using acetic acid as the example of organic matter that is oxidized. Among the two types of oxidation that occur (denitrifying and sulfur reducing), one milligram of TOC requires roughly four milligrams of nitrate or sulfate to achieve complete conversion of the organic compound to CO_2.

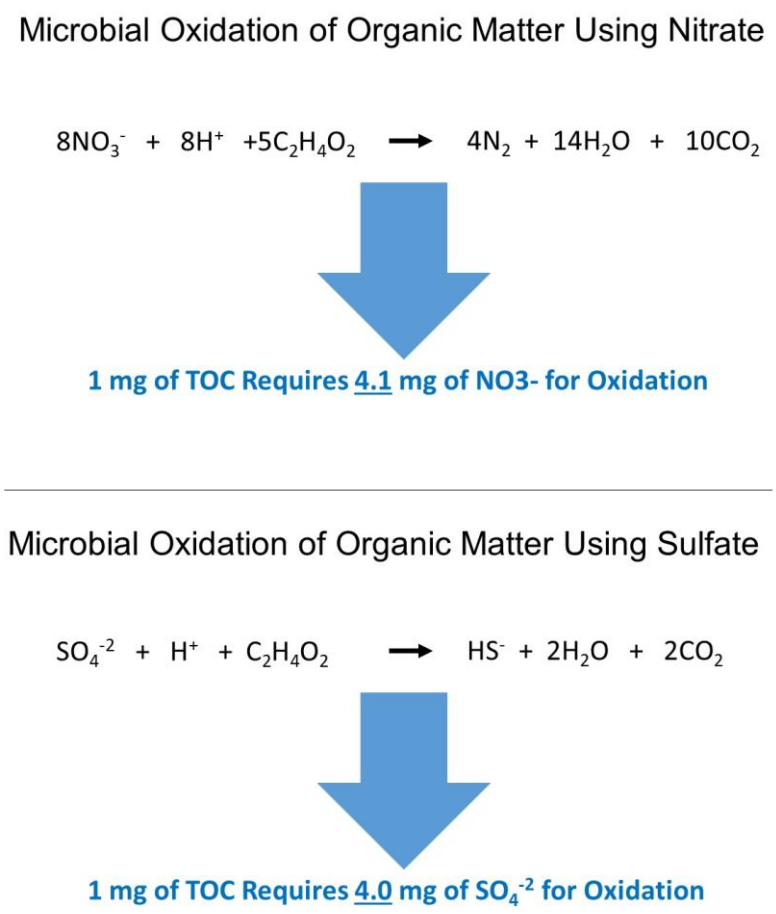


Figure 10: Balanced Equations Describing the Microbial Oxidation of Organic Matter Using Nitrate and Sulfate.

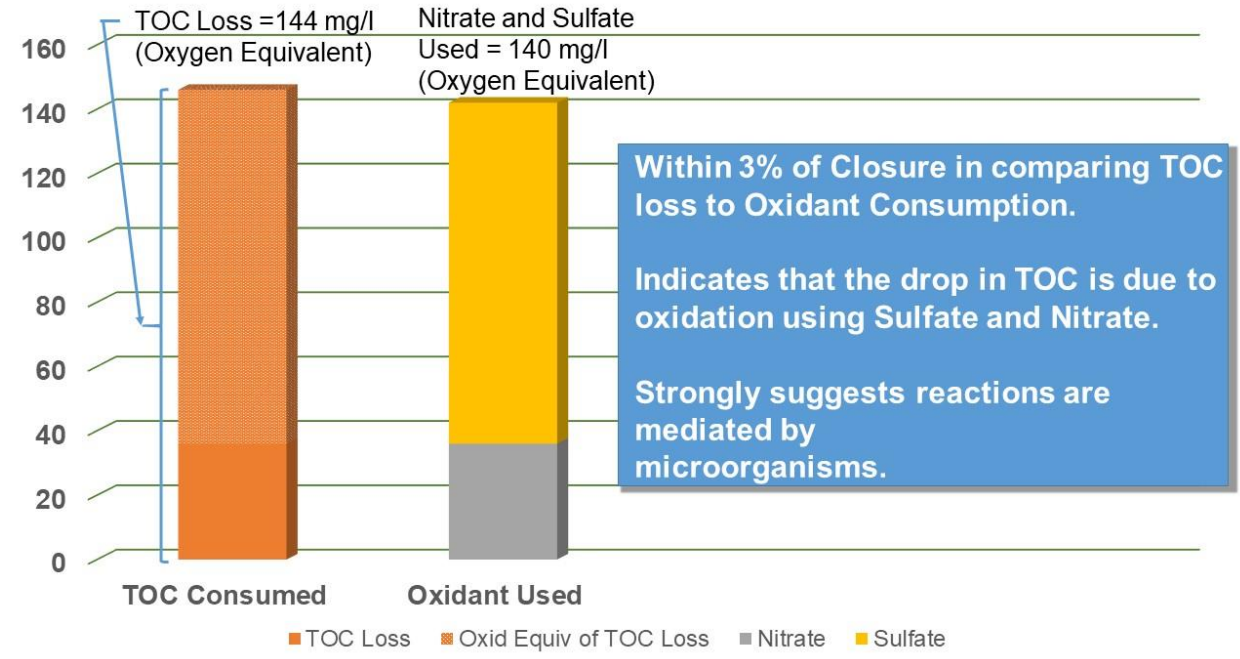


Figure 11: Comparison of Oxidant and TOC Conversion in the Downhole Aquatic Environment During the Initial 14 Days of Flowback Release.

When these stoichiometric conversion factors are considered along with the concentration reductions during the first 14 days of flowback release, it appears that the decreased concentration of TOC in the downhole water in terms of oxygen equivalent is very close in value to the oxygen equivalent of sulfate and nitrate consumed during this same period. This is shown in a comparison of oxidant and TOC conversion shown in Figure 11 where the loss of

soluble TOC (oxygen equivalent) came within 3% of the consumption of nitrate and sulfate in terms oxygen equivalents. This would indicate that the drop in soluble TOC is due to oxidation using nitrate and sulfate. More important, this would strongly suggest that the oxidative transformations of TOC utilizing sulfate and nitrate are mediated by microbial consortia in the downhole environment.

If the concentrations in the flowback samples are indicative of the levels of TOC, sulfate and nitrate of the in-place injected water (with a total initial volume of 10 million gallons per completed well), then mass flow calculations show that within two weeks following the release of flowback about 1.5 tons of TOC was converted to CO2 through the action of microbes with the concomitant reduction of 1.5 tons of nitrate to nitrogen gas and 4.2 tons of sulfate to sulfide amounting to about 1.4 tons. While the nitrogen gas is inert, the formation of over a ton of sulfide from sulfate conversion could potentially be problematic in terms of corrosion or sour gas formation. If all the 104 mg/L of transformed sulfate was converted to soluble sulfide and distributed in the formation, the resultant concentration of soluble sulfide would be at least 30 mg/L as HS-.

The results of sulfide analysis of all flowback and produced water samples, however, show soluble sulfide levels at below detection (< 1 mg/L). This is likely due to the presence of soluble iron at concentrations of 15 to 170 mg/L in the downhole aquatic environment; at these concentrations, iron levels at the pH level of the produced water (pH 7.5 to 8.0) may be sufficient to precipitate the sulfide as ferrous sulfide, thereby reducing soluble sulfide concentrations to below 1 mg/L. A similar observation of low sulfide (<1.2 mg/L) in the presence of 25-200 mg/L of iron has also been described in another study where produced waters were characterized at 19 locations in the Marcellus Shale (Hayes, 2010) and in the Barnett Shale (Hayes and Severin, 2012).

Sulfide may also be complexed with metals associated with the well corrosion materials and be rapidly generated in biofilms that may be involved with microbiologically influenced corrosion. More downhole chemistry information as well as microbial community analysis will shed further light on transformation mechanisms and the role of microbes in the fate of key constituents under down-hole conditions. Analysis of key microbial consortia that may be active in sulfate and nitrate transformations is presented and discussed in a separate microbiology report associated with sampling at the HFTS facility.

The methodical characterization of produced waters from three of the eleven horizontal wells of the HFTS facility has shown good agreement in the cumulative flow and composition determined with time starting from the day of the initiation of flowback release. At all three wells, about 2.4-2.9 million gallons of flowback water was collected in a two-month period which amounted to about a quarter of the total water that was injected which is in the range of normal yields of flowback reported in the literature for wells in Texas and the Marcellus (Hayes, 2012). All three wells showed produced water TDS profiles with time that approached about 120,000 mg/L TDS, approximately consistent with TDS levels measured in produced waters from three mature horizontal wells at nearby well fields. More important, careful sample collection and analysis has revealed several substantial downhole transformations in terms of the disappearance of 36 mg/L of soluble organic carbon coupled with the simultaneous reduction of sulfate and nitrate where the oxygen equivalent of carbon that is converted to

CO2 is nearly equal to the oxygen equivalent of the sum of the oxygen equivalents of sulfate and nitrate that disappeared during the first 14 days of flowback water sampling. These produced water characterization results strongly point to the likelihood that microbial communities were stimulated downhole to perform denitrification and sulfate reduction using soluble TOC as the carbon source. If the composition measurements in the flowback samples is representative of the composition of the total mass of injected water, then it is also likely that downhole microbial communities were sufficiently active to achieve the reduction of multiple tons of nitrate and sulfate as well as the oxidation of over 1.5 tons of soluble carbon in the short interval in the downhole environment.

Associated microbial genetic testing, discussed in the accompanying HFTS Microbiology Report (Eisenlord & Hayes, 2017) provides confirmation of the growth of key microbial species during this critical chemical transformation period. This microbial sampling and characterization work was closely coordinated with the flowback composition sampling. The totality of results of changing chemical composition compared to the timing and nature of shifts in microbial community structure can provide substantial insights into the deep shale as a possible environment of substantial biotransformations that may occur that may be tied into corrosion and gas quality.

Alternative transformations which could occur in the subsurface, attributing to a decrease in measurable sulfate include the formation of calcium sulfate or barium sulfate scale. However, levels of Ca in produced water increased from 1,900 ppm to 2,410 ppm over the year and a half of production. Ba concentration was low, between BDL and 2.5 mg/L over the year and a half of production. Therefore, we do not have strong evidence of Ca or Ba reacting with sulfate to create a precipitate at a large enough scale to account for the marked decline in sulfate in PW over time.

Air Quality Analysis

The purpose of the air monitoring effort was to determine the effect of shale gas well development operations on the quality of ambient air at ground level and at distances that are proximal to shale energy well pads. The positioning of air quality monitoring was intended to be indicative of temporary exposure of well pad operation emissions to near-by residential areas.

Methods and Approach

A Vantage Pro2 weather station (Model No. 6152C) measured the prevailing wind direction and speed at the HFTS center pad to place air quality sampling stations 1,000 feet upwind and downwind of the HFTS well pads for the duration of the air monitoring sampling events. Sampling equipment was placed on tables, approximately 4 ft. above ground level. Field data acquisition was conducted by HSE Solutions and Kane Environmental Engineering; data analysis was conducted by AHIA accredit laboratories ALS (Salt Lake City, UT) and HIH Laboratories (Webster, TX) data compilation and analysis was conducted by GTI. Air monitoring included the collection of air monitoring data at four separate time intervals related to HFTS activity: 1) during the time before hydraulic fracturing equipment arrived at the site to establish a baseline (site-prep activities were on-going, transitioning from drilling to hydraulic fracturing) ; 2) during hydraulic fracturing; 3) during flowback water collection; and, 4)

during the phase of production. The schedule of sampling and locations of the air monitoring are described in Table 10. An example of the positioning of air monitoring equipment to perform the air quality measurements is depicted in Figure 12.

Table 10: Schedule and Locations of Air Monitoring Sampling at the HFTS.

Phase of HFTS Activity	Dates of Sampling	Comment
Background	October 12-14, 2015	Sampling from one downwind location, 1,000 ft. from HFTS.
Hydraulic Fracturing	November 10-12, 2015	Upwind and Downwind Sampling, 1,000 ft. from center well pad.
Flowback Collection	January 4-6, 2016	Upwind and Downwind Sampling, 1,000 ft. from center well pad.
Production	May 3-5, 2016	Sampling at one downwind location, 1,000 ft. from center well pad – after completion equipment was removed.

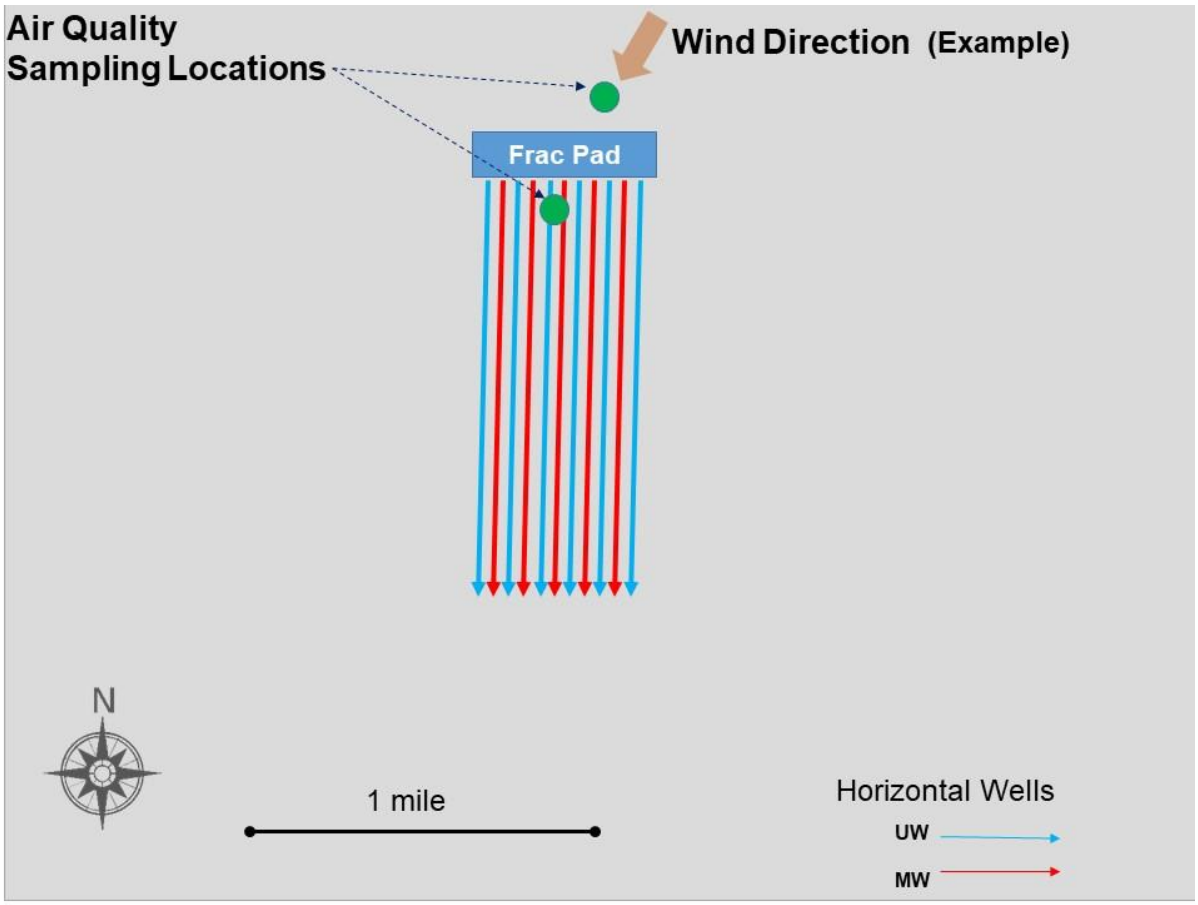


Figure 12: Example of Air Monitoring Locations at the HFTS Facility.

As shown in Table 10, each phase of air quality monitoring at the HFTS location involved continuous sampling over the three-day period. Air quality parameters include methane, particulate matter (PM-10), BTEX (benzene, toluene, ethylbenzene, and total xylenes), nitrogen oxide, nitrogen dioxide, hydrogen sulfide, and total volatile organic compounds (VOCs). The same air quality monitoring was performed at a location in downtown Midland to serve as a comparison for reference purposes, May 3rd through 5th 2016. Methods used for measuring air quality constituents at HFTS are described in Table 11. Blank references were used each day of sampling for all parameters at all sample points.

Table 11: Methods for Determination of Air Quality Constituents at HFTS Facility.

Parameter	Collection	Sample Frequency	Analysis Method
BTEX/Methane	Summa Can (6L) with 24-hour valving	12 hour	Modified EPA TO-15 method & T-03 Method
VOCs	Direct Read Data Logger: RaePPB	Every minute	Direct Read: photoionization detector
Hydrogen Sulfide	Direct Read Data Logger: ToxiRae Pro	Every minute	Direct Read: electrochemical technology sensor
Nitrogen Dioxide Nitric Oxide	Pump and Treated Sorbent Tube: SKC 226-40 tube	24 hour	Visible Absorption Spectrophotometry (NIOSH 6014)
Particulates PM10	Direct Read Data Logger	Every minute	TSI Dustrak DRX 8533

Results and Discussion

Air monitoring results of the HFTS field experiment during the four phases of activity, including baseline and Midland TX sampling events, are summarized in Table 12. All air quality data is presented in Appendix tables A14-A18. Table 12 presents average concentrations (12 or 24 hour) for each parameter, calculated from both upwind and downwind measurements. Upwind and downwind measurements were combined due to the lack of a constant wind direction for each 72-hour sampling effort and the limitation of having only two monitoring stations per sampling. Therefore, this data represents the concentrations of key air quality parameters 1,000 feet away from the oil and gas development site, HFTS. Not included in this table were constituents that were consistently not detected: nitrogen dioxide, nitric oxide and hydrogen sulfide. It should be noted, no nitrogen oxide or nitrogen dioxide was detected at the sampling locations at any of the four sampling time points, most notably during hydraulic fracturing when multiple diesel engines were running to pressurize fluids for hydraulic fracturing. This indicates the methods deployed may have been inadequate to accurately measure true emissions at the HFTS field site. Regardless, the data collected are presented and discussed below. Nearly all air monitoring parameters measured during fracturing and in the production, phases were lower or comparable to the HFTS baseline values, the Midland baseline, and literature values for the DFW and Fort Worth measurements (Rich, et al., 2011; Bunch, et al., 2014). The concentrations of BTEX measured at HFTS were orders of magnitude lower than the OSHA limits (Table 13).

The authors acknowledge the improper comparison between our 12-hour data and OSHA's 8-hour averages; however, we still believe in the merit of the compassion as the recorded HFTS concentrations are several orders of magnitude below OSHA's limits. PM-10 values were not detected in the high quantities expected during hydraulic fracturing from to truck traffic and sand loading. HFTS operations used high quality filters on all silica proppant silos to prevent particulate matter pollution, and the installation and use of water, gas, and oil pipelines across the Laredo facility limited truck traffic during this time. The highest 24-hour average of PM-10 was measured during production, at 5.23 mg/m^3.

Average concentrations of BTEX, total VOCs, methane, and PM 10 are displayed in the bar charts of Figures 13 & 14. Average values for BTEX, VOCs and methane for the hydraulic fracturing and production phases were either less than or comparable to the HFTS Baseline and Midland air monitoring values. Figures 13 & 14 also show BTEX, VOC and methane

concentrations during the flowback phase were substantially greater in magnitude in terms of average and median values than the air monitoring results obtained from the baseline, fracturing, and production phases, as well as from the Midland location.

Table 12: Air Quality Data (Averages) at the HFTS (2015-2016)

Background	Units	Timing	Average	Max	Min	Std Error
Benzene	ppb	12 hour composite	0.478	0.570	0.380	0.034
Ethylbenzene	ppb	12 hour composite	0.206	0.550	0.000	0.127
Toluene	ppb	12 hour composite	15.53	56.00	0.390	10.51
Xylenes	ppb	12 hour composite	0.752	1.800	0.000	0.394
Methane	ppm	12 hour composite	2.720	3.000	2.500	0.192
PM 10	mg/m3	24 hour average	0.786	2.320	0.014	0.594
VOC	ppb	24 hour average	68.33	205.0	0.000	52.93
Fracturing			Average	Min	Max	Std Error
Benzene	ppb	12 hour composite	0.487	0.000	1.100	0.194
Ethylbenzene	ppb	12 hour composite	0.000	0.000	0.000	0.000
Toluene	ppb	12 hour composite	0.390	0.000	0.870	0.148
Xylenes	ppb	12 hour composite	0.000	0.000	0.000	0.000
Methane	ppm	12 hour composite	2.700	2.300	3.200	0.144
PM 10	mg/m3	24 hour average	0.062	0.013	0.107	0.018
VOC	ppb	24 hour average	46.42	1.000	153.5	24.57
Flowback			Average	Min	Max	Std Error
Benzene	ppb	12 hour composite	16.29	0.230	82.00	13.30
Ethylbenzene	ppb	12 hour composite	1.583	0.000	7.900	1.290
Toluene	ppb	12 hour composite	14.76	0.180	73.00	11.82
Xylenes	ppb	12 hour composite	4.588	0.000	22.00	3.560
Methane	ppm	12 hour composite	15.50	10.00	32.00	4.491
PM 10	mg/m3	24 hour average	0.004	0.001	0.012	0.002
VOC	ppb	24 hour average	853.6	333.5	1377	226.9
Production			Average	Min	Max	Std Error
Benzene	ppb	12 hour composite	0.400	0.000	1.200	0.400
Ethylbenzene	ppb	12 hour composite	0.000	0.000	0.000	0.000
Toluene	ppb	12 hour composite	0.983	0.000	2.600	0.815
Xylenes	ppb	12 hour composite	0.000	0.000	0.000	0.000
Methane	ppm	12 hour composite	3.500	3.200	3.700	0.153
PM 10	mg/m3	24 hour average	1.777	0.010	5.230	1.727
VOC	ppb	24 hour average	7.667	3.500	10.00	2.088
Midland			Average	Min	Max	Std Error
Benzene	ppb	12 hour composite	0.327	0.000	0.540	0.166
Ethylbenzene	ppb	12 hour composite	0.000	0.000	0.000	0.000
Toluene	ppb	12 hour composite	0.860	0.640	1.000	0.111
Xylenes	ppb	12 hour composite	0.000	0.000	0.000	0.000
Methane	ppm	12 hour composite	3.100	2.700	3.300	0.200
PM 10	mg/m3	24 hour average	0.060	0.023	0.097	0.021
VOC	ppb	24 hour average	25.17	65.00	2.500	19.98

Figure 15a and 15b display the upwind and downwind concentrations of total BTEX, VOC, and methane during fracturing and flowback operations. Measurements taken during fracturing operations indicate there was no significant positive pickup of organic constituents due to site specific activities. During flowback, greater concentrations of BTEX were detected downwind from the HFTS pad compared to upwind. The comparison of Figure 15a to 15b conveys the magnitude of the increase in BTEX and VOC concentrations during flowback operations

compared to fracturing operations.

Table 13: OSHA 8hr TWA average for BTEX and PM10

Pollutant	OSHA Limits – 8 hour basis
Benzene, ppb	1000
Toluene, ppb	200,000
Ethylbenzene, ppb	100,000
Xylenes, ppb	100,000
PM-10, mg/m^3	15

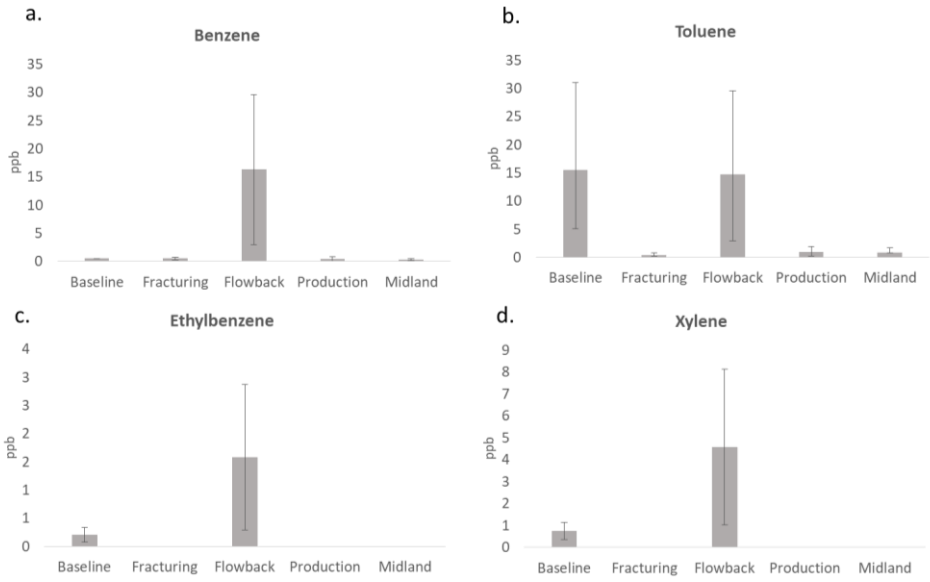


Figure 13: Air Monitoring Results for BTEX for the Duration of Experiment. (a) Benzene; (b) Toluene; (c) Ethylbenzene; (d); Total Xylenes

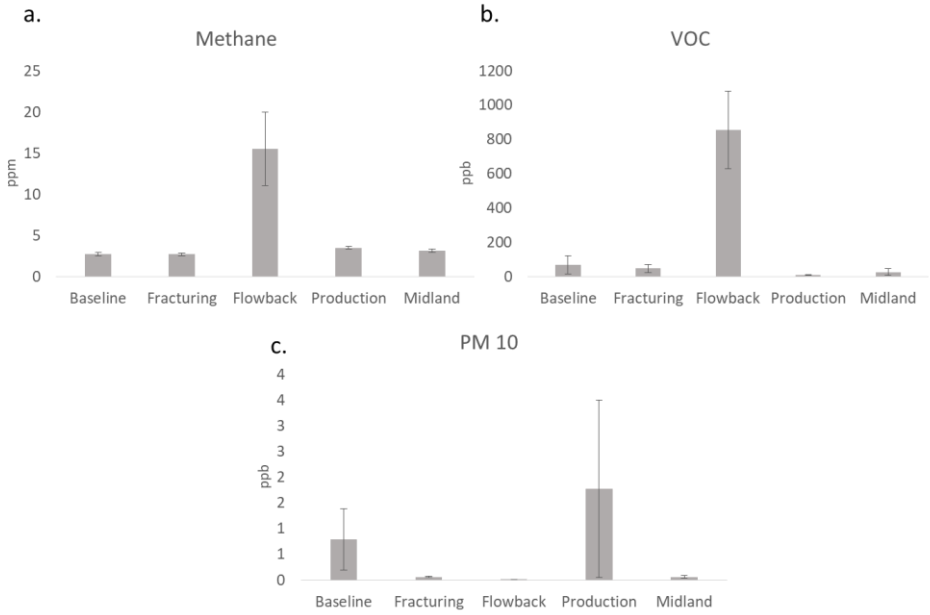


Figure 14: Total VOCs (a) Methane (b) and PM 10 (c) in Ambient Air during HFTS Experiment.

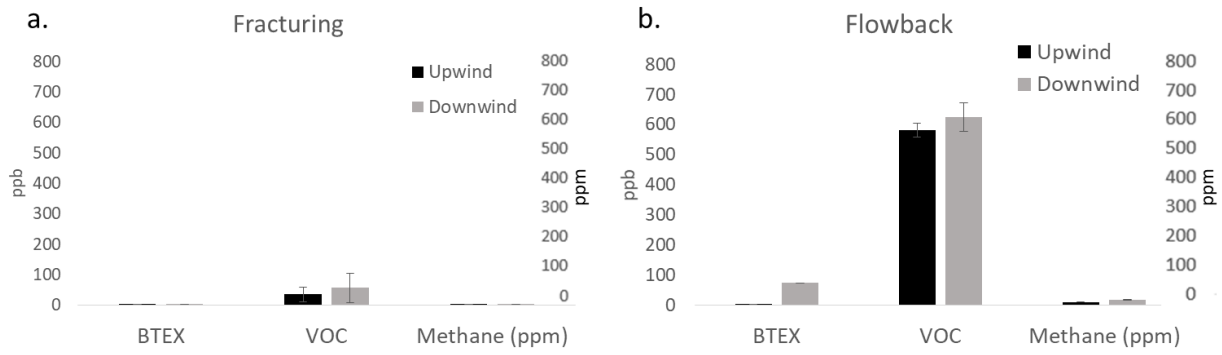


Figure 15: Air Monitoring Results for BTEX, VOCs, and Methane during (a) Fracturing Operations and (b) Flowback Operations, Comparing Upwind and Downwind values.

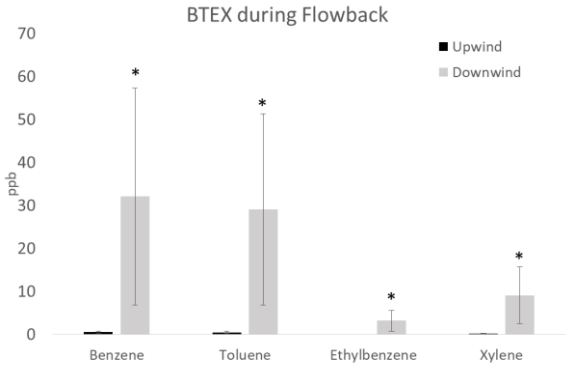


Figure 16: BTEX Concentrations during Flowback Operations, Comparing Upwind and Downwind Values

Figure 16 displays the individual BTEX components upwind and downwind of the HFTS pad during flowback. These organic constituents are in elevated concentrations in flowback water when it is released from the downhole environment, and when large volumes of flowback water are collected and stored at the HFTS facility at atmospheric pressure, releases of methane, BTEX and VOCs occur.

Overall, our limited air monitoring effort indicates the HFTS experiment had a minimal impact on concentrations of key pollutants related to oil and gas development. Concentrations of these key pollutants substantially increased during the flowback period of operations. However, even the highest measured levels of BTEX and benzene were levels at orders of magnitude below the OSHA limits for 8-hour worker safety exposure (See Table 12 and 13). The OSHA limit for benzene in air is 1,000 ppb compared to the maximum 12-hour benzene concentration measured was 82 ppb during flowback operations. If mitigation is deemed necessary, granular sorbents (such as granular activated carbon) would likely be effective and economical in the control of BTEX and VOCs emitted from frac tank vents.

Discussion of Overall Environmental Impact

Environmental monitoring performed during the HFTS operations in this effort indicate there was no detrimental impact to groundwater and minimal impact to ambient air quality within 1,000 feet of the site. About impacts to groundwater, the constituent of greatest potential for transport through the various deep and shallow strata of the subsurface is methane; for this reason, methane is a very good sentinel constituent for detecting impacts from natural gas production wells to groundwater. Methane, a constituent that is found naturally in groundwater aquifers throughout the U.S. at concentrations as high as 1 mg/l or more, was consistently below 0.001 mg/l (< 1 ppb) in all the samples collected from the five groundwater

wells surrounding the HFTS facility. Likewise, the other important indicator compounds of benzene, toluene, ethylbenzene, and xylenes were below detection limit in all groundwater samples –throughout all the HFTS operational phases. The rise in TDS levels of about 350 to 400 mg/l TDS occurred during the period of hydraulic fracturing when large amounts of well water were withdrawn for use in the fracturing operations. Even during this brief time of salt infiltration due to localized well drawdown conditions, the TDS levels in the groundwater wells did not come close to the widely accepted criterion for brackish water (3,000 mg/l TDS) and within 2 months following the TDS peak, groundwater dissolved solids levels recovered back to the baseline levels below 500 mg/l TDS. This information taken together indicates that impact to groundwater from HFTS operations was not deleterious and the results strongly suggest that there was no migration of constituents of interest from the deep shale or from the well bore through the subsurface to groundwater during the period of monitoring.

Regarding impacts to air, using the methods described in this report, results show that nearly all phases of HFTS operations (except for flowback collection) had minimal impact to air quality when compared to the baseline HFTS samples and to monitoring conducted in downtown Midland. Even the flowback stage, though measurably higher than the baseline, fracturing, and production phases, was less than 3% of the OSHA limit (worker safety, 8-hour daily exposure) for benzene and less than 0.01% of the OSHA limit for toluene, ethylbenzene, and total xylenes. In consideration that each of the active phases of HFTS development (fracturing and flowback) only lasts 4-6 weeks, and in view of the temporal nature of all aspects of well pad development (including completion) extending for a limited period of 3-5 months, residents are further protected by the relatively short time of potential exposure.

These findings are based on the monitoring of only one shale system involving the construction of 11 horizontal wells. The well installation and completion methods utilizing state-of-the-art technologies were sufficient to limit measurable impacts to groundwater and to ambient air quality. More site-specific monitoring involving other locations in other plays will add more insight into the impacts of shale energy development across a wide span of field conditions.

Conclusions

In consideration of the monitoring results obtained by this evaluation effort, the following summary conclusions are drawn:

1. Application and testing of advanced technologies of drilling, completion, and production at the HFTS facility did not result in lasting deterioration of groundwater.

2. Air monitoring measurements conducted at the HFTS including VOC, PM-10, benzene, toluene, ethylbenzene, total xylenes, and methane indicate that nearly all phases of HFTS operations (except for flowback collection) had no discernable impact to air quality when compared to the baseline HFTS samples, monitoring conducted in downtown Midland, and to literature values from other urban locations in Texas.

3. The collection and storage of initial produced water released from each well (flowback) does result in measurable release of VOCs and BTEX to the atmosphere; however, near-site air quality values for BTEX are less than 10% of OSHA limits for worker safety (8-hour exposure) and the short-term nature of the flowback collection phase limits local

residential exposure to air emissions. If needed, however, these small emissions can be economically controlled through engineering controls (adsorbents) applied to frac tank vents.

4. Groundwater was not impacted by HFTS operations through migration of constituents from the well bore or from the shale strata to groundwater aquifers. In the monitoring of groundwater before and during each phase of operation, no evidence of migration of methane, benzene, toluene, ethylbenzene, xylenes or total organic carbon (TOC) was detected.

5. The temporary rise in median salinity of the groundwater measured at the five groundwater wells (increasing from about 500 mg/l to 800 mg/l) was likely due to the infiltration of water from neighboring aquifers of higher salinity occurring during the fracturing phase when extensive pumping (amounting to tens of millions of gallons) could have caused groundwater drawdown of each of the five wells. The effect was short termed: dissolved solids returned to baseline TDS levels within 50 days.

6. Flowback collection efficiencies amounted to approximately 25% of the 10 million gallons of water injected in each of the three HFTS wells monitored for produced water characterization. Delaying flowback release by 6 weeks following the completion of each well provided more contact time of the injected aliquot to equilibrate with downhole materials and causes higher salinities to be measured in early flowback samples. Upon release, median TDS levels in flowback water were measured at around 90,000 mg/l in the first day of release increasing to a plateau of 120,000 mg/l in about 3 months, close in value with the salinity of produced waters generated from mature wells of nearby Wolfcamp shale well fields.

7. As salinity in the flowback increased with time, concentrations of several constituents decreased simultaneously, the nature of which strongly pointed to the likelihood of substantial microbial mediated transformations of hydrocarbons and oxidants. Within the first 14 days following initial release of flowback, TOC decreased by 95% while nitrate decreased by 100% (mediated by denitrifier microbial populations) and sulfate (initially present at over 420 mg/l) decreased by 24% (mediated through the action of sulfate reducing bacteria). The measured TOC loss was in stoichiometric balance with nitrate and sulfate consumption: The oxygen equivalents of TOC oxidized to CO2 were within 3% of the measured losses of sulfate and nitrate oxygen equivalents in the flowback at 14 days. In this project, sampling for microbial community characterization was closely coordinated with compositional sampling; microbiological results are described in a separate report (Eisenlord & Hayes, 2017).

8. If the changes in concentration in the flowback water samples were indicative of the 10 million gallons of injected water, more than 1.4 tons of sulfide could have been generated in place in the fractured shale. The non-detect levels of soluble sulfide measured in the flowback water samples together with the presence of excess soluble iron point to the substantial formation of iron sulfide precipitate. More than 3.8 tons of ferrous sulfide precipitate may have formed along the lateral of each horizontal well. This in-place precipitate may later move toward the horizontal well bore as water is removed and may over time mechanically impede the movement of fluids and gases from a horizontal well and become a factor in overall well performance. More research will be needed to determine the fate of sulfide and management approaches to prevent deleterious effects on well performance.

References

1. Anaya, R. and I. Jones. 2009. "Groundwater Availability Model for the Edwards-Trinity (Plateau) and Pecos Valley Aquifers of Texas: Texas Water Development Board Report 373. (103 pages).
2. Brock, T. 1970. Biology of Microorganisms. Prentice Hall, Inc. Englewood, NJ., pp. 486-487.
3. Bunch, A.G., et al. 2014. "Evaluation of Impact of Shale Gas Operations in the Barnett Regions on Volatile Organic Compounds and Potential Health Risks." Science of the Total Environment: 468-469. pp. 832-842.
4. Clark, C., A. Burnham, C. Harto, and R. Horner. 2013. "Hydraulic Fracturing and Shale Gas Production: Technology, Impacts, and Regulations." USDOE Office of Scientific and Technology Information, Oak Ridge, TN. Report No. ANL/EVS/R-12/5.
5. EIA. 2017. "International Energy Outlook 2017." Report No. IEO2017. U.S. Energy Information Administration. p. 55.
6. Eisenlord, S. and T. Hayes. 2017. "Microbiological Analysis of Hydraulic Fracture Test Site (HFTS) Operations. Final Report. Gas Technology Institute, Des Plaines, IL.
7. USEPA. 2016. "Hydraulic Fracturing for Oil and Gas: Impacts from the Hydraulic Fracturing Water Cycle on Drinking Water Resources in the U.S." Report No. EPA-600-R-16-236Fa. December 2016.
8. Gallegos, T.J., B.A. Valera, S.S. Haines, and M.A. Engle. 2015. Hydraulic Fracturing in the U.S." AGU Water Resources Research. pp 5830-5845.
9. Hayes, T.D. 2010. "Sampling and Analysis of Water Streams Associated with the Development of Marcellus Shale Gas," Final Report to the Marcellus Shale Coalition. Gas Technology Institute, Des Plaines, Il.
10. Hayes, T.D. and B.F. Severin. 2012. "Barnett and Appalachian Shale Water Management and Reuse Technologies," RPSEA Report No. 08122-05.FINAL.2.
11. Hayes, T.D. and B.F. Severin. 2012. "Characterization of Flowback Waters from the Marcellus and the Barnett Regions." RPSEA Report No. 08122-05.09.
12. Rich, A., J.P. Grover, and M.L. Sattler. 2014. "An Exploratory Study of Air Emissions Associated with Shale Gas Development and Production in the Barnett Shale." Journal of the Air and Waste Management Association. Vol 64(1): 61-72.
13. Small, M.J., et al. 2014. "Risk and Risk Governance in Unconventional Shale Gas Development." ES&T, 48: 8289-8297.
14. Stumm, W. and J.J. Morgan. 1981. Aquatic Chemistry. John Wiley & Sons, Inc., Hoboken, NJ. pp. 458-461.

Appendix

Table A1. Methane Concentrations (mg/L) in Groundwater Wells during Monitoring.

	Sampling Time				
Groundwater Well	Baseline 10/12/15	Hydraulic Fracturing 12/1/15	Flowback 1/14/16	Production 6/3/16	Production 1/4/17
1	0.00049	0.00060	0.00031	0.00057	0.00015
2	0.00047	0.00103	0.00063	0.00072	0.00056
3	0.00030	0.00037	0.00018	0.00086	0.00010
4	0.00039	0.00032	0.00018	0.00031	0.00072
5	0.00109	0.00016	0.00019	N/A	N/A

Table A2. Summary of BTEX Concentrations in Groundwater Wells during Monitoring.

Constituent	Sampling Time

	Baseline 10/12/15	Hydraulic Fracturing 12/1/15	Flowback 1/14/16	Production 6/3/16	Production 1/4/17
Benzene	--- All Wells: < 0.00050 mg/L Across All Sampling Times ---				
Toluene	--- All Wells: < 0.00050 mg/L Across All Sampling Times ---				
Ethylbenzene	--- All Wells: < 0.00050 mg/L Across All Sampling Times ---				
Xylenes	--- All Wells: < 0.0010 mg/L Across All Sampling Times ---				

Table A3. Results for groundwater Well 184

S-184 Parameter	Units	Det. Limit	10/12/15	12/1/15	1/14/16	6/3/16	1/4/17
Organics							
Methane	mg/L	0.00010	0.00049	0.00060	0.00031	0.00057	0.00015
Benzene	mg/L	0.00015	0.00050	<0.00050	<0.00050	<0.00050	0.00050
Toluene	mg/L	0.00015	0.00050	<0.00050	<0.00050	<0.00050	0.00050
Ethyl Benzene	mg/L	0.00018	0.00050	<0.00050	<0.00050	<0.00050	0.00050
Xylenes	mg/L	0.00022	0.0010	<0.0010	<0.0010	<0.0010	0.0010
Total Organic Carbon	mg/L	0.23	0.70	0.83	0.24	0.59	0.48
Total Petroleum Hydrocarbons	mg/L	0.51	1.3	<5.1	1.00	<5.1	3.60
Oil & Grease	mg/L	0.56	1.3	<5.1	1.00	<5.1	6.70
General							
pH			8.06	7.60	7.95	7.55	7.81
Total Dissolved Solids	mg	10	470	670	490	850	600
Conductivity	µS/cm, 25°C	5	775	1,110	739	1,050	772
Alkalinity	mg/l CaCO3	0.1	193	209	192	206	207
Cations							
Arsenic	mg/L	0.3	BDL	BDL	BDL	BDL	BDL
Barium	mg/L	0.02	0.03	0.03	0.03	0.06	0.03
Boron	mg/L	0.2	0.4	2.4	BDL	BDL	0.80
Cadmium	mg/L	0.03	BDL	BDL	BDL	BDL	BDL
Calcium	mg/L	0.7	66.6	86.8	56.8	77.7	72.5
Chromium	mg/L	0.1	BDL	BDL	BDL	BDL	BDL
Copper	mg/L	0.07	BDL	BDL	BDL	BDL	BDL
Iron	mg/L	0.2	BDL	BDL	1.0	BDL	BDL
Lead	mg/L	0.3	BDL	BDL	BDL	BDL	BDL
Magnesium	mg/L	0.7	39.3	48.4	32.5	43.7	38.4
Manganese	mg/L	0.03	BDL	BDL	0.03	BDL	BDL
Nickel	mg/L	0.1	BDL	BDL	BDL	BDL	BDL
Potassium	mg/L	0.3	3.9	5.4	4.3	5.6	6.9
Sodium	mg/L	1.7	42.0	89.8	63.3	88.9	66.9
Zinc	mg/L	0.07	0.09	0.07	BDL	BDL	BDL
Anions							
Fluoride	mg/L	0.1	1.6	1.5	0.9	BDL	1.5
Chloride	mg/L	0.1	27.6	44.7	16.0	49.4	49.6
Nitrate	mg/L	0.1	24.2	17.9	13.1	21.0	20.3
Sulfate	mg/L	0.1	118	224	83	246	235

	BDL = Below Detection Limit			

Table A4. Results for Groundwater Well 195

S-195 Parameter	Units	Method Detection Limit	10/12/2015	12/1/2015	1/14/2016	6/3/2016	1/4/2017
Organics							
Methane	mg/L	**0.00010**	0.00047	0.00103	0.00063	0.00072	0.00056
Benzene	mg/L	**0.00015**	0.00050	<0.00050	<0.00050	<0.00050	<0.00050
Toluene	mg/L	**0.00015**	0.00050	<0.00050	<0.00050	<0.00050	<0.00050
Ethyl Benzene	mg/L	**0.00018**	0.00050	<0.00050	<0.00050	<0.00050	<0.00050
Xylenes	mg/L	**0.00022**	0.0010	<0.0010	<0.0010	<0.0010	<0.001
Total Organic Carbon	mg/L	**0.23**	0.71	0.45	0.25	0.47	1.10
Total Petroleum Hydrocarbons	mg/L	**0.51**	2.3	1.50	2.10	<5.1	2.90
Oil & Grease	mg/L	**0.56**	2.3	<5.0	2.10	<5.1	2.90
General							
pH			8.13	7.64	7.63	7.44	7.99
Total Dissolved Solids	mg	**10**	370	1,950	420	520	320
Conductivity	µS/cm, 25°C	**5**	631	2,870	722	739	373
Alkalinity	mg/l CaCO3	**0.1**	188	292	192	195	179
Cations							
Arsenic	mg/L	**0.3**	BDL	BDL	BDL	BDL	BDL
Barium	mg/L	**0.02**	0.08	0.08	0.05	0.09	0.05
Boron	mg/L	**0.2**	BDL	0.6	BDL	BDL	1.20
Cadmium	mg/L	**0.03**	BDL	BDL	BDL	BDL	BDL
Calcium	mg/L	**0.7**	60.3	76.7	58.3	57.8	41.6
Chromium	mg/L	**0.1**	BDL	BDL	BDL	BDL	BDL
Copper	mg/L	**0.07**	BDL	BDL	BDL	BDL	BDL
Iron	mg/L	**0.2**	0.4	2.0	BDL	BDL	0.80
Lead	mg/L	**0.3**	BDL	BDL	BDL	BDL	BDL
Magnesium	mg/L	**0.7**	30.1	47.2	26.9	27.8	25.9
Manganese	mg/L	**0.03**	BDL	0.09	BDL	BDL	0.10
Nickel	mg/L	**0.1**	BDL	BDL	BDL	BDL	BDL
Potassium	mg/L	**0.3**	3.9	8.6	4.6	4.4	5.1
Sodium	mg/L	**1.7**	39.5	207	58.5	46.7	36.6
Zinc	mg/L	**0.07**	BDL	0.1	BDL	BDL	BDL
Anions							
Fluoride	mg/L	**0.1**	1.2	2.1	0.7	BDL	1.1
Chloride	mg/L	**0.1**	21.8	614	17.6	30.4	32.8
Nitrate	mg/L	**0.1**	19.7	2.7	13.9	24.8	BDL
Sulfate	mg/L	**0.1**	68.6	390	65	102	67.4
	BDL = Below Detection Limit						

Table A5. Results for Groundwater Well 142

S-142 Parameter	Units	Method Detection Limit	10/12/2015	12/1/2015	1/14/2016	6/3/2016	1/4/2017
Organics							
Methane	mg/L	0.00010	0.00030	0.00037	0.00018	0.00086	0.00010
Benzene	mg/L	0.00015	0.00050	<0.00050	<0.00050	<0.00050	<0.00050
Toluene	mg/L	0.00015	0.00050	<0.00050	<0.00050	<0.00050	<0.00050
Ethyl Benzene	mg/L	0.00018	0.00050	<0.00050	<0.00050	<0.00050	<0.00050
Xylenes	mg/L	0.00022	0.0010	<0.0010	<0.0010	<0.0010	<0.0010
Total Organic Carbon	mg/L	0.23	0.41	0.46	0.26	0.69	0.62
Total Petroleum Hydrocarbons	mg/L	0.51	2.7	1.00	1.10	<5.1	2.10
Oil & Grease	mg/L	0.56	2.7	1.00	1.10	<5.1	2.10
General							
pH			8.23	7.83	7.84	7.62	7.82
Total Dissolved Solids	mg	10	484	708	443	490	450
Conductivity	µS/cm, 25°C	5	762	854	756	691	463
Alkalinity	mg/l CaCO3	0.1	192	185	183	184	187
Cations							
Arsenic	mg/L	0.3	BDL	BDL	BDL	BDL	BDL
Barium	mg/L	0.02	0.05	0.04	0.1	BDL	0.04
Boron	mg/L	0.2	0.2	0.4	BDL	BDL	0.80
Cadmium	mg/L	0.03	BDL	BDL	BDL	BDL	BDL
Calcium	mg/L	0.7	69.9	75.3	139	61.4	61.4
Chromium	mg/L	0.1	BDL	BDL	BDL	BDL	BDL
Copper	mg/L	0.07	BDL	BDL	BDL	BDL	0.10
Iron	mg/L	0.2	0.5	0.8	5.8	BDL	BDL
Lead	mg/L	0.3	BDL	BDL	BDL	BDL	BDL
Magnesium	mg/L	0.7	42.0	43.6	81.2	36.0	35.7
Manganese	mg/L	0.03	BDL	0.04	0.2	0.03	BDL
Nickel	mg/L	0.1	BDL	BDL	BDL	BDL	BDL
Potassium	mg/L	0.3	4.1	4.0	10.0	3.8	5.5
Sodium	mg/L	1.7	23.1	29.6	85.1	34.2	30.2
Zinc	mg/L	0.07	0.08	0.1	BDL	BDL	0.30
Anions							
Fluoride	mg/L	0.1	1.6	1.5	0.9	BDL	1.6
Chloride	mg/L	0.1	28.9	26.0	15.6	22.8	26.7
Nitrate	mg/L	0.1	21.6	16.1	10.6	18.7	18.0
Sulfate	mg/L	0.1	135	145	89	112	132
	BDL = Below Detection Limit						

Table A6. Results for Groundwater Well 158

S-158 Parameter	Units	Method Detection Limit	10/12/2015	12/1/2015	1/14/2016
Organics					
Methane	mg/L	**0.00010**	0.00039	0.00032	0.00018
Benzene	mg/L	**0.00015**	0.00050	<0.00050	<0.00050
Toluene	mg/L	**0.00015**	0.00050	<0.00050	<0.00050
Ethyl Benzene	mg/L	**0.00018**	0.00050	<0.00050	<0.00050
Xylenes	mg/L	**0.00022**	0.0010	<0.0010	<0.0010
Total Organic Carbon	mg/L	**0.23**	2.20	0.96	2.30
Total Petroleum Hydrocarbons	mg/L	**0.51**	2.0	1.20	1.60
Oil & Grease	mg/L	**0.56**	2.0	1.20	1.60
General					
pH			8.05	7.61	7.79
Total Dissolved Solids	mg	**10**	722	844	290
Conductivity	µS/cm, 25°C	**5**	928	1550	478
Alkalinity	mg/l CaCO3	**0.1**	217	246	210
Cations					
Arsenic	mg/L	**0.3**	BDL	BDL	BDL
Barium	mg/L	**0.02**	0.04	0.07	0.05
Boron	mg/L	**0.2**	0.5	0.5	BDL
Cadmium	mg/L	**0.03**	BDL	BDL	BDL
Calcium	mg/L	**0.7**	90.8	76.4	157
Chromium	mg/L	**0.1**	BDL	BDL	0.3
Copper	mg/L	**0.07**	BDL	BDL	0.3
Iron	mg/L	**0.2**	3.9	1.3	2.6
Lead	mg/L	**0.3**	BDL	BDL	BDL
Magnesium	mg/L	**0.7**	49.6	31.1	41.8
Manganese	mg/L	**0.03**	0.10	0.06	2.4
Nickel	mg/L	**0.1**	BDL	BDL	0.3
Potassium	mg/L	**0.3**	7.2	10.8	54.7
Sodium	mg/L	**1.7**	67.5	233	22.7
Zinc	mg/L	**0.07**	0.14	0.1	0.5
Anions					
Fluoride	mg/L	**0.1**	1.5	1.8	BDL
Chloride	mg/L	**0.1**	52.2	134	8.0
Nitrate	mg/L	**0.1**	22.7	3.4	8.3
Sulfate	mg/L	**0.1**	254	247	17
	BDL = Below Detection Limit				

Table A7. Results for Groundwater Well 168

168 Parameter	Units	Det. Limit	10/12/2015	12/1/2015	1/14/2016	6/3/2016	1/4/2017
Organics							
Methane	mg/L	0.00010	0.00109	0.00016	0.00019	0.00031	0.00072
Benzene	mg/L	0.00015	0.00050	<0.00050	<0.00050	<0.00050	<0.00050
Toluene	mg/L	0.00015	*0.00120*	<0.00050	<0.00050	<0.00050	<0.00050
Ethyl Benzene	mg/L	0.00018	0.00050	<0.00050	<0.00050	<0.00050	<0.00050
Xylenes	mg/L	0.00022	0.0010	<0.0010	<0.0010	<0.0010	<0.0010
Total Organic Carbon	mg/L	0.23	0.79	0.43	0.23	0.5	0.64
Total Petroleum Hydrocarbons	mg/L	0.51	1.4	2.30	2.60	1.8	2.9
Oil & Grease	mg/L	0.56	1.4	2.30	2.60	1.8	2.9
General							
pH			7.96	8.01	7.98	7.63	7.69
Total Dissolved Solids	mg	10	552	895	703	750	440
Conductivity	µS/cm, 25°C	5	756	1390	1060	766	457
Alkalinity	mg/l CaCO3	0.1	199	207	197	193	191
Cations							
Arsenic	mg/L	0.3	BDL	BDL	BDL	BDL	BDL
Barium	mg/L	0.02	0.04	0.02	BDL	BDL	0.12
Boron	mg/L	0.2	0.6	0.5	BDL	BDL	0.8
Cadmium	mg/L	0.03	BDL	BDL	BDL	BDL	BDL
Calcium	mg/L	0.7	81.3	108	70.3	59.6	59.2
Chromium	mg/L	0.1	BDL	BDL	BDL	BDL	BDL
Copper	mg/L	0.07	BDL	BDL	BDL	BDL	BDL
Iron	mg/L	0.2	0.9	0.2	8.8	4.2	12
Lead	mg/L	0.3	BDL	BDL	BDL	BDL	BDL
Magnesium	mg/L	0.7	42.6	56.4	36.8	34.1	32.3
Manganese	mg/L	0.03	0.00	0.03	0.2	0.2	1.9
Nickel	mg/L	0.1	BDL	BDL	BDL	BDL	BDL
Potassium	mg/L	0.3	4.9	7.4	BDL	4.4	5.6
Sodium	mg/L	1.7	61.1	128	66.5	39.7	31.2
Zinc	mg/L	0.07	0.08	0.08	BDL	BDL	0.1
Anions							
Fluoride	mg/L	0.1	1.2	1.5	0.7	BDL	1.1
Chloride	mg/L	0.1	37.5	71	33.8	29.2	28.4
Nitrate	mg/L	0.1	22.6	12.2	9.4	19.3	18.0
Sulfate	mg/L	0.1	163	327	185	138	118
	BDL = Below Detection Limit						

Table A8. Results for Produced Water Collected from Shale Well 6-SM at 0-14 Days.

Parameter	Units	Det. Limit	Results (On Days Following Initiation of Flowback Release)			
			0-Day	1-Day	5-Day	14-Day
General						
pH	-	-	7.17	6.7	7.26	6.62
Total Dissolved Solids (TDS)	mg/L	10	91,300	88,500	92,900	62,100
Conductivity	µS/cm	5	50,900	51,400	45,800	41,900
Alkalinity	mg/L**	1	450	407	419	321
Organics						
Total Organic C	mg/L	0.2	98	33	31	8.5
Total Petroleum Hydrocarbons	mg/L	0.5	18	80	42	16
Benzene	mg/L	0.0073	5	2.2	4.4	1.5
Toluene	mg/L	0.0076	5.7	1.2	5	0.71
Ethylbenzene	mg/L	0.0091	1.1	0.11	1.1	0.056
Xylenes	mg/L	0.011	4.6	0.51	4.4	0.31
Anions						
Chloride	mg/L	500	48,400	48,600	53,000	33,800
Nitrate	mg/L	3	36.3	35.3	34.9	13.7
Sulfate	mg/L	5	432	432	435	308
Sulfide	mg/L	1	BDL	BDL	BDL	BDL
Cations						
Arsenic	mg/L	1	BDL	BDL	BDL	BDL
Barium	mg/L	0.05	1.9	1.9	1.7	1.6
Boron	mg/L	0.5	36.5	28.7	29.3	16.9
Cadmium	mg/L	0.1	BDL	BDL	BDL	BDL
Calcium	mg/L	10	1,890	2,060	1,800	1,610
Chromium	mg/L	0.3	BDL	BDL	BDL	BDL
Copper	mg/L	0.2	BDL	BDL	BDL	BDL
Iron	mg/L	0.5	50.2	14.3	17.2	45.3
Lead	mg/L	1	BDL	BDL	BDL	BDL
Magnesium	mg/L	10	303	282	291	224
Manganese	mg/L	0.1	0.9	0.3	0.2	0.7
Nickel	mg/L	0.3	BDL	BDL	BDL	BDL
Potassium	mg/L	10	422	402	509	247
Sodium	mg/L	5	30,200	30,100	34,100	31,900
Zinc	mg/L	0.2	0.8	0.7	BDL	2.7

* *Alkalinity Units in mg/L as $CaCO_3$*

Table A9. Results for Produced Water Collected from Shale Well 6-SM at 36-550 Days.

Parameter	Units	Det. Limit	Results (On Days Following Initiation of Flowback Release)				
			36-Day	90-Day	210-Day	365-Day	550-Day
General							
pH	-	-	6.41	6.39	6.54	6.57	6.26
Total Dissolved Solids (TDS)	mg/L	10	102,000	115,000	118,000	120,000	128,400
Conductivity	µS/cm	5	40,000	81,200	80,700	65,000	73,500
Alkalinity	mg/L**	1	517	413	429	394	374
Organics							
Total Organic C	mg/L	0.2	0.23	0.72	1	150	0.5
Total Petroleum Hydrocarbons	mg/L	0.5	13	180	143	3.2	111
Benzene	mg/L	0.0073	3.7	2.8	3.4	3.3	4.2
Toluene	mg/L	0.0076	1.8	1.5	1.7	1.6	2.1
Ethylbenzene	mg/L	0.0091	0.12	0.086	0.13	0.099	0.13
Xylenes	mg/L	0.011	0.47	0.35	0.48	0.35	0.051
Anions							
Chloride	mg/L	500	67,100	67,100	69,300	65,900	37,400
Nitrate	mg/L	3	35.8	BDL	45.6	BDL	BDL
Sulfate	mg/L	5	367	318	297	257	895
Sulfide	mg/L	1	BDL	BDL	BDL	BDL	BDL
Cations							
Arsenic	mg/L	1	BDL	BDL	BDL	BDL	BDL
Barium	mg/L	0.05	2.1	BDL	2.9	1.3	2.29
Boron	mg/L	0.5	28.8	39.7	39.7	39.2	39.7
Cadmium	mg/L	0.1	BDL	0.2	BDL	BDL	BDL
Calcium	mg/L	10	2,640	2,170	2,550	2,880	2,900
Chromium	mg/L	0.3	BDL	BDL	BDL	BDL	BDL
Copper	mg/L	0.2	BDL	0.2	BDL	0.2	BDL
Iron	mg/L	0.5	165	97	156	52.7	18.4
Lead	mg/L	1	BDL	BDL	BDL	BDL	BDL
Magnesium	mg/L	10	362	343	345	361	502
Manganese	mg/L	0.1	2.3	3.1	1.4	1.3	1.3
Nickel	mg/L	0.3	BDL	1	BDL	0.3	BDL
Potassium	mg/L	10	509	475	386	694	505
Sodium	mg/L	5	38,500	34,700	37,800	40,300	41,200
Zinc	mg/L	0.2	BDL	BDL	BDL	0.8	BDL

** *Alkalinity Units in mg/L as $CaCO_3$*

Table A10. Results for Produced Water Collected from Shale Well 4-SU at 0-14 Days.

Parameter	Units	Det. Limit	Results (On Days Following Initiation of Flowback Release)			
			0-Day	1-Day	5-Day	14-Day
General						
pH	-	-	6.71	6.55	7.41	7.33
Total Dissolved Solids (TDS)	mg/L	10	88,900	87,600	94,500	103,000
Conductivity	µS/cm	5	44,400	46,000	45,100	45,900
Alkalinity	mg/L**	1	438	441	422	393
Organics						
Total Organic C	mg/L	0.2	9.9	39	34	12
Total Petroleum Hydrocarbons	mg/L	0.5	5.6	15	54	50
Benzene	mg/L	0.0073	0.93	1.7	4.9	0.78
Toluene	mg/L	0.0076	0.43	0.88	7	0.47
Ethylbenzene	mg/L	0.0091	0.025	0.068	1.6	0.059
Xylenes	mg/L	0.011	0.13	0.3	6.6	0.25
Anions						
Chloride	mg/L	500	49,200	50,000	52,500	56,100
Nitrate	mg/L	3	36.6	36	34.9	BDL
Sulfate	mg/L	5	416	414	422	292
Sulfide	mg/L	1	BDL	BDL	BDL	BDL
Cations						
Arsenic	mg/L	1	BDL	BDL	1.1	BDL
Barium	mg/L	0.05	2.1	2.1	2.5	2
Boron	mg/L	0.5	25	32.5	25.2	30.2
Cadmium	mg/L	0.1	BDL	BDL	BDL	BDL
Calcium	mg/L	10	1,900	1,990	1,790	2,000
Chromium	mg/L	0.3	BDL	BDL	BDL	BDL
Copper	mg/L	0.2	BDL	BDL	1	0.3
Iron	mg/L	0.5	24.6	19.2	11.3	11.6
Lead	mg/L	1	BDL	BDL	BDL	BDL
Magnesium	mg/L	10	296	313	285	326
Manganese	mg/L	0.1	0.5	0.5	0.9	BDL
Nickel	mg/L	0.3	BDL	BDL	0.7	BDL
Potassium	mg/L	10	385	421	513	590
Sodium	mg/L	5	28,500	29,600	33,900	36,400
Zinc	mg/L	0.2	0.8	0.8	0.8	0.2

* *Alkalinity Units in mg/L as $CaCO_3$*

Table A11. Results for Produced Water Collected from Shale Well 4-SU at 36-210 Days.

Parameter	Units	Det. Limit	Results (On Days Following Initiation of Flowback Release)				
			36-Day	90-Day	210-Day	365-Day	550-Day
General							
pH	-	-	6.43	6.67	6.49	6.68	6.26
Total Dissolved Solids (TDS)	mg/L	10	105,000	114,000	123000	120,000	121,000
Conductivity	µS/cm	5	42,200	81,700	77800	63,500	75,800
Alkalinity	mg/L**	1	683	537	450	438	355
Organics							
Total Organic C	mg/L	0.2	1	2.6	1	220	0.5
Total Petroleum Hydrocarbons	mg/L	0.5	3	200	142	46.5	91.1
Benzene	mg/L	0.0073	0.95	3.3	3.5	7.4	3.2
Toluene	mg/L	0.0076	0.52	1.8	1.9	3.8	1.9
Ethylbenzene	mg/L	0.0091	0.051	0.13	0.15	0.29	0.18
Xylenes	mg/L	0.011	0.21	0.45	0.51	0.98	0.55
Anions							
Chloride	mg/L	500	63,900	68,100	68,900	64,000	34,000
Nitrate	mg/L	3	35.6	BDL	43.3	BDL	BDL
Sulfate	mg/L	5	387	349	307	290	279
Sulfide	mg/L	1	BDL	BDL	BDL	BDL	BDL
Cations							
Arsenic	mg/L	1	BDL	BDL	BDL	BDL	BDL
Barium	mg/L	0.05	1.6	BDL	2.3	2.3	2.1
Boron	mg/L	0.5	30.1	40.3	43.0	40.0	45.7
Cadmium	mg/L	0.1	0.1	0.2	BDL	BDL	BDL
Calcium	mg/L	10	2,150	1,640	2,020	2,150	2,250
Chromium	mg/L	0.3	BDL	BDL	BDL	BDL	BDL
Copper	mg/L	0.2	BDL	0.2	BDL	0.2	BDL
Iron	mg/L	0.5	351	168	93.0	57.5	51.4
Lead	mg/L	1	BDL	BDL	BDL	BDL	BDL
Magnesium	mg/L	10	358	332	347	345	422
Manganese	mg/L	0.1	4.3	4.3	1.8	1.2	1.2
Nickel	mg/L	0.3	BDL	0.9	BDL	0.3	BDL
Potassium	mg/L	10	642	630	519	845	625
Sodium	mg/L	5	41,000	36,300	40,500	34,100	39,300
Zinc	mg/L	0.2	BDL	0.3	BDL	0.7	BDL

* *Alkalinity Units in mg/L as $CaCO_3$*

Table A12. Results for Produced Water Collected from Shale Well 7-SU at 0-14 Days.

Parameter	Units	Det. Limit	Results (On Days Following Initiation of Flowback Release)			
			0-Day	1-Day	5-Day	14-Day
General						
pH	-	-	6.62	6.55	6.39	6.27
Total Dissolved Solids (TDS)	mg/L	10	93,400	96,700	97,000	102,000
Conductivity	µS/cm	5	50,200	50,600	51,100	49,200
Alkalinity	mg/L**	1	445	371	481	396
Organics						
Total Organic C	mg/L	0.2	6.8	23	23	0.94
Total Petroleum Hydrocarbons	mg/L	0.5	63	25	190	190
Benzene	mg/L	0.0073	3.9	3	1.7	0.084
Toluene	mg/L	0.0076	5.2	3.6	1.2	0.69
Ethylbenzene	mg/L	0.0091	1.1	0.7	0.14	0.083
Xylenes	mg/L	0.011	4.6	2.5	0.57	0.031
Anions						
Chloride	mg/L	500	51,000	53,300	54,600	56,100
Nitrate	mg/L	3	37.2	36.6	35.4	BDL
Sulfate	mg/L	5	448	443	441	297
Sulfide	mg/L	1	BDL	BDL	BDL	BDL
Cations						
Arsenic	mg/L	1	BDL	BDL	BDL	BDL
Barium	mg/L	0.05	1.7	1.7	1.8	1.9
Boron	mg/L	0.5	36.2	36.3	38.1	29.5
Cadmium	mg/L	0.1	BDL	BDL	BDL	BDL
Calcium	mg/L	10	1,940	1,990	2,070	1,990
Chromium	mg/L	0.3	BDL	BDL	BDL	BDL
Copper	mg/L	0.2	BDL	BDL	BDL	BDL
Iron	mg/L	0.5	65.7	57.1	153	158
Lead	mg/L	1	BDL	BDL	BDL	BDL
Magnesium	mg/L	10	322	336	348	333
Manganese	mg/L	0.1	1	1	2.1	2
Nickel	mg/L	0.3	BDL	BDL	BDL	BDL
Potassium	mg/L	10	439	465	503	618
Sodium	mg/L	5	29,400	32,300	38,500	39.4
Zinc	mg/L	0.2	0.7	BDL	0.8	BDL

** *Alkalinity Units in mg/L as $CaCO_3$*

Table A13. Results for Produced Water Collected from Shale Well 7-SU at 36-210 Days.

Parameter	Units	Det. Limit	Results (On Days Following Initiation of Flowback Release)				
			36-Day	90-Day	210-Day	365-Day	550-Day
General							
pH	-	-	6.46	6.44	6.36	7.36	6.26
Total Dissolved Solids (TDS)	mg/L	10	112,000	118,000	118,000	970*	117,500
Conductivity	µS/cm	5	40,900	81,100	84,400	2280*	73,500
Alkalinity	mg/L**	1	475	524	564	493	415
Organics							
Total Organic C	mg/L	0.2	1.6	1.4	1.0	3.867	0.5
Total Petroleum Hydrocarbons	mg/L	0.5	220	250	87.7	3.8	808
Benzene	mg/L	0.0073	1.6	1.8	3.4	7.4	0.49
Toluene	mg/L	0.0076	1.3	1.2	1.7	3.8	3.3
Ethylbenzene	mg/L	0.0091	0.18	0.11	0.13	0.29	0.44
Xylenes	mg/L	0.011	0.65	0.37	0.44	0.98	1.4
Anions							
Chloride	mg/L	500	63,600	68,000	69,200	618*	34,000
Nitrate	mg/L	3	35.3	BDL	43.2	BDL	BDL
Sulfate	mg/L	5	394	321	246	0.6*	279
Sulfide	mg/L	1	BDL	BDL	BDL	BDL	BDL
Cations							
Arsenic	mg/L	1	BDL	BDL	BDL	BDL	BDL
Barium	mg/L	0.05	1.8	0.8	2.0	0.5	2.1
Boron	mg/L	0.5	31.7	41.5	41.1	BDL	51.9
Cadmium	mg/L	0.1	BDL	0.2	BDL	BDL	BDL
Calcium	mg/L	10	2,130	2,040	2,010	18.6*	2,080
Chromium	mg/L	0.3	BDL	BDL	BDL	BDL	BDL
Copper	mg/L	0.2	BDL	0.1	BDL	BDL	0.3
Iron	mg/L	0.5	171	159	156	15.0	78.3
Lead	mg/L	1	BDL	BDL	BDL	BDL	BDL
Magnesium	mg/L	10	359	336	330	3.2	355
Manganese	mg/L	0.1	2.4	5.1	3.6	0.1	1.8
Nickel	mg/L	0.3	BDL	1	BDL	BDL	BDL
Potassium	mg/L	10	638	608	511	5.8	565
Sodium	mg/L	5	39,400	33,100	34,900	311*	36,800
Zinc	mg/L	0.2	0.2	0.3	BDL	BDL	BDL

* *Value considered to be an outlier in the analysis of the data.*

** *Alkalinity Units in mg/L as $CaCO_3$*

Table A.14: Baseline Air Quality Data

Date	Chemical	Result Avg.	Units
10/12/2015	Benzene	0.500	ppb
10/12/2015	Benzene	0.420	ppb
10/13/2015	Benzene	0.570	ppb
10/14/2015	Benzene	0.380	ppb
10/14/2015	Benzene	0.520	ppb
10/12/2015	Ethylbenzene	0.550	ppb
10/12/2015	Ethylbenzene	0.000	ppb
10/13/2015	Ethylbenzene	0.000	ppb
10/14/2015	Ethylbenzene	0.000	ppb
10/14/2015	Ethylbenzene	0.480	ppb
10/12/2015	m,p, Xylene	1.600	ppb
10/12/2015	m,p, Xylene	0.000	ppb
10/13/2015	m,p, Xylene	0.000	ppb
10/14/2015	m,p, Xylene	0.360	ppb
10/14/2015	m,p, Xylene	1.800	ppb
10/12/2015	Methane	2.600	ppb
10/12/2015	Methane	2.500	ppb
10/13/2015	Methane	3.000	ppb
10/14/2015	Methane	2.800	ppb
10/14/2015	Methane	2.700	ppb
10/12/2015	PM 10	0.014	mg/m3
10/13/2015	PM 10	0.025	mg/m3
10/14/2015	PM 10	2.320	mg/m3
10/12/2015	Toluene	56.000	ppb
10/12/2015	Toluene	0.390	ppb
10/13/2015	Toluene	0.680	ppb
10/14/2015	Toluene	4.600	ppb
10/14/2015	Toluene	16.000	ppb
10/12/2015	VOC	0.000	ppb
10/13/2015	VOC	0.001	ppb
10/14/2015	VOC	205.000	ppb

Table A.15: Hydraulic Fracturing Air Quality Data: Upwind (UW) and Downwind (DW)

Date	Chemical	Result Avg.	Units	Location	Date	Chemical	Result Avg.	Units	Location
11/10/2015	Benzene	**0.000**	ppb	UW	11/10/2015	Methane	2.500	ppm	UW
11/10/2015	Benzene	**0.000**	ppb	DW	11/10/2015	Methane	2.400	ppm	DW
11/11/2015	Benzene	0.460	ppb	UW	11/11/2015	Methane	2.900	ppm	UW
11/11/2015	Benzene	1.100	ppb	DW	11/11/2015	Methane	2.900	ppm	DW
11/12/2015	Benzene	1.000	ppb	UW	11/12/2015	Methane	3.200	ppm	UW
11/12/2015	Benzene	0.360	ppb	DW	11/12/2015	Methane	2.300	ppm	DW
11/10/2015	Toluene	0.000	ppb	UW	11/10/2015	PM 10	0.029	mg/m 3	UW
11/10/2015	Toluene	0.000	ppb	DW	11/10/2015	PM 10	0.103	mg/m 3	DW
11/11/2015	Toluene	0.330	ppb	UW	11/11/2015	PM 10	0.025	mg/m 3	UW
11/11/2015	Toluene	0.740	ppb	DW	11/11/2015	PM 10	0.107	mg/m 3	DW
11/12/2015	Toluene	0.870	ppb	UW	11/12/2015	PM 10	0.013	mg/m 3	UW
11/12/2015	Toluene	0.400	ppb	DW	11/12/2015	PM 10	0.093	mg/m 3	DW
11/10/2015	Ethyl-benzene	**0.000**	ppb	UW	11/10/2015	VOC	1.000	ppb	UW
11/10/2015	Ethyl-benzene	**0.000**	ppb	DW	11/10/2015	VOC	1.000	ppb	DW
11/11/2015	Ethyl-benzene	**0.000**	ppb	UW	11/11/2015	VOC	81.000	ppb	UW
11/11/2015	Ethyl-benzene	**0.000**	ppb	DW	11/11/2015	VOC	17.500	ppb	DW
11/12/2015	Ethyl-benzene	**0.000**	ppb	UW	11/12/2015	VOC	24.500	ppb	UW
11/12/2015	Ethyl-benzene	**0.000**	ppb	DW	11/12/2015	VOC	153.50	ppb	DW
11/10/2015	m,p, Xylene	**0.000**	ppb	UW					
11/10/2015	m,p, Xylene	**0.000**	ppb	DW					
11/11/2015	m,p, Xylene	**0.000**	ppb	UW					
11/11/2015	m,p, Xylene	**0.000**	ppb	DW					
11/12/2015	m,p, Xylene	**0.000**	ppb	UW					
11/12/2015	m,p, Xylene	**0.000**	ppb	DW					

Table A.16: Flowback Air Quality Data, Upwind (UW) and Downwind (DW)

Date	Chemical	Result Avg.	Units	Location	Date	Chemical	Result Avg.	Units	Location
1/4/2016	Benzene	0.990	ppb	UW	1/4/2016	Methane	10	ppm	UW
1/4/2016	Benzene	1.200	ppb	DW	1/4/2016	Methane	10	ppm	DW
1/5/2016	Benzene	0.230	ppb	UW	1/5/2016	Methane	10	ppm	UW
1/5/2016	Benzene	13.000	ppb	DW	1/5/2016	Methane	10	ppm	DW
1/6/2016	Benzene	0.300	ppb	UW	1/6/2016	Methane	10	ppm	UW
1/6/2016	Benzene	82.000	ppb	DW	1/6/2016	Methane	32	ppm	DW
1/4/2016	Toluene	0.970	ppb	UW	1/4/2016	PM 10	0.002	mg/m3	DW
1/4/2016	Toluene	1.200	ppb	DW	1/5/2016	PM 10	0.001	mg/m3	UW
1/5/2016	Toluene	0.180	ppb	UW	1/5/2016	PM 10	0.001	mg/m3	DW
1/5/2016	Toluene	13.000	ppb	DW	1/6/2016	PM 10	0.003	mg/m3	UW
1/6/2016	Toluene	0.220	ppb	UW	1/6/2016	PM 10	0.012	mg/m3	DW
1/6/2016	Toluene	73.000	ppb	DW	1/4/2016	VOC	32.000	ppb	UW
1/4/2016	Ethylbenzene	ND	ppb	UW	1/4/2016	VOC	171.000	ppb	DW
1/4/2016	Ethylbenzene	ND	ppb	DW	1/5/2016	VOC	333.500	ppb	UW
1/5/2016	Ethylbenzene	ND	ppb	UW	1/5/2016	VOC	415.000	ppb	DW
1/5/2016	Ethylbenzene	1.600	ppb	DW	1/6/2016	VOC	1377.000	ppb	UW
1/6/2016	Ethylbenzene	ND	ppb	UW	1/6/2016	VOC	1289.000	ppb	DW
1/6/2016	Ethylbenzene	7.900	ppb	DW					
1/4/2016	m,p, Xylene	0.380	ppb	UW					
1/4/2016	m,p, Xylene	0.450	ppb	DW					
1/5/2016	m,p, Xylene	ND	ppb	UW					
1/5/2016	m,p, Xylene	4.700	ppb	DW					
1/6/2016	m,p, Xylene	ND	ppb	UW					
1/6/2016	m,p, Xylene	22.000	ppb	DW					

Table A.17: Production Air Quality Data

Date	Chemical	Result Avg.	Units
5/3/2016	Benzene	0.000	ppb
5/4/2016	Benzene	1.200	ppb
5/5/2016	Benzene	0.000	ppb
5/3/2016	Ethylbenzene	0.000	ppb
5/4/2016	Ethylbenzene	0.000	ppb
5/5/2016	Ethylbenzene	0.000	ppb
5/3/2016	Toluene	0.350	ppb
5/4/2016	Toluene	2.600	ppb
5/5/2016	Toluene	0.000	ppb
5/3/2016	m,p, Xylene	0.000	ppb
5/4/2016	m,p, Xylene	0.000	ppb
5/5/2016	m,p, Xylene	0.000	ppb
5/3/2016	Methane	3.2	ppm
5/4/2016	Methane	3.6	ppm
5/5/2016	Methane	3.7	ppm
5/3/2016	PM 10	0.01	mg/m3
5/4/2016	PM 10	5.230	mg/m3
5/5/2016	PM 10	0.091	mg/m3
5/3/2016	VOC	3.500	ppb
5/4/2016	VOC	9.500	ppb
5/5/2016	VOC	10.000	ppb

Table A.18: Midland Air Quality Data

Date	Chemical	Result Avg.	Units
5/3/2016	Benzene	0.540	ppb
5/4/2016	Benzene	0.440	ppb
5/5/2016	Benzene	0.000	ppb
5/3/2016	Ethylbenzene	0.000	ppb
5/4/2016	Ethylbenzene	0.000	ppb
5/5/2016	Ethylbenzene	0.000	ppb
5/3/2016	Toluene	0.940	ppb
5/4/2016	Toluene	1.000	ppb
5/5/2016	Toluene	0.640	ppb
5/3/2016	m,p, Xylene	0.000	ppb
5/4/2016	m,p, Xylene	0.000	ppb
5/5/2016	m,p, Xylene	0.000	ppb
5/3/2016	Methane	3.3	ppm
5/4/2016	Methane	2.7	ppm
5/5/2016	Methane	3.3	ppm
5/3/2016	PM 10	0.097	mg/m3
5/4/2016	PM 10	0.061	mg/m3
5/5/2016	PM 10	0.023	mg/m3
5/3/2016	VOC	65.000	ppb
5/4/2016	VOC	8.000	ppb
5/5/2016	VOC	2.500	ppb

Appendix E: Scaleup and Demonstration of Membrane Distillation

Research Entity: University of Pittsburg, Department of Civil and Environmental Engineering

Final Report Membrane Distillation, December 31, 2021

Prepared by Radisav D. Vidic, Ritesh Pawar, Zhewei Zhang

Executive Summary

This study evaluated technical feasibility of using membrane distillation for treatment of produced water from unconventional oil and gas wells in the Permian Basin in West Texas with the objective to recover high-quality water for agricultural/industrial use and reduce the volume of produced water that needs to be sent to disposal facilities.

Prior to field demonstration, extensive lab-scale experiments using a direct contact membrane distillation (DCMD) system were performed with actual produced water from the Permian Basin with total dissolved solids (TDS) of about 100,000 mg/L. The lab- scale system operated with feed and permeate temperatures of 60 and 20°C, respectively achieved permeate flux of 13 Liters/m2/hr. (LMH) at 50% water recovery. No membrane fouling was observed at these operating conditions. Conductivity monitoring of the permeate revealed a slow but steady increase in permeate TDS, which was attributed to ammonia transfer from the raw produced water to the permeate side, which led to the increase in pH and conductivity of the permeate.

Comparison between commercial polyethylene (PE) and polytetrafluoroethylene (PTFE) membranes revealed slightly better and more robust performance of the PTFE membrane that was selected for field demonstration. Two trials were conducted with a pilot-scale system equipped with two membrane modules with 26 m2 of membrane area in each. This pilot system was designed to treat 1 gpm of produced water and achieve 50% water recovery. The first field demonstration conducted in May 2021 failed due to the addition of surfactant-based biocide solution to the feed solution, which caused membrane wetting. In addition, lack of produced water pretreatment that was originally planned for this field demonstration and ineffective control of pilot-plant operation led to premature termination of the field demonstration. The second field demonstration conducted in September 2021 included produced water pretreatment to remove dissolved iron and reduce sulfate concentration to prevent scale formation in the system. Appropriate analytical capabilities to control system operation were added in this trial. Field demonstration of MD technology in this trial involved 5 days of continuous operation at steady-state conditions treating 0.8 gpm of produced water at 48% water recovery. The permeate conductivity of about 600 mS/cm indicated 99.7% TDS rejection by the PTFE membrane and very high quality of recovered permeate (i.e., the conductivity of tap water ranges from 200-800 mS/cm) from the pretreated produced water with TDS of 123,000 mg/L.

This study demonstrated technical feasibility of using MD for treatment of produced water generated in the Permian Basin to recover high-quality water suitable for industrial/agricultural use. MD treatment for water recovery represents a viable technical solution in the arsenal of produced water management strategies that would dramatically reduce the water footprint of unconventional oil and gas industry.

A supplement to this report, entitled "Forecasting of Benefits of Membrane Distillation in the Treatment of Produced Water for Beneficial Use", was prepared by Thomas Hayes of the Gas Technology Institute and Blaine Severin of Environmental Process Dynamics. The supplement includes analysis aimed at forecasting the benefits of membrane distillation for the treatment of produced water for beneficial use with particular emphasis on the Permian Basin in Texas and the Bakken Shale in North Dakota.

Acknowledgements

This report is based upon work supported by the U.S. Department of Energy under award number DE-FE0024292. Additionally, we thank the following individuals for helping us throughout the project: Joana Carvalho and Bart Nelemans (Aquastill, NL) for pilot plant training and help with operation and maintenance, Joe Hamende, Jonathan Reeves, Bert, Colton (Permian Basin host site) for all the help in the field, Drs. Jens Blotevogel and Andrea Hanson (Colorado State University) for Q-ToF analysis, Sarah Pitell (University of Pittsburgh) for help with biodegradation experiments, Dr. Lei Li (University of Pittsburgh) for help with contact angle measurements, and Dr. David Malehorn (Lab Manager, University of Pittsburgh) for help with TOC analysis.

Introduction

Wastewater from Hydraulic Fracturing

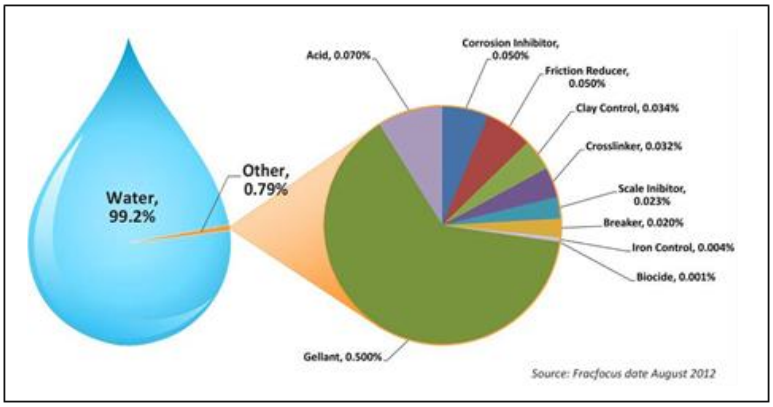


Figure 1. Average hydraulic fracturing fluid composition for U.S. Shale Plays [7]

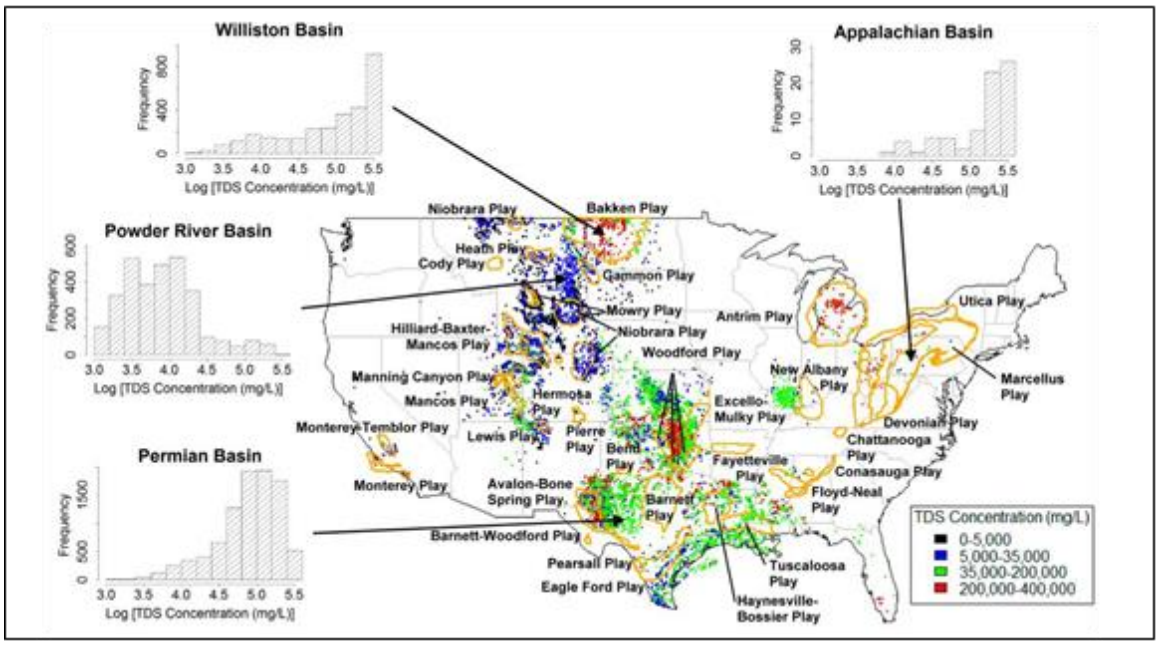


Figure 2. Map illustrating the locations of active shale plays in the contiguous United States and the ranges of produced water total dissolved solids (TDS) concentrations from the U.S. Geological Survey's Produced Waters Database [13].

Extraction of oil and gas from unconventional reservoirs by hydraulic fracturing has been widely employed by the U.S. oil and gas industry [1]. The unconventional oil and gas extraction is a promising energy source with major economic benefits but is accompanied by a host of

environmental challenges, including an increased level of methane emissions at shale gas production sites [2,3], and the potential for drinking water [4] and groundwater contamination [5]. One of the critical challenges for this industry is the management of vast quantities of high salinity wastewater generated in the process of hydraulic fracturing [6]. The extraction process generates large volumes of produced water [8], which contains chemicals that were added to the fracturing fluid as well as salts and hydrocarbons from the geologic formations. During hydraulic fracturing, a mixture of water and chemicals (Figure 1) known as fracturing fluid [9] is injected in a horizontal well to fracture the formation rock, increase its permeability and facilitate the flow of oil and gas into the well. The water that is extracted from the well in the early period (2-3 weeks) is typically designated as flowback water [10] with a total volume between 10-40% of the fracturing fluid volume [11]. Wastewater continues to be produced throughout the lifetime of the well but at a rate that is much lower than during the flowback period [8]. This wastewater is known as produced water (PW) and generally contains various organic and inorganic constituents, bacteria, sand or mud, oil, and grease, as well as Naturally Occurring Radioactive Materials (NORM) and is not amenable to conventional wastewater treatment [11]. The composition of produced water depends on the well location, and it varies during the lifetime of the well [12]. Figure 2 indicates how oil and gas wells are distributed across the United States with the ranges of total dissolved solids (TDS) concentration in produced water [13]. There are vast differences in salinity and chemical composition [1] of the produced water in the US, which increases management complexity between different plays.

The current global generation of produced water is estimated at 250 million barrels per day compared to 80 million barrels per day of oil and is expected to increase even further, thus leading to an increase in the cost of produced water management [14]. A comprehensive 10-year study has shown that PW generation in the United States has sharply increased by 15.2 % from 2012 to 2017, as opposed to just 1% increase from 2007 to 2012[15,16]. The generation of PW in the United States in 2017 was dominated by three states, Texas, California, and Oklahoma, which generated 41, 13, and 12% of the total volume, respectively, of the total [16]. The Permian Basin, which is the most productive tight oil and gas play in the US, currently contributes more than 2 million barrels of oil per day (~18 % of total U.S. production) and a considerably larger volume of produced water [17–19]. Figure 3 shows the increase in produced water generated in the Permian Basin in the last decade (2010-2019).

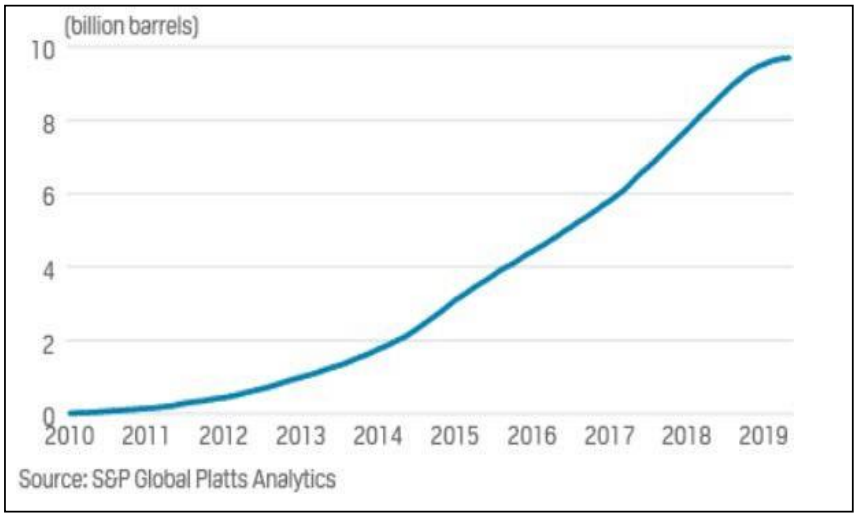


Figure 3. Volume of produced water generated in the Permian Basin (obtained from S&P Global Platts Analytics)

Current Management Strategies

The produced water is the largest volume byproduct associated with oil and gas exploration and production; the cost of managing such a large volume of wastewater is a large fraction of capital and O&M costs for oil and gas producers. The management strategy employed by the oil and gas industry varies largely with location, regulatory landscape, and existing infrastructure.

As shown in Figure 4, 91.5 % of the produced water is injected either for enhanced oil recovery or in commercial and non-commercial disposal wells [16]. The least expensive produced water management method is injection in class II disposal wells that are geologically isolated from the underground sources of drinking water [20]. However, the disposal of produced water in the injection wells leads to a total loss of water from the ecosystem. In addition, these disposal wells have been linked with seismic activity [18,21,22]. In the regions where disposal wells are not readily available (e.g., Pennsylvania), the cost associated with transportation of produced water to out-of-state disposal facilities significantly increases the overall management costs [23]. In areas of limited disposal capacity or where water resources are under pressure due to overuse or climate change impacts, reuse and recycling of produced water are an attractive alternative to direct underground disposal.

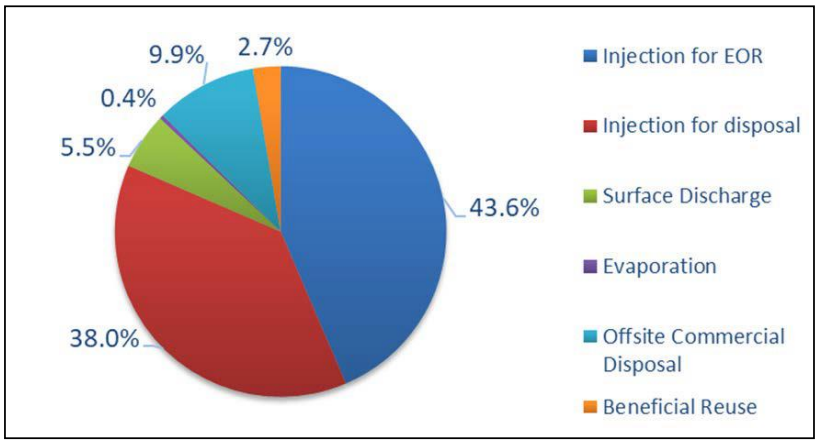


Figure 4. Produced water management practices by percentage in 2017[16]

The issues with the current management strategies and increasing demand for water conservation drive the need for the development of innovative management strategies for produced water to reduce environmental footprint of oil and gas industry.

Membrane Distillation

Desalination has emerged as a promising technology to address the problems related to water treatment [25]. These technologies have proven to be commercially successful in effectively treating the wastewater and producing good quality water. Membrane-based processes like Reverse Osmosis (RO) and Multistage Flash (MSF) are some of the leading examples of desalination technologies used on a commercial scale [26]. However, RO is limited to about 70,000 mg/L of TDS as it reaches the operational limit for the feed osmotic pressure [27]. Membrane Distillation (MD) is an emerging technology for desalination of produced water [28] that offers 100% rejection of non-volatile compounds, lower operating temperature than conventional distillation processes, the ability to utilize low-grade thermal energy, less

stringent requirements for membrane mechanical properties, and lower operating pressure than conventional pressure-driven membrane processes [29–31].

Over the past two decades, there have been considerable improvements in the membranes for MD applications as well as improvements in the performance and energy cost of MD systems [32]. MD can achieve up to 99.9 and 99.5% rejection of salts [33,34] and organic compounds [35,36], respectively and has been shown to be effective in removing heavy metals from wastewater [37] and concentrated radioactive waste [38]. MD has been evaluated for brackish water [39] and seawater desalination [40,41], food industry applications [42], and acid recovery [43,44]. Like any other membrane-based separation process, MD faces a major challenge from fouling due to the accumulation of inorganic and organic contaminants on the membrane surface [22,45,46]. Additionally, membrane wetting is a unique feature in MD systems that might be more critical than fouling as it leads to a decrease in performance and permeate quality [47–49]. In short, both membrane fouling and wetting have adverse impacts on MD and need to be mitigated to maintain stable performance and requisite water recovery [50,51].

There are numerous studies related to membrane distillation that are done on the laboratory scale [22,52]. However, membrane distillation is not yet used for water treatment on a commercial scale. There are very few studies that are done on the pilot-scale with the majority focused on seawater or brackish water desalination [53,54]. Recently, there has been an increase in drive to further these studies with coal seam gas produced water [55] and even with high salinity sodium chloride solutions [56]. Transferability of results from bench-scale to pilot-scale and then full-scale is associated with variability of operational and system parameters [57].

Study Objectives

The objective of this project was to evaluate technical feasibility of treating produced water generated by the unconventional oil and gas industry in Permian Basin using membrane distillation (MD) technology to reduce the volume of water that needs to be disposed of and to recover high-quality water for use in agriculture and/or industrial applications. The first phase of the project involved laboratory-scale prototype testing on actual Permian Basin produced waters to determine optimal design and operating parameters for the operation of this technology in the field. These results were used to construct a pilot scale MD system that was tested in the lab before deployment to the field. The final phase of this project included deployment and operation of the pilot MD system to treat actual produced water in Permian Basin to validate operating and performance parameters.

Laboratory scale studies

Materials and Methods

Produced water was obtained from the Wolfcamp formation in the Permian Basin, TX, and was filtered through a 0.22-µm membrane to remove any suspended solids before analysis. The total dissolved solids (TDS) concentration was determined using the EPA gravimetric method (EPA Method 160.1). Dissolved Organic Carbon (DOC) content of the produced water was analyzed using a TOC analyzer (Shimadzu, TOC-L) while cations and anions were analyzed using Inductively Coupled Plasma – Optical Emission Spectrometry (ICP-OES, 5100, Agilent Technologies) and Ion Chromatography with an IonPac Carbonate Eluent Anion-Exchange

Column (IC, Dionex ICS-1100, Thermoscientific), respectively. The composition of the filtered produced water is shown in Table 1.

Organic chemicals, such as nonylphenol ethoxylates (NPEOs, ~10 EO units, average mol wt. 680 gm/mol), polyethylene glycols (PEGs), nonylphenol (NP), 2-butoxyethoxy acetic acid (2-BE), benzyl dimethyldecylammonium chloride (ADBAC), were obtained from Millipore Sigma. Ammonium chloride (NH_4Cl), ammonium acetate (CH_3COONH_4), and sodium acetate (CH_3COONa) were also purchased from Millipore Sigma. These organic and inorganic compounds were used to prepare synthetic solutions based on the analysis shown in Table 1. Hydrochloric acid (HCl), sodium hydroxide (NaOH), hydrogen peroxide (H_2O_2, 30%), barium chloride ($BaCl_2$, 2 H_2O), and sodium chloride (NaCl) were procured from Fisher Scientific. Filtrasorb® 400 granular activated carbon (Calgon Carbon Corporation, Pittsburgh, PA) was used to filter the produced water to remove organic constituents. Deionized (DI) water with a resistivity of 18.2 Mohm-cm was obtained from a MilliQ water system. Chlorine dioxide solution (4000 mg/L) was prepared by mixing the sachets purchased from GO2 International (Buena Park, CA).

Table 1. Composition of the filtered produced water sample

Ion	Unit	Concentration
Sulfate (SO_4^{2-})	mg/L	550
Chloride (Cl^-)	mg/L	60,200
Sodium (Na^+)	mg/L	30,800
Calcium (Ca^{2+})	mg/L	2000
Potassium (K^+)	mg/L	350
Magnesium (Mg^{2+})	mg/L	350
Barium (Ba^{2+})	mg/L	20
Strontium (Sr^{2+})	mg/L	400
Ammonium (NH_4^+)	mg/L	450
DOC	mg/L	120
Total dissolved solids (TDS)	mg/L	100,000
Conductivity	mS/cm	140
pH	-	7

Table 2. Properties of PTFE and PE membranes used in this study.

Membranes	Mean Pore size (μm)	Thickness (mm)	Contact angle (^{o})	Liquid Entry Pressure (bar)	% porosity of the membrane
PTFE	0.45	0.13-0.23	139.6	2.5	85
PE	0.16	0.11	126.4	4.2	85

Commercially available hydrophobic microporous polytetrafluoroethylene (PTFE) with polypropylene support and polyethylene (PE) membranes were obtained from Aquastill, Netherlands. The properties of these membranes as provided by the manufacturer are shown

in Table 2.

All experiments in this study were carried out using a DCMD module with a 40 cm^2 (20 cm x 2 cm) flat sheet membrane in the experimental system operated in batch (concentrating) mode shown in Figure 5. The 1-mm thick spacers with a porosity of 0.77 (Delstar Technologies, PA) were stacked on top of the membrane from both sides to ensure even distribution of the feed and permeate flow. The feed solution was heated to a desired temperature (60°C) using a hot plate and was circulated using a centrifugal pump (Baldor Reliance, Fort Smith, AZ). DI water was circulated on the permeate side using a centrifugal pump and its temperature was maintained at 20°C using a chiller (M75, Thermo Fisher Scientific Inc., Pittsburgh, PA). The overflow from permeate tank was collected in a beaker and its weight was monitored with a balance (Ohaus Corp., Parsippany, NJ) while its conductivity was continuously monitored using a conductivity meter (Orion VersaStar Pro, Thermo Fisher Scientific Inc., Pittsburgh, PA). The laboratory-scale experimental DCMD setup is shown in Figure 6. Water recovery was calculated using the following equation:

$$\%\ \text{Recovery} = \frac{\text{Total mass of permeate collected at time t (g)}}{\text{Initial mass of the feed solution (g)}} \text{ X } 100$$

The permeate flux was calculated using the following equation:

$$\text{Flux (LMH)} = \frac{\text{Mass of permeate collected during the period } \Delta t\text{ (g)}}{A\ (\text{cm}^2) * \Delta t\ (\text{min}) * \rho''\ (\text{g/mL})} \text{ X } 600$$

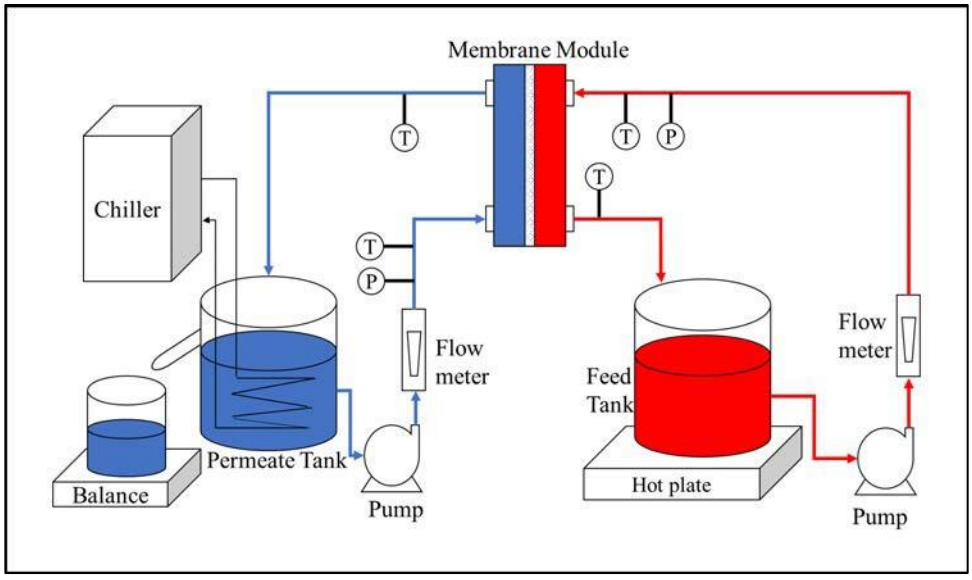


Figure 5. Schematic of laboratory-scale DCMD system

Biological treatment

Produced water was stored in a refrigerator at 4°C. Prior to the DCMD experiment, the desired volume of refrigerated produced water was transferred to Erlenmeyer flasks and incubated in a shaker at 37°C. Samples were taken every 2 days, filtered through a 0.22-µm membrane, and analyzed for DOC.

Activated carbon treatment.

Filtrasorb® 400 was wetted overnight in DI water to remove air trapped in the pores [58] and charged in a glass column (40 cm in height and 2.54 cm in diameter). The packed adsorber

column was flushed with deionized water at a flow rate of 50 ml/min to remove the fines prior to filtering the produced water at a flow rate of (10-20 ml/min). Empty Bed Contact Time (EBCT) in the adsorber was varied between 10-20 min [59] by adjusting the flow rate.

Chemical Oxidation

Hydrogen peroxide [21,60] at a dose of 5 mM was added to produced water at pH 3.0 and 12.0 and stirred overnight prior to treatment in a laboratory-scale DCMD system. Different concentrations of Fe2+ were added to the solution using a ferrous sulfate solution to promote the Fenton reaction [60–62]. Chlorine dioxide [19,59,60] stock solution at 4,000 mg/l was used to add chlorine dioxide to produced water at 50% of DOC concentration and the solution was stirred overnight.

Major organics present in the produced water were analyzed using ultrahigh-pressure liquid chromatography (UHPLC) with quadrupole time-of-flight mass spectrometry (LC- QToF MS). Prior to instrumental analysis, all samples were processed through a solid-phase extraction (SPE) procedure to concentrate organics and remove salts. Samples (~250 mL) were first vacuum-filtered through a 0.2-µm glass fiber filter and the pH was adjusted to 3 with HCl. For SPE, Supel Select HLB cartridges (200 mg/6 mL, Supelco, Bellefonte, PA) were sequentially conditioned with 10 mL each of methanol (Thermo Fisher Scientific, Pittsburgh, PA), double-deionized water, and double-deionized water at pH 3. Samples were extracted under vacuum and the SPE columns were rinsed with 5% methanol before being dried for 15 min. The cartridges were eluted with 10 mL of methanol and immediately stored at -20 °C until analysis by LC-QToF MS (Agilent 1100 series LC and Agilent G3250AA QToF) using previously developed methods [63,64]. Agilent Mass Hunter Qualitative Analysis 10.0 software was used for data analysis using an abundance cutoff of 10σ to extract molecular features. Identification of surfactant species used an in-house database of known polyethoxylated surfactants, including polyethylene glycols (PEGs), alkyl ethoxylates (AEOs), octylphenol ethoxylates (OPEOs), and nonylphenol polyethoxylates (NPEOs), in addition to polypropylene glycols (PPGs) that had been previously reported for produced waters [63–65]. Surfactant species identified in the samples (the most predominant series present in the samples) for which chemical formulas were assigned based on accurate masses were also added to the database. For positive surfactant identification, species had to be visible within a series in the chromatogram following the correct elution order, have the same computed Kendrick mass defect (KMD) for a given surfactant series [63], and have a mass error of less than 5 ppm compared to the species in the surfactant database.

Contact angle measurement for virgin and used membranes was performed using a sessile drop method (VCA optima, AST Products, Inc.) and 1 µl DI water droplet released from a needle tip onto the flat membrane surface. The Liquid Entry Pressure (LEP) [66] was measured using the method described previously [22].

Results and Discussion

Effect of membrane properties on DCMD performance with raw produced water

The produced water was first treated to completely remove SO42- ions in the form of BaSO4 precipitate by adding $BaCl_2$ at the molar ratio of Ba^{2+} to SO_4^{2-} of 1.2[67]. The solution was allowed to settle for 4 h and was filtered through 0.22 µm membrane before use in the DCMD

module. Unless stated otherwise, the feed side operating temperature was always 60°C and the permeate side temperature was 20°C. The flow rate on each side was 0.2 GPM (0.756 L/min) and the experiment was concluded at 30% water recovery. A new membrane was used for each experiment after the initial test with NaCl solution to ensure leak-free module operation.

Figure 7 shows the performance of PE and PTFE membranes with pretreated produced water. The permeate flux with both PE and PTFE membranes was nearly constant over a 3-hr period with the permeate flux for the PTFE membrane slightly higher than that for the PE membrane. However, the permeate conductivity increased monotonically during both tests.

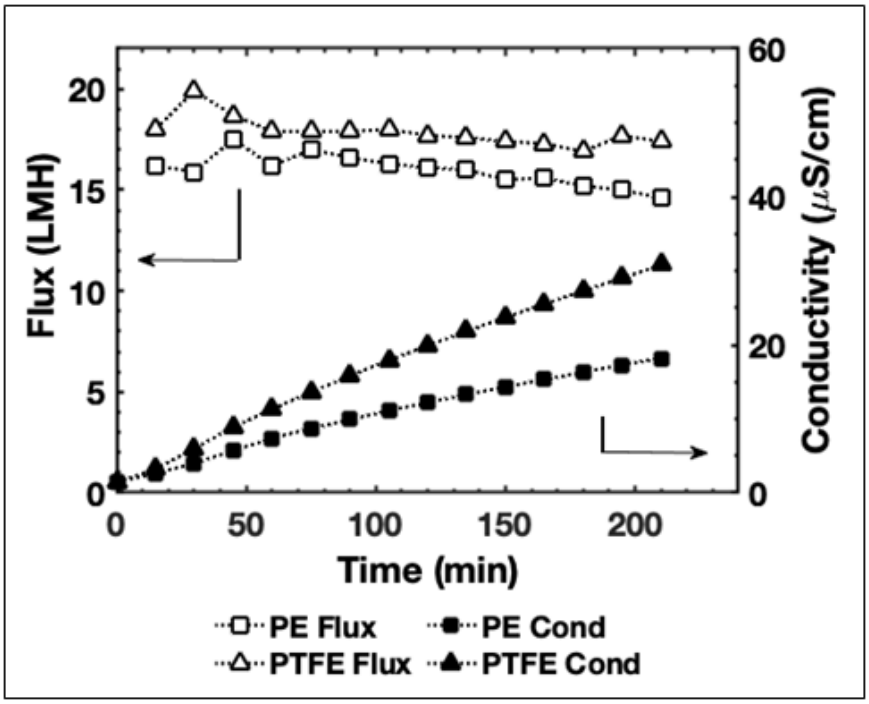


Figure 7. Permeate flux and conductivity for PTFE and PE membranes treating raw produced water.

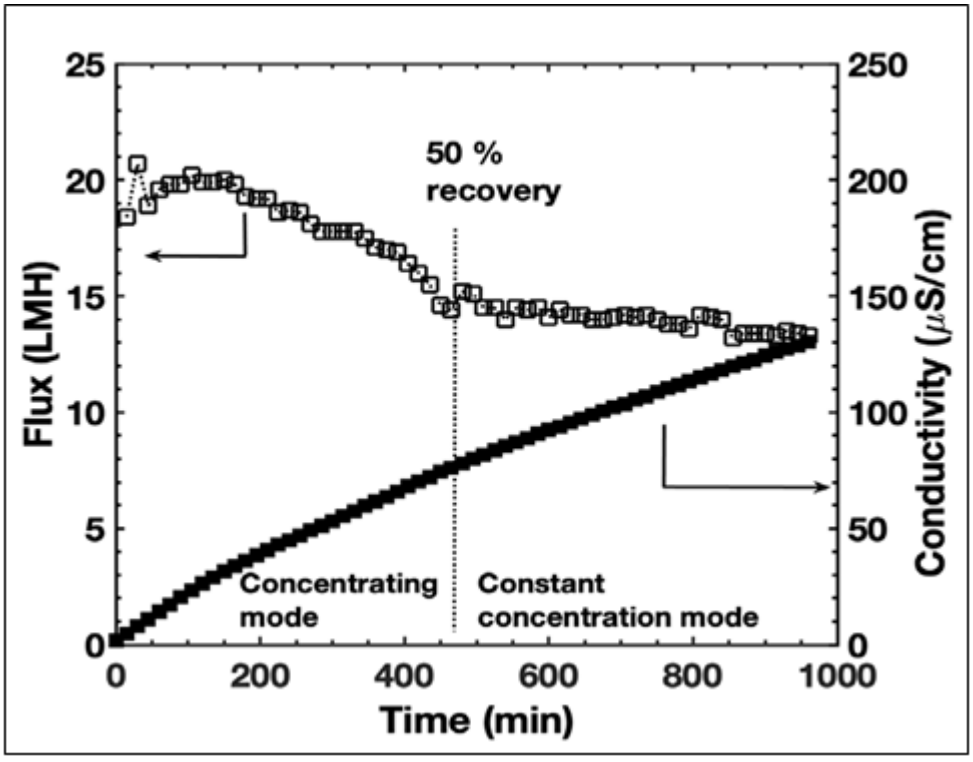


Figure 8. Permeate flux and conductivity in a long-term DCMD test with PTFE membrane.

The increase in permeate conductivity observed in Figure 7 can be due to the following reasons: (i) membrane wetting due to fouling/scaling [68,69], (ii) presence of low surface tension organic compounds in the feed that would alter the hydrophobicity of the membrane [70,71], or (iii) passage of volatile compounds to the permeate side that leads to conductivity increase [68,72,73]. Each of these possibilities was evaluated in subsequent analyses.

Deposition of inorganic scales on the membrane surface and crystallization inside the membrane pores can reduce the hydrophobicity of the membrane leading to wetting [68] and transport of non-volatile compounds from the feed to permeate side that leads to an increase in permeate conductivity [74]. If scaling is the primary reason for membrane wetting, it should be accompanied by a rapid increase in permeate conductivity along with the permeate flux decline [68,75]. Because such behavior may not be evident during short-term experiments, a long-term experiment (16 h) was performed using raw produced water as shown in Figure 8.

The raw produced water was concentrated from 100 g/L to 200 g/L to achieve 50% recovery, which took about 460 min. A decrease in permeate flux observed during this period was due to an increase in feed salinity and an associated decrease in vapor pressure. After this initial period, the feed salinity was maintained at 200 g/L by continuously adding a make-up stream of raw produced water and withdrawing the overflow purge stream from the feed tank. The conductivity continued to increase steadily even after the feed concentration was maintained at a constant level. A constant permeate flux during the system operation with constant feed composition (Figure 8) suggests that the increase in permeate conductivity was not due to scaling/fouling of the membrane. Moreover, the permeate flux with the raw feed solution and the feed solution after barite precipitation was identical (data not shown), indicating that no barite precipitation on the membrane surface was observed with this produced water. Hence, feed pretreatment with barite precipitation was not performed in subsequent experiments.

DCMD performance with pretreated produced water

Table 3. DOC reduction by various treatment methods.

Pre-treatment method	Operating Conditions	DOC (mg/L)
Untreated Water	-	120
Biodegradation	7 days	20
Biodegradation	15 days	19
Biodegradation	30 days	19
Biodegradation (15 d) + Adsorption	10 min EBCT	1.6
Biodegradation (15 d) + Adsorption	20 min EBCT	1.5
H_2O_2	pH = 3.0	106
H_2O_2	pH = 12.0	107
Fenton Reagent		113
ClO_2		100

As shown in Table 1, the raw produced water had a DOC content of 120 mg/L, and it is possible that some of the organic compounds present in this water could reduce the surface

tension to reduce both membrane hydrophobicity and Liquid Entry Pressure (LEP) and allow the passage of salts to the permeate side [76]. Several different treatment approaches were utilized to remove organics from the raw produced water to evaluate this hypothesis.

It has been reported that 91% reduction in DOC can be achieved within 6.5 days by aerobic biodegradation of Synthetic Fracturing Fluid (SFF), which is similar in composition to produced water from the Marcellus Shale play [77]. Hence, aerobic biodegradation was evaluated for its ability to reduce the DOC content of the produced water obtained from the Permian Basin in TX. As shown in Table 3, the DOC in the produced water decreased from 120 mg/L to 20 mg/L (83% reduction) after 7 days of continuous aeration, but it could not be reduced any further even after 30 days of treatment [78].

After biological treatment, produced water was filtered through a fixed bed activated carbon adsorber operated at Empty Bed Contact Time (EBCT) of 10 min and 20 min. The DOC in the produced water was reduced from 19 mg/L to 1.6 mg/L (91.5 % reduction) by an adsorber with EBCT of 10 min and to 1.5 mg/L (92.1% reduction) by an adsorber with EBCT of 20 min (Table 3).

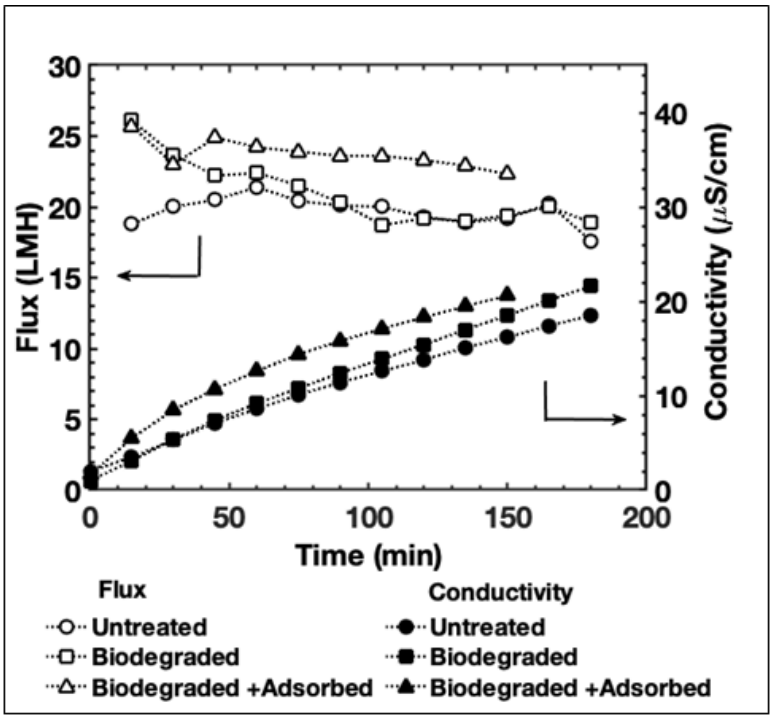


Figure 9. Impact of produced water treatment on permeate flux and conductivity with the PE membrane.

Chemical oxidation with hydrogen peroxide [60], Fenton reagent [62,79], and chlorine dioxide was also evaluated as an option to reduce the organic content in this produced water. Hydrogen peroxide was added to the feed solution at 5 mM concentration at pH of 3.0 and 12.0 [62], and the reaction was allowed to proceed overnight before analyzing the DOC content. The DOC of raw produced water decreased to 106 mg/L (11.6 % reduction) after treatment with H_2O_2 under acidic conditions and to 105 mg/L (10.8 % reduction) under alkaline conditions (Table 3). These results indicate that oxidation with hydrogen peroxide is not very effective in reducing the DOC of raw produced water.

Fenton reaction was performed using 5 mM H_2O_2 and 2 mM Fe^{2+} without any pH adjustment. The DOC value obtained after the Fenton reaction was 112 mg/L (5.8 % reduction) and it was

concluded that this method is also not effective in reducing the organic content of produced water, which supports previous findings [60]. The ability of chlorine dioxide to oxidize organics in this produced water was evaluated using the ClO_2/DOC mass ratio of 0.5 and it was able to reduce the DOC in raw produced water from 120 mg/L to 100 mg/L (16.6% reduction).

Because the maximum DOC reduction in the produced water was observed after biological treatment followed by activated carbon adsorption (Table 3), DCMD tests were performed with produced water after these pretreatment steps. Experimental results shown in Figure 9 indicate that the combination of biological degradation and activated carbon adsorption, which resulted in close to 92% reduction in DOC of the produced water, had minimal impact on the observed permeate flux and conductivity when compared to the results obtained with raw produced water (Figure 9). Considering that most low surface tension organic compounds (surfactants) are easily removed by biodegradation or activated carbon adsorption [77], the results shown in Figure 9 suggest that the presence of low surface tension organics in the raw produced water was not responsible for the observed deterioration in permeate quality.

Impact of produced water on membrane characteristics

Previous reports have shown that some organics in produced water can permanently wet a membrane, and neither membrane cleaning nor physical cleaning by air-drying was successful in restoring the original membrane properties, resulting in permeate flux decline with each cleaning cycle and consistently low permeate quality [80]. As such, the impact of membrane exposure to produced water on its ability to achieve requisite performance in terms of permeate flux and quality was evaluated using 100 g/L NaCl feed solution. As shown in Figure 10, both PE and PTFE membranes performed quite well with NaCl solution where permeate conductivity remained below 2 mS/cm during the first 100 min of operation.

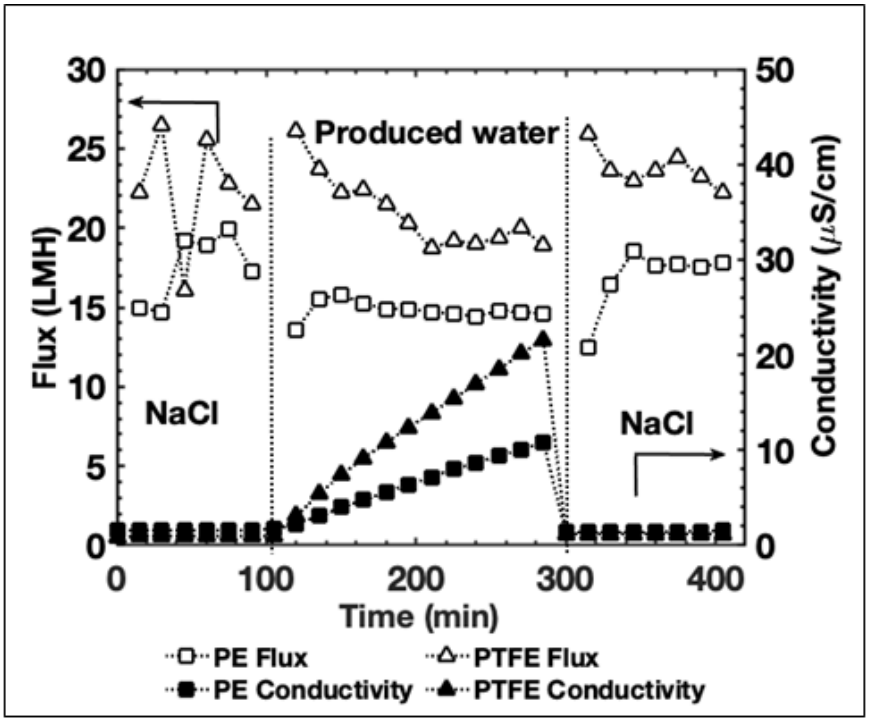


Figure 10. Impact of exposure to produced water on permeate flux and conductivity for PE and PTFE membranes treating NaCl solution.

When the NaCl feed solution was replaced with untreated produced water, the permeate flux

decreased slightly compared to that observed with NaCl solution despite the almost identical salinities of the two solutions. Such behavior can be explained by the presence of other ions in the produced water that have a more significant impact on vapor pressure lowering compared to monovalent Na+ and Cl-. Like the behavior observed in previous tests (Figure 7 and Figure 9), a monotonous increase in permeate conductivity was observed when the produced water was treated in the DCMD module. It is important to note that the PTFE membrane had higher permeate flux compared to the PE membrane, which can be explained by its larger pore size (Table 2). However, the PTFE membrane also had a more significant increase in permeate conductivity, which suggested that the permeate conductivity increase may be due to the compounds that are transferred in the vapor phase.

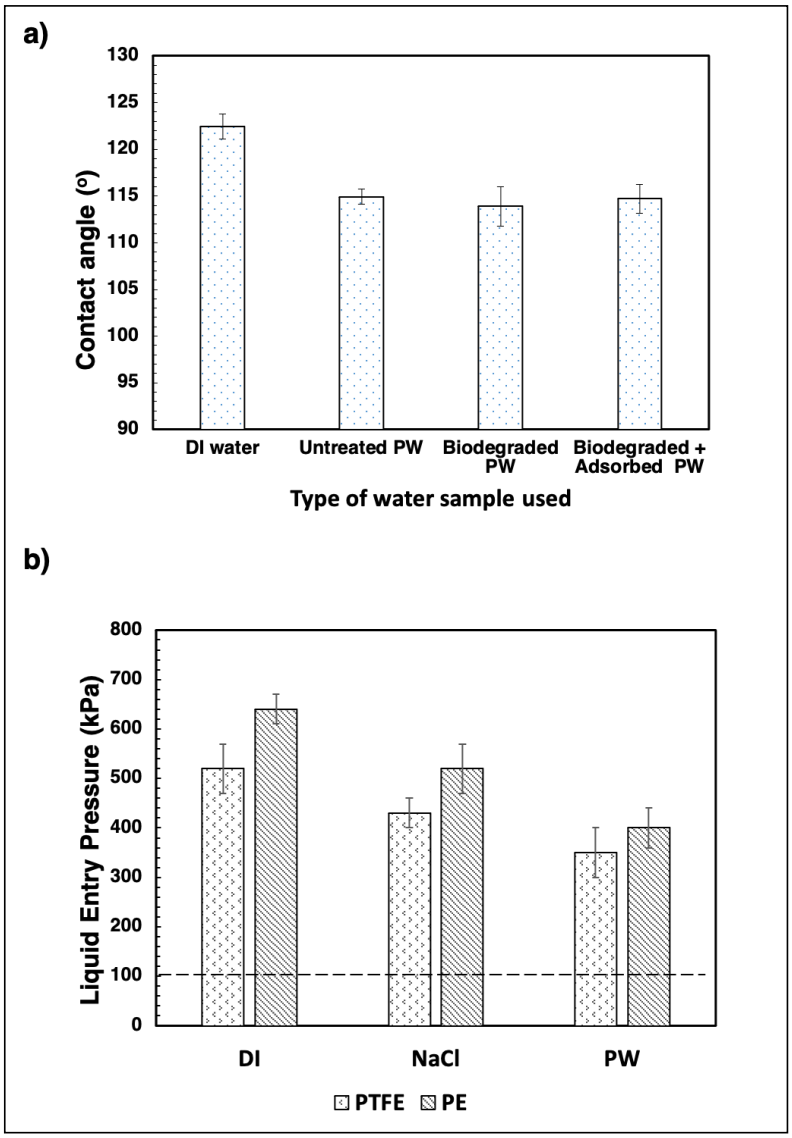


Figure 11. Membrane characterization: a) contact angle for PE membrane exposed to different feed solutions; b) Liquid Entry Pressure (LEP) for PE and PTFE membranes with DI water, NaCl solution, and raw produced water (PW). The error bars represent a range of results from triplicate measurements.

After 200 min of treating produced water, the system was first flushed with DI water and the feed was switched back to 100 g/L NaCl solution. The performance of the DCMD system was identical to that observed in the first 100 min of operation with virgin membranes whereby the permeate conductivity returned to below 2 mS/cm indicating no permanent wetting of the membrane. Such behavior suggests that the increase in permeate conductivity when treating

the produced water was not caused by strongly adsorbing (hydrophobic) organic species or scales.

To further pinpoint the observed behavior with produced water, the PE membrane exposed to different feed solutions was characterized with respect to contact angle with DI water while both PE and PTFE membranes were analyzed for liquid entry pressure with different solutions (i.e., DI Water, NaCl solution and produced water). The results of these tests are shown in Figure 11.

The contact angle measured for virgin PE membrane with DI water was 122.5° and it was 114.5° in the case of produced water regardless of the pretreatment evaluated in this study. The reduction in contact angle with produced water samples can be attributed to non-adsorbable low surface tension organic compounds that pass through the membrane and do not permanently damage the membrane. The LEP for virgin PE and PTFE membranes was 640 $\pm$ 30 and 520 $\pm$ 50 kPa, respectively. These values decreased to 520 $\pm$ 50 and 430 $\pm$ 30 kPa with NaCl solution, and to 400 $\pm$ 40 and 350 $\pm$ 50 kPa with raw produced water. Because the operating pressure in the laboratory-scale MD system was around 100 kPa, it can be concluded that none of the feed solutions evaluated in this study could achieve complete membrane wetting.

The results described above suggest that neither membrane underwent irreversible scaling/fouling/wetting due to exposure to produced water. The only mechanism that can explain the increase in permeate conductivity observed when treating this produced water from the Permian Basin is the passage of volatile compounds from the feed side to the permeate side.

Impact of specific organics on DCMD performance

Nontargeted high-resolution accurate mass spectrometric analysis of the untreated produced water revealed the presence of the following predominant organic compounds: PEGs, polyethylene glycol carboxylates (PEGCs), polypropylene glycols (PPGs), NPEOs, nonylphenol ethoxylate carboxylates (NPECs), octylphenol ethoxylates (OPEOs), 2- butoxyethoxy acetic acid (2-BE), the C10-ADBAC species decyldimethylbenzylammonium chloride, and quaternary ammonium salts. Comparison of sequentially treated and untreated produced water revealed an apparent reduction in higher molecular weight PEGs (n=5-13 in treated water vs. n=9-23 in untreated water) and PPGs (n=3-6 in treated water vs. n=4-13 in untreated water); in addition, OPEOs were below the detection thresholds in the treated produced water, suggesting significant removal with pretreatment (data not shown). Lastly, while NPEOs persisted in the treated produced water, NPECs were also detected (TableA 2 and FigureA 1, Appendix), indicating biological transformation in agreement with previous studies [65]. ADBAC, which is a widely used biocide in this industry, and other similar quaternary ammonium salts that were present in the produced water, were likely responsible for the reduction in the LEP when compared to the values obtained with DI water (Figure 11).

To help elucidate whether a specific organic compound in the sequentially treated produced water was responsible for the observed decrease in permeate quality, the permeate was further analyzed by LC-QToF-MS/MS. It is interesting to note that NPEOs, NPECs, and 2-BE were detected in the permeate (TableA 2 and FigureA 1, Appendix). These compounds might have

passed through the membrane either due to their lower vapor pressure or if they acted as surfactants to reduce membrane hydrophobicity. As such, the organic compounds listed above were purchased in their pure form and used in DCMD tests to assess their ability to cause the increase in permeate conductivity observed in the tests depicted in Figures 2, 4, and 5. Each compound was added at a concentration of 5 mg/L in 100 g/L NaCl solution to simulate reasonable concentrations that may be encountered in actual produced waters [61,81]. As shown in Figure 8a, adding PEGs, ADBAC, 2-BE, and NP to NaCl solution did not affect permeate conductivity in the case of PTFE membrane when compared to the results observed with NaCl solution. Therefore, it can be concluded that none of these compounds were responsible for the increase in permeate conductivity observed with untreated produced water.

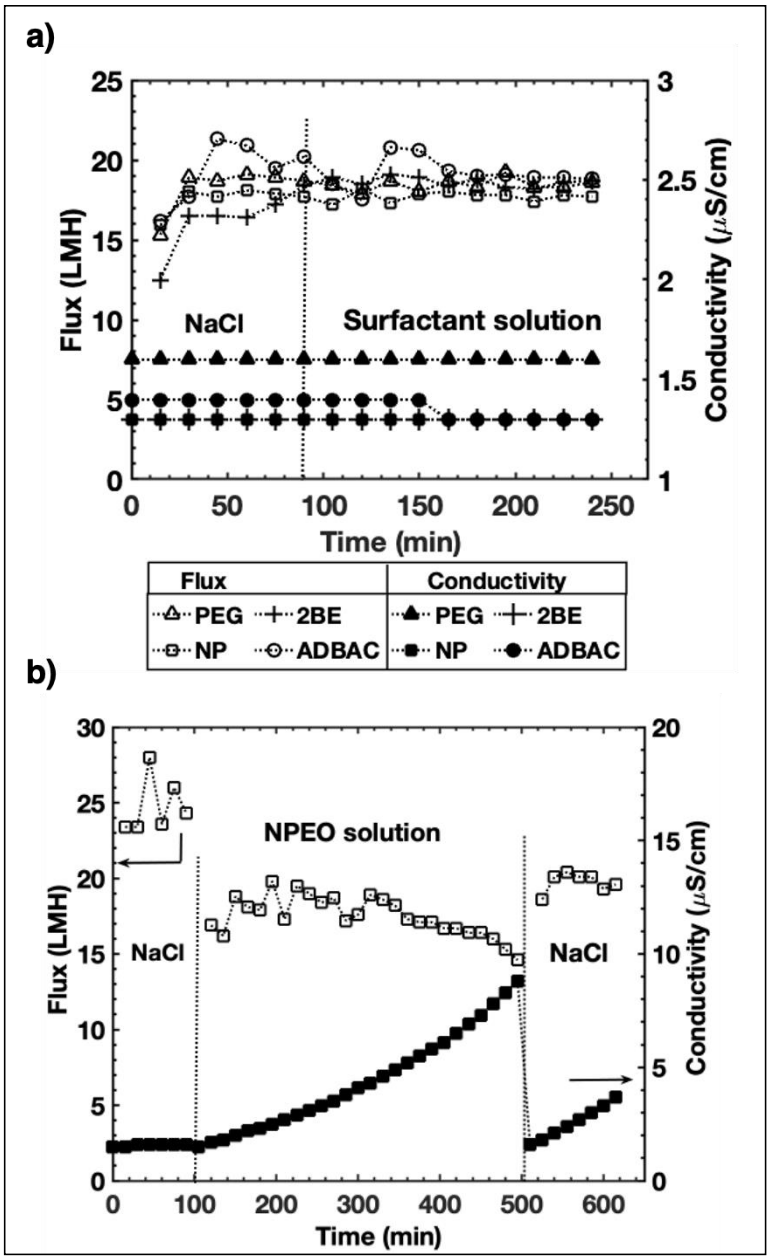


Figure 12. Impact of individual organics on DCMD performance with PTFE membrane in 100 g/L NaCl solution: a) PEG, NP, ADBAC, 2-BE, and b) NPEO

As shown in Figure 12, the increase in permeate conductivity was observed when NPEO was added to NaCl solution on the feed side, suggesting membrane wetting had occurred. NPEOs can act as surfactants, which can change the surface properties of the membrane to reduce the

LEP and lead to membrane wetting. To test the reversibility of wetting caused by NPEOs in the feed, the feed side of the DCMD system was flushed with DI water and pure NaCl solution was used as a feed after 500 min of operation.

Contrary to the behavior observed with raw produced water depicted in Figure 10, an increase in permeate conductivity was observed in the last phase of this test (Figure 8b). Such behavior suggests that the wetting observed in the presence of NPEOs is permanent and cannot be restored by simple flushing with DI water. One possible explanation for this behavior is the adsorption of NPEOs on the membrane that cannot be removed by mere washing with DI water. The difference in the behavior observed with NPEOs in the produced water and that in the synthetic NaCl solution can be due to the difference in NPEO concentration in the produced water or the difference in the number of ethoxylate groups in NPEOs found in the produced water and NPEO purchased for this study. The test with 1 mg/L NPEO, which is much lower than the critical micelle concentration (CMC) of 40 mg/L, showed similar behavior with respect to conductivity increase and permanent change in the membrane characteristics as that shown in Figure 8b. The synthetic solution was prepared with NPEO with an average of ~10 ethoxylate groups, whereas the number of ethoxylate groups present in NPEOs detected in the produced water ranged from 3 to 17 units. The number of ethoxylate groups present in NPEOs determines the Hydrophilic-Lypophilic Balance (HLB) of the surfactant [82] that also governs the surface activity of these compounds. A higher HLB value indicates more hydrophilic surfactant [83]. The NPEOs purchased for these tests had a lower HLB value (~11) than the NPEOs with more ethoxylate units present in the produced water (HLB ranging from 8 to 15) and were able to permanently change the hydrophobicity of the membrane to cause wetting.

DCMD performance with synthetic solutions of volatile salts

Based on the experimental results presented above, it can be concluded that membrane scaling/fouling or low surface tension compounds in the feed solution were not responsible for the observed deterioration in permeate quality when treating produced water from the Permian Basin in TX. The possibility that the increase in permeate conductivity was caused by the transfer of volatile compounds that protonate on the permeate side of the PTFE membrane was tested using 100 g/L NaCl solution containing 500 mg/L of ammonium and acetate salts, which are usually found in hydraulic fracturing fluids [58,84,85]. As shown in Figure 13, the increase in permeate conductivity was observed with ammonium-based salts but not with acetic acid salts. The conductivity did not increase when the solution containing volatile salts was replaced with pure NaCl solution after the module was flushed with DI water, which is identical to the behavior that was observed when treating produced water.

To further confirm the cause of permeate conductivity increase, the DCMD module was used to treat produced water in several cycles. The DCMD module was flushed with DI water between the cycles, and the same produced water was returned to the feed tank. As shown in Figure 13, the increase in conductivity was reduced with each subsequent treatment cycle, which can be explained by the removal of ammonia from the feed side during the previous treatment steps. These results support the hypothesis that the increase in permeate conductivity was due to the transfer of volatile ammonia from the feed side to the permeate side followed by protonation to form an ammonium ion.

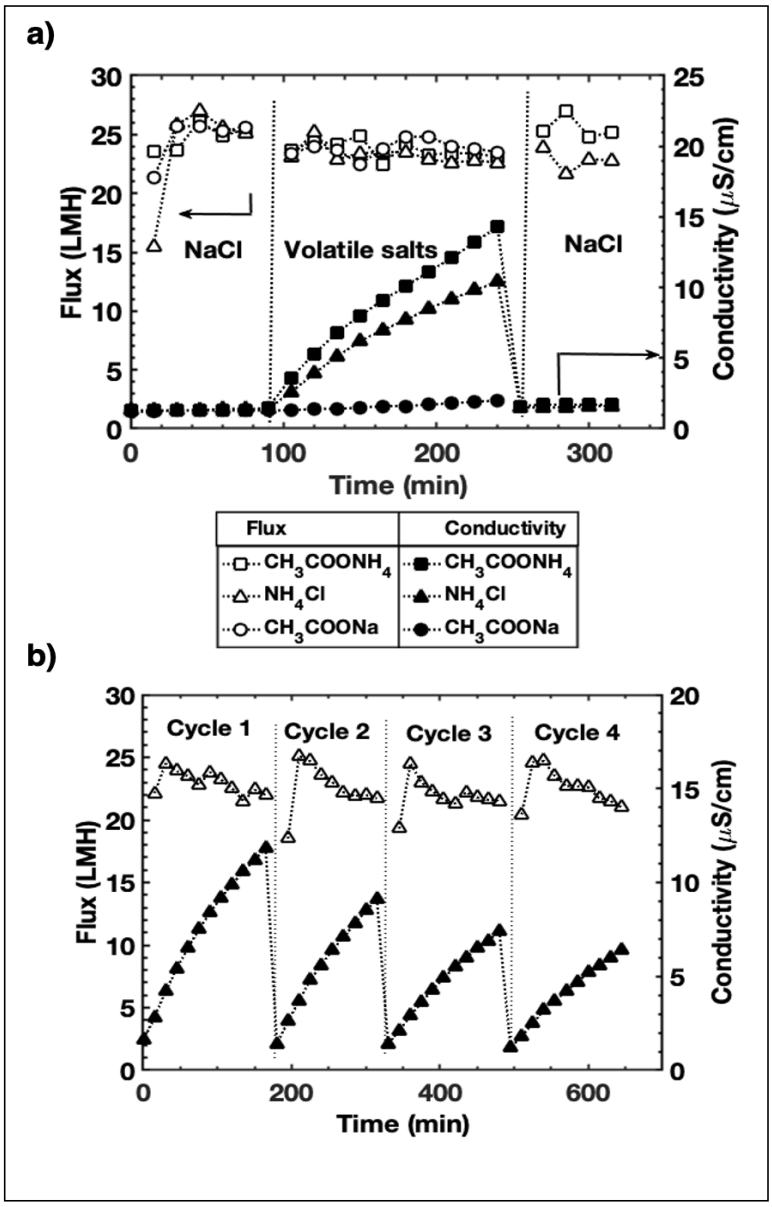


Figure 13. Flux and conductivity with PTFE membrane in DCMD module treating a) synthetic solutions of volatile salts, b) multiple cycles of produced water.

Conclusions

The feasibility of using direct contact membrane distillation (DCMD) for desalination of produced water from the Wolfcamp formation of the Permian Basin in West Texas was evaluated in this study. An increase in permeate conductivity was observed when produced water was treated in the laboratory-scale DCMD module with both PE and PTFE membrane. Membrane scaling/fouling was excluded as the primary reason for the observed increase in permeate conductivity based on the results of extended tests with raw produced water.

Pretreatment of the produced water with biodegradation followed by activated carbon adsorption removed 92% of organic compounds in the produced water but had no impact on permeate quality in DCMD tests conducted with treated produced water. A detailed analysis of organic constituents revealed the presence of nonylphenol ethoxylates (NPEOs), nonylphenol ethoxylate carboxylates (NPECs), and 2-butoxyethoxy acetic acid (2-BE) in both the concentrate and permeate stream of DCMD treating raw produced water. Except for NPEOs, other organics detected in the permeate had no impact on the performance of the DCDM system. While the

membrane wetting observed with the produced water was reversible with DI water flushing, a synthetic solution containing NPEOs caused irreversible wetting of the membrane. The difference in wetting behavior observed with produced and synthetic NPEO solution was not due to the concentration effect but was most likely due to the difference in the number of ethoxylate units present in the NPEOs found in produced water and that available commercially. Testing with ammonium and acetate salts revealed that the permeate conductivity rise was likely due to the passage of volatile salts like ammonia from the feed side to the permeate side followed by protonation to form ionic species in the permeate.

This study shows that membrane distillation can be used for the desalination of produced water from the Permian Basin. The conductivity of the permeate can be a concern if it is due to the passage of salts because of membrane wetting. However, the permeate conductivity due to the presence of ammonium is not a major concern if its concentration remains within the limits for beneficial reuse. The results of this study emphasize the need to develop predictive models for the conductivity increase caused by the passage of volatile components that may be present in the produced water to enable the further application of this technology in the unconventional oil and gas industry.

Pilot scale demonstration

Materials and Methods

Pilot plant design

Table 4. Pilot plant design parameters

Parameters	Value	Units Process Conditions
Circulation/module	1.6	m3/h
T membrane, in	80	°C
T condenser, out	71	°C
T condenser, in	35	°C
T membrane, out	40.6	°C
Salinity at start	98	gr/kg
Recovery req.	50	%
Airgap pressure	550	mbar
T feed	30	°C
Module Parameters		
Area of module modeled	25.9	m2
Envelope length	2.7	m
Flux, calculated	2.4	LMH
Gain output ratio	2.7	--
Spec. Energy consumption	855.7	kJ/kg
Electrical consumption	0.4	kWh/m3
Produced Distillate per module	63.2	L/h
Hydraulic Pressure losses module	175.1	mbar
T distillate estimated	50	°C

Table 5. System specifications

Parameters	Value	Units
Distillate required	113	L/h
Feed	226	L/h
Brine	113	L/h
Feed Salinity	196	gr/kg
Number of modules	2	pcs
Total circulation flow	3.2	m^3/h
Heating HX	27	kW, thermal
Cooling CX	18	kW, thermal

The design and manufacturing of the pilot plant were done by Aquastill, NL. The pilot plant was specifically designed for this project to generate 0.5 gpm permeate from 1 gpm produced water with TDS of approximately 100,000 mg/L (50% water recovery). The design and operating parameters are summarized in Table 4, while system specifications are listed in Table 5.

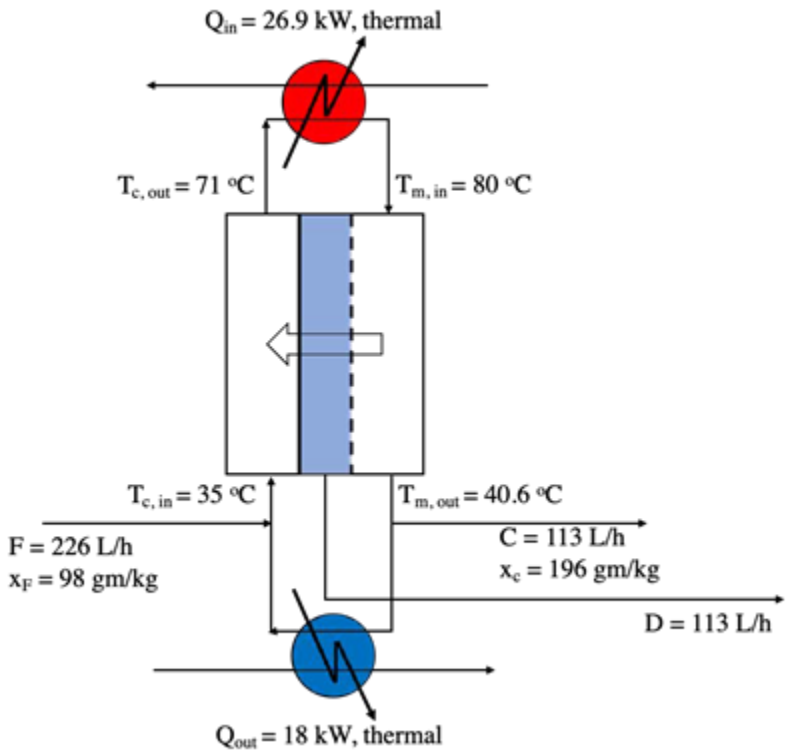


Figure 14. Steady-state heat and mass balance design conditions

The mass and energy balance at steady-state operation is shown in Figure 14.

Pilot plant setup and operation

The pilot plant system is used to produce distillate and concentrated brine from the inlet produced water. The pilot plant consists of four modules with PTFE membrane with PP support, with two modules in operation and 2 as stand by. The membrane modules are spiral wound Air Gap Membrane Distillation (AGMD) modules with approximately 26 m^2 membrane area per module. Figure 15 shows the details of the channels inside the module. The hot brine channel and air gap are separated by the membrane. The air gap is in contact with the cold

brine channel through the condenser. The brine to be treated is circulated in hot and cold brine channels and permeate is obtained in the air gap channel.

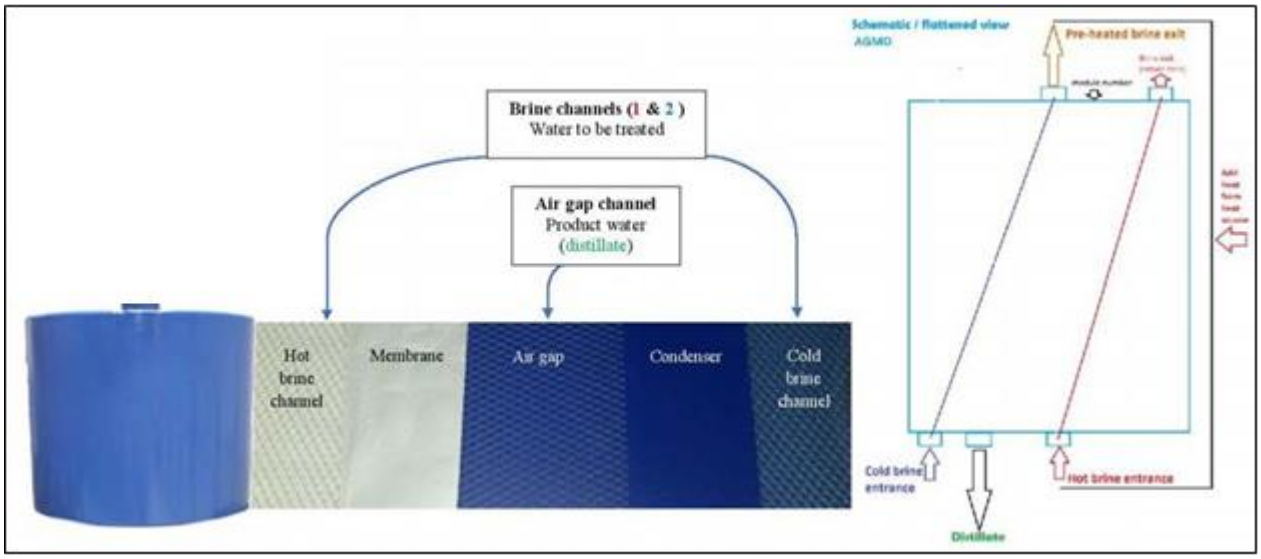


Figure 15. Schematic of membrane module showing channels for hot and cold brine as well for the permeate.

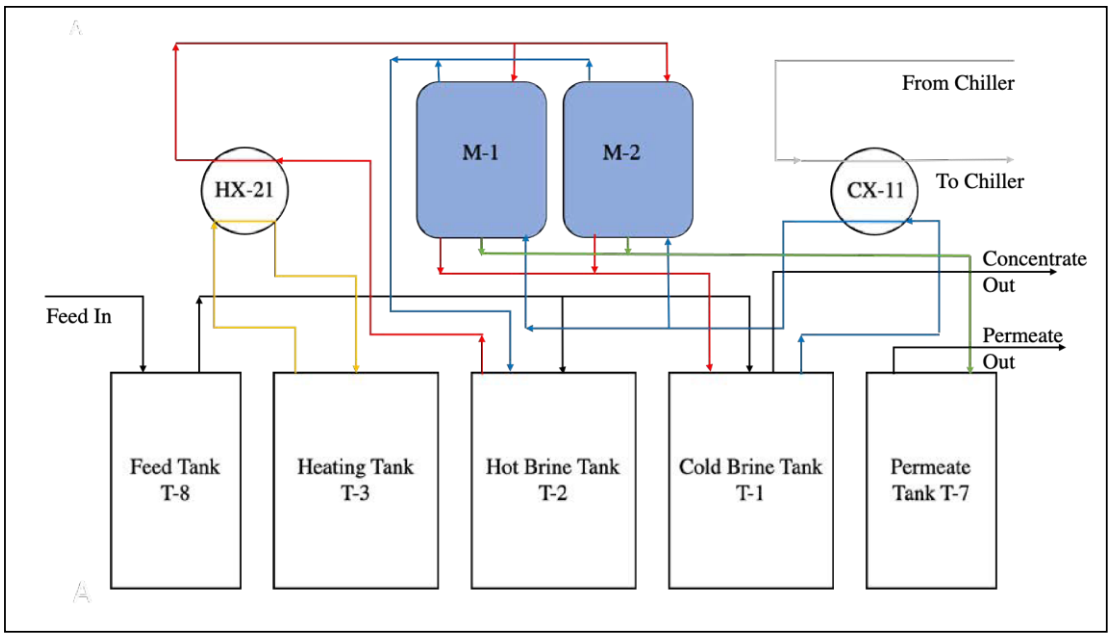


Figure 16. Process flow diagram of the pilot plant system

Figure 16 shows the process flow diagram of the pilot plant system. The pilot plant consists of five tanks; Feed Tank (T-8), Heating Tank (T-3), Hot Brine Tank (T-2), Cold Brine Tank (T-1), and Permeate Tank (T-7). Pretreated produced water is fed in the pilot plant (Tank T-8) using gravity through a water meter for measuring the feed flow rate. Feed from tank T-8 is transferred to tanks T-2 and T-1 using pump P-7(pumps not shown). Autofill mode operation maintains the levels of tanks T-2 and T-1 at desired values. The heating tank is equipped with four 9 kW heating elements to maintain the temperature of the heating tank. The water from the heating tank is circulated through the hot side heat exchanger (HX-21) using pump P-3. The brine from tank T-2 is pumped to the other side of HX-21 using pump P-2. The heated feed from tank T-2 goes through the hot side of the modules and is returned to the tank T-1. At the same time, brine from tank T-1 is pumped through the cold side heat exchanger (CX-11) using pump P-1. The other side of CX-11 circulates cooling fluid (35% Propylene Glycol

Solution) from the chiller. The cooled brine from Tank T-1 is circulated in the cold brine channel of the membrane module and returned to Tank T-2.

Due to the temperature difference between the hot and cold brine channels, vapor transfer occurs across the membrane and these vapors are condensed in the air gap channel. The condensed distillate is sucked from the modules using a vacuum which is generated in the tank T-8 using a submersible pump (P-10) and venturi meter.

The permeate from tank T-8 and concentrate from tank T-1 are pumped out of the pilot plant system using pumps P-8 and P-9, respectively. The number and volume of these discharges were recorded to evaluate the pilot plant performance. The temperatures in the heating tank, permeate tank, and inlet and outlet of both the channels in the module are continuously monitored. Also, the pressure at the inlet and outlet of both the channels in the module and the vacuum line is monitored. In addition, the conductivity of brine inlet from Tank T-1 and permeate from the modules is recorded. The detailed piping and instrumentation diagram can be obtained in Appendix FigureA 2.



Figure 17. Picture of pilot plant system with four modules

The pilot plant can be operated in 'balance mode' or 'feed and bleed mode'. In balance mode, the brine from T-1 is transferred to T-2 through the cold channel in the module while the brine from T-2 is transferred to T-1 through the hot channel in the module. As membrane distillation happens, distillate is produced, and fresh brine is fed to these tanks using autofill mode to maintain the desired levels in all tanks. In the "feed and bleed" mode, the system operates to maintain the brine conductivity at the desired level by removing the concentrate from Tank T-1. To maintain the desired range of concentrate, pump P-9 will pump out the concentrate, and pump P-7 will feed in fresh brine from Tank T-7. The concentrate brine discharge, fresh feed

addition and stabilizing occur in series to maintain the brine conductivity between the desired conductivity values. Figure 17 shows the picture of the pilot plant system.

Pilot plant set-up with pretreatment

Figure 18 shows the schematic of the setup used for the first field trial in West TX conducted during May 23-June 07, 2021. The pilot plant skid is housed in a 20-ft shipping container that was positioned close to two frack tanks. Raw produced water was transferred from the produced water pipeline using a 2" pipe and one frac tank was filled with 20,000 gallons of produced water. The other frack tank was empty, and both permeate and concentrate from the pilot system were transferred to that tank during the system operation.

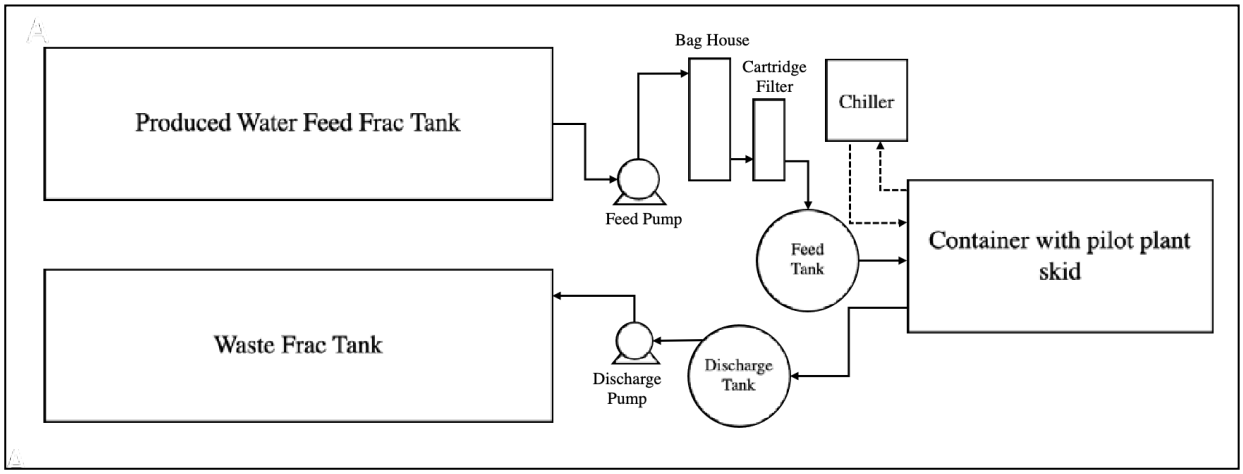


Figure 18. Schematic of pilot plant setup with pretreatment (Trial 1)

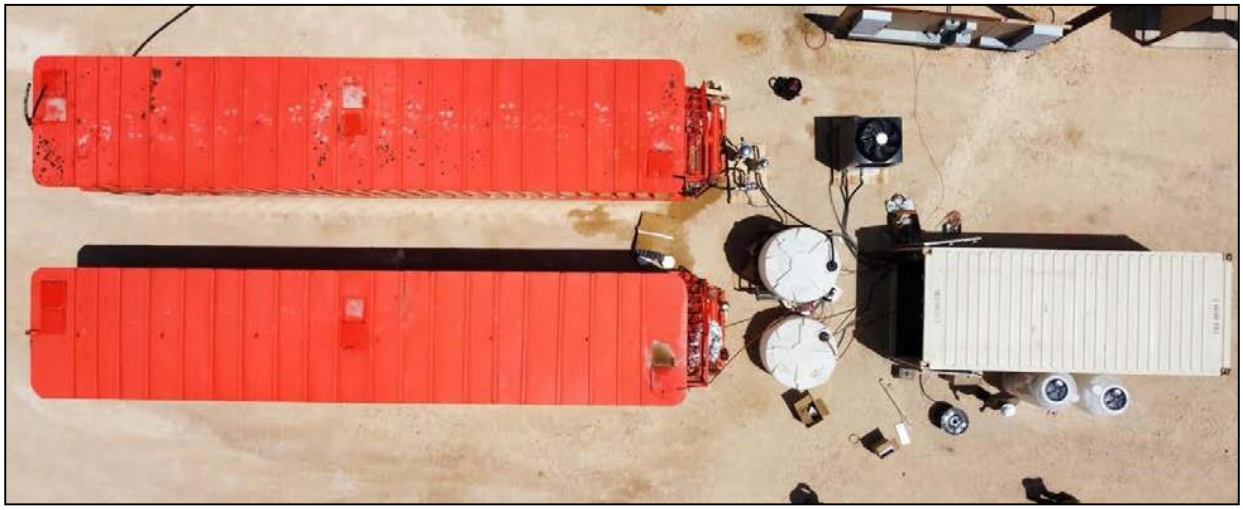


Figure 19. Aerial view of the pilot plant set-up (Trial 1)

Raw produced water from the feed frack tank was filtered through a 25-micron oil absorption baghouse filter (OAS-25-M02E, Filtra-systems, Farmington Hills, MI) followed by the filtration through 0.22-micron polypropylene cartridge filter (FS-PR-0.2-20-226-B, Filtra- systems, Farmington Hills, MI) using a 1 HP 5-stage feed pump (3HM05N07T6PBQE, Xylem Inc., Auburn, NY). The baghouse was used for oil and grease removal and a cartridge filter for the removal of suspended solids. The filtered water was stored in a 500-gallon feed tank and fed to the pilot plant by gravity. After MD, concentrate and permeate from the pilot plant are pumped to the 500-gal discharge tank. The brine from the discharge tank was pumped to the waste frack tank using a 3/4 HP self-priming pump (285E-95, Odessa Pumps, Odessa, TX).

A 10-ton chiller (OPC10-A7, Haskris, Elk Grove Village, IL) was used to meet the cooling needs of the pilot system while a 35% propylene glycol solution was used as a working fluid. Figure 19 shows the aerial view of the treatment system setup used in the first trial.

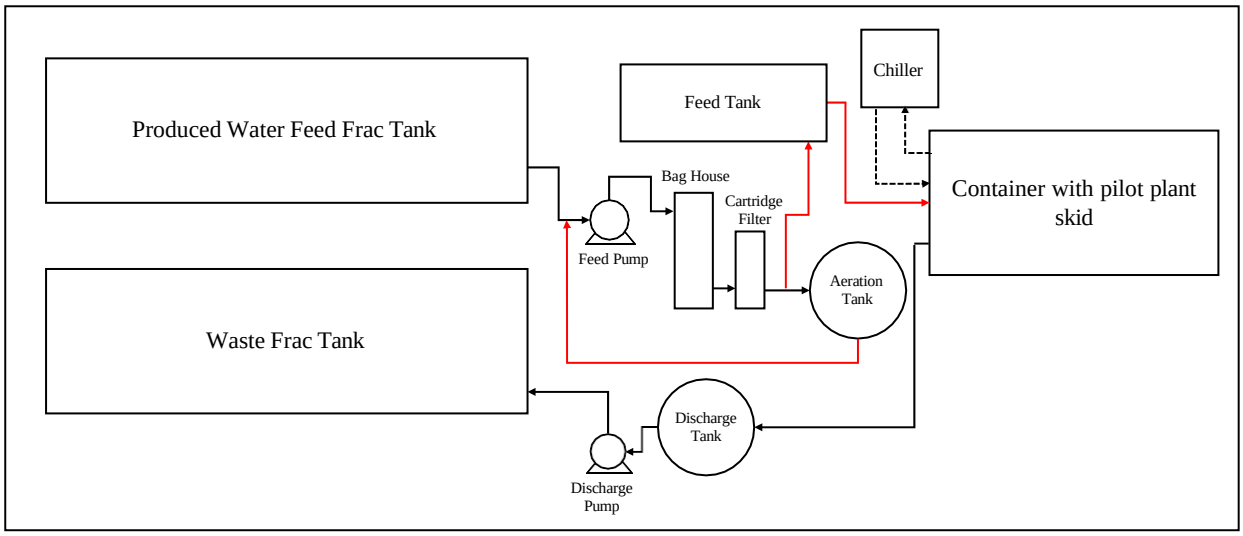


Figure 20. Schematic of pilot plant set-up with pretreatment (Trial 2)



Figure 21. Aerial view of the pilot plant set-up (Trial 2)

Figure 20 shows the schematic of the treatment system setup used for the second trial that was conducted at the same location from September 6-21, 2021. Raw produced water from the feed frack tank was filtered through a 5-micron oil absorption baghouse filter (OAS-5- M02E, Filtra-systems, Farmington Hills, MI) followed by the filtration through 0.45-micron polypropylene cartridge filter (FS-PR-0.45-20-226-B, Filtra-systems, Farmington Hills, MI) using a 1 HP 5-stage feed pump (3HM05N07T6PBQE, Xylem Inc., Auburn, NY). The filtered produced water was stored in a 1,000-gallon 15o conical bottom tank (N-44241, Plastic- Mart.com). The conical bottom tank was equipped with an aeration system which included a 1 HP air compressor (RV100, Gast, Benton Harbor, MI) and 6 rubber membrane air diffusers (RAD2475, Living Water Aeration, Lafayette, LA). Filtered produced water mixed with Barium Chloride Dihydrate (Allan Chemical Corporation, Ringwood, NJ) and Sodium Hydroxide (Duda Energy LLC, Decatur, AL) and aerated for 1 hour to promote barium sulfate precipitation and iron oxidation. The mixture was allowed to settle for 6 hours and the sludge from the conical

bottom tank was transferred to the discharge frack tank using a 3/4 HP pump (368A-98, AMT, Royersford, PA). The supernatant was then filtered through the 5-micron baghouse and 0.45-micron cartridge filter and transferred to a 1000-gallon horizontal feed tank. As mentioned earlier, the concentrate and permeate from the pilot plant were collected in a 1000-gallon vertical discharge tank and then pumped to the waste frack tank. The aerial view of the complete treatment system used in Trial 2 is shown in Figure 21.

Figure 22 shows the aeration step in the 15° conical bottom tank, filtration system, chiller, and feed tank used in the pilot-scale studies.

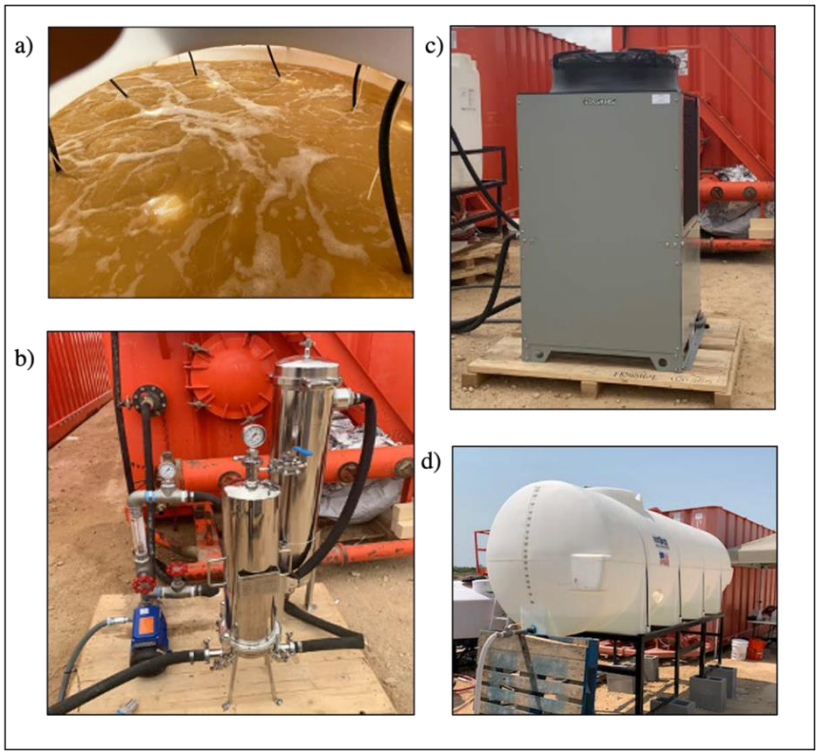


Figure 22. a) Pretreatment using aeration for iron oxidation and barite precipitation, b) filtration system, c) 10-ton chiller for cooling circuit, and d) 1000-gallon horizontal feed tank.

Results and Discussion

Trial 1

The first trial was conducted with only one treatment module with a total membrane area of 26 m^2. During the first part of this trial, the pilot plant was operated in recirculation mode. The hot side module inlet temperature was 60°C and the cold side module inlet temperature was 20°C. Feed conductivity was maintained at 40 mS/cm (~ one-third of TDS in the produced water) and the pilot plant was operated at constant feed concentration.

Figure 23 shows the permeate flux and conductivity over the operating period of 22 h. The average permeate flux obtained during this period was constant at 2.1 LMH. Since the value of the permeate flux was close to that obtained with clean water, it can be concluded that there was no scaling on the membrane. The permeate conductivity started at about 200 mS/cm and decreased to about 100 mS/cm during more than 20 hours of continuous operation. Low permeate conductivity (100-200 ▪ S/cm) indicated 99.5 – 99.8% TDS rejection by PTFE membranes. The pH of permeate increased to ~9.5, which indicated ammonia transfer from the feed side to the permeate side. The observed decrease in permeate conductivity was most

likely due to ammonia stripping from the feed solution during continuous recirculation of the feed in the pilot system. The observed permeate flux and the results shown in Figure 23 suggest that the pilot system was operated according to specifications provided by the manufacturer.

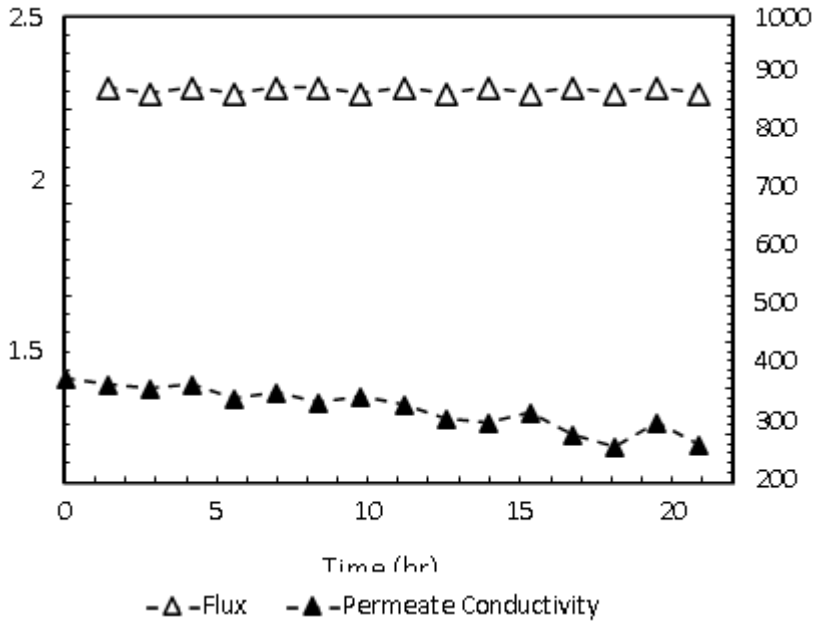


Figure 23. Permeate flux and conductivity using the pilot plant in recirculation mode.

After this initial period, the pilot plant was operated in the feed and bleed mode to achieve the concentrate conductivity of 250 mS/cm, corresponding to 50% water recovery. Figure 24 shows that the permeate flux experienced a continuous decline as the salt concentration in the feed increased. During this period, a continuous increase in permeate conductivity was also observed due to enhanced passage of ammonia from the fresh feed that was continuously added to the system operated in the fed and bleed mode to the permeate side. TDS rejection by the PTFE membrane was continuously above 99.6 %. The permeate flux decline and conductivity increase continued for 26h when the concentrate conductivity reached ~220 mS/cm (Figure 25). The increase in permeate flux observed between 20 and 26 hours of operation was due to the increase in the hot side temperature from 60°C to 75°C while the cold side temperature was always maintained at 20°C.

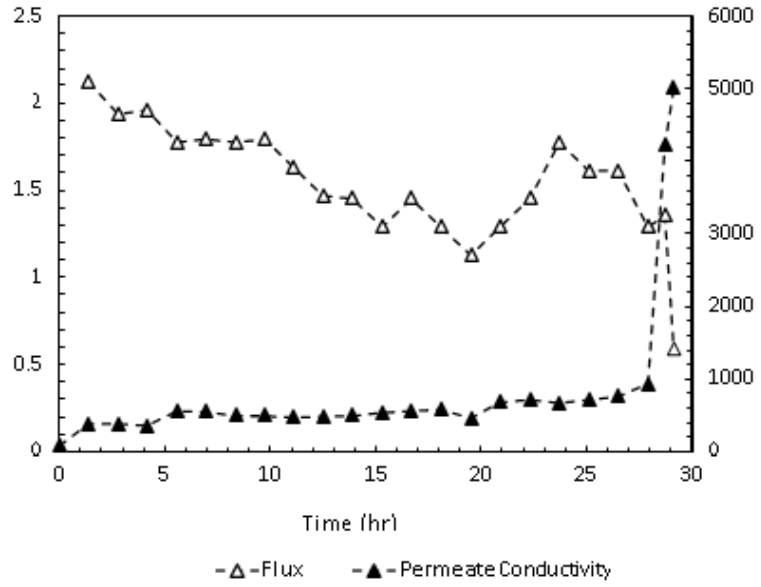


Figure 24. Permeate flux and conductivity during brine concentration in the feed and bleed mode.

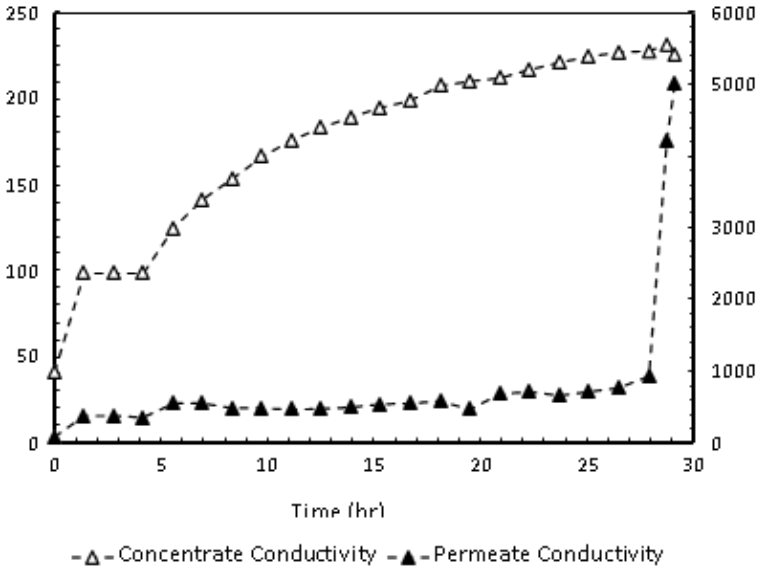


Figure 25. Concentrate and permeate conductivity data during brine concentration in the feed and bleed mode.

After 27 hours of increasing TDS concentration on the feed side, a sudden increase in permeate conductivity was observed. As seen in Figure 24, the observed slow increase in permeate conductivity was accompanied by a continuous decrease in permeate flux. The flux decreased from 1.35 LMH to 0.59 LMH thereby suggesting scale accumulation on the membrane surface. The permeate conductivity increased from about 900 mS/cm to more than 5,000 mS/cm after 27 hours of continuous operation, which suggested that the PTFE membrane was wetted due to scale accumulation. Concentrate conductivity at the end of 27 hours was 235 mS/cm (Figure 25). A sudden and severe increase in the feed side pressure after 27 hours of operation (Figure 26) confirmed severe scale accumulation on the membrane surface. Pilot plant operation was stopped after 28 h of continuous operation due to membrane failure (i.e., scaling and wetting).

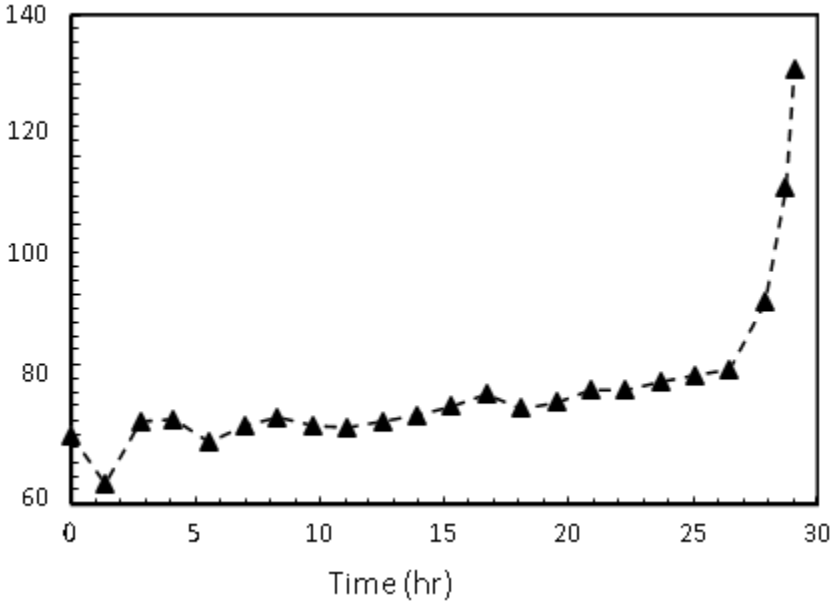


Figure 26. Feed side pressure recorded with an increase in the brine concentration.

The samples that were collected during pilot plant operation were analyzed for major ions and Table 6 shows water quality analysis for samples collected after 26 h of continuous operation. The results in Table 6 suggest produced water feed TDS of ~ 126 gm/L while the concentrate TDS was over 300 mg/L. Water recovery based on these TDS values was 58%, which was greater than the desired value. As seen from Table 6, the concentration of iron in the acidified feed was much higher than in the raw feed, which suggested precipitation of iron oxides and oxyhydroxides inside the pipes, tanks as well as inside the module at the feed at pH of 6.97.

Table 6. Water quality analysis of samples collected during Trial 1

	Acidified Feed	Feed	Acidified Concentrate	Concentrate	Permeate
Ba2+	8	9.5	5.3	4.1	0.01
Ca2+	2548	2252	7197	6925	2.7
Fe	55.3	0.12	66.5	0.02	0.01
K+	298	285	858	888	0.65
Mg2+	368	411	1136	1094	0.64
Na+	39207	39416	104216	102392	50.8
Sr2+	542	540	1281	1233	0.61
Cl-		65288		236856	120.3
SO42-		685		1367	0.88
TDS		126105		302688	253.7

Conductivity		156.6 mS/cm		252.2 mS/cm	773.4 µS/cm
pH		6.97		7.08	8.95

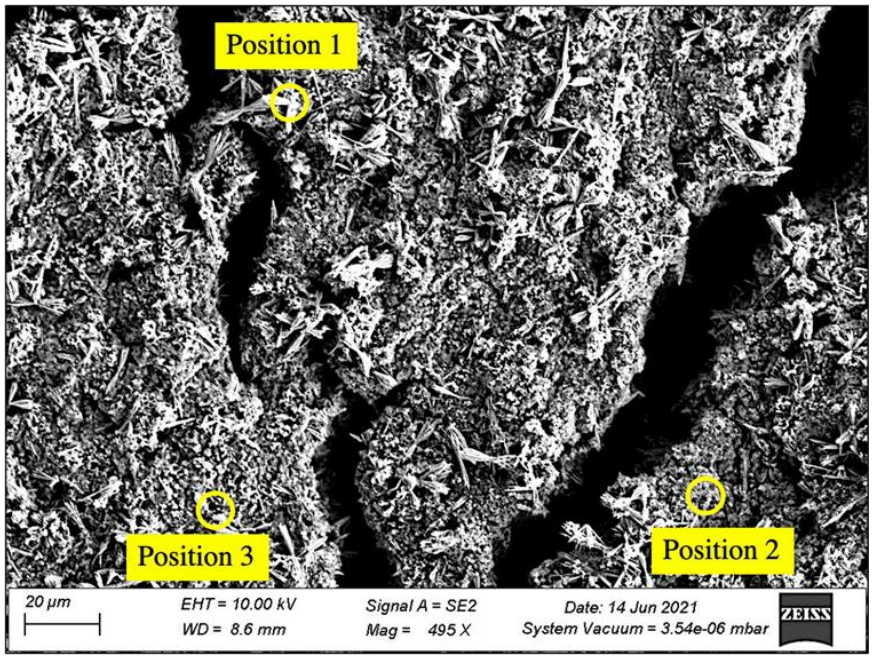


Figure 27. SEM image of the filtered concentrate from Trial 1.

Considering that the concentration polarization coefficient in MD systems can be as high as 1.4, it is highly likely that the ion concentration at the membrane surface was higher than the solubility limits of some inorganic salts, which led to their precipitation on the membrane surface. SEM/EDS analysis of filtered concentrate from Trial 1 shown in Figure 27 indicates predominantly the presence of NaCl, SrSO4, and Iron Oxide at three different locations (Table 7).

To further confirm the reason for scale formation on the membrane, theoretical calculations with PHREEQC chemical speciation software using the bulk composition and concentration polarization coefficient of 1.4 were performed. Figure 28 shows the results of the simulation indicating increased precipitation of solids with an increase in water recovery.

Table 7. Chemical compositions of selected locations (unit: wt.%)

Spectrum Label	Position 1	Position 2	Position 3
O	17.63	13.1	17.92
Na	3.86	29.1	25.24
Mg			
Si		3.83	3.17
S	14.62		0
Cl	7.28	35.58	27.12
K			0.33
Ca	2.65	2.87	3.04
Fe	6.44	15.52	23.18
Sr	44.23		
Ba	3.28		
Total	100	100	100

The simulation results using the bulk composition of the feed show a minimal increase in $SrSO_4$ and $Fe(OH)_3$ precipitation, which most probably would not cause significant membrane scaling and affect its operation. However, results with CPC = 1.4 show that there is a huge increase in NaCl precipitation at ~60% recovery (TDS > 300,000 mg/L) with minor increase in $SrSO_4$ and $Fe(OH)_3$ concentration. Thus, confirming the failure of the membrane with heavy scale formation due to exceedance of the solubility limit for sodium chloride.

Trial 2

Based on the results of Trial 1, on-site pretreatment of produced water was included in Trial 2 to avoid the risk of membrane scaling due to salt precipitation. The produced water from the feed frack tank was transferred to the conical bottom tank after filtering through the 5 mm baghouse and 0.45 mm cartridge filter. As mentioned earlier, filtered produced water was mixed with NaOH to adjust the pH above 8 and promote iron oxidation and BaCl2 to induce sulfate removal through barite precipitation. Raw water was aerated for 1 hour to ensure adequate mixing and complete iron oxidation followed by 6 hours of settling to remove solids formed during this pretreatment step. The settled sludge was transferred to the empty frack tank using the discharge pump while the supernatant was transferred to a 1,000-gallon horizontal feed tank after filtering through the baghouse and cartridge filter. The pretreated produced water feed was fed from the feed tank pilot-plant by gravity while concentrate and distillate (permeate) were collected in a 1,000-gallon vertical discharge tank.

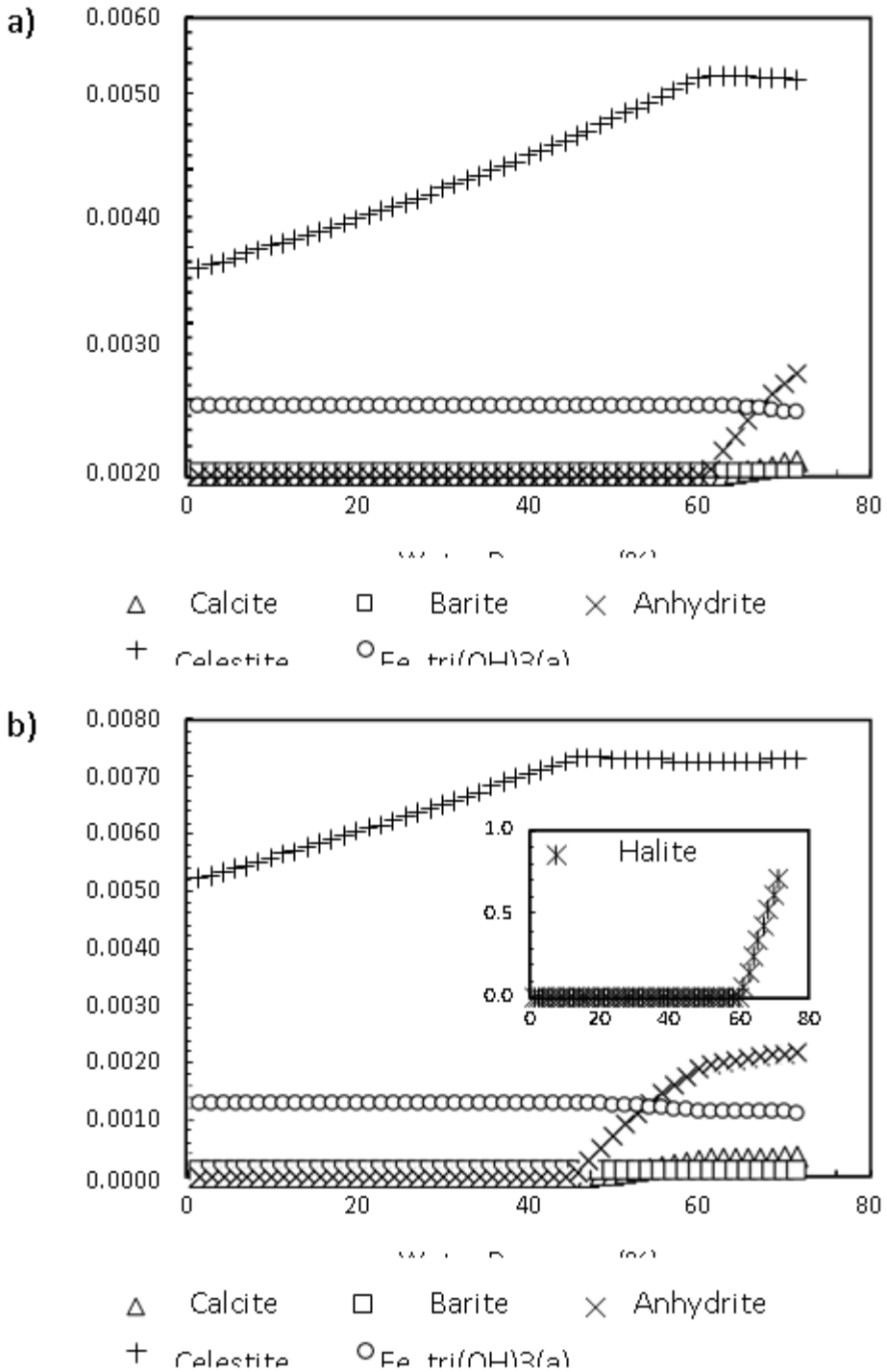


Figure 28. PHREEQC simulations with a) filtered produced water, and b) filtered produced water with CPC = 1.4.

The operating parameters used for the membrane distillation pilot-scale tests are summarized in Table 8. The pilot plant operating parameters chosen for this trial were different from the original design parameters and those used in the first trial to void membrane scaling, adjust for the higher salinities, and obtain higher distillate production rates. The recirculation flow rate chosen was higher than in Trial 1 to avoid scaling of the membrane and to reproduce the laboratory-scale operating parameters.

The initial stage of Trial 2 included the side operation of the pilot plant in the recirculation mode for 12 hours with ~2,000 mg/L synthetic NaCl solution (conductivity = 3.8 mS/cm) as feed. During this test, the permeate conductivity remained low (< 10 mS/cm), indicating proper operation of membrane modules with salt rejection greater than 99.7%. After validating plant

operation with NaCl solution, pretreated produced water was continuously added to the system while permeate was discharged (feed and bleed mode) to achieve a target feed salinity of about 240,000 mg/L, which took about 14 hours. Figure 29 shows the decrease in permeate flux with an increase in feed side concentration due to vapor pressure lowering by TDS increase and continuous permeate conductivity increase due to the passage of the ammonia from the feed side to the permeate side. The concentration of the feed was continued until the TDS on the feed side reached about 235,000 mg/L (conductivity of 200 mS/cm), which represents 47.5 % water recovery. Figure 30 and Figure 31 depict the feed and permeate flow rate during this transition period and feed and permeate conductivity, respectively.

Table 8. Summary table of parameters used in the pilot plant operation.

Parameters	Value	Units
Process Conditions		
T membrane, in	73.1	°C
T condenser, out	62.5	°C
T condenser, in	20.7	°C
T membrane, out	32.1	°C
T feed	30	°C
Module Parameters		
Circulation/module	2.8	m3/h
Area of module	25.9	m2
Number of modules	2	--
Produced Distillate per module	48.8	L/h
Vacuum (airside pressure)	57.1	mbar
Cold side hydraulic pressure loss	100	mbar
Hot side hydraulic pressure loss	165	mbar
System specifications		
Average permeate flux	1.86	LMH
Permeate production rate	97.6	L/h
Feed usage rate	181.7	L/h
Concentrate discharge rate	84.1	L/h
Permeate salinity	0.748	gm/kg
Feed salinity	123	gm/kg
Concentrate salinity	234	gr/kg
Recovery	47.5	%

After concentrating the produced water to the desired value to achieve 47.5% water recovery, the pilot plant was operated in a steady-state mode to maintain these conditions. Figure 32 shows the permeate flux and conductivity for 120 hours of steady-state operation. Permeate flux was virtually constant during this period of operation while the permeate conductivity decreased with time because of the reduction in ammonia concentration in the feed caused by continuous volatilization of ammonia in the feed frack tank. The steady flux and permeate conductivity in the range of 500-600 mS/cm indicate successful long-term operation of MD system in the field to recover high quality permeate that can be reused in industry/agriculture

and reduce the volume of produced water that needs to be disposed of.

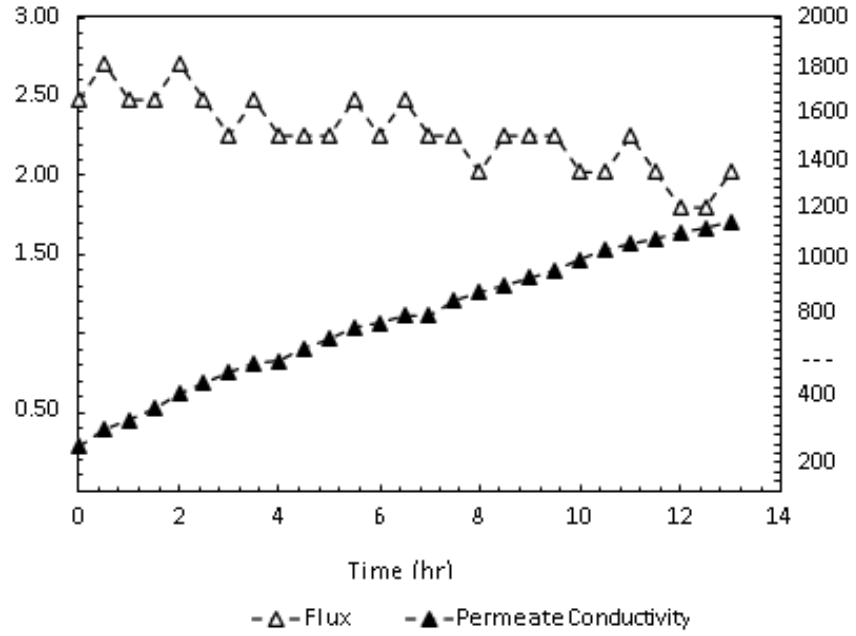


Figure 29. Permeate flux and conductivity witan h increase in the brine concentration.

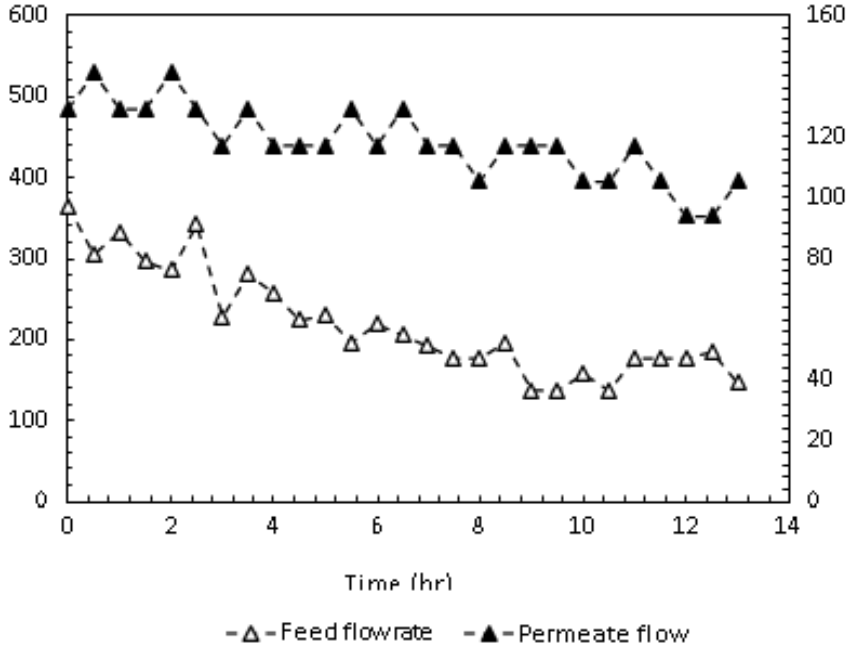


Figure 30. Feed and permeate flow rate with increase in brine concentration.

Table 9 shows water quality analysis of samples collected after 115 h of continuous operation. Pretreatment implemented in the field reduced dissolved iron concentration from 70 mg/L to < 0.1 mg/L and SO42- concentration from 321 mg/L to 191 mg/L. The results in Table 9 confirmed that the pretreated produced water feed had TDS of about 123 g/L while the concentrate TDS was about 234 g/L, thereby indicating 47.5 % water recovery. The permeate TDS of 248 mg/L suggests 99.8% salt rejection by the commercial PTFE membrane used in the pilot system.

The analysis of concentrate samples showed that the divalent ions are not in agreement with theoretical calculations based on the observed water recovery. This discrepancy is most probably due to the precipitation of divalent ions in the system/modules. To further test this

hypothesis, theoretical calculations were performed using PHREEQC. Figure 33 shows the results of the theoretical calculations to assess salt precipitation in the feed with and without considering CPC. The modeling results show likely precipitation of Barite, Calcite, and Anhydrite at ~50% recovery when considering CPC =1.4. These values are very small as compared to the halite concentration predicted for Trial 1 (Figure 28) and would not significantly affect system performance.

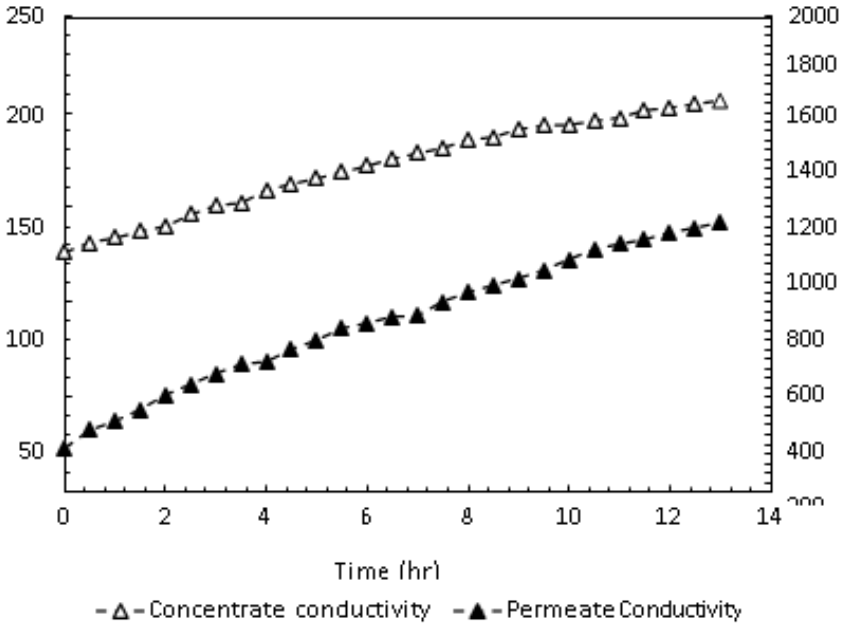


Figure 31. Concentrate and permeate conductivity with an increase in brine concentration.

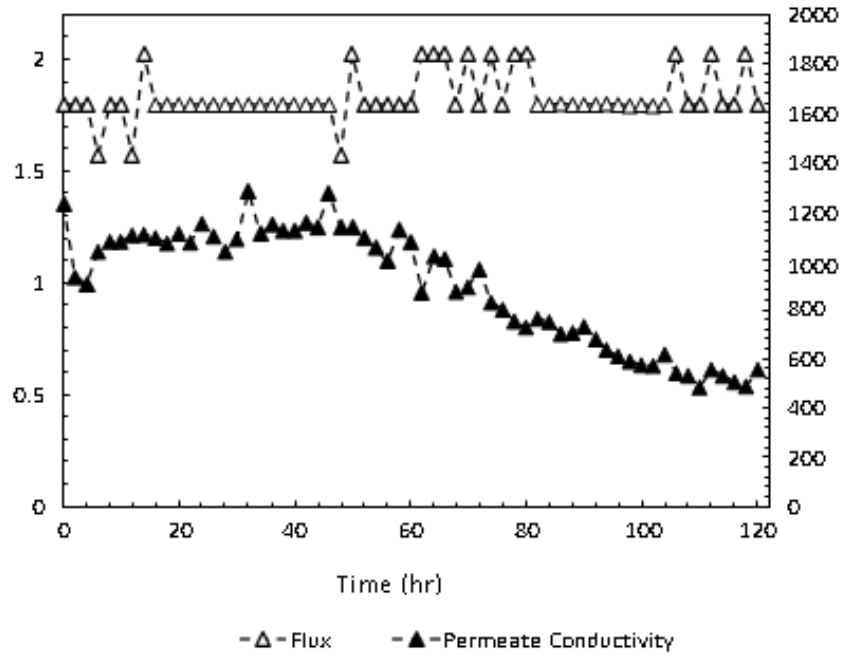


Figure 32. Flux and conductivity data for 120 h of pilot plant operation.

To support this hypothesis, Figure 34 depicts the observed pressure in membrane modules during Trial 2. A negligible increase in module pressure confirms minimal salt accumulation on the membrane surface that did not result in membrane wetting as indicated by permeate conductivity results during Trial 2 shown in Figure 32 (i.e., membrane wetting would have caused a severe increase in permeate conductivity).

Table 9. Analysis results of samples collected from Trial 2.

	Raw Produced Water	Pretreated Produced Water Feed	Concentrate	Permeate
Ba^{2+}	8.1	18.9	21.2	0.0312
Ca^{2+}	2490	2430	3720	4.3
Fe	70	< 0.5	< 1	-
Mg^{2+}	375	418	634	0.92
Mn^{2+}	175	321	802	0
Sr^{2+}	535	497	789	0.99
Cl^-	93100	84900	213000	244
SO_4^{2-}	321	191	334	0.76
Alkalinity as $CaCO_3$	370	299	357	249
Ammonia	190	220	222	61.7
TDS	181000	123000	234000	248
Conductivity	145.5 mS/cm	153.5 mS/cm	240.2 mS/cm	676.4 µS/cm
pH	6.5	8.14	7.53	9.62

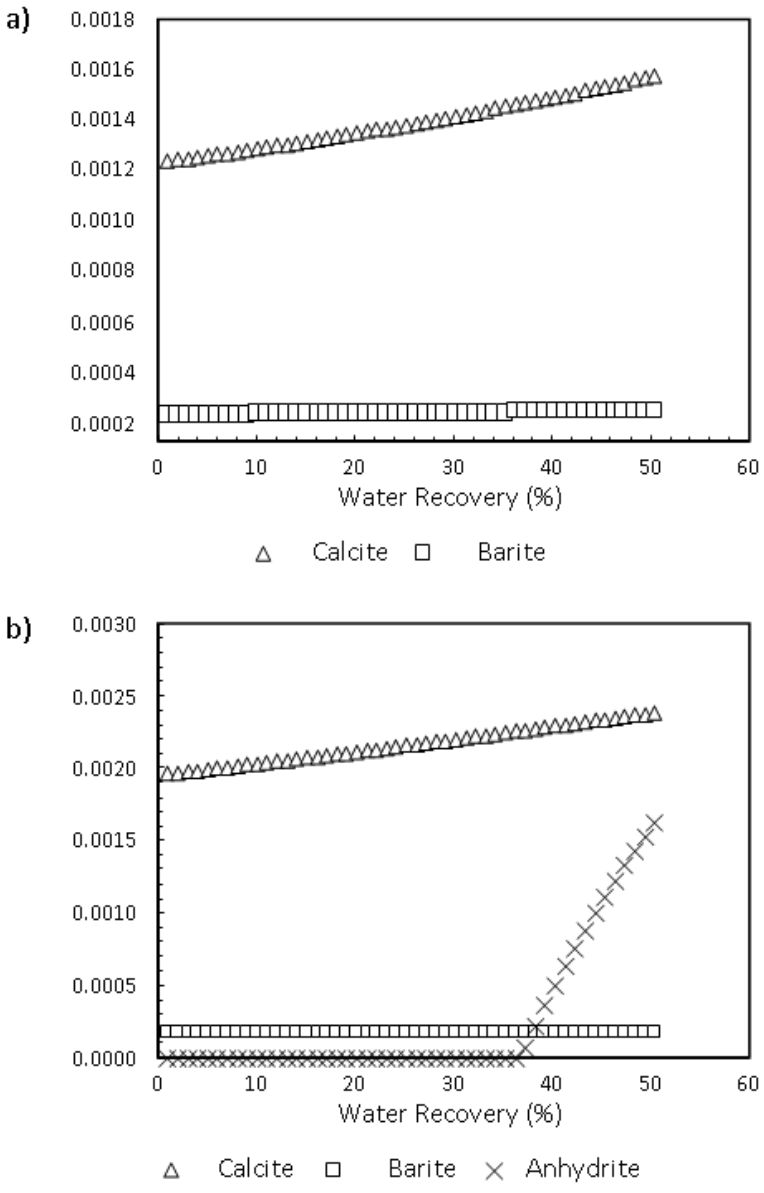


Figure 33. PHREEQC simulations for a) pretreated produced water, b) pretreated produced water considering CPC =1.4.

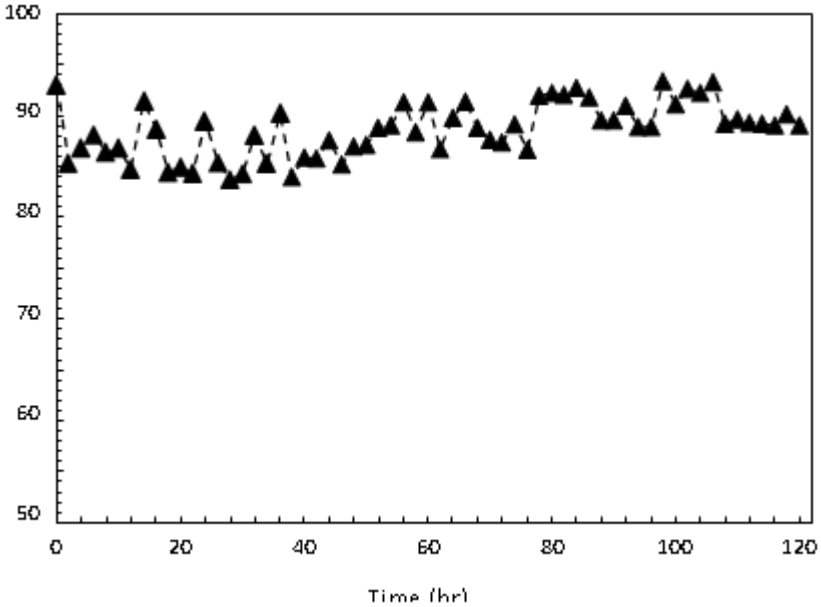


Figure 34. Feed side pressure recorded with constant brine concentration.

Conclusions

The technical feasibility of using membrane distillation for desalination of produced water from the Wolfcamp formation in the Permian Basin in West Texas was evaluated in this study. Treatment of raw produced water by membrane distillation can lead to precipitation of some salts inside the membrane modules (e.g., iron oxyhydroxide, celestite). However, pretreatment of produced water by aeration and barite precipitation, membrane distillation was very effective to ensure a stable operation with 47.5% of the produced water recovered as high-quality permeate suitable for beneficial reuse. The flux of permeate remained constant at 1.86 LMH throughout 120 hours of continuous operation while permeate conductivity was about 500-600 mS/cm. Even though some loss of divalent cations was observed in these tests, there was no permanent scaling of the membrane with any adverse consequences.

Conclusions

This study evaluated technical feasibility of using membrane distillation for desalination of produced water from the unconventional reservoirs in Permian Basin, Western Texas. Laboratory scale studies showed that membrane distillation can be used to recover 50% of high-quality permeate from the produced water with a TDS of 123 g/L. An increase in permeate conductivity observed in the laboratory-scale DCMD module was due to the passage of ammonia from the feed side to the permeate side followed by protonation to ammonium ion. The permeate flux remained constant indicating no scaling/fouling of the membrane during the long-term laboratory tests.

Based on a successful laboratory-scale experiments, a pilot-scale system to achieve 50% water recovery when treating 1 gpm of produced water was deployed to Permian Basin in West Texas. The pilot plant was first operated using produced water without any chemical pretreatment. Permian Basin produced water subjected to filtration through 25 mm baghouse and 0.22 mm cartridge filter can lead to precipitation of some salts in the system depending on their solubility limits. However, chemical pretreatment using pH adjustment, aeration, and barite precipitation, resulted in successful steady-state operation of the pilot system for 5 days

where the produced water was concentrated from 123,000 mg/L to 234,000 mg/L (47.5% water recovery) while recovering high quality permeate suitable for industrial/agricultural use. This study demonstrated the operation a of commercial PTFE membrane with a steady flux of 1.86 LMH for 120 hours with 99.7% ion rejection from the feed. Successful demonstration of MD technology under realistic fed conditions offers additional management strategies for produced water generated by the unconventional oil and gas industry to reduce its water footprint.

Like most membrane processes, MD can be easily scaled-up to full-scale applications to treat high salinity wastewaters from oil and gas industry. However, membrane modules used for longer time can experience wear and tear due to continuous use as well as scaling and fouling when treating high salinity brines. Thus, membrane modules might require cleaning at regular intervals and replacement in case of leakage or physical damage. Further application of MD technology for produced water treatment would also require pilot-scale studies that are conducted for a longer period (i.e., months). These tests would provide a better idea of the membrane cleaning requirements and will be used to validate the initial operating cost estimates. Also, these long-term tests would provide insights into continuously operating MD system with produced water of variable quality and quantity. This enhanced pilot-scale testing should be done using many membrane modules (e.g., several tens) operating in parallel to demonstrate system performance at a larger scale (e.g., feed flowrate of 25 gpm). In addition, it would be necessary to optimize pretreatment process for continuous and reliable operation for each produced water quality that may be encountered in the field to enable further penetration of MD technology into oil and gas industry.

References

[1] H. Chang, T. Li, B. Liu, R.D. Vidic, M. Elimelech, J.C. Crittenden, Potential and implemented membrane-based technologies for the treatment and reuse of flowback and produced water from shale gas and oil plays: A review, Desalination. 455 (2019) 34–57. https://doi.org/10.1016/j.desal.2019.01.001.

[2] A.L. Mitchell, D.S. Tkacik, J.R. Roscioli, S.C. Herndon, T.I. Yacovitch, D.M. Martinez, T.L. Vaughn, L.L. Williams, M.R. Sullivan, C. Floerchinger, M. Omara, R. Subramanian, D. Zimmerle, A.J. Marchese, A.L. Robinson, Measurements of methane emissions from natural gas gathering facilities and processing plants: Measurement results, Environ. Sci. Technol. 49 (2015) 3219–3227. https://doi.org/10.1021/es5052809.

[3] A.T. Dale, V. Khanna, R.D. Vidic, M.M. Bilec, Process based life-cycle assessment of natural gas from the marcellus shale, Environ. Sci. Technol. 47 (2013) 5459– 5466. https://doi.org/10.1021/es304414q.

[4] R.B. Jackson, A. Vengosh, T.H. Darrah, N.R. Warner, A. Down, R.J. Poreda, S.G. Osborn, K. Zhao, J.D. Karr, Increased stray gas abundance in a subset of drinking water wells near Marcellus shale gas extraction, Proc. Natl. Acad. Sci. U. S. A. 110 (2013) 11250– 11255. https://doi.org/10.1073/pnas.1221635110.

[5] G.T. Llewellyn, F. Dorman, J.L. Westland, D. Yoxtheimer, P. Grieve, T. Sowers, E. Humston-Fulmer, S.L. Brantley, Evaluating a groundwater supply contamination incident attributed to Marcellus Shale gas development, Proc. Natl. Acad. Sci. U. S. A. 112 (2015) 6325–6330.

https://doi.org/10.1073/pnas.1420279112.

[6] E. Mielke, L. Diaz Anadon, V. Narayanamurti, Water Consumption of Energy Resource Extraction, Processing, and Conversion, A review of the literature for estimates of water intensity of energy-resource extraction, processing to fuels and conversion to electricity, Energy Technol. Innov. Policy Discuss. Pap. (2010). http://belfercenter.ksg.harvard.edu/%5C-files/ETIP-DP-2010-15-final-4.pdf.

[7] D.J. Soeder, S. Sharma, N. Pekney, L. Hopkinson, R. Dilmore, B. Kutchko, B. Stewart, K. Carter, A. Hakala, R. Capo, An approach for assessing engineering risk from shale gas wells in the United States, Int. J. Coal Geol. 126 (2014) 4–19. https://doi.org/10.1016/j.coal.2014.01.004.

[8] K.B. Gregory, R.D. Vidic, D.A. Dzombak, Water management challenges associated with the production of shale gas by hydraulic fracturing, Elements. 7 (2011) 181–

186. https://doi.org/10.2113/gselements.7.3.181.

[9] R.D. Vidic, S.L. Brantley, J.M. Vandenbossche, D. Yoxtheimer, J.D. Abad, Impact of shale gas development on regional water quality, Science (80-.). 340 (2013). https://doi.org/10.1126/science.1235009.

[10] K.B. Gregory, R.D. Vidic, D.A. Dzombak, Water management challenges associated with the production of shale gas by hydraulic fracturing, Elements. 7 (2011) 181–

186. https://doi.org/10.2113/gselements.7.3.181.

[11] L.O. Haluszczak, A.W. Rose, L.R. Kump, Geochemical evaluation of flowback brine from Marcellus gas wells in Pennsylvania, USA, Appl. Geochemistry. 28 (2013) 55–61. https://doi.org/10.1016/j.apgeochem.2012.10.002.

[12] E. Barbot, N.S. Vidic, K.B. Gregory, R.D. Vidic, Spatial and temporal correlation of water quality parameters of produced waters from Devonian-age shale following hydraulic fracturing, Environ. Sci. Technol. 47 (2013) 2562–2569. https://doi.org/10.1021/es304638h.

[13] D.L. Shaffer, L.H. Arias Chavez, M. Ben-Sasson, S. Romero-Vargas Castrillón,

N.Y. Yip, M. Elimelech, Desalination and reuse of high-salinity shale gas produced water: Drivers, technologies, and future directions, Environ. Sci. Technol. 47 (2013) 9569–9583. https://doi.org/10.1021/es401966e.

[14] Y. Hedar, Budiyono, Pollution Impact and Alternative Treatment for Produced Water, E3S Web Conf. 31 (2018) 1–12. https://doi.org/10.1051/e3sconf/20183103004.

[15] J. Veil, U . S . Produced Water Volumes and Management Practices in 2012, US. Prod. WaternManag.(2015)

[16] J. Veil, V. Environmental, U . S . Produced Water Volumes and Management Practices in, Gr. Water Res. Educ. Found. (2020).

[17] B.R. Scanlon, R.C. Reedy, F. Male, M. Walsh, Water Issues Related to Transitioning from Conventional to Unconventional Oil Production in the Permian Basin, Environ. Sci. Technol. 51 (2017) 10903–10912. https://doi.org/10.1021/acs.est.7b02185.

[18] B.R. Scanlon, R.C. Reedy, P. Xu, M. Engle, J.P. Nicot, D. Yoxtheimer, Q. Yang, S. Ikonnikova,

Can we beneficially reuse produced water from oil and gas extraction in the U.S.?, Sci. Total Environ. 717 (2020) 137085. https://doi.org/10.1016/j.scitotenv.2020.137085.

[19] K. Guerra, K. Dahm, S. Dundorf, Oil and Gas Produced Water Management and Beneficial Use in the Western United States, U.S. Dep. Inter. Bur. Reclamation, Manag. Water West. (2011) 129. http://www.usbr.gov/research/AWT/reportpdfs/report157.pdf.

[20] Z. Anari, A. Sengupta, K. Sardari, S.R. Wickramasinghe, Surface modification of PVDF membranes for treating produced waters by direct contact membrane distillation, Sep. Purif. Technol. 224 (2019) 388–396. https://doi.org/10.1016/j.seppur.2019.05.032.

[21] A. Butkovskyi, H. Bruning, S.A.E. Kools, H.H.M. Rijnaarts, A.P. Van Wezel, Organic Pollutants in Shale Gas Flowback and Produced Waters: Identification, Potential Ecological Impact, and Implications for Treatment Strategies, Environ. Sci. Technol. 51 (2017) 4740–4754. https://doi.org/10.1021/acs.est.6b05640.

[22] O.R. Lokare, S. Tavakkoli, S. Wadekar, V. Khanna, R.D. Vidic, Fouling in direct contact membrane distillation of produced water from unconventional gas extraction, J. Memb. Sci. 524 (2017) 493–501. https://doi.org/10.1016/j.memsci.2016.11.072.

[23] J. Slutz, J. Anderson, R. Broderick, P. Horner, Key shale gas water management strategies: An economic assessment tool, Soc. Pet. Eng. - SPE/APPEA Int. Conf. Heal. Saf. Environ. Oil Gas Explor. Prod. 2012 Prot. People Environ. - Evol. Challenges. 3 (2012) 2343– 2357. https://doi.org/10.2118/157532-repeat-ms.

[24] S. Mondal, S.R. Wickramasinghe, Produced water treatment by nanofiltration and reverse osmosis membranes, J. Memb. Sci. 322 (2008) 162–170. https://doi.org/10.1016/j.memsci.2008.05.039.

[25] U.K. Kesieme, N. Milne, H. Aral, C.Y. Cheng, M. Duke, Economic analysis of desalination technologies in the context of carbon pricing, and opportunities for membrane distillation, Desalination. 323 (2013) 66–74. https://doi.org/10.1016/j.desal.2013.03.033.

[26] T. Mezher, H. Fath, Z. Abbas, A. Khaled, Techno-economic assessment and environmental impacts of desalination technologies, Desalination. 266 (2011) 263–273. https://doi.org/10.1016/j.desal.2010.08.035.

[27] G.P. Thiel, E.W. Tow, L.D. Banchik, H.W. Chung, J.H. Lienhard V, Energy consumption in desalinating produced water from shale oil and gas extraction, Desalination. 366 (2015) 94–112. https://doi.org/10.1016/j.desal.2014.12.038.

[28] A. Subramani, J.G. Jacangelo, Emerging desalination technologies for water treatment: A critical review, Water Res. 75 (2015) 164–187. https://doi.org/10.1016/j.watres.2015.02.032.

[29] K.W. Lawson, D.R. Lloyd, Membrane distillation, 124 (1997) 1–25.

[30] L.M. Camacho, L. Dumée, J. Zhang, J. de Li, M. Duke, J. Gomez, S. Gray, Advances in membrane distillation for water desalination and purification applications, Water (Switzerland). 5 (2013) 94–196. https://doi.org/10.3390/w5010094.

[31] A. Alkhudhiri, N. Darwish, N. Hilal, Produced water treatment: Application of Air Gap Membrane Distillation, Desalination. 309 (2013) 46–51.

https://doi.org/10.1016/j.desal.2012.09.017.

[32] B. Li, K.K. Sirkar, Novel membrane and device for direct contact membrane distillation-based desalination process, Ind. Eng. Chem. Res. 43 (2004) 5300–5309. https://doi.org/10.1021/ie030871s.

[33] T.Y. Cath, V.D. Adams, A.E. Childress, Experimental study of desalination using direct contact membrane distillation: A new approach to flux enhancement, J. Memb. Sci. 228 (2004) 5–16. https://doi.org/10.1016/j.memsci.2003.09.006.

[34] A.M.M. Shirazi, c r v i h o e f c r v i h o e f, 17 (2011) 28–36.

[35] M. Xie, L.D. Nghiem, W.E. Price, M. Elimelech, A forward osmosis-membrane distillation hybrid process for direct sewer mining: System performance and limitations, Environ. Sci. Technol. 47 (2013) 13486–13493. https://doi.org/10.1021/es404056e.

[36] M. Gryta, K. Karakulski, A.W. Morawski, Purification of oily wastewater by hybrid UF/MD, Water Res. 35 (2001) 3665–3669. https://doi.org/10.1016/S0043-1354(01)00083-5.

[37] V.V.U.I.B.V. and V.N.N. P.P. Zolotarev, Karpov Physico-Chemical Research Institute, ul. Obukha 10. Moscow 103064. Russia, J. Hazard. Mater. 37 (1994) 77–82.

[38] M. Khayet, Treatment of radioactive wastewater solutions by direct contact membrane distillation using surface modified membranes, Desalination. 321 (2013) 60–66. https://doi.org/10.1016/j.desal.2013.02.023.

[39] Z. Zhang, O.R. Lokoare, A. V Gusa, R.D. Vidic, Pretreatment of brackish water reverse osmosis (BWRO) concentrate to enhance water recovery in inland desalination plants by direct contact membrane distillation (DCMD), Desalination. 508 (2021) 115050. https://doi.org/10.1016/j.desal.2021.115050.

[40] S.T. Hsu, K.T. Cheng, J.S. Chiou, Seawater desalination by direct contact membrane distillation, Desalination. 143 (2002) 279–287. https://doi.org/10.1016/S0011-9164(02)00266-7.

[41] X. Ji, E. Curcio, S. Al Obaidani, G. Di Profio, E. Fontananova, E. Drioli, Membrane distillation-crystallization of seawater reverse osmosis brines, Sep. Purif. Technol. 71 (2010) 76–82. https://doi.org/10.1016/j.seppur.2009.11.004.

[42] J. Kujawa, E. Guillen-Burrieza, H.A. Arafat, M. Kurzawa, A. Wolan, W. Kujawski, Raw Juice Concentration by Osmotic Membrane Distillation Process with Hydrophobic Polymeric Membranes, Food Bioprocess Technol. 8 (2015) 2146–2158. https://doi.org/10.1007/s11947-015-1570-4.

[43] U.K. Kesieme, N. Milne, C.Y. Cheng, H. Aral, M. Duke, Recovery of water and acid from leach solutions using direct contact membrane distillation, Water Sci. Technol. 69 (2014) 868–875. https://doi.org/10.2166/wst.2013.788.

[44] A.A. Hassan, H. Adel Jabbar, Direct Contact Membrane Distillation for Separation of Hcl From A Mixture of Acids, J. Eng. 24 (2018) 41. https://doi.org/10.31026/j.eng.2018.06.04.

[45] H. Julian, Y. Ye, H. Li, V. Chen, Scaling mitigation in submerged vacuum membrane distillation and crystallization (VMDC) with periodic air-backwash, J. Memb. Sci. 547 (2018) 19–33. https://doi.org/10.1016/j.memsci.2017.10.035.

[46] X. Du, Z. Zhang, K.H. Carlson, J. Lee, T. Tong, Membrane fouling and reusability in membrane distillation of shale oil and gas produced water: Effects of membrane surface wettability, J. Memb. Sci. 567 (2018) 199–208. https://doi.org/10.1016/j.memsci.2018.09.036.

[47] X. Wen, F. Li, B. Jiang, X. Zhang, X. Zhao, Effect of surfactants on the treatment of radioactive laundry wastewater by direct contact membrane distillation, J. Chem. Technol. Biotechnol. 93 (2018) 2252–2261. https://doi.org/10.1002/jctb.5568.

[48] H. Chang, B. Liu, Z. Zhang, R. Pawar, Z. Yan, J.C. Crittenden, R.D. Vidic, A Critical Review of Membrane Wettability in Membrane Distillation from the Perspective of Interfacial Interactions, Environ. Sci. Technol. (2021). https://doi.org/10.1021/acs.est.0c05454.

[49] M. Gryta, Long-term performance of membrane distillation process, J. Memb. Sci. 265 (2005) 153–159. https://doi.org/10.1016/j.memsci.2005.04.049.

[50] S. Goh, J. Zhang, Y. Liu, A.G. Fane, Fouling and wetting in membrane distillation (MD) and MD-bioreactor (MDBR) for wastewater reclamation, Desalination. 323 (2013) 39–47. https://doi.org/10.1016/j.desal.2012.12.001.

[51] Z. Wang, S. Lin, Membrane fouling and wetting in membrane distillation and their mitigation by novel membranes with special wettability, Water Res. 112 (2017) 38–47. https://doi.org/10.1016/j.watres.2017.01.022.

[52] O.R. Lokare, Direct Contact Membrane Distillation for Desalination Brine Solution, J. Eng. 24 (2018) 18. https://doi.org/10.31026/j.eng.2018.11.02.

[53] R.G. Raluy, R. Schwantes, V.J. Subiela, B. Peñate, G. Melián, J.R. Betancort, Operational experience of a solar membrane distillation demonstration plant in Pozo Izquierdo- Gran Canaria Island (Spain), Desalination. 290 (2012) 1–13. https://doi.org/10.1016/j.desal.2012.01.003.

[54] J. Koschikowski, M. Wieghaus, M. Rommel, V.S. Ortin, B.P. Suarez, J.R. Betancort Rodríguez, Experimental investigations on solar driven stand-alone membrane distillation systems for remote areas, Desalination. 248 (2009) 125–131. https://doi.org/10.1016/j.desal.2008.05.047.

[55] H.C. Duong, A.R. Chivas, B. Nelemans, M. Duke, S. Gray, T.Y. Cath, L.D. Nghiem, Treatment of RO brine from CSG produced water by spiral-wound air gap membrane distillation - A pilot study, Desalination. 366 (2015) 121–129. https://doi.org/10.1016/j.desal.2014.10.026.

[56] J. Minier-Matar, A. Hussain, A. Janson, F. Benyahia, S. Adham, Field evaluation of membrane distillation technologies for desalination of highly saline brines, Desalination. 351 (2014) 101–108. https://doi.org/10.1016/j.desal.2014.07.027.

[57] R. Schwantes, K. Chavan, D. Winter, C. Felsmann, J. Pfafferott, Techno- economic comparison of membrane distillation and MVC in a zero liquid discharge application, Desalination. 428 (2018) 50–68. https://doi.org/10.1016/j.desal.2017.11.026.

[58] A.Z. Rodriguez, H. Wang, L. Hu, Y. Zhang, P. Xu, Treatment of produced water in the permian basin for hydraulic fracturing: Comparison of different coagulation processes and innovative filter media, Water (Switzerland). 12 (2020). https://doi.org/10.3390/w12030770.

[59] D.E. Freedman, Biologically Active Filtration for Treatment of Produced Water and

Fracturing Flowback Wastewater in the O&G Industry, J. Chem. Inf. Model. 53 (1970) 1689–1699.

[60] S. Jiménez, M. Andreozzi, M.M. Micó, M.G. Álvarez, S. Contreras, Produced water treatment by advanced oxidation processes, Sci. Total Environ. 666 (2019) 12–21. https://doi.org/10.1016/j.scitotenv.2019.02.128.

[61] F. Ricceri, M. Giagnorio, G. Farinelli, G. Blandini, M. Minella, D. Vione, A. Tiraferri, Desalination of Produced Water by Membrane Distillation: Effect of the Feed Components and of a Pre-treatment by Fenton Oxidation, Sci. Rep. 9 (2019) 1–12. https://doi.org/10.1038/s41598-019-51167-z.

[62] P.R. Gogate, A.B. Pandit, A review of imperative technologies for wastewater treatment I: Oxidation technologies at ambient conditions, Adv. Environ. Res. 8 (2004) 501–551. https://doi.org/10.1016/S1093-0191(03)00032-7.

[63] E.M. Thurman, I. Ferrer, J. Blotevogel, T. Borch, Analysis of hydraulic fracturing flowback and produced waters using accurate mass: Identification of ethoxylated surfactants, Anal. Chem. 86 (2014) 9653–9661. https://doi.org/10.1021/ac502163k.

[64] M.C. McLaughlin, T. Borch, J. Blotevogel, Spills of Hydraulic Fracturing Chemicals on Agricultural Topsoil: Biodegradation, Sorption, and Co-contaminant Interactions, Environ. Sci. Technol. 50 (2016) 6071–6078. https://doi.org/10.1021/acs.est.6b00240.

[65] A.J. Hanson, J.L. Luek, S.S. Tummings, M.C. McLaughlin, J. Blotevogel, P.J. Mouser, High total dissolved solids in shale gas wastewater inhibit biodegradation of alkyl and nonylphenol ethoxylate surfactants, Sci. Total Environ. 668 (2019) 1094–1103. https://doi.org/10.1016/j.scitotenv.2019.03.041.

[66] K. Smolders, A.C.M. Franken, Terminology for Membrane Distillation, Desalination. 72 (1989) 249–262. https://doi.org/10.1016/0011-9164(89)80010-4.

[67] T. Zhang, K. Gregory, R.W. Hammack, R.D. Vidic, Co-precipitation of radium with barium and strontium sulfate and its impact on the fate of radium during treatment of produced water from unconventional gas extraction, Environ. Sci. Technol. 48 (2014) 4596– 4603. https://doi.org/10.1021/es405168b.

[68] M. Rezaei, D.M. Warsinger, J.H. Lienhard V, M.C. Duke, T. Matsuura, W.M. Samhaber, Wetting phenomena in membrane distillation: Mechanisms, reversal, and prevention, Water Res. 139 (2018) 329–352. https://doi.org/10.1016/j.watres.2018.03.058.

[69] D.M. Warsinger, J. Swaminathan, E. Guillen-Burrieza, H.A. Arafat, J.H. Lienhard V, Scaling and fouling in membrane distillation for desalination applications: A review, Desalination. 356 (2015) 294–313. https://doi.org/10.1016/j.desal.2014.06.031.

[70] M.R. Choudhury, N. Anwar, D. Jassby, M.S. Rahaman, Fouling and wetting in the membrane distillation driven wastewater reclamation process – A review, Adv. Colloid Interface Sci. 269 (2019) 370–399. https://doi.org/10.1016/j.cis.2019.04.008.

[71] Z. Wang, Y. Chen, X. Sun, R. Duddu, S. Lin, Mechanism of pore wetting in membrane distillation with alcohol vs. surfactant, J. Memb. Sci. 559 (2018) 183–195. https://doi.org/10.1016/j.memsci.2018.04.045.

[72] N. Dow, S. Gray, J. de Li, J. Zhang, E. Ostarcevic, A. Liubinas, P. Atherton, G. Roeszler, A. Gibbs, M. Duke, Pilot trial of membrane distillation driven by low grade waste heat: Membrane fouling and energy assessment, Desalination. 391 (2016) 30–42. https://doi.org/10.1016/j.desal.2016.01.023.

[73] J.M. Winglee, N. Bossa, D. Rosen, J.T. Vardner, M.R. Wiesner, Modeling the Concentration of Volatile and Semivolatile Contaminants in Direct Contact Membrane Distillation (DCMD) Product Water, Environ. Sci. Technol. 51 (2017) 13113–13121. https://doi.org/10.1021/acs.est.6b05663.

[74] M. Gryta, Influence of polypropylene membrane surface porosity on the performance of membrane distillation process, J. Memb. Sci. 287 (2007) 67–78. https://doi.org/10.1016/j.memsci.2006.10.011.

[75] M. Gryta, Separation of saline oily wastewater by membrane distillation, Chem. Pap. 74 (2020) 2277–2286. https://doi.org/10.1007/s11696-020-01071-y.

[76] G. Naidu, S. Jeong, S.J. Kim, I.S. Kim, S. Vigneswaran, Organic fouling behavior in direct contact membrane distillation, Desalination. 347 (2014) 230–239. https://doi.org/10.1016/j.desal.2014.05.045.

[77] D. Kekacs, B.D. Drollette, M. Brooker, D.L. Plata, P.J. Mouser, Aerobic biodegradation of organic compounds in hydraulic fracturing fluids, Biodegradation. 26 (2015) 271–287. https://doi.org/10.1007/s10532-015-9733-6.

[78] E. Olkowska, M. Ruman, Z. Polkowska, Occurrence of surface active agents in the environment, J. Anal. Methods Chem. 2014 (2014). https://doi.org/10.1155/2014/769708.

[79] R. Chen, J.J. Pignatello, Role of quinone intermediates as electron shuttles in fenton and photoassisted fenton oxidations of aromatic compounds, Environ. Sci. Technol. 31 (1997) 2399–2406. https://doi.org/10.1021/es9610646.

[80] Y. Yin, N. Jeong, T. Tong, The effects of membrane surface wettability on pore wetting and scaling reversibility associated with mineral scaling in membrane distillation, J. Memb. Sci. 614 (2020) 118503. https://doi.org/10.1016/j.memsci.2020.118503.

[81] C. Boo, J. Lee, M. Elimelech, Omniphobic Polyvinylidene Fluoride (PVDF) Membrane for Desalination of Shale Gas Produced Water by Membrane Distillation, Environ. Sci. Technol. 50 (2016) 12275–12282. https://doi.org/10.1021/acs.est.6b03882.

[82] J.M. Green, Effect of Nonylphenol Ethoxylation on the Biological Activity of Three Herbicides with Different Water Solubilities Author (s): Jerry M . Green Published by : Cambridge University Press on behalf of the Weed Science Society of America Stable URL : https, 13 (1999) 840–842.

[83] R.A. Frazier, Physical Chemistry of Foods, 2004. https://doi.org/10.1016/s0308-8146(03)00246-2.

[84] K.M. Heyob, J. Blotevogel, M. Brooker, M. V. Evans, J.J. Lenhart, J. Wright, R. Lamendella, T. Borch, P.J. Mouser, Natural Attenuation of Nonionic Surfactants Used in Hydraulic Fracturing Fluids: Degradation Rates, Pathways, and Mechanisms, Environ. Sci. Technol. 51 (2017) 13985–13994. https://doi.org/10.1021/acs.est.7b01539.

[85] M. Yao, Y.C. Woo, L.D. Tijing, J.S. Choi, H.K. Shon, Effects of volatile organic compounds on water recovery from produced water via vacuum membrane distillation, Desalination. 440 (2018) 146–155. https://doi.org/10.1016/j.desal.2017.11.012.

Appendix

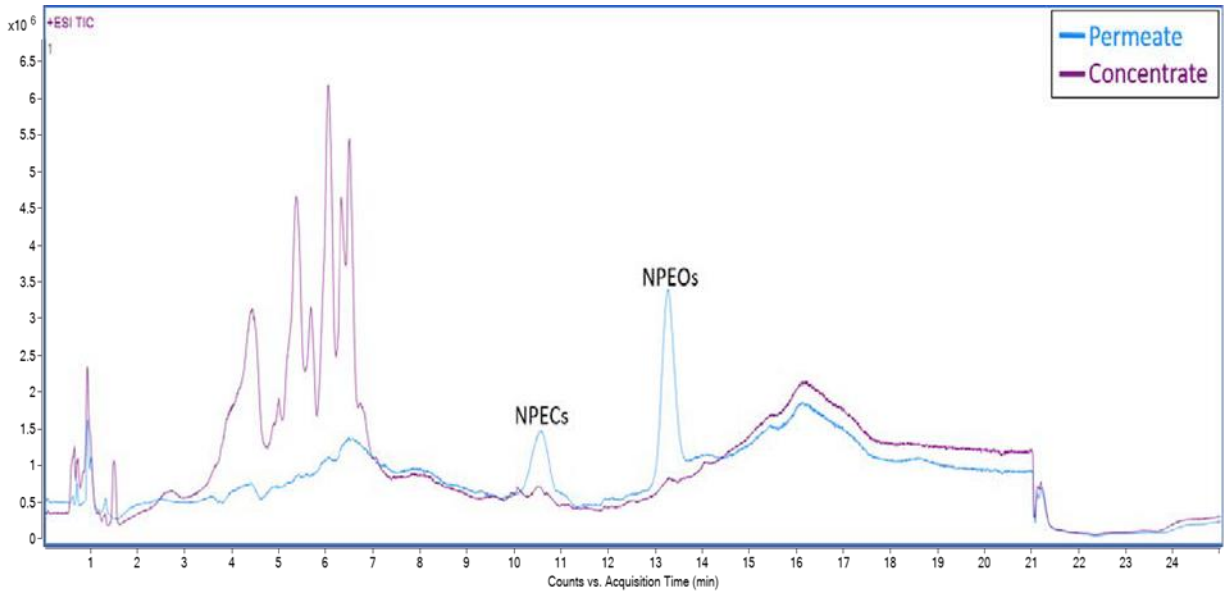
Appendix A. Experimental data

TableA 1. LC-QToF-MS information for tentatively identified compounds detected in the untreated produced water.

Name	Formula	Major adduct	Observed m/z	Theoretical m/z	Error (ppm)
2-BE	C8 H16 O4	[M+H]+	177.112	177.1122	-1.13
ADBAC-C10	C21 H38 N	[M+H]+	305.3097	305.3109	-3.93
PEG-EO9	C18 H38 O10	[M+NH4]+	432.282	432.2803	3.93
PEG-EO10	C20 H42 O11	[M+NH4]+	476.3077	476.3065	2.52
PEG-EO11	C22 H46 O12	[M+NH4]+	520.3342	520.3328	2.69
PEG-EO13	C26 H54 O14	[M+Na]+	613.3419	613.3406	2.12
PEG-EO14	C28 H58 O15	[M+Na]+	657.3679	657.3668	1.67
PEG-EO15	C30 H62 O16	[M+Na]+	701.394	701.3930	1.43
PEG-EO16	C32 H66 O17	[M+Na]+	745.4199	745.4173	3.46
PEG-EO18	C36 H74 O19	[M+Na]+	833.4725	833.4695	3.58
PEG-EO19	C38 H78 O20	[M+Na]+	877.4986	877.4956	3.40
PEG-EO22	C44 H90 O23	[M+Na]+	1009.5766	1009.5739	2.66
PEG-EO23	C46 H94 O24	[M+Na]+	1053.6031	1053.6000	2.93
PPG-4PO	C12 H26 O5	[M+Na]+	273.1675	273.1672	1.10
PPG-5PO	C15 H32 O6	[M+Na]+	331.2104	331.2091	3.92
PPG-6PO	C18 H38 O7	[M+Na]+	389.2523	389.2510	3.34
PPG-7PO	C21 H44 O8	[M+Na]+	447.2923	447.2928	-1.12
PPG-8PO	C24 H50 O9	[M+Na]+	505.3348	505.3347	0.20
PPG-9PO	C27 H56 O10	[M+NH4]+	558.4203	558.4212	-1.61
PPG-11PO	C33 H68 O12	[M+NH4]+	674.5027	674.5049	-3.26

PPG-12PO	C36 H74 O13	[M+NH4]+	732.5475	732.5468	0.96
PPG-13PO	C39 H80 O14	[M+NH4]+	790.5885	790.5886	-0.13
C8-EO11	C30 H62 O12	[M+NH4]+	632.4561	632.4562	-0.19
C8-EO12	C32 H66 O13	[M+NH4]+	676.4815	676.4823	-1.22
OP-EO4	C22 H38 O5	[M+Na]+	405.2625	405.2601	5.88
OP-EO6	C26 H46 O7	[M+NH4]+	488.3602	488.3569	6.71
OP-EO7	C28 H50 O8	[M+NH4]+	532.386	532.3830	5.59
OP-EO8	C30 H54 O9	[M+NH4]+	576.4113	576.4091	3.78
OP-EO9	C32 H58 O10	[M+NH4]+	620.4378	620.4352	4.15
OP-EO10	C34 H62 O11	[M+NH4]+	664.4651	664.4613	5.68
OP-EO11	C36 H66 O12	[M+NH4]+	708.4912	708.4874	5.33
OP-EO12	C38 H70 O13	[M+NH4]+	752.5175	752.5135	5.28
OP-EO13	C40 H74 O14	[M+NH4]+	796.5436	796.5396	4.99
OP-EO14	C42 H78 O15	[M+NH4]+	840.5709	840.5657	6.16
OP-EO15	C44 H82 O16	[M+NH4]+	884.5974	884.5918	6.30
OP-EO16	C46 H86 O17	[M+NH4]+	928.6209	928.6179	3.21
OP-EO17	C48 H90 O18	[M+NH4]+	972.6472	972.6440	3.27
NP-EO3	C21 H36 O4	[M+Na]+	375.2517	375.2506	2.93
NP-EO4	C23 H40 O5	[M+Na]+	419.2783	419.2768	3.58
NP-EO5	C25 H44 O6	[M+NH4]+	458.3486	458.3476	2.18
NP-EO6	C27 H48 O7	[M+NH4]+	502.3762	502.3738	4.78
NP-EO7	C29 H52 O8	[M+NH4]+	546.4021	546.4000	3.84
NP-EO8	C31 H56 O9	[M+NH4]+	590.428	590.4263	2.88
NP-EO10	C35 H64 O11	[M+NH4]+	678.4813	678.4787	3.83
NP-EO11	C37 H68 O12	[M+NH4]+	722.5059	722.5049	1.38

NP-EO12	C39 H72 O13	[M+NH4]+	766.5327	766.5311	2.09
NP-EO13	C41 H76 O14	[M+NH4]+	810.5585	810.5573	1.48
NP-EO14	C43 H80 O15	[M+NH4]+	854.586	854.5835	2.93
NP-EO15	C45 H84 O16	[M+NH4]+	898.6109	898.6098	1.22
NP-EO16	C47 H88 O17	[M+NH4]+	942.6372	942.6335	3.90
NP-EO17	C49 H92 O18	[M+Na]+	991.6207	991.6150	5.73

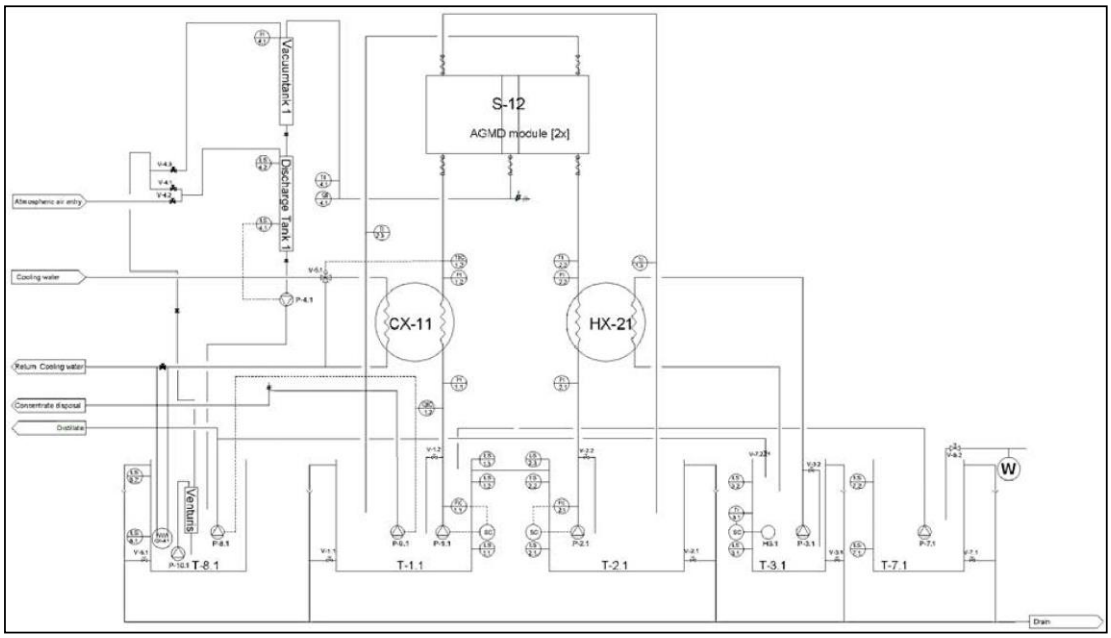


FigureA 1. Total ion chromatogram (TIC) obtained under positive electrospray ionization for the concentrated feed (purple) and permeate (blue) from biodegraded + adsorbed produced water experiment (Figure 4). The relative abundances of the most predominant surfactant.

TableA 2. LC-QToF-MS information for tentatively identified compounds detected in the permeate.

Name	Formula	Major adduct	Observed m/z	Theoretical m/z	Error (ppm)
2-BE	C8 H16 O4	[M+H]+	177.1124	177.1122	1.13
NPEC-EO5	C25 H42 O7	[M+NH4]+	472.3278	472.3257	4.40
NPEC-EO6	C27 H46 O8	[M+NH4]+	516.3543	516.3518	4.80
NPEC-EO7	C29 H50 O9	[M+NH4]+	560.3806	560.3779	4.78
NPEC-EO8	C31 H54 O10	[M+NH4]+	604.4068	604.4040	4.59

NPEC-EO9	C33 H58 O11	[M+NH4]+	648.4328	648.4301	4.13
NPEC-EO10	C35 H62 O12	[M+NH4]+	692.4588	692.4562	3.72
NPEC-EO11	C37 H66 O13	[M+NH4]+	736.4847	736.4823	3.23
NPEC-EO12	C39 H70 O14	[M+NH4]+	780.5107	780.5084	2.92
NPEC-EO13	C41 H74 O15	[M+NH4]+	824.5366	824.5345	2.52
NPEC-EO14	C43 H78 O16	[M+NH4]+	868.5625	868.5606	2.16
NP-EO4	C23 H40 O5	[M+NH4]+	414.3223	414.3214	2.17
NP-EO5	C25 H44 O6	[M+NH4]+	458.3487	458.3476	2.40
NP-EO6	C27 H48 O7	[M+NH4]+	502.3751	502.3738	2.59
NP-EO7	C29 H52 O8	[M+NH4]+	546.4015	546.4000	2.75
NP-EO8	C31 H56 O9	[M+NH4]+	590.4277	590.4263	2.37
NP-EO9	C33 H60 O10	[M+NH4]+	634.4538	634.4525	2.05
NP-EO10	C35 H64 O11	[M+NH4]+	678.4801	678.4787	2.06
NP-EO11	C37 H68 O12	[M+NH4]+	722.5061	722.5049	1.66
NP-EO12	C39 H72 O13	[M+NH4]+	766.532	766.5311	1.17
NP-EO13	C41 H76 O14	[M+NH4]+	810.5577	810.5573	0.49
NP-EO14	C43 H80 O15	[M+NH4]+	854.5836	854.5835	0.12
NP-EO15	C45 H84 O16	[M+NH4]+	898.6092	898.6098	-0.67
NP-EO16	C47 H88 O17	[M+NH4]+	942.6349	942.6335	1.46
NP-EO17	C49 H92 O18	[M+NH4]+	986.6609	986.6596	1.29



FigureA 2. PID Diagram of the pilot-scale system.

Appendix F: Forecasting of Benefits of Membrane Distillation in the Treatment of Produced Water for Beneficial Use

Research Entity: GTI Energy

Final Report Benefits forecast for membrane distillation, December 6, 2021

Prepared by Tom Hayes, Blaine Severin

Legal Notice

This information was prepared by Gas Technology Institute (“GTI”) for NETL-DOE.

Neither GTI, the members of GTI, the Sponsor(s), nor any person acting on behalf of any of them:

a. Makes any warranty or representation, express or implied with respect to the accuracy, completeness, or usefulness of the information contained in this report, or that the use of any information, apparatus, method, or process disclosed in this report may not infringe privately-owned rights. Inasmuch as this project is experimental in nature, the technical information, results, or conclusions cannot be predicted. Conclusions and analysis of results by GTI represent GTI's opinion based on inferences from measurements and empirical relationships, which inferences and assumptions are not infallible, and with respect to which competent specialists may differ.

b. Assumes any liability with respect to the use of, or for any and all damages resulting from the use of, any information, apparatus, method, or process disclosed in this report; any other use of, or reliance on, this report by any third party is at the third party's sole risk.

c. The results within this report relate only to the items tested.

Acknowledgment

"This material is based upon work supported by the Department of Energy under Award Number DE-FE0024292."

Disclaimer: "This report was prepared as an account of work sponsored by an agency of the United States Government. Neither the United States Government nor any agency thereof, nor any of their employees, makes any warranty, express or implied, or assumes any legal liability or responsibility for the accuracy, completeness, or usefulness of any information, apparatus, product, or process disclosed, or represents that its use would not infringe privately owned rights. Reference herein to any specific commercial product, process, or service by trade name, trademark, manufacturer, or otherwise does not necessarily constitute or imply its endorsement, recommendation, or favoring by the United States Government or any agency thereof. The views and opinions of authors expressed herein do not necessarily state or reflect those of the United States Government or any agency thereof."

Executive Summary

In the past two decades, the United States has seen a rapid growth of unconventional oil and gas exploration and production that has come about from energy obtained from the successful development of the shale across the U.S. During hydraulic fracturing activities, large volumes of freshwater along with fracturing fluids (including proppant and polyacrylamide friction reducers) are injected under high pressure to fracture the underlying shale strata to stimulate hydrocarbon generation which is accompanied by a concomitant production of substantial amounts of wastewater or “produced water” containing hydrocarbons and elevated concentrations of salts including heavy metals and radioactive materials. Currently, the nearly 1 million producing wells in the United States generate approximately 24.4 billion barrels of produced water each year or about 2.8 billion gallons per day; much of this production occurs

in the areas of the U.S. that are water stressed. In these areas, there is growing interest in technologies that can economically process produced water to generate demineralized water streams suitable for beneficial use. Effective treatment that demineralizes produced water and removes hazardous components at treatment efficiencies that are protective of human health and environment at a reasonable cost will be critical to achieve if produced water is to be beneficially reused.

Membrane distillation (MD) has emerged as a promising technology for the renovation of produced water for the generation of demineralized water supplies that are suitable for beneficial use in agriculture and industry. Direct contact membrane distillation or DCMD is a hybrid thermal membrane desalination in which a partial vapor pressure difference established between the heated feed water and the cold permeate stream drives the transport of water vapor across a microporous and hydrophobic membrane. An ASPEN Plus simulation of DCMD was used to optimize the design and operation of commercial scale systems and estimate the energy requirements of the DCMD process. (Lokare, et al.). The testing and optimization of this process treating actual produced water from shale wells has been the focus of the current work performed by the University of Pittsburgh. This development effort has included extensive laboratory testing as well as scaleup and pilot testing of the DCMD process at a shale wellfield managed by Laredo Petroleum. In parallel with this effort, GTI and Environmental Process Dynamics (EPD) have teamed up to assess the practical feasibility of using sources of waste energy (waste heat, streams of natural gas that are flared, etc.) for generating substantial flows of demineralized water suitable for beneficial use in agriculture and industry for two major shale energy regions of the U.S. (the Permian Basin in Texas and the Bakken Basin in North Dakota).

The overall purpose of this effort was to provide a year-by-year projection of the benefits of DCMD in the conversion of produced waters to substantial flows of demineralized water suitable for beneficial use and to base these projections on an examination of shale well databases obtained from North Dakota and Texas while considering the water-based life-cycle characteristics of shale wells with time as well as the waste energy management advantages of key equipment that could be used to establish the temperature conditions required for efficient DCMD water treatment. This effort examined the databases to forecast spatial distributions of produced water generation and the proximal availability of low-cost natural gas and thermal waste energy according to geographic locations and over time spanning the life cycle of shale well fields (about 45 years). The analysis then used this information to determine the year-by- year magnitude of benefits that could be achieved with DCMD processing in the conversion of produced water to water streams suitable for beneficial use. This was performed for the example plays of the Permian Basin of Texas and the Bakken Shale of North Dakota. These projections of produced water generation, DCMD processing opportunities, process economics, together with water renovation benefits for the Permian and Bakken regions have been incorporated into a spreadsheet model that is available upon request from the Department of Energy.

Major findings of the GTI-EPD projections of water treatment benefits analysis for DCMD are as follows:

1. Membrane Distillation: Membrane distillation is a thermal process for the desalination of salty water. Much of the heat of the inlet water transfers to the distillate. It requires a 75° F temperature differential between the salty feed water (warm) and the distillate (cool).
2. Minimum Heat Required: The minimum theoretical heat required to remove 50% (forward flow) of the water from a barrel of produced water (as distillate) is around 244,300 BTU/BBL. The various heat sources to operate the process, including reasonable estimates of the heat transfer are as follows:
    a. Diesel Engines: Exhaust from 440 HP diesel engines carries a low-quality heat at around 900°F with limited contact area for heat recovery. Exhaust from a single engine has the potential to treat around 15 BBL/day PW. However, heat transfer equipment is not available and is not being developed. A cool water reservoir is required to offset the warm water inflow. These types of engines are seldom near sources of PW.
    b. Steam Boilers: Direct firing of a boiler would require around 407,000 BTU/BBL. About 540 MCF/BBL PW of low-quality gas at 750 BTU/CF would be required per barrel. Heat transfer equipment would need to be adapted for contact between the boiler steam and the produced water. A cool water source is required.
    c. Heat Pumps: Conceptually, the heat pump could remove heat from a cool reservoir and transfer it to the warm side, thus guaranteeing a consistent source of cool water for the process. The heat pump option would require approximately 74,040 BTU/BBL PW. The natural gas demand with low-quality gas at 750 BTU/CF would be around 100 CF/BBL. Heat pumps driven by natural gas are readily available, however heat transfer equipment would need to be adapted.
3. Cost Model: A cost model was generated including reasonable costs for equipment, buildings, and water storage, and 10% unknowns. The membranes were estimated at 2 LMH (liter per square meter per hour) with a cost of $120 per square meter. Capital costs were amortized at 4% for 10 years. Operational Costs included fully loaded operator costs for hours per day equipment maintenance. Membrane replacement was 10% per annum. Pre-commercial gas was priced at $3 per million BTU. The following cost results are for a 1000 BBL/day treatment plant producing 500 BBL/day distilled water over a 10-year period.
    a. Diesel Engines: Costs were not evaluated due to the impossibility of providing enough heat for 1000 BBL/day.
    b. Steam Boilers: The present worth of a 1000 BBL/day facility was estimated at $2.3 million ($823/day capital costs). The daily operational costs totaled $1,307. The sum of these values gives a cost of $2.1/BBL PW treated or $4.2/BBL distilled water generated.
    c. Heat Pumps: The present worth capital was estimated at $4.0 million which translates to a daily cost of around $1,433/day. The daily operational costs totaled $874/day. The sum of these two costs gives an estimate of $2.3/BBL PW applied or $4.6/BBL distilled water generated.
4. Produced Water in the Bakken: The average number of active wells in the Bakken ranged from 11,000 to 15,000 wells between 2015 to 2020 with an average completion

rate of 800 new wells/yr. The average production per well was 5,500 BBL/month oil, 5,600 BBL/month produced water and 10,100 million cubic feet of natural gas. The total produced water was approximately 73 million barrels per month which translates into about 186 barrels per well per day. On average, 41% of the produced water was injected for re-pressurization or disposal.

   a. Present Water Management Issues: Based on the assumption that flared gas can be reasonably diverted for water treatment, then around 15% of the wells exceed the base assumption that 540 cubic feet of natural gas is required per barrel of PW based on the boiler option for the heat source. The percentage of wells that can be treated using only flare gas increases to 80% when the base assumption is that only 100 CF/BBL are required for a heat pump option.
   b. Future Water Management Issues: There will be potentially 52,000 total wells (nearing or at drilling saturation) with 47,000 active wells by 2020 generating upwards of 3.2 billion BBL of produced water/yr. About 1.3 billion BBL/yr will be injected, and 1.9 billion BBL/yr. of produced water will require treatment other than injection. If a treatment system (such as membrane distillation) is compatible at 65% of the wells, then the future market for advanced treatment may be nearly 1.2 billion BBL/yr., leaving 0.64 billion BBL/yr. for other treatment methods.

5. Produced Water in the Permian There are 63 counties impacted by oil and gas production in the region with some 102,000 active oil wells, 19,200 gas wells oil. Approximately 3,000 new wells were completed per year averaged over the last five years. These wells produced 600 million barrels of oil and 1.1 trillion cubic feet of natural gas in 2018. The rate of PW generation in the Permian accounts for upwards of 50% of the total PW produced in the US. Estimates of the rate of generation ranges from 4 to 10 BBL PW/BBL oil which occurs predominantly at oil producing wells. The total rates of generation of PW are estimated at 9–5 million BBL/day, with 5 million BBL/d in-excess of the volumes reused or deep well injected. This excess PW needs either convention or advanced treatment.

   a. Present Water Management Issues: Venting or flaring of excess gas is discouraged by State statures, limiting the use of flared gas as an alternative energy source. Based on the thermal requirements for membrane distillation and assuming the ability to divert gas for water treatment, about 38% of the wells could treat the produced water with the boiler option and 65% of the wells could treat the produced water with a heat pump.
   b. Future Water Management Issues: By 2060 there will be nearly 250,000 total wells with 210,000 remaining active and 40,000 closures. Based on based on 65% acceptance of the technology, the market for DCMD treatment of produced water for beneficial use could reach 136,000 wells. The remaining 74,000 of the wells would be reliant on more traditional disposal means. The projections for the yearly production of produced water suggest that by year 2060 the annual rate of production will reach 25 billion barrels with 14 billion barrels injected for disposal or re-fracture, and 11 billion barrels requiring treatment of which 7.4 billion barrels of produced water could be treated with

an advanced treatment such as membrane distillation. The remaining 3.6 billion barrels of produced water would need conventional treatment.

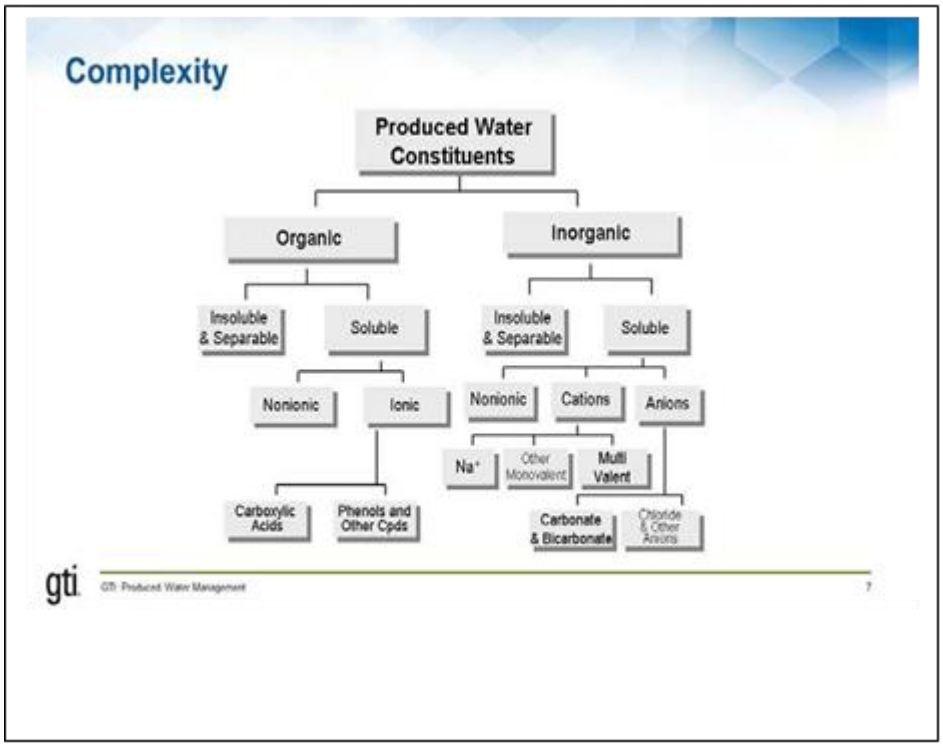
List of Acronyms

CF	Cubic Ft		NA	Not Analyzed
COP	Coefficient of Performance		NETL	National Energy Technology Laboratory
DCMD	Direct Contact Membrane Distillation		NGCS	Natural Gas Test Site
DOE	United States Department of Energy		NORM	Naturally Occurring Radioactive Materials
DW	Distilled Water		ppb	Parts per billion w/w basis
HFTS	Hydraulic Fracturing Test Site		ppm	Parts per million w/w basis
HP	Horsepower		psig	Pounds per Sq Inch
Influent	In-flow water blend stream pumped into a well during fracturing		PW	Produced Water
LMH	Liters per Hour per Square Meter of Membrane (Flux)		RO	Reverse Osmosis Process
M	Thousand		RPSEA	Research Partnership to Secure Energy for America
MM	Million		RRC	Texas Railroad Comission
MD	Membrane Distillation		tcf	Trillion cubic feet of natural gas
MG	Million gallons		TDS	Total Dissolved Solids
mg/l	Milligrams per liter		η	Efficiency of Heat Transfer

Introduction

Over the past 15 years, the United States has experienced a remarkable growth of unconventional oil and gas (UOG) exploration and production that has been accompanied with a large demand for water used in hydraulic fracturing employed for horizontal well completions and a large generation of wastewater (or produced water) that is coproduced with the oil and gas generated from the shale formations. Currently, more than half of the crude oil and natural gas produced from onshore well fields are supplied by the shale energy industry. Water management for each horizontal well that is constructed and operated in the shale industry involves the sourcing of millions of gallons of fresh water and injecting 4-15 million gallons of water combined with friction reducers(polyacrylamide organics) and other chemicals into the well to achieve hydraulic fracturing in the shale strata under great pressure; water in contact with the formation is then released from the well; water released and co-produced with the oil and gas is called “produced water”. In performing each hydraulic fracture, the influent blend of water and additives usually also contains about 25% by volume of produced water obtained from nearby wells. During the construction phase of each well field, most produced waters are recovered and utilized for reuse in hydraulic fracturing of other shale

wells (either within the same well field or in proximal well fields) (Hayes et al 2010). Thus, the flowback and produced waters from nearby wells that have been completed are reused in the hydraulic fracturing operation of the next wells to be completed. Energy development in the shale industry has driven a growth in demand for water treatment and water management. Water is the largest volume of waste that is handled and managed by the oil and gas industry. The oil and gas industry now operates 1 million oil and gas wells; from these wells, the industry handles and manages over 1 trillion gallons of produced water per year (equivalent to 24.4 billion bbl per year). The produced water flow per day is now approximately 2.8 billion gallons per day (GWPC, 2019).



Having been in intimate contact with oil and gas formation materials, flowback and produced water in the shale industry and from conventional wells is best described as a complex mixture or inorganic salts and organics as schematically depicted in Figure 35. Also included in the composition are low concentrations of naturally occurring radioactive materials ("NORM").

Contributing to the complexity, produced water may contain:

1. Mineral salts including cations and anions dissolved in water measured in terms of total dissolved solids (TDS)
2. Organic compounds including volatile and semi-volatile organics (such as naphthalene), organic acids, oils, and waxes.
3. Inorganic metals and other inorganic constituents such as ammonia.
4. Chemical additives to improve drilling, microbial control, and production operations.
5. Naturally occurring radioactive material (NORM) that leached into the produced water from the formation strata.

Currently, treatment of produced water in the shale industry has been aimed at conditioning produced water for reuse in the hydraulic fracture of the next wells to be constructed. Treatment for this purpose has usually consisted of low-cost removal of particulates and microbes, friction reducers, free oils and grease, and reduction of hardness. The state-of-the

art alternative to reuse has consisted of transportation of the water to a Class II well for disposal via deep well injection. As shale energy regions progress in their life cycle from well construction and hydraulic fracturing to long term production characterized by continuous daily generation of 5-25 barrels of produced water per well among thousands of shale wells per region, many companies are considering environmentally sound approaches for reducing the cost of large scale produced water management, including treatment for volume reduction of brines and generation of demineralized (desalinated) water streams suitable for beneficial use.

Early efforts to demineralize produced water mostly focused on reverse osmosis (RO) membrane processing. Numerous field trials of RO treatment of conventional and unconventional produced waters were unsuccessful due to rapid fouling and degradation of the membranes and an inability to handle influent streams with salt concentrations above 40,000 mg/l (Hayes, et al., 2011). These early tests showed that state-of-the-art reverse osmosis processing would not be of great help with most produced waters that are "hypersaline" and range from 80,000 to more than 150,000 mg/l of total dissolved solids (TDS). At these concentrations, the pressure driven RO process required operating pressures of over 700 psig to achieve even a 60% recovery of demineralized water from produced waters; these conditions incurred considerable electrical energy costs. In addition to the high salt concentrations, produced waters also contain residuals of soluble oils and divalent scale-forming cations that degrade the membrane surfaces of RO and decrease membrane life by more than 90% (Hayes, et al., 2011).

In view of this experience, the industry has searched for membrane processes that resist fouling and are capable of dewatering hypersaline brines at reasonable energy inputs. In recent years, membrane distillation has gained considerable attention as a promising technology that can demineralize hypersaline and complex produced waters such as those generated in the shale energy industry while using energy inputs that could potentially be obtained from low-cost energy sources proximal to well fields (Robbins, et al., 2020). A processing advantage of membrane distillation (MD) is that the process is a hybrid thermal-membrane distillation process in which a partial vapor pressure difference generated between the heated feed water and the cold permeate stream drives the transport of water vapor across the microporous membrane. On the feed water side, membrane distillation requires modest temperatures of 60- 80º C and therefore has the potential to utilize low grade thermal energy. These performance characteristics point to a potential of MD to utilize low grade energy sources in the well field to process produced water to generate a demineralized water stream for beneficial use while reducing and minimizing the brine volumes requiring transportation and ultimate disposal. The question, of course, is whether sufficient low-cost waste energy (e.g., conducted waste heat from engines at compressor stations or low-Btu natural gas that may be flared) can be harnessed at or near each well field to support MD processing of produced water to provide sufficient benefits in terms of produced water transportation and disposal savings while generating significant amounts of demineralized water for beneficial use.

Under the current program, the technical feasibility of treating produced water generated by the shale well fields of the unconventional oil and gas industry using membrane distillation has

been the centerpiece of the water processing research work performed under the Hydraulic Fracture Test Site-1 (HFTS-1) project by the University of Pittsburgh. The first phase of the work involved laboratory scale testing on actual Permian Basin produced waters provided by the host site operated by Laredo Petroleum. The results from these runs were used to construct the pilot scale direct contact membrane distillation process (DCMD). The final phase of the University of Pittsburgh effort in this project was to test the pilot DCMD skid at the shale well field (hosted by Laredo Petroleum). These tests are critically needed to assess the performance of DCMD with actual hypersaline produced waters under realistic field conditions.

In parallel with this effort, GTI and Environmental Process Dynamics (EPD) have teamed up in a companion task to conduct a detailed assessment of the practical feasibility of accessing various sources of waste energy (waste heat, streams of natural gas that are flared, etc.) for supporting DCMD operations on a large scale in selected example shale plays of the U.S. (i.e., Permian of Texas and the Bakken of North Dakota) where beneficial use of demineralized produced water is of growing interest as a significant source of water supplies for agricultural and industrial use.

The overall purpose of this water management systems analysis effort is to provide a year by year projection of the benefits of DCMD in the conversion of produced waters to substantial flows of demineralized water suitable for beneficial use and to base these projections on an examination of shale well databases of North Dakota and Texas while considering the water-based life cycle characteristics of shale wells with time as well as the waste energy management advantages of key equipment that could be used to establish the temperature conditions required for efficient DCMD water treatment. The state databases of Texas and North Dakota that were examined included the availability of waste energy sources in the Permian and Bakken plays (including conductive heat from natural gas compression site (NGCS) units and natural gas diverted from flaring) that could be used to support the operation of DCMD conversion of produced waters for the generation of demineralized water streams suitable for beneficial use. This analysis also incorporates process performance information from the University of Pittsburgh (PITT) tests on DCMD treatment of actual produced waters in terms of process operating conditions, salt separation (desalination) efficiencies, and membrane life.

Objectives

The overall objective of this engineering analysis is to perform projections of the potential of direct contact membrane distillation (DCMD) to provide substantial benefits in terms of harnessing low-cost energy that is available at or near the well fields (e.g., waste heat or low-cost natural gas) to convert hypersaline produced water to generate demineralized water supplies suitable for beneficial use within the Permian Basin of Texas and the Bakken Shale Region of North Dakota. Specific objectives of this effort include the following:

1. Review the recent trends of shale well drilling activity, gas production oil production, and produced water generation for the two geographic regions of the Permian of Texas and the Bakken of North Dakota and use these data along with water-based life cycle demographics to project water production rates and forecast the water production rates and water management issues into the future (45 years).

2. Evaluate potential sources of waste or low-cost energy available at the well field to drive the DCMD process in converting produced water to demineralized water, including:
    a. Waste heat recovery from diesel engine exhaust at compressor stations.
    b. Utilization of flare gas or low value pre-distribution natural gas to fuel boilers supporting DCMD operations; and,
    c. Flare gas or low-value natural gas for operating heat pumps that provide benefits of heating and cooling for DCMD processing.
3. Review the alternatives and hardware that can be employed for capturing waste energy to support DCMD in the conversion of produced water to demineralized water supplies for beneficial use.
4. Develop a computer model to provide forecasting of the potential benefits of DCMD in the conversion of produced water to include savings in transportation and disposal of produced water (through reducing volumes of hypersaline wastewaters) and potential revenues arising from the generation of demineralized water suitable for beneficial use.
5. Develop a computer model that compares capital and operating costs of each of the above options for the use of waste heat and low-value natural gas for the operation of DCMD in the treatment and management of produced water for the improved sustainability of the shale energy industry.

Overall Approach

This effort consisted of an engineering analysis of information obtained from multiple sources to estimate the level of benefits that can potentially be provided by DCMD in the conversion of produced water to generate demineralized waters suitable for beneficial use in the Permian Basin of Texas and in the Bakken Shale of North Dakota. From the state-based agencies that monitor the fossil energy data from the shale plays of Texas and North Dakota, computer databases covering the well drilling, completions, oil and gas production and water consumption and produced water generation from the Permian and Bakken shale regions were purchased and examined. In addition, site specific information on the locations of water management and compressor stations (where sources of waste heat from diesel engines can be found) were documented, and region-specific information on the availability of waste heat energy recovery equipment was sought from site managers at Laredo and from suppliers of diesel equipment in the Midland area. This region-specific survey effort was important in that it provided an indicator of the current availability of waste energy recovery equipment that is employed in the shale industry at this present time. The analysis also included a review of the waste energy recovery hardware that could be employed in the future to support DCMD operations for the beneficial renovation of produced water in future years to identify the cost-effective and the highest impact directions of commercial application.

The information bases from these parallel efforts were used in the construction of a computer model capable of describing current trends and providing forecasting of the potential benefits of DCMD in capture of waste energy or low-cost natural gas support the renovation of shale field produced waters for the generation of demineralized water supplies for beneficial use. This model was constructed to allow the user to enter certain inputs that would enable "what if" analyses of various produced water management scenarios.

Background

The production of gas and oil in the Bakken (North Dakota) and the Permian (West Texas) Reserves generates a large volume of produced water (PW). Estimates of water production range from 1-4 barrels (BBL) PW per barrel oil in the Bakken to 4-10 BBL PW per BBL oil in the Permian. While much of the PW is reused in the hydraulic fracture of new wells, or otherwise disposed-of by deep-well injection, there remain millions of barrels per day PW that are either not treated or minimally treated with conventional methods such as settling basins or evaporation ponds. While there are many examples of pilot trials for advanced treatment aimed at desalination of PW for beneficial reuse such as mechanical vapor recompression (Hayes and Severin 2012a), electrodialysis (Hayes and Severin 2012b), and freeze-thaw (Boyson et al 2002), there are few examples that have been demonstrated at full scale.

Membrane distillation is a thermal process that desalinates salt water by vapor transport across a membrane (Comanchero 2013). A temperature differential must be maintained across the membrane. The objective of this report is to investigate whether membrane distillation has a substantial place in the arsenal of options for treating excess PW for beneficial reuse, and whether there are low-cost energy options available for use with this treatment technology. More specifically, this section of the report investigates potential sources for waste heat to drive the distillation process. These include 1) waste heat from diesel engine exhaust at compressor stations, 2) diversion of flare gas or use of low value pre-distribution natural gas to fuel boilers, 3) and the use of flare gas or low-value gas to drive heat pumps.

The volumes and chemical make-up of PW vary widely by geographic region, drilling methods, and whether the region is primarily oil or gas producing. A review of the recent history of drilling activity, gas production, oil production, and produced water generation for two geographic regions, the Bakken in North Dakota and the Permian in S.W. Texas are provided. These data are used to project water production rates and provide a guide as to the magnitude of the water management issues into the future (45 years). These data also provide insight into the opportunity to generate water for alternative uses by applying a technology such as membrane distillation.

A survey of the gas and oil industry and the companies that provide waste heat recovery equipment indicated that there is very little experience for heat recovery in the gas and oil business except at very large installations such as refineries. Additionally, the highly concentrated salts of variable composition associated with PW means that examples of real-world materials costs and equipment life are unavailable. As such, the cost analysis provided, herein, for boilers, heat pumps, and heat transfer elements is highly subjective. Cost elements are gleaned from general reviews (Kesieme et al 2013), groundwater distillation (Pangarkar et al 2011), seawater desalination (Comanchero et al 2013 and Duong et al 2021), or other reports of membrane distillation in the gas and oil industry (Lakare et al 2017, Zhang 2019, and Robbins et al 2020). While the costs of these options remain basically unknown due to lack of engineering experience, a rudimentary cost model is presented. The model is available in the public domain and contains sufficient input variables; and rationale for use of certain input values, so that the reader can estimate their own costs for the boiler or heat pump option. The use of waste heat from diesel exhaust is far from commercial reality due to low quality, minimal quantity, and availability and a cost model for this option is not provided.

Summary of Information Considered in the Analysis

Membrane Distillation. Membrane distillation is a thermal process for the desalination of salty water. Other sections of the final report evaluate the use of membrane distillation to treat produced water (PW). This process requires that a thermal differential of around 75 °F be applied across the membrane. In all calculations, the warm side of the membrane is assumed to be 150 °F and the cool side is set at 75 °F. The minimum heat required to remove 50% (forward flow) of the water from a barrel of produced water (as distillate) is around 244,300 BTU/BBL. The process requires both a warm influent and a constant cool reservoir to be effective. There is a potential to treat PW using waste heat or inexpensive flare or pre-commercial gas to heat the water. Inexpensive sources of waste were evaluated such as exhaust from diesel engines, boilers, and heat pumps.

Waste Heat from Diesel Engines. This is the most efficient heat source since no fuel is solely dedicated to heating the produced water. A 440 HP engine has the potential to treat around 15 BBL/day PW. The heat recovery and transfer equipment are not commercially available, and a survey of equipment manufacturers covering Texas and North Dakota indicate no present interest in the recovery of this low quality and low quantity heat source. A further disadvantage is that diesel engines are mostly used at gas lift or re-pressurization stations along a transmission pipe, which may not be in close proximity to the PW generated at the wellheads. Costs estimates for this option were not evaluated.

Heat from Boilers. There is an option to use diverted flare gas or inexpensive pre- commercial gas to fuel steam boilers. Based on estimates of boiler and transfer efficiencies the boiler option would require around 407,000 BTU/BBL to treat the PW (at 50% forward flow). Using low-quality gas at 750 BTU/CF would require approximately 540 CF/BBL PW applied to the process. While commercial boilers are readily available, heat transfer equipment would need adaptation for contact between the boiler steam and the produced water. The boiler option has an added disadvantage in that there is no guarantee that there is sufficient supply of cool water. Cooling ponds or other cooling mechanisms would potentially be needed. Despite the lack of commercial equipment and process experience, a rudimentary cost estimate is provided.

Heat Pumps. There is a potential to use diverted flare gas or inexpensive pre- commercial gas to drive a heat pump. Conceptually, the heat pump could remove heat from a cool reservoir (75°F) and transfer it to the warm side (150° F), thus guaranteeing a consistent source of cool water for the process. At these target temperatures, the theoretical coefficient of performance (Carnot Cycle) of a heat pump is around 8.1. Based on estimates of heat pump and transfer efficiencies, the heat pump option would require approximately 74,040 BTU/BBL PW applied to the process. At 750 BTU/CF precommercial gas, the gas required would be around 100 CF/BBL. While heat pumps driven by natural gas are readily available, there is no industrial experience coupling these units to low-quality or precommercial gas. Furthermore, as with the boiler option, there is no industrial experience coupling the heat transfer process between a heat pump and a produced water source. Despite the lack of commercial equipment and process experience, a rudimentary cost estimate is provided.

Cost Model. Despite the lack of commercial equipment and process experience, rudimentary cost estimates are provided for the boiler option and the heat pump option. A cost model was generated and is publicly available. Since there are few references available with reliable costs, the model contains many "placeholder" values. The following values were used in the analysis. These numbers are readily changed if desired by a user of the model. Capital costs include the boiler ($75,000 per million BTU/hr) or heat pump ($200,000 per million BTU/hr); heat transfer units at ($60,000 per million BTU/hr, one unit for the boiler and two units for the heat pump); building ($250 per BBL/day); warm and cold reservoirs ($200/BBL/day). The membranes were estimated for a distilled water generation rate of 2 LMH (liter per square meter per hour) with a cost of $120 per square meter. Pipes, pumps, and controls were estimated at $150 per BBL/day. Unknown capital costs of 10% were added to the total. Capital was amortized at 4% interest for 10 years. Operational costs included fully loaded operator costs at $47/hr at 4 hours per day. The operational time of the process was prorated by the operator maintenance (4 hr per day). Membrane replacement was estimated at 10% per annum. Pre-commercial gas was priced at $3 per million BTU.

Cost Model Results. The following cost results were obtained using the placeholder data listed immediately above for the heat pump and boiler options for a 1000 BBL/day membrane treatment plant. For the boiler option, the present worth capital was estimated at $2.3 million which translates to a daily cost of around $823/day. The daily operational costs totaled to $1,307. The sum of these values gives a cost of $2.1/BBL PW applied or $4.2/BBL distilled water generated. For the boiler option, the present worth capital was estimated at $4.0 million which translates to a daily cost of around $1,433/day. The daily operational costs totaled to $874/day. The sum of these two costs gives an estimate of $2.3/BBL PW applied or $4.6/BBL distilled water generated. The obvious difference between the boiler option and the heat pump option is the trade-off of capital costs for operational costs. The differential capital costs are ($4.0 mm–$2.3mm= $1.7mm). The differential operational cost excluding capital amortization are ($1,307/day- $847/day = $460/day). The ratio of the capital differential to the daily costs indicate that the heat pump payback period (relative to the boiler option) is just over 10.1 years. The major driver in the payback period for the heat pump is the cost of the natural gas expended for the process. Because the heat pump is more efficient than the boiler option the payback term for the more capital-intensive heat pump decreases as the natural gas price increases. If the cost of natural gas is $2/million BTU, then the payback relative to tne boiler option is 19.3 years. If the gas is $4/million BTU, then the payback is 7.5 years.

Produced Water in the Bakken. The average number of active wells in the Bakken ranged from 11,000 to 15,000 wells between 2015 to 2020. The average completion rate for new wells was approximately 800 wells per year. The average production per well was 5,500 BBL/month oil, 5,600 BBL/month produced water and 10,100 million cubic feet of natural gas. The total produced water was approximately 73 million barrels per month which translates into about 186 barrels per well per day. On average, 41% of the produced water was injected for re-pressurization disposal (76 BBL/well per day). Not all wells are equal. Some wells are considered gas wells where the gas to oil ratio (cubic feet gas per barrel oil) is around 1000. Other wells considered oil wells where the gas to oil ratio is less than 30. The high-volume gas producing wells tend to produce less water per well than the low-volume gas producing wells

which produce a higher volume of water per well. Older oil wells tend to produce more water than mid-age wells, and freshly completed wells tend to produce more water than mid-age wells. Furthermore, some wells flare much of the gas and other wells capture most of the gas for sale or reinject it to maintain well pressure. When considering which wells are suitable for treatment by membrane distillation using flare gas or low quality pre-commercial gas it is necessary to approximate the volume of gas per volume of produced water. Based on the assumption that flared gas can be reasonably diverted (safely) then around 15% of the wells exceed the base assumption that 540 cubic feet per barrel PW based on the boiler option for the heat source. The percentage of wells that can be treated using only flare gas increases to 80% when the base assumption is that only 100 CF/BBL are required.

Projected Water Production in the Bakken. A life-cycle model was developed to estimate the production of water in the Bakken 45 years into the future. The Bakken reserves in North Dakota are being re-developed in the "Unit" mode to accommodate between 6 and 8 wells per 2 Unit area. Each Unit covers 2 square miles. The area of Bakken reserves in North Dakota covers 28,000 square miles. Drilling to 67% saturation would cover 7,000 2-Unit areas with between 28,000 and 37,000 new wells. There are presently 33,000 older wells with approximately 13,000 listed as active in this system. The model assumes 13,000 active wells, 1,000 new wells per year, 5% closure per year, and produced water generation of 5,600 BBL/month per well. Of this PW, 2,300 is injected for re-pressurization or disposal. Of the remaining 3,300 BBL/month per well, it is assumed that 65% (2,145 BBL/month per well) is treated with membrane distillation and 33% (1055 BBL/month/well) is treated by conventional methods or orphaned. By this model, it is projected that by 2060, there will be potentially 52,000 total wells (nearing or at drilling saturation) with 47,000 active wells. There will potentially be a total produced water generation of 3.2 billion BBL/yr. of which 1.3 billion BBL/yr. will be injected, and 1.9 billion BBL/yr. will require treatment other than injection. Assuming that a treatment system (such as membrane distillation) is compatible at 65% of the wells, then the future market for advanced treatment may be nearly 1.2 billion BBL/yr., leaving 0.64 billion BBL/yr. for other treatment methods. By 2060 the total (cumulative) volume of produced water (since 2020) generated will be 84 billion BBL with an injected volume of 35 billion BBL. The potentially treated volume using an advanced treatment system such as membrane distillation could represent a market of 32 billion BBL with a volume representing convention disposal of 17 billion BBL.

Produced Water in the Permian. The Texas Railroad Commission (RRC) lists 63 counties impacted by oil and gas production with some 102,000 active oil wells, 19,200 gas wells, and roughly 3,000 new wells per year averaged over the last five years. These wells produced 600 million barrels of oil and 1.1 trillion cubic feet of natural gas in 2018. The calculated reserves are estimated to be 50 billion barrels of oil and 300 trillion cubic feet of natural gas. The rate of generation of produced water in the Permian accounts for upwards of 50% of the total in the US. Rates of produced water per BBL oil range from 4 to 10 BBL/BBL which occurs predominantly at oil producing wells. Older wells generate more water per volume oil due to re-pressurization of the field with injected water. Newer wells also generate high volumes of water because of the use of higher volumes of hydraulic fracture water with deeper and longer well runs. Of the produced water that is disposed, 25% is through reuse as pressure fluid in old

wells or as hydraulic fracture water in new drilling. About 75% of the disposal is through deep well injection. Rates of generation of PW are estimated at 9–15 million BBL/day with 5 million BBL/d in-excess of the volumes reused or deep well injected. This excess PW needs either convention or advanced treatment. By State Statute flaring or venting of excess gas is discouraged. Temporary discharge permits for flared gas are issued for a 10-day period during final completion of a new well. Emergency extensions for a 45-day period may be issued under extreme duress. Therefore, capture and use of flared gas as an alternative energy source for water treatment is a restricted alternative in the Permian. Data in Table E1, Appendix E were analyzed by county and by assuming that the oil production in the county accounts for 4.4 BBL PW per BBL oil and that the gas produced within the county was available to treat the produced water in that county. The county average ratio of CF gas per BBL PW was calculated, and indicated that 15% wells have ratios that exceed 2,500 CF/BBL and 20% or the wells have a ratio approximating 0 CF/BBL. Based on the thermal requirements of for membrane distillation by boiler option (540 BTU/CF) and by heat pump (100 CF/BTU) it is estimated that about 38% of the wells could treat the produced water with the boiler option and 65% of the wells could treat the produced water with the heat pump option by diverting 100% of the gas production for wastewater treatment.

Projected Water Production in the Permian. The Life-Cycle analysis for the Permian assumes that there presently are 102,000 active wells and that a constant number (3,600 per year) of new wells drilled with a rate of closure of 0.5% of the active wells per year. Each active well is assumed to generate an average volume of 10,000 BBL/month produced water. The fate of the water is injection (55% or 5,500 BBL/well per month), with membrane treatment with membrane distillation applied to (65% of active wells) and the remainder (35%) relying on conventional treatment of produced water. This model projects that by 2060 there will be nearly 250,000 total wells with 210,000 remaining active due to 40,000 closures during the period between 2020 and 2060. Based on based on 65% acceptance of the technology that the market for treatment could reach 136,000 wells. The remaining 74,000 wells would be reliant on more traditional disposal means. The projections for the yearly production of produced suggest that by year 2060, the annual rate of production will reach 25 billion barrels with 14 billion barrels injected for disposal or re-fracture, and 11 billion barrels requiring treatment of which 7.4 billion could be treated with an advanced treatment such as membrane distillation, and the remaining 3.6 billion barrels would need to receive conventional treatment. The cumulative projections for produced water in the Permian indicated that by 2060, the production will reach 780 billion barrels with 430 billion barrels injected for disposal or re-fracture, and 350 billion barrels requiring treatment of which 230 billion could be treated with an advanced treatment such as membrane distillation, and the remaining 120 billion barrels would need to receive conventional treatment.

Membrane Distillation and Potential Heat Sources

Membrane Distillation

Membrane distillation is a thermal process that separates soluble salts from water by vapor distillation across a membrane. A warm feedstock, typically at around 150°F such as seawater or produced water containing salts, is contacted with a membrane. The opposite side of the membrane is supplied with cool water typically at around 75 F°. If a temperature differential of

more than 50 °F is maintained, water is vaporized across the membrane. The advantage of the process is that there is no need to boil the water at a conventional temperature (approximately 212 °F). The optimum temperature differential appears to be about 75 °F and heat demand calculations provided, herein, are on these temperatures. Because the vapor carries about 1008 BTU/lb from the warm side to the cool side, the temperature of the cool side plus permeate rises rapidly. This demands the assumption that there is a sufficiently large supply of cool side water to adsorb the thermal exchange when considering the boiler option. While this may be true at sites across North Dakota, there may not be readily available cool water resources S.W. Texas. This is the main reason why a heat pump option was evaluated; it can provide the constant cool side flow demanded by the process.

Minimum Heat Required to Treat Produce Water

Table 1: Estimate of Theoretical Minimum Heat to Generate DW from PW at 60° F									
Forward Flow	40%			50%			60%		
Brine Flow	60%			50%			40%		
Heat Demand and Total	BTU/lb PW App.	BTU/BBL PW App.	BTU/BBL DW Gen.	BTU/lb PW App.	BTU/BBL PW App.	BTU/BBL DW Gen.	BTU/lb PW App.	BTU/BBL PW App.	BTU/BBL DW Gen.
	594	208,040	520,390	698	244,340	488,770	801	280,540	467,590
PW = Produced Water		DW = Distilled Water		Warm Side 150 °F		Cool Side 75 °F		BBL = 42 gallons	

The heat required to treat produced water is based on the sensible heat to bring the process streams (warm side and cool side) to process temperature plus the latent of vaporization to pass the treated water (permeate) through the membrane. There is also an unknown conductive heat transfer across the membrane which is assumed to be 10% of the total sensible and latent heat transfers. The permeate flow through the membrane from the warm side to the cool side is herein called the forward flow. For all subsequent calculations, the forward flow is 50% of the produced water flow applied to the membrane on the warm side. The heat demand can therefore be calculated based on the volume of produced water applied to the membrane or based on the volume of distilled water produced. In all subsequent

calculations, the distinction is made between the PW applied or DW generated. See Appendix A for a detailed analysis of the heat requirements for membrane distillation.

The heat required to treat produced water is around 244,340 BTU/BBL applied to the membrane with a forward flow through the membrane of 50% and ambient water at 60°F. The heat required on a per BBL DW generated is roughly double this value at 488,700 BTU/BBL. This heat requirement changes with the estimate of forward flows; for completeness, values of heat demand at 40% and 60% forward flow are summarized in Table 1. Note that the heat demand increases as the forward flow increases.

Comparison of Heat Sources

Table 2: Estimate of Heat Demand Using Different Heat Sources

Method	Heat Source	COP	η_{source}	$\eta_{transfer}$	*Operating Estimate BTU/BBL		**Operating Estimate CF/BBL	
Engine Exhaust	Diesel Engines at Pump Stations	1	0.8	0.8	382,000 BTU/BBL PW Applied	764,000 BTU/BBL DW Generated	NA	NA
Boiler	Flare gas	1	0.80	0.75	407,000 BTU/BBL	814,000 BTU/BBL	543 CF/BBL	1,085 CF/BBL
	or low-quality NG				PW Applied	DW Generated	PW Applied	DW Generated
Heat Pump	Flare gas or low-quality NG	8.1	0.55	0.75	74,040 BTU/BBL PW Applied	148,000 BTU/BBL DW Generated	99 CF/BBL PW Applied	197 CF/BBL PW Applied

Operating Estimate = Basis /(COP x η_{source} x $\eta_{transfer}$)

PW = Produced Water, DW = Distilled Water, CF= Cubic Foot, Calculated for 50% Forward Flow

*Basis is a minimum requirement of 244,320 BTU/BBL

**Basis is a pre-commercial gas rated at 750 BTU/CF

Three types of heat sources were evaluated (See Appendices B and C). The technical correlations can be found in any standard heat transfer text such as Bennet and Meyers (1974) or Smith and Van Ness (1975).

1. Exhaust from diesel engines at lift stations (no flare gas nor pre-commercial gas required).

2. Direct heating of PW with boilers using by (flare or precommercial gas)
3. Heating and cooling the warm-side and cool-side waters with heat pumps (flare or precommercial gas).

Based on the type of heat equipment envisioned, there is a wide range of heat required to produce distilled water, DW, from produced water, PW. The calculation for the information in Table 2 follows the general equation:

$$Heat_{actual} = \frac{Heat_{theoretical}}{COP\ x\ \eta_{source\ x}\ \eta_{heat\ transfer}}$$

For waste heat captured from diesel exhaust and heat generated from a boiler, the coefficient of performance is unity (COP = 1). For a heat pump operating between 75°F and 150 °F where TF is the temperature of the feed and TC is the temperature of the cool side of the membrane, evaluation of the Carnot cycle gives the theoretical efficiency COP = 8.1; meaning that for every BTU of heat transferred, only 1/8.1th must be supplied.

$$COP = \frac{Heat\ Transfered\ to\ Warm\ Side}{Work\ Required} = \frac{T_F}{T_F - T_P} = \frac{150+460}{150+460-(75+460)} = 8.1$$

The relation between heat to treat one volume of applied PW and the heat to generate one volume DW for the case of 50% forward flow is:

$$Heat_{Generation\ DW} = \frac{Heat_{Application}}{Fraction\ Forward\ Flow}$$

Different types of equipment may be compared on a basis of BTU delivered. Table 3 is a comparison of the three heat sources based on approximately 1 million BTU delivered per hour. The exception is the rating for a 440 HP diesel engine which converts to about 1.1 million BTU/hr.

Table 3: Rate of PW Applied per Unit Engine (Roughly 1- Million BTU/Hr Delivered)					
	Rate	Energy Expended	Source (Delivered)	Note	Equipment Available
Engine Exhaust	15 BBL/D	None	440-HP Engine 1.1 mm BTU/hr	40% glycol in heat transfer fluid.	No, never been tried.
Boiler	44 BBL/D	1.6 mm BTU/hr	1 mm BTU/hr	80% efficient, and 75% Transfer Efficiency	Maybe, would need reliable heat transfer unit
Heat Pump	40 BBL/D	0.3 mm Btu/hr	1 mm BTU/hr	COP = 8.1, 55% efficient 75% transfer efficiency	Maybe, would need reliable heat transfer unit
1 mm = one million					

Table 4: Advantages and Disadvantages of the Heat Sources		
Source	Advantages	Disadvantages
Heat from Diesel Exhaust	1. This is an untapped resource available at many sites, especially at compressor stations.	1. The engines are located a gas lift stations which are not usually located near produced water sources. 2. Low quality heat source yields Insufficient heat to treat more than a few barrels per day. 3. A constant cool-side water source must be obtained to maintain the temperature differential across the membrane. 4. Present utility is limited to heating buildings or pre-heating diesel fuel to improve engine performance. 5. There is no industrial experience for this application. The first attempts would be capital intensive.
Boiler Option using Flare Gas low quality precommercial gas	1) Many sites in the Bakken have sufficient flare gas to treat most of the produced water generated. 2) The cost of the gas is minimal once the equipment for diversion is installed. 3) Lower capital cost than the heat pump option	1) There are site safety reasons for flares. Diversion of flares must be carefully evaluated. 2) Sites in Texas are issued only short-term permits for flaring. The expectation is that this gas is controlled as soon as possible for commercial recovery. 3) There is an unknown capital cost associated with the diversion of the flare gas. 4) The quality of the gas is highly variable and may require some treatment to be usable in an engine. 5) A constant cool-side water source must be obtained to maintain the temperature differential across the membrane. This may be possible in the northern climate of the Bakken, by problematic in the S.W. Texas climate of the Permian.
Heat Pump Option using Flare or low-quality precommercial gas	1) With a COP of 4-4.5, heat transfer could be performed for 25% of the energy of a steam boiler. 2) The heat pump removes heat from the cool side	1) Higher equipment costs than the boiler option. This must be offset by lower energy costs. 2) Warm-side and cool-side reservoirs must be designed to allow for heat transfer. 3) There are no comparable engineered systems. Seawater distillation units use steam heating and the ambient
	water and moves it to the warm side.	temperature of the source water for maintaining the temperature differential.

The most efficient option is the engine exhaust providing a capacity of 15 BBL/day PW applied for minimal energy expended. The major drawbacks to this process are the relatively low treatment capacity per engine retrofitted coupled with the complete unfamiliarity in the commercial equipment business with tapping this waste energy source. A secondary drawback is that the compressor stations located along a natural gas pipeline may not be near a produced water source (at the wellhead). It must be assumed that there is sufficient cool water capacity to accommodate the heat transfer from the permeate flow. These disadvantages are sufficiently great that the development of this heat source for the purpose of membrane distillation is unlikely. The second most efficient option is the heat pump option. It has a rating of 40 BBL/day treatment capacity for an expenditure of 0.3 million BTU/Hr. It has the

advantage that the transfer of heat from the cool side to the warm side is thermodynamically efficient (vis. the effective COP) and that this heat transfer automatically regenerates the cool water flow required by the membrane. It has the disadvantage that this type of unit process has not been adapted (yet) to this application. The method of heat transfer from the heat pump to the warm fluid has not been designed. The expected capital cost of the equipment is expected to be higher than for the boiler option.

The least efficient option is the heating of PW with boilers. The rating is 44 BBL/day for 1 million BTU/hr delivered, but the various inefficiencies of heat conversion and transfer require the expenditure of 1.6 million BTU/hr. The disadvantages include lack of experience with heat transfer from steam to the variable environment created with produced water, and the need to supply cool water to maintain the temperature differential demanded by the membrane process. The cost of a boiler is expected to be much less than a heat pump. The choice of the boiler option over the heat pump option will be based, in part, on the operating expense of the gas expenditure. Table 4 is a summary of the advantages and disadvantages of each heat source.

Bakken Shale

The Bakken and Lodgepole geographic region extend from west North Dakota to East Montana to Southern part of Saskatchewan, Canada with an estimated reserve of 3.6 billion BBL oil and 1,860 billion cubic feet of gas (USGS 2008). The Bakken reserves in North Dakota are being re-developed in the "Unit" mode to accommodate between 6 and 8 wells per 2 Unit area. Each Unit covers 2 square miles. The area of Bakken reserves in North Dakota covers approximately 28,000 square miles. Drilling to 67% saturation would cover 7,000 2-Unit areas with between 28,000 and 37,000 new wells. There are presently 33,000 older wells with approximately 13,000 listed as active in this system.

Produced Water in the Bakken

Table 5: Existing and Spudded Wells During 6-Month Period in ND (Bakken Only)

	July-Dec 2015	Jan-June 2016	July-Dec 2016	Jan-June 2017	July-Dec 2017	Jan-June 2018	July-Dec 2018	Jan-June 2019	July-Dec 2019	Jan-June 2020
Active Wells at Start	11,168	11,716	11,968	12,704	13,201	13,769	14,378	14,913	15,148	15,154
New During Period	548	252	302	434	497	568	609	535	235	6
Undated	6463 wells do not list spud date									

The focus of this report are the Bakken shale reserves covering more than 40% of area of north- west North Dakota (approximately 28,000 square miles). The Bakken oil is in tight shale formation and requires hydraulic fracture and horizontal drilling for efficient capture. There is a long history of oil production from the area, meaning that there are older (and still productive wells) plus modern hydraulically fractured wells. Table 5 is a summary of the ND data for active wells and new wells from July 2015 to June 2020. The average number of active wells in the

Bakken ranged from 11,000 to 15,000 wells between 2015 to 2020. The average completion rate for new wells was approximately 800 wells per year.

Table 6 shows the activity of the active wells on a per-well per-month basis. The average production per well was 5,500 BBL/month oil, 5,600 BBL/month produced water and 10,100 million cubic feet of natural gas. The total produced water was approximately 73 million barrels per month which translates into about 186 barrels per well per day. On average, 41% of the produced water was injected for re-pressurization or deep-well disposal (76 BBL/well per day). Handling methods for the remaining 59% of the produced water are not mentioned in the database and it is assumed that these waters are minimally treated in evaporation or storage basins.

Table 6: Production per-Well per-Month for Bakken Wells During Each 6-Month Period

M = Thousand	2015 July-Dec	2016 Jan-June	2016 July-Dec	2017 Jan-June	2017 July-Dec	2018 Jan-June	2018 July-Dec	2019 Jan-June	2019 July-Dec	2020 Jan-June
Oil (BBL)	3,141	2,834	2,511	2,465	2,576	2,643	2,832	2,921	2,968	2,569
Water (BBL)	2,589	2362	2,239	2,285	2,536	2,726	3,135	3,304	3,580	3,176
Gas (MCF)	4,420	4,396	4,169	4,299	4,687	4,987	5,526	6,034	6,396	5,837
Gas Sold (MCF)	3,536	3,769	3,538	3,672	3,865	4,049	4,217	4,517	4,948	4,849
Flared (MCF)	684	428	442	426	591	683	987	1,178	1,124	698
Flared CF/BBL	264	181	198	187	233	251	315	357	314	220

While most recovered natural gas is sold to market, there is significant flaring (per average well) that overall ranges between 10 to 15% of the total gas recovered. When considering flared gas as an alternative fuel for heating the produced water for membrane distillation, the broad determinant is the volume of gas required for heating with a boiler option (540 CF/BBL) or the heat pump option (100 CF/BBL). The final row in Table 6 is a calculation of the ratio of flared gas to produced water generated which averages 250 CF/BBL meaning that if all wells were "average" then flared gas is sufficient to treat all the PW using the heat pump option and none of the water using the boiler option.

Not all wells are equal, however. The data used to generate Table 6 are reviewed extensively by named geographic regions in Appendix D. Some regions produce copious volume of gas relative to oil and are considered gas wells, while other regions generate large volumes of oil and little gas and are considered oil wells. Many of the regions generate a mixture of both products.

When considering flare gas as an option for heat powering the membrane distillation process, it is necessary to look closely at the ratio of flared gas to produced water generated. Figure 36 is a probability plot (Blue Curve) of a well having less than the stated value of flared gas per barrel of produced water generated. The horizontal lines represent the targets of 100 CF/BBL for a heat pump option (Orange Line) and 540CF/BBL for a boiler option (Grey Line) as a heat source for membrane distillation. The orange line intersects the blue curve at 20%, therefore, 20% of the wells have insufficient flare gas to treat all the water. Conversely, 80% have sufficient gas to treat the water using the heat pump option. On the other hand, the grey line is 0.5 MCF/BBL and represents the minimum gas needed to treat the water with the boiler option. This intersects the blue curve at 85%, therefore 85% of the wells have insufficient flare gas to treat all the water. Conversely, only 15% have sufficient gas to treat the water using the boiler option.

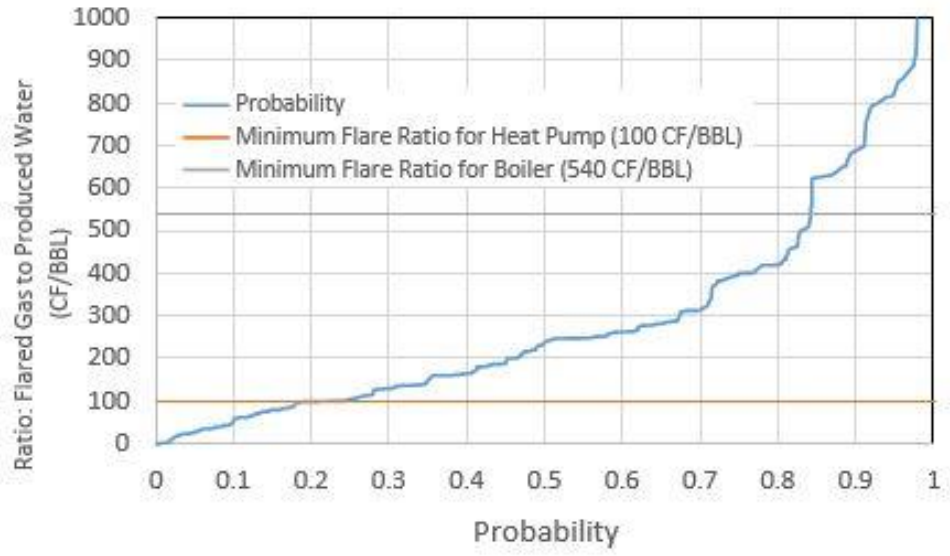


Figure 36: Probability of Less than Ratio (Flared Gas/Water)

Produced Water Life-Cycle Analysis for the Bakken

The Bakken reserves in North Dakota are being re-developed in the "Unit" mode to accommodate between 6 and 8 wells per 2 Unit area. Each Unit covers 2 square miles. The area of Bakken reserves in North Dakota covers 28,000 square miles. Drilling to 67% saturation would cover 7,000 2-Unit areas with between 28,000 and 37,000 new wells. In general, there is presently a great need for water treatment based on many active old-style wells. The Impact new well activity; along with the closure of the old-style wells; on water needs will be discussed in the Appendix E.

Table 5 was presented above as a summary from the North Dakota database attributed to the Bakken oil pool. Showing on-average that around 800 wells are completed per year, with a range of 50-1100 per year depending on economic conditions. It is noteworthy that there are some 33,000 wells in the database, some of these are inactive and some lay outside the Bakken fields. Table 6 was presented above as a summary of the data for active wells listed by North Dakota from July 2015 to June 2021. These two tables for the general basis for the life-cycle model as will be described in Table 6 below.

The number of existing and future wells were estimated to 45 years. Base assumptions for the model are summarized in Table 7. The assumption is that there are a constant number of new wells drilled per year with a constant rate of closure of active wells per year. Each active well is assumed to generate an average volume of produced water per month. The fate of the water is injection (41%), treatment with membrane distillation (65% of active wells able to treat water) and the remainder to be untreated.

Table 7: Data Used in the Life-Cycle Model for the Bakken		
Parameter	Number	Basis (Tables 4 and 5)
Existing Active Wells	13,000 Wells	Average over Last 7.5 Years
Wells per Year Drilled	1000 Wells	Yearly Average over Last 7.5 Years
Future Wells (Existing + New)	50,500 Wells	7000 Double-Units (DU) at 8 wells per DU + Existing Wells, at 67% Drilling Saturation
Produced Water Generated	5,600 BBL	per-well per-month (100 BBL/D)
Produced Water Injected	2,300 BBL	per-well per-month (41% of PW)
Well Closure	0.5%	Of Active Wells per Year
Gas Production	5	million CF per well per month
Gas Flared	1	million CF per well per month
Treatment Potential	65%	Wells that have both flare gas and water to treat

The projected information on the status of the wells over the projected time are presented in Figure 37. The projections indicate that by 2060, there will be potentially 53,400 total wells (nearing or at saturation) with 46,600 active wells, and 7,000 wells closed during the analysis period. If the produced water from 65% of the active wells can be treated using membrane treatment technology (powered by flare gas) then the potential market for this treatment system can potentially be used at 33,300 wells.

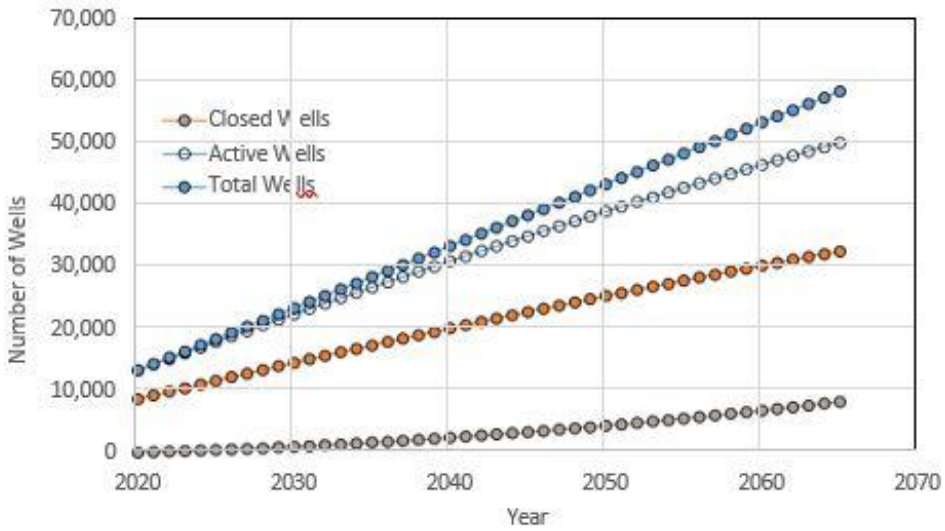


Figure 37: Total, Active, and Closed Wells Projected for the Bakken over 45 Years

Figure 37 is a plot of the future yearly volumes of the produced water including total production, water injection for re-pressurization deep-well disposal, the volume of water that may be treated by membrane distillation powered by flared gas (heat pump option), and the remaining water that is to receive conventional treatment such as storage in evaporation

ponds. These projections indicate that by 2060 there will potentially be a total produced water generation of 3.2 billion BBL/yr. of which 1.3 billion BBL/yr. will be injected. If an advanced treatment such as membrane distillation is introduced for 65% of the wells, the volume of advanced treated water will be around 1.2 billion BBL/yr. and the remaining 0.64 million BBL/yr. will need to be handled by conventional disposal.

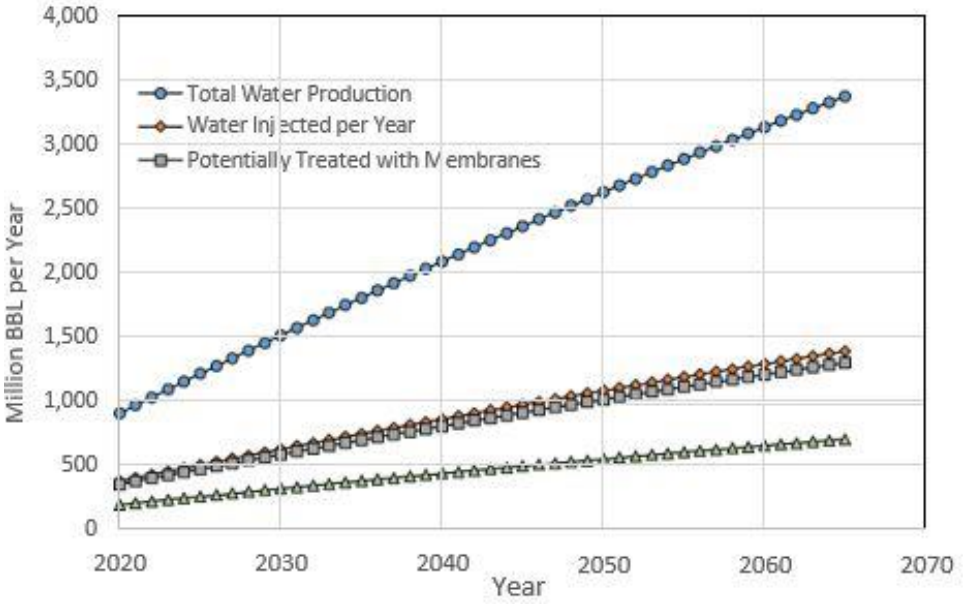


Figure 38: Projection of PW and Potentially Treated Water per Year in the Bakken

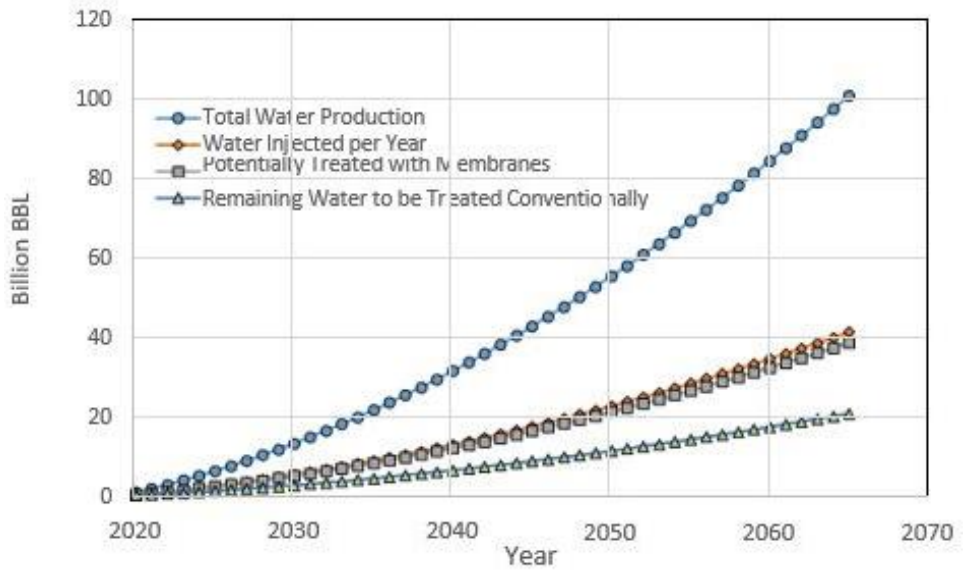


Figure 39: Cumulative Projection of PW and Potentially Treated Water in the Bakken

The projections for growth in the Bakken at 1000 wells/year and an existing 13,000 active wells at present are roughly linear. The values in the Figure 38 are based on yearly projections. One aspect of the rates of water treatment, injection, and produced water generation is that any water untreated today, is still water untreated tomorrow; the results are cumulative. Figure 39 is a summary of the cumulative effects of the continued generation of produced water. By 2060 the total (cumulative) volume of produced water (since 2020) generated will be 84 billion BBL with an injected volume of 35 billion BBL. The potentially treated volume using an advanced treatment system such as membrane distillation could represent a market of 32 billion BBL with a volume representing convention disposal of 17 billion BBL. Obviously, if all

the non-injected produced water is to be treated by conventional storage in evaporation ponds, there will be a very large capacity of ponds that need to be constructed.

Summary of the Bakken Results

The average number of active wells in the Bakken ranged from 11,000 to 15,000 wells between 2015 to 2020. The average completion rate for new wells was approximately 800 wells per year. The average production per well was 5,500 BBL/month oil, 5,600 BBL/month produced water and 10,100 million cubic feet of natural gas. The total produced water was approximately 73 million barrels per month which translates into about 186 barrels per well per day. On average, 41% of the produced water was injected for re-pressurization disposal (76 BBL well per day). Not all wells are equal. Some wells are considered gas wells where the gas to oil ratio (cubic feet gas per barrel oil) is around 1000. Other wells considered oil wells where the gas to oil ratio is less than 30. The high-volume gas producing wells tend to produce less water per well than the low-volume gas producing wells which produce a higher volume of water per well. Older oil wells tend to produce more water than mid-age wells, and freshly completed wells tend to produce more water than mid-age wells. Furthermore, some wells flare much of the gas and other wells capture most of the gas for sale or reinject it to maintain well pressure. When considering which wells are suitable for treatment by membrane distillation using flare gas or low quality pre-commercial gas it is necessary to approximate the volume of gas per volume of produced water. Based on the assumption that flared gas can be reasonably diverted (safely) then around 15% of the wells exceed the base assumption that 540 cubic feet per barrel PW based on the boiler option for the heat source. The percentage of wells that can be treated using only flare gas increases to 80% when the base assumption is that only 100 CF/BBL are required.

A life-cycle model was developed to estimate the production of water in the Bakken 45 years into the future. The Bakken reserves in North Dakota are being re-developed in the "Unit" mode to accommodate between 6 and 8 wells per 2 Unit area. Each Unit covers 2 square miles. The area of Bakken reserves in North Dakota covers 28,000 square miles. Drilling to 67% saturation would cover 7,000 2-Unit areas with between 28,000 and 37,000 new wells. There are presently 33,000 older wells with approximately 13,000 listed as active in this system. The model assumes 13,000 active wells, 1,000 new wells per year, 5% closure per year, and produced water generation of 5,600 BBL/month per well. Of this PW, 2,300 is injected for re-pressurization or disposal. Of the remaining 3,300 BBL/month per well, it is assumed that 65% (2,145 BBL/month per well) is treated with membrane distillation and 33% (1055 BBL/month/well) is treated by conventional methods or orphaned. By this model, it is projected that by 2060, there will be potentially 52,000 total wells (nearing or at drilling saturation) with 47,000 active wells. There will potentially be a total produced water generation of 3.2 billion BBL/yr. of which 1.3 billion BBL/yr. will be injected, and 1.9 billion BBL/yr. will require treatment other than injection. If a treatment system (such as membrane distillation) is compatible at 65% of the wells, then the future market for advanced treatment may be nearly 1.2 billion BBL/yr., leaving 0.64 billion BBL/yr. for other treatment methods. By 2060 the total (cumulative) volume of produced water (since 2020) generated will be 84 billion BBL with an injected volume of 35 billion BBL. The potentially treated volume using an advanced treatment system such as

membrane distillation could represent a market of 32 billion BBL with a volume representing convention disposal of 17 billion BBL.

Permian Shale

The Permian Shale oil reserves are in Western Texas and South-Eastern Wyoming north of Mexico and occupy some 86,000 square miles. The modern hydraulic fracture technologies have opened the region as perhaps the largest oil field on earth. The Texas Railroad Commission lists 63 counties impacted by oil and gas production with some 102,000 active oil wells, 19,200 gas wells oil and roughly 3,000 new wells per year averaged over the last five years. These wells produced 600 million barrels of oil and 1.1 trillion cubic feet of natural gas in 2018. The calculated reserves are estimated to be 50 billion barrels of oil and 300 trillion cubic feet of natural gas.

Produced Water Generation in the Permian

Table 8: Estimates of the Drilling and Production Rates for the Permian Basin (Horizontal Wells Only)

	2014	2015	2016	2017	2018	2019	2020	Avg
New Wells	2,864	2,723	2,855	3,614	5,249	5,067	3,216	3655
Total Active Wells	7,064	9,955	12,024	16,009	20,905	25,972	29,630	17,366
Oil M BBL Daily Avg	590	674	784	1,374	2,258	2,452	1,907	1434
Gas MM CF Daily	1,540	1,538	1,719	3,291	5,249	6,589	3,508	3348
Avg Oil BBL /well/D	83.5	67.7	65.2	85.8	108.0	94.4	64.4	81
Avg Gas M-CF/well/D	218	154	143	206	251	254	118	192
PW BBL/well/D (est.)	367	298	287	378	475	415	283	358
The ratio of PW/BBL oil is set at 4.4								

According to several sources (Hart Energy 2018, Permian Produced Water Society 2019) the Permian is the most active and productive oil drilling regions in the world. According to these sources, the rate of generation of produced water in the Permian accounts for upwards of 50% of the total in the US. Rates of produced water per BBL oil range from 4 to 10 BBL/BBL. Older wells generate more water per volume oil due to re-pressurization of the field. Newer well also generate high volumes of water because of the use of higher volumes of hydraulic fracture water with deeper and longer well runs. Of the produced water that is disposed, 25% is through reuse as pressure fluid in old wells or as hydraulic fracture water in new drilling. About 75% of the disposal is through deep well injection. Rates of generation of PW are estimated at

9–5 million BBL/day with 5 million BBL/d more than the volumes reused or deep well injected. Some estimates are for 30 million BBL/d generation within 5- 10 years to the future.

Table 8 is a compilation of the various sources (Hart Energy 2018, Permian Produced Water Society 2019, Shale Profile.com 2021) and apparently include only horizontal wells. The ratio of PW per oil production in this table is set at 4.4 based on the estimate that 10,000 BBL/d were generated in 2018.

According to the Texas Railroad Commission (TRR) (See Appendix E), there were 19,200 operating gas wells and 102,000 operating oil wells in the Permian during 2018 as summarized in Table 9. Appendix E shows sorted profiles of the production by county. Seven counties had no production. Sixteen counties had oil production only, whereas 37 counties showed production of oil and gas. The average daily oil production is similar in 2018 in Tables 8 and 9, however the gas production reported by TRR is about one-half reported by Shale Profile.com. This is somewhat at-odds with the smaller number of operating wells estimated by Shale Profile.com in Table 8 and may be reflective of many vertical wells, or lower producing wells reported in TRR data. This is examined more closely in Appendix E. The median TRR reported production was around 11.2 BBL/well-day. There are 40,000 wells that produce less than 6 BBL/d.

Table 9: Summary of the Texas Railroad Commission Report for 2018

	Counties	Wells Operating		Production in 2018	
		Oil	Gas	Gas MM CF	Oil M BBL
No Production	7	0	0	0	0
Only Oil Reported	16	12,839	0	0	41,928
Both Oil and Gas	37	89,175	19,198	1,143,370	817,919
Daily Average				3,133	2,356

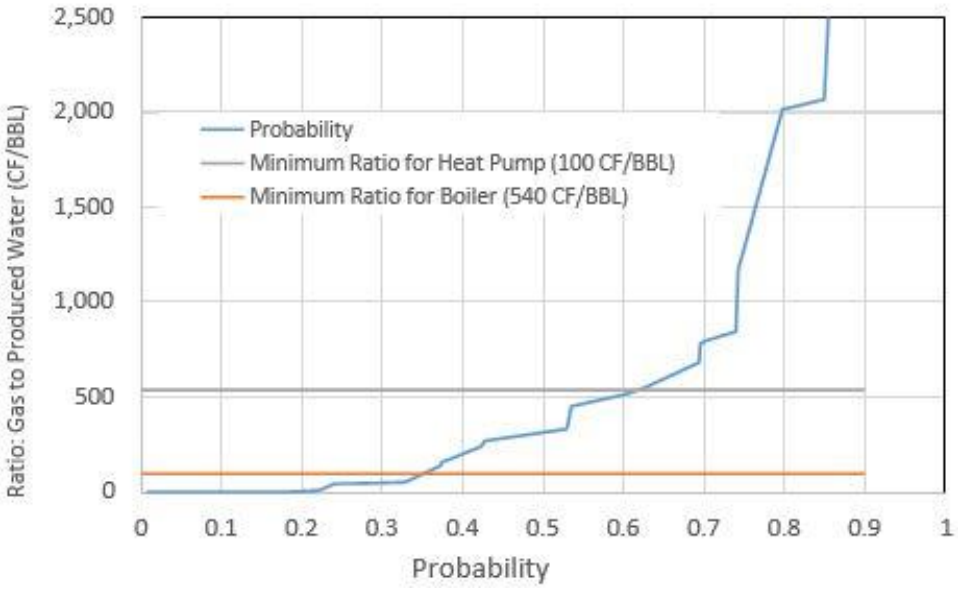


Figure 40: Probability of Permian Wells with Less than Ratio (Gas/Water)

Figure 40 is a plot of the probability sufficient gas generation at a well (on a county- wide basis) to support treatment of the produced water. Note that 20 % of the wells do not generate natural gas and 15% generate more than 2,500 CF/BBL. There are 65% of the wells that produce sufficient gas to treat the water by the heat pump option and 35% of the wells that could treat using the boiler option.

Produced Water Lifecycle in the Permian

The Life-Cycle analysis for the Permian is based on a combination of the data collected from the mentioned references. The number of existing and future wells were estimated to 45 years. The assumption is that there are a constant number (3,600 per year) of new wells drilled with a constant rate of closure of 0.5% of the active wells per year. Each active well is assumed to generate an average volume of 10,000 BBL/month produced water. The fate of the water is injection (55% or 5,500 BBL/well per month), with membrane treatment with membrane distillation applied to (65% of active wells) and the remainder (35%) relying on conventional treatment of produced water (Table 10).

Table 10: Data Used in the Life-Cycle Model for the Permian

Parameter	Number	Basis (Tables 8, 9, E1 Appendix E)
Existing Active Wells	102,000 Wells	Active Oil Wells, Table E1, Appendix E
Wells per Year Drilled	3,600 Wells	Yearly Average over Last 5 Years (Table 8)
Future (Existing + New)	NA	Drilling Saturation Unknown
Produced Water Generated	10,000 BBL	per-well per-month (4.4 BBL PW/BBL Oil)
Produced Water Injected	5,500 BBL	per-well per-month (55% of PW)
Well Closure	0.5%	Of Active Wells per Year
Gas Production	5.7	Million CF per-well per-month
Gas Flared	None	Million CF per-well per-month
Treatment Potential	65%	Percent of wells that implement technology

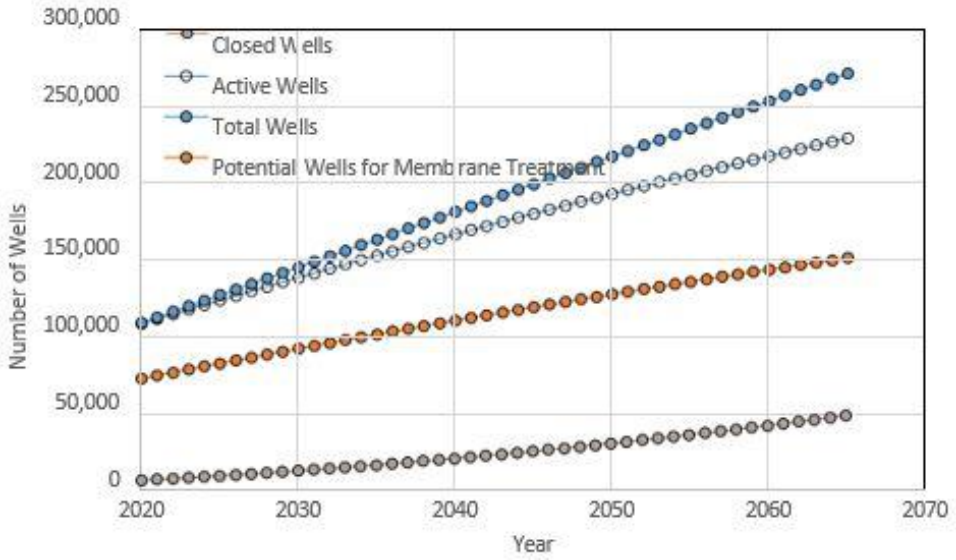


Figure 41: Total, Active, and Closed Wells Projected for the Permian over 45 Years

Figure 41 is a projection of the total wells, active wells, and wells closed during the analysis period. This figure indicates there will be nearly 250,000 total wells by 2060 with 210,000

remaining active due to 40,000 closures during the period between 2020 and 2060. Figure 41 also shows that (based on 65% acceptance of the technology) that the market for treatment equipment could reach (136,000 wells).

The projections for the yearly production of produced water in the Permian are presented in Figure 42. By the year 2060, the annual rate of production will reach 25 billion barrels with 14 billion barrels injected for disposal or re-fracture, and 11 billion barrels requiring treatment of which 7.4 billion could be treated with an advanced treatment such as membrane distillation, and the remaining 3.6 billion barrels would need to receive conventional treatment.

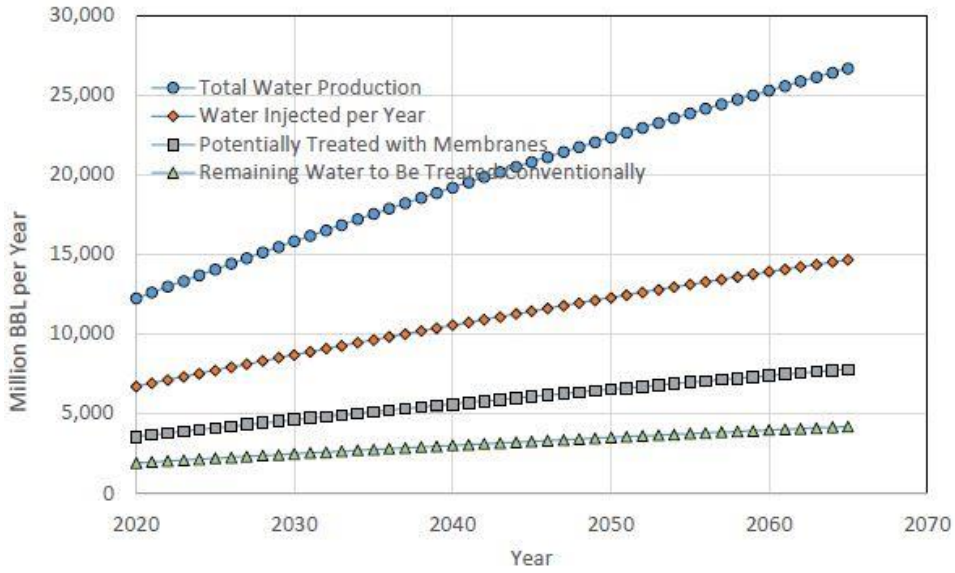


Figure 42: Yearly Projection for PW and Potentially Treated Water in the Permian

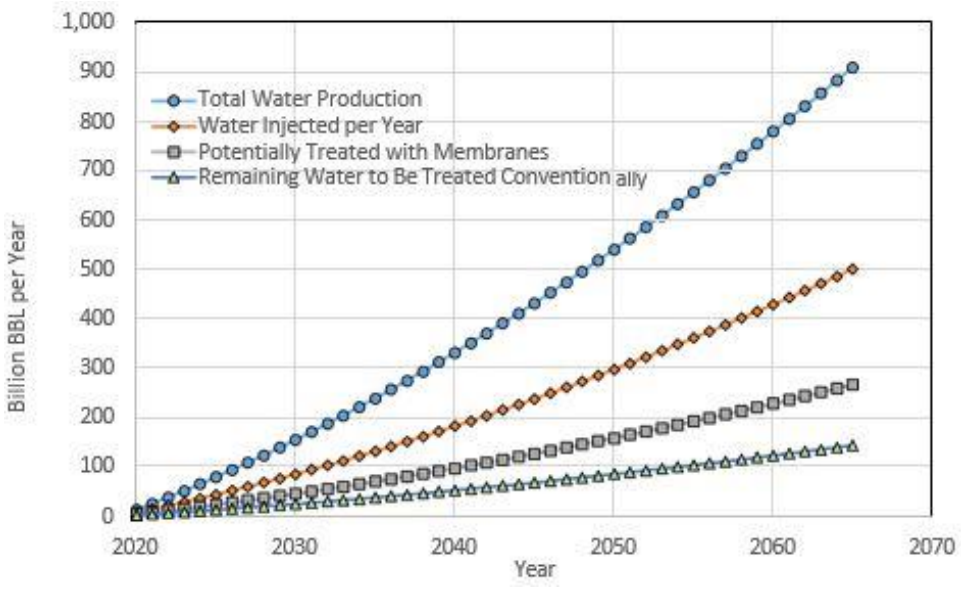


Figure 43: Cumulative Projection for Produced Water and Potentially Treated Water in the Permian

The cumulative projections for produced water in the Permian are presented in Figure 43. By the year 2060, the production will reach 780 billion barrels with 430 billion barrels injected for disposal or re-fracture, and 350 billion barrels requiring treatment of which 230 billion could be treated with an advanced treatment such as membrane distillation, and the remaining 120 billion barrels would need to receive conventional treatment.

Summary of the Permian Results

The average number of active wells in the Bakken ranged from 11,000 to 15,000 wells between 2015 to 2020. The average completion rate for new wells was approximately 800 wells per year. The average production per well was 5,500 BBL/month oil, 5,600 BBL/month produced water and 10,100 million cubic feet of natural gas. The total produced water was approximately 73 million barrels per month which translates into about 186 barrels per well per day. On average, 41% of the produced water was injected for re-pressurization disposal (76 BBL well per day). Not all wells are equal. Some wells are considered gas wells where the gas to oil ratio (cubic feet gas per barrel oil) is around 1000. Other wells considered oil wells where the gas to oil ratio is less than 30. The high-volume gas producing wells tend to produce less water per well than the low-volume gas producing wells which produce a higher volume of water per well. Older oil wells tend to produce more water than mid-age wells, and freshly completed wells tend to produce more water than mid-age wells. Furthermore, some wells flare much of the gas and other wells capture most of the gas for sale or reinject it to maintain well pressure. When considering which wells are suitable for treatment by membrane distillation using flare gas or low quality pre-commercial gas it is necessary to approximate the volume of gas per volume of produced water. Based on the assumption that flared gas can be reasonably diverted (safely) then around 15% of the wells exceed the base assumption that 540 cubic feet per barrel PW based on the boiler option for the heat source. The percentage of wells that can be treated using only flare gas increases to 80% when the base assumption is that only 100 CF/BBL are required.

A life-cycle model was developed to estimate the production of water in the Permian 45 years into the future. The number of existing and future wells were estimated based on the assumption that there are a constant number (3,600 per year) of new wells drilled with a constant rate of closure of 0.5% of the active wells per year. Each active well is assumed to generate an average volume of 10,000 BBL/month produced water. The fate of the water is injection (55% or 5,500 BBL/well per month), with membrane treatment with membrane distillation applied to (65% of active wells) and the remainder (35%) relying on conventional treatment of produced water. It is projected that there will be nearly 250,000 total wells by 2060 with 210,000 remaining active and approximately 40,000 closed wells. Based on 65% acceptance of the technology, the market for treatment equipment could reach 136,000 wells. The projections for the yearly production of produced water in the reach 25 billion barrels with 14 billion barrels injected for disposal or re-fracture, and 11 billion barrels requiring treatment of which 7.4 billion could be treated with an advanced treatment such as membrane distillation, and the remaining 3.6 billion barrels would need to receive conventional treatment. By the year 2060, the cumulative production will reach 780 billion barrels with 430 billion barrels injected for disposal or re-fracture, and 350 billion barrels requiring treatment of which 230 billion could be treated with an advanced treatment such as membrane distillation, and the remaining 120 billion barrels would need to receive conventional treatment.

Cost of Treatment with Membrane Distillation

The project cost estimator is presented as a tool for providing a superficial overview of the utility of membrane distillation for a potential produced water source. The output is an estimate of the cost per barrel ($/BBL) to treat the produced water. Other outputs include an estimate of the capital costs, operating costs, size of the distillation unit (m2 of membrane),

BTU capacity of a heat pump to provide warm and cool water for the process, and the natural gas requirements for the heat required.

The membrane distillation process operates by "vaporizing" water across a membrane from a warm side to a cool side. The warm side is the retentate and retains the salts. The cool side is the distillate which is relatively ion free. The heat loss from the warm side to the cool side is calculated as the heat of vaporization of the warm saltwater times the volume transferred across the membrane. In general, from 35-65% of the warm side water is transferred to the cool side. The efficiency of transfer is dependent upon the temperature differential across the membrane and optimal at ΔT = 40°C (74 °F). While the rate of transfer is roughly 12-16 LMH (liters per hour per square meter of membrane) for seawater, the rate projected in this report is discounted to 2 LMH. To maintain a high efficiency, there needs to be a constant source of warm water. The high rate of latent heat transfer from the warm side to the cool side rapidly increases temperature of the cool water.

The energy demand to treat the produced water is estimated from the latent heat requirement plus a small sensible conduction transfer across the membrane. The theoretical COP of the heat pump is calculated at the input temperatures for the warm side reservoir and the cool side reservoir. An efficiency input (around 50%) discounts the COP to a rational operating value. An efficiency input (nominally 60%) for the heat transfer units in the warm and cool reservoirs is used to further discount the actual heat transfer. The model calculates a rational volume of natural gas required to treat the produced water based on an input value for the BTU quality of the gas burned in the heat pump (nominally 650 – 900 BTU/cubic ft).

The design tool has both a boiler option and a heat pump option, which comprise different worksheets in the program. NOTE: Most input parameters are established on the HEAT PUMP worksheet and directly transported to the BOILER worksheet with the exception of the cost $/million BTU Line 40 delivered for the boiler and the efficiency of the boiler Line 12, both on the BOILER worksheet. Additionally, the heat pump option requires two sets of heat transfer equipment, whereas the boiler option relies on passive cooling and requires only one set of transfer equipment on the heated side. The input and output parameters are described in Appendix G.

Example Cost Model Output

An example cost model output was generated to compare the cost of membrane distillation with heat pump (Table 11) and boiler option (Table 12) for a 1000 BBL/day facility. Note that the heat pump capital cost was assumed to be $175,000 per million BTU/hr and the boiler was set at $75,000 per million BTU/hr. The efficiency of the heat pump was set at 55% whereas, the boiler efficiency was set to 75%. The cost for heat transfer equipment for the heat pump is twice that of the boiler due to the passive nature of cooling with the boiler option. The gas cost was estimated at $3/million BTU. The forward flow was set to 50%. The amortization discount factor was calculated for 4% interest over a 10-year equipment life. All other parameters in the model were the same for both heat source options.

Cost results are show in red colored cells at the end of each Table 11 and Table 12. For this example, the cost of heat pump option is estimated with a total capital cost of $3.7 million, a daily (amortized) equipment cost of $1,323/ day, an operational cost of $641/day for a total

daily cost of $1,964/day which translates into just over $1.95/BBL produced water applied to the unit. The cost of heat pump option is estimated with a total capital cost of $2.29 million, a daily (amortized) equipment cost of $881/ day, an operational cost of $1,131/day for a total daily cost of $1,943/day which translates into just under $1.95/BBL produced water applied to the unit.

Table 11:

Volume of Produced Water (10 to 1000)	1000	BBL/Day
Salt content of Produced Water (Range 0.1 to 7))	8	% weight
Expected Forward Flow (Percent Distillate to PW)	50	% volume
Temperature of Produced Water from Source	70	°F
Temperature of Hot Side Reservoir (to membrane)	150	°F
Cool Side Reservoir (to membrane)	75	°F
Base Efficiency of Membrane (Range 1-16)	2	liter/m^2hour
Maintenance Downtime (hours per day)	3	hours per day
Quality of the Natural Gas used in the Heat Pump	750	BTU/cuft
Cost of the Natural Gas Supplied ($/million BTU)	3	$/million BTU
Efficiency of the heat pump	55	%
Efficiency of the Transfer Coils	80	%
Interest Rate (% yearly) format enter (2 for 2%)	5	i = %
Loan Term (years) Useful Equipment Life	10	Years (n)
Capital Recovery (Annuity/Present Worth, (%,n))	0.130	Discount Factor
Fully Loaded Operator Costs per Annum	$95,000	$/year
Hourly Labor Basis (Work Hours per Annum)	2020	hours per year
Attention to Membrane Distillation (Hours/Day)	3	hours per day

Membrane Replacement (percent per year)	10	%/yr.
Fully Loaded Operator Cost per hour	$47	$/hour
Membrane Cost	$120	$/$m^2$
Pumps, Pipes, Controls	$150	$/BBL-day
Heat Pump	$175,000	$/mmBTU delivered
Transfer Coils	$60,000	$/mmBTU delivered
Physical Structure (Building)	$250	$/BBL-day
Physical Structure (Truck Station)	$0	$/BBL-day
Resevoirs (cool and warm)	$200	$/BBL-day
Miscellaneous Capital Costs	10	Percent of

Estimated Membrane Efficiency based on ΔT	2.0	liter/m^2hour
Size of Membrane Distillation Unit (meter sq)	1832	m^2
Theoretical COP of the Heat Pump	7.6	
Actual COP based on Efficiency Rating	4.2	
Pounds of Distilled Water per day	169,200	
Pounds of Brine Produced per day	201,336	
Specific Gravity of the Brine Produced	1.12	
Concentration of the Brine Produced (% salt)	16.00	% weight
BTU/hr required for latent and sensible heat	10,082,000	BTU/hr
BTU/hr required for for Heat Pump and Transfer	3,005,000	BTU/hr
BTU/BBL PW treated	72,100	BTU/BBL
CF gas/BBL PW Treated	100	CF/BBL

Capital Cost for Membrane Stack	$219,840	Present Worth
Capital Cost for Pumps and Piping, Controls	$150,000	Present Worth
Physical Structure (Building)	$250,000	Present Worth
Truck Station	$0	Present Worth
Capital for Heat Pump	$1,764,350	Present Worth
Capital for Heat Transfer Coil (warm and cool)	$604,920	Present Worth
Capital for Hot and Cool Reservoir	$400,000	Present Worth
Miscellaneous Capital Costs	$338,911	Present Worth
TOTAL Capital	$3,728,021	Present Worth
Natural Gas at Rated BTU value	$216	per day
Downtime (Unused Capital)	$165	per day
Operator Pay	$141	per day
Membrane Replacement	$60	per day
Miscellaneous at 10%	$58	per day
TOTAL Operating Cost	$641	per day
Amortized Capital on a Daily Basis	$1,323	per day
Operating Cost on a Daily Basis	$641	per day
Total Costs on a Daily Basis	$1,964	per day
Amortized Capital per BBL (treated)Basis	$1.32	per BBL
Operating Cost on a per BBL Basis	$0.64	per BBL
Total Costs on a per BBL Basis	$1.96	per BBL

Operator Pay	$141	per day
Membrane Replacement	$60	per day
Miscellaneous at 10%	$58	per day
TOTAL Operating Cost	$641	per day
Amortized Capital on a Daily Basis	$1,323	per day
Operating Cost on a Daily Basis	$641	per day
Total Costs on a Daily Basis	$1,964	per day
Amortized Capital per BBL (treated)Basis	$1.32	per BBL
Operating Cost on a per BBL Basis	$0.64	per BBL

	Total Costs on a per BBL Basis	$1.96	per BBL

Table 12: Membrane Distillation Design and Cost Estimator, Boiler Option

	INPUTS FOR CHARACTER OF PRODUCED WATER		
1	Volume of Produced Water (10 to 1000)	1000	BBL/Day
2	Salt content of Produced Water (Range 0.1 to 7))	8	% weight
3	Expected Forward Flow (Percent Distillate to PW)	50	% volume
	INPUT OPERATING RANGE FOR THE DISTILLATION UNIT		
4	Temperature of Produced Water from Source	70	°F
5 6	Temperature of Hot Side Reservoir (to membrane)	150	°F
7	Cool Side Reservoir (to membrane)	75	°F
8	Base Efficiency of Membrane (Range 1-16)	2	liter/m^2hour
	Maintenance Downtime (hours per day)	3	hours per day
	INPUT DETAILS FOR THE BOILER		
10	Quality of the Natural Gas used in the Heat Pump	750	BTU/cuft
11	Cost of the Natural Gas Supplied ($/million BTU)	3	$/million BTU
12	Efficiency of the Boiler	75	%
13	Efficiency of the Transfer Coils	80	%
	INPUT DETAILS FOR THE ECONOMIC AMMORTIZATION		
14	Interest Rate (% yearly) format enter (2 for 2%)	5	i = %
15	Loan Term (years) Useful Equipment Life	10	Years (n)
16	Capital Recovery (Annuity/Present Worth, (%,n))	0.130	Discount Factor
	INPUT DETAILS ON LABOR AND MAINTAINCE		
17	Fully Loaded Operator Costs per Annum	95000	$/year

18	Hourly Labor Basis (Work Hours per Annum)	2020	hours per year
19	Attention to Membrane Distillation (Hours/Day)	3	hours per day
20	Membrane Replacement (percent per year)	10	%/yr
21	Fully Loaded Operator Cost per hour	$47	$/hour
INPUT ON CAPTIAL			
22	Membrane Cost	120	$/m^2
23	Pumps, Pipes, Controls	150	$/BBL-day
24	Boiler	$75,000	$/mmBTU delivered
25	Transfer Coils	60000	$/mmBTU delivered
26	Physical Structure (Building)	250	$/BBL-day
27	Physical Structure (Truck Station)	0	$/BBL-day
28	Resevoirs (warm)	200	$/BBL-day
29	Miscellaneous Capital Costs	10	Percent of Total

OUTPUT DETAILS ON THE MEMBRANE DISTILLATION UNIT Boiler Option			
30	Estimated Membrane Efficiency based on ΔT	2.0	liter/m^2hour
31	Size of Membrane Distillation Unit (meter sq)	1832	m^2
	OUTPUT DETAILS ON THE HEAT TRANSFER EQUIPMENT		
32	Theoretical COP of the Heat Pump	NA	
33	Actual COP based on Efficiency Rating	NA	
	OUTPUT DETAILS ON THE PROCESS STREAMS		
34	Pounds of Distilled Water per day	169,200	
35	Pounds of Brine Produced per day	201,336	
36	Specific Gravity of the Brine Produced	1.12	
37	Concentration of the Brine Produced (% salt)	16.00	% weight
	OUTPUT DETAILS ON THE ENERGY REQUIREMENTS		
38	BTU/hr required for latent and sensible heat	10,082,000	BTU/hr
39	BTU/hr reqired for for Boiler and Transfer	16,803,333	BTU/hr
40	BTU/BBL PW treated	403,300	BTU/BBL
41	CF/BBL	538	CF/BBL
	OUTPUT DETALS ON THE CAPITAL COSTS (present worth)		
42	Capital Cost for Membrane Stack	$219,840	Present Worth
43	Capital Cost for Pumps and Piping, Controls	$150,000	Present Worth
44	Physical Structure (Building)	$250,000	Present Worth
45	Truck Station	$0	Present Worth
46	Capital for Boiler	$756,150	Present Worth
47	Capital for Heat Transfer Coil (warm and cool)	$302,460	Present Worth
48	Capital for Hot and Cool Reservoir	$400,000	Present Worth
49	Miscellaneous Capital Costs	$207,845	Present Worth
50	TOTAL Capital	$2,286,295	Present Worth
	OUTPUT DETALS ON THE OPERATING COSTS		
51	Natural Gas at Rated BTU value	$726	per day

52	Downtime (Unused Capital)	$101	per day
53	Operator Pay	$141	per day
54	Membrane Replacement	$60	per day
55	Miscellaneous at 10%	$103	per day
56	TOTAL Operating Cost	$1,131	per day
	TOTAL DAILY COSTS		
57	Amortized Capital on a Daily Basis	$811	per day
58	Operating Cost on a Daily Basis	$1,131	per day
59	Total Costs on a Daily Basis	$1,943	per day
	TOTAL COSTS ON A PER Barrel Basis		
60	Amortized Capital per BBL (treated)Basis	$0.81	per BBL
61	Operating Cost on a per BBL Basis	$1.13	per BBL
62	Total Costs on a per BBL Basis	$1.94	per BBL

Cost Sensitivity to the Price of Pre-commercial Gas

Table 13: Capital Differential Between Heat Pump and Boiler vs Cost of Pre-Commercial Gas			
Membrane Distillation Plant Size	500 BBL/d	1,000 BBL/d	1,500 BBL/d
Capital Heat Pump Option ($ millions)	$1.85	$3.73	$5.58
Capital Boiler Option ($ millions)	1.14	1.85	2.55
Δ Capital (Millions)	0.72	1.88	3.04
$/million BTU	Δ Fuel $/day		
$1	$84/d	170	254
2	168	340	508
3	252	509	763
4	337	679	1017
5	421	849	1271
$/million BTU	Payback of the Cost Differential (Δ Capital) Years		
$1	23.3 Yr.	30.4	32.8
2	11.6	15.2	16.4
3	7.8	10.1	10.9
4	5.8	7.6	8.2
5	4.7	6.1	6.6

The heat pump option is projected to be more capital intensive than the boiler option while the boiler option is more expensive to operate. There is a cost benefit to the heat pump if the cost of

the natural gas is expensive. This benefit can be estimated based on the ratio of the difference in capital divided by the difference in the yearly cost of fuel. Table 13 examines the capital costs (using inputs in Tables 11 and 12) for these plant sizes ranging from 500 to 1500 BBL/day and the difference in fuel costs between for the heat sources with fuel costs ranging from $1 to $5/million BTU. The time to pay-off the difference in capital costs is from 4.7 to 33 years.

Conclusions

Heat sources for membrane distillation of produced water were evaluated. The baseline heat required for treatment of a barrel of PW is 244,030 BTU/BBL assuming a 50% forward flow (50% distilled water 50% brine, latent and sensible heat demand, and 10% conductive heat transfer across the membrane. Based on the efficiency of boilers and heat pumps, the heat demand is around 407,000 BTU/BBL for boilers and 74,030 BTU/lb for heat pumps with a theoretical COP of 7.6 and an operating COP of 4.2. The capture of heat from diesel engines, is discouraged because of the low quality, low quantity, inadequate availability near PW sources, and lack of interest from equipment vendors. The heat pump option is more capital intensive than the boiler option while the boiler demands more fuel. The fuel difference is estimated at 100 CF/BBL for the heat pump and 540 CF/BBL for the boiler option using 750 million BTU/CF pre-commercial gas.

While there are no examples of equipment for the transfer of heat to produced water, conservative estimates for establishing a membrane distillation treatment site are estimated at $2.11, $1.96, and $1.91/BBL for the heat pump and $2.09, $1.96, and $1.89/BBL for the boiler option at plant sizes of 500, 1000, and 1500 BBL/day, respectively. The excess capital cost of the heat pump option is covered by lower fuel costs. At $3/CF for pre-commercial gas, and at an interest rate of 4% for a project life of 10 years, the excess capital for a 1,000 BBL/day plant is recovered at the end of service life of 10 years. A cost model is supplied for readers to apply their own cost and operating parameters.

One potential source of pre-commercial gas is the diversion of flare gas as the fuel for the heat pump or the boiler. Most of the Bakken oil wells also generate natural gas, and flaring is a common occurrence throughout the region and accounts for 10-15% of the generated gas. If the diversion of flare gas can be achieved safely and economically, there is a natural market for a technology such as membrane distillation which potentially be applied to 15% of the currently active wells using boilers as the heat source and 80% of the currently active wells using heat pump technology using recovered flared gas. There are currently some 13,000 active wells generating 850 million BBL/yr. of produced water. The current rate of injection for pressure or disposal is 41% leaving 500 million BBL for conventional treatment. Application of a technology such as membrane distillation to 65% of the wells would open a market for 325 million BBL/year on flared gas alone. By 2060 there is a potential for 53,000 active wells producing 3.1 billion BBL/year PW. Using the current rate of injection, this leaves 1.8 billion BBL/yr. needing treatment. Using the same criteria of 65% of the wells accessible to treatment using a technology such as membrane distillation, the would be a potential at, of which Incorporation of 34,300 wells and 1.2 billion BBL/yr. The market for advanced treatment would expand if pre-commercial gas were also to be utilized for water treatment.

Texas has strict ordinances against flaring natural gas at the wellheads. As such, the recovery of flared gas as a heat source is unavailable as an option. Well production in the Permian is very

diverse as the recovery of natural gas and oil. In some Permian counties, the oil production is low, and the gas volume is large. In other counties, the oil production is high, and the gas volume is low. Other counties generate a wide range of oil/gas. Most of the produced water in the Permian is generated by the oil wells, and the range of produced water per unit oil production ranges from 4 to 10 BBL/BBL. Rates of generation of PW are estimated at 9–15 million BBL/day (3.3 billion to 5.5 billion BBL/year) with 5 million BBL/d in-excess of the volumes reused or deep well injected. Based on an assumed average of 4.4 BBL PW/BBL oil the average production of PW is 10,000 BBL/month per well is 12.2 billion BBL/yr. Due to the wide range of gas and oil production (as rated on a county-wide basis), about 20 % of the wells do not generate natural gas and 15% generate more than 2,500 CF/BBL. There are 65% of the wells that produce sufficient gas to treat the water by the heat pump option and 35% of the wells that could treat using the boiler option. The projections for the yearly production of produced suggest that by year 2060, the annual rate of production will reach 25 billion barrels with 14 billion barrels injected for disposal or re-fracture, and 11 billion barrels requiring treatment of which 7.4 billion could be treated with an advanced treatment such as membrane distillation, and the remaining 3.6 billion barrels would need to receive conventional treatment.

References

1. Al-Obaidani, S., Curcio E., Macedonio, F. Di Profio, G., Al-Hina, H., and Drioli, E. (2008) Potential of Membrane Distillation in Seawater Desalination: Thermal Efficiency, Sensitivity Study and Cost Estimation. J. Membrane Science, pp 85-98.
2. Bennet, C.O., and Myers J.E. (1974) Momentum, Heat, and Mass Transfer, Second Edition, McGraw-Hill NY, Chapter 4; Chapter 17: Conduction and Thermal Conductivity pp. 246-253; Chapter 24: Some Design Equations for Convective Heat Transfer pp. 370-397.
3. Boysen, J.E., D. Boysen, and T. Larson. 2002. Field Application of the Freeze Thaw Evaporation (FTE) Process for the Treatment of Natural Gas Produced Water in Wyoming. GRI Report No. GRI-02/0221. Available from the Gas Technology Institute, Des Plaines, IL.
4. Comancho, L.M., et al., 2013. Advances in Membrane Distillation for Water Desalination and Purification Applications. Water 5, 94-196.
5. Dow Chemical Company, A Guide to Glycols, http://msdssearch.dow.com/PublishedLiteratureDOWCOM/dh_091b/0901b8038091b508.pdf?filepath=pro
6. Duong, H.C., et al., 2021. Seawater Membrane Distillation Desalination for Potable Water Provision on Remote Islands – Case Study in Vietnam. Case Studies in Chemical and Environmental Engineering 4: 100110.
7. Guerra, K., K. Dahm, and S.D. Anderson. 2011. Oil and Gas Produced Water Management and Beneficial Use in the Western U.S. In: Bureau of Reclamation Science Technology Report No. 157. 113 p.
8. GWPC, 2019. Produced Water Report: Regulation, Current Practices and Research Needs. Groundwater Protection Council (GWPC), 310 p.
9. Hart Energy (2018) HartEnergy.com, Hart Energy 2018 Permian Basin Playbook.,

10. Hayes, T.D. and B.F. Severin. 2012a. Evaluation of the Aqua Pure Mechanical Vapor Recompression System in the Treatment of Shale Gas Flowback Water. DOE Contract 08122-05. Available from the Gas Technology Institute, Des Plaines, IL.
11. Hayes T.D., and Severin B.F. 2012b. Evaluation of Electrodialysis for the Demineralization of Shale Gas Flowback Water. DOE Contract 08122-05. Available from the Gas Technology Institute, Des Plaines, IL.
12. Hayes, T.D., and Smith T. , 2012. Techno-economic Assessment of Shale Gas Water Management Solutions. GTI Report No. GTI-12/0004. Available from the Gas Technology Institute, Des Plaines, IL.
13. Khattab I.S., Bandarkar, F., Khoubnasabjafari, M., and Jouyban, A., (2017) Density, viscosity, surface tension, and molar volume of propylene glycol + water mixtures from 293 to 323 K and correlations by the Jouyban–Acree model. Arabian Journal of Chemistry Volume 10, Supplement 1, February 2017, Pages S71-S75.
14. Kesieme U.K., Milne N., Aral H., Cheng C.Y. and Duke,M. (2013) Economic Analysis of Desalination Technologies in the Context of Carbon Pricing, and Opportunities for Membrane Distillation. Distillation, August 15, pp 66-74.
15. Lokare, O.R., Tsvakkoli, S., Rodriguez, G., Khanna, V., Vidic, R.D. 2017. Integrating membrane distillation with waste heat from natural gas compressor stations for produced water treatment in Pennsylvania. Desalination 413, 144-153.
16. Pangarkar, B.L,Sane, M.G.,Parjane, S., and Guddad, M. V. (2014). Status of Membrane Distillation for Water and Wastewater Treatment—A review. Desalination and Water Treatment 52(28-30) DOI: 10.1080/19443994.2013.808422
17. Permian Produced Water Society (2019), https://producedwatersociety.com/the-rise- of-recycling-in-the-permian/
18. Robbins, C.A., B.M. Granberger, S.D. Garland, K.H. Carlson, S. Lin, T.M. Bandhauer, and T. Tong. 2020. On-site treatment capacity distillation powered by waste heat or natural gas for unconventional oil and gas wastewater in the Denver-Julesburg Basin. Environment International Journal 145: 106142.
19. Shale Profile.com 2021) https://shaleprofile.com/blog/permian/permian-update-through-August-2021.
20. Smith J.M., and Van Ness, H. C. (1975) Introduction to Thermodynamics, Third Edition, McGraw-Hill NY., Chapter 11.
21. Texas Railroad Commission (2019) https://www.rrc.state.tx.us/oil-gas/research-and-statistics/production-data/ Data sources,by County. contain different types of data; as such, the approaches to identifying geographic (by county) that might have flare gas available are different.
22. Texas Railroad Commission (2019) https://rrc.texas.gov/about-us/resource-center/faqs/oil- gas-faqs/faq-flaring-regulation/ Summary of Flaring Regulations
23. USGS (2008) R.M. Pollastro, L.N.R. Roberts, T. A. Cook, and M.D. Lewan, Assessment of

Undiscovered Technically Recoverable Oil and Gas Resources of the Bakken Formation, Williston Basin, Montana and North Dakota, 2008

24. Zhang, Z., 2019. Thesis Treatment of Shale Oil and Gas Produced Water Using Membrane Distillation Combined with Effective Pretreatment. Department of Civil and Environmental Engineering In partial fulfillment of the requirements For the Degree of Master of Science Colorado State University Fort Collins, Colorado Spring 2019.

Appendices

Appendix A: Basis for Minimum Heat Demand for Membrane Distillation

The theoretical heat demand for membrane distillation of produced water (PW) may be estimated from thermodynamic principles. Figure A1 is a summary of the complexity of the overall process. The use of waste heat for membrane distillation involves a complex cascade of heat and mass transfer (Figure A1). Heated brine is contacted with cool water across the membrane stack. Heated brine releases water to the cool water, heating the cool water by conduction (about 20% sensible heat) plus latent heat of vaporization of the water transferred across the membrane. If no further heat loss occurs during the process (i.e., ideal insulation), the finished process water is the recipient of most the heat transferred upstream. Because the membrane is most efficient with a constant temperature differential between the warm brine and the cool water (ΔT = 75°F), it is unacceptable to directly reuse the finished water without some method of cooling.

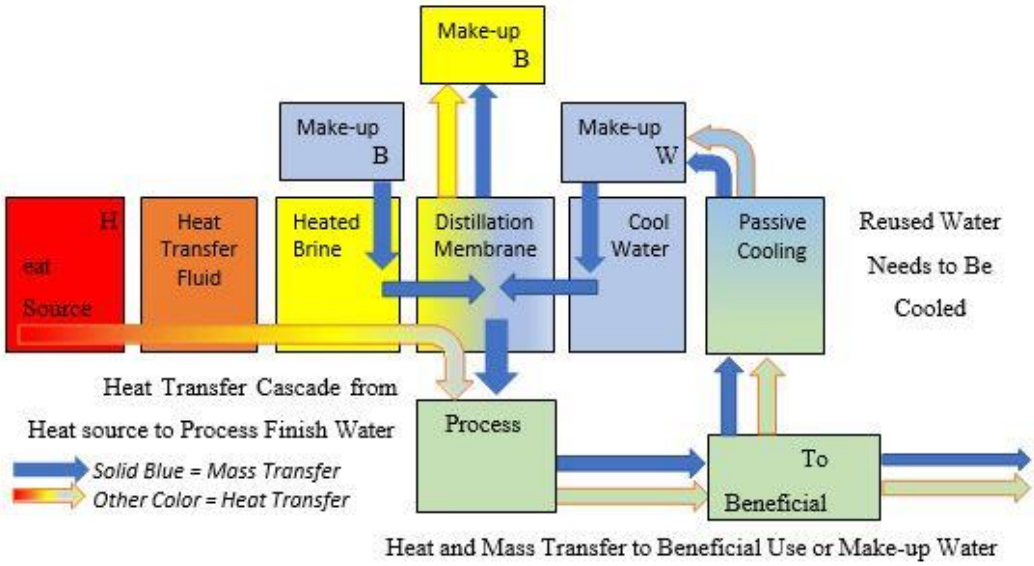


Figure A1. Heat and Mass Transfer in a Waste Heat Membrane Distillation Process

Disregarding any loss of efficiency such as encountered with steam generators, heat pumps, or capture with annular shells envisioned for diesel engine exhaust, there is a minimum heat requirement that follows as in Table A1. Table A1 shows the calculations for the BTU per pound PW applied to the process, the BTU demand per barrel PW applied, and the BTU/BBL of distilled water (DW) generated. Most of the heat loss is the latent heat of vaporization. A conductive heat loss of 10% of the latent heat is assumed and is the second largest heat loss. The third largest heat demand is the heating of the source PW from 60 °F to 150°F, followed by losses of heat in the discharge brine and DW flows. Note that the salt component has minimal impact on heat demand, since the salt mass a few percent of the water mass, and the heat capacity of salt is

about 15% that of water.

Table A 1:Estimate of Theoretical Minimum Heat Required to Generate DW from PW at 60 F									
Forward Flow	40%			50%			60%		
Brine Flow	60%			50%			40%		
Heat Demand	BTU/lb PW Applied	BTU/BBL	BTU/BBL DW Generated	BTU/lb PW Applied	BTU/BBL PW Applied	BTU/BBL DW Generated	BTU/lb PW Applied	BTU/BBL PW Applied	BTU/BBL DW Generated
Heat Source Water to 150 F	90	31,500	78,800	90	31,500	63,100	90	31,500	52,500
Vaporization at Membrane	403	141,200	353,100	504	176,500	353,100	605	211,800	353,100
Conductive Heat at Membrane	40	14,100	35,300	50	17,700	35,300	60	21,200	35,300
Brine Discharge from Warm Side	54	18,900	47,300	45	15,800	31,500	36	12,600	21,000
Distilled Water from Cool Side	6	2,100	5,300	8	2,600	5,300	9	3,200	5,300
Salt at 5% in Produced Water	1	240	590	1	240	470	1	240	390
Total	594	208,040	520,390	698	244,340	488,770	801	280,540	467,590
PW = Produced Water		DW = Distilled Water		Warm Side = 150 °F		Cool Side = 75 °F		BBL = 42 gallons	

Appendix B: Heat Pumps Applied to the Membrane Distillation Process

B.1 Summary:

The membrane distillation process uses a temperature differential between two water streams to cause water to vaporize (across the membrane) from the warm water (feed) to the cool water (permeate). Salts concentrate in the feed. The cool permeate is generated as a distillate without salt. This project investigates the ability to use the membrane process on shale gas produced water. In previous reports on the potential use of the membrane process to treat produced water, there have been claims that there is sufficient flare gas available to use as direct heat (via a boiler) to treat all of the produced water generated.

An estimate of the energy needed to operate a membrane distillation unit with a gas fired with boiler is about 595,000 BTU/BBL (about 590 CF/BBL) assuming a 55% efficient boiler and 75% efficiency in heat transfer coils. Unfortunately, many well fields have little or no source for the cool-side water and ambient cooling ponds would need to be constructed. Not stated in this estimate is the need for a constant source of cool permeate water to maintain the temperature differential across the membrane.

The ability to treat water using flare gas to operate a heat pump has a thermodynamic advantage over using the energy required to operate a boiler. A heat pump would operate by removing heat from a cool reservoir and transfer it to a warm feed reservoir. By setting the feed temperature at 150°F and the cool permeate reservoir at 75°F means that theoretical "Carnot Engine" would transfer 8.1 units of energy for every unit of energy expended. By including some estimates of efficiency losses, 55% efficient heat pump and 75% efficiency in transfer coils, a heat pump could potentially transfer 4.4 times more heat than a boiler and require 134,000 BTU/BBL (about 134 CF/BBL). A heat pump has the added advantage over direct heating in that the cool reservoir is actively targeted to remain at an optimal temperature.

B.2 Objective

The purpose of this report is to determine the base-line performance expected if heat pump technology could be adapted to the membrane distillation process. The membrane distillation process works by the application of a warm, salty water on the feed side, and a cool water (relatively fresh) on the permeate side of an ion exclusionary membrane. By virtue of the difference in the between the vapor pressures between the two solutions, water passes from the warm water to the cool water. Water molecules pass through the membrane by "vaporization" hence this is a true distillation process. Salts are retained on the warm water side of the membrane. As a result, the warm water becomes saltier, and the cool side becomes less salty. Because the vapor pressure differential is the driving force for water transport, the process fails if a cool water (heat sink) is not readily available. In previous heat models in this report, the assumption has been that there is always readily available cool water. This assumption fails for certain well fields that either lack sufficient cool water resources, or there is a constant demand for the fresh water generated by the membrane process.

B.3 Results

The intent of the heat pump model is to estimate of the energy required to generate one barrel of distilled water. This value (BTU/lb water) will be used to estimate the total volume of produced water that can be treated from waste flare gas or low BTU (pre-commercial) available at many well heads. Since the volume of produced water generated per well and the volume of gas flared

at a site are highly variable, there is no present need to have more than a crude estimate of the energy required per barrel of water generated. As such, several assumptions are made to simplify the calculation.

The following analysis (Table B1) is based on the water fraction of the produced water, as the heat capacity of salt adds only 15% if the sensible heat and none of the latent heat of vaporization. For a source of produced water at 60 °F and 50% of the produced water is passed through the membrane, and assuming a latent heat of 1008 BTU/lb water (at 150 °F) and sensible heat transfer across the membrane of 0.1 x latent heat, then including bleed loss from removal of processed (cool) water from the cool-side reservoir, the theoretical BTU demand to treat a barrel of produced water is around 1396 WM BTU per Lb water passed through the membrane where WM is the mass flow rate of water passing through the membrane. There are about 350 Lb water in one barrel or 488,770 BTU/BBL DW produced, or 244,340 BTY/BBL applied to the system.

The theoretical coefficient of performance (COP) of a heat pump is calculated from the temperature differential. If reservoirs of warm-side brine and cool-side water are available for continuous feed to the membrane process, the COP may be calculated from the temperatures of the fluids. For the case where the warm-side reservoir is maintained at 150 °F (630 °R) and the cool-side is maintained at 75 °F (535 °R) then the theoretical COP is 8.1.

$$COP = \frac{Heat\ Transfered\ to\ Warm\ Side}{Work\ Required} = \frac{H_H + H^*}{H^*} = \frac{T_F}{T_F - T_P} = \frac{150+460}{150+460-(75+460)} = 8.1$$

Assuming that the heat pump is n= 55% efficient, then the performance of the heat pump is estimated to be 4.4. This means that the heat pump requires (1/4.4 = 23%) of the input energy necessary to vaporize the water by boiling with direct heat.

$$COP_{actual} = \eta COP = 4.4$$

The heat required with a heat pump and with 75% efficient heat transfer is:

$$Heat_{actual} = \frac{Heat_{theoretical}}{COP\ x\ \eta_{source\ x}\ \eta_{heat\ transfer}}$$

Table B 1: Estimate of Heat Required to Generate DW from PW, Heat Pump Compared to Boiler

Forward Flow	50%			
Brine Flow	50%			
Heat Demand	BTU/lb PW Applied	BTU/BBL PW Applied	BTU/lb DW Generated	BTU/BBL DW Generated
Heat Source Water to 150 F	90	31,500	180	63,100
Vaporization at Membrane	504	176,500	1008	353,100
Conductive Heat at Membrane	50	17,700	100	35,300

Brine Discharge from Warm Side	45	15,800	90	31,500
Distilled Water from Cool Side	8	2,600	18	5,300
Salt at 5% in Produced Water	1	240	2	470
Total Heat Needed	698	244,340	1,396	488,770
Heat Pump ηCOP of 4.4 and 75% heat fin efficiency	212	74,042	414	148,084
Boiler Demand with 60% boiler and 75% transfer efficiency	1551	542,977	31,022	1,086,000

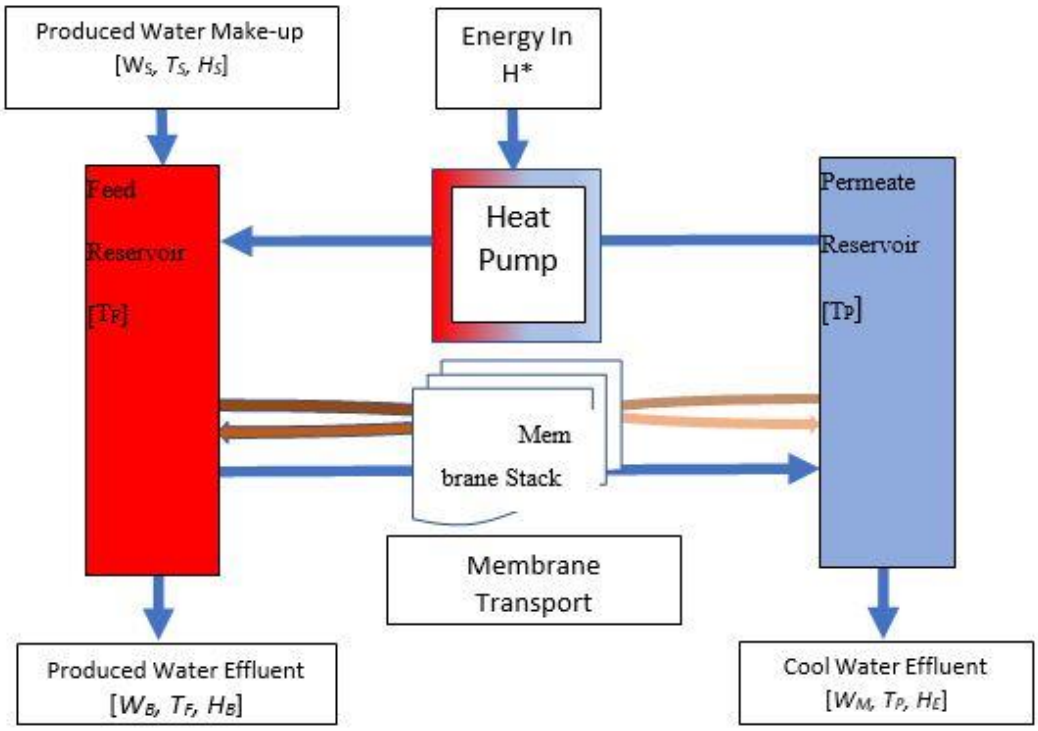


Figure B1. A Simple Heat Pump Calculation

B.4 Heat and Mass Transfer Calculation

The intent of the heat pump model is to estimate of the energy required to generate one barrel of distilled water. This value (BTU/lb water) will be used to estimate the total volume of produced water that can be treated from waste flare gas. Since the volume of produced water generated per well and the volume of gas flared at a site are highly variable, there is no present need to have more than a crude estimate of the energy required per barrel of water generated. As such, several assumptions are made to simplify the calculation. The model is presented as Figure B1 with accompanying term definitions in Table B2.

Table B 2: Nomenclature for the Heat Pump Calculation							
		Feed Reservoir (Warm)		Membrane	Heat Pump	Permeate Reservoir (Cool)	
Term	Units	Source	Bleed			Feed	Effluent
Heat	BTU·min^{-1}	H_S	H_B	H_M = (1+α) H_V	H*= energy in H_H = work out	H_M = (1+α)	H_E
Water	Lb·min^{-1}	W_S	W_B	W_M	NA	W_M	W_M
Temp	°R	T_S	T_F	T_F			T_P

Note that there is a conductive heat loss (α =0.1) added to the latent heat to account for heat transfer without mass transfer. The heat needed to be supplied by the heat pump is the heat to treat distill Wm pounds of water were reviewed in the Table B1. The influence of salt on the heat balance is minimal and has been neglected for simplicity. For example, salt has a heat capacity about 15% that of water. For the purposes of the present calculation the salt concentration may be assumed 5% in the source water. Salt enters with the feed stream WS at 60 °F, and leaves in the bleed stream WB at 150°F. Therefore, the heat load on the system due to the salt component is small compared to the other heat demands. A sample calculation is presented in Table B3.

$BTU_{Salt} = 0.05 \times 0.15 \times (150\text{-}60)\ W_s = 0.67\ W_S = 1.35\ W_M$

Subscripts	Constants or Parameters
$_B$ - Bleed Stream from Feed Reservoir	C_P - Heat Capacity of Water ~1 BTU Lb^{-1} °R^{-1}
$_F$ - Feed Reservoir	H_V - Heat to Vaporize Water ~1008 BTU Lb^{-1}
$_H$ - Heat Pump	α - Conductive Heat Transport Factor ~0.2 Dimensionless
$_M$ - Transport across Membrane	COP- Heat Pump Carnot Efficiency Dimensionless
$_P$ - Permeate Reservoir	η - Efficiency of a Heat Pump ~55%
$_S$ - Feed Source (Produced Water)	β - Efficiency of a Heat Transfer Coil ~75%
$_V$ - Vapor	T - Reference Temperature (32°F, 492°R)
*- Energy Supplied to a Heat Pump	

B.5 Discussion and Conclusions:

The ability to treat water using flare gas to operate a heat pump has a thermodynamic advantage over using the energy to operate a boiler. To run the distillation unit with boiler heat requires a minimum heat demand of 244,340 BTU/BBL. With a 60% boiler efficiency and 75% heat transfer efficiency, actual demand is closer to 244,340/ (0.6 x 0.75)) = 543,000 BTU/BBL applied. This is about 4.4 (the value of ηCOP) times greater than the 74,042 BTU/BBL needed with a 55% efficient heat pump with 75% heat transfer efficiency. The effectiveness of the heat pump is that it delivers heat from the cool permeate reservoir to the warm feed reservoir. It has the added advantage over direct heating in that the cool reservoir is actively targeted to remain at an optimal temperature (in this example 75°*F*) and does not require the need to constantly provide cool water to maintain the desired temperature differential across the membrane.

Table B 3: Material and Energy Balances (See Figure B1)			
Balance	Feed Reservoir (Warm)	Permeate Reservoir (Cool)	Overall System
Water	$W_S = W_B + W_M$	$W_M = W_E$	$W_S = W_B + W_M$
Heat	$H_S + H_H + H^* = H_M + H_B$	$H_M = (1+\alpha)\, H_V = H_E + H_H$	$H_S + H^* = H_B + H_E$
Note: Any flows associated with the RECYCLE LOOPS are written as internal to the Feed or Permeate Control Volumes and can be neglected.			

Table B4: Assumptions and Derivation of Energy Required per Lb Water Treated			
		Note	
H_V @150°F =	1008 BTU/Lb	The error if T_F is incorrect is about 0.05% per °F	
T_S =	60 °F		
T_F=	150°F		
T_P=	75°F		
C_P=	1.0 BTU/Lb-°F		
α=	0.1	Estimate for the sensible heat loss at membrane	
Bleed Ratios	$W_B = 0.5\, W_S$	$W_S = 2\, W_M$	$W_B = 1\, W_M$
Term	Equation		
H_S	$= C_P\, W_S\, (T_S\text{-}T)$	$= 1\, W_S\, (150\text{-}90)$	$= 90\, W_M$
H_B	$= C_P\, W_B\, (T_F\text{-}T)$	$= 1\, W_B\, (150\text{-}60)$	$= 45\, W_M$
H_E	$= C_P\, W_E\, (T_P\text{-}T)$	$= 1\, W_E\, (75\text{-}60)$	$= 7.5\, W_M$
H_M	$= (1+\alpha)\, H_V W_M$	$= 1.1\, W_M\, (1008)$	$= 1109\, W_M$

Appendix C: Heat Transfer from Diesel Engine Exhaust

C.1 Summary:

Diesel engines are commonly used at natural gas pumping stations located to maintain pressure in the transmission lines. The recovery of heat from the engines was suggested as one method to heat produced water for treatment by the membrane distillation unit. The example used in this report was a pumping station with nine 440 HP engines, each engine producing 12,000 CFM of exhaust at 900 °F. The following discussion is based on the collection of waste heat from one engine and assumes that the latent heat of vaporization is 1000 BTU/lb fluid or 380,000 BTU/BBL treated. It was assumed that the exhaust pipes could be incorporated into annular heat exchangers with the inner pipe being the exhaust and the ring of the annulus containing a benign heat transfer fluid. Three fluids were considered, single pass air, infinite loop air, and infinite loop propylene glycol. Single pass air would be insufficient to treat more than 0.3 BBL/d at a warm-side temperature of 140 °F. There was no condition where 150 °F inlet water was easily reached. Running the air in an infinite loop could provide sufficient thermal capacity to produce provide insufficient heat transfer and at best could generate enough heat to bring between 6

and 14 BBL/d to 140 °F. With propylene glycol as the heat transfer fluid,

C.2 Objective:

One proposal for use as a heat source from that waste heat can be recovered from various natural gas production processes to make the membrane distillation of produced waters to be essentially "energy free". One source of waste heat is generated by diesel engines at natural gas pumping stations. One example pumping station has nine 440 HP engines. Each engine produces 12,000 CFM of exhaust at 900 °F. The purpose of this report is to examine the feasibility of heat recovery from diesel exhaust pipes without major engine retrofits or interfering with the engine efficiency.

The use of waste heat for membrane distillation involves a complex cascade of heat and mass transfer (Figure C1). An existing heat source, such as an exhaust pipe from a diesel engine, must be carefully retrofitted with heat transfer equipment such that the loss of heat or pressure does not impede the normal operation of the engine. The heat transfer device uses a heat transfer fluid to move a heated fluid to secondary transfer device that heats a tank of brine. Because of the caustic nature of the brine, direct use of the brine as the heat transfer fluid is dismissed for the inevitable damage done to the diesel engine. Therefore, a benign fluid such as air or propylene glycol is used in the present examples.

Heated brine is contacted with cool water across the membrane stack. Heated brine releases water to the cool water, heating the cool water by conduction (about 20% sensible heat) plus latent heat of vaporization of the water transferred across the membrane. If no further heat loss occurs during the process (i.e., ideal insulation), the finished process water is the recipient of most the heat transferred upstream. Because the membrane is most efficient with a constant temperature differential between the warm brine and the cool water (ΔT = 75°F), it is unacceptable to directly reuse the finished water without some method of cooling, passive or otherwise.

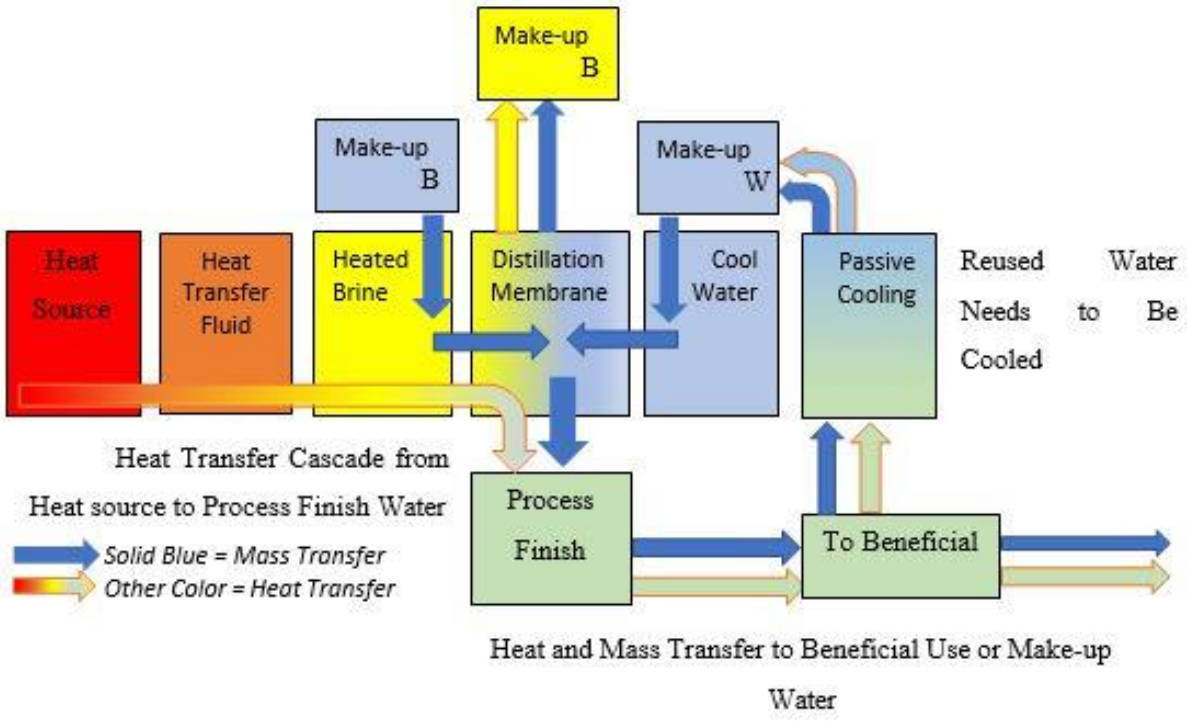


Figure C 1: Heat and Mass Transfer in a Waste Heat Membrane Distillation Process

A considerable effort was expended to determine if commercial heat extraction devices were available. None of a dozen or more companies were able to recommend a method, except for one suggestion that a single-pass air system ducted around the exhaust pipe would potentially be beneficial. Based on this suggestion, it was determined that a heat transfer model should be constructed to look at the extraction of heat from diesel exhaust pipes. In this report we examine various modification of a concept for a shell contactor around an exhaust pipe and a plenum of tubes within a tank of brine. The three examples are:

- Single-pass air through a shell to a plenum of tubes in a tank of brine.
- Infinite recycle of air through a shell into a plenum of tubes with air returned to the shell.
- Infinite recycle of propylene glycol through a shell into a plenum with return to the shell.

C.3 Model Heat Transfer System:

Inputs: An engine exhaust stack is retrofitted with an external pipe to form an annular shell around the exhaust stack as in Figure C2. The temperature of the inlet stack gas and transfer fluid are variables, as are the volume of the stack gas and the heat transfer fluid. The diameter of the stack and the annular shell and the length of the contact of the shell with the stack are variables.

A heat transfer fluid, such as air or propylene glycol is flowed into the annulus of the shell. The warm fluid from the annular shell then sent to a plenum of tubes within a passively mixed brine tank. The number of tubes in the plenum is a variable. The diameter of the "n" tubes in the plenum is set such that the total cross-sectional area of the "n" tubes is to equal the cross-sectional area of the outer ring of the annular shell. The length each tube is a variable. The tank is assumed to have passive mixing with a recommended value of 0.5 to 2 feet/sec across a tube (a variable).

The brine tank is of infinite capacity such that the temperature of the brine is always at a target temperature sufficient to meet the needs of the warm side of the membrane distillation system. A very small portion of the warm brine is sent to the membrane distillation unit. This small portion of brine is replenished with make-up brine. The temperature of the make-up brine is variable. The salinity of the brine is a variable. The mass of brine that can be treated by the membrane distillation unit is based on the heat transferred across the plenum to the brine. As such, the ability to transfer heat to the brine tank is a function of the ability to transfer heat from the exhaust to the transfer fluid.

The model does not consider any heat transfer issues concerning the distillation membrane or the cooling of the finished water.

Calculations: The principles of heat transfer used to generate the model are reviewed in Appendix A. The fluid thermodynamic properties: density, thermal conductivity, heat capacity, and viscosity are presented in Appendix B. To facilitate calculation, each thermodynamic property was correlated over a range of values. Each correlation is also presented in Appendix B.

The model calculates the fluid thermodynamic properties based on the arithmetic average of the temperature in the inlet-side and the fluid temperature on the outlet-side. The outlet temperature is input as initially an estimate input by the model user.

Heat transfer coefficients are calculated based on flow velocities, pipe or annular diameters, and

the thermodynamic properties at the average temperature. The heat transferred to a fluid is calculated. The transferred heat is used to re-estimate the outlet fluid temperature.

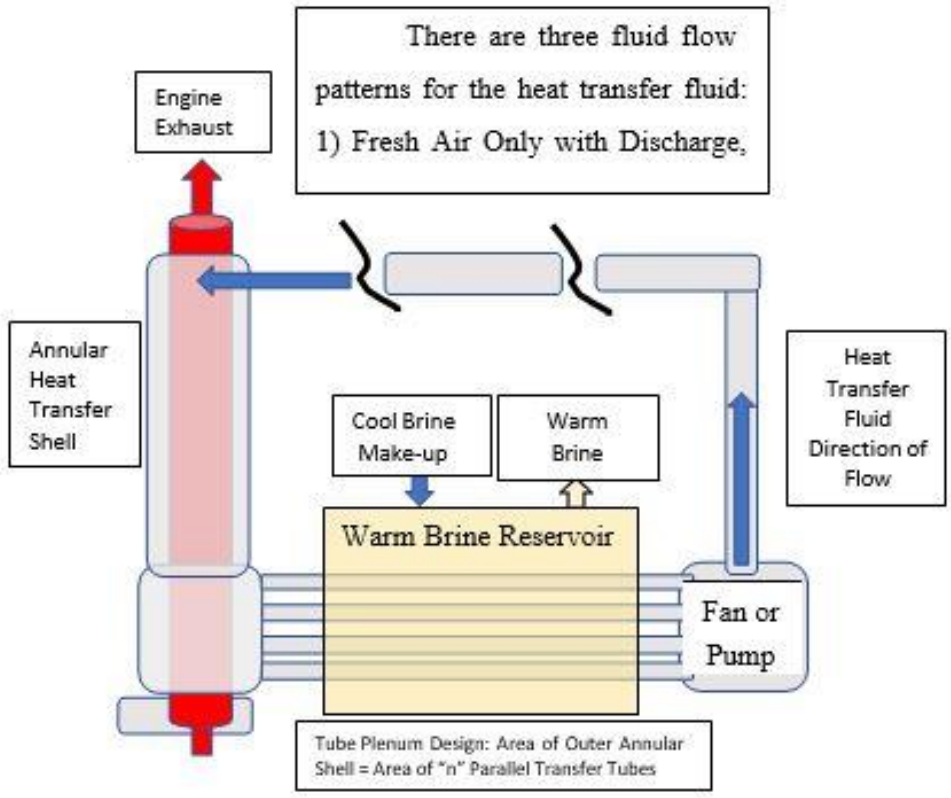


Figure C 2: Concept of the Heat Transfer Model

Two iteration loops are available to the user. One loop treats the heat transfer fluid as if it is used only once in a single pass through the process. Estimates for the outlet fluid temperatures from the shell and plenum are first entered into the model. A heat balance is calculated based on these estimates. Outlet fluid temperatures are then calculated based on the heat balance.

The new outlet fluid temperatures are re-entered, and a new heat balance is generated. This recalculation loop is run for 15 cycles. The loop can be re-run until the calculation stabilizes. A second iteration loop treats the heat transfer fluid as if it is reused through the process. The loop performs as discussed above with the added feature that the outlet temperature of the plenum is entered as the inlet temperature of the shell. This loop is also set to 15 cycles. It usually requires several iterative loops to stabilize.

C.4 Model Results:

Example 1, Single Pass Ducted Air:

The simplest construct for the model (Figure C2) is single pass air ducted from outside air through the shell and plenum with direct discharge to the outside. The test case was based on a shell and exhaust pipe contact of 30 ft2 with a contact length of just over 9 ft; and a tube-in tank plenum with 25 ft2 with 10 tubes each 15 ft. This configuration was established as the standard reference for all model runs.

The other design parameters for the single pass example are presented at the end of Table C1. This table is an example of the mass of brine (lb/minute) that can be raised from 65°F to the target temperature of the brine tank and provided with the required latent heat. If the target

brine temperature is 140 °F and the air temperature is 100°F, then less than 0.1 BBL/day brine can be accommodated by the waste heat from a single 440 HP engine. This indicates that the concept of single pass air is not feasible as a heat recovery mechanism.

Table C1: Heat Brine (lb/min) with Single Pass Air and Brine Make-up at 65°F						
	Inlet Air					
Brine Tank Temp.	55°F		70°F		100°F	
	BTU/min	BBL/d	BTU/min	BBL/d	BTU/min	BBL/d
120°F	0	0	0	0	35.2	0.13
130°F					20.2	0.08
140°F					6.0	0.02
Other Data Used in Model Runs						
Exhaust	900 °F		Shell area		30 ft^2	
Air Duct	400 CFM		Plenum area		25 ft^2	
ft/sec (0.5 to 2)	0.5		Brine Salinity		12%	
Make-up Brine	65°F		Treatment		380,000 BTU/BBL	

Example 2, Ducted Air with Infinite Recycle:

Table C 2: Heated Brine (lb/min) with Infinite Air Recycle and Brine Make-up at 65°F						
	Air Duct Flow Rate CFM					
Brine Tank	200		400		600	
	BTU/min	BBL/d	BTU/min	BBL/d	BTU/min	BBL/d
120°F	127	0.5	220	0.8	297	1.1
130°F	124	0.5	215	0.8	293	1.1
140°F	120	0.5	210	0.8	285	1.1
Other Data Used in Model Runs						
Exhaust	900 °F		Shell area		30 ft^2	
Air Duct	Varied CFM		Plenum area		25 ft^2	
ft/sec (0.5 to 2)	0.5		Brine Salinity		12%	
Make-up Brine	65°F		Treatment		380,000 BTU/BBL	

An incremental improvement in heat capture may be made by feeding the outlet air from the tank plenum to the inlet of the shell around the exhaust pipe. This essentially represents infinite recycle of the air. The net effect is to raise temperature of the air in the entire loop. Results in Table C2 are based on the standard test case defined in the section above. Since the outside air is no longer a variable, data in this table compare a range of duct air flow (200, 400, and 600 CFM). At a reference of 400 CFM, the model predicts that less than 1 BBL/d brine can be brought to a target temperature of 140°F and provide the required latent heat of vaporization from brine

at an ambient temperature of 65°F. This indicates that the concept of single pass air is not feasible as a heat recovery mechanism.

Example 3, Propylene Glycol:

In this example, a 40% (by mass) solution of glycol in water is modeled as the heat transfer fluid in infinite recycle around the process. The test case was based on a shell and exhaust pipe contact of 30 ft^2 with a contact length of just over 9 ft; and a tube-in tank plenum with 25 ft^2 with 10 tubes each 15 ft. Additionally, the standard test was based on a flow of glycol of 35 CFM. Table C3 is a summary of results (BTU/sec transferred to the contents of the brine tank) from several variations around the standard unit. The variations are plenum area, shell area, glycol flow and exhaust temperature.

Note the color code on the bottom of the table. The green columns are standard conditions and are repeated throughout the table for reference. The tan cells represent the parameter that is varied. The blue boxes represent the results of the variation. When glycol is used, there is a finite temperature that can be imposed on the fluid. The red cells indicate that the stated conditions are at a 200°F limit.

The plenum area was varied from 15 to 30 ft^2. The major effect was that as the plenum area increased, the overall unit could accommodate higher target brine temperatures before reaching a glycol limit of 200 °F. Whenever the target temperature did not result in the temperature exceedance, the steady state heat transfer rate remained remarkably stable at just over 69 BTU/sec. This is because while the inlet and outlet temperatures of the heat transfer fluid in the plenum changed with surface area, the net average driving force for heat transfer was self-regulating and nearly constant; the inlet temperature and the outlet temperature were ultimately functions of the temperature of the brine.

The shell area was varied from 20 to 35 ft^2. As the area of the shell increased, the brine temperature that allowed the glycol to exceed 200° F decreased. As the shell area increased, the overall heat transfer rate increased indicating that in this design the limiting rate is determined by the shell area.

The glycol flow rate was varied from 30 to 40 CFM which had the effect of slightly increased heat transfer with increased flow. The major contribution of the glycol flow rate in the heat transfer equations is to increase the value of the velocity, which governs the value of the overall heat transfer coefficient. A 30% increase in the flow rate yielded a 3% increase in heat transfer.

The exhaust flow was varied from 800 to 1000 °F with a resulting increase of 27% heat transfer. Data from Table C3 were rewritten in Table C4 to estimate the BBL/d of produced water that could be treated assuming the latent heat of the water is 1000 BTU/lb. The rate of treatment for the glycol adaptation is theoretically very low.

C.5 Discussion and Conclusion

This modeling exercise determined that simple systems, such as a shell annulus around an exhaust pipe and a tubular plenum transfer unit in a brine tank cannot capture enough heat to increase the temperature of a sufficient volume of brine to be of engineering value. This is true whether the envisioned system is a single pass air exchanger, or if the air is returned (infinite loop) from the plenum to the inlet to the shell. Table C5 is a summary of terms used in the

model.

If the heat transfer fluid is a solution of glycol and water, then a more reasonable (but still low) volume of brine can be heated to a desired temperature. As an example, the referenced standard unit potentially could produce about 15 BBL/d of brine to 138°F with make-up brine initially at an ambient temperature of 65°F. This is still not a large flow rate of treated brine, compared to the rates of water recovery at most well heads. Multiple heat capture units covering multiple diesel engines would need to be utilized to produce a large enough flow of heated brine to have utility.

The limiting heat exchange (by the results of this model) is the contact between the exhaust pipe and the heat transfer fluid. Considerable retrofitting to construct a pressurized shell around the exhaust pipe would be needed. This could be augmented to increase contact area, such the addition of finned exhaust pipes within the shell.

In conclusion, one of the most reliable sources of waste heat generated at a natural gas facility is the exhaust from transfer pumps. This modeling exercise demonstrates that the capture of waste heat is difficult and requires considerable design effort. Furthermore, the heat is of insufficient quality to supply the energy needed to vaporize large quantities of water.

Table C 3: Heat Transfer (BTU/sec) Using Infinite Recycle of 40% Propylene Glycol

	Tank Plenum Area Varied				Duct Shell Area Varied				Glycol Flow Varied			Exhaust Temperature Varied		
Exhaust °F	900	900	900	900	900	900	900	900	900	900	900	800	900	1000
Glycol CFM	35	35	35	35	35	35	35	35	30	35	40	30	35	40
Shell Area ft^2	30.0	30.0	30.0	30.0	20.0	25.0	30.0	35.0	30.0	30.0	30.0	30.0	30.0	30.0
Plenum ft^2	15.0	20.0	25.0	30.0	25.0	25.0	25.0	25.0	25.0	25.0	25.0	25.0	25.0	25.0
Brine Tank	Heat Transferred (BTU/sec) from Exhaust to Brine in Tank at Target Temperature °F													
130°F	69.6	69.5	69.2	68.9	46.3	58.0	69.5	80.5	66.9	69.5	71.4	61.3	69.5	77.7
138°F	69.6	69.5	69.2	69.0	46.3	58.1	69.5	80.6	67.0	69.5	71.6	61.3	69.5	77.7
153°F		69.6	69.3	69.1	46.5	58.2	69.5	80.7	67.2	69.5	71.7	61.3	69.5	77.7
156°F			69.4	69.2	46.8	58.2	69.5	80.8	67.3	69.5	71.8	61.3	69.6	77.6
158°F			69.5	69.3	46.8	58.2	69.5		67.4	69.5	72.0	61.3	69.6	77.6
163°F			69.6	69.4	46.8	58.2	69.6			69.6	72.6	61.3	69.6	
167°F				69.5	46.8	58.2					72.7	61.3		
168°F				69.6	46.8	58.2								

169°F					46.8	58.2								
174°F					46.8									
Glycol %		40	Shell Diameter ft		1.2		Brine Salinity %		12	Tank Mixing ft/sec		0.5		
Exhaust Flow CFM		12000	Exhaust Diameter ft		1.0		Parallel Tubes in Plenum		10					
Color Key														
Variable that is varied		Value of variable or results					Reference Standard Run			Glycol Overheated >200°F				

Table C 4: Heat Transfer (BBL/d Treated) Using Infinite Recycle of 40% Propylene Glycol

	Tank Plenum Area Varied				Duct Shell Area Varied				Glycol Flow Varied			Exhaust Temperature Varied		
Exhaust °F	900	900	900	900	900	900	900	900	900	900	900	800	900	1000
Glycol CFM	35	35	35	35	35	35	35	35	30	35	40	30	35	40
Shell Area ft^2	30.0	30.0	30.0	30.0	20.0	25.0	30.0	35.0	30.0	30.0	30.0	30.0	30.0	30.0
Plenum ft^2	15.0	20.0	25.0	30.0	25.0	25.0	25.0	25.0	25.0	25.0	25.0	25.0	25.0	25.0
Brine Tank	Heat Transferred (BBL/d) from Exhaust to Brine in Tank at Target Temperature °F													
130°F	15.9	15.8	15.8	15.7	10.6	13.2	15.8	18.4	15.3	15.8	16.3	14.0	15.8	17.7
138°F	15.9	15.8	15.8	15.7	10.6	13.2	15.8	18.4	15.3	15.8	16.3	14.0	15.8	17.7
153°F		15.9	15.8	15.8	10.6	13.3	15.8	18.4	15.3	15.8	16.3	14.0	15.8	17.7
156°F			15.8	15.8	10.7	13.3	15.8	18.4	15.3	15.8	16.4	14.0	15.9	17.7
158°F			15.8	15.8	10.7	13.3	15.8		15.4	15.8	16.4	14.0	15.9	17.7
163°F			15.9	15.8	10.7	13.3	15.9			15.9	16.6	14.0	15.9	
167°F				15.8	10.7	13.3					16.6	14.0		
168°F				15.9	10.7	13.3								
169°F					10.7	13.3								
174°F					10.7									
Glycol %	40	Shell Diameter ft		1.2	Brine Salinity %			12	Tank Mixing ft/sec			0.5		
Exhaust Flow CFM	12000	Exhaust Diameter ft		1.0	Parallel Tubes in Plenum			10						
Variable that is varied	Value of variable or results				Reference Standard Run			Glycol Overheated >200°F						

C.6 Nomenclature:

Table C 5: Definition of Parameters		
Nu	Nusselt number = $[hD/k]$	dimensionless
Pr	Prandlt number = $[C_p\mu/k]$	dimensionless

Re	Reynolds number = [DρU/μ]	dimensionless
A	A_L = heat transfer contact area (eg., wall of a pipe)	ft^{-2}
	A_x =cross sectional area (eg., across the diameter of a pipe)	
C_p	heat capacity of fluid	$BTU \cdot lb_m \cdot °F^{-1}$
d	Thickness of a pipe wall	ft
D	D_1 = diameter of a pipe	ft
	D_2 = diameter of the outer pipe of an annulus	
%G	percent propylene glycol by weight in a solution with water	percent
h	h_o = overall transfer coefficient	$BTU \cdot ft^{-2} \cdot sec^{-1} \cdot °F^{-1}$
	h_{hot} = transfer coefficient of hot fluid boundary	
	h_{cool} = transfer coefficient of the cool fluid boundary	
	$h_{material}$ = transfer coefficient of the construction material	
L	length of a transfer unit, e.g., a pipe	ft
M	mass flow rate of a fluid	$lb_m \cdot sec^{-1}$
k	thermal transfer coefficient of the material or fluid	$BTU \cdot ft^{-1} \cdot sec^{-1} \cdot °F^{-1}$
q	heat transfer	$BTU \cdot sec^{-1}$
U	fluid velocity through cross-sectional area A_x	$ft \cdot sec^{-1}$
ρ	density	$lb_m \cdot ft^{-3}$
μ	dynamic viscosity	$lbm \cdot ft^{-1} \cdot sec^{-1}$
T	T_{inlet} = Temperature of the bulk fluid inlet	°F
	T_{outlet} = Temperature of the bulk fluid outlet	
	$T_{average}$= Average of the inlet and outlet temperature for a fluid	
	T_{target} = Temperature of the fluid (salt brine) in a large tank	
	ΔT^*= mean driving force	
%TDS	percent mass of salt in solution with water	

X	X_1 = mole fraction propylene glycol in a glycol-water solution	moles·mole^{-1}
	X_2 = mole fraction water in a glycol-water solution	
α	Power coefficient on Reynolds number e.g., $[Re]^{\alpha}$	dimensionless
β	Power coefficient on Prandlt number e.g., $[Pr]^{\beta}$	dimensionless
δ	Multiplier for cool side transfer coefficient in a large tank	dimensionless

C.7 Model Development

General Considerations: Steady state heat transfer is calculated using Equation 1 for heat transferred from a fluid at inlet conditions to the fluid at the outlet conditions.

Equation 1: $$q = MC_p(T_{outlet} - T_{inlet})$$

Steady state heat transfer from one fluid to another fluid across a resistant boundary is estimated with Equation 2:

Equation 2: $$q = h_o A_L \Delta T^*$$

The average temperature driving force, ΔT*, is calculated as the difference between the average temperature of the hot fluid minus the average temperature of the cool fluid. The average temperature of a fluid is based on the inlet and outlet temperatures is assumed as in Equation 3:

Equation 3: $$T_{average} = \frac{T_{inlet} + T_{outlet}}{2}$$

By the definition of Equation 3, the mean driving force is given in Equation 4.

Equation 4: $$\Delta T = (T_{average})_{hot} - (T_{average})_{cool}$$

The area available for transfer is approximated using outside diameter of a pipe and its length.

Equation 5: $$A_L = \pi L D_1$$

Heat Transfer Coefficients in an Annular Heat Exchanger: Resistance to heat transfer from one fluid to another is considered to occur at any boundary that occur between the fluids. For simplicity, this is usually calculated as a series resistance across 1) the cool-side fluid boundary between the bulk fluid ($1/h_{cool}$) and a material; 2) the resistance across the material; and 3) a fluid boundary between the wall and the hot-side bulk fluid. Figure C3 is a conceptual depiction of the boundary and fluid conditions in an annular heat transfer problem. The overall transfer coefficient, ho, is estimated as in Equation 6.

Equation 6: $$h_o = \left(\frac{1}{h_{hot}} + \frac{1}{h_{material}} + \frac{1}{h_{cool}}\right)^{-1}$$

The individual heat transfer coefficients are generated from definitions and correlations given in Bennet and Myers (1974). For solid materials such as a pipe wall, the transfer coefficient is given as Equation 7.

$$Equation\ 7: \quad Nu = \frac{h_{material} d}{k} = 1.0$$

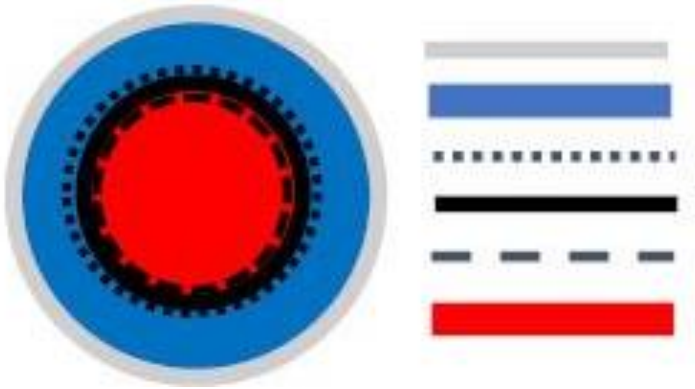


Figure C 3: Fluids and Boundary Conditions in an Annular Heat Exchanger

The stagnant fluid boundary coefficients on the inside pipe wall are of a form given by Equation 8:

$$Equation\ 8: \quad Nu = 0.023 Re^{\alpha} Pr^{\beta}$$

Where the fluid is in the inner pipe of an annulus and is being cooled, β = 0.3. If the fluid is being heated, β = 0.4. For the case of cooling of exhaust gas, the heat transfer coefficient, h_{hot} is written as Equation 9.

$$Equation\ 9: \quad \frac{h_{hot} D_1}{k} = 0.023 \left[\frac{D_1 U \rho}{\mu}\right]^{0.8} \left[\frac{C_p \mu}{k}\right]^{0.3}$$

For heat transfer from the outer wall of the inner pipe (with diameter D1) in an annulus with an outer pipe (diameter D2) the transfer coefficient, h_{cool}, is given by Equation 10:

$$Equation\ 10: \quad \frac{h_{cool}(D_2 - D_1)}{k} = 0.023 \left[\frac{(D_2 - D_1) U \rho}{\mu}\right]^{0.8} \left[\frac{C_p \mu}{k}\right]^{0.4} \left[\frac{D_2}{D_1}\right]^{0.45}$$

Note that the various thermodynamic properties of the exhaust gas (air); k, ρ, C_p and ρ are temperature dependent. These same parameters for water are also dependent on the salinity of water. Tables of these parameters and equations used to interpolate these parameters are given in following sections of Appendix C. All estimates of the various transfer coefficients are based the thermodynamic properties at the mean temperature of the inlet and outlet conditions.

The velocity term, U, is calculated as the fluid flow rate divided by the cross-sectional area. For a pipe, the velocity is given by Equation 11:

$$Equation\ 11: \quad U = \frac{A_x M}{\rho}$$

For the pipe, the area A_x is:

$$Equation\ 12: \quad A_x = \frac{\pi D_1^2}{4}$$

For the outside ring of the annulus, the area is:

Equation 13: $$A_x = \frac{\pi(D_2^2 - D_1^2)}{4}$$

Heat Transfer from a Hot Pipe to a Large Tank: The transfer coefficient for the pipe material is given by Equation 7. The hot-side transfer coefficient on the inside of the pipe is given by Equation 9. The cool-side transfer coefficient is evaluated for passive mixing (Equation 14).

Equation 14: $$\frac{h_{cool} D_1}{k} = \delta \left[\frac{D_1 U \rho}{\mu}\right]^{\alpha}$$

Where α and δ are presumed to be a function of the Reynolds number. For ease of calculation, the following correlations were generated from Table 24-3 in Bennet and Myers (1974).

Equation 15: $$\alpha = 0.155[Re]^{0.13}$$

Equation 16: $$\delta = 0.286[Re]^{0.77}$$

The velocity across the outside of the hot pipe is taken as passive mixing with a nominal value U = 0.5 ft•sec^{-1}. The fluid (salt brine) in the tank is assumed to be a constant bulk temperature defined by the target temperature for the inlet to the membrane distillation unit.

Thermal Transfer Coefficients (k). Due to the corrosive nature of the brine, material choice is problematic. The model uses the value for steel in all calculations. Coefficients for various pipe material are as follows:

Aluminium	k = 0.033
Copper	k = 0.062
Iron	k = 0.011
Steel	k = 0.007 BTU•ft^{-1}•sec^{-1}•°F^{-1}

Specific Heat (Heat Capacity) of Salt Water (C_p): The specific heat of salt water is a function of salt concentration (Table C6). In these correlations, the salinity is entered as the percent of fluid mass as total dissolved solids (%TDS). For example, a brine with salinity of 50,000 ppm as NaCl would be entered as 5% TDS. The correlation is Equation 16. Examples of correlated results are in Table C6.

Equation 16: $$C_p = 0.0002388[0.8(\%TDS)^2 - 58(\%TDS) + 4199]$$

Density of Brine: The density of brine is a function of both temperature and salinity (Table C7). The correlation used in this study was generated from Equation. Note this equation is in °K which is by conversion:

$$°K = 273.1 + (°F\text{-}32) \times 5/9$$

Equation 17: $$\rho = 62.34(0.0074[\%TDS] - 3.23x10^{-6}[°K]^2 + 0.0016[°K] + 0.8047)$$

Table C 6: Density of Brine											
% TDS	35°F	50°F	65°F	80°F	95°F	110°F	125°F	140°F	155°F	170°F	195°F
0	62.4	62.3	62.2	62.0	61.8	61.6	61.4	61.1	60.8	60.5	59.9
5	64.7	64.6	64.5	64.3	64.2	63.9	63.7	63.4	63.1	62.8	62.2
10	67.0	66.9	66.8	66.6	66.5	66.2	66.0	65.7	65.4	65.1	64.5
15	69.4	69.3	69.1	69.0	68.8	68.6	68.3	68.0	67.7	67.4	66.8
20	71.7	71.6	71.4	71.3	71.1	70.9	70.6	70.3	70.0	69.7	69.1
25	74.0	73.9	73.7	73.6	73.4	73.2	72.9	72.7	72.3	72.0	71.4
Density of Brine $\rho = lb_m \cdot ft^{-3}$											

Thermal Transfer Coefficient k: The thermal transfer coefficient for brines is correlated by Equation 18 and shown by example in Table C8.

Equation 18: $$k = \frac{0.0408 ln(°F) - 6.73x10^{-4} + 0.0.1754}{3600}$$

Table C 7: Thermal Capacity (k) of Brine											
% TDS	35°F	50°F	65°F	80°F	95°F	110° F	125° F	140° F	155° F	170° F	195° F
0	8.908 E-05	9.313 E-05	9.610 E-05	9.846 E-05	1.004 E-04	1.021 E-04	1.035 E-04	1.048 E-04	1.060 E-04	1.070 E-04	1.086 E-04
5	8.814 E-05	9.219 E-05	9.517 E-05	9.753 E-05	9.948 E-05	1.011 E-04	1.026 E-04	1.039 E-04	1.050 E-04	1.061 E-04	1.076 E-04
10	8.721 E-05	9.126 E-05	9.423 E-05	9.659 E-05	9.854 E-05	1.002 E-04	1.017 E-04	1.029 E-04	1.041 E-04	1.051 E-04	1.067 E-04
15	8.627 E-05	9.032 E-05	9.330 E-05	9.566 E-05	9.761 E-05	9.927 E-05	1.007 E-04	1.020 E-04	1.032 E-04	1.042 E-04	1.058 E-04
20	8.534 E-05	8.939 E-05	9.236 E-05	9.472 E-05	9.667 E-05	9.833 E-05	9.979 E-05	1.011 E-04	1.022 E-04	1.033 E-04	1.048 E-04
25	8.440 E-05	8.845 E-05	9.143 E-05	9.378 E-05	9.574 E-05	9.740 E-05	9.885 E-05	1.001 E-04	1.013 E-04	1.023 E-04	1.039 E-04
$k = BTU \cdot ft^{-1} \cdot sec^{-1} \cdot °F^{-1}$											

Dynamic Viscosity of Brine: The correlation for the dynamic viscosity of brine solutions is Equation 9 and example viscosity generated from the equation are in Table C9.

Equation 19: $\mu = 0.081 + (2.26x10^{-5}x\ [\%TDS] + 0.00106)\ x\ e^{\frac{[3.861x[\%TDS]+3558]}{°F+459.6}}$

Table C 8: Viscosity of Brine											
% TDS	35°F	50°F	65°F	80°F	95°F	110° F	125° F	140° F	155°F	170°F	195°F
1	1.538	1.259	1.046	0.880	0.749	0.645	0.562	0.494	0.438	0.392	0.332
5	1.709	1.397	1.157	0.972	0.825	0.709	0.616	0.540	0.478	0.426	0.359
10	1.936	1.579	1.305	1.093	0.926	0.793	0.687	0.600	0.530	0.471	0.395
15	2.179	1.773	1.462	1.222	1.032	0.882	0.762	0.664	0.584	0.519	0.432
20	2.439	1.980	1.630	1.358	1.146	0.977	0.842	0.732	0.642	0.569	0.472
25	2.716	2.201	1.808	1.504	1.266	1.077	0.926	0.803	0.704	0.621	0.514
$\mu = lb_m \cdot ft^{-1} \cdot sec^{-1}$											

Thermodynamic Data for Air: The approximations for the thermodynamic properties for air are presented in Table 5 based on Equations 20-23.

Equation 20: $\rho = \frac{39.645}{(°F + 459.6)} + 1.2\ x\ 10^{-5}$

Equation 21: $\mu = -4\ x\ 10^{-7}\ (°F)^2 + 0.00176(°F) + 1.1036$

Equation 22: $C_p = 0.0104\ \left(\frac{°F}{1000}\right)^2 + 0.0127\ \left(\frac{°F}{1000}\right) + 0.2392$

Equation 23: $k = \frac{(0.0195\ °F + 0.014)}{3600}$

Table C 9: Thermal Conductivity of Air										
		10°F	50°F	80°F	150°F	250°F	400°F	750°F	1000°F	1200°F
Density	ρ	0.0844	0.0778	0.0735	0.0650	0.0559	0.0461	0.0328	0.0272	0.0239
Viscosity	μ	1.12	1.19	1.24	1.36	1.52	1.74	2.20	2.46	2.64
specific heat	C_p	0.239	0.239	0.240	0.241	0.243	0.245	0.254	0.262	0.269
Thermal conductivity	k	5.81 E-05	2.75 E-04	4.37 E-04	8.16 E-04	1.36 E-03	2.17 E-03	4.07 E-03	5.42 E-03	6.50 E-03
Units: { $\rho = lb_m \cdot ft^{-3}$ } { $\mu = lb_m \cdot ft^{-1} \cdot sec^{-1}$} { $C_p = BTU \cdot lb_m \cdot °F^{-1}$} { $k = BTU \cdot ft^{-1} \cdot sec^{-1} \cdot °F^{-1}$}										

Thermodynamic properties of propylene glycol: Some of the data used below were presented initially as mole fraction glycol in water. In keeping with the use of percent of mass, the Conversion used from mole fraction propylene glycol (X1) to (%G) in a water solution is given in Equation 24:

$$Equation\ 24: \quad \%G = \frac{100}{\left(1 + \frac{\frac{1}{X_1} - 1}{4.22}\right)}$$

Thermal Conductivity of Glycol in Water: The Equation for correlation of the thermal conductivity of propylene glycol is given as Equation 25 and example results are given in Table B6,

$$Equation\ 25: \quad k = \frac{\frac{(0.121(\%G) - 12.981)[°\mathrm{F}]^2}{10^7} + (-5.84\ x\ 10^{-6}(\%G) + 0.0006)[°\mathrm{F}] - 0.0019(\%G) + 0.2848}{3600}$$

Heat Capacity of Propylene Glycol in Water:

$$Equation\ 26: \quad C_p = (9.03x10^{-6}x\ \%G - 2.00x10^{-5})[°\mathrm{F}] - 0.00544\ x\ \%G + 1.0829$$

%G	35	45	55	65	75
10°F	6.17E-05	5.62E-05	5.08E-05	4.53E-05	3.99E-05
20°F	6.27E-05	5.71E-05	5.15E-05	4.59E-05	4.03E-05
50°F	6.55E-05	5.95E-05	5.35E-05	4.75E-05	4.14E-05
70°F	6.71E-05	6.08E-05	5.46E-05	4.83E-05	4.21E-05
90°F	6.85E-05	6.20E-05	5.56E-05	4.91E-05	4.26E-05
110°F	6.97E-05	6.31E-05	5.64E-05	4.98E-05	4.31E-05
130°F	7.08E-05	6.39E-05	5.71E-05	5.03E-05	4.35E-05
110°F	6.97E-05	6.31E-05	5.64E-05	4.98E-05	4.31E-05
150°F	7.16E-05	6.46E-05	5.77E-05	5.07E-05	4.38E-05
170°F	7.22E-05	6.52E-05	5.81E-05	5.10E-05	4.40E-05
190°F	7.27E-05	6.55E-05	5.84E-05	5.12E-05	4.41E-05

Table C 10: Thermal Conductivity k of Propylene Glycol (%wt) in Water

Density of Propylene Glycol in Water:

$$Equation\ 27: \quad \rho = -a[°\mathrm{F}]^2 + b[°\mathrm{F}] + c$$

$$a = 3.02x10^{-6}\left[\frac{\%G}{100}\right]^2 - 0.0011\left[\frac{\%G}{100}\right] + 0.1645$$

$$b = 4.27x10^{-6}\left[\frac{\%G}{100}\right]^2 - 0.0017\left[\frac{\%G}{100}\right] + 0.2524$$

$$c = -1.44x10^{-6}\left[\frac{\%G}{100}\right]^2 + 0.0002\left[\frac{\%G}{100}\right] + 0.979$$

Dynamic Viscosity of Propylene Glycol:

$$Equation\ 28: \quad \mu = 0.000673\ \ (exp(a\ ln[\%G] + b))$$

$$a = -0.01448[°\mathrm{F}] + 0.8686$$

$$b = 0.1[°\mathrm{F}] + 3.447$$

Table C 11: Heat Capacity of Glycol Solutions in Water C_p					
%G	100	80	60	40	20
60°F	0.59	0.69	0.79	0.89	0.98
80°F	0.61	0.70	0.80	0.89	0.99
100°F	0.63	0.72	0.81	0.90	0.99
120°F	0.65	0.73	0.82	0.91	0.99
140°F	0.66	0.75	0.83	0.91	1.00
160°F	0.68	0.76	0.84	0.92	1.00
180°F	0.70	0.77	0.85	0.93	1.00
200°F	0.72	0.79	0.86	0.93	1.01
220°F	0.73	0.80	0.87	0.94	1.01
240°F	0.75	0.82	0.88	0.95	1.01

Table C 12: Density of Glycol (%Wt) in Water						
%Glycol	30	60	90	120	150	180
20	63.55	63.25	62.87	62.42	61.88	61.27
30	64.41	63.94	63.43	62.87	62.26	61.60
50	65.63	64.92	64.20	63.48	62.75	62.02
70	66.18	65.35	64.53	63.71	62.91	62.11
80	66.21	65.36	64.52	63.69	62.86	62.04
100	65.75	64.97	64.18	63.36	62.52	61.66
$\rho = lb_m \cdot ft^{-3}$						

Table C 13: Viscosity of Glycol and Water Solutions								
%Glycol	25°F	50°F	75°F	100°F	125°F	150°F	175°F	200°F
	25	50	75	100	125	150	175	200
20	0.00375	0.00168	0.00105	0.00075	0.00058	0.00047	0.00039	0.00034
30	0.00640	0.00259	0.00153	0.00105	0.00079	0.00062	0.00051	0.00043
50	0.01862	0.00617	0.00324	0.00205	0.00143	0.00107	0.00084	0.00068
70	0.05417	0.01469	0.00685	0.00398	0.00262	0.00186	0.00139	0.00108
80	0.09240	0.02267	0.00996	0.00556	0.00354	0.00244	0.00179	0.00136
μ=lbm · ft^{-1} · sec^{-1}								

Appendix D: Analysis of the Bakken Production Data

D.1. Summary

The Bakken and Lodgepole geographic region extents from west North Dakota to East Montana to Southern part of Saskatchewan, Canada with an estimated reserve of 3.6 billion BBL oil and 1,860 billion cubic feet of gas (USGD 2008). The focus of this report are the Bakken reserves covering more than 40% of area of north-west North Dakota (approximately 28,000 square

miles). The Bakken oil is in tight shale formation and requires hydraulic fracture and horizontal drilling for efficient capture. There is a long history of oil production from the area, meaning that there are older (and still productive wells) plus modern hydraulically fractured wells. Older vertical wells were able to collect gas and oil from an area not more than 40 acres per well. In 2019, North Dakota (15,348 active wells) with special reference to the Bakken oil fields (336 named fields with 12,141 active wells).

Modern horizontal wells are up to 2 miles deep and traverse 2 miles horizontally. To accommodate this new technology North Dakota is allocating mineral rights in "Units" where each unit is one mile by two miles (1280 acres). To minimize surface activity, units are paired into 2 Units. Each 2 Unit property is planned to accommodate between 6 to 8 wells. In the previous report, the performance of 1320 Unit wells were described. These wells implemented active re-injection of produced water and natural gas to re-pressurize the oil field. With localized surface collection, the sale of natural gas was accelerated (compared to the older wells) and the opportunity for use of membrane distillation was limited to about 20% of the wells. The present report covers the wells extant from 2015 to 2020 and included many older wells plus the new "Unitized" wells. The present report covers some 12,141 active wells in the Bakken. The data for this report were extracted from the millions of lines of code available in the North Dakota Department of Mineral Resources data base (Table D1).

Table D 1: Reference to the North Dakota Department of Mineral Resources; Oil and Gas Division	
Monthly Production Report Index	https://www.dmr.nd.gov/oilgas/mprindex.asp
Well Index	https://www.dmr.nd.gov/oilgas/basic/well_index.zip
Field-Pool Production and Injection Data	https://www.dmr.nd.gov/oilgas/basic/fieldprodinj.asp

The Bakken reserves in North Dakota are being re-developed in the "Unit" mode to accommodate between 6 and 8 wells per 2 Unit area. Each Unit covers 2 square miles. The area of Bakken reserves in North Dakota covers 28,000 square miles. Drilling to 50% saturation would cover 7,000 2-Unit areas with between 21,000 and 28,000 wells. In general, there is presently a great need for water treatment based on many active old-style wells. The Impact new well activity; along with the closure of the old-style wells; on water needs will be discussed in the Appendix D.

D.2 Status of the Existing Bakken Wells

The Well Index lists the status, spud date, owner, and location of some 38,425 wells dating back to 1929. Table D2 is a summary of wells listed by status in all North Dakota and wells listed as being in the Bakken oil reserve. Approximately 79% of the current resource recovery available to the public is occurring in the Bakken. Starting in 2017 and increasing until the latest available reports (January-June 2020) are "Confidential" and do not list spud dates and/or oil pools. Many of the 1,202 Confidential wells listed for Total ND can be attributed to Bakken activity.

Drilling Activity in Bakken Reserves: Table D3 is a summary of drilling activity from July 2015 to June 2020 in six-month intervals. There are three categories Bakken, All North Dakota, and Confidential wells. There were 4920 wells drilled in North Dakota in this 5- year period, with 3992

attributed to Bakken activity and 195 confidential wells. Peak activity occurred in July-December 2018 with a strong downturn in drilling in 2020.

Table D 2: Reported Wells in ND & Bakken September 2020			
Code	Definition	Total ND	Bakken
A	Active	15,348	12,141
AB	Abandoned (Shut-In > 12 Months)	714	139
C	Confidential	1,202	
DRL	Drilling	68	
DRY	Dry Hole	6,375	11
EXP	Expired Permit	156	
IA	Inactive (Shut-In >= 3 and <= 12 Months)	3,283	2,325
IAW	Inactive Well Waiver	129	53
LOC	Permitted Location to Drill	764	
LOCR	Permitted Reentry of Plugged	3	
NC	Not Completed (Drilled to TD, Awaiting Completion)	625	134
NCW	Not Completed Waiver	5	
PA	Plugged and abandoned	4,849	247
PNC	Permit Now Cancelled	4,418	8
PNS	Permit Now Suspended	16	
TA	Temporarily Abandoned	393	93
TAI	Temp Abandoned, SoD (Intermediate Casing Set)	7	
TAO	Temporarily Abandoned - Observation	17	
TASC	Temp Abandoned, SoD (Surface Casing Set)	17	
TATD	Temp Abandoned, Drilled to Total Depth	36	
TOTAL	All Status	38,425	15,151

Table D 3: Drilling Activity in ND by 6 Month Period										
Attributed to the Bakken Pool of Wells by Spud Dates										
	July-Dec 2015	Jan-June 2016	July-Dec 2016	Jan-June 2017	July-Dec 2017	Jan-June 2018	July-Dec 2018	Jan-June 2019	July-Dec 2019	Jan-June 2020
Existing at Start	11,168	11,716	11,968	12,704	13,201	13,769	14,378	14,913	15,148	15,154
New During Period	548	252	302	434	497	568	609	535	235	6
Undated	3 wells do not list spud date									
All ND Wells Spud Date										
	July-Dec 2,015	Jan-June 2,016	July-Dec 2,016	Jan-June 2,017	July-Dec 2,017	Jan-June 2,018	July-Dec 2,018	Jan-June 2,019	July-Dec 2,019	Jan-June 2,020
Existing at Start	33,253	33,858	34,130	34,477	34,963	35,540	36,163	36,883	37,548	38,173
New During Period	605	272	347	486	577	623	720	665	625	252
Undated	6463 wells do not list spud date									
Listed as Confidential Without Attribution to Pool										
	July-Dec 2,015	Jan-June 2,016	July-Dec 2,016	Jan-June 2,017	July-Dec 2,017	Jan-June 2,018	July-Dec 2,018	Jan-June 2,019	July-Dec 2,019	Jan-June 2,020
New During Period	NL	NL	NL	NL	3	NL	2	12	112	66
Undated	500 wells are listed as "confidential" without spud date nor oil pool									

Total and Well Average Production and Flaring: Table D4 shows the total production activity over each 6-month period from July 2015 to June 2020. For this report, the important line is the flare activity (final row) indicating that there are between 27 and 92 billion cubic feet of flared gas in each period. Table D5 shows the activity of the active wells on a per-well per-month basis. The important line is the flare activity (final row highlighted grey) indicating that the flare activity for each well exceeds 181 CF per BBL produced water, indicating that there is insufficient resources to treat the PW with the boiler option with the boiler option, however, on average, there is sufficient flared gas to treat the produced water using membrane distillation based on the presumed value of 100 cubic feet per barrel for using a heat pump as the heat source.

The minimum theoretical heat needed to treat PW with 50% forward flow through a membrane distillation unit was established at 244,340 BTU/barrel applied to the membrane which requires 382,000 BTU/BBL for heating with a 60% efficiency steam boiler and 74,000 BTU/BBL with a 55%

heat pump with a COP of 8.1 (See Table 2 Main Text). If natural gas is available as recovered flared gas or low-quality source gas at 750 BTU/CF, then the treatment ratio of flared gas required to barrels treated is around 500 CF/BBL for the boiler and around 100 CF/BBL for the heat pump option.

Table D 4: Total Reported Production for Bakken Wells per 6 Month Period										
MM = million MM-M = billion	2015 July-Dec	2016 Jan-June	2016 July-Dec	2017 Jan-June	2017 July-Dec	2018 Jan-June	2018 July-Dec	2019 Jan-June	2019 July-Dec	2020 Jan-June
Active Wells	10,294	10,593	10,889	11,261	11,725	12,126	12,753	13,058	13,571	12,854
Oil (MM BBL)	194	180	164	167	181	192	217	229	242	198
Water (MM BBL)	160	150	146	154	178	198	240	259	291	245
Gas (MM-MCF)	273	279	272	290	330	363	423	473	521	450
Gas Sold (MM-MCF)	218	240	231	248	272	295	323	354	403	374
Flared (MM- MCF)	42	27	29	29	42	50	76	92	92	54

Table D 5: Production per Well per Month for Bakken Wells During Each 6-Mo Period										
M = Thousand	2015 July-Dec	2016 Jan-June	2016 July-Dec	2017 Jan-June	2017 July-Dec	2018 Jan-June	2018 July-Dec	2019 Jan-June	2019 July-Dec	2020 Jan-June
Oil (BBL)	3,141	2,834	2,511	2,465	2,576	2,643	2,832	2,921	2,968	2,569
Water (BBL)	2,589	2362	2,239	2,285	2,536	2,726	3,135	3,304	3,580	3,176
Gas (MCF)	4,420	4,396	4,169	4,299	4,687	4,987	5,526	6,034	6,396	5,837
Gas Sold (MCF)	3,536	3,769	3,538	3,672	3,865	4,049	4,217	4,517	4,948	4,849
Flared (MCF)	684	428	442	426	591	683	987	1,178	1,124	698
Flared CF/BBL	264	181	198	187	233	251	315	357	314	220

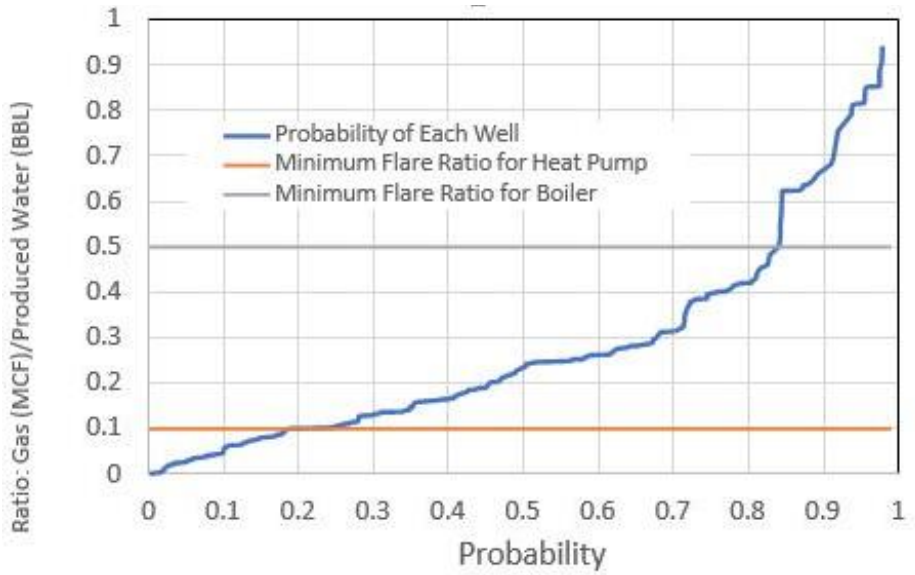


Figure D 1: Probability of Less than Ratio (Gas/Water)

Figure D1 is a probability plot (Blue Curve) of a well having less than the stated value of flared gas per barrel of produced water generated. The horizontal lines represent the targets of 0.100

MCF/BBL for a heat pump option (Orange Line) and 0.500 MCF/BBL for a boiler option (Grey Line) as a heat source for membrane distillation. \ The orange line intersects the blue curve at 20%, therefore, 20% of the wells have insufficient flare gas to treat all the water. Conversely, 80% have sufficient gas to treat the water using the heat pump option. On the other hand, the grey line is 0.5 MCF/BBL and represents the minimum gas needed to treat the water with the boiler option. This intersects the blue curve at 83%, therefore 83% of the wells have insufficient flare gas to treat all the water. Conversely, only 17% have sufficient gas to treat the water using the boiler option.

Table D 6:Bakken Field Production Data (Jan 1- Dec 31, 2019) and Potential for Treatment									
FieldName	Active Wells Number	Oil MBBL BBL/D	Produced Water BBL/D	Gas Thousand CF/D	Gas Sold Thousand CF/D	Flared Thousand CF/D	Ratio CF Flared/ BBL Water	Heat Pump BBL Treatable at 99 CF/BBL	Boiler BBL Treatable at 545 CF/BBL
ALEXANDER	11.3	482	1,104	1,208	1,104	60	55	609	111
ALEXANDRIA	17.4	778	1,704	803	556	8	5	83	15
ALGER	333.0	16,734	19,997	27,962	23,211	3,455	173	19,997	6,339
ALKABO	1.0	14	38	14	0	5	143	38	10
ALKALI CREEK	197.5	29,274	23,847	62,364	51,882	9,381	393	23,847	17,213
AMBROSE	113.9	3,016	6,701	4,956	3,792	236	35	2,380	432
ANTELOPE	18.8	46,921	37,255	115,918	73,466	34,140	916	37,255	37,255
ANTELOPE CREEK	258.3	715	1,282	1,351	1,055	184	143	1,282	337
ARNEGARD	22.2	753	858	1,896	1,581	230	268	858	422
ASH COULEE	1.0	79	293	126	82	8	28	83	15
ASSINIBOINE	3.4	74	101	90	79	3	27	28	5
AVOCA	24.8	5,444	8,737	8,003	6,951	973	111	8,737	1,785
BAILEY	169.7	20,173	24,841	23,693	11,882	9,647	388	24,841	17,700
BAKER	69.8	2,578	5,526	6,195	5,008	595	108	5,526	1,091
BANKS	328.3	55,978	75,633	222,425	197,159	22,468	297	75,633	41,227

BARTA	3.0	55	96	71	33	0	0	0	0
BASKIN	11.4	849	866	882	764	121	139	866	221
BATTLEVIEW	2.0	41	104	156	129	3	26	28	5
BAUKOL NOONAN	4.3	36	99	66	19	8	83	83	15
BEAR BUTTE	5.8	93	148	277	178	22	148	148	40
BEAR CREEK	60.0	19,671	19,992	26,532	20,077	6,236	312	19,992	11,441
BEAR DEN	39.6	3,534	2,252	7,510	5,814	1,471	653	2,252	2,252
BEAVER CREEK	3.9	219	71	156	110	11	154	71	20
BEAVER LODGE	80.5	3,863	4,296	11,041	10,181	671	156	4,296	1,232
BELL	80.5	4,792	4,482	13,838	13,496	151	34	1,522	276

FieldName	Active Wells Number	Oil MBBL BBL/ D	Produced Water BBL/D	Gas Thousand CF/D	Gas Sold Thousand CF/D	Flared Thousand CF/D	Ratio CF Flared/ BBL Water	Heat Pump BBL Treatable at 99 CF/BBL	Boiler BBL Treatable at 545 CF/BBL
BENNETT CREEK	85.3	49	96	66	55	0	0	0	0
BICENTENNIAL	12.6	137	60	134	3	58	955	60	60
BIG BEND	168.4	31,438	31,184	30,674	20,827	5,773	185	31,184	10,592
BIG BUTTE	52.3	2,381	2,482	3,863	3,184	674	272	2,482	1,237
BIG DIPPER	5.0	249	679	211	25	137	202	679	251

BIG GULCH	23.3	1,030	499	2,299	2,170	11	22	111	20
BIG MEADOW	2.0	68	208	249	27	186	895	208	208
BIG STICK	6.9	93	159	148	129	5	34	55	10
BIG STONE	10.4	362	647	847	77	712	1,102	647	647
BLACK SLOUGH	3.0	52	68	66	0	38	560	68	68
BLACKTAIL	2.0	25	68	36	0	11	160	68	20
BLOOMING PRAIRIE	32.3	655	1,740	1,529	1,112	121	69	1,218	221
BLUE BUTTES	223.9	41,332	18,123	87,074	69,047	16,348	902	18,123	18,123
BLUE RIDGE	7.0	647	1,430	1,068	912	115	80	1,162	211
BLUFFTON	10.8	195	562	348	145	79	141	562	146
BONETRAIL	7.9	578	1,244	816	641	104	84	1,052	191
BORDER	4.9	88	211	197	134	5	26	55	10
BOUNTY SCHOOL	2.0	27	96	68	0	25	257	96	45
BOWLINE	4.0	110	79	197	164	3	34	28	5
BOXCAR BUTTE	26.8	907	2,304	1,970	1,721	44	19	443	80
BRIAR CREEK	17.7	923	2,077	1,268	1,000	208	100	2,077	382
BROOKLYN	103.3	10,775	17,167	30,058	26,115	2,814	164	17,167	5,163
BUCKHORN	5.0	22	3	66	27	25	9,000	3	3
BUFFALO WALLOW	7.4	334	627	803	773	14	22	138	25

FieldName	Active Wells Number	Oil MBBL BBL/D	Produced Water BBL/D	Gas Thousand CF/D	Gas Sold Thousand CF/D	Flared Thousand CF/D	Ratio CF Flared/ BBL Water	Heat Pump BBL Treatable at 99 CF/BBL	Boiler BBL Treatable at 545 CF/BBL
BUFORD	3.0	137	236	137	82	47	198	236	85
BULL BUTTE	37.2	808	1,721	1,238	825	123	72	1,245	226
BULL MOOSE	1.9	27	71	49	0	41	577	71	71
BULLSNAKE	1.0	8	5	27	3	3	500	5	5
BULLY	25.0	926	1,564	2,301	1,441	759	485	1,564	1,392
BURG	27.8	1,540	4,307	2,696	2,304	173	40	1,743	317
BUTTE	1.0	16	33	27	22	0	0	0	0
CABERNET	40.2	2,477	2,679	2,238	1,641	192	72	1,937	352
CAMEL BUTTE	51.3	9,419	7,233	27,249	24,082	2,907	402	7,233	5,334
CAMP	145.3	8,386	10,852	21,085	17,888	1,827	168	10,852	3,353
CANDAK	1.8	19	153	60	5	27	179	153	50
CAPA	58.3	10,063	10,890	28,630	23,975	4,170	383	10,890	7,651
CARTWRIGHT	4.0	101	153	175	153	14	89	138	25
CATWALK	17.3	1,622	2,701	2,866	1,937	737	273	2,701	1,352
CEDAR COULEE	32.2	4,564	3,323	6,474	5,603	668	201	3,323	1,227

CHARBONNEAU	13.0	488	1,301	1,162	1,041	33	25	332	60
CHARLIE BOB	2.0	27	36	52	25	0	0	0	0
CHARLSON	119.1	26,184	7,940	54,521	40,132	13,570	1,709	7,940	7,940
CHERRY CREEK	28.8	1,126	847	2,504	2,096	153	181	847	282
CHIMNEY BUTTE	79.8	11,570	12,912	16,532	11,068	4,466	346	12,912	8,194
CHURCH	3.0	90	129	96	33	55	426	129	101
CINNAMON CREEK	5.0	173	268	178	74	8	31	83	15
CLARKS CREEK	39.3	5,811	6,559	22,416	19,310	1,953	298	6,559	3,584
CLAYTON	1.8	25	118	33	25	0	0	0	0
Field Name	Active Well Number	Oil MBBL BBL/D	Produced Water BBL/D	Gas Thousand CF/D	Gas Sold Thousand CF/D	Flared Thousand CF/D	Ratio CF Flared/ BBL Water	Heat Pump BBL Treatable at 99 CF/BBL	Boiler BBL Treatable at 545 CF/BBL
CLEAR CREEK	73.3	3,929	1,866	12,559	10,778	1,395	747	1,866	1,866
CLEAR WATER	66.1	1,449	3,285	1,474	822	205	63	2,076	377
CLIMAX	11.8	156	458	293	49	162	353	458	297
COLGAN	61.9	1,367	2,573	1,882	849	71	28	720	131
COOKS PEAK	1.0	19	16	5	5	0	0	0	0
CORINTH	20.0	797	1,866	1,507	723	605	325	1,866	1,111

CORRAL CREEK	190.3	31,353	27,049	36,044	28,830	6,419	237	27,049	11,778
COTEAU	1.8	30	159	44	36	0	0	0	0
COTTONWOOD	92.3	2,022	5,937	3,989	2,444	397	67	4,013	729
COVERED BRIDGE	1.1	49	55	52	16	36	650	55	55
COW CREEK	44.8	2,096	4,112	3,515	2,726	575	140	4,112	1,056
CRAZY MAN CREEK	60.8	5,386	6,995	16,726	13,197	986	141	6,995	1,810
CROFF	27.9	6,225	2,216	11,910	9,679	2,123	958	2,216	2,216
CROOKED CREEK	13.4	323	501	342	205	33	66	332	60
CROSBY	0.8	11	22	30	8	3	125	22	5
CUSTOMS	1.0	22	479	16	11	0	0	0	0
DANEVILLE	2.0	47	236	58	3	5	23	55	10
DAVIS BUTTES	1.0	25	47	8	0	3	59	28	5
DEEP WATER CREEK BAY	35.9	1,422	1,397	1,088	510	342	245	1,397	628
DEMORES	7.0	153	493	115	66	14	28	138	25
DEVILS PASS	1.0	0	0	30	25	0	0	0	0
DICKINSON	9.0	205	112	156	126	3	24	28	5
DIMMICK LAKE	34.5	9,567	8,978	23,784	19,370	4,197	468	8,978	7,701
DIMOND	33.4	1,323	6,395	1,132	301	696	109	6,395	1,277
DOLLAR JOE	91.5	2,986	5,526	11,233	9,447	981	177	5,526	1,800

FieldName	Active Wells Number	Oil MBBL BBL/D	Produced Water BBL/D	Gas Thousand CF/D	Gas Sold Thousand CF/D	Flared Thousand CF/D	Ratio CF Flared/ BBL Water	Heat Pump BBL Treatable at 99 CF/BBL	Boiler BBL Treatable at 545 CF/BBL
DOLPHIN	16.4	260	342	915	647	79	232	342	146
DORE	5.2	271	389	301	175	115	296	389	211
DUBLIN	18.8	2,301	4,633	4,384	3,995	340	73	3,432	623
DUTCH HENRY BUTTE	24.8	562	318	512	397	27	86	277	50
EAGLE NEST	109.7	11,329	9,189	18,342	12,249	3,825	416	9,189	7,018
EAST FORK	157.5	16,964	33,885	30,764	20,175	9,060	267	33,885	16,624
EAST TIOGA	20.9	786	1,773	1,233	975	71	40	720	131
EDGE	7.0	1,362	860	3,586	3,296	74	86	747	136
EIGHTMILE	11.9	1,408	3,052	2,096	668	1,359	445	3,052	2,493
ELIDAH	85.8	19,049	19,364	54,068	45,712	7,622	394	19,364	13,985
ELK	59.4	4,589	9,688	6,647	6,121	378	39	3,819	694
ELKHORN RANCH	16.2	441	619	819	532	74	119	619	136
ELLISVILLE	33.3	3,627	9,808	6,447	5,036	1,236	126	9,808	2,267
ELLSWORTH	44.5	2,014	2,937	4,222	3,321	622	212	2,937	1,141
ELM TREE	102.7	27,112	22,789	60,104	52,151	7,321	321	22,789	13,432

ENGET LAKE	11.7	885	1,740	1,255	1,088	126	72	1,273	231
EPPING	74.4	10,932	16,411	25,395	20,663	3,696	225	16,411	6,781
ESTES	6.6	121	162	142	68	66	407	162	121
FAIRFIELD	3.0	52	41	107	58	11	267	41	20
FANCY BUTTES	8.5	3,805	3,186	8,764	7,110	1,614	506	3,186	2,961
FAYETTE	53.8	3,649	4,910	2,589	1,811	184	37	1,854	337
FERTILE VALLEY	3.6	356	1,340	301	0	247	184	1,340	452
FLAT LAKE EAST	8.1	0	0	0	0	0	0	0	0
Field Name	Active Wells Number	Oil MBBL BBL/D	Produced Water BBL/D	Gas Thousand CF/D	Gas Sold Thousand CF/D	Flared Thousand CF/D	Ratio CF Flared/ BBL Water	Heat Pump BBL Treatable at 99 CF/BBL	Boiler BBL Treatable at 545 CF/BBL
FLAT TOP BUTTE	8.1	38	16	181	115	36	2,167	16	16
FLAXTON	2.0	33	321	33	22	0	0	0	0
FOOTHILLS	10.3	214	312	504	0	288	921	312	312
FOREMAN BUTTE	29.2	2,581	4,803	3,679	3,000	485	101	4,803	890
FORTHUN	6.0	123	408	219	0	181	443	408	332
FORTUNA	14.0	290	1,923	375	129	88	46	886	161
FOUR BEARS	42.9	3,414	3,488	7,027	3,819	2,890	829	3,488	3,488

FOUR EYES	1.0	5	3	5	5	0	0	0	0
FRAZIER	13.9	392	592	814	595	55	93	553	101
FRYBURG	8.1	164	282	416	397	0	0	0	0
FT. BUFORD	6.9	195	249	351	225	63	253	249	116
GARDEN	19.3	1,312	1,658	5,740	5,255	381	230	1,658	699
GARNET	4.0	90	266	104	79	0	0	0	0
GAYLORD	12.6	121	145	214	189	0	0	0	0
GLADE	2.0	16	8	41	5	0	0	0	0
GLASS BLUFF	40.0	2,186	3,967	3,027	1,964	770	194	3,967	1,413
GOOD LUCK	6.0	115	186	167	27	96	515	186	176
GOOSENECK	3.9	104	436	126	58	38	88	387	70
GRAIL	192.6	14,641	11,378	53,874	47,756	3,732	328	11,378	6,847
GREEN LAKE	2.0	44	140	77	44	0	0	0	0
GREEN RIVER	9.6	211	156	200	162	3	18	28	5
GRINNELL	67.8	2,597	3,030	15,751	12,332	1,997	659	3,030	3,030
GROS VENTRE	39.5	1,140	2,395	2,721	1,416	512	214	2,395	940
HAMLET	47.5	984	1,677	2,649	1,995	93	56	941	171
HANKS	2.5	38	115	52	0	33	286	115	60

Field Name	Active Wells Number	Oil MBBL BBL/D	Produced Water BBL/D	Gas Thousand CF/D	Gas Sold Thousand CF/D	Flared Thousand CF/D	Ratio CF Flared/ BBL Water	Heat Pump BBL Treatable at 99 CF/BBL	Boiler BBL Treatable at 545 CF/BBL
HANSON	5.9	90	170	301	181	47	274	170	85
HARDING	7.1	132	189	258	181	66	348	189	121
HARDSCRABBLE	2.0	104	170	140	115	11	65	111	20
HAWKEYE	111.1	5,597	1,863	18,219	13,268	4,362	2,341	1,863	1,863
HAY CREEK	6.5	145	211	241	181	49	234	211	90
HAY DRAW	2.0	249	359	575	521	38	107	359	70
HAYLAND	12.3	115	334	515	392	0	0	0	0
HAYSTACK BUTTE	65.6	5,378	5,882	12,748	10,137	2,162	367	5,882	3,966
HEART BUTTE	227.3	23,293	33,455	18,485	10,573	3,488	104	33,455	6,399
HEART RIVER	20.0	436	337	510	416	14	41	138	25
HEBRON	14.8	293	384	345	68	156	407	384	287
HOFFLUND	31.5	2,518	1,964	5,433	4,301	819	417	1,964	1,503
HUNGRY MAN BUTTE	4.7	471	1,266	915	849	5	4	55	10
ICE CAVES	1.6	11	3	5	0	0	0	0	0
INDIAN HILL	31.9	1,581	2,627	2,192	1,671	192	73	1,937	352

JIM CREEK	74.3	11,049	11,849	18,132	15,118	2,268	191	11,849	4,162
JOHNSON CORNER	27.3	1,627	608	3,444	2,701	679	1,117	608	608

Bakken Field Production Data Jan1-(Dec 31, 2019) and Potential for Treatment									
Field Name	Active Wells Number	Oil MBBL BBL/D	Produced Water BBL/D	Gas Thousand CF/D	Gas Sold Thousand CF/D	Flared Thousand CF/D	Ratio CF Flared/ BBL Water	Heat Pump BBL Treatable at 99 CF/BBL	Boiler BBL Treatable at 545 CF/BBL
JUNIPER	10.3	389	463	1,227	888	288	621	463	463
JUNO	10.5	345	951	825	236	468	493	951	860
KILLDEER	47.4	8,016	10,416	8,005	2,586	4,677	449	10,416	8,581
KIMBERLY	1.0	16	55	47	0	36	650	55	55
KITTLESON SLOUGH	34.7	1,274	2,279	1,208	756	227	100	2,279	417
LAKE ILO	14.2	373	737	315	99	74	100	737	136
LAKE TRENTON	5.8	195	362	293	162	63	174	362	116
LARSON	3.9	151	449	214	148	58	128	449	106
LAST CHANCE	21.3	1,063	1,896	2,652	1,704	704	371	1,896	1,292
LEAF MOUNTAIN	5.0	121	236	227	140	30	128	236	55

LIGNITE	1.0	5	25	8	0	5	222	25	10
LINDAHL	27.9	1,203	1,540	3,022	2,685	110	71	1,107	201
LITTLE BUTTE	4.5	77	277	90	58	16	59	166	30
LITTLE KNIFE	153.8	8,636	10,353	11,447	9,611	814	79	8,219	1,493
LITTLE MUDDY	16.9	479	1,342	627	400	195	145	1,342	357
LITTLE TANK	4.0	395	893	649	485	44	49	443	80
LONE BUTTE	11.1	458	611	855	490	326	534	611	598
LONE TREE LAKE	66.9	14,800	36,107	21,126	12,384	7,929	220	36,107	14,548
LONESOME	14.9	515	682	1,129	934	134	197	682	246
LONG CREEK	27.8	1,685	1,723	10,071	8,414	1,296	752	1,723	1,723
LOST BRIDGE	81.9	14,159	13,126	22,858	13,468	8,773	668	13,126	13,126
LOSTWOOD	2.0	16	197	25	14	3	14	28	5
LUCY	2.0	66	96	156	99	8	86	83	15
MAGPIE	0.8	16	44	11	0	8	188	44	15

Field Name	Active Wells Number	Oil MBBL BBL/D	Produced Water BBL/D	Gas Thousand CF/D	Gas Sold Thousand CF/D	Flared Thousand CF/D	Ratio CF Flared/ BBL Water	Heat Pump BBL Treatable at 99 CF/BBL	Boiler BBL Treatable at 545 CF/BBL
MAGPIE	0.8	16	44	11	0	8	188	44	15
MANDAREE	125.8	23,668	18,992	26,638	19,995	2,970	156	18,992	5,449
MANITOU	55.6	2,438	2,195	4,170	3,474	668	305	2,195	1,227
MANNING	34.0	1,532	4,364	1,025	605	88	20	886	161
MARMON	36.7	4,715	10,142	5,479	3,858	1,474	145	10,142	2,705
MARY	3.0	104	96	184	159	3	29	28	5
MCGREGOR	48.7	1,307	3,611	6,208	5,616	93	26	941	171
MCGREGORY BUTTES	138.8	16,488	19,995	24,975	13,838	7,997	400	19,995	14,674
MIDWAY	31.1	926	1,277	3,173	2,068	222	174	1,277	407
MISSOURI RIDGE	39.1	3,019	6,386	4,641	4,088	258	40	2,601	473
MOCCASIN CREEK	87.9	13,501	14,008	14,195	8,751	3,047	217	14,008	5,590
MOLINE	5.0	178	452	373	337	0	0	0	0
MONDAK	38.3	879	1,099	1,422	556	463	421	1,099	850
MORAINE	4.0	90	416	137	115	0	0	0	0
MORGAN DRAW	10.8	227	148	332	225	25	167	148	45

MURPHY CREEK	198.3	7,707	11,789	6,477	3,455	1,433	122	11,789	2,629
MUSTA	8.0	312	1,008	326	216	19	19	194	35
NAMELESS	9.9	321	570	562	485	49	87	498	90
NELSON BRIDGE	3.8	90	126	173	153	14	109	126	25
NEW HOME	21.3	775	1,896	1,956	1,479	304	160	1,896	558
NEW HRADEC	7.0	93	110	96	71	3	25	28	5
NOHLY LAKE	2.9	66	110	77	52	16	150	110	30
NOONAN	3.0	126	304	205	58	107	351	304	196

Bakken Field Production Data Jan1-(Dec 31, 2019) and Potential for Treatment									
Field Name	Active Wells Number	Oil MBBL BBL/D	Produced Water BBL/D	Gas Thousand CF/D	Gas Sold Thousand CF/D	Flared Thousand CF/D	Ratio CF Flared/ BBL Water	Heat Pump BBL Treatable at 99 CF/BBL	Boiler BBL Treatable at 545 CF/BBL
NORTH BRANCH	1.0	5	14	14	0	0	0	0	0
NORTH CREEK	8.0	90	170	142	126	0	0	0	0
NORTH ELKHORN RANCH	1.0	11	22	115	107	5	250	22	10
NORTH FORK	80.9	15,263	12,321	42,334	30,805	10,493	852	12,321	12,321

NORTH TIOGA	77.3	2,315	3,981	4,975	3,567	792	199	3,981	1,453
NORTH TOBACCO GARDEN	72.9	6,797	9,978	33,877	29,633	3,271	328	9,978	6,002
NORTHEAST FOOTHILLS	2.4	49	219	52	38	3	13	28	5
NORTHWEST MCGREGOR	21.3	696	984	2,011	1,685	66	67	664	121
OAKDALE	28.1	8,225	5,299	9,830	8,271	1,241	234	5,299	2,277
OLIVER	58.3	10,203	25,658	13,732	7,260	5,690	222	25,658	10,441
OTTER	16.3	438	1,060	663	378	205	194	1,060	377
PAINTED WOODS	71.5	5,230	13,233	6,622	4,767	1,490	113	13,233	2,735
PARK	38.7	3,008	2,778	6,255	6,000	184	66	1,854	337
PARSHALL	470.4	25,293	20,893	48,589	40,830	2,411	115	20,893	4,424
PATENT GATE	12.2	1,296	2,003	2,203	2,005	121	60	1,218	221
PAULSON	2.0	16	41	58	0	27	667	41	41
PEMBROKE	74.1	11,367	15,466	32,384	20,137	11,444	740	15,466	15,466
PERSHING	61.8	11,178	8,463	28,638	22,800	5,411	639	8,463	8,463
PHELPS BAY	2.8	33	8	244	233	3	333	8	5
PICKETT	2.8	33	236	36	22	0	0	0	0
PIERRE CREEK	8.6	101	101	175	104	25	243	101	45

Bakken Field Production Data Jan1-(Dec 31, 2019) and Potential for Treatment									
Field Name	Active Wells Number	Oil MBBL BBL/D	Produced Water BBL/D	Gas Thousand CF/D	Gas Sold Thousand CF/D	Flared Thousand CF/D	Ratio CF Flared/ BBL Water	Heat Pump BBL Treatable at 99 CF/BBL	Boiler BBL Treatable at 545 CF/BBL
PLEASANT HILL	37.1	973	1,219	2,504	2,090	340	279	1,219	623
PLEASANT VALLEY	11.8	964	1,134	1,666	1,332	310	273	1,134	568
PLUMER	6.0	79	175	115	74	0	0	0	0
POE	115.5	7,405	8,984	19,049	17,551	822	91	8,302	1,508
POWERS LAKE	1.0	22	25	27	19	0	0	0	0
PRONGHORN	24.4	1,660	3,093	2,192	2,132	44	14	443	80
RAGGED BUTTE	22.5	997	2,049	1,921	1,504	353	172	2,049	648
RAINBOW	14.6	422	532	663	205	345	649	532	532

RANCH COULEE	3.7	44	58	74	19	16	286	58	30
RANCH CREEK	7.9	142	329	227	123	60	183	329	111
RANDOLPH	1.0	22	36	19	14	3	77	28	5

Bakken Field Production Data Jan1-(Dec 31, 2019) and Potential for Treatment									
Field Name	Active Wells Number	Oil MBBL BBL/D	Produced Water BBL/D	Gas Thousand CF/D	Gas Sold Thousand CF/D	Flared Thousand CF/D	Ratio CF Flared/ BBL Water	Heat Pump BBL Treatable at 99 CF/BBL	Boiler BBL Treatable at 545 CF/BBL
RATTLESNAKE POINT	39.0	6,814	8,099	12,449	10,318	1,753	217	8,099	3,217
RAWSON	30.5	1,244	1,921	2,997	2,811	153	80	1,550	282
RAY	52.9	1,353	3,874	4,671	3,803	584	151	3,874	1,071
RED WING CREEK	2.8	47	63	123	110	0	0	0	0
RENNIE LAKE	1.0	11	44	8	5	0	0	0	0
REUNION BAY	233.6	67,559	54,882	106,186	51,090	46,655	850	54,882	54,882
ROBINSON LAKE	185.2	12,025	12,049	21,364	17,504	3,452	286	12,049	6,334
ROOSEVELT	10.9	411	964	367	271	47	48	470	85
ROSEBUD	17.6	1,244	2,310	1,329	504	693	300	2,310	1,272
ROSS	79.8	4,225	7,145	3,586	2,649	534	75	5,396	980

ROUGH RIDER	9.2	25	11	107	88	11	1,000	11	11
ROUND PRAIRIE	12.0	236	359	356	233	8	23	83	15
RUSSIAN CREEK	9.8	181	301	153	82	0	0	0	0
SADDLE BUTTE	4.9	44	137	68	30	0	0	0	0
SADLER	25.0	597	1,548	1,740	1,329	126	81	1,273	231
SAKAKAWEA	3.5	608	1,090	816	748	68	63	692	126
SAND CREEK	102.8	12,778	11,542	48,625	41,910	5,186	449	11,542	9,516
SANDROCKS	25.5	1,011	953	2,340	2,049	148	155	953	271
SANISH	618.7	36,912	32,759	80,277	69,975	8,101	247	32,759	14,865
SATHER LAKE	7.8	227	318	400	247	63	198	318	116
SAUK	16.8	425	458	1,205	964	30	66	304	55
SAXON	1.0	36	85	19	8	3	32	28	5

Bakken Field Production Data Jan1-(Dec 31, 2019) and Potential for Treatment									
Field Name	Active Wells Number	Oil MBBL BBL/ D	Produce d Water BBL/D	Gas Thousan d CF/D	Gas Sold Thousan d CF/D	Flared Thousan d CF/D	Ratio CF Flared/ BBL Water	Heat Pump BBL Treatable at 99 CF/BBL	Boiler BBL Treatable at 545 CF/BBL
SHEEP BUTTE	4.9	118	353	222	184	8	23	83	15
SHORT CREEK	1.9	16	88	14	0	14	156	88	25
SIMON BUTTE	6.0	101	216	66	3	19	89	194	35
SIOUX	11.7	134	142	266	233	27	192	142	50
SIOUX TRAIL	3.8	219	1,351	370	132	25	18	249	45
SIVERSTON	315.9	30,225	41,756	118,288	85,679	27,225	652	41,756	41,756
SIXMILE	3.4	90	159	123	74	25	155	159	45
SKABO	8.9	184	721	340	219	52	72	526	96
SKJERMO	9.8	219	721	304	68	11	15	111	20
SMOKY BUTTE	14.9	395	1,085	581	318	25	23	249	45
SNOW	2.0	38	55	66	49	0	0	0	0
SORKNESS	10.8	260	271	460	184	208	768	271	271
SOUTH COTEAU	4.0	71	348	82	63	3	8	28	5
SOUTH FORK	36.6	5,449	6,627	5,411	3,923	584	88	5,895	1,071

SOUTH HEART	6.8	151	203	145	132	0	0	0	0
SOUTH MEADOW	7.2	129	277	386	268	49	178	277	90
SOUTH TOBACCO GARDEN	40.1	5,044	6,052	8,723	7,699	660	109	6,052	1,212
SPENCER	1.0	19	79	14	0	3	34	28	5
SPOTTED HORN	149.5	33,260	25,436	59,184	41,392	12,584	495	25,436	23,089
SPRING CREEK	9.7	926	2,156	3,162	2,666	477	221	2,156	875
SPRINGBROOK	12.8	907	1,863	4,460	4,099	247	132	1,863	452
SQUAW CREEK	58.9	13,723	11,041	21,326	16,170	3,236	293	11,041	5,937
SQUAW GAP	8.0	104	19	112	25	8	429	19	15
SQUIRES	65.3	5,258	13,805	8,397	6,019	1,403	102	13,805	2,574
ST. ANTHONY	18.9	438	1,370	321	192	8	6	83	15

Bakken Field Production Data Jan1-(Dec 31, 2019) and Potential for Treatment									
Field Name	Active Wells Number	Oil MBBL BBL/D	Produced Water BBL/D	Gas Thousand CF/D	Gas Sold Thousand CF/D	Flared Thousand CF/D	Ratio CF Flared/ BBL Water	Heat Pump BBL Treatable at 99 CF/BBL	Boiler BBL Treatable at 545 CF/BBL
ST. DEMETRIUS	28.0	710	811	1,408	981	79	98	803	146
STANLEY	90.5	4,071	3,058	5,271	3,784	641	210	3,058	1,176
STOCKYARD CREEK	104.5	10,197	15,375	30,277	25,058	2,721	177	15,375	4,992
STONEVIEW	74.0	1,803	2,655	5,079	3,638	622	234	2,655	1,141
STONY CREEK	46.3	3,660	6,847	8,416	6,151	1,614	236	6,847	2,961
STRANDAHL	32.4	553	1,222	844	271	405	332	1,222	744
SUGAR BEET	2.0	71	132	99	55	36	271	132	65
TEMPLE	24.3	838	1,636	2,600	1,937	416	255	1,636	764
THOMPSON LAKE	7.8	145	315	197	134	11	35	111	20
TIMBER CREEK	25.9	682	1,066	2,578	2,381	107	100	1,066	196
TIOGA	27.3	784	948	1,748	1,586	101	107	948	186

TOBACCO GARDEN	56.0	3,279	3,200	10,652	8,707	962	301	3,200	1,764
TODD	61.9	4,282	7,874	5,079	4,049	756	96	7,638	1,387
TRAILSIDE	1.0	25	36	44	36	0	0	0	0
TREE TOP	3.8	162	553	403	370	8	15	83	15
TRENTON	2.0	118	156	85	47	19	123	156	35
TRUAX	231.0	26,107	40,510	94,674	65,512	28,551	705	40,510	40,510
TWIN BUTTES	24.0	1,395	1,775	1,564	0	882	497	1,775	1,619
TWIN VALLEY	34.2	5,540	3,770	23,989	22,682	1,162	308	3,770	2,131
TYRONE	78.6	8,230	17,151	11,005	5,466	5,112	298	17,151	9,380
UKRAINA	10.0	173	277	252	123	11	40	111	20
UNION CENTER	20.5	1,589	789	5,318	4,584	578	733	789	789
UPLAND	20.0	422	603	981	608	123	205	603	226
VAN HOOK	177.3	17,233	14,381	17,737	9,071	6,203	431	14,381	11,381
VANVILLE	1.0	11	33	16	5	0	0	0	0

Bakken Field Production Data Jan1-(Dec 31, 2019) and Potential for Treatment									
Field Name	Active Wells Number	Oil MBBL BBL/D	Produced Water BBL/D	Gas Thousand CF/D	Gas Sold Thousand CF/D	Flared Thousand CF/D	Ratio CF Flared/ BBL Water	Heat Pump BBL Treatable at 99 CF/BBL	Boiler BBL Treatable at 545 CF/ BBL
VIKING	4.8	121	186	312	238	16	88	166	30

WERNER	16.3	2,074	4,981	1,085	718	173	35	1,743	317
WEST AMBROSE	96.8	2,830	6,247	4,674	3,726	263	42	2,657	483
WEST BANK	12.0	282	145	822	636	55	377	145	101
WEST CAPA	32.4	3,192	3,690	10,019	7,066	2,718	736	3,690	3,690
WEST TIOGA	7.3	55	22	90	68	5	250	22	10
WESTBERG	86.7	3,904	1,910	14,545	12,233	1,723	902	1,910	1,910
WHEELOCK	28.8	2,301	3,734	5,630	4,425	978	262	3,734	1,795
WHISKEY JOE	1.0	5	19	11	8	0	0	0	0
WHITE EARTH	6.0	510	997	737	644	77	77	775	141
WHITEAKER	21.0	373	1,101	704	496	49	45	498	90
WHITETAIL	3.1	52	101	85	58	0	0	0	0
WILDROSE	15.8	247	504	693	395	137	272	504	251
WILLISTON	37.9	8,178	16,721	11,721	8,077	3,510	210	16,721	6,440
WILLMEN	26.3	397	512	488	296	5	11	55	10
WILLOW CREEK	61.8	7,244	12,036	19,425	17,392	1,430	119	12,036	2,624
WINNER	20.2	3,096	8,140	4,562	3,751	696	85	7,029	1,277
WOBURN	2.0	19	241	30	22	0	0	0	0
WOLF BAY	26.3	6,797	10,932	4,499	1,153	2,362	216	10,932	4,333
WRITING ROCK	14.0	441	1,696	551	252	66	39	664	121
ZAHL	6.8	129	452	255	129	27	61	277	50
ZENITH	30.6	737	625	1,268	1,134	27	44	277	50

D.3. Life Cycle Analysis for the Bakken

Summary:

This section of the report describes a continuation of the practical engineering evaluation of applying membrane distillation to field use and represents an analysis of the opportunity to utilize flared gas as a source of heat to drive the distillation equipment. The target areas include the gas and oil fields in North Dakota (15,348 active wells) with special reference to the Bakken oil fields (336 named fields with 12,141 active wells). In previous quarterly reports, the quantity of gas needed to provide the heat need for membrane distillation has been estimated at >0.59 MCF/BBL (thousand cubic feet/barrel) for boilers as the heat source, and >0.134 MCF/BBL for the use of heat pumps as the heat source. By these criteria, 15% of active Bakken field wells have enough flared gas to treat water using a boiler, whereas 65-70% of wells should have sufficient flared gas to treat water using the heat pump option.

Life Cycle Model:

This section presents the values for the parameters the GTI Water Based Life Cycle Model to forecast future water treatment needs in the Bakken shale play. The number of existing and future wells were estimated to 45 years. Base assumptions for the model are summarized in Table D7. The assumption is that there are a constant number of new wells drilled per year with a constant rate of closure of active wells per year. Each active well is assumed to generate an average volume of produced water per month. The fate of the water is injection (41%), treatment with membrane distillation (65% of active wells able to treat water), and the remainder to accounted as untreated.

Table D 7: Data Used in Fife-Cycle Model for Bakken

Parameter	Number	Basis
Existing Active Wells	13,000 Wells	Average over Last 7.5 Years
Wells per Year Drilled	650 Wells	per Year Average over Last 7.5 Years
Future Wells	50,500 Wells	7000 Double-Units (DU) at 8 wells per DU + Existing Wells, at 67% Drilling Saturation
Produced Water Generated	3,000 BBL	per well per month
Produced Water Injected	1,250 BBL	per well per month
Well Closure	0.5%	of Active Wells per Year
Gas Production	5	million CF per well per month
Gas Flared	1	million CF per well per month
Treatment Potential	65%	Wells that have both flare gas and water to treat

Results:

The number of active wells, closed wells, wells that have potential to treat the produced water and total wells is given in Figure D2. About 9000 wells can presently treat water with membrane distillation using flared gas and heat pumps. That number increases each year to around 22,000 wells by 2060.

The present rate of produced water generation is around 600 million BBL per year with about 250 million BBL injected for well pressure maintenance and/or initial hydraulic fracture. As shown in Figure D2, in the future, the water generation will rise to 1.65 billion BBL per year with only 0.7 billion BBL re-injected. About 220 million BBL/yr. (present) to 620 million BBL/yr. (45 years) can be treated with membrane technology. This leaves 100 million BBL/yr. (present) to 270 million BBL/yr (45 years) needing treatment. It is reasonable to expect that the composition of the produced water will degrade with time, meaning that either more waste heat must be extracted, or some technology (in addition to membrane distillation) must be applied.

Figure D3 shows the gas production rate at present to be about 800 billion CF per year and expanding to 2,000 billion per year by 2060. The flare rate increases from around 160 billion CF per year to just over 400 billion CF per year.

Discussion:

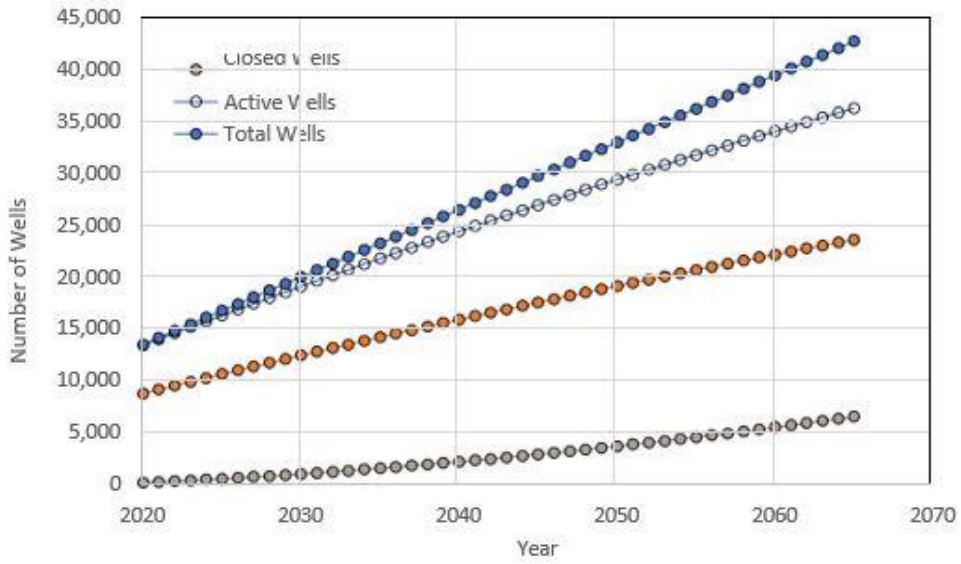


Figure D 2: Total, Active, and Closed Wells Projected for the Bakken over 45 Years

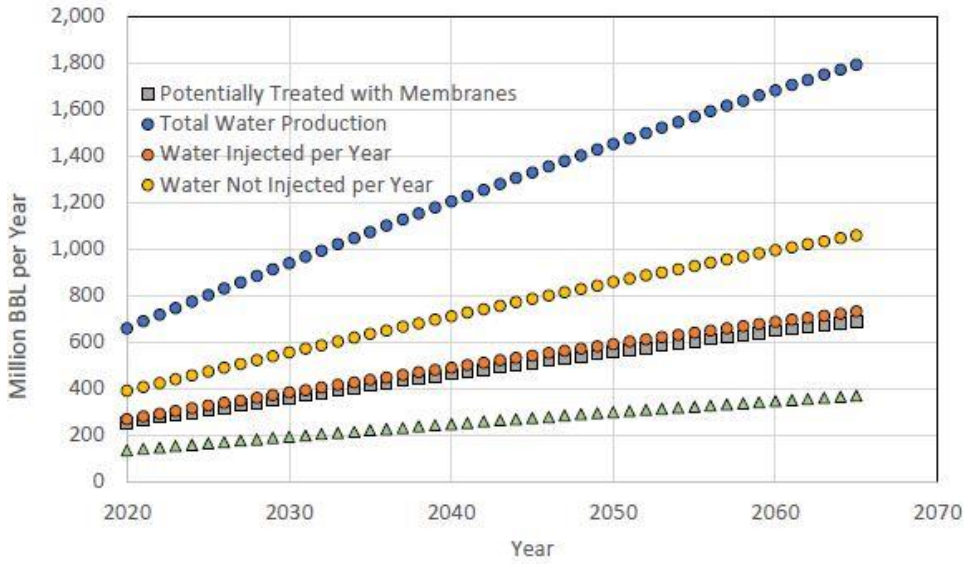


Figure D 3: Produced Water and Potentially Treated Water per Year in Bakken

The value for wells drilled per year (650) is the average for the last 7.5 years which includes one "boom" and one "bust" cycle. The total number of well to be drilled is based on 65% drilling

saturation over the entire range of the Bakken which will reach saturation sometime beyond 2070. Water production and water injection data were based on the last 7.5 years data from "Field Production Database" for approximately 13,000 active wells in the Bakken. The average produced water generation excels 3,000 BBL/well per month. Gas Production and Flared Gas data were based on the last the last 7.5 years data from "Field Production Database" for approximately 13,000 active wells in the Bakken.

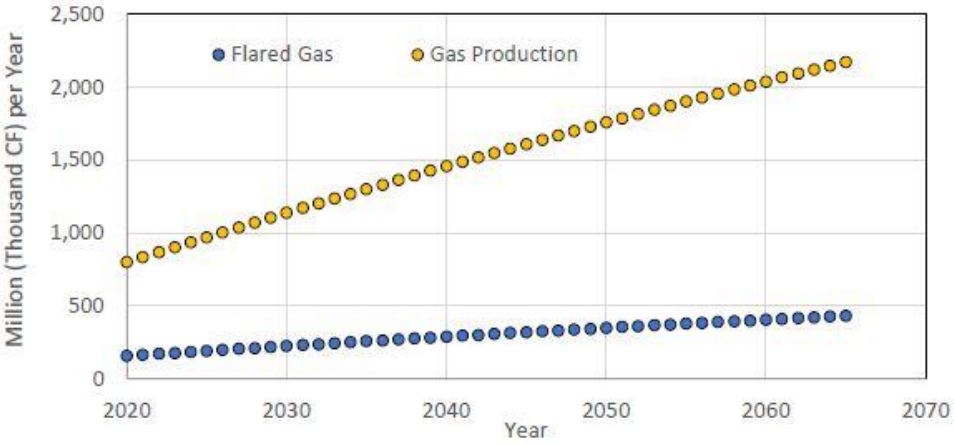


Figure D 4: Flared and Total Gas Production Projected for the Bakken

Appendix E: Analysis of the Permian Basin (Texas) Production

E.1 Summary

The Permian oil reserves are in Western Texas and South-Eastern Wyoming north of Mexico and occupy some 86,000 square miles. The modern hydraulic fracture technologies have opened the region as perhaps the largest oil field on earth. The Texas Railroad Commission lists 63 counties impacted by oil and gas production with some 30,000 active wells and roughly 3,000 new wells per year averaged over the last five years. These wells produced 600 million barrels of oil and 1.1 trillion cubic feet of natural gas in 2018. The calculated reserves are estimated to be 50 billion barrels of oil and 300 trillion cubic feet of natural gas.

Table E 1:Gas and Oil Production for the Permian Basin Counties, Texas 2018

	Natural Gas Production				Oil Production		
	Producing Wells	Inactive Wells	Total Gas MMCF		Producing Wells	Inactive Wells	Total Crude (Mbbl)
Andrews	131	102	3,464		10,420	3814	42,450
Bailey	0	0	0		0	0	0
Bordon	0	0	0		655	565	4,808
Brewster	0	0	0		0	0	0
Cochran	19	24	62		1,632	849	2,772
Coke	20	20	313		268	183	361
Concho	58	21	156		200	126	285
Cottle	79	11	2,889		43	15	117

Crane	444	123	8,287	4,006	1472	7,034
Crockett	5,649	448	44,851	2563	817	7,741
Crosby	0	0	0	656	376	1,004
Culberson	419	89	271,126	146	146	931
Dawson	0	0	0	1325	609	3,635
Dickens	0	0	0	202	81	485
Ector	67	79	3,709	7145	3487	20,176
Edwards	332	201	5,367	29	105	1
El Paso	0	0	0	0	0	0
Fisher	9	13	23	521	199	984
Floyd	0	0	0	0	3	0
Gaines	84	79	3,314	3917	1134	24,453
Garza	0	0	0	2007	498	2,297
Glasscock	102	22	627	4538	810	45,795
Hale	0	0	0	207	107	1,240
Hockley	13	8	32	3843	1067	12,370
Howard	18	23	255	4915	704	66,260
Hudspeth	0	0	0	0	0	0
Irion	216	53	1,280	2322	571	10,532
Jeff Davis	0	0	0	0	3	0
Kent	0	0	0	538	322	3,458
Kimble	13	11	16	1	2	0.3
Lamb	0	0	0	64	29	227
Loving	470	153	139,345	1496	460	77,171
Lubbock	0	0	0	430	76	989
Lynn	0	0	0	98	48	320
Martin	2	2	9	5897	817	93,225
McCulloch	1	5	0	58	22	41
Menard	6	2	20	127	53	95
Midland	133	73	4,572	6701	1812	151,379
Mitchel	0	0	0	2638	721	2,640
Motley	0	5	0	15	21	35
Nolan	33	11	266	589	304	1,160
Pecos	1,283	349	47,074	3156	1729	25,673

Presidio	0	0	0		0	0	0
Reagan	45	25	1,205		4992	1593	47,067
Real	4	0	66		0	2	0.06
Reeves	804	316	504,865		2291	670	92,391
Runnels	23	17	113		418	249	351
Schleicher	718	126	5,307		347	148	304
Scurry	0	0	0		2448	1512	15,309
Sterling	622	193	2,622		1293	390	725
Stonewall	0	0	0		587	388	2,040
Sutton	5,610	878	23,859		59	16	20
Terrell	647	77	19,723		22	9	32
Terry	0	0	0		848	344	3,400
Tom Green	59	23	477		600	251	502
Upton	302	98	11,331		5623	1690	6,050
Val Verde	237	28	4,667		14	4	2
Ward	255	77	17,471		3502	1907	36,268
Winkler	271	208	14,432		1669	1194	27,443
Yoakum	1	17	175		3870	807	15,799
Inactive wells include non-eligible, temporary shut-in, and shut-in as of February 2019 Gas and Oil Production is for calendar year 2018. Source Texas Railroad Commission, 2019. (MM = millions) (M = thousands)							

Table E 2: Counties in Permian NOT Producing in 2018							
Natural Gas Production					Oil Production		
	Producing Wells	Inactive Wells	Total Gas MMCF		Producing Wells	Inactive Wells	Total Crude
Bailey	0	0	0		0	0	0
Brewster	0	0	0		0	0	0
El Paso	0	0	0		0	0	0
Floyd	0	0	0		0	3	0
Hudspeth	0	0	0		0	0	0
Jeff Davis	0	0	0		0	3	0
Presidio	0	0	0		0	0	0

Table E 3: Counties in Permian that Produce Oil but NOT Gas							
	Natural Gas				Oil		
	Producing Wells	Inactive Wells	Total Gas MMCF		Producing Wells	Inactive Wells	Total Crude (Mbbl)
Bordon	0	0	0		655	565	4,808
Crosby	0	0	0		656	376	1,004
Dawson	0	0	0		1325	609	3,635
Dickens	0	0	0		202	81	485
Garza	0	0	0		2,007	498	2,297
Hale	0	0	0		270	107	1,240
Kent	0	0	0		538	322	3,458
Lamb	0	0	0		64	29	227
Lubbock	0	0	0		430	76	989
Lynn	0	0	0		98	48	320
McCulloch	1	5	0		58	22	41
Mitchel	0	0	0		2,638	721	2,640
Motley	0	5	0		15	21	35
Scurry	0	0	0		2,448	1,512	15,309
Stonewall	0	0	0		587	388	2,040
Terry	0	0	0		848	344	3,400

Table E 4: Counties in Permian that Produce Gas AND Oil in 2018							
	Natural Gas				Oil		
	Producing Wells	Inactive Wells	Total Gas MMCF		Producing Wells	Inactive Wells	Total Crude (Mbbl)
Andrews	131	102	3,464		10,420	3814	42,450
Cochran	19	24	62		1,632	849	2,772
Coke	20	20	313		268	183	361
Concho	58	21	156		200	126	285
Cottle	79	11	2,889		43	15	117
Crane	444	123	8,287		4,006	1472	7,034
Crockett	5,649	448	44,851		2563	817	7,741
Culberson	419	89	271,126		146	146	931
Ector	67	79	3,709		7145	3487	20,176

Edwards	332	201	5,367	29	105	1
Fisher	9	13	23	521	199	984
Gaines	84	79	3,314	3917	1134	24,453
Glasscock	102	22	627	4538	810	45,795
Hockley	13	8	32	3843	1067	12,370
Howard	18	23	255	4915	704	66,260
Irion	216	53	1,280	2322	571	10,532
Kimble	13	11	16	1	2	0.3
Loving	470	153	139,345	1496	460	77,171
Martin	2	2	9	5897	817	93,225
Menard	6	2	20	127	53	95
Midland	133	73	4,572	6701	1812	151,379
Nolan	33	11	266	589	304	1,160
Pecos	1,283	349	47,074	3156	1729	25,673
Reagan	45	25	1,205	4992	1593	47,067
Real	4	0	66	0	2	0.06
Reeves	804	316	504,865	2291	670	92,391
Runnels	23	17	113	418	249	351
Schleicher	718	126	5,307	347	148	304
Sterling	622	193	2,622	1293	390	725
Sutton	5,610	878	23,859	59	16	20
Terrell	647	77	19,723	22	9	32
Tom Green	59	23	477	600	251	502
Upton	302	98	11,331	5623	1690	6,050
Val Verde	237	28	4,667	14	4	2
Ward	255	77	17,471	3502	1907	36,268
Winkler	271	208	14,432	1669	1194	27,443
Yoakum	1	17	175	3870	807	15,799

Inactive wells include non-eligible, temporary shut-in, and shut-in as of February 2019 Gas and Oil Production is for calendar year 2018. Source Texas Railroad Commission, 2019. (MM = millions) (M = thousands)

The Texas Railroad Commission lists the following 61 Counties in Table E1 as being impacted by oil and gas production in the Permian Basin and totaling more than 102,000 oil and 19,200 gas wells. Note that there are several counties that produce neither gas nor oil (Table E2), counties that produce a predominance of oil and little natural gas (Table E3), and counties that produce

both (Table E4). Significant quantities of both oil and gas (as arbitrarily having > 150 active natural gas wells AND > 500 oil wells are produced in only a few counties (Table E5). Figure E1 is a probability plot showing the number of wells having less than the stated daily production rate (BBL/well). The median production rate is around 11.2 BBL/well-day.

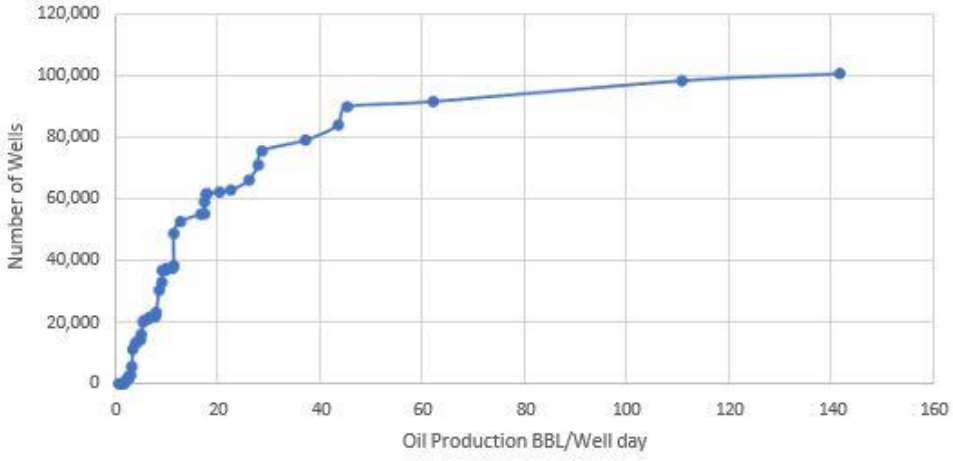


Figure E 1: Number of Wells Producing Less than Stated BBL/Well Day

Table E 5: Counties with Gas AND Oil with >150 Gas Wells and >500 Oil Wells

	Natural Gas				Oil		
	Producing Wells	Inactive Wells	Total Gas MMCF		Producing Wells	Inactive Wells	Total Crude (Mbbl)
Andrews	131	102	3,464		10,420	3814	42,450
Crane	444	123	8,287		4,006	1472	7,034
Crockett	5,649	448	44,851		2563	817	7,741
Glasscock	102	22	627		4538	810	45,795
Irion	216	53	1,280		2322	571	10,532
Loving	470	153	139,345		1496	460	77,171
Midland	133	73	4,572		6701	1812	151,379
Pecos	1,283	349	47,074		3156	1729	25,673
Reeves	804	316	504,865		2291	670	92,391
Sterling	622	193	2,622		1293	390	725
Upton	302	98	11,331		5623	1690	6,050
Ward	255	77	17,471		3502	1907	36,268
Winkler	271	208	14,432		1669	1194	27,443

Inactive wells include non-eligible, temporary shut-in, and shut-in as of February 2019 Gas and Oil Production is for calendar year 2018. Source Texas Railroad Commission, 2019. (MM = millions) (M = thousands)

E.2 Lifecycle in the Permian

The Life-Cycle analysis for the Permian is based on a combination of the data collected from the references. The number of existing and future wells were estimated to 45 years. The assumption is that there are a constant number of new wells drilled per year with a constant rate of closure of active wells per year. Each active well is assumed to generate an average volume of produced water per month. The fate of the water is injection (55%), treatment with membrane distillation (65% of active wells able to treat water) and the remainder to be untreated (Table %6).

Table E 6: Data Used in Life-Cycle Model for the Permian

Parameter	Number	Basis (Tables 4 and 5)
Existing Active Wells	30,000 Wells	Average over Last 7.5 Years
Wells per Year Drilled	3,000 Wells	Yearly Average over Last 5 Years
Future Wells (Existing + New)	190,000 Wells	Linear Growth Potential
Produced Water Generated	10,000 BBL	per-well per-month (4.4 BBL PW/BBL Oil/)
Produced Water Injected	5,500 BBL	per-well per-month (55% of PW)
Well Closure	0.5%	Of Active Wells per Year
Gas Production	5.7	million CF per-well per-month
Gas Flared	none	million CF per-well per-month
Treatment Potential	65%	percent of wells that implement technology

Figure E2 indicates that by 2060, there will be potentially 175,000 total wells with 150,000 active wells. Figure E3 indicates that there will potentially be a total produced water generation of 18 billion BBL/yr. of which 8.1 billion BBL/yr. will require treatment other than injection. Figure E4 is a projection for the gas production nearing 15 trillion CF/yr. by 2060.

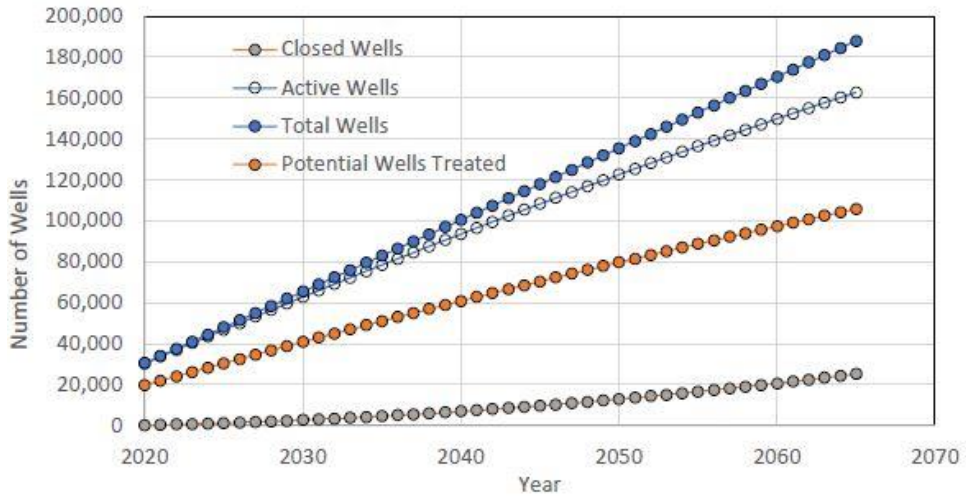


Figure E 2: Total, Active, and Closed Wells Projected for the Permian over 45 Years

The projections for growth in the Permian at 3,000 wells/year and an existing 30,000 active wells at present are roughly linear. The values in the Figures 4 and are based on yearly production. One aspect of the rates of water treatment, injection, and produced water generation is that any

water untreated today, is still water untreated tomorrow; the results are cumulative. Table E7 is a summary of the cumulative effects of the continued generation of produced water. If the water that is presently untreated, were to remain in a reservoir, by 2061 that reservoir would have collected 212 billion barrels.

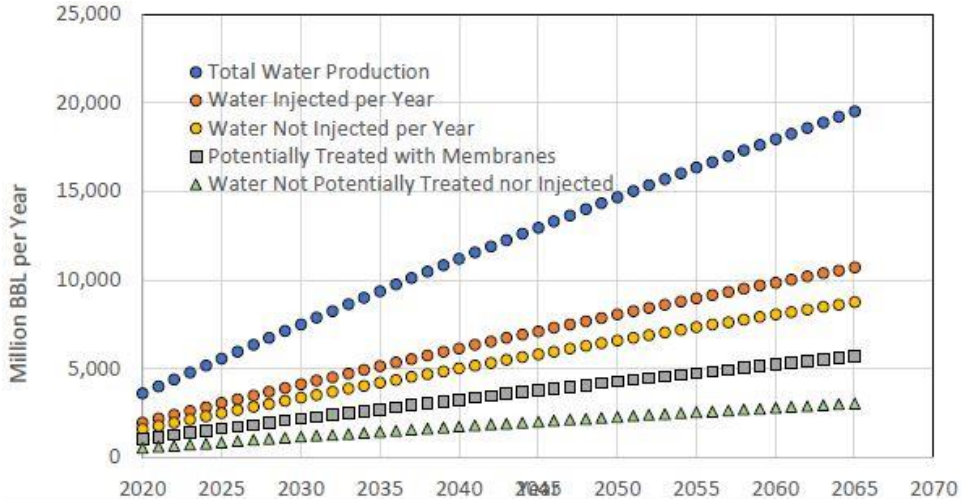


Figure E 3: Projection for PW and Potentially Treated Water per Year in the Permian

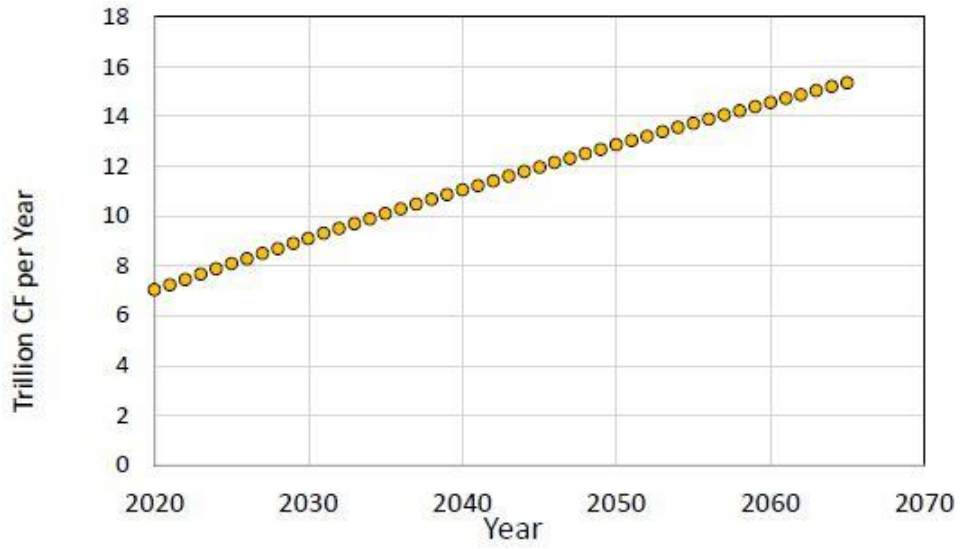


Figure E 4: Total Gas Production Projected for the Permian

Table E 7: Cumulative Volumes Projected for Permian (Millions BBL at Year-End)					
Year	2021	2031	2041	2051	2061
Produced Water Generated (Total)	7,700	69,500	169,000	304,000	472,500
Injected at 41% (Total)	4,200	38,200	92,900	167,200	259,900
Produced Water Presently Not Treated (Total)	3,400	31,300	76,000	136,800	212,600

Appendix F. Flaring Regulations in the Permian

The goal of this report is to present the likelihood that the membrane distillation process can be employed to de-brine produced water using waste flare gas as the heat source. Two natural gas production plays, Permian region (SW Texas) and Bakken (North Dakota) were investigated for

overlap between available flare gas and regions of produced water generation. Data were collected from summary data from the Texas Railroad Commission https://www.rrc.state.tx.us/oil-gas/research-and-statistics/production-data/ These data sources contain different types of data; as such, the approaches to identifying geographic (by county) that might have flare gas available are different. Most notably, Texas is highly restrictive on the release of permits to flare and does not keep data on the quantity of flare gas available. Conversely, North Dakota has does not restrict flaring; yet gas production data include loses to flare (and venting).

Flaring Regulations for the Texas Railroad Commission:

While flaring of natural gas is performed in the Permian (SW Texas), the flaring mostly occurs at new oil wells, and according to The Texas Railroad Commission, flared gas is considered a wasted resource. Flare permits are of limited duration. The following paragraphs are copied from the TRC website "question and answer section" https://rrc.texas.gov/about-us/resource-center/faqs/oil-gas-faqs/faq-flaring-regulation/. Some material has been reordered into paragraph structure for clarity. A simple summary is that natural gas wells are discouraged from flaring, and oil wells are allowed temporary permits.

"Flaring is a process used primarily in the production of crude oil in which excess natural gas produced with the oil is burned off at the well head, rather than released into the atmosphere. Operators are required to report to the Commission volumes of gas flared on their monthly Production Report form (Form PR). The Form PR must include actual, metered volumes of both gas well gas and casinghead gas reported by operators at the lease level.

"As the state's primary regulator of energy resource production, the Railroad Commission has jurisdiction over permitting of flaring operations with respect to prevention of waste of natural resources. The Texas Commission on Environmental Quality has jurisdiction over air quality issues related to flaring. The TCEQ handles all complaints regarding air quality and air pollution. For more information on TCEQ's role, please visit https://www.tceq.texas.gov/assistance/industry/oil-and-gas/oilgas.html.

"The Commission's Statewide Rule 32 (16 Texas Administrative Code §3.32) allows an operator to flare gas while drilling a well and for up to 10 days after a well's completion to conduct well potential testing. The majority of flaring permit requests received by the Commission are for flaring cashing head gas from oil wells. Permits to flare from gas wells are not typically issued as natural gas is the main product of a gas well. Rule 32 authorizes the flaring of gas while drilling a well and for up to 10 days after a well's completion for operators to conduct well potential testing. Outside of that time period, the Commission requires operators to obtain a permit to flare for most short-term requests and in every instance where the request is for an extended time period. Our trained staff works closely with operators to ensure compliance with Commission rules. RRC District Offices have inspectors available to witness operations, conduct inspections, provide information about permitting requirements, and ensure compliance with permits issued by the Commission.

"Flaring of casinghead gas for extended periods of time may be necessary if the well is drilled in areas new to exploration. In new areas of exploration, pipeline connections are not typically constructed until after a well is completed and a determination is made about the well's

productive capability. Other reasons for flaring include: gas plant shutdowns; repairing a compressor or gas line or well; or other maintenance. In existing production areas, flaring also may be necessary because existing pipelines may have reached capacity. Commission staff issue flare permits administratively for 45 days at a time, for a maximum limit of 180 days. Extensions beyond 180 days must be granted through a Commission Final Order.

"See specifics on Statewide Rule 32 at the following link under §3.32 (Gas Well Gas and Casinghead Gas Shall Be Utilized for Legal Purposes):
http://texreg.sos.state.tx.us/public/readtac$ext.ViewTAC?tac_view=4&ti=16&pt=1&ch=3&rl=Y

"If operators want to pursue an additional 45 days past the initial 45-day flare permit time period, they must provide documentation that progress has been made toward establishing the necessary infrastructure to produce gas rather than flare it. A copy of the Statewide Rule 32 Exception Data Sheet can be found here.

"The most common reason for granting an extension to an initial flaring permit is the operator is waiting for pipeline construction scheduled to be completed by a specified date. Other reasons for granting an extension include operators needing additional time for well cleanup and pending negotiations with landowners.

"The majority of flaring permit requests that the Commission receives are for flaring casinghead gas from oil wells. The Commission does not issue long-term permits for flaring from natural gas wells as natural gas is the main product of a gas well. Both oil and gas wells are allowed under Commission rules to flare during the drilling phase and for up to 10 days after a well's completion for well potential testing. Rare exceptions for long-term flaring may be made in cases where the well or compressor needs repair.

"Total venting and flaring permits approved statewide by the Railroad Commission of Texas:

"To put these numbers in context, as of August 31, 2019 Texas had 264,877 producing oil and gas wells, so venting and flaring involves just a small fraction of the state's oil wells."

Flare Permits Issued in Permian Region, Texas			
FY 2008	107	FY 2014	5,285
FY 2009	158	FY 2015	5,689
FY 2010	306	FY 2016	4,870
FY 2011	651	FY 2017	3,708
FY 2012	1,963	FY 2018	5,488
FY 2013	3,092	FY 2019	6,972

Appendix G: Cost Analysis Model Inputs and Outputs

G.1 Input Parameters:

The model is fully annotated for input factors and input cells are value-protected to allow applicable ranges of requested parameters. Most input parameters are located on the HEAT PUMP worksheet. The input parameters follow the ranges presented in Table G10. Because membrane distillation of produced water is a new technology for the gas and oil industry, and

especially when this process is coupled with the capture of waste heat or low-quality fuel, there are few references for cost evaluations. The reader must accept that costs for certain process components are estimates (place-holder values), often without reference. All these values are variables that a user can enter themselves into the model if they are interested in refining the output. The input values are listed in Table G1 with upper, lower, and baseline ranges. Table G2 is the only new input used in the BOILER model.

G.2 Technical Outputs:

THE DESIGN SPECIFIC TECHNICAL OUTPUTS ARE FOR THE HEAT PUMP ARE SHOWN IN TABLE G3 AND INCLUDE AN ESTIMATE OF THE MEMBRANE FLUX WHICH IS PRORATED FOR OPTIMUM OCCURRING AT A MEMBRANE ΔT OF 70 °F; THE NUMBER OF SQUARE METERS OF MEMBRANE NEEDED, THE THEORETICAL COP AND ACTUAL COP PRORATED BY THE EFFICIENCY OF THE HEAT PUMP, THE POUNDS OF DISTILLED WATER AND BRINE GENERATED PER DAY, AND THE DENSITY AND SALINITY OF THE BRINE. ENERGY OUTPUTS INCLUDE THE LATENT AND SENSIBLE HEAT DEMAND, THE HEAT REQUIRED BY THE HEAT PUMP, THE BTU EXPENDED PER POUND OF PW APPLIED TO THE SYSTEM, AND THE CUBIC FEED OF GAS REQUIRED BASED ON THE INPUT QUALITY OF THE GAS. THE TECHNICAL OUTPUTS FOR THE BOILER OPTION ARE SOMEWHAT DIFFERENT. THESE DIFFERENCES ARE PRESENTED IN TABLE G4.

G.3 Cost Output Parameters:

The capital cost for the membrane is based on the surface area (Line 31 Table G3) times the membrane costs (Line 22 Table G1). Heat transfer coils and Heat pump capital are based on the delivered BTU (Line 38 Table G3) and the input costs (Lines 24 and 25 Table G1). The physical structure, truck station, water reservoirs and pumps pipes and controls are estimated based on the volume of produced water treated (Line 1 Table G1 times the input costs (Lines 26,27, 28, and 23 Table G1). A miscellaneous capital cost adder (Line 49 Table G3) is applied to the total of the other capital costs (sum of Lines 42 through 49) by the cost factor in the input (Line 29). The amortized cost for the total capital is presented in (Line 57 Table G1) and is calculated as the total capital times the discount factor (Line 16 Table G1, as calculated from the project life (Line 15 and interest rate Line 14 Table G1). This is presented as a daily cost (Line 57 Table G4) by division by 365 days per year.

The operating costs are the natural gas calculated from the cubic feet per barrel (Line 41 Table G3) and the cost of gas (Line 11 Table G1). The operating cost for the operator is based on the operator rate (Line 21) times the operator attention time (Line 19 Table G1). The operator rate is based on the fully loaded (salary, fringes, vacation) which is derived from Line 17 and Line 18 (Table G1). There is additional "opportunity cost" assessed Line 52 Table G3 which arises from the downtime Line 8 Table G1.

Capital and operating costs for the boiler option follow the protocol as established for the heat pump option with attention to the different input parameters identified in Table G5.

Table G 1: Inputs and Ranges for Heat Pump Cost Model

	Volume of Produced Water (100 to 1500)	100	1000	1500	BBL/Day

Salt content of Produced Water (Range 0.1 to 10))	0.1	8	10	% weight
Expected Forward Flow (Percent Distillate to PW)	30	50	65	% volume
Temperature of Produced Water from Source	33	70	100	°F
Temperature of Hot Side Reservoir (to membrane)	130	150	170	°F
Cool Side Reservoir (to membrane)	70	75	80	°F
Base Efficiency of Membrane (Range 1-16)	1	2	14	liter/m^2hour
Maintenance Downtime (hours per day)	0	3	6	hours per day
Quality of the Natural Gas used in the Heat Pump	700	750	1000	BTU/cuft
Cost of the Natural Gas Supplied ($/million BTU)	0	4	5	$/million BTU
Efficiency of the heat pump	45	52	65	%
Efficiency of the Transfer Coils	75	90	90	%
Interest Rate (% yearly) format enter (2 for 2%)	0	5	10	i = %
Loan Term (years) Useful Equipment Life	5	10	15	Years (n)
Capital Recovery (Annuity/Present Worth, (%,n))		0.13		Discount Factor
Fully Loaded Operator Costs per Annum	$45,000	$95,000	$100,000	$/year
Hourly Labor Basis (Work Hours per Annum)	2020	2020	2020	hours per year

Attention to Membrane Distillation (Hours/Day)	0	4	8	hours per day
Membrane Replacement (percent per year)	5	10	15	%/yr
Fully Loaded Operator Cost per hour		$47		$/hour
Membrane Cost	$80	$120	$140	$/m^2
Pumps, Pipes, Controls	100	$150	200	$/BBL-day
Heat Pump	$150,000	$175,000	$250,000	$/mmBTU del.
Transfer Coils	$30,000	$60,000	$90,000	$/mmBTU del.
Physical Structure (Building)	$150	$250	$300	$/BBL-day
Physical Structure (Truck Station)		$0		$/BBL-day
Reservoirs (cool and warm)	$150	$200	$300	$/BBL-day
Miscellaneous Capital Costs	0	10	25	% of Total

Table G 2: Technical Outputs for the Heat Pump Option		
Estimated Membrane Efficiency based on ΔT	2.0	liter/m²hour
Size of Membrane Distillation Unit (meter sq)	1832	m²
Theoretical COP of the Heat Pump	7.6	
Actual COP based on Efficiency Rating	4.2	
Pounds of Distilled Water per day	169,200	
Pounds of Brine Produced per day	201,336	
Specific Gravity of the Brine Produced	1.12	
Concentration of the Brine Produced (% salt)	16.00	% weight
BTU/hr required for latent and sensible heat	10,082,000	BTU/hr
BTU/hr required for Heat Pump and Transfer	2,671,000	BTU/hr
BTU/BBL PW treated	64,100	BTU/BBL
CF gas/BBL PW Treated	90	CF/BBL

Table G 4: Special Outputs for the Boiler Option		
OUTPUT DETAILS ON THE ENERGY REQUIREMENTS		
BTU/hr required for latent and sensible heat	10,082,000	BTU/hr
BTU/hr required for Boiler and Transfer	14,936,296	BTU/hr
BTU/BBL PW treated	358,500	BTU/BBL
CF/BBL	478	CF/BBL

Table G 5: Economic Evaluation of the Heat Pump Option		
Capital Cost for Membrane Stack	$219,840	Present Worth
Capital Cost for Pumps and Piping, Controls	$150,000	Present Worth
Physical Structure (Building)	$250,000	Present Worth
Truck Station	$0	Present Worth
Capital for Heat Pump	$1,764,350	Present Worth

Capital for Heat Transfer Coil (warm and cool)	$604,920	Present Worth
Capital for Hot and Cool Reservoir	$400,000	Present Worth
Miscellaneous Capital Costs	$338,911	Present Worth
TOTAL Capital	$3,728,021	Present Worth

Natural Gas at Rated BTU value	$192	per day
Downtime (Unused Capital)	$165	per day
Operator Pay	$141	per day
Membrane Replacement	$60	per day
Miscellaneous at 10%	$56	per day
TOTAL Operating Cost	$615	per day

Amortized Capital on a Daily Basis	$1,323	per day
Operating Cost on a Daily Basis	$615	per day
Total Costs on a Daily Basis	$1,938	per day

Amortized Capital per BBL (treated)Basis	$1.3	per BBL
Operating Cost on a per BBL Basis	$0.6	per BBL
Total Costs on a per BBL Basis	$1.9	per BBL

Appendix G: Microbiological Analysis of Hydraulic Fracture Test Site (HFTS) Operations

Research Entity: GTI Energy

Final Report Microbial Analysis, November 21, 2017

Prepared by Sarah Eisenlord and Tom Hayes

Research by Sarah Eisenlord, Karen Crippen, Alan Janos, Russ Bora, Yuliana Drobit, Brian Landreth, Amanda Harmon, Scott Leleika

Legal Notice

This information was prepared by Gas Technology Institute (“GTI”) for NETL-DOE.

Neither GTI, the members of GTI, the Sponsor(s), nor any person acting on behalf of any of them:

a. Makes any warranty or representation, express or implied with respect to the accuracy, completeness, or usefulness of the information contained in this report, or that the use of any information, apparatus, method, or process disclosed in this report may not infringe privately-owned rights. Inasmuch as this project is experimental in nature, the technical information, results, or conclusions cannot be predicted. Conclusions and analysis of results by GTI represent GTI's opinion based on inferences from measurements and empirical relationships, which inferences and assumptions are not infallible, and with respect to which competent specialists may differ.

b. Assumes any liability with respect to the use of, or for any and all damages resulting from the use of, any information, apparatus, method, or process disclosed in this report; any other use of, or reliance on, this report by any third party is at the third party's sole risk.

c. The results within this report relate only to the items tested.

Acknowledgment: "This material is based upon work supported by the Department of Energy under Award Number DE-FE0024292."

Disclaimer: "This report was prepared as an account of work sponsored by an agency of the United States Government. Neither the United States Government nor any agency thereof, nor any of their employees, makes any warranty, express or implied, or assumes any legal liability or responsibility for the accuracy, completeness, or usefulness of any information, apparatus, product, or process disclosed, or represents that its use would not infringe privately owned rights. Reference herein to any specific commercial product, process, or service by trade name, trademark, manufacturer, or otherwise does not necessarily constitute or imply its endorsement, recommendation, or favoring by the United States Government or any agency thereof. The views and opinions of authors expressed herein do not necessarily state or reflect those of the United States Government or any agency thereof."

Executive Summary

The Hydraulic Fracture Test Site (HFTS) experiment, co-funded by the oil and gas industry and NETL-DOE, tested advanced fracturing and completions technologies and techniques to better understand fracture geometry and optimize well spacing, ultimately limiting the environmental impact of future shale hydrocarbon development. As a part of this research program water sourced for hydraulic fracturing and produced water from three of the eleven test wells were studied for chemical and microbiological attributes, as there is widespread evidence for microbial growth and activity in shale petroleum reservoirs across the United States. Microbiological mechanisms of interest include microbially influenced corrosion of well infrastructure, biomass accumulation leading to bio-plugging and biodegradation of crude oil, to name a few. As the practice of supplementing fresh water with recycled produced water for hydraulic fracturing increases, so does the likelihood of unwanted microbiological activity in the subsurface. A deeper

understanding on the chemistry and biology will lead to improved bio-control efforts while increasing water re-use potential.

Major findings of this effort determined water injected into each well contained high concentrations of bacteria, some of which survived the subsurface temperature, lack of oxygen, and high salinity. Incomplete treatment of recycled produced water used in injection combined with a relatively long residence time of injection water held in before production lead to the establishment of populations capable of biofilm formation and microbially influenced corrosion. Notably, there were substantial and persistent populations of sulfate reducing bacteria and methanogens as detected with qPCR and metagenomic sequencing. Due to the hardness of the water in the stimulated reservoir volume (SRV) and the composition of microorganisms present, biocide dosing one year after production with 55 gallons of B-1203 in each well was insufficient to substantially reduce the concentration of bacteria or sulfate reducing bacteria within the SRV. Furthermore, due to the high naturally occurring levels of sulfate in injection water, we calculate up to 1.4 tons of sulfide was produced though microbiological transformations. Besides being highly corrosive, the sulfide is thought to have reacted with soluble iron, resulting in iron sulfides that would drop out of solution and potentially build up within the fracture network.

Introduction

Hydrocarbons derived from shale deposits in the United States are poised to become instrumental in our energy independence and a clean energy future. These resources are projected to constitute over 38% of the national hydrocarbon energy portfolio by 2040. The Permian Basin is the largest petroleum-producing basin in the United States and has produced a cumulative 28.9 billion barrels of oil and 75 trillion cu ft. of gas. Currently, nearly 2 million barrels of oil a day are being produced from the basin. Constant innovations in horizontal drilling and hydraulic fracturing technologies are increasing shale hydrocarbon production efficiency and minimizing environmental impact.

Economic recovery of these resources is dependent on the pressurized injection of large volumes of chemically treated water to hydraulically fracture the shale and alter its permeability through the generation of extensive fracture networks. As horizontal wells become longer and fracture treatments more complex, water use, and management needs will increase. The practice of produced water recycling and re-use substantially decreases the industry's reliance on fresh water sources yet may introduce new and unforeseen risks to infrastructure integrity and formation productivity. Biogeochemical processes carried out by microorganisms in the deep subsurface has been of much interest to microbiologists and geochemists since shale hydrocarbon extraction began to expand in the United States (Magot 2000); (Roling 2003); (Voordouw 2009); (Mohan 2013); (Strutchtemeryer 2012); (Daly 2016); (Lipus 2017).

There is widespread evidence of microbial growth with complex metabolic abilities in shale petroleum reservoirs across the United States (Magot 2000); (Galperin 2011); (Gaspar J. 2014); (Daly 2016). Potential microbial mechanisms include (1) increased methane production from microbially produced hydrogen and carbon dioxide, (2) biodegradation of crude oil, (3) biomass accumulation leading to bio-plugging of fractures or surface equipment, (4) iron sulfide deposition decreasing permeability, (5) corrosion of steel well infrastructure, and (6) production of sour gas. Despite the potential impacts, little is known about the function, activity, and

controls of microorganisms in hydraulically fractured shale. Key questions remain regarding the introduction and proliferation of microorganisms in the subsurface, mechanisms for mitigating deleterious impact, and how production operations influence the subsurface environment regarding microbial activity.

The research presented in this report is aimed to illuminate some of these questions by examining microbial population dynamics in injection fluids, drill-out mud, produced water (over one year of production) and treated, recycled produced water all at the Hydraulic Fracture Test Site (HFTS) in the Permian Basin, TX. The HFTS experiment was designed to test new extraction and production techniques and technologies aimed at increasing the efficiency of shale hydrocarbon production. Eleven test wells were drilled in the Wolfcamp Formation, hydraulically fractured, and produced. This study examines the microbiological populations in three of the eleven wells.

Objective

The overall purpose of the effort to characterize waters associated with the hydraulic fracturing and production at the HFTS facility was to obtain information of value for long-term produced water management (including reuse) and to gain some insight into possible bio-transformations that may have implications for future impacts such as corrosion. The scope of this effort included chemical and microbiological analysis of samples from water impoundments that provided the freshwater and recycled produced water for hydraulic fracturing operations, injection water once mixed with fracture treatment chemicals, fluids used for drilling out frac plugs, and a time series of samples to characterize the produced water from three selected shale wells.

HFTS Site & Operations Description

Situated about 55 miles southeast of Midland, TX, the hydraulic fracturing test site, comprising of oil and gas assets owned and operated by Laredo Petroleum, is in the Northeast quadrant of Reagan County near the northern boundary of the county as shown in Figure 1. Rural in nature with a small population of 3,367 (according to the Year 2010 Census), the county and the immediate area containing the facility is sparsely populated containing less than three people per square mile. The Edward-Trinity Plateau Aquifer provides fresh water for this region.

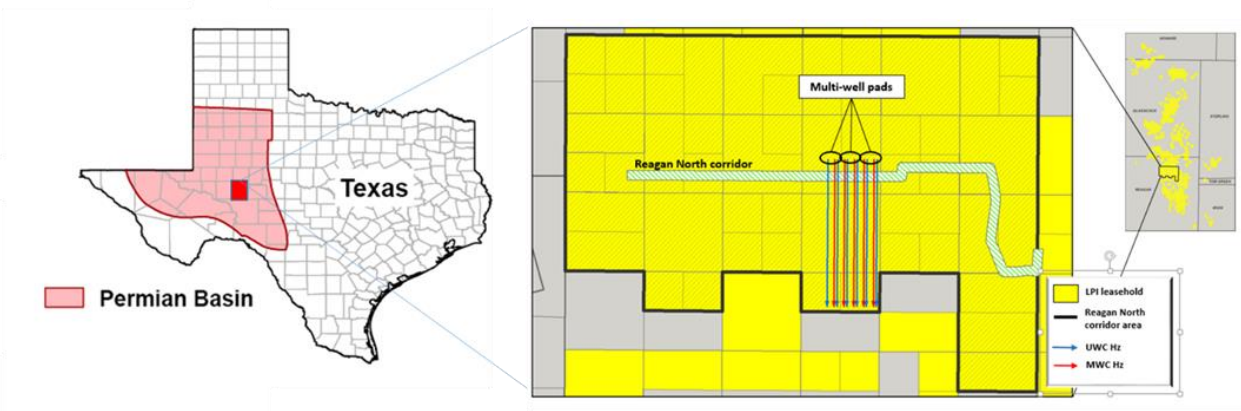


Figure 1: Location of the Hydraulic Fracture Test Site

The HFTS itself is comprised of three well pads from which eleven horizontal wells were drilled during the HFTS project. A layout of the well pad system is shown in Figure 2. In this array, six

horizontal wells were drilled into the Upper Wolfcamp Horizontal oil play (UW Hz, in blue) and five horizontal wells were drilled into the Middle Wolfcamp Horizontal oil play (MW Hz, in red) as depicted in the figure. Three wells were chosen for this research, two of the test wells (4SU and 7SU) were in the Upper Wolfcamp, one well (6SM) was located in the Middle Wolfcamp. Also shown in this diagram are the five groundwater wells used to obtain the freshwater required for hydraulic fracturing and the water impoundment positioned in proximity to the well pad facility containing fresh and recycled treated produced water (Poseidon Tank).

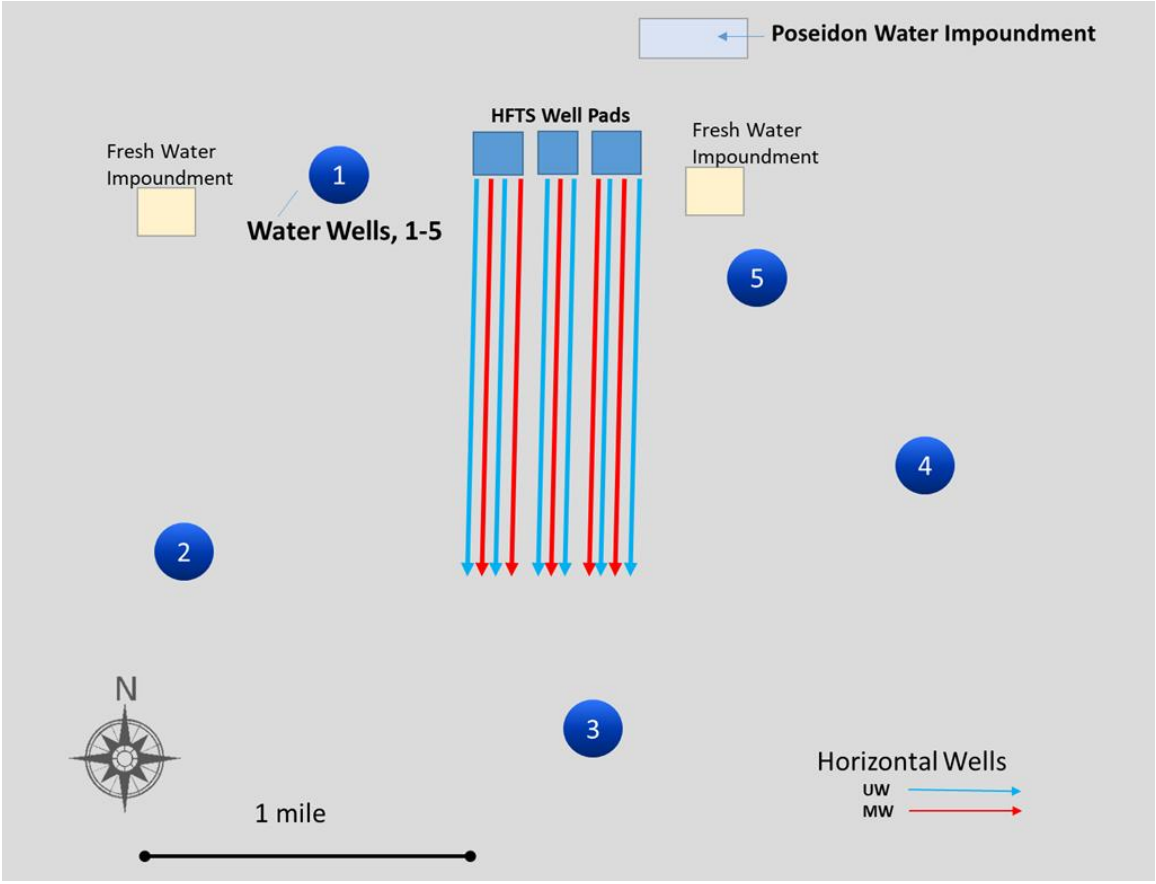


Figure 2: Layout of the Hydraulic Fracture Test Site and Water Wells

Procedures that involved handling of water supporting the main activities of HFTS and are of interest for microbiological characterization included the following:

• During hydraulic fracturing, freshwater and recycled produced water from the storage impoundments was sent to a blending stage where influent water is mixed (80% fresh with 20% recycled water), and where chemicals and sand are added. This water blend is subsequently pumped downhole under high pressure in 35 fracture stages per well. The fracturing process took place over 12-14 days depending on the complexity of the fracture design and number of fracture stages.

• After stimulation, the wells were shut in for up to six weeks while topside operations continued.

• Fracture stages were isolated using frac plugs, before production these plugs were drilled out using trucked in water-based drilling fluid.

• When each completed well was put on production, produced water was separated from oil and gas in water drop-out separators before stored on site in frac tanks.

• Large volumes of produced water were collected, treated, and stored on site in double lined impoundment ponds for use in subsequent stimulation operations.

Methods and Approach

Sampling

This sampling campaign collected water for microbiological and chemical analyses from five types of water:

• Poseidon Tank Impoundment Water (Poseidon): treated, recycled, produced water was sampled weekly for five weeks from this on-site, open top, impoundment.

• Fresh Water Impoundment (FW): Groundwater pumped from the Edward-Trinity Plateau Aquifer and stored on site in freshwater impoundments.

• Frac Water (FW): An 80% / 20% fresh water to recycled water mix was sampled after fracture chemicals were added, before silica proppant and pressurization. Water pumped into each of the three wells was sampled three times: first day of fracturing, sixth day of fracturing, and final day of fracturing. This typically occurred over 12-14 days.

• Drill-out Water (DW): A water-based fluid was introduced to each well to drill out fracture plugs which isolated each fracture stage. This was sampled once for each well.

• Produced Water (PW): Water produced from each of the three wells was collected over a time series at days: 0, 1, 5, 14, 36, 90, 210, 365, and 550. Water was collected from the water dropout at each well.

All water samples were collected by EnviroClean Cardinal (Tulsa, OK). The following Table 1 details the preservation and analytical methods for all analytical categories. After collection, samples were kept cold at 4°C until overnight shipment on ice to GTI within 4 days of collection. Water samples for metals, TOC, BTEX, anions, and general chemistry analyses were placed in a 4°C refrigerator until analysis. For microbiological analysis, 2.5 liters of water was vacuum filtered through 0.2um PES filters upon arrival and filters were immediately frozen at -80°C until DNA extraction. The full suite of analytics was performed on all PW samples. IW, FW, and Poseidon received microbiology, general chemistry, TOC, nitrate, sulfate, and chloride analysis. Statistical analyses were performed in PRIMER-E, MATLAB, R, and Excel.

Table 1: Methods and instrumentation for HFTS water analysis

Parameter	Sample Preservation	Standard Method	Instrumentation	Comments
Microbiology				
DNA Analysis	Ice	NACE Standards TM0106-2006 and TM0212-2012	Qiagen qPCR Thermocycler, Illumina HiSeq Sequencer	Standard for qPCR and Sequencing
General Chemistry				
pH	Ice	EPA 9040	Electrometric Equipment	Suitable for water analysis
Total Dissolved Solids	Ice	SM18 2540 C	Gravimetric Apparatus	Standard USEPA Method
Specific Conductance	Ice	EPA 120.1	Self-Contained Conductivity Meter	Standard USEPA Method
Alkalinity	Ice	SM18	Titration Equipment	

		2320 B		21st Ed. Standard Methods (2015)
Organic Compounds				
Total Organic Carbon	Sulfuric Acid	EPA 415.1	Combustion and Infrared Detection	Provides the concentration of total organics as Carbon.
Total Petroleum Hydrocarbons	Ice	EPA 1664B	Gravimetric Apparatus	Involves Hexane Extraction
Volatile Organic Compounds	Hydrochloric Acid	EPA 8260B or 8021B	Gas Chromatography with Mass Spectroscopy or Photoionization and Flame Ionization Detection	Benzene, Toluene, Ethylbenzene, Xylenes
Inorganic Species				
Cations	Ice	EPA 6010B, 6020, or 200.7	Inductively Coupled Plasma Emission Spectroscopy	As, Ba, Bo, Cd, Ca, Cr, Cu, Fe, Pb, Mg, Mn, Ni, K, Na, Zn
Anions	Ice	EPA 300.0	Ion Chromatography	Chloride, Fluoride, Sulfate, Nitrate
		EPA 9030B (modified)	Distillation / Ion Chromatography	Total Sulfide

Microbiological Analysis

Microbial DNA was extracted from the frozen filters with an optimized protocol using the MP Biomedicals FastDNA Spin Kit for Soil DNA Extraction Kit. Extracted DNA was quantified with the Qbit (ThermoFisher), and aliquoted for archive, qPCR analysis, and metagenomic analyses.

DNA sequencing and bioinformatics was carried out by the Wrighton lab at Ohio State University and is described below. 16S DNA was sequenced using Illumina MiSeq with 2 x 301 base pair paired end reads following established HMP protocols (Caporaso et al., 2011). Briefly, primers 515F and 806R targeting bacterial and archaeal 16S rRNA were used for PCR amplification of the V4 hypervariable region with 35 cycles and 10 µl of template DNA. Data processing was performed using QIIME 1.9.0, with specific processing steps as follows (Solden et al., 2017; Caporaso et al., 2010). Raw fastq data were demultiplexed and quality filtered to a Phred score of 20. Organized taxonomic units (OTUs) were chosen in a two-step process. First, sequences were clustered into OTUs at 97% using UCLUST followed by de novo OTU picking. OTUs were checked for chimeras using RDP gold database and assigned taxonomy using the 97_SILVA_111 rep set (Quast et al., 2013). Sequence abundance was used for calculation of the relative abundance of OTUs detected in at least 2 samples.

Quantitative PCR was conducted on 1:10 dilutions of extracted DNA according to the NACE TM0106-2006 and TM0212-2012 standards.

Chemistry Results

Injection Water

10 million gallons of water was injected into each well during hydraulic fracturing. Hydraulic fracturing for each 10,000 ft lateral occurred over a time span of 10-14 days. Frac Water (FW) was sampled at the first, sixth, and last day of hydraulic fracturing. There was on average 35 fracture stages/well. Frac fluids were composed of 80% fresh water from onsite open top impoundments

of groundwater and 20% recycled produced water, cleaned through a series of settling tanks and stored on-site in the open top Poseidon tank. FW water samples were obtained after chemical additions and before the addition of proppant. Fluids used during the drilling out of fracture plugs was sampled once for each well.

Concentrations of select chemical compounds in the FW are shown in Figure 3. Fluids pumped into the three wells varied slightly in sulfate, TDS, conductivity, and chloride concentrations, though not statistically (P=0.52, PERMANOVA). The drill out water (DW) chemistry was similar for all three wells as well (P=0.58), furthermore FW and DW samples were not found to be statistically distinct (P=0.73) and therefore will be considered together as frac water (FW) in this report.

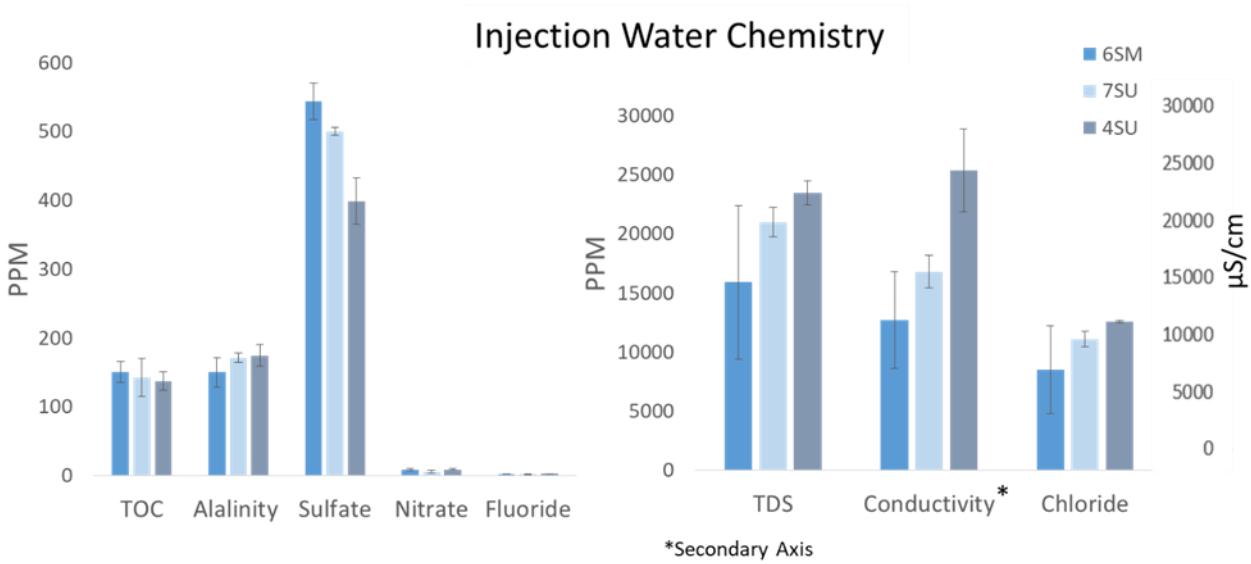


Figure 3. Average concentration of chemicals of interest in Frac Water for three HFTS wells.

Chemical makeup of the source waters (FW and Poseidon) and injected water are discussed thoroughly in the HFTS Environmental Monitoring Report (Hayes & Eisenlord, 2017). Characteristics of the source waters and injected waters are presented in Table 2 below.

Produced Water

After hydraulic fracturing, water was held in the formation for 4-6 weeks before the wells were put on production. The chemical composition of PW was significantly different than the water introduced to the wells based on the multivariate statistical analysis of pH, TOC, TDS, conductivity, alkalinity, chloride, nitrate, and sulfate (P=0.001). This difference is expected due to the long residence time of the injected water for interaction with the shale formation and dilution with extant formation water. The hierarchical clustering of PW, IW, Poseidon, and fresh water (FW) samples based on the similarity of 8 chemical variables is seen in the Cluster Diagram in Figure 4. All water samples cluster by type of sample; IW and FW have distinct chemistry from one another (P=0.001), and from PW (P=0.001) according to PERMANOVA analysis. The recycled treated Poseidon tank water grouped within PW samples. PW samples often, but do not always cluster by day.

Table 2: Characteristics of Freshwater Impoundments, Recycled Produced Water in the Poseidon Impoundment, and Injection Fluids Used for Fracturing at HFTS

Parameter	Freshwater Impoundment		Poseidon Impoundment		Injection Fluids	
	Range	Median	Range	Median	Range	Median
pH	8.03-8.30	8.17	6.64-7.03	6.81	6.28-7.08	6.66
TDS, mg/L	1,790-3,800	2,580	75,400-104,000	98,500	3,370-25,300	21,700
Conductivity, µS/cm	1,460-5,270	3,790	13,000-69,100	47,850	4,960-29,500	18,200
Alkalinity, mg/L as $CaCO_3$	143-183	177	236-383	344	114-190	178
Chloride, mg/L	149-1,380	793	730-1,380	1,220	1,310-13,800	12,200
Nitrate, mg/L	6.7-15.1	13	<1	<1	2-11	8
Sulfate, mg/L	340-650	494	185-310	230	342-570	490

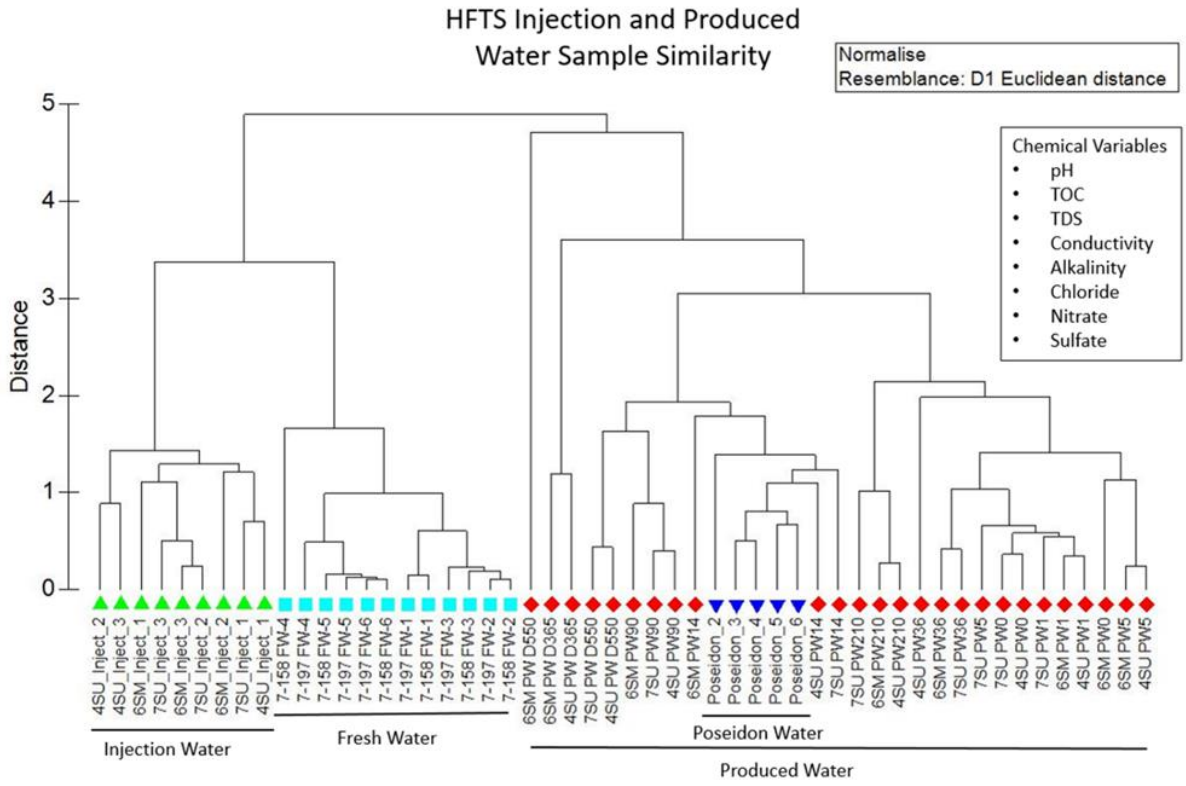


Figure 4: Cluster Diagram of Injection, Fresh, Poseidon and Produced Water Chemistry during HFTS.

Produced water chemistry changed substantially over one and a half years of production. All PW chemistry results can be seen in Appendix A and are discussed thoroughly in the Environmental Monitoring Report. The major changes occurred in alkalinity, conductivity, sulfate, nitrate, chloride and TOC (Figures 5 and 6). Alkalinity, a measurement of a solution's ability to neutralize acid and reported in units of $CaCO_3$, ranged from 300 mg/L to 700 mg/L during the first 36 days of production, after 36 days the alkalinity averaged 500 mg/L with little variation. Conductivity measurements doubled from 40,000 µs/cm to 80,000 µs/cm between 36 and 90 days, and slowly declined to 60,000 µs/cm by the end of the first year. The change in conductivity indicates a change of dissolved inorganic solids or organic hydrocarbon content in the early days of production. Also, within the first 36 days, chloride concentrations increased from 50,000 mg/L to

65,000 mg/L and TDS concentrations increased from 90,000 mg/L to 105,000 mg/L. Concentrations stabilized over the next 6 to 9 months.

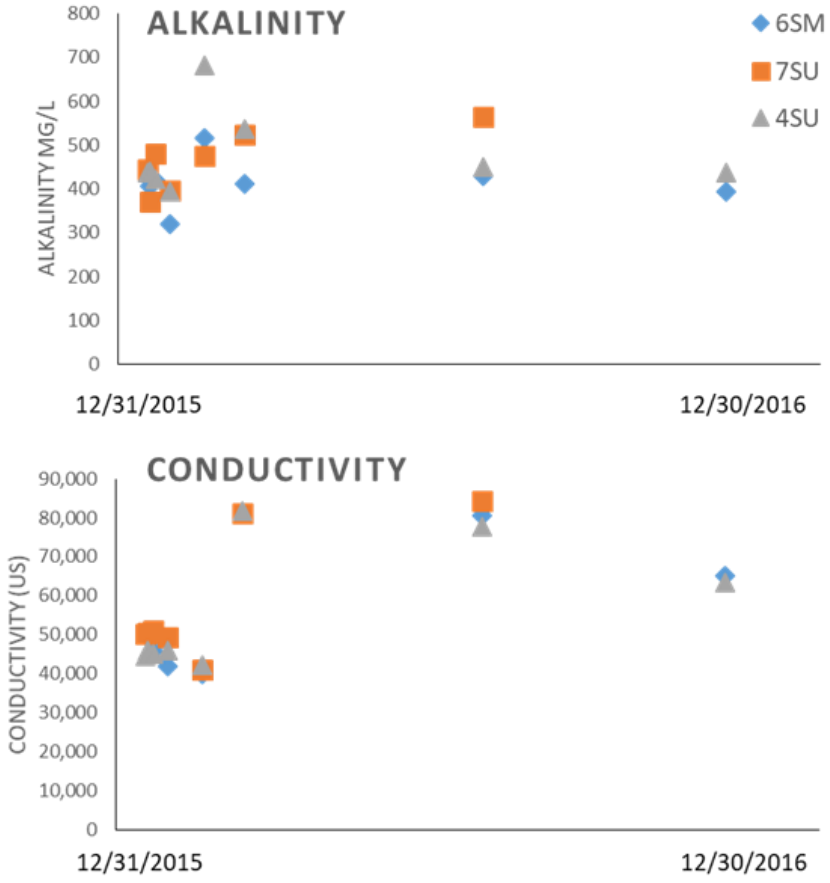


Figure 5: Alkalinity and Conductivity measurements of the HFTS wells over one year

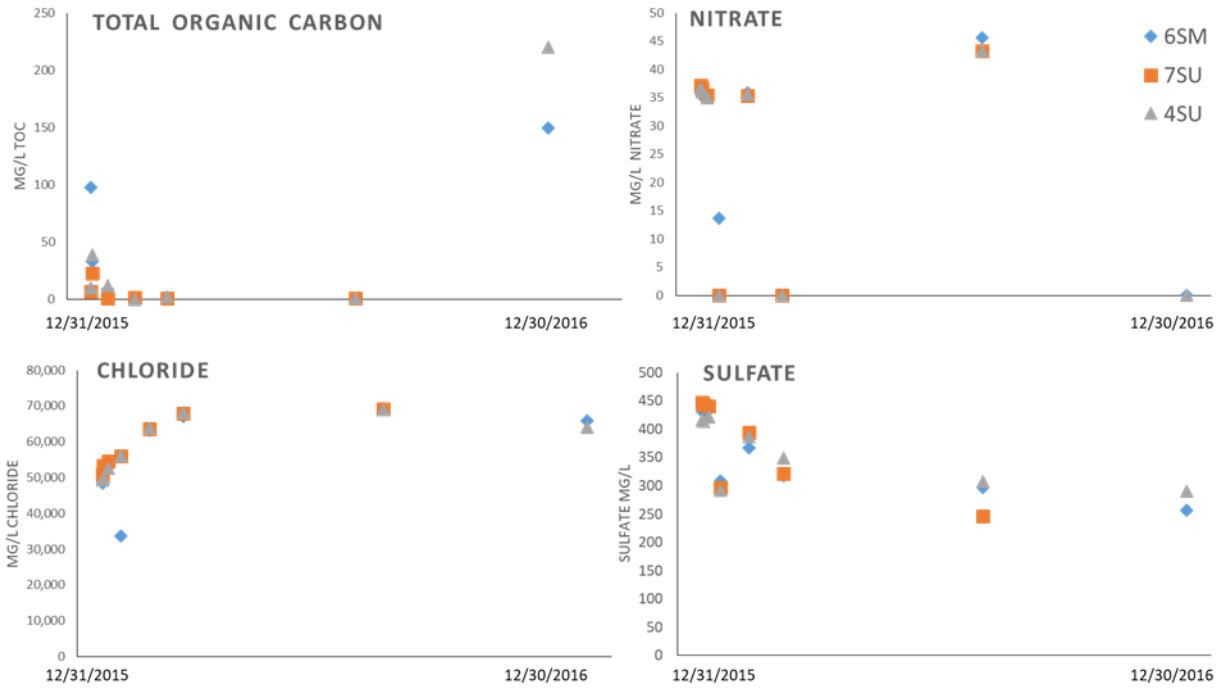


Figure 6: TOC, Nitrate, Chloride and Sulfate measurements of the HFTS wells over one year.

Sulfate concentrations of produced water decreased from 420 mg/L to 350 mg/L within the first 14 days of production and continued to decline over the next several months to 260 mg/L. TOC

effectively disappears after 14 days of production, only to increase at one year into production when biocides were introduced to the wells. Also relevant to microbial function is nitrate concentration, which initially declines during the first 14 days, and then hovers around 30 PPM for the extent of the study. All data is presented in Appendix A and thoroughly discussed in the HFTS Environmental Monitoring Report (Hayes & Eisenlord, 2017).

When analyzed across all PW samples, measured chemical variables grouped into four main categories, except for Zinc, during a Hierarchical Clustering for Variables conducted in MATLAB, see Figure 7. All Anions clustered together with chloride and TDS, indicating that changes in TDS and chloride occurred in tandem. Nitrate, sulfate, and TOC clustered together, as did BTEX and total petroleum hydrocarbon measurements. This preliminary analysis highlights the future ability to analyze fewer variables in produced water and gain predictive ability for other, more difficult, or expensive to measure yet operationally important compounds.

Based on this grouping of chemical variables, patterns in PW chemistry were evaluated on the full suite of 29 chemical analyses and the select suite of 8 variables measured to assess all water samples. The nMDS of these analyses is seen in Figure 8. Both data sets, full and partial, group PW significantly in to early (<36 days), late (>36 days), and post biocide (D365) categories (P=0.001). According to both models, concentrations of nitrate and TOC contribute the most to the distinction between groups (30% and 23% respectively).

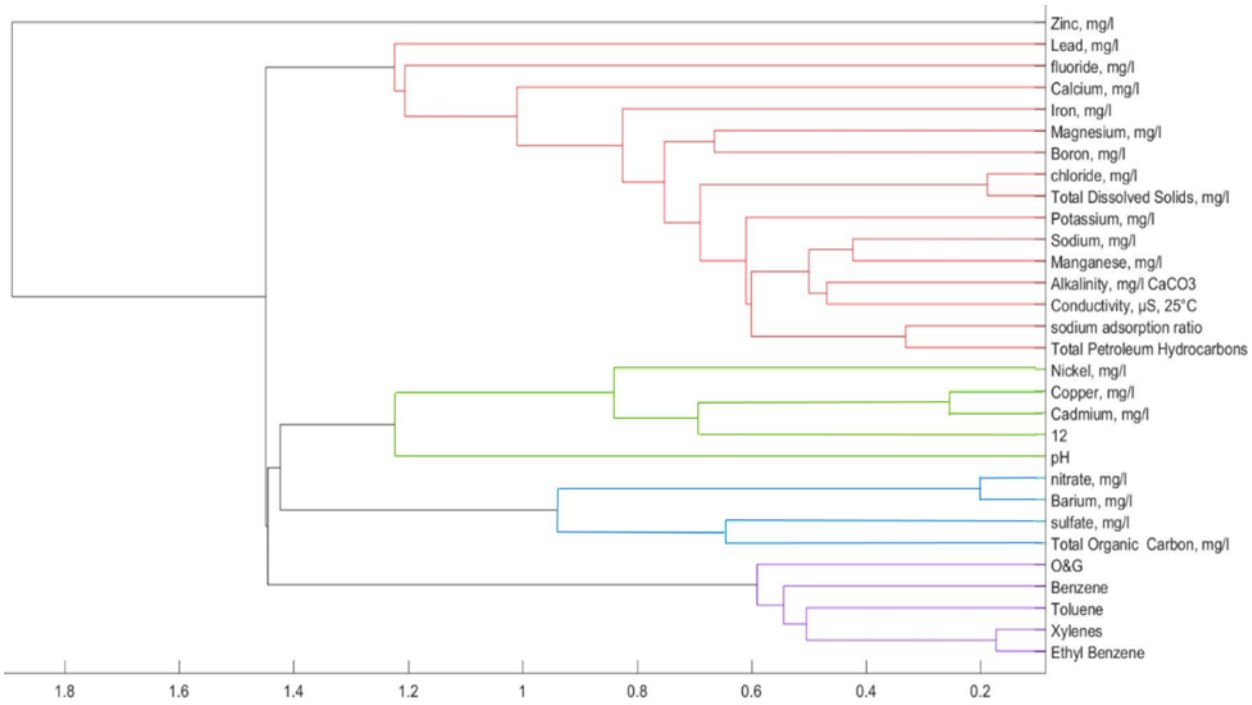


Figure 7: Hierarchical Clustering for Chemistry Variables in HFTS Produced Water.

The RELATE statistic identifies how similar these two multivariate data sets are by reporting a Rho value between 0 and 1; not related to completely identical. The Rho statistic for these two data sets is 0.38, with a P-value of 0.002, indicating these data sets are significantly similar. This provides further evidence that a select set of variables can be used to evaluate large changes in produced water chemistry, the added information from the full set of variables does not elucidate significantly more meaning from the produced water sample set.

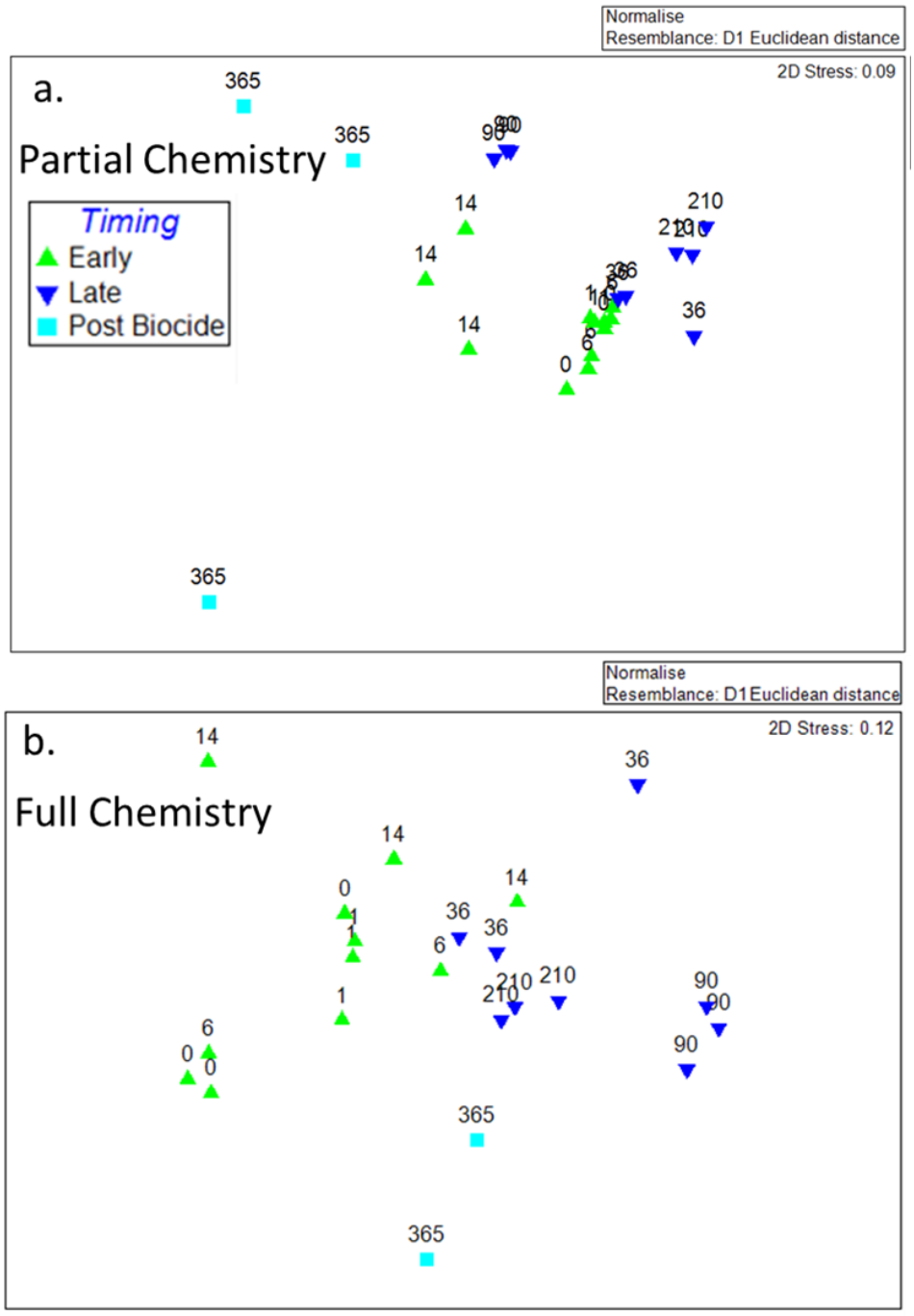


Figure 8: nMDS of PW samples based on chemical variables (a) partial suite of 8 variables (b) full suite of 29 variables.

Microbiological Results

16S sequencing and quantitative PCR of microbial DNA extracted from recycled produced water (Poseidon tank), IW (fracturing fluids and drill out muds) and PW over one year has yielded insight to how microorganisms and chemistry introduced to these three wells has influenced the microbial populations established in the subsurface, on casings, tubing, and on the formation itself. With this information we can hypothesize microbial mechanisms of biocorrosion and biofouling, and postulate ways to prevent such activity in the future.

Total Bacteria (BA) was quantified in water samples using qPCR of the 16S rRNA gene common to all living organisms (Figure 9). Levels in the FW samples were around 1x104 gene copies per mL, Poseidon samples had considerably higher concentrations of bacteria, up to 1x108 16S copies per mL; the total copy number of 16S genes can be considered analogous to the total

number of bacterial cells per mL. The differences in BA concentration are expected as Poseidon water is recycled produced water that is stored in open top pits without anti-microbial treatment. Drillout water (DW) contained similarly high concentrations of bacteria, the biocide treatment of these fluids is unknown so we cannot know what percentage of these organisms were living and active when introduced to the wells.

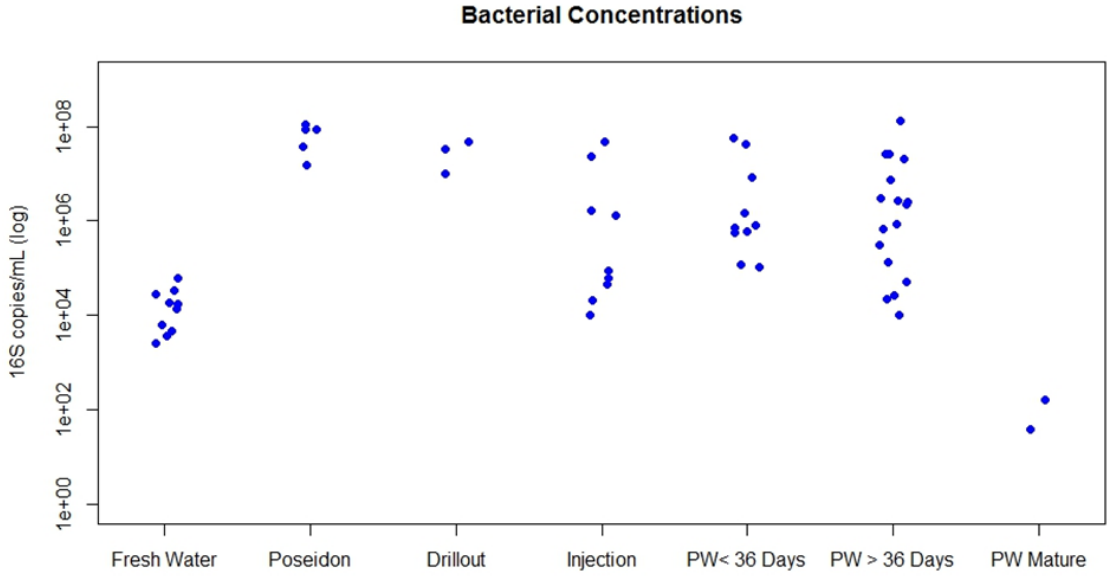


Figure 9: Concentration of Bacterial 16S Genes in HFTS Injection, Impounded, and Produced Water.

IW, a combination of FW and Poseidon, varied in BA concentration over the timeline of fracturing. For each well, DNA was successfully extracted from at least two of the three IW samples; chemical additives used for fracturing often act as inhibitors to DNA extraction and amplification. With the data collected, we observed water-containing microorganisms ranging in concentration from 6x104 to 5x107 cells per mL was injected during the fracturing of each well, and then held in the well for up to six weeks before production. Bacterial concentrations in PW samples (Early samples < 36 days, and Late samples > 36 days) ranged in concentrations between wells and over time from 1x104 to 1x108 cells per mL produced water. After 550 days of production, the HFTS wells still contained BA populations around 3x106 cells per mL. For comparison, we tested produced water from 2 adjacent producing wells on Laredo property which had been on-line for over 3 years, these wells contained less than 5x102 cells per mL.

It is commonly thought that temperatures and salinity in the reservoir would limit microbial survival and proliferation, as indicated by low microbial counts in the mature producing wells. Bottom hole temperature gauges in the HFTS wells measured reservoir temperature to be around 65°C, while lethal to the majority of surface organisms, this level of temperature selects for specific thermo- and hyperthermophilic organisms adapted to thrive in hot environments. These organisms are commonly known as extremophiles, organisms which grow optimally in extreme environments such as deep-sea hydrothermal vents, Yellowstone hot springs, and the deep sub-surface. Indeed, our sequencing results indicate the dominant organisms found in PW samples have the evolutionary capability of surviving up to 80°C. We discuss the sequencing results for each type of water used at HFTS in the next several sections of this report.

Metagenomic Sequencing Results

A total of 1,684 unique operational taxonomic units (OTUs) were identified in IW, Poseidon, and PW samples. Each unique OTU is the grouping of microbial DNA sequences of greater than 97% similarity, each OTU can be considered as a unique species of bacteria. These 1,684 OTUs belong to 91 phylogenetic families in the Bacteria and Archaea Domains. Out of these, 24 types of microorganism (grouped by phylum, family, or genus) were identified as dominant across all sample types. The relative abundance of these 24 phylotypes in each sample is presented in Appendix B.

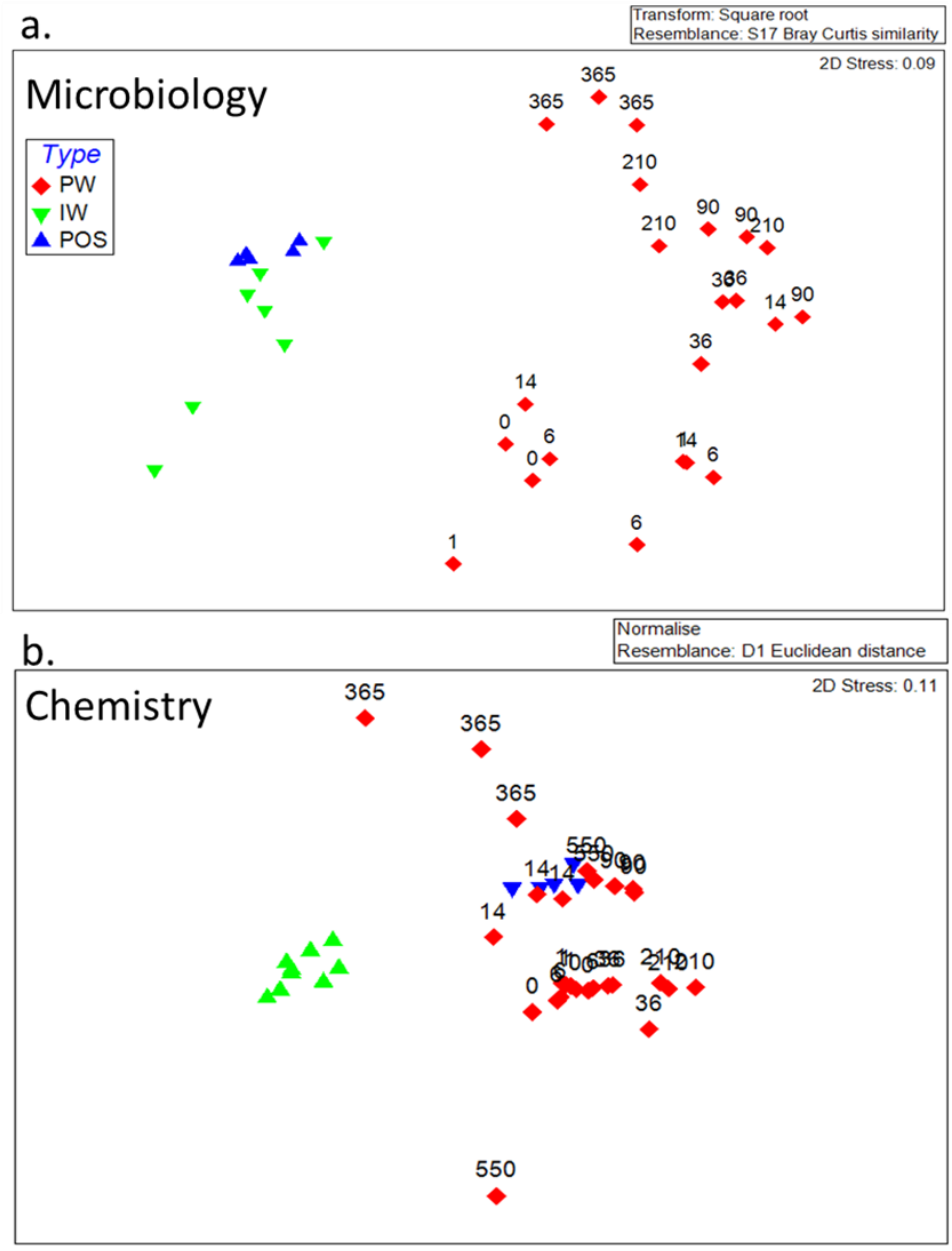


Figure 10: nMDS of all water samples based on (a) microbiology (b) chemical variables.

A graphical representation in non-metric, multidimensional space (nMDS) of the multivariate statistical analysis of the relative abundance of these phylotypes across all samples is seen in Figure 10a. compared to the results of the same analyses conducted on the selected 8 chemical variables for all water samples (Figure 10b). Samples group by water type whether analyzed by chemical or microbiological attributes. Produced water chemistry and microbiology is different from that in injection fluids (P=0.001, PERMANOVA). Interestingly, the microbiology of the

Poseidon samples is more like that of PW samples, however, chemically these Poseidon samples are more similar to IW. This is likely due to the exposure of Poseidon water to oxygen and ambient temperatures, selecting for a substantially different microbial community from the anaerobic produced water, even though the two types of samples have similar chemical variables.

The SIMPR analysis determines which variables, or phylotypes, contribute most to the differences between the types of water samples, these results are presented in Table 3. TOC, sulfate, alkalinity, and nitrate are the primary chemical variables contributing to the difference between sample types. The relative abundance of Pseudomonas, Roseovarius, Methanothermococcus and Arcobacter are driving the microbiological differences between sample types.

Table 3: SIMPER results for variables contributing most to the differences in (a) sample chemistry and (b) sample microbiology.

a.

Chemistry	Variable	Contribution %
IW - POS	TOC	30%
	Sulfate	18%
IW - PW	TOC	21%
	Alkalinity	19%
POS - PW	Nitrate	40%
	Sulfate	20%

b.

Microbiology	Phylotype	Contribution %
IW - POS	*Pseudomonas*	17%
IW - PW	*Roseovarious*	13%
	Methanothermococcus	12%
POS - PW	*Arcobacter*	13%

Poseidon Tank

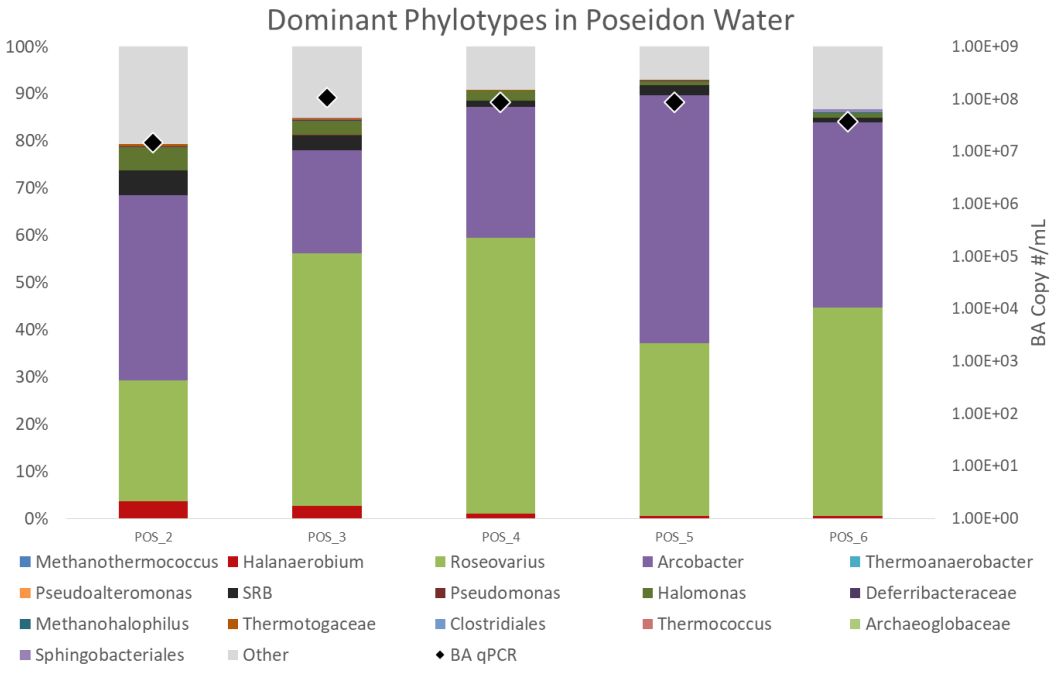


Figure 11: Relative abundance of dominant groups in Poseidon recycled produced water.

The Poseidon tank water had a consistent microbial community composition, as measured weekly for five weeks (Figure 11). Roseovarius and Arcobacter were the predominant organisms, and the water contained an average total bacterial population size of 6.66x107 cells/mL. Roseovarius bacteria have been known to create bio-clogging issues (Lim 2011), and therefore

may be relevant for surface water handling equipment and storage. Also, in the Poseidon water is small to moderate concentrations of SRB and Halanaerobium species which are found in microbial populations in later stage produced water samples.

Injection Water

Injection water at HFTS for hydraulic fracturing was comprised of freshwater from nearby groundwater wells (80%), recycled produced water held in the Poseidon tank (20%) and chemicals required for hydraulic fracturing. Injection water was mixed independently and on the fly for all three wells, resulting in large variations in microbial abundance and community structure. The drill out water (DW) used to remove the plugs after fracturing was included in the injection water analysis to determine potential sources of microorganisms. The concentration of total bacteria injected into the wells during hydraulic fracturing ranged from 1x104 to 5x107 bacterial cells per mL, population size and community structure can be seen in Figure 12. Relative abundances of bacterial phylotypes can be seen in Appendix B.

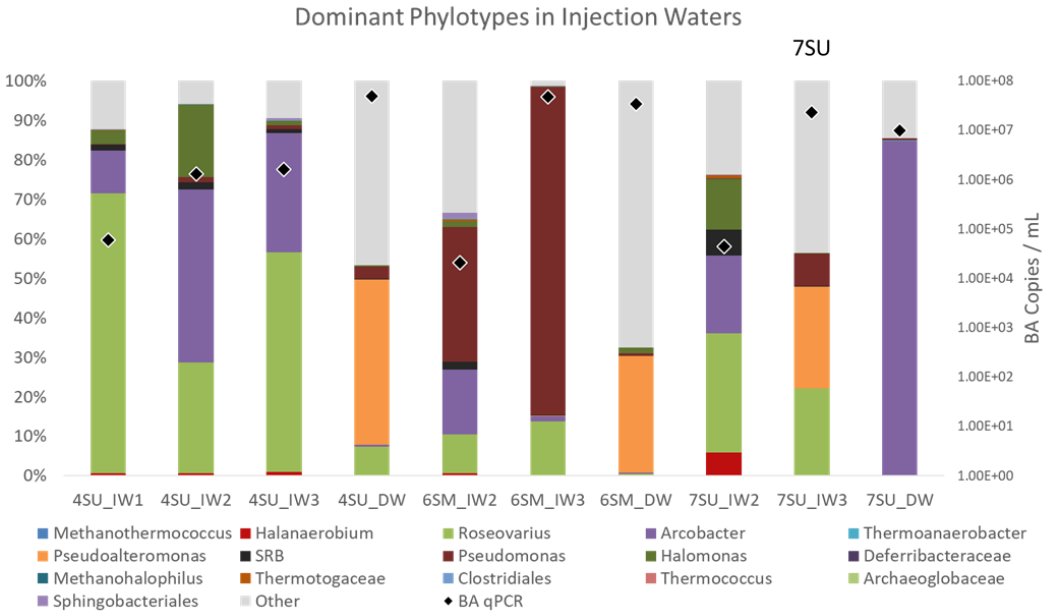


Figure 12: Relative abundance of dominant organisms in Influent Water (IW) and drill out water (DW) for all three HFTS wells.

IW samples contained populations comprised of primarily Roseovarius and Arcobacter, resembling the recycled produced water in the Poseidon impoundment tank. Although Roseovarius bacteria have been known to create bioclogging issues, no Roseovarius organisms were detected after the wells were put on production, and therefore likely do not contribute to subsurface microbial community structure long term.

Arcobacter, which comprised 20-50% of Poseidon and IW microbial populations was detected as high as 17% of the PW population 14 days after the wells were put on production. Some Arcobacter species contain metabolic capabilities to reduce nitrate and oxidize sulfide to elemental sulfur (Fera 2004). Incomplete microbial reduction of nitrate produces nitrite, which in turn inhibits the dissimilatory sulfite reductase enzyme produced by SRB during sulfate reduction. This biological mechanism, encouraging nitrate reducer growth to limit sulfate reduction and corrosion, has been used by the industry as an alternative to biocides to inhibit or slow SRB corrosion with mixed results (Gaspar J. 2014).

Pseudoalteramonas organisms were detected in the water injected into the wells in moderate to high concentrations. Pseudomonas was introduced to well 6SM in the IW. These groups of organisms were not detected in the Poseidon water, so it was likely introduced through fresh water, additives, or drill out muds. Pseudoalteramonas was detected as over 80% of the microbial population coming from 6SM on the first day of production. Pseudoalteramonas and Pseudomonas bacteria are known for their antimicrobial qualities, however more notably for their ability to establish and promote biofilm formation.

Produced Water

Average bacteria concentration, as measured by qPCR, in the PW for the first year and a half of production is shown in Table 4 along with sulfate-reducing bacteria (SRB) and denitrifying bacteria (DNB) concentrations. Total bacterial populations peaked at 1.3x108 cells per mL after 36 days of production in well 6SM, the lowest measured concentration of bacteria to date is 1x104 cells per ml after 210 days of production in well 4SU. Concentrations of SRB increased over the first year and a half of production and concentrations of DNB decreased.

Table 4: Average concentrations of total bacteria, sulfate-reducing bacteria, and denitrifying bacteria in produced water sampled over 550 days of production.

	Date	BA	SRB	DNB
PW0	**12/31/2015**	1.13E+05	1.29E+01	3.31E+02
PW1	**1/1/2016**	3.25E+07	3.91E+01	7.58E+02
PW6	**1/5/2016**	6.96E+05	3.73E+02	1.78E+01
PW14	**1/14/2016**	1.46E+07	1.12E+02	1.37E+02
PW36	**2/5/2016**	5.34E+07	1.73E+03	4.95E+01
PW90	**3/2/2016**	1.56E+07	9.62E+02	4.09E+00
PW210	**8/2/2016**	6.57E+04	4.54E+02	3.70E+00
PW365	**12/30/2016**	9.51E+05	8.14E+03	2.31E+00
PW550	**6/30/2017**	3.41E+06	1.68E+03	9.61E+00

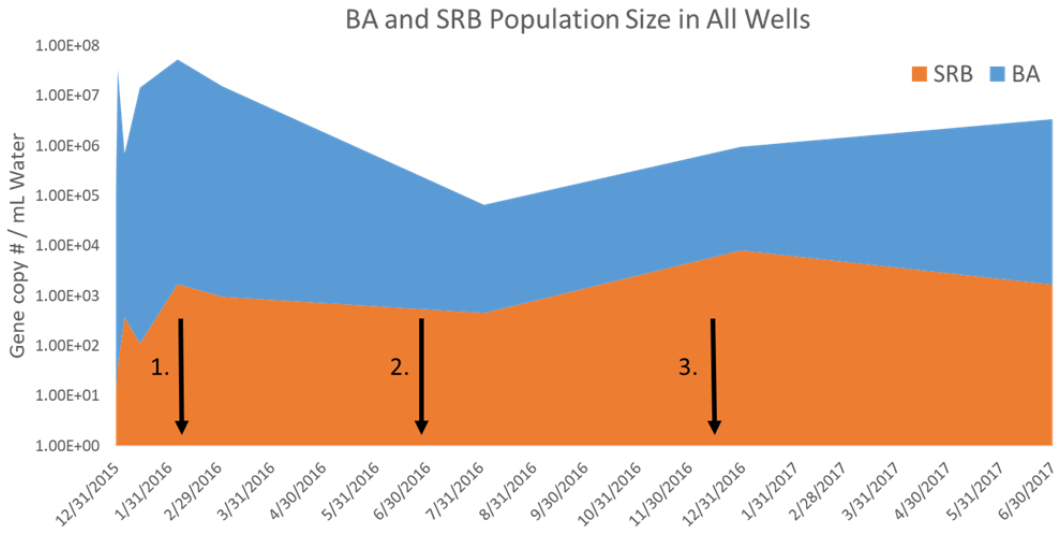


Figure 13: Average total BA and SRB gene copies/mL across 6SM, 7SU, and 4SU. (1) Date of community composition shift (2) Well 6SM tubing pulled (3) Biocide applied to all wells.

Three time points are highlighted in Figure 13 below which visually displays the BA and SRB concentration in PW over time. The first is at sample Day 36 (2/5/2016) when the microorganisms

present in the produced water drastically and significantly change in diversity, relative abundance, and metabolic function. The second event occurred in June 2016 when well 6SM was pulled to remove and replace the tubing which was extensively corroded by microbially influenced processes. The well was not treated with biocide at this time. Thirdly, in November and December 2016, well 4SU's tubing was pulled due to microbial corrosion and all wells were dosed with biocide B-1203. Wells were sampled in late December, days after biocide treatment and six months later in June, it is notable that total BA concentrations continued to increase over this time. We do not yet have sequencing results for the 550-day samples taken in June 2017.

Out of the dominant groups in the drill out mud and injection water, (Roseovarius, Halamonas, Pseudomonas, Pseudoalteramonas, Arcobacter, Psycrobacter), few persist in the downhole environment with the lack of oxygen and high salinity, temperature, and pressure. The lack of oxygen selects for microbial communities with the ability to use alternative electron acceptors for metabolic energy, such as sulfate or nitrate.

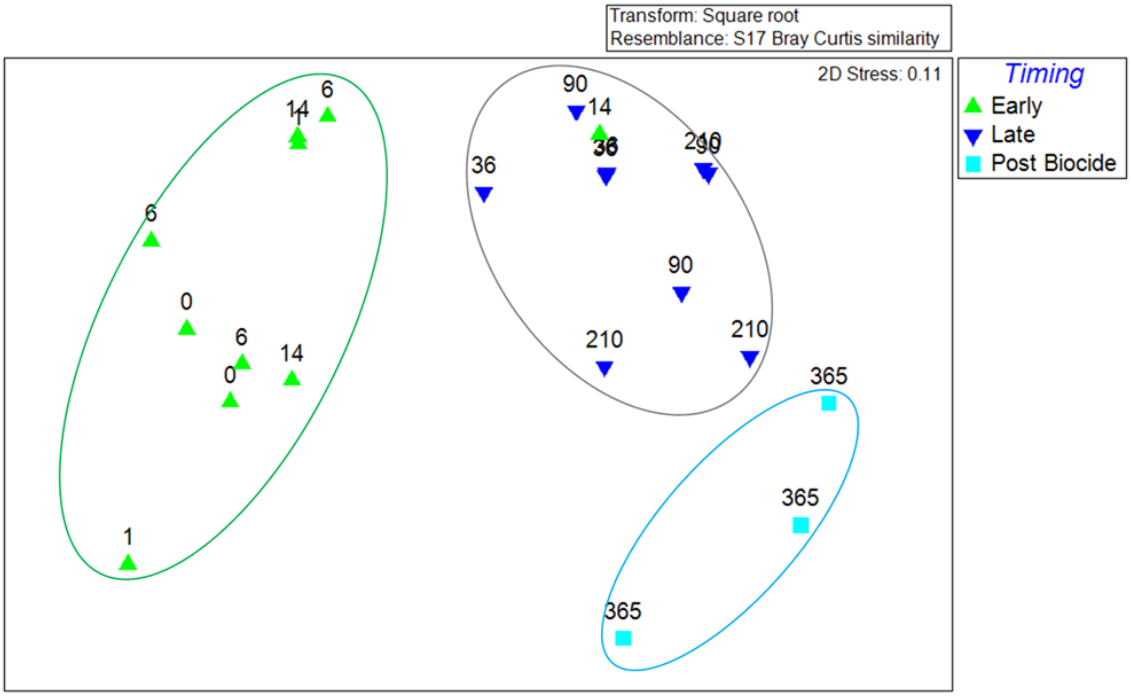


Figure 14: nMDS of PW microbial communities, grouping samples into Early, Late, and Post Biocide categories.

Produced water microbial composition does not resemble injection fluids, however, a few of phylotypes that became dominant in the later stages of well development (>36 days) were present in small quantities in the injection fluids (<5% relative abundance). For example, Halanaerobium and Methanothermococus were detected in injection fluids and drill out water. Other organisms detected in injection fluids which became established in the down environment include the sulfate reducing Archaeoglobus, Desulfitibacter, and Desulferrvibrio, and iron reducing bacteria in the Deferribacter phylotype.

When plotted in non-metric multi-dimensional space, the difference between "early", "late", and "post biocide" microbial communities is clearly evident (PERMANOVA P=0.001), see Figure 14. The phylotypes contributing the most to the difference are shown in Table 5. Distance based redundancy analysis reveals that changes TOC and sulfate explain a significant proportion of the

variation in the biological communities (P=0.002), however it was weak model fitting to environmental variables with less than 20% of the variation accounted for.

Table 5: SIMPER results identify Phylotypes contributing to differences between Early, Late, and Post Biocide samples.

	Phylotype	Contribution
Early to Late	↑ *Halanaerobium*	20%
	↓ *Thermoanaerobacter*	12%
Late to Post Biocide	↓ *Methanothermococcus*	15%
	↑ *Methanohalophilus*	9.30%

Early Produced Water Microbiology

DNA extraction and amplification was not successful for the initial 7SU well PW samples. 4SU and 6SM wells produced early populations dominated by anaerobic Thermoanaerobacter, Gram positive organisms which produce corrosive acetic acid (Ben-Bassat 1981). It is noteworthy IW and Poseidon populations contained less than 5% Thermoanaeobacter species and at Day 1 of production these organisms make up as much as 50% of the PW population, indicating the prime conditions for microbial growth during the 6 weeks injection fluids were held in the well. There is evidence that the length of time water is held in the reservoir before flowback influences produced water microbial community size, composition, and response to biocides (Gaspar J. 2014); (Strutchtemeryer 2012). Pseudoalteromonas, although only found in small concentrations in most wells comprised 80% of the microbial population in well 6SM the first day of production and are known for biofilm formation ability in a wide variety of environments (Rao D. 2005). Deferribacter were detected in PW water from all wells with high concentrations in well 4SU. These organisms have the metabolic ability to solubilize Fe (III) to Fe (II) contributing to the corrosion of steel (Slobodkina G 2009).

Early water produced from well 6SM, where extensive corrosion was identified, contained slightly different populations than well 4SU. The relative abundance of phylotypes and total bacterial population sizes for all samples can be seen in Figure 15. Arcobacter, Thermococcus, and Archaeoglobous were found in higher concentrations in 6SM, with Deferribacter and Methanothermococcus in lower concentrations when compared to well 4SU. Arcobacter form filamentous sulfur mats (Wirsen 2004) which are able to anchor bacteria to rocky surfaces where there is high fluid flow, as seen in hydrothermal vents (Wirsen 2004), yet these organisms also reduce nitrate and oxidize sulfide to elemental sulfur; mechanisms which can reduce corrosion impacts. Thermococcus, known hyperthermophiles, transform elemental sulfur into corrosive hydrogen sulfide and generate white-grey plaques or scale on surfaces (Rivas-Pardo J 2013). Additionally, the Archaeoglobus are sulfate reducing archaea with optimal growth at 83°C, commonly found in oilfield systems with the ability to reduce sulfate to sulfide with the oxidation of complex carbon polymers (Stetter, 1989).

Methanothermococcus were detected in moderate to high concentrations in nearly all early and late PW samples. These organisms utilize H+ from fermentative heterotrophic organisms, sulfate from the environment, and available C sources (TOC, biomass, light alkane hydrocarbons) to generate methane and biomass.

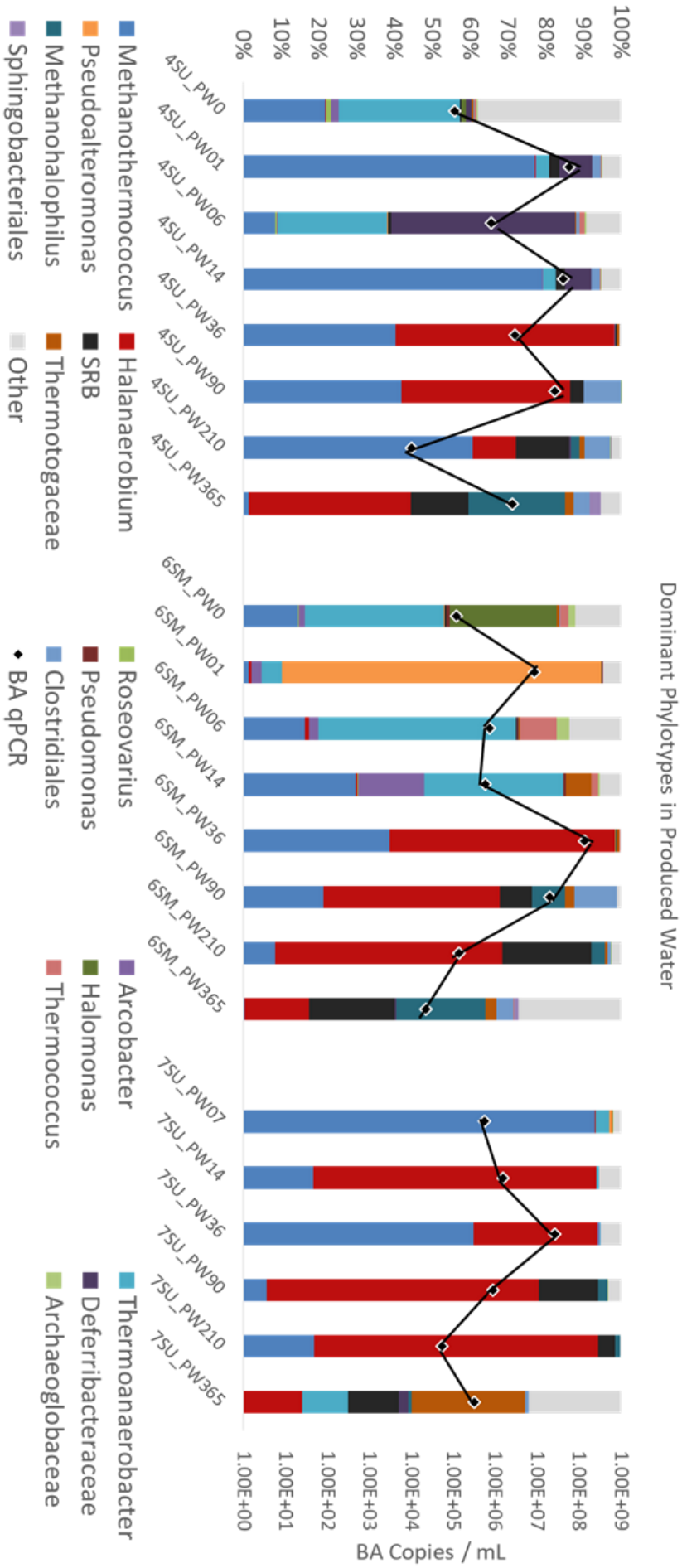


Figure 15: Relative abundance of dominant phylotypes and total bacterial population size in HFTS PW samples.

Late Produced Water Microbiology

After 36 days production, bacterial population size begins to decrease from approximately 1.5x107 cells per mL to an average 3.4x106 cells per mL. Microbial community composition in all three wells become similar after 36 days (Figure 14; PermDisp; P=0.014). This pattern indicates strong selection pressures from the subsurface environment. These later water sample populations are dominated by Halanaerobium and Methanothermococcus. Sulfur-Reducing bacteria are a small but consistently increasing part of this community around 5-7%, as corroborated by qPCR results (Table 4, Appendix B). Sulfate reducing bacteria identified through metagenomics include the Desulfonatronum, Desulfovibrio, Desulformondaceae, Desulfonatronovibrio, Desulfovermiculus, Desulfobacteraceae. Halanaerobium are fermentative bacteria often found in produced waters which feed on ethylene glycol, a common additive to injection water. These bacteria produce hydrogen which is then a primary energy source for SRB, methanogens, and iron reducing bacteria in the formation of sulfides, methane, or dissolution of iron in steel (Singh A. 2014). It appears, regardless of differences chemistry or microbiology introduced to the wells, the ultimate population returning to the surface in produced water from the three wells was similar.

The convergence of microbial populations may lead one to conclude that operation activities have limited impact on microbial population dynamics due to the extreme environment selecting for specific organisms. However, it should be noted that early populations returning to the surface indicate differences in well populations in the first several weeks of production. These differences can be the difference between biofilm establishment and propagation or not. 6SM had early substantial populations of biofilm forming and sulfur-cycling organisms including Pseudoalteramonas, Arcobacter, Thermococcus, and Archaeoglobus, when the other wells did not, and exhibited highly corrosive activity before the rest. Additionally, the operational decision to hold the water in after fracturing can impact microbial growth in the subsurface, allowing more contact time for microorganisms to interact with the fractured shale and form biofilms. Furthermore, many of the fracture chemicals feed microbial metabolism, a portion of which are analyzed as total organic carbon (TOC). Influent water had TOC concentrations of 150mg/L whereas water produced at on the first day of flowback contained less than 50mg/L TOC indicating microbiological utilization may be occurring along with dilution from mixing with in-situ formation water.

Post Biocide Water Microbiology

Produced water samples taken days after biocide dosing (D365 samples) contain microbial communities higher in diversity and with significantly different community composition than previous PW samples Figure 15 (P=0.001). The most drastic impact of the biocide is the near complete disappearance of Methanothermococcus organisms and decrease in Halanaerobium species. However, the relative abundance of SRB was not impacted by the biocide, as they comprise 15% of the population in Well 4SU, 22% of the population in 6SM and 13% of the population in 7SU (up from 4% of the population 210 days into production). qPCR results found the total amount of bacterial cells / mL increased by an order of magnitude 6 months after biocide dosing (Table 4, Figure 13).

Discussion

Microbial Control

Biocides are used in the oil and gas industry to prevent the breakdown of fracture fluid chemicals, microbiologically induced corrosion, sour gas production, and decreased formation permeability due to biofilm. During this experiment, recycled produced water was treated with Chlorine Dioxide, a strong oxidizing biocide, and stored in impoundment tanks before being mixed with fresh water, fracturing fluid chemicals and sand, and then injected into the reservoir. The wells were then shut in for 4-6 weeks after hydraulic fracturing. Our microbiology results indicated high concentrations of bacterial populations persisting in the subsurface, up to 550 days after production began, and the detrimental impact of biofilms was observed on site as corrosion failures.

Two factors likely contributed to the establishment of viable microbial communities in the subsurface. First, injection water was not treated to adequately kill all microorganisms before hydraulic fracturing, as communicated by Laredo operations. This introduced living, thermo- and halo-tolerant, biofilm promoting organisms into the SRV. Secondly, the wells were shut in for a period of several weeks after hydraulic fracturing. Post-fracture biocide treatments are found to be most successful when flowback occurs within 24 hours of hydraulic fracturing (Struchtemeyer C. 2012). The shorter residence time of fracturing fluids limits the amount of time for cell – surface interactions required for anaerobic biofilm growth and proliferation. Once established however, biofilms are notoriously difficult to remove from the formation and steel surfaces, so produced water microbiology must be monitored and managed.

In November and early December 2016, wells were shut in for 12 hours for biocide treatment after microbiologically influenced corrosion was observed on tubing and pressure gauges. Approximately 55 gallons of B-1203, a Glutaraldehyde/ Didecyldimethylammonium Chloride blend, was pumped downhole. Gluteraldehyde binds to cell's amine groups, killing microorganisms by inhibiting the transport of essential nutrients. Didecyldimethylammonium chloride, is a quaternary ammonium compound, otherwise known as "quats". Quats are added to glutaraldehyde biocides for their ability to disrupt cell membranes and grant access for amine binding. Quaternary compounds are most effective on Gram positive cell membrane structure. Sequencing results of produced water revealed the majority or organisms growing in the reservoir since the early days of production were Gram negative.

qPCR results from samples taken one month after biocide application indicate bacteria concentrations have remained steady or increased in some wells (Table 4, Figure 13). The persistence of high concentrations of bacterial DNA in the subsurface indicates an incomplete kill job in these wells. Although we did not conduct an activity or live vs. dead test for these samples, sampling over time with quantitative methods indicates populations are alive and sustaining growth in the SRV. Furthermore, the sequencing of DNA in samples taken days after the biocide treatment indicate the subsurface population is now dominated by Gram negative organisms, and organisms with natural defenses to quats such as double membranes or protective sheaths around the cell body. There are strategies for enhancing biocide effectiveness against Gram negative bacteria (Denyer 2002) which can be determined based on fracturing fluid and formation chemistry.

Incomplete kill jobs from biocide treatments are common in the unconventional oil and gas industry (Gaspar J. 2014). Chemically, quaternary ammonium compounds work best in soft water, with calcium concentrations below 60 mg/L. The ground water introduced to the reservoir during hydraulic fracturing at HFTS was only moderately hard (Ca = 75 mg/L), however the produced water has Ca >2,000 mg/L. The biocide treatment in November introduced 55 gallons of B-1203 to a reservoir containing considerably hard water, likely compromising the biocide effectiveness.

Microbial response to biocide uses and duration for fracturing fluids to be in contact with the formation indicate operation activities have an influence on ultimate subsurface microbiological community structure and activity.

TOC, S, N shaping microbial PW communities.

Changes in the chemistry of the water in the subsurface can strongly influence microbiological metabolism by providing available carbon, electron acceptors, and electron donors for microbial metabolism and energy. Evidence for this is seen over the first few weeks of production in the three wells by examining qPCR results and water chemistry data.

Sulfate reducing organisms use sulfate to draw electrons through their electron transport chain so they may generate energy, like how humans use the oxygen that we breathe. Nitrate reducing organisms do the same with nitrate as their primary electron acceptor. As energy is generated, organisms require carbon to grow, the most easily consumed carbon is generally measured as TOC. However, other carbon compounds can also fuel cell growth, such as light chain hydrocarbons, aromatic species, and long chain hydrocarbons. Microbial metabolism plays a large role in the degradation of oil from light to dark crude over large time spans. Other sources of microbially available carbon in the subsurface include additives to the fracturing fluids as surfactants, friction reducers, and chelating agents as well as the biomass of other bacterial cells.

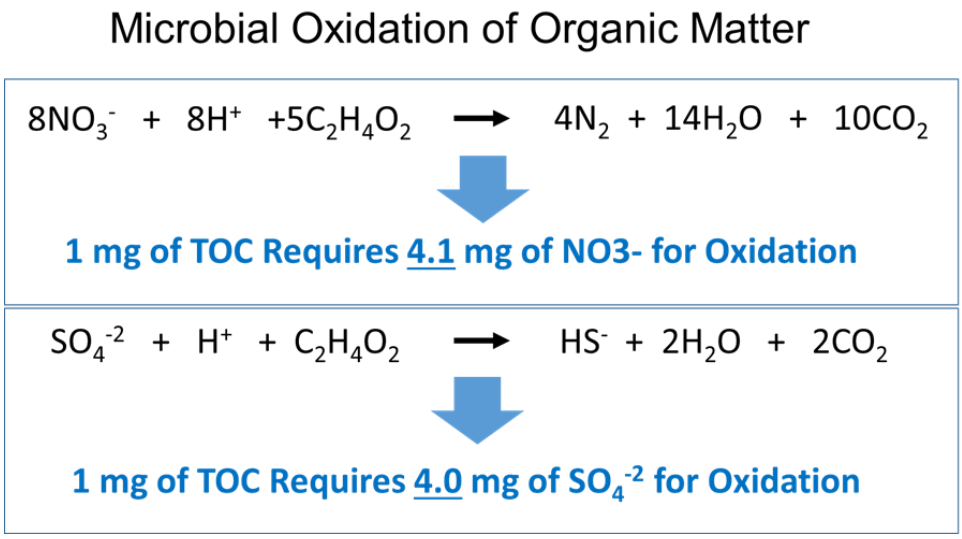


Figure 16: Equations and equivalencies for microbial oxidation of organic matter using Sulfate and Nitrate.

Based on the redox reactions in Figure 16, we calculate the bacterial reduction of 4mg of sulfate will oxidize 1mg TOC. Similarly, the bacterial reduction of 4.1mg of nitrate will oxidize 1mg of TOC. Within the first 14 days of production, sulfate concentrations dropped approximately 100 mg/L, nitrate dropped 30 mg/L, and TOC concentrations decreased approximately 30mg/L. If we are considering TOC to be acetate, easily available carbon, the TOC oxidant equivalent is reduced

by 144mg/L. This brings the system within 3% of closure in comparing TOC loss to oxidant consumption. It indicates the loss of TOC is due to microbially mediated sulfate and nitrate reduction. Correspondingly, we see a disappearance of denitrifying bacteria (DNB) once the nitrate is depleted in the reservoir (Table 4). A considerable amount of sulfate remains however, which sulfate reducing organisms use for energy to fuel carbon consumption and the production of corrosive acids, sour gas, and feed into the intimate relationships of bacterial redox reactions and food webs in biofilms. As the available TOC disappears in the system and biofilms have established on the steel or shale surfaces, SRB can use dead biomass as a carbon source for their own growth and continued sulfate reduction.

Mass flow calculations, discussed in the Environmental Monitoring Report, indicate that within two weeks of production, about 1.5 tons of TOC was converted to CO2 though microbial mechanisms with the concomitant reduction of 1.5 tons of nitrate to nitrogen gas and 4.2 tons of sulfate to 1.4 tons of sulfide. The sulfide likely reacted with the soluble iron in the SRV to produce iron sulfide. Iron sulfide drops out of solution and may lead to build up and clogging in the fracture network.

Conclusions

The conclusion of the microbiological and chemical analysis of waters used in and produced from the HFTS wells are summarized below:

1. 10 million gallons of water was injected into each HFTS well and remained in the formation for 4-6 weeks, during which time water chemistry and microbiology was significantly altered (Figure 10). Downhole temperatures of 65°C does not impede the growth of microorganisms but selects for organisms tolerant of extreme heat and salinity. Bacterial populations fluctuated by several orders of magnitude over the first year and a half of production and have been steadily increasing for 6 months into production.
2. Water injected into the wells for hydraulic fracturing contained high concentrations of bacteria (Figure 9) compared to fresh water sources. The Poseidon tank recycled produced water and drill out fluids used in drilling out fracture plugs contributed to the high concentration of bacteria in injection waters. Organisms present in these injection waters established populations in the SRV while wells were shut-in before production.
3. Microorganisms found in early produced water samples from well 6SM contain the metabolic functions for biofilm formation and sulfate reduction to corrosive sulfide. Tubing was pulled from this well 6 months into production after substantial microbially influenced corrosion occurred. Sulfate reducing bacteria, biofilm forming bacteria, and iron reducing bacteria were also found in well 4SU in which premature corrosion occurred on bottom-hole gauges less than one year into production.
4. Inadequate biocide treatment of injection water and relatively long residence time of injected water before flow back contributed to the establishment of microbial communities in the HFTS wells.
5. Later stage microbiological communities (from 36 days of production to 210) were dominated by methane generating organisms, thermo- and halo-tolerant fermentative bacteria, and sulfate reducing bacteria.

6. Biocide dosing in December 2016 decreased the population of methane producing bacteria, however it did not substantially reduce overall bacterial population sizes or the relative abundance of sulfate reducing bacteria. The biocide used targeted Gram-positive bacteria and works optimally in soft water (<60mg/L Ca). At this point microbial communities were composed of mostly Gram-negative organisms with a Ca concentration over 2,000 mg/L.
7. Based on redox reactions, microbial mechanisms lead to the creation of 1.4 tons of sulfide in the subsurface. The sulfide likely reacted with soluble iron in the SRV to produce iron sulfide which precipitates out of solution and may build up within fracture networks decreasing formation production.

Recommendations

1. Based on the study results a re-designed bacteria treatment program needs to be developed for Permian basin hydraulic fracturing operations. This should include treatment recommendations for fresh water, stored water and a treatment schedule for wells after production commences. The types of biocides being utilized should be reviewed for efficacy.
2. Further research needs to be performed on the impact of potential precipitates to well production. Precipitation of iron sulfide may be contributing to the rapid production decline typical of Wolfcamp shale wells. All shale wells from around the country tend to decline rapidly and it is attributed to low permeability within the formation matrix outside of the stimulated region. Determining the impact of precipitate damage will not be a trivial exercise.

References

1. Ben-Bassat, A., J Zeikus. 1981. "Thermobacteroides acetothylicus gen. nov. and spec. nov. a new chemoorganotropic, anaerobic, thermophilic bacterium." Archives of Microbiology 365-370.
2. Caporaso JG, Kuczynski J, Stombaugh J, Bittinger K, Bushman FD, Costello EK, Fierer N, Pena AG, Goodrich JK, Gordon JI, Huttley GA, Kelley ST, Knights D, Koenig JE, Ley RE, Lozupone CA, McDonald D, Muegge BD, Pirrung M, Reeder J, Sevinsky JR, Turnbaugh PJ, Walters WA, Widmann J, Yatsunenko T, Zaneveld J, Knight R. QIIME allows analysis of high-throughput community sequencing data. Nat Methods. 2010; 7(5):335-6
3. Caporaso JG, Lauber CL, Walters WA, Berg-Lyons D, Lozupone CA, Turnbaugh PJ, Fierer N, Knight R. Global patterns of 16S rRNA diversity at a depth of millions of sequences per sample. Proc Natl Acad Sci. 2011; 108(Supplement 1):4516-22.
4. Fera, M., T Maugeri, C Gugliandolo, C Beninati, M Giannone, E La Camera, M Carbone. 2004. "Detection of Arcobacter spp. in the costal environemnt of the mediterranean sea." Applied and Environmental Microbiology 1271-1276.
5. Gaspar J., J Mathiew, Y Yang, R Tomson, J Leyris, K Gregory, P Alvarez. 2014. "Microbioal dynamics and control in shale gas production." Enviornmental Science and Technology 465-473.

6. Lim, C.P, D Zhao, Y Takase, K Miyanaga, T Watanabe, Y Tomoe, Y Tanjii. 2011. "Increased bioclogging and corrosion risk by sulfate additions during iodine recovery at a natrual gas production plant." Applied Microbiology Biotechnology 825-834.
7. Rao D., J Webb, S Kjelleber. 2005. "Competative interactions in mixed-species biofilms containing the marine bacterium Pseudoalteromonas tunicata." Applied and Environmental Microbiology 1729-1736.
8. Rivas-Pardo J, V Castro-Fernandez, F Fernandez, M Vega, V Guixe. 2013. "Crystal structure, SAXS and kinetic mechanism of hyperthomophilic ADP-Dependent glucosinase from Thermococcus litoralis reveal a conserved mechanism for catalsis." PLoS ONE 12.
9. Singh A., J CVan Hamme, R Kuhad, N Parmar, O Ward. 2014. "Subsurface Petrolium Microbiology." Geomicrobiology and Geochemistry 39.
10. Slobodkina G, T Kolganova, N Chernyh, J Querellou, E Bonch-Osmolovskaya, A Slovodkin. 2009. "Deferribacter autotriphicus sp. nov., an iron(III)-reducing bacterium from a deep-sea hydrothermal vent." International Journal of Systematic and Evolutionary Microbiology 1508-1512.
11. Solden LM, Hoyt DW, Collins WB, Plank JE, Daly RA, Hildebrand E, Beavers TJ, Wolfe R, Nicora CD, Purvine SO, Carstensen M, Lipson MS, Spalinger DE, Firkins JL, Wolfe BA, Wrighton KC. New roles in hemicellulosic sugar fermentation for the uncultivated Bacteroidetes family BS11. ISME J. 2017; 11(3):691-703.
12. Quast C, Pruesse E, Yilmaz P, Gerken J, Schweer T, Yarza P, Peplies J, Glockner FO. The SILVA ribosomal RNA gene database project: improved data processing and web-based tools. Nucleic Acids Res. 2013; 41(D1):D590-6.
13. Wirsen, C. 2004. "Is life thriving beneath the sea floor." Oceanus 72+.

Appendix A: Produced Water Chemistry

Table A1. Results for Produced Water Collected from HFTS Well 6SM at 0-14 Days.

Parameter	Units	Det. Limit	Results (On Days Following Initiation of Flowback Release)			
			0-Day	1-Day	5-Day	14-Day
General						
pH	-	-	7.17	6.7	7.26	6.62
Total Dissolved Solids (TDS)	mg/L	10	91,300	88,500	92,900	62,100
Conductivity	µS/cm	5	50,900	51,400	45,800	41,900
Alkalinity	mg/L	1	450	407	419	321
Organics						
Total Organic Carbon	mg/L	0.2	98	33	31	8.5
Total Petroleum Hydrocarbons	mg/L	0.5	18	80	42	16
Benzene	mg/L	0.0073	5	2.2	4.4	1.5
Toluene	mg/L	0.0076	5.7	1.2	5	0.71
Ethylbenzene	mg/L	0.0091	1.1	0.11	1.1	0.056
Xylenes	mg/L	0.011	4.6	0.51	4.4	0.31
Anions						
Chloride	mg/L	500	48,400	48,600	53,000	33,800
Nitrate	mg/L	3	36.3	35.3	34.9	13.7
Sulfate	mg/L	5	432	432	435	308

Sulfide	mg/L	1	BDL	BDL	BDL	BDL
Cations						
Arsenic	mg/L	1	BDL	BDL	BDL	BDL
Barium	mg/L	0.05	1.9	1.9	1.7	1.6
Boron	mg/L	0.5	36.5	28.7	29.3	16.9
Cadmium	mg/L	0.1	BDL	BDL	BDL	BDL
Calcium	mg/L	10	1,890	2,060	1,800	1,610
Chromium	mg/L	0.3	BDL	BDL	BDL	BDL
Copper	mg/L	0.2	BDL	BDL	BDL	BDL
Iron	mg/L	0.5	50.2	14.3	17.2	45.3
Lead	mg/L	1	BDL	BDL	BDL	BDL
Magnesium	mg/L	10	303	282	291	224
Manganese	mg/L	0.1	0.9	0.3	0.2	0.7
Nickel	mg/L	0.3	BDL	BDL	BDL	BDL
Potassium	mg/L	10	422	402	509	247
Sodium	mg/L	5	30,200	30,100	34,100	31,900
Zinc	mg/L	0.2	0.8	0.7	BDL	2.7

Table A2. Results for Produced Water Collected from HFTS Well 6SM at 36-550 Days.

Parameter	Units	Det. Limit	Results (On Days Following Initiation of Flowback Release)				
			36-Day	90-Day	210-Day	365-Day	550-Day
General							
pH	-	-	6.41	6.39	6.54	6.57	6.26
Total Dissolved Solids (TDS)	mg/L	10	102,000	115,000	118,000	120,000	128,400
Conductivity	µS/cm	5	40,000	81,200	80,700	65,000	73,500
Alkalinity	mg/L	1	517	413	429	394	374
Organics							
Total Organic Carbon	mg/L	0.2	0.23	0.72	1	150	0.5
Total Petroleum Hydrocarbons	mg/L	0.5	13	180	143	3.2	111
Benzene	mg/L	0.0073	3.7	2.8	3.4	3.3	4.2
Toluene	mg/L	0.0076	1.8	1.5	1.7	1.6	2.1
Ethylbenzene	mg/L	0.0091	0.12	0.086	0.13	0.099	0.13
Xylenes	mg/L	0.011	0.47	0.35	0.48	0.35	0.051
Anions							
Chloride	mg/L	500	67,100	67,100	69,300	65,900	37,400
Nitrate	mg/L	3	35.8	BDL	45.6	BDL	BDL
Sulfate	mg/L	5	367	318	297	257	895
Sulfide	mg/L	1	BDL	BDL	BDL	BDL	BDL
Cations							
Arsenic	mg/L	1	BDL	BDL	BDL	BDL	BDL
Barium	mg/L	0.05	2.1	BDL	2.9	1.3	2.29
Boron	mg/L	0.5	28.8	39.7	39.7	39.2	39.7
Cadmium	mg/L	0.1	BDL	0.2	BDL	BDL	BDL
Calcium	mg/L	10	2,640	2,170	2,550	2,880	2,900
Chromium	mg/L	0.3	BDL	BDL	BDL	BDL	BDL

Copper	mg/L	0.2	BDL	0.2	BDL	0.2	BDL
Iron	mg/L	0.5	165	97	156	52.7	18.4
Lead	mg/L	1	BDL	BDL	BDL	BDL	BDL
Magnesium	mg/L	10	362	343	345	361	502
Manganese	mg/L	0.1	2.3	3.1	1.4	1.3	1.3
Nickel	mg/L	0.3	BDL	1	BDL	0.3	BDL
Potassium	mg/L	10	509	475	386	694	505
Sodium	mg/L	5	38,500	34,700	37,800	40,300	41,200
Zinc	mg/L	0.2	BDL	BDL	BDL	0.8	BDL

Table A3. Results for Produced Water Collected from HFTS Well 4SU at 0-14 Days.

Parameter	Units	Det. Limit	Results (On Days Following Initiation of Flowback Release)			
			0-Day	1-Day	5-Day	14-Day
General						
pH	-	-	6.71	6.55	7.41	7.33
Total Dissolved Solids (TDS)	mg/L	10	88,900	87,600	94,500	103,000
Conductivity	µS/cm	5	44,400	46,000	45,100	45,900
Alkalinity	mg/L	1	438	441	422	393
Organics						
Total Organic Carbon	mg/L	0.2	9.9	39	34	12
Total Petroleum Hydrocarbons	mg/L	0.5	5.6	15	54	50
Benzene	mg/L	0.0073	0.93	1.7	4.9	0.78
Toluene	mg/L	0.0076	0.43	0.88	7	0.47
Ethylbenzene	mg/L	0.0091	0.025	0.068	1.6	0.059
Xylenes	mg/L	0.011	0.13	0.3	6.6	0.25
Anions						
Chloride	mg/L	500	49,200	50,000	52,500	56,100
Nitrate	mg/L	3	36.6	36	34.9	BDL
Sulfate	mg/L	5	416	414	422	292
Sulfide	mg/L	1	BDL	BDL	BDL	BDL
Cations						
Arsenic	mg/L	1	BDL	BDL	1.1	BDL
Barium	mg/L	0.05	2.1	2.1	2.5	2
Boron	mg/L	0.5	25	32.5	25.2	30.2
Cadmium	mg/L	0.1	BDL	BDL	BDL	BDL
Calcium	mg/L	10	1,900	1,990	1,790	2,000
Chromium	mg/L	0.3	BDL	BDL	BDL	BDL
Copper	mg/L	0.2	BDL	BDL	1	0.3
Iron	mg/L	0.5	24.6	19.2	11.3	11.6
Lead	mg/L	1	BDL	BDL	BDL	BDL
Magnesium	mg/L	10	296	313	285	326
Manganese	mg/L	0.1	0.5	0.5	0.9	BDL
Nickel	mg/L	0.3	BDL	BDL	0.7	BDL
Potassium	mg/L	10	385	421	513	590
Sodium	mg/L	5	28,500	29,600	33,900	36,400
Zinc	mg/L	0.2	0.8	0.8	0.8	0.2

Table A4. Results for Produced Water Collected from HFTS Well 4SU at 36-550 Days.

Parameter	Units	Det. Limit	Results (On Days Following Initiation of Flowback Release)				
			36-Day	90-Day	210-Day	365-Day	550-Day
General							
pH	-	-	6.43	6.67	6.49	6.68	6.26
Total Dissolved Solids (TDS)	mg/L	10	105,000	114,000	123000	120,000	121,000
Conductivity	µS/cm	5	42,200	81,700	77800	63,500	75,800
Alkalinity	mg/L	1	683	537	450	438	355
Organics							
Total Organic Carbon	mg/L	0.2	1	2.6	1	220	0.5
Total Petroleum Hydrocarbons	mg/L	0.5	3	200	142	46.5	91.1
Benzene	mg/L	0.0073	0.95	3.3	3.5	7.4	3.2
Toluene	mg/L	0.0076	0.52	1.8	1.9	3.8	1.9
Ethylbenzene	mg/L	0.0091	0.051	0.13	0.15	0.29	0.18
Xylenes	mg/L	0.011	0.21	0.45	0.51	0.98	0.55
Anions							
Chloride	mg/L	500	63,900	68,100	68,900	64,000	34,000
Nitrate	mg/L	3	35.6	BDL	43.3	BDL	BDL
Sulfate	mg/L	5	387	349	307	290	279
Sulfide	mg/L	1	BDL	BDL	BDL	BDL	BDL
Cations							
Arsenic	mg/L	1	BDL	BDL	BDL	BDL	BDL
Barium	mg/L	0.05	1.6	BDL	2.3	2.3	2.1
Boron	mg/L	0.5	30.1	40.3	43.0	40.0	45.7
Cadmium	mg/L	0.1	0.1	0.2	BDL	BDL	BDL
Calcium	mg/L	10	2,150	1,640	2,020	2,150	2,250
Chromium	mg/L	0.3	BDL	BDL	BDL	BDL	BDL
Copper	mg/L	0.2	BDL	0.2	BDL	0.2	BDL
Iron	mg/L	0.5	351	168	93.0	57.5	51.4
Lead	mg/L	1	BDL	BDL	BDL	BDL	BDL
Magnesium	mg/L	10	358	332	347	345	422
Manganese	mg/L	0.1	4.3	4.3	1.8	1.2	1.2
Nickel	mg/L	0.3	BDL	0.9	BDL	0.3	BDL
Potassium	mg/L	10	642	630	519	845	625
Sodium	mg/L	5	41,000	36,300	40,500	34,100	39,300
Zinc	mg/L	0.2	BDL	0.3	BDL	0.7	BDL

Table A5. Results for Produced Water Collected at HFTS Well 7SU at 0-14 Days.

Parameter	Units	Det. Limit	Results (On Days Following Initiation of Flowback Release)			
			0-Day	1-Day	5-Day	14-Day
General						
pH	-	-	6.62	6.55	6.39	6.27

Total Dissolved Solids (TDS)	mg/L	10	93,400	96,700	97,000	102,000
Conductivity	µS/cm	5	50,200	50,600	51,100	49,200
Alkalinity	mg/L	1	445	371	481	396
Organics						
Total Organic C	mg/L	0.2	6.8	23	23	0.94
Total Petroleum Hydrocarbons	mg/L	0.5	63	25	190	190
Benzene	mg/L	0.0073	3.9	3	1.7	0.084
Toluene	mg/L	0.0076	5.2	3.6	1.2	0.69
Ethylbenzene	mg/L	0.0091	1.1	0.7	0.14	0.083
Xylenes	mg/L	0.011	4.6	2.5	0.57	0.031
Anions						
Chloride	mg/L	500	51,000	53,300	54,600	56,100
Nitrate	mg/L	3	37.2	36.6	35.4	BDL
Sulfate	mg/L	5	448	443	441	297
Sulfide	mg/L	1	BDL	BDL	BDL	BDL
Cations						
Arsenic	mg/L	1	BDL	BDL	BDL	BDL
Barium	mg/L	0.05	1.7	1.7	1.8	1.9
Boron	mg/L	0.5	36.2	36.3	38.1	29.5
Cadmium	mg/L	0.1	BDL	BDL	BDL	BDL
Calcium	mg/L	10	1,940	1,990	2,070	1,990
Chromium	mg/L	0.3	BDL	BDL	BDL	BDL
Copper	mg/L	0.2	BDL	BDL	BDL	BDL
Iron	mg/L	0.5	65.7	57.1	153	158
Lead	mg/L	1	BDL	BDL	BDL	BDL
Magnesium	mg/L	10	322	336	348	333
Manganese	mg/L	0.1	1	1	2.1	2
Nickel	mg/L	0.3	BDL	BDL	BDL	BDL
Potassium	mg/L	10	439	465	503	618
Sodium	mg/L	5	29,400	32,300	38,500	39.4
Zinc	mg/L	0.2	0.7	BDL	0.8	BDL

Table A6. Results for Produced Water Collected from HFTS Well 7SU at 36-550 Days.

Parameter	Units	Det. Limit	Results (On Days Following Initiation of Flowback Release)				
			36-Day	90-Day	210-Day	365-Day	550-Day
General							
pH	-	-	6.46	6.44	6.36	7.36	6.26
Total Dissolved Solids (TDS)	mg/L	10	112,000	118,000	118,000	970*	117,500
Conductivity	µS/cm	5	40,900	81,100	84,400	2280*	73,500
Alkalinity	mg/L	1	475	524	564	493	415
Organics							
Total Organic Carbon	mg/L	0.2	1.6	1.4	1.0	3.867	0.5

Total Petroleum Hydrocarbons	mg/L	0.5	220	250	87.7	3.8	808
Benzene	mg/L	0.0073	1.6	1.8	3.4	7.4	0.49
Toluene	mg/L	0.0076	1.3	1.2	1.7	3.8	3.3
Ethylbenzene	mg/L	0.0091	0.18	0.11	0.13	0.29	0.44
Xylenes	mg/L	0.011	0.65	0.37	0.44	0.98	1.4
Anions							
Chloride	mg/L	500	63,600	68,000	69,200	618*	34,000
Nitrate	mg/L	3	35.3	BDL	43.2	BDL	BDL
Sulfate	mg/L	5	394	321	246	0.6*	279
Sulfide	mg/L	1	BDL	BDL	BDL	BDL	BDL
Cations							
Arsenic	mg/L	1	BDL	BDL	BDL	BDL	BDL
Barium	mg/L	0.05	1.8	0.8	2.0	0.5	2.1
Boron	mg/L	0.5	31.7	41.5	41.1	BDL	51.9
Cadmium	mg/L	0.1	BDL	0.2	BDL	BDL	BDL
Calcium	mg/L	10	2,130	2,040	2,010	18.6*	2,080
Chromium	mg/L	0.3	BDL	BDL	BDL	BDL	BDL
Copper	mg/L	0.2	BDL	0.1	BDL	BDL	0.3
Iron	mg/L	0.5	171	159	156	15.0	78.3
Lead	mg/L	1	BDL	BDL	BDL	BDL	BDL
Magnesium	mg/L	10	359	336	330	3.2	355
Manganese	mg/L	0.1	2.4	5.1	3.6	0.1	1.8
Nickel	mg/L	0.3	BDL	1	BDL	BDL	BDL
Potassium	mg/L	10	638	608	511	5.8	565
Sodium	mg/L	5	39,400	33,100	34,900	311*	36,800
Zinc	mg/L	0.2	0.2	0.3	BDL	BDL	BDL

Appendix B: Relative Abundance of Dominant Phylotypes in HFTS Water Samples

Table B1: Relative abundance of dominant phylotypes in Poseidon water samples

	POS 1	POS 2	POS 3	POS 4	POS 5
Methanothermococcus	0.001	0.007	0.001	0.003	0.000
Halanaerobium	3.610	2.700	1.099	0.585	0.617
Roseovarius	25.730	53.454	58.456	36.626	44.054
Arcobacter	39.149	21.923	27.682	52.506	39.191
Thermoanaerobacter	0.003	0.003	0.006	0.006	0.004
Pseudoalteromonas	0.001	0.003	0.000	0.001	0.002
SRB	5.319	3.070	1.245	2.101	1.124
Pseudomonas	0.008	0.088	0.001	0.003	0.002
Alteromondaceae	16.210	12.552	7.791	5.796	11.862
Psychrobacter	0.004	0.001	0.000	0.000	0.002
Halomonas	4.926	3.063	2.100	0.882	0.962
Deferribacteraceae	0.065	0.034	0.026	0.025	0.018
Methanohalophilus	0.055	0.037	0.012	0.089	0.043
Thermotogaceae	0.450	0.359	0.158	0.128	0.102
Shewanella	0.000	0.000	0.000	0.000	0.000

Clostridiales	0.050	0.032	0.021	0.010	0.045
Synergistetes	0.017	0.015	0.004	0.009	0.004
Vibrio	0.001	0.000	0.000	0.000	0.002
Anaerophaga	0.064	0.311	0.145	0.022	0.005
Spirochaetes	0.188	0.115	0.105	0.104	0.290
Xanthomonadales	0.002	0.001	0.000	0.000	0.001
Thermococcus	0.000	0.000	0.000	0.000	0.000
Archaeoglobaceae	0.000	0.000	0.000	0.000	0.000
Sphingobacteriales	0.034	0.073	0.068	0.025	0.526
Other	4.113	2.159	1.080	1.077	1.142
BA qPCR	1.49E+07	1.08E+08	8.64E+07	8.61E+07	3.75E+07

Table B2: Relative abundance of dominant phylotypes in injection water samples.

	4SU IW 2	**4SU IW 3**	**4SU DW**	**7SU IW 2**	**7SU IW 3**	**7SU DW**	**6SM IW 2**	**6SM IW 3**	**6SM DW**
Methanothermococcus	0.002	0.001	0.002	0.003	0.002	0.000	0.002	0.000	0.001
Halanaerobium	0.683	0.918	0.035	5.916	0.017	0.003	0.567	0.140	0.023
Roseovarius	28.073	55.674	7.340	30.156	22.059	0.004	9.864	13.664	0.471
Arcobacter	43.712	30.176	0.503	19.732	0.098	84.870	16.480	1.263	0.273
Thermoanaerobacter	0.003	0.003	0.015	0.001	0.006	0.097	0.017	0.001	0.004
Pseudoalteromonas	0.002	0.003	41.836	0.007	25.777	0.001	0.010	0.179	29.518
SRB	1.763	1.016	0.058	6.537	0.045	0.005	1.890	0.137	0.116
Pseudomonas	1.438	0.874	3.140	0.043	8.288	0.407	34.108	83.074	0.607
Alteromondaceae	3.954	7.508	0.401	16.651	0.059	0.058	4.561	0.272	0.047
Psychrobacter	0.015	0.006	2.969	0.095	38.210	0.005	0.552	0.002	55.257
Halomonas	18.274	1.188	0.344	12.804	0.146	0.005	1.487	0.151	1.500
Deferribacteraceae	0.016	0.028	0.002	0.043	0.001	0.000	0.032	0.003	0.001
Methanohalophilus	0.020	0.009	0.002	0.043	0.000	0.000	0.062	0.000	0.006
Thermotogaceae	0.083	0.087	0.003	0.811	0.006	0.000	0.434	0.057	0.001
Shewanella	0.020	0.002	32.707	0.000	0.002	1.217	0.031	0.000	8.351
Clostridiales	0.011	0.036	0.002	0.032	0.000	0.000	0.252	0.003	0.004
Synergistetes	0.016	0.010	0.001	0.019	0.001	0.007	0.012	0.002	0.002
Vibrio	0.002	0.001	0.041	0.011	0.000	13.238	0.115	0.000	0.002
Anaerophaga	0.020	0.006	0.001	0.131	0.024	0.000	0.070	0.052	0.000
Spirochaetes	0.098	0.216	0.014	0.132	0.005	0.000	0.047	0.006	0.001
Xanthomonadales	0.001	0.001	3.160	0.026	0.019	0.055	0.195	0.104	0.446
Thermococcus	0.000	0.000	0.000	0.000	0.000	0.000	0.000	0.000	0.000
Archaeoglobaceae	0.001	0.000	0.000	0.000	0.000	0.000	0.000	0.000	0.000
Sphingobacteriales	0.025	0.522	0.047	0.121	0.001	0.000	1.430	0.019	0.011
Other	1.770	1.717	7.375	6.684	5.234	0.027	27.782	0.870	3.360
BA qPCR	1.29E+06	1.63E+06	4.87E+07	4.43E+04	2.28E+07	9.84E+06	2.05E+04	4.72E+07	3.40E+07

Table B3a: Relative abundance of dominant phylotypes in Produced Water samples.

	4SU PW0	4SU PW01	4SU PW06	4SU PW14	4SU PW36	4SU PW90	4SU PW210	4SU PW365	6SM PW0	6SM PW01	6SM PW06
Methanothermococcus	21.667	77.119	8.359	79.063	40.130	42.749	60.679	1.465	14.355	1.327	16.153
Halanaerobium	0.018	0.082	0.012	0.049	58.034	45.909	11.437	42.725	0.020	0.604	1.117
Roseovarius	1.477	0.061	0.344	0.049	0.032	0.006	0.002	0.006	0.215	0.023	0.125
Arcobacter	1.913	0.123	0.239	0.197	0.055	0.050	0.008	0.009	1.628	2.672	2.374
Thermoanaerobacter	32.148	3.543	29.113	3.264	0.029	0.006	0.018	0.004	36.782	5.396	52.222
Pseudoalteromonas	0.063	0.010	0.006	0.025	0.003	0.001	0.002	0.004	0.297	84.847	0.088
SRB	0.394	2.573	0.975	2.378	0.438	3.678	14.173	15.298	0.388	0.016	0.347
Pseudomonas	0.074	0.010	0.020	0.008	0.134	0.000	0.006	0.001	0.814	0.060	0.153
Alteromondaceae	1.339	1.327	0.151	2.493	0.005	0.010	0.004	0.001	0.345	0.656	0.298
Psychrobacter	0.346	0.020	0.048	0.000	0.001	0.000	0.000	0.001	0.101	0.027	0.175
Halomonas	0.982	0.031	0.059	0.000	0.001	0.003	0.000	0.001	28.355	0.069	0.050
Deferribacteraceae	1.775	8.679	48.767	6.946	0.004	0.011	0.472	0.003	0.000	0.000	0.188
Methanohalophilus	0.003	0.000	0.000	0.000	0.001	0.000	2.079	25.596	0.000	0.000	0.000
Thermotogaceae	0.301	0.010	0.050	0.008	0.634	0.001	1.440	2.275	0.632	0.072	0.316
Shewanella	0.982	0.041	0.126	0.041	0.001	0.031	0.000	0.000	0.199	0.805	0.900
Clostridiales	0.321	2.318	0.889	2.296	0.007	10.075	6.604	4.243	0.264	0.000	0.002
Synergistetes	1.012	2.777	6.353	2.075	0.265	0.392	1.358	0.031	7.620	0.078	1.488
Vibrio	6.442	0.153	0.630	0.230	0.000	0.096	0.002	0.001	0.842	2.392	5.152
Anaerophaga	0.003	0.000	0.000	0.000	0.001	0.000	0.164	0.148	0.000	0.000	0.000
Spirochaetes	0.001	0.000	0.000	0.000	0.000	0.000	1.532	2.346	0.000	0.000	0.000
Xanthomonadales	10.033	0.102	1.771	0.254	0.000	0.001	0.006	0.001	1.293	0.386	2.380
Thermococcus	0.499	0.235	1.368	0.205	0.005	0.001	0.014	0.000	2.242	0.137	9.742
Archaeoglobaceae	0.273	0.265	0.597	0.172	0.005	0.029	0.220	0.002	1.808	0.048	3.350
Sphingobacteriales	0.047	0.000	0.005	0.000	0.000	0.000	0.271	2.874	0.007	0.001	0.005
Other	17.887	0.521	0.118	0.246	0.213	0.000	0.000	2.966	1.794	0.383	3.375
BA qPCR	1.1E+05	5.6E+07	8.0E+05	4.2E+07	3.0E+06	2.6E+07	1.0E+04	2.5E+06	1.2E+05	8.6E+06	7.3E+05

Table B3b: Relative abundance of dominant phylotypes in Produced Water samples.

	6SM PW14	6SM PW36	6SM PW90	6SM PW210	6SM PW365	7SU PW07	7SU PW14	7SU PW36	7SU PW90	7SU PW210	7SU PW365
Methanothermococcus	29.592	38.613	21.156	8.318	0.303	93.074	18.335	60.836	6.128	18.704	0.097
Halanaerobium	0.578	59.856	46.670	60.184	17.065	0.043	75.095	32.791	71.963	75.164	15.427
Roseovarius	0.049	0.009	0.004	0.002	0.003	0.008	0.001	0.003	0.000	0.017	0.001
Arcobacter	17.688	0.044	0.031	0.007	0.005	0.140	0.024	0.364	0.012	0.008	0.010
Thermoanaerobacter	36.684	0.030	0.012	0.002	0.010	3.621	0.659	0.281	0.118	0.022	12.134
Pseudoalteromonas	0.016	0.001	0.008	0.002	0.004	0.581	0.000	0.001	0.001	0.000	0.001
SRB	0.078	0.265	8.515	23.547	22.575	0.083	0.009	0.124	15.555	4.431	13.414
Pseudomonas	0.545	0.097	0.019	0.000	0.001	0.006	0.003	0.006	0.001	0.061	0.002
Alteromondaceae	0.070	0.003	0.008	0.009	0.001	0.121	0.001	0.004	0.002	0.005	0.003
Psychrobacter	0.137	0.001	0.005	0.002	0.001	0.097	0.001	0.006	0.001	0.002	0.002
Halomonas	0.008	0.000	0.003	0.004	0.001	0.017	0.001	0.000	0.000	0.000	0.001
Deferribacteraceae	0.102	0.003	0.004	0.009	0.362	0.001	0.000	0.000	0.000	0.000	2.426
Methanohalophilus	0.000	0.003	8.744	3.652	23.680	0.000	0.000	0.007	2.523	1.303	0.972
Thermotogaceae	6.811	0.663	2.518	0.703	3.019	0.006	0.004	0.010	0.000	0.041	30.089
Shewanella	0.255	0.000	0.004	0.000	0.000	0.026	0.001	0.063	0.009	0.000	0.001
Clostridiales	0.016	0.013	11.070	0.860	4.489	0.074	0.013	0.077	0.005	0.000	0.774
Synergistetes	0.568	0.257	0.546	0.370	1.735	1.310	5.438	3.219	2.846	0.019	0.025
Vibrio	0.659	0.000	0.000	0.001	0.001	0.183	0.036	1.292	0.086	0.000	0.001
Anaerophaga	0.001	0.000	0.317	0.870	0.131	0.000	0.000	0.000	0.000	0.000	21.629
Spirochaetes	0.001	0.000	0.001	0.069	16.808	0.000	0.000	0.000	0.000	0.000	0.308
Xanthomonadales	1.256	0.002	0.044	0.000	0.001	0.032	0.006	0.205	0.072	0.000	0.001
Thermococcus	1.652	0.005	0.009	0.047	0.027	0.094	0.021	0.030	0.008	0.008	0.000
Archaeoglobaceae	0.443	0.002	0.010	0.028	0.015	0.118	0.020	0.097	0.246	0.047	0.003
Sphingobacteriales	0.073	0.000	0.000	0.000	1.253	0.000	0.000	0.001	0.002	0.000	0.000
Other	2.717	0.133	0.303	1.313	8.510	0.364	0.330	0.582	0.421	0.167	2.680
BA qPCR	5.9E+05	1.3E+08	2.0E+07	1.3E+05	2.2E+04	5.6E+05	1.5E+06	2.6E+07	8.8E+05	5.3E+04	3.1E+05

Appendix H: Impact of Stress Shadowing and Reservoir Heterogeneity on the Propagation of Complex Fractures: Comparison with Field Data

Research Entity: The University of Texas at Austin

Final Report Fracture Simulation, June 30, 2017

Prepared by Mukul M. Sharma

Disclaimer

"This report was prepared as an account of work sponsored by an agency of the United States Government. Neither the United States Government nor any agency thereof, nor any of their employees, makes any warranty, express or implied, or assumes any legal liability or responsibility for the accuracy, completeness, or usefulness of any information, apparatus, product, or process disclosed, or represents that its use would not infringe privately owned rights. Reference herein to any specific commercial product, process, or service by trade name, trademark, manufacturer, or otherwise does not necessarily constitute or imply its endorsement, recommendation, or favoring by the United States Government or any agency thereof. The views and opinions of authors expressed herein do not necessarily state or reflect those of the United States Government or any agency thereof."

Abstract

The large volume of log, core and fracturing data collected in the Hydraulic Fracturing Test Site (HFTS) was analyzed using models for fracture propagation and fracture interference due to stress shadowing. Such data integration and modeling are essential if the results of the HFTS are going to the generalized and applied in other field locations. Three types of models were used to analyze the data and to compare the model results with field observations.

An analysis of the cores analyzed from the cored well (adjacent to the hydraulically fractured well) showed a very complex network of fractures had been generated in each stage. A few of these fractures had evidence of proppant in them. However, most of the fractures showed no indication of proppant. These were characterized as activated natural fractures or induced unpropped fractures. The data also indicated a higher density of fractures near the heel of the frac stage.

The proppant distribution into the different clusters for Stage 23 in well 6SU (the stage closest to the cored well) was simulated using a coupled wellbore-fracture model that had been developed earlier (PROPP-P). Results from this model show that the primary reason for the heel dominated fractures observed in the HFTS wells (and in other horizontal wells) is the inertia of the proppant particles. This leads to very high proppant concentrations towards the toe of the well. Ultimately this leads to a screen out of the toe-side clusters. This results in most of the fluid and proppant going into the heel-side clusters as seen in the core data.

The stress distribution and stress interference effects caused by both the mechanical opening of the fractures and pore pressure effects around fractures in a single stage were computed based on models developed at the University of Texas. Fracture propagation models for both planar (EFRAC) and non-planar complex fractures (MULTI-FRAC) were used to compute the fracture width and fracture complexity for the 6SU well. The effects of stress interference were clearly visible as three fractures propagated from the three perforation clusters. These finite element and finite volume models propagate fractures while solving for the stresses and strains everywhere in the rock. They have a difficult time dealing with natural fractures and heterogeneity.

A Peridynamics based model was attempted next. Such models have been found to handle heterogeneity very well. However, due to the long run times they have only a limited ability to

deal with large scale rock heterogeneity and intersecting planes of weakness in the rock at the length scale of the pad. The geo-mechanical model results were compared with the results from core data and microseismic measurements, to see if these different data sets can be reconciled. It was clear from these results that the fracture geometry generated in the field was much more complex than that obtained from the simulations. There were a lot more induced unpropped fractures in the core than were predicted by the model.

This data set clearly shows that for highly naturally fractured formations such as the Wolfcamp, traditional hydraulic fracture models based on finite volume or finite elements solutions are not adequate. A follow-up study to simulate the observed complex fracture geometry was proposed. This model (MULTI-FRAC-NF) is designed to deal with highly naturally fractured rock formations where thousands of natural fractures may exist in the simulation domain.

Finally, the water hammer fracture signatures from the HFTS site were analyzed to see if some fracture diagnostics could be performed from simulating the water hammer signature. Results from this analysis indicate that this analysis provides a very reasonable estimate of the fracture geometry.

Introduction

Reducing the high cost associated with drilling and completing long laterals with many hydraulic fractures requires us to better understand and model the geometry of these fractures for a better description of the stimulated rock volume (SRV) around the wellbore. Significant questions remain about what the optimum spacing of the laterals should be as well as the optimum spacing between fracture stages and between perforation clusters[2–5]. The inability to conduct such an analysis stems from the difficulty in determining, with any degree of certainty, the geometry of the fractures created through multiple clusters and multiple stages along the lateral. It is estimated that more efficient reservoir drainage could potentially reduce well costs by up to 25%[2,6].

Recent studies using micro-seismic monitoring have shown that in many instances the geometry of hydraulic fractures can be much more complicated than the single planar geometry that has been historically assumed. A picture is now emerging of a region around the wellbore, the stimulated rock volume (SRV), in which multiple complex fractures propagate from each of the perforation clusters that results in a much more complex pattern of fractures. The physics of how such a complex pattern of fractures is created is far from clear as is our ability to model such complex fracture patterns.

To address the relatively high cost of these wells, it is essential for us to first be able to model the stimulated rock volume (SRV) and understand the primary factors that control its creation and its properties. This study aims to develop models that, for the first time, allow us to model the propagation of multiple, non-planar competing fractures in shales. This will be accomplished by modifying a new mathematical method that is well suited to modeling fracture propagation. The method called peridynamics[15–18], will allow arbitrarily complex fracture geometries to be modeled in 3-dimensions and will allow for the growth of competing and interacting fractures in naturally fractured media.

No current models exist for modeling the propagation and performance of simultaneous multiple fractures in horizontal wells in naturally fractured formations. While many finite element studies have focused on modeling the propagation of planar fractures in shales, these studies are unable to deal with multiple, non-planar fractures. The collection of field data to physically observe the geometry of the propped fractures in a test well provides a unique opportunity to compare recent models we have developed with such observations.

Finally, fracture trajectories and complexity obtained from the model for the stages in the well next to the cored well will be modeled and compared with the best estimates from the field. Regions of high propped fracture complexity and regions of high microseismic activity were predicted from the model and compared to the field data. For example, stimulated regions that have a lower horizontal stress contrast are likely to have higher propped fracture complexity. The model predictions of the propped fracture complexity locations (lower horizontal stress contrast locations) can be correlated to the production estimates from the DTS data and the produced chemical tracer concentrations. The effect of the number of active clusters per stage in the fractured well and the fracture spacing and well spacing were assessed both from the data and the model.

The primary objective of this research is to compare results from a new generation of hydraulic fracturing models, that allow us to model multiple, non-planar, competing fractures in heterogeneous shales with direct observations of fracture geometry in the field.

Preparation and analysis of field core data

Introduction

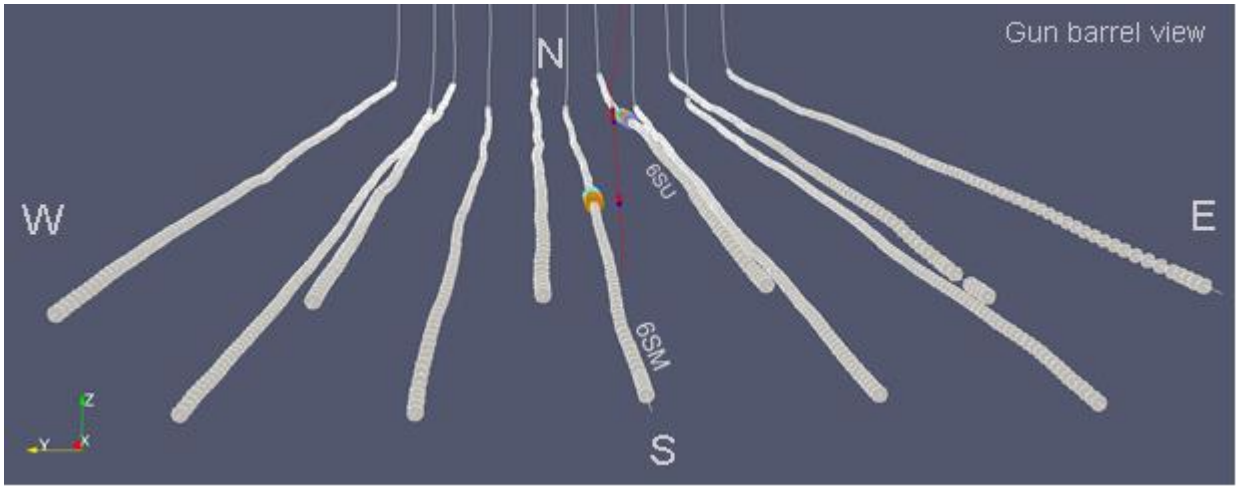


Fig. 2.1. Gun barrel view of wells, cores, and perforation clusters in the Hydraulic Fracturing Test Site. Red line indicates the wellbore of Sugg A 171 6TW slant well where 6 cores were taken for the systematic core description.

We have visualized and analyzed the core description data which BEG has completed for six cores from the well Sugg A 171 6TW. This slant coring well has 4 cores (Cores 1 to 4) located in Upper Wolfcamp with the MD range of 9276–9717 ft, and 2 cores (Cores 5 and 6) in Mid Wolfcamp with the MD range of 11525–11685 ft. Core description contains information of type, number, location and orientation of fractures, morphology and features of fracture faces, and so on. Cores 1 to 4 contains fractures mainly propagated from the well Sugg A 171 6SU, and Cores 5 and 6 contains fractures from the well Sugg A 171 6SM.

We used the type (origin), dip and dip direction of fractures described in BEG core description datasheet, and visualized orientations/types of fractures along with wellbores, and perforation clusters in the field-scale 3-dimensional space. The number densities and orientations of fractures indicated that hydraulically created fractures are significantly bifurcating and splitting over the course of fracture treatment. It also showed that many natural fractures are also reactivated along with the hydraulic fractures. The difference in fracture densities from toe to heel also indicated the nature of stage-wise fracture treatment and fluid/proppant transport in the wellbore and in the clusters of perforations.

Objectives

By visualizing the core descriptions, we intend to understand the primary origins of fractures in terms of hydraulic, natural, and reactivated natural fractures. The density of individual types of fractures along the core depths, and dominant orientations of each fracture type over the relative locations of cores to the fracturing wells/stages/clusters are an important component for understanding (by visualization) the complex core description data obtained. This information helps us understanding the impact of the natural fracture network, stress interference, fracture reorientation during stimulation and transport of fluid/proppant in the wellbore. Various simulation results from different models, e.g., 3-dimensional compositional fracture model, multiple fracturing model coupled with reservoir geomechanics, displacement-discontinuity method, can be benchmarked with this 3-D visualization from systematic core descriptions based on actual field observations.

Methods

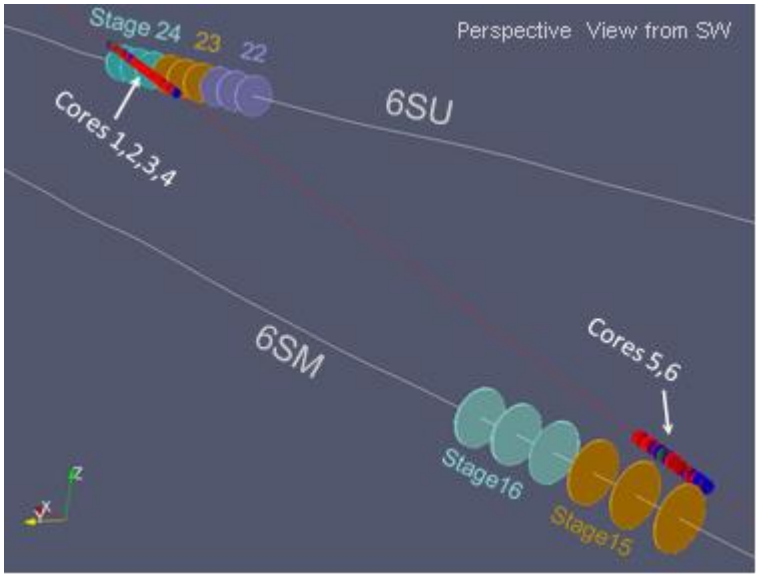


Fig. 2.2. Perspective view of wells Sugg A 171 6SU, 6SM and 6TW (red line).

The systematic core description and core analysis data (prepared by BEG and Core Labs) contains fracture depth/numbers, fracture orientation, fracture tip/termination types, morphology/fracture surface features, apertures, fill, faults, and fracture origin (type). We have taken the fracture location in measured depth (MD), fracture dip angle, dip direction, fracture origin from the raw datasheet. Fractures induced by drilling, coring, or handling process were ignored to distinguish from intact natural fractures (N), reactivated natural fractures (NR), and hydraulically induced fractures (HF) only.

Once other types of fractures are filtered out, only the fractures (N, NR and HF) are visualized as circles with their dip and dip directions at their corresponding measured depth. To better understand the spatial location of fractures relative to their initiation points (perforation clusters), the well trajectories of the slant cored well 6TW (red line in Fig. 2.2) as well as those of 6SU and 6SM wells were taken from the latest well survey results. The adjacently located perforation clusters were also visualized by a large disk with different colors for each treatment stage. Three perforation clusters per stage were placed in the fracturing wells. Each perforation clusters have a density of 6 perforation shots per ft with a cluster length of 2.5 ft. For cores 1 to 4, stages 23 and 24 of the well Sugg A 171 6SU are most adjacently located, and stages 15 and 16 of well 6SM were close to cores 5 and 6 as in Fig. 2.2.

Presentation of Core Data – Cores 1 to 4

Cores 1 to 4 are in the range of 9276 to 9717 ft MD in the slant well Sugg A 171 6TW. The distance between cores and adjacent 6SU wellbore is approximately 100 ft. In Fig. 3, three perforation clusters from stage 23 and two toe-side perforation clusters from stage 24 of 6SU well are closely located. Fractures described in cores 1 to 4 are the fracture treatments mainly from those clusters. In Fig. 2.3 to 3.5, the individual fractures are shown as circles with different colors. Red circles represent hydraulic fractures (HF), blue circles are intact natural fractures (N), and green circles are natural fractures reactivated during fracture treatment (NR). They are drawn in orientations from core descriptions. Fig. 2.4 shows fractures in a map view, and Fig. 2.5 shows them in a side view from the West.

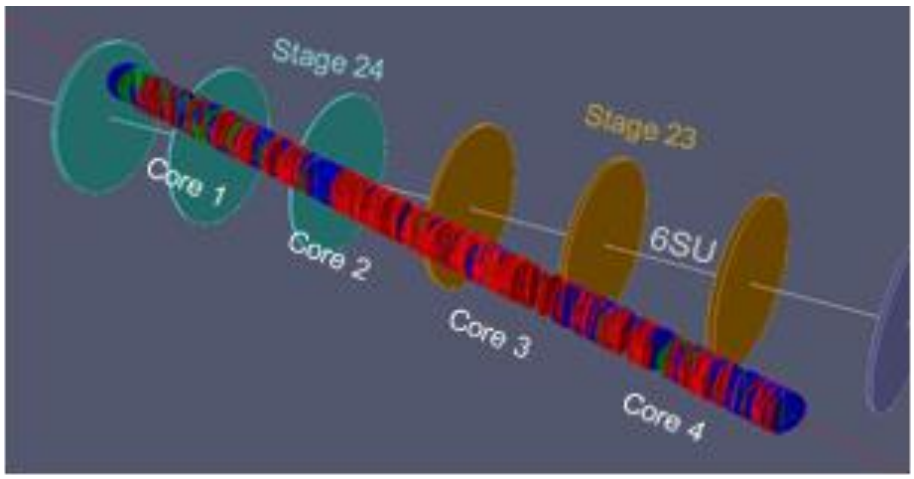


Fig. 2.3. Perspective view of fractures in cores 1 to 4 from southwest. Large circles are centered at locations of perforation cluster from stages 23 and 24 of well Sugg A 171 6SU.

The number of fractures in cores 1 to 4 are 298, 132, 66 respectively for HF, N, and NR. When compared with the limited length (2.5 ft) of the perforation clusters and considering the distance from the treatment well, it is evident that fractures have bifurcated and split repeatedly to create a very large number of fractures that ultimately make up the stimulated rock volume. In the visualized fracture orientations, the dip angle is very close to vertical plane for all types of fractures. The direction of dip, however, shows different trends between hydraulic fractures and natural fractures (intact or reactivated). Hydraulic fractures are largely in the East-West direction, while the natural fractures are trending in NE-SW and WNW-ESE directions. The fracture orientations from the BEG core description results can be visually seen in Fig. 2.4.

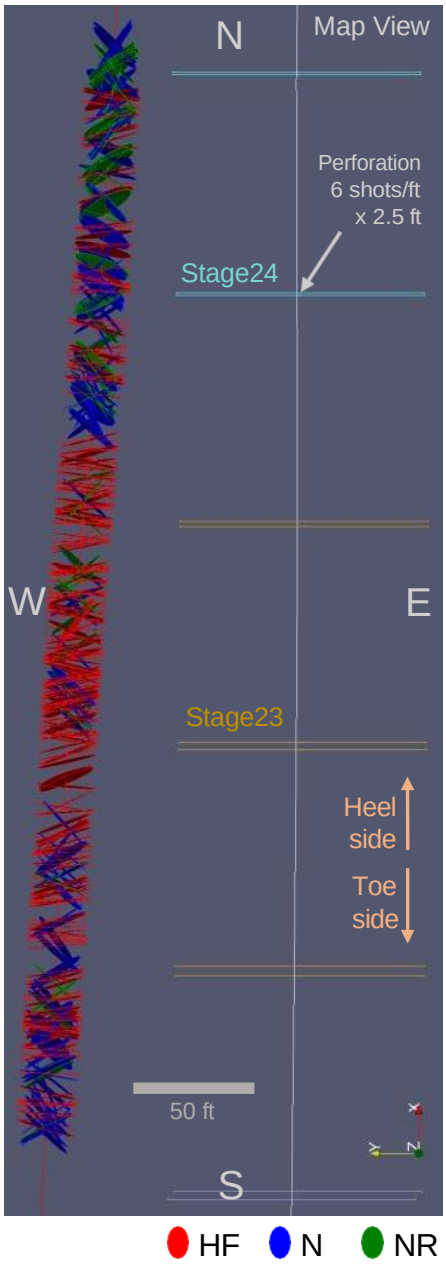


Fig. 2.4. Map view of fractures in cores 1 to 4 with well 6SU.

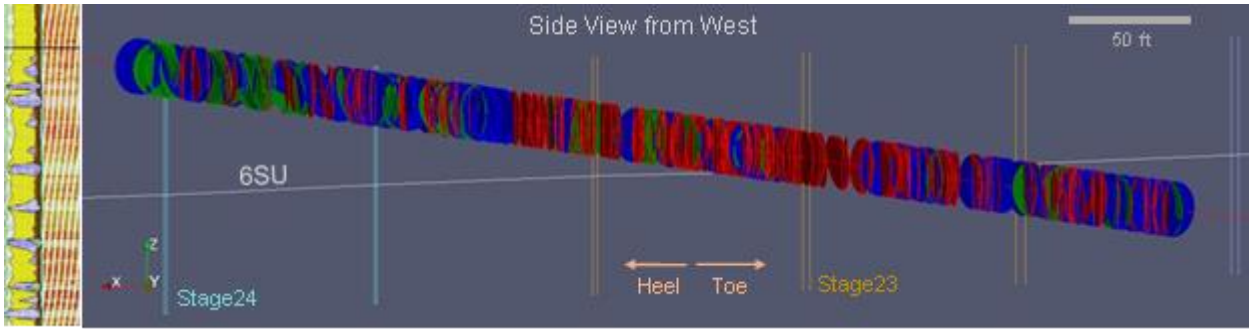


Fig. 2.5. Side view of fractures in cores 1 to 4. The viewpoint is from West. Lithology logs and borehole image logs are compared for reference purpose. Color codes for fracture types are HF: hydraulic fractures, N: intact natural fractures, and NR: natural fractures reactivated.

Presentation of Core Data – Cores 5 and 6

Cores 5 and 6 are in the measured depth range of 11528 to 11684 ft MD in the slant well Sugg A 171 6TW. The distance between cores and adjacent well Sugg A 171 6SM is approximately 125 ft,

which is slightly farther than the distance between 6SU and cores 1 to 4. In Fig. 2.6, two heel-side perforation clusters from stage 15 of 6SM well are the closely located. Fractures observed in cores 5 and 6 are the fracture treatments mainly from those clusters. In Fig. 2.6 to 3.8, the individual fractures are shown as circles with different colors. Color codes are the same as previous figures. Fig. 2.7 shows fractures in a map view, and Fig. 2.8 shows them in a side view from West.

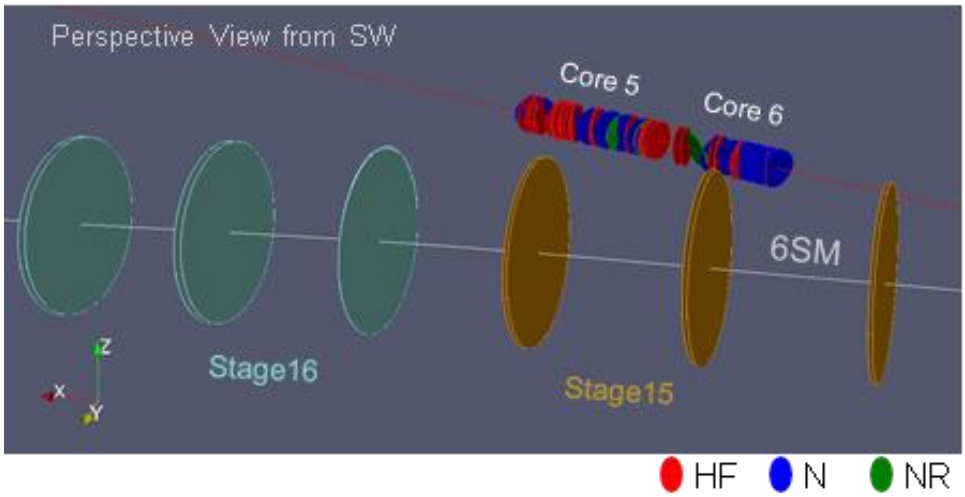


Fig. 2.6. Perspective view of fractures in cores 1 to 4 from southwest. Large circles are centered at locations of perforation cluster from stages 23 and 24 of well Sugg A 171 6SU.

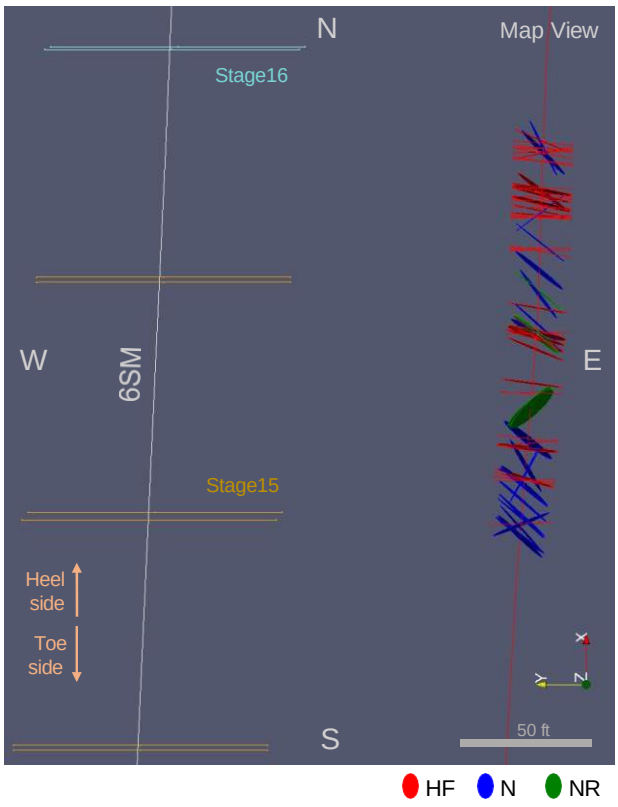


Fig. 2.7. Map view of fractures in cores 1 to 4 with well 6SU.

The number of fractures in cores 5 and 6 are 54, 26 and 8 respectively for HF, N, and NR. As in the previous cores, the large number of fractures observed in the core seems to indicate that many additional fractures have been created by the growth of the main hydraulic fractures. Similar trends in the fracture orientations are observed in cores 5 and 6. The dip angle is very

close to vertical plane for all types of fractures again. The direction of dip also shows similar trends. Hydraulic fractures are largely in East-West direction, but natural fractures are trending in primarily WNW-ESE directions. Dip directions in NE-SW are less frequently observed in Middle Wolfcamp cores. The fracture orientations in BEG core description results can be visually seen in Fig. 2.6 to 3.8.

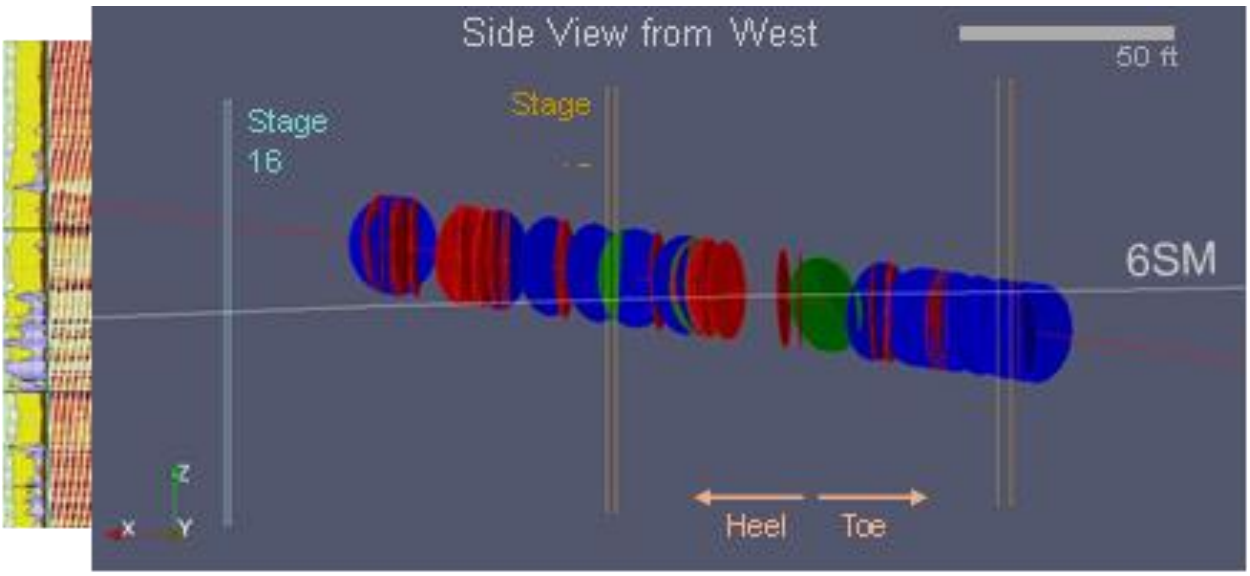


Fig. 2.8. Side view of fractures in cores 1 to 4. The viewpoint is from west. Lithology logs and borehole image logs are compared for reference purpose. Color codes for fracture types are HF: hydraulic fractures, N: (intact) natural fractures, NR: natural fractures reactivated.

Analysis of Core Data

From the compiled and visualized core description data, we conducted a statistical analysis to better understand how fracture propagation is impacted by the relative spatial locations of stages and clusters. In Fig. 2.9a, fractures are visualized separately for the different fracture types. All types of fractures are mainly in a vertical plane. Horizontal fractures are typically not observed. As a general trend fractures in cores 1 to 4 are trending in the E-W direction indicating direct propagation from the 6SU well with the creation of many new fracture planes. These new fractures may be created by shear failure or activation of natural fractures or the bifurcation and splitting of hydraulic fractures during propagation. Natural fractures including both intact and reactivated fractures show two dominant orientations, the NE-SW and WNW-ESE directions.

Impact of fluid/proppant transport over multiple clusters in a stage. We counted the number of fractures per foot to show the fracture density of different types of fractures over the length of cores 1 to 4 as shown in Fig. 9b. The number of all fractures per unit distance of 10 ft was approximately 11.2. In cores 1 to 4, average fracture densities are 6.7, 3.0, and 1.5 fractures per 10 ft length of MD respectively for hydraulic fractures (HF), intact natural fractures (N), and reactivated natural fractures (NR). In cores 5 and 6, average fracture densities are 3.5, 1.7 and 0.5 fractures per 10 ft length of MD, respectively for HF, N and NR.

The primary trend in the fracture density is that there are more hydraulic fractures at the heel-side cluster of stage 23 compared to toe-side clusters of either stage 23 or subsequent stage 24 as seen in Fig. 9c. This behavior of more fractures close to heel-side clusters than toe-side is a direct observation from actual propagated fractures using a direct core description. There have

been many indirect observations of this preferred fracture stimulations in heel-side of a treatment stage (Wheaton et al., 2016, Ugueto et al., 2016, Haustveit et al., 2017). The primary reason for this heel-side domination is the preferred transport of fluid and proppant into the heel-side cluster. This has been verified by extensive numerical simulation and resulting correlations as well as field observations reported recently. (Wu et al., 2017).

Impact of inter-stage stress interference on natural fracture reactivation.

In Fig. 2.9d, the ratio of reactivated natural fracture (NR) to the total number of pre-existing natural fractures (N and NR) over the length of MD has been shown. The general trend is that the ratio of natural fracture reactivation increases from toe- to heel-side in a stage. The ratio increases from 9700 ft MD (toe-side of stage 23) to 9550 ft MD (heel-side of stage 23) in cores 1 to 4. In the subsequent stage 24, the reactivation ratio becomes small at the toe-side and increases again toward the heel- side of the same stage.

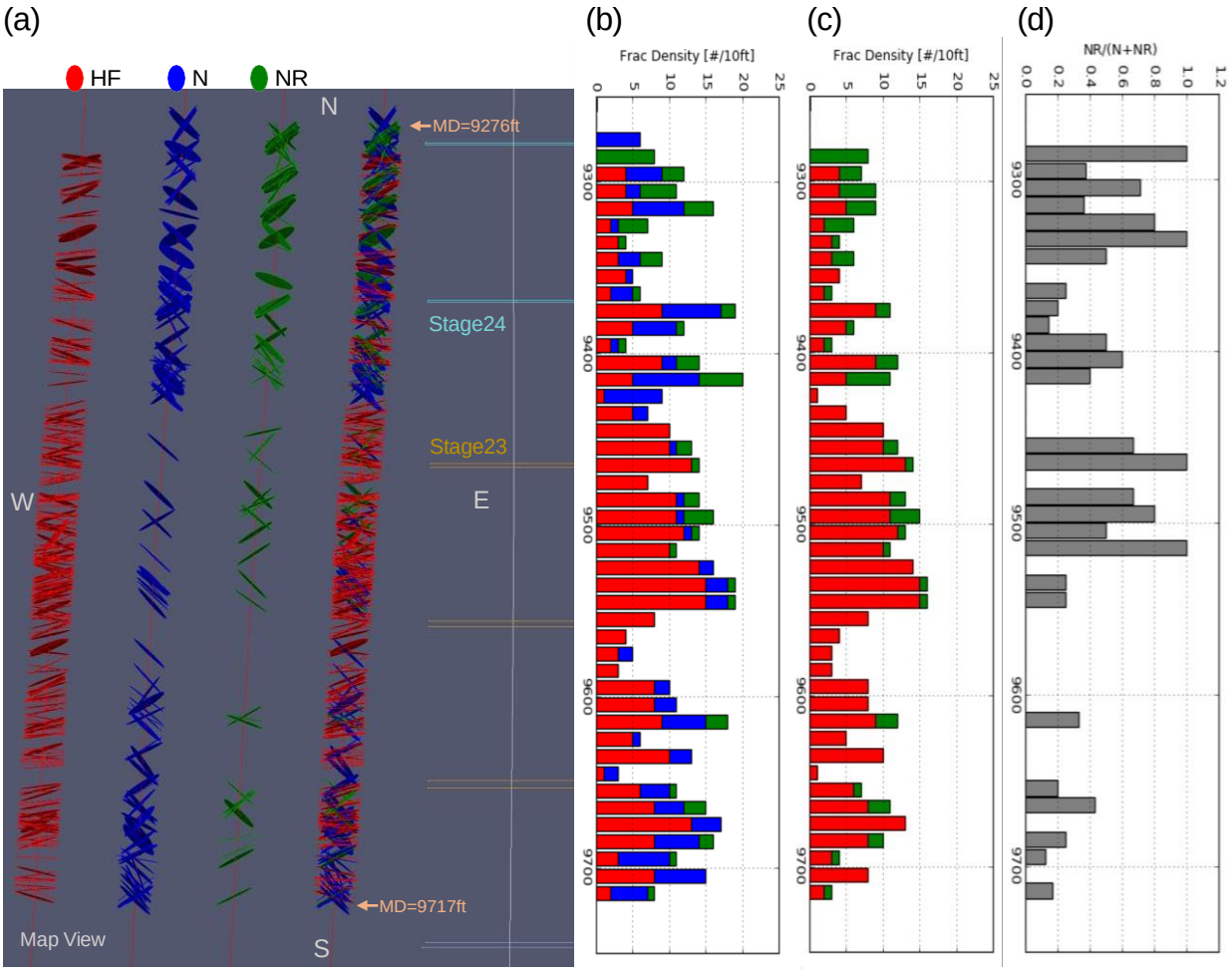


Fig. 2.9. (a) Map view of fractures in cores 1 to 4. From left to right, fractures are shown individually for types of HF, N and NR, and all types are shown together. Each group of fractures are shown separately, but the spatial location of fractures does not represent actual subsurface location. (b) Fracture density by number of fractures per 10 ft. (c) Fracture density by number of fractures per 10 ft. Only HF and NR types are shown to represent the degree of stimulation. (d) Ratio of reactivated natural fractures per total number of initial natural fractures. Vertical axis of plot is measured depth (MD) in feet.

When Stage 23 is pumped and fractures are created/propped, the magnitudes of stress increase in subsequent Stage 24. The stress change is primarily caused by mechanical opening of the fractures in Stage 23. The effect of mechanical opening increases the components of the stress

tensor, however the stress component in the North-South direction increases much more than the East-West stress. As a result, the stress anisotropy increases before fracturing stage 24 due to the stress shadow effect of Stage 23. This increased stress anisotropy at the toe-side of stage 24 results in the natural fractures being less reactivated from 9550 ft MD to 9450 ft MD (smaller reactivation ratio as seen in Fig. 2.9d). As the magnitude of stress shadows decreases towards the heel-side of Stage 24, the reactivation ratio increases.

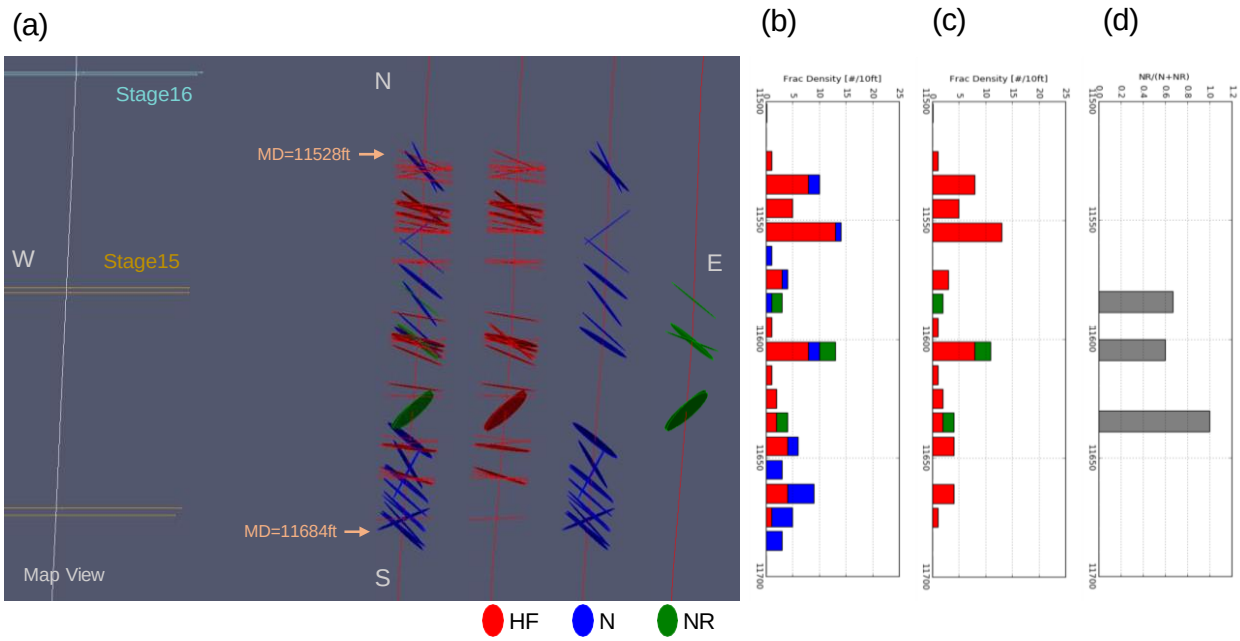


Fig. 2.10. (a) Map view of fractures in cores 5 and 6. From left to right, all types of fractures are shown together, and fractures are shown individually for types of HF, N and NR. Each group of fractures are shown separately, but the spatial location of fractures does not represent actual subsurface location. (b) Fracture density by number of fractures per 10 ft. (c) Fracture density by number of fractures per 10 ft. Only HF and NR types are shown to represent the degree of stimulation. (d) Ratio of reactivated natural fractures per total number of initial natural fractures. Vertical axis of plot is measured depth (MD) in feet.

Conclusion

In this chapter, the core description work conducted by BEG has been visualized and analyzed to help understand the locations and orientations and types of fractures in 3-dimensional space relative to perforation clusters. Considering the limited lengths of each perforation cluster, the high fracture density indicates a substantial degree of natural fracture reactivation and fracture bifurcation and splitting as they interact with bed boundaries and natural fractures during propagation. The unique and different directions of the hydraulic fractures versus the natural fractures shows the relative number of reactivated vs hydraulic fractures. Orientations of natural fractures can be grouped into two main directions of NE-SW and WNW-ESE, and hydraulic fractures are primarily trending in the E-W direction.

Analysis of fracture density revealed that heel-side clusters in a treatment stage show more stimulation in terms of both hydraulic fractures and activated natural fractures. Higher stimulation in the heel-side cluster is likely to be a combined result of fluid/proppant distribution and the inter- stage stress shadow. From the intact and reactivated natural fracture densities, it was also understood that inter-stage stress shadow changes the stress anisotropy leading to a trend in the ratio of reactivated fractures to the total number of natural fractures.

Non-planar Fracture Propagation from Multiple Perforation Clusters in Horizontal Wells

Summary

Increasing the efficiency of completions in horizontal wells is an important concern in the oil and gas industry. To decrease the number of fracturing stages per well it is common practice to use multiple clusters per stage. This is done with the hope that most of the clusters in the stage were effectively stimulated. Diagnostic evidence, however, suggests that in many cases only 1 or 2 clusters out of 4 or 5 clusters in a stage are effectively stimulated.

In this report strategies to maximize the number of effectively stimulated perforation clusters are discussed. A fully 3-D poroelastic model that simulates the propagation of non-planar fractures in heterogeneous media is developed and used to model the propagation of multiple competing, fractures. A parametric study is first conducted to show how important fracture design variables such as limited entry perforations and cluster spacing; and formation parameters such as permeability, lateral and vertical heterogeneity affect the growth of competing fractures. The effect of stress shadowing due to both mechanical and poroelastic effects is accounted for.

3-D numerical simulations have been performed to show the impact of some operational and reservoir parameters on simultaneous competitive fracture propagation. It was found that an increase in stage spacing decreases the stress interference between propagating fractures and increases the number of propagating fractures in a stage. It was also found that an increase in reservoir permeability can decrease the stress interference between propagating fractures because of poroelastic stress changes. A modest (about 25%) variability in reservoir mechanical properties along the wellbore is shown to be enough to alter the number of fractures created in a hydraulic fracturing stage and mask the effects of stress shadowing. Inter-stage fracture simulations show post-shut-in fracture extension induced by stress interference from adjacent propagating fractures. The impact of poro-elasticity is highlighted for infill well fracture design and preferential fracture propagation towards depleted regions is clearly observed in multi-well pad fracture simulations.

The results in this report attempt to provide practitioners with a better understanding of multi-cluster fracturing dynamics. Based on these findings' recommendations are made on how best to design fracture treatments that will not only lead to the successful placement of fluid and proppant in a single fracture, but in a set of fractures that are competing with each other for growth. The ability to successfully stimulate all perforation clusters is shown to be a function of key fracture design parameters.

Introduction

Horizontal wells are completed in stages with each stage having clusters of perforations that serve as initiation points for fractures. Each stage is fractured with the hope of creating fractures from each cluster. However, diagnostic data in the field has shown that in most cases all clusters do not create dominant fractures (Fisher et al. 2004; Miller et al. 2011, Molenaar et al. 2011). Distributed Temperature Sensing (DTS) and Distributed Acoustic Sensing (DAS) data show that about a third of the clusters might not contribute to production, while another third are not effectively stimulated. The increase in the compressive stresses in the vicinity of the fracture can

inhibit fracture growth from nearby perforation clusters (Fisher et al. 2004; Manchanda and Sharma 2014). Some researchers have also concluded that if the perforation clusters were kept very close to each other then there is a possibility of fracture coalescence or longitudinal growth of fractures (Daneshy 2011; Rousell and Sharma 2011, Wong et al. 2013).

Past experimental work has also clearly shown that the perforation cluster spacing influences the fracture growth pattern. When closely spaced multiple fractures were propagated simultaneously, some fractures were much larger than others (El-Rabaa 1982; Abass et al. 1996). It was shown that in some cases one fracture could become the dominant fracture propagating amongst the clusters.

Bunger, Zhang, and Jeffrey (2012) used an analytical model and performed a dimensional analysis to understand the most important parameters that need to be addressed when optimizing multiple fracture growth problems. They investigated the deflection patterns that are generated due to interaction of the fractures with existing fractures. They applied their model to a 2-D fracture growth simulator. In a later paper their model was used to understand the impact of viscosity and toughness dominated regimes on multiple fracture propagation (Ames and Bunger 2015). They used a mathematical model to couple the contribution of fluid flow, rock breakage and perforation pressure drop to the total power requirement for the growth of multiple hydraulic fractures. Their model predicts that when the stage spacing is less than the created fracture height, the probability of multiple fracture growth is small. The fundamental understanding their model provides can be very useful in explaining observations from numerical models.

Many researchers have used the displacement discontinuity method (DDM) to model the stress interference created by hydraulic fractures. Using this method, researchers have attempted to analyze the impact of simultaneous multiple fracture growth (Yamamoto et al. 2004; Min and Ghassemi 2012; Wong et al. 2013; Lecampion and Desroches 2015; Wu and Olson 2015). Several of these methods have been extended to allow for interaction with heterogeneities in the reservoir (Weng et al. 2011; Sesetty and Ghassemi 2012; McClure and Horne 2013; Wu and Olson 2013; McClure et al. 2015). Castonguay et al. (2013) developed a boundary element method for modeling the competitive growth of cracks in an elastic domain. Their model was based on a single fracture model developed earlier (Rungamornrat et al. 2005) and was able to generate three-dimensional growth of competing fractures. DDM does not model the effects of poro-elasticity and is not able to include the effect of heterogeneity in material properties. These effects can play an important role in problems where prior production and pore pressure depletion has occurred.

The finite element method (FEM) can be used as an alternative when the discretization of the reservoir domain is important. Dahi-Taleghani and Olson (2011) have used the extended finite element method (XFEM) for 2D fracture propagation and interaction with existing flaws. Shin and Sharma (2014) also used XFEM to analyze the impact of various factors controlling the simultaneous propagation of multiple competing fractures. Haddad and Sepehrnoori (2014) used a similar method coupled with a cohesive zone model to look at the propagation of 3D competing fractures. The authors showed competitive growth with fracture curving in another publication (Haddad and Sepehrnoori 2015). These models grid the entire reservoir domain and

hence are computationally expensive. Numerical enhancements and efficiency upgrades are necessary for practical simulations.

In this work we look at an alternative method and use finite volume methods (FVM) to model competitive multiple fracture propagation. FVM is considered a simpler, less complex alternative to FEM and allows incorporation of multi-physics system of equations with relative ease (Jasak and Weller 2000, Tang et al. 2015, Tukovic et al. 2012). Reservoir domain discretization using FVM and 2-D single fracture propagation using cohesive zone method has been discussed before (Carolan et al. 2013, Bryant et al. 2015, Lee et al. 2015). In the current work, the application of a new 3-D, non-planar, fracture propagation model that solves a coupled system of equations involving the wellbore fluid compressibility, perforation pressure drop, fluid distribution between simultaneously propagating fractures and the poro-elastic stress changes in the reservoir domain is discussed.

Model Formulation

In the current formulation, Biot's poro-elastic equations are solved in the reservoir domain (Biot 1955). The displacement field variable and the pressure field variable are the system unknowns. The displacement equation (Eq. (1)), conserving momentum, and pressure equation (Eq. (2)), conserving fluid mass, are iteratively coupled, and are solved implicitly to a desired solution tolerance every time-step.

$$\nabla.[G\nabla\mathbf{u} + G(\nabla\mathbf{u})^T + \lambda\mathbf{I}tr(\nabla\mathbf{u})] - \alpha\nabla p\mathbf{I} + \rho\mathbf{f} = 0 \quad (1)$$

$$\nabla.\left(\frac{kM}{\mu}\nabla p\right) = \frac{\partial p}{\partial t} + \alpha M\frac{\partial}{\partial t}(\nabla.\mathbf{u}) \quad (2)$$

These equations and the corresponding fracture propagation model have been discussed, verified, and validated in Bryant et al. (2015), and Lee et al. (2015) for 2-D fracture propagation. In this work, this poro-elastic framework is used to simulate fracture propagation in 3-D including wellbore fluid compressibility, perforation pressure drops and fluid distribution into multiple simultaneously propagating fractures (Manchanda (2015)). The fractures are modeled as a discontinuity (an internal boundary) within the reservoir mesh and a cohesive zone model is used for the fracture propagation criteria. The fracture boundary is dynamically updated during fracture propagation by splitting mesh faces and adding them to the fracture boundary (Cardiff et al. 2015). The fracture is then allowed to propagate along arbitrary trajectories following the faces of the reservoir mesh.

Wellbore Storage

The treatment fluid in the wellbore is assumed to be slightly compressible. The bulk modulus of the fluid is defined as,

$$\kappa = -V\frac{dP}{dV} = -V\frac{\Delta P}{\Delta V} \quad (3)$$

$$\Delta V_w = V_{out} - V_{in} = (Q_{out} - Q_{in})\Delta t \quad (4)$$

$$P_w - P_w^o - \frac{K_f}{V_w}(Q_{in} - Q_{out})\Delta t = 0 \qquad (5)$$

Wellbore storage can be formulated assuming uniform pressure in the wellbore. The pressure drop in the wellbore is ignored here. This is a simplifying assumption to avoid discretizing the wellbore. Perforation Pressure Drop. The pressure drop through a cluster of cylindrical perforations is approximated by the following expression,

$$\Delta P_i^{perf} = P_w - P_i = \frac{\overline{\rho}}{2{\alpha_d}^2 {n_{perfs}}^2 (\pi {r_i}^2)^2} {q_i}^2 = a_i {q_i}^2 \qquad (6)$$

or

$$P_w - P_i - a_i q_i |q_i| = 0 \qquad (7)$$

Flow Distribution into Multiple Fractures. The flow distribution from the fluid exiting the bottom of the well through the perforations into the fractures (assuming fluid incompressibility) can be expressed as,

$$Q_{out} - \sum_{i=1}^{n} q_i = 0 \qquad (8)$$

Using the same definition of bulk modulus shown above, the compliance of the fracture can be simulated. The fluid leak-off and the change in volume of the fracture is included in this formulation. Vic is a constant initial volume that represents the volume associated with the storage in the stage and the initial perforations. The change in volume of a fracture is given as,

$$\Delta V_f = (q_i - q_{L,i} - q_{V,i})\Delta t \qquad (9)$$

$$P_i - P_i^o - \frac{K_f}{(V_i^o + V_i^c)}(q_i - q_{L,i} - q_{V,i})\Delta t = 0 \qquad (10)$$

This gives us a system of 2n + 2 equations with 2n + 2 variables namely, $\boldsymbol{Pw}$, $\boldsymbol{Qout}$, $\boldsymbol{Pi}$, and $\boldsymbol{qi}$. This non-linear system of equations can be solved using a Newton Raphson method to a desired solution tolerance to obtain an estimate of the flow distribution into the individual fractures. Further details can be found in Manchanda (2015).

Multiple Fracture Propagation: Parametric Analysis

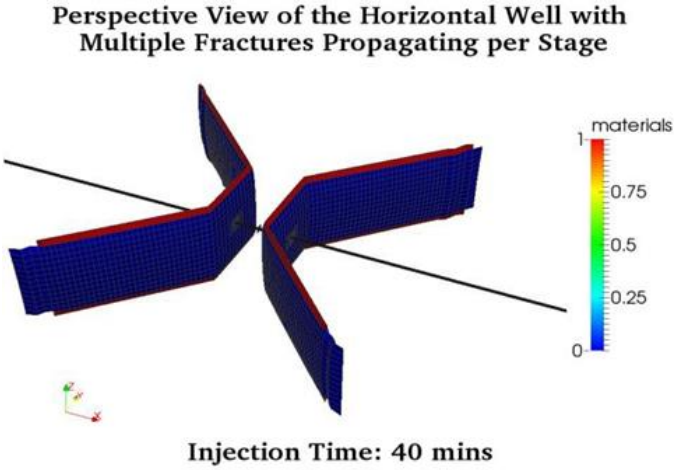


Fig. 3.11 Fracture geometry of the created fractures in a horizontal well stage after 40 minutes of injection.

A parametric analysis was performed to analyze the impact of various operational and reservoir parameters on simultaneous multiple fracture propagation. The base case parameters and the respective sensitivity case parameters are shown in Table 3.1. Other simulation parameters such as Young's modulus (2.9 MMpsi), Poisson's ratio (0.2), horizontal stress contrast (100 psi), and injection rate (60 bpm) were kept constant.

The impact of these simulation parameters and more details about the simulation setup can be found in Manchanda (2015). For each sensitivity case, only the corresponding parameter value was changed. The clusters were modelled as starter fractures to model simultaneous propagation of multiple fractures. The results for the base case simulation show that the outer fractures turn away from each other and propagate symmetrically (Fig. 3.11). The stress shadow caused by the propagating outer fractures inhibits the growth of the middle fracture.

Table 3.1 Base case and sensitivity case parameter values (Manchanda 2015)

Parameter	Base Case	Sensitivity Case
Matrix Permeability	1 microDarcy	1 milliDarcy
Number of Clusters per Stage	3	5
Cluster Spacing	35 ft	50 ft
Perforation Coefficient	1e9	4e9

Impact of Operationally Controllable Variables.

The most important parameters that the operators can control to increase the number of fractures created per stage are the number of clusters per stage, cluster spacing, and perforation parameters.

Impact of number of clusters and stage size.

Simulations were conducted to show that increasing the number of clusters in a stage for the same cluster spacing can reduce the interference between the propagating fractures. The number of clusters was increased from 3 to 5 for the same cluster spacing. Thus, the stage size (distance between the first and the last cluster in a stage) was increased from 70 ft to 140 ft.

In the Base Case the fractures diverted away from each other because of their proximity and high stress interference (Fig. 3.11). After fracture diversion or turning, the fracture length increased rapidly causing a reduction in the fracture width. Also, the increased distance between the turning, outer fractures caused a reduction in the stress interference (Fig. 3.12) This reduced stress interference promotes further fracture propagation after turning. This in-turn leads to most of the fluid going into the outer fractures and the middle cluster does not propagate a fracture.

In contrast to the Base Case, if we increase the number of clusters to 5 while keeping the same cluster spacing, we observe that the outer fractures propagate symmetrically and transversely away from the wellbore. The larger distance between the outer fractures reduces the stress interference and thus, the outer fractures do not turn away from each other.

Another observation (from Fig. 3.12 and Fig. 3.13) is that for the 5-cluster simulation the middle cluster also creates a small fracture. The large stress interference induced by the surrounding bigger fractures inhibits further growth of this middle fracture. However, this suggests that

increasing the number of clusters in a stage while keeping the same cluster spacing could promote more fractures to propagate.

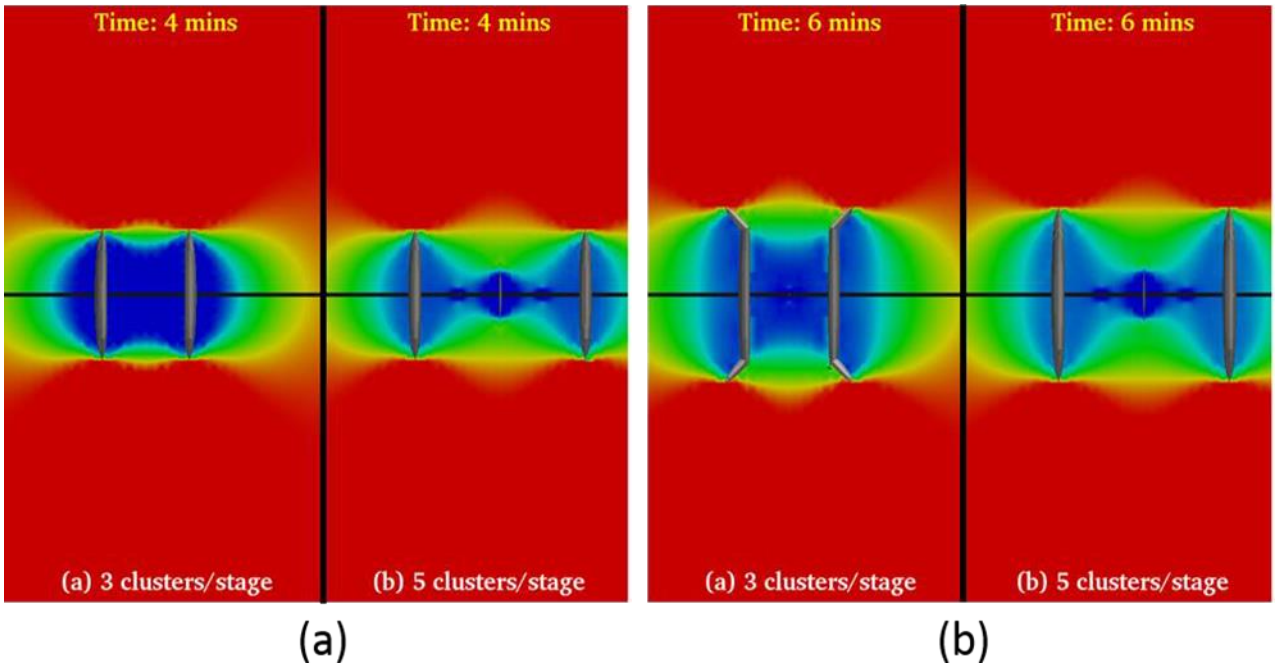


Fig. 3.12 Stress relaxation between fractures caused by fracture turning (a) stress interference before fracture turning, and (b) stress interference after fracture turning for the number of clusters per stage parametric analysis case. Colors show the total compressive stress in the left-right direction. Blue color indicates high compressive stress and red color indicates low compressive stress.

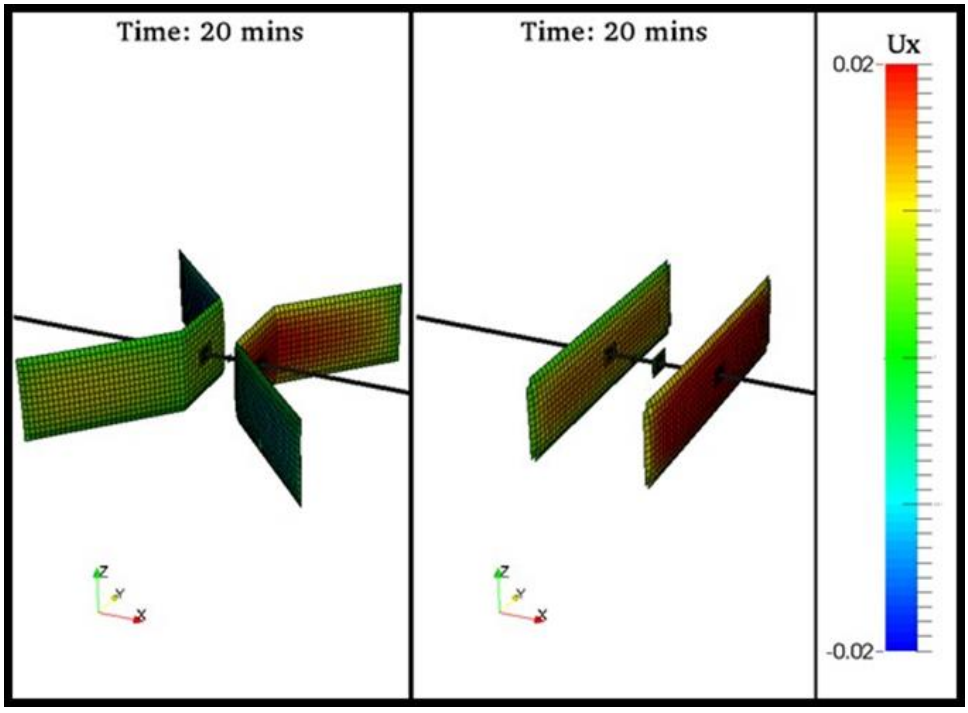


Fig. 3.13 Impact of number of clusters per stage on fracture trajectory and width distribution. Left figure shows the resulting fracture trajectory for 3 cluster per stage and the right figure shows the resulting fracture trajectory for 5 clusters per stage.

Impact of perforation parameters.

As shown in Eq. (6) there are various parameters that control the perforation pressure drop. At the high injection rates used in fracturing operations, perforation parameters can lead to a large

perforation pressure drop. The Base Case perforation pressure drop coefficient chosen to be 1x109, is equivalent to a cluster with 12 active perforations, 1 cm perforation diameter, 0.9 damage factor, and 1500 kg/m3 slurry density. The comparison case perforation pressure drop coefficient was chosen to be 4x109, which can be obtained by reducing the active number of perforations to 6 or decreasing the perforation diameter to 0.707 cm.

Fig. 3.14 shows the impact of perforation coefficient on the observed pressure trends. Fig. 3.14(a) shows the wellbore pressure to be higher for the case of larger perforation coefficient. Fig. 3.14(b) shows that the perforation pressure drop for the larger perforation coefficient case is approximately 4 times the perforation pressure drop observed for the smaller perforation coefficient case. Thus, the fracture pressure is much smaller for the second case. This suggests that the perforation variables can potentially be varied for the various clusters in a stage to promote multiple fracture growth.

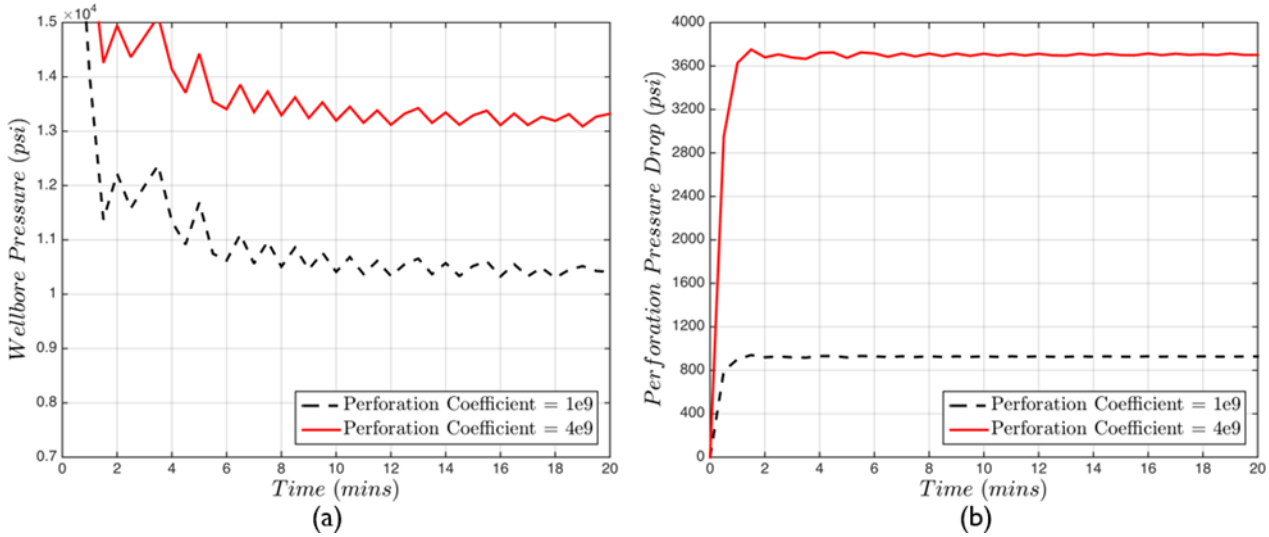


Fig. 3.14 Impact of perforation coefficient on (a) wellbore pressure, and (b) perforation pressure drop.

Impact of Formation Properties.

Formation variables such as matrix permeability, horizontal stress contrast, mechanical properties, and lateral and vertical heterogeneity can impact the trajectory of fracture propagation in a horizontal well stage. For example, it has been shown before (Manchanda et al. 2012, Manchanda 2015) that higher Young's modulus can induce greater stress interference between propagating fractures. This implies that a higher cluster spacing should be used in higher modulus rocks to reduce fracture interference. Another observation in the past has been that in higher in-situ horizontal stress contrast formations, the probability of stress re-orientation is reduced. In these cases, the fractures are resistant to turning. The impact of some parameters is, however, not as intuitively obvious and has not been explored by earlier work. These non-intuitive parameter sensitivities are presented here.

Impact of matrix permeability.

When the simulated matrix permeability was increased from 1 microDarcy to 1 milliDarcy, our simulations suggested lower probability of fracture turning in the higher permeability case. Higher reservoir permeability increases the fluid leak-off which causes a decrease in the fracture

volume. This decrease in fracture volume reduces the fracture width, which causes a decrease in the stress interference between the fractures as shown in Fig. 3.15.

The secondary impact of higher reservoir permeability is the increase in the poro-elastic stresses resulting from fluid leak-off. The poro-elastic impact on fracture propagation has been discussed using analytical models (Detournay et al. 1989; Boone and Detournay 1990; Detournay and Cheng 1993; Berchenko and Detournay 1997). Greater leak-off causes the pressure in the vicinity of the fracture to increase in the high permeability case. The poro-elastic impact of increased pressure in the reservoir increases the compressive stresses on the fracture surface thus decreasing the fracture width because of the additional back-stress and hence further reducing the stress interference. This decrease in stress interference restricts fracture turning in higher permeability rocks (Fig. 3.15).

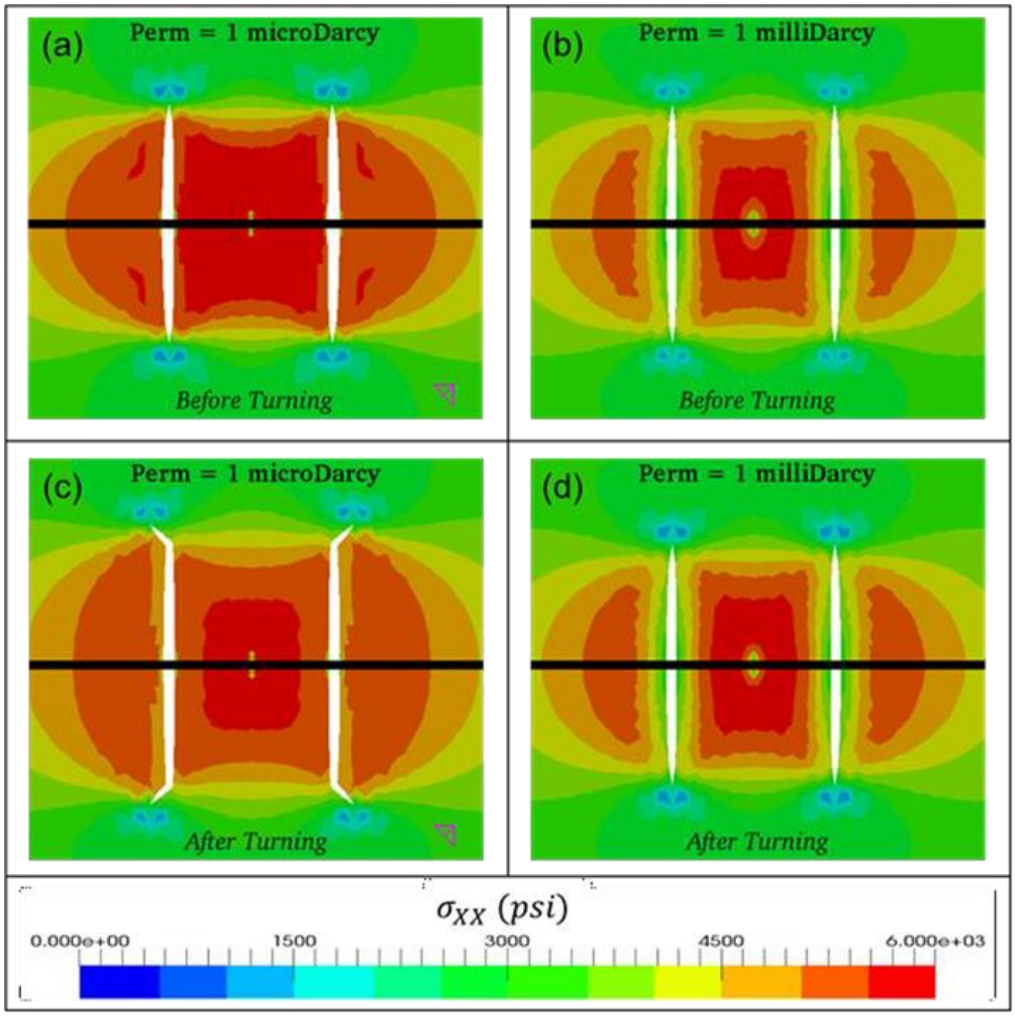


Fig. 3.15 Permeability and induced stress interference (a) low perm, before turning, (b) high perm, before turning, (c) low perm, after turning, (d) high perm, after turning. Color represents the compressive effective stress in the left-right direction.

The poro-elastic impact of the fluid leaking off also impacts the stress orientations and, therefore, the fracture trajectories. In Fig. 3.16 we take a close look at the region near the fracture tip of the left fracture in the low and high permeability cases and observe the pressure contours and the pressure gradient vectors before fracture turning and after fracture turning. The pressure contours show that after 4 minutes of fluid injection the pressure ahead of the fracture tip is smaller in the low matrix permeability case than in the high matrix permeability case. Another

distinction is in the calculated pressure gradient directions and magnitude at the mesh faces adjacent to the fracture tip. These differences are induced because of poro-elasticity and suggest that fracture turning may be influenced by poroelastic effects and the permeability in the SRV around the fracture.

Impact of lateral heterogeneity.

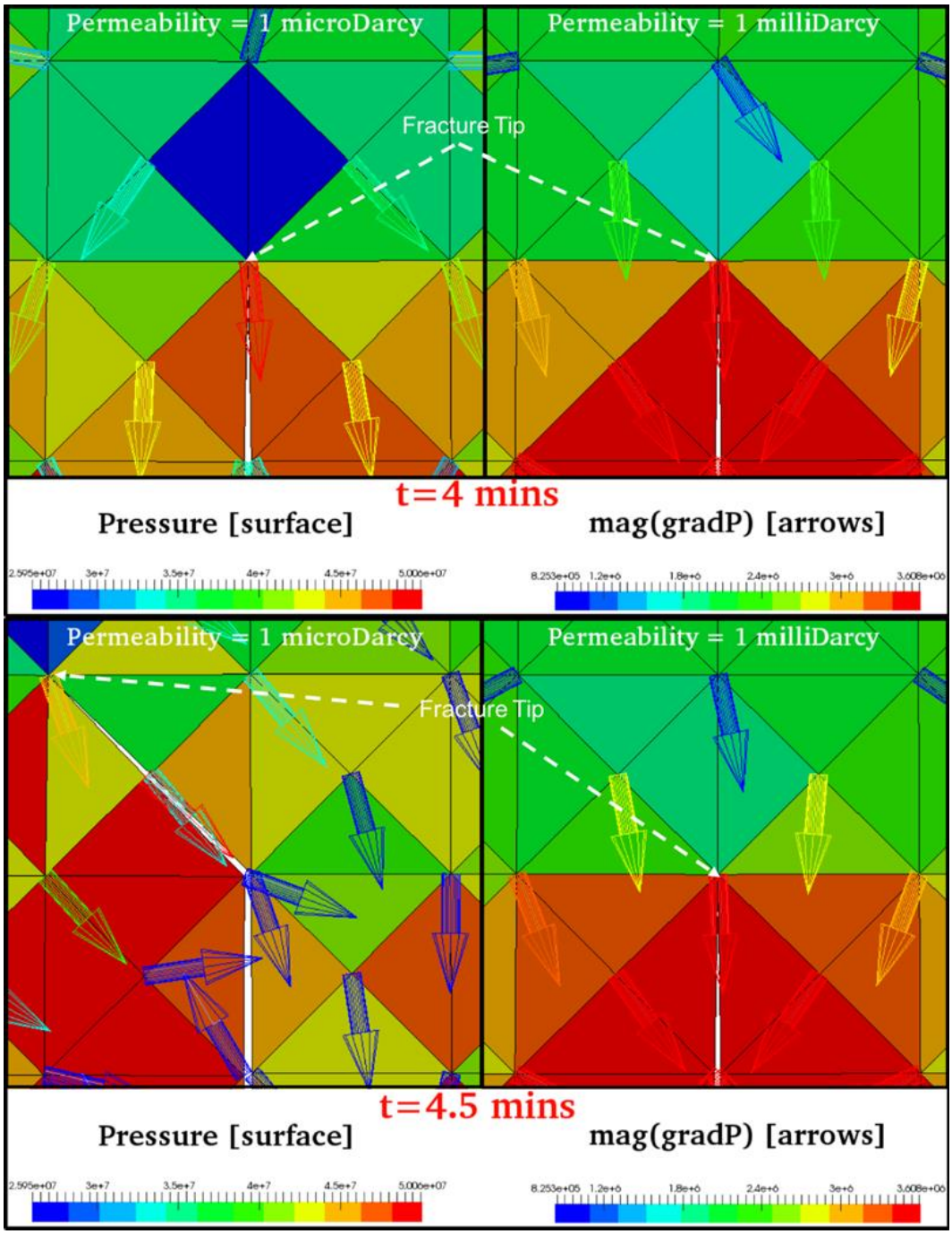


Fig. 3.16 Pressure contours and pressure gradient vectors in the vicinity of the fracture tip for the two cases of matrix permeability after injection for (top) 4 minutes (before turning), (bottom) 4.5 minutes.

Heterogeneity in formation properties along the horizontal well has been used to select locations for perforation in regions of good "fracability" (Mullen and Enderlin 2012; Fang and Amro 2014; Jahandideh and Jafarpour 2014; Jin et al. 2014, 2015; Su et al. 2014; Cudjoe et al. 2016). Different researchers pose different ways to determine the fracability of the reservoir in the vicinity of horizontal well stages. Sometimes brittleness is taken as a surrogate for fracability. Several

models to calculate brittleness exist (Kias et al. 2015). New logging techniques are enabling engineered completion design to get away from geometric spacing between fracturing clusters and have more customized fracture placement (Dahl et al. 2015a; Dahl et al. 2015b). Pin-point perforating methods of fracturing have shown to reduce water use, increase productivity of wells and create efficient fracture networks (Lane et al. 2013; Carrasco et al. 2014).

We address the following question here: How big a role does formation heterogeneity play relative to stress shadowing in controlling the competitive growth of fractures? The formation properties of the red and blue regions in Fig. 3.17 are shown in Table 3.2. Four simulations were run to address the impact of each property separately. In

all four simulations, the cluster in the red region propagated a dominant fracture. More details about the simulation setup can be found in Manchanda (2015).

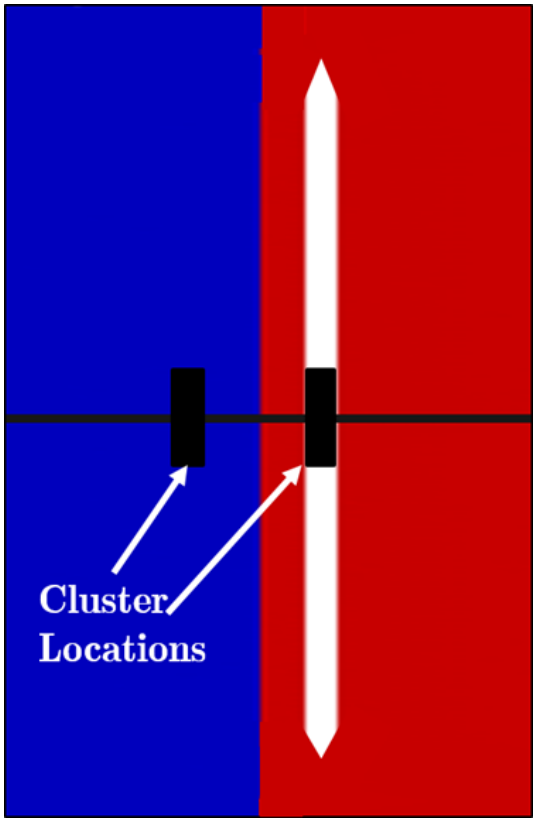


Fig. 3.17 Impact of lateral heterogeneity on fracture propagation. The blue region and the red region have contrasting values in all the simulations. All cases led to fracture.

At the beginning of the treatment the pressure in the clusters is similar. However, the difference in mechanical properties causes the displacements to be different in the two domains. The tensile strength criterion is met in the high Young's modulus region and a fracture is initiated in this region. According to linear elastic fracture mechanics (LEFM), the less energy required to propagate a fracture in a higher Young's modulus material. After fracture initiation in the higher modulus region, the initiated fracture continues propagating. This continued propagation induces a strong stress shadow and prevents the propagation of a fracture from the other cluster. Relatively small changes (5-10%) in the elastic moduli of the rock can induce stresses that are comparable in magnitude to the stress shadow. This implies that the effects of rock heterogeneity were superimposed on the stress shadow and poroelastic effects presented earlier

and, in some instances, can play a dominant role in determining how many fractures are effectively stimulated.

Table 3.2 Formation properties in blue and red region of Fig. 3.7

	Young's modulus (GPa)		**Poisson's ratio**		**Porosity (%)**		**Permeability (microDarcy)**	
Simulation #	Blue region	Red region	Blue region	Red region	Blue region	Red region	Blue region	Red region
1	**20**	**25**	0.2	0.2	10	10	1	1
2	20	20	**0.2**	**0.3**	10	10	1	1
3	20	20	0.2	0.2	**10**	**20**	1	1
4	20	20	0.2	0.2	10	10	**1**	**10**

To understand the impact of porosity we consider the definition of the hydraulic diffusivity generally used in reservoir engineering (Eq. (11)).

$$Diffusivity = \frac{k}{\phi \mu c} \qquad (11)$$

Higher porosity will reduce the hydraulic diffusivity. Lower diffusivity implies slower pressure change in the system. From the simulations conducted we have observed that the fracturing process reduces the pressure ahead of a fracture tip to a value below the reservoir pore pressure (because of poro-elasticity). A smaller change in this pressure is expected for a smaller value of hydraulic diffusivity. Thus, for the high porosity case the pressure ahead of the fracture tip is closer to the reservoir pore pressure. This higher pressure ahead of the fracture tip (compared to the low porosity case) leads to a higher tensile effective stress. The calculated traction will then meet the criteria of fracture propagation earlier in the high porosity case and this will lead to faster fracture propagation.

Higher matrix permeability induces more leak-off. Higher permeability also increases the diffusivity. More leak-off coupled with more diffusion causes higher pressure ahead of the fracture tip. Higher pressure induces more tensile effective stress and hence more tensile effective traction ahead of the fracture tip. Thus, the fracture propagates preferentially in the high permeability region. This effect is particularly important when competing fractures are propagating.

Table 3.3 Young's modulus and Poisson's ratio used for the cases shown in Fig. 3.18.

Simulation	Young's modulus			Poisson's ratio		
	Blue region	Red region	% heterogeneity	Blue region	Red region	% heterogeneity
Fig. 3.18**(a)**	20 GPa	21 GPa	**5%**	0.2	0.2	0%
Fig. 3.18**(b)**	20 GPa	25 GPa	**25%**	0.2	0.2	0%
Fig. 3.18**(c)**	20 GPa	20 GPa	0%	0.2	0.21	**5%**
Fig. 3.18**(d)**	20 GPa	20 GPa	0%	0.2	0.25	**25%**

Thus, it has been shown that poro-elastic stresses can cause changes in fluid distribution and fracture propagation in multi-cluster stages. Estimates of porosity can be obtained from density, neutron, and sonic logs. Permeability estimates can be obtained from core analysis. These

estimates can then be included in the simulation model to analyze their impact on fracture propagation.

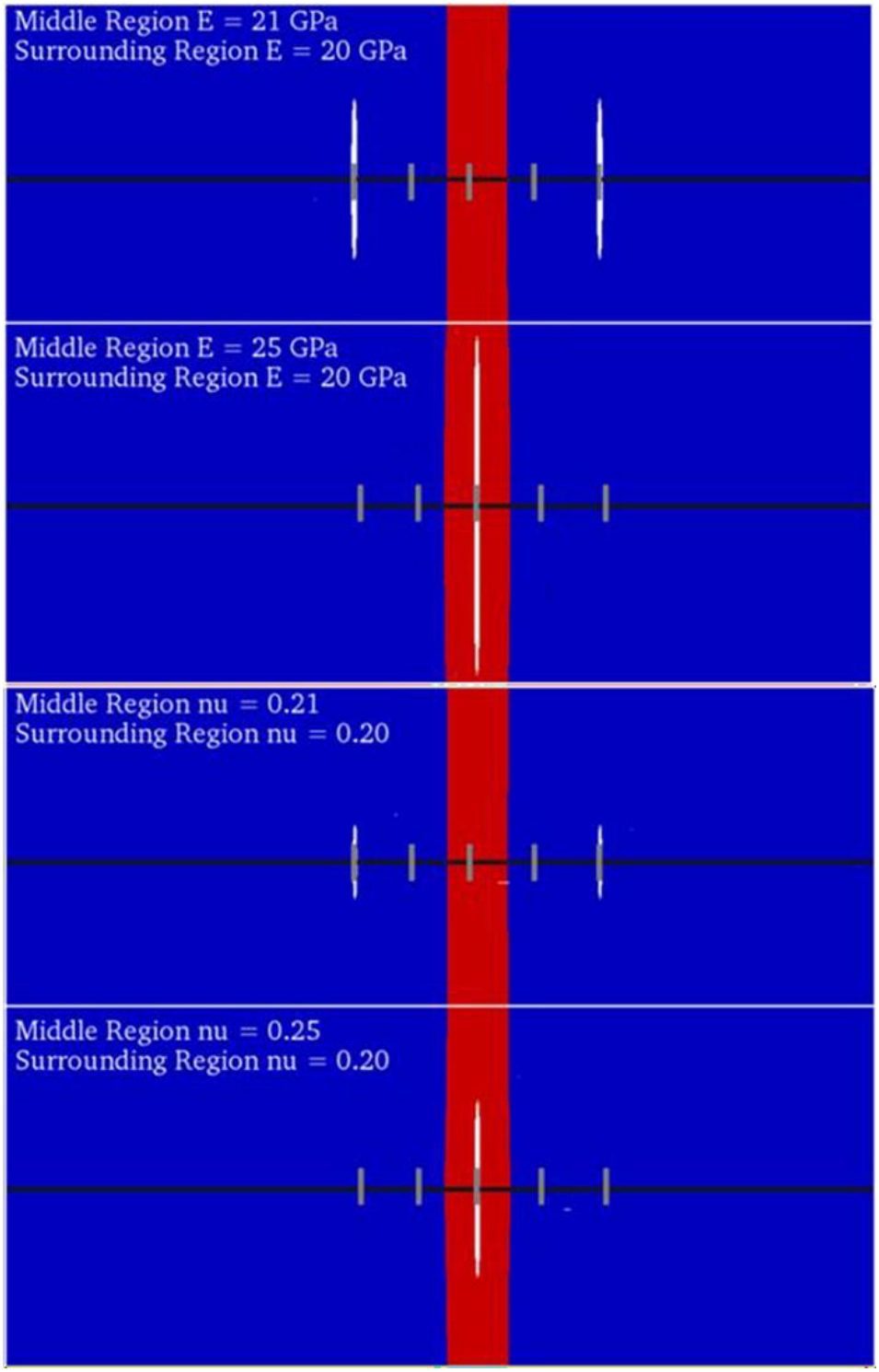


Fig. 3.18 Impact of lateral heterogeneity on multiple fracture propagation in a 5-cluster stage (a) variation in Young's modulus, (b) variation in Poisson's ratio. Grey vertical lines represent the clusters in the fracturing stage. The mechanical properties in the red band region depict the lateral heterogeneity.

In the above simulations we only addressed fluid distribution between two clusters. In the next results we discuss, the impact of heterogeneity in Young's modulus and Poisson's ratio on the propagation of fractures and fluid distribution when the injection fluid is distributed between 5 clusters spaced 15 m apart. The values used for Young's modulus and Poisson's ratio have been described in Table 3.3 and the simulation results are shown in Fig. 3.18. In all the cases, a red

band of heterogeneity was introduced at the location of the middle cluster. In this red region one of the parameter values was increased by a certain percentage. For example, in Fig. 3.18(a), Young's modulus in the red region was increased by 5%. This percentage heterogeneity is defined as the percentage increase in the value of the chosen parameter in the red region relative to the blue region.

For both the cases of heterogeneity in Young's modulus and heterogeneity in Poisson's ratio we observe that 5% heterogeneity does not impact the fluid distribution and fracture propagation as only the outer fractures propagate. When the material property is varied by 25%, the heterogeneous band promotes fracture propagation and only the middle cluster is stimulated with a fracture. Thus, there is a critical value of percentage heterogeneity above which the stress shadow effect becomes insignificant, and heterogeneity governs the simulated fracture trajectories.

Impact of vertical heterogeneity. Geological deposition can induce vertical heterogeneity in reservoir properties. These geological bedding planes can be of varying sizes and can affect the height growth of fractures. A representative simulation depicting the impact of these heterogeneous layers was performed by fracturing in the middle of an intermediate (40 GPa) Young's modulus layer which was bounded by small (5 GPa) and high (70 GPa) Young's modulus layers. More details of the simulation setup can be found in Manchanda (2015). The results from this simulation are shown in Fig. 3.19.

Fracture propagation begins from the center of the middle layer. The fracture initially propagates downwards to the low Young's modulus layer. For a propagating fracture the stress ahead of a fracture tip is a function of the mechanical properties of the rock in the vicinity of the fracture tip. The impact of reservoir heterogeneity can thus be integrated in a non-local manner. In the current case, the pressure in the fracture induces strain in the matrix. The variation in layer properties causes the induced strain to be asymmetric. For the same traction at the fracture face, the reservoir deforms more in the low Young's modulus layer. The strain in the low Young's modulus layer is felt further away from the layer interface. This reduces the compressive stresses in the downward direction. Thus, the fracture initially propagates downwards till it reaches the interface between the intermediate Young's modulus layer and the small Young's modulus layer. When the presence of the material boundary/interface is felt at the propagating tip of the fracture, the traction calculations at the tip automatically guide the fracture along the path of least resistance.

The fracture does not propagate into the bottom layer because of the impact of Young's modulus on fracture width (Eq. (12), Schechter 1992). The equation suggests that the fracture width in the low Young's modulus region will have to be 8 times the fracture width in the intermediate Young's modulus region for the same value of net pressure. This is an improbable possibility in a continuum model since the displacements must be continuous at the interface. Thus, the fracture does not propagate into the low Young's modulus layer.

$$w(z,t) = \frac{2(1-v^2)}{E}\sqrt{(h^2 - z^2)}P_{net}(t) \qquad (12)$$

After the fracture reaches the lower interface, the fracture starts propagating radially upwards towards the high Young's modulus layer. When the fracture reaches the upper interface, it is

easily able to break through the interface and propagate further into the stiffer material. The propagation rate is faster in the high Young's modulus layer because the effective tractions calculated are higher. The vertical cross-section of the fracture after it propagates into the high Young's modulus layer is shown in Fig. 3.19(b). The continuity of displacement at the layer interface is observed and the pinching of the fracture in the high Young's modulus layer in accordance with the above equation is also evident.

The vertical layer heterogeneity can be decisive in altering the fracture growth pattern when estimating the fracture lengths and trajectories in multi-cluster, multi-stage fracturing.

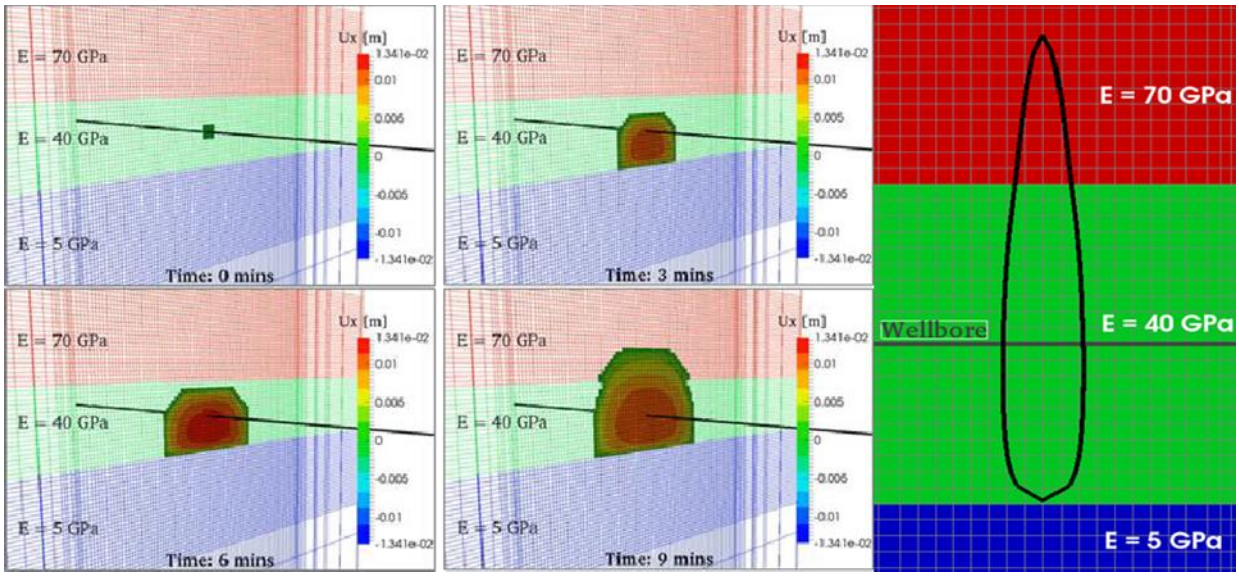


Fig. 3.19 (a) Impact of layer heterogeneity on fracture height growth. (b) Impact of layer heterogeneity on fracture width profile.

Inter-Stage Stress Shadow Effects

In this section we examine the impact of the fractures created in a horizontal-well stage on the fractures formed in the next hydraulic fracture stage in the same well.

A two-stage fracture treatment simulation was performed to understand the impact of fractures in one stage on the fractures in a subsequent stage for the treatment profile shown in Fig. 3.20(a). The simulated fracture patterns are presented in Fig. 3.20(b) at various times during the fracture treatment. The clusters in the stages are simulated 50 ft away from each other. More details of the simulation setup can be found in Manchanda (2015). Symmetric fractures are observed in the first stage. Limited stress interference is observed in the fractures propagating in the first stage as the fractures do not turn away from each other. The stress interference is, however, enough to prevent the propagation of fractures from the middle cluster in stage 1. After fluid injection into stage 1 is stopped, the created fractures start closing. The stress shadow from the first stage, allows only one fracture to propagate in the next stage. The stress shadow from the fractures created in stage 1 is least at the location of the furthest cluster in stage 2. Thus, the single propagating fracture from the second stage is created in the cluster furthest from the first stage.

Fig. 3.21 shows the simulated treatment pressures in the two fracture stages. The pressures recorded in Stage 1 show that Frac 1 and Frac 3 are symmetric during the first 60 minutes of treatment. The pressure in Frac 2 and the wellbore was observed to be the same suggesting that

there was negligible perforation pressure drop in the middle fracture. Differences in the pressure trends for the fractures in stage 1 appear when the treatment is started in the second stage. Fracture propagation in the second stage induces changes in the pressures recorded in the first stage. The pressures observed in the well during fracture propagation in stage 2 are much higher than the pressures observed in stage 1. Since all the injected fluid goes through a single cluster the perforation pressure drop is increased for the cluster that creates a fracture in stage 2. This higher perforation pressure drop leads to higher wellbore pressure needed to propagate the fracture (Fig. 3.21(b)).

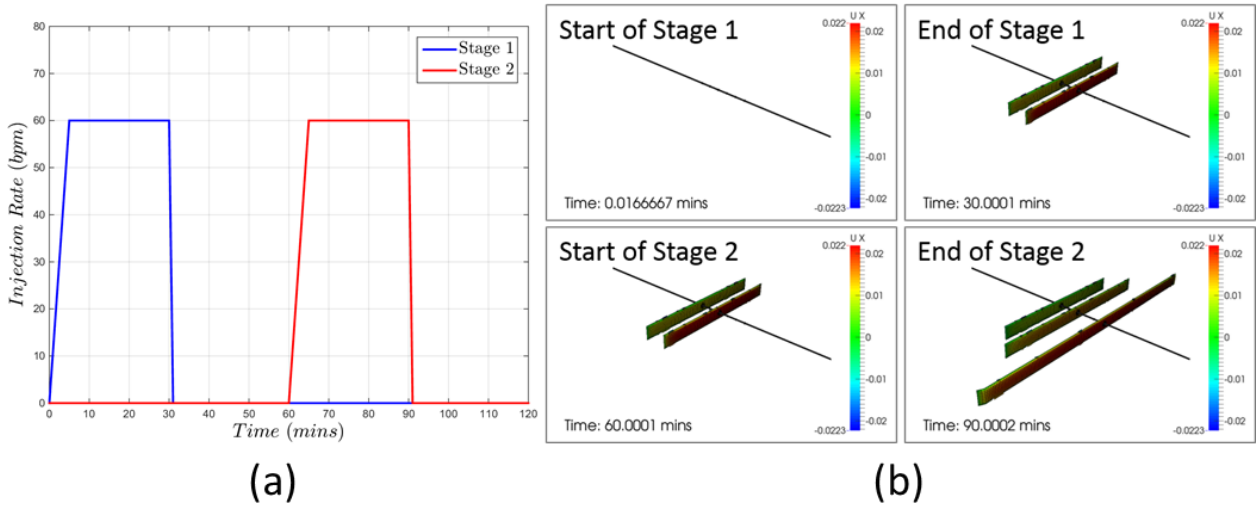


Fig. 3.20 (a) Treatment profile for the two fracturing stages. (b) Fracture trajectories in multi-cluster multi-stage fracturing simulation.

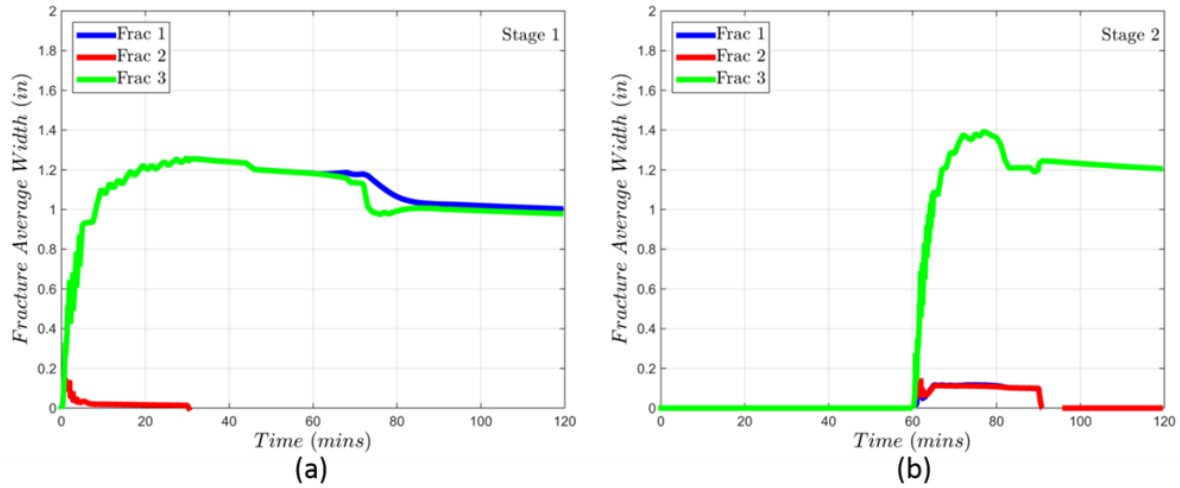


Fig. 3.22 Simulated fracture widths for (a) stage 1, (b) stage 2.

The fracture geometries are shown in Fig. 3.22, Fig. 3.23, and Fig. 3.24. For the first 30 minutes, fluid injected into stage 1 causes an increase in the fracture width for the fractures formed from cluster 1 and cluster 3. From time 30 minutes to 60 minutes, the fracture width and fracture volume slowly decrease because of leak-off while the fracture area remains constant. During this period no fluid is injected into any of the clusters and hence during this period the created fractures close. Injection of fluid into stage 2 is started at 60 mins. The third cluster in stage 2 starts propagating a fracture within a minute after starting the treatment. The impact of this fracture's stress shadow is observed in the fractures in the previous stage. The width of fracture 3 in stage 1 decreases more than the width of fracture 1 because stress interference is larger on

the fracture closer to stage 2. This decrease in width compresses the fluid in the existing fractures and increases the pressure inside the fractures hence causing fracture 3 in stage 1 to propagate. This increase in fracture area decreases the fracture width. Increase in the third fracture's area impacts the first fracture's area by decreasing its width. This decrease in width of the first fracture redistributes the fluid to the third fracture and allows for further fracture propagation.

Fig. 3.25 shows the fluid injection rate into the two stages. There are some blips that are seen in Fig. 3.25(a) from 60 to 90 minutes. In the simulation framework, a positive injection rate signifies fluid entering a fracture and a negative injection rate signifies fluid exiting a fracture. The opposite injection rate trends shown between 60 min and 90 min in Fig. 3.25(a) signify the exchange of fluid between fracture 1 and 3 in stage 1. This fluid exchange occurs because of the changes in fracture dimensions (both width and length) of the fractures in stage 1 during fracture propagation in stage 2.

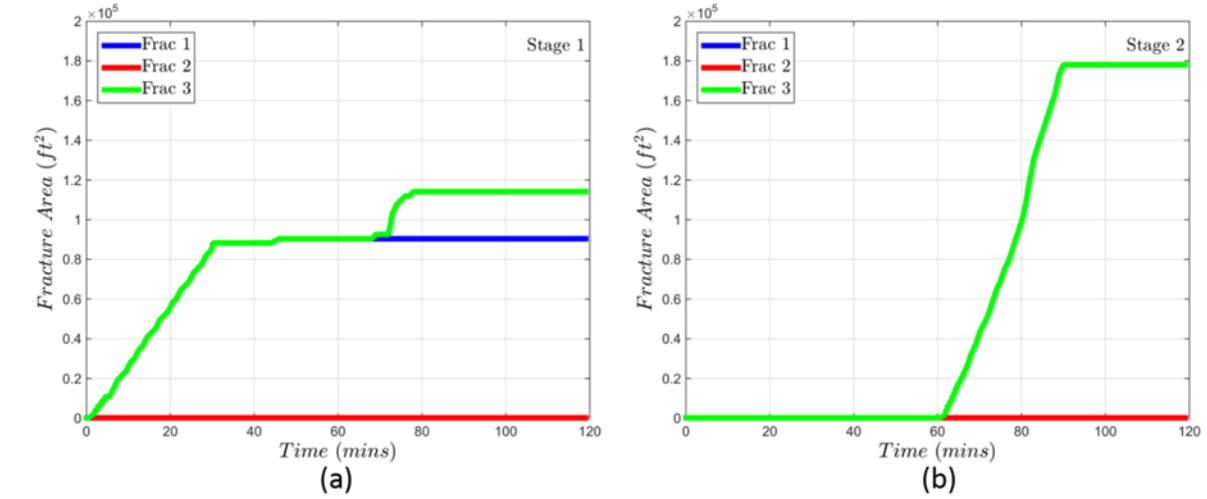


Fig. 3.23 Simulated fracture area for (a) stage 1, (b) stage 2.

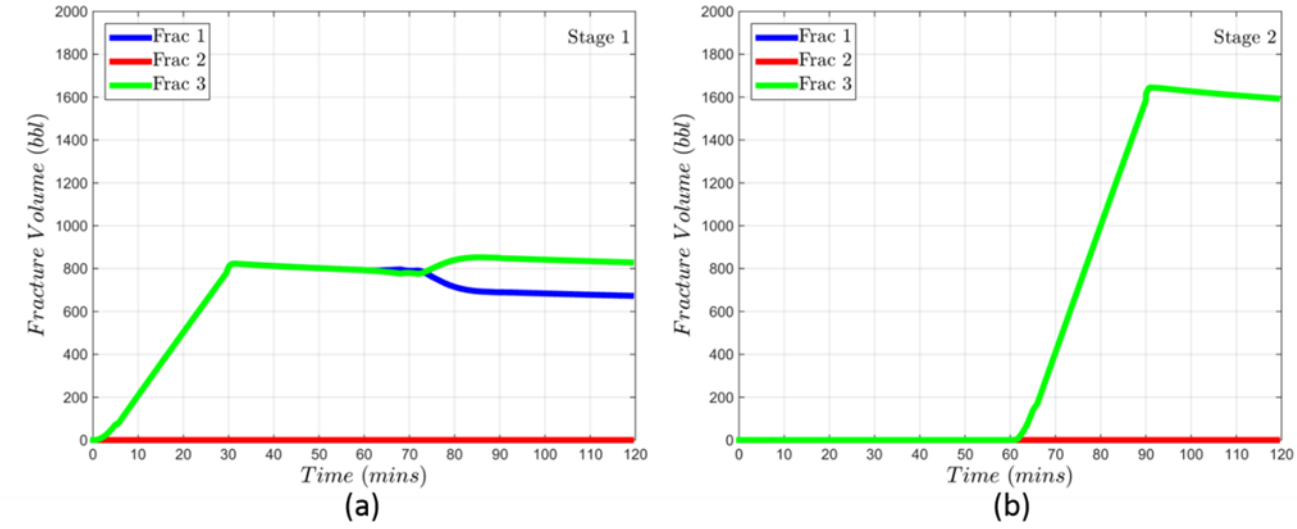


Fig. 3.24 Simulated fracture volume for (a) stage 1, (b) stage 2.

The workflow described above can now be applied to simulate multi-stage multi-cluster fracturing in horizontal well pads. Heterogeneity in reservoir properties can be included in this model to predict competitive growth and interaction between rock heterogeneities and the hydraulic fractures. This can help in estimating the number of active clusters per stage in a horizontal well. Such an analysis can help in reducing costs by helping optimize the spacing

between clusters and helping optimize the number of clusters per stage while taking into consideration the impact of reservoir mechanical and flow properties as well as treatment and completion parameters.

Infill Well Hydraulic Fracturing

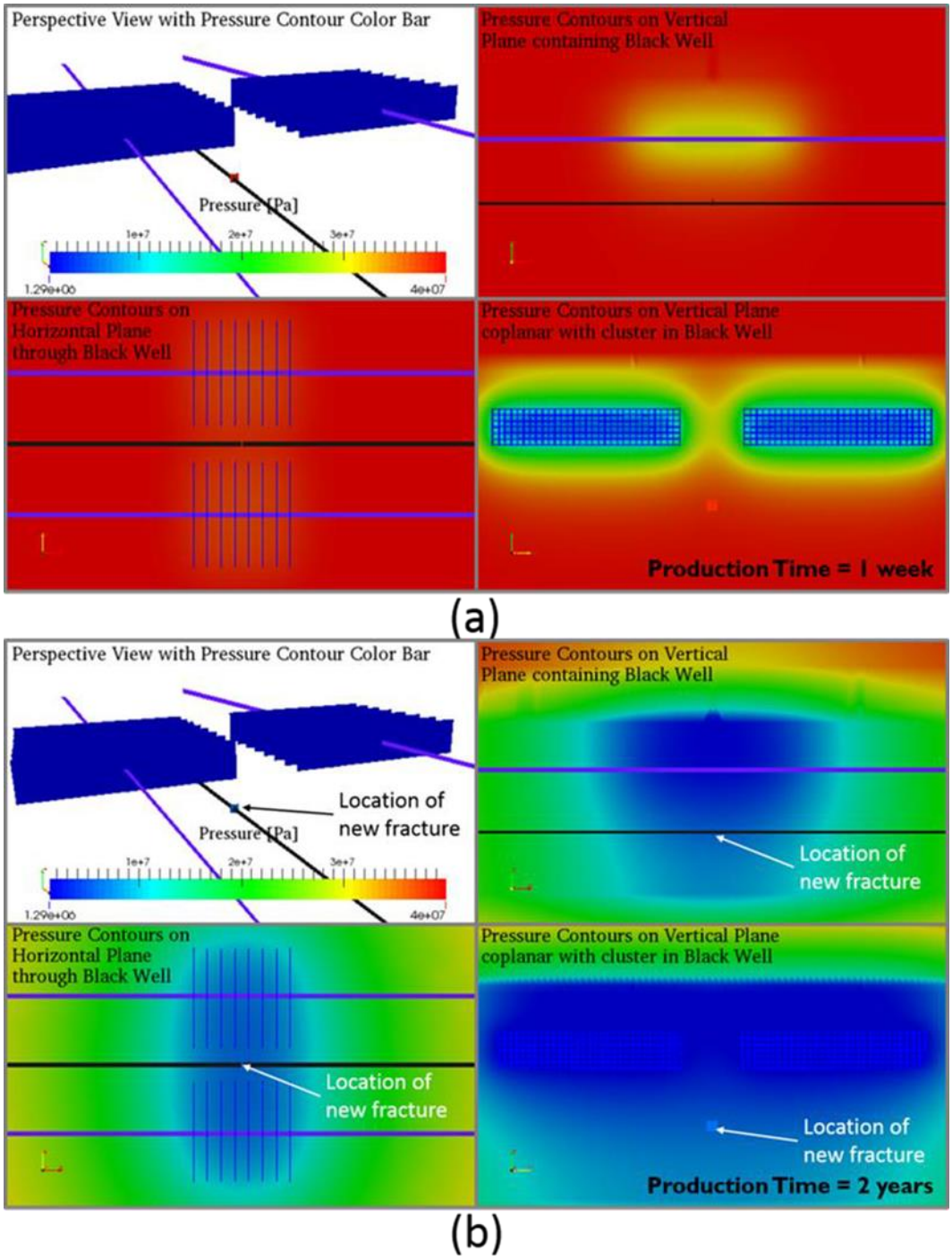


Fig. 3.26 Impact of horizontal well production on pressure depletion in a multi-zone multi-well hydraulic fracturing pad (a) pressure distribution after 1 week of production, (b) pressure distribution after 2 years of production.

Poro-elastic stress reorientation and its impact on the trajectory of hydraulic fractures has been studied with field data (Warpinski and Branagan 1989; Weng and Siebrits 2007; Fischer et al. 2009; Dahm et al. 2010; Ajani and Kelkar 2012), lab experiments (Bruno and Nakagawa 1991), analytical estimations (Berchenko and Detournay 1997) and numerical simulations (Weng and Siebrits 2007; Singh et al. 2008; Roussel 2011; Gupta et al. 2012; Roussel et al. 2013).

In this section we show simulation results of hydraulic fracture propagation from an infill horizontal well in a pad with multiple fractured wells that had been on production for two years. As shown in the top left section of Fig. 3.26(a) and Fig. 3.26(b), the outer purple wells are simulated with 8 fractures each (dimensions are 100 ft x 250 ft) spaced 65 ft apart from each other. The outer purple wells are positioned 1000 ft apart from each other and are in a horizontal plane that is 200 ft above the infill well.

Fig. 3.26(a) shows the pore pressure contours after 1 week of depletion and Fig. 3.26(b) shows the pore pressure contours after 2 years of depletion. Exaggerated depletion trends were simulated by applying a 0-pressure boundary condition on the outer fractures for 2 years. In-situ reservoir pore pressure is simulated to be approximately 5800 psi and the in-situ horizontal stress contrast is simulated to be 1000 psi. The pressure contours show extensive depletion in the reservoir for a matrix permeability of 100 microDarcy. A decreasing pressure trend is observed from the infill well to the producing wells after 2 years of production. More details about the simulation setup can be found in Manchanda (2015).

A single fracture is simulated in the infill well at the location shown in Fig. 3.26(b). The reservoir depletion induces poro-elastic stress changes in the reservoir causing asymmetric fracture propagation from the infill well as shown in Fig. 3.27. The figure shows that the fracture propagates towards the outer wells. Pressure reduction causes the total stress to be less compressive following Eq. (13). A decrease in pressure for constant effective stress causes the total stress to be less compressive.

$$\mathbf{S} = \boldsymbol{\sigma} - \alpha P \mathbf{I} \qquad (13)$$

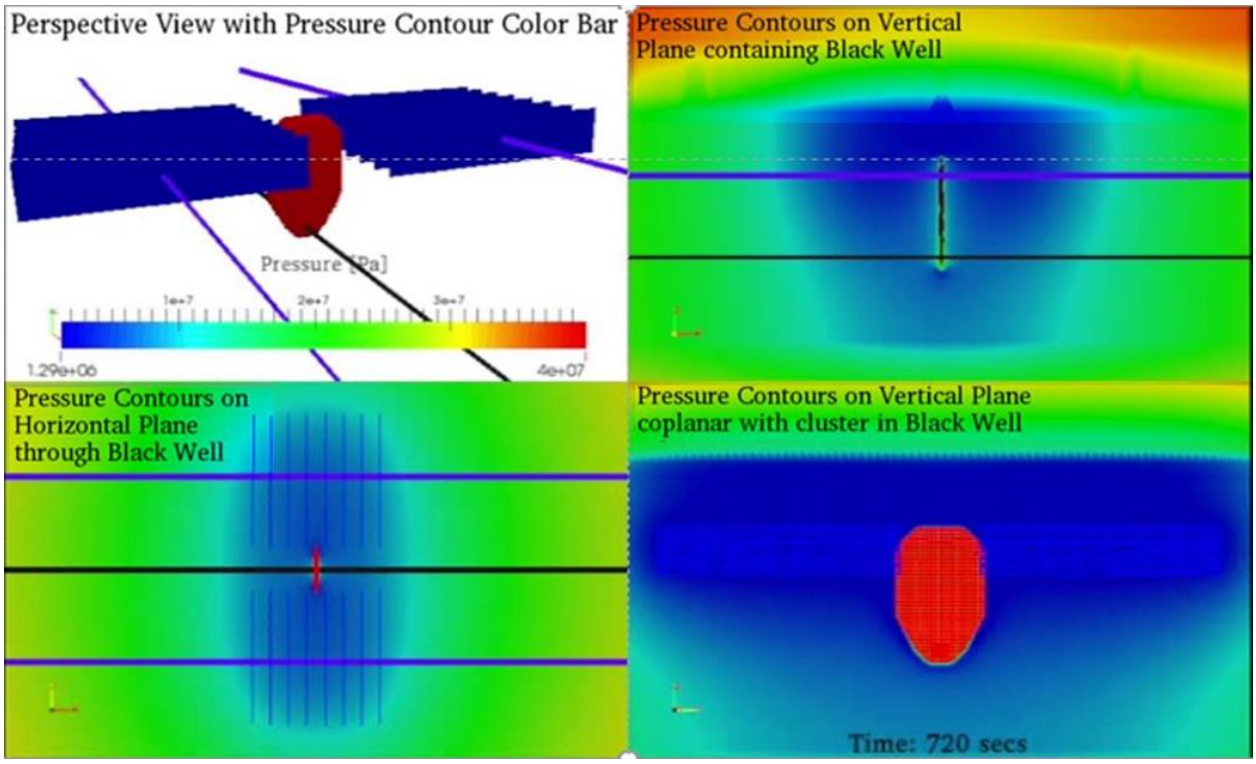


Fig. 3.27 Poro-elastic stress changes induced by depletion causes the hydraulic fracture to propagate towards the depleted region.

Depletion of pore pressure in the vicinity of the producing fractured wells also induces the effective stress to be less compressive around the depleted region. There are two coupled reasons for this. Firstly, a decrease in pressure in a system causes the volume of the solid skeleton to decrease. In a continuum system, the contraction of the solid introduces tensile stresses and subsequently makes the effective stress less compressive in the vicinity of the compressed region. Secondly, local pressure reduction induces pressure gradients in the reservoir. The pressure gradient acts as a body force on the matrix and an outward pressure gradient introduces tensile forces on the matrix thus making the effective stress less compressive.

Conclusions

A new geomechanical simulation framework (FROGG – Framework for Research and Operations in General Geomechanics) was used to simulate pad scale fracturing. The model allows competitive propagation of multiple, non-planar fractures (in multiple clusters in sequential or simultaneous stages in multiple wells) with poroelastic and stress shadow effects included. The model allows us to investigate problems such as the influence of cluster spacing and stage spacing on fracture propagation in multiple wells in a pad and fracturing of infill wells in a partially depleted reservoir. Example results are shown to illustrate how the model can be used to simulate complex pad-scale scenarios with multiple wells such as, zipper fracturing, frac wave (Sardinha et al. 2014) and other innovative fracture sequencing strategies. Fracture closure is also automatically handled in the formulation. Thus, stress shadow reduction in the vicinity of closing fractures can be modelled and operations that involve variation in times between fractures can be simulated such as minifrac tests, alternate fracture sequences (Roussel and Sharma 2011b) etc. The model can readily accommodate reservoir heterogeneity and thus can be used to include variations in rock petrophysical data when it is available. The capability to simulate depletion and associated poro- elastic stress changes implies that the simulation model can also be used for simulating re- fracturing processes.

Some specific conclusions arrived at based on the simulation results presented are listed below.

1. Increasing cluster spacing decreases the stress interference between the outer propagating fractures and prevented the fractures from turning/diverting/rotating away from each other. This mechanism can lead to multiple inactive clusters in the fracturing stage.

2. Increasing the number of clusters, while keeping the same cluster spacing (larger stage spacing) can result in larger number of effective fractures because of less fracture interference.

3. Perforation parameters such as perforation diameter, number of perforations etc. can be varied to change the perforation pressure drop and help to propagate multiple simultaneous fractures from a stage (Eq. (6)).

4. Higher reservoir permeability can induce an increase in pore pressure in the vicinity of the fracture. The poro-elastic impact of hydraulic fracturing reduced the stress interference between simultaneously propagating fractures in the high permeability case. Simulations showed less probability of fracture turning in the higher permeability case.

5. Fracture height growth was shown to be sensitive to reservoir layer heterogeneity. A fracture propagating in a material layer propagated preferentially towards a softer layer. Fracture

breakthrough into a soft layer from a harder layer was shown to be less probable. Fracture breakthrough into a harder layer from a softer layer was shown to be easier. This knowledge can be used when drilling to optimize the position of a well with layers of productive pay.

6. Heterogeneity along the length of a horizontal well was shown to impact the propagation of fractures from the clusters in a stage.

a. Higher Young's modulus and higher Poisson's ratio induced preferred fracture propagation.

1b. Higher porosity and higher permeability induced preferred fracture propagation because of the induced poroelastic impact.

c. There is a balance between heterogeneity and stress interference. For fracture initiation and propagation, a 25% variation in material properties shows the dominance of heterogeneity but a 5% variation in material properties shows the dominance of stress shadow effects.

7. Results from a multi-stage, multi-cluster simulation shows that fractures in one stage induce stress shadow on the subsequent stage. This stress shadow limited the number of active clusters in the next stage. In this example, only the cluster furthest from the previous stage created an effective fracture.

8. The multi-stage simulation also showed that fractures created in a previous stage were extended further because of the stress shadow induced by the fractures propagating in the next stage. This provides an explanation of some observations of induced microseismic events observed in stages after fluid injection was stopped in a stage (Fischer et al. 2008). The extension and closure of the fractures in the previous stage can be diagnosed using the shut-in pressure data of the previous stage.

9. The poroelastic impact of reservoir depletion is observed in the height growth of fractures in an infill well simulation. Fracture growth was observed to be preferentially oriented towards the depleted regions in the reservoir. Thus, the model can be used to simulate fracture hits.

Proppant Distribution Among Multiple Perforation Clusters in a Horizontal Wellbore

Summary

Plug-and-perf fracturing stages with multiple perforation clusters have become common practice in the industry. However, it is usually unclear whether the fluid and proppant are distributed evenly among all clusters. In this study we present a method for computing the proppant distribution into each cluster in a fracturing stage. By integrating proppant transport into a multi-cluster hydraulic fracturing model and implementing a simple screenout criterion, we show that the proppant distribution in a fracturing stage can be very uneven with a strong bias towards the heel-side clusters even when the initial fluid distribution is uniform among all clusters.

In this work, we present results to show why heel dominated fractures are created (as observed in the HFTS data). We define the efficiency of proppant transport into a perforation by the proppant transport efficiency (PTE), which is defined as the mass fraction of proppant transported through a perforation relative to the total mass of proppant approaching the perforation. The dynamic proppant distribution in a fracturing stage is modeled using the PTE

concept in 3 steps. First, a series of coupled computational fluid dynamics - discrete element method (CFD-DEM) simulations were performed to obtain PTE under controlled flow conditions. Then, the CFD-DEM simulation results were statistically analyzed to generate a PTE correlation as a function of wellbore, perforation, fluid, and proppant properties. Finally, the PTE correlation was incorporated into a multi-cluster hydraulic fracturing model to compute the dynamic distribution of fluid and proppant among multiple clusters in a fracturing stage.

Results from this work show that proppant concentration in the toe-side clusters can be several times higher than the injected concentration. This occurs because the high wellbore flow rate near the heel-side clusters provides proppant particles a large enough inertia that prevents them from turning into the perforations. Proppant concentration in the wellbore is thus increased as the slurry flows towards the toe side and the fluid preferentially leaks off from the heel side perforations. The highly concentrated slurry increases the screenout risk of the toe-side clusters. Our modeling results show that if toe-side clusters screen out early of a proppant stage, fluid and proppant are re-distributed to the heel-side clusters. In such a case, cumulative fluid and proppant distributions will be heel biased. Simulation results are compared with field observations and are shown to be completely consistent with DTS and DAS observations on proppant distribution made in three different studies.

The method presented in this work provides a way to quantify proppant transport at a wellbore scale. It shows that the uneven proppant distribution among perforation clusters is a function of fluid, perforation and proppant properties. An estimate of proppant placement in different perforation clusters can be computed for any pumping schedule and wellbore/perforation geometry using this method. This can be used to optimize perforation clusters that will result in a more even distribution of proppant in each cluster.

Introduction

Plug-and-perf completions are one of the most used completion methods for horizontal wells in unconventional reservoirs. The method stimulates the well with several isolated fracturing stages. Each fracturing stage usually involves 3 to 6 perforation clusters that are simultaneously stimulated by injected fluid. The operation begins from the toe-side of a well and proceeds towards the heel side with drillable plugs placed between each stage for zonal isolation. After completing all the fracturing stages, the plugs are drilled and circulated out of the well before the well is put into production. Previous studies found that shale plays completed with the plug-and-perf approach often have under-performing perforation clusters with almost one third of all perforation clusters not contributing to production (Baihly et al. 2010; Miller et al. 2011). Recent observations made from distributed acoustic sensing (DAS) and distributed temperature sensing (DTS) during each fracturing stage showed that it is common to have a few dominant clusters taking the majority of the treatment volumes while leaving other clusters in the same stage understimulated (Ugueto et al. 2016; Wheaton et al. 2016).

There can be many possible reasons to explain these observations: stress interference between fractures, local heterogeneity of the reservoir, difference in the effectiveness of zonal isolation between stages, differences in stimulation job design (pumping schedules and fluid/proppant selection), and differences in natural fracture systems surrounding the well. Although all these

reasons can lead to the uneven stimulation of a reservoir volume, it is still hard to explain why most of the dominant clusters are located near the heel-side of a fracturing stage.

In this work we propose an alternate explanation for the heel-side treatment bias: the bias can occur because of premature near-wellbore screen out of toe-side perforation clusters at early pumping times in any fracture stage. By numerically simulating the flow of proppant particles under downhole conditions we show that the proppant distribution among multiple perforation clusters can be highly uneven even when the fluid is uniformly distributed in all clusters. Our results show that it is difficult for the proppant to make the turn into perforations at typical high wellbore flow rates because of the effect of proppant inertia. This implies that the proppant concentration in toe-side clusters can be significantly higher than the proppant concentration in heel-side ones when the proppant slurry is first pumped. This can lead to premature near-wellbore screenout of toe-side clusters and create the heel-side treatment bias commonly seen in the field.

Simulation of Proppant Transport (Step 1)

A coupled computational fluid dynamics and discrete element method (CFD-DEM) approach (Goniva et al. 2012; Mondal et al. 2016) is used to evaluate the effect of proppant inertia on proppant transport in this work. The unresolved CFD-DEM model assumes incompressible flow and solves the mass conservation equation and the volume-averaged Navier-Stokes equation for the fluid:

$$\frac{f\alpha_f}{ft} + \nabla \cdot (\alpha_f \mathbf{u}_f) = 0 \qquad (1)$$

$$\frac{\partial(\rho_f \alpha_f \mathbf{u}_f)}{\partial t} + \nabla \cdot (\rho_f \alpha_f \mathbf{u}_f \mathbf{u}_f) = -\alpha_f \nabla p + \mathbf{R}_{pf} + \nabla \cdot (\alpha_f \tau) \qquad (2)$$

Where α_f is the volume fraction of the fluid phase in the CFD cell, u_f is the fluid velocity, ρ_j is the fluid density. R_{pj} Is the particle-fluid momentum exchange term that is computed by assembling particle-based drag forces in each cell. Movement of particles is computed through the DEM coupling, which accounts for the hydrodynamic drag, the viscous shear, the pressure gradient forces from fluid-particle interaction, and the collision force from particle-particle interaction. The transport of proppant slurry is simulated for a section of horizontal wellbore with a single perforation. Fig.4.1 shows the schematic of the modeled geometry.

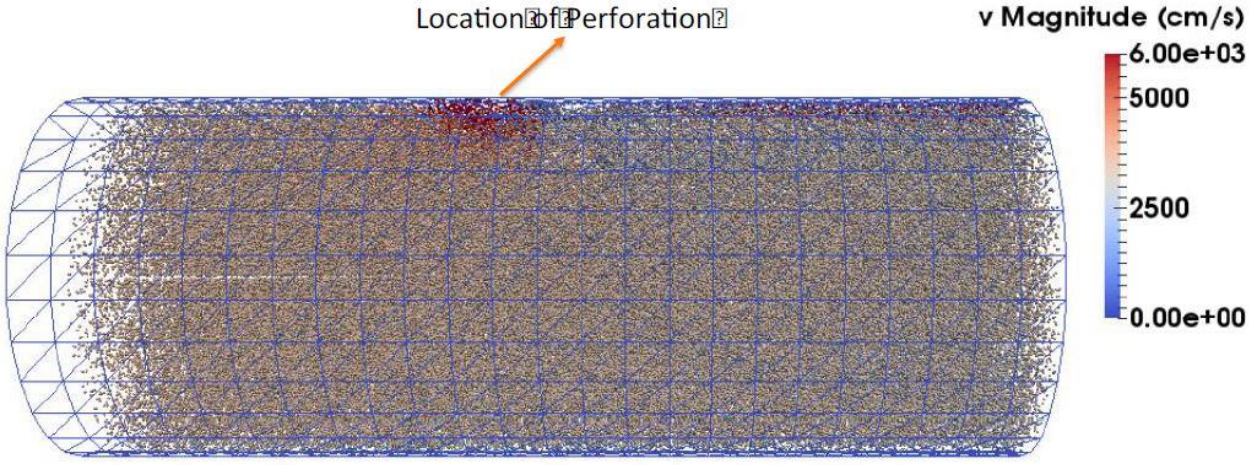


Fig. 4.1—Schematic of the CFD-DEM model geometry used in this work. (Wu and Sharma, 2016).

Results from CFD-DEM simulations are used to compute the proppant transport efficiency (PTE). The PTE is defined as the rate of proppant transport into a perforation divided by the rate of proppant transport upstream of that perforation (Eq. 3). The PTE for a given perforation depends on the rate proppant size, proppant density, fluid flow rate, fluid density, rheology, wellbore diameter, and perforation flow ratio (PFR). The PFR is defined as the fluid flow rate through the perforation relative to the fluid flow rate upstream of that perforation (Eq. 4):

$$\text{Particle Transport Efficiency, PTE} \equiv \frac{\dot{m}_{perf}}{\dot{m}_{upstream}} \quad (3)$$

$$\text{Perforation Flow Ratio, PFR} \equiv \frac{\dot{q}_{perf}}{\dot{q}_{upstream}} \quad (4)$$

where $\dot{m}_{perf}$ and $\dot{m}_{upstream}$ are proppant mass flow rates, $\dot{q}_{perf}$ and $\dot{q}_{upstream}$ are volumetric fluid flow rates, through the perforation and upstream of that perforation, respectively. The computed PTEs were plotted against the PFRs (see Fig. 4.2 for an example).

Proppant Transport Efficiency Correlations (Step 2)

A total of 45 PTE versus PFR plots were generated based on the results of 180 CFD-DEM simulations for a wide range of proppant sizes, flow rates, proppant densities, wellbore diameters and fluid viscosities. Each of the PTE curve was fitted with a fourth-order polynomial in the form of Eq. 5:

$$\text{PTE} = C_1(\text{PFR})^4 + C_2(\text{PFR})^3 + C_3(\text{PFR})^2 + C_4(\text{PFR}) \quad (5)$$

where C_1, C_2, C_3, and C_4 are the fitting coefficients. Note that these fitting coefficients reflect how PTE changes with PFR for a given set of fluid, proppant, wellbore, and perforation properties. The range of simulation parameters used in this work is shown in Table 4.1.

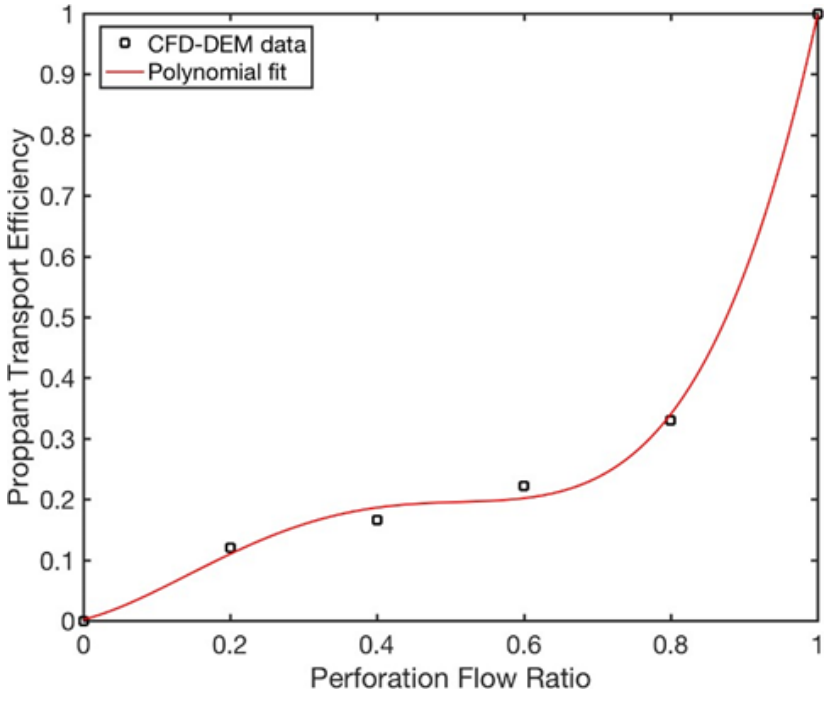


Fig. 4.2—An example of PTE versus perforation flow ratio plot. Note that the plot is composed of four simulation results with perforation flow ratio ranging from 0.2 to 0.8 for a given set of fluid, proppant, wellbore, and perforation properties. A 1 lbm/gal, 600 μm proppant slurry flowing at a wellbore flow rate of 60 bbl/min was used in this example. The perforation size is 3/8″ oriented on the side of a 6″ casing. The data is fitted by a fourth-order polynomial curve.

After obtaining the fitting coefficients from all 45 PTE versus PFR curves, the least absolute shrinkage and selection operation (LASSO) method was used to perform a multivariate linear regression analysis for the fitting coefficients (James et al. 2013). The LASSO selects a subset of simulation parameters (variables) that best predicts the trends for C_1, C_2, C_3, and C_4. We limited the subset selection to only the independent variables to ensure the simplicity and interpretability of the statistical model. The functional form for predicting C_1 to C_4 is shown in Eq. 6.

$$C_i = f\left(\mathrm{D}_{\mathrm{casing}}, \mathrm{D}_{\mathrm{perf}}, \mathrm{C}_{\mathrm{proppant}}, \mathrm{d}_{\mathrm{proppant}}, \rho_{\mathrm{proppant}}, \dot{\mathrm{Q}}_{\mathrm{f}}\right), \ \mathrm{i} = 1 \text{ to } 4 \quad (6)$$

Table 4.1—Range of simulation parameters used in this work

Parameter	Range
Casing Diameter (in.)	3, 6
Perforation Orientation	High-side, Low-side, Side
Perforation Diameter (in.)	3/8, 1/2
Proppant Diameter (μm)	600, 1260
Proppant Density (g/cm^3)	1.54, 2.65, 3.56
Proppant Concentration (lbm/gal)	1, 3
Wellbore Flow Rate (bbl/min)	6, 15, 30, 60, 120
Fluid Density (g/cm^3)	1
Fluid Viscosity (cp)	0.1, 1, 100

where D_{casing} is the casing diameter, D_{perf} is the perforation diameter, $C_{proppant}$ is the proppant concentration, $d_{proppant}$ is the proppant size, $\rho_{proppant}$ is the proppant density, and Q_f is the wellbore fluid rate.

We observe that the PTE is insensitive to the orientation of a perforation when the wellbore flow rate is larger than 6 bbl/min. It is also worth noting that fluid density and fluid viscosity are not included in Eq. 6; the former is not included because it was fixed in our parametric study, the latter is shown to have less impact at a high wellbore flow rate (60 bbl/min) and thus is not part of the equation. Our results also show that increasing the proppant concentration, proppant density, wellbore flow rate, or casing size can lower the PTE at a perforation. Proppant size and fluid viscosity have less influence on PTE when the wellbore flow rate is high enough to suspend the proppant. More details can be found in Wu and Sharma (2016). Fig. 4.3 shows the effect of increasing casing size and wellbore flow rate on PTE (after Wu and Sharma 2016).

The solutions of Eq. 6 can be used in Eq. 5 to obtain PTE versus PFR curves for flow conditions within the range of our parametric investigation (as listed in Table 4.1). These PTE correlations represent how efficiently proppant particles are transported into perforations under different

flow conditions and can be used to solve proppant transport at a wellbore scale. The proppant concentration entering a perforation is very different from the injected proppant concentration. Toe-side perforation clusters tend to accept more proppant at the beginning of a proppant stage.

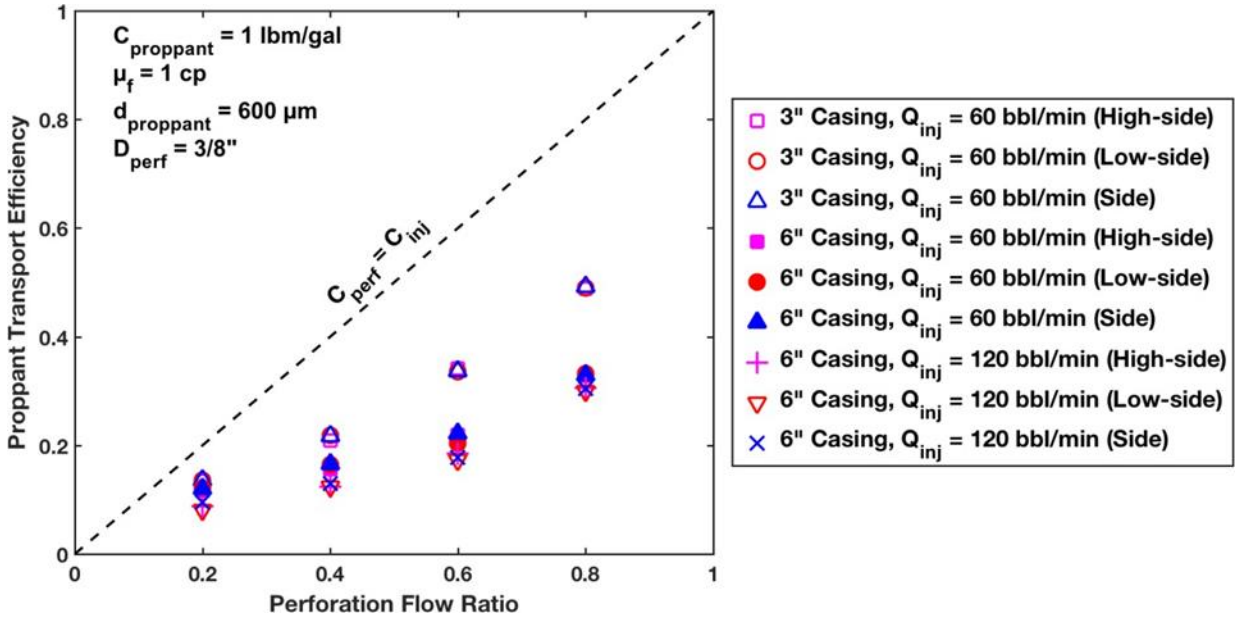


Fig. 4.3—Effect of increasing casing size and wellbore flow rate on PTE. After Wu and Sharma (2016).

Modeling Proppant Distribution among Multiple Clusters in a Fracturing Stage (Step 3)

The PTE correlation (Eq. 5) described above computes proppant transport through a single perforation with a given fluid distribution. This section describes how these calculations of PTE can be incorporated into a multi-cluster hydraulic fracturing model to calculate the dynamic proppant distribution among multiple perforations and clusters during a fracturing stage.

Calculation of Proppant Distribution among Multiple Clusters

The fluid and proppant distribution into each cluster can be obtained by incorporating the PTE correlation when solving the mass conservation of fluid and proppant in the wellbore. Eq. 7 is the mass balance equation for an incompressible fluid.

$$\dot{Q}_{inj} = \sum_{i=1}^{k} \dot{q}_{perf,i} \qquad (7)$$

Where $\dot{Q}_{inj}$ is the injection rate (pumping rate), $\dot{q}_{perf,i}$ is the flow rate entering perforation i, and k is the total number of perforations in a fracturing stage. Eq. 8 is the mass balance equation for proppant transport.

$$\dot{m}_{inj} = \sum_{i=1}^{k} \dot{m}_{perf,i} = \sum_{i=1}^{k} (\dot{m}_{upstream,i} \times \mathrm{PTE}_{perf,i}) \qquad (8)$$

Where $\dot{m}_{inj}$ is the proppant mass injection rate, $\dot{m}_{perf,i}$ is the proppant mass flow rate entering perforation i, $\dot{m}_{upstream,i}$ is the proppant mass flow rate at the upstream location of perforation i, and $\mathrm{PTE}_{perf,i}$ is the PTE at perforation i at current time.

Eq. 9 shows the functional form of PTE *perf* , *i* , which is governed by the PFR, and wellbore, fluid, and proppant properties. Note that since PTE *perf* , *i* varies with PFR, it should be re-solved whenever $\dot{q}_{perf,i}$ is re-evaluated.

$$\mathrm{PTE}_{perf,i} = f\left(\frac{\dot{q}_{perf,i}}{\dot{q}_{upstream,i}}, \text{ wellbore, fluid, and proppant properties}\right) \qquad (9)$$

The following steps summarize how the equations are solved to obtain the dynamic proppant distribution:

1. Calculate fluid distribution among multiple clusters, solve Eq. 7 to get $\dot{q}_{perf,i}$.

2. For each perforation, solve Eq. 6, and use the solutions of coefficients in Eq. 5 to get the PTE versus PFR curve. Then, find the PTE value on the curve using the PFR value at the perforation.

3. Solve Eq. 8 to get the proppant distribution into each perforation at the current time.

Implications of the PTE versus PFR curve

Fig. 4.4 shows an example of what the proppant concentration looks like at the beginning of a proppant stage. The flow rate in this example is 30 bbl/min, and the injected proppant concentration is 3 lbm/gal. Proppant distribution is evaluated by assuming the fluid is evenly distributed among 3 clusters, each with 4 perforations. This example demonstrates that the proppant distribution can be quite non-uniform even when fluid is uniformly distributed among all clusters. Proppant particles tend to accumulate near the toe-side perforations; and proppant concentration increases as slurry flows from the heel-side perforations to the toe-side perforations. This can be explained by the physics presented in the PTE vs PFR curve.

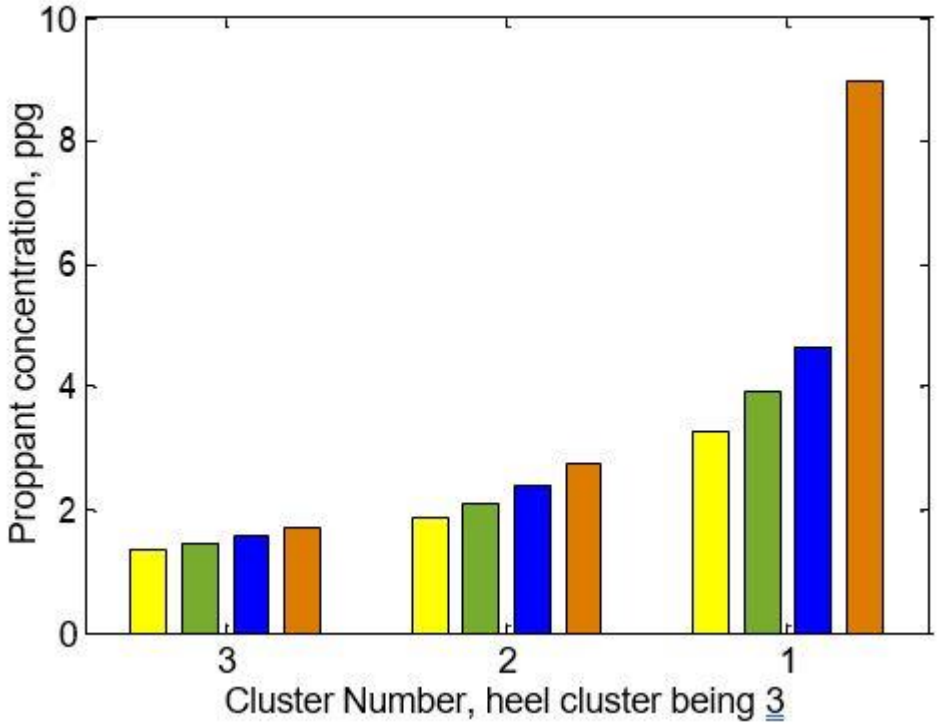


Fig. 4.4—An example of simulated proppant distribution using the PTE correlation. Slurry is injected at 30 bbl/min with 3 lbm/gal proppant concentration. Each cluster has 4 perforations. Cluster 3 is on the heel side and cluster 1 is on the toe side. Uniform fluid distribution among the 3 clusters is assumed. Result shows that proppant distribution is quite non-uniform. The heel-side perforations receive a dilute slurry, and the toe-side perforations receive a concentrated slurry.

The unit slope line in a PTE versus PFR curve represents a condition in which the proppant exactly follows the fluid. However, it was shown in our parametric study that most PTE versus PFR curves is below the unit slope line (see Fig. 4.3 for an example). This implies that under most flow conditions proppant particles are not transported efficiently into perforations. Instead, they tend to accumulate in the wellbore slurry and flow towards the toe cluster. Therefore, the heel-side perforation receives a proppant concentration that is lower than the injected value while the toe-side perforation receives a proppant concentration that is several times higher than the injected value.

Incorporation of the PTE Correlation into a Multi-Cluster Hydraulic Fracturing Model

The PTE correlation is incorporated in a multi-cluster hydraulic fracturing model to calculate dynamic fluid and proppant distribution during a fracturing stage. The PTE correlation was extrapolated when perforation flow conditions were outside the range of the parametric study shown in Table 1. As we have seen earlier, proppant particle inertia causes it to stay in the wellbore instead of turning into perforations. This increases the proppant concentration in the slurry near the toe-side clusters. The highly concentrated slurry increases the risk of screen-out in the near-wellbore regions at the toe-side clusters. In this work, we assume that when the proppant concentration flowing into a perforation exceeds 25% volume concentration, near-wellbore fractures connected to that perforation will screen out. When the near wellbore complex fractures are packed by proppant, the perforation is considered screened out and it no longer accepts any more fluid or proppant. It is important to point out that, proppant screen-out is not likely to happen in the perforation tunnel (Tran et al. 2009; Lafond et al. 2013) but is much more likely to happen in the near-wellbore region (in complex near-wellbore fractures). Once perforation screenout occurs, fluid and proppant are re-distributed into the other active perforations. This process continues until the proppant concentration in all perforations is below the plugging limit, and all these remaining perforations continue to receive fluid and proppant.

Multi-Cluster Hydraulic Fracturing Model

The model calculates simultaneous propagation of multiple planar fractures. In the model, fracturing fluid is distributed among multiple fractures using a flow resistance model. The flow resistance of a fracture is defined as the summation of the flow resistance in the wellbore, in the perforations, inside the fracture, as well as the reservoir. The distribution of fracturing fluid is inversely proportional to the flow resistance of fractures. In other words, a fracture with higher flow resistance receives less treating fluid than a fracture with lower resistance.

A detailed description of the flow resistance calculation and fracture discretization and propagation calculation is available in Yi and Sharma (2016). A simple flow chart for this method is shown in Fig. 4.5. The calculation of pressure drop in the perforation and the stress shadow effect is briefly discussed below.

$$\Delta P_{perf} = 0.2369 \frac{Q^2 \rho_f}{n^2 \mathrm{D}_{\mathrm{perf}}^{\ 4} C^2} \qquad \text{(10-a)}$$

$$C = 0.56 + 1.65 \times 10^{-4} M, \qquad (C \leq 0.89) \qquad \text{(10-b)}$$

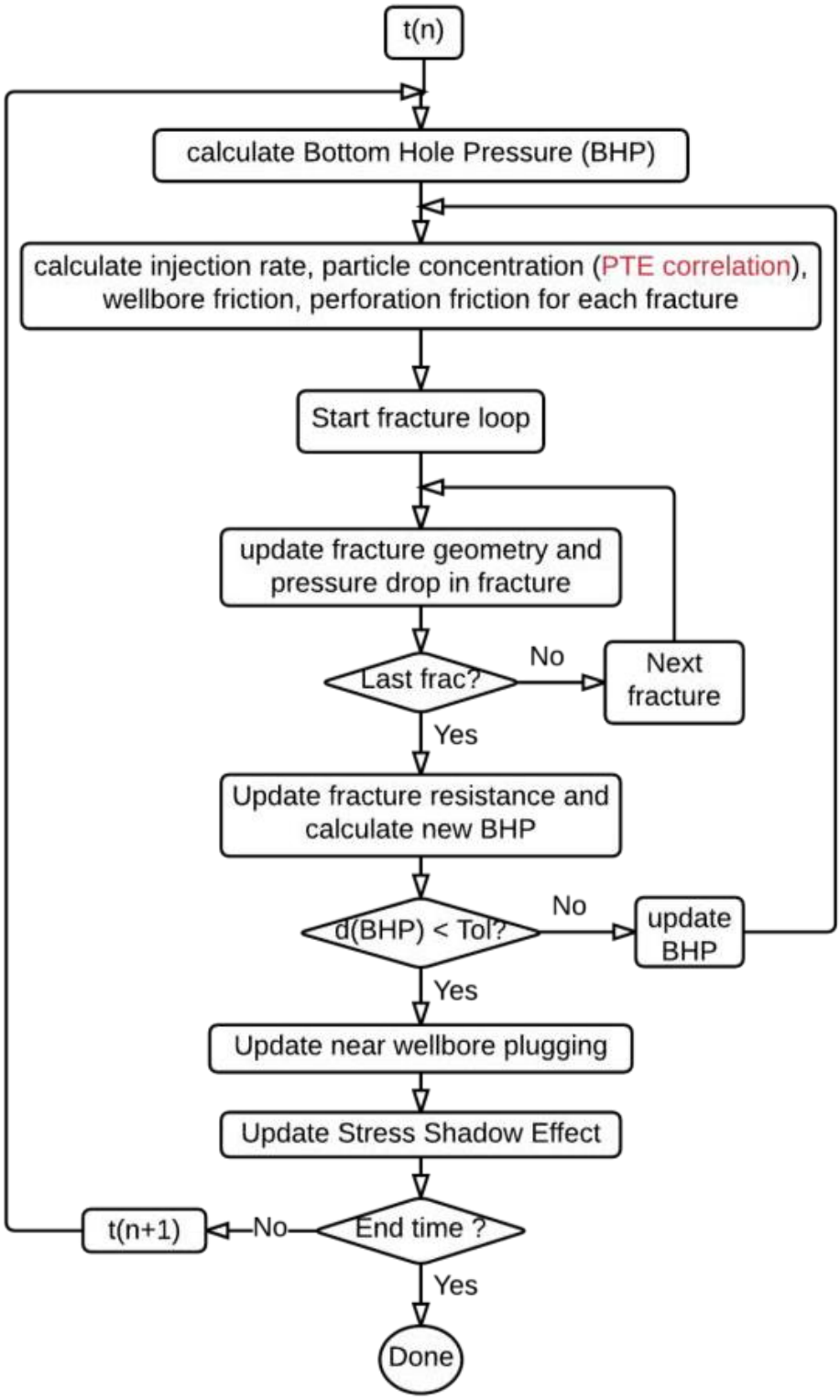


Fig. 4.5—Calculation flow chart of the multi-cluster hydraulic fracturing model.

Where Q is the total flowrate through perforations (bbl/min), ρ_f is the fluid density (lbm/gal), n is the number of unplugged perforations, D_{perf} is the perforation diameter (in), C is the discharge coefficient, and M is the total mass of proppant passed through perforations (lbm). Eq. 10-a shows that the perforation pressure drop is proportional to the square of total flow rate and is strongly influenced by the number of active perforations in a cluster. Eq. 10-b accounts for the erosion of perforations induced by sand slurries.

The opening of a fracture induces additional stress in its neighborhood and suppresses the propagation of its neighboring fractures. This effect is known as the stress shadow effect

(Roussel and Sharma 2012). In this model, the stress shadow effect is computed using the Westgaard's solution (Sneddon 1946) as shown in Fig. 4.6. For each fracture, the stress shadow effect from other fractures is calculated by superposition of the Westgaard solution.

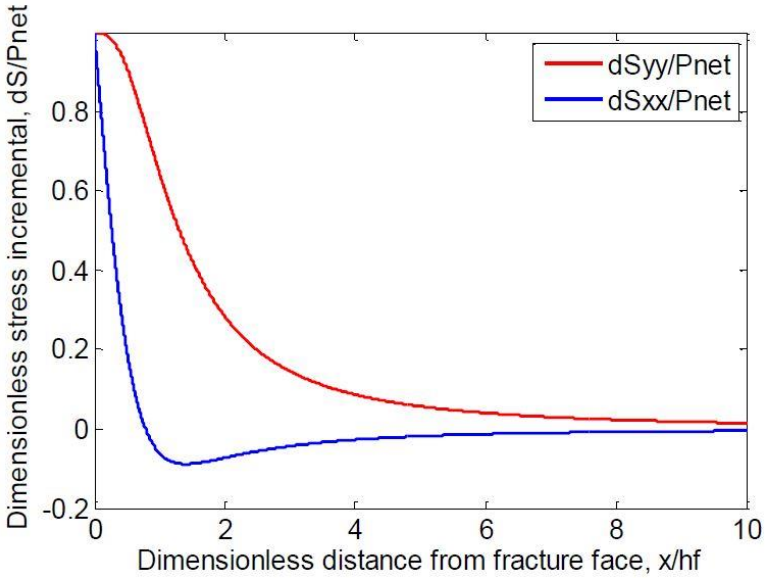


Fig. 4.6—Westgaard's solution describes the distribution of stress in an infinite 2D elastic medium resulting from the opening of a fracture under a uniform liquid pressure: x is the axis along the fracture face and y is the axis perpendicular to the fracture face; hf is fracture half height. The stress shadow effect is considered in this work by superposition of the Westgaard solution.

Results and Discussion

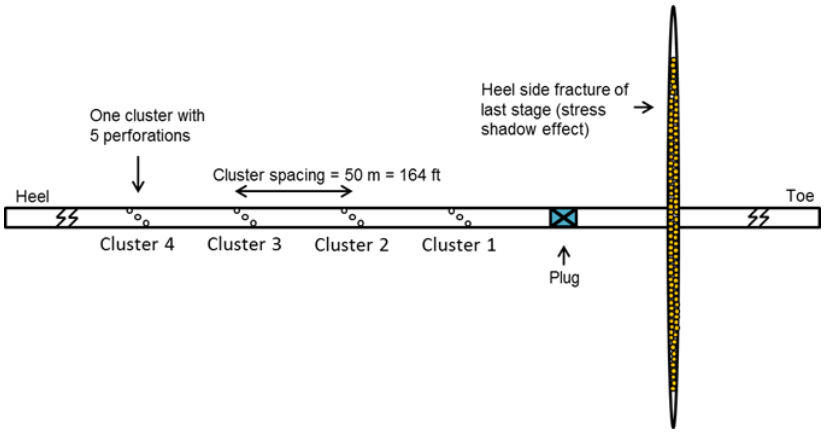


Fig. 4.7—Simulation case set up: 4 clusters with 50 m spacing, each cluster has 5 perforations. The heel-side fracture from the previous stage is included for stress shadow considerations. The toe cluster of the current stage is most affected by the fracture from the previous stage and the heel cluster of the current stage is least affected. The distance between the toe cluster of the current stage to the heel fracture of previous stage is 50 m.

The multi-cluster hydraulic fracturing model introduced above, combined with the PTE correlation for proppant transport, can be used to calculate the dynamic fluid distribution and sand distribution during a fracturing stage. In this section, simulation results for a typical horizontal well stimulation stage based on a field case are presented. The results are compared with field measurements made available by fiber optics (DTS and DAS). The simulated proppant distribution agrees very well with the field observations. The commonly observed trend of heel-biased sand placement is explained and the factors controlling the heel-biased treatment distribution are discussed. A fiber optic DAS and DTS monitored multi-stage cemented liner

completion case in "a low permeability over-pressured sand/siltstone reservoir" was published by Molenaar and Cox (2013). The fracturing stage was completed with 4 clusters with 50 m spacing. During the treatment, the two clusters close to the toe were found to screen out early in the proppant stage. And the heel- side two clusters ended up receiving most of the treatment. The final sand placement was severely heel biased.

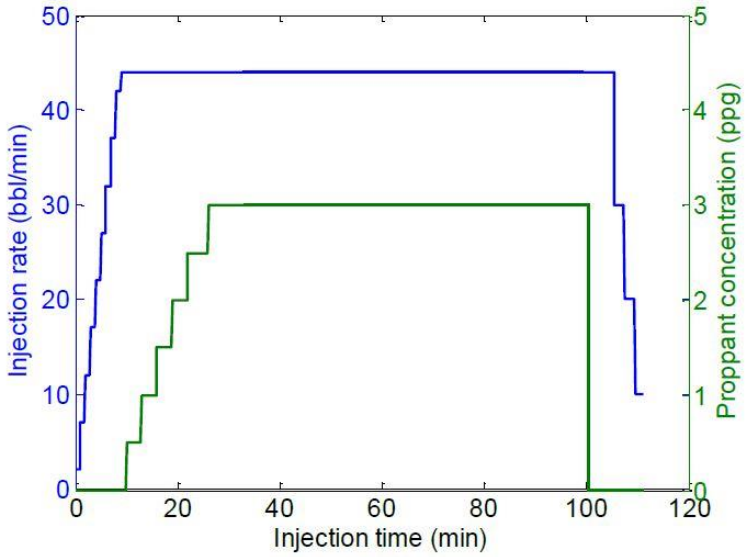


Fig. 4.8—Pumping schedule simulated. Maximum slurry injection rate 44 bbl/min; proppant concentration ramps up from 0 to 3 ppg. The whole treatment lasts for about 2 hours. Designed total proppant mass to pump is 100,000 lbm per cluster.

Simulations were performed based on this field case using all the information provided, such as: cluster number, cluster spacing, maximum injection rate, injected proppant concentration range. Some other parameters not given in the paper are estimated, such as pore pressure, minimum horizontal stress, Young's modulus, and wellbore diameter. The cluster arrangement is shown in Fig. 4.7. The heel-side fracture from the previous stage was included for stress shadow effect. The pumping schedule used in simulation is shown in Fig. 4.8. Estimated simulation parameters are shown in Table 4.2.

Table 4.2—Simulation Parameters

Parameter	Value	Parameter	Value
Wellbore Inner Diameter (in.)	3	Stimulation Depth (ft)	6818
Perforation Diameter (in.)	3/8	Pore Pressure (psi/ft)	0.44
Proppant Diameter (μm)	600	Minimum Horizontal Stress (psi/ft)	0.62
Proppant Density (g/cm^3)	2.65	Poisson's Ratio	0.23
Fluid Density (g/cm^3)	1	Young's Modulus (GPa)	5
Fluid Viscosity (cp)	0.1	Fracture Half Height (ft)	82

Simulation results showing the injection rate into each cluster are shown in Fig. 4.9. In the pad stage (first 10 min of treatment), cluster 1 (toe side cluster) receives less fluid than the other clusters mainly because of the stress shadow effect from the fracture of the previous stage, which induces additional stress that suppresses fracture propagation. The stress shadow effect from the previous stage has the most influence on the nearest cluster (cluster 1) and the least influence on the furthest cluster (cluster 4).

In the proppant stage, as predicted by the PTE correlation, the proportion of proppant entering a perforation is lower than the proportion of fluid entering the perforation at a high wellbore flow rate (Fig. 4.3). Therefore, the heel-side perforations receive only a small proportion of injected proppant at the beginning of the proppant stage. This increases the proppant concentration in the slurry as the slurry flows from the heel side to the toe side. The proppant concentration into the toe-side perforations is several times higher than the injected concentration. The highly concentrated slurry flowing into the toe-side perforations increases the risk of premature screenout.

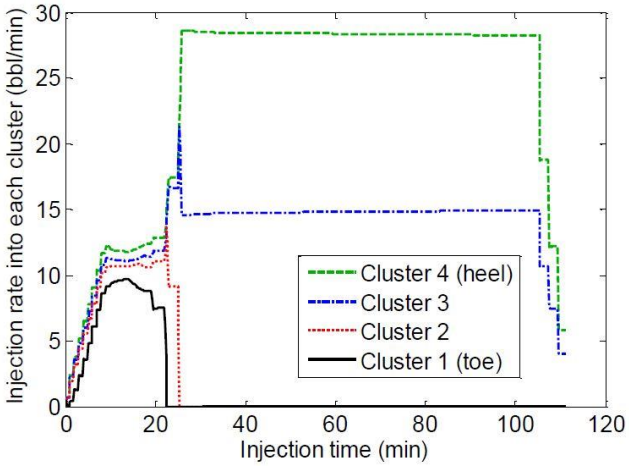


Fig. 4.9—Simulation results showing the injection rate into each cluster. Cluster 1 receives less fracturing fluid during the pad stage mainly because of the stress shadow effect from the fracture in the previous stage. At early pumping time (proppant stage), cluster 1 and cluster 2 screened out because of the highly concentrated slurry close to the toe side of the fracturing stage. Treatment fluid was quickly re-distributed into the other active perforations after the screenout of toe-side clusters. Each cluster has 5 perforations.

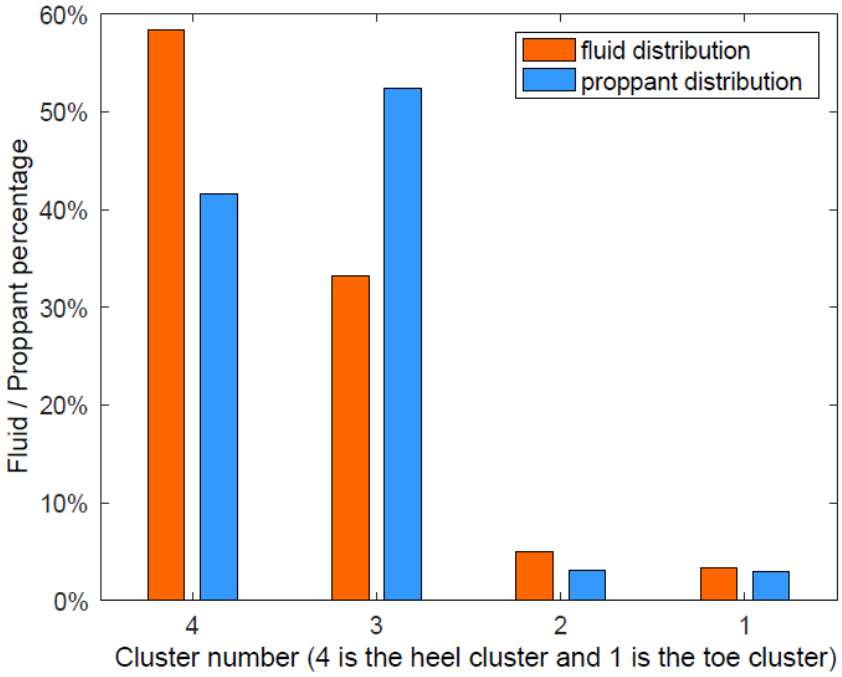


Fig. 4.10—Cumulative fluid and proppant distribution among the 4 clusters from simulation results. Two trends can be observed: (1) the fluid distribution and the proppant distribution are different. The fluid distribution declines from the heel-side cluster to the toe-side cluster, with the heel cluster receiving the majority of fracturing fluid. Cluster 3 receives less fluid, but more proppant than cluster 4, and (2) there is a strong heel-side bias in proppant placement. Each cluster has 5 perforations.

As stated in the previous section, a 25% proppant volume concentration into a perforation is used as an empirical criterion for the beginning of proppant screen-out in the near wellbore region. Fig. 9 clearly shows that the toe-side proppant concentration is high and this results in the near-wellbore region of cluster 1 (toe-side cluster) gradually screening-out. The flow rate into cluster 1 decreases as screenout occurs and fracturing fluid is re-distributed into the other active perforations. Eventually, all perforations in cluster 1 are screened out (at approximately 22 min). Shortly after that, cluster 2 also screens out (at about 25 min), leaving only the two heel-side clusters that continue to receive treatment. In fact, 3 out of 5 perforations in cluster 3 reached the critical concentration and were plugged later in the treatment as well. At the end of this simulation, there were only 2 active perforations in cluster 3 while all 5 perforations of cluster 4 remained active.

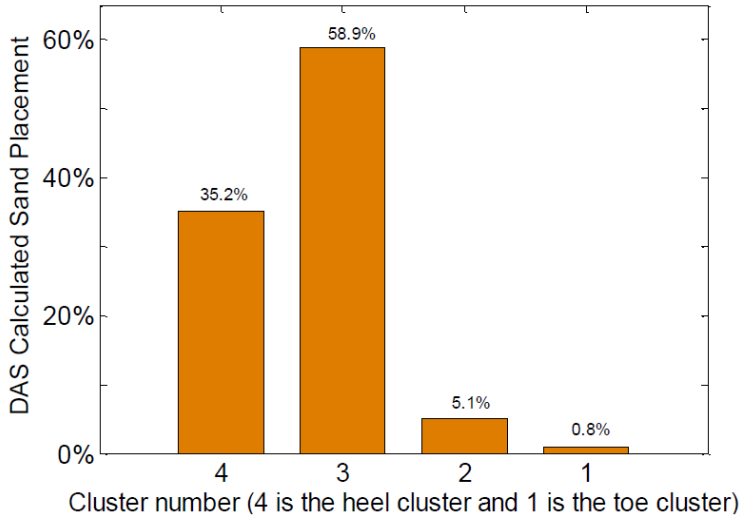


Fig. 4.11—Field data of sand placement calculated from DAS measurement. After Molenaar and Cox (2013).

The final cumulative fluid and sand distribution is shown in Fig. 4.10. The fluid distribution and the proppant distribution trends are different. First, cluster 1 receives more fluid, but less proppant than cluster 2. Second, the treatment distribution shows a declining trend from the heel-side clusters to the toe-side clusters. The main reason is that the numbers of active perforations in each cluster after about three-fourths of the treatment are: 5 – 2 – 0 – 0 (from heel to toe), respectively. With cluster 1 and 2 fully screened out, all the treatment fluid (44 bbl/min) has to flow through the remaining active perforations in clusters 3 and 4. The fluid distribution between clusters 3 and 4 is determined by the perforation pressure drop (Eq. 10). With fewer perforations open to flow, the perforation flow resistance of cluster 3 is higher than cluster 4 at the same flow rate. Therefore, cluster 4 will take more fluid than cluster 3 when the system is balanced. Third, more proppant ended up in cluster 3 even though cluster 4 receives more fluid. This can be explained by the inertia of the proppant particles reflected in the PTE. When flowing at a high velocity, it is difficult for proppant to turn 90 degrees into the perforation. Therefore, the ratio of proppant entering the perforation is less than the ratio of fluid entering it. This phenomenon is quantified by the PTE curve (see Fig. 4.3 for an example), which is below the 1:1 uniform particle distribution line. It is worth pointing out that the proppant volume entering a cluster is the slurry rate multiplied by the proppant concentration. If more fluid enters cluster 4, then even if the proppant concentration in cluster 4 is lower than cluster 3, the total amount of proppant entering cluster 4 could still be more than cluster 3.

The sand placement estimated from DAS data for this field case is published by Molenaar and Cox (2013) and shown in Fig. 4.11. A comparison between Figs. 10 and 11 show that the proppant distribution among the 4 clusters is well captured by the simulation. The two clusters on the heel side receive most of the proppant while the two toe-side clusters receive very little proppant. More proppant ended up in the second cluster from the heel (cluster 3) than the first cluster from the heel (cluster 4).

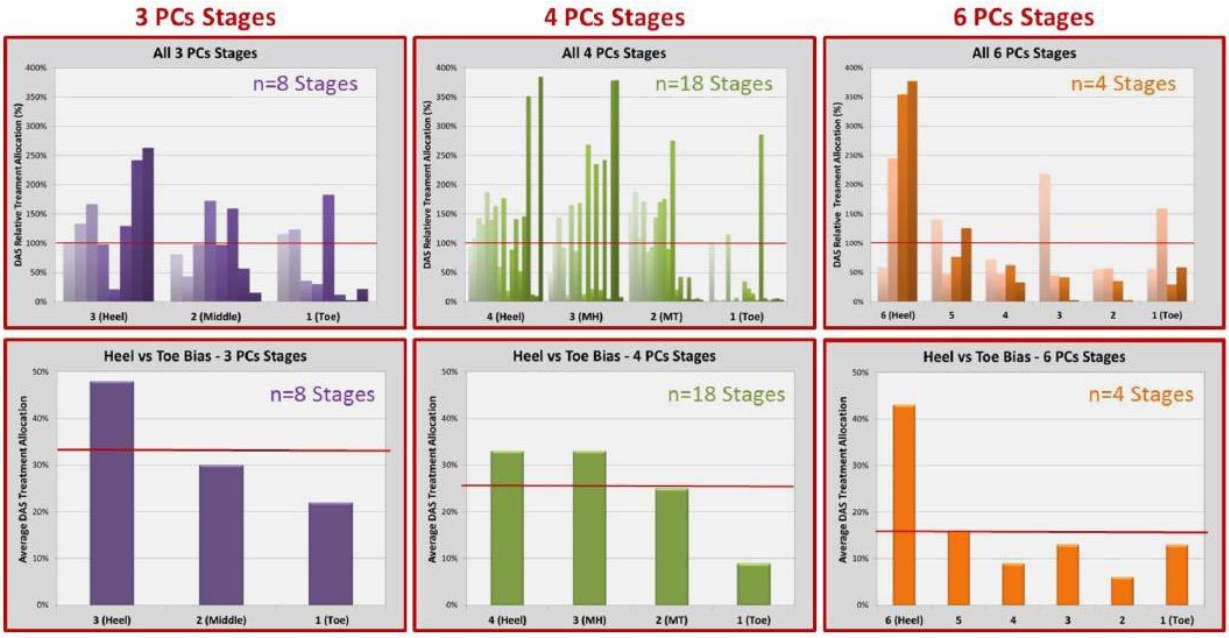


Fig. 4.12—Field data published by Ugueto et al. (2016). Heel-biased treatment distribution was observed repeatedly in all 3-cluster, 4-cluster, and 6-cluster stages. In each column, the top figure shows the DAS measured treatment allocation among clusters in multiple fracturing stages, the bottom figure shows the averaged treatment allocation from the observed trend.

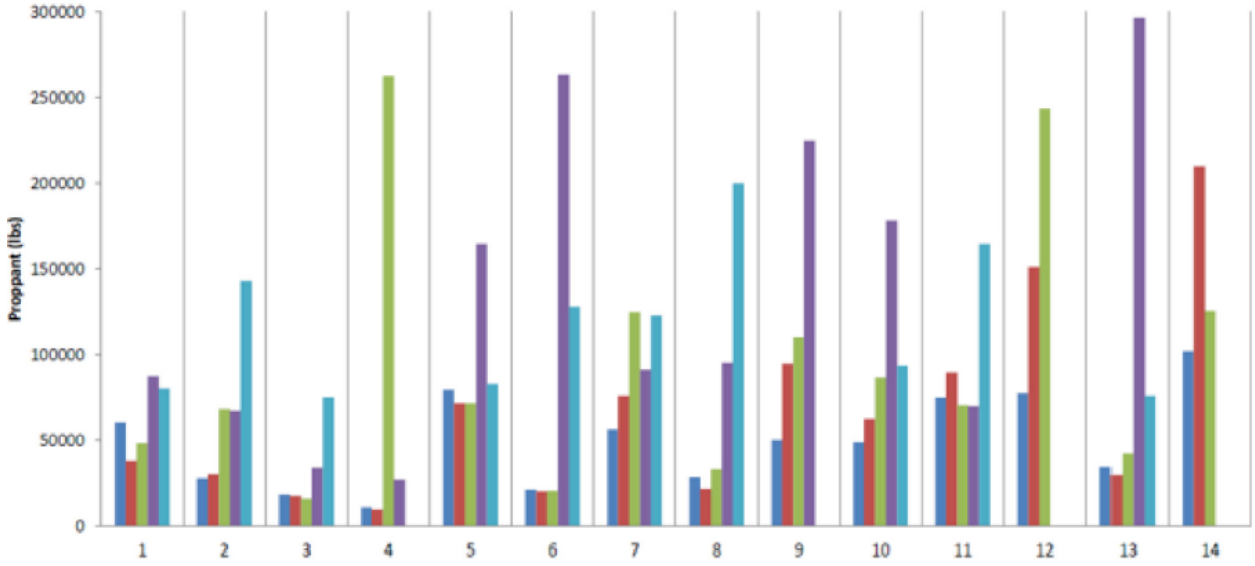


Fig. 4.13—Field data published by Wheaton et al. (2016). Proppant distribution of 14 stimulation stages is presented. For each stage, the bars from left to right show the proppant placement from the toe cluster to the heel cluster. These results show a general trend of biased proppant distribution towards the heel-side clusters. In some cases, the heel cluster gets most of the proppant. In other cases, the second cluster from the heel gets most of the proppant.

The biased proppant placement towards the heel has also been independently reported by Ugueto et al. (2016) and Wheaton et al. (2016). These papers present the treatment distribution

estimated using DTS and DAS measurements. Fig. 4.12 from Ugueto et al. (2016) and Fig. 4.13 from Wheaton et al. (2016) show two field examples.

Fig. 4.12 presents the treatment distribution as measured by DAS for eight 3-cluster stages, eighteen 4-cluster stages, and four 6-cluster stages. Heel-biased treatment distribution was observed consistently in all 3-cluster, 4-cluster and 6-cluster stages.

Fig. 4.13 shows data published by Wheaton et al. (2016). 14 stimulation stages are presented in the figure. For each stage, the bars from left to right shows the proppant placement from toe cluster to heel cluster. These results clearly show the biased proppant placement towards to heel side. In some cases, the heel cluster gets most proppant; in other cases, the second cluster from the heel gets most proppant. One important observation in their work is that in many stages, the use of diverter to improve proppant placement did not change the distribution of proppant in the clusters. The dominant fracture cluster remained dominant throughout the treatment.

To summarize, heel-biased proppant distribution had been observed multiple times in the field in plug-and-perf stimulation stages. According to the analysis above, the factors causing the heel-biased distribution are the following:

1. The stress shadow induced by fractures created in the previous stage influences the toe cluster the most and the heel cluster the least. This can lead to a non-uniform fluid distribution that favors the heel-side fractures.

2. As shown in the PTE correlation, the proppant ratio entering a perforation is less than the fluid ratio entering the perforation. This makes the proppant concentration flowing into the heel-side clusters lower than the injected concentration. The proppant concentration in the wellbore is therefore increased as the slurry flows from the heel side to the toe side.

3. The highly concentrated slurry in the toe-side clusters increases the risk of premature screenout. Screenout risk is high especially early in the proppant stage, when near-wellbore complexity causes a large pressure drop.

4. As toe-side clusters screen out, fluid and proppant are re-distributed into heel-side clusters. At the end of the stimulation, the cumulative fluid distribution and proppant distribution are heel biased.

Proppant and Fluid Distribution in the HFTS 6SU Well

Table 4.3 Layer properties for the 6SU well (Stage 23).

LayerName	Thickness (ft)	Top Depth (ft)	Porosity	k (D)	Biot's Coeff	Shmin (psi)	Shmax (psi)	Sv (psi)	Pore Pressure (psi)	YM(Mpsi)	PR
Dean	147.6	7214.6	0.05	5.01E-05	0.7	4149.5	4649.9	7787.1	2880.5	2.16	0.25
UWTop	121.4	7362.2	0.07	7.01E-05	0.7	4790.6	5291.0	7945.2	3494.0	2.25	0.24
UW1	45.9	7483.6	0.07	7.01E-05	0.7	4921.1	5421.5	8075.7	3594.0	2.32	0.24
UW1Base_1	72.2	7529.5	0.067	6.71E-05	0.7	4999.5	5499.8	8125.0	3646.3	2.34	0.24
UW1Base_2	36.1	7601.7	0.067	6.71E-05	0.7	5324.3	5824.7	8201.9	3670.9	2.34	0.24
UW1Base_3	42.7	7637.8	0.067	6.71E-05	0.7	4829.8	5330.1	8241.1	3689.8	2.34	0.24
UW2	95.1	7680.4	0.063	6.31E-05	0.7	5048.8	5549.2	8287.5	3917.5	2.44	0.26
UW2Base +	49.2	7775.6	0.056	5.58E-05	0.7	6049.5	6549.9	8389.0	4422.6	2.40	0.27
MW1Base_Co	150.9	7824.8	0.064	6.41E-05	0.7	5572.6	6073.0	8399.5	4397.4	2.02	0.27

The analysis presented above was applied to the 6SU well to see if the heel dominated effects could be seen in this well. The Inputs used of the simulation are shown in Table 4.3. The computed injection rate of each fluid into each cluster and the proppant distribution are shown

below in Figure 4.15 and 4.16. Heel dominated fractures will develop in this well. Evidence of premature screenout in Cluster #3 is clearly seen in Figure 4.14.

Table 4.4 Wellbore and perforation information for the 6SU well (Stage 23).

Cluster Number	3
Cluster Spacing (ft)	90
Wellbore Diameter(in)	4.892
Perf per cluster	15, 15, 15
Perf Phasing	60, 60, 60
Perf Diameter(in)	0.42

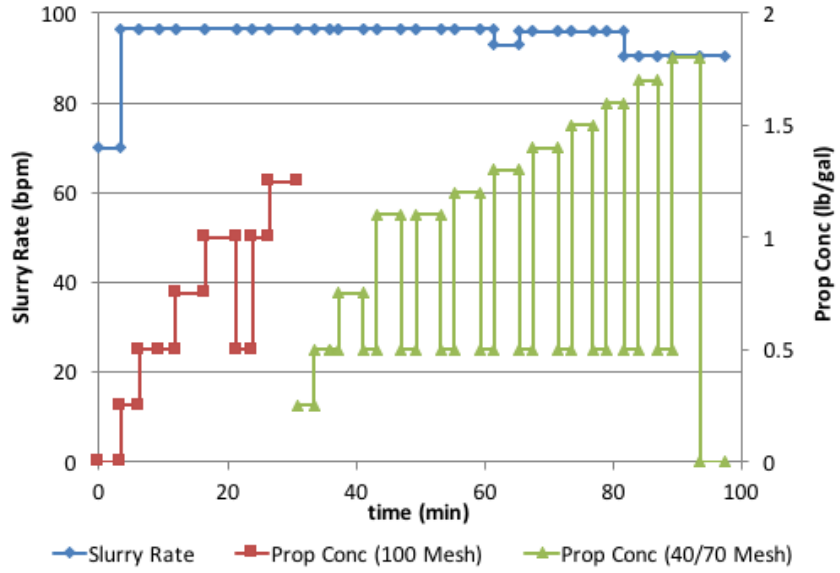


Figure 4.14 The pumping schedule for the 6SU well (Stage 23).

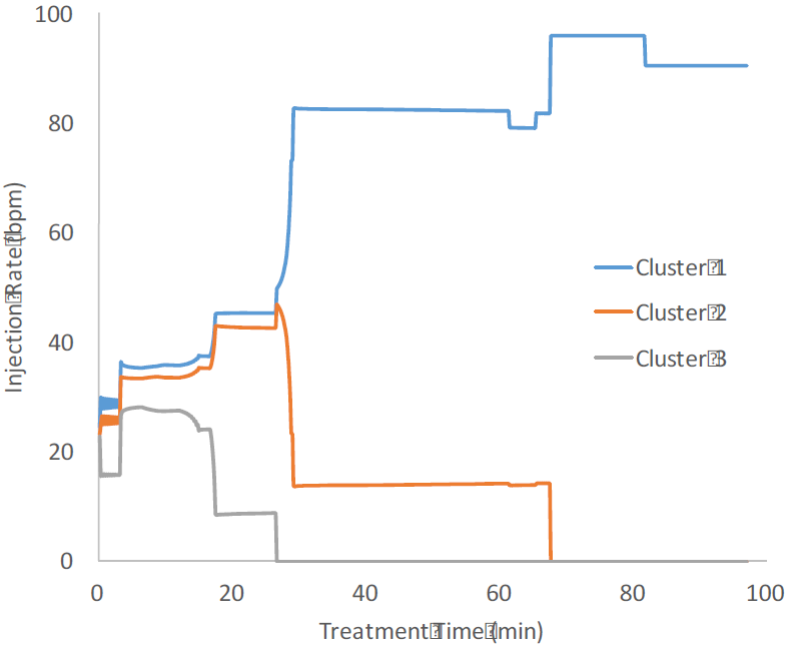


Fig. 4.15. Simulation injection rate into each cluster.

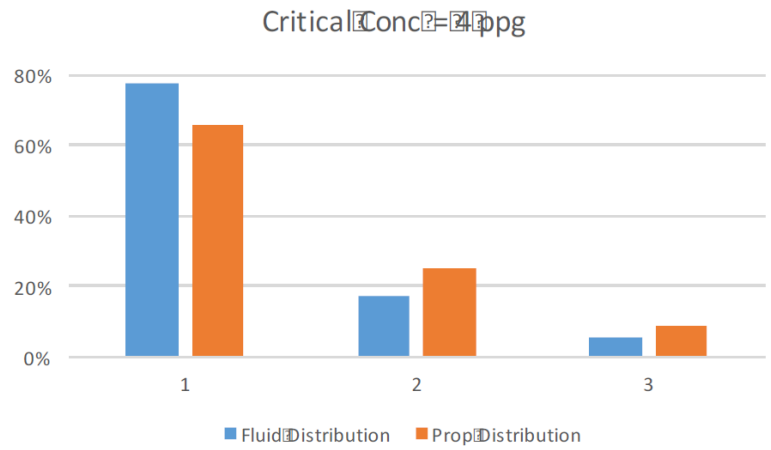


Fig. 4.16 Cumulative fluid and proppant distribution into each cluster.

Conclusions

In this work, a method is presented to compute the distribution of proppant and fluid into proppant clusters for any given wellbore and perforation geometry and proppant pumping schedule. The method is based on CFD-DEM simulations of proppant transport in wellbores. It is shown that proppant particles do not flow into perforations in the same proportion as the fluid. At high wellbore velocities, the inertia of the proppant particles prevents them from turning the corner and entering perforations. This effect is quantified through the proppant transport efficiency (PTE) correlations we have developed based on our CFD-DEM results. This causes much higher proppant concentrations near the toe clusters leading to premature cluster screenout. The PTE correlation has been incorporated into a multi-cluster hydraulic fracturing model to simulate dynamic fluid and proppant distribution among multiple clusters in plug-and-perf stimulation stages. The simulated proppant distribution for a field case agrees very well with field observations based on DAS and DTS data. The frequently observed trend of heel-biased proppant distribution has been explained and factors causing the heel-biased distribution to have been discussed.

More specific conclusions of this work are summarized as follows:

1. A PTE correlation has been developed by fitting the CFD-DEM simulation results. The PTE correlation quantifies the ratio of proppant entering a perforation based on given fluid flow ratio entering the perforation as slurry flows in the wellbore.

2. The PTE curve in most occasions is below the 1:1 uniform distribution line, implying that the proppant ratio entering a perforation is less than the fluid ratio entering the perforation because of the inertia of the denser solid particles.

3. The proppant concentration entering the heel-side clusters is lower than the injected concentration. The proppant concentration in the slurry increases as the slurry flows from the heel side to the toe side. At the toe cluster, the slurry concentration can be several times higher than the injected proppant concentration.

4. The highly concentrated slurry increases the risk of premature screenout of the toe-side clusters. Screenout risk is especially high early in the proppant stage, when the pressure drop caused by near-wellbore complexity is significant.

5. As perforations in the toe-side clusters screen out, fluid and proppant are re-distributed into other active perforations. At the end of a fracturing stage, the cumulative fluid and proppant distributions among multiple clusters are heel-biased. Furthermore, the cumulative fluid distribution and proppant distributions can be different from one another.

6. The influence of stress shadow effect has been considered. The stress shadow effect from fractures of previous stage suppresses fracture propagation from the toe-side clusters. This also promotes a heel-biased fluid distribution.

Effect of Reservoir Heterogeneity on the Vertical Migration of Hydraulic Fractures

Summary

The HFTS data set shows that the Wolfcamp formation is very heterogeneous and natural fractures and bedding planes play a very important role in controlling he fracture geometry. In this chapter the effect of different types of vertical reservoir heterogeneities on fracture propagation was systematically investigated. A fully 3-D, poroelastic model that does not prescribe the crack propagation path is used to estimate the fracture geometry in vertically heterogeneous rocks. Complex fracture trajectories are shown to occur and this limits fracture height growth. It is shown that the presence of bedding planes, layer interfaces and even smaller scale heterogeneities can lead to fracture turning, kinking or branching. The mechanisms that control these characteristic fracture propagation behaviors (“turning”, “kinking”, and “branching”) near the layer interface are explored in detail. In layered systems, the mechanical property contrast between layers, the dip angle, the stress contrast and the mechanical properties of the layer interface all play an important role in controlling the fracture trajectory. Conditions under which each type of behavior is expected to occur are clearly delineated.

Introduction

Shale gas/oil reservoirs inherently contain heterogeneities at multiple length scales (Filder, 2011; Mokhtari et al., 2014). Examples of this include micrometer scale heterogeneities at the grain scale, and meter scale heterogeneities such as bedding planes (Maxwell et al., 2009; Walton and McLennan, 2013). All of them may influence hydraulic fracture propagation. However, the effect of these heterogeneities on fracture propagation has not been fully investigated. The effect of layer-scale heterogeneity on fracture propagation was investigated by several authors (Gu and Siebrits, 2008; Thiercelin et al., 1989; van Eekelen, 1982). They studied the effect of such layering on width growth in planar fractures. However, contrasts in mechanical properties and weak interfaces between different layers, not only affect the width of planar fractures, but can also cause complicated fracture propagation patterns. As Fisher et al. (Fisher and Warpinski, 2012) point out, fractures can show complicated behavior such as “bending”, “kinking”, and “offsetting” at layer interfaces. When these phenomena occur, fracture height growth is limited when compared with a planar fracture due to the narrower fracture width at the fracture turning point. Moreover, this is likely to cause proppant bridging or screen out (Fisher and Warpinski, 2012). Therefore, understanding the mechanism of fracture propagation near layer interfaces is important from a fracture design viewpoint. A few authors have tried to investigate such complicated fracture propagation behavior near layer interfaces. Based on an energy analysis and comparisons with experimental results, Wu et al. (Wu et al., 2004) have shown that hydraulic

fractures can turn (bend), kink, and be arrested at the layer boundary when fractures go from a softer layer to a harder layer. Zhang et al. (Zhang et al., 2007) have demonstrated that the magnitude of far field stresses acting on a layer interface and the frictional strength of a layer interface mainly affect fracture turning along the layer interface. Garcia et al. (Garcia et al., 2013) have shown that the contrast in fracture toughness could also cause different types of complicated fracture propagation behavior ("turning", "kinking", and "offsetting") near the layer interface. However, a comprehensive study of the conditions under which the different fracture propagation behavior should be expected to occur for multi-layered rocks has not been conducted yet. Part of the reason for this has been the inability of past models to simulate complex fracture propagation patterns without prescribing the fracture propagation direction. Allowing the fracture to propagate in any direction (controlled by the underlying physics and material properties) and to branch into multiple fractures is essential to simulating fracture complexity in heterogeneous rocks.

Peridynamics is a recently developed nonlocal theory of continuum mechanics that accounts for discontinuities such as fractures naturally (Silling and Askari, 2005; Silling et al., 2007; Silling et al., 2010b). Its integral formulation eliminates the spatial derivatives in the classical theory that are incompatible with the nature of cracks. The validity and applicability of peridynamics to solid and fracture mechanics has been demonstrated (Askari et al., 2008; Askari et al., 2006; Bobaru, 2007; Silling and Bobaru, 2005; Silling et al., 2010a; Xu et al., 2007). We have recently derived a new peridynamics fluid flow formulation (Katiyar et al., 2014) and developed a new peridynamics-based hydraulic fracturing model (Ouchi et al., 2015a; Ouchi et al., 2015b). This model can simulate non-planar, multiple fracture growth in arbitrarily heterogeneous reservoirs by solving fracture propagation, deformation, fracturing fluid pressure, and pore pressure simultaneously.

In order to investigate the effect of vertical heterogeneity on fracture propagation at different scales, we use this new peridynamics-based hydraulic fracturing model to simulate fracture propagation in vertically heterogeneous porous media. We systematically investigate how the four types of phenomena ("crossing", "turning (bending)" "kinking", and "branching") take place near the layer interface depending on the contrast in the layer mechanical properties, the layer dip angle and the properties of the interface.

Mathematical Model

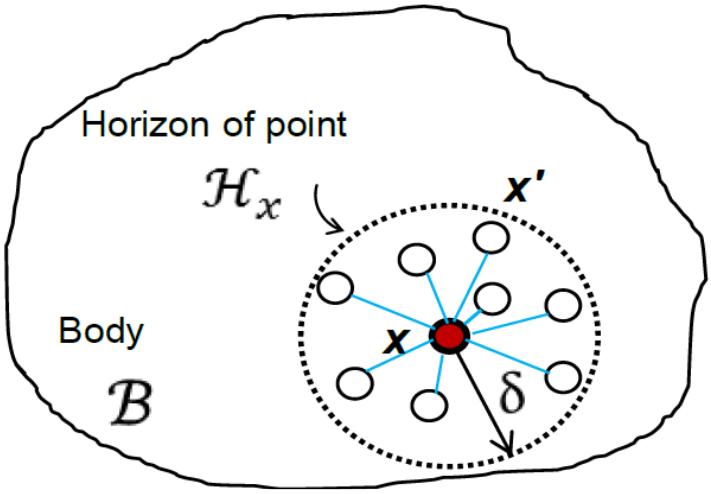


Fig. 5.1. "Horizon" and "Bond" (Ouchi et al., 2015b).

The details of the model used in this study have been presented by Ouchi et. al (Ouchi et al., 2015a; Ouchi et al., 2015b). This model takes into account fracture propagation and poroelastic effects by simultaneously solving the three governing equations for mechanics, porous flow, and fracture flow. FEM, FVM and other classical models discretize and solve the governing equations in the form of PDEs. In contrast, peridynamics-based model solves the integral equations obtained by integrating the PDEs over an influence region called the 'horizon'.

The peridynamics equations have one to one correspondence with the classical PDEs. For example, the rock momentum balance is written as:

In classical theory:

$$\rho[\boldsymbol{x}]\ddot{\boldsymbol{u}}[\boldsymbol{x},t] = \boldsymbol{\nabla}\cdot\boldsymbol{\sigma}[\boldsymbol{x},t] + b[\boldsymbol{x},t]$$

In peridynamics theory:

$$\rho[\boldsymbol{x}]\ddot{\boldsymbol{u}}[\boldsymbol{x},t] = \int_{\mathcal{H}_x}\left(\underline{T}[\boldsymbol{x},t]\langle\boldsymbol{\xi}\rangle - \underline{T}[\boldsymbol{x}',t]\langle-\boldsymbol{\xi}\rangle\right)dV_{x'} + b[\boldsymbol{x},t]$$

where, T is the peridynamic force vector state [N/m^6], V is material volume [m^3] and $\mathcal{H}_x$ is the 'horizon'.

Results and Discussion

Investigation of Fracture Propagation Behavior near a Layer Boundary

Model Description

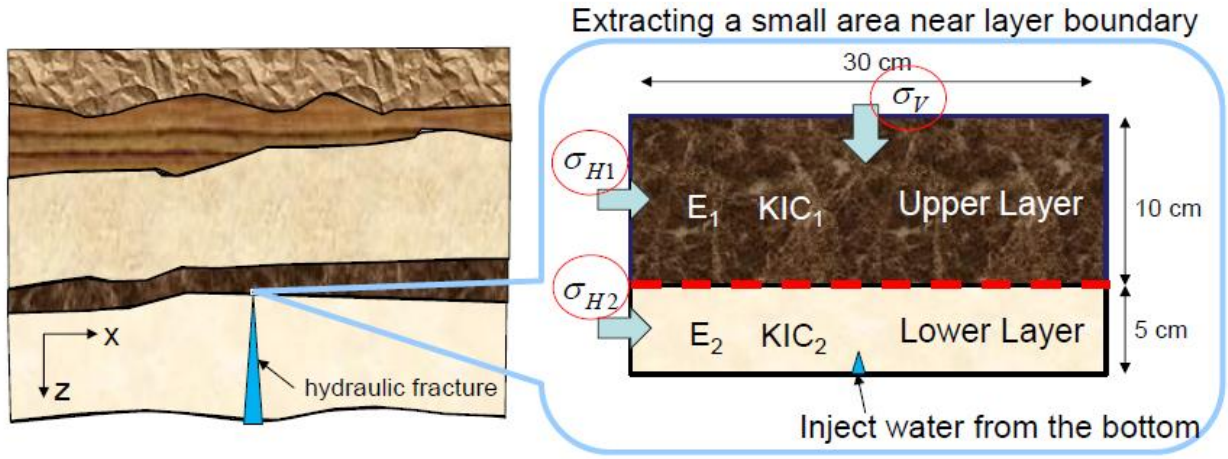


Fig. 5.2. Schematic view of the 2-layer model.

To investigate the effect of mechanical property contrast and layer dip angle on fracture propagation near a layer boundary, as shown in Fig. 5.2., we constructed a two-layer model and conducted a comprehensive parametric study of the model. The model domain (30 cm15 cm) is divided into 150 x 75 elements. The upper two-thirds of the domain (10 cm from the top) is assigned to Layer 1 and the lower one-third of the domain (5cm from the bottom) is assigned to Layer 2. For fluid flow calculations, a no-flow boundary condition is applied to every boundary (top, bottom, left side, and right side). For mechanical calculations, a normal stress of magnitude is applied as a maximum principal stress at the top boundary, and a normal stresses of magnitude (horizontal stress for layer 1) and (horizontal stress for layer 2) are applied to Layer 1 and Layer 2 respectively. Note that to avoid stress concentration near the layer interface due to

the different magnitude of strains in the two different layers, the same stress condition as the far field stresses mentioned above are directly assigned to each element as a background force vector (in the same manner as explained in the above section). As shown in Fig. 5.2., to simulate fracture propagation, a fluid injection point is set as a "dual injection point" at the bottom of the model and no vertical displacement is allowed at the bottom boundary so that the boundary can only deform in the horizontal direction. By changing the mechanical properties, horizontal stress, and layer dip angle, we investigated the fracture propagation behavior near the layer interface. The parameters we changed in this section are summarized in Table 5.1. Calculation settings are summarized in Table 5.2.

Effect of Young's Modulus, Fracture Toughness, Horizontal/Vertical Stress Contrast, and Layer Dip Angle

Table 5.1. Parameter list for 2-layer model.

Parameters	Variation
Young's modulus in layer 1 (GPa)	10, 20, 40, 80
Young's modulus in layer 2 (GPa)	10, 20, 40, 80
Fracture toughness in layer 1 (MPa $m^{0.5}$)	0.25, 0.5, 1.0, 1.4, 2.0, 2.5, 3.0, 5.0
Fracture toughness in layer 2 (MPa $m^{0.5}$)	0.25, 0.5
Layer dip angle (degree)	0, 15, 30
Vertical stress (MPa)	41, 47, 50, 60
Horizontal stress in layer 1 (MPa)	40, 45, 50

Table 5.2. Calculation settings.

Parameter	Value
Dimension in horizontal direction L_x (cm)	30.0
Dimension in vertical direction L_y (cm)	15.0
Layer 1 thickness (cm)	10.0
Layer 2 thickness (cm)	5.0
Boundary stress in vertical direction σ_V (MPa)	Table 5.1
Boundary stress in layer 1 in horizontal direction σ_{H1} (MPa)	Table 5.1
Boundary stress in layer 2 in horizontal direction σ_{H2} (MPa)	40.0
Young's modulus in layer 1	Table 5.1
Young's modulus in layer 2	Table 5.1
Poisson's ratio	0.25
Initial pore pressure (MPa)	30.0
Injection rate (kg/s)	0.005
Fracturing fluid viscosity (cp)	1.0
Medium permeability (mD)	0.00001
Number of elements	150×75
Horizon size ($=\frac{\delta}{\Delta x}$)	3.0

The effect of Young's modulus, fracture toughness contrast, horizontal/vertical stress difference, and layer dip angle are summarized in Fig. 5.3-5.5. All other properties are fixed as shown in Table 5.3. Different fracture propagation patterns are observed by changing the stress contrast (= σ_V- σ_H plotted on the x axis), fracture toughness of the first layer (plotted on the y axis), and layer dip angle. As shown in Fig. 5.3-5.5, three types of fracture propagation behavior near the layer interface are observed: "turning", "branching", and "kinking". For each fracture propagation behavior, we first explain the propagation mechanism based the results of some specific cases. After that, we discuss the effect of each parameter on the propagation behavior.

Table 5.3. List of fixed and changed parameters.

Parameters	Condition	Variation
Young's modulus in layer 1 (GPa)	Changed	10, 20, 40, 80
Young's modulus in layer 2 (GPa)	Changed	10, 40, 80
Fracture toughness in layer 1 (MPa $m^{0.5}$)	Changed	0.25, 0.5, 1.0, 1.4, 2.0, 2.5, 3.0, 5.0
Fracture toughness in layer 2 (MPa $m^{0.5}$)	Fixed	0.5
Layer dip angle (degree)	Changed	0, 15, 30
Vertical stress (MPa)	Changed	41, 47, 50, 60
Horizontal stress in layer 1 (MPa)	Fixed	40
Medium permeability (mD)	Fixed	0.00001

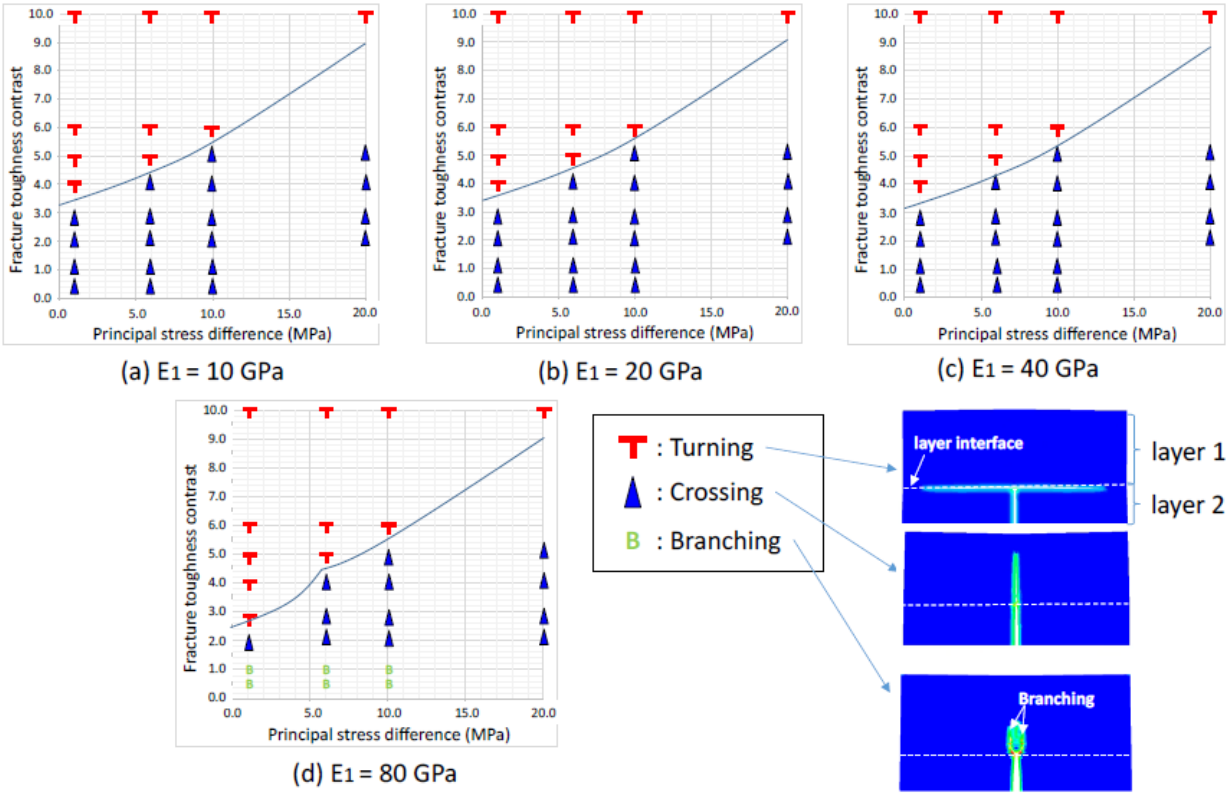


Fig. 5.3. Fracture turning behavior (layer dip angle = 0 degree, E2=10 GPa).

Fracture Turning Mechanism

Fig. 5.6 shows the bottom-hole (BHP) change with time in the two different cases where only the fracture toughness contrast is different (1.41 MPa $m^{0.5}$ and 2.0 MPa $m^{0.5}$). All the other parameters are fixed as follows: layer dip angle = 0 degree, Young's modulus contrast 1.0 (= 10GPa/10GPa), and principal stress difference = 1 MPa. As shown in Fig. 5.6, the fracture passes through the layer interface in the case where fracture toughness of the first layer (KIC1) is 1.41

MPa $m^{0.5}$ (we call this case the "crossing" case) while the fracture turns along the layer interface in the case where the fracture toughness in Layer 1 is 2.0 MPa m0.5 (we call this case the "turning" case).

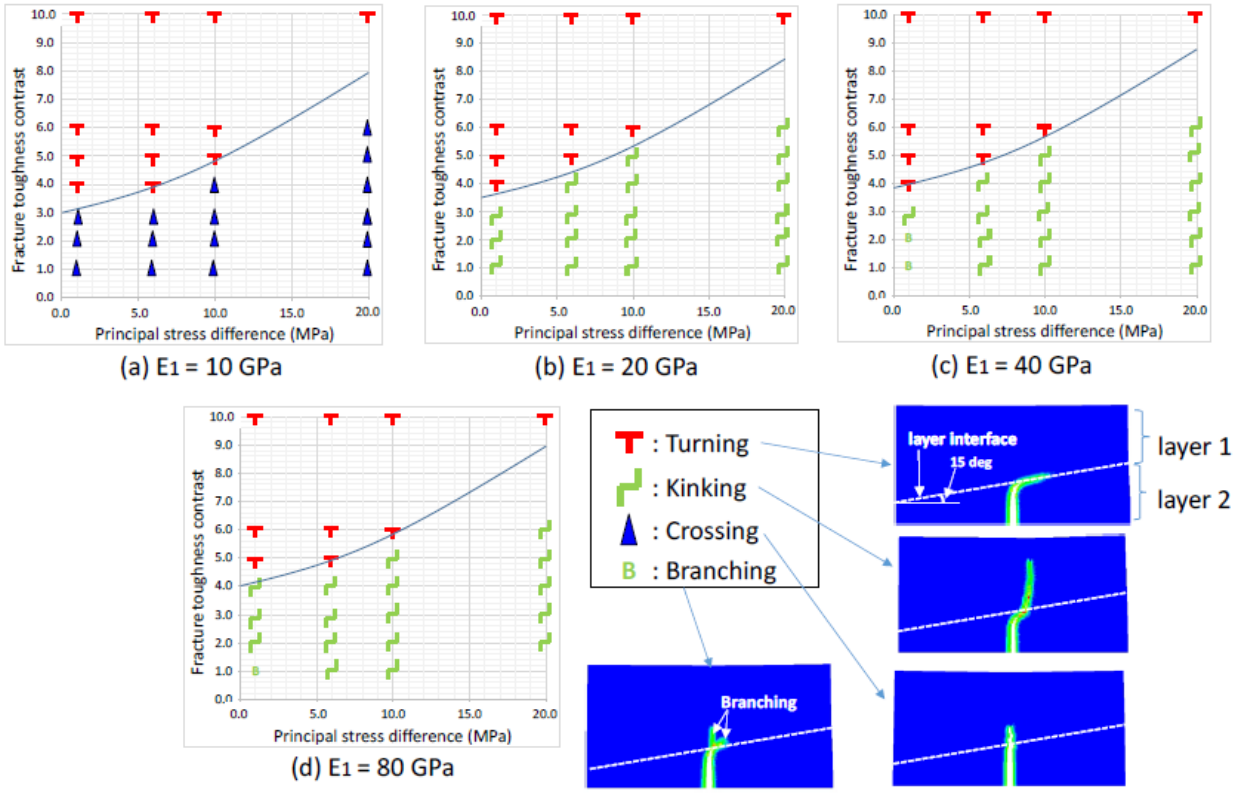


Fig. 5.4. Fracture turning behavior (layer dip angle = 15 degree, E2=10 GPa).

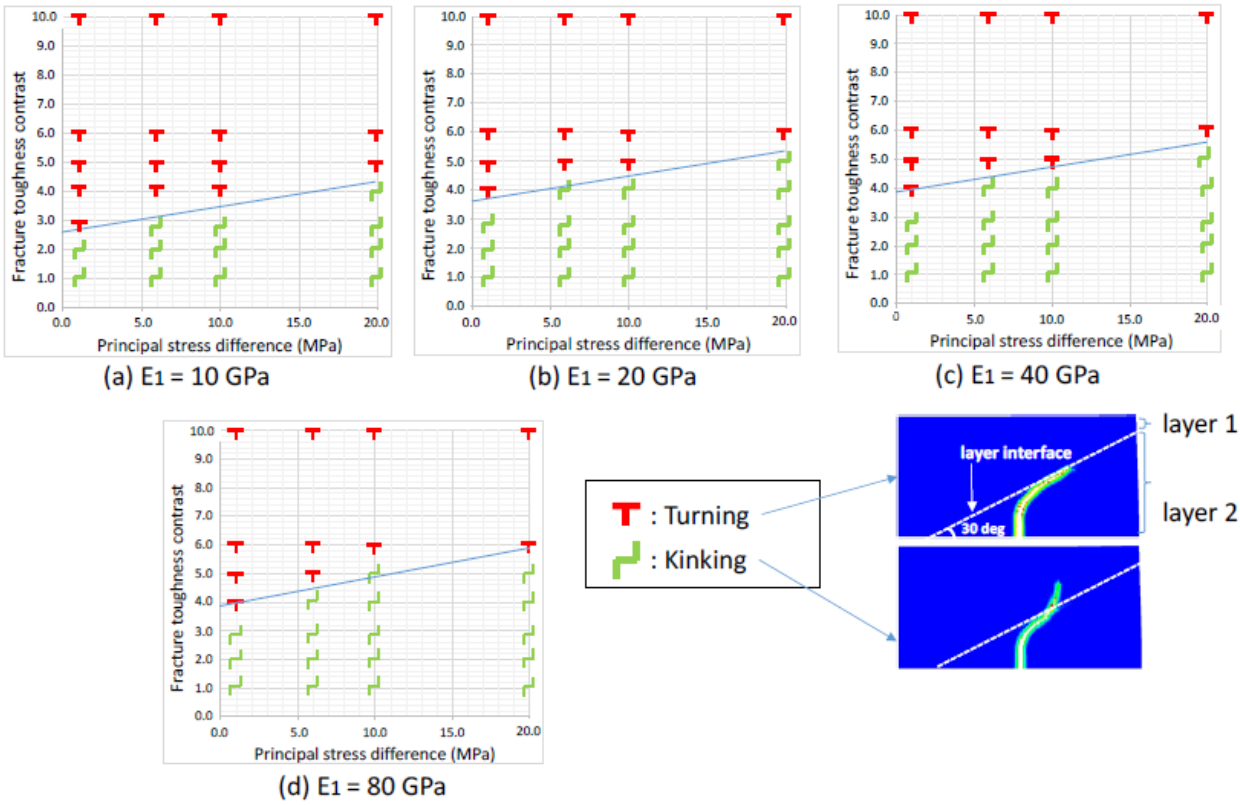


Fig. 5.5. Fracture turning behavior (layer dip angle = 30 degree, E2=10 GPa).

In both cases, at an early stage (t < 0.27 sec), the BHP decreases with time due to the fracture volume expansion. Then, from (0.27 sec <= t < 0.5 sec), the BHP begins to increase since the fracture propagation stops at the layer interface due to the higher energy requirement for breaking bonds in the first layer compared to the second layer. During this time, the fracture width continues to increase due to the BHP increase.

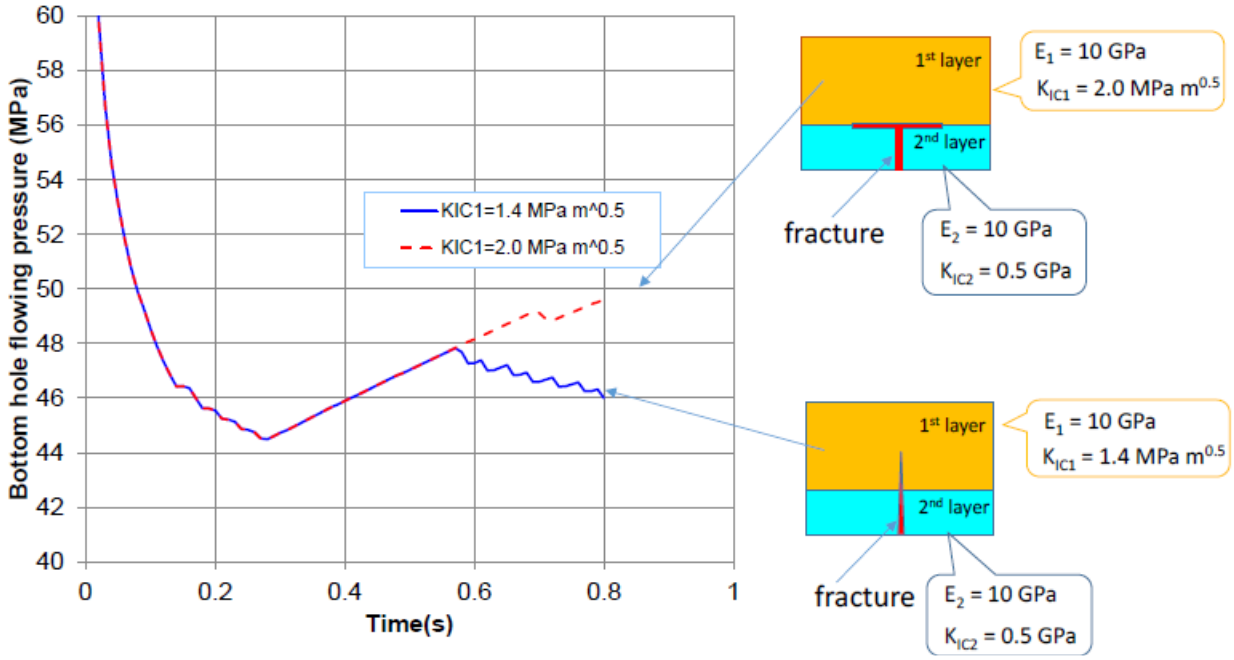


Fig. 5.6. Bottomhole pressure change with time (E2 = 10GPa, principal stress difference = 1 MPa).

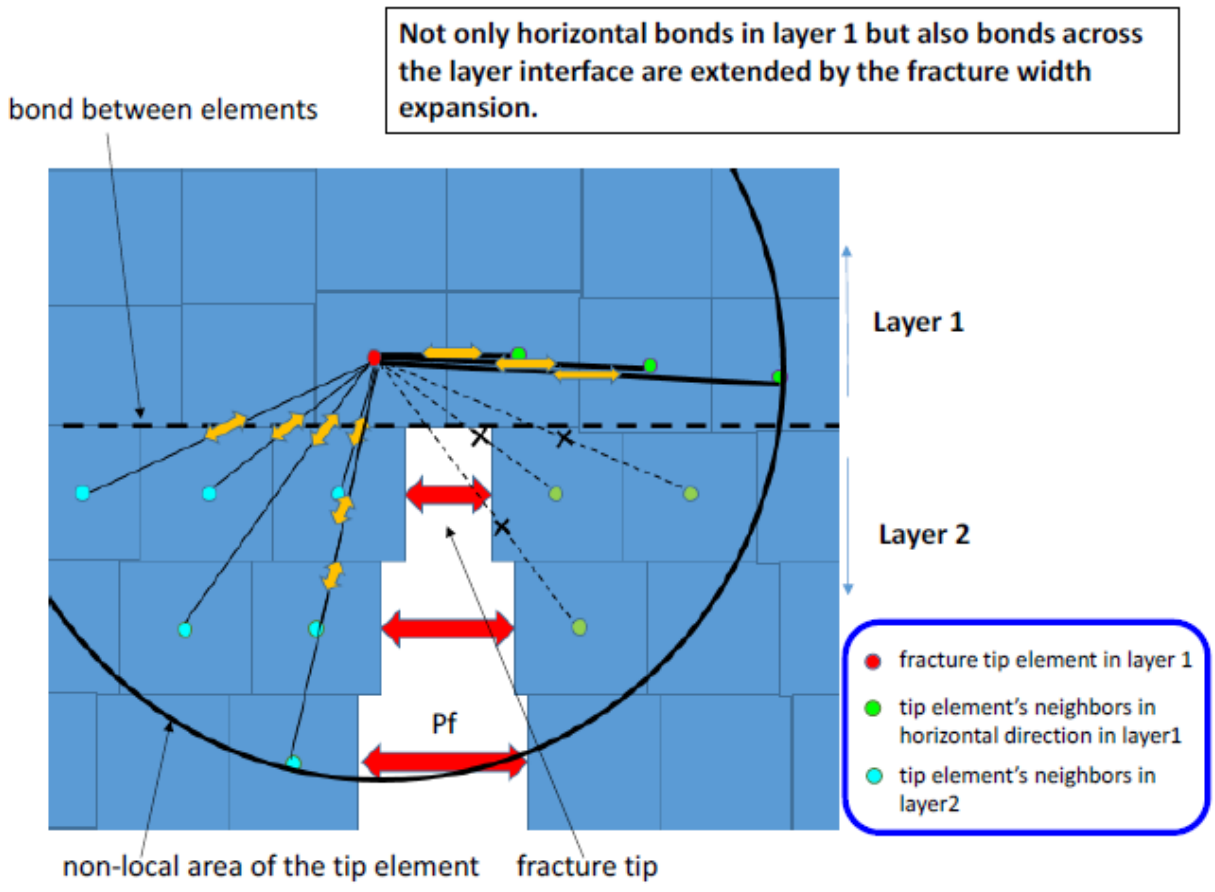


Fig. 5.7. Schematic view of bond extension near layer interface.

As shown in Fig. 5.7, the fracture width expansion causes the bonds to stretch both in the horizontal direction in Layer 1 and in the bonds across the layer interface between Layer 1 and Layer2. Therefore, if the horizontal bonds in Layer1 shown in Fig. 5.7 break sooner than the bonds across the layer interface, the fracture crosses the layer interface. Conversely, if all the bonds across the layer interface break sooner than the horizontal bonds in Layer1 due to a shear like displacement along the layer interface, the fracture turns along the layer interface. In essence, if the bonds' connection across the layer interface break faster than the bonds in the upper layer, "turning" occurs. Please note that if "turning" does not occur, "crossing" always occurs in our models since the models investigated in this research are two dimensional. However, in real (three dimensional) situations, no "turning" does not always mean "crossing". A fracture can stop at a layer interface and can propagate in the 3rd lateral direction (maximum horizontal stress direction). Part of the "crossing" results in this research represent fracture "stopping" at the layer interface in real situations. In the next section, we discuss how the following parameters (fracture toughness contrast, principal stress difference, Young's modulus contrast, and layer dip angle) affect the timing of bond failure.

Effect of fracture toughness and principal stress difference on turning

As shown in Fig. 5.3, the turning criterion is mainly affected by the principal stress difference between vertical and horizontal stresses, and the toughness contrast between the two layers. A hydraulic fracture is more likely to turn along the layer interface for a lower principal stress difference and a higher fracture toughness contrast. A two to four times fracture toughness contrast (K_{IC1} / K_{IC2} > 2-4) is necessary for the fracture to turn under a low principal stress difference condition ($\Delta\sigma$ < 1.0 MPa), while a fracture toughness contrast of about eight to ten times is necessary for a high principal stress difference condition ($\Delta\sigma$ = 20.0 MPa). Since the published values of fracture toughness range from 0.2 ≈ 3.0 MPa $m^{0.5}$ (Rijken and Cooke, 2001; Senseny and Pfeifle, 1984; Thiercelin et al., 1989), the possible fracture toughness contrast is less than fifteen even in extreme cases. In many cases, the contrast is less than around 2.0 to 3.0 at best. This suggests that fracture turning along a layer interface is unlikely to occur especially in deep reservoirs. This is consistent with field observations by tiltmeter surveys. Horizontal fracture propagation is not commonly observed deeper than 4000 ft, whereas a horizontal fracture component begins to appear in measurements made for fractures shallower than 4000 ft, as reported by Fisher et al. (Fisher and Warpinski, 2012).

Effect of Young's modulus on Turning

As shown in Fig. 5.3, the effect of Young's modulus contrast on fracture turning is not as significant. No apparent differences are observed among the different Young's modulus contrast cases. Regardless of the Young's modulus contrast, a fracture turns at a fracture toughness contrast of three to four (turning fracture toughness contrast K_{IC1} / K_{IC2} > 3-4) in the lower principal stress difference cases ($\Delta\sigma$ <= 1.0 MPa) and at eight to ten fracture toughness contrast in the higher principal stress difference cases ($\Delta\sigma$ = 20.0 MPa). Please note that the same kind of results are obtained for fracture propagation from the harder layer to the softer layer, although the figures are not shown in this paper.

Effect of Layer Dip on Turning

As shown in Fig. 5.4 and Fig 5.5, for dipping layers, the minimum fracture toughness contrasts for which fracture turning occurs mainly depends on the principal stress difference. It is not affected much by the Young's modulus contrast. This is the same tendency as when the layer dip angle is 0 ("0 degree cases"). The main difference between the 0 degree layer dip cases and the dipping bedding planes is that the fractures only turn updip along the layer interface in the dip angle cases since the updip side is less compressive due to the layer inclination. As shown in Fig. 5.4, in the cases where the layer dip angle is 15 degree ("15 degree cases"), since the initial effective stress acting on the layer interface in the 15 degree cases is almost the same as the 0 degree cases, the fracture turning criterion is almost the same as the 0 degree cases regardless of the Young's modulus contrast. The minimum fracture toughness contrast for fracture turning is around 3.0 – 4.0 (1.5 MPa $m^{0.5}$/0.5 MPa $m^{0.5}$ – 2.0 MPa $m^{0.5}$/0.5 MPa $m^{0.5}$) in the lower principal stress difference cases (Δσ <= 1.0 MPa) and around 8.0 – 10.0 in the high principal stress difference cases (Δσ = 20.0 MPa). As shown in Fig. 5.5, in the cases where the layer dip angle is 30 degrees (30 degree cases), the minimum fracture toughness contrast for fracture turning becomes lower than for the low layer dip angle cases (the 0 degree cases and the 15 degree cases). For a 30 degree layer dip angle, the minimum fracture toughness contrast for fracture turning is around 3.0 – 4.0 (1.5 MPa $m^{0.5}$/0.5 MPa $m^{0.5}$ – 2.0 MPa $m^{0.5}$/0.5 MPa $m^{0.5}$) for a low principal stress difference (Δσ < MPa) and around 5.0 – 6.0 for a high principal stress difference condition (Δσ = 20.0 MPa). Since the initial normal effective stress acting on the layer interface in the 30 degree cases is smaller than the 0 degree cases, especially in the high principal stress condition, the fracture propagation along the layer interface is easier than for the low dip angle cases. A fracture toughness contrast of the order of 5.0 – 6.0 is still extremely high. Judging from the minimum fracture toughness contrast obtained in this simulation study, no fracture turning is expected in a deep reservoir even if the layer interface is highly inclined.

Kinking Mechanism

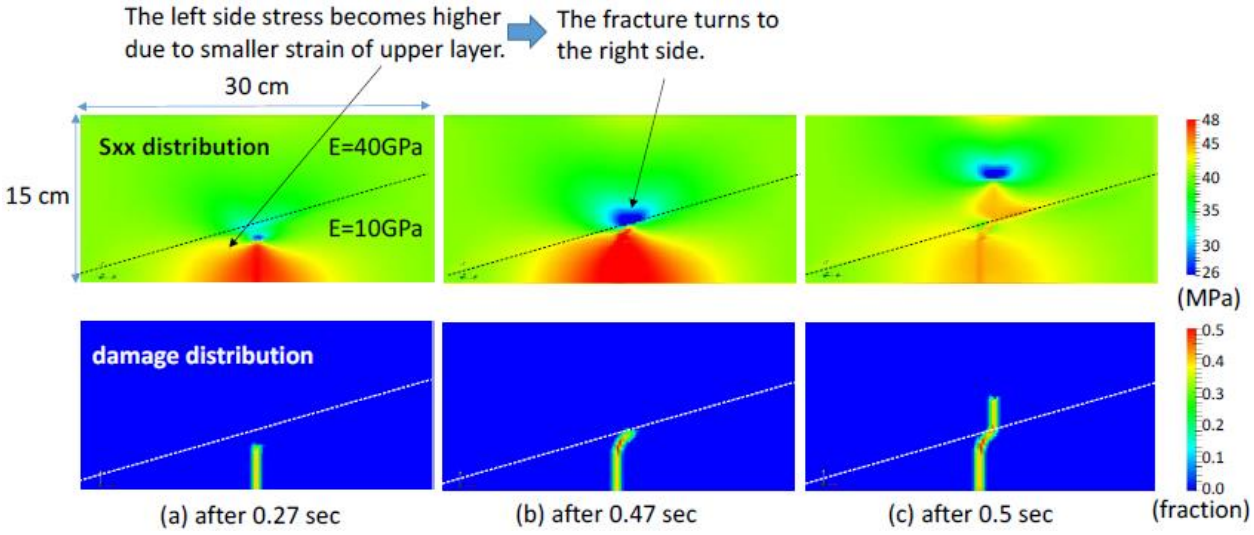


Fig. 5.8. Horizontal stress and damage distribution (layer dip angle = 15 degree, E_1/E_2=40 GPa/10 GPa, K_{IC1}/K_{IC2}=1.41MPa $m^{0.5}$/0.5MPa $m^{0.5}$, principal stress difference = 1.0 MPa).

As shown in Fig. 5.4 and Fig. 5.5, if the layer interface is inclined, the fractures do not go straight but kink before they reach the layer interface in many cases. Here, we explain the basic mechanism of "kinking" and the important parameters that control fracture kinking.

Fig. 5.8. shows the distribution of horizontal stress and damage at different time steps in the case where the dip angle is 15 degrees, the Young's modulus contrast is 4.0, and the principal stress difference is 1.0 MPa. As shown in Fig. 5.8, if the dip angle is not zero and the Young's modulus contrast is more than 1.0, the fracture turns to the right before it hits the layer interface. Since the displacement of Layer 2 is prevented more by the smaller displacement of Layer 1 to the left of the fracture, the crack propagation becomes relatively difficult on the left side, which results in the fracture turning toward the right. Note that if the fractures propagate from the harder layer to the softer layer, the fracture turns to the left instead of right since the direction perpendicular to the layer interface is the easiest direction for fracture propagation.

Effect of Young's modulus contrast on kinking

Fig. 5.9. shows the damage distribution just before crossing the layer interface for the different Young's modulus contrast cases. In these cases, the other parameters are fixed as follows (layer dip angle = 15 degree, the fracture toughness contrast = K_{IC1}/K_{IC2}= =1.4 / 0.5, and the principal stress difference = 1.0 MPa). As shown in Fig. 5.9, since the fracture turning is caused by the difference of the displacement between Layer 1 and Layer 2, a higher Young's modulus contrast causes more fracture turning. As shown in Fig. 5.4 (a) and Fig. 5.9 (a), if the fracture toughness contrast is 1.0 and the layer dip angle is 15 degrees, no fracture turning is expected before the fracture reaches the layer interface. However, as shown in Fig. 5.5 (a), if the layer dip angle is 30 degrees, the kinking region appears even if the fracture toughness contrast is 1.0. In these cases, there is no kinking before the fracture reaches the layer interface, but the kinking occurs along the layer interface due to the fracture toughness contrast.

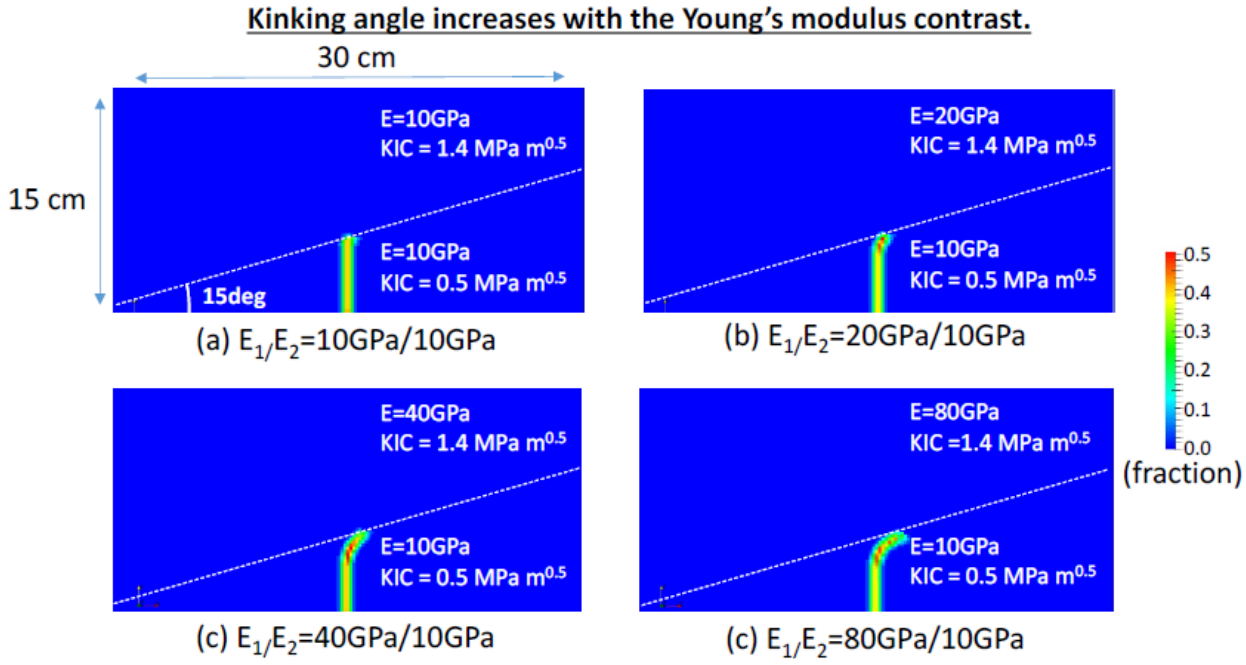


Fig. 5.9. Damage distribution in the different Young's contrast cases (layer dip angle = 15 degree, K_{IC1}/K_{IC2}=1.41MPa $m^{0.5}$/0.5MPa $m^{0.5}$, principal stress difference = 1.0 MPa).

Effect of fracture toughness contrast on kinking

Fig. 5.10 shows the damage distribution just before the fracture crosses the layer interface for the different fracture toughness contrast cases. In these cases, the other parameters are fixed as follows (layer dip angle = 15 degree, the Young's modulus contrast = E_1 / E_2 = 40 / 10, and the

principal stress difference = 1.0 MPa). As shown in Fig. 5.10, the degree of fracture kinking (kinking angle) is not different for the different fracture toughness contrast cases. Since the kinking is caused by the displacement difference between the two layers under compression, the parameters which are not directly related to the compressional displacement such as fracture toughness do not affect the degree of kinking.

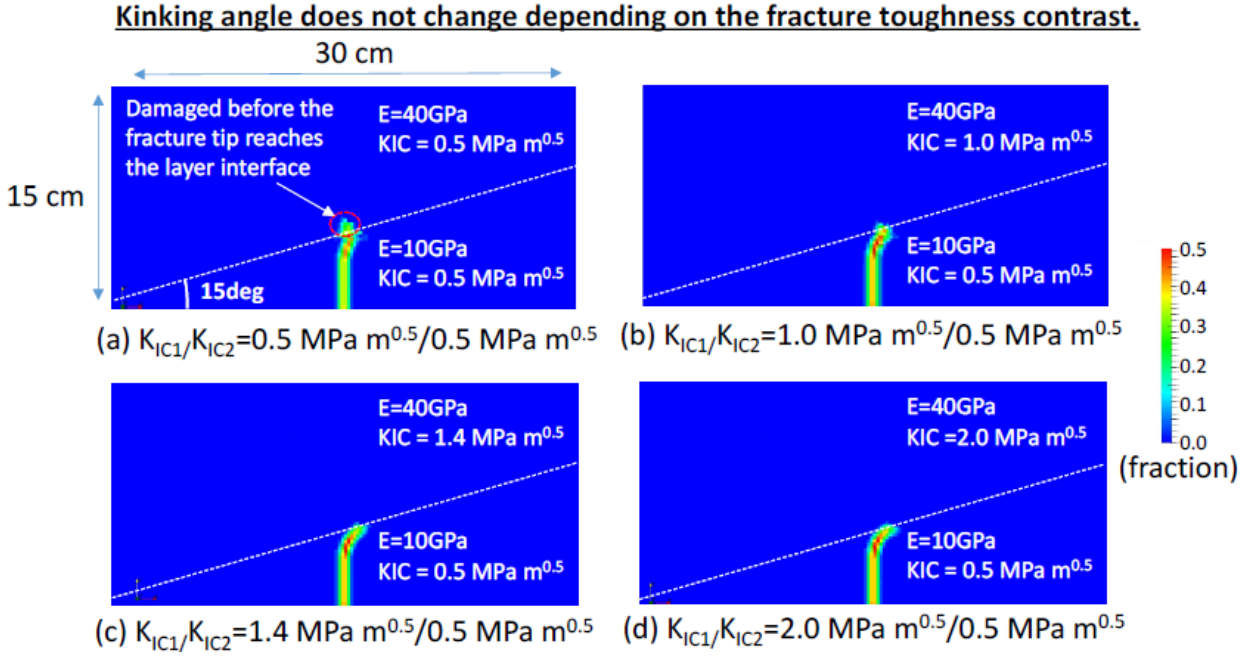


Fig. 5.10. Damage distribution in the different fracture toughness contrast (layer dip angle = 15 degree, E_1/E_2=40 GPa/10 GPa, principal stress difference = 1.0 MPa).

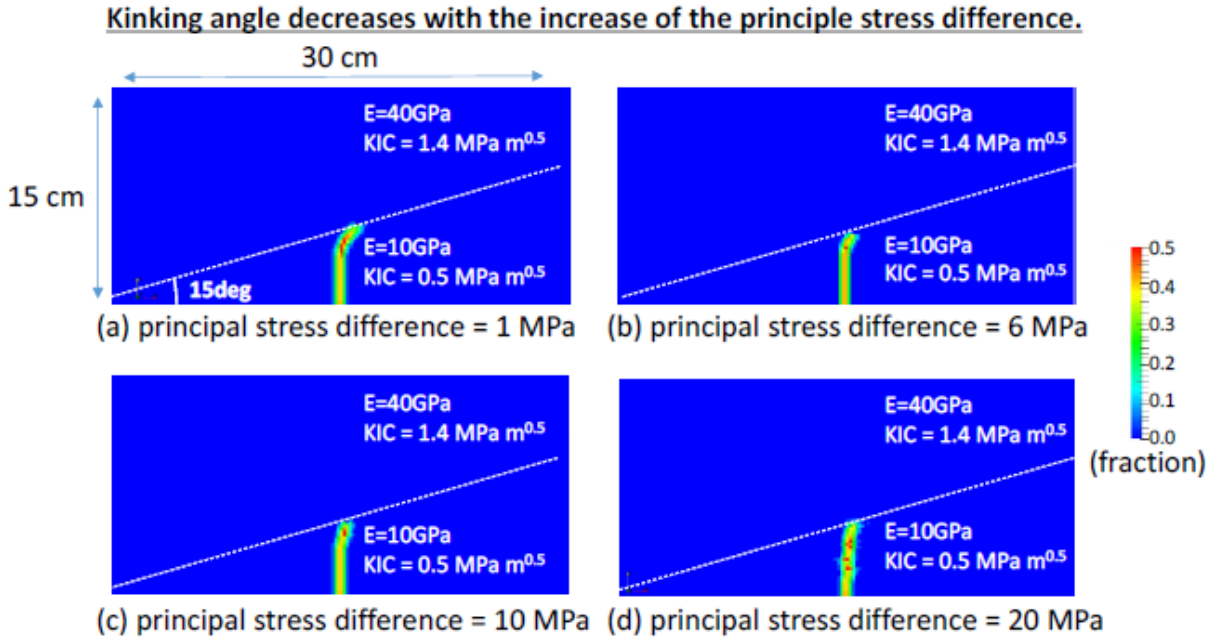


Fig. 5.11. Damage distribution in the different principal stress difference cases (layer dip angle = 15 degree, E_1/E_2=40 GPa/10 GPa, K_{IC1}/K_{IC2}=1.41MPa $m^{0.5}$/0.5MPa $m^{0.5}$.

Fig. 5.11 shows the damage distribution just before the fracture crosses the layer interface for the different principal stress difference cases. In these cases, the other parameters are fixed as follows (layer dip angle =15 degree, the Young's modulus contrast = E_1 / E_2 = 40 / 10, and the fracture toughness contrast = K_{IC1}/K_{IC2}= =1.4 / 0.5). As shown in Fig. 5.11, the more the principal

stress difference is, the less the fracture turns before it reaches the layer interface. Since the larger vertical stress makes the bonds in the vertical direction have a higher compressional stress than the bonds in the horizontal direction, breaking the vertical bonds becomes more difficult. Therefore, the fracture turning into the horizontal direction is more difficult in the larger principal stress difference case.

Effect of layer dip angle on kinking

Fig. 5.12 shows how the fracture turning angle is different depending on the layer dip angle. As shown in Fig. 5.12, the fractures turn more in the cases where the layer dip angle is 30 degrees than the cases where the layer dip angle is 15 degrees. In the larger dip angle cases, since the horizontal displacement in Layer2 is more influenced by Layer 1 at the left of the fracture, the fracture propagates more toward the right.

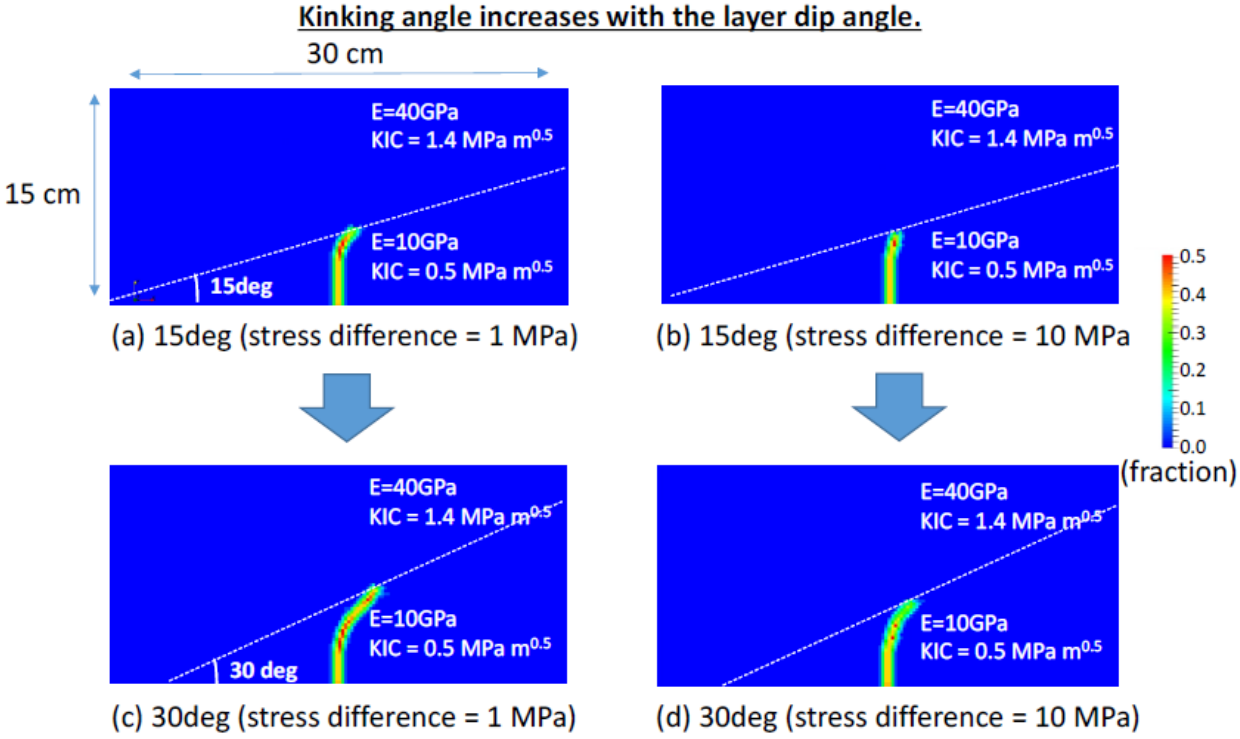


Fig. 5.12. Damage distribution in the different layer dip angle and different principal stress cases (E_1/E_2=40 GPa/10 GPa, K_{IC1}/K_{IC2}=1.41MPa $m^{0.5}$/0.5MPa $m^{0.5}$).

Branching

As shown in Fig. 5.3 (d), our results show that if the following conditions are satisfied, the fracture branches at the layer interface (first turns along the layer interface and then quickly move into the first layer).

1. Fracture propagates from the low Young's modulus layer to the high Young's modulus layer

2. Young's modulus contrast between the two layers is high.

3. Fracture toughness contrast is less than 1.0.

In essence, if the upper layer material is very brittle (high Young's modulus and low fracture toughness), fracture branching will occur. Fig. 5.13 shows the damage distribution near the fracture tip in the branching case where the Young's modulus contrast, fracture toughness contrast, and principal stress difference are 8 (E_1/E_2= 80GPa/10GPa), 1.0 (=0.5 MPa $m^{0.5}$/0.5 MPa

m0.5), and 1.0 MPa respectively. As shown in Fig. 5.13, if Layer 1 is much more brittle than Layer 2 as mentioned above, the damage zone begins to grow before the fracture tip reaches the layer interface due to the much smaller energy requirement for the bond breakage in Layer 1 than for Layer 2. In this case, the energy required for breaking bonds in Layer 1 is just 12.5 % of the energy required to break bonds in Layer 2. Hence, even small deformations, induced by the fracture propagation in Layer2, which do not break bonds in Layer 2 can break the bonds near the layer interface and in Layer 1. As shown in Fig. 5.13 (c), since Layer 1 has already been damaged when the fracture reaches the layer interface, the fracture continues to propagate through the pre-damaged zone in Layer 1. Note that the fracture perfectly branches in this example case due to the perfect symmetry of the mechanical properties in front of the fracture tip. However, for most cases, the mechanical properties in front of the fracture tip are not fully symmetric at the layer interface. For such cases, fracture "kinking" may occur (in other words, one side of the branch may grow) instead of "branching" since the fracture always propagates through the weakest path (the easiest open path).

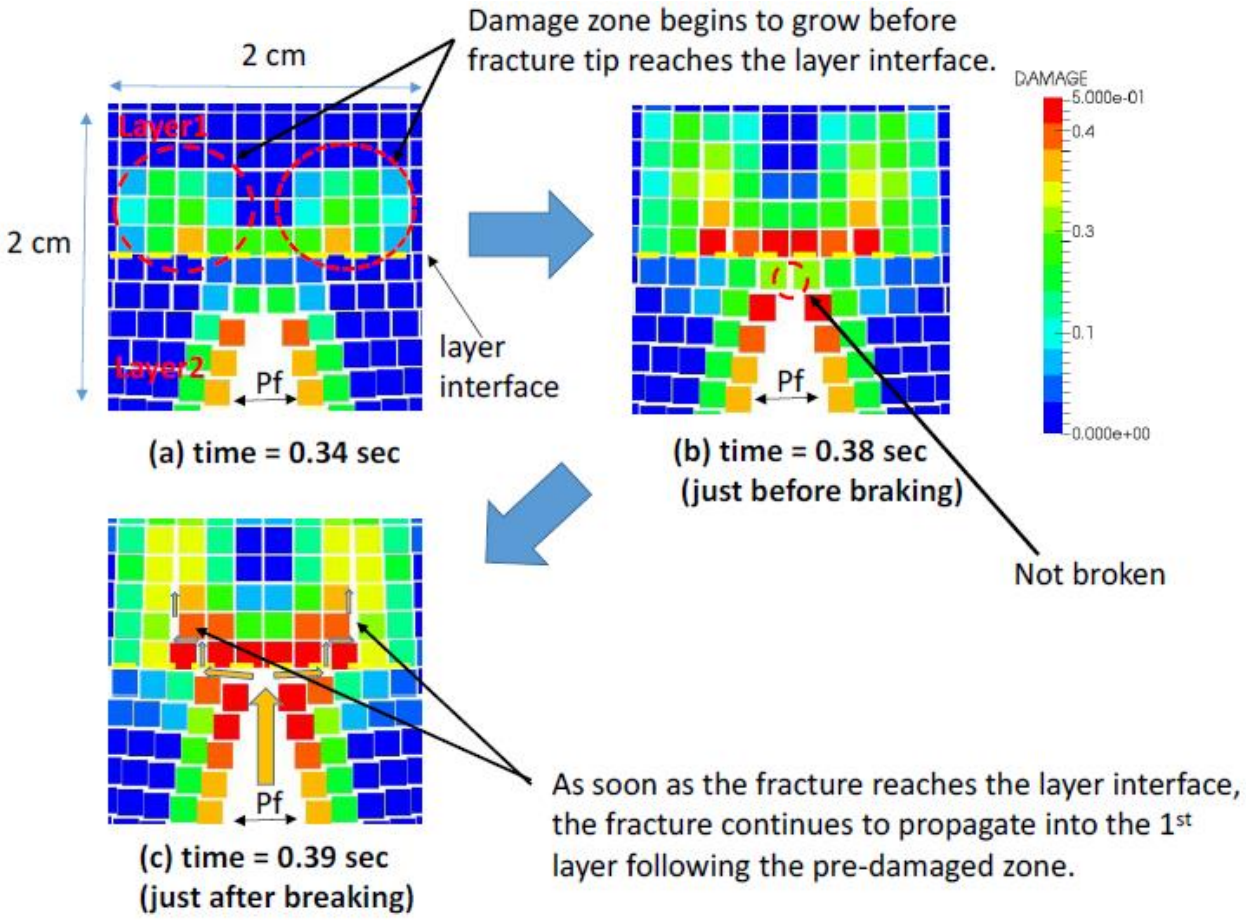


Fig. 5.13. Damage distribution change near the fracture tip ("branching" case).

Effect of Layer Thickness

In order to investigate how the layer thickness affects the fracture propagation near the layer interface, as shown in Fig. 5.14, we prepared three different models by changing the 2nd layer thickness for two different layer dip angles (0 degrees and 30 degrees). We selected the following reference cases (please see Table 5.4) from the previous cases shown in Fig. 5.3 (c) and

Fig. 5.5 (c) and simulated fracture propagation by changing the 2nd layer thickness for each of the reference cases.

Table 5.4. Reference case settings (investigation of the effect of layer thickness).

Case Name	Layer dip angle (degree)	Principal stress difference (MPa)	Fracture toughness contrast
0deg_1MPa_1	0.0	1.0	4.0
0deg_1MPa_2	0.0	1.0	5.0
0deg_1MPa_3	0.0	1.0	6.0
0deg_1MPa_4	0.0	1.0	10.0
0deg_10MPa_1	0.0	10.0	6.0
0deg_10MPa_2	0.0	10.0	10.0
30deg_1MPa_1	30.0	1.0	4.0
30deg_1MPa_2	30.0	1.0	5.0
30deg_1MPa_3	30.0	1.0	6.0
30deg_1MPa_4	30.0	1.0	10.0
30deg_10MPa_1	30.0	10.0	5.0
30deg_10MPa_2	30.0	10.0	6.0
30deg_10MPa_3	30.0	10.0	10.0

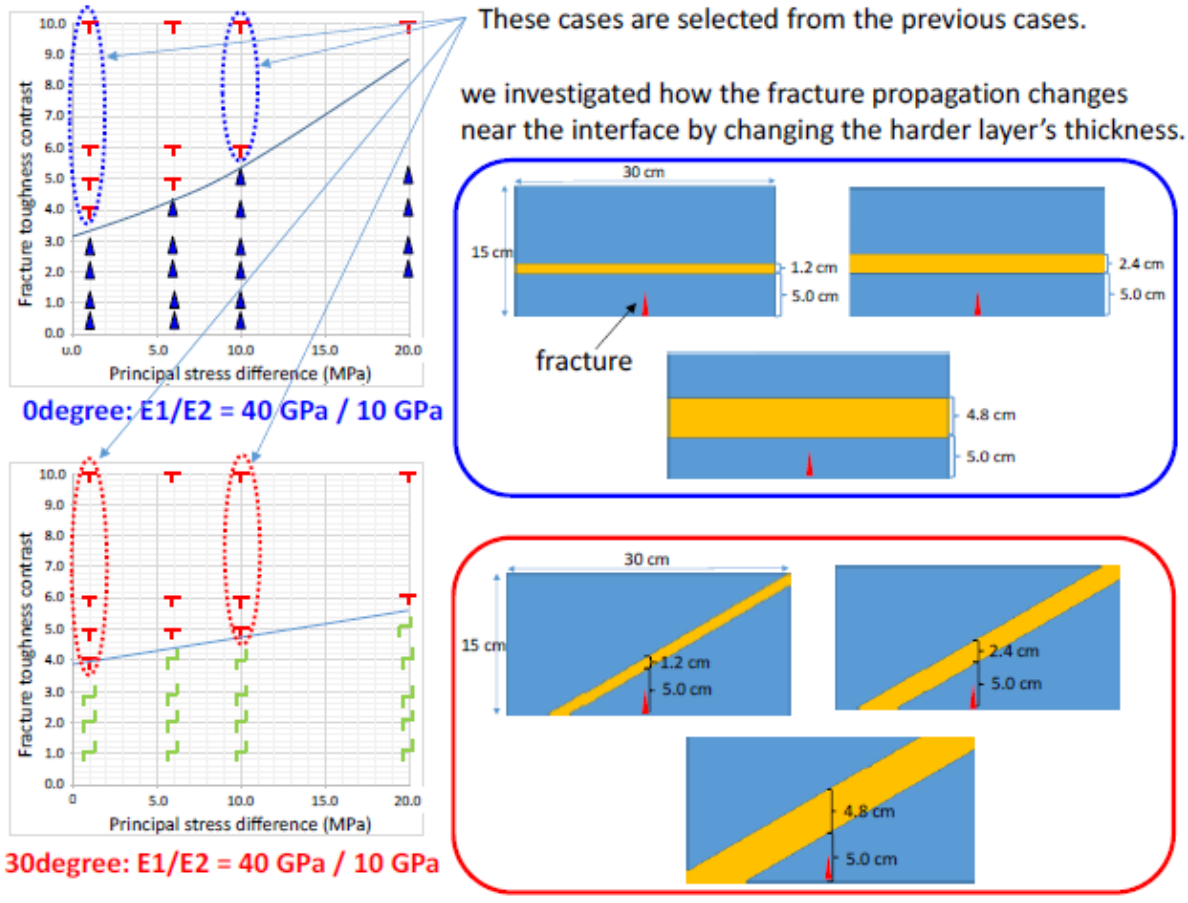


Fig. 5.14. Damage distribution in the different layer dip angle and different principal stress cases (E1/E2=40 GPa/10 GPa, KIC1/KIC2=1.41MPa m0.5/0.5MPa m0.5).

Fig. 5.15 and Fig. 5.16 show the results for fracture propagation for the different layer thickness cases. As shown in these figures, the thinner the 2nd layer thickness is, the higher the minimum fracture toughness contrast needed for fracture turning. These results clearly show that not only the mechanical properties of the interface layers but also those of other layers affect the fracture

propagation behavior at the target layer interface in accordance with the distance from the layer interface. Fig. 5.17 shows the horizontal stress difference between the thinnest layer case (l = 1.2 cm) and the reference case (l = 10.0 cm) in the 0 degree case. As shown in Fig. 5.17, if the 2nd layer thickness is thin, since the existence of the softer layer (the 1st layer) makes the displacement of the 2nd layer larger, the stress reduction near the layer interface between the 2nd layer and the 3rd layer is bigger for the thinnest 2nd layer thickness case than for the reference case. This leads to easier fracture penetration in the 2nd layer in the thinnest layer cases.

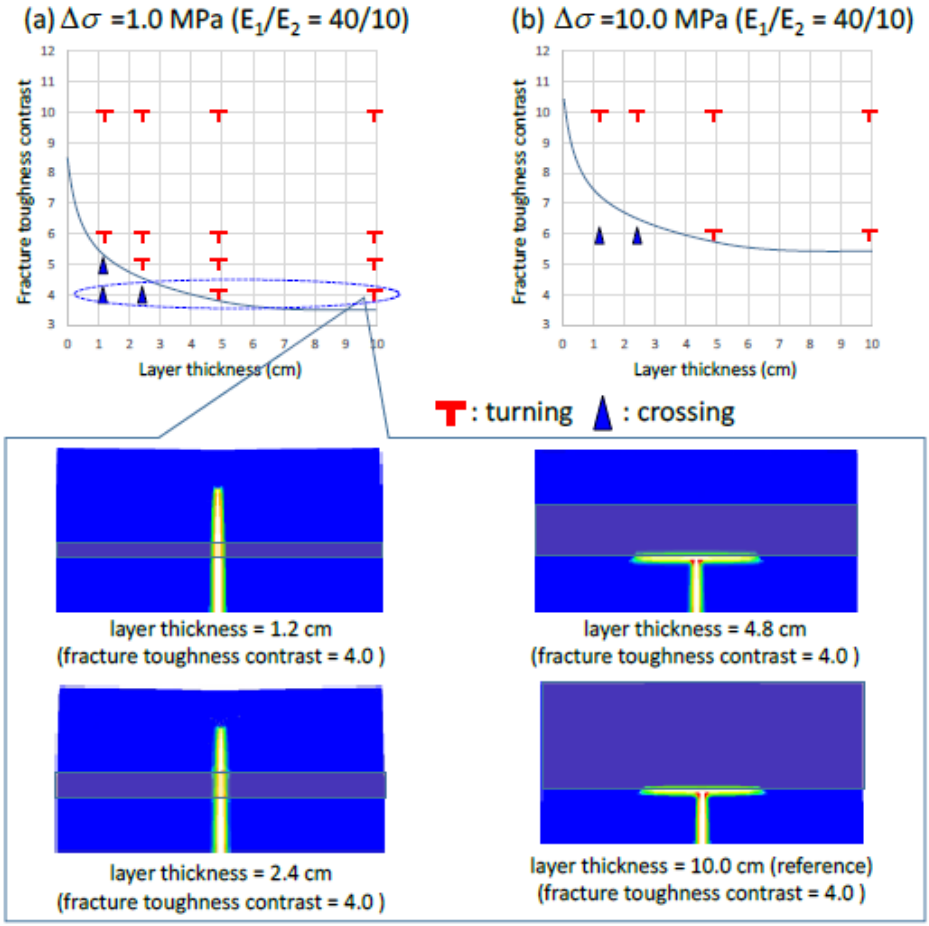


Fig. 5.15. Fracture propagation behavior for the different layer thickness cases (0 degree dip cases).

As shown in Fig. 5.15, in the 0 degree case, if the 2nd layer thickness is more than 4.8 cm, the fracture turning criteria is the same as the reference case regardless of the principal stress difference. However, in the 30 degree case, if the principal stress difference is high, the fracture turning behavior is still different from the reference case even in the case where the 2nd layer thickness is 4.8 cm. On the other hand, if the principal stress is low, the fracture propagation behavior is the same as the reference case in the cases where the layer thickness is more than 2.4 cm. These differences may be caused by the kinking angle difference between the two different cases. Since the fracture has already turned before reaching the layer interface in the low principal stress difference case, the horizontal stress reduction near the fracture tip in the 2nd layer is not as large as in the high principal stress difference case. Therefore, if the principal stress difference is low, the layer thickness difference does not significantly affect the fracture propagation behavior in the 30 degree cases. Note that, in the 30 degree cases, as shown in Fig. 5.16, regardless of the 2nd layer thick ness, the magnitudes of fracture turning before the

fracture reaches the layer interface are almost same even for the thinnest 2nd layer thickness case. These results suggest that fractures can frequently kink in most reservoirs which have some degree of bed dipping and vertical heterogeneity in mechanical properties.

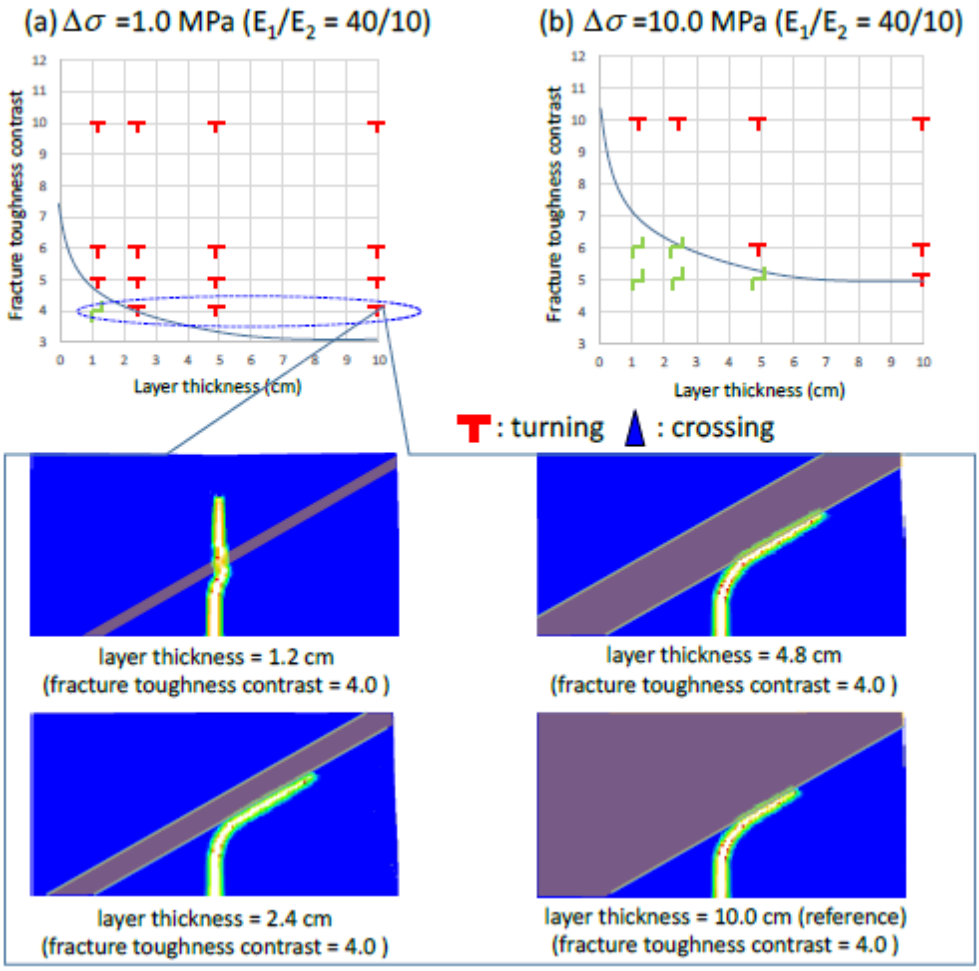


Fig. 5.16. Fracture propagation behavior for the different layer thickness cases (30 degree dip cases).

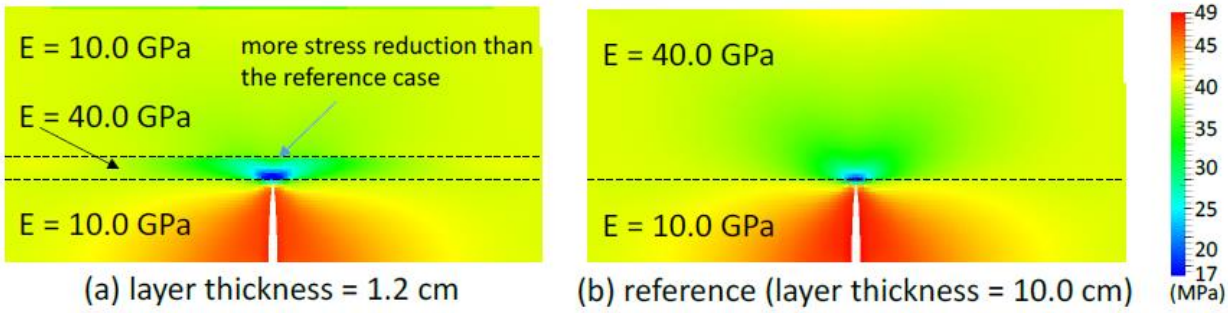


Fig. 5.17. Stress distribution near the layer interface (the thinnest layer case vs. reference case).

Effect of Horizontal Stress Difference

For investigating the effect of horizontal principal stress difference between the layers, we choose the eight reference cases from the previous cases shown in Fig. 5.3 (two cases for each Young's modulus contrast). All these reference cases have the same layer dip angle (θ=0 degree), the same principal stress difference (Δσ =10 MPa), the same horizontal principal stress both in Layer 1 and Layer 2 (σ_H =40.0 MPa), and a smaller fracture toughness contrast than the minimum fracture toughness contrast for fracture turning. As shown in Fig. 5.18, by applying a 5 MPa

higher effective horizontal principal stress to Layer 1 than in the reference cases, we simulate how fracture turning criterion changes as the horizontal stress is increased. Table 5.5 shows the reference cases for the simulations in this section.

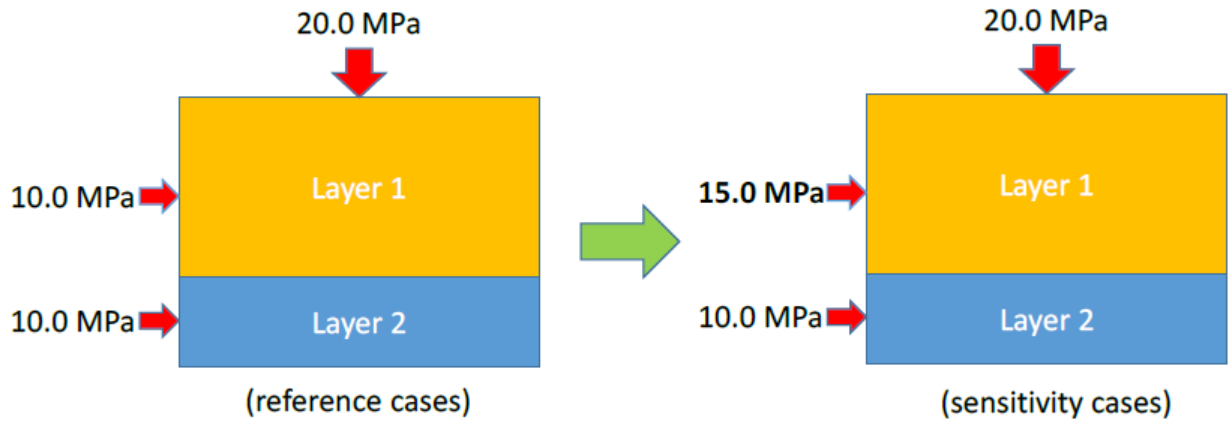


Fig. 5.18. Horizontal stress modification from the reference cases.

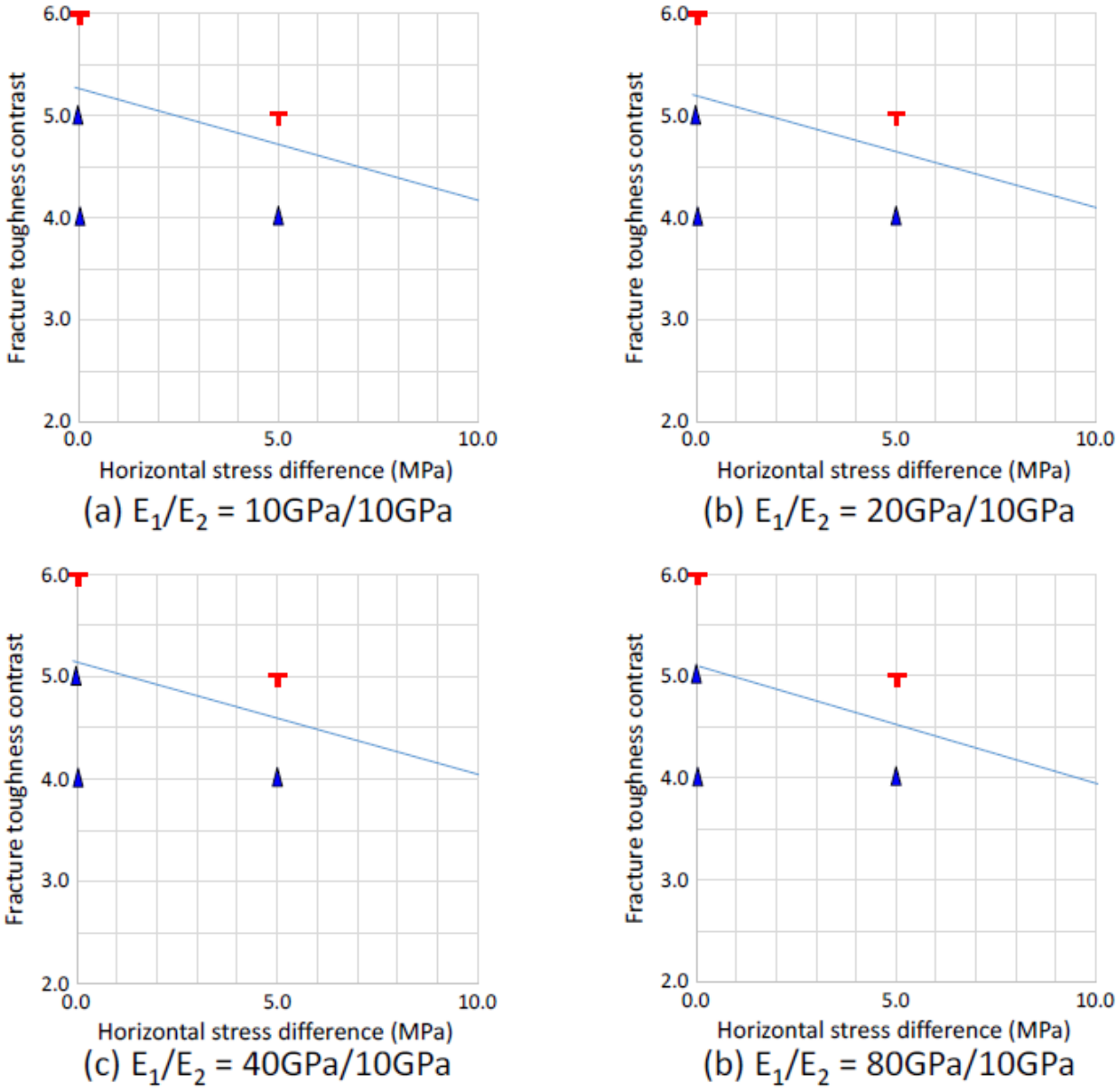


Fig. 5.19. Effect of horizontal stress difference.

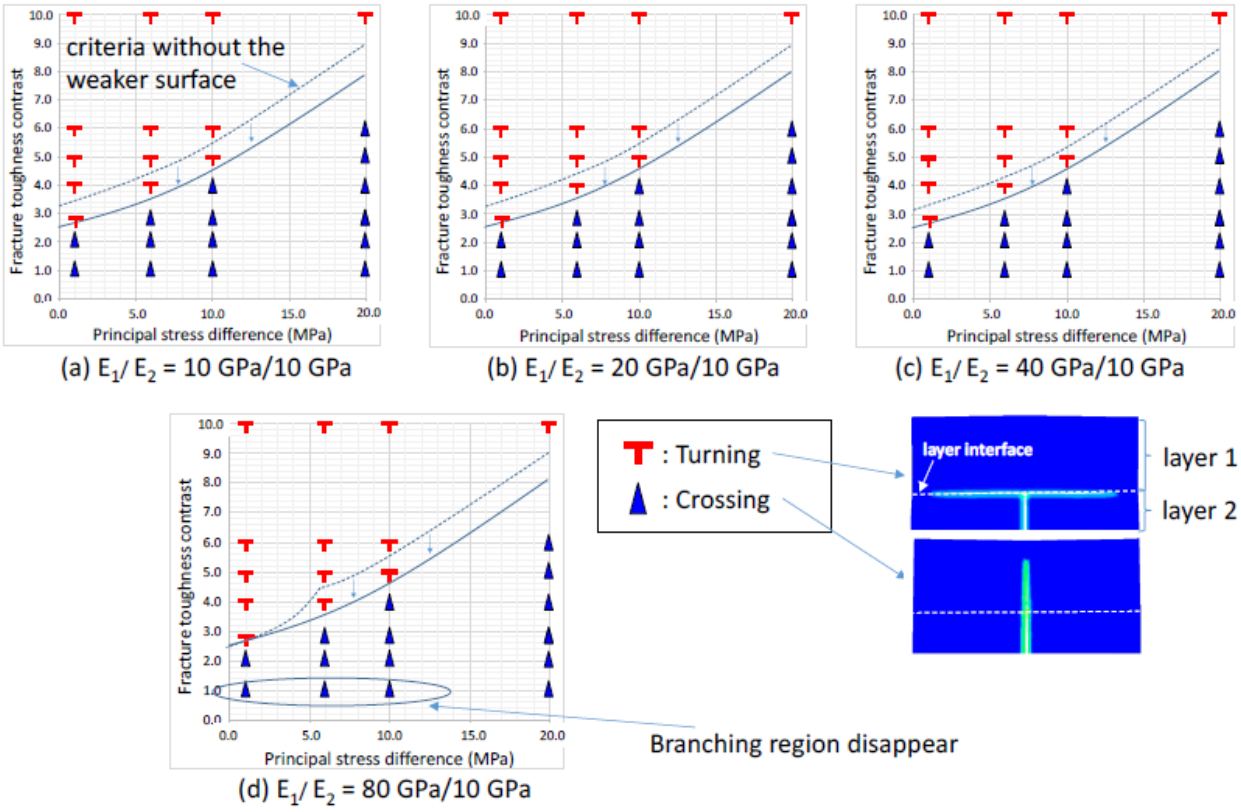


Fig. 5.20. Fracture turning behavior (weak surface cases: layer dip angle = 0 degree).

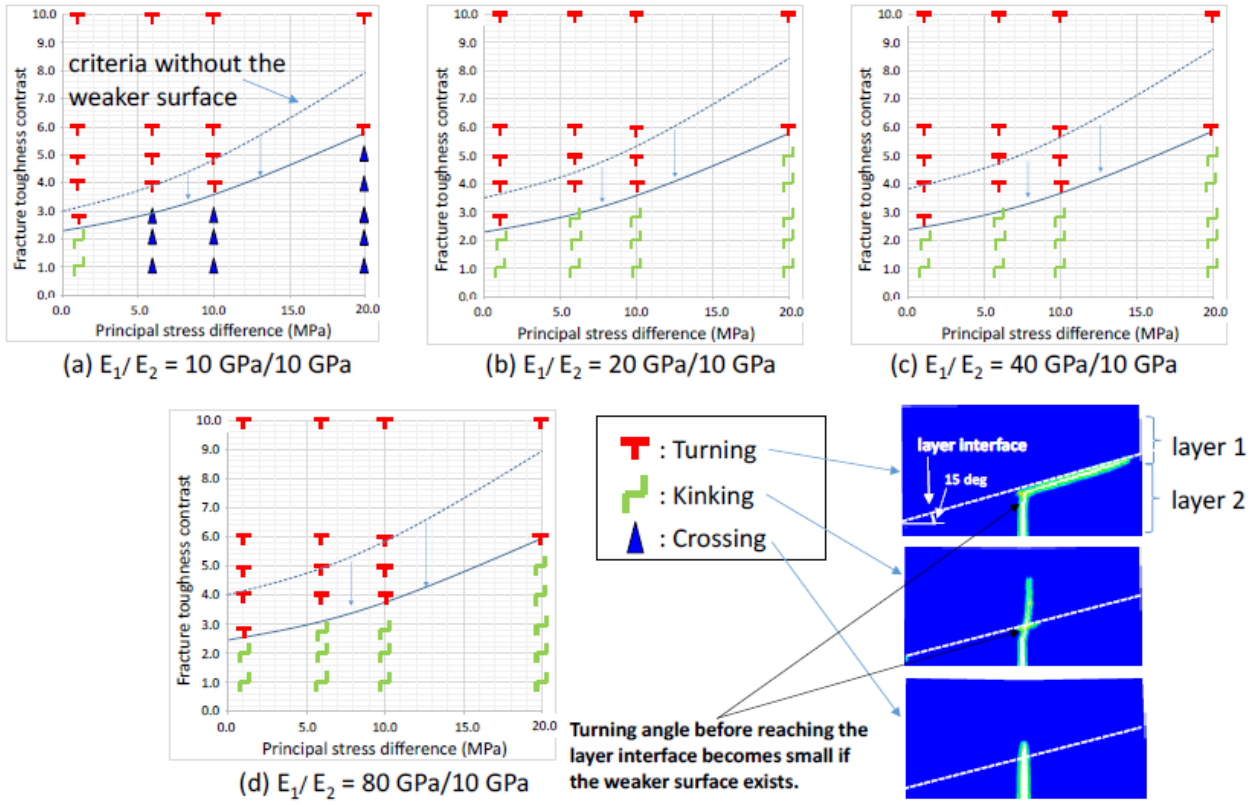


Fig. 5.21. Fracture turning behavior (weak surface cases: layer dip angle = 15 degree).

Fig. 5.19 shows a summary of the simulation results in this section. As shown in Fig. 5.19, the fractures turn at a smaller fracture toughness value than the reference cases (in every instance). These results show that increasing the horizontal principal stress difference between layers lowers the minimum fracture toughness contrast for fracture turning. However, when we

consider the fact that a large horizontal stress difference is only expected in deep reservoirs where the required fracture toughness contrast for the fracture turning is around eight to ten, the effect of horizontal principal stress difference (the reduction of the minimum fracture toughness change order of 1.0 – 2.0) may not significantly affect the fracture turning behavior (practically turning is not caused only by horizontal stress difference).

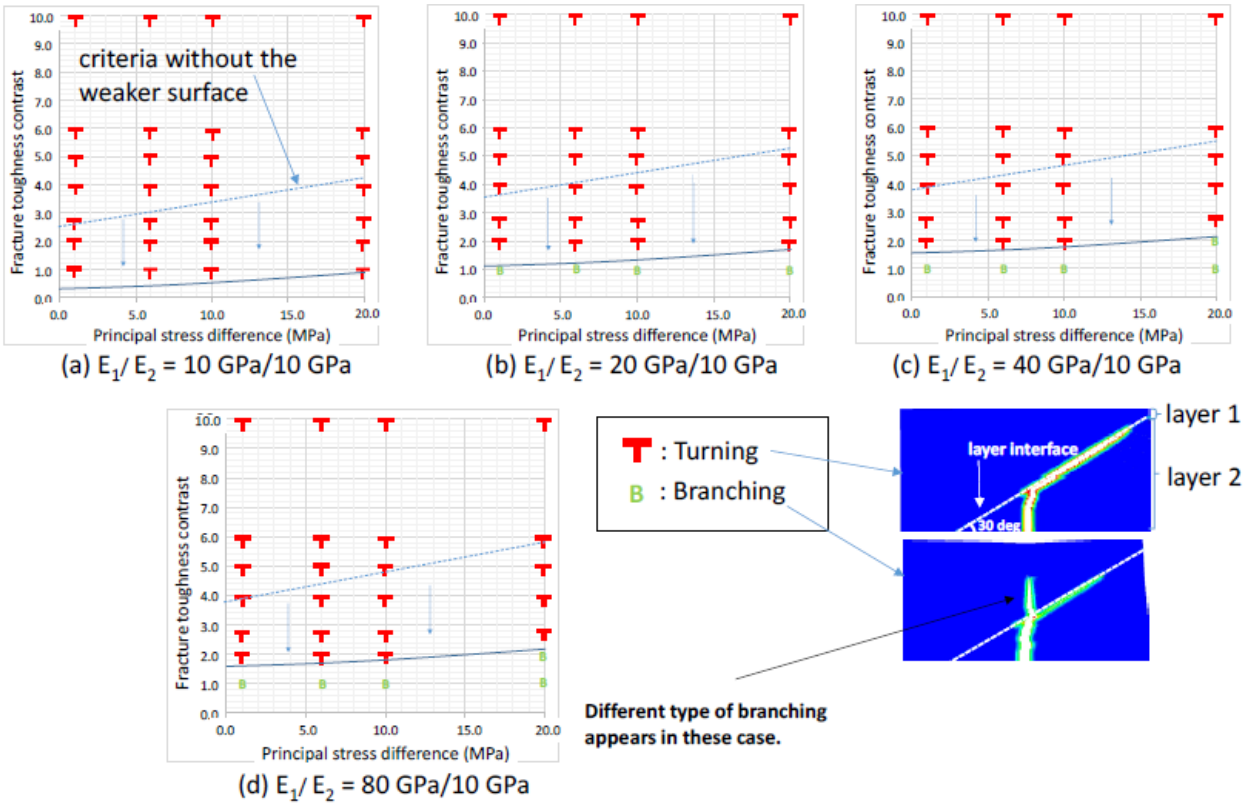


Fig. 5.22. Fracture turning behavior (weak surface cases: layer dip angle = 30 degree).

Table 5.5. Reference cases for the investigation of the effect of horizontal stress difference.

Case Name	σ_1 (MPa)	σ_2 (MPa)	E_1 (GPa)	E_2 (GPa)	K_{IC1}/K_{IC2}
Case1_1	10.0	20.0	10.0	10.0	5.0
Case1_2	10.0	20.0	10.0	10.0	4.0
Case2_1	10.0	20.0	20.0	10.0	5.0
Case2_2	10.0	20.0	20.0	10.0	4.0
Case3_1	10.0	20.0	40.0	10.0	5.0
Case3_2	10.0	20.0	40.0	10.0	4.0
Case4_1	10.0	20.0	80.0	10.0	4.0
Case4_2	10.0	20.0	80.0	10.0	2.8

Effect of Weak Surface

In the previous sections, we investigated the effect of several mechanical properties based on the assumption that the layer interface is fully bonded (in other words, the layer interface is not allowed to be damaged). However, layer interfaces are not always strongly bonded. Sometimes, they can be weakly bonded and easily slip along the layer interface. In order to analyze the effect of a weak layer interface on fracture propagation (turning, kinking and branching), we apply the following shear failure parameter (shear coefficient = 0.6, cohesion = 0.0 MPa) to the layer interface in the cases shown in Fig. 5.3, Fig. 5.4, and Fig. 5.5 ("original cases"), and simulate

fracture propagation in these cases ("weak surface cases"). Note that, in these cases, all the parameters except the shear failure parameters are the same as the original cases.

Fig. 5.20 - Fig. 5.22 show the fracture propagation behavior near the layer interface for the different layer dip angle cases (0 degree, 15 degree, and 30 degree cases in the weak surface cases respectively). As shown in these figures, the minimum fracture toughness contrasts for fracture turning in the weak surface cases are lower than the original cases for all layer dip angles. However, the degree and the criteria for fracture turning are very different depending on the layer dip angles. As shown in Fig. 5.20, in the 0 degree cases, even if the cohesion of the layer interface is zero, the difference of the minimum fracture toughness contrast for fracture turning between the original cases and the weak surface cases is less than 1.0. Since the initial normal stress acting on the layer interface is equivalent to the maximum principal stress in these cases, shear failure along the layer interface is difficult and unlikely to occur. These results show that fracture turning is not expected in deep reservoirs even if the layer interface is weak. Note that fracture branching is not observed in the low fracture toughness region in the highest Young's modulus case (see Fig. 5.20 (d)). Since the part of the bonds across the layer interface break in shear failure due to the low shear failure criteria, the displacement of the softer layer cannot fully transfer to the harder layer in these cases. Shear slip prevents fracture branching in highest Young's modulus contrast case.

As shown in Fig. 5.21, in the 15 degree cases, the differences of the minimum fracture toughness contrast for fracture turning between the original cases and the weak surface cases are larger than the 0 degree cases since shear failure is more likely to occur along the layer interface. A 1.5 to 2.0 reduction in fracture toughness contrast is observed in these cases. Note that, as shown in Fig. 5.21, the extent of fracture kinking is smaller in the weak surface cases than in the original cases. In these cases, since Layer 2 can slip along the layer interface, the displacement of Layer 2 is not limited by Layer 1, which results in more straight fracture propagation into Layer 2.

As shown in Fig. 5.22, in the 30 degree cases, the fractures always turn along the layer interface regardless of the principal stress difference and the fracture toughness contrast since shear failure always occurs along the layer interface. A weak layer interface has a significant influence on fracture turning in high dip angle layers. These results show that if the layer is highly inclined and the layer interface is not fully bonded, turning can occur even in the deep reservoir.

Investigation of the fracture propagation behavior in multiple layer cases

In shale gas reservoirs, mechanical property distribution in vertical direction is highly heterogeneous. As Passey et al. (2010) point out, mineralogical changes in shale gas reservoirs can be observed at the order of mm and cm scale as well as meter scale (Fig. 5.23).

In this section we investigate how fracture propagation is affected if this kind of small scale heterogeneity (cm scale heterogeneity) exists in the reservoir. We prepare the two types of models ("Model 1" and "Model 2") which have a 30 cm × 30 cm model domain and consist of 150 × 150 elements. Both models are divided into multiple layers which have constant thickness (= 2 cm). The layer dip angle of Model 1 is 0 degrees, while the layer dip angle for Model 2 is 30 degrees. As shown in Fig. 5.24, in order to represent small scale vertical heterogeneity, we alternately assign two different sets of mechanical properties to each layer in both models. As

shown in Fig. 5.25, to investigate the effect of initial stress distribution, one of two different stress initialization methods is applied in each case (Initialization 1 or Initialization 2).

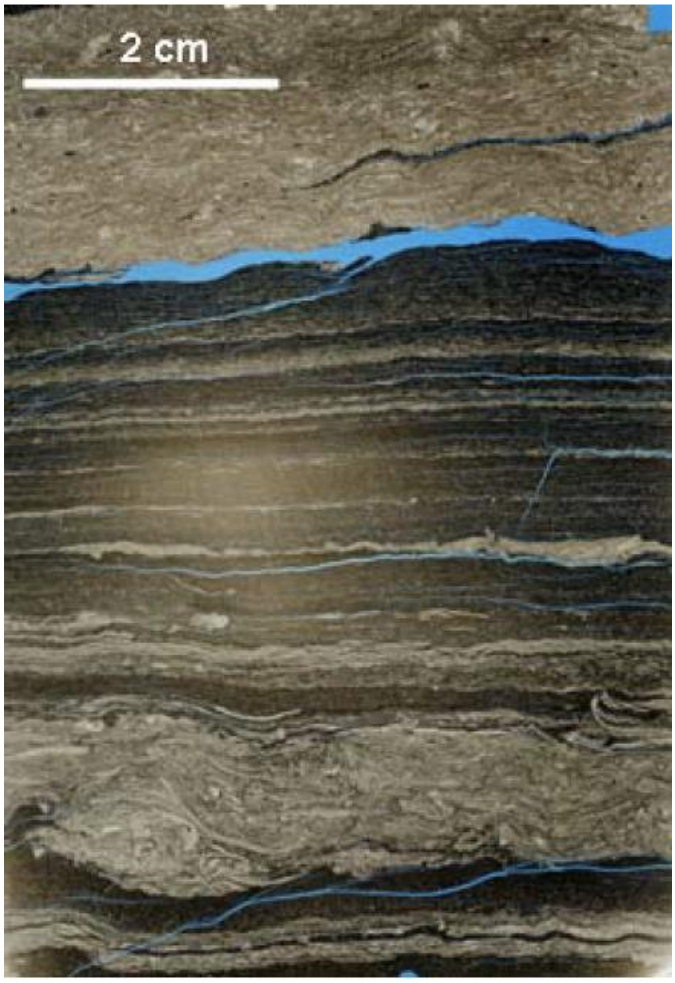


Fig. 5.23. Example of the cm order vertical heterogeneity (taken from Passey et al., 2010)).

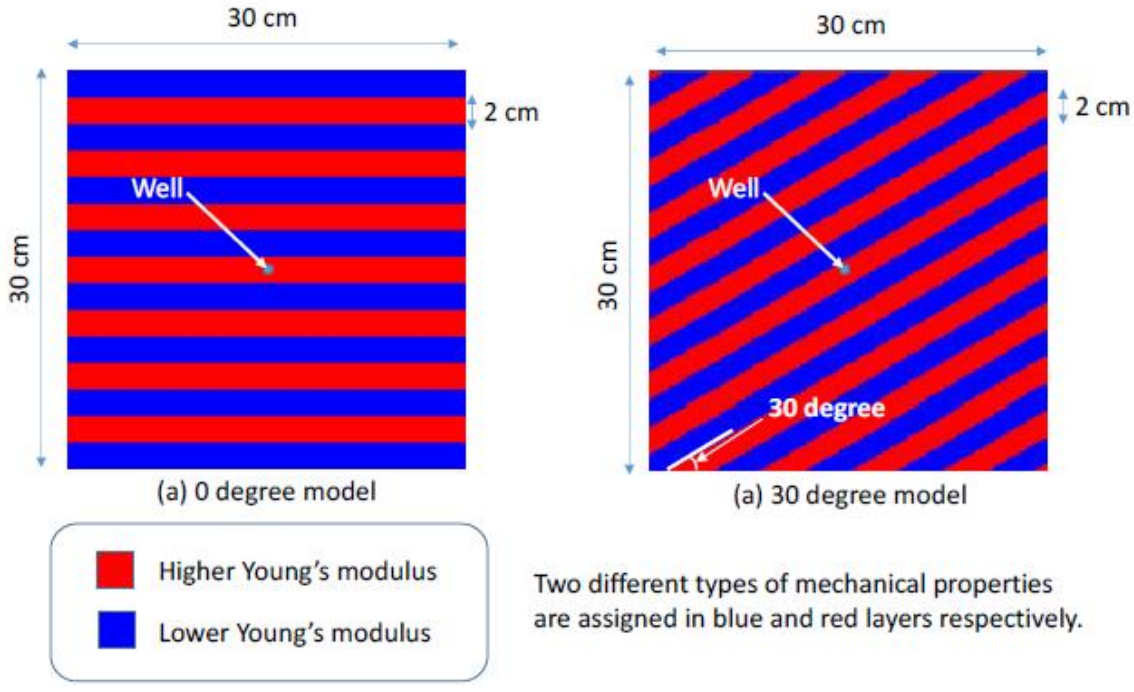


Fig. 5.24. Model description (0 degree and 30-degree dip).

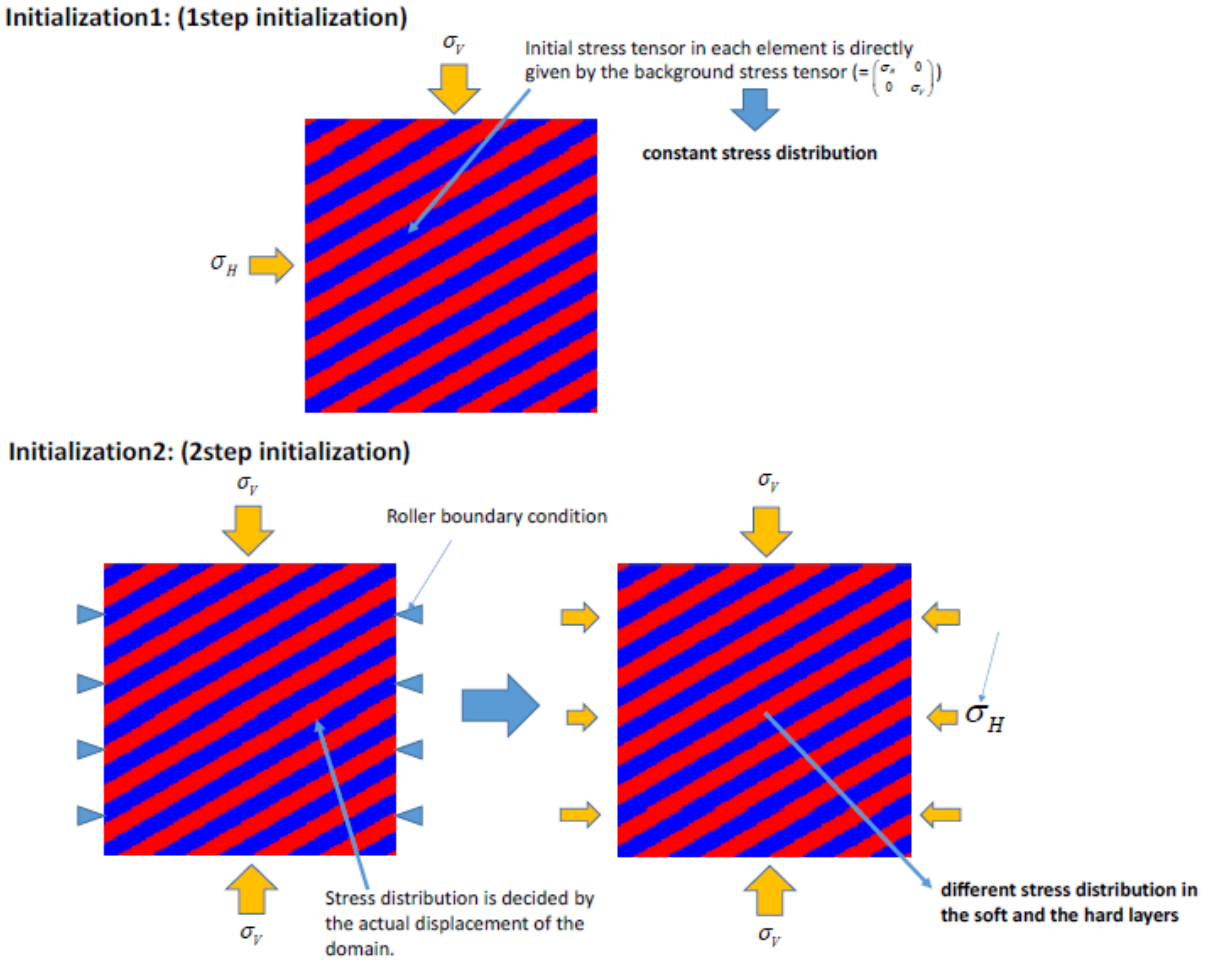


Fig. 5.25. Two different initialization.

1. **Initialization 1 (assuming homogeneous stress distribution)**: At time t < 0, a constant horizontal stress (σ_H = 40 MPa) and vertical stress (σ_V = 60 MPa) are assigned to each element through the background stress tensor method.
2. **Initialization 2 (assuming zero strain in horizontal direction):** At time t < 0, a roller boundary condition is applied to the side boundaries (no deformation in the horizontal direction) and only a normal traction of magnitude (σ_V = 60MPa) is applied to the top and the bottom boundary. At time t >= 0, the roller boundary condition applied to the side boundaries is replaced by constant traction boundaries which gives the same traction as the roller boundary condition in order to allow horizontal displacement of the side boundaries due to fracture propagation.

After stress initialization (at time t >= 0), fluid is injected from the "injection dual point" at the center of the model domain at constant rate to propagate a fracture. We investigated the effect of small-scale heterogeneity on fracture propagation by changing the contrast in mechanical properties and the initial stress distribution in both models. Table 5.6 shows the case settings. Table 5.7 shows the common calculation settings for these cases. In these cases, we assumed that the energy release rate is the same both in the higher Young's modulus layer and the smaller Young's modulus layer (except in the contrast-high 2 case and contrast-high 2_dip case). Fig. 5.26 shows the initial stress distribution in the cases where Initialization 2 method is applied. Note that in Model 1 (layer dipping angle = 0), we only apply Initialization 1 to all the cases.

Since the same Poisson's ratio is applied in every layer in these cases, even if Initialization 2 is applied, it also gives the same initial stress distribution as Initialization 1 in Model 1.

Table 5.6. Case settings for multi-layer cases.

Case name	Initialization method	E_1 (GPa)	E_2 (GPa)	K_{IC1} (MPa $m^{0.5}$)	K_{IC2} (MPa $m^{0.5}$)	G_{c1}/G_{c2} (hard/soft)	Layer Dip Angele (θ)
low_contrast	1	10	20	0.5	0.707	1.00	0
middle_contrast	1	10	40	0.5	1.000	1.00	0
high_contrast	1	10	80	0.5	1.414	1.00	0
high_contrast2	1	10	80	0.5	0.707	0.25	0
low_contrast_dip	1	10	20	0.5	0.707	1.00	30
low_contrast_dip2	2	10	20	0.5	0.707	1.00	30
middle_contrast_dip	1	10	40	0.5	1.000	1.00	30
middle_contrast_dip2	2	10	40	0.5	1.000	1.00	30
high_contrast_dip	1	10	80	0.5	1.414	1.00	30
high_contrast_dip2	2	10	80	0.5	1.414	1.00	30
high_contrast2_dip	1	10	80	0.5	0.707	0.25	30
high_contrast2_dip2	2	10	80	0.5	0.707	0.25	30

Table 5.7. Common calculation settings for multi-layer cases.

Parameter	Value
Dimension in horizontal direction L_x (cm)	30.0
Dimension in vertical direction L_y (cm)	30.0
Layer thickness (cm)	2.0
Boundary stress in vertical direction σ_V (MPa)	60.0
Boundary stress in horizontal direction σ_V (MPa)	40.0
Young's modulus E_1, E_2 (GPa)	Table 5.6
Poisson's ratio	0.25
Fracture toughness K_{IC1}, K_{IC2}	Table 5.6
Initial pore pressure P (MPa)	28.5
Injection rate (kg/s/m)	0.01
Fracturing fluid viscosity (cp)	1.0
Medium permeability (mD)	0.00001
Number of elements	150×150
Horizon size ($=\frac{\delta}{\Delta x}$)	3.0

Fig. 5.27 – Fig. 5.29 show the mechanical and fluid property distributions after fracture propagation (note that the displacements are 50 times exaggerated in these figures.) As shown in Fig. 5.27 (A) and Fig. 5.27 (B), in the cases where the layer dip angle is zero and the Young's modulus contrast is not very high (less than 4.0), the fractures just propagate in the maximum principal stress direction even if vertical heterogeneity exists in the reservoir. However, as shown in Fig. 5.27 (C), in the cases where the layer dip angle is zero and the Young's modulus contrast is very high (= 8.0), the fracture propagation is affected by the small scale heterogeneity in the reservoir. In this case, the fracture does not go straight, but branches at the layer interface when it propagates from the lower Young's modulus layer (softer layer) to the higher Young's modulus layer (harder layer) due to the pre-damage zone in the higher Young's modulus layer. As

explained in the previous section, if the Young's modulus between the two layer is highly different, the required displacement for the fracture propagation in the harder layer is much smaller than the softer layer (in this case, the critical displacement of the softer layer is about one-third of the harder layer). Therefore, the displacement induced by the fracture propagation in the softer layer can cause damage in the harder layer before the fracture tip reaches the layer interface, which finally causes fracture branching.

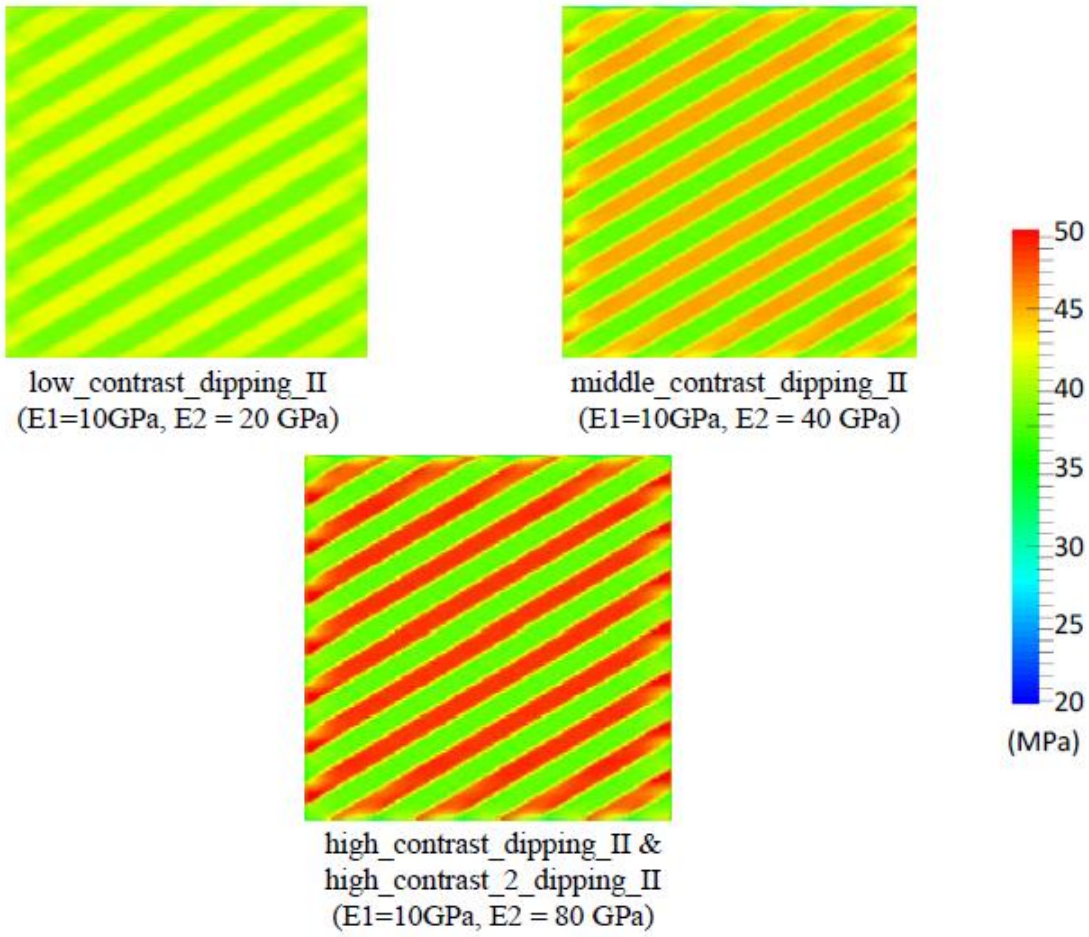


Fig. 5.26. Initial horizontal stress distribution (Initialization2 Cases)

As shown in Fig. 5.27 (D), if the harder layer's energy release rate is smaller than the softer layer (high_contrast2 case: G_{E_hard} / G_{E_soft} = 0.25), branching is more clearly observed due to the higher critical displacement contrast between the harder layer and the softer layer. These high Young's modulus contrast cases demonstrate that even a thin (order 1 cm) high Young's modulus layer such as a calcite vein can cause fracture branching at the layer interface between the softer layer and the harder layer. When we consider the published mechanical property of calcite (E = 84.3 GPa, K_{IC} = 0.19 MPa $m^{0.5}$) (Atkinson, 1987; Gray Mavko, 2009), branching may occur in some reservoirs where calcite veins exist. Note that, due to the difficulty of convergence of the calculation when the fracture tips reach the pre-damage zone in the harder layer, the symmetricity of the fracture propagation is not perfectly kept in these high Young's modulus contrast cases. However, since the pre-damage zone in the harder layer has already existed before the fracture tip reaches the layer interface, branching in these cases is not the result of numerical instability.

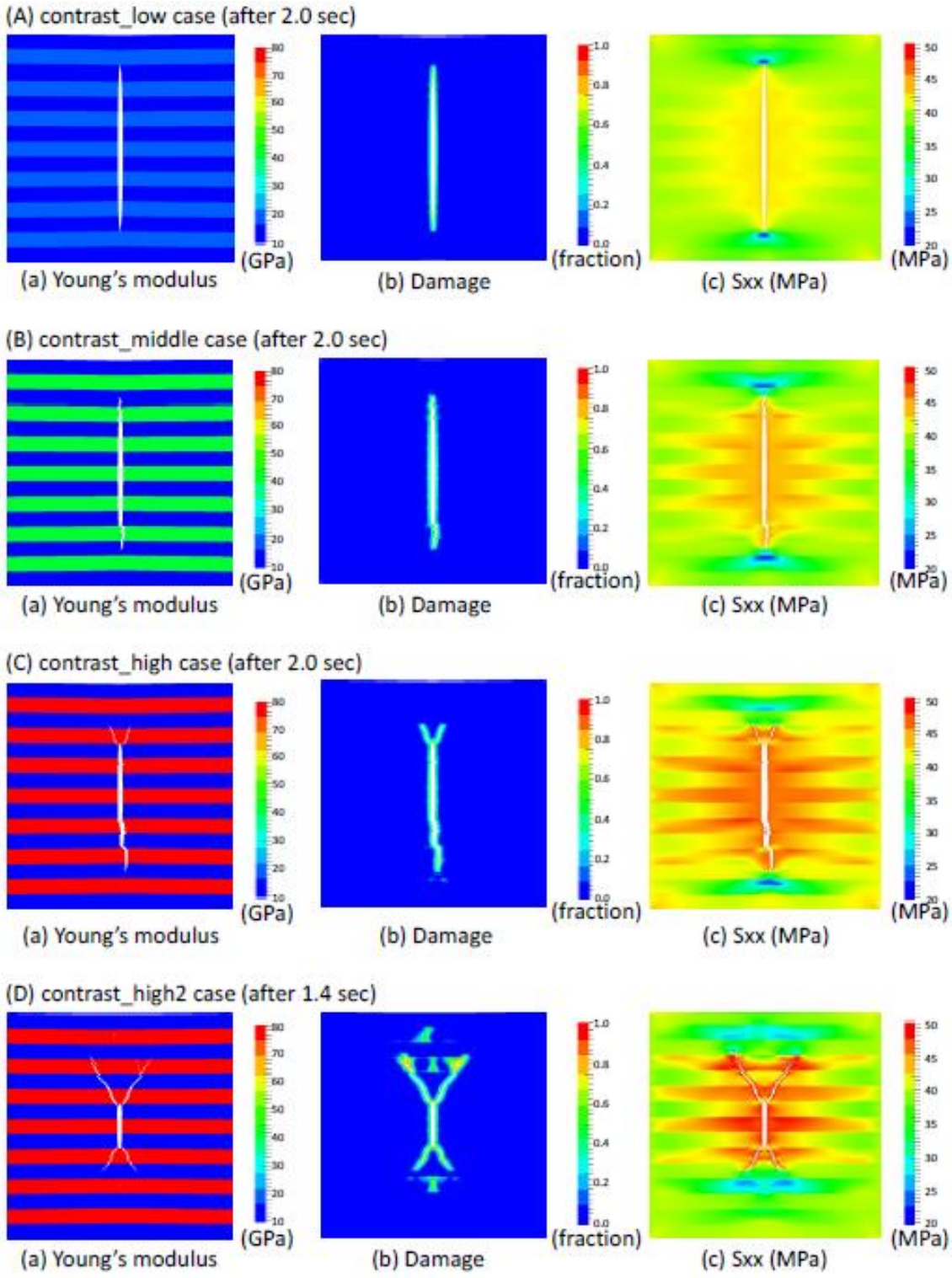


Fig. 5.27. Reservoir property distributions (0-degree cases)

If the layer has a high dip angle (30 degrees), regardless of the initial stress distribution (Initialization 1, assuming a homogeneous stress distribution) and Initialization 2 (assuming zero strain in the horizontal direction)), the fracture kinks at the layer interface even in the low Young's modulus contrast case (E_{hard} / E_{soft} = 2.0) since the fracture propagates in the propagation direction offering the least resistance. As shown in Fig. 5.28 (A) and Fig. 5.29 (A), in the dipping layers, the fracture turns as if avoiding the harder layer and staying in the softer layer. In addition, the fracture also turns towards the softer layer when propagating in the harder layer. Due to the combination of these two types of kinking in the softer layer and the harder

layer, the total kinking angle at the layer interface finally becomes more than 60 degrees in these cases.

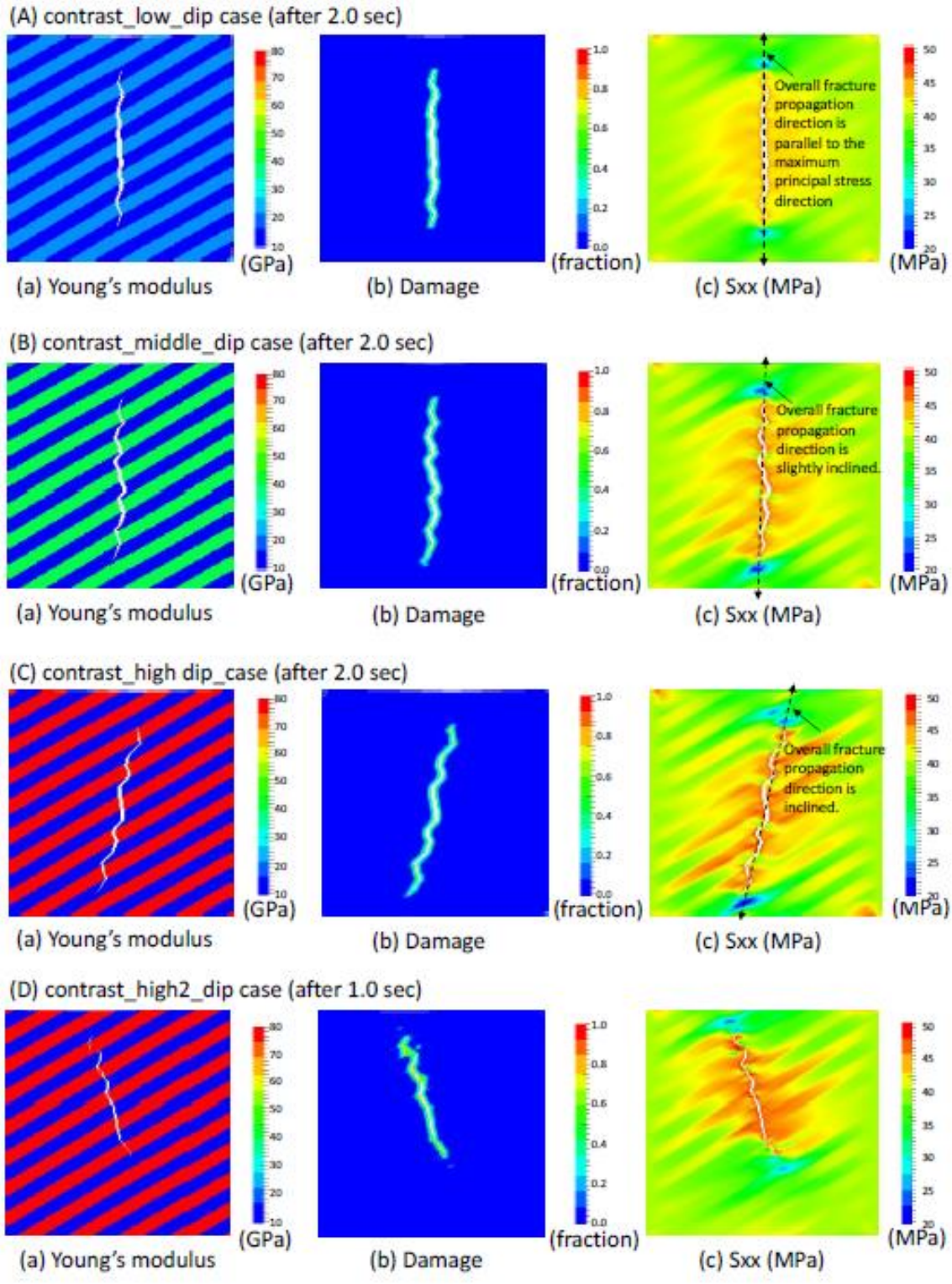


Fig. 5.28. Reservoir property distributions (30-degree dip cases: Initialization Case I)

When the two different stress initializations are compared, Initialization 2 which has a higher horizontal stress contrast between the high Young's modulus layer and the low Young's modulus layer, the fracture is more likely to turn in the "low_contrast_dip2" case (non-homogeneous stress distribution case) than the "low_contrast_dip" case (homogeneous stress distribution case). The stress difference caused by mechanical property variations enhances fracture turning. As shown

in Fig. 5.28 (B) and Fig. 5.29 (B), in the cases where the Young's modulus contrast is not as large (E_{hard} / E_{soft} = 4.0), the kinking angle of the fracture at the layer interface becomes higher (more than 70 – 80 degrees) than the lower Young's modulus contrast cases. The fracture turning angle in the non-homogeneous stress distribution case (middle_contrast_dip2 case) is higher than the homogeneous stress distribution case (middle_contrast_dip case). In the cases where the Young's modulus contrast is the highest (E_{hard} / E_{soft} = 8.0), as shown in Fig. 5.28 (C) and Fig. 5.29 (C), the fracture kinks at around 80 – 90 degrees at the layer interface in both stress distribution cases.

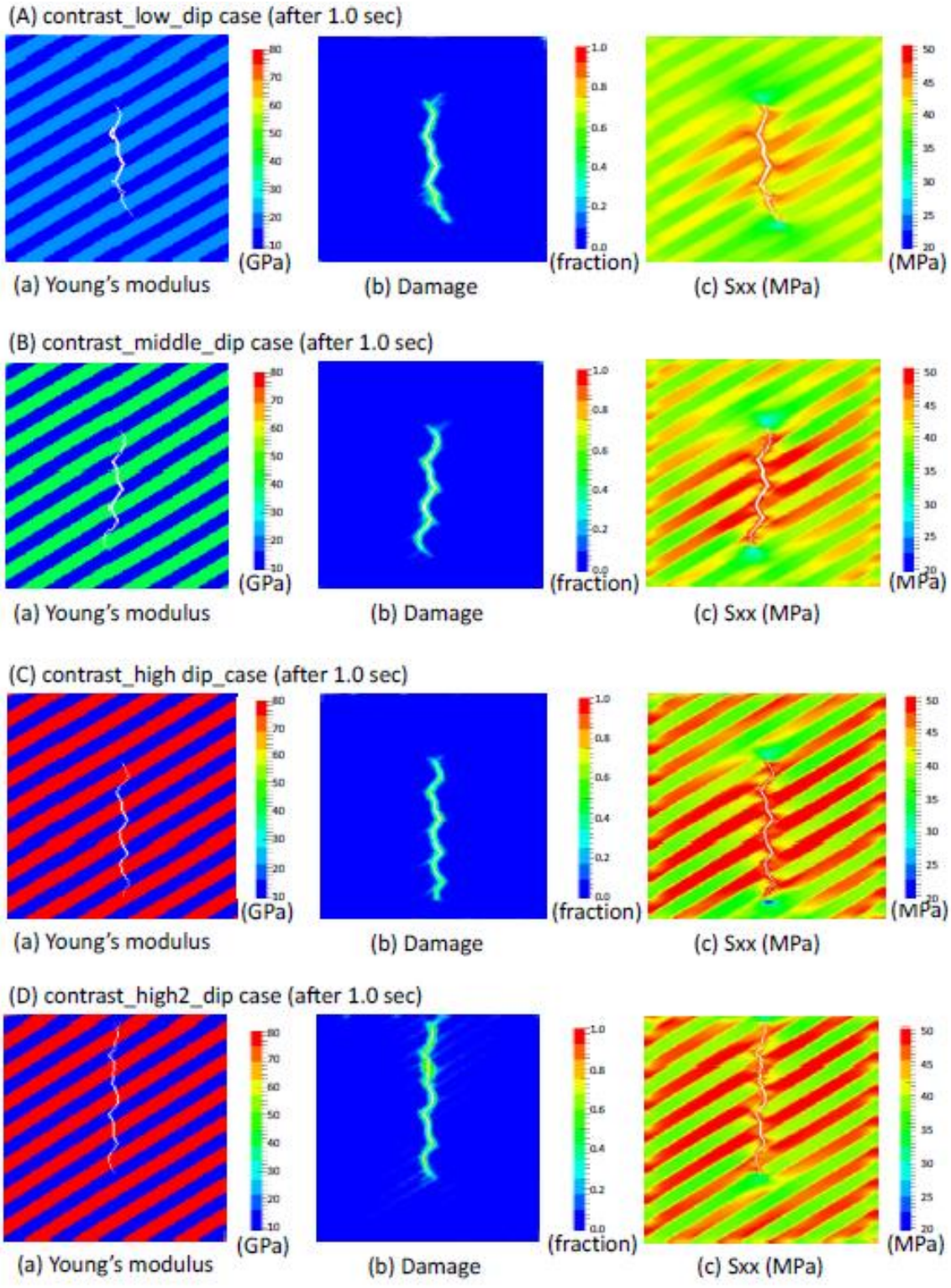


Fig. 5.29. Reservoir property distributions (30 degree dip cases: Initialization Case II)

These layer dipping cases clearly show the tendency that the higher the Young's modulus contrast, the more local kinking is expected in a dipping layer. When compared with the two different stress initialization cases, the overall fracture propagation direction in the homogeneous initial stress distribution case is about 12 degrees deviated from the maximum principal stress direction (Fig. 5.28 (C)) while the overall fracture propagation direction in the non-homogeneous initial stress distribution case is almost parallel to the maximum principal stress direction (Fig. 5.29 (C)). As shown in Fig. 5.28 (D) and Fig. 5.29 (D), if the energy release rate in the harder layer is 25 % of the softer layer in the highest Young's modulus contrast cases, the fracture propagation geometries in the different stress initialization cases (high_contrast2_dip case and high_contrast2_dip case) also show very high turning angle (80 – 90 degrees). However, the global fracture propagation direction in the uniform initial stress distribution case (high_contrast2_dip case) is different from the non-uniform initial stress distribution case (high_contrast2_dip2 case). In the "high_contrast2_dip" case, as shown in Fig. 5.30, one observes the same kind of pre-damaged zone, as in the case where the layer dip angle is zero and the other conditions are the same. However, due to the layer dipping angle, the magnitude of the two pre-damage zones ahead of the fracture tip is not equivalent. One of the pre-damage zones which is closer to the principal stress direction in the softer layer grows more than the other side of the pre-damage zone due to the ease of fracture propagation. Therefore, the fracture preferentially selects the larger pre-damaged zone and the overall fracture propagation direction in this case is different from the "high_contrast_dip" case. In the non-uniform stress distribution case (high_contrast2_dip2 case), the pre-damage zones do not appear in the high Young's modulus layers due to the high stress concentration in the high Young's modulus layers. Therefore, the global fracture propagation direction is still same as the high_contrast_dip2 case even if the fracture toughness in the high Young's modulus layer is low.

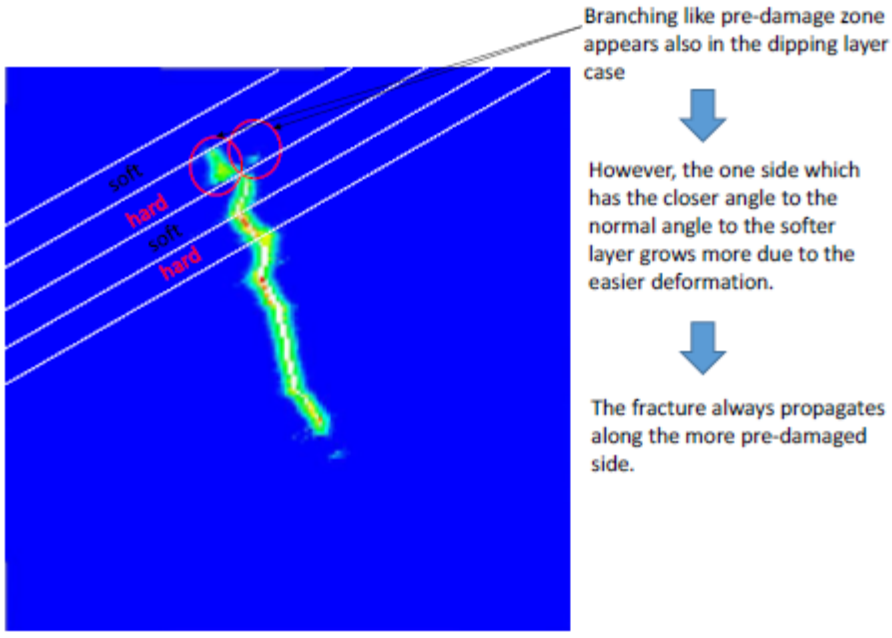


Fig. 5.30. Preferential fracture propagation direction (contrast_high2_dip case).

These simulation results clearly show that, if the layer interface is inclined, the effect of cm scale sublayers on fracture propagation cannot be neglected. Kinking at the layer interface will affect

proppant transport (screen out could occur) due to changes in the fracture width at the kinking point. In addition, the frequent kinking could also have a significant influence on the net pressure (fracturing fluid pressure distribution in the frequently kinked fracture geometry may be totally different from a single planar fracture). Judging from the kinking angle, even if the Young's modulus contrast is low, inclined sub-layers could be an obstacle to fluid flow, fracture growth and proppant transport.

Conclusions

We systematically investigated fracture propagation in heterogeneous reservoirs by using different geological models with different types of heterogeneity (two-layer, three-layer and multi-layer models, arbitrary micro-scale heterogeneity).

In the two-layer model, we observed three characteristic fracture propagation behaviors near the layer interface: "turning", "kinking", and "branching". The following conclusions were drawn from this study.

Fracture Turning

1. If the layer interface is not damaged, fracture turning along the layer interface is primarily controlled by the fracture toughness contrast and the principal stress difference. A lower principal stress difference and a higher toughness contrast facilitates fracture turning along the layer interface. The effect of other parameters (Young's modulus contrast, layer dip angle, and horizontal stress contrast between layers) on turning is limited.
2. If the layer interface is damaged (weak), the fracture always turns more easily for high interface dip angles (θ >= 30 degree) regardless of the toughness contrast between layers or the principal stress difference. However, if the interface dip angle is low (θ <= 15 degree), fracture turning is primarily controlled by fracture toughness contrast and principal stress difference.
3. Layer thickness also affects fracture turning along the layer interface. The thinner the layer in front of the fracture tip, the easier it is for the fracture to cross the layer interface.
4. Based on the required fracture toughness contrast, fracture turning along the layer interface is expected only in shallow reservoirs in which the principal stress contrast is less than 1 MPa or in reservoirs which have highly dipping or weak layer interfaces.

Fracture Kinking

1. If the layer interface is inclined, the propagating fracture kinks before it reaches the layer interface. If the fracture propagates from a softer layer to a harder layer, it turns as if avoiding the layer interface. On the other hand, if the fracture propagates from a harder layer to a softer layer, it turns as if trying to cross the layer interface at a right angle.
2. The magnitude of fracture kinking is primarily controlled by the magnitude of Young's modulus contrast and layer dip angle. The effects of fracture toughness contrast and layer thickness on fracture kinking are limited, which suggests that, if layers are inclined enough, the fracture can kink in reservoirs which contain small scale heterogeneities in Young's modulus (bedding planes in the vertical direction) as are commonly observed in shale reservoirs.

Branching

1. If the Young's modulus contrast is very high (E_1/E_2 >= 8.0), fracture toughness contrast is low (K_{IC1} / K_{IC2} <=1.0), and the layer interface is not inclined, a propagating fracture branches in the harder layer due to the damage ahead of the fracture tip in the harder layer.
2. In a multi-layer model, we investigated the effect of many sub-layers or bedding planes on fracture propagation. The following conclusions can be made.
    a. If the layers are not inclined, the effect of small-scale heterogeneity (sub-layers) on fracture geometry is limited. Only in the case where a small vein which has very high Young's modulus and low fracture toughness contrast exists, a fracture can branch in such a layer. The fracture propagation pressure increases as the contrast between the Young's moduli and fracture toughness in the layers increases.
    b. If the layers are inclined, the fracture can frequently kink at a high angle in the small scale sub-layers even if the Young's modulus contrast is low (<= 2.0) and the principal stress difference is high. This result suggests that proppant screen out or proppant bridging is likely to happen when highly inclined bedding planes are present in a vertically heterogeneous reservoir.

A Peridynamics Model For The Propagation of Hydraulic Fractures in Naturally Fractured Reservoirs

Summary

A novel fully coupled hydraulic fracturing model based on a non-local continuum theory of peridynamics is presented and applied to the hydraulic fracture propagation problem. It is shown that this modeling approach provides an alternative to finite element and finite volume methods for solving poroelastic and fracture propagation problems. In this paper we specifically investigate the interaction between a hydraulic fracture and natural fractures. The peridynamics model presented here allows us to simulate the propagation of multiple, non-planar, interacting fractures and provides a novel approach to simulate the interaction between hydraulic fractures and natural fractures. The model predictions in two-dimensions have been validated by reproducing published experimental results where the interaction between a hydraulic fracture and a natural fracture is controlled by the principal stress contrast and the approach angle. A detailed parametric study involving poroelasticity and mechanical properties of the rock is performed to understand why a hydraulic fracture gets arrested or crosses a natural fracture. This analysis reveals that poroelasticity, resulting from high fracture fluid leak-off, has a dominant influence on the interaction between a hydraulic fracture and a natural fracture. In addition, the fracture toughness of the rock, the toughness of the natural fracture, and the shear strength of the natural fracture also affect the interaction between a hydraulic fracture and a natural fracture. We also investigate the interaction of multiple completing fractures with natural fractures in two-dimensions and demonstrate the applicability of the approach to simulate complex fracture networks on a field scale. Finally, the 3-D interaction study elucidated that the height of the NF, the position of the NF, and the opening resistance of the NF all have a significant impact on the three-dimensional interaction between a HF and a NF.

Introduction

In many shale gas/oil fields, microseismic mapping techniques have shown the growth of complex fracture networks and asymmetric fracture propagation. Studies suggest that the creation of such complicated fracture networks is generated by the interaction between hydraulic fractures and natural fractures. To fully understand how such complex fracture networks are formed, we need to understand how a hydraulic fracture (HF) interacts with a single natural fracture (NF) or a network of natural fractures or planes of weakness such as faults.

Many researchers have tried to investigate the mechanism of this interaction through experiments and numerical simulations. Blanton et al. (Blanton 1982) conducted experiments on naturally fractured Devonian shale and hydrostone. They found that hydraulic fractures crossed natural fractures under a high stress contrast and a high angle of approach, and dilated or were arrested by natural fractures under low stress contrast conditions and low approach angles. Warpinski et al. (Warpinski and Teufel 1987) conducted the same type of experiments and got results that were consistent with Blanton. Zhou et al. (Zhou et al. 2008) conducted experiments on sand blocks and concluded that in addition to stress contrast and angle of approach, shear strength also affects the interaction between hydraulic fractures and natural fractures. Gu et al. (Gu et al. 2012) conducted similar experiments to verify his proposed equation (Gu and Weng 2010) for determining whether a fracture crossed a natural fracture or not; their results agreed with prior findings.

Zhao et al.(Zhao and Young 2009) developed a two-dimensional (2D) DEM model and showed that his model could match the experimental data. Chuprakov et al. (Chuprakov et al. 2010) investigated the interaction between a hydraulic fracture and a natural fracture in an impermeable rock. This research suggested that in addition to the stress contrast and the angle of approach, the effect of net pressure and friction coefficient on the interaction between a hydraulic fracture and natural fracture was also significant. Taleghani and Olson (Dahi Taleghani and Olson 2014) investigated how a hydraulic fracture interacts with sealed natural fractures based on the ratio of the cement fracture energy to the rock fracture energy. They demonstrated that a sealed natural fracture can still be the path for a hydraulic fracture to divert. All previous modeling efforts in this area have neglected poroelasticity and assume purely elastic interactions. While this may be a good approximation in nano-Darcy rock, it is certainly not a good assumption in more permeable rocks. This study, for the first time, solves the complete poroelastic problem of the interaction of a propagating hydraulic fracture with a natural fracture.

Peridynamics is a recently developed nonlocal theory of continuum mechanics that accounts for discontinuities such as fractures naturally (Silling and Askari 2005, Silling et al. 2007, Silling et al. 2010). The validity of the peridynamic theory for solid and elastic fracture mechanics has been fully demonstrated (Silling and Bobaru 2005, Askari, Xu, and Silling 2006, Bobaru 2007, Xu et al. 2007, Askari et al. 2008). However, the peridynamic theory did not have a formulation for fluid flow. Hence, it could not simulate fluid induced fracture propagation (hydraulic fracturing). In order to simulate hydraulic fracturing using peridynamics, a peridynamics based fluid flow and poroelastic model was developed by our group (Katiyar et al. 2014). Later, we fully coupled the existing peridynamic theory for solid and fracture mechanics with the peridynamic model for fluid flow in pores and fractures (Ouchi et al. 2015). Since this coupled formulation simulates the stresses and the pore pressure both inside and outside a fracture, it allows us to consider the

effect of poroelasticity and reservoir heterogeneity. It should be noted that recently Nadimi and Miskovich (Nadimi and Miskovich 2016) claim to use the peridynamics implementation within the LAMMPS (Plimpton 1995) molecular dynamics code to model hydraulic fractures interacting with natural fractures. However, their paper does not discuss the multi-physics coupling to fluid flow in any detail, nor cite the implementation they used, as this is not a standard feature in the LAMMPS code. For this reason, we take serious exception to their methodology and findings. They oddly use a viscoelastic material model along with "randomly deleting" a small percentage of the problem domain to model porosity and poroelastic effects. This methodology conflicts with well-established poroelastic theory in which the deformation of a solid skeleton material and fluids are super-imposed at every continuum point and their mechanical interactions are enforced through Lagrange-multipliers that result in the well-known "effective stress" model. Their results show very strange fracture patterns that involve crack-branching and turning that we will demonstrate do not occur with a robust numerical implementation of the peridynamics poroelastic formulation (Ouchi et al. 2015).

In this paper, we briefly review the mathematical models for the peridynamics based hydraulic fracturing model. We then introduce the new formulations for defining tensile failure and shear failure of NF (a pre-existing fracture) in peridynamics and define NF as a special surface which has both tensile and shear failure criteria. We derive the discretization of the governing equations and the numerical solution method in the peridynamics based hydraulic fracturing model. Subsequently, we demonstrate the validity of our NF model by comparing the experimental results for interaction between hydraulic fractures and natural fractures. The key parameters for the interaction between a hydraulic fracture and a natural fracture are also investigated through a sensitivity analysis. Then, we highlight the applicability of our model to predict the generation of complex fracture networks by simulating multiple competing hydraulic fractures through a network of natural fractures in a 2D field-scale domain. Finally, the effect of 3D interactions between a HF and a NF is investigated by using a parallelized 3D fracture propagation model.

Mathematical Model

The details of the poroelastic fracture propagation model used in this study have been presented earlier (Ouchi et al. 2015). This model simultaneously solves the three governing equations for mechanics, porous flow, and fracture flow. In this paper, to simulate the interaction between a HF and NF, we introduce new formulations for defining a NF (pre-existing fracture) and its interaction with a hydraulic fracture in peridynamics. In the following section, we review the mathematical models for the peridynamics based hydraulic fracturing model and explain the new formulations for defining a NF in peridynamics.

Definition of Natural Fracture (Pre-existing Fracture) in Peridynamics

To simulate the interaction between a HF and a NF in peridynamics, we define a NF (pre-existing fracture) as a special surface where all the bonds passing through the surface have different failure criteria than all the other ordinary bonds. All the bonds crossing the pre-existing fracture follow the same constitutive law as the ordinary bonds. But, since they have the following (special) tensile failure criteria and shear failure criteria, the time when these bonds break is different from the bonds representing the rock matrix.

Tensile Failure Criteria for Natural Fracture

The failure criteria for pre-existing fractures (NF) is given by the following formulation where the modification factor α_{NF} is multiplied by the failure criterion for the rock.

$$s_{c_NF} = \alpha_{NF} s_{c_rock} \quad (0 \le \alpha_{NF} \le 1)$$

Shear Failure Criteria for Natural Fracture

To capture the first order effect of shear failure on the interaction of HF and NF, we introduce one based on a Mohr-Coulomb type shear failure criterion in our hydraulic fracturing model.

$$\|\tau\|_{NF} > K_{shear}\sigma_{NF} + \tau_0$$

Where, $\|\tau\|_{NF}$ is a shear stress acting on a natural fracture surface, σ_{NF} is a normal stress acting on a natural fracture surface, K_{shear} is the shear strength of a natural fracture, and τ_0 is the cohesion of a natural fracture.

Verification: Comparison with Experimental Results (Interaction of a Hydraulic Fracture with a Single Natural Fracture)

To validate simulator's predictions for interaction between a HF and NF, we compare simulation results with the experimental results presented by Zhou et al (2008). Zhou et al. performed a series of hydraulic fracturing experiments where ordinary paper was used to mimic a natural fracture. Fig. 6.1 shows the schematic of these experiments. By changing three parameters —shear strength of the natural fracture (types of the paper), the angle between the hydraulic fracture and the natural fracture, and the stress contrast— Zhou et al. investigated how a HF interacted with a NF. We simulated their reported hydraulic fracturing experiments with 0.11 mm thickness paper. Table 6.1 reports the parameters for the experiments and the corresponding numerical simulations. To calibrate the model, we simulate the unconfined stress test with different critical strain values to reproduce the UCS measured in the experiments reported by Zhou et al. Fig. 6.2 shows the results of numerical simulations and the resulting critical strain value. The critical strain value of $1.183*10^{-3}$ shows good agreement with experimental results and was used for the rest of the numerical simulations unless mentioned otherwise.

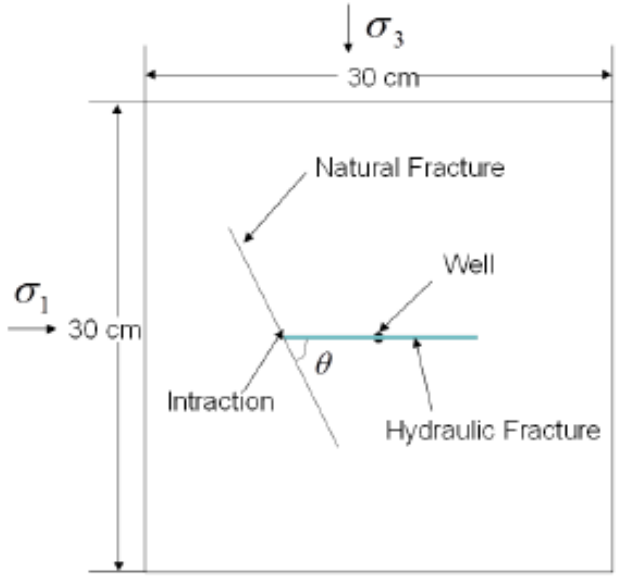
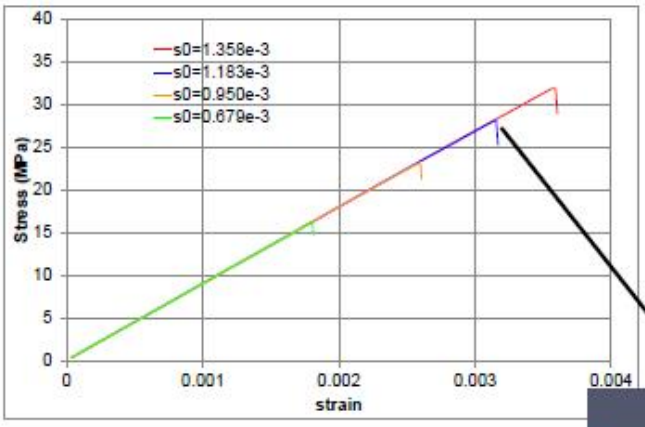
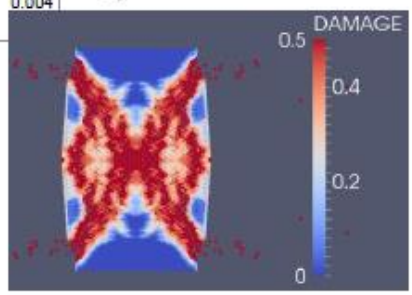


Fig. 6.1. Schematic view of experiments conducted by Zhou (modified from Zhou et al. (2008)).

Table 6.1. Basic Conditions (experiment vs. simulation)

Parameters	Value (experiment)	Value (simulation)
Domain size (cm*cm)	30*30*30	30*30
Bulk modulus (GPa)	5.18	5.18
Poisson's ratio	0.23	0.23
Unconfined compressive stress (MPa)	28.34	28.10
Permeability (mD)	0.1	0.10
Porosity	1.85	1.85
Injected fluid viscosity (cp)	135.0	135.0
Injection rate	$4.2*10^{-9}$ (m^3/s)	$2.1*10^{-8}$ ($m^3/s/m$)
Distance between well and natural fracture (cm)	around 4.0	4.0
Natural fracture length (cm)	around 8.0	8.0
Approach angle (degree)	30, 60, 90	30, 60, 90
Horizontal stress difference (MPa)	3, 5, 7, 10	3, 5, 7, 10
Vertical stress (MPa)	20.0	-
Shear failure coefficient	0.89	0.89
Cohesion (MPa)	3.2	3.2
Numerical section		
Number of material points	-	200*200
Horizon size ($=\frac{\delta}{\Delta x} = 0.45$ cm / 0.15 cm)	-	3.0
Critical strain	-	$1.183*10^{-3}$
Critical damage	-	0.25





Experimental critical stress (= 28.3 Mpa) is well reproduced by simulation when $s_0 = 1.183*10^{-3}$ (28.1 Mpa)

Fig. 6.2. Simulation results of unconfined compressive stress tests.

Table 6.2 reports a summary of each experiment, where "arrested" means fracturing fluid flows along a natural fracture without dilating the natural fracture due to shear slippage, and "dilated" means the natural fracture is dilated by the fracturing fluid. As shown in Table 6.2, the hydraulic fracture tends to cross the natural fracture if the approach angle is more than 60˚ and the hydraulic fracture tends to dilate the natural fracture at low stress contrast.

Table 6.2. Summary of the experiments and simulations (case numbers are added for simulations)

Case	Approching Angle (deg)	Sigma1 (MPa)	Sigma3 (MPa)	Result (experiment)	Result (simulation)
case1	90	10	5	Crossed	Crossed
case2	90	10	3	Crossed	Crossed
case3	60	10	3	Crossed	Crossed
case4	60	13	3	Crossed	Crossed
case5	60	8	5	Dilated	Dilated
case6	30	10	5	Dilated	Dilated
case7	30	8	5	Dilated	Dilated
case8	30	13	3	Arrested	Dilated

To simulate these experiments, a 30 cm square 2D domain is divided into 40,000 (= 200 x 200) 2D square material points. As shown in Fig. 6.3, a natural fracture surface is explicitly defined in the simulation domain. Bonds which cross the natural fracture surface are given a critical strain S0 = $0.592*10^{-3}$ —half of the critical strain for the rock as no experimental data exists for the tensile failure criteria. The shear failure criterion is the same as the experiment (shear coefficient = 0.89 and cohesion = 3.2 MPa). The fluid injection rate was equally allocated into the four center-most material points which act as injection points.

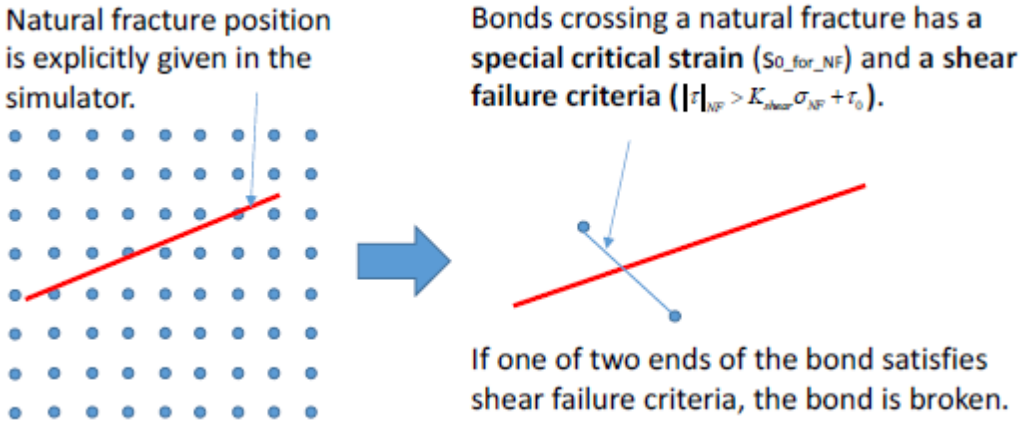


Fig. 6.3. Definition of natural fractures.

Fig. 6.4 shows the initial stress acting on a natural fracture. Fig. 6.4 shows good agreement between the experimental results and the simulation results. For the 30˚approach angle cases shown in Fig. 6.6, on approaching the natural fracture, the hydraulic fracture did not cross it as shear failure occurred on the natural fracture surface due to high leak-off leading to a decrease in the effective stress. Once shear failure occurs on the two natural fracture surfaces, the surface closer to the hydraulic fracture slips but due to the discontinuity (broken bonds across the natural fracture), less force acts on the other surface. This makes it difficult for the natural fracture to open in Mode I along the original hydraulic fracture propagation direction and,

therefore, the hydraulic fracture does not pass through the natural fracture. In addition, as shown in Fig. 6.5 for an approach angle of 30˚, the normal stress acting on the natural fracture surface is closer to the minimum principal stress. This makes it easier for the fracture fluid to dilate the natural fracture which has a smaller fracture toughness.

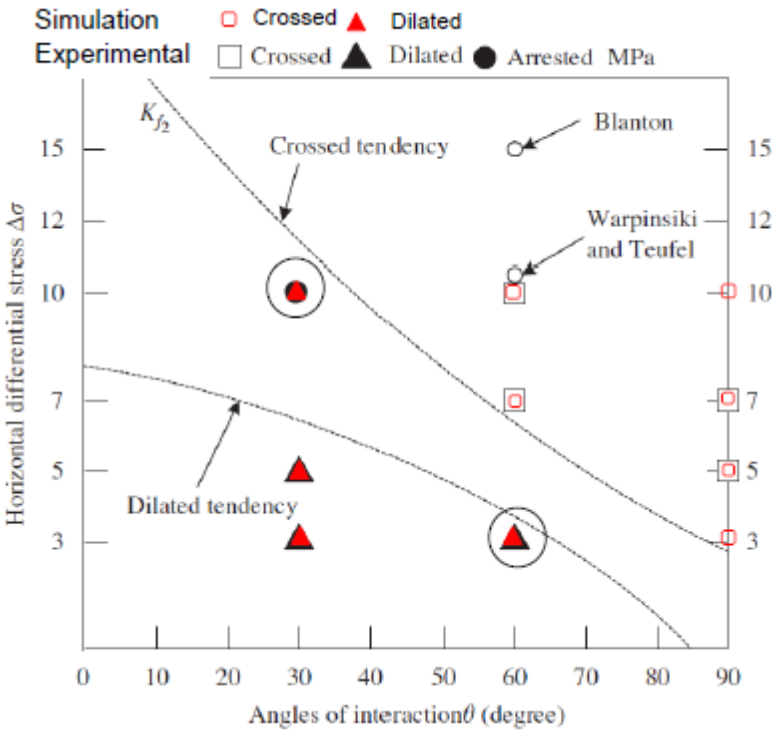


Fig. 6.4. Comparison between experimental results and simulation results (modified from Zhou et al. (2008)).

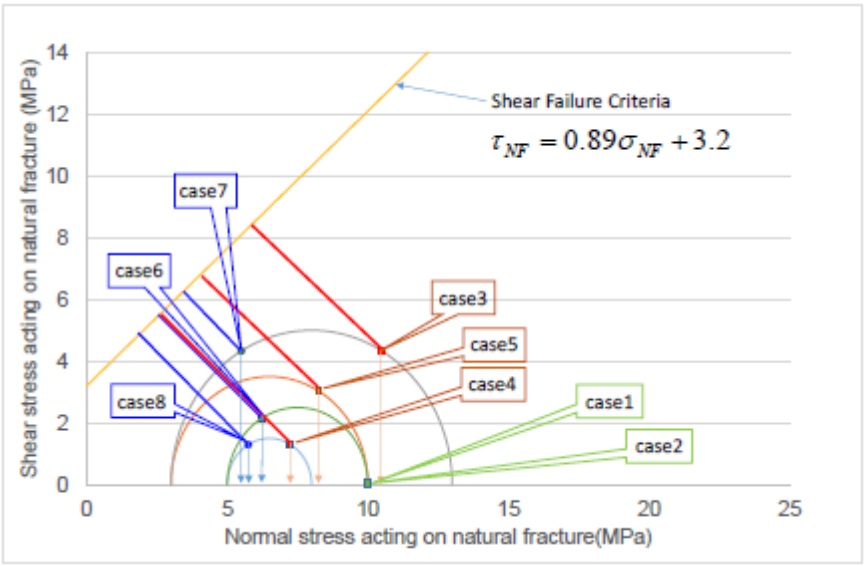


Fig. 6.5. Shear failure criteria and initial natural fracture stress condition in each case.

The simulated 60˚approach angle cases in Fig. 6.7 also show good agreement with experiments. The hydraulic fracture dilates the natural fracture in the lower stress contrast case (Case5), while the hydraulic fracture continues to propagate immediately after dilating the natural fracture in the higher stress contrast cases (Case3 and Case 4). As shown in Fig. 6.8, since the pore pressure around the fracture increases due to the high matrix permeability (= 0.1 mD), the effective stress near the fracture tip decreases from the initial condition and on approaching the natural fracture causes it to fail under shear. However, in the higher stress contrast cases, although the hydraulic

fracture initially dilates the natural fracture, the hydraulic fracture finally crosses the natural fracture because the normal stress acting on the natural fracture is close to the maximum principal stress.

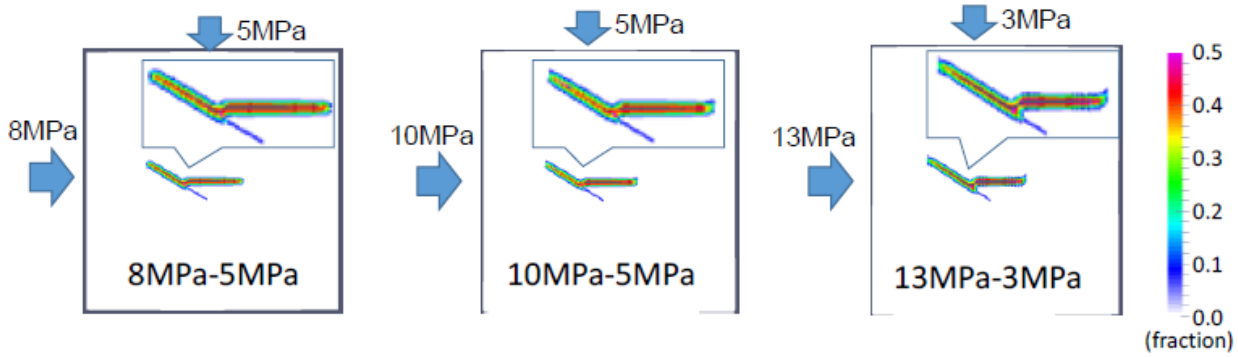


Fig. 6.6. Damage distribution after 300 sec (approach angle = 30 degree).

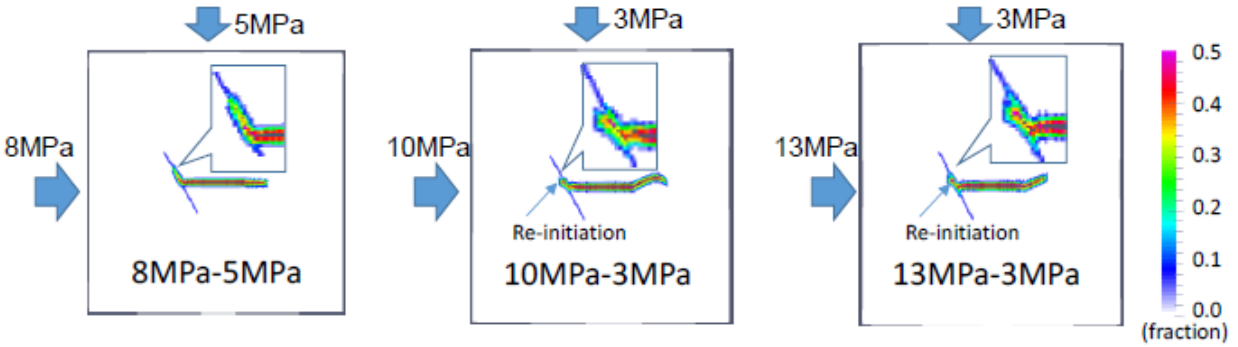


Fig. 6.7. Damage distribution after 300 sec (approach angle = 60 degree).

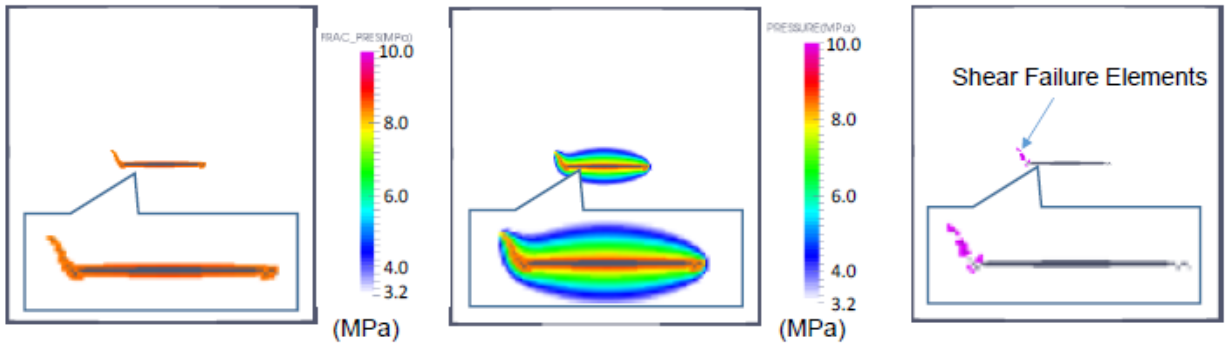


Fig. 6.8. Fracture pressure, pore pressure, and shear failure distribution after 200 sec (approach angle = 60 degree, stress contrast 8MPa-5MPa).

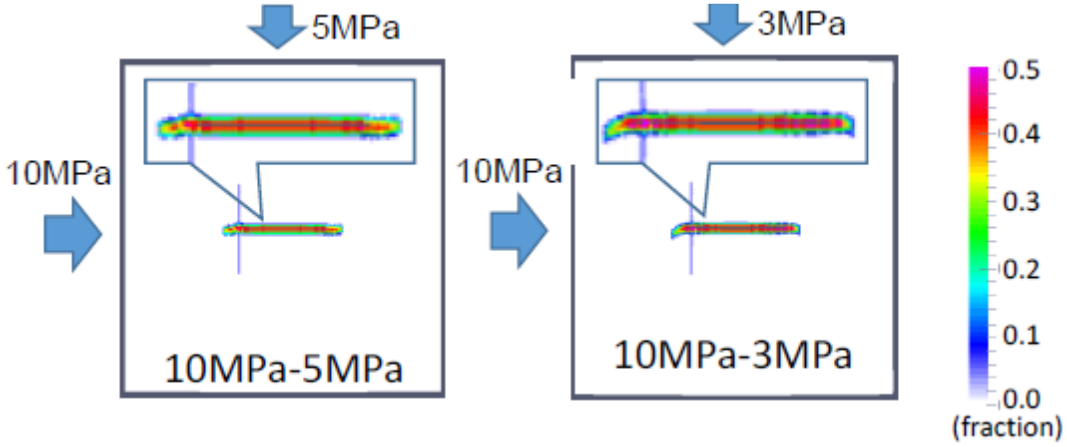


Fig. 6.9. Damage distribution after 300 sec (approach angle = 90 degree).

The simulated 90˚ approach angle cases shown in Fig. 6.9 also show good agreement with experiments. As shown in Fig. 6.5, the initial stress condition in the 90˚cases is far from the shear failure criteria. In addition, the initial normal stress acting on the natural fracture surface is the maximum principal stress. Therefore, the hydraulic fracture passes through the natural fracture without any offset.

Sensitivity Analysis

Table 6.3. Summary of the experiments and simulations

Parameter	Case	Value
Young's modulus & Critical strain	1	E = 4.0 GPa, $S_{crit} = 0.81*10^{-3}$
	2	Base (E = 8.4 GPa, $S_{crit} = 1.18*10^{-3}$)
	3	E = 20.0 GPa, $S_{crit} = 1.82*10^{-3}$
NF critical strain	1	$S_{crit} = 1.18*10^{-3}$
	2	Base ($S_{crit} = 0.59*10^{-3}$)
	3	$S_{crit} = 0.0$
Injection rate	1	$1.1*10^{-8}$ $m^3/s/m$
	2	Base ($2.1*10^{-8}$ $m^3/s/m$)
	3	$1.1*10^{-8}$ $m^3/s/m$
Rock permeability	1	0.001 mD
	2	0.01 mD
	3	Base (0.1 mD)
Shear strength	1	Coefficient = 0.89, Cohesion = 0.0 MPa
	2	Base(Coefficient = 0.89, Cohesion = 3.2 MPa)
	3	Coefficient = 0.89, Cohesion = 7.0 MPa
Initial natural fracture permeability	1	Base (0.0 mD)
	2	1.0 mD

To analyze the effect of rock properties and poroelasticity on the interaction between a hydraulic fracture and a natural fracture, we conducted a sensitivity analysis for these parameters based on Case 5 (Base Case) in the previous section (approach angle = 60º and stress contrast = 3 MPa). The following parameters are changed in these simulations: critical strain and the Young's modulus of the rock, critical strain of the natural fracture, matrix permeability, injection rate, initial natural fracture permeability, and shear failure criteria. In the critical strain and Young's modulus sensitivity case, critical strain is modified as a function of square root of Young's modulus. Also, in the initial natural fracture permeability cases, since our simulator does not allow us to keep constant initial fracture space and initial fracture permeability regardless of deformation, the initial natural fracture permeability is assumed to be equal to the matrix permeability. Modified parameters in each case are summarized in Table 6.3. Fracture propagation and damage distribution after 350 sec in each case is shown in Fig. 6.10 – Fig. 6.15. This sensitivity analysis reveals that poroelasticity has a significant effect on the interaction between a hydraulic fracture and a natural fracture if the leak-off rate is high. In addition, the relative magnitude of the following mechanical properties (fracture toughness of the rock, fracture toughness of the natural fracture, and shear strength of the natural fracture) also affect the interaction between a hydraulic fracture and a natural fracture.

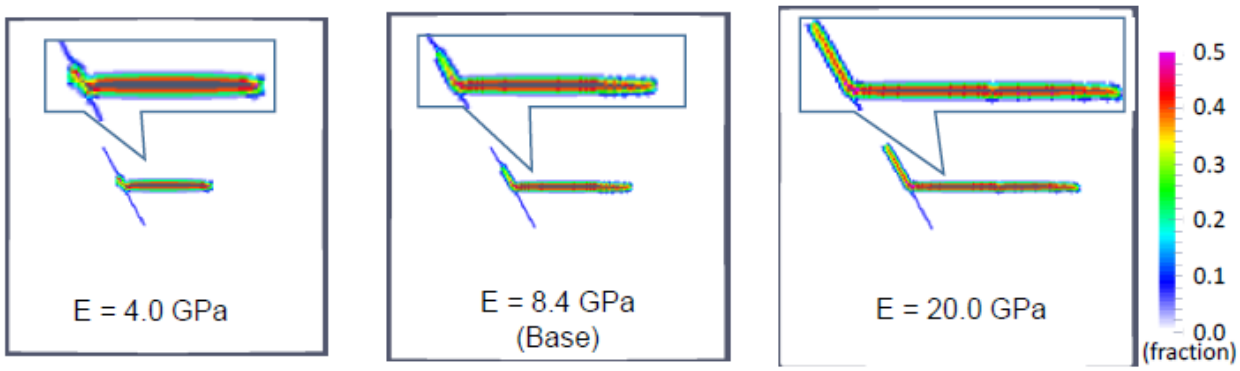


Fig. 6.10. Effect of Young's modulus and accordingly modified critical strain of the rock (Damage distribution after 350 sec).

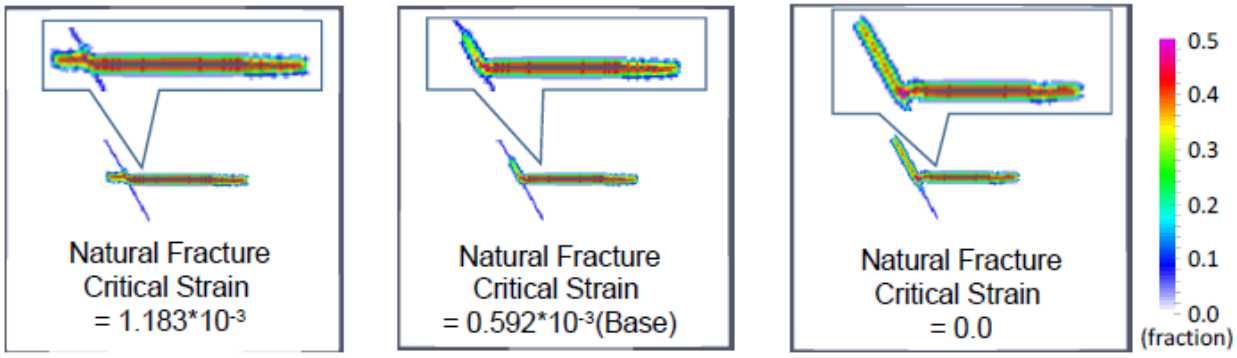


Fig. 6.11. Effect of critical strain of the natural fracture (damage distribution after 350 sec).

In Fig. 6.11, we vary the critical strain of the bonds crossing the natural fracture. The hydraulic fracture crossed the natural fracture for the highest critical strain case (S_{crit} = 1.18*10^{-3}) though it turned along the natural fracture for the zero critical strain case and the Base Case (S_{crit} = 0.59*10^{-3}). These results suggest that a high fracture toughness of a natural fracture would restrict the hydraulic fracture to turn along the natural fracture. These results also suggest that the arbitrarily chosen values of the toughness of the natural fracture in Cases 3 and 4 in the previous section may be smaller than the experiment allowing the fracture to turn towards the natural fracture.

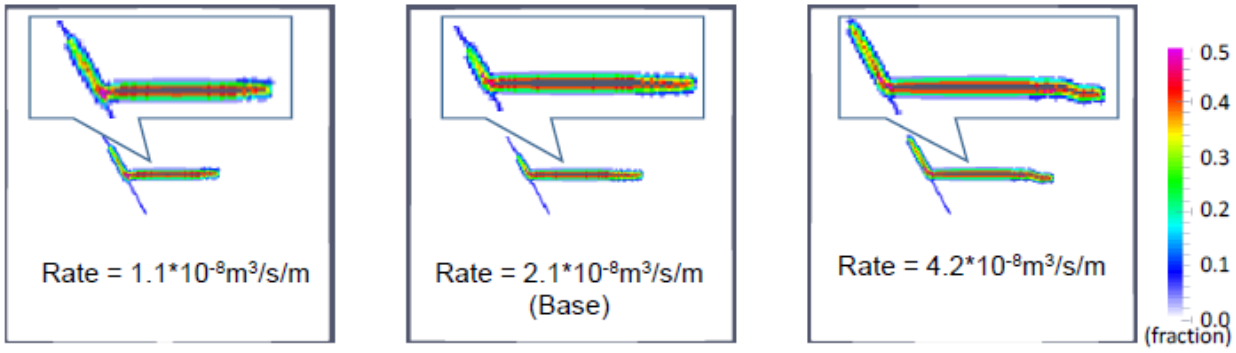


Fig. 6.12. Effect of injection rate (damage distribution after 700 sec, 350 sec, 175 sec respectively).

In Fig. 6.12, we investigate the impact of injection rate on the interaction of the hydraulic fracture with the natural fracture. For comparison between the different injection rate cases, we keep the injected volume the same, therefore, we select the injection time accordingly. The chosen injection rates do not affect the interaction mode between the hydraulic fracture and the natural

fracture; in all three cases, the hydraulic fracture turns along the natural fracture. However, it is curious to note that the higher and the lower injection rate cases in comparison to the base case yield longer fracture lengths. In the lower injection rate case with the longer injection time, due to relatively large leak-off and the resulting lower effective stress on the natural fracture, the larger shear failure causes longer fracture length along the natural fracture than base case. On the other hand, in the higher injection rate case with smaller injection time, fracture length along the natural fracture is longer than base case due to relatively smaller leak-off.

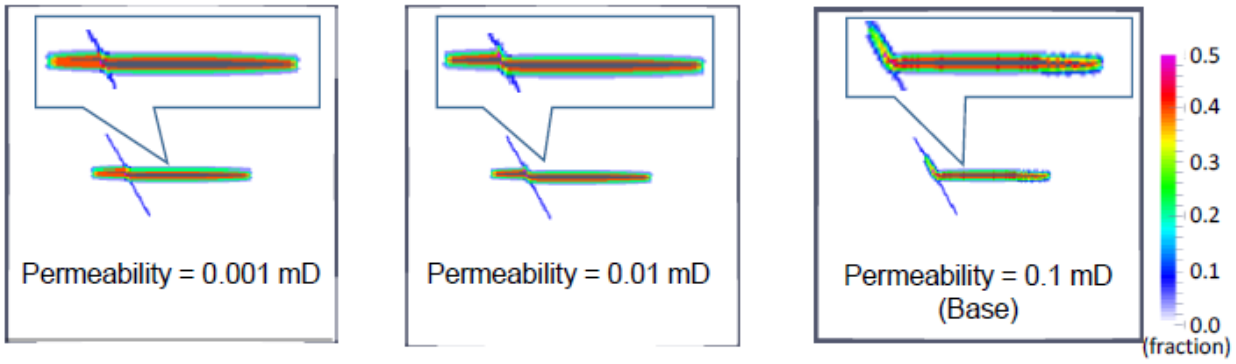


Fig. 6.13. Effect of rock permeability (damage distribution after 350 sec).

The matrix permeability shows a significant influence on the interaction between a natural fracture and a hydraulic fracture (Fig. 6.13). In the lower matrix permeability cases (k = 0.001 mD and k = 0.01 mD), the fractures passed through the natural fractures. In contrast, the fracture turned along the natural fracture for the base case (k = 0.1 mD). As shown in Fig. 6.8 (k = 0.1 mD), higher matrix permeability causes high leak-off and a significant increase in pore pressure. This leads to large reduction in the normal effective stress acting on a natural fracture surface, which makes it easier for a natural fracture to fail both in tensile and in shear modes. The fracture propagation pattern in the presence of natural fractures can completely change under high leak-off conditions. This result highlights the fact that poroelasticity plays an important role in the interaction between a natural fracture and a hydraulic fracture if leak-off is significant. This is consistent with the findings of Agarwal and Sharma (2011). Note that if we set the matrix permeability to more than 1 mD, the hydraulic fracture does not propagate. A matrix permeability of 0.1 mD is almost the maximum value that allows fracture initiation under the given injection rate.

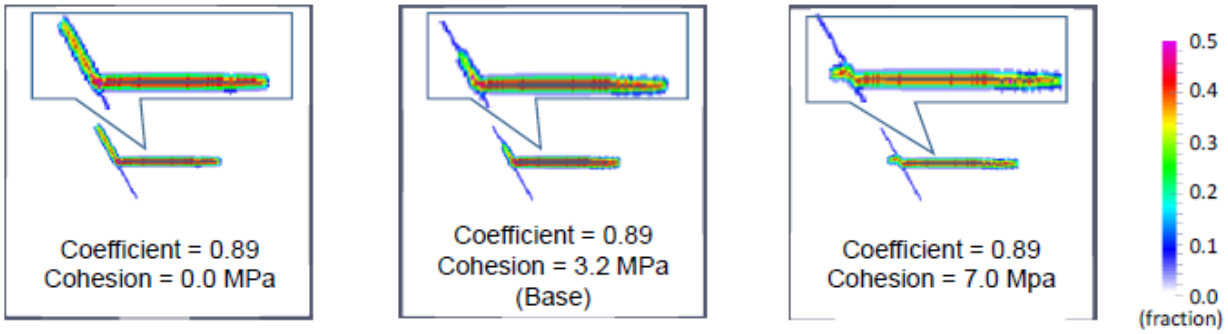


Fig. 6.14. Effect of shear strength (damage distribution after 350 sec).

In Fig. 6.14, we simulate different cohesion values to modify the shear failure criterion of the natural fracture. With the larger cohesion value (shear coefficient = 0.89, cohesion = 7.0 MPa), as

expected, the hydraulic fracture did not turn along the natural fracture even under high leak-off conditions. This suggests that the shear failure controls whether a fracture turns along a natural fracture or not. We also find that the fracture propagation speed along a natural fracture changes depending on the failure criterion. The fracture propagation speed in the lowest cohesion case (shear coefficient = 0.89, cohesion = 0.0 MPa) was faster than the second lowest cohesion case (shear coefficient = 0.89, cohesion = 3.2 MPa) due to the larger shear failure region.

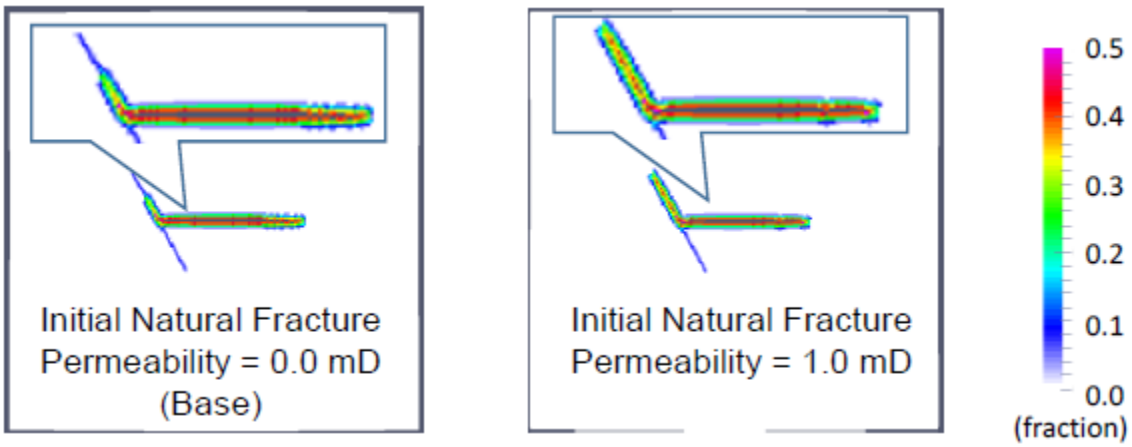


Fig. 6.15. Effect of initial natural fracture permeability (damage distribution after 350 sec).

We also find in Fig. 6.15 that the higher initial permeability of the natural fracture (than the surrounding rock) causes the hydraulic fracture to accelerate as the fracturing fluid preferentially flows into the natural fracture.

Growth of Multiple Hydraulic Fractures in Naturally Fractured Reservoirs

To demonstrate the applicability of our peridynamic hydraulic fracturing model to a field scale simulation, two cases of domain size 5,200 ft x 5,200 ft are considered. The only difference between the two cases is the presence or absence of natural fractures. As shown in Fig. 6.16, one model has 100 arbitrarily oriented natural fractures (NF case) and another has no natural fractures (no-NF case). Five equi-spaced perforation clusters 200 ft apart are placed as shown in Fig. 6.16.

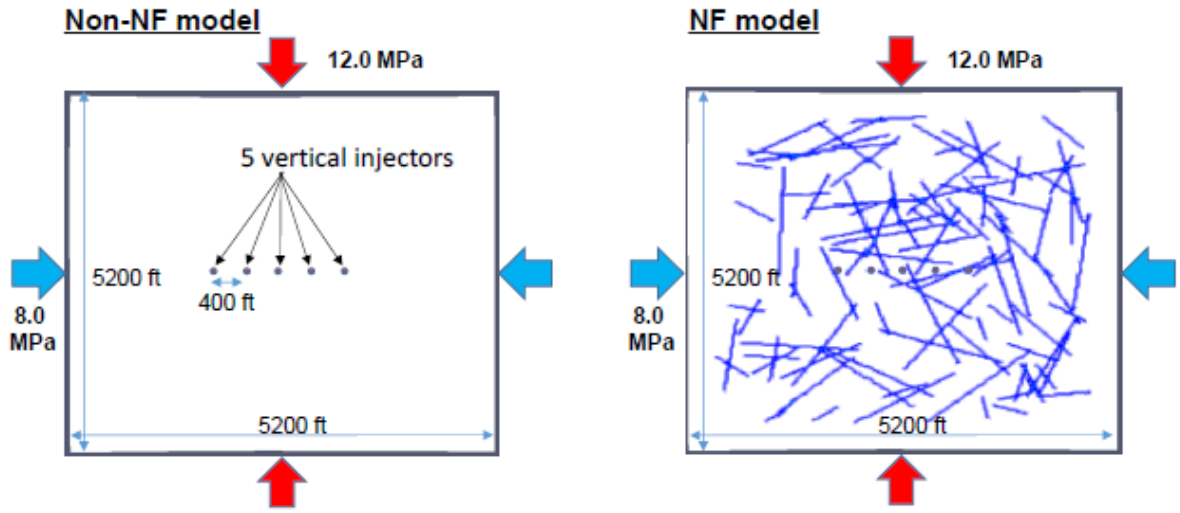


Fig. 6.16. Model description (No-NF model & NF model).

Water is injected from the five clusters at a flow rate of 0.12 bbl/min/ft to propagate fractures. Competing fracture growth from the five perforation clusters is simulated in both cases. Table 6.4 shows the simulation parameters for these cases. Fig. 6.17 and Fig. 6.18 show the property distribution (damage, fracturing fluid pressure, matrix pressure, matrix porosity, normal stress in the x direction (S_{xx}), normal stress in the y direction (S_{yy})) after 2000 sec and 4000 sec for No-NF case respectively. Fig. 6.19 and Fig. 6.20 show the property distribution after 3000 sec and 6000 sec for the NF case.

Table 6.4. Simulation parameters for fracture propagation (field case)

Parameter	Value
Dimension of the 2D domain in X direction L_x (ft)	5200
Dimension of the 2D domain in Y direction L_y (ft)	5200
Boundary stress in x direction T_x (psia)	1740
Boundary stress in y direction T_y (psia)	1160
Young's modulus of the domain (psia)	1.60*10 6
Shear modulus of the domain (psia)	0.96*10 6
Reference pore pressure p_0 (psia)	464
Injection rate (bbl/min/ft)	0.05
Fracturing fluid viscosity (cp)	1
Medium permeability (nD)	10
Critical damage	0.25
Shear failure coefficient	0.89
Cohesion (psia)	464
Number of material points	200*20 0
Horizon size ($=\frac{\delta}{\Delta x} = 78$ ft / 26 ft)	3

In the no-NF case, as shown in Fig. 6.17, at an early stage of the injection, although water was injected at the same rate from each cluster, fracture geometry and fracture pressures were slightly different for each cluster due to stress interference among clusters. The center fracture showed a shorter and wider geometry and a higher fracture pressure, while the outer fracture showed a longer and narrower geometry and a lower fracture pressure. However, at the late stage of the injection, as shown in Fig. 6.18, the center fracture (the third fracture from the left) grows longer than the intermediate fractures (second fracture and fourth fracture from the left). As the five fractures simultaneously propagate, the area under tensile stress conditions (blue S_{xx} area in Fig. 6.18 (e)) gradually grows in front of each fracture. Due to the superposition effect of every fracture, the tensile domain becomes largest in front of the center fracture (the third fracture from the left). This may induce the center fracture to propagate into the tensile domain more than the intermediate ones. Once the center fracture becomes longer than the intermediate fractures, the propagation of intermediate fractures is severely impeded by the stress interference from the center fracture and the outside fractures. However, the width of the

center fracture near the injection point becomes narrowest since this point still has the maximum stress interference from the other wells.

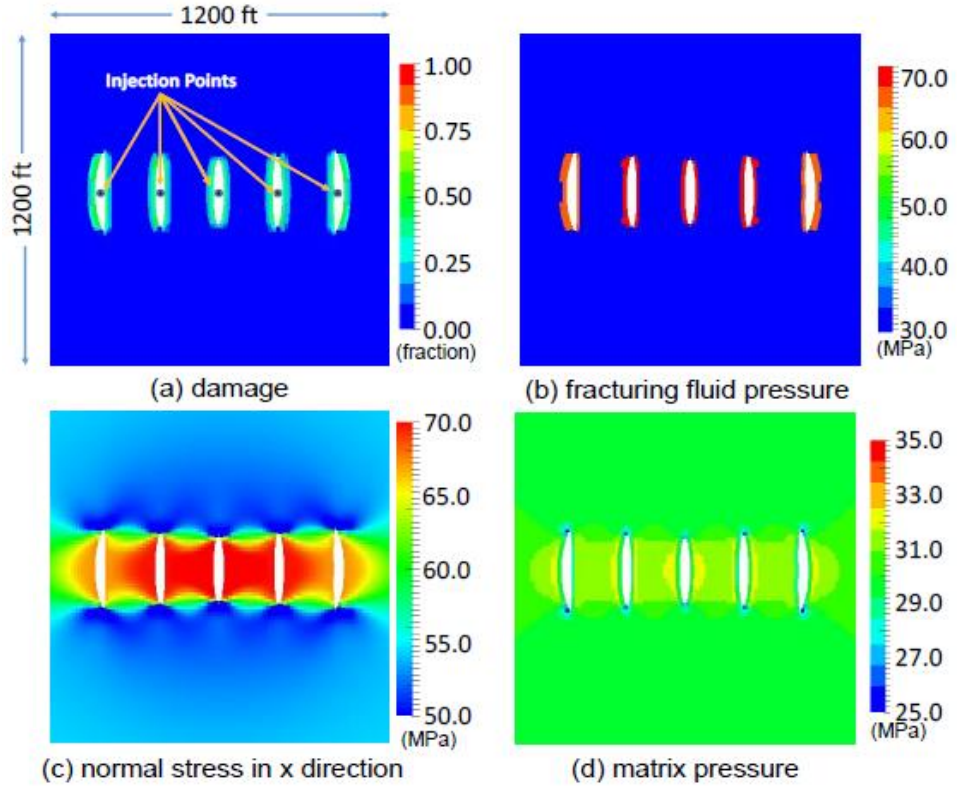


Fig. 6.17. Stress and reservoir property distribution after 2,000 sec in No-NF case.

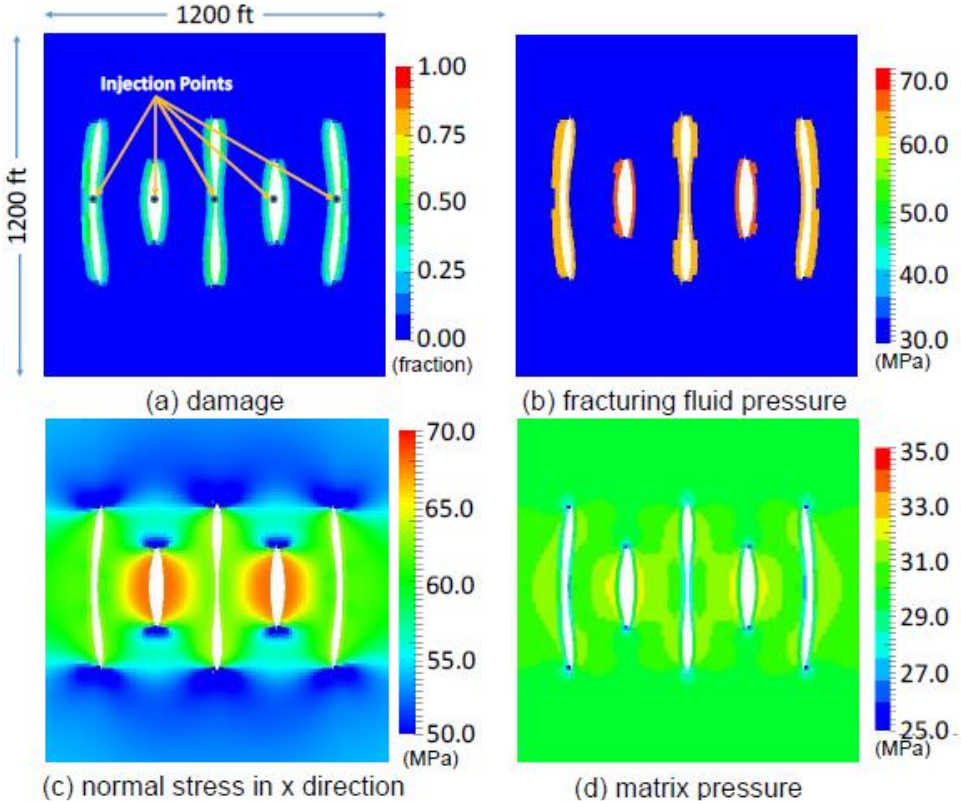


Fig. 6.18. Normal stress and reservoir property distribution after 4,000 sec in no NF case.

On the other hand, the NF case shows a completely different fracture propagation pattern. Each fracture tends to grow more in a region that has a higher density of natural fractures, compared

to those regions are already damaged and easier to open. This leads to asymmetrical fracture propagation from the well, longer fracture length and smaller fracture pressure than no-NF case. Also, in agreement with the observations made in the previous section, fractures dilate low approach angle natural fractures and cross high approach angle ones (Fig. 6.19 and Fig. 6.20).

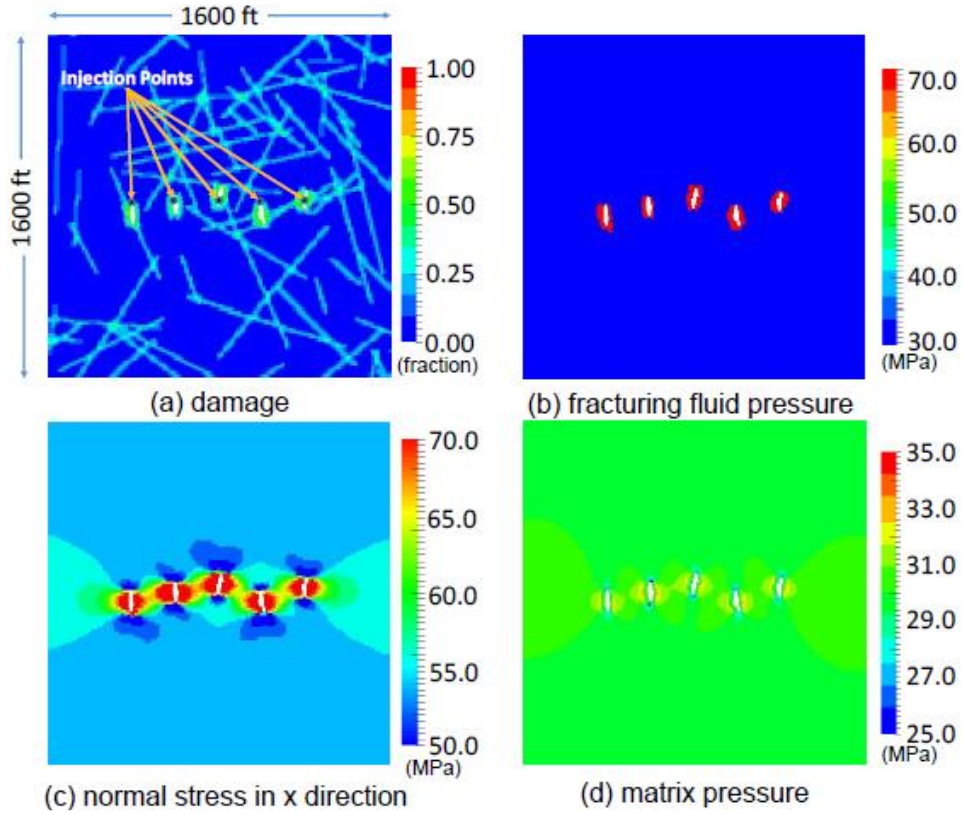


Fig. 6.19. Normal stresses and reservoir property distribution after 3,000 sec in NF case.

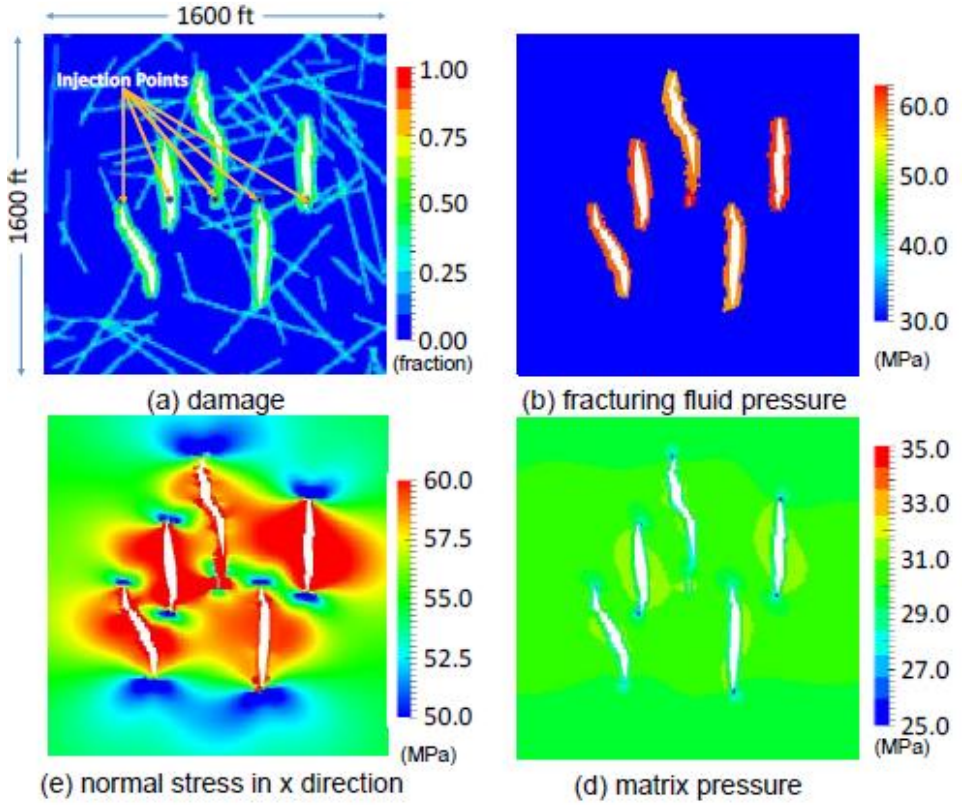


Fig. 6.20. Normal stresses and reservoir property distribution after 6,000 sec in NF case.

These results show the ability of a peridynamics-based fracture propagation theory to easily model heterogeneity and complex networks of natural fractures. The existence of natural fractures drastically changes fracture propagation patterns and generates a complicated fracture geometry.

3-D Interaction between a hydraulic fracture and a natural fracture

In the previous sections, we demonstrated our model's validity by comparing with experimental results, and our model's applicability to predict interaction behaviors between HF and NF through two dimensional simulations. As we showed in these cases, our model can properly predict the three basic interaction behaviors between HF and NF: crossing, turning (or arresting), and reinitiating a new fracture (Fig. 6.21).

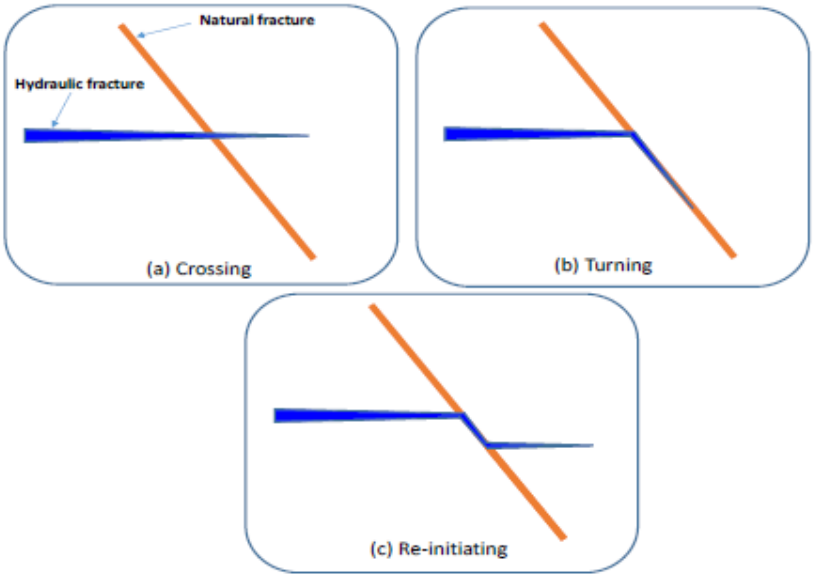


Fig. 6.21. Basic hydraulic fracture interactions with a natural fracture.

Bahorich et al. (2012) reveal, through their experiments, that when a HF turns along a NF, if the NF does not fill the entire height of the pay-zone, it can display more complicated behavior as shown in Fig. 6.22 (combination of bypassing NF and turning along NF, or a combination of turning along the NF and diverting propagation along the top and bottom of the NF).

Predicting this kind of complex interaction behavior requires full 3-D simulations, something that most state-of-the-art simulators cannot do. Two-dimensional interactions between HF and NF shown in Fig. 6.21 cannot simulate this behavior. However, our peridynamics based hydraulic fracturing model is fully capable of simulating such complicated interaction behavior. In this section, we demonstrate our simulator's applicability to model complex 3-D fracture interaction problems.

As shown in Fig. 6.23, we consider a simulation domain of 1.6 m X 1.6 m X 0.68 m where three different principal stresses (Sx=41 MPa, Sy=40 MPa, Sz=60 MPa) are applied from the x, y, and z planes respectively (exactly the same as the experiments). At x = 0, an injection point is defined as an injector. Water is injected from this injection point at the rate of 0.003 kg/s. By changing the height of NF and cohesion parameter, we investigate how a HF interacts with a NF. Common input parameters for the simulations are summarized in Table 6.5.

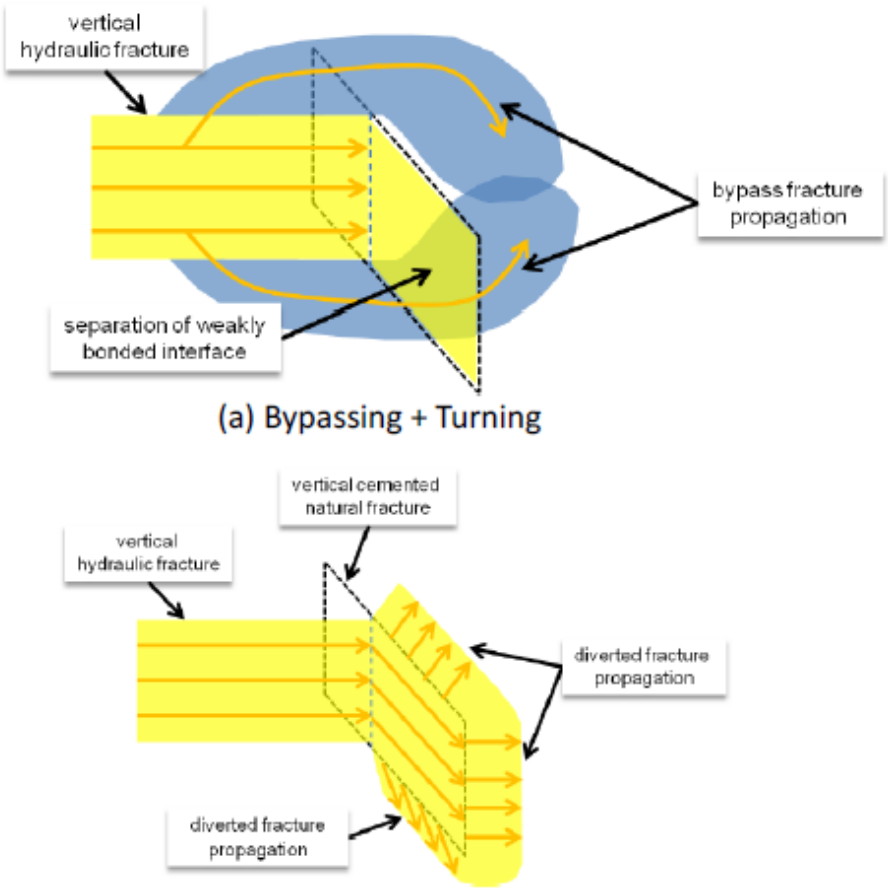


Fig. 6.22. Complicated fracture propagation in 3-D (Figures are taken from (Bahorich et al, 2012)).

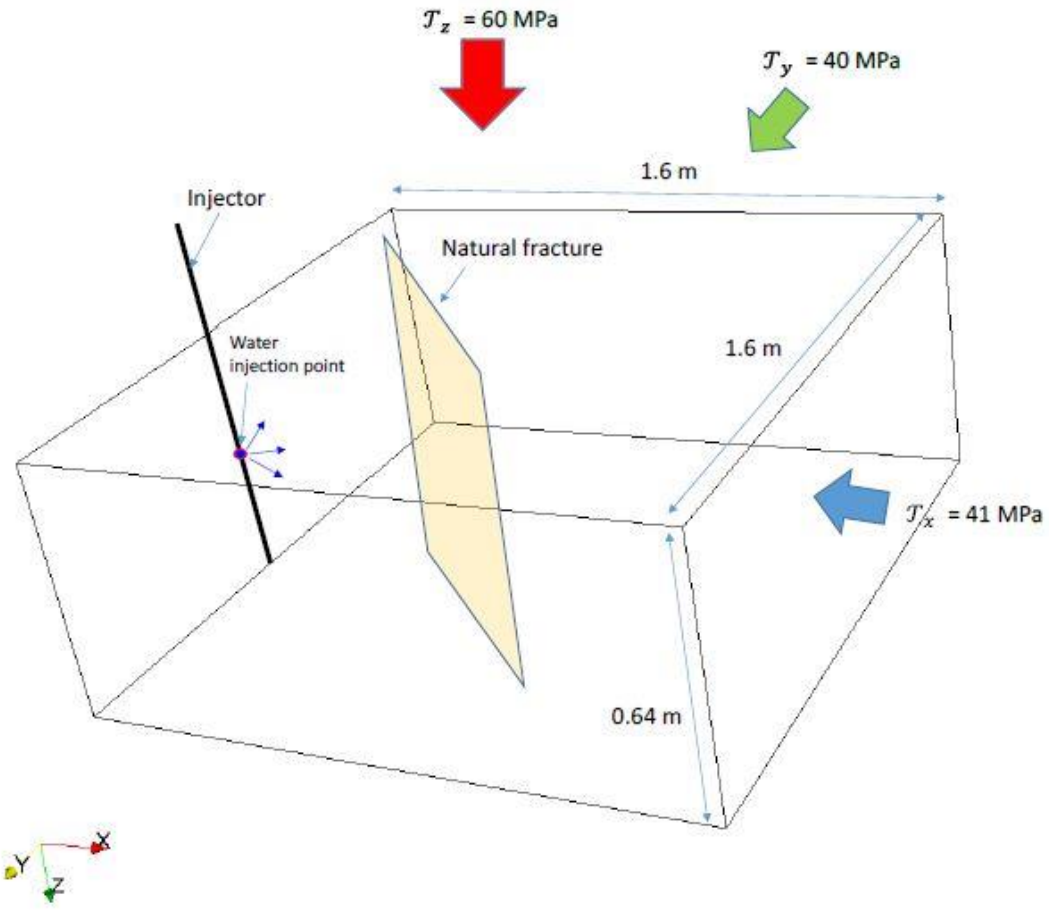


Fig. 6.23. Model description for 3-D interaction between a HF and a NF.

Parameters particular to the different cases are summarized in Table 6.6. Note that numerical convergence of the simulations is quite slow in these complicated 3-D interaction problems once the HF interacts with the NF. To complete the simulations in a reasonable time, poroelastic effects are neglected. This is a reasonable assumption for nano-Darcy permeability shales and when comparing our results with lab results (where there is very little leak-off). We don't solve pore pressure in these cases (constant initial pore pressure is used for the leak-off calculation and effective stress calculation). In addition, to reduce the calculation time further, instead of simulating bounding layers which have higher stress than the pay-zone, the displacement in the non-local area of the top and bottom boundary elements are fixed for mimicking the bounding layer.

Table 6.5. Simulation parameters for 3-D fracture propagation cases.

Parameter	Value
Dimension of the 3D domain in X direction L_x (cm)	160.0
Dimension of the 3D domain in Y direction L_y (cm)	160.0
Dimension of the 3D domain in Y direction L_z (cm)	68.0
Boundary stress in x direction $\mathcal{T}_x$ (MPa)	41.0
Boundary stress in y direction $\mathcal{T}_y$ (MPa)	40.0
Boundary stress in y direction $\mathcal{T}_z$ (MPa)	60.0
Young's modulus of the domain (MPa)	30.0
Shear modulus of the domain (MPa)	12.0
Initial pore pressure p_0 (MPa)	30.0
Injection rate (kg/s)	0.003
Fracturing fluid viscosity (cp)	1.0
Medium permeability (nD)	10.0
Critical damage (%)	25.0
Number of material points	80*80*34
Horizon size ($=\frac{\delta}{\Delta x}$)	2.0

Table 6.6. Case settings (3-D fracture propagation cases).

Case	Approaching angle (degree)	Shear failure coefficient	Cohesion (MPa)	tensile strength multiplier	Natural fracture height (cm)
Case1	60.0	0.5	0.0	0.5	60.0 (z=4 – 64 cm)
Case2	60.0	0.5	0.0	0.5	30.0 (z=34 – 64 cm)
Case3	60.0	0.5	0.0	0.0	30.0 (z=34 – 64 cm)
Case4	60.0	0.5	0.0	0.5	30.0 (Z=19 – 49 cm)
Case5	60.0	0.5	0.0	0.0	20.0 (Z=44 – 64 cm)

Fig. 6.24 shows the fracturing fluid pressure distribution in Case 1 after 26 seconds. This is the reference case. In this case, since NF fills the entire pay-zone (60 cm) and the horizontal principal

stress difference and cohesion of NF surface is low enough (ΔS = 1.0MPa, cohesion = 0.0MPa) to cause shear failure along the NF surface, the HF turns along the NF, which is the same behavior as was observed in the 2-D plain strain simulation.

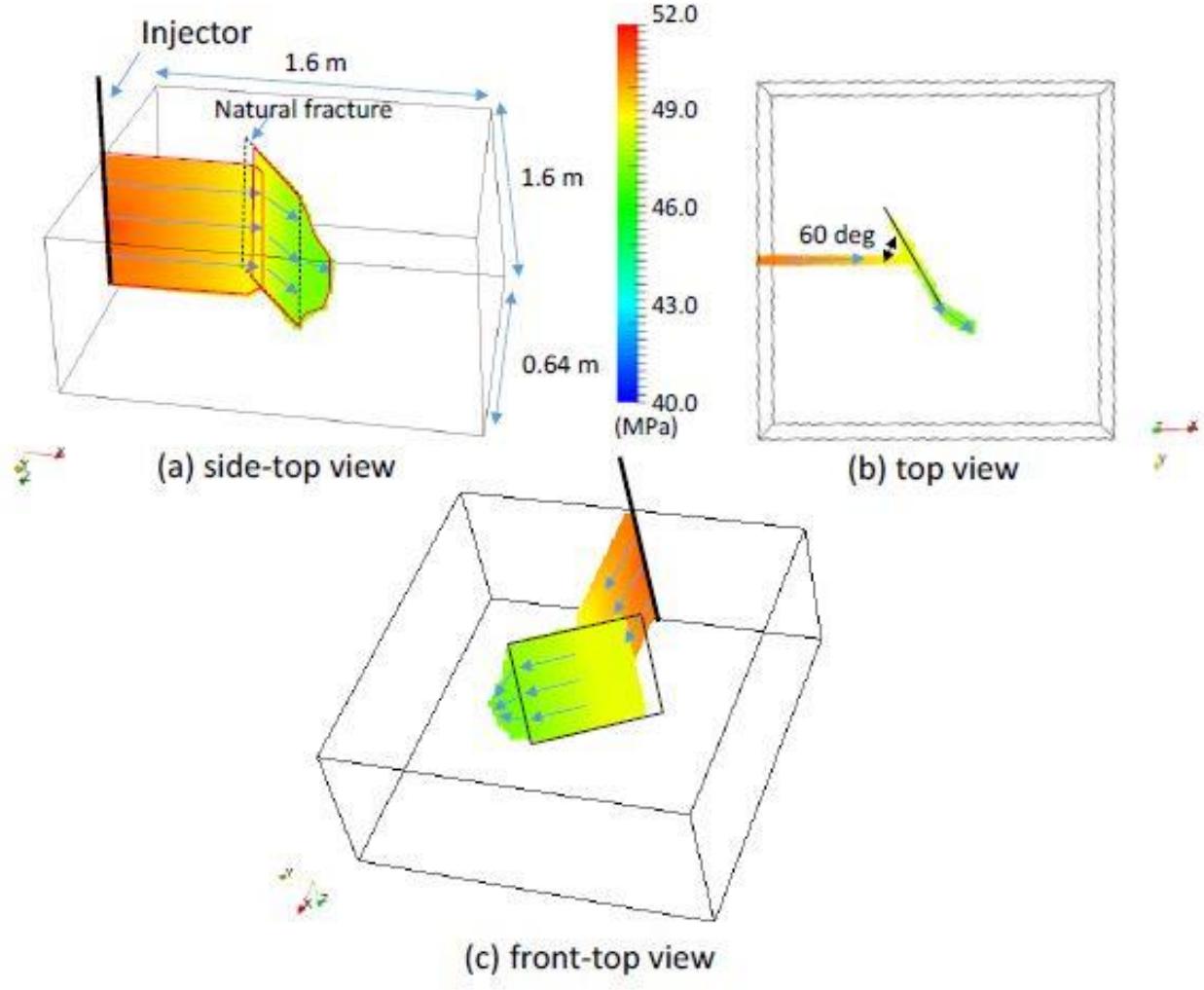


Fig. 6.24. Fracturing fluid pressure distribution (Case1, after 26 sec).

However, as shown in Fig. 6.25, if the NF fills only the lower half of the pay-zone (Case 2, with all other conditions being the same as Case1), the HF does not fully turn along NF but shows a combination of bypassing and turning behavior which is the same as the behavior shown in Fig. 6.22 (a). In this case, as shown in Fig. 6.26 (a), once the tip of the HF reaches the NF, the HF begins to turn along the NF in the lower half of the pay-zone due to shear failure at the point where it hits the NF. However, since the NF does not fill in the upper half of the pay-zone, the HF continues to propagate without turning in the upper half of the pay-zone (Fig. 6.26 (b)). Once the HF overcomes the NF in the upper part of the pay-zone, it gradually moves down to the lower part of the pay zone and fills it again (Fig. 6.26 (c)). With the main fracture moving down from the upper part of the pay-zone, fracture propagation in the NF slows down due to the stress interference from the main fracture, and finally it stops before reaching the end of the NF (Fig. 6.26 (d)). This case suggests that the height of the NF (the ratio of NF to the pay-zone) is also one of the important parameters which control the interaction between the HF and the NF.

Case 3 shows different HF propagation behavior from Case 2. In this case, the tensile strength multiplier for the NF is set lower than for Case 2 (all other conditions are the same as Case 2). As

shown in Fig. 6.27, in the lower part of the pay-zone, the HF completely turns along the NF, while, in the upper part of the pay-zone, the HF also turns along the NF with some diverting angle from the vertical axis. This is the same propagation behavior as in Fig. 6.22 (b) (turning + diverting). In this case, after the tip of the HF reaches the NF, most of the injected water moves into the NF rather than going straight due to the lower tensile resistance caused by the lower tensile strength of the NF. After water reaches the end of the NF, the HF begins to propagate from the top of the NF at some diverting angle from the vertical axis. This case shows that the degree of resistance to open the NF also affects the 3-D interaction behavior between the HF and the NF. The lower opening resistance of the NF causes more turning and diverting behavior rather than bypassing and turning.

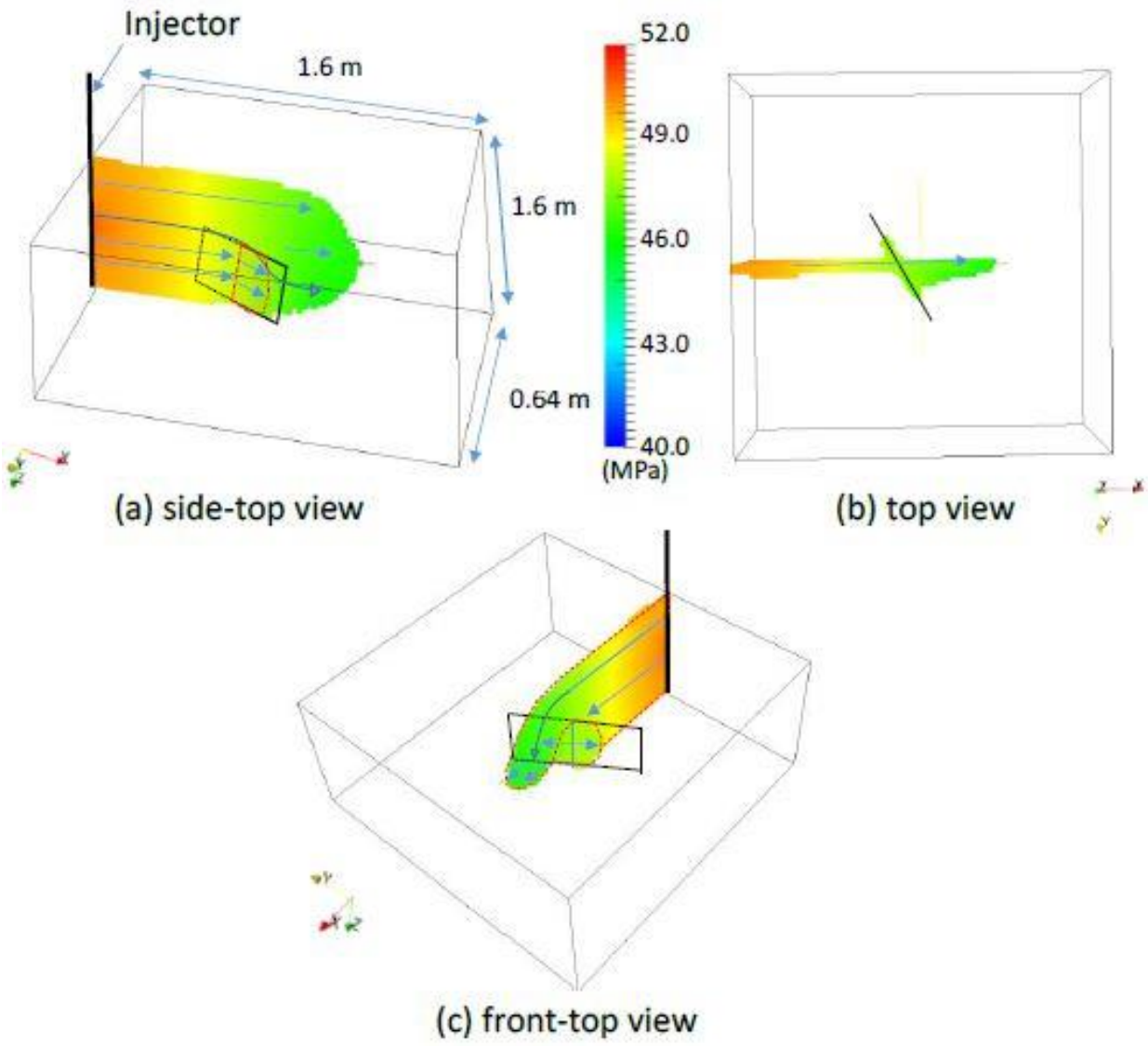


Fig. 6.25. Fracturing fluid pressure distribution (Case 2, after 26 sec).

In Case 4, the NF fills half of the pay-zone (same as Case 2), but it is set in the middle of the pay-zone instead of the bottom of the pay-zone. All the other conditions are the same as Case 2. As shown in Fig. 6.28, the fracture propagation behavior in Case 4 is also different from Case 2. It shows (turning + diverting) behavior instead of (bypassing + turning) behavior. In this case, since the tip of the HF shows a circular or elliptic shape, the middle part of the HF propagates faster than the upper and lower parts.

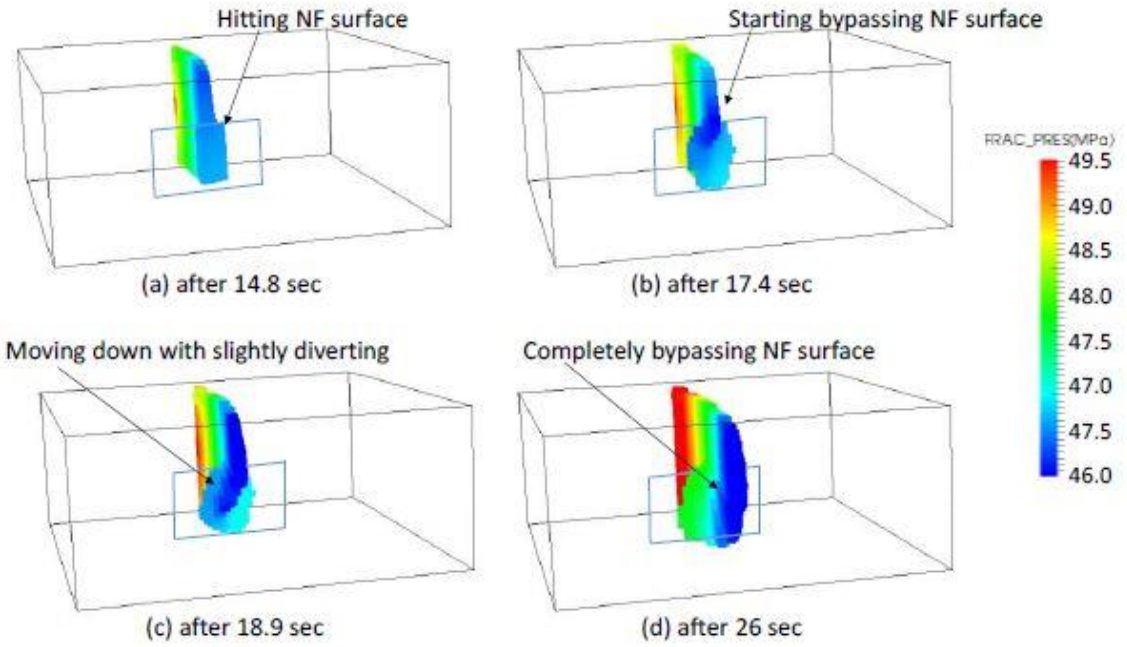


Fig. 6.26. Fracture bypassing (Case 2).

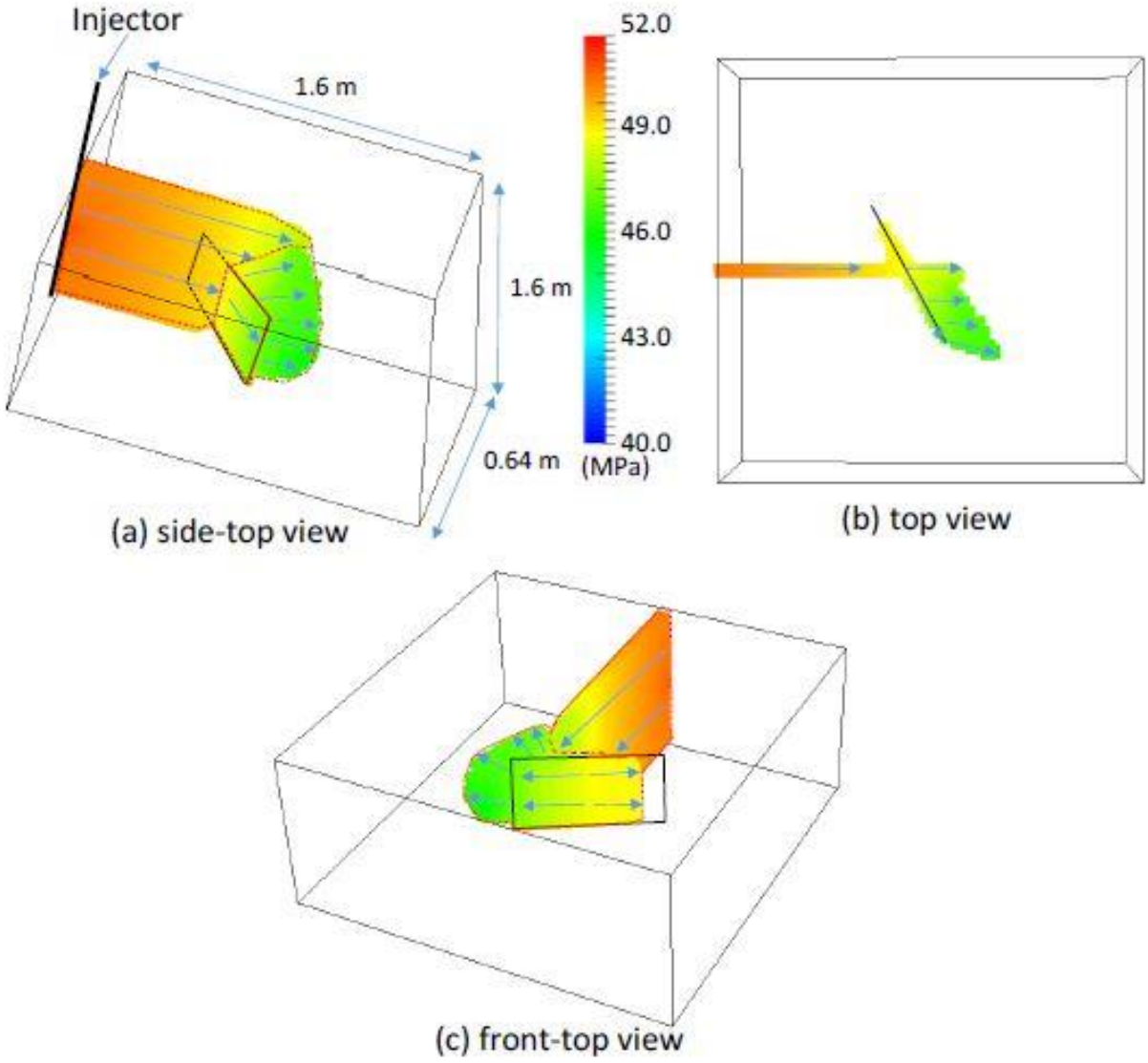


Fig. 6.27. Fracturing fluid pressure distribution (Case 3, after 26 sec).

When the upper part and lower quarter part of the HF just reach the NF, as shown in Fig. 6.29, a certain amount of water has already moved into the NF and this increase in pore pressure and resulting stress interference prevents the crossing of the NF by the HF. This case suggests that the position of the NF also affects the interaction between the HF and NF. A NF located in the center of pay-zone is more likely to cause HF turning.

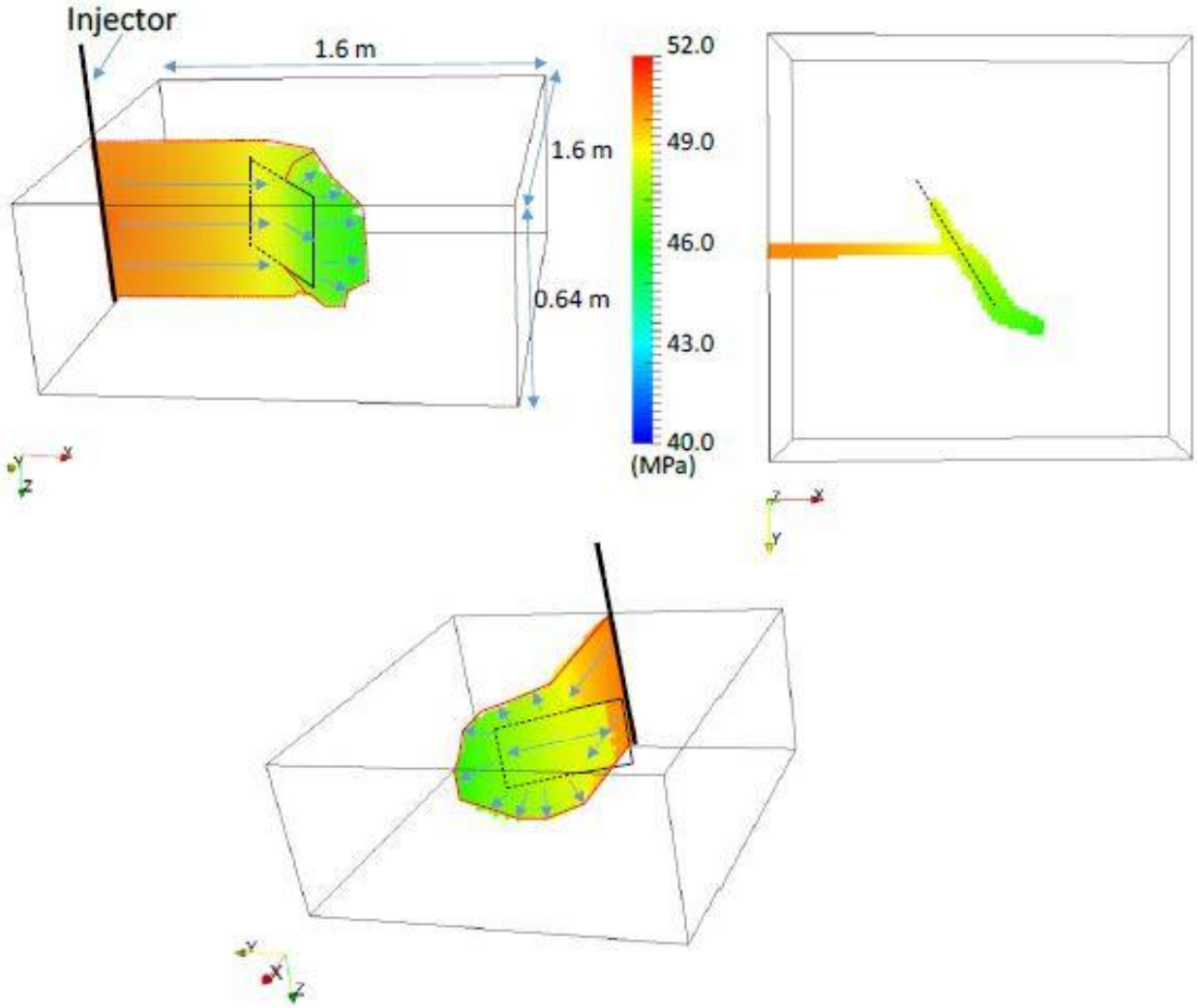


Fig. 6.28. Fracturing fluid pressure distribution (Case 4, after 26 sec).

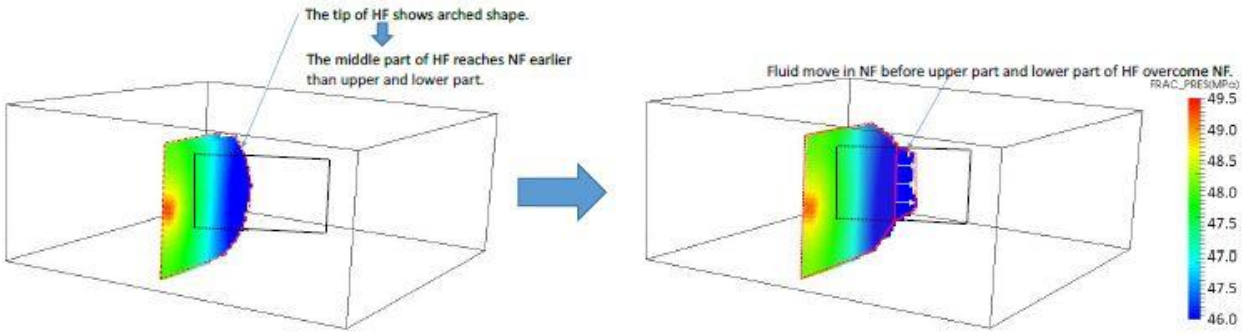


Fig. 6.29. Investigation of fracture propagation behavior for Case 4.

In Case 5, the NF has the same shear and tensile strength as Case 3 but the NF fills the lower one-third of the pay-zone. All the other settings except NF height are the same as Case 3. In this case, as shown in Fig. 6.30, the HF bypasses the NF though the tensile strength multiplier is as

low as Case 3. The main reason for the bypassing is that the middle part of the HF crosses the NF before the lower part of the HF hits the NF. In addition, even if the NF opens as easily as Case 3, a relatively small amount of water can move into the NF than Case 3 due to the smaller height of the NF, which allows more water / energy to be used for straight fracture propagation.

Simulations with HFTS Log Data

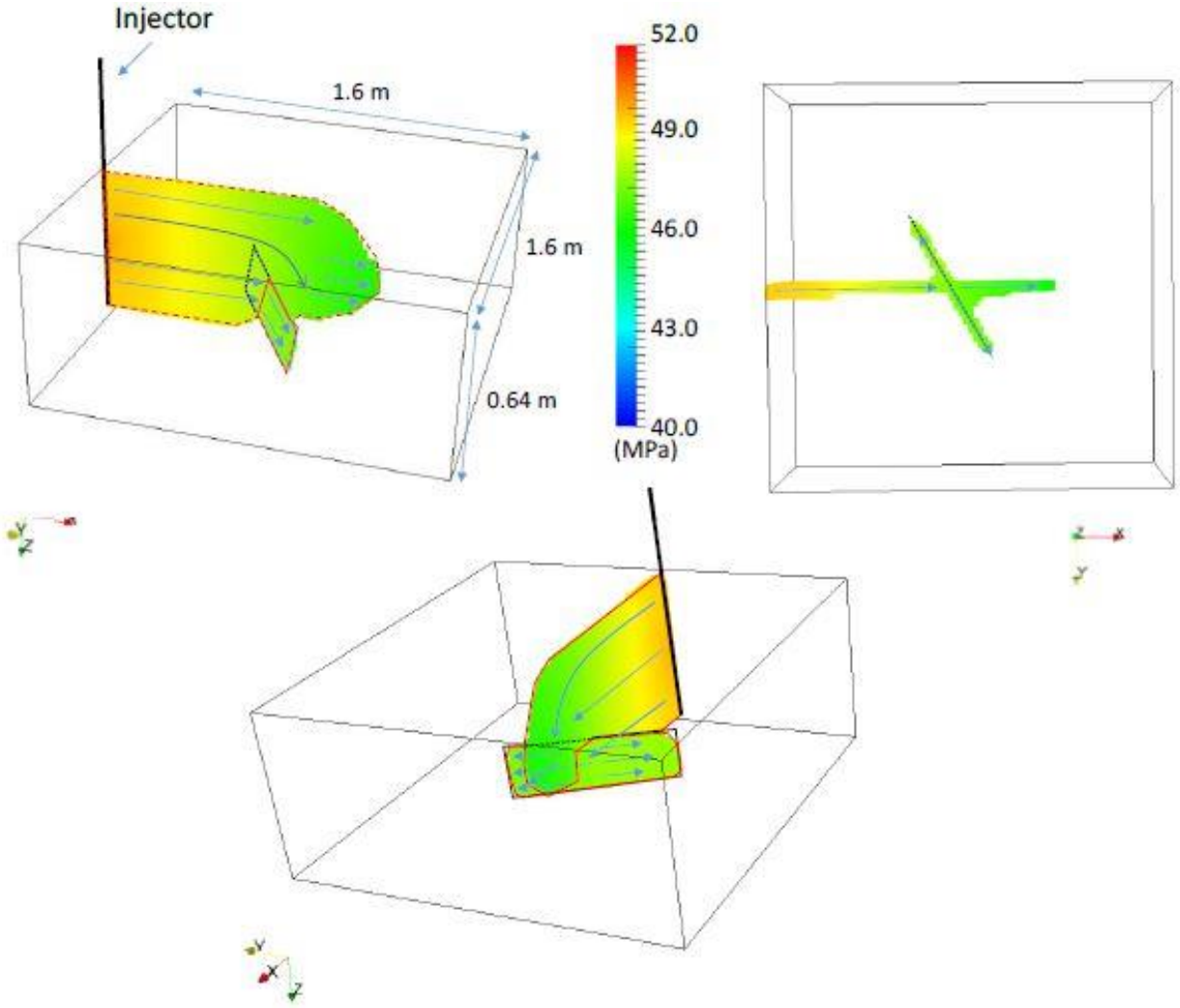


Fig. 6.30. Fracturing fluid pressure distribution (Case 5, after 26 sec).

Table 6.7. Parameters for layer simulations

Parameters	Values
Fracture toughness (MPa m^0.5)	1.05
Fracturing fluid	Water
Nodes	223*223
Cell size (ft)	1

Simulations were performed with the peridynamics-based hydraulic fracturing simulator using the HFTS log data. Layer properties corresponding to UW1Base to MW1 (7680-7903 ft) were input to the simulator. The resolution of the log data is 0.5 ft. However, to reduce the computational time, the data was approximated per 1 ft and a grid block of 1 ft was used. Appropriate correction for depth shift was applied to use the data of 7SU well for simulating

fracturing in 6SU well. Some of the simulation parameters are provided in Table 6.7, and the rest were taken from the log data.

As shown in Fig. 6.31 and Fig. 6.32, 2-layer models with dip angles of 10o and 30o were considered. For each of the models, 2 simulations were performed – one with isotropic stresses and the other with 1% contrast in stresses.

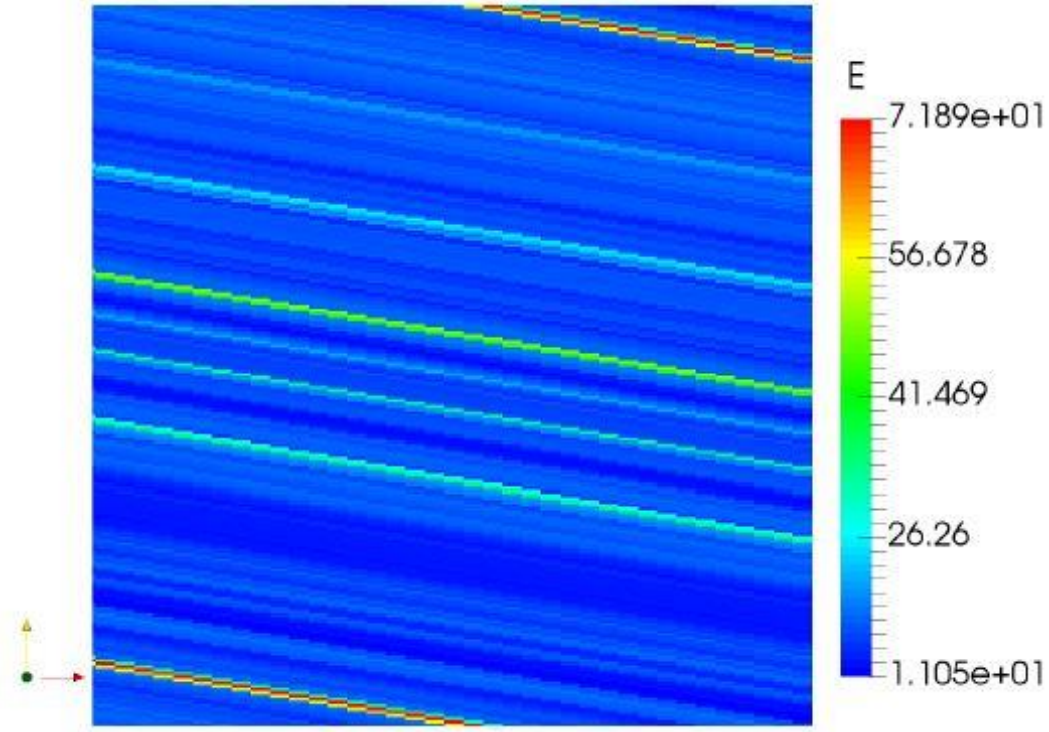


Fig. 6.31. Layer model with a dip angle of 10°. The colors represent Young's modulus.

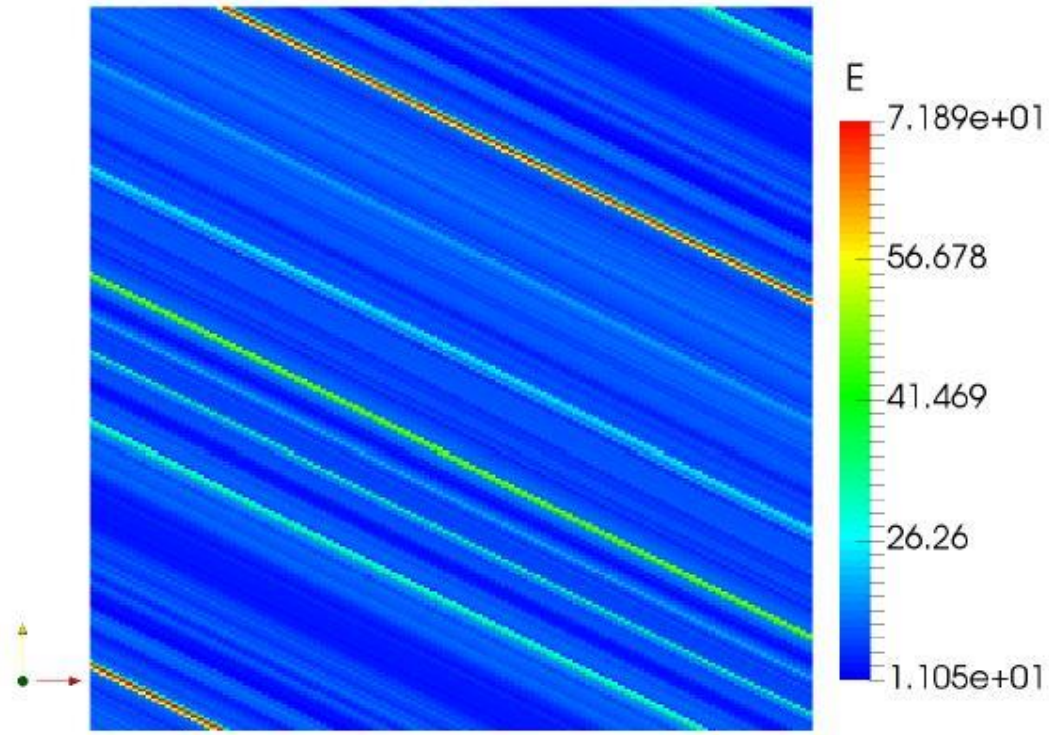


Fig. 6.32. Layer model with a dip angle of 30°. The colors represent Young's modulus.

For the 10° dipping model, the results are shown in Fig. 6.33 – 6.34. Frequent kinking at layer interfaces is observed in the isotropic setting. Even a 1% stress contrast causes the kinking to become less prominent. It can be noted that not as much kinking is seen as in the results we published in the paper (Chapter 5 of this report). This is because the contrast in mechanical properties between adjacent layers is not very high in these simulations.

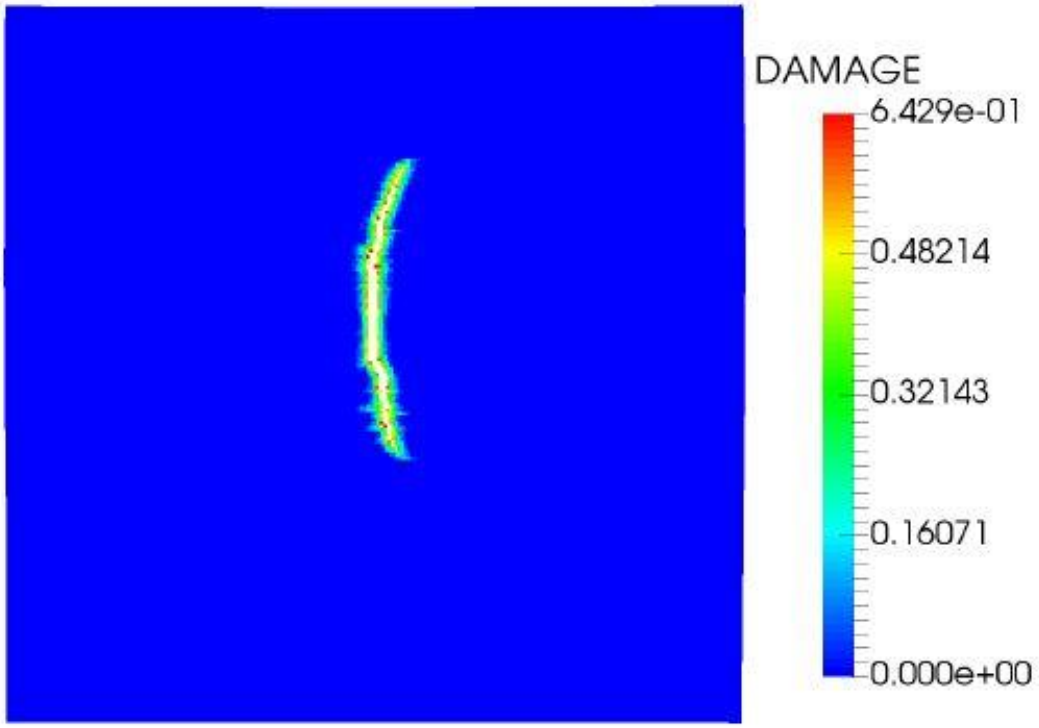


Fig. 6.33. Fracture propagation with isotropic stresses, 10° dipping model (Layers not shown in Figs. 6.33 – 6.36 for clarity)

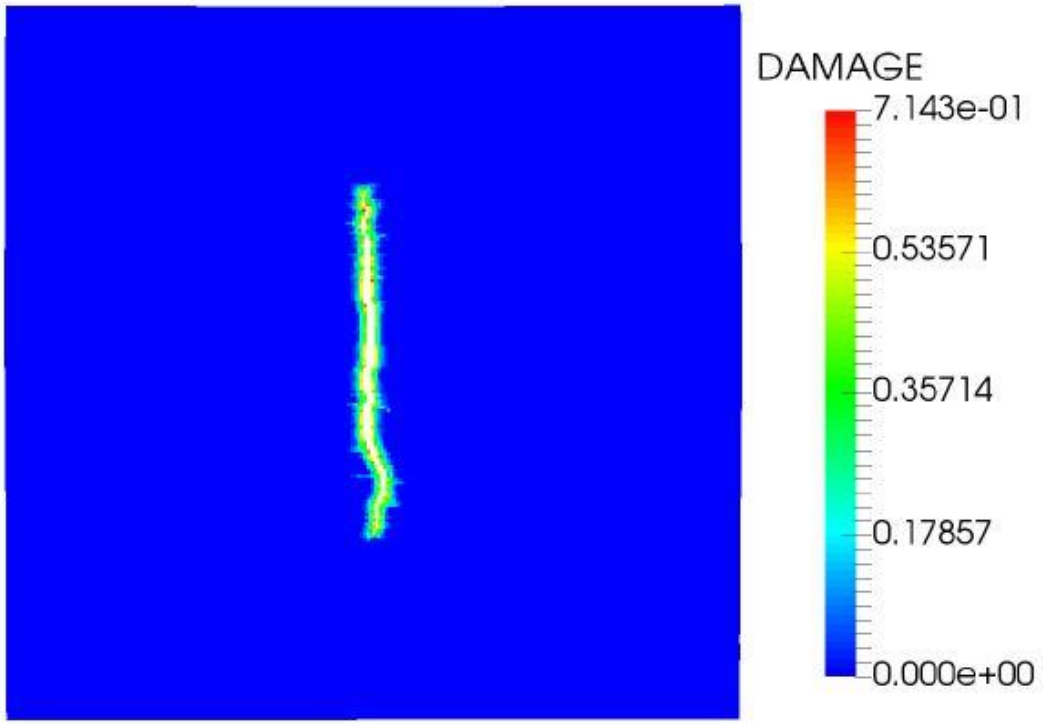


Fig. 6.34. Fracture propagation with 1% contrast in stresses, 10° dipping model.

For the 30° dipping model, the results are shown in Fig. 6.35 – 6.36. The results are consistent with our published results. A higher dipping angle causes the global fracture propagation direction to change and not remain parallel to maximum stress direction (vertical in these cases).

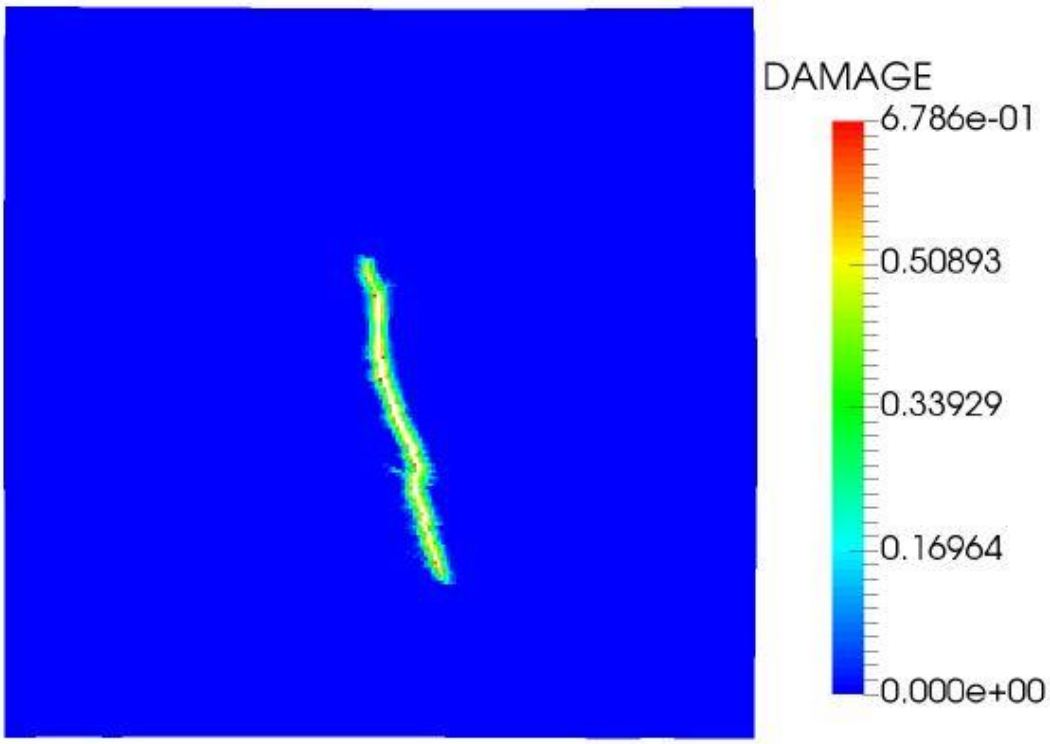


Fig. 6.35. Fracture propagation with isotropic stresses, 30° dipping model.

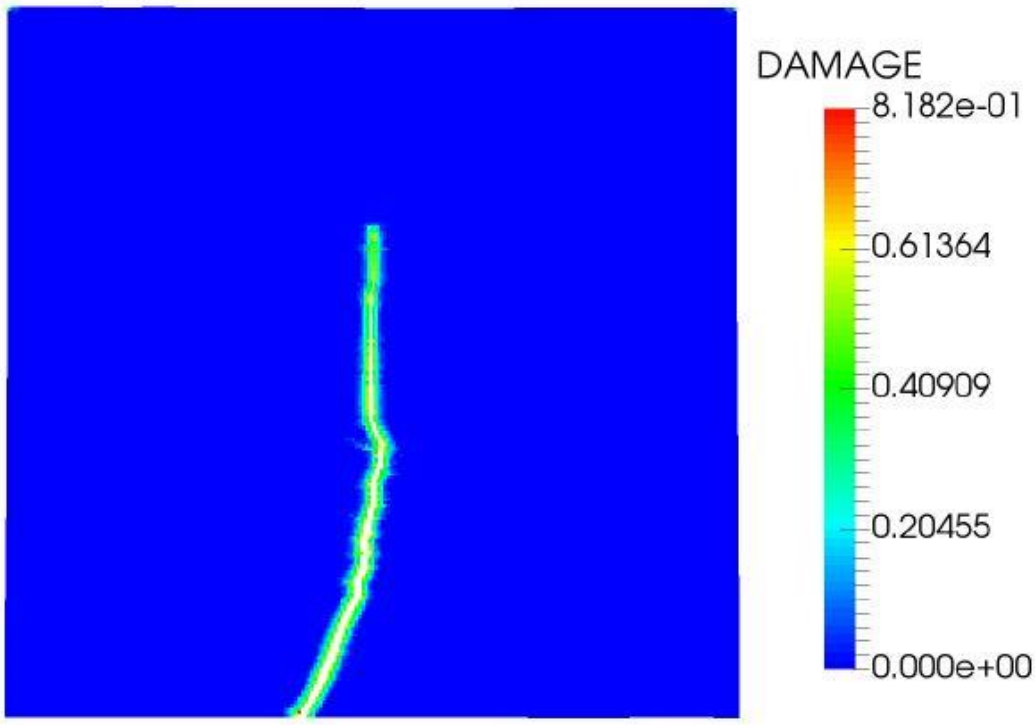


Fig. 6.36. Fracture propagation with 1% contrast in stresses, 30° dipping model.

HFTS Simulations with Natural Fractures

Competing fracture growth from 3 perforation clusters was simulated in this section. The provided injection schedule was scaled and used as input in these simulations. The cores had

fractures oriented in 2 distinct directions. To estimate the first order effects of angle of interaction, 2 models with natural fractures dipping at angles of 260 and 640 to the horizontal were considered. The simulation parameters are given in Table 6.8.

Table 6.8. HFTS parameters for natural fracture simulations

Parameters	Values
Pore pressure (MPa)	25.42
Minimum horizontal stress (MPa)	34.81
Vertical stress (MPa)	38.26, 44.26
Young's modulus (GPa)	16.80
Poisson' ratio	0.25
Fracture toughness (MPa m^0.5)	1.05
Porosity (%)	6.3
Permeability (nD)	21
Viscosity (cP)	1
Injection rate (bbl/min)	9
Nodes	180*80, 120*140
Cell size (m)	1
Fracture toughness (MPa m^0.5)	1.05
Fracturing fluid	Water
Nodes	223*223
Cell size (ft)	1

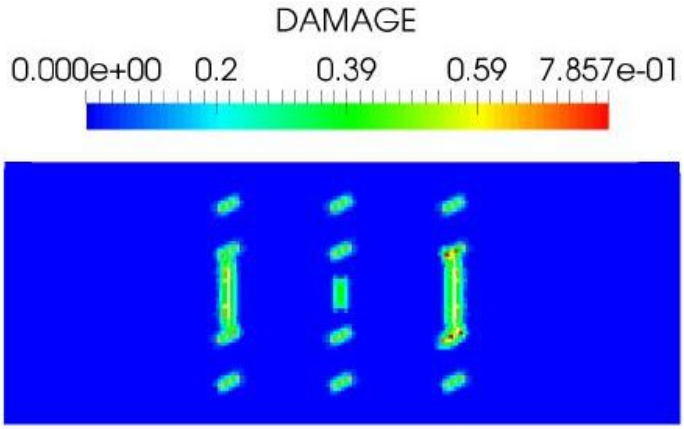


Fig. 6.37. Fracture propagation at low stress contrast, natural fractures at 26°

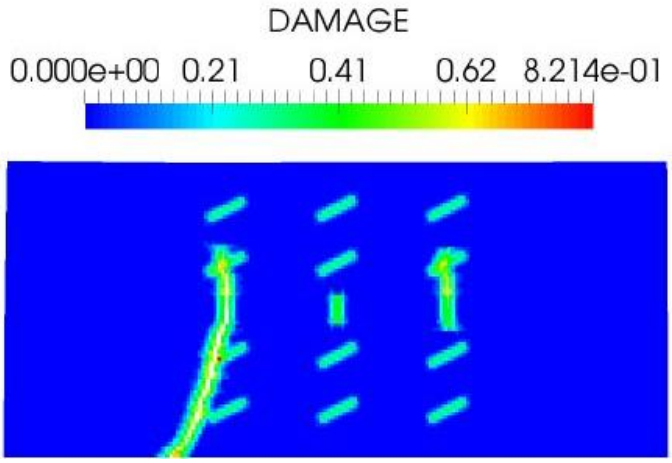


Fig. 6.38. Fracture propagation at high stress contrast, natural fractures at 26°

For each of the models, 2 simulations were performed – one with low stress contrast and the other with high stress contrast.

For the 26° model, the results are shown in Fig. 6.37 – 6.38. All the clusters begin to grow, but due to stress shadow effect, the outer ones take off while the middle fracture gets suppressed. In this model the hydraulic fractures intersect the natural fractures at a high angle of interaction. At low stress contrast, hydraulic fracture dilates the natural fracture. At high stress contrast, hydraulic fracture crosses the natural fracture. This observation is consistent with our published results (Chapter 6).

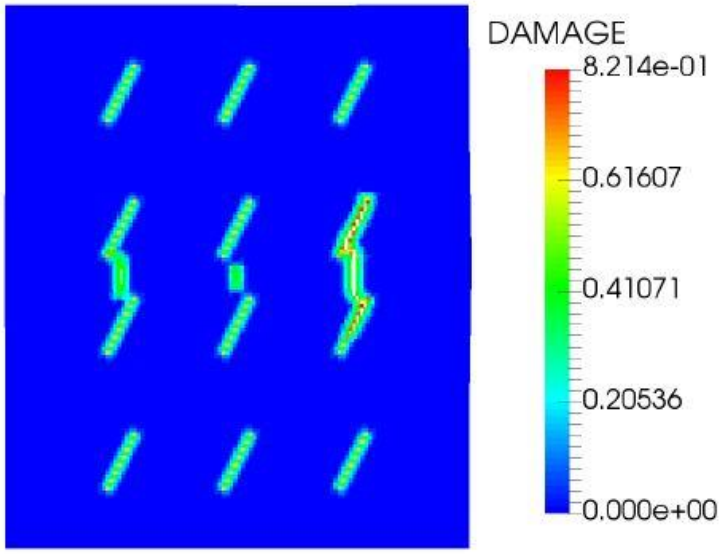


Fig. 6.39. Fracture propagation at low stress contrast, natural fractures at 64°

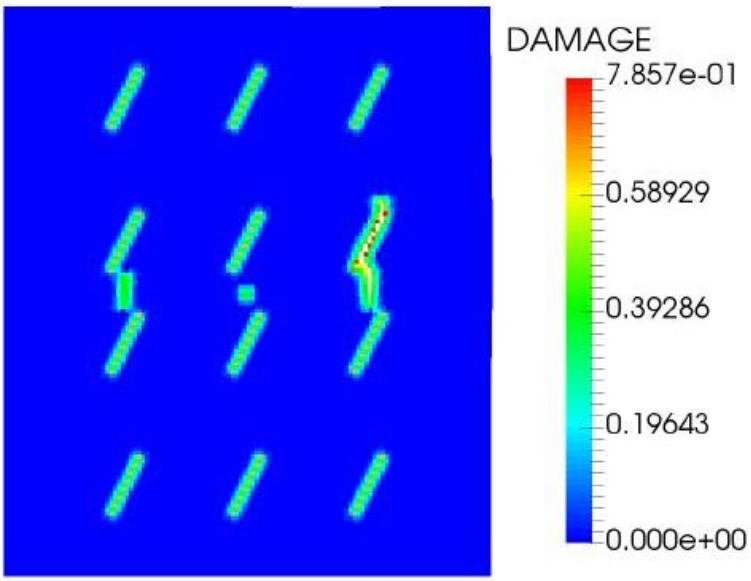


Fig. 6.40. Fracture propagation at high stress contrast, natural fractures at 64°

Conclusions

In this chapter, we used the new 3-D peridynamic model for simulating fracture growth for the HFTS dataset. It is shown that it is possible to include layers, natural fractures, and other heterogeneities with relative ease. In addition, the propagation of multiple, non-planar fractures can also be modelled without specifying the direction of the fractures *a priori*. Poroelastic effects are also included in the computations. To demonstrate the capability of our model to predict the

results of interaction between a HF and a NF, the simulation results are compared with large block experiments conducted with simulated natural fractures. A sensitivity analysis is conducted by changing the rock mechanical properties, rock permeability, natural fracture permeability, and injection rate to examine the key controlling parameters. We show that poroelastic effects have a large influence on the interaction between HF and NF if leak-off is high. In addition, we also demonstrate that the fracture toughness of the rock, the fracture toughness of the natural fracture, and the shear failure criteria of the natural fracture affect the interaction between HF and NF. In addition, the principal stress contrast and the approach angle have a first order effect. These results are consistent with published experiments. Furthermore, we have demonstrated our simulator's applicability to simulate field scale hydraulic fracturing simulations. Simulation results are presented for the growth of multiple fractures, while considering the mechanical stress shadow and pore pressure effects created by the growing fractures. Finally, through three dimensional simulations, we also demonstrate that our peridynamics based hydraulic fracturing model can capture the complicated three-dimensional interaction behavior between a HF and a NF (bypassing, turning, diverting and combinations of these). These simulation results reveal that the height of the NF, the position of the NF, and the opening resistance of the NF have a huge impact on the three-dimensional interaction behavior between a HF and a NF.

The model is not able to simulate the large number of natural fractures that are seen in the HFTS data set in a reasonable period due to computational limitations.

Hydraulic Fracture Diagnostics and Stress Interface Analysis by Water Hammer Signatures in Multi-Stage Pumping Data

Summary

When fluid injection is shut-off after a fracture stage has been pumped, the sudden change in injection rate leads to a pressure fluctuation called a water hammer. These pressure pulses are observed and available at no additional cost because the pressure and rate data are recorded for every shut-in during field treatments. This abundant field data is commonly ignored.

In this report, we show that this water hammer signature can provide diagnostic information on fracture geometry. We simulated the transient flow problem in a wellhead-wellbore-fracture system to match the water hammer signature, and the solution provides the fracture dimensions based on the resistance-capacitance-inertance (R-C-I) circuit analogy. The analysis of water hammer signatures has been applied to multi-stage hydraulic fracture treatments to show the effect of input parameters and stress interference between stimulation stages.

Water hammer simulation also suggests an accurate method to estimate instantaneous bottom-hole shut-in pressure (ISIP). This ISIP estimation for multi-stage treatments clearly shows the impact of the inter-stage stress shadow effect when applied to multi-stage fracture diagnosis. Simulated results which include stress interference effects indicate variations in fracture dimensions. This analysis also shows that the net fracturing pressure, near-wellbore frictional pressure drops, and stress magnitudes are changed by the stress shadow in multi-stage fracture treatments. This work has demonstrated that water hammer simulations can provide valuable fracture diagnostic information which compliments other diagnostic methods such as microseismicity and long-term production.

Introduction

A pressure pulse is created when the fluid flow in a pipe is suddenly shut in. This fluctuation of pressure is called a water hammer signature. It is observed in many instances in the oilfield. When an offshore water injection well is shut down or pumping of fluid is shut in during hydraulic fracture treatment, a water hammer signature is almost always observed as shown in Fig. 7.28a. This pressure fluctuation originates from the momentum change of the fluid in the conduit when the fluid experiences a sudden change of flow rate in a confined system. This pressure pulse propagates through the wellbore up and down within a few seconds as shown in Fig. 1b and attenuates over time (typically within a few seconds to nearly a minute, depending on the condition of wellbore, fluid, fracture, and reservoir).

Although recent work on water hammer signatures has focused on wellbore stability issues in the field which can be caused by large pressure fluctuations in the well, some recent studies focused on the diagnostic usefulness from water hammer analysis during hydraulic fracturing. In this work, we simulate the water hammer signature to estimate fracture dimensions in multi-stage hydraulic fracturing stimulations and suggest a work process incorporating the inter-stage stress shadow effect to properly solve the momentum balance and continuity equation in the wellbore-fracture system.

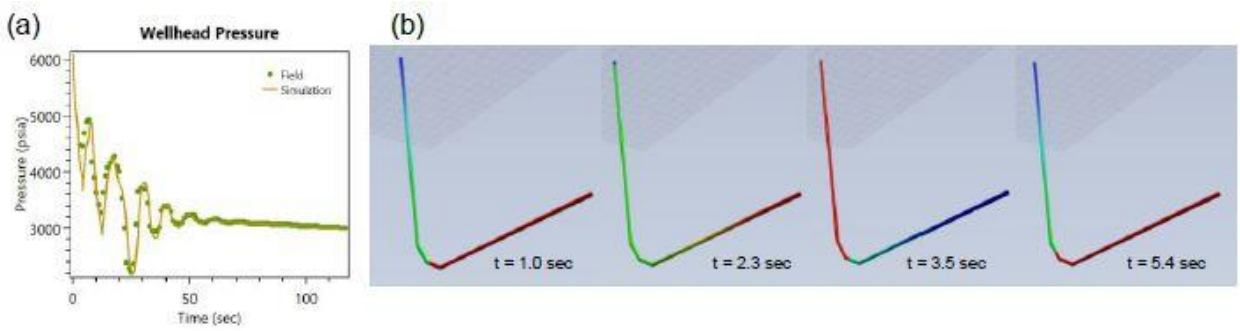


Fig. 7.28. (a) Typical wellhead pressure response showing a water hammer signature immediately after shut-in of fracturing fluid injection. (b) Typical pressure changes in the wellbore during water hammer response. Red color represents high pressure, and blue represents low pressure; Courtesy of Anand S. Nagoo; Adapted from Carey (2014).

Simulation Model for Water Hammer Signature in Wellbore-Fracture System

Observation by Ferrick et al. (1982) suggested that water hammer signatures are altered by the existence of a fracture connected to the wellbore. Holzhausen and Gooch (1985) have shown that the fracture dimensions and its connectivity to the wellbore change the water hammer signature by using hydraulic impedance testing (HIT) method wherein they showed the impact of a pressure pulse on the reflected pressure fluctuations. In Mondal's (2010) work, continuity and momentum equations are solved in the wellbore containing slightly compressible single-phase fluid by the method of characteristics (MOC). In this model, the boundary condition at the surface side of the wellbore is the changing flow rate during shut-in, and the one at the downhole is a resistance-capacitance-inertance (R-C-I) circuit representing a single fracture connected to the wellbore. Based on this work, Carey (2014) extended the wellbore-fracture system to an analogous R-C-I circuit with multiple capacitors to represent multiple identical fractures in a treatment stage.

Carey et al. (2015) have summarized key components in the current model which is used in this

work. Readers are recommended to refer to the papers for more details on the model formulations. Assumptions used in the model are as follows:

A. Fluid in wellbore-fracture system is single-phase.
B. Fractures are planar fractures with constant height.
C. Fracture length is constant during the water hammer.
D. Fracture compliance is only due to a change in width.
E. Fluid leak-off is negligible during the water hammer period.
F. Flow resistance is dominated by near-wellbore and perforation friction and negligible along the fracture.
G. Minimum horizontal stress (S_{hmin}) before fracture stimulation is estimated from a DFIT or other source.

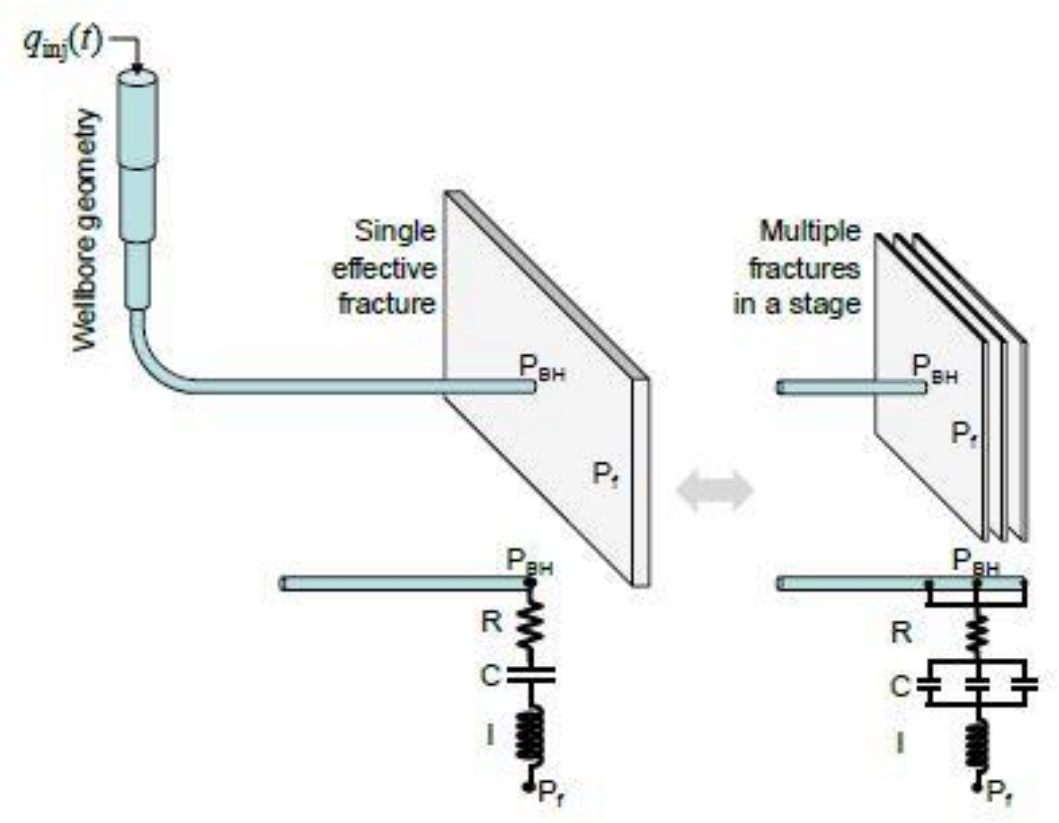


Fig. 7.29. Schematic diagram showing wellbore-fracture system. Fracture is assumed to be either a single effective fracture or multiple identical fractures of width and length less than the single effective fracture model. Corresponding analogous R-C-I circuits are shown as well.

In this series of works by Mondal (2010) and Carey (2014), the simulation model calculates the transient pressure changes along the wellbore segments. Based on the R, C and I values used for fracture boundary conditions, the simulation model also provides pressure oscillations at the wellbore and bottomhole conditions which exhibit the water hammer signature. This simulated signature can be matched to the field data by changing R, C and I values. Once these R, C and I values which match the pressure are obtained by iteratively changing them, the fracture dimensions are estimated based on following equations:

$$L_f = \sqrt{\frac{CI\overline{\Delta P_o}}{\rho}} \quad (1)$$

$$h_f = \begin{cases} \frac{4E'E(m)C}{\pi^2 L_f^2} & short \\ \sqrt{\frac{4E'E(m)C}{\pi^2 L_f}} & long \end{cases} \quad (2)$$

$$w_f = \frac{\rho L_f}{I h_f} \quad (3)$$

where L_f is the half length of the fracture, $\overline{\Delta P_0}$ is the net pressure, h_f is the fracture height, E' is the plane-strain Young's modulus, ρ is the density of fluid in the fracture, and $E(m)$ is the complete elliptical integral of the second kind. As length, width, and height are functions of each other and R-C-I values, iterative methods are required to solve for fracture dimensions. Only the important equations are shown here, the actual procedure to calculate the fracture dimensions can be found in Carey et al. (2015).

Once pressure-matching R-C-I values are found, the fracture dimensions for the multiple identical fractures in a stage can also be found based on the multiple-capacitor analogy shown in Fig. 7.2:

$$L_{f_E} = \sqrt{\frac{I_T}{\rho}\sum_{i=1}^{n} C_i \overline{\Delta P_{o_i}}} = \sqrt{\sum_{i=1}^{n} L_{f_i}^2} \quad (4)$$

$$\overline{w_E} = \sqrt{\sum_{i=1}^{n} \overline{w_i^2}} \quad (5)$$

where L_{fE} is a single equivalent fracture half-length and is a summation of the half-lengths of individual fractures, L_{fi}. The equivalent single fracture width $\overline{w_E}$, is a function of individual fracture width, $\overline{w_i}$. Fracture height remains the same when a single equivalent fracture is interpreted to be multiple fractures in a stimulation stage.

Recent Approaches to Use Water Hammer for Diagnostic Purposes

There have been recent approaches to use water hammer signatures to diagnose the effectiveness of fracturing stimulation. Ciezobka et al. (2016) interpreted water hammer signatures to understand fracture complexity. They hypothesized that the decay rate over the water hammer cycle is higher when pressure pulses move through a more complex fracture network. When fluids transport through a more extensive fracture network, the higher frictional loss leads to a shorter pressure oscillation.

Iriarte et al. (2017) conducted a quantitative assessment based on an extensive database of hydraulic fracturing from several fields. In this work, water hammer signatures across many stages, wells and fields were investigated for amplitudes, period, and decay rate. They compared these characteristic parameters of water hammer with completion parameters to find correlations between them. They explained that qualitative differences in the water hammer signals are caused by different completion systems including completion types (plug and perf or sliding sleeve), injection fluids, wellbore geometry (length and casing size) and so on. These factors affected the wavelength and magnitude of water hammer signals. Chemical tracer recovery observed in the neighboring wells suggested fracture connections through certain stages between wells, and this observation was supported by a higher decay rate in water hammer signals in those stages.

Fracture diagnostics based on a simulation approach have been compared with other type of diagnosis for stimulation effectiveness. Carey et al. (2016) compared fracture dimensions and R-C-I values obtained from water hammer analysis (the same model used in this work) with microseismic-derived SRV, fracture complexity index (FCI), and long-term production data. A strong correlation has been found for the water-hammer-derived fracture length and SRV- and FCI-derived fracture lengths, which supports the underlying theory behind water hammer simulations.

Haustveit et al. (2017) have compared results from various fracture diagnostic methods, which include electromagnetic imaging, microseismicity, pressure interference tests, fracture simulations, and water hammer simulations used in this work. The fracture length estimated from water hammer simulation was longer than those from other methods and comparable to microseismic-derived fracture lengths. As water hammer simulation assumes a single "effective" fracture per stimulation stage, it is expected that the actual fracture lengths in the fracture network are shorter than the simulated water hammer fracture length.

Analysis of period, decay rate, and amplitude may explain correlations between completion related factors and production. However, water hammer signatures observed from field data are a result of the combined effects of shut-in, wellbore, fluid, fracture, and reservoir parameters. Quantitative approaches (data mining) using limited characteristic parameters only may not capture these combined effects. In contrast, the simulation approach better captures details of the comprehensive nature of water hammer signatures. Some examples on how the water hammer signal changes by completion type and operational factors are shown in the following sections.

Impact of R, C, and I

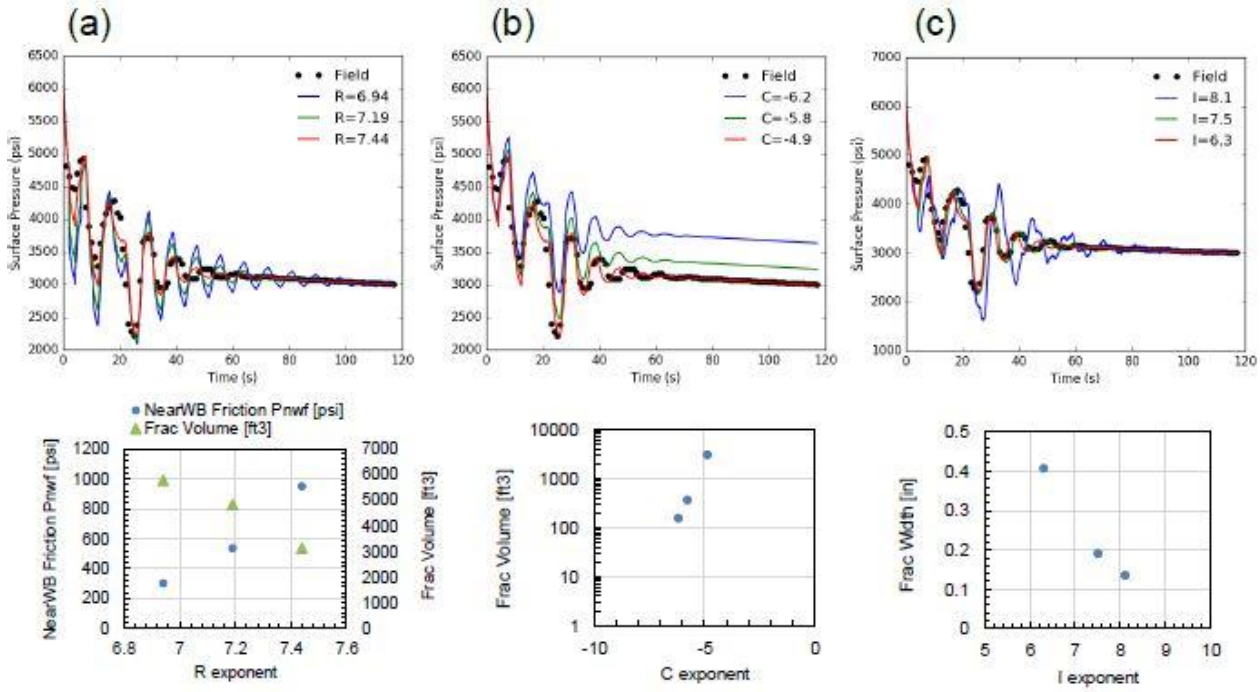


Fig. 7.30. Impact of R, C and I parameters on pressure solution and fracture dimensions. Exponents of R, C and I are used for actual R, C and I values, e.g., actual R value in SI unit is $10^{(R\ exponent)}$.

Our simulation model calculates transient pressure responses after shut-in. As the water hammer

signatures change depending on R, C and I values, the estimated fracture dimensions also change. By changing R, C and I values, it can be demonstrated how amplitude, wavelength and the rate of attenuation change in the resulting water hammer signatures (as shown in Fig. 7.3). A larger resistance value leads to a quicker attenuation in the pressure response and a larger near-wellbore frictional pressure drop. The fracture volume also becomes smaller with increasing resistance.

Capacitance is a critical parameter to determine fracture length and volume because it controls fracture compliance. For a very small fracture volume estimated, the water hammer signature shows a very high deviation from the actual water hammer response of a fractured well. This behavior can be used to detect any underperforming stages during fracture stimulation. Inertance is also a parameter affecting both pressure response and fracture dimensions (especially width) based on the relations in Eq. (3).

Impact of Wellbore Geometry and Injection Fluid

As the simulation model takes wellbore, reservoir and fluid parameters into consideration, their impacts also have been investigated in this section. The conduit length from the wellhead to the fracture is primarily related to the wavelength (or period) of water hammer signature. As the wellbore becomes longer, the wavelength increases (Fig. 7.4a). This is a direct result of the time for the momentum changes to propagate in the wellbore.

The wellbore diameter (or casing size) also changes the water hammer signatures when other parameters remain the same (Fig. 7.4b). Amplitude decreases with increasing casing size, indicating that the increased total fluid volume in the wellbore reduces the magnitude of momentum transfer through the wellbore. The increased wavelength associated with the larger casing size can be understood in a similar manner. That is, for a given flow rate, it takes longer for momentum to transfer in a larger casing size compared to a smaller one.

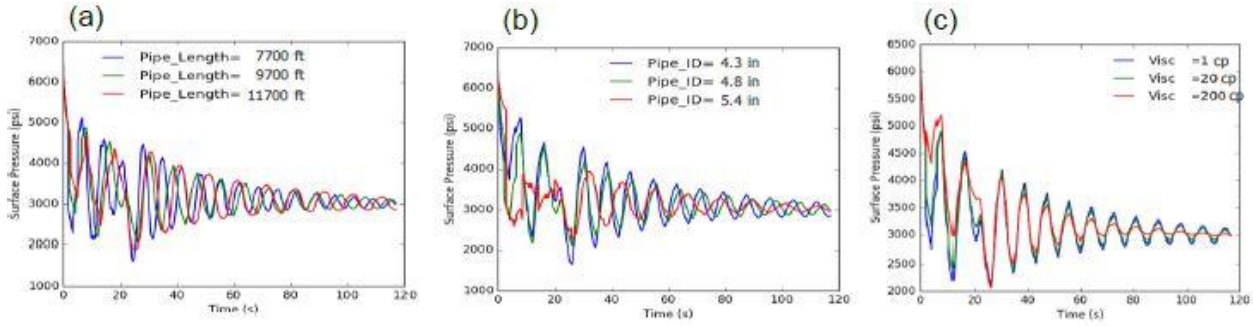


Fig. 7.31. Impact of wellbore and fluid parameters on water hammer signatures.

Fluid properties also change the pressure responses. To represent stimulations using slickwater and gel as the injection fluid system, the effect of viscosity was tested. High viscosity leads to a quicker attenuation in water hammer signatures as in Fig 7.4c. This can be understood that, with high-viscosity fluid, the momentum transport in the wellbore dissipates at a quicker rate. The high flow resistance at the wellbore-fracture connection caused by high viscosity also contributes to the quicker attenuation.

Impact of Shut-in Process

Operational factors need to be considered as well. As shown in Fig 7.5, if the shut-in process of

fluid injection occurs over a relatively short period of time, the attenuation may occur quickly. In contrast, the pressure fluctuation may last longer for a longer shut-in process.

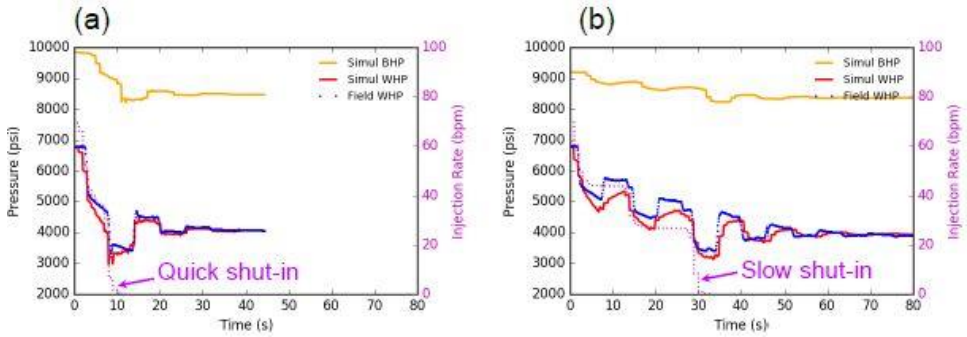


Fig. 7.32. Impact of flow rate changes on water hammer signatures during shut in.

The flow rate change during shut-in is essentially treated as a transient process that occurs as multiple events of smaller flow rate changes. The pressure responses in Fig. 7.5 have changed significantly only because of the shut-in process without changes in physical representation of R-C-I analogous circuit. The signature lasts longer with slow shut-in, and decays quickly with a quick shut-in. Hence, the advantage of this physics-based simulation model lies in the fact that it can represent a comprehensive impact from multiple components in wellbore-fracture systems, e.g., shut-in, fluid, reservoir, and wellbore properties.

Data Requirements for Water Hammer Analysis

Most of the pressure and rate data acquired from the field has a sampling rate of 1 to 10 samples per second (frequency of 1/sec to 10/sec) although transducers are available that can handle even higher sampling rates. The rate of sampling during data acquisition is directly related to the resolution of the results from the simulation. Pressure data were compared for different sampling rates of 1 and 10 per seconds in Fig. 7.6. The resolution of the water hammer signature is more distinct in the data with 10 samples per second. However, the signature becomes obscure in lower frequency data. This clearly shows the importance of sampling rate in the analysis of water hammer signatures.

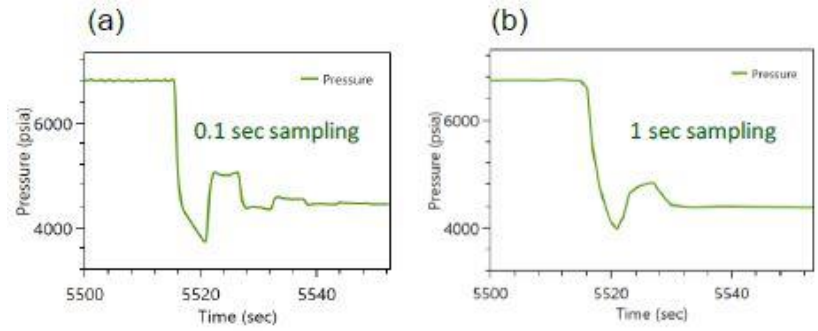


Fig. 7.33. Example of water hammer pressure data sampled at different sampling rates. (a) Pressure data was collected every 0.1 second. (b) Pressure data was collected every 1 second.

Another aspect on the high sampling rate is its potential to distinguish clusters in a stimulation stage. As the water hammer pressure pulse propagates at the speed of sound in the wellbore, e.g., 1500 m/s, the high-frequency data may contain signals from multiple fractures (or perforation clusters) spaced by a few meters. Perforation clusters spaced by 15m, at least theoretically, would require 0.01 sec sampling rate to be distinguished by water hammer

signatures.

Once fracture dimensions are obtained, other datasets should be compared with results from the water hammer analysis. Some examples of those data are production logs obtained for stages; DTS/DAS; long-term production data; microseismicity; SRV estimations and so on. In this report, this comparison work has not been shown. However, Carey et al. (2016) discussed a series of comparisons between results from this water hammer model and microseismic-derived SRV and fracture complexity index (FCI). In their work, SRV had a strong correlation with water-hammer-derived capacitance values (which are related to the fracture volume and compliance).

Workflow of Water Hammer Simulation for Single-Stage Data

A single stage of a fracture treatment typically contains the water hammer signature immediately after shutting down the pumps. There may be multiple shut-in events and associated water hammer signatures during pumping for a single stage. Pressure and injection rate data during the water hammer period were extracted from the raw field data (Fig. 7.7b). The injection rate was used as input data, and pressure data were compared with simulation results.

Table 7.1. Example of input parameters used for water hammer simulation

Parameter	Value	Parameter	Value
R-C-I Parameters		**Fluid Properties**	
R [psi/bpd]	7.35E-03	Fluid density in wellbore [ppg]	8.34
C [bbl/psi]	5.46E-01	Fluid density in fracture [ppg]	8.34
I [psi/(bbl/d^2)]	6.16E-10	Fluid viscosity in wellbore [cp]	1
Initial Conditions		Fluid viscosity in fracture [cp]	1
WHP before shut-in [psi]	6415	Fluid modulus in wellbore [psi]	320000
Injection rate before shut-in [bpm]	89.5	**Completions**	
Reservoir Properties		Number of clusters in a stage	6
S_{hmin} [psi]	5340		
TVD [ft]	5600		
Young's modulus [psi]	2000000		
Poisson's ratio	0.28		

Wellbore Properties

	Section 1	Section 2	Section 3	Section 4
Section deviation from horizontal [deg]	90	60	30	0
Section length [ft]	5200	500	500	3500
Section ID [in]	4.778	4.778	4.778	4.778
Section OD [in]	5.5	5.5	5.5	5.5
Section Young's modulus [psi]	29000000	29000000	29000000	29000000
Section Poisson's ratio	0.25	0.25	0.25	0.25
Section roughness factor	6E-05	6E-05	6E-05	6E-05

An example of input parameters is shown in Table 1. Fluid, reservoir, and wellbore data as well as estimated R, C and I values are used as input parameters. R, C and I values will then be iteratively changed to match the pressure data. R is altered to match amplitude and rate of attenuation. C and I are also altered to match frequency and the final (falloff) pressure value in the signatures. R, C and I values matching the pressure then result in fracture dimensions including height, length and width for a single effective fracture in a stage. The equivalent fracture dimensions for multiple identical fractures are then calculated by the analogous R-C-I circuit representation described in the previous section.

The input and output data used in water hammer simulation can be grouped as follows: Input parameters, simulated downhole and wellhead pressure, distribution of pressure drops in the wellbore-fracture system, and estimated fracture dimensions. When simulations are performed,

all output data must show physically reasonable ranges of values. For example, although pressure matches are reasonable, individual pressure drops, e.g., net fracturing pressure, frictional pressure drops may be beyond a physically reasonable range. In this case, input parameters including R, C and I values should be accordingly adjusted to make all groups of parameters within a reasonable range.

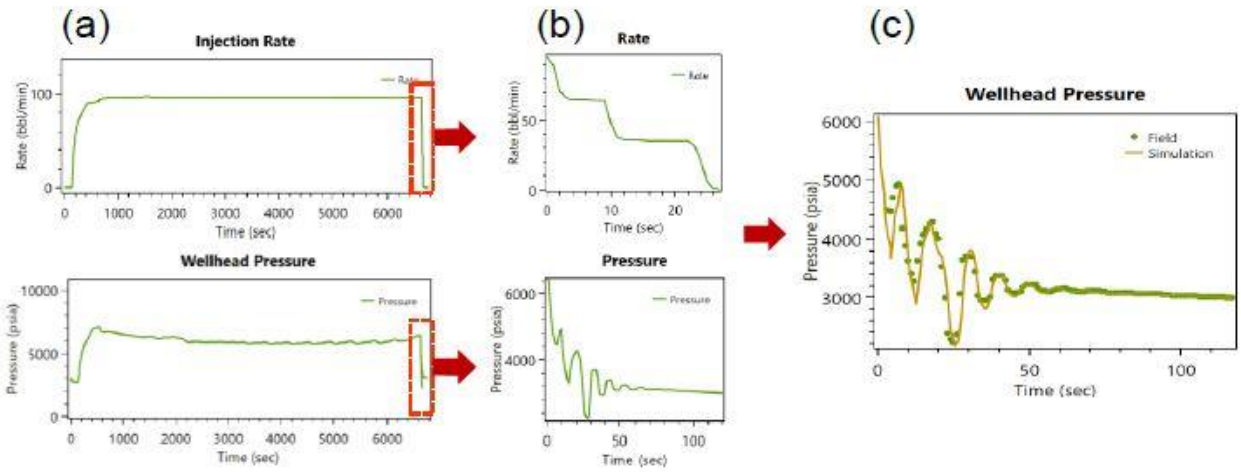


Fig. 7.34. Procedure to simulate a single water hammer signature from a single stimulation stage. (a) Raw field data of injection rate and wellhead pressure are read. (b) Portion of field data which exhibits water hammer signature is extracted for simulation. (c) Simulated wellhead or bottom-hole pressure is compared with field data.

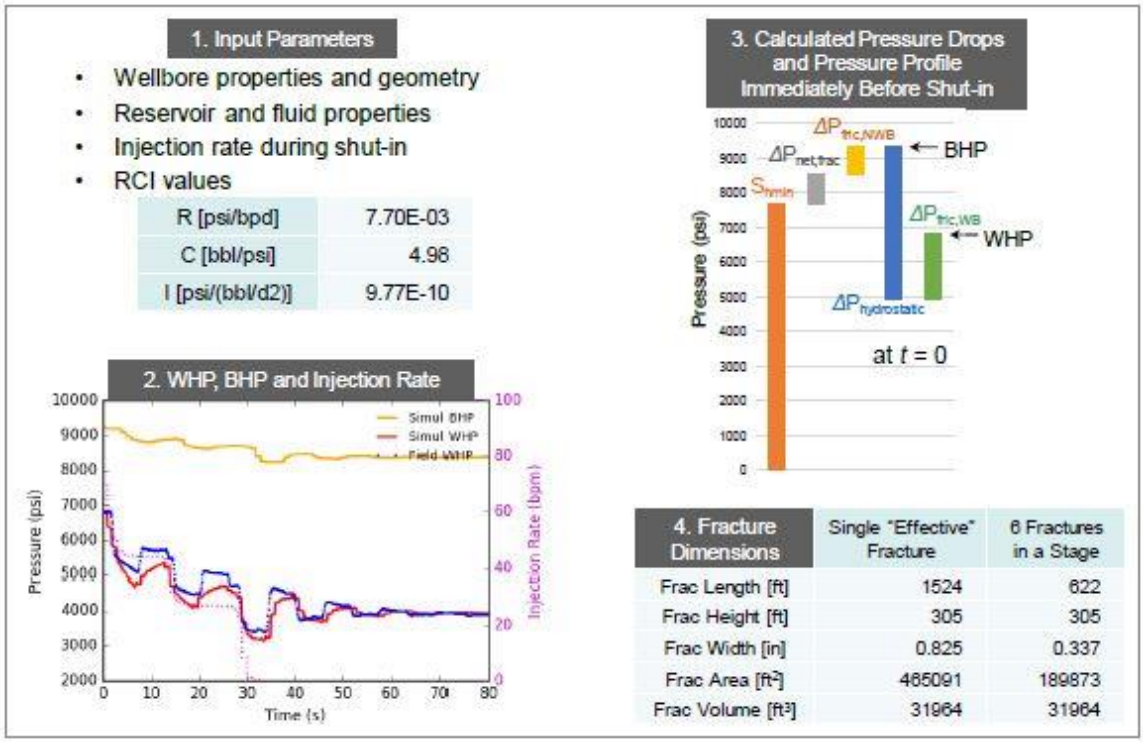


Fig. 7.35. Four groups of input and output parameters. Each group of parameters must be within a physically reasonable range to be used for fracture diagnostics.

Estimation of ISIP by Water Hammer Simulation

One of the most critical input parameters is the minimum horizontal stress (S_{hmin}). Minimum horizontal stress is used as the starting value when the bottomhole and wellhead pressures are calculated. When the net fracturing pressure ($\Delta P_{net,frac}$) and near-wellbore frictional pressure drop ($\Delta P_{fric,NWB}$) are added to the minimum horizontal stress it provides us the bottomhole pressure.

The relation between bottomhole and wellhead pressures that uses hydrostatic and wellbore frictional pressure drop should be satisfied.

As the model will be applied to the analysis of multi-stage water hammer data, changes in the stress magnitudes caused by inter-stage stress shadow effect (i.e. the increase in S_{hmin} caused by poroelastic and mechanical opening effects of previous-stage fractures) must be considered here. The in-situ stress is expected to increase by several hundred psi over many stages. This increase will depend on the sequencing, initial reservoir properties, and injection strategies. Without accounting for stress changes over stages, subsequent pressure calculations to acquire net fracturing pressure ($\Delta P_{net,frac}$) and near-wellbore frictional pressure drop ($\Delta P_{fric,NWB}$) can be over-estimated significantly. Hence, S_{hmin} values for each stage reflect this stress shadow effect should be used to calculate proper pressure distributions and fracture dimensions.

To estimate S_{hmin} for each stage (reflecting inter-stage stress shadow), we suggest using instantaneous shut-in pressure (ISIP) information which can be acquired from our water hammer simulation model. The ISIP value at wellhead conditions for each stage can be estimated from field data. The stabilized wellhead pressure trend after the water hammer has attenuated can be extrapolated back to earlier time to find the point where pressure decreases below the trendline (as in Fig. 7.9). This is the ISIP at wellhead conditions. At the same time, the calculated bottomhole pressure can also be extrapolated in the same manner to find the bottomhole ISIP (as in Fig. 7.9). This is a better estimation of ISIP at subsurface conditions as the obtained ISIP is based on hydrodynamic calculations for a wellbore-fracture system whereas conventional ISIP estimation accounts for the wellbore only.

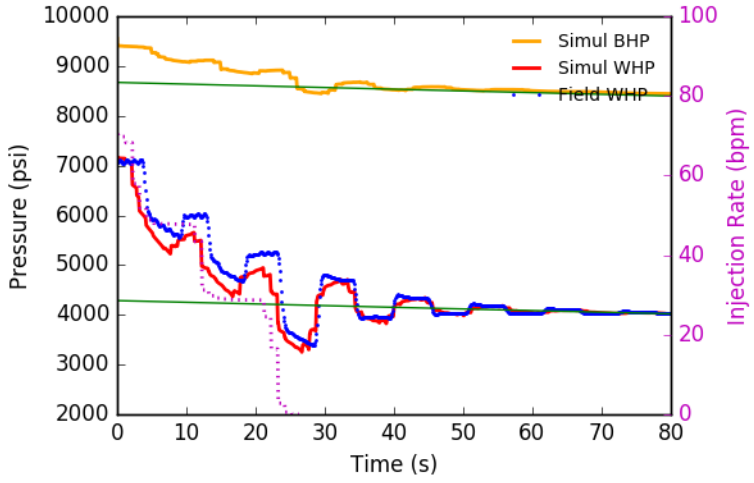


Fig. 7.36. ISIP at wellhead is obtained by finding a pressure value which decreases below the extrapolated decline curve from the field data of wellhead pressure. At the same time, the ISIP at bottomhole can be obtained from the extrapolated line of simulated bottomhole pressure.

Water Hammer Simulation for Multi-Stage Fracturing

Once ISIP at bottomhole conditions is obtained, it is compared with the known original S_{hmin} prior to hydraulic fracturing treatment. This is typically available from a diagnostic fracture injection test (DFIT), or an extended leak-off test (XLOT). If the difference between ISIP and S_{hmin} is assumed to remain unchanged over treatment stages, then S_{hmin} changes in the same manner as ISIP over stages. This S_{hmin} trend over stages can be used as new input for water hammer

simulation for each stage.

One iteration of the water hammer simulation may be required when stress shadow is large, because the magnitude of stress increase is unknown before a simulation. The ISIP trend from water hammer analysis is useful for many important applications to estimate parameters such as pore pressure and reservoir properties as well as stress. Another application to estimate fracture dimensions from the observed ISIP escalation trend can be found in Roussel (2017). The ISIP estimation method introduced in this work can be used for Roussel's application.

The S_{hmin} estimation procedure to account for stress shadow effect has been applied to a multi-stage water hammer analysis. ISIP increased from 7,804 (stage 1) to 8,642 psi (stage 17) (Fig. 7.10). The available S_{hmin} value in this field was 6,714 psi, and it was used for stage 1. S_{hmin} was assumed to increase with the same trend as ISIP, and a S_{hmin} of 7,552 psi was used for stage 17. Although the bottomhole pressure immediately before shut-in fluctuated over stages, ISIP at bottomhole condition was gradually increasing over stages as shown in Fig. 10a. Results of net fracturing pressure and near-wellbore frictional pressure drops over stages are shown in Fig. 10b. They remain within a reasonably constant range of values as stress increases over stages. Without addressing the stress shadow effect in S_{hmin} used for water hammer simulations, the calculated pressure drops will increase over stages leading to incorrect fracture dimensions and pressure distributions in the wellbore-fracture system. It should be noted that rock heterogeneity can lead to decreases in the minimum horizontal stress from the toe to the heel (see Figure 7.10). However, the general trend is consistent, the in-situ stress generally increases as more stages are pumped.

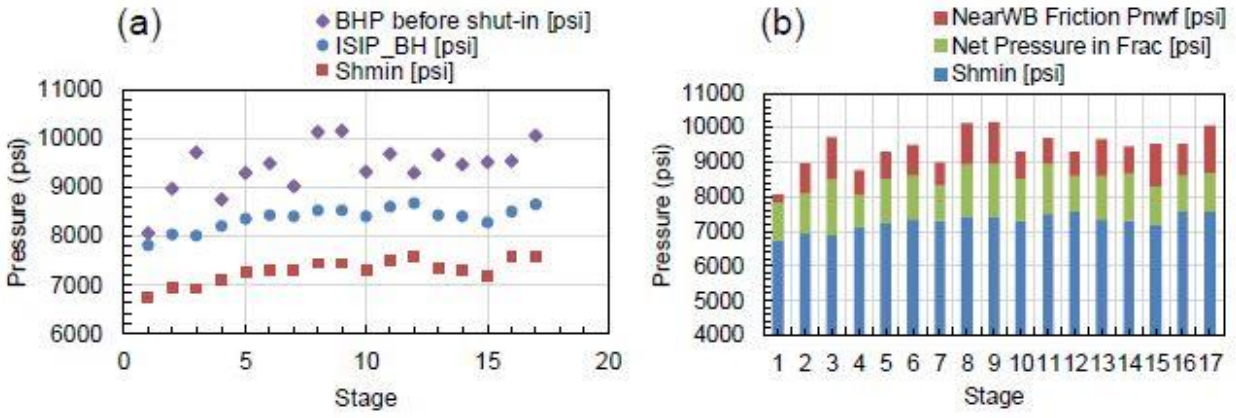


Fig. 37. (a) Estimated ISIP at bottomhole over stages are shown with estimated minimum horizontal stress over stages. (b) Net fracturing pressure drop (green) and near-wellbore frictional pressure drop (red) over stages are shown.

By addressing the stress shadow and heterogeneity effects in multi-stage water hammer analysis, fracture dimensions for 17 treatment stages were obtained. Fracture half-length of a single "effective" fracture ranges between 1,294 and 1,869 ft. They comprise a reasonable distribution, and no abnormal length was observed. Fracture width of single effective fracture was between 0.54 and 1.16 inches, and fracture height was between 204 and 347 ft.

As each treatment stage had 6 clusters, we assumed 6 identical fractures in a treatment stage. These individual fracture dimensions were also calculated as shown in Fig. 7.11 based on an analogous R-C-I circuit of 6 capacitors. The fracture length for 6 identical fractures in a stage is estimated to be between 579 and 836 ft. Width was between 0.24 to 0.52 inches per fracture,

and height is the same as the single effective fracture.

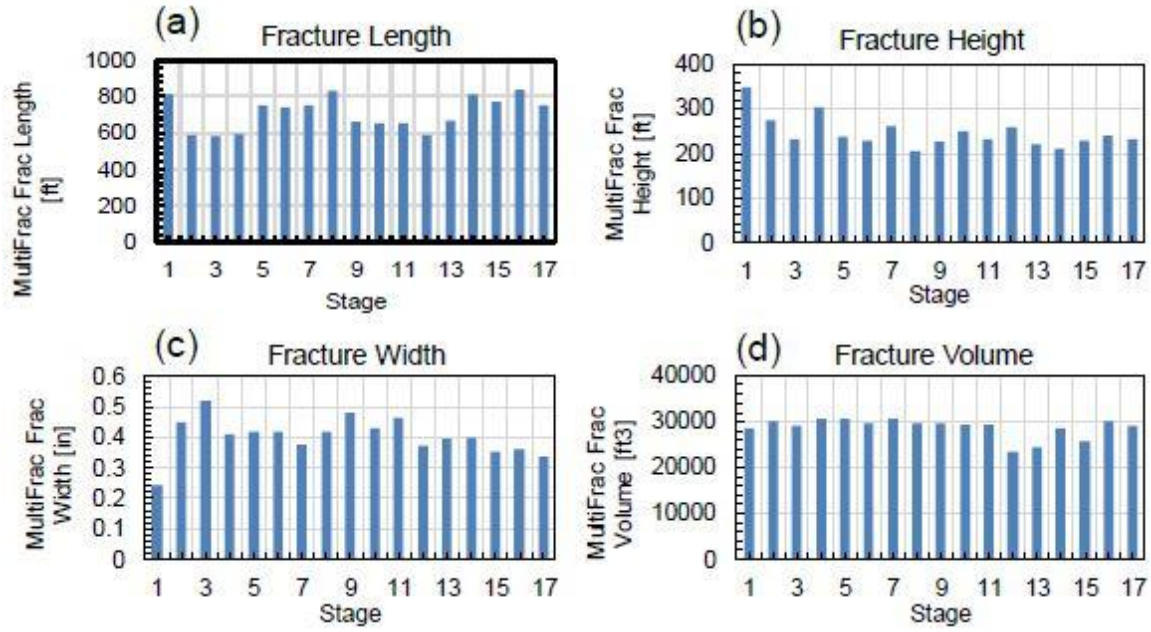


Fig. 38. Fracture dimensions calculated from the water hammer simulation are shown for all stages.

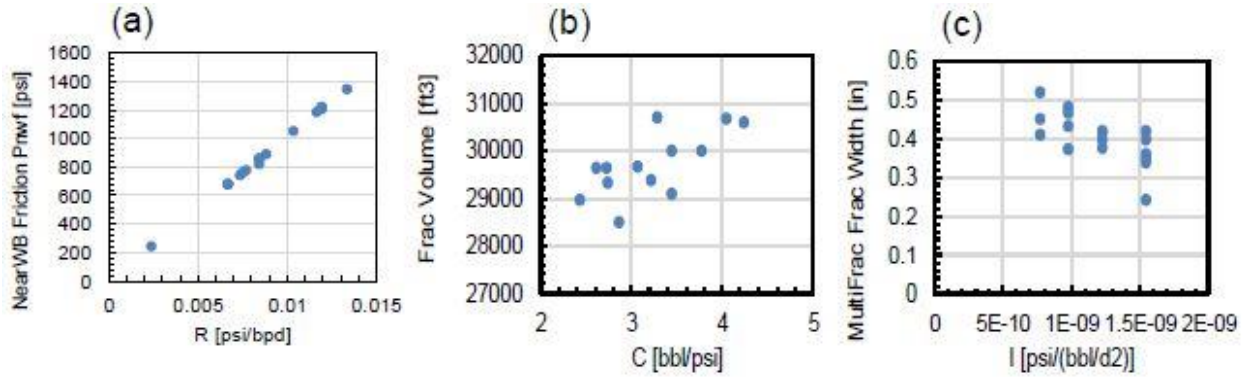


Fig. 39. Impact of R, C and I on pressure drop and fracture dimensions.

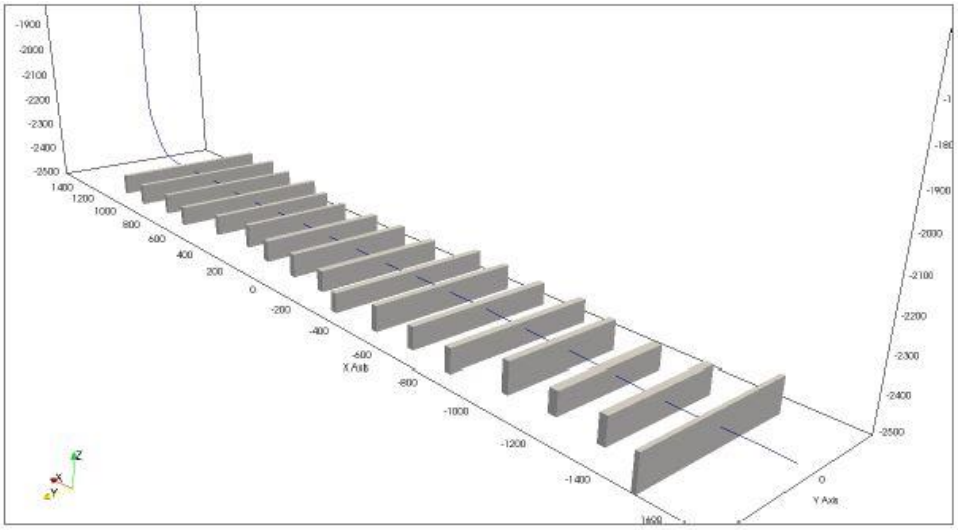


Fig.7.13. Fracture dimensions calculated from water hammer simulation are shown for each stage. Numbers are in meters. The width is exaggerated 1000 times to represent the simulated fractures as SRV.

Simulated fracture dimensions and pressure distributions from multi-stage water hammer

analysis validated the physical implications of R, C and I values. The near-wellbore frictional pressure drop was directly proportional to the R value, which indicates the wellbore-fracture connectivity (Fig. 7.12a). Any stages showing deviations from average would be investigated for different conditions experienced during stimulations. The relation between C and fracture length and volume can be verified again in Fig. 7.12b. The C value from a water hammer simulation conveys significant information in fracturing effectiveness. The fracture width decreased with increasing I values, verifying Eq. 7.3 again.

The fracture dimensions from water hammer analysis were shown by a 3-dimensional rendering in Fig. 7.13 representing a single effective fracture estimation. In the figure, fracture width has been exaggerated to represent the SRV extent of each stage. If microseismic data is available, this rendering can directly be compared. Water hammer diagnostics from data that is available at no cost can be used to support other more costly fracture diagnostic methods.

Conclusions

Our water hammer model numerically solves continuity and momentum equations in the wellbore-fracture system during the transient stage of a shut-in, which can last up to a minute. The wellbore-fracture connection is represented by a circuit composed of resistance-capacitance-inertance (R-C-I) components. The amplitude, wavelength and attenuation of the pressure pulse are all strong functions of the near-wellbore frictional pressure resistance, compliance of the fracture, and the flow resistance associated with fluid moving in and out of the fracture. The R-C-I magnitudes that allow for a match between simulated and actual pressure transients are converted to an effective fracture geometry including fracture height, width, and length.

For multi-stage fracture diagnostics, magnitudes of S_{hmin} for each stage were critical input data for the calculation of pressure distributions and fracture dimensions. We suggested a method to estimate ISIP and S_{hmin} over stimulation stages based on water hammer simulations to account for the inter-stage stress interference and heterogeneity effects. ISIP trends obtained from water hammer simulation clearly showed a general trend of stress escalation over stages, and associated S_{hmin} trends were used for water hammer simulation again to accurately calculate fracture dimensions, net fracturing pressure, and frictional pressure drop in the wellbore-fracture system.

The fracture diagnostic method based on the water hammer simulation allowed us to estimate the fracture geometry and its variation over stages. The advantage of this method is that it can be obtained from readily available, essentially “free” field data. This does not require any additional expensive operations intended for diagnostics but can be added to other diagnostic methods and augment the reliability of an SRV estimation. The method also provides insights on stress changes along stages which can be used as a guide for future fracture designs.

References

1. Abass, H.H., Hedayati, S., and Meadows, D.L. 1996. Nonplanar Fracture Propagation From a Horizontal Wellbore: Experimental Study. SPE Prod. & Fac. 11 (03): 133–137. SPE-24823-PA. http://dx.doi.org/10.2118/24823-PA.

2. Ajani, A.A., and Kelkar, M.G. 2012. Interference Study in Shale Plays. Presented at the SPE

Hydraulic Fracturing Technology Conference, The Woodlands, Texas, 6-8 February. SPE-151045-MS. http://dx.doi.org/10.2118/151045-MS.

3. Ames, B.C., and Bunger, A. 2015. Role of Turbulent Flow in Generating Short Hydraulic Fractures With High Net Pressure in Slickwater Treatments. Presented at the SPE Hydraulic Fracturing Technology Conference, The Woodlands, Texas, 3-5 February. SPE-173373-MS. http://dx.doi.org/10.2118/173373-MS.
4. Askari, E. et al., 2008. Peridynamics for multiscale materials modeling. Journal of Physics: Conference Series, 125: 012078.
5. Askari, E., F. Bobaru, R. B. Lehoucq et al. 2008. Peridynamics for multiscale materials modeling (in Journal of Physics: Conference Series 125: 012078.
6. Askari, Ebrahim, Jifeng Xu, Stewart Silling. 2006. Peridynamic Analysis of Damage and Failure in Composites. Reston, Virigina: 44th AIAA Aerospace Sciences Meeting and Exhibit, American Institute of Aeronautics and Astronautics (Reprint). http://arc.aiaa.org/doi/pdfplus/10.2514/6.2006-88.
7. Atkinson, B.K., 1987. Fracture mechanics of rock. Academic Press.
8. Bahorich, Ben, Jon Edward Olson, Jon Holder. 2012. Examining the Effect of Cemented Natural Fractures on Hydraulic Fracture Propagation in Hydrostone Block Experiments. Proc.
9. Baihly, J., Malpani, R., Edwards, C. et al. 2010. Unlocking the Shale Mystery: How Lateral Measurements and Well Placement Impact Completions and Resultant Production. Paper SPE 138427 presented at the SPE Tight Gas Completions Conference, San Antonio, Texas, USA, 2-3 November 2010. http://dx.doi.org/10.2118/138427-MS.
10. Berchenko, I., and Detournay, E. 1997. Deviation of hydraulic fractures through poroelastic stress changes induced by fluid injection and pumping. Int. J. Rock. Mech. Min. 34 (6): 1009–1019. http://dx.doi.org/10.1016/S1365-1609(97)80010-X.
11. Biot, M.A. 1955. Theory of Elasticity and Consolidation for a Porous Anisotropic Solid. J. App. Phy. 26 (2): 182-185. http://dx.doi.org/10.1063/1.1721956.
12. Blanton, Thomas L. 1982. An Experimental Study of Interaction Between Hydraulically Induced and Pre-Existing Fractures: SPE Unconventional Gas Recovery Symposium, Society of Petroleum Engineers (Reprint).
13. Bobaru, F. 2007. Influence of van der Waals forces on increasing the strength and toughness in dynamic fracture of nanofibre networks: a peridynamic approach (in Modelling and Simulation in Materials Science and Engineering 15: 397-417. http://iopscience.iop.org/0965- 0393/15/5/002/pdf/0965-0393_15_5_002.pdf.
14. Boone, T.J., and Detournay, E. 1990. Response of a vertical hydraulic fracture intersecting a poroelastic formation bounded by semi-infinite impermeable elastic layers. Int. J. Rock. Mech. Min. Sci. Geomech Abstr. 27 (3): 189–197. http://dx.doi.org/10.1016/0148-9062(90)94327-P.
15. Bruno, M.S., and Nakagawa, F.M. 1991. Pore pressure influence on tensile fracture

propagation in sedimentary rock. Int. J. Rock. Mech. Min. Sci. Geomech. Abstr. 28 (4): 261–273. http://dx.doi.org/10.1016/0148-9062(91)90593-B.

16. Bryant, E.C., Hwang, J., and Sharma, M. M. 2015. Arbitrary Fracture Propagation in Heterogeneous Poroelastic Formations Using a Finite Volume-Based Cohesive Zone Model. Presented at the SPE Hydraulic Fracturing Technology Conference, The Woodlands, Texas, 3-5 February. SPE-173374-MS. http://dx.doi.org/10.2118/173374-MS.
17. Bunger, A., Zhang, X., and Jeffrey, R. 2012. Parameters Affecting the Interaction Among Closely Spaced Hydraulic Fractures. SPE J. 17 (1): 292–306. SPE-140426-PA. http://dx.doi.org/10.2118/140426-PA.
18. Carey, M. A. (2014). Water Hammer Fracture Diagnostics. Thesis, The University of Texas at Austin.
19. Carey, M. A., Mondal, S., & Sharma, M. M. (2015). Analysis of Water Hammer Signatures for Fracture Diagnostics. Presented at the SPE Annual Technical Conference and Exhibition, 28- 30 September, Houston, Texas, USA, Paper SPE 174866. doi:10.2118/174866-MS.
20. Carolan, D., Tukovic, Z., Murphy, N. Et al. 2013. Arbitrary crack propagation in multi-phase materials using the finite volume method. Comp. Mat. Sci. 69:153-159. http://dx.doi.org/10.1016/j.commatsci.2012.11.049.
21. Carrasco, A., DeGeare, J., and Hunter, J. 2014. Achieving a More Efficient Frac Network for Horizontal Development of the Bone Spring Sandstone. Presented at the SPE Hydraulic Fracturing Technology Conference, The Woodlands, Texas, 4-6 February. SPE-168633-MS. http://dx.doi.org/10.2118/168633-MS.
22. Castonguay, S.T., Mear, M.E., Dean, R.H. et al. 2013. Predictions of the Growth of Multiple Interacting Hydraulic Fractures in Three Dimensions. Presented at the SPE Annual Technical Conference and Exhibition, New Orleans, Louisiana, 30 September–2 October. SPE-166259- MS. http://dx.doi.org/10.2118/166259-MS.
23. Chuprakov, Dmitry A, Anna Akulich, Eduard Siebrits et al. 2010. Hydraulic Fracture Propagation in a Naturally Fractured Reservoir: SPE Oil and Gas India Conference and Exhibition, Society of Petroleum Engineers (Reprint).
24. Ciezobka, J., Maity, D., & Salehi, I. (2016). Variable Pump Rate Fracturing Leads to Improved Production in the Marcellus Shale. Presented at the SPE Hydraulic Fracturing Technology Conference, 9-11 February, The Woodlands, Texas, USA, Paper SPE 179107. doi:10.2118/179107-MS.
25. Cox, B.E. and Molenaar, M.M., 2013. Field cases of hydraulic fracture stimulation diagnostics using fiber optic distributed acoustic sensing (DAS) measurements and Analyses. Paper SPE 164030 presented at the SPE Unconventional Gas Conference and Exhibition, Muscat, Oman, 28-30 January 2013. http://dx.doi.org/10.2118/164030-MS.
26. Cudjoe, S., Vinassa, M., Gomes, J.H et al. 2016. A comprehensive approach to sweet-spot mapping for hydraulic fracturing and CO2 huff-n-puff injection in Chattanooga shale

formation. Journal of Natural Gas Science and Engineering. 33: 1201-1218. http://dx.doi.org/10.1016/j.jngse.2016.03.042.

27. Dahi Taleghani, Arash, Jon E Olson. 2014. How Natural Fractures Could Affect Hydraulic-Fracture Geometry (in SPE Journal 19: 161-171.
28. Dahi-Taleghani, A., and Olson, J.E. 2011. Numerical Modeling of Multistranded-Hydraulic-Fracture Propagation: Accounting for the Interaction Between Induced and Natural Fractures. SPE J. 16 (3): 575-581. SPE-124884-PA. http://dx.doi.org/10.2118/124884-PA.
29. Dahl, J., Samaripa, J., Spaid, J., et al. 2015a. Optimized Fracture Stage and Perforation Placement in Horizontal Wells using a New Calibrated Pulsed-Neutron Log Workflow. Presented at the SPE Annual Technical Conference and Exhibition, Houston, Texas, 28-30 September. SPE- 174757-MS. http://dx.doi.org/10.2118/174757-MS.
30. Dahl, J., Samaripa, J., Spaid, J., et al. 2015b. Application of an Engineered Completion Methodology in the Eagle Ford to Improve Economics. Presented at the Unconventional Resources Technology Conference, San Antonio, Texas, 20-22 July. http://dx.doi.org/10.15530/urtec-2015-2153805.
31. Dahm, T., Hainzl, S., and Fischer, T. 2010. Bidirectional and unidirectional fracture growth during hydrofracturing: Role of driving stress gradients. J. of Geo. Res. 115 (B12):322. http://dx.doi.org/10.1029/2009JB006817.
32. Daneshy, A. 2011. Hydraulic Fracturing of Horizontal Wells: Issues and Insights. Presented at the SPE Hydraulic Fracturing Technology and Conference, The Woodlands, Texas, 24-26 January. SPE-140134-MS. http://dx.doi.org/10.2118/140134-MS.
33. Degroote, J., Bathe, K.J., and Vierendeels, J. 2009. Performance of a new partitioned procedure versus a monolithic procedure in fluid-structure interaction. Comp. Struct. 87 (11-12): 793– 801. http://dx.doi.org/10.1016/j.compstruc.2008.11.013.
34. Degroote, J., Haelterman, R., Annerel, S., et al. 2010. Performance of partitioned procedures in fluid-structure interaction. Comp. Struct. 88 (7-8): 446–457. http://dx.doi.org/10.1016/j.compstruc.2009.12.006.
35. Detournay, E., and Cheng, A.H.-D. 1993. Fundamentals of Poroelasticity. In Comprehensive Rock Engineering: Principles, Practice and Projects, first edition, ed. J.A. Hudson and C. Fairhurst, Chap. 5, 113-171. Tarrytown, New York: Permagon Press.
36. Detournay, E., Cheng, A.H.-D., Roegiers, J.-C., et al. 1989. Poroelasticity considerations in In Situ stress determination by hydraulic fracturing. Int. J. Rock. Mech. Min. Sci. Geomech. Abstr. 26(6): 507–513. http://dx.doi.org/10.1016/0148-9062(89)91428-9.
37. El-rabaa, W. 1982. Experimental Study of Hydraulic Fracture Geometry Initiated From Horizontal Wells. Presented at the SPE Annual Technical Conference and Exhibition, 8-11 October. SPE- 19720-MS. http://dx.doi.org/10.2118/19720-MS.
38. Fang, C., and Amro, M. 2014. Influence Factors of Fracability in Nonmarine Shale. Presented at the SPE/EAGE European Unconventional Resources Conference and Exhibition, Vienna, Austria. 25-27 Frbruary. SPE-167803-MS.

http://dx.doi.org/10.2118/167803-MS.

39. Ferrick, M. G., Qamar, A., & St. Lawrence, W. F. (1982). Source mechanism of volcanic tremor. Journal of Geophysical Research: Solid Earth, 87(B10), 8675–8683. doi:10.1029/JB087iB10p08675.

40. Filder, L.J., 2011. Natural Fracture Characterization of the New Albany Shale, The University of Texas at Austin.

41. Fischer, T., Hainzl, S. and Dahm, T. 2009. The creation of an asymmetric hydraulic fracture as a result of driving stress gradients. Geophy. J. Int. 179 (1): 634–639. http://dx.doi.org/10.1111/j.1365-246X.2009.04316.x.

42. Fischer, T., Hainzl, S., Eisner, L., et al. 2008. Microseismic signatures of hydraulic fracture growth in sediment formations: Observations and modeling. J. Geophy. Res. 113 (B2): B02307. http://dx.doi.org/10.1029/2007JB005070.

43. Fisher, M.K. and Warpinski, N.R., 2012. Hydraulic-Fracture-Height Growth: Real Data.

44. Fisher, M.K., Heinze, J.R., Harris, C.D., et al. 2004. Optimizing Horizontal Completion Techniques in the Barnett Shale Using Microseismic Fracture Mapping. Presented at the SPE Annual Technical Conference and Exhibition, Houston, Texas. 26-29 September. SPE-90051- MS. http://dx.doi.org/10.2118/90051-MS.

45. Foster, J.T., Silling, S.A. and Chen, W.N., 2011. An Energy Based Failure Criterion for Use with Peridynamic States. International Journal for Multiscale Computational Engineering, 9(6): 675-687.

46. Garcia, X., Nagel, N., Zhang, F., Sanchez-Nagel, M. and Lee, B., 2013. Revisiting Vertical Hydraulic Fracture Propagation Through Layered Formations – A Numerical Evaluation. American Rock Mechanics Association.

47. Goniva, C., Kloss, C., Deen, N.G., Kuipers, J.A.M., and Pirker, S. 2012. Influence of Rolling Friction on Single Spout Fluidized Bed Simulation. Particuology 10, no. 5, pp. 582–91. http://dx.doi.org/10.1016/j.partic.2012.05.002.

48. Gray Mavko, T.M., Jack Dvokin, 2009. The rock physics handbook: Tools for seismic analysis of porous media. Cambridge university press.

49. Gu, H. and Siebrits, E., 2008. Effect of Formation Modulus Contrast on Hydraulic Fracture Height Containment.

50. Gu, H., X. Weng. 2010. Criterion For Fractures Crossing Frictional Interfaces At Non-orthogonal Angles. Proc., 44th U.S. Rock Mechanics Symposium and 5th U.S.-Canada Rock Mechanics Symposium, Salt Lake City, Utah.

51. Gu, Hongren, X Weng, Jeffrey Lund et al. 2012. Hydraulic Fracture Crossing Natural Fracture at Nonorthogonal Angles: A Criterion and Its Validation (in SPE Production & Operations 27: 20-26.

52. Gunzburger, M. and Lehoucq, R., 2010. A Nonlocal Vector Calculus with Application to Nonlocal Boundary Value Problems. Multiscale Modeling & Simulation, 8(5): 1581-1598.

53. Gupta, J., Zielonka, M., Albert, R., et al. 2012. Integrated Methodology for Optimizing Development of Unconventional Gas Resources. Presented at SPE Hydraulic Fracturing Technology Conference and Exhibition, The Woodlands, Texas, 6-8 February. http://dx.doi.org/10.2118/152224-MS.

54. Haddad, M., and Sepehrnoori, K. 2014. Simulation of Multiple-Stage Fracturing in Quasibrittle Shale Formations Using Pore Pressure Cohesive Zone Model. Presented at the Unconventional Resources Technology Conference, Denver, Colorado, 25-27 August. http://dx.doi.org/10.15530/urtec-2014-1922219.

55. Haddad, M., and Sepehrnoori, K. 2015. Integration of XFEM and CZM to Model 3D Multiple- Stage Hydraulic Fracturing in Quasi-brittle Shale Formations : Solution-Dependent Propagation Direction. Presented at the AADE National Technical Conference and Exhibition, San Antonio, Texas, 8-9 Apr.

56. Haustveit, K., Dahlgren, K., Greenwood, H., Peryam, T., Kennedy, B., & Dawson, M. 2017. New Age Fracture Mapping Diagnostic Tools-A STACK Case Study. Paper 184862 presented at the SPE Hydraulic Fracturing Technology Conference and Exhibition, 24–26 January, The Woodlands, Texas, USA. http://dx.doi.org/10.2118/184862-MS.

57. Holzhausen, G. R., & Gooch, R. P. (1985). Impedance of Hydraulic Fractures: Its Measurement and Use for Estimating Fracture Closure Pressure and Dimensions. Presented at the SPE/DOE Low Permeability Gas Reservoirs Symposium, Society of Petroleum Engineers. doi:10.2118/13892-MS.

58. Iriarte, J., Merritt, J., & Kreyche, B. (2017). Using Water Hammer Characteristics as a Fracture Treatment Diagnostic. Presented at the SPE Oklahoma City Oil and Gas Symposium, 27–31 March, Oklahoma City, Oklahoma, USA, Paper SPE 185087. doi:10.2118/185087-MS.

59. Jahandideh, A., and Jafarpour, B. 2014. Optimization of Hydraulic Fracturing Design Under Spatially Variable Shale Fracability. Presented at the SPE Western North American and Rocky Mountain Joint Meeting, Denver, Colorado. 17-18 April. SPE-169521-MS. http://dx.doi.org/10.2118/169521-MS.

60. James, G., Witten, D., Hastie, T. et al. 2013. An Introduction to Statistical Learning: With Applications in R. Springer, New York. http://dx.doi.org/10.1007/978-1-4614-7138-7.

61. Jasak, H., and Weller, H. 2000. Application of the finite volume method and unstructured meshes to linear elasticity. Int. J. Num. Meth. Engg. 48(2):267-287.

62. Jin, X., Shah, S.N., Roegiers, J., et al. 2014. Fracability Evaluation in Shale Reservoirs - An Integrated Petrophysics and Geomechanics Approach. Presented at the SPE Hydraulic Fracturing Confernece, The Woodlands, Texas, 4-6 February. SPE-168589-MS. http://dx.doi.org/10.2118/168589-MS.

63. Jin, X., Shah, S.N., Roegiers, J., et al. 2015. An Integrated Petrophysics and Geomechanics Approach for Fracability Evaluation in Shale Reservoirs. SPE J. 20 (03): 518–526. SPE-168589-PA. http://dx.doi.org/10.2118/168589-PA.

64. Katiyar, A., Foster, J.T., Ouchi, H. and Sharma, M.M., 2014. A peridynamic formulation of pressure driven convective fluid transport in porous media. Journal of Computational Physics, 261: 209-229.

65. Kias, E., Maharidge, R., and Hurt, R. 2015. Mechanical versus Mineralogical Brittleness Indices Across Various Shale Plays. Presented at the SPE Annual Technical Conference and Exhibition, Houston, Texas, 28-30 September. SPE-174781-MS. http://dx.doi.org/10.2118/174781-MS.

66. Lafond, P.G., Gilmer, M.W., Koh, C.A. et al, 2013. Orifice jamming of fluid-driven granular flow.

67. Physical Review E, 87(4), p.042204. https://doi.org/10.1103/PhysRevE.87.042204.

68. Lane, C., Laun, L.E., and Schlosser, D. 2013. Reducing Water Volume in Multistage Fracturing Using Sliding Sleeves and Coiled-Tubing-Deployed Resettable Frac Isolation. Presented at the SPE/ICoTA Coiled Tubing & Well Intervention Conference & Exhibition, The Woodlands, Texas. 26-27 March. SPE-163935-MS. http://dx.doi.org/10.2118/163935-MS.

69. Lecampion, B., and Desroches, J. 2015. Simultaneous initiation and growth of multiple radial hydraulic fractures from a horizontal wellbore. J. Mech. Phy. Sol. 82: 235–258. http://dx.doi.org/10.1016/j.jmps.2015.05.010.

70. Lee, D., Cardiff, P., Bryant, E.C., et al. 2015. A New Model for Hydraulic Fracture Growth in Unconsolidated Sands with Plasticity and Leak-Off. Presented at the SPE Annual Technical Conference and Exhibition, Houston, Texas. 28-30 September. SPE-174818-MS. http://dx.doi.org/10.2118/174818-MS.

71. Malhotra, S., Lehman, E.R. and Sharma, M.M. 2014. Proppant Placement Using Alternate-Slug Fracturing. SPE J. 19 (05): 974–985. SPE-163851-PA. http://dx.doi.org/10.2118/163851-PA. Manchanda, R. 2015. A General Poro-Elastic Model for Pad-Scale Fracturing of Horizontal Wells.

72. PhD Dissertation. University of Texas at Austin, Austin, Texas (December 2015).

73. Manchanda, R. and Sharma, M.M. 2013. Time-Delayed Fracturing: A New Strategy in Multi- Stage, Multi-Well Pad Fracturing. Paper SPE 166489 presented at SPE Annual Technical Conference and Exhibition, New Orleans, Louisiana, 30 September-2 October. http://dx.doi.org/10.2118/166489-MS.

74. Manchanda, R. and Sharma, M.M. 2014. Impact of Completion Design on Fracture Complexity in Horizontal Shale Wells. SPE Drill & Compl. 29 (1): 78-87. SPE-159899-PA. http://dx.doi.org/10.2118/159899-PA.Montana Geological Society: 1991 Guidebook to Geology and Horizontal Drilling of the Bakken Formation, 1991 pp 69-88.

75. Manchanda, R., Roussel, N.P. and Sharma, M.M. 2012. Factors Influencing Fracture Trajectories and Fracturing Pressure Data in a Horizontal Completion. Paper presented at 46th US Rock Mechanics / Geomechanics Symposium, Chicago, Illinois, 24-27 June.

76. Manchanda, R., Sharma, M.M., and Holzhauser, S. 2014. Time-Dependent Fracture-

Interference Effects in Pad Wells. SPE Prod. & Oper. 29 (04): 274–287. SPE-164534-PA. http://dx.doi.org/10.2118/164534-PA.

77. Maxwell, S.C. et al., 2009. Fault Activation During Hydraulic Fracturing. Society of Exploration Geophysicists.

78. McClure, M., and Horne, R.N. 2013. Discrete Fracture Network Modeling of Hydraulic Stimulation: Coupling Flow and Geomechanics. Springer Science & Business. http://dx.doi.org/bfm:978-3-319-00383-2.

79. McClure, M., Babazadeh, M., Shiozawa, S., et al. 2015. Fully Coupled Hydromechanical Simulation of Hydraulic Fracturing in Three-Dimensional Discrete Fracture Networks. Presented at the SPE Hydraulic Fracturing Technology Conference, The Woodlands, Texas, 3-5 February. SPE-173354-MS. http://dx.doi.org/10.2118/173354-MS.

80. Miller, C.K., Waters, G.A., and Rylander, E.I. 2011. Evaluation of Production Log Data from Horizontal Wells Drilled in Organic Shales. Presented at the North American Unconventional Gas Conference and Exhibition, The Woodlands, Texas, 14-16 June. SPE-144326-MS. http://dx.doi.org/10.2118/144326-MS.

81. Min, K. S., and Ghassemi, A. 2012. Simulation of fracture clusters in unconventional reservoir using fully coupled thermo-hydro-mechanical FEM analysis. Presented at the 46th US Rock Mechanics/Geomechanics Symposium, Chicago, Illinois, 24-27 June.

82. Mokhtari, M., Honarpour, M.M.M., Tutuncu, A.N. and Boitnott, G.N., 2014. Acoustical and Geomechanical Characterization of Eagle Ford Shale -Anisotropy, Heterogeneity and Measurement Scale. Society of Petroleum Engineers.

83. Molenaar, M., Hill, D., Webster, P., et al. 2011. First downhole application of distributed acoustic sensing (DAS) for hydraulic fracturing monitoring and diagnostics. Presented at the SPE Hydraulic Fracturing Technology Conference, The Woodlands, Texas, 24-26 Jan. SPE- 140561-MS. http://dx.doi.org/10.2118/140561-MS.

84. Mondal S., Wu C.-H., and Sharma M.M. 2016. Coupled CFD-DEM Simulation of Hydrodynamic Bridging at Constrictions. Int. J. Multiph. Flow, Volume 84, September 2016, pp. 245-263. http://dx.doi.org/10.1016/j.ijmultiphaseflow.2016.05.001.

85. Mondal, S. (2010). Pressure Transients in Wellbores: Water Hammer Effects and Implications for Fracture Diagnostics. Thesis, The University of Texas at Austin.

86. Morsy, S., J. J. Sheng, and M. Y. Soliman. 2013a. Waterflooding in the Eagle Ford Shale Formation: Experimental and Simulation Study. in SPE Unconventional Resources Conference and Exhibition-Asia Pacific. Society of Petroleum Engineershttp://dx.doi.org/10.2118/167056-MS.

87. Morsy, S., J. J. Sheng, and R. O. Ezewu. 2013b. Potential of Waterflooding in Shale Formations. in SPE Nigeria Annual International Conference and Exhibition. Society of Petroleum Engineers1–9. http://dx.doi.org/10.2118/167510-MS.

88. Mullen, M.J., and Enderlin, M.B. 2012. Fracability Index - More Than Rock Properties. Presented at the SPE Annual Technical Conference and Exhibition, San Antonio, Texas, 8-

10 October. SPE-159755-MS. http://dx.doi.org/10.2118/159755-MS.

89. Nadimi, S, I Miskovich. 2016. A 3D PERIDYNAMIC SIMULATION OF HYDRAULIC FRACTURE PROCESS IN A HETEROGENEOUS MEDIUM (in Journal of Petroleum Science and Engineering.
90. Ouchi, H., 2016. Development of a Peridynamics-based Hydraulic Fracturing Model for Fracture Growth in Heterogeneous Reservoirs, The University of Texas at Austin.
91. Ouchi, H., Katiyar, A., Foster, J. and Sharma, M.M., 2015a. A Peridynamics model for the propagation of hydraulic fractures in heterogeneous, naturally fractured reservoirs, SPE Hydraulic Fracturing Technology Conference. Society of Petroleum Engineers.
92. Ouchi, H., Katiyar, A., York, J., Foster, J. and Sharma, M., 2015b. A fully coupled porous flow and geomechanics model for fluid driven cracks: a peridynamics approach. Computational Mechanics, 55(3): 561-576.
93. Ouchi, Hisanao, Amit Katiyar, Jason York et al. 2015. A fully coupled porous flow and geomechanics model for fluid driven cracks: a peridynamics approach (in English). Computational Mechanics 55 (3): 561-576. http://dx.doi.org/10.1007/s00466-015-1123-8.
94. Passey, Q.R., Bohacs, K., Esch, W.L., Klimentidis, R. and Sinha, S., 2010. From Oil-Prone Source Rock to Gas-Producing Shale Reservoir - Geologic and Petrophysical Characterization of Unconventional Shale Gas Reservoirs. Society of Petroleum Engineers.
95. Plimpton, Steve. 1995. Fast parallel algorithms for short-range molecular dynamics (in Journal of computational physics 117 (1): 1-19.
96. Rijken, P. and Cooke, M.L., 2001. Role of shale thickness on vertical connectivity of fractures: application of crack-bridging theory to the Austin Chalk, Texas. Tectonophysics, 337(1–2): 117-133.
97. Romero, J., Mack, M.G. and Elbel, J.L., 1995. Theoretical model and numerical investigation of near-wellbore effects in hydraulic fracturing. Paper SPE 30506 Presented at the SPE Annual Technical Conference and Exhibition, Dallas, Texas, 22-25 October. http://dx.doi.org/10.2118/30506-MS.
98. Roussel, N. P. (2017). Analyzing ISIP Stage-by-Stage Escalation to Determine Fracture Height and Horizontal-Stress Anisotropy. Presented at the SPE Hydraulic Fracturing Technology Conference and Exhibition, 24–26 January, The Woodlands, Texas, USA, Paper SPE 184865. doi:10.2118/184865-MS.
99. Roussel, N. P., and Sharma, M.M. 2011a. Optimizing Fracture Spacing and Sequencing in Horizontal-Well Fracturing. SPE Prod. & Oper. 26(02): 173–184. SPE-127986-PA. http://dx.doi.org/10.2118/127986-PA.
100. Roussel, N.P. 2011. Stress Reorientation in Low Permeability Reservoirs. PhD dissertation, University of Texas at Austin, Austin, Texas (August 2011).
101. Roussel, N.P. and Sharma, M.M. 2011b. Strategies to Minimize Frac Spacing And Stimulate Natural Fractures in Horizontal Completions. Paper SPE 146104 presented at SPE Annual Technical Conference and Exhibition, Denver, Colorado, 30 October-2

November. http://dx.doi.org/10.2118/146104-MS.

102. Roussel, N.P. and Sharma, M.M. 2012. Role of stress reorientation in the success of refracture treatments in tight gas sands. SPE Production and Operations, 27(04), pp.346-355. http://dx.doi.org/10.2118/134491-PA.

103. Roussel, N.P., H.A. Flores, and A.A. Rodriguez. 2013. Hydraulic Fracture Propagation from Infill Horizontal Wells. Paper SPE 166503 presented at SPE Annual Technical Conference and Exhibition, New Orleans, Louisiana. http://dx.doi.org/10.2118/166503-MS.

104. Roussel, N.P., Manchanda, R. and Sharma, M.M. 2012. Implications of Fracturing Pressure Data Recorded during a Horizontal Completion on Stage Spacing Design. Paper SPE 152631 presented at SPE Hydraulic Fracturing Technology Conference and Exhibition, The Woodlands, Texas, 6-8 February. http://dx.doi.org/10.2118/152631-MS.

105. Rungamornrat, J., Wheeler, M., and Mear, M. 2005. A Numerical Technique for Simulating Non- Planar Evolution of Hydraulic Fractures. Proceedings of SPE Annual Technical Conference and Exhibition, Dallas, Texas, 9-12 October. SPE-96968-MS. http://dx.doi.org/10.2523/96968-MS.

106. Sahai, V., Jackson, G., Lalehrokh, F., et al. 2013. An Examination of Infill and Offset Drilling Patterns on Field Development for Shale Wells. Presented at the SPE Eastern Regional Meeting, Pittsburgh, Pennsylvania, 20-22 August. SPE-165722-MS. http://dx.doi.org/10.2118/165722-MS.

107. Sardinha, C.M., Petr, C., Lehmann, J., et al. 2014. Determining Interwell Connectivity and Reservoir Complexity Through Frac Pressure Hits and Production Interference Analysis. Presented at the SPE/CSUR Unconventional Resources Conference – Canada. Calgary, Alberta, Canada, 30 September-2 October. SPE-171628-MS. http://dx.doi.org/10.2118/171628-MS.

108. Schechter, R.S. 1992. Oil Well Stimulation. Englewood Cliffs, New Jersey: Prentice Hall.

109. Seleson , Pablo, Michael Parks. 2011. On the role of the influence function in the peridynamic theory (in 9 (6): 689-706). http://dl.begellhouse.com/journals/61fd1b191cf7e96f,5dbda3444284ba35,0a8c180d218057a 8.html.

110. Seleson, P.D., 2010. Multiscale Models for the Mechanics of Materials: Constitutive Relations, Upscaling from Atomistic Systems, and Interface Problems., The Florida State University.

111. Senseny, P.E. and Pfeifle, T.W., 1984. Fracture Toughness Of Sandstones And Shales. American Rock Mechanics Association.

112. Sesetty, V., and Ghassemi, A. 2012. Simulation of Hydraulic Fractures and their Interactions with Natural Fractures. Paper presented at 46th US Rock Mechanics / Geomechanics Symposium, Chicago, Illinois, 24-27 June.

113. Shin, D.H., and Sharma, M.M. 2014. Factors Controlling the Simultaneous Propagation of Multiple Competing Fractures in a Horizontal Well. Presented at the SPE Hydraulic

Fracturing Technology Conference, The Woodlands, Texas, 4-6 February. SPE-168599-MS. http://dx.doi.org/10.2118/168599-MS.

114. Silling, S. A., E. Askari. 2005. A meshfree method based on the peridynamic model of solid mechanics (in Computers & Structures 83 (17-18): 1526-1535.

115. Silling, S. A., M. Epton, O. Weckner et al. 2007. Peridynamic States and Constitutive Modeling (in Journal of Elasticity 88 (2): 151-184.

116. Silling, S. A., O. Weckner, E. Askari et al. 2010. Crack nucleation in a peridynamic solid (in International Journal of Fracture 162 (1-2): 219-227.

117. Silling, S.a. 2000. Reformulation of elasticity theory for discontinuities and long-range forces (in Journal of the Mechanics and Physics of Solids 48: 175-209. http://ac.els-cdn.com/S0022509699000290/1-s2.0-S0022509699000290-main.pdf?_tid=9d0c2f10-185a- 11e4-b320-00000aab0f6c&acdnat=1406773998_d2fe1d304af3415380345e6e6128211a.

118. Silling, S.a. and Bobaru, F., 2005. Peridynamic modeling of membranes and fibers. International Journal of Non-Linear Mechanics, 40: 395-409.

119. Silling, S.a., Weckner, O., Askari, E. and Bobaru, F., 2010a. Crack nucleation in a peridynamic solid. International Journal of Fracture, 162: 219-227.

120. Silling, S.A., Weckner, O., Askari, E. and Bobaru, F., 2010b. Crack nucleation in a peridynamic solid. International Journal of Fracture, 162(1-2): 219-227.

121. Singh, V., Roussel, N.P., and Sharma, M.M. 2008. Stress Reorientation and Fracture Treatments in Horizontal Wells. Presented at the SPE Annual Technical Conference and Exhibition, Denver, Colorado, 21-24 September. SPE-116092-MS. http://dx.doi.org/10.2118/116092-MS. Sneddon, I., 1946. The distribution of stress in the neighbourhood of a crack in an elastic solid. Proc., the Royal Society of London A: Mathematical, Physical and Engineering Sciences, 22 October. Vol. 187, No. 1009, pp. 229-260. http://dx.doi.org/10.1098/rspa.1946.0077.

122. Su, K., Onaisi, A., and Garnier, A. 2014. A Comprehensive Methodology of Evaluation of the Fracability of a Shale Gas Play. Presented at the 2nd Unconventional Resources Technology Conference, Denver, Colorado, 25-27 August. http://dx.doi.org/10.15530/urtec-2014- 1932416.

123. Tang, T., Hededal, O., and Cardiff, P. 2015. On finite volume method implementation of poro- elasto-plasticity soil model. 39(13):1410-1430. http://dx.doi.org/10.1002/nag.2361.

124. Thiercelin, M., Jeffrey, R.G. and Naceur, K.B., 1989. Influence of Fracture Toughness on the Geometry of Hydraulic Fractures.

125. Tran, D., Settari, A. and Nghiem, L., 2004. New Iterative Coupling Between a Reservoir Simulator and a Geomechanics Module. SPE Journal, 9: 362-369.

126. Tran, David, Antonin Settari, Long Nghiem. 2004. New Iterative Coupling Between a Reservoir Simulator and a Geomechanics Module (in SPE Journal 9: 362-369.

127. Tran, T.V., Civan, F. and Robb, I.D., 2009. Correlating flowing time and condition for perforation plugging by suspended particles. SPE Drilling & Completion, 24(03), pp.398-403. SPE- 120847-PA. http://dx.doi.org/10.2118/120847-PA.

128. Tukovic, Z., Ivankovic, A., and Karac, A. 2012. Finite-volume stress analysis in multi-material linear elastic body. Int. J. Num. Meth. Engg. 93(4):400-419. http://dx.doi.org/10.1002/nme.4390.

129. Turner, D.Z., 2012. Modeling Reactive Transport in Deformable Porous Media Using the Theory of Interacting Continua. 1-38.

130. Turner, Daniel Z. 2012. A nonlocal model for fluid-structure interaction with applications in hydraulic fracturing.

131. Ugueto, C., Gustavo, A., Huckabee, P.T. et al. 2016. Perforation Cluster Efficiency of Cemented Plug and Perf Limited Entry Completions; Insights from Fiber Optics Diagnostics. Paper SPE 179124 presented at the SPE Hydraulic Fracturing Technology Conference, the Woodlands, Texas, 9-11 February. http://dx.doi.org/10.2118/179124-MS.

132. van Eekelen, H.A.M., 1982. Hydraulic Fracture Geometry: Fracture Containment in Layered Formations.

133. Walton, I. and McLennan, J., 2013. The Role of Natural Fractures in Shale Gas Production. International Society for Rock Mechanics.

134. Warpinski, N.R., and Branagan, P.T. 1989. Altered-Stress Fracturing. J. of Pet. Technol. 41 (09): 990–997. SPE-17533-PA. http://dx.doi.org/10.2118/17533-PA.

135. Warpinski, N.R., L.W. Teufel. 1987. Influence of Geologic Discontinuities on Hydraulic Fracture Propagation (includes associated papers 17011 and 17074), in Journal of Petroleum Technology 39: 209-220.

136. Weng, X. and Siebrits, E. 2007. Effect of Production-Induced Stress Field on Refracture Propagation and Pressure Response. Paper SPE 106043 presented at the SPE Hydraulic Fracturing Technology Conference, College Station, Texas, 29-31 January. SPE-106043-MS. http://dx.doi.org/10.2118/106043-MS.

137. Weng, X., Kresse, O., Cohen, C.E., et al. 2011. Modeling of Hydraulic Fracture Network Propagation in a Naturally Fractured Formation. SPE Prod. & Oper. 26 (4): 368-380. SPE-140253-PA. http://dx.doi.org/10.2118/140253-PA.

138. Wheaton, B., Haustveit, K., Deeg, W. et al. 2016. A Case Study of Completion Effectiveness in the Eagle Ford Shale Using DAS/DTS Observations and Hydraulic Fracture Modeling. Paper SPE 179149 presented at the SPE Hydraulic Fracturing Technology Conference, the Woodlands, Texas, 9-11 February. http://dx.doi.org/10.2118/179149-MS.

139. Wheaton, B., Haustveit, K., Deeg, W. et al. 2016. A Case Study of Completion Effectiveness in the Eagle Ford Shale Using DAS/DTS Observations and Hydraulic Fracture Modeling. Paper SPE 179149 presented at the SPE Hydraulic Fracturing Technology Conference, the Woodlands, Texas, 9-11 February. http://dx.doi.org/10.2118/179149-MS.

140. Willenbring, James M., Michael Allen Heroux. 2003. Trilinos users guide. Report No.

SAND2003-2952; TRN: US200818%%226 United States10.2172/918334TRN: US200818%%226Thu Oct 02 07:27:31 EDT 2008SNLEnglish.

141. Wong, S.-W., Geilikman, M., and Xu, G. 2013. Interaction of Multiple Hydraulic Fractures in Horizontal Wells. Presented at the SPE Unconventional Gas Conference and Exhibition. SPE- 163982-MS. http://dx.doi.org/10.2118/163982-MS.

142. Wu C.-H., Sharma, M.M. 2016. Effect of Perforation Geometry and Orientation on Proppant Placement in Perforation Clusters in a Horizontal Well. Paper SPE 179117 presented at the SPE Hydraulic Fracturing Technology Conference, The Woodlands, Texas, USA, 9-11 February 2016. http://dx.doi.org/10.2118/179117-MS.

143. Wu, C-H., Yi, S., & Sharma, M.M. 2017. Proppant Distribution Among Multiple Perforation Clusters in a Horizontal Wellbore. Paper 184861 presented at the SPE Hydraulic Fracturing Technology Conference and Exhibition, 24–26 January, The Woodlands, Texas, USA. http://dx.doi.org/10.2118/184861-MS.

144. Wu, H., Chudnovsky, A., Dudley, J.W. and Wong, G.K., 2004. A Map Of Fracture Behavior In The Vicinity Of An Interface. American Rock Mechanics Association.

145. Wu, K., and Olson, J. 2013. Investigation of the Impact of Fracture Spacing and Fluid Properties for Interfering Simultaneously or Sequentially Generated Hydraulic Fractures. SPE Prod. & Oper. 28 (4): 4–6. SPE-163821-PA. http://dx.doi.org/10.2118/163821-PA.

146. Wu, K., and Olson, J.E. 2015. Simultaneous Multifracture Treatments: Fully Coupled Fluid Flow and Fracture Mechanics for Horizontal Wells. SPE J. 20 (02): 337–346. SPE-167626-PA. http://dx.doi.org/10.2118/167626-PA.

147. Xu, J., Askari, A., Weckner, O., Razi, H. and Silling, S., 2007. Damage and Failure Analysis of Composite Laminates under Biaxial Loads, 48th AIAA/ASME/ASCE/AHS/ASC Structures, Structural Dynamics, and Materials Conference. American Institute of Aeronautics and Astronautics, Reston, Virigina, pp. 1-9.

148. Xu, Jifeng, Abe Askari, Olaf Weckner et al. 2007. Damage and Failure Analysis of Composite Laminates under Biaxial Loads. Reston, Virigina: 48th AIAA/ASME/ASCE/AHS/ASC.

149. Structures, Structural Dynamics, and Materials Conference, American Institute of Aeronautics and Astronautics (Reprint). http://arc.aiaa.org/doi/pdfplus/10.2514/6.2007-2315.

150. Yamamoto, K., T. Shimamoto, and S. Sukemura. 2004. Multiple Fracture Propagation Model for a Three-Dimensional Hydraulic Fracturing Simulator. Int. J. Geomech. 4 (1): 46–57. http://dx.doi.org/10.1061/(ASCE)1532-3641(2004)4:1(46).

151. Yi, S. and Sharma, M., 2016. A Model for Refracturing Operations in Horizontal Wells Employing Diverting Agents. Paper SPE 181795 presented at the SPE Asia Pacific Hydraulic Fracturing Conference, Beijing, China, 24-26 August. http://dx.doi.org/10.2118/181795-MS.

152. Zhang, X., Jeffrey, R.G. and Thiercelin, M., 2007. Deflection and propagation of fluid-

driven fractures at frictional bedding interfaces: A numerical investigation. Journal of Structural Geology, 29(3): 396-410.

153. Zhao, X. P., RP Young. 2009. Numerical Simulation of Seismicity Induced by Hydraulic Fracturing in Naturally Fractured Reservoirs: SPE Annual Technical Conference and Exhibition, Society of Petroleum Engineers (Reprint).

154. Zhou, Jian, Mian Chen, Yan Jin et al. 2008. Analysis of fracture propagation behavior and fracture geometry using a tri-axial fracturing system in naturally fractured reservoirs (in International Journal of Rock Mechanics and Mining Sciences 45 (7): 1143-1152.